Handbook of Nanostructured Materials and Nanotechnology

3

Electrical Properties



Edited by Hari Singh Nalwa

Foreword by George A. Olah, Nobel Laureate

ACADEMIC PRESS

Handbook of Nanostructured Materials and Nanotechnology

This Page Intentionally Left Blank

Handbook of Nanostructured Materials and Nanotechnology

Volume 3

Electrical Properties

Edited by

Hari Singh Nalwa, M.Sc., Ph.D.
Hitachi Research Laboratory
Hitachi Ltd., Ibaraki, Japan



ACADEMIC PRESS

A Harcourt Science and Technology Company

San Diego San Francisco New York Boston
London Sydney Tokyo

The images for the cover of this book were reprinted with generous permission from:

(Top left) R.P. Andres, J.D. Bielefeld, J.I. Henderson, D.B. Janes, V.R. Kolagunta, C.P. Kubiak, W. Mahoney, and R.G. Osifchin, *Science* 273, 1690 (1996). Copyright 1996 American Association for the Advancement of Science.

(Top right) Bruce Godfrey, Volume 5, Chapter 12 in this series.

(Middle left) M.R. Sorensen, K.W. Jacobsen, and P. Stoltze, *Phys. Rev. B* 53, 2101–2113 (1996).

(Middle right) T.W. Ebbesen et al., *Nature* 382, 54 (1996) copyright 1996 Macmillan Magazines Ltd.

(Bottom left) R.H. Jin, T. Aida, and S. Inoue, *J. Chem. Soc., Chem. Commun.*, 1260 (1993). Copyright by The Royal Society of Chemistry.

(Bottom right) NANO*SENSORS*.

This book is printed on acid-free paper. ♾

Copyright © 2000 by Academic Press

All rights reserved.
No part of this publication may be reproduced or transmitted in any form or by any means, electronic or mechanical, including photocopy, recording, or any information storage and retrieval system, without permission in writing from the publisher.

The appearance of the code at the bottom of the first page of a chapter in this book indicates the Publisher's consent that copies of the chapter may be made for personal or internal use of specific clients. This consent is given on the condition, however, that the copier pay the stated per-copy fee through the Copyright Clearance Center, Inc. (222 Rosewood Drive, Danvers, Massachusetts 01923), for copying beyond that permitted by Sections 107 or 108 of the U.S. Copyright Law. This consent does not extend to other kinds of copying, such as copying for general distribution, for advertising or promotional purposes, for creating new collective works, or for resale. Copy fees for pre-2000 chapters are as shown on the title pages; if no fee code appears on the title page, the copy fee is the same as for current chapters. $30.00.

The information provided in this handbook is compiled from reliable sources but the authors, editor, and the publisher cannot assume any responsibility whatsoever for the validity of all statements, illustrations, data, procedures, and other related materials contained herein or for the consequence of their use.

ACADEMIC PRESS
A Harcourt Science and Technology Company
525 B Street, Suite 1900, San Diego, CA 92101-4495, USA
http://www.apnet.com

Academic Press
24–28 Oval Road, London NW1 7DX, UK
http://www.hbuk.co.uk/ap/

Library of Congress Cataloging-in-Publication Data
Nalwa, Hari Singh, 1954–
Handbook of nanostructured materials and nanotechnology / Hari Singh Nalwa.
p. cm.
Includes indexes.

ISBN 0-12-513760-5
1. Nanostructured materials. 2. Nanotechnology. I. Title.
TA418.9.N35 N32
620′.5–dc21

98-43220
CIP

International Standard Book Number: 0-12-513763-X

Printed in the United States of America
99 00 01 02 03 MB 9 8 7 6 5 4 3 2 1

To my children,
Surya, Ravina and Eric

This Page Intentionally Left Blank

Foreword

Nanostructured materials are becoming of major significance and the technology of their production and use is rapidly growing into a powerful industry. These fascinating materials whose dimension range for 1–100 nanometer (1 nm $= 10^{-9}$ m, i.e., one billionth of a meter) include quantum dots, wires, nanotubes, nanorods, nanofilms, nanoprecision self assemblies and thin films, nanosize metals, semiconductors, biomaterials, oligomers, polymers, functional devices, etc. etc. It is clear that the number and significance of new nanomaterials and application will grow explosively in the coming twenty-first century.

This dynamical fascinating new field of science and its derived technology clearly warranted a comprehensive treatment. Dr. Hari Singh Nalwa must be congratulated to have undertaken the task to organize and edit such a massive endeavor. His effort resulted in a truly impressive and monumental work of fine volumes on nanostructured materials covering synthesis and processing, spectroscopy and theory, electrical properties, and optical properties, as well as organics, polymers, and biological materials. One hundred forty-two authors from 16 different countries contributed 62 chapters encompassing the fundamental compendium. It is the merit of these authors, their contributions coordinated most knowledgeably and skillfully by the editor, that the emerging science and technology of nanostructured materials is enriched by such an excellent and comprehensive core-work, which will be used for many years to come by all practitioners of the field, but also will inspire many others to join in expanding its vistas and application.

Professor George A. Olah
University of Southern California
Los Angeles, USA
Nobel Laureate Chemistry, 1994

This Page Intentionally Left Blank

Preface

Nanotechnology is the science and engineering of making materials, functional structures and devices on the order of a nanometer scale. In scientific terms, "Nano" means 10^{-9} where 1 nanometer is equivalent to one thousandth of a micrometer, one millionth of a millimeter, and one billionth of a meter. In Greek, "nanotechnology" derives from the *nanos* which means dwarf and *technologia* means systematic treatment of an art or craft. Nanostructured inorganic, organic, and biological materials may have existed in nature since the evolution of life started on Earth. Some evident examples are micro-organisms, fine-grained minerals in rocks, and nanosize particles in bacterias and smoke. From a biological viewpoint, the DNA double-helix has a diameter of about 2 nm (20 angstrom) while ribosomes have a diameter of 25 nm. Atoms have a size of 1-4 angstrom, therefore nanostructured materials could hold tens of thousands of atoms all together. Moving to a micrometer scale, the diameter of a human hair is 50-100 μm. Advancements in microscopy technology have made it possible to visualize images of nanostructures and have largely dictated the development of nanotechnology. Manmade nanostructured materials are of recent origin whose domain sizes have been precision engineered at an atomic level simply by controlling the size of constituent grains or building blocks. About 40 years ago, the concept of atomic precision was first suggested by Physics Nobel Laureate Richard P. Feynman in a 1959 speech at the California Institute of Technology where he stated, "*The principles of physics, as far as I can see, do not speak against the possibility of maneuvering things atom by atom . . .*". Research on nanostructured materials began about two decades ago but did not gain much impetus until the late 1990s. Nanotechnology has become a very active and vital area of research which is rapidly developing in industrial sectors and spreading to almost every field of science and engineering. There are several major research and development government programs on nanostructured materials and nanotechnology in the United States, Europe, and Japan. This field of research has become of great scientific and commercial interest because of its rapid expansion to academic institutes, governmental laboratories, and industries. By the turn of this century, nanotechnology is expected to grow to a multibillion-dollar industry and will become the most dominant technology of the twenty-first century.

In this handbook, nanostructures loosely define particles, grains, functional structures, and devices with dimensions in the 1-100 nanometer range. Nanostructures include quantum dots, quantum wires, grains, particles, nanotubes, nanorods, nanofibers, nanofoams, nanocrystals, nanoprecision self-assemblies and thin films , metals, intermetallics, semiconductors, minerals, ferroelectrics, dielectrics, composites, alloys, blends, organics, organominerals, biomaterials, biomolecules, oligomers, polymers, functional structures, and devices. The fundamental physical and biological properties of materials are remarkably altered as the size of their constituent grains decreases to a nanometer scale. These novel materials made of nanosized grains or building blocks offer unique and entirely different electrical, optical, mechanical, and magnetic properties compared with conventional micro or millimeter-size materials owing to their distinctive size, shape, surface chemistry, and topology. On the other hand, organics offer tremendous possibilities of chemical modification by tethering with functional groups to enhance their responses. Nanometer-sized organic materials such as molecular wires, nanofoams, nanocrystals, and dendritic molecules have been synthesized which display unique properties compared with their counterpart conventionally sized materials. An abundance of scientific data is now available to make useful comparisons between nanosize materials and their counterpart microscale or bulk materials. For example, the hardness of nanocrystalline copper increases with decreasing grain size and 6 nm copper grains show five times hardness than the conventional copper. Cadmium selenide (CdSe) can yield any color in the spectrum simply by controlling the size of its constituent grains. There are many such examples in the literature where physi-

cal properties have been remarkably improved through nanostrucure maneuvering. Nanostructured materials and their base technologies have opened up exciting new possibilities for future applications in aerospace, automotive, cutting tools, coatings, X-ray technology, catalysts, batteries, nonvolatile memories, sensors, insulators, color imaging, printing, flat-panel displays, waveguides, modulators, computer chips, magneto-optic disks, transducers, photodetectors, optoelectronics, solar cells, lithography, holography, photoemitters, molecular-sized transistors and switches, drug delivery, medicine, medical implants, pharmacy, cosmetics, etc. Apparently, a new vision of molecular nanotechnology will develop in coming years and the twenty-first century could see technological breakthroughs in creating materials atom by atom where new inventions will have intense and widespread impact in many fields of science and engineering.

Over the past decade, extraordinary progress has been made on nanostructured materials and a dramatic increase in research activities in many different fields has created a need for a reference work on this subject. When I first thought of editing this handbook, I envisaged a reference work covering all aspects of nanometer scale science and technology dealing with synthesis, nanofabrication, processing, supramolecular chemistry, protein engineering, biotechnology, spectroscopy, theory, electronics, photonics, and other physical properties as well as devices. To achieve this interface, researchers from different disciplines of science and engineering were brought together to share their knowledge and expertise. This handbook, written by leading international experts from academia, industries, and governmental laboratories, consists of 62 chapters written by 142 authors coming from 16 different countries. It will provide the most comprehensive coverage of the whole field of nanostructured materials and nanotechnology by compiling up-to-date data and information.

Each chapter in this handbook is self-contained with cross references. Some overlap may inevitably exist in a few chapters, but it was kept to a minimum. It was rather difficult to scale the overlap that is usual for state-of-the-art reviews written by different authors. This handbook illustrates in a very clear and concise fashion the structure-property relationship to understand a broader range of nanostructured materials with exciting potential for future electronic, photonic, and biotechnology industries. It is aimed to bring together in a single reference all inorganic, organic, and biological nanostructured materials currently studied in academic and industrial research by covering all aspects from their chemistry, physics, materials science, engineering, biology, processing, spectroscopy, and technology to applications that draw on the past decade of pioneering research on nanostructured materials for the first time to offer a complete perspective on the topic. This handbook should serve as a reference source to nanostructured materials and nanotechnology. With over 10,300 bibliographic citations, the cutting edge state-of-the art review chapters containing the latest research in this field is presented in five volumes:

Volume 1: Synthesis and Processing
Volume 2: Spectroscopy and Theory
Volume 3: Electrical Properties
Volume 4: Optical Properties
Volume 5: Organics, Polymers, and Biological Materials

Volume 1 contains 13 chapters on the recent developments in synthesis, processing and fabrication of nanostructured materials. The topics include: chemical synthesis of nanostructured metals, metals alloys and semiconductors, synthesis of nanostructured coatings by high velocity oxygen fuel thermal spraying, nanoparticles from low-pressure and low-temperature plasma, low temperature compaction of nanosize powders, kinetic control of inorganic solid state reactions resulting from mechanistic studies using elementally modulated reactants, strained-layer heteroepitaxy to fabricate self-assembled semiconductor islands, nanofabrication via atom optics, preparation of nanocomposites by sol-gel methods: processing of semiconductors quantum dots, chemical preparation and characteriza-

tion of nanocrystalline materials, rapid solidification processing of nanocrystalline metallic alloys, vapor processing of nanostructured materials and applications of micromachining to nanotechnology. The contents of this volume will be useful for researchers particularly involved in synthesis and processing of nanostructured materials.

Volume 2 contains 15 chapters dealing with spectroscopy and theoretical aspects of nanostructured materials. The topics covered include: nanodiffraction, FT-IR surface spectrometry of nanosized particles, specification of microstructure and characterization by scattering techniques, vibrational spectroscopy of mesoscopic systems, advanced interfaces to scanning-probe microscopes, microwave spectroscopy on quantum dots, tribological experiments with friction force microscopy, electron microscopy techniques applied to study of nanostructured ancient materials, mesoscopic magnetism in metals, tools of nanotechnology, and nanometrology. The last five chapters in this volume describe computational technology associated with the stimulation and modeling of nanostructures. The topics covered are tunneling times in nanostructures, theory of atomic-scale friction, theoretical aspects of strained-layer quantum-well lasers, carbon nanotube-based nanotechnology in an integrated modeling and stimulation environment, and wavefunction engineering: a new paradigm in quantum nanostructure modeling.

Volume 3 has 11 chapters which exclusively focus on the electrical properties of nanostructured materials. The topics covered are: electron transport and confining potentials in semiconductor nanostructures, electronic transport properties of quantum dots, electrical properties of chemically tailored nanoparticles and their applications in microelectronics, design, fabrication and electronic properties of self-assembled molecular nanostructures, silicon-based nanostructures, semiconductor nanoparticles, hybrid magnetic-semiconductor nanostructures, colloidal quantum dots of III-V semiconductors, quantization and confinement phenomena in nanostructured superconductors, properties and applications of nanocrystalline electronic junctions, and nanostructured fabrication using electron beam and its applications to nanometer devices.

Volume 4 contains 10 chapters dealing with different optical properties of nanostructured materials. The topics include: photorefractive semiconductor nanostructures, metal nanocluster composite glasses, porous silicon, 3-dimension lattices of nanostructures, fluorescence, thermoluminescence and photostimulated luminescence of nanoparticles, surface-enhanced optical phenomena in nanostructured fractal materials, linear and nonlinear optical spectroscopy of semiconductor nanocrystals, nonlinear optical properties of nanostructures, quantum-well infrared photodetectors and nanoscopic optical sensors and probes. The electronic and photonic applications of nanostructured materials are also discussed in several chapters in Volumes 3 and 4.

All nanostructured organic molecules, polymers, and biological materials are summarized in Volume 5. This volume has 13 chapters that include: Intercalation compounds in layered host lattices-supramolecular chemistry in nanodimensions, transition-metal-mediated self-assembly of discrete nanoscopic species with well-defined shapes and geometries, molecular and supramolecular nanomachines, functional nanostructures incorporating responsive modules, dendritic molecules: historical developments and future applications, carbon nanotubes, encapsulation and crystallization behavior of materials inside carbon nanotubes, fabrication and spectroscopic characterization of organic nanocrystals, polymeric nanostructures, conducting polymers as organic nanometals, biopolymers and polymers nanoparticles and their biomedical applications, and structure, behavior and manipulation of nanoscale biological assemblies and biomimetic thin films.

It is my hope that *Handbook of Nanostructured Materials and Nanotechnology* will become an invaluable source of essential information for academic, industrial, and governmental researchers working in chemistry, semiconductor physics, materials science, electrical engineering, polymer science, surface science, surface microscopy, aerosol science, spectroscopy, crystallography, microelectronics, electrochemistry, biology, microbiology,

bioengineering, pharmacy, medicine, biotechnology, geology, xerography, superconductivity, electronics, photonics, device engineering and computational engineering.

I take this opportunity to thank all publishers and authors for granting us copyright permissions to use their illustrations for the handbook. The following publishers kindly provided us permissions to reproduce originally published materials: Academic Press, American Association for the Advancement of Science, American Ceramic Society, American Chemical Society, American Institute of Physics, CRC Press-LLC, Chapman & Hall, Electrochemical Society, Elsevier Science Ltd., Huthig-fachverlag, IBM, Institute of Physics (IOP) Publishing Ltd., IEEE Industry Applications Association, Japan Society of Applied Physics, Jai Press, John Wiley & Sons, Kluwer Academic Publishers, Materials Research Society, Macmillan Magazines Ltd., North-Holland, Pergamon Press, Plenum, Physical Society of Japan, Optical Society of America, Springer Verlag, Steinkopff Publishers, Technomic Publishing Co. Inc., The American Physical Society, The Mineral, Metal, and Materials Society, The Materials Information Society, The Royal Society of Chemistry, Vacuum Society of America, VSP, Wiley-Liss Inc., Wiley-VCH Verlag, World Scientific.

This handbook could not have reached fruition without the marvelous cooperation of many distinguished individuals who contributed to these volumes. I am fortunate to have leading experts devote their valuable time and effort to write excellent state-of-the-art reviews which led foundation of this handbook. I deeply express my thanks to all contributors. I am very grateful to Dr. Akio Mukoh and Dr. Shuuichi Oohara at Hitachi Research Laboratory, Hitachi Ltd., for their kind support and encouragement. I would like to give my special thanks to Professor Seizo Miyata of the Tokyo University of Agriculture and Technology (Japan), Professor J. Schoonman of the Delft University of Technology (The Netherlands), Professor Hachiro Nakanishi of the Tohoku University (Japan), Professor G. K. Surya Prakash of the University of Southern California (USA), Professor Padma Vasudevan of Indian Institute of Technology at New Delhi, Professor Toskiyuki Watanabe, Professor Richard T. Keys, Dr. Christine Peterson, and Dr. Judy Hill of Foresight Institute in California, Rakesh Misra, Krishi Pal Reghuvanshi, Rajendra Bhargava, Jagmer Singh, Ranvir Singh Chaudhary, Dr. Hans Thomann, Dr. Ho Kim, Dr. Thomas Pang, Ajit Kelkar, K. Srinivas, and other colleagues who supported my efforts in compiling this handbook. Finally, I owe my deepest appreciation to my wife, Dr. Beena Singh Nalwa, for her cooperation and patience in enduring this work at home; I thank my parents, Sri Kadam Singh and Srimati Sukh Devi, for their moral support; and I thank my children, Surya, Ravina, and Eric, for their love.

I express my sincere gratitude to Professor George A. Olah for his insightful Foreword.

Hari Singh Nalwa

Contents

About the Editor xxi
List of Contributors xxiii

Chapter 1. ELECTRON TRANSPORT AND CONFINING POTENTIALS IN SEMICONDUCTOR NANOSTRUCTURES

J. Smoliner, G. Ploner

1. Introduction 1
   1.1. Aim of This Review 2
2. Quantized States in Low-Dimensional Systems 4
   2.1. Electrons in One-Dimensional Potentials 5
   2.2. Parabolic Confinement 6
3. Basic Methods for Self-Consistent Calculations in One and Two Dimensions . 8
   3.1. Self-Consistent Treatment of One-Dimensional Problems 9
   3.2. Self-Consistent Calculations in Two Dimensions 13
   3.3. Three-Dimensional Modeling of Quantum Dots 19
4. Transport Spectroscopy of Quantum Wires 20
   4.1. Magnetic Depopulation Experiments 21
   4.2. Magnetosize Effects and Weak Localization in Quantum Wires . . . 25
   4.3. Magnetophonon Resonances in Quantum Wires 31
5. Weakly and Strongly Modulated Systems 41
6. Vertical Tunneling through Quantum Wires 48
   6.1. Experimental 48
   6.2. Transfer Hamiltonian Formalism 53
   6.3. Influence of the Potential Profile on Two-Dimensional–One-Dimensional Tunneling Processes 56
7. Vertical Transport Through Quantum Dots 68
   7.1. First Experiments 68
   7.2. Lateral and Vertical Transport through Quantum Dots: Coulomb Blockade Effects 71
   7.3. Tunneling via Zero-Dimensional Donor States 77
   7.4. Zero-Dimensional–Two-Dimensional Tunneling 82

Acknowledgments 86
References 86

Chapter 2. ELECTRONIC TRANSPORT PROPERTIES OF QUANTUM DOTS

M. A. Reed, J. W. Sleight, M. R. Deshpande

1. Introduction 93
   1.1. Fabricated Quantum Dots: Vertical and Horizontal Systems 93
   1.2. Impurity Dot System: Coulomb Potential Confinement 95
2. Theory 96
   2.1. Energy States of a Fabricated Quantum Dot 96
   2.2. Energy States of the Impurity Dot 97
   2.3. Current–Voltage Characteristics of Vertical Dot: Fabricated and Impurity Systems 100
3. Sample Growth and Fabrication 101
4. Experimental Results 101
   4.1. Current–Voltage Characteristics 101

4.2. Variable-Temperature Measurements . . . 103
4.3. Magnetotunneling Measurements: Diamagnetic Shifts and Current Suppression . . . 106
4.4. Magnetotunneling Measurements: Fine Structure . . . 113
4.5. Magnetotunneling Measurements: Spin Splitting and g^* Factor . . . 117
4.6. Magnetotunneling Measurements: Electron Tunneling Rates . . . 121
5. Conclusions . . . 128
Acknowledgments . . . 129
References . . . 129

Chapter 3. ELECTRICAL PROPERTIES OF CHEMICALLY TAILORED NANOPARTICLES AND THEIR APPLICATION IN MICROELECTRONICS

U. Simon, G. Schön

1. Introduction . . . 131
1.1. Physical Background . . . 132
2. Preparation Techniques and Classification of Chemically Tailored Nanoparticles . . . 139
2.1. Ligand-Stabilized Nanoparticles . . . 139
2.2. Nanoparticles in Block Copolymers . . . 141
2.3. Host/Guest Composites . . . 142
2.4. Electrochemical Composition of Nanoparticles . . . 143
3. Arrangements and Deposition Techniques . . . 143
3.1. Three-Dimensional Arrangements . . . 144
3.2. Two-Dimensional Arrangements . . . 145
3.3. One-Dimensional Arrangements . . . 149
4. Electrical Properties of Zero- to Three-Dimensional Arrangements of Nanoparticles . . . 154
4.1. Single-Particle Properties . . . 154
4.2. One-Dimensional Arrangements . . . 158
4.3. Two-Dimensional Arrangements . . . 159
4.4. Three-Dimensional Arrangements . . . 162
5. Working Principles of Single-Electron Tunneling Devices and the Use of Chemically Built Nanoparticles . . . 165
5.1. Single-Electron Tunneling Devices and Circuits . . . 165
5.2. Metal Nanoparticles as Elements for Single-Electron Devices . . . 169
5.3. Time Scales of Recharging, Charge Relaxation, and Tunneling . . . 172
6. Applications and Concluding Remarks . . . 174
Acknowledgments . . . 175
References . . . 175

Chapter 4. THE DESIGN, FABRICATION, AND ELECTRONIC PROPERTIES OF SELF-ASSEMBLED MOLECULAR NANOSTRUCTURES

R. P. Andres, S. Datta, D. B. Janes, C. P. Kubiak, R. Reifenberger

1. Introduction . . . 180
2. Molecular Wire Synthesis . . . 181
2.1. Overview . . . 181
2.2. Recent Advances in the Synthesis of Molecular Wires . . . 181
2.3. The Chemistry of Self-Assembled Monolayers . . . 184
2.4. Chemical Self-Assembly of Aryl Dithiol Monolayers on Gold . . . 185
2.5. Self-Assembly of "Chemically Sticky" Surfaces . . . 189
2.6. Concluding Remarks . . . 189

3. Metal Cluster Synthesis 189
3.1. Overview 189
3.2. Gas Phase Synthesis 190
3.3. Capture of Clusters as Bare Metal Particles 193
3.4. Capture of Clusters as Colloidal Particles 193
3.5. Precipitation of Colloidal Networks from Solution 194
3.6. Formation of an Unlinked Cluster Array 195
3.7. Formation of a Linked Cluster Network 197
3.8. Concluding Remarks 199
4. Theory of Electronic Conduction through Organic Molecules 200
4.1. Overview 200
4.2. Theoretical Model 200
4.3. Factors Affecting the Current–Voltage Characteristics 203
4.4. Concluding Remarks 206
5. Electronic Properties of Molecular Nanostructures 207
5.1. Overview 207
5.2. Experimental Considerations 207
5.3. Electronic Properties of Individual Molecules 209
5.4. Electronic Conduction through Supported Clusters 209
5.5. Electronic Properties of Encapsulated Gold Clusters 211
5.6. Electronic Properties of Tethered Gold Clusters 212
5.7. Estimating the Electrical Resistance of a Molecule 215
5.8. Concluding Remarks 216
6. Electronic Properties of Cluster Arrays and Networks 216
6.1. Overview 216
6.2. Sample Preparation 217
6.3. Electrical Measurements 220
6.4. Conduction Model 221
6.5. Concluding Remarks 224
7. Summary 225
Acknowledgments 226
References 226

Chapter 5. SILICON-BASED NANOSTRUCTURES

Tamim P. Sidiki, Clivia M. Sotomayor Torres

1. Introduction 233
2. Optical Properties of Silicon and Related Materials 235
2.1. General Remarks 235
2.2. Group IV Heterostructures: Electronic Zone Folding 236
2.3. The Direct-Gap Material $FeSi_2$ as a Silicon-Based Light Emitter . . . 238
2.4. Erbium-Doped Silicon Light Emitters 240
3. Quantum Confinement 242
3.1. Two-, One-, and Zero-Dimensional Confinement 242
3.2. Si–SiGe Quantum Wells 244
3.3. Porous Silicon 246
3.4. Postgrowth Nanofabrication by Lithography and Etching 249
3.5. Self-Organized Growth 258
3.6. Selective Epitaxial Growth 262
3.7. V-Groove Growth 265
3.8. Local Growth of Dots and Wires through Shadow Masks 266
3.9. Silicon Nanocrystallites 270
3.10. Si/III–V Light-Emitting Nanotips 275
4. Single-Electron Electronics 278

5. Tips for Atomic Force Microscopy and Field Emission 282
6. Conclusions 284
Acknowledgments 284
References 285

Chapter 6. SEMICONDUCTOR NANOPARTICLES

Prashant V. Kamat, Kei Murakoshi, Yuji Wada, Shizo Yanagida

1. Introduction 292
2. Preparation and Characterization 293
   2.1. Size Control 293
   2.2. Crystalline Phase Control 294
   2.3. Size Quantization Effects 296
   2.4. Nonlinear Optical Properties 297
   2.5. Emission Characteristics 297
   2.6. Trapping of Charge Carriers 298
3. Interfacial Charge Transfer Processes in Colloidal Semiconductor Systems . . 299
   3.1. Reductive Process 300
   3.2. Oxidative Process 300
   3.3. Kinetics of Interfacial Electron Transfer 301
4. Photocatalytic Applications 303
   4.1. Organic Synthesis 304
   4.2. Fixation of Carbon Dioxide into Organic Compounds 304
   4.3. Reduction of Dinitrogen 308
   4.4. Decomposition of Nitrogen Oxides and Their Anions 308
   4.5. Photocatalytic Degradation of Organic Contaminants 308
5. Surface Modification of Semiconductor Colloids 309
   5.1. Deposition of Metals on Semiconductors 309
   5.2. Capping with Organic and Inorganic Molecules 310
   5.3. Surface Modification with Sensitizing Dyes 312
   5.4. Ultrafast Charge Injection into Semiconductor Nanocrystallites . . . 314
   5.5. Designing Multicomponent Semiconductor Systems 315
6. Ordered Nanostructures using Semiconductor Nanocrystallites and Their Functionality 318
   6.1. Preparation and Characterization of Nanostructured Semiconductor Films 319
   6.2. Electron Storage and Photo- and Electrochromic Effects 322
   6.3. As a Photosensitive Electrode 323
   6.4. Sensitization of Large-Band-Gap Semiconductors 325
   6.5. Single-Electron Tunneling Devices 327
7. Concluding Remarks 329
Acknowledgments 329
References 329

Chapter 7. HYBRID MAGNETIC–SEMICONDUCTOR NANOSTRUCTURES

François M. Peeters, Jo De Boeck

1. Introduction 346
2. Electrons in Microscopically Inhomogeneous Magnetic Fields 347
3. Magnetic Field Profiles 348
   3.1. One-Dimensional Profiles 348
   3.2. Periodic Structures 351

4. Quantum Motion in Nonhomogeneous Magnetic Fields 353
4.1. Magnetic Step 354
4.2. Magnetic Barrier 356
4.3. Magnetic Quantum Well 359
4.4. Resonant Tunneling Structures 361
4.5. Magnetic Dot 363
5. Diffusive Transport of Electrons through Magnetic Barriers 366
5.1. Theoretical Formalism 367
5.2. Single Magnetic Barrier 368
5.3. Magnetic Barriers in Series 370
6. One-Dimensional Magnetic Modulation 371
6.1. Weak Magnetic Modulation 372
6.2. Electric and Magnetic Modulations 377
6.3. Magnetic Minibands 380
7. Two-Dimensional Magnetic Modulation 386
7.1. Periodic Two-Dimensional Modulation 386
7.2. A Random Array of Identical Magnetic Disks 387
7.3. Random Magnetic Fields 388
8. Hall Effect Devices 390
8.1. Ballistic Hall Magnetometry 391
8.2. Hall Magnetometry in the Diffusive Regime 395
8.3. Hybrid Hall Effect Device 399
9. Nonpolarized Current Injection from Semiconductor into Ferromagnets . . . 403
10. Spin Injection Ferromagnetic/Semiconductor Structures 404
10.1. Spin-Polarized Electronic Current from Ferromagnets 404
10.2. Optical Detection of Spin-Polarized Tunnel Current 404
10.3. Spin-Polarized Electronic (Tunnel) Current from Optically Pumped Semiconductors 405
10.4. Spin-Polarized Current from Magnetic Contacts to Semiconductors . 406
11. Ferromagnetic/Semiconductor Experimental Structures 408
11.1. The Need for Epitaxy 408
11.2. General Metal Epitaxy Criteria 409
11.3. Elemental Ferromagnetic Metal Epitaxy on Semiconductors 410
11.4. Magnetic and Electrical Properties of Ferromagnets at the Ferromagnetic/Semiconductor Interfaces 411
11.5. Properties of Manganese-Based Epitaxial Magnetic Layers on III–V Semiconductors 412
11.6. Semiconductor/Ferromagnetic/Semiconductor Multilayers 413
12. Nanoscale Magnets 414
12.1. Introduction 414
12.2. Self-Organized Magnetic Nanostructures in Semiconductor Thin Films 414
12.3. Experimental Conditions for Thin Films with Nanoclusters by Molecular Beam Epitaxy + Annealing 415
13. Superlattices of Nanoscale Magnet Layers and Semiconductors 418
13.1. Engineering Aspects of Superlattices of Nanoscale Magnet Layers and Semiconductors 418
13.2. Structural and Magnetic Properties of the Superlattices 418
13.3. Current Perpendicular to the Plane Magnetotransport 418
13.4. Conclusions 419
Acknowledgments 420
References 420

Chapter 8. COLLOIDAL QUANTUM DOTS OF III–V SEMICONDUCTORS

Olga I. Mićić, Arthur J. Nozik

1. Introduction . . . 427
2. Synthesis of Colloidal Quantum Dots . . . 429
   - 2.1. Synthesis of Colloidal InP Quantum Dots . . . 430
   - 2.2. Etching of Colloidal InP Quantum Dots with HF . . . 431
   - 2.3. Synthesis of Colloidal GaP Quantum Dots . . . 431
   - 2.4. Synthesis of Colloidal $GaInP_2$ Quantum Dots . . . 431
3. Properties of III–V Quantum Dots . . . 432
   - 3.1. InP Quantum Dots . . . 432
   - 3.2. GaP Quantum Dots . . . 442
   - 3.3. $GaInP_2$ Quantum Dots . . . 444
   - 3.4. GaAs Quantum Dots . . . 446
4. Summary . . . 447

Acknowledgment . . . 447

References . . . 447

Chapter 9. QUANTIZATION AND CONFINEMENT PHENOMENA IN NANOSTRUCTURED SUPERCONDUCTORS

V. V. Moshchalkov, V. Bruyndoncx, L. Van Look, M. J. Van Bael, Y. Bruynseraede, A. Tonomura

1. Introduction . . . 452
   - 1.1. Quantization and Confinement . . . 452
   - 1.2. Nanostructuring . . . 452
   - 1.3. Confining the Superconducting Condensate . . . 454
   - 1.4. Vortex Lattice in a Type II Superconductor . . . 457
2. Individual Nanostructures . . . 464
   - 2.1. Line . . . 464
   - 2.2. Loop . . . 465
   - 2.3. Dot . . . 468
3. Clusters of Loops and Antidots . . . 473
   - 3.1. One-Dimensional Clusters of Loops . . . 473
   - 3.2. Two-Dimensional Clusters of Antidots . . . 477
4. Huge Arrays of Nanoscopic Plaquettes in Laterally Nanostructured Superconductors . . . 479
   - 4.1. The $T_c(H)$ Phase Boundary of Superconducting Films with an Antidot Lattice . . . 480
   - 4.2. Pinning in Laterally Nanostructured Superconductors . . . 482
   - 4.3. Regular Pinning Arrays with $n_s = 1$ . . . 485
   - 4.4. Multiquanta Vortex Lattices ($n_s > 1$) . . . 505
   - 4.5. Crossover from a Pinning Array to a Network ($n_s \gg 1$) . . . 517
5. Conclusions . . . 520

Acknowledgments . . . 521

References . . . 522

Chapter 10. PROPERTIES AND APPLICATIONS OF NANOCRYSTALLINE ELECTRONIC JUNCTIONS

Michael Grätzel

1. General Properties of Nanocrystalline Semiconductor Junctions . . . 527
2. Majority Carrier Injection Devices . . . 531

2.1. Electrochromic Displays . . . 531
2.2. Cross-Surface Electron Transfer on Nanocrystalline Oxide Films . . 534
2.3. Luminescent Diodes Based on Mesoscopic Oxide Cathodes 534
3. Light-Induced Charge Separation in Nanocrystalline Semiconductor Films . . 536
4. Nanocrystalline Injection Solar Cells . . . 537
4.1. Solar Light Harvesting . . . 539
4.2. Conversion Efficiencies . . . 539
4.3. Photovoltaic Performance Stability . . . 545
4.4. Development of Series-Connected Modules . . . 545
4.5. Cost and Environmental Compatibility of the New Injection Solar Cell . . . 547
4.6. Current Research Issues . . . 547
5. Sensitized Solid-State Heterojunctions . . . 548
6. Tandem Cells for the Cleavage of Water by Visible Light . . . 550
7. Nanocrystalline Intercalation Batteries . . . 551
References . . . 552

Chapter 11. NANOSTRUCTURE FABRICATION USING ELECTRON BEAM AND ITS APPLICATION TO NANOMETER DEVICES

Shinji Matsui

1. Introduction . . . 555
2. Nanofabrication Using Electron Beam . . . 556
2.1. Nanometer Electron Beam Direct Writing System . . . 556
2.2. 10-Nanometer Lithography Using Organic Positive Resist . . . 558
2.3. 10-Nanometer Lithography Using Organic Negative Resist . . . 560
2.4. Sub-10-Nanometer Lithography Using Inorganic Resist . . . 561
2.5. Nanometer Fabrication Using Electron-Beam-Induced Deposition . . 563
3. Material Wave Nanotechnology: Nanofabrication Using a de Broglie Wave . . 565
3.1. Electron Beam Holography . . . 565
3.2. Atomic Beam Holography . . . 569
4. Nanometer Devices . . . 572
4.1. 40-Nanometer-Gate-Length Metal-Oxide-Semiconductor Field-Emitter-Transistors . . . 572
4.2. 14-Nanometer-Gate-Length Electrically Variable Shallow Junction MOSFETs . . . 574
4.3. Operation of Aluminum-Based Single-Electron Transistors at 100 Kelvins . . . 576
4.4. Room Temperature Operation of a Silicon Single-Electron Transistor 579
5. Summary . . . 582
References . . . 582

Index . . . 585
Contents of Volumes in This Set . . . 593

This Page Intentionally Left Blank

About the Editor



Dr. Hari Singh Nalwa has been working at the Hitachi Research Laboratory, Hitachi Ltd., Japan, since 1990. He has authored over 150 scientific articles in refereed journals, books, and conference proceedings. He has 18 patents either issued or applied for on electronic and photonic materials and their based devices. Dr. Nalwa has published 18 books, including *Ferroelectric Polymers* (Marcel Dekker, 1995), *Handbook of Organic Conductive Molecules and Polymers, Volumes 1–4* (John Wiley & Sons, 1997), *Nonlinear Optics of Organic Molecules and Polymers* (CRC Press, 1997), *Organic Electroluminescent Materials and Devices* (Gordon & Breach, 1997), *Handbook of Low and High Dielectric Constant Materials and Their Applications, Volumes 1-2* (Academic Press, 1999), and *Advanced Functional Molecules and Polymers, Volumes 1–4* (Gordon & Breach, 1999).

Dr. Nalwa is the founder and Editor-in-Chief of the *Journal of Porphyrins and Phthalocyanines* published by John Wiley & Sons and serves on the editorial board of *Applied Organometallic Chemistry, Journal of Macromolecular Science-Physics* and *Photonics Science News*. He is a referee for the *Journal of American Chemical Society, Journal of Physical Chemistry, Applied Physics Letters, Journal of Applied Physics, Chemistry of Materials, Journal of Materials Science, Coordination Chemistry Reviews, Applied Organometallic Chemistry, Journal of Porphyrins and Phthalocyanines, Journal of Macromolecular Science-Physics, Optical Communications*, and *Applied Physics*.

He is a member of the American Chemical Society (ACS), the American Association for the Advancement of Science (AAAS), and the Electrochemical Society. He has been awarded a number of prestigious fellowships in India and abroad that include National Merit Scholarship, Indian Space Research Organization (ISRO) Fellowship, Council of Scientific and Industrial Research (CSIR) Senior fellowship, NEC fellowship, and Japanese Government Science & Technology Agency (STA) fellowship. Dr. Nalwa has been cited in the *Who's Who in Science and Engineering*, *Who's Who in the World*, and *Dictionary of International Biography*. He was also an honorary visiting professor at the Indian Institute of Technology in New Delhi.

He was a guest scientist at Hahn-Meitner Institute in Berlin, Germany (1983), research associate at University of Southern California in Los Angeles (1984–1987) and State University of New York at Buffalo (1987–1988). He worked as a lecturer from 1988–1990 in the Tokyo University of Agriculture and Technology in the Department of Materials and Systems Engineering. Dr. Nalwa received a B.Sc. (1974) in biosciences from Meerut University, a M.Sc. (1977) in organic chemistry from University of Roorkee, and a Ph.D. (1983) in polymer science from Indian Institute of Technology in New Delhi, India. His research work encompasses ferroelectric polymers, electrically conducting polymers, electrets, organic nonlinear optical materials for integrated optics, electroluminescent materials, low and high dielectric constant materials for microelectronics packaging, nanostructured materials, organometallics, Langmuir-Blodgett films , high temperature-resistant polymer composites, and stereolithography.

This Page Intentionally Left Blank

List of Contributors

Numbers in parenthesis indicate the pages on which the author's contribution begins.

R. P. ANDRES (179)
Purdue University, West Lafayette, Indiana, USA

V. BRUYNDONCX (451)
Laboratorium voor Vaste-Stoffysica en Magnetisme, Katholieke Universiteit Leuven, Leuven, Belgium

Y. BRUYNSERAEDE (451)
Laboratorium voor Vaste-Stoffysica en Magnetisme, Katholieke Universiteit Leuven, Leuven, Belgium

S. DATTA (179)
Purdue University, West Lafayette, Indiana, USA

JO DE BOECK (345)
IMEC, Leuven, Belgium

M. R. DESHPANDE (93)
Departments of Physics, Applied Physics, and Electrical Engineering, Yale University, New Haven, Connecticut, USA

MICHAEL GRÄTZEL (527)
Institute of Photonics and Interfaces, Swiss Federal Institute of Technology, Lausanne, Switzerland

D. B. JANES (179)
Purdue University, West Lafayette, Indiana, USA

PRASHANT V. KAMAT (291)
Notre Dame Radiation Laboratory, Notre Dame, Indiana, USA

C. P. KUBIAK (179)
Purdue University, West Lafayette, Indiana, USA

SHINJI MATSUI (555)
Laboratory of Advanced Science and Technology for Industry, Himeji Institute of Technology, Hyogo, Japan

OLGA I. MIĆIĆ (427)
Center for Basic Sciences, National Renewable Energy Laboratory, Golden, Colorado, USA

KEI MURAKOSHI (291)
Chemical Process Engineering, Faculty of Engineering, Osaka University, Suita, Osaka, Japan

V. V. MOSHCHALKOV (451)
Laboratorium voor Vaste-Stoffysica en Magnetisme, Katholieke Universiteit Leuven, Leuven, Belgium

ARTHUR J. NOZIK (427)
Center for Basic Sciences, National Renewable Energy Laboratory, Golden, Colorado, USA

FRANÇOIS M. PEETERS (345)
Departement Natuurkunde, Universiteit Antwerpen, Antwerpen, Belgium

G. PLONER (1)
Institut für Festkörperelektronik und Mikrostukturzentrum der TU-Wien, Floragasse 7, A-1040 Vienna, Austria

M. A. REED (93)
Departments of Physics, Applied Physics, and Electrical Engineering, Yale University, New Haven, Connecticut, USA

R. REIFENBERGER (179)
Purdue University, West Lafayette, Indiana, USA

G. SCHÖN (131)
Institute of Inorganic Chemistry, University of Essen, 45127 Essen, Germany

TAMIM P. SIDIKI (233)
Institute of Materials Science and Department of Electrical Engineering, University of Wuppertal, 42097 Wuppertal, Germany

U. SIMON (131)
Institute of Inorganic Chemistry, University of Essen, 45127 Essen, Germany

J. W. SLEIGHT (93)
Departments of Physics, Applied Physics, and Electrical Engineering, Yale University, New Haven, Connecticut, USA

J. SMOLINER (1)
Institut für Festkörperelektronik und Mikrostukturzentrum der TU-Wien, Floragasse 7, A-1040 Vienna, Austria

CLIVIA M. SOTOMAYOR TORRES (233)
Institute of Materials Science and Department of Electrical Engineering, University of Wuppertal, 42097 Wuppertal, Germany

A. TONOMURA (451)
Advanced Research Laboratory, Hitachi, Ltd., Hatoyama, Saitama, Japan

M. J. VAN BAEL (451)
Laboratorium voor Vaste-Stoffysica en Magnetisme, Katholieke Universiteit Leuven, Leuven, Belgium

L. VAN LOOK (451)
Laboratorium voor Vaste-Stoffysica en Magnetisme, Katholieke Universiteit Leuven, Leuven, Belgium

YUJI WADA (291)
Chemical Process Engineering, Faculty of Engineering, Osaka University, Suita, Osaka, Japan

SHIZO YANAGIDA (291)
Chemical Process Engineering, Faculty of Engineering, Osaka University, Suita, Osaka, Japan

Chapter 1

ELECTRON TRANSPORT AND CONFINING POTENTIALS IN SEMICONDUCTOR NANOSTRUCTURES

J. Smoliner, G. Ploner

Institut für Festkörperelektronik und Mikrostukturzentrum der TU-Wien, Floragasse 7, A-1040 Vienna, Austria

Contents

1. Introduction 1
   1.1. Aim of This Review 2
2. Quantized States in Low-Dimensional Systems 4
   2.1. Electrons in One-Dimensional Potentials 5
   2.2. Parabolic Confinement 6
3. Basic Methods for Self-Consistent Calculations in One and Two Dimensions 8
   3.1. Self-Consistent Treatment of One-Dimensional Problems 9
   3.2. Self-Consistent Calculations in Two Dimensions 13
   3.3. Three-Dimensional Modeling of Quantum Dots 19
4. Transport Spectroscopy of Quantum Wires 20
   4.1. Magnetic Depopulation Experiments 21
   4.2. Magnetosize Effects and Weak Localization in Quantum Wires 25
   4.3. Magnetophonon Resonances in Quantum Wires 31
5. Weakly and Strongly Modulated Systems 41
6. Vertical Tunneling through Quantum Wires 48
   6.1. Experimental 48
   6.2. Transfer Hamiltonian Formalism 53
   6.3. Influence of the Potential Profile on 2D–1D Tunneling Processes 56
7. Vertical Transport Through Quantum Dots 68
   7.1. First Experiments 68
   7.2. Lateral and Vertical Transport through Quantum Dots: Coulomb Blockade Effects 71
   7.3. Tunneling via Zero-Dimensional Donor States 77
   7.4. 0D–2D Tunneling 82
   Acknowledgments 86
   References 86

1. INTRODUCTION

Before nanofabrication processes became available, the fundamental electronic properties of semiconductor devices were independent of their geometrical size. Through nanofab-

Handbook of Nanostructured Materials and Nanotechnology, edited by H.S. Nalwa
Volume 3: Electrical Properties
Copyright © 2000 by Academic Press
All rights of reproduction in any form reserved.
ISBN 0-12-513763-X/$30.00

rication, however, the geometrical dimensions of a semiconductor device can be made smaller than any of the other characteristic lengths of the electron system, such as the mean free path or the Fermi wavelength. Consequently, the device geometry is expected to influence the fundamental device and transport properties, which has made the investigation of the electronic properties of nanostructured systems a continuously growing field of solid-state research. Together with advances in molecular beam epitaxy (MBE) growth, nanofabrication allows for so-called "band structure engineering" in the vertical and lateral directions suitable for the design of semiconductor devices of almost any desired properties.

In the very beginning of nanofabrication, quantum wire structures were suggested to provide efficient semiconductor lasers, because the artificial confinement of carriers in the active region of a nanolaser was expected to give a better performance [1, 2] than a bulk system. After that, the electronic properties of the wires themselves and their possible use for device applications became the center of worldwide activities [3]. In 1985, Luryi and co-workers [4] were the first to report a quantum wire device with negative transconductance, and it was demonstrated that this kind of quantum device is interesting for practical applications, for example, as field effect transistors [5]. With forthcoming advances in nanotechnology, the idea of an "artificial atom" or quantum dot became realizable and a topic of great interest. As ohmic contacts to quantum dots are difficult to establish, the first investigations of quantum dots concentrated on optical properties such as size effects in the absorption spectra [6] and the exciton dynamics [7]. Later tunneling spectroscopy [8, 9] was established as the genuine method for the investigation of the electronic transport properties of quantum dot structures [10].

After the presence of size quantization effects and quantum interference phenomena in wires and dots was demonstrated in the early experiments, further investigations revealed numerous other features that were partially not predicted by theoretical considerations, such as the quantized conductance in ballistic quantum wires [11, 12] or the quenching of the quantum Hall effect in strong magnetic fields [13, 14].

An artificially imposed lateral potential modulation is expected to induce a miniband structure similar to that obtained by MBE-grown perpendicular superlattices. Lateral surface superlattices (LSSLs) provide the possibility of creating artificial crystals made of quantum dot "atoms." Because the electron mean free path in these LSSLs extends over many periods, they are expected to reveal interesting quantum or band structure effects that are not accessible in conventional crystal lattices [15]. In particular, the evolution of the band structure in magnetic fields is expected to display several interesting features [16]. Indeed, the experiments performed on one-dimensional (1D) and two-dimensional (2D) LSSLs in a perpendicular magnetic field revealed a wealth of additional structure in the magnetoresistance, which has been shown, however, to be due to a geometrical commensurability between the electron's cyclotron orbit and the periodic potential landscape [17–21]. For details on these so-called (magnetic) *commensurability oscillations*, see Section 5.

LSSLs were also investigated by tunneling experiments using a coupled quantum well system and equilibrium tunneling spectroscopy [22] (see Section 6). Tunneling spectroscopy principally offers the interesting possibility of studying electron transfer between systems of different dimensionality, for example, using a 2D gas as the emitter and a system of quantum wires [23] or dots [24] as the collector electrode. The tunneling characteristics give rather direct information on the Fourier transforms of the low-dimensional electron wave functions. Moreover, it turns out that the results obtained in the simulation of tunneling spectra are very sensitive to the actual shape of the potential, which brings us to the main motivation for writing this review.

1.1. Aim of This Review

While writing this chapter, it became clear that the lack of space and time as well as the huge amount of material published in the field of nanostructured systems makes it necessary to restrict the material presented here to several characteristic topics, selected with

regard to a few guiding aspects. The main emphasis in this chapter will be put on the role of the confining potential in low-dimensional systems. We will discuss the extent to which the confinement potential has a direct influence on the obtained results of lateral and vertical transport experiments, which serve as standard characterization methods for nanostructures. It will be shown how the different transport methods can be used to obtain a consistent picture of the shape and magnitude of confinement potentials and related parameters. Furthermore, in writing this review, we wanted to give the beginning experimentalist in the field some basic idea of the phenomena typically encountered in a transport investigation of low-dimensional systems and how the observed features will allow him or her to estimate the various sample parameters necessary for a detailed knowledge of the systems under investigation.

From the preceding discussion, it is clear that the present review will be far from giving a complete overview on all the transport investigations performed on nanostructured systems in the past decade. As a major omission, we only mention the transport experiments in the ballistic regime. One reason for this is the fact that the topics of interest in the ballistic regime have only marginally to do with the major guiding aspect of this review, that is, the confinement potential and its direct influence on various transport properties. Another reason is, of course, that this transport regime has been extensively reviewed previously (see, e.g., the excellent review articles by Beenakker and van Houten [25, 26], covering the developments up to the year 1991) and that an in-depth account of the recent progress in this field deserves a review of its own.

We would just like to mention some of the outstanding experimental achievements in this field, such as the study of the phase correlation behavior of electronic matter waves in semiconductor devices by ballistic transport experiments [27, 28]. Some other highlights include a modification of Young's double-slit experiment for ballistic electrons [29], as well as the experimental proof that lateral tunneling through a quantum dot is at least a partially coherent process [30], which was achieved with an extremely sophisticated device structure. Until very recently, the observation of ballistic transport phenomena was possible only in very short and narrow constrictions, the so-called quantum point contacts. Recent progress in the fabrication techniques of quantum wires and dots such as, for example, cleaved edge overgrowth [31, 32], however, has made it possible to create long conducting channels exhibiting the phenomena characteristic of ballistic transport [33, 34]. This allows an experimental test of several theoretical predictions on the behavior of one-dimensional systems of interacting electrons (Luttinger liquid state) [35, 36]. Considerable progress has also been made in adapting suitable fabrication processes for narrow channels on very high mobility 2D electron gases at relatively large distances below the sample surface [34, 37]. This led to the first experimental evidence of specifically one-dimensional electron–electron interaction effects such as a theoretically predicted [38] zero-field spin polarization in short and narrow constrictions [39].

We also do not discuss fabrication techniques in great detail. This is partly due to the fact that the complexity of the transport investigations makes highly specialized solutions necessary. Almost any new fundamental experiment uses innovations and improvements especially conceived for its special purposes. The very fundamental fabrication principles in the nanotechnology of low-dimensional systems, however, were already reviewed earlier. Some basic references on these topics can be found in [25, 40, 72] and, of course, the literature cited therein.

This chapter is divided into three main parts. In the first part (Sections 2 and 3), a survey of the basic electronic properties of low-dimensional systems is given, including the discussion of some simple numerical methods for self-consistent calculations in one and two dimensions. The second part (Sections 4 and 5) mainly deals with magnetotransport in quantum wires and lateral surface superlattices with an emphasis on the experimental determination of fundamental wire parameters and on methods to gain information on the actual shape of the confining potential. The third part (Sections 6 and 7) is dedicated to

tunneling phenomena in low-dimensional systems. The systems and experiments reviewed in this last part are also selected under the aspect to which extent they allow access to potential parameters and/or the shape of the corresponding wave functions. Because in the theoretical apparatus underlying the analysis of tunneling phenomena the notation is not as unified in the literature as in the conventional magnetotransport sector, we decided to use the same notation as in the original articles in all cases where model calculations are discussed. This makes the description of the formalism somewhat incoherent but facilitates the direct reference to the cited articles.

2. QUANTIZED STATES IN LOW-DIMENSIONAL SYSTEMS

Low-dimensional electron systems are commonly defined by lateral potentials artificially imposed on the two-dimensional electron gas (2DEG) situated at the interface of a modulation-doped semiconductor heterostructure. Throughout this chapter, we shall focus on results obtained using the GaAs–AlGaAs system. Several methods exist to create a lateral modulation of the effective potential at the heterointerface, which all use advanced lithographic or crystal growing techniques. For details of nanostructure fabrication and nanolithographic techniques, see [25, 40, 41] and the references cited therein.

The common starting point in the study of the electronic properties of low-dimensional systems is provided by confining the electrons of a 2DEG into narrow electron lines through an additional nanofabrication process. In case the lines are sufficiently narrow, lateral size quantization effects will occur and quasi one-dimensional electron systems, so-called quantum wires, are established. A typical quantum wire sample, fabricated by laser holography and subsequent wet chemical etching, is shown in Figure 1.

To analyze the electronic properties of a quantum wire, we consider the electrons as independent particles moving in a confining potential $V(x, z)$. Here $V(x, z)$ describes the joint influence of the confinement in the growth (z) direction and the lateral confinement in the x direction induced by nanolithographic patterning. The latter is thought to leave only the y direction for free motion of the electrons. This one-particle point of view ignores the presence of correlations resulting from the Coulomb interaction between different electrons and summarizes the effects of electron–electron interactions by an average global contribution to the potential. The problem is often simplified further by assuming that the confining potential $V(x, z)$ can be decomposed into a sum of two independent contributions $V(x, z) = V(z) + V(x)$, where the first term is due to the confinement at the heterointerface and the second term accounts for the lateral potential modulation. It will be shown later that this treatment is not quite correct but it can be used in many situations as a good approximation to understand the results obtained in various experimental situations. This approximation also allows the separation of the motion in the growth (z) direction

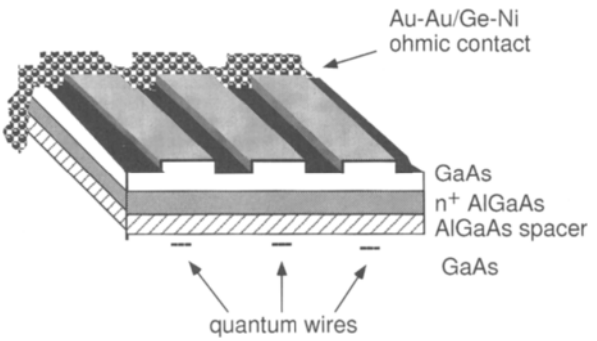


Fig. 1. Schematical view of a typical multiple quantum wire sample, which was fabricated by laser holography and subsequent wet chemical etching.

from the one-particle Schrödinger equation describing the confined electrons by a separation ansatz $\Psi(x, y, z) = \Phi(x, y)\varphi(z)$, where $\varphi(z)$ corresponds to the ground state of the underlying 2DEG with energy E_z^{2D}. Higher subbands in the z direction are not considered here, because commonly only the lowest subband is occupied in typical high-mobility GaAs–AlGaAs heterostructures. Within the effective mass approximation, this leaves us with the equation

$$H\Phi = \left(\frac{P_x^2}{2m^*} + \frac{P_y^2}{2m^*} + V(x)\right)\Phi = E^{1D}\Phi \tag{1}$$

which gives the quantized states in the quantum wire and also the corresponding energy levels. The bottom of the 2D subband E_z^{2D} is commonly taken as the zero point of the energy scale and all quantization energies are given relative to this origin.

In general, the confining potential $V(x, z)$, or $V(x)$ if the x and z dependence have been separated, has to be determined from a self-consistent solution of the Schrödinger and Poisson equations. In the following sections, we will summarize the simplest methods for such self-consistent calculations, which can be used to analyze the electronic properties of quantum wires and quantum dots. To give some insight into the physics of quantum-confined motion and to introduce several notions used in nanostructure physics, we also show how the actual confining potential can be approximated by simple and analytically tractable functions. From the self-consistent calculations, it will become evident that these approximations are often sufficient to describe the experimental data, but not always and not under all conditions.

2.1. Electrons in One-Dimensional Potentials

As stated before, we describe a one-dimensional electron system by a Schrödinger equation of the form

$$H\Phi = \left(\frac{P_x^2}{2m^*} + \frac{P_y^2}{2m^*} + V(x)\right)\Phi = E\Phi \tag{2}$$

Because the motion along the wire axis in the y direction is assumed to be free, one can use the following factorized form of the wave function:

$$\Phi(x, y) = \frac{1}{\sqrt{L}} \exp(ik_y y)\, \psi(x) \tag{3}$$

where L is the wire length. Inserting this wave function into the Schrödinger equation shows that the energy eigenvalues of the laterally confined electrons are quantized into subbands according to

$$E_n(k_y) = E_n + \frac{\hbar^2 k_y^2}{2m^*} \tag{4}$$

To determine the 1D subband energies E_n, it is necessary to know the shape of the lateral confining potential $V(x)$. There are several ways to model $V(x)$ in a more or less realistic way. The two most familiar examples for analytical model potentials are the square-well potential

$$V(x) = \begin{cases} 0 & \text{if } -W/2 \leqslant x \leqslant W/2 \\ \infty & \text{otherwise} \end{cases} \tag{5}$$

where W is the wire width, and the parabolic potential

$$V(x) = \tfrac{1}{2} m^* \omega_0^2 x^2 \tag{6}$$

It turns out [23] that these two are the limiting forms of the more general Woods–Saxon model potential, known from the shell model of atomic nuclei [42]:

$$V(x) = V_{\text{mod}}\left[\frac{1}{1+\exp\left(\frac{\alpha(w/2-x)}{w}\right)} + \frac{1}{1+\exp\left(\frac{\alpha(w/2+x)}{w}\right)}\right] - V_{\text{min}}$$
$$V_{\text{min}} = V_{\text{mod}}\left[\frac{2}{1+\exp(\alpha/2)}\right] \tag{7}$$

Depending on the parameter α, the Woods–Saxon potential interpolates between an approximately parabolic form ($\alpha = 8$) and an approximately square-well form ($\alpha = 200$). For intermediate values of α, it develops a flat bottom, which, as we shall see later, is necessary to describe quantum channels defined by a split-gate geometry at relatively high electron densities (or low gate voltages).

2.2. Parabolic Confinement

It is very instructive to consider a parabolic confinement in more detail for several reasons. First, it allows a completely analytical treatment of quantum wires in a magnetic field, and, second, it turns out that in many cases this simple model describes the actual situation reasonably well. It is, therefore, a useful tool for the analysis of magnetotransport data.

We now assume that a quantum wire is extended in the y direction and described by a lateral confining potential of the form of Eg. (6). From the beginning, we include the additional influence of a magnetic field applied in the z direction, which we describe as usual within the Landau gauge by a vector potential $\mathbf{A} = B(0, x, 0)$. The corresponding Schrödinger equation for a single electron state reads

$$-\frac{\hbar^2}{2m^*}\left[\frac{\partial^2}{\partial x^2} + \left[\frac{\partial}{\partial y} - \frac{ieB}{\hbar}x\right]^2\right]\Phi(x,y) + \frac{1}{2}m^*\omega_0^2 x^2\Phi(x,y) = E\Phi(x,y) \tag{8}$$

Together with Eq. (3), using $\omega_c = eB/m^*$ for the cyclotron frequency and introducing the center coordinate $x_0 = \hbar k_y/m^*\omega_c = \hbar k_y/eB$, one obtains

$$\left[-\frac{\hbar^2}{2m^*}\frac{\partial^2}{\partial x^2} + \frac{1}{2}m^*\omega_c^2(x-x_0)^2 + \frac{1}{2}m^*\omega_0^2 x^2\right]\psi(x) = E\psi(x) \tag{9}$$

A simple quadratic substitution transforms this equation into the Schrödinger equation for a shifted harmonic oscillator

$$\left[-\frac{\hbar^2}{2m^*}\frac{\partial^2}{\partial x^2} + \frac{1}{2}m^*\omega^2\left(x-\bar{x}_0\right)^2 + \frac{\hbar^2}{2m^*}k_y^2\frac{\omega_0^2}{\omega^2}\right]\psi(x) = E\psi(x) \tag{10}$$

where we used $\omega^2 = \omega_0^2 + \omega_c^2$ and a new, magnetic field–dependent center coordinate

$$\bar{x}_0 = x_0\frac{\omega_c^2}{\omega^2} = \frac{\hbar k_y \omega_c}{m^*\omega^2} \tag{11}$$

The solutions to this equation are the well-known harmonic oscillator functions $\psi_n(\sqrt{m\omega/\hbar}(x-\bar{x}_0))$ with $\psi_n(x) \equiv (\sqrt{\pi}2^n n!\sqrt{m\omega/\hbar})^{-1/2}\exp(-x^2/2)\,H_n(x)$. $H_n(x)$ denotes the nth Hermite polynomial. The corresponding energy eigenvalues are given by

$$E_n(k_y) = \hbar\omega\left(n+\frac{1}{2}\right) + \frac{1}{2}\frac{\hbar^2 k_y^2}{m_{\text{eff}}(B)} \qquad n = 0, 1, 2, \ldots \tag{12}$$

Here, we have used the abbreviation $m_{\text{eff}}(B) = m^*\omega^2/\omega_0^2$ for the magnetic field–dependent effective mass. In zero magnetic field, the lateral parabolic confinement gives rise to equidistant 1D subbands $E_n(k_y) = \hbar\omega_0(n+\frac{1}{2}) + \frac{1}{2}\hbar^2 k_y^2/m^*$ whose dispersion is parabolic and determined by the electron effective mass m^*. In nonzero magnetic field, the subbands are still equally spaced but with a field-dependent subband spacing $\hbar\sqrt{\omega_0^2+\omega_c^2}$ and

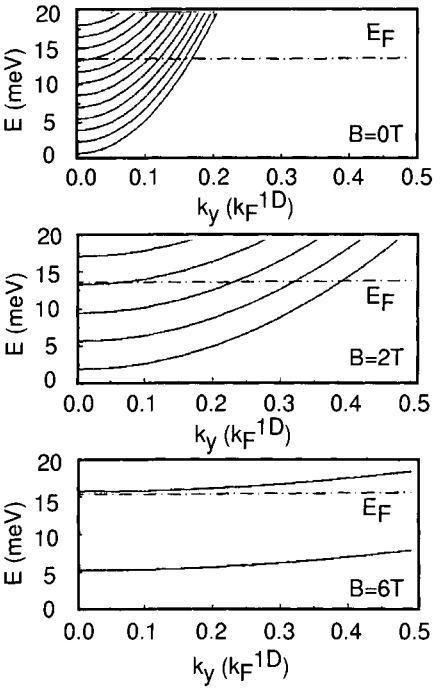


Fig. 2. Dispersion relation of a typical quantum wire plotted for three different magnetic fields.

a dispersion that becomes increasingly flat with increasing B. This behavior is due to the influence of $m_{\text{eff}}(B)$ and is illustrated in Figure 2, where the dispersion of these so-called magnetoelectric hybrid levels is drawn for three different magnetic fields.

The figure nicely visualizes that with increasing magnetic field strength, fewer and fewer subbands remain occupied for a given Fermi level E_F. This *magnetic depopulation* of 1D subbands gives rise to an oscillatory structure in the magnetoresistance. Its use for the determination of wire parameters such as the energy spacing and the electron density will be discussed later in detail.

Note the difference to the corresponding situation in purely 2D systems. In this case, the magnetic field quantizes the energy levels into *dispersionless* Landau levels at energies $\hbar\omega_c(n + \frac{1}{2})$. The group velocity of electrons in a Landau level is zero, which classically corresponds to the fact that electrons are forced on circular cyclotron orbits by the magnetic field. An analogous correspondence of the magnetoelectric hybrid states to classical orbits can be used to explain the persistence of a nonzero group velocity in a parabolic quantum wire at finite magnetic fields. As has been pointed out by Beenakker et al. [43], every point on a quantum mechanical dispersion relation can be related to a corresponding classical orbit. This is illustrated on the left-hand side of Figure 3, which shows the allowed energy values of a particle moving classically under the influence of a perpendicular magnetic field in a quantum channel described by a square-well confining potential. The (X, E) phase space shown in the figure is divided into four different sections by the two parabolas defined according to $(x_0 \pm W/2)^2 = R_c^2 = 2mE/(eB)^2$. Here, R_c is the cyclotron radius and x_0 is the center of the classical cyclotron orbit, whose quantum mechanical counterpart is the center coordinate appearing in Eqs. (10) and (11). Each section corresponds to one of the cases where the cyclotron orbit of the particle interacts with one, two, or none of the side walls. Those classical cyclotron orbits that do not interact with the wire walls correspond to undisturbed Landau levels and would be situated on completely flat sections of the dispersion relation, as shown on the right-hand side of Figure 3. Those orbits that interact with both walls (traversing orbits) correspond to magnetoelectric hybrid levels and

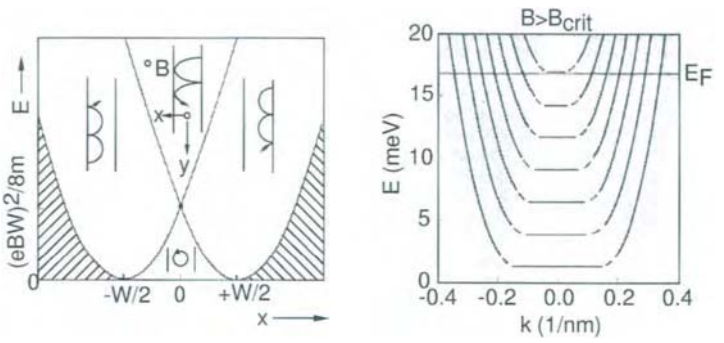


Fig. 3. Left: Possible combinations of kinetic energy and cyclotron orbit center in a narrow channel of width W, when specular boundary scattering dominates. The shaded area is forbidden. The four sections delimited by the two parabolas correspond to different types of classical orbits. Right: Dispersion relation $E(k)$ calculated for $W = 200$ nm and $B = 1.5$ T by applying the Bohr–Sommerfeld quantization condition to the classical trajectories shown on the left. The shaded areas indicate the parabolas drawn on the left-hand side of the figure. (Source: Reprinted with permission from [25].)

those orbits interacting with only one side wall of the wire (skipping orbits) correspond quantum mechanically to so-called edge states. It is clear that in each real quantum channel the dispersion relation should develop flat regions at high magnetic fields. This is when the spatial extension of the wave function, which corresponds to the classical cyclotron diameter, is substantially smaller than the effective wire width. The parabolic model potential describes this situation only in an approximate fashion since the curvature of the dispersion relation [(Eq. (12)] becomes very small at high magnetic fields but never completely flat as for a Landau level. This is due to the fact that any flat sections in the potential landscape are missing and even at very high magnetic fields there will be some net interaction of the electron orbit with the side walls of the channel.

Finally, it is interesting to note that any value X for the center coordinate of a classical cyclotron orbit (on the left-hand side of Fig. 3) corresponds directly to a particular state k_y in the dispersion relation (on the right-hand side of Fig. 3) by means of the relation $\hbar k = -eBX$. X can be interpreted as the classical equivalent to the center coordinate x_0 introduced in Eq. (9). Hence, in some sense, the dispersion relation shows the energy of a confined electron as a function of its lateral position in the wire.

3. BASIC METHODS FOR SELF-CONSISTENT CALCULATIONS IN ONE AND TWO DIMENSIONS

The model potentials described in the previous section are helpful for a qualitative and also quantitative interpretation of many experimental situations. However, as simple as they are, they need some justification from more realistic calculations taking into account an appropriately chosen distribution of impurities or the electric fields created by the gate on top of the sample. A realistic calculation should also account for the fact that, in response to the externally applied potentials, the electron gas will change its equilibrium configuration and thereby modify the effective confinement. In other words, a fully *self-consistent* treatment of the Schrödinger and Poisson equations has to be performed. From an experimentalist's point of view, such calculations will often be numerically too expensive to allow an efficient comparison with a particular experimental situation. However, these self-consistent calculations provide a lot of useful information about the corresponding sample parameters, such as the effective confinement width, the electron density, or the potential amplitude as a function of gate voltages or other external parameters. With this knowledge,

it is then possible to choose an appropriately tailored model potential that is numerically more tractable and that can be used to fit the experimental data. For this reason, some of the very basic methods for a self-consistent description of confining potentials are introduced in the following. We also reproduce some numerical results that are obtained for the most frequently encountered experimental situations.

Concerning the methodical part, we will restrict ourselves to the simple Hartree approximation and ignore all many-body corrections and scattering processes. Moreover, magnetic fields are not considered explicitly throughout this section. We disregard these topics in order to give a simple and ready-to-use exposition of the numerical and analytical details intended as a basis for quick first-principles calculations that any experimentalist might be interested in. Those readers who are interested in more theoretical details are referred to [44–47]. From more recent work, we mention [48, 49] and, in particular, the efficient numerical simulation methods of electron states in quantum wires presented by Kerkhoven et al. [50].

The organization of this section is as follows. First, we describe a simple and straightforward discretization method and some practical details of the numerical solution of the Schrödinger and Poisson equations in one dimension. Then we discuss how self-consistency is achieved numerically and how the corresponding procedure can be simplified by using the Thomas–Fermi approximation. The latter takes the electron response to an external potential into account without referring to an explicit solution of the Schrödinger equation. Finally, a simple way to solve two-dimensional problems self-consistently is presented together with some results on the potential shape in quantum wires defined by shallow etching and the split-gate techniques.

3.1. Self-Consistent Treatment of One-Dimensional Problems

3.1.1. Solving Schrödinger's Equation

In the following discussion, we assume that the problem of a laterally confined electron gas can be treated in a one-particle approximation and that the contributions to the potential in the x and z directions can be separated as outlined previously. To solve the Schrödinger equation for an arbitrary potential in one dimension, a simple finite-difference method can be used, which is sufficient for many problems. For this purpose, the stationary Schrödinger equation is written in discretized form as

$$-\frac{\hbar^2}{2m^*}\frac{D_i\Psi}{\delta_i^2} + V_i\Psi_i = E\Psi_i \tag{13}$$

with

$$D_i\Psi = (\Psi_{i+1} - 2\Psi_i + \Psi_{i-1}) \qquad \text{and} \qquad \delta_i = x_{i+1} - x_i \tag{14}$$

where i denotes the discretization index, δ_i is the spacing between the mesh points, V_i is the value of the confining potential at point i, and E is the energy of the eigenstates. The total number of grid points in the x direction is N. For simplicity, a constant effective mass is assumed in the following. The wave functions are assumed to vanish at the boundaries of the mesh ($\Psi_0 = 0$, $\Psi_{N+1} = 0$). This allows us to transform Eq. (13) into a symmetric band matrix problem, where the elements of the Hamiltonian matrix $\mathbf{H}$ are given by

$$H_{k,k} = +\frac{\hbar}{m^*}\frac{1}{\delta_k^2} + V_k \tag{15}$$

and

$$H_{k,k+1} = H_{k+1,k} = -\frac{\hbar^2}{2m^*}\frac{1}{\delta_k^2} \qquad \text{for } k = 1, \ldots, N-1 \tag{16}$$

All other elements of **H** are zero. To calculate the eigenstates and eigenvectors of the matrix, any standard numerical software can be used. Later, we shall discuss some results that were obtained using EISPACK [51] routines, which simultaneously yield both the eigenvectors and the energy eigenvalues of the problem. Note that the EISPACK routines are reasonably fast on a conventional personal computer, even if a 1-Å resolution is used on a 200-nm-wide system (2000 mesh points).

3.1.2. Solving the Poisson Equation

In the following discussion, we consider a quantum wire with the axis of free motion along the y direction. The translational invariance along y reduces the problem of calculating the confinement potential to the calculation of any arbitrary cut through the potential landscape in the x direction. The total electrostatic potential in the quantum wire is determined by the distribution of charged donors (in the case of a wire defined by etching) or the distribution of electric fields (for a split-gate wire), on the one hand, and by the spatial distribution of the free electrons, on the other hand. In the following, we consider the case of an etched wire, whose confinement is determined by some spatial modulation of the donor distribution with no external electric fields being applied.

A simple and numerically effective way to solve the one-dimensional Poisson equation is obtained, if the spatial region in which the electrostatic problem is to be solved is split into N intervals with a piecewise-constant charge density. We denote the charge density in the nth interval by the constant ρ_n, where ρ_n is composed of the contributions of the ionized donors in the structure and the electrons in the conducting regions. Because, in general, both will depend on temperature, we can write

$$\rho_n = e\left[N_D^*(x, T) - n(x, T)\right] \tag{17}$$

where $N_D^*(x, T)$ is the temperature-dependent density of ionized donors and $n(x, T)$ is the local electron density in the nth interval with $x_n \leqslant x \leqslant x_{n+1}$. Any residual acceptor concentrations or holes are ignored in this consideration. If we further assume a piecewise-constant dielectric constant ε_n, the Poisson equation on the nth interval reads

$$\frac{\partial^2 \varphi_n}{\partial x^2} = -\frac{e\rho_n}{\varepsilon_n \varepsilon_0} \tag{18}$$

where φ denotes the electrostatic potential. Integration yields the following quadratic expression for the electrostatic potential in the nth interval:

$$\varphi_n = -\frac{e\rho_n}{\varepsilon_n \varepsilon_0} \frac{(x - x_n)^2}{2} + c_n(x - x_n) + d_n \tag{19}$$

where c_n and d_n are integration constants. To calculate c_n and d_n, we define $x_0 = 0$ and introduce, for simplicity, the following boundary conditions:

$$\begin{aligned} \varphi_0(x_0) &= 0 \\ \left.\frac{\partial \varphi}{dx}\right|_{x=0} &= F \end{aligned} \tag{20}$$

That is, the potential is chosen to be zero at $x = 0$, whereas an electric field F of any desired value can be present at this point. These boundary conditions can be chosen arbitrarily without restricting the generality of the described procedure. The preceding boundary conditions lead to recursion relations for the coefficients d_n and c_n. As starting values, they give $d_0 = 0$ and $c_0 = F$ and, if we require the potential values in adjacent intervals to match at each intersection x_{n+1},

$$\varphi_n(x_{n+1}) = \varphi_{n+1}(x_{n+1}) \tag{21}$$

and the same for the displacement

$$\varepsilon_n \frac{\partial \varphi_n}{\partial x}\bigg|_{x=x_{n+1}} = \varepsilon_{n+1} \frac{\partial \varphi_{n+1}}{\partial x}\bigg|_{x=x_{n+1}} \tag{22}$$

we get the following recursive relations for c_{n+1} and d_{n+1}:

$$d_{n+1} = -\frac{e\rho_n}{2\varepsilon_n \varepsilon_0}(x_{n+1} - x_n)^2 + c_n(x_{n+1} - x_n) + d_n \tag{23}$$

and

$$c_{n+1} = -\frac{e\rho_n}{\varepsilon_{n+1}\varepsilon_0}(x_{n+1} - x_n) + \frac{\varepsilon_n c_n}{\varepsilon_{n+1}} \tag{24}$$

Having discretized the Schrödinger and Poisson equations in this way, it is now easy to obtain a self-consistent solution of these two equations by carrying out the usual Hartree iteration scheme, which will be summarized later.

3.1.3. Self-Consistency

To obtain a self-consistent solution of the Poisson and Schrödinger equations, one chooses, as a first step, an initial spatial electron distribution. It may, in principle, be of any shape provided that the integrated electron density equals the predefined one-dimensional electron density in the quantum wire: $\int n(x, T)^{\text{it}=1}\, dx = n^{1\text{D}}$. Here, the superscript it denotes an iteration index; it = 1 denotes the first iteration step. In practice, $n(x, T)^{\text{it}=1}$ is chosen to have some "realistic" shape, given by, for example, the Gaussian distribution function, which will accelerate the convergence of the iteration procedure. The Poisson equation, solved with the initial density $\rho(x)^{\text{it}=1} = e(N_{\text{D}}^*(x, T) - n(x, T)^{\text{it}=1})$, now gives the starting configuration of the electrostatic potential, $\varphi^{\text{it}=1}(x)$. The so-obtained potential is then inserted into the Schrödinger equation, whose solution yields a first approximation for the wave functions, and eigenenergies. With these wave functions, the local electron density in the wire can be expressed as

$$n(x, T) = \sum_{i=1}^{N} n_i(T)\left|\psi_i(x)\right|^2 \tag{25}$$

where N denotes the number of occupied subbands and $n_i(T)$ is the temperature-dependent number of electrons per unit length (in the y direction) in each 1D subband. At finite temperature, the Fermi distribution entering into the $n_i(T)$ (see the following discussion) extends to infinite energy. The cutoff number N of subbands used in the sum is, therefore, determined by the required numerical accuracy.

For a given total 1D electron density $n^{1\text{D}}$ in the quantum wire, $n_i(T)$ is obtained from the relation

$$n_i(T) = \int_0^\infty g_i^{1\text{D}}(E) f(E - E_{\text{F}})\, dE \tag{26}$$

where $g_i^{i\text{D}}(E)$ is the one-dimensional density of states in the ith 1D subband, $f(E - E_{\text{F}})$ is the Fermi distribution function, and E_{F} is the Fermi energy in the quantum wire.

For zero temperature, the previous equation simplifies to

$$n_i(T = 0\text{ K}) = \int_0^{E_{\text{F}}} g_i^{1\text{D}}(E)\, dE \tag{27}$$

Because most of the transport investigations on quantum wires are carried out at liquid helium temperatures or below, the assumption of zero temperature in the calculation will be a valid approximation. It can immediately be seen that $n_i(T)$ cannot be calculated directly

because this would require knowledge of the Fermi energy. The Fermi energy itself, however, depends on n^{1D} and the calculated subband energies. Consequently, to obtain $n_i(T)$, one first has to calculate the Fermi energy from the implicit relation

$$n^{1D} = \sum_i n_i(T) = \sum_i \int_0^{E_F} g_i^{1D}(E - E_i)\, dE \tag{28}$$

where, again, $T = 0$ K is assumed. The summation is carried out over all occupied subbands. The outlined procedure yields a local electron density $n(x, T)$, which can now be inserted into the next iteration step. In practice, however, it is not simply $n(x, T)$ that is used, but rather a linear combination of $n(x, T)^{it=1}$ and $n(x, T)$:

$$n^{it=2}(x, T) = (1 - \alpha)n^{it=1}(x, T) + \alpha n(x, t) \tag{29}$$

with the so-called mixing parameter $\alpha \in [0, 1]$. Using this mixing trick, the iteration is repeated until the resulting potential and electron distribution are left unchanged by consecutive iterations. The mixing relation of Eq. (29) is introduced because the self-consistent calculation scheme tends to be unstable. Frequently, the position of the center of the self-consistently calculated potential [and, consequently, that of the charge distribution $\rho(x)$] starts to oscillate about its equilibrium value during the iteration process. Equation (29) serves to damp these oscillations and to achieve fast convergence. Increasing the value of α, in principle, reduces the number of iterations but increases the risk of oscillations. The optimum choice of α depends on the investigated system, but usually α will be of order 0.2 for reasonably fast convergence.

3.1.4. Thomas–Fermi Approximation

In more complex situations, particularly in the field of real device simulation, the solution of the Schrödinger equation becomes numerically very expensive. Therefore, there is a need for approximation methods that take the response of the electron gas to an externally applied potential efficiently into account. A particularly simple approximation scheme is provided by the well-known Thomas–Fermi approach [52–55]. It was originally conceived to make the problem of many electron atoms tractable. In this context, it serves to estimate the local charge density in the atom without invoking a solution of the Schrödinger equation for all energy levels.

Consider a uniform electron gas in some external potential $\varphi_{ext}(x)$, which can be due to the space charge distribution created by charged donors or to externally applied electric fields. The electrons will change their configuration in response to $\varphi_{ext}(x)$, thereby creating an effective potential $\varphi(x, T)$ that will, in general, be temperature dependent even if φ_{ext} is not. In the Thomas–Fermi approach, it is assumed that $\varphi(x, T)$ originates in a spatially varying electron density $n(x, T)$ that is in thermal equilibrium with the local value of the effective potential. Taking the requirements of Fermi statistics into account, this means that the electron density can be written as

$$n(x, T) = \int_0^\infty g(E)\left[1 + \exp\left\{\left(E - E_F - e\varphi(x, T)\right)/k_B T\right\}\right]^{-1} dE \tag{30}$$

where $g(E)$ is the density of states in the semiconductor. The preceding equation is then evaluated as

$$n(x, T) = N_c(x, T) F_{1/2}\left(\left(E_F + e\varphi(x, T)\right)/k_B T\right) \tag{31}$$

where $N_c = 2[m^*(x)k_B T/(2\pi\hbar^2)]^{3/2}$, $m^*(x)$ is a piecewise-constant effective mass, and $F_{1/2}$ is the Fermi–Dirac integral conventionally defined by

$$F_\alpha(\eta) = \frac{1}{\Gamma(\alpha + 1)} \int_0^\infty \xi^\alpha \left[1 + \exp(\xi - \eta)\right]^{-1} d\xi \tag{32}$$

T symbolizes the Gamma function. Now, to apply these considerations to a quantum wire, one identifies the external potential $\varphi_{\text{ext}}(x)$ with the potential formed by a fixed space charge resulting from ionized donors, separated from the active region of the wire by a spacer layer. This would be a typical situation for etched quantum wires, but the following considerations also apply to split-gate structures if the proper boundary conditions are chosen. As before, z denotes the growth direction, y is the direction of the wire axis, and x is the direction of the lateral confinement produced by the nanofabrication process. Using Eq. (31) for the electron density in the presence of $\varphi_{\text{ext}}(x)$, one may write the Poisson equation in the following way:

$$\nabla\big[\varepsilon_0\varepsilon(x)\nabla\varphi(x,T)\big] = -\rho(x,T) = -e\big[N_{\text{D}}^*(x,T) - n(x,T)\big] \tag{33}$$

Here, $\rho(x,T)$ is the total charge density, $\varepsilon(x)$ is the spatially varying dielectric constant, and $N_{\text{D}}^*(x,T)$ is the concentration of ionized donors. Equation (33) already contains the response of the system of conduction electrons to the external potential without requiring the Schrödinger equation to be solved. The price that has to be paid for this convenience is that the Poisson equation now becomes a nonlinear differential equation. It can be solved numerically, using an iteration method similar to the one described previously: One assumes a piecewise-constant charge density $N_{\text{D}}^*(x,T)$ and starts with some initial distribution of electrons from which a potential $\varphi(x,T)$ is calculated using the Poisson equation. Then, the iteration step in Eq. (29), which previously required the solution of the Schrödinger equation, is now replaced by simply inserting $n(x,T)$ obtained from the Thomas–Fermi approach. Again, the procedure is repeated until the calculated potential becomes stationary. We refer the reader to [56–58] for more details.

3.2. Self-Consistent Calculations in Two Dimensions

3.2.1. Discretization Scheme and Boundary Conditions

Until now, all considerations and calculations were based on the assumption that the confining potential for narrow electron channels at a GaAs–AlGaAs interface can be separated into two independent components, one describing the approximately triangular potential well at the heterointerface and the other giving the lateral confinement induced by nanofabrication. The numerical problem was then reduced to the solution of equations that only depended on the x coordinate. We now relax this assumption and consider the unrestricted two-dimensional problem. This will enable a more realistic view of the "true" shape of the confining potential. Furthermore, it will become clear that the separation of the potential components underlying the simple models discussed at the beginning of this chapter has to be used with some care.

The principal procedure for the solution of the two-dimensional problem is analogous to that used in the one-dimensional case. As in the preceding section, we start by giving a particularly simple discretization method for the Schrödinger equation. Although there are many advanced methods to solve the Schrödinger equation numerically (see, e.g., [59, 60]), the finite-difference scheme described later [61] will, because of its simplicity, prove to be particularly helpful in any first-principles analysis of commonly encountered experimental situations.

In the two-dimensional Schrödinger equation

$$-\frac{\hbar^2}{2m^*}\left(\frac{\partial^2}{\partial x^2} + \frac{\partial^2}{\partial y^2}\right)\Psi(x,z) + V(x,z)\Psi(x,z) = E\Psi(x,z) \tag{34}$$

where $V(x,z)$ now describes the joint influence of the electric field at the heterostructure interface and the lateral nanostructuring process, we replace the differential quotients by finite differences just as in the preceding section:

$$-\frac{\hbar^2}{2m^*}\left(\frac{D_i\Psi}{\delta_i^2} + \frac{D_j\Psi}{\delta_j^2}\right) + V_{i,j}\Psi_{i,j} = E\Psi_{i,j}$$

with

$$D_i\Psi = (\Psi_{i+1,j} - 2\Psi_{i,j} + \Psi_{i-1,j})$$

and

$$D_j\Psi = (\Psi_{i,j+1} - 2\Psi_{i,j} + \Psi_{i,j-1}) \tag{35}$$

Here, $\delta_i = x_{i+1} - x_i$ and $\delta_j = z_{j+1} - z_j$ are the mesh spacings in the x and z directions, respectively. One now performs an index transformation and defines a new index $k = (i-1)N_j + j$, where N_i and N_j are the number of mesh points in the x and z directions. This gives

$$-\frac{\hbar^2}{2m^*}\left(\frac{\Psi_{k+N_j} - 2\Psi_k + \Psi_{k-N_j}}{\delta_i^2} + \frac{\Psi_{k-1} - 2\Psi_k + \Psi_{k+1}}{\delta_j^2}\right) + V_k\Psi_k = E_k\Psi_k \tag{36}$$

where k runs in the interval between 1 and $N = N_iN_j$. As boundary conditions, one again assumes vanishing wave functions at the borders of the mesh: $\Psi_0 = 0$, $\Psi_{N+1} = 0$. This transforms the eigenvalue equation into a symmetric band matrix problem, where the elements of the Hamiltonian matrix $\mathbf{H}$ are now given by

$$\begin{aligned} H_{k,k} &= +\frac{\hbar^2}{m^*}\left(\frac{1}{\delta_i^2} + \frac{1}{\delta_j^2}\right) + V_k \\ H_{k,k-N_j} &= H_{k-N_j,k} = -\left(\frac{\hbar^2}{2m^*\delta_i^2}\right) \\ H_{k,k+1} &= H_{k+1,k} = \begin{cases} 0 & \text{if } k = nN_j \text{ and } 1 \leqslant n \leqslant N \\ -\left(\frac{\hbar^2}{2m^*\delta_j^2}\right) & \text{otherwise} \end{cases} \end{aligned} \tag{37}$$

All other elements of $\mathbf{H}$ are zero. Once again, one obtains a practical discretization of the Schrödinger equation, which can easily be implemented on a personal computer using standard numerical algorithms for the solution of the resulting sets of linear equations. Later, some results will be shown that were obtained using the same EISPACK routines already mentioned in the context of the one-dimensional self-consistent calculations.

The next important step is the discretization of the Poisson equation. Usually, it is not reasonable to discretize and to solve both the Poisson and the Schrödinger equations in the whole discretization range because the electronic wave functions are expected to contribute only in the vicinity of the heterostructure interface. To achieve high accuracy and to reduce computation times, the Schrödinger equation is, therefore, solved only on a subset of the Poisson mesh. An example of this gives Figure 4, which shows the two discretization meshes used for a self-consistent simulation of a shallow etched quantum wire. As shown in this figure, the Schrödinger equation is solved only in the nonetched regions of the sample and there only in the area immediately adjacent to the heterostructure interface. The rest of the sample is assumed to be totally depleted. The two-dimensional Poisson equation can be solved on a rectangular mesh using the so-called simultaneous overrelaxation method [62]. As in the one-dimensional case, we assume zero temperature and define a local charge density

$$\rho(z,x) = N^*(z,x) + n^{1D}(z,x) \tag{38}$$

which consists of the contribution $N^*(z,x)$ of the ionized donors and the local electron concentration $n^{1D}(z,x)$. The discretized 2D Poisson equation can then be written in the following matrix form:

$$a_{i,j}\varphi_{i+1,j} + b_{i,j}\varphi_{i-1,j} + c_{i,j}\varphi_{i,j+1} + d_{i,j}\varphi_{i,j-1} + e_{i,j}\varphi_{i,j} = \frac{e\delta_i\delta_j\rho_{i,j}}{\varepsilon\varepsilon_0} \tag{39}$$

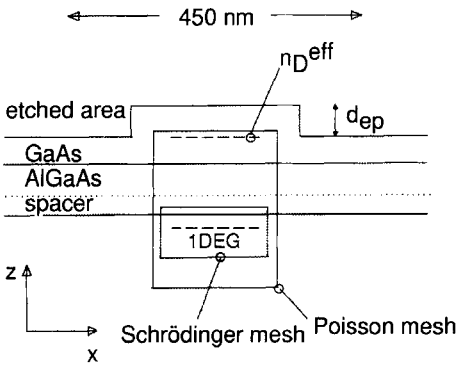


Fig. 4. Typical choice of the Schrödinger and Poisson mesh for a shallow etched quantum wire. A typical discretization grid for the solution of the Schrödinger equation often encountered in the literature consists of 51 × 51 points. (Source: Reprinted with permission from [61].)

Here, i counts the mesh points in the x direction, j those in the z (growth) direction, and δ_i, δ_j are the mesh spacings in the two directions. $\rho_{i,j}$ and $\varphi_{i,j}$ are the values of the charge density and the electrostatic potential at the point (i, j), respectively. The elements of the matrices **a**, **b**, **c**, **d**, and **e** in Eq. (39) are $a_{ij} = b_{ij} = c_{ij} = d_{ij} = 1$ and $e_{ij} = -4$ at the inner mesh points. To define them at the boundary of the mesh, one introduces suitable electrostatic boundary conditions. In the next subsection, several results of calculations using to the outlined method will be discussed. There, Neumann boundary conditions (zero electric field) are used on three sides of the underlying mesh (see Fig. 4). To fix the potential scale, Dirichlet conditions are used at the upper side. Note that, for simplicity, one assumes a position-independent dielectric constant ε in Eq. (39). This is a good approximation for quantum wires fabricated on GaAs–AlGaAs heterostructures, because there is little difference in the relative dielectric constants of GaAs and AlGaAs.

Self-consistency of the numerical solutions for the wave functions, energy levels, and the potential shape are now obtained in the same way as described for the one-dimensional case. Starting with an arbitrary electron distribution $n^{1D}(x, z, T)$, one first calculates the corresponding electrostatic potential. From this, a first approximation to the subband energies and wave functions is obtained. The electrons are then distributed among their energy levels taking the 1D form of the density of states into account. In most cases, zero temperature can be assumed for simplicity. The resulting new electron distribution $n(x, z, T)^{it=i}$ is again mixed with $n(x, z, T)$ using a weighting factor α ($\alpha = 0, \ldots, 1$) according to

$$n^{it=i+1}(x, z, T) = (1 - \alpha)n^{it=i}(x, z, T) + \alpha n(x, z, T) \tag{40}$$

The new value of $n(x, z, T)^{it=i+1}$ is then used in the subsequent iteration for the Poisson equation.

3.2.2. Some Numerical Results

In the following, some examples for self-consistently calculated confinement potentials of quantum wires are given. They serve as an illustration for the calculation methods outlined previously and will also indicate the limits of validity of the assumptions made previously, namely on the approximation of confining potentials by simple analytical functions and on the separate treatment of the confinement in lateral and growth direction.

Figure 5 shows the confinement potential obtained from a solution of the two-dimensional Poisson–Schrödinger (PS) model for a wire fabricated by shallow etching on a GaAs–AlGaAs heterostructure. Figure 4 shows the parametrization of the system used in the numerical calculation. The etching process, which removes a layer of thickness d_{ep}

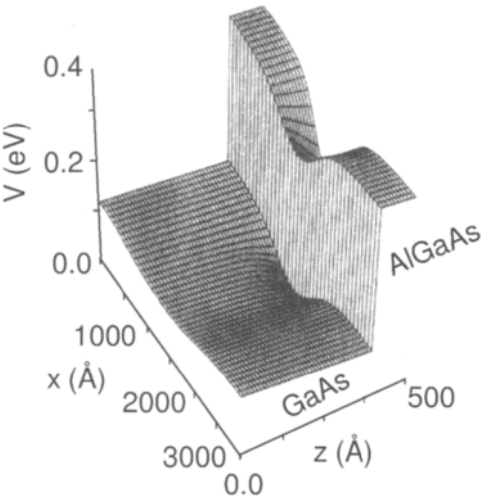


Fig. 5. Three-dimensional view of a quantum wire potential. The vertical potential step is the conduction band offset at the interface of the GaAs and the AlGaAs. For clarity, only a subset of the Poisson mesh is shown.

from the GaAs cap, induces a lateral modulation of the density of charged donors. Because the exact distribution of the donors and the surface states is not known exactly, it is modeled by a sheet of positively charged donors with thickness δ_z, positioned at $z = d_{\text{ep}}$. The profile of the charge distribution $n_{\text{D}}^{\text{eff}}$ is assumed to be constant in the z direction and to be correlated with the profile of the free carrier distribution in the wire itself. This can be formally expressed as

$$n_{\text{D}}^{\text{eff}}(y, z = d_{\text{ep}}) = \frac{1}{\delta_z} \int n_{\text{s}}^{\text{1D}}(y, z)\, dz \tag{41}$$

To accelerate the convergence of the calculation, a Broyden algorithm [63, 64] can be used. The self-consistent solution is then obtained typically after 15 iterations with average changes in the subband energies of less than 0.1 meV between the iteration steps. Note that the discretization grid of the PS model has to be fine enough to resolve all the extrema of all wave functions involved in the calculation of the charge density.

From the shape of the potential, it is obvious that it is not possible to separate the contributions of the z confinement from that of the x confinement over the entire integration region. However, within the range of the corresponding wave functions, the relation between the two contributions may be "linearized" and their separation can be considered to be a good approximation in many cases.

A common way to give a one-dimensional representation of the results of a two-dimensional calculation is to perform a cut through the potential profile at the maximum of the electron charge density $n_{\text{s}}^{\text{1D}}(y, z)$, as shown in Figure 6. This also allows us to decide what form an analytical model potential should have in order to give a fair approximation of the self-consistently calculated potential. Figure 6 reveals that, in the case of shallow etched quantum wires, the self-consistent confinement potential has a sinusoidal shape. The small oscillations superimposed on the sine potential of Figure 6 are due to small local variations in the self-consistently calculated electron density. Note that the situation shown in Figure 6 is typical for a relatively high electron density, which occurs, for example, after illumination. The Fermi level is located near the upper edge of the potential modulation and the highest lying of the eight occupied subbands are situated in the nonparabolic part of the potential.

Note also that there is a considerable "offset" in the zero-point energy, that is, a large energetic distance between the conduction band bottom and the lowest subband. This offset

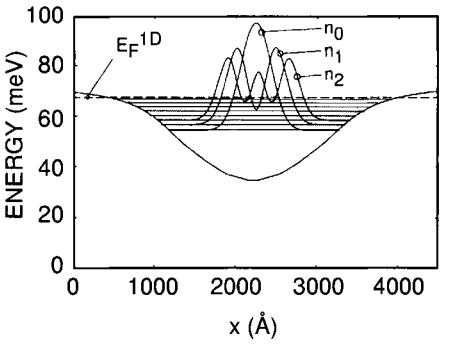


Fig. 6. Cut through a quantum wire potential at the total charge density maximum. The 1D subband energies and the squared wave functions of the lowest three subbands are also shown. (Source: Reprinted with permission from [61].)

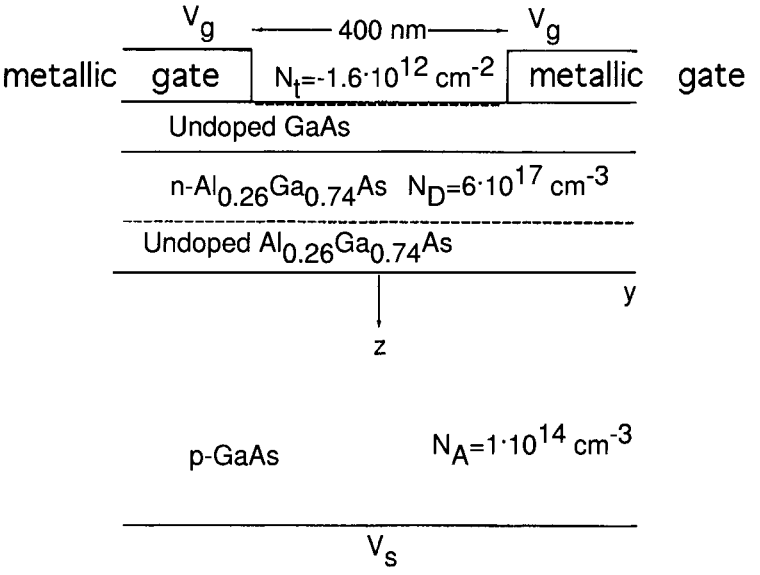


Fig. 7. Sample geometry and sample parameters for a typical split-gate wire fabricated on a GaAs–AlGaAs heterostructure. (Source: Reprinted from [44], with permission of Elsevier Science.)

reflects the position of the lowest occupied subband of the underlying 2D electron gas, which is the zero point for the superposed quantization into 1D subbands. (Fermi energies considered later on will generally not be given with respect to the conduction band bottom but with respect to the bottom of the lowest 2D subband.) This is another manifestation of the fact that the x and z components of the total confining potential cannot be considered separately. It is another interesting feature of the calculated results that the spatial extension of the wave functions corresponding to the highest occupied subbands can even exceed the geometrical width of the wire structure (which is on the order of 200 nm in Fig. 6).

In the case of low electron densities, the overall cosine shape of the confinement potential is conserved. However, the Fermi level and the occupied subbands are then located near the bottom of the potential where it may be well approximated by a parabolic shape.

We now compare these results to those obtained from self-consistent calculations performed for a split-gate geometry. The corresponding sample structure is depicted in Figure 7. In contrast to the shallow etching method, the lateral confinement is now induced by the external voltage applied to metallic gates on top of the GaAs–AlGaAs heterostructure.

The main advantage of the split-gate geometry is the possibility of tuning the confinement strength. This allows us to change the behavior of the confined electron system from effectively two dimensional to strongly confined one dimensional. Self-consistent wire potentials for the split-gate geometry of Figure 7 are shown in Figure 8 for various values of the gate voltage. The corresponding charge density distributions are reproduced in Figure 9.

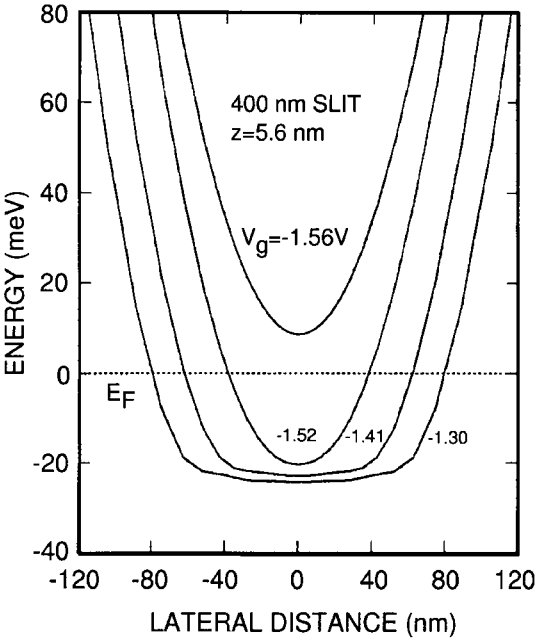


Fig. 8. Self-consistently calculated potential for a quantum wire in split-gate geometry. The potential is plotted for $z = 56$ Å below the GaAs–AlGaAs interface and for four different gate voltages. (Source: Reprinted from [44], with permission of Elsevier Science.)

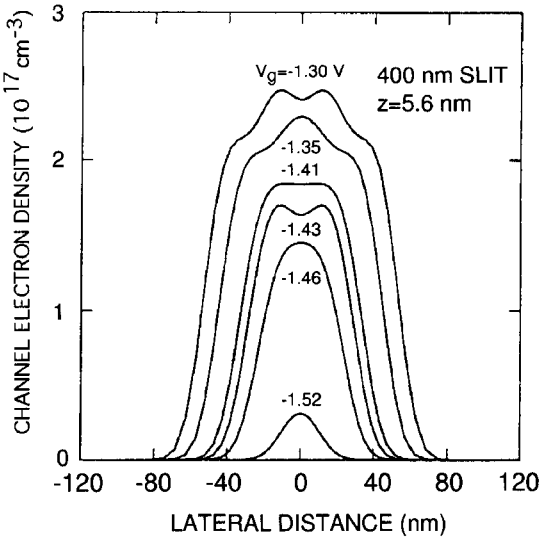


Fig. 9. Self-consistently calculated electron density for a quantum wire in split-gate geometry. The electron density is plotted for different gate voltages. (Source: Reprinted from [44], with permission of Elsevier Science.)

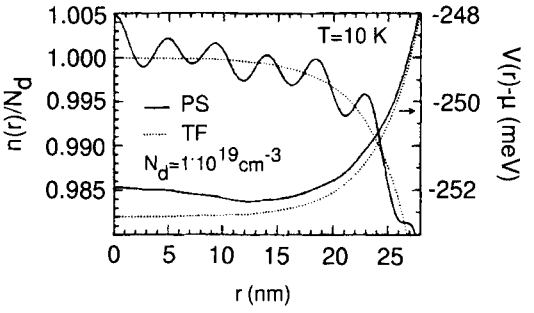


Fig. 10. Self-consistently calculated potential and charge distribution of a cylindrical quantum wire. The dotted lines are the results obtained through the Thomas–Fermi (TF) approximation; the solid lines are obtained through a self-consistent solution of the Schrödinger and Poisson equations. (Source: Reprinted with permission from [54]. © 1992 American Physical Society.)

Figure 8 reveals the main qualitative difference between the split-gate and the shallow etching geometry: For low electron density, both cases yield an approximately parabolic potential, whereas, at higher electron densities, the split-gate potential develops a flat bottom. The electron density plotted in Figure 9 shows several oscillations, which, in fact, reflect the structure of the corresponding 1D wave functions. The position and the amplitude of these oscillations depend on the gate voltage, which nicely reflects the increasing number of occupied subbands as the gate bias is lowered.

3.2.3. Thomas–Fermi Approximation in Two Dimensions

In the last paragraph of this section, we take a brief look at the application of the Thomas–Fermi (TF) approximation to two-dimensional problems. In principle, there is no difference to the one-dimensional case considered earlier, except for the number of independent variables. We, therefore, restrict the following discussion to a comparison of the results generated by the TF and PS approaches in Figure 10. The figure shows the potential and the local charge density as a function of the radius for a cylindrical, homogeneously doped quantum wire [54]. Dotted lines represent the Thomas–Fermi results; solid lines correspond to a fully self-consistent solution of the Poisson and Schrödinger equations. As discussed previously and as also seen in the figure, the PS approach leads to oscillations in the electron density, which are not revealed by the TF approximation. This is because the latter yields some kind of "average" behavior of the electron density and the confinement potential. The difference between the two approaches will become weaker when the number of occupied subbands or the temperature increases. In general, the Poisson–Schrödinger results are expected to approach the Thomas–Fermi results, as soon as the energy spacing between the occupied subbands becomes smaller than $k_B T$.

3.3. Three-Dimensional Modeling of Quantum Dots

In this section, we give a very brief survey on the self-consistent treatment of quantum dots without going into great detail. For the reader particularly interested in this subject, we give a short list of references, which may serve as a starting point for finding more detailed information on this topic.

There are mainly three obvious possibilities for calculating the electronic properties of quantum dots: As a first approximation, again a one-dimensional model potential such as, for example, an anharmonic oscillator potential suggests itself (Luban et al. [65]) for the simulation of electronic properties of a quantum dot nanostructure. As a next step, one might consider a circular symmetric "quantum disk" system. This implies the use of cylinder coordinates and, consequently, the solution of a two-dimensional Schrödinger equation

using the methods described in the previous sections. Finally, and also numerically most challenging, is a fully self-consistent simulation in three dimensions. The first to do this were Kumar et al. [66], who calculated the electron states of a quantum dot including the presence of a magnetic field. Recently, fully self-consistent calculations became more important because of progress in nanofabrication and the need for a three-dimensional (3D) device simulator for practical applications. The interested reader is referred to the work of Udipi et al. [67] for a model of lateral quantum dots on silicon and Scholze et al. [68] for various other aspects of device simulation.

The case of a circular dot geometry has been intensively investigated during the past years. The most popular examples of this are pillar-shaped double-barrier resonant tunneling diodes with diameters in the nanometer range, the dot being formed in the well between the barriers. The intensive work on these systems was performed mainly at Texas Instruments (see, e.g., [55]) and was motivated by two major aspects. First, the increasing scale of integration in commercial devices strongly requires this kind of calculation and, second, nanostructured double-barrier resonant tunneling diodes (DBRTDs) are useful for certain applications that require ultralow power consumption. The efforts in this field aim at the conception of a nanodevice simulation tool capable of calculating current–voltage characteristics from the given fabrication parameters. The computer simulations always employ the Thomas–Fermi approximation to keep the computational expense reasonably low. It should be noted, however, that the calculation of IV characteristics requires not only the self-consistent treatment of confinement potentials but also the calculation of tunneling currents. Therefore, scattering processes have to be included [69] for realistic simulations, which is a topic that we have completely omitted in the preceding discussion. Pioneering work in this field was done by Frensley [70] and Luban and Luscombe [71]. Detailed accounts on the problems and methods encountered in nanodevice simulation can be found in their work and in the other references given in the context of the Thomas–Fermi approximation.

4. TRANSPORT SPECTROSCOPY OF QUANTUM WIRES

In the following, we discuss the magnetotransport properties of quantum wires in the diffusive transport regime. We shall focus on those phenomena that provide a more or less direct access to those quantum wire properties directly related to the confinement potential, such as the subband spacing or the wire width. The standard example for an experiment yielding the subband spacing is the magnetic depopulation measurement. A second example that has only recently been shown to be suitable for the subband spectroscopy on quantum wires is the observation of the magnetophonon resonance at elevated temperatures. In the interpretation of the experimental results, the confinement will be approximated by simple and frequently used model potentials, as they are suggested by the self-consistently calculated results introduced in the preceding chapter. We shall discuss the limits of the validity of these approximations and also outline a method that gives direct information on the shape of the actual potential from the comparison of high- and low-temperature magnetoresistance measurements. Several other phenomena exhibited in a magnetoresistance experiment, such as the suppression of backscattering in a magnetic field or the weak localization effect, are also considered. They provide additional information on several characteristic lengths important for the characterization of long quantum channels in the diffusive regime. The particular magnetoresistance "anomalies" occurring in lateral surface superlattices and their use for the determination of potential parameters will be discussed in the subsequent chapter.

According to the objective of this chapter, ballistic transport phenomena are completely neglected in the following. This is mainly because the phenomena typically examined in this regime, in general, do not rely strongly on a detailed knowledge of the properties

of confinement potentials. The reader who is especially interested in a review on ballistic transport is referred to the excellent articles by Beenakker and van Houten [25], van Houten et al. [26], Timp [72], or the textbook of Datta [73] as well as the references cited therein.

4.1. Magnetic Depopulation Experiments

4.1.1. Determination of Subband Energies

The "classic" method to gain information on the confining potential in quantum wires and, in particular, on the energy spacing of the 1D subbands is the so-called magnetic depopulation measurement [74–76]. It exploits the particular features of the low temperature ($T \leqslant 4.2$ K) longitudinal magnetoresistance of a quantum wire sample with a magnetic field applied in the growth direction of the underlying heterostructure. As already mentioned earlier, the magnetic field enlarges the energetic separation of the 1D subband edges and, therefore, the number of occupied subbands is successively reduced with increasing magnetic field. This is shown in Figure 11, where the magnetic field–dependent density of states of a one-dimensional system is plotted for three different magnetic fields. The position of the Fermi level E_F is defined through the electron density in the quantum wire and also depends on the magnetic field strength.

As shown in Section 1, the energy dispersion for a parabolic confinement potential in a perpendicular magnetic field is given by

$$E_n(k_y) = \hbar\omega\left(n + \frac{1}{2}\right) + \frac{1}{2}\frac{\hbar^2 k_y^2}{m_{\text{eff}}(B)} \qquad n = 0, 1, 2, \ldots \tag{42}$$

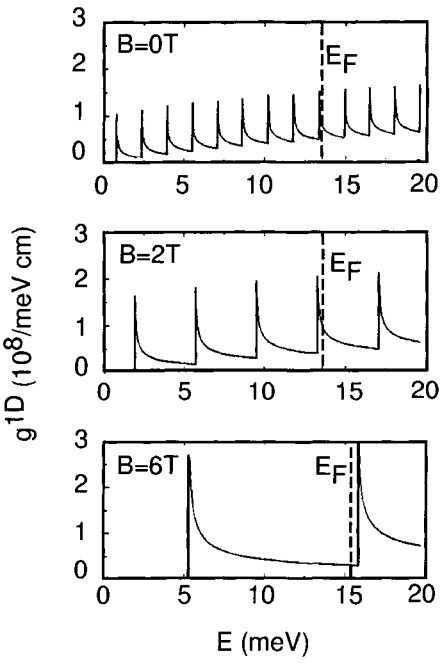


Fig. 11. One-dimensional density of states according to Eq. (43) plotted for magnetic fields of $B = 0$ T, 2 T, and 6 T, respectively. Because constant carrier density is assumed, the position of the Fermi level is dependent on the magnetic field. The density of states is calculated for the ideal case of absent lifetime broadening of the magnetoelectric hybrid levels. As shown by Berggren et al. [75], realistic assumptions for the lifetime broadening leave the main qualitative features of the magnetic depopulation process unchanged. The lifetime broadening in a magnetic field is found to be strongly dependent on the wavevector component k_y.

The density of states for a particular subband is given by the expression

$$g_n^{1D}(E) = \frac{1}{\pi}\left(\frac{dE}{dk_y}\right)^{-1} = \frac{\sqrt{2m_{\text{eff}}(B)}}{\pi\hbar}\frac{1}{\sqrt{E-\hbar\omega(n+1/2)}} \tag{43}$$

If we sum this expression over all N occupied subbands, we obtain

$$g^{1D}(E) = \frac{\sqrt{2m_{\text{eff}}(B)}}{\pi\hbar}\sum_{n=0}^{N}(E-E_n)^{-1/2}\Theta(E-E_n) \tag{44}$$

which is plotted in Figure 11. The density of states at the Fermi energy oscillates as a function of magnetic field and gives rise to an oscillating impurity scattering time. A semi-quantitative way to see this is to consider the scattering from a set of dilute impurities in first-order perturbation theory. If the scattering potential is delta function like with a strength V_0 it can be shown that [77]:

$$\tau^{-1} = \frac{\pi}{\hbar}g^{1D}(E_F)c_{\text{imp}}V_0^2 \tag{45}$$

Here, c_{imp} denotes the sheet concentration of impurities. At low temperatures, impurity scattering may be considered to be the dominant contribution to the resistivity. The magnetic depopulation effect will, therefore, manifest itself in the oscillatory behavior of the semiclassical magnetoresistivity $\rho_{xx} \propto \tau^{-1} \propto g^{1D}(E_F)$.

To reveal the oscillatory structure in the magnetoresistance, it is advantageous to consider arrays of identical quantum wires. For a single quantum wire, the low-field magnetic depopulation oscillations may be obscured by the so-called aperiodic conductance fluctuations (for an introduction to this topic, see, e.g., [25]). This quantum interference effect originates in the large-phase coherence length in a mesoscopic electron system and it is averaged out if an ensemble of quantum wires is investigated.

Several methods for the fabrication of such arrays of quantum wires have been successfully applied. The simplest possible sample layout consists of a two-terminal configuration where an array of quantum wires is extended between two large contacts. To get rid of the contact resistance, one may evaporate a metal gate on top of the wire array intended for the application of a small modulation voltage [78]. This sample geometry is shown in Figure 12a.

The magnetoresistance is then measured using a lock-in technique and gives the resistance of only those regions covered by the modulating gate. The influence of the contact resistance is thereby effectively eliminated. A variation of this method was used by Brinkop et al. [79, 80, 119]. Their fabrication principle exploits a modified split-gate technique to create the wire array as indicated schematically in Figure 12b. In contrast to the sample

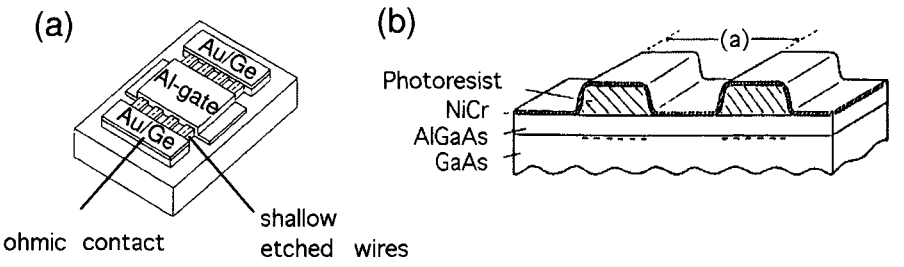


Fig. 12. Two different fabrication principles for arrays of parallel quantum wires. (a) Wires fabricated by laser holography and shallow etching. The top Al gate serves as a modulation electrode for lock-in measurements intended to eliminate the contribution of the contact resistance. (b) A Ni/Cr gate evaporated over nanostructured photoresist stripes. This modified split-gate geometry allows one to tune the confinement strength. (Source: Part b reprinted with permission from [119]. © 1989 American Physical Society.)

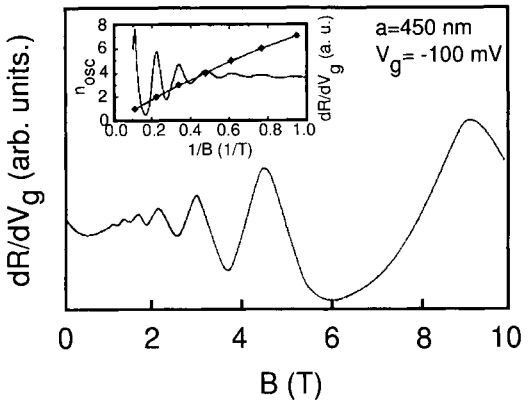


Fig. 13. Derivative of the magnetoresistance with respect to the modulated gate voltage V_g, measured for an array of quantum wires. The sample layout is shown in Figure 12a. The period of the shallow etched grating was 450 nm. The inset shows the same data plotted as a function of the inverse magnetic field together with a Landau plot of the corresponding magnetoresistance maxima.

shown in Figure 12a, where the confinement is achieved by shallow etching, the purpose of the gate in this configuration scheme is twofold. First, it produces the 1D confinement and, second, it serves as a modulating gate for contact resistance elimination. For the purpose of spectroscopic investigations, it furthermore provides an effective grating coupler for far-infrared radiation (see [79]). This sample configuration has the advantage of supplying quantum wires with a *tunable* confinement strength.

Figure 13 shows a typical magnetoresistance trace obtained for a sample structure as depicted in Figure 12a, using a modulated gate voltage to eliminate the contact resistance [78]. A minimum occurs whenever the Fermi level is shifted across the bottom of the highest occupied magnetoelectric subband, where a sharp maximum in the density of states is followed by a region of minimal density of states (DOS). If a running subband index n_{osc} is assigned to each minimum and the index n_{osc} is plotted against the inverse magnetic field position of the corresponding minimum in R_{xx}, a fan chart or so-called Landau plot is obtained (cf. the inset of Fig. 13). The characteristic feature in this plot, which demonstrates the presence of a 1D confinement, is the deviation from linearity at low magnetic fields. This behavior can be understood from Eq. (42), which describes the subband energies in a parabolic confinement potential. For the subband edge ($k_y = 0$) of the nth subband, Eq. (42) yields $E_n(B) = \hbar\sqrt{\omega_c^2 + \omega_0^2}(n + \frac{1}{2})$. For large magnetic fields, ω_0 may be neglected and the resulting dependence of n_{osc} on B^{-1} is linear. This is the well-known behavior of the Shubnikov–de Haas oscillations observed in the magnetoresistance of unstructured 2DEGs. The presence of the lateral confinement characterized by the additional frequency ω_0 becomes visible only when it is at least of the same order of magnitude as the cyclotron frequency. For those magnetic fields where this is the case, the relation between n_{osc} and $1/B$ is no longer linear. This is the general signature of lateral confinement in narrow channels, no matter what the actual shape of the confining potential is [74, 81].

It is instructive to analyze the $n_{\mathrm{osc}}(B^{-1})$ dependence in terms of a parabolic confinement potential [75] because this allows the analytical treatment of the magnetic depopulation effect and provides a particularly simple way to determine wire parameters from an actual measurement. The situation encountered in a magnetic depopulation experiment is depicted in Figure 14, which shows the energy of the magnetoelectric subband edges as a function of B. Whenever the Fermi level crosses the edge of the highest occupied magnetoelectric hybrid subband, that is, whenever $E_{\mathrm{F}} = N\hbar\omega(B)$, a minimum in the magnetoresistance is observed. Because the 1D electron density in the channel is constant, the

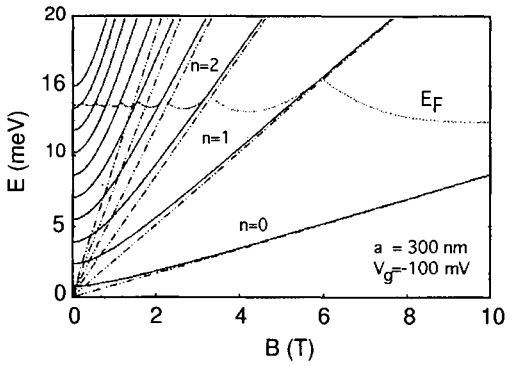


Fig. 14. Dependence of the magnetoelectric subband energy on magnetic field strength, calculated for a parabolic confinement with $\hbar\omega_0 = 1.57$ meV. The dashed–dotted lines show the corresponding behavior of the Landau levels in an unstructured 2DEG. Also shown is the oscillating Fermi energy, calculated for a 1D carrier density of $n_{1D} = 5.68 \times 10^6$ cm^{-1}. n is the subband index.

Fermi level oscillates with increasing magnetic field. From the 1D carrier density at zero temperature

$$n_{1D} = \int_0^{E_F} g^{1D}(E, B)\, dE \tag{46}$$

one obtains, together with Eq. (44) and $E_F = E_N$,

$$n_{1D} = \frac{2}{\pi}\sqrt{\frac{2m^*}{\hbar}}\,\frac{\omega^{3/2}}{\omega_0}\sum_{n=0}^{N} n^{1/2} \tag{47}$$

This finally leads to the following relation between the index N of the highest occupied subband and the magnetic field position of the corresponding magnetic depopulation minimum in R_{xx}:

$$B_N = \frac{m^*}{\hbar e}\sqrt{\left[\frac{\pi\hbar n_{1D}\hbar\omega_0}{\sqrt{8m^*\sum_{n=0}^{N} n^{1/2}}}\right]^{4/3} - (\hbar\omega_0)^2} \tag{48}$$

If this relation is fitted to the experimentally determined Landau plot, N plays the role of the previously introduced n_{osc}. As fit parameters, one obtains the subband spacing $E_0 = \hbar\omega_0$ and the 1D carrier density n_{1D}. The latter is related to the approximately linear behavior of the $n_{osc}(1/B)$ plot for high-magnetic-field values [75], which is obtained by replacing in Eq. (47) ω by ω_c:

$$N \approx \frac{m^*/e}{(2m^*\hbar)^{1/3}}\left(\frac{3\pi}{4}n_{1D}E_0\right)^{2/3}\frac{1}{B_N} \tag{49}$$

In the preceding section, we have seen that in the case of quantum channels defined by a split-gate geometry the confining potentials as obtained from self-consistent calculations have the shape of a Woods–Saxon potential with a flat bottom. Only for very narrow channels or at quite low electron densities does the potential assume an approximately parabolic form [44]. In the case of quantum wires defined by the shallow etching method, the self-consistent calculations showed that the effective potential felt by the electrons is of a sinusoidal shape [61]. It is again for relatively low electron densities that the electronic wave functions are concentrated near the bottom of the sinusoidal potential where it is well described by a parabola. Only in these cases will the parabolic model and the described fitting procedure be able to reproduce the experimental depopulation data and give results

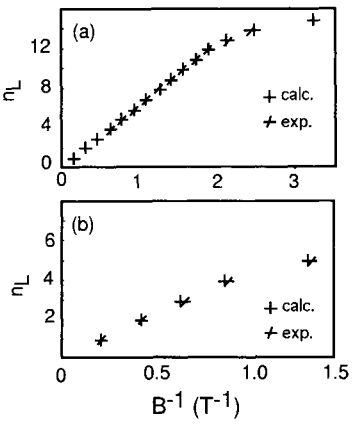


Fig. 15. Experimental and calculated sublevel index n_L versus the inverse magnetic field positions of the resistance minima for two different samples. The theoretical values are calculated under the assumption of a square-well potential and fitted to the experimental points with the channel width and the 1D carrier density as fit parameters. (a) Wide channel (estimated width and carrier density are 378 nm and 1.16 nm^{-1}, respectively). (b) Narrow channel (162 nm, 0.38 nm^{-1}). The wide-channel sample is well described by a square-well potential. The parabolic approximation is found to give better results for the narrow channel (cf. [75]), but turned out not to be suitable for a description of the wide-channel experiment. (Source: Reprinted with permission from [81].)

for channel width and electron density that are in good agreement with independently estimated values.

The second strongly simplified model potential, the square well, does not lend itself to as simple an analytical treatment as the parabolic potential. Rundquist [81] applied a numerical fitting procedure to describe wide and narrow channels defined by the split-gate geometry using a square-well confinement potential. As expected, the square-well model is able to describe wide channel experiments where the parabolic model does not give convincing results and vice versa (cf. Fig. 15, where the experimental results are plotted together with a numerical fit of the results with a square-well model). However, even in the simple case of a square well, the fitting procedure becomes numerically very expensive and is not easily implemented in routine investigations.

Another model potential used to approximate the flat bottom potential of split-gate wires at high electron densities (or, alternatively, low gate voltages) is given by $V(x) = (m^*\omega_0^2/2)(|x| - t/2)^2$ for $|x| \geqslant t/2$ and zero otherwise. It has been investigated in Wentzel, Kramers, Brillouin (WKB) approximation by Berggren and Newson [76]. The use of this potential in the numerical analysis of an experimental situation requires one additional fit parameter, namely the width t of the flat potential section. If, in addition, a modulating gate configuration is used for the magnetoresistance measurement, a phase shift in the dR_{xx}/dV_G traces has also to be taken into account, which requires adding a further unknown parameter B_{offset} to the positions of the magnetic depopulation minima. Altogether, one thus needs four fit parameters for the analysis of the Landau plot. The so obtained values of E_0 and n_0 are questionable in particular when the Landau plot consists of only a few data points.

4.2. Magnetosize Effects and Weak Localization in Quantum Wires

4.2.1. Magnetosize Effects

A useful quantity for the characterization of quantum channels is the electrical width W, which can be estimated from several independent effects in the magnetic field and temperature dependence of the sample resistance. The values extracted for W allow us to

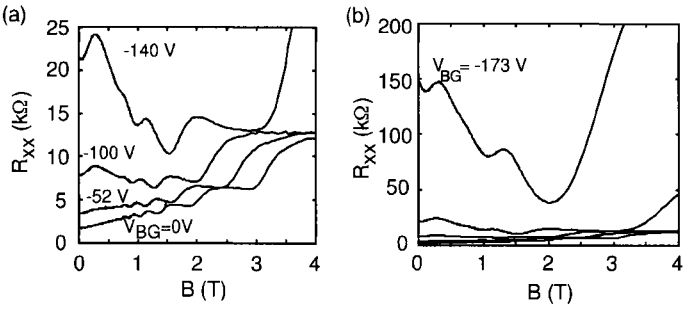


Fig. 16. Low-temperature ($T = 2$ K) magnetoresistance of an array of shallow etched quantum wires, measured with different back-gate voltages applied to the substrate. At low back-gate voltages, the behavior of the system corresponds to a modulated 2D gas. At higher gate voltages, the Fermi level is reduced below the modulation potential amplitude and typical 1D features are observed, such as the large magnetosize peak at $B = 0.27$ T and the negative differential magnetoresistance caused by a suppression of 1D weak localization at $B \leqslant 0.1$ T. The pronounced negative differential magnetoresistance superimposed on the depopulation oscillations at $V_G \geqslant -100$ V is due to the suppression of backscattering by a magnetic field (cf. Fig. 17). The -173-V trace has been drawn separately for clarity (b). The squeezed traces at the bottom of part b are the same curves as in part a.

cross-check whether a model potential used in the analysis of magnetic depopulation experiments is well suited to describe the experimental situation.

Figure 16 shows two-terminal magnetoresistance traces for an array of quantum wires fabricated by laser holography and shallow etching. The etching is very shallow in this case such that without additional measures only a periodic potential modulation is superimposed on the 2DEG. The results of Figure 16 were obtained without application of a modulating front-gate voltage and, therefore, contain the contribution of the contact resistance which, however, is small in this case. The electron density was reduced by applying a negative back-gate voltage on the substrate side of the sample. In this way, the Fermi energy becomes gradually smaller than the amplitude of the potential modulation, eventually leading to a system of well-separated quantum wires. The magnetoresistance traces depicted in the figure clearly show the evolution of two magnetoresistance phenomena typical for narrow electron channels in the diffusive transport regime: magnetosize effects and weak localization.

We first consider magnetosize effects. With increasing back-gate voltage, that is, increasing confinement of the electrons to 1D channels, a magnetoresistance peak evolves at about 0.3 T. This so-called *magnetosize peak* has been shown by Thornton et al. [82, 83] to be due to *diffuse* scattering from the channel walls of electrons moving on cyclotron orbits. It can be shown that this effect can be explained by purely classical arguments and that the presence of diffuse boundary scattering is an essential prerequisite for the observation of a magnetosize peak. Note that the mean free path of the electrons has to be large enough that boundary scattering contributes appreciably to the total wire resistance. The situation is depicted schematically in Figure 17, which shows two classical electron trajectories at two different field strengths [25]. For field strengths where the cyclotron radius is of the order of $R_c \approx W/2$ (Fig. 17a, W is an effective wire width), the probability for electron backscattering is considerably larger than in the case of $R_c \ll W/2$ (Fig. 17b), provided that the scattering from the channel boundaries is predominantly diffuse. The reduction of backscattering for $R_c \ll W/2$ is also responsible for the negative differential magnetoresistance observed in the field range beyond the magnetosize peak for the most strongly confined channels in Figure 16.

As has been found experimentally by Thornton et al. [82], the magnetic field position B_{ms} of the magnetosize peak can be related to the effective width W_{eff} of the quantum wire by $W_{eff} \approx 0.55 R_c^{ms}$, where $R_c^{ms} = \hbar k_F / e B_{ms}$. It is not straightforward to give an unambiguous meaning to the effective wire width W_{eff} obtained from the magnetosize peak.

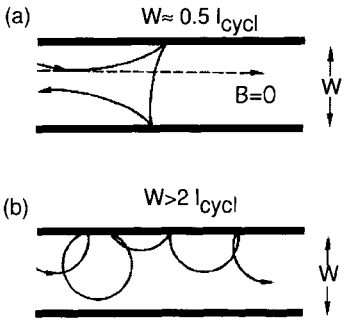


Fig. 17. Classical cyclotron trajectories in a narrow channel with diffuse side-wall scattering, illustrating the origin of the magnetosize peak. (a) If the cyclotron radius (l_{cycl}) is near the indicated value, diffuse side-wall scattering can reverse the motion of an electron, leading to an enhanced resistance. (b) At higher magnetic fields, backscattering is suppressed and the resistance is reduced below the zero-field value. (Source: Reprinted with permission from [25].)

The definition of W_{eff} depends on the underlying model potential. Even if a particular model has been chosen, there are several possibilities to define W_{eff}. Consider as an example the parabolic confinement potential. One way to define W_{eff} is to take the distance between the turning points of the classical motion at the Fermi energy:

$$W_{\text{eff}} = \frac{2\hbar k_{\text{F}}}{m\omega_0} \tag{50}$$

(ω_0 is the confining frequency). An alternative definition is given by $W_{\text{eff}} = n_{1\text{D}}/n_{2\text{D}}$. $n_{1\text{D}}$ can, for example, be estimated from the approximately linear section of the Landau plot. If one starts from Eq. (47), replaces the summation over ν by an integration, and takes into account that in the limit of high magnetic fields $\omega \approx \omega_{\text{c}}$, one obtains

$$n_{1\text{D}} \approx \frac{4}{3\pi\omega_0 m^*}\sqrt{\frac{2}{\hbar}}(eBN)^{3/2} \tag{51}$$

This formula describes a situation analogous to the depopulation of pure Landau levels in a two-dimensional electron system. Taking the corresponding relation between the Landau level index N and the sheet electron density of the underlying 2DEG:

$$n_{2\text{D}} = \frac{e}{\pi\hbar}NB \tag{52}$$

one obtains, as a final result for W_{eff},

$$W_{\text{eff}} = 2\pi\left[\frac{2\hbar}{3\pi m^*\omega_0}\right]^{2/3} n_{1\text{D}}^{1/3} \tag{53}$$

Note that the application of Eq. (50) or Eq. (53) implicitly assumes that the overall sheet electron density $n_{2\text{D}}$ is not affected by the nanofabrication process, which will be the case only for relatively wide channels. In general, the lateral confinement will raise the conduction band bottom also in ungated or nonetched regions of the quantum wire (cf. Fig. 8).

Several other definitions for effective wire widths are possible. They rely, for example, on the lateral extension of the wave function in the Nth magnetoelectric hybrid level [84]. All these definitions give values for W_{eff} that differ from each other, but nevertheless allow one to estimate the correct order of magnitude. A comparison of W_{eff}, as obtained from a model potential, with the experimentally determined value therefore allows one to decide if the applied model gives reasonable results.

It should be emphasized that not every quasi one-dimensional system will display a magnetosize maximum. For wires defined by split gates, for example, it was shown by

Thornton et al. [82] that the confining electric field gives relatively smooth side walls and the boundary scattering is predominantly specular. A magnetosize maximum is, therefore, only weakly established or completely missing. One, therefore, has to resort to alternative methods for the independent determination of the wire width, one of which will be briefly outlined in the following discussion.

4.2.2. Weak Localization and Interaction Correction to the One-Dimensional Conductivity

In Figure 16b, a magnetoresistance trace for very high applied back-gate voltage is shown. The number of subbands is now considerably reduced because of the low remaining electron density. At very low magnetic fields ($\leqslant 0.1$ T), the differential magnetoresistance is seen to be negative for these strongly confined wires. The effect is also observed in a less pronounced form in the 140-V trace of Figure 16a and is attributed to the *suppression of* 1*D weak localization* by a magnetic field. Note that this effect has nothing to do with the reduced backscattering observed beyond the magnetosize peak ($B > 0.3$ T). In the following, we sketch only the very basic idea underlying the phenomenon of weak localization and indicate briefly how its investigation may serve as a tool for the determination of relevant wire parameters. A detailed and clear account of the physics of weak localization can be found in [25] and the references cited therein. Our very brief introductory argumentation follows closely the exposition at the beginning of Section 6 of [25].

Weak localization is assumed to occur in the diffusive transport regime because of the phase coherence of electron waves that are propagating or elastically backscattered by an impurity. It can be shown that elastic impurity scattering does not affect the phase coherence length l_ϕ and that, in order to achieve phase randomization, inelastic scattering events are necessary [72, 85]. Bergmann [86] has given an intuitive interpretation of the quantum mechanical weak localization effect. Its treatment within the framework of the path integral formalism, which forms the basis of this qualitative interpretation, is discussed in some detail in [87]. Consider an electron propagating along a narrow channel from a starting point $\mathbf{r}$ to the point $\mathbf{r}'$. Quantum mechanically, one may assign a probability amplitude A_i to each path (labeled by an index i) the electron can take between the two points. The probability of finding the electron at $\mathbf{r}'$ after a time t is then given by the absolute square of the coherent sum of these amplitudes

$$P(\mathbf{r}, \mathbf{r}', t) = \left| \sum_i A_i \right|^2 = \sum_i |A_i|^2 + \sum_{i \neq j} A_i A_j^* \tag{54}$$

If a sequence of elastic scattering events is considered that brings an electron back to its starting point, $\mathbf{r}$ and $\mathbf{r}'$ coincide and the preceding sum is taken over closed Feynman paths. It may then be split up into a sum over time-reversed pairs of amplitudes A^+ and A^-, assigned to clockwise and counterclockwise propagation along the same closed path. Because of time reversal symmetry, the two amplitudes are equal and if they are added coherently, they give a probability for returning to the starting point (after several phase-conserving elastic scattering events) of $|A^+ + A^-|^2 = 4|A|^2$. Without phase coherence, if scattering gives rise to a purely classical diffusive motion, the squared probabilities have to be added noncoherently. This would give for the same process a classical return probability of $2|A|^2$. In other words, quantum mechanical phase coherence yields a return probability that is twice the probability of the corresponding classical noncoherent diffusion process. It may, therefore, be expected that this will give rise to an additional contribution to the conductivity of a low-dimensional semiconductor system, which exhibits quite large phase coherence lengths at low temperatures. This contribution has to be added to the classically obtained result

$$g_{1D} = g_{\text{Boltzmann}} + \delta g_{1D}^{\text{loc}} \tag{55}$$

where the sign of δg_{1D}^{loc} will be *negative*, because an enhanced *return* probability reduces the resulting conductivity.

On the other hand, if a weak magnetic field is applied, time reversal symmetry is broken. There will be appreciable flux through any closed electron trajectory, which gives rise to an Aharonov–Bohm like phase shift acquired along the corresponding Feynman paths. This phase shift will be different for clockwise and counterclockwise propagation along the closed paths. Different possible orbits will enclose different flux and after averaging over all possible closed trajectories (or Feynman paths) phase coherence will be destroyed at sufficiently large magnetic fields. This, consequently, leads to an effective suppression of the weak localization corrections to the 1D conductivity. It has been shown by Altshuler and Aronov [88] (see also [25, 89, 90]) that this magnetic field dependence of the weak localization effect can be taken into account by adding to the 1D conductivity a term of the form

$$\delta g_{loc}^{1D} = -\frac{e^2}{\pi\hbar}\left(\frac{1}{l_\phi^2} + \frac{W^2}{3l_m^4}\right)^{-1/2} \qquad \text{for } l_m, l_\phi \gg W \gg l \tag{56}$$

Here, W is the width of the channel, l is the mean free path, $l_m = \sqrt{\hbar/eB}$ is the magnetic length, and $l_\phi = \sqrt{D\tau_\phi}$, where D denotes the diffusion constant, is the phase coherence length. A first-principles justification of Eq. (56) can be found in the review article of Beenakker and van Houten [25].

The preceding relation is derived under two assumptions. First, the magnetic length l_m has to be larger than the effective width of the channel; otherwise, the localization is of a 2D nature. This requirement is usually well established at the low magnetic fields for which the suppression of weak localization is observed. The second condition requires that the width W be larger than the electronic mean free path l, which is usually not the case for the conventional high-mobility GaAs–AlGaAs samples used to study the effect. It has been shown by Beenakker and van Houten [90] that in the opposite regime $l \gg W$ one has to take into account the effects of boundary scattering on the phase accumulated along a closed trajectory enclosing a magnetic flux (flux cancellation effect). Equation (56) has then to be replaced by

$$\delta g_{loc}^{1D} = -\frac{e^2}{\pi\hbar}\left(\left[\frac{1}{l_\phi^2} + \frac{W^2}{3l_m^4}\right]^{-1/2} - \left[\frac{1}{l_\phi^2} + \frac{W^2}{3l_m^4} + \frac{2}{l^2}\right]^{-1/2}\right) \tag{57}$$

The weak localization correction turns out to be much weaker in the case of an unstructured 2DEG (which also finds its expression in the W dependence of δg_{loc}^{1D}), so that the negative magnetoresistance at low field becomes more and more pronounced as the 1D confinement becomes stronger. This is what is observed in parts a and b of Figure 16, where a pronounced negative differential magnetoresistance is observed only for the highest back-gate voltages and, hence, the narrowest channels.

The magnetic field dependence of the weak localization correction can be exploited to obtain wire parameters such as the width W and the phase coherence length l_ϕ. One simply fits one of the expressions Eq. (56) or Eq. (57), chosen appropriately to the sample geometry, to a plot of $G(B) - G(0) = 1/R_{xx}(B) - 1/R_{xx}(0)$ versus magnetic field, using W and l_ϕ as adjustable parameters. This is done in a field range where $l_m > W$ and the suppression of weak localization is clearly observed in the magnetoresistance. This method was applied for the first time by Thornton et al. [91] for a 15-μm-long channel defined by a split gate on top of a GaAs–AlGaAs heterojunction. We reproduce their results, obtained for various temperatures below 1 K, in Figure 18. The solid curves are fitted according to Eq. (56). It has been discussed if the "dirty metal" expression Eq. (56) for δg_{loc}^{1D} is suitable in this case, because the estimated mean free path is larger than the channel width. However, the extracted values for the different characteristic lengths give a more or less consistent picture, if one assumes that the damage induced by the electron beam lithography [74] has led to a

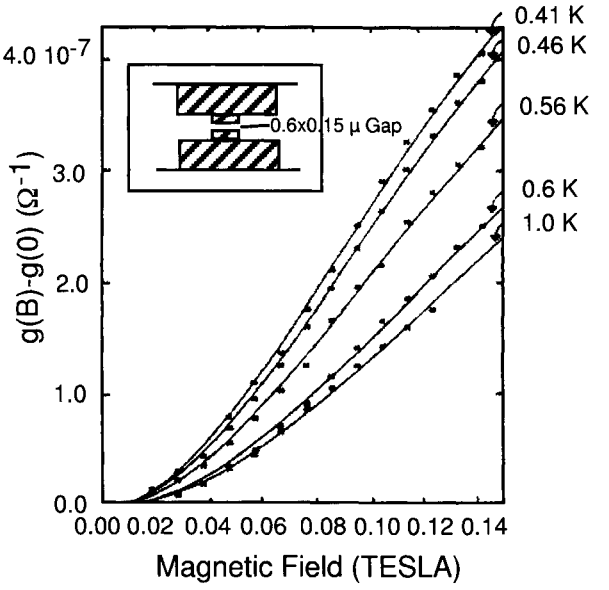


Fig. 18. Difference of magnetoconductance and zero-field conductance for a split-gate wire, measured at different temperatures. The sample geometry is shown in the inset. The solid lines stem from a two-parameter fit according to Eq. (56). (Source: Reprinted with permission from [91]. © 1986 American Physical Society.)

drastic reduction of the mean free path in the wire, compared to the value of the unstructured 2DEG. The values for the phase coherence length l_ϕ (200 nm or below) found from the fits shown in Figure 18 together with the condition $l_\phi \gg l$ underlying Eq. (56) would be consistent with a mean free path that certainly is not reduced below the estimated width of 50 nm, but could have reached the same order of magnitude.

An example of the application of the correct expression Eq. (57) to the low-field magnetoresistance in short and narrow channels defined by the shallow etching technique can be found, for example, in [92].

For the sake of completeness, it should be mentioned that there is another correction to the Boltzmann–Drude conductivity g_0 that is due to electron–electron interactions. Because both the weak localization and the interaction effects are relatively weak, they may to first order be taken into account as additive corrections to g_0:

$$g_{1D} = g_0 + \delta g_{1D}^{loc} + \delta g_{e-e} \tag{58}$$

The interaction correction has been estimated to be [93]:

$$\delta g_{e-e} = -\alpha \frac{e^2}{\pi\hbar}\sqrt{\frac{\hbar D}{2k_B T}} \tag{59}$$

which is valid if the thermal length $\sqrt{\hbar D/k_B T} < W$. α is a coupling constant that depends on the electron density and on the screening length in the system under consideration. Its magnitude is usually of order unity and in the commonly encountered experimental situations its sign is positive [25]. Electron–electron interactions thus reduce the conductivity of a narrow channel. The localization correction can be easily distinguished from the interaction correction in a magnetic field. As is obvious from Eq. (56) or Eq. (57), the former is completely suppressed already at very weak fields, whereas the latter is almost unaffected in this field regime. Theoretical considerations indicate that there is a small contribution to δg_{e-e} which is also sensitive to weak magnetic fields. But the main contribution to the conductivity correction reveals its magnetic field dependence only in strong fields. Usually, the weak-field-dependent part of δg_{e-e} is neglected, which makes the distinction between

the two corrections feasible [94]. If one wishes, one may use the T dependence of the interaction correction, determined from the magnetoconductance after subtraction of the weak localization correction, to estimate the diffusion constant D of the narrow channel [74, 91].

4.3. Magnetophonon Resonances in Quantum Wires

In 1961, Gurevich and Firsov [95] discovered that the quantization into Landau levels at high magnetic fields should lead to resonant longitudinal-optical (LO) phonon scattering of electrons between these equidistant Landau levels. As the LO phonons are assumed to be dispersionless in the interesting k-space region, resonant scattering between Landau levels is expected whenever the phonon energy equals an integer number of Landau levels:

$$\hbar\omega_{\mathrm{LO}} = N\hbar\omega_{\mathrm{c}} \tag{60}$$

This so-called magnetophonon effect has been shown to result in an oscillatory behavior of the magnetoresistance at temperatures high enough to ensure a sufficient population of the phonon states (usually at $T \geqslant 100$ K). Since then, magnetophonon resonances (MPRs) have been observed in a variety of semiconductor systems (for a review of the work until 1975, see [96]). In the bulk, MPRs have become a standard method for the determination of effective masses [97, 98] and proved to be a useful tool for the investigation of the conduction band nonparabolicity in ternary compounds for temperatures up to 400 K [99, 100]. After the first detection of MPRs in 2D systems [101], a wealth of phenomena was investigated also in 2D electron gases using the magnetophonon effect. Besides the determination of effective masses, an important subject that could be investigated using the magnetophonon effect in 2DEGs was the influence of the reduced dimensionality on the electron-phonon interaction [102–104].

As discussed previously, in quantum wires the energy spacing of magnetoelectric hybrid levels does not only depend on the magnetic field strength, but also on the 1D subband spacing induced by the lateral confinement. If, for example, parabolic confinement is assumed, the energy levels are calculated according to $E_n(B) = \hbar\omega(n + \frac{1}{2}) = \hbar\sqrt{\omega_{\mathrm{c}}^2 + \omega_0^2}(n + \frac{1}{2})$. This leads to a modification of the magnetophonon resonance condition Eq. (60) where now $\hbar\omega$ has to be used instead of $\hbar\omega_{\mathrm{c}}$. As a consequence, the magnetic field positions of the magnetophonon resonances should be shifted to slightly lower fields compared to the 2D case. Because this shift depends on the subband energy $\hbar\omega_0$, it is expected that MPRs can be used for subband spectroscopy of 1D quantum channels.

After a brief résumé of the relevant theoretical work on MPRs in quantum wires, it will be shown in the following that MPRs are indeed useful for the experimental determination of 1D subband energies. The obtained results for the sublevel spacings turn out to be different from the values extracted from low-temperature magnetic depopulation investigations. We discuss the reasons for this difference and show that it gives direct qualitative information on the shape of the wire potential.

4.3.1. Magnetophonon Resonances in Quantum Wires: Theory

The first theoretical investigation of MPRs in quasi one-dimensional electron systems was performed by Vasilopoulos et al. [105]. To determine the contribution to the magnetoconductivity due to electron-LO phonon scattering, they started from a quantum transport equation of the form

$$\sigma_{xx} = \frac{e^2}{2k_{\mathrm{B}}TV_0}\sum_{\zeta,\zeta'}\langle n_\zeta\rangle\big(1 - \langle n_{\zeta'}\rangle\big)W_{\zeta,\zeta'}\big(\langle\zeta|y|\zeta\rangle - \langle\zeta'|y|y\zeta'\rangle\big)^2 \tag{61}$$

which follows from a modification of the formalism developed to describe the magnetophonon effect in 2D systems [106]. Here, $\langle n_\zeta\rangle$ denotes the Fermi–Dirac distribution

function, y is the coordinate along the wire axis, and $W_{\zeta,\zeta'}$ is the usual Fröhlich-type transition probability between the two states ζ and ζ'. The $|\zeta\rangle$ denote the one-particle states of the 1D confined electrons. For their calculation, it is assumed that the confinement in the growth direction can be separated from the lateral confinement and that the latter is well described by the usual harmonic oscillator potential. The z component $\varphi_0(z)$ of the wave function is approximated by the well-known Fang–Howard trial functions $\varphi_0(z) = b_0^{3/2} z \exp(-b_0 z/2)$. Thus,

$$\langle r|\zeta\rangle = \psi_n\left(\sqrt{m\omega/\hbar}(x-\bar{x})\right) 1/\sqrt{L} \exp(ik_y y)\varphi_0(z)$$

where the harmonic oscillator functions, given in the paragraph following Eq. (11), have been used.

It turns out that in the case of relatively weak confinement ($\omega_0 < \omega_c$) σ_{xx} may be calculated analytically. The LO phonon–mediated magnetoconductivity consists of a contribution falling off monotonically with increasing B and an additional oscillatory part σ_{xx}^{osc}, which is given by [105]:

$$\sigma_{xx}^{\text{osc}} \propto \left(\frac{\omega_c}{\omega}\right) \frac{N_s^{1D} \tilde{l}_B^2}{k_B T \hbar\omega} \frac{\cos(2\pi\omega_{LO}/\omega) - \exp(-2\pi\Gamma_N/\hbar\omega)}{\cosh(2\pi\Gamma_N/\hbar\omega) - \cos(2\pi\omega_{LO}/\omega)} \tag{62}$$

A plot of this relation is shown in Figure 19. The total magnetoconductivity, including the monotonic part, is obtained from Eq. (62) by replacing the numerator $\cos(2\pi\omega_{LO}/\omega) - \exp(-2\pi\Gamma_N/\hbar\omega)$ by $\sinh(2\pi\Gamma_N/\hbar\omega)$. ω is again the combined "renormalized" frequency $\omega = \sqrt{\omega_0^2 + \omega_c^2}$, Γ_N is the magnetic field–dependent width of the Nth magnetoelectric hybrid level. $\tilde{l}_B^2 = \hbar/m^*\omega$ is a modified magnetic length and, finally, ω_{LO} is the frequency of the LO phonons, which is assumed to be given by its bulk value.

In the case of weak confinement the oscillatory part of the magnetoconductivity is thus described by a series of exponentially damped cosine oscillations just as it is well known from the magnetophonon theory in the bulk and in 2D systems [107, 108]. Whenever the resonance condition $\hbar\omega_{LO} = \nu\hbar\omega$ with integer ν is satisfied, a maximum in the magnetoconductivity is observed (cf. Fig. 19). The main effect of a weak 1D confinement on the magnetoconductance is thus simply a shift of the resonant maxima in σ_{xx} to smaller magnetic fields as compared to the resonance condition [Eq. (60)], valid for bulk and 2D systems.

This first investigation of the 1D magnetophonon effect has been followed by several improvements of the theory, mainly concerning the extension to the case of arbitrary confinement strength. Mori et al. [109] pointed out that, in the case of strong confinement, the influence of the confining potential on the electron motion may not be neglected. Employing a Green's function approach to the general Kubo formula and using the same parametrization of the confinement as before, they were able to show that, in addition to the weak confinement expression already given by Vasilopoulos et al. [105], there is a second, qualitatively different contribution to the 1D magnetoconductance. To understand the difference between the two contributions, one may resort to a simple classical picture. Consider a wide, weakly confined quantum wire. In sufficiently strong magnetic fields, a considerable part of the electrons will be in Landau level–like states. Classically, they are localized on circular cyclotron orbits. LO phonon scattering will lead to hopping motion between these localized orbits and, therefore, to an enhancement of the electron mobility. This is why maxima occur at resonance in the magnetoconductance as indicated in Figure 19. On the other hand, if the confinement is strong and the wire narrow, a considerable fraction of electrons will be in edge states corresponding to skipping orbits propagating along the wire. The LO phonons will scatter electrons off their propagating modes, thereby reducing their mobility. This is expected to lead to resonant minima in the magnetoconductance. In Figure 20, the second derivative of σ_{xx}, calculated according to the model of Mori et al. [109], is plotted for the two cases of low and high confinement energy.

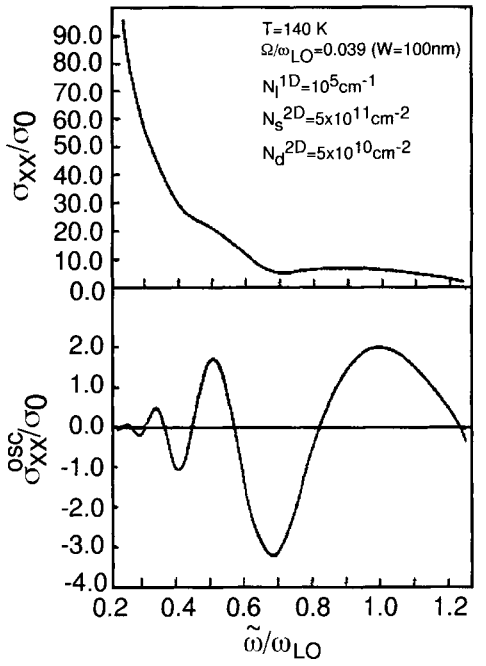


Fig. 19. Top: Magnetoconductivity in units of $\sigma_0 = e^2/hk_{LO}$ as a function of the combined frequency ω ($=\widetilde{\omega}$ in the figure). The parameters used in the calculation are also shown. Ω is the confining frequency of the parabolic potential; N_d^{2D} is the depletion charge density, needed for the calculation of Γ_N. Bottom: Oscillatory part σ_{xx}^{osc} according to Eq. (62). (Source: Reprinted with permission from [105]. © 1989 American Physical Society.)

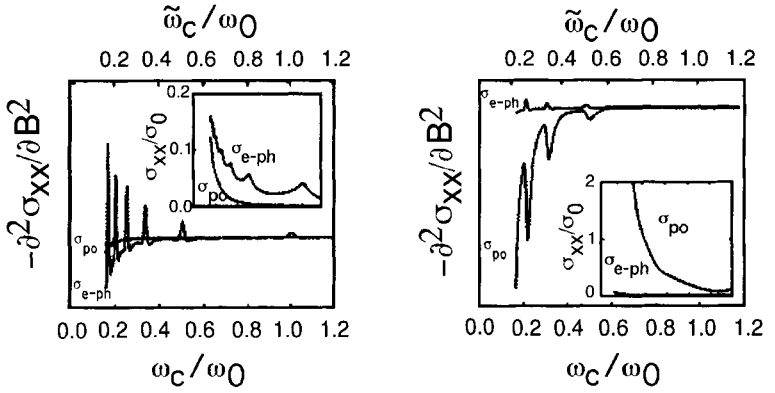


Fig. 20. Calculated second derivative of the two contributions to the magnetoconductivity for weak (left) and strong (right) confinement. σ_{po} denotes the contribution corresponding to the skipping motion of electrons along the wire boundaries, σ_{e-ph} is due to electrons without interaction with the channel boundaries. The traces are calculated for $T = 100$ K, a level broadening Γ of 1 meV, and a confining frequency of the parabolic potential of 1 meV (left) and 5 meV (right). The insets show the corresponding underived quantities in units of $\sigma_0 = ne^2/\alpha\omega_0 m^*$, α being the Fröhlich coupling constant. In the figure, ω_0 is the LO phonon frequency, ω_c is the cyclotron frequency, and $\widetilde{\omega}_c$ is again the combined frequency of the magnetoelectric hybrid levels. (Source: Reprinted with permission from [109]. © 1992 American Physical Society.)

These results have been confirmed theoretically by Ryu and O'Connell [110, 111], who used a different quantum transport approach [112] to describe the influence of resonant LO phonon scattering on the magnetoconductance. Their model calculations also assume a parabolic confinement potential and again give two contributions to the magnetoconduc-

tivity, the first being almost identical to the result of Vasilopoulos et al. [105]. The second term was attributed to a "nonhopping" contribution to the electron conduction, which is qualitatively reminiscent of Mori's skipping orbit motion term.

4.3.2. *Magnetophonon Resonances in Quantum Wires: Experimental Results*

Regarding the nature of the magnetic depopulation experiments discussed previously and the methods of calculating the subband spacing from the resulting Landau plots, it is clear that it is necessary to have a sufficient number of occupied subbands in order to obtain reliable results for E_0 and n_{1D}. It is the main advantage of the magnetophonon method of subband spectroscopy that the number of occupied subbands is largely irrelevant for its application. It is, therefore, a transport characterization technique for quantum wires with low carrier densities or relatively large subband spacing. It could even be used to characterize quantum channels in or at least very near to the quantum limit where only one 1D subband is occupied (provided, of course, the subband spacing is substantially smaller than $\hbar\omega_{LO}$).

However, it has been shown experimentally [103] and theoretically [108] in the case of MPRs in 2D systems that the oscillation amplitude of the magnetoresistance strongly depends on various scattering mechanisms such as scattering from charged donor impurities. These scattering mechanisms influence the broadening of the Landau levels or magnetoelectric hybrid levels in 2D and 1D, respectively. The experimental results [113, 114] indicate that if the influence of charged donors is reduced by low total doping and large spacer layers of the underlying heterostructures, a much more pronounced magnetoresistance oscillation is obtained at high temperatures. Consequently, the low-density regime is the natural field of application of the magnetophonon effect for the characterization of quantum wires both because this regime is not readily accessible to magnetic depopulation measurements and because the magnetophonon effect is more easily resolved. On the other hand, one has to be aware of the considerable amount of unwanted scattering sources that are introduced by any nanofabrication process. The shallow etching method, in particular, introduces considerable side-wall roughness in the narrow channels. This, in turn, will reduce the amplitude of the high-temperature magnetoresistance oscillations and be disadvantageous for their resolution.

For this reason the following experiments discussed briefly were conducted on a set of quantum wires obtained by very shallow etching on a low density, high mobility heterostructure. The most prominent features of the sample material used in the experiments are the low integral doping and the relatively wide spacer layer. Due to these features very shallow etching is sufficient to obtain appreciable 1D confinement, keeping the amount of sidewall roughness within tolerable limits. Some details of the sample structure are given in the caption of the following Figure 21. This figure shows a set of typical magnetoresistance traces, recorded at $T = 100$ K and revealing pronounced oscillatory structure due to the magnetophonon effect.

Figure 22 shows two examples of the oscillatory part of the magnetoresistance ΔR_{osc}, which were obtained from similar data as those shown in Figure 22 after subtraction of a monotonous background resistance. The lower trace corresponds to a sample (labeled "1" in the following), where slightly deeper etching is done in comparison to sample "2". The two samples are otherwise identical. The $R(B)$ traces shown in Figure 21 were obtained for sample "2". Note that for the more shallow wires of sample "2" the oscillation amplitude is almost an order of magnitude greater than for sample "1". On the other hand, the oscillation of sample "1" does not seem considerably broadened as compared to the ΔR_{osc} of the other sample. The most interesting feature of the traces of Figure 22 is that they seem to be "phase-shifted" with respect to each other.

This phase shift together with the large reduction of the oscillation amplitude observed for sample "1" indicates that for the more strongly confined wires of this sample one en-

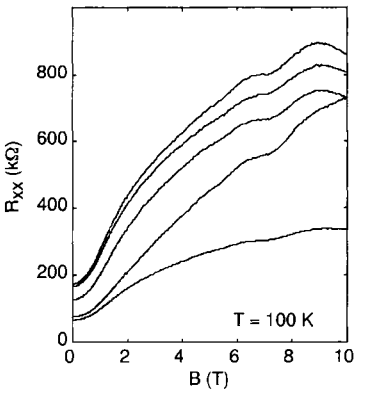


Fig. 21. Typical magnetoresistance data measured on an array of shallow etched quantum wires at $T = 100$ K. The various traces correspond to sample "2" for different electron densities (see text). The underlying heterojunction consists of 100 Å GaAs cap undoped, followed by 300 Å $Al_{0.4}Ga_{0.6}As$, doped to 2×10^{18} cm^{-3}, and 600 Å undoped $Al_{0.4}Ga_{0.6}As$ spacer.

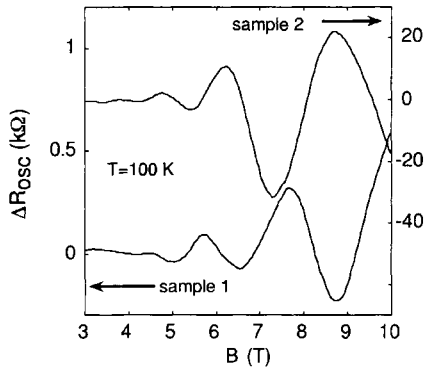


Fig. 22. Oscillatory part of the magnetoresistance ΔR_{osc} plotted for two different samples. The curves are obtained after subtraction of the monotonic background from the $R(B)$ traces, some examples of which are shown in Figure 21. Sample "1" (bottom curve) was slightly deeper etched than sample "2" (top curve). This slight increase of the etching depth leads to a reduction of the oscillation amplitude by almost an order of magnitude as well as to a drastic "phase shift" of the oscillation. Note the different y-axis scales valid for the two traces.

counters a situation where there is a crossover between the two transport regimes discussed in the previous section. For sample "1" scattering off skipping orbits seems to be the dominant source that influences the magnetoresistance. Therefore one observes resistance *maxima* at resonance whereas the other sample "2" displays minima at resonance. It turns out that this assumption leads to a consistent explanation of the features of ΔR_{osc} observed in Figure 22.

To analyze the experimental data quantitatively, one assumes a parabolic confinement $V(x) = \frac{1}{2}m^*\omega_0^2 x^2$ for the quantum wire. Again, x is the direction perpendicular to the wire and m^* is the electron effective mass (frequently called the *polaron mass* in the context of MPR). In a perpendicular magnetic field, the bottoms of the magnetoelectric hybrid levels are quantized according to $E(B) = \hbar\omega_{\text{eff}}(n + \frac{1}{2})$ with $\hbar\omega_{\text{eff}} = \sqrt{(\hbar\omega_c)^2 + E_0^2}$ and $E_0 = \hbar\omega_0$ being the 1D subband spacing.

As discussed before, one assumes that the weak confinement case is valid for sample "2". The resonance condition

$$N\hbar\omega_{\text{eff}} = \hbar\omega_{\text{LO}} \tag{63}$$

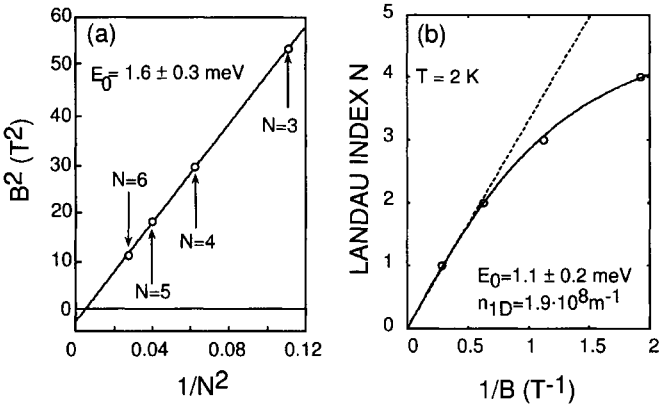


Fig. 23. (a) Plot of the squared magnetic field position of the resonance minima in $\Delta R_{\rm osc}$ versus $1/N^2$, obtained from the data shown in Figure 22 for sample "2". The corresponding value of the subband spacing obtained from the intersection of the resulting straight line with the B^2-axis is 1.6 meV. (b) Landau Plot obtained from magnetic depopulation data for the same sample and electron density as in (a). The solid line represents a fit using a harmonic oscillator model, which gives a subband spacing of 1.1 meV.

thus applies to the minima in the magnetoresistance oscillation $\Delta R_{\rm osc}$ [109]. For sample "1" this condition is related to the resonant maxima in $\Delta R_{\rm osc}$.

Using $E_{\rm LO} = \hbar\omega_{\rm LO}$, this resonance condition may be rewritten as follows:

$$B^2 = \left(\frac{m^*}{e\hbar}\right)^2 \frac{E_{\rm LO}^2}{N^2} - \left(\frac{m^*}{e\hbar}\right)^2 E_0^2. \tag{64}$$

According to this equation, the B^2 values, corresponding to the resonant extrema in $\Delta R_{\rm osc}$, plotted versus $1/N^2$ should lie on a straight line. Its slope is a measure of the effective mass of the confined electrons, whereas its intersection with the B^2-axis is proportional to the squared subband spacing E_0. It should be emphasized that this simple relationship is only valid if the confining potential can be approximated by the harmonic oscillator form given above.

Figure 23a shows the positions of the resonant minima in $\Delta R_{\rm osc}$ taken from the upper curve in Figure 22 (corresponding to sample "2"). The solid straight line stems from a fit of the data according to Eq. (64), using the LO phonon energy for bulk GaAs, $E_{\rm LO} = 36.6$ meV. The simple parabolic model potential is seen to describe the experimental data quite well. As parameters of the fit one obtains a magnetophonon effective mass of $(0.069 \pm 0.007)m_e$ and a subband spacing E_0 of (1.6 ± 0.3) meV. The value for E_0 can now be compared to the corresponding low temperature value, obtained from a magnetic depopulation measurement on the same sample at $T = 2$ K. The resulting Landau plot is shown in Figure 23b. The deviation of the plot from a straight line clearly shows the 1D behavior of the laterally confined electrons. The solid line interpolates between calculated points fitted to the data according to the model of Berggren et al. [75] (see Section 4.1.1), which also assumes a parabolic confinement potential. The resulting subband spacing is $E_0 = (1.1 \pm 0.2)$ meV, which is somewhat smaller than the corresponding high temperature subband energy.

When one changes the carrier density of the quantum wires, for example by illuminating the samples with a red light emitting diode, one obtains the subband spacing as a function of the 1D carrier density as shown in Figure 24. Solid circles correspond to data obtained from an analysis of the MPR signal of sample "1". Open diamonds represent the same data for sample "2". The open circles were obtained from magnetic depopulation experiments on sample "2". Figure 21 shows a set of typical magnetoresistance traces measured for varying carrier density of sample "2". To arrive at the plot of Figure 24 the electron density

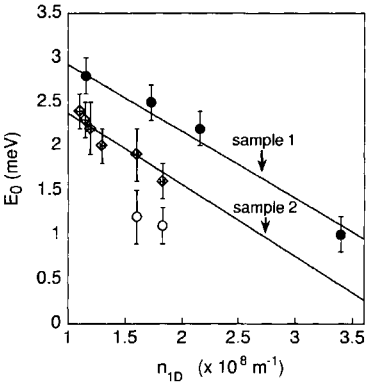


Fig. 24. Subband spacing as a function of the 1D electron density for the two samples considered in the text. Solid circles: Magnetophonon results for sample "1". Open diamonds: Magnetophonon results for sample "2". Open circles: Subband energies obtained by magnetic depopulation from sample "2". The increase of E_0 with decreasing n_{1D} is attributed to screening effects, as discussed in [115].

was determined from the linear part of the low temperature Landau plots according to Eq. (49). Details of the experimental procedure can be found in [114] and [115]. Note that in order to determine the low temperature subband spacing from the magnetic depopulation data it is necessary that the number of occupied subbands in the wires is large enough for the usual evaluation methods to be applicable. This is the case only for sample "2" at relatively high carrier densities. In all cases where a direct comparison was possible, the low temperature subband spacing turned out to be systematically smaller than the high temperature value by 30–50%.

Before giving an explanation of this apparent difference, it is worth mentioning that both in the theoretical and the experimental analysis the LO photon energy of 36.6 meV of bulk GaAs is assumed. Note that there is experimental evidence that the presence of the GaAs–AlGaAs interface leads to a modification of the photon energies. From a combination of cyclotron resonance and magnetophonon resonance experiments on various GaAs–AlGaAs heterojunctions, Brummell et al. [102] found that the LO phonon energy appears to be reduced by approximately 5% to 34.8 meV. However, this possible slight modification of the LO phonon energy has no influence on the above analysis. The reason for this insensitivity is that the statistical error of the fit in Figure 23a is, in spite of the excellent correlation to the data, not very much smaller than approximately 10%. This experimental error far exceeds that introduced by any uncertainty in the phonon energies.

To explain the difference in the E_0 values obtained at low and high temperatures, respectively, we first note that the thermal rearrangement of the electrons among the 1D sublevels at elevated temperatures cannot account for the observed difference. If this rearrangement is considered in a self consistent calculation, it can be shown [116] that it will indeed lead to a slight enhancement of the subband spacing. However, these changes in E_0 are small (less than 10%) unless one assumes considerable recharging and reordering of the electrically active impurities, which is not a very realistic assumption.

It rather turns out that the observed difference can be consistently explained if one takes into account that the actual confinement potential for shallow etched quantum wires is not exactly parabolic but sinusoidal. To demonstrate this, we model the experimental situation by choosing a one-dimensional potential of the form $V(y) = V_{\mathrm{mod}}(\cos(2\pi y/w) + 1)/2$ that best approximates the self-consistently calculated potential for a shallow etched wire (cf. Fig. 6). Using this model potential, we calculate both the magnetoelectric confinement and the corresponding energy states as a function of magnetic field, simply using the one-dimensional Schrödinger equation and the discretization schemes described in Section 2.

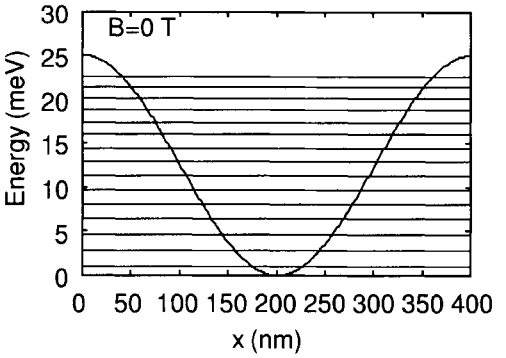


Fig. 25. Cosine-shaped model potential with a period of 400 nm and a modulation amplitude of 25 meV. The energy levels are calculated for zero magnetic field. Because of the shape of the potential the subband spacing decreases with increasing energy.

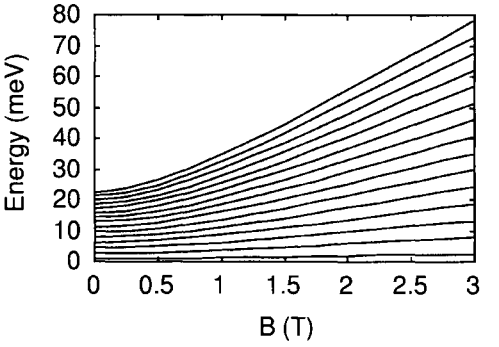


Fig. 26. Magnetoelectric subband edges as a function of magnetic field calculated for the cosine potential shown in Figure 25.

Figure 25 shows the energy levels for a cosine potential with $V_{\text{mod}} = 25$ meV and a period of 400 nm for zero magnetic field. To calculate their magnetic field dependence, one adds the magnetic confinement according to

$$V(y) = V_{\text{e}}(y) + V_{\text{m}}(y) = \frac{V_{\text{mod}}}{2}\left[\cos\left(\frac{2\pi}{w}\right) + 1\right] + \frac{1}{2}m^*\omega_{\text{c}}^2(x - x_0)^2 \qquad (65)$$

To cover the essential features of a magnetophonon or magnetic depopulation experiment, it is sufficient to consider the positions of the sublevel bottoms, that is, to calculate the magnetic field dependence of the 1D subbands setting the center coordinate $x_0 = 0$. The resulting B dependence of the hybrid level energies is shown in Figure 26.

Two main features are interesting. First, the subband spacing of the high-lying subbands is obviously smaller than that of the low-lying levels of the cosine potential. This is important when considering the information on the subband spacing E_0 obtained from the magnetic depopulation method. E_0 is found from that part of the Landau plot where it deviates from a straight line. That is, the main information is obtained from those high-lying subbands that are depopulated at low magnetic fields. If the Landau plot is fitted with a model curve calculated from a simple parabolic potential (Section 4.1.1), one has to be aware that this will only reproduce the subband spacings for the high-lying levels.

Numerically, one can simulate this situation by determining the magnetic field positions, where the magnetoelectric subbands cross the Fermi level. The resulting Landau plot is then evaluated using the simple harmonic oscillator model. In fact, performing this procedure for the model potential of Figure 25, we obtain an energy spacing of 1.35 meV, which excellently reproduces the subband spacing of the high-lying subbands (1.3 meV)

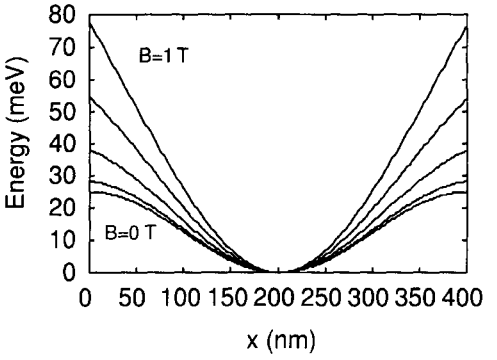


Fig. 27. Sum of the electrostatic and magnetic confinement potentials in the range between $B = 0$ T and $B = 1$ T, plotted in steps of 0.25 T. The parameters of the cosine potential are the same as in Figure 25.

in the cosine-shaped potential. Note that, in the numerical simulation of the magnetic depopulation experiment, the Fermi level has to be calculated as a function of magnetic field, taking into account the one-dimensional density of states. Because this is easily achieved only for the harmonic oscillator potential but computationally very expensive for an arbitrarily shaped electrostatic potential, one may assume an approximately constant Fermi level at low magnetic fields. As can be seen from Figure 14, this assumption is justified at low magnetic fields. The oscillations of the Fermi level are relatively small there and the error introduced by assuming a constant E_F will be negligible.

We now consider the situation encountered in a magnetophonon resonance experiment. Because of the strong damping of the magnetophonon (MP) magnetoresistance oscillations with decreasing magnetic field, it is clear that, in contrast to the magnetic depopulation experiment, the relevant information is drawn from the structure in $R_{xx}(B)$ observed at *high* magnetic fields ($B > 4$ T). As can be seen from Figure 27, the magnetic confinement strongly dominates over the electrostatic one already at fields of 2 T. The resulting total potential is parabolic to a good approximation with the nonparabolic parts of the superposed electrostatic potential entering only as a weak perturbation. At the high magnetic fields at which MP resonances are observed (cf. Fig. 22), only the lowest subbands are occupied. Because the transition probability between the subbands at elevated temperatures is weighted by a Boltzmann factor, resonant LO phonon scattering mainly occurs between the lowest subbands. Hence, what is probed by the magnetophonon effect is the subband spacing of those levels lying near the bottom of the cosine confinement potential, which is larger than that of the high-lying levels. Quantitatively, we demonstrate this by the following considerations. In analogy to the previous simulation of the magnetic depopulation experiment, we calculate those magnetic field positions where an integer number (N) of subbands equals the LO phonon energy (36.6 meV) and plot their squared values against the inverse-squared N (see Fig. 28). The solid straight line in the figure is a fit according to Eq. (64), ignoring all nonparabolic contributions to the electrostatic confinement. As can be seen from Figure 28, the parabolic model fits perfectly with the simulated data points. The values for the effective mass and the subband spacing obtained from the fit are $m^* = 0.070$ and $\Delta E = 2.0$ meV, respectively. The latter reproduces almost exactly the subband spacing at the bottom of the underlying cosine potential.

To summarize these considerations, one may state that magnetic depopulation experiments always probe the subband energies at the Fermi energy, whereas magnetophonon resonance experiments are sensitive to the sublevels near the bottom of the confinement potential. This not only explains the experimentally observed difference between the energy values determined by the two methods. It also shows that the combination of the two methods provides in a simple manner direct information on the actual shape of the underlying confinement potential, in that it allows us to decide immediately if the potential is

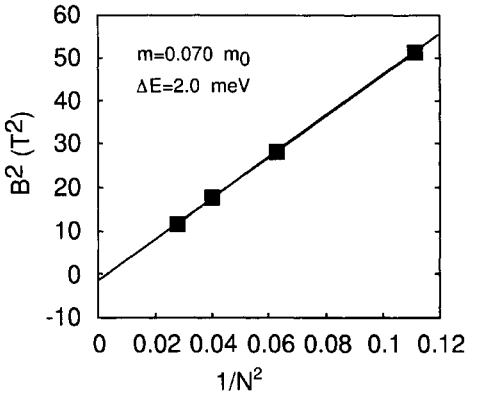


Fig. 28. Simulated magnetophonon resonance experiment for a wire with cosine-shaped confinement. The squares correspond to those magnetic fields, where an integer number of the low-lying subbands fits the LO phonon energy. The straight line stems from a fit using a simple harmonic oscillator potential. The subband spacing extracted from the intersection of the straight line with the B^2 axis is $\Delta E = 2.0$ meV. This value reproduces the subband spacing at the bottom of the cosine potential almost exactly. The mass value obtained from the slope of the line is $m^* = 0.070 m_e$.

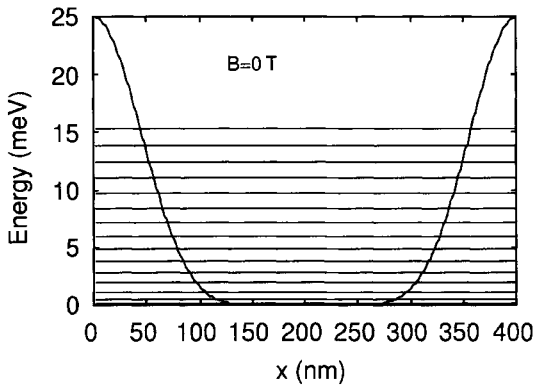


Fig. 29. Confinement potential according to Eq. (66) plotted together with the calculated energy levels at zero magnetic field.

cosine or square well like. Consider as an example a potential calculated according to

$$V(y) = \frac{V_{\text{mod}}}{2}\left(\cos\left(\frac{2\pi y}{w}\right) + 1\right)^4 \tag{66}$$

which is shown in Figure 29 together with the corresponding subbands. This model potential exhibits a flat bottom and has relatively steep side walls as is typical for a split-gate wire at high carrier densities. Inversely to the previous case of a simple cosine potential, the upper subbands now have a higher spacing than the low-lying ones. Again, the simulation of the magnetic depopulation and the magnetophonon resonance experiment shows that the former will give the higher subband spacing of the top levels, the latter that of the bottom levels.

Finally, it is worth noting that the estimate of the 1D carrier density from a magnetic depopulation experiment should be interpreted with some care. The application of the standard parabolic model to the interpretation of a Landau plot also yields the 1D carrier density of the wire [cf. Eq. (49)]. If the "true" confinement is sinusoidal, however, the so-obtained n_{1D} slightly underestimates the actual value, because the procedure leading to Eq. (49) presupposes that the subband spacing appropriate for the high-lying levels is valid for all occupied subbands.

5. WEAKLY AND STRONGLY MODULATED SYSTEMS

A practical problem that sometimes arises when one fabricates an array of shallow etched quantum wires is that one needs to know whether one has really achieved a system of separated quantum wires or only imposed a periodic potential modulation on the underlying 2D electron gas. Also, the variation of the potential amplitude with varying etching depth or gate voltage is sometimes of interest for theoretical or technological reasons. As will be shown in the following, the magnetoresistance measured *perpendicular* to the equipotential lines of a lateral potential modulation contains a wealth of information on the relevant potential parameters. Depending on whether the modulation is only weak, that is, the potential amplitude V_0 is much smaller than the Fermi energy, or whether V_0 is no longer negligible in comparison to E_F, different characteristic features of the magnetoresistance can be used for the characterization of the potential. This will be the topic of the present section. Because modulated systems are of great interest not only from the point of view of potential properties, they have been extensively investigated and reviewed in the past (see, e.g., [84]). We will consider these systems only under the aspect of obtaining insight into the shape and magnitude of the periodic potential. In order to do this, we restrict our discussion to the very simplest (semiclassical) model considerations commonly employed for the explanation of the observed effects.

We start with the case of a weakly modulated system. A weak potential modulation can be realized by different techniques such as *very* shallow etching, by application of small voltages to a grating gate, or even by brief illumination with two interfering laser beams [19]. The magnetoresistance $\rho_\perp$ measured perpendicular to the equipotentials of the so-introduced modulation exhibits a number of characteristic low-field oscillations (see Fig. 30). The oscillations are periodic in $1/B$, just as the Shubnikov–de Haas oscillations of the unstructured 2DEG, but, as the different field scale indicates, of an obviously different origin. After the first observation of these oscillations [19], which have later on been termed *commensurability oscillations*, several equivalent models were developed to explain their origin [117–120]. In the following, we give a very brief account of the semiclassical model of Beenakker [117], because it facilitates an intuitive understanding of the underlying physics. Its basic ideas can also be used to explain the special features occurring if the modulation height is gradually increased.

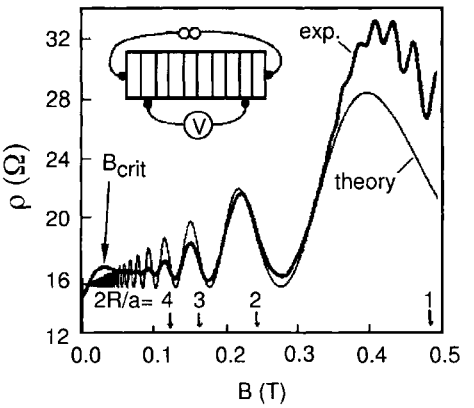


Fig. 30. Longitudinal magnetoresistance of a weakly modulated 2DEG with current flowing perpendicular to the equipotential lines (see inset). The thick solid line represents data from Weiss et al. [19], showing commensurability oscillations below $B = 0.4$ T and the onset of Shubnikov–de Haas oscillations for $B \geqslant 0.4$ T. The thin solid line is calculated from the semiclassical guiding center drift resonance model of Beenakker [117]. The vertical arrows indicate those magnetic field values where the cyclotron diameter matches the period of the grating. The commensurability oscillations are phase shifted relative to these values by $\pi/4$. B_{crit} is the critical field for magnetic breakdown and will be discussed later in this section. (Source: Reprinted with permission from [25].)

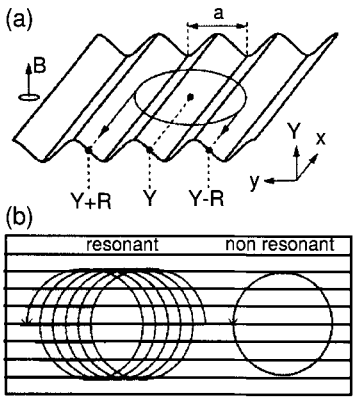


Fig. 31. Illustration of the electron motion in a weakly modulated 2DEG with a magnetic field applied perpendicular to the electron gas. (a) Potential landscape with cyclotron orbit. (X, Y) are the coordinates of the orbit center (guiding center); $Y \pm R$ are the extremal points, where the orbit center acquires a net $\mathbf{E} \times \mathbf{B}$ drift. (b) Numerically calculated cyclotron orbits in a sinusoidal potential. Horizontal lines indicate the equipotential lines of the periodic modulation. The figure shows a resonant orbit at $2R/a = 6.25$ and a nonresonant one at $2R/a = 5.75$ with negligible drift. (Source: Reprinted with permission from [25].)

Figure 31 shows the classical cyclotron trajectory of an electron moving in a weak periodic potential modulation with a magnetic field applied perpendicular to the plane of the 2DEG. (X, Y) denotes the center of the cyclotron orbit and $R = \hbar k_F/eB$ is the cyclotron radius. Because the modulating potential is assumed to be very weak, it can be considered as a small perturbation that leaves the cyclotron orbits essentially undistorted. The simultaneously present electric ($\mathbf{E} = -\nabla V_{\text{mod}}(y)$) and magnetic fields classically give rise to an $\mathbf{E} \times \mathbf{B}$ drift of the center of the otherwise unaffected cyclotron orbit. Because at low magnetic fields the electronic orbit extends over many periods of the potential modulation, only the drift acquired at its extremal points $Y \pm R$ will be essential. This is depicted in Figure 31b. If the position and radius of the orbit are such that the drift acquired at opposite extremal points adds up constructively, one speaks of a guiding center drift resonance. Off resonance, the drift acquired at one extremal of the orbit will cancel that at the other extremal, leading to zero net drift. At resonance, the electron drift, which is directed parallel to the equipotential lines, will lead to a maximum in $\rho_\perp$. An off-resonant, stationary orbit accordingly corresponds to a resistance minimum. This qualitatively accounts for the oscillatory behavior shown in Figure 30. The preceding ideas can be integrated into a rigorous solution of the semiclassical Boltzmann equation. If the strength of the potential modulation is characterized by the parameter $\varepsilon \equiv e\overline{V}/E_F$, the magnetoresistance is then obtained to second order in ε:

$$\frac{\rho_{yy}}{\rho_0} = 1 + \frac{1}{2}\left(\frac{2\pi}{a}\varepsilon l\right)^2 \frac{J_0^2(2\pi R_c/a)}{1 - J_0^2(2\pi R_c/a)} \tag{67}$$

Here, ρ_0 is the usual semiclassical expression for the longitudinal magnetoresistivity, a is the period of the potential modulation, and $l = v_F\tau$ is the mean free path. J_0 is a Bessel function. The exact analysis gives the condition $2R_c/a = n - 1/4$ for a resistance minimum and $2R_c/a = n + 1/4 - \text{order}(1/n)$ for a maximum. In the limit $2\pi(R_c/a) \gg 1$, Eq. (67) can be shown to reduce to the following frequently quoted expression for $\rho_\perp$ [117]:

$$\rho_\perp = \rho_0\left(1 + 2\varepsilon^2\left(\frac{l^2}{aR_c}\right)\cos^2\left(2\pi\frac{R_c}{a} - \frac{\pi}{4}\right)\right) \tag{68}$$

Basically, the same result can also be derived directly from the simple classical picture outlined previously [117]. Note that the $\overline{V}$ entering the definition of ε is a root mean square

average of the modulation potential amplitude. If, for example, a sinusoidal modulation $V_{\mathrm{mod}}(y) = V_0 \cos(2\pi y/a)$ is considered, one has $V_0 = \sqrt{2\overline{V}}$.

The guiding center drift oscillations have also been explained on purely quantum mechanical grounds [118, 119]. If the weak periodic modulation $V(x)$ is treated by simple first-order perturbation theory, it is easily shown that this leads to a widening of the Landau levels to Landau bands according to $E_N(k_y) = (N+1/2)\hbar\omega_c + \langle Nk_y|V(x)|Nk_y\rangle$. The kets in the matrix element denote the Nth Landau state with center coordinate $x_0 = \hbar k_y/eB$ of the unperturbed system. If the matrix element is replaced by the classical expectation value, which can be done because high numbers of Landau levels are occupied at low fields, an expression very similar to Eq. (68) can be derived for $\rho_\perp$.

The result of the semiclassical calculation is shown in Figure 30 (thin solid line). A parameter value $\varepsilon = 0.015$ is assumed to reproduce best the corresponding experimental trace. The most interesting feature of Eq. (68) is the phase shift of $\pi/4$ appearing in the argument of the cosine term. The value of this phase shifts depends on the shape of the modulating potential and equals $\pi/4$ only if a simple sinusoidal potential is assumed. The perfect agreement with the phase shift of the experimental trace indicates that this assumption describes the actual shape of the potential very well.

Another important source of information on the potential parameters is the positive magnetoresistance at very low magnetic fields (denoted by the arrow labeled B_{crit} in Fig. 30). This property of $\rho_\perp$ is clearly not accounted for by the strongly simplified classical picture of undistorted cyclotron orbits undergoing a resonant drift. Beton et al. [121] investigated this positive magnetoresistance systematically by using a grating gate geometry similar to that used by Brinkop et al. [79] (cf. Fig. 12), which allowed them to vary the height of the modulating potential. We reproduce their results in Figure 32, where several magnetoresistance traces are shown for different voltages applied to the modulating gate.

As shown in the figure, with increasing gate voltage and thus increasing potential amplitude, the positive magnetoresistance is significantly enhanced and extends over a larger field range. Simultaneously, the number and peak-to-valley ratio of the commensurability oscillations are reduced. This behavior is easily explained by a modification of the simple

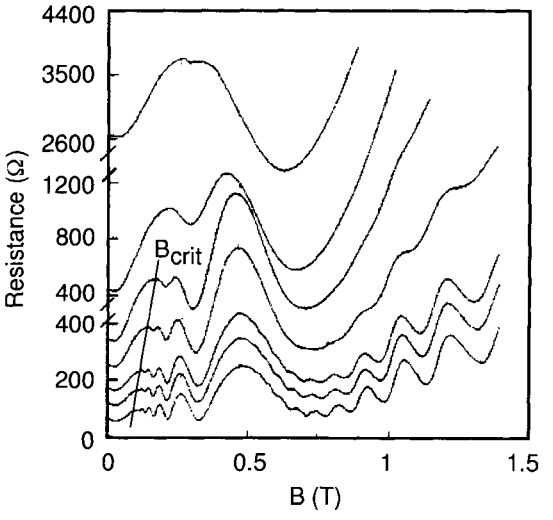


Fig. 32. Magnetoresistance traces measured at 2 K for different top-gate voltages. From top to bottom, $V_G = -1.0, -0.8, -0.6, -0.5, -0.3, -0.2$, and 0 V. The curves are displaced for clarity. The period of the modulation potential was $a = 300$ nm. B_{crit} is the critical field for magnetic breakdown (see also Fig. 30). For $B \geqslant 0.5$ T the usual Shubnikov–de Haas oscillations are observed. (Source: Reprinted with permission from [121]. © 1990 American Physical Society.)

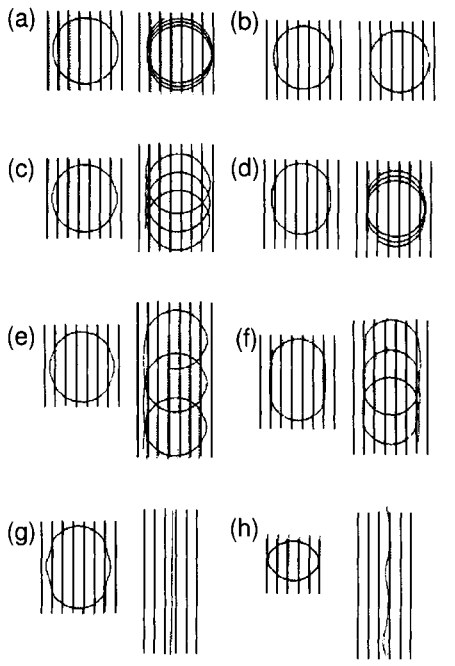


Fig. 33. Numerically calculated classical electron orbits in a periodic potential with a magnetic field applied perpendicular to the 2DEG. The straight lines symbolize the equipotential lines of the periodic potential. The orbits (a), (c), (e), and (g) correspond to $2R_c/a = 6.25$; the orbits (b), (d), (f), and (h) correspond to $2R_c/a = 5.75$. The left-hand orbit of each partial figure is symmetric with respect to the periodic potential; the right-hand one is positioned asymmetrically with respect to the equipotential lines. The values of the parameter $\varepsilon = eV_0/E_F$ are (a), (b) 0.01; (c), (d) 0.05; (e), (f) 0.09; and (g), (h) 0.15. (Source: Adapted from [121].)

classical picture outlined previously. The main ideas become clear from Figure 33, which shows numerically calculated classical trajectories for different potential heights (characterized by the parameter ε defined previously). The left-hand set of orbits is calculated for $2R_c/a = 6.25$, which, in the case of a weak modulation, would correspond to a maximum of $\rho_\perp$; the right-hand orbits were obtained for $2R_c/a = 5.75$, corresponding to a resistance minimum.

If the potential amplitude is increased, the corresponding electric field consequently enhances the $\mathbf{E} \times \mathbf{B}$ drift. On the other hand, this also leads to an increasing distortion of the cyclotron orbits. As a consequence those trajectories begin to drift (right-hand trajectories of parts b, d, f, and h of Figure 33), which are stationary in the weak potential case and lead to a distinct minimum in $\rho_\perp$. This fact explains the reduction of contrast of the commensurability oscillations with increasing potential amplitude. As shown in parts g and h of Figure 33, there is also a possibility of open orbits traversing parallel to the equipotential lines. Beton et al. [121] conclude from their classical model that a certain fraction of open orbits is present even for the smallest magnetic field values. Because the open orbits are traversed with the Fermi velocity v_F rather than with the slower $\mathbf{E} \times \mathbf{B}$ drift velocity, they dominate the resistivity at very low magnetic fields and lead to the observed positive magnetoresistance. As shown in Figure 32, the magnetoresistance (caused by open orbits) remains positive up to a certain magnetic field B_{crit} where it has a maximum, followed by commensurability oscillations resulting from closed and drifting orbits. It was shown by Beton et al. [121] that the maximum in $\rho_\perp$ occurs when the Lorentz force equals the electric force caused by the potential gradient:

$$2\pi \frac{V_0}{a} = eB_{crit}v_F \tag{69}$$

Magnetic fields weaker than B_{crit} are unable to force an electron on a closed cyclotron orbit against the action of the potential wells, which leads to a dominant fraction of open orbits. When the magnetic field exceeds the critical value determined by Eq. (69), the number of open orbits is drastically reduced ("magnetic breakdown"). It can be easily shown [121] that the magnetoresistance can be approximated by

$$\frac{\Delta\rho_{xx}}{\rho_0} \approx 2\omega_c^2\tau\frac{N_0}{N_T} \tag{70}$$

where N_0/N_T denotes the fraction of open orbits relative to the total number of trajectories and ρ_0 is the resistivity at zero magnetic field. In Eq. (70), the magnetic field dependence contained in ω_c together with the drastic reduction of N_0/N_T at

$$B \geqslant B_{crit} = \frac{2\pi V_0}{ea v_F} \tag{71}$$

leads to the observed peak in $\rho_\perp$ at low magnetic fields.

Beton et al. also gave a semiqualitative quantum mechanical explanation of the observed low-field behavior [122]. A rigorous analysis of the semiclassical dynamics in lateral superlattices was given by Streda and Kucera [123, 124], who analyzed the detailed features of the electronic energy spectrum and obtained the characteristic low-field magnetic breakdown peak from the Chambers solution of the semiclassical Boltzmann equation. A similar magnetic breakdown concept had been used earlier by Streda and MacDonald [125] for an investigation of the weak modulation limit. In principle, the classical considerations made responsible for the magnetoresistance peak remain a valid picture also in the more detailed study of Streda and Kucera. In contrast to the classical model of Beton et al. [121], however, the latter does not predict a magnetoresistance that falls off abruptly for fields $B \geqslant B_{crit}$, but behaves smoothly in this field regime. Also the relation for the expected peak position is slightly modified to $B_{crit} = 4V_0/ea v_F$.

According to Eq. (69), the determination of B_{crit} allows the characterization of the amplitude V_0 of the periodic potential, if the Fermi velocity v_F is known. An example of the application of Eqs. (68) and (69) to the systematic study of V_0 and its dependence on various sample parameters is given in Figure 34 [126]. The shown data were obtained from the magnetoresistance of an inverted, back-gated heterostructure. The lateral superlattice is induced by a grating metal gate, fabricated on top of the heterostructure. The gate fingers had a width of only 25 nm and formed a grating with period $a = 200$ nm. The height of the potential modulation was tuned by a voltage V_G applied to the top Schottky gates, whereas the electron density could be independently varied by a back-gate voltage. The different symbols in Figure 34 indicate different methods used to extract the value of V_0. The squares are obtained from an analysis of the magnetic breakdown peak discussed previously. The circles and triangles stem from a comparison of the $n = 1$ and $n = 2$ commensurability oscillations (labeled $i = 1, 2$ in the figure) to the theoretical expression Eq. (68), where this was possible. As shown in Figure 30, this approximate relation not only reproduces the correct period and phase of these oscillations, but also gives a fair approximation of their amplitude for low values of n. For higher n, the calculated amplitude generally overestimates the measured one, which is due to the previously discussed reduction of the oscillation "contrast" by distorted orbits not accounted for by the simple classical picture of [117].

Figure 34a shows the dependence of the potential amplitude on the gate voltage for a certain fixed back-gate voltage, that is, for fixed electron density. The two different evaluation methods approximately give the same results when the modulation is very weak. This is the regime for which Eq. (68) is conceived and where it gives a fair representation of the actual situation. For higher V_G, Eq. (68) yields smaller values than Eq. (71). It is expected that in the case of stronger modulation Eq. (68) overestimates the oscillation amplitude, particularly at higher indices n and, consequently, underestimates V_0. In part b of the figure, the same analysis is performed for fixed V_G but at different electron densities, varied by a back-gate voltage. Again, the two evaluation methods give different results for the

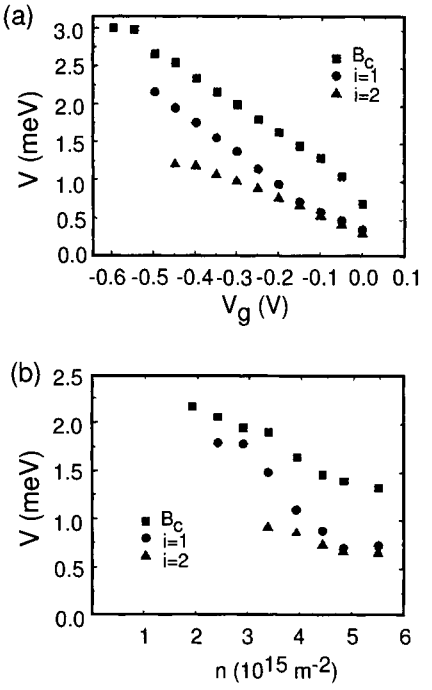


Fig. 34. Amplitude V of the periodic potential modulation for a back-gated inverted heterostructure, plotted as a function of the voltage applied to a grating gate, fabricated on top of the sample. Squares are obtained from an analysis of the magnetic breakdown peak at B_{crit}; circles and triangles are obtained from the application of Eq. (68) to the $i = 1$ and $i = 2$ commensurability oscillation. (Source: Adapted from [126].)

same reasons as before. However, all values confirm the observed trend of an increasing modulation amplitude (at fixed top gate voltage) with decreasing carrier density n_s. This carrier density dependence is a signature of screening effects that should be independent of n_s in a purely 2D electron system. The results of Figure 34b, therefore, nicely illustrate the reduction of screening when the potential amplitude increases and an increasing number of electrons become bound in one dimension.

A similar analysis has been applied to the characterization of short-period ($a = 100$ nm) lateral surface superlattices, fabricated by a plasma etching process [127]. An additional blanket gate on top of the etched superlattice has been used to improve the properties of the potential modulation. Indeed, the analysis of the phase of the commensurability oscillations shows that the blanket gate smooths the periodic potential and suppresses most of its higher harmonics; that is, the potential is sinusoidal to a very good approximation and, consequently, yields a phase shift of the commensurability oscillations equal to $\pi/4$. According to Davies and Larkin [128], a potential that is not perfectly sinusoidal creates higher harmonics in the magnetoresistance commensurability oscillations. Thus, an additional possibility to obtain information on the shape of $V_{\text{mod}}(y)$ is to analyze the Fourier transform of the low-field oscillatory magnetoresistance, taken as a function of $1/B$. This method was also applied in [127] and was found to confirm the results obtained from the phase analysis.

When the lateral superlattice potential becomes still stronger, the magnetoresistance anomalies change their character. This is illustrated in Figure 35 [129]. In this example, the periodic potential is created by shallow etching on a GaAs–AlGaAs heterostructure. The potential amplitude relative to the Fermi level is tuned by brief illumination from a red LED. In part a of the figure, V_0 and E_F, measured relative to the subband bottom in the wells of the lateral potential, are nearly equal. In this case, there is no trace of

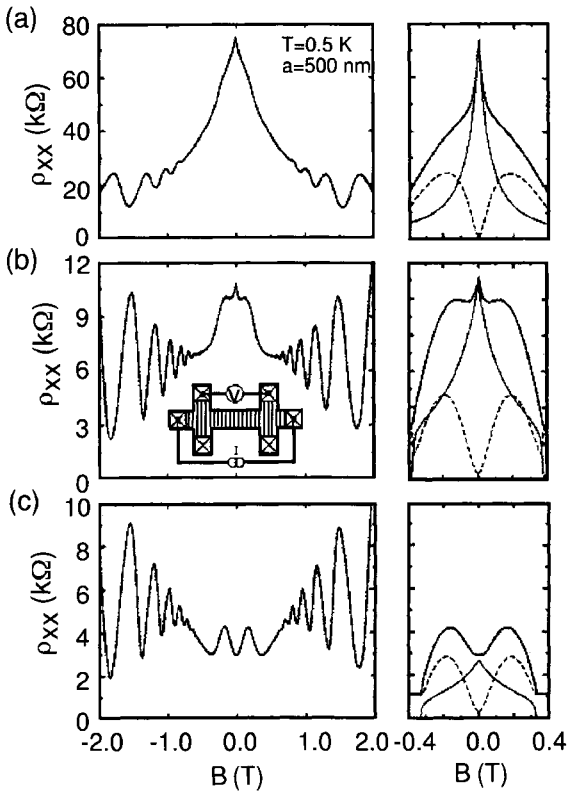


Fig. 35. The left-hand curves show experimental magnetoresistance traces for different amplitudes of the modulating potential. The top curve corresponds to the strongest modulation, the bottom curve to the weakest one. The inset in part b shows the experimental setup. The right-hand figures display the calculated magnetoresistance (thick solid lines; see text). The dashed curves correspond to the isotropic contribution to ρ_{xx}, thin solid lines to the anisotropic part, which dominates for very strong modulation. The Fermi level (measured from the bottom of the potential wells) and the potential amplitudes used in the calculation are: (a) $E_F^{weil} = 8.1$ meV, $V_0 = 7.8$ meV; (b) 8.6 meV, 7.0 meV; (c) 9.0 meV, 6.7 meV. (Source: Adapted from [129].)

a positive magnetoresistance, which, on the contrary, becomes negative. With increasing difference between V_0 and E_F, that is, decreasing ε, a positive contribution to the low-field magnetoresistance becomes visible, which dominates for the lowest value of ε (part c of the figure).

This behavior can be explained semiclassically if one assumes different scattering times for electrons bound in the wells and for those having sufficient energy to overcome the barriers and to move freely [129]. In the following outline of the underlying semiclassical model, we suppose that the potential modulation is in the x direction. One assigns a scattering time τ_0^b to those electrons bound in the well and τ_0^f to those electrons whose energy is high enough to overcome the barriers, both defined for zero magnetic field. With an applied magnetic field, the number of free electrons is not constant, because due to the Lorentz force electrons can acquire an additional momentum component in the x direction, which transforms previously bound electrons into free ones. Thus, for $B \neq 0$, one can define an average, magnetic field–dependent scattering time for free electrons

$$\frac{1}{\tau_f} = \frac{\theta_0}{\theta_B}\frac{1}{\tau_0^f} + \frac{\theta_B - \theta_0}{\theta_B}\frac{1}{\tau_0^b} \tag{72}$$

which is equivalent to the assumption that the phase space average of the scattering probability is not changed by a weak magnetic field. The angles θ_0 and θ_B delimit those regions in k space (at zero and nonzero magnetic field, respectively) that correspond to a free-electron

dispersion, that is, where the electrons have sufficient kinetic energy in the x direction to overcome the barriers. One finds from a semiclassical treatment [129] that the resistivity in the x direction may be split up into two components:

$$\rho_{xx} = \rho_{xx}^{\mathrm{iso}}(\tau_y) + \Delta\rho_{xx} \tag{73}$$

The first term follows from the Chambers solution of the Boltzmann equation

$$\rho_{xx}^{\mathrm{iso}}(\tau) = \frac{m^*}{e^2 n_s \tau} \frac{1 + \omega_c^2 \tau^2 C(\theta_B)}{1 - C(\theta_B)} \tag{74}$$

if for τ an *isotropic* scattering time is used, which is given by

$$\tau_y = \tau^f + \frac{\pi + \theta_B + \sin\theta_B}{\pi}(\tau_0^b - \tau^f) \tag{75}$$

The effect of anisotropy, induced by the presence of two different scattering times, is subsumed in the second term of Eq. (73):

$$\Delta\rho_{xx} = \frac{m^*}{e^2 n_s \tau_y} \frac{\pi - \theta_B + \sin\theta_B}{\theta_B + \sin\theta_B} \frac{\tau_0^b - \tau^f}{\tau^f} \tag{76}$$

In Figure 35, the magnetoresistance traces calculated according to Eqs. (74) and (76) are shown on the right-hand side. The dashed lines correspond to ρ_{xx}^{iso} which, in analogy to the strongly modulated case discussed previously, exhibits a positive magnetoresistance followed by a breakdown peak. The solid lines correspond to the anisotropic contribution $\Delta\rho_{xx}$. It can be seen that at large values of ε the anisotropic part strongly dominates the low-field magnetoresistance, leading to the characteristic spiked helmet form. The model calculations also allow one to estimate the amplitude of the periodic potential. However, the involved formalism is much more intricate than the methods described previously and does not lend itself to systematic routine investigations. The V_0 values corresponding to the different experimental situations shown in Figure 35 are given in the caption.

In conclusion, it is worth mentioning that the semiclassical modeling of magnetotransport in a periodic potential gives in a way complementary information on the underlying potential for weak and strong modulation. In the first case, the commensurability oscillations provide phase information that allows one to draw conclusions on the shape of the potential. However, because the semiclassical model treats the potential modulation as vanishingly small, the potential amplitude is not well reproduced by the semiclassical expressions (see [126]). In contrast to that, the magnetic breakdown picture yields a particularly simple tool for the determination of potential amplitudes but it is basically insensitive to the exact shape of the modulating potential. Sinusoidal or Kronig–Penney-like model potentials give essentially the same results [123, 129].

6. VERTICAL TUNNELING THROUGH QUANTUM WIRES

6.1. Experimental

In this section, we discuss the use of tunneling spectroscopy as a tool for the investigation of confining potentials and wave functions of 1D systems. Experimentally, tunneling via 1D states can be realized in various ways. Lateral tunneling between a quantum wire and 2D systems, for example, can be implemented on modulation-doped heterostructures using a split-gate geometry with a "leaky" channel. In this geometry, electrons are allowed to tunnel out of a 1DEG through a thin side-wall barrier into an adjacent 2D electron bath [130, 131]. A pronounced oscillatory structure can be observed in the 1D–2D tunneling current when the carrier concentration in the 1D channel is modulated through the split gates. These features reflect the modulation of the 1D density of states as the 1D subbands are successively depopulated with increasing split-gate bias.

However, tunneling between electron systems of different dimensionality in the vertical (growth) direction turned out to be the more interesting situation. In vertical geometry, epitaxial regrowth techniques either on V-groove etched substrates, as proposed by Luryi and Capasso [132], or on the edge of *in situ* cleaved substrates [133] can be used for devices, where electrons tunnel resonantly from a 2D emitter state into the 1D subbands of a quantum wire [134]. In such a sample, tunneling proceeds from the edge of a two-dimensional electron source through a bound state in a quantum wire into the edge of another 2D electron system and the combined effects of the longitudinal and perpendicular motion of electrons allows a detection of the excited wire states. On double-barrier resonant tunneling diodes, the lateral dimension can be restricted by use of focused Ga ion beam implantation [135]. In this case, the mixing of 2D emitter subbands and 1D subbands in the double-barrier region can be observed [136]. In theoretical models, these subband mixing and coupling effects turned out to be important and have, therefore, to be taken into account [137, 138].

The most instructive way to investigate tunneling processes through quantum wires, however, is to use a nanostructured double-layer electron system consisting of two coupled two-dimensional electron gas (2DEG) systems separated by a thin tunnel barrier. Three types of such bilayer structures have been extensively investigated: the double heterostructure with a two-dimensional electron gas on both sides of an AlGaAs barrier, the double-barrier resonant tunneling diode with two-dimensional emitter, and the coupled quantum well system. On all types of samples, either the upper 2D-channel, lying closer to the sample surface, or both channels can be patterned into quantum wires. In this way, tunneling processes from a 2D emitter into a system of one or more quantum wires and also vertical tunneling between insulated quantum wires can be investigated. In all these cases, the fundamental technological problem, which makes the construction of a vertical tunneling device a challenging task, is the formation of independent ohmic contacts to each of the barrier-separated low-dimensional systems. In the following, we discuss three representative experiments, each performed on one of the three mentioned systems of coupled electron channels. We describe briefly the sample geometry used and show some typical data obtained for each of these devices. In a subsequent section, we shall discuss briefly the theoretical models underlying the interpretation of these data. In the discussion, the emphasis will be put on the influence of the confining potential on the resonant tunneling characteristics or, vice versa, on the question to which extent the latter can provide substantial information on the former.

The double GaAs–AlGaAs–GaAs heterostructure, used in [23, 139–142], is shown in Figure 36a. The sample structure is made up of a nominally undoped GaAs layer

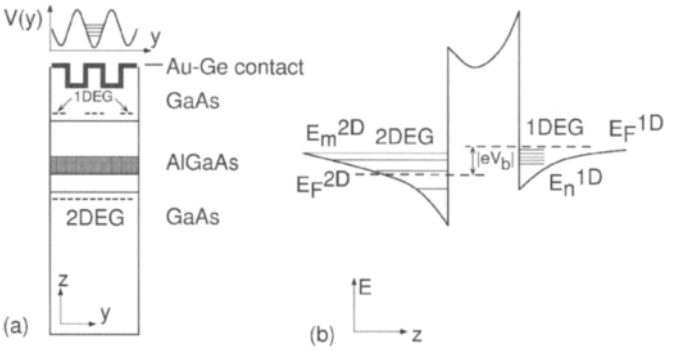


Fig. 36. (a) Schematic cross section of a processed single-barrier resonant tunneling device and resulting surface potential in the y direction (top). (b) Corresponding conduction band profile in the z direction. E_m and E_n denote the energy levels on the 2D and 1D side, respectively. E_F is the Fermi energy; V_b is the applied sample bias.

($N_A \leqslant 1 \times 10^{14}$ cm^{-3}) grown on a semiinsulating substrate, followed by an undoped AlGaAs spacer ($d = 50$ Å), doped $Al_xGa_{1-x}As$ ($d = 50$ Å, $N_D \leqslant 3 \times 10^{18}$ cm^{-3}, $x = 0.36$), another spacer ($d = 100$ Å), and n^--doped GaAs ($d = 800$ Å, $N_D \leqslant 1.2 \times 10^{15}$ cm^{-3}). An additional highly doped GaAs cap layer ($d = 150$ Å, $N_D = 6.4 \times 10^{18}$ cm^{-3}) was added on the surface. This structure provides an inversion layer at the lower GaAs/$Al_xGa_{1-x}As$ interface, containing several 2D subbands, and an accumulation layer at the upper $Al_xGa_{1-x}As$/GaAs interface, both separated by a barrier of only 200-Å thickness. From Shubnikov–de Haas measurements, it was deduced that in both 2DEG systems only one subband is occupied with values of $n_s^{inv} = 6.0 \times 10^{11}$ cm^{-2} and $n_s^{acc} = 5.5 \times 10^{11}$ cm^{-2} for the electron densities, respectively.

With this sample structure, 1D–2D tunneling can be realized if the upper channel is structured into quantum wires using, for example, standard laser holographic techniques and wet chemical etching. The etching process will induce a potential modulation only in the upper electron system, because the lower 2DEG is screened by the highly doped barrier separating the two channels. More details concerning sample preparation, particularly on the question of independent ohmic contacts to the low-dimensional systems, can be found in [140]. A bias voltage V_b, applied between the top and the bottom electron systems across the barrier, will shift the 1D states energetically with respect to the 2D electron gas as indicated in Figure 36b. It can be shown from self-consistent calculations that the externally applied voltage drops almost completely across the potential barrier. Consequently, the relative energy shift ΔE between the 1D and 2D system is equal to eV_b to a very good approximation, which considerably simplifies a quantitative analysis of the experimental data. Note that for this geometry both the initial and the final states involved in a tunneling process are quantized in a way that no free momentum component exists in the direction of the tunneling current.

Some typical tunneling data are shown in Figure 37. For reference purposes, consider first the results for the unstructured sample (upper curve in Fig. 37), where the resonant tunneling processes occur between two 2D electron gases and lead to a series of sharp peaks in dI/dV_b. Because in the geometry discussed the transverse electron momentum (parallel to the barriers) is conserved during the tunneling process, resonant tunneling occurs whenever the subband in the accumulation layer is energetically aligned with a subband in the inversion layer [141, 142].

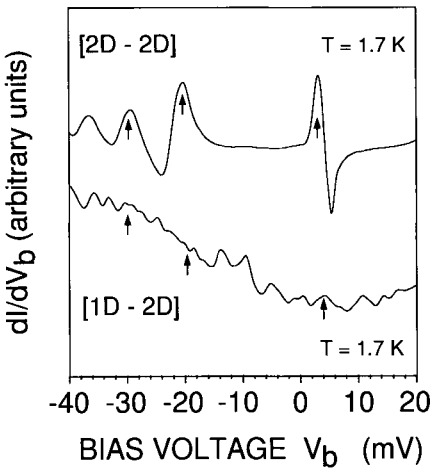


Fig. 37. dI/dV_b curves of an unstructured sample (2D–2D tunneling), recorded at $T = 1.7$ K and dI/dV_b characteristics of a nanostructured sample (1D–2D tunneling). The upward arrows indicate the resonance positions of the unstructured sample.

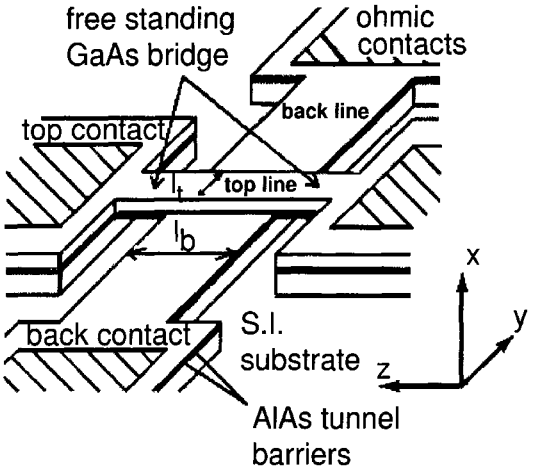


Fig. 38. Schematic diagram of a 1D–1D tunneling device based on a double-barrier resonant tunneling structure. (Source: Reprinted with permission from [143]. © 1994 American Physical Society.)

The trace at the bottom of Figure 37 shows the corresponding low-temperature dI/dV_b characteristics for a nanostructured sample. A wealth of additional structure appears in the differential tunneling characteristics in the investigated bias regime. It turns out that the identification of single peaks is not as straightforward as in the case of 2D–2D tunneling. It will be shown later in detail that for 1D–2D tunneling individual peaks in dI/dV_b cannot be simply assigned to the energetic alignment of the 2D emitter level with a special 1D wire state.

Vertical tunneling between single quantum wires (1D–1D tunneling) was demonstrated by Wang et al. [143, 157] in a very appealing way. They used a conventional double-barrier resonant tunneling diode with symmetric barriers having a thickness of 47 Å and enclosing a 90-Å-wide well. On both sides of the double barrier, 200-Å-thick spacer layers were grown to minimize the unintentional incorporation of donors into the well. The sample geometry depicted in Figure 38 is achieved by optical lithography and a series of selective wet chemical etch steps [157]. The top line has a submicrometer width and forms an air bridge to the top contact regions. This allows one to establish independent ohmic contacts to the top and back lines of the device. Its active area is formed by the overlap region of the top and back lines, as shown in Figure 39a. When a bias voltage is applied, the spacer in front of the double barrier forms an accumulation layer, which acts as a 1D emitter (see the conduction band profile in Fig. 39b). The 1D quantization energy $\hbar\omega_e$ in the emitter is determined by the width l_t of the top line and the side-wall depletion induced by the etching process. In general, the 1D quantization of the emitter will be much weaker than in the double-barrier region.

If the width l_t of the top line is in the micrometer range, a conventional small-area resonant tunneling diode is obtained, whose current–voltage characteristics display the usual region of negative differential resistance. The reduction of l_t to submicrometer dimensions leads to the observation of a rich additional structure in the I–V curves, which is due to resonant tunneling through the quantized 1D states between the AlAs barriers of the active area (cf. Fig. 48). Using magnetotunneling experiments, even the probability density of the quantum confined states can be determined with this device [144–146].

As a third example, we mention a vertical tunneling device that is based on coupled quantum wells [147–149]. Both wells are 180 Å wide and separated by a 125-Å AlGaAs barrier. The reported electron concentrations are typically 3×10^{11} cm^{-2} (μ = 800,000 cm^2/V s) and 1.8×10^{11} cm^{-2} (μ = 200,000 cm^2/V s) in the upper and the lower wells, respectively. On these samples, independent contacts to the electron systems in the

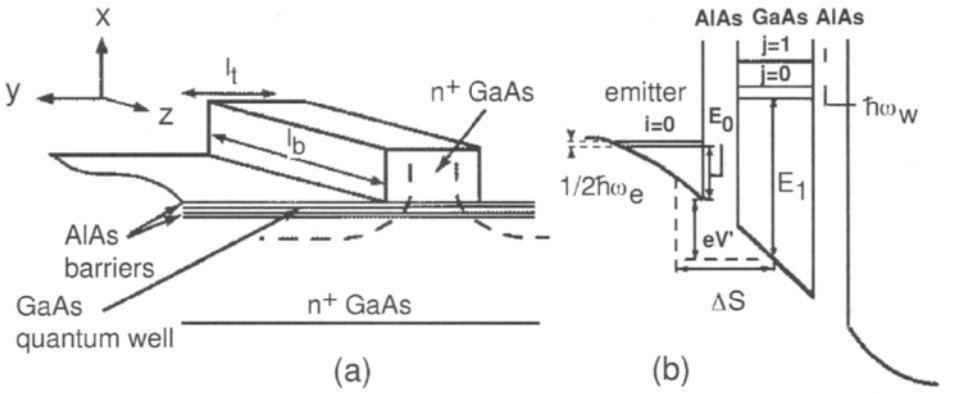


Fig. 39. (a) Side view of the 1D–1D tunneling device. The wires are formed by side-wall depletion underneath the GaAs bar. (b) Corresponding conduction band profile. $\hbar\omega_e$ and $\hbar\omega_w$ are the subband spacings in the 1D emitter and well. E_0 and E_1 are the energy levels resulting from quantization in the growth direction. (Source: Reprinted with permission from [144]. © 1995 American Physical Society.)

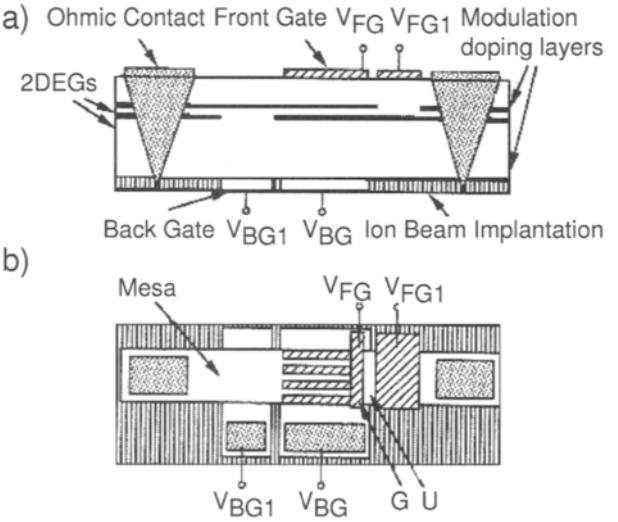


Fig. 40. Cross-sectional view (a) and top view (b) of the device structure. The selective depletion technique, which is used to contact each 2DEG separately, is shown in (a) and definitions of the different tunneling regions in (b). G denotes the gated, U the ungated region of the device leading to the q- and k-peaks shown in Figure 41. (Source: Reprinted with permission from [147]. © 1996 American Institute of Physics.)

upper and lower wells were established by *in situ* focused ion beam lithography and selective gate depletion techniques. A schematic view of the sample geometry is shown in Figure 40. The gates BG1, formed by an *in situ* patterned n^+ layer, and FG1 are used for the local depletion of the lower and upper channels, respectively. In this way, independent contacts to both 2D systems can be achieved. The back gate BG is used to tune the electron concentration in the lower channel. A potential modulation can be imposed on the upper well by means of the nanostructured top (front) Schottky gate FG.

The back gate allows the variation of the electron density (i.e., the Fermi level) in the lower channel. By recording the tunneling conductance as a function of the back-gate voltage, the resonant tunneling between the barrier-separated electron systems can be studied

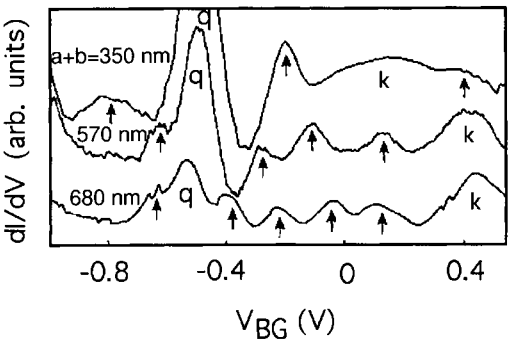


Fig. 41. Tunneling differential conductance for $V_{sl} = -0.25$ V and three different grating periods. The arrows mark the peaks, which are due to the crystal part of the 1DSSL band structure. Definition of separated quantum wires occurs at $V_{sl} = -0.45$ V. (Source: Reprinted with permission from [148]. © 1996 American Physical Society.)

without applying a bias voltage across the tunnel junction. This technique, first introduced by Eisenstein et al. [150–152], is called "equilibrium tunneling spectroscopy." In the case of 2D–2D tunneling, the net effect of the back-gate voltage is, just as in the previously discussed "biased" cases, a relative shift of the emitter and collector subband energies. As soon as the bottoms of the two subbands on both sides of the barrier are energetically aligned, the requirements of energy and momentum conservation are fulfilled and resonant tunneling between the subbands can occur. To study 1D–2D tunneling processes, a voltage V_{sl} can be applied to the front Schottky gate. This induces a potential modulation in the upper 2DEG whose amplitude can be tuned from zero up to a value where an array of independent quantum wires is established in the upper channel. At intermediate values of V_{sl}, the strength of the modulation is not sufficient to create a set of independent wires but rather leads to the formation of a lateral superlattice. For this latter situation, typical tunneling spectra are shown in Figure 41, where the differential tunneling conductance is plotted for three different grating periods and a front-gate voltage of $V_{sl} = -0.25$ V.

It can be shown (see the following sections) that the two large peaks, labeled k and q, are due to resonant 2D–2D tunneling between the 2D emitter and the 2D gases in the gated (q-labeled peak) and the ungated (k-labeled peak) regions of the device. They occur at back-gate voltages where the 2D electron densities in the emitter (lower) 2DEG and in the respective regions of the upper channel coincide. The small peaks, denoted by arrows, correspond to back-gate voltages where k_y at the Fermi energy in the 2DEG is equal to k_y in the one-dimensional surface superlattice (1DSSL) to within a reciprocal lattice vector $G_n = 2n\pi/(a+b)$ of the superlattice. Here, n is an integer, $a+b$ is the superlattice period (i.e., the sum of the width of a gate finger and the gate separation). The y axis is oriented perpendicular to the 1DSSL gates. In other words, the regular series of small-amplitude peaks can be assigned to the "crystal part" of the superlattice band structure.

Before continuing the discussion of these experiments, we briefly introduce the theoretical machinery of the transfer Hamiltonian formalism [153–155], which forms the basis of a quantitative analysis of all the vertical tunneling experiments discussed in this review.

6.2. Transfer Hamiltonian Formalism

Consider a tunneling process starting in an electron system, which we shall call the *emitter* in the following, and ending in some collector electron bath. To support the intuitive understanding of the following, one might imagine a 2DEG as the emitter and a second 2DEG, separated from the first through a barrier, as the collector system. In the formalism of the

transfer Hamiltonian approach, one treats, in a first step, both 2DEGs as independent systems. Each one is characterized by a complete set of eigenfunctions $\{\Psi_i\}_\mathrm{I}$ and $\{\Psi_k\}_\mathrm{F}$ and the corresponding eigenenergies, respectively (the indices I and F indicate the initial and final state of a tunneling process). If the two systems are brought into contact, for example, by a thin tunneling barrier, one may approximate the wave function of the total system by an expansion of the form

$$\Psi(t) = \sum_i a_i(t)\Psi_i \exp\left(\frac{iE_i t}{\hbar}\right) + \sum_k b_k(t)\Psi_k \exp\left(\frac{iE_k t}{\hbar}\right) \tag{77}$$

The indices i denote the emitter states and k those of the collector system. Equation (77) will be a good approximation if the coupling between the two systems is weak and the barriers are relatively thick. If the electron is assumed to start from a state $\{\Psi_0\}_\mathrm{I}$, one has as initial conditions for the coefficients $a_0(t=0) = 1$ and $a_i(0) = b_k(0) = 0$. The preceding total wave function may now be inserted into the time-dependent Schrödinger equation $i\hbar\dot{\Psi} = H\Psi$. If one assumes a weakly coupled system, a perturbation approach may be taken, which starts with the assumptions $a_i(t) \approx 1$, $b_k(t) \approx 0$, and $da_i(t)/dt \approx 0$ for all times t. This leads to the expression $\Psi(t) \approx \Psi_{i=0} \equiv \Psi_\mathrm{I}$ for the total wave function, and the time-dependent Schrödinger equation takes the form

$$\sum_k i\hbar \frac{db_k}{dt}\Psi_k \exp\left(-\frac{iE_k t}{\hbar}\right) = (H - E_\mathrm{I})\Psi_\mathrm{I} \exp\left(-\frac{iE_\mathrm{I} t}{\hbar}\right) \tag{78}$$

After multiplication with a state Ψ_F taken from the set of possible states in the collector system and repeating the same procedure familiar from standard time-dependent perturbation theory, one obtains for the transition probability between the states Ψ_I and Ψ_F the expression

$$\frac{|b_\mathrm{F}(t)|^2}{t} = \frac{2\pi}{\hbar}|M_\mathrm{IF}|^2 \delta(E_\mathrm{F} - E_\mathrm{I}) \tag{79}$$

with a transition matrix element given by $M_\mathrm{IF} = \langle\Psi_\mathrm{F}|H - E_\mathrm{I}|\Psi_\mathrm{I}\rangle$. Note that in the present context E_F does not denote the Fermi level but the energy of the final state. To obtain the total transition probability, one has to sum over all initial and final states and to weight every term in the usual way by the combined probability to find the initial state occupied and the final state empty. This leads to the expression

$$P_\mathrm{IF} = \frac{2\pi}{\hbar}\sum_{m,n}\sum_{k_\mathrm{I},k_\mathrm{F}} |M_\mathrm{IF}|^2 \big[f(E_\mathrm{I}) - f(E_\mathrm{F})\big]\delta(E_\mathrm{I} - E_\mathrm{F} + eV_\mathrm{b}) \tag{80}$$

The δ function ensures the conservation of energy. Note that in the previous equation it is already assumed that a bias voltage is applied, which drops completely across the tunneling barrier and, hence, simply leads to a relative shift in the Fermi levels of the emitter and collector systems. Furthermore, the summation is carried out over all electron wave vectors k_x and k_y parallel to the barrier and all 2D subbands n, m of the initial and final 2DEGs. It can be easily shown that the matrix element M_IF can be transformed into the following expression [154]:

$$M_\mathrm{IF} = -\frac{\hbar^2}{2m^*}\int\!\!\int_{z=z_0} d^2S\left[\Psi_\mathrm{F}^* \frac{\partial\Psi_\mathrm{I}}{\partial z}\bigg|_{z=z_0} - \Psi_\mathrm{I}\frac{\partial\Psi_\mathrm{F}^*}{\partial z}\bigg|_{z=z_0}\right] \tag{81}$$

The integration over the surface elements dS has to be carried out in the plane of the barrier, which separates the initial and final side at $z = z_0$.

We first evaluate the matrix element M_IF for the case where both the initial and the final states are purely two-dimensional electron systems, as is the case for unstructured 2D–2D tunneling samples. In a two-dimensional system, the states are quantized in the z direction,

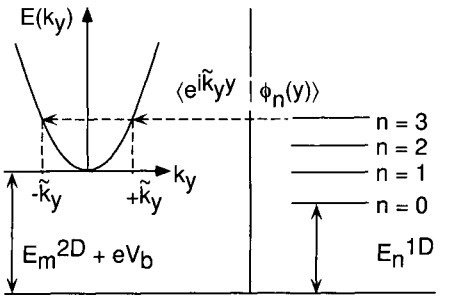


Fig. 42. Schematic illustration of a 1D–2D tunneling process. The arrow represents an electron tunneling from the quantum wire system into the 2DEG. The x component of the electron momentum is not considered here, as it is conserved during the tunneling process.

but free motion of electrons exists parallel to the barrier in the x and y directions. The wave functions for the initial and final states thus have the form

$$\begin{aligned} \Psi_{\mathrm{I}} &= \psi_{\mathrm{I}}(z)\exp(ik_{x,\mathrm{I}}x)\exp(ik_{y,\mathrm{I}}y) \\ \Psi_{\mathrm{F}} &= \psi_{\mathrm{F}}(z)\exp(ik_{x,\mathrm{F}}x)\exp(ik_{y,\mathrm{F}}y) \end{aligned} \tag{82}$$

Inserting these wave functions into the expression for the matrix element and evaluating the integrals yields

$$M_{\mathrm{IF}} = -\frac{\hbar^2}{2m^*}\left[\psi_{\mathrm{F}}^*\frac{\partial\psi_{\mathrm{I}}}{\partial z}\bigg|_{z=z_0} - \psi_{\mathrm{I}}\frac{\partial\psi_{\mathrm{F}}^*}{\partial z}\bigg|_{z=z_0}\right]\delta(k_{x,\mathrm{I}}-k_{x,\mathrm{F}})\,\delta(k_{y,\mathrm{I}}-k_{y,\mathrm{F}}) \tag{83}$$

The first term defines the *transmission coefficient of the barrier* in the z direction:

$$T_{\mathrm{IF}} = \left|\psi_{\mathrm{F}}^*\frac{\partial\psi_{\mathrm{I}}}{\partial z}\bigg|_{z=z_0} - \psi_{\mathrm{I}}\frac{\partial\psi_{\mathrm{F}}^*}{\partial z}\bigg|_{z=z_0}\right|^2 \tag{84}$$

The δ functions in Eq. (83) are the evaluated overlap integrals between the wave functions in the x and y directions of the initial and final states. Because for tunneling between 2D states these wave functions are plane waves, the overlap integrals reduce to δ functions. In this case, one thus obtains as a condition for resonant tunneling between 2D states that the electron wave vectors (k_x, k_y) parallel to the barrier have to be conserved during the tunneling process.

Next, we consider transitions between a 2D system and a quantum wire as the emitter. In this case, the wave functions are plane waves in the x and y directions in the 2D collector. For the quantum wire side, however, one has plane waves in the x direction but quantized states in the y direction. This situation is schematically sketched in Figure 42 for an electron tunneling from a 1D quantum wire state ($n = 3$) into an unoccupied 2D subband. For this situation, the wave functions are written as

$$\begin{aligned} \Psi_{\mathrm{I}} &= \psi_{\mathrm{I}}(z)\exp(ik_{x,\mathrm{I}}x)\exp(ik_{y,\mathrm{I}}y) \\ \Psi_{\mathrm{F}} &= \psi_{\mathrm{F}}(z)\exp(ik_{x,\mathrm{F}}x)\,\Phi_{n,\mathrm{F}}(y) \end{aligned} \tag{85}$$

and the corresponding matrix element for the 1D–2D tunneling process reads

$$\begin{aligned} M_{\mathrm{IF}} = &-\frac{\hbar^2}{2m^*}\left[\psi_{\mathrm{F}}^*\frac{\partial\psi_{\mathrm{I}}}{\partial z}\bigg|_{z=z_0} - \psi_{\mathrm{I}}\frac{\partial\psi_{\mathrm{F}}^*}{\partial z}\bigg|_{z=z_0}\right] \\ &\times\delta(k_{x,\mathrm{I}}-k_{x,\mathrm{F}})\int\exp(ik_{y,\mathrm{I}}y)\,\Phi_{n,\mathrm{F}}(y)\,dy \end{aligned} \tag{86}$$

We now assume that a voltage V_{b} is applied across the tunneling barrier and use Eq. (86) to calculate the total tunneling probability per unit time according to Eq. (80). The corresponding tunneling current is then given by $I = 2eP_{\mathrm{IF}}$, where the factor of 2 accounts

for the spin. The tunneling matrix element, Eq. (86), has two remarkable features. First, the δ function indicates that the x component of the electronic momentum is still conserved in a tunneling process. The second feature is the appearance of the overlap integral $\int \exp(ik_{y,\mathrm{I}}y)\,\Phi_{n,\mathrm{F}}(y)\,dy$ between the final and initial states in the y direction, which is recognized to be simply the Fourier transform of the quantized wire state forming the starting point of the tunneling process. This means that there are two main contributions to P_{IF}, leading to observable structure in the measured tunnel current: the transmission coefficient of the tunneling barrier [see Eq. (84)] and the overlap integral. For a single-barrier tunneling device, the transmission coefficient T_{IF} of the barrier adds no resonance structures to the tunneling current. Consequently, it will only be the overlap integral between the initial and final states that is responsible for all structures in the tunneling current. If we assume that the electron systems on both sides of the barrier are shifted in energy by eV_{b} with respect to each other, total energy conservation requires that

$$E_{n,\mathrm{I}} + \frac{\hbar^2 k_{x,\mathrm{I}}^2}{2m^*} + \frac{\hbar^2 k_{y,\mathrm{I}}^2}{2m^*} + eV = E_{\mu,\mathrm{F}} + \frac{\hbar^2 k_{x,\mathrm{F}}^2}{2m^*} \tag{87}$$

where μ is the subband index. Because we can ignore the free-electron motion in the x direction, this equation can be expressed in terms of k_y:

$$k_y(V) = \pm\sqrt{\frac{2m^*}{\hbar^2}[E_{\mu,\mathrm{F}} - E_{n,\mathrm{I}} - eV]} \tag{88}$$

This means that the wavevector of the tunneling electron, k_y, appearing in the overlap integral, is controlled by the external voltage. Consequently, the measured current–voltage characteristics of the tunneling device basically reflect the Fourier transform of the 1D emitter wave functions.

6.3. Influence of the Potential Profile on 2D–1D Tunneling Processes

The "real" profile of the confining potential in a quantum wire is determined by various effects such as Fermi-level pinning at exposed surfaces, free-carrier contributions, and many-body effects such as electron–electron interactions or screening at low temperatures. The bottom part of the quantum wire potential is especially influenced by the densities of free as well as fixed carriers, resulting in potential shapes ranging from almost parabolic to almost square well like.

To analyze the influence of the shape of the confining potential on the overlap integral in Eq. (86), one may calculate the wave function overlap for different model potentials. To do this, we consider as the emitter system an array of shallow etched quantum wires. If one assumes periodic boundary conditions, the following cosine-shaped potential can be considered as a reasonably good approximation of the real situation:

$$V(y) = V_{\mathrm{mod}}\left[\frac{1}{2} + \frac{1}{2}\cos\left(\frac{2\pi}{w}\left(y - \frac{w}{2}\right)\right)\right] \tag{89}$$

Here, V_{mod} is the potential amplitude and w is the electrical width of an individual quantum wire. Using Eq. (88), we now calculate the overlap integrals $I_n = |\langle \exp(ik_y y)|\phi_n(y)\rangle|^2$ as a function of the applied bias voltage. The results for the tunneling transitions from the four lowest 1D subbands ($n = 0, \ldots, 3$) into an unoccupied 2D subband are plotted in Figure 43. We first discuss the result for the lowest 1D subband ($n = 0$), which is shown in the uppermost curve.

At bias voltages where the 1D subband edge is energetically below the 2D subband edge ($V_{\mathrm{b}} > V_0$), resonant tunneling is forbidden because the total energy cannot be conserved in such a process. If the bias voltage reaches $V_{\mathrm{b}} = V_0$, the subband edges of the 2D subband

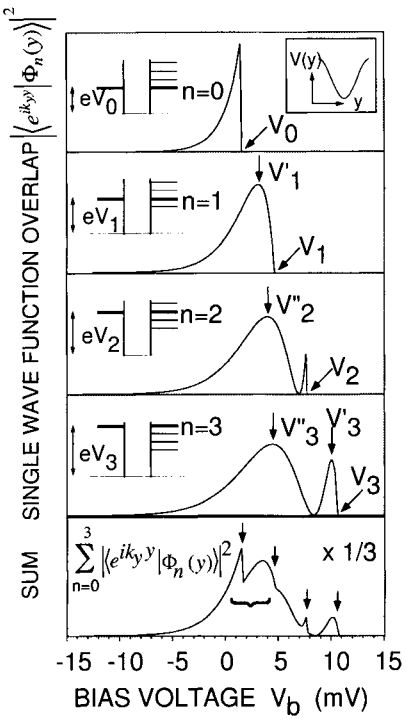


Fig. 43. Plot of the overlap integrals for the lowest four 1D subbands ($n = 0, \ldots, 3$) in a cosine-shaped potential [Eq. (89)], with a single 2D subband; V_n is the resonance position of the subband edges ($k_y = 0$), whereas ΔV_n denotes the deviation between the first overlap maximum and the position of the subband edge resonance V_n (only present for even n). The parameters for the 1D potential were $V_{\text{mod}} = 60$ mV, $w = 350$ nm. The lowest curve represents the sum of the upper four. (Source: Reprinted with permission from [23]. © 1993 American Physical Society.)

and of the lowest 1D subband ($n = 0$) are in resonance, and the overlap integral of the lowest 1D subband, I_0, reaches its maximum value. As V_b is decreased further, I_0 drops gradually toward zero. Note that I_0 indirectly reflects the spatial extent of the wave function, because it is nothing else than its Fourier transform. For the first excited 1D subband ($n = 1$), the tunneling probability, moreover, reflects the parity of this state. If the subband edges of both the 2D and the $n = 1$ subband coincide at $V_b = V_1$, I_1 is still zero because the corresponding 1D state has odd parity, $I_1(k_y = 0) = 0$. The tunneling probability then increases with decreasing bias voltage and reaches its maximum, which is slightly shifted by ΔV_1 from the subband edge resonance. With further decreasing bias voltage, I_1 drops toward zero. The behavior of the tunneling probabilities for the higher 1D subbands can, in principle, be understood in an analogous way.

It is obvious from Figure 43 that the maxima of I_n at the positions of the subband edge resonances (even 1D subband index, V_{2n}) or most close to them (odd 1D subband index, $V_{2n+1} + \Delta V_{2n+1}$) are much more pronounced than all the other structures caused by the nodes of the 1D wave functions. In addition, the values of ΔV_{2n+1} become smaller and smaller with increasing n (e.g., $\Delta V_1 > \Delta V_3$ etc.). Therefore, resonances caused by an energetic alignment between the subband edges of the 1D and 2D states can be expected to be dominant in the 1D–2D tunneling experiments, but are by no means the only reason for structures in the tunneling characteristics.

As has been shown previously, the confining potential in split-gate structures is rather "boxlike" than cosine shaped. Therefore, it is necessary to study also the influence of the steepness of the confinement walls. For this purpose, we choose an analytical expression

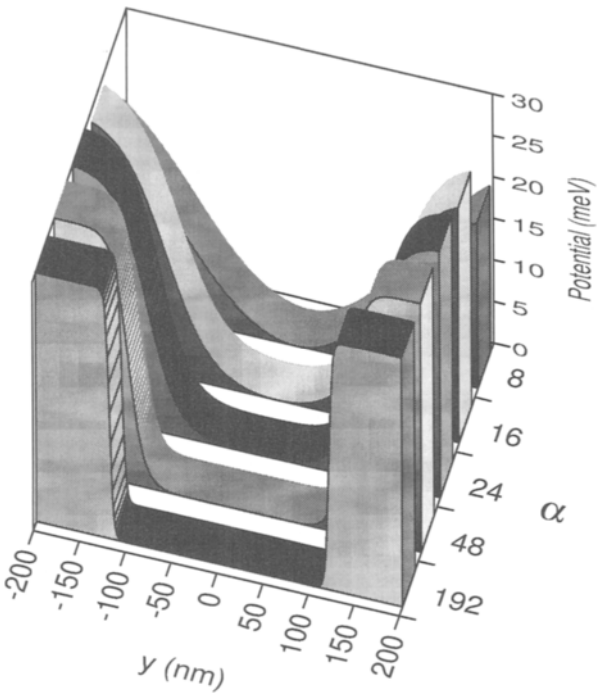


Fig. 44. Potential profiles for a series of α values, tuning the shape of $V(y)$ from smooth parabolic like ($\alpha = 8$) to almost rectangular box like ($\alpha = 192$).

for the potential, which allows us to control the steepness by a single parameter α. To obtain a potential profile that is smooth within one period of the multiple quantum wire system under consideration, we use the one-dimensional Woods–Saxon potential [42], which was already introduced in Section 2:

$$V(y) = V_{\text{mod}}\left[\frac{1}{1+\exp\left(\frac{\alpha(w/2-y)}{w}\right)} + \frac{1}{1+\exp\left(\frac{\alpha(w/2+y)}{w}\right)}\right] - V_{\text{min}} \tag{90}$$

The last term $V_{\text{min}} = V_{\text{mod}}\{2/[1+\exp(\alpha/2)]\}$ sets the potential minimum to zero. The parameter α allows a continuous variation of the potential shape from an approximately parabolic to a nearly rectangular form.

Figure 44 shows the potential profiles for a series of α values, starting at $\alpha = 8$ (nearly parabolic) and ending at $\alpha = 192$ (nearly rectangular box). The other parameters used in the calculation are $V_{\text{mod}} = 50$ meV and $w = 250$ nm.

In analogy to the case depicted in Figure 43, the overlap integral for the 1D ground state $n = 0$ and the third excited 1D subband $n = 3$ as well as their sum ($\sum n = 0, \ldots, 3$) is calculated for various values of α. The results are plotted in parts a–c of Figure 45.

Because of the variation of the potential profile, the energies of all 1D subband edges are shifted to lower values with increasing parameter α. The change in shape of the wave functions has a pronounced effect on the corresponding overlap integrals. This is illustrated for the 1D ground state in Figure 45a. With rising α, the spatial extent of the wave function is increased. As a result, the overlap integral of the single 1D wave function is squeezed on the wavevector scale k_y and, consequently, on the bias voltage scale V_b, too. In addition, the maximum tunneling probability is increased by more than 50%, whereas the integral tunneling probability, which is represented by the area enclosed by the curve, decreases simultaneously by a factor of 2. This behavior is even more pronounced for the overlap integrals of the higher quantum wire states, as shown in Figure 45b for the subband index $n = 3$. While α increases, the resonance structure close to the position of the subband

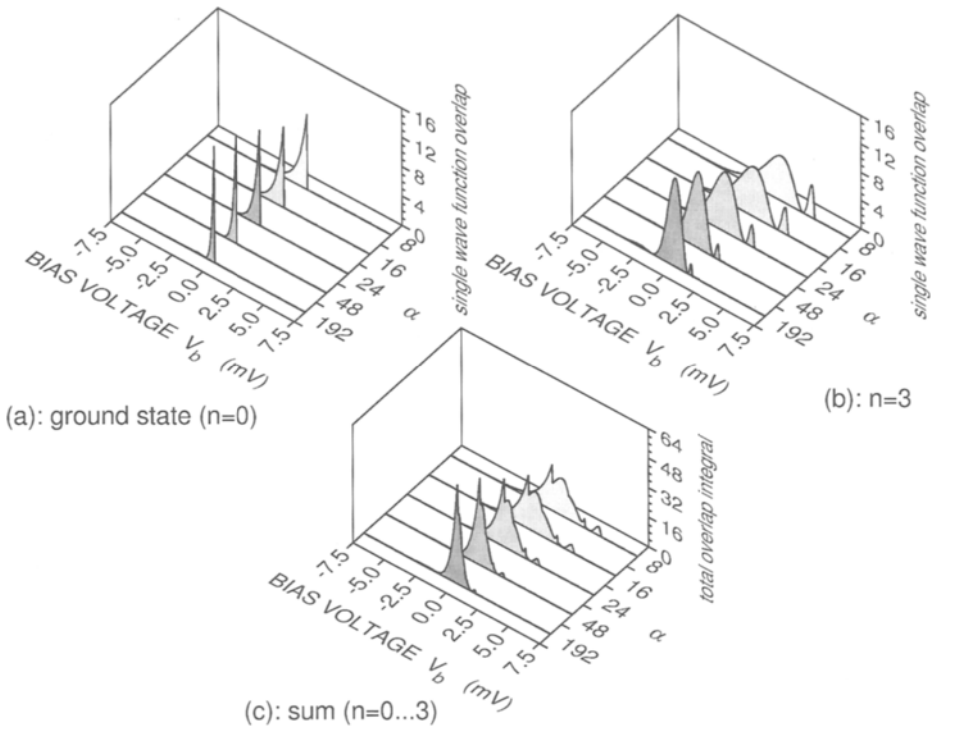


Fig. 45. Plot of the overlap integrals for the 1D subbands $n = 1$ (a) and $n = 3$ (b) with a single 2D subband as a function of the parameter α. (c) Sum of the overlap integrals of the lowest four subbands. (Source: Reprinted with permission from [23]. © 1993 American Physical Society.)

edge resonance (labeled V_3' in Fig. 43) is systematically degraded. In contrast to that, the tunneling probability at the bias voltage position of the second maximum (labeled V_3'' in Fig. 43) is drastically increased and becomes the by far most dominant structure for high values of α. Comparing the amplitudes of the overlap integral at the voltage positions V_3' and V_3'', their ratio increases from 1.4 for $\alpha = 8$ to above 8 for $\alpha = 192$. For the rectangular potential profile, the maximum in the tunneling probability at V_3'' coincides with the subband resonance position of the lowest 1D subband, that is, $V_b = V_0$.

To illustrate this remarkable behavior more clearly, we have recalculated the results shown in Figure 43 for a box potential with infinitely high walls and a width of $w = 100$ nm. For this potential profile, the values of I_n ($n = 0, \ldots, 3$) as well as their sum are plotted in Figure 46. Although the shapes of the curves are qualitatively identical with the corresponding curves of Figure 43, the intensity ratios of the structures within a curve show a completely different behavior. As pointed out previously, only the structures in the vicinity of the resonance of the lowest 1D subband (labeled V_0, V_1', V_2'', and V_3'') remain important. The width of these resonance structures, however, increases as the 1D quantum number increases. All other peaks of I_n for the higher 1D subbands at voltage positions $V_b > V_0$ are of minor importance, because their intensity can be neglected. All these features are also present in the sum of all overlap integrals, which determines the total tunneling probability (lowest curve of Fig. 46). There is only one broad maximum dominant, peaking at a bias voltage of V_0. This result is valid for all quantum wire subbands, but particularly pronounced for higher subband indices.

The total tunneling probability exhibits less and less structures as the potential profile is tuned from a smooth parabolic shape to a rectangular shape, as shown in Figure 45c. In the latter case, just one broadened maximum, located at $V_b = V_0$, characterizes the tunneling probability for all 1D subbands. Therefore, a single, but broad resonance structure

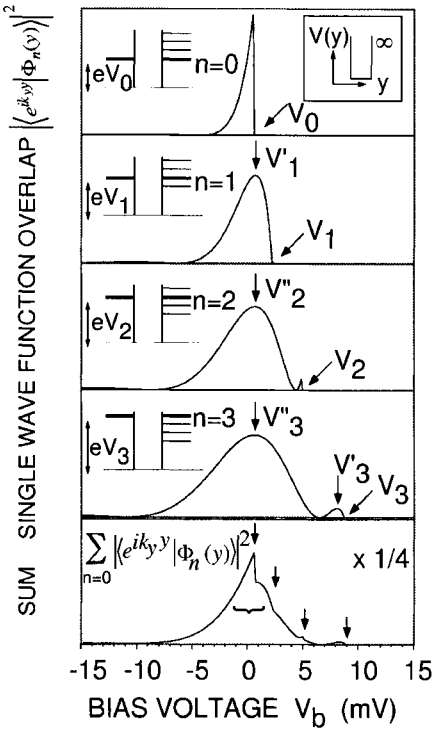


Fig. 46. Plot of the overlap integrals for the lowest four 1D subbands ($n = 0, \ldots, 3$) with a single 2D subband (not occupied) for a box potential with infinite high walls and a width of 100 nm. The lowest curve represents the sum of the overlap integrals for the four lowest subbands. (Source: Reprinted with permission from [23]. © 1993 American Physical Society.)

is expected at the position of the former 2D–2D resonance (which in the ideal case of zero-level broadening is a δ function), but only very weak additional structures resulting from the 1D subbands should occur at higher bias voltages. For a smooth potential profile, however, all quantum wire states give rise to a series of resonances that interfere within the voltage range mentioned previously.

With these insights into the nature of the 1D–2D tunneling process, an attempt can be made to simulate the corresponding tunneling characteristics and to compare them with the experimental results depicted in Figure 37. First, note that the experimental I–V curve displays a multitude of resonant structures. From the preceding analysis we know that a rectangular potential would lead only to a weak fine structure in the overlap integrals and, consequently, in the total tunneling probability P_{IF} [cf. Eqs. (80) and (86)]. One therefore concludes that the confinement leading to the characteristics of Figure 37 is due to a smooth potential profile. In the following, we shall only be interested in the numerical reproduction of the average number and spacing of the experimental tunneling structures. We, therefore, describe the 1D confinement by the cosine function of Eq. (89), which was found previously to be a good approximation of the potential of shallow etched wires [140]. The resonant tunneling current $I(V_{\mathrm{b}})$ is calculated according to $I = 2eP_{\mathrm{IF}}$ together with Eq. (88) and its first derivative $dI(V_{\mathrm{b}})/dV_{\mathrm{b}}$ is obtained numerically. To account for generic broadening effects caused by the limitation of the carrier lifetime in the states involved in the resonant tunneling process and by the interaction between electrons and acoustic phonons, the tunneling probability near a resonance at V_{b}' is assumed to have Lorentz form, which we denote by $L(V_{\mathrm{b}} - V_{\mathrm{b}}')$:

$$L(V_{\mathrm{b}} - V_{\mathrm{b}}') = \frac{1}{\pi} \frac{\Gamma}{(V_{\mathrm{b}} - V_{\mathrm{b}}')^2 + \Gamma^2} \tag{91}$$

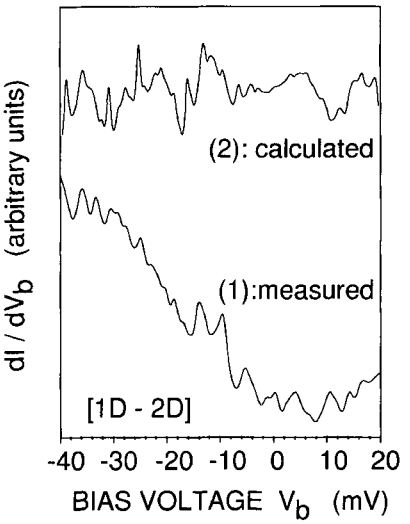


Fig. 47. Comparison of the measured and calculated 1D–2D tunneling characteristics (see also Fig. 37). (Source: Reprinted with permission from [23]. © 1993 American Physical Society.)

In this equation, Γ represents the linewidth of any resonance position on the scale of the applied voltage. The application of Eq. (91) to the model calculation also accounts for broadening effects caused by the sample preparation technique, such as fluctuations of the wire width and so on. The total tunneling current is then given by the convolution of the current represented by the bare tunneling probability and the Lorentz function given previously [154, 156]:

$$j_{\mathrm{tot}} \to \int dV_{\mathrm{b}}' j_{\mathrm{tot}}(V_{\mathrm{b}}') L(V_{\mathrm{b}} - V_{\mathrm{b}}') \tag{92}$$

The positions of the 2D subbands in the inversion (collector) layer needed for the calculation can be obtained from the tunneling experiments on non-nanostructured samples.

The final result is shown in Figure 47, curve 2, assuming a temperature of $T = 2$ K and a level width $\Gamma = 0.5$ mV. The parameters of the cosine potential were chosen to be $V_{\mathrm{mod}} = 55$ meV and $w = 350$ nm. The corresponding experimental result is plotted as curve 1 in the figure. All structures in the calculated dI/dV_{b} curves are mainly caused by the overlap integral. As a major difference between the measured and calculated curve, one may note that in the former the resonant tunneling structure is superposed on a background that increases monotonically with decreasing bias voltage. This background presumably reflects a possible energy (i.e., bias voltage) dependence of the transmission coefficient of the tunneling barrier [Eq. (84)]. Note that the structures of the calculated curve are determined by the sum of overlap integrals as discussed previously. Any influence of the applied bias voltage on the transmission coefficient of the barrier itself is neglected in the calculation. Nevertheless, the qualitative features of the measured tunneling characteristics, for example, the average peak amplitude and peak distance, are well reproduced within the outlined model. However, as one has to sum up over all closely spaced 1D emitter and 2D collector subbands, it is not possible to identify and analyze the contributions of each single 1D state to the total tunneling current. The main factor, which limits the resolution, is the doped barrier between the 1D and 2D systems. It introduces scattering in the tunneling process and, therefore, broadens the linewidth of the resonances in the dI/dV_{b} curves. Because of the large number of resonance structures in the dI/dV_{b} curves, the peaks will overlap and also smear out, which makes a more detailed quantitative analysis rather difficult.

6.3.1. *1D–1D Tunneling: Probing the Fourier Transform of One-Dimensional Wave Functions*

In the experiment outlined previously, it was not possible to explain all measured features of the tunneling characteristics in detail, although its numerical analysis gave valuable insight into how the presence of numerous 1D subbands influences the 1D–2D tunneling current when the conservation of the k_y momentum component is relaxed because of the confinement in the y direction. The particular form of the tunneling matrix element in Eq. (86) also suggests the possibility of measuring directly the Fourier transform of the wave functions of the confined emitter states. To this end, however, the number of 1D subbands contributing to the tunneling characteristics within a given bias voltage interval has to be considerably reduced. Progress in this direction has been achieved by manufacturing single-wire tunneling devices from double-barrier resonant tunneling diode (DBRTD) structures [157]. The corresponding device geometry is shown in Figure 39 together with the definitions of some notation used later on. Depending on the width l_t of the top line, a situation can be achieved where only one 1D subband is occupied in the emitter and the subband spacing in the well, $\hbar\omega_w$, is on the order of 10 meV [144]. For this situation, a set of tunneling I–Vs is shown in Figure 48, obtained for different magnetic fields applied perpendicular to the tunneling direction (and parallel to the top line). Each of the displayed tunneling peaks now corresponds to transitions from the single 1D emitter level (labeled by $i = 0$) into a single collector level(labeled by the index j).

For the numerical analysis of the measured I–Vs, a modified form of the transfer Hamiltonian formalism is applied [145, 146]. In the form used by Beton et al. [144] and Wang et al. [143], level broadening is included in the formalism from the very beginning by replacing the δ functions used in Eq. (80) with spectral density functions [158, 159]. The corresponding expression for the tunneling current as a function of bias voltage V, applied across the barrier, is

$$I = 2e \sum_{k_y,k_z} \sum_{jk'_z} |T_{jk'_z,k_y,k_z}|^2 \int \frac{d\varepsilon}{2\pi} A_e(k_y, k_z, \varepsilon) \times A_w\left(jk'_z, \varepsilon + eV\right) f(\varepsilon) \qquad (93)$$

The coordinate system underlying this equation is shown in Figure 38. T denotes the tunneling matrix element already introduced in Eq. (86). The spectral density functions A_e and A_w for the emitter and the well have Lorentzian shape. In addition, it is assumed that there is no charge accumulation in the well and that all collector states are empty. If a

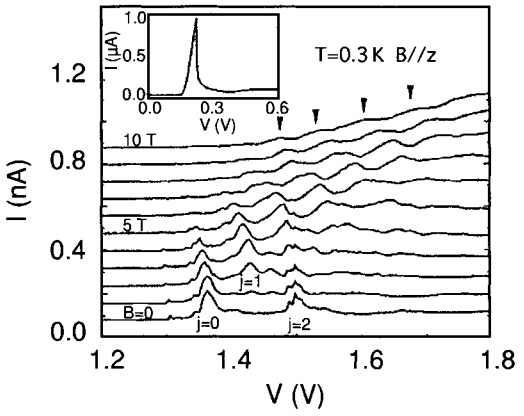


Fig. 48. I–V characteristics of a 1D–1D submicrometer tunneling diode in the presence of a magnetic field applied parallel to the z direction. The curves are measured for magnetic field strengths ranging from 0 T (lowest curve) up to 10 T (uppermost curve), varied in 1-T steps. The curves are offset for clarity. The inset shows I–V at $B = 0$ T for a large-area device. The device geometry is shown in Figure 38. (Source: Reprinted with permission from [144]. © 1995 American Physical Society.)

magnetic field is applied parallel to the top line (cf. Fig. 39), the tunneling current can be expressed as [145]:

$$\frac{I}{I_0} = \frac{1}{\pi} \sum_{ij} \left\{ \frac{2[\varepsilon_F - (i+1/2)\hbar\hat{\omega}_e]}{\hbar\omega_e} \right\}^{1/2} M_{ij}^2(B) \frac{\Gamma^2}{(\varepsilon_i + eV^* - \varepsilon_j)^2 + \Gamma^2} \tag{94}$$

Here, ω_e is the confining frequency of the emitter quantum wire whose confinement potential is assumed to be parabolic. $\hat{\omega}_e = \omega_e(\Omega/\sqrt{\Omega_e^2 + \omega_c^2})$ is the emitter frequency in the presence of a magnetic field.* I_0 is a renormalized tunneling current that is solely due to the transmission coefficient t of the barrier: $I_0 = 4et^2\sqrt{m\omega_e/\hbar}(L_z/\Gamma)$. The main information on the tunneling process is contained in the matrix element M_{ij}, which now reads

$$M_{ij}(B) = \int \frac{dk_y}{2\pi} \Phi_i\left(l_e^{-2}\hat{l}_e; k_y - \frac{eB\Delta s}{\hbar}\right) \Phi_j\left(l_w^{-2}\hat{l}_w; k_y\right) \tag{95}$$

Here, $\Phi_{i,j}$ are the Fourier transforms of the corresponding wave functions in the emitter (i) and the well (j) and the $l_{e,w}$ are given by $l_{e,w} = (\hbar/m\omega_{e,w})^{1/2}$ (in $\hat{l}_{e,w}$ the corresponding frequencies $\hat{\omega}_e$ have to be inserted). The magnetic field dependence enters through a parameter $k_0 = eB\Delta s/\hbar$ in the tunneling matrix element, where Δs is the spatial separation of the 1D states in the emitter and in the well. The k_0 dependence can be derived quantum mechanically, but it can also be motivated from a simple classical picture. In the given geometry of $B \| z$, an electron moves on a curved orbit. While it is traveling the distance Δs in the x direction, the electron momentum in the y direction changes by $eB\Delta s = \hbar k_0$ through the influence of the Lorentz force. In a quantum mechanical picture of 2D–2D tunneling, this means that the magnetic field introduces a wavevector shift of k_0 between the initial and final states, which is achieved by applying the translation operator ($\exp(-ik_0y)$) to the corresponding wave function. For 1D–1D tunneling, however, k_0 enters as a wavevector shift between the Fourier transforms of the initial and final wave functions of the 1D states.

Now, if only one subband is occupied in the emitter and the subband spacing in the well is large enough, one has realized the unique situation that the Fourier transform of the probability density of the laterally confined states in the well can be determined directly, if the resonant tunneling current is measured as a function of the magnetic field applied parallel to the wires. Note that the occupation of only one emitter state is crucial for this purpose; otherwise, the measured $I(B)$ curve will be a convolution of many resonances of all occupied states. In the case of a single-emitter subband, resonant 1D–1D tunneling via the jth state in the well occurs when the voltage is adjusted in a way that the emitter state is aligned in energy with the jth state in the well, which is for (see also Fig. 39)

$$eV^* + E_0 + \frac{\hbar\hat{\omega}_e}{2} = E_1 + \left(j + \frac{1}{2}\right)\hbar\hat{\omega}_w \tag{96}$$

Here, E_0 is the emitter subband energy, E_1 the subband energy in the well (both are magnetic field dependent in the special notation used in [145]), V^* is the voltage drop across the barrier, and $\hat{\omega}_e$ and $\hat{\omega}_w$ the magnetic field–dependent oscillator frequencies of the lateral confining potentials in the emitter and the well, respectively. At resonance, the current flowing through the jth state, $I_j(B)$, is proportional to the modulus squared of the overlap integral $M_j(B)$ between the initial and final state. This is given by Eq. (95), which can be rewritten as [144]:

$$\begin{aligned} M_j(B) &= \int_{-\infty}^{+\infty} \exp(-ik_0y)\, \varphi_0^e(y)\, \varphi_j^w(y)\, dy \\ &= \int_{-\infty}^{+\infty} \Phi_0^e(k_y - k_0)\, \Phi_j^w(k_y)\, dk_y \end{aligned} \tag{97}$$

* In the special notation used by Mori et al. [145], Ω_e quantifies the confinement in the growth direction, which is assumed to be parabolic for simplicity. In a magnetic field, this confining frequency also becomes magnetic field dependent.

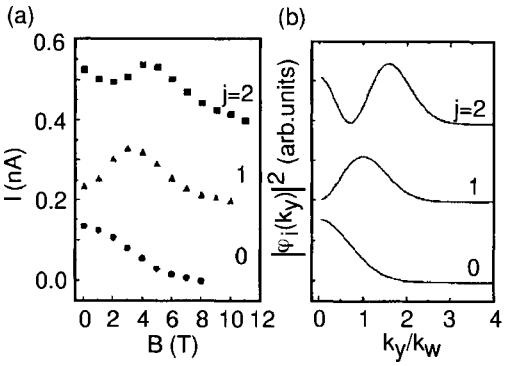


Fig. 49. (a) Peak currents as a function of magnetic field for the $j = 1, 2, 3$ resonance peak. The experimental data are displaced for clarity. (b) Probability densities for the $j = 0, 1, 2$ simple harmonic oscillator states plotted versus k_y/k_w. A value of $\hbar\omega_w = 10$ meV was assumed for this calculation. (Source: Reprinted with permission from [143]. © 1994 American Physical Society.)

where $\Phi_0^e(k_y) = \int_{-\infty}^{+\infty} \varphi_0^e(y) \exp(ik_y y)\, dy$ and $\Phi_j^w(k_y)$ are the Fourier transforms of the emitter and well wave functions. As discussed previously, the magnetic field thus induces a relative shift in k space between the emitter and the collector states. If the emitter state has a narrow spread in k space, Eq. (97) shows that the Fourier transform of the jth 1D wave function in the well can be probed by simply measuring the peak tunneling current as a function of the magnetic field. Due to the asymmetry of the 1D–1D tunneling device, the assumption of narrow k spread of the emitter wave function is justified because the confining potential in the y direction is much stronger between the double barriers than for the emitter electrode owing to side-wall depletion.

Figure 49a shows the peak currents of the magnetotunneling peaks labeled $j = 0, 1, 2$ in Figure 48, plotted as a function of the magnetic field. In Figure 49b the calculated Fourier transforms of the probability densities, corresponding to the three lowest states in a simple harmonic oscillator potential, are also shown for the purpose of comparison. For convenience, the calculated probability density was plotted versus k_y/k_w, where $k_w = (m\omega_w/\hbar)^{1/2}$ and k_y is calculated from $k_y = eB\Delta s/\hbar$. If one chooses $\hbar\omega_w$ such that the measured and the calculated positions of the $j = 1$ maximum coincide, one obtains excellent agreement between the measured and the calculated results. However, one has to be aware of the fact that the width of the emitter Fourier transform $\Phi_0^e(k_y) = 1/(\pi k_e^2)^{1/4} \exp(-k_y^2/k_e^2)$, characterized by $k_e \equiv (m\omega_e/\hbar)^{1/2}$ is finite. This limits the resolution of the minimum of the $j = 2$ state.

6.3.2. 2D–1D Surface Superlattice Tunneling: Measuring Potential Profiles

In the preceding experiment, vertical transport through quantum wires and the transfer Hamiltonian formalism were used to determine the probability density for electrons in quantum wire states. The measured (k space) probability density was found to agree well with the one expected for a parabolic confinement potential. This justifies the assumptions on the shape of the confinement made to get tractable expressions in the formalism used for the analysis of the experiments. As will be shown in this section, this type of wave function spectroscopy allows one to gain even more detailed information on the shape of confining potentials. A particularly well elaborated example of this is ? by the results of Kardynal et al. [147–149], who have used the tunneling geometry shown in Figure 40.

As already mentioned earlier, their device allows them to perform equilibrium tunneling spectroscopy, that is, the measurement of the differential tunneling conductance as

a function of the Fermi energy in the emitter without applying a bias voltage across the tunneling barrier. Due to the particular sample layout this can be done as a function of different parameters, such as magnetic fields or front-gate voltages. The latter offers the possibility of using, alternatively, a set of independent quantum wires [147] or a lateral surface superlattice (1DSSL) [148] as the collector system. For the quantitative analysis of their experimental results, Kardynal et al. also employ a transfer Hamiltonian formalism similar to the model discussed in the previous section. They obtain for the derivative of the tunneling current the following expression [148]:

$$\frac{dI}{dV} \propto t^2 \sum_{k_x,k_y} B_1(k_x, k_y, \mu) A_2(k_x, k_y, \mu) \tag{98}$$

where the so-called augmented spectral function

$$B_1(k_x, k_y, \mu) = \sum_{\nu} \left|\widetilde{\varphi}_{k_x,\nu}(-k_y)\right|^2 A_1(k_x, k_y, \nu, \mu) \tag{99}$$

has been introduced, whose detailed form will be discussed later for the case of tunneling into a lateral 1DSSL. A_1 and A_2 are Lorentzian spectral functions accounting for level broadening just as in Eq. (93). t^2 is again the transmission coefficient of the tunneling barrier. In fact, Eq. (98) is equivalent to Eq. (93), because the differentiation with respect to V removes the integration over the energy ε. Note, however, that in the preceding expression the general overlap integrals are already cast in a form appropriate for a 2D emitter and a set of tightly bound superlattice states in the collector. In the notation of Kardynal et al. [148], the spectral functions are written as

$$A_{(1,2)}(s_{1,2}, \mu) = \frac{\Gamma}{2\pi[(\Gamma/2)^2 + (\mu - \xi^{(1,2)}_{s_{(1,2)}})^2]} \tag{100}$$

where $s_1 = (k_x, k_y, \mu)$ and $s_2 = (k_x, k_y)$ are the relevant quantum numbers for the 2DEG and the 1DSSL, $\hbar/\Gamma$ is the quasiparticle lifetime, and μ is the electrochemical potential. $\xi^{(1)}_{s2} = (\hbar^2/2m)(k_x^2 + k_y^2) + V_2$ is the energy dispersion in the 2DEG. If tunneling into a 1DSSL is studied, the energy dispersion of the collector electron gas is written as $\xi^{(1)}_{s1} = \hbar^2 k_x^2/2m^* + E_{k_y,\nu} + V_1$, where the miniband structure of the 1DSSL is characterized by $E_{k_y,\nu}$ (termed the *crystal part* of the 1DSSL band structure in [148]), ν being the miniband index. $V_{(1,2)}$ are the energy levels of the 2D subbands in the upper and lower channels, respectively. Because of the superlattice nature of the collector system, the wave functions perpendicular to the 1DSSL are Bloch functions. If a tight binding picture is adopted, they are given by a linear combination of the $\varphi_{k_y,\nu}(y)$ obtained by solving the Schrödinger equation in the range $0 \leqslant y \leqslant a + b$ for a single potential well of the 1DSSL:

$$\Phi_{k_y,\nu}(y) = \sum_n \exp\big(ik_y n(a+b)\big)\varphi_{k_y,\nu}\big(y - n(a+b)\big) \tag{101}$$

The Fourier transforms of $\varphi_{k_y,\nu}(y)$ will be denoted by $\widetilde{\varphi}_{k_y,\nu}(k)$. They already appear in the definition Eq. (99) of the augmented spectral density function.

To illustrate the meaning of the spectral density functions, we first consider the case of zero potential modulation. In this case, Eq. (98) describes pure 2D–2D tunneling processes and the spectral density functions at the Fermi energy simply have circular shape. The circles will be broadened by the linewidth Γ. If an appropriate front-gate voltage is applied to the nanostructured front gate, the electron density is modulated under the gated area and a 1DSSL is induced. A typical situation is shown in Figure 50.

The spectral density function A_1 for a 1DSSL, calculated according to Eq. (100) and with the appropriate dispersion relation given previously, is plotted in Figure 51a. The 1DSSL induces a set of Brillouin zone boundaries in k space. In the extended-zone scheme, a cut through the spectral density function at the Fermi energy will consequently appear as a set of circles displaced by the reciprocal lattice vector $G_n = 2\pi n/(a + b)$, as is shown

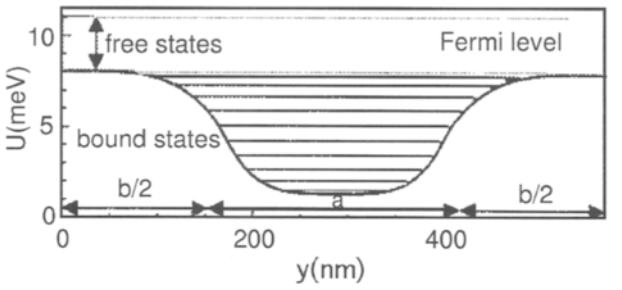


Fig. 50. 1DSSL potential, which is induced by the nanostructured front gate. The total period of the 1DLSSL is equal to $(a+b)$. (Source: Reprinted with permission from [148]. © 1996 American Physical Society.)

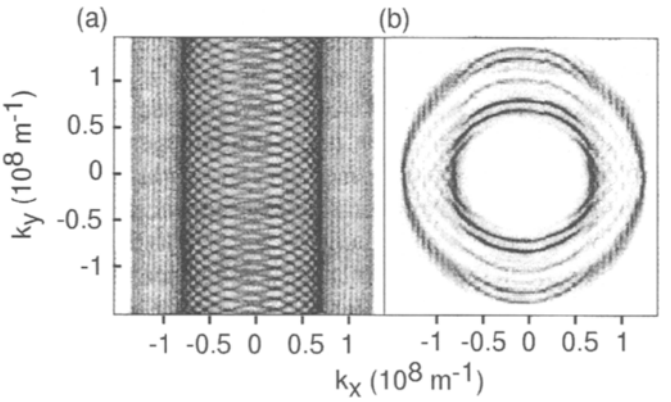


Fig. 51. (a) Cut at the Fermi energy through the spectral density function A_1 of the potential discussed in the text. (b) Same as (a) but for the augmented spectral density function B_1. (Source: Reprinted with permission from [148]. © 1996 American Physical Society.)

in Figure 51. If the 1DSSL potential is sufficiently deep, bound states will also exist in the potential wells. These states have no dispersion in k_y and appear, therefore, as lines parallel to the k_y direction in Figure 51a.

According to Eq. (98), the tunneling differential conductance (TDC) is proportional to the convolution of A_2 and the augmented spectral function B_1. The main features of the measured TDC, shown in Figure 41, are, therefore, due to the overlap integrals contained in B_1. Assume a shape of the confining potential as shown in Figure 50, giving rise to a number of tightly bound Bloch states. The k_y dependence of the bound states will be weak and, consequently, the overlap integrals in the expression for B_1 will essentially be given by the Fourier transform $\widetilde{\varphi}_{k_y,\nu}(-k_y)$ of the wave functions corresponding to a single well. The corresponding k-space plot of B_1 is given in Figure 51b. The vertical lines in Figure 51a are now replaced by the modulus squared of the Fourier transforms of the bound state wave functions. In addition to the quasi–bound states, quasi–free states will also be present in the 1DSSL. These give rise to the approximately circular features of B_1 in Figure 51b. To see this, one may approximate the free-state Bloch functions according to Kardynal et al. [148] by Kronig–Penney wave functions. If $\varphi_{k_y,\nu}(y) = A\exp(iky) + B\exp(-iky)$ represents the free states in the ungated regions and $\varphi_{k_y,\nu}(y) = C\exp(iqy) + D\exp(-iqy)$ the free states in the gated regions of the LSSL, it becomes immediately clear that $|\widetilde{\varphi}_{k_y,\nu}(-k_y)|^2$ will display peaks at $k_y = \pm k$ and $k_y = \pm q$. If a smooth potential is assumed instead of the rectangular Kronig–Penney potential, these peaks will be broadened but otherwise remain at the same k-space positions. They are responsible for the k and q peaks in the experimental

data shown in Figure 41. Their position in the differential tunneling conductance gives the electron concentration in the gated and ungated regions of the 1DSSL and, consequently, the values of the potential minima and maxima. The positions of the smaller peaks, denoted by arrows in Figure 41, are exclusively determined by the shape of the 1DSSL potential. Excellent agreement between the calculated dI/dV curves and the experimental data can be achieved, if the 1DSSL potential is properly chosen. The potential shown in Figure 50 gives the best fit to the experimental data in a broad range of the top-gate and back-gate voltages V_{SI} and V_{BG}. It has the typical shape expected for confinement potentials induced by the split-gate technique at relatively low gate bias.

With the same sample layout, the voltage applied to the nanostructured front gate can be increased to yield a collector system that consists of a set of separated quantum wires. For this case the analysis of potential shapes can be extended by performing magnetotunneling spectroscopy, just as it was discussed in the previous section [149]. For this purpose, a magnetic field is applied parallel and also perpendicular to the layers of the sample and the equilibrium tunneling conductance dI/dV is measured as a function of the magnetic field B. Typical experimental results are shown in Figure 52 (solid lines).

From the discussion of the transfer Hamiltonian formalism given previously, it is clear that the detailed shape of the confining potential will have a strong influence on the measured tunneling conductance. Hence, a plot of dI/dV versus magnetic field is a unique fingerprint of the confining potential. By incorporating the magnetic field into the calculation of the tunneling differential conductance [Eq. (98)] and by fitting the calculated curves to the corresponding experimental data, a quite realistic picture of the confining potential and the corresponding wave functions can be constructed (see parts e and f of Fig. 52). To

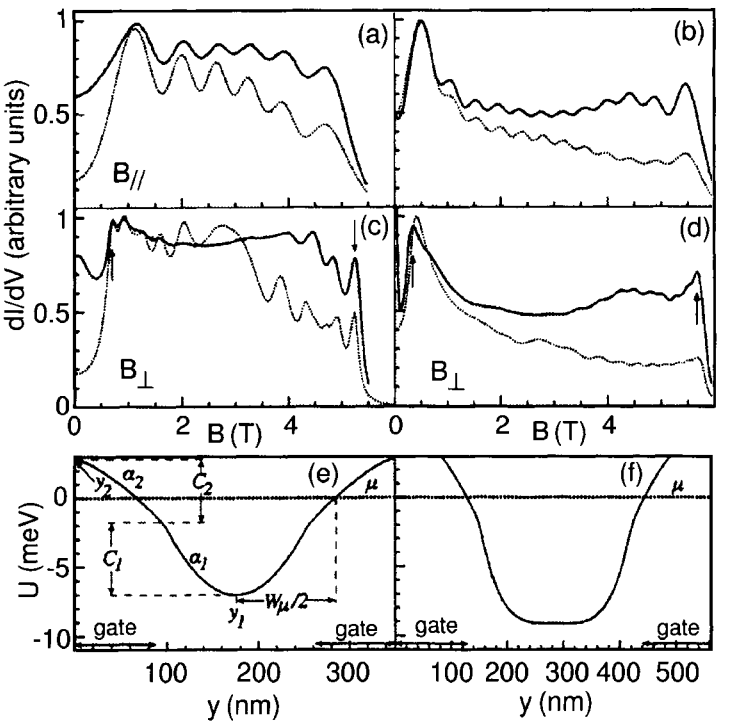


Fig. 52. Experimental (solid lines) and calculated tunneling conductance (dotted lines) for $V_{SL} = -0.48$ V for $B_{\|}$ (a) and (b) and $B_{\perp}$ (c) and (d). (a) and (c) are the data of a device with a 350-nm superlattice period; (b) and (d) belong to a device with a 570-nm grating period. (e) shows the best fitting potential profile for the 350-nm-period device and (f) for the 570-nm-period device. (Source: Reprinted with permission from [148]. © 1996 American Physical Society.)

obtain better results, the fitting procedure was carried out simultaneously for both magnetic field directions [149].

As shown in Figure 52, the overall features of the tunneling characteristics are well reproduced by the transfer Hamiltonian approach. Parts e and f of Figure 52 show the fitted potential profiles of a 350-nm- and a 570-nm-period device, respectively. For the short-period device, the confining potential is approximately parabolic at the bottom, giving rise to equidistant subband spacing. For higher energies, the nonparabolic widening of the potential will lead to decreasing subband spacings. For the longer-period device, the confining potential is approximately square well like. The reason for this difference is simply the different "overlap" of the electrostatic depletion fields of the two gate electrodes defining the wire region. For the small-period device, the wire region is depleted by the gate voltage from the very beginning, resulting in an approximately cosine-shaped potential. The depletion of the wire region is also reflected by the fact that the bottom of the potential in Figure 52e is higher in energy than in Figure 52f. The electron density in the short-period wire will, therefore, be substantially influenced by the gate voltage. For the long-period wire, this will only be the case at high gate voltages, where the confinement potential will change its character and develop from a flat bottom, nearly rectangular well into an approximately parabolic one. The discussed experiment, therefore, gives a rather direct experimental proof for the validity of the general results obtained by the self-consistent treatment of split-gate-induced confining potentials (see Section 3.2).

7. VERTICAL TRANSPORT THROUGH QUANTUM DOTS

In this section, vertical tunneling through quantum dots will be discussed on the basis of a few instructive experiments. Lateral transport through quantum dots will be ignored almost completely because, owing to the vastness of this field, it is beyond the scope of the present chapter. The lateral transport geometry will only be treated in the context of Coulomb blockade effects, which are most easily introduced and discussed for this case. For a comprehensive treatment of lateral tunneling through quantum dots, see, for example, the book *Single Charge Tunneling* [160], the clear and concise exposition by Meirav and Foxman [161], or the very recent article by Kouwenhoven et al. [162], and, of course, the references cited therein.

In the following, emphasis will again be placed on the question of how to gain some information on the confining potential and the corresponding wave functions in quantum dots. In this respect, it is important to note that the $I-V$ curves of quantum dot devices have to be interpreted with some care. As shown in the previous section, information on confining potentials is obtained from the resonance structures in the $I-V$ curves. However, in the case of 0D tunneling, a wealth of structure is observed in the $I-V$ characteristics that is not necessarily due to resonant tunneling processes in the sense discussed previously for quantum wires. Other physical effects such as tunneling via donor states or Coulomb blockade effects can also lead to a multitude of structures in the $I-V$ curves. The discussion of early experiments on tunneling in quantum dots is, therefore, followed by a brief discussion of these "parasitic" effects and of some instructive experiments that allow us to separate Coulomb blockade–mediated structure from resonant tunneling through quantum dot states.

7.1. First Experiments

The first measurements on vertical quantum dot tunneling were reported by Reed and coworkers [163] in 1988. In this early work, GaAs–AlGaAs–InGaAs–AlGaAs–GaAs double-barrier resonant tunneling diodes (DBRTDs) were used as the basic material. The InGaAs was introduced between the barriers because it allows us to lower the quantum well states

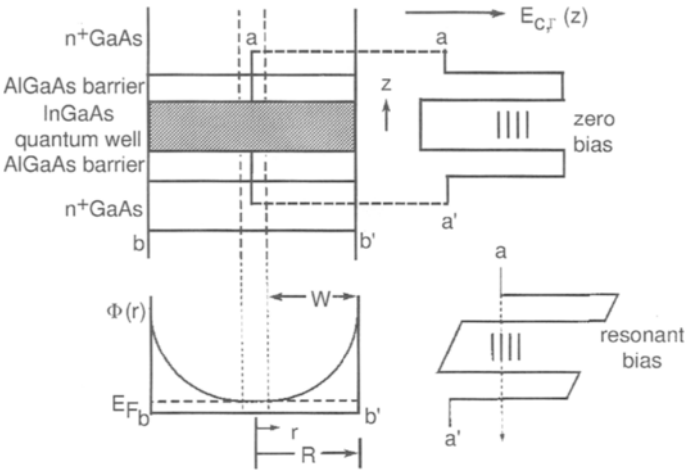


Fig. 53. Left, top: Schematical view of a quantum dot sample realized on double-barrier resonant tunneling diodes. The barriers have a thickness of 40 Å; the undoped InGaAs well is 50 Å wide. On both sides of the barriers, there is an undoped GaAs spacer (100 Å) and a graded region, where the doping is changed from 1×10^{16} cm^{-3} to 2×10^{18} cm^{-3}. The top contact is highly n doped. Left, bottom: Radial component of the confining potential in the pillar-shaped structure. Right: Conduction band profile of the quantum dot structure. The discrete states in the dot are indicated schematically. (Source: Reprinted with permission from [163]. © 1988 American Physical Society.)

with respect to the conduction band edge without changing the width of the quantum well. More details about the sample structure are shown in Figure 53. On these samples, ultrafine pillars were fabricated by electron beam lithography and reactive ion etching. The pillars had a typical diameter of 250 nm and a height of 0.5 μm. The main technological problem in the beginning was the formation of ohmic contacts to the tops of these pillars. For this purpose, the structures were planarized by covering the whole sample with polyimide, followed by a reactive ion etch back. In this way, only the uppermost parts of the pillars were exposed, which finally could be coated by an evaporated gold contact. More details on the fabrication process can be found in [164, 165].

Current–voltage curves were measured at low temperatures and also capacitance measurements were performed to characterize large quantum dot arrays [166]. We restrict the discussion to the I–V measurements that are more instructive in the present context. Figure 54 shows a typical I–V curve of a nanostructured DBRTD. An unstructured sample fabricated on the same wafer behaves "normal" and a clear negative differential resistance region is observed above $V = 0.9$ V.

The nanostructured sample, however, exhibits several extra features at low temperatures. As shown in Figure 54, the expected negative differential resistance region is somewhat less pronounced and a series of equidistant structures in the I–V curve is revealed instead. These peaks are due to resonant tunneling processes through the zero-dimensional states in the quantum "dot" or quantum "disk," which is formed in the InGaAs well cladded by the two AlGaAs barriers and the radial confinement in the small pillar. At higher temperatures, these small peaks disappear again and the I–V curves of the nanostructured DBRTD resemble those of large-area samples. The equidistant peak spacing suggests a parabolic confinement, which can be estimated quantitatively using the following considerations: The edge depletion width in the pillars, W, can be derived if one assumes that the current density in the small pillars is the same as in the large-area samples. Because the Fermi level pins at the midgap position of $\Phi_T = 0.7$ eV, the confining potential can be written as

$$\Phi(r) = \Phi_T \left[\frac{1 - (R - r)}{W} \right]^2 \tag{102}$$

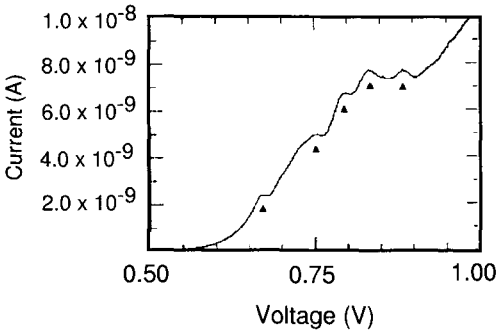


Fig. 54. Typical current–voltage characteristics of a single quantum dot measured at liquid helium temperatures. (Source: Reprinted with permission from [163]. © 1988 American Physical Society.)

where r is the radial coordinate, R is the geometrical radius of the pillar, and W is the depletion width ($R - W \leqslant r \leqslant R$). For $R \approx W$, the corresponding energy spacing between the single electron levels is given by

$$\Delta E = \left(\frac{2\Phi_T}{m^*}\right)^{1/2} \frac{\hbar}{R} \tag{103}$$

This yields a value of 26 meV for the 0D states in the InGaAs well, which can be compared with the peak positions in the measured I–V curve. If one assumes that the applied voltage drops homogeneously across the whole structure, approximately half of the voltage will drop between the emitter and the confined states at the center of the well. As a consequence, the measured energy spacing ΔE is equal to e times half the voltage spacing ΔV between the peaks. One obtains a subband spacing of approximately 25 meV from the experimental I–V curve, showing that the preceding considerations give a fairly accurate description of the situation.

For the previous analysis, however, an important assumption was made that caused some confusion in the early stages of low-dimensional tunneling experiments. As already stated by Reed et al., their samples represent a system with electrons in the pillar traveling through a freestanding quantum wire, tunneling through a quantum dot, and continuing to flow in another quantum wire. The correct description of this 1D–0D–1D tunneling process necessitates the calculation of transmission coefficients that takes the dimensionality of the involved states into account [167–169].

In the previous experiment, however, excellent agreement with the experiment is achieved by simply assuming that resonance structures in the I–V curve occur whenever the Fermi energy in the emitter electrode is energetically aligned with a zero-dimensional state in the dot. Because this assumption is only true if the emitter and collector electrodes do not contain any quantized states and can, therefore, be considered as perfectly three-dimensional systems, one might conclude that the sample quality was too poor to observe the influence of the different dimensionality in the emitter and collector electrodes.

At this point, it should be mentioned, however, that besides poor sample quality there are also several other possibilities for the missing evidence of 1D–0D–1D tunneling processes even if the sample quality is sufficiently good. To illustrate this, we just consider one possible example: To improve the sample quality, undoped spacer layers were introduced in front of the double-barrier structure, which under bias form a triangular potential well, resulting in electron confinement in the growth direction (cf. Fig. 39b for a similar situation in the 1D–1D case). Together with the radial confinement caused by the etching process, the emitter itself will represent a second quantum dot in front of the double barrier, which, in principle, should lead to 0D–0D–1D tunneling behavior. Because confinement in the growth direction is weak, many closely spaced subbands will exist in this direction,

each of them having a ladder of corresponding (and also closely spaced) 0D states resulting from the lateral confinement. These states will be broadened at finite temperatures and in the presence of a certain amount of scattering. The overlap of the resonant peaks and the scattering-induced broadening will smear out the expected fine structure completely and only the main resonances resulting from the 0D states in the InGaAs well will be dominant. Thus, proper sample design is required if tunneling processes between states of different dimensionality are to be studied on quantum dot samples.

Tarucha et al. [170] were the first to report experimental evidence of the expected dimensionality effects for the emitter electrode in DBRTDs. In their work, focused ion beam implantation is used to define rectangular quantum dot or quantum wire structures of variable size. This also allows one to vary the dimensionality as well as the geometry of the nanostructured collector system and enables studies of tunneling processes through 0D and 1D states in rectangular geometry. Although the experimental results look very similar to the results of Reed et al., additional spectral features in the measured I–V curves suggested a mixing of the 1D or 0D states between the barriers and the 2D states in the contacts.

7.2. Lateral and Vertical Transport through Quantum Dots: Coulomb Blockade Effects

7.2.1. Coulomb Blockade in Planar Quantum Dots

In the previous section, vertical resonant tunneling through quantum dots was used for an investigation of the energy spectrum caused by 0D lateral quantization. The structure observed in the tunneling characteristics was thereby assigned to resonant tunneling processes via 0D states, just as in the case of quantum wires discussed in Section 6. For quantum dots, especially for those containing only a few electrons, this simple interpretation can be obscured by other mechanisms, which will also lead to structure in I–V characteristics. One of them, the so-called Coulomb blockade, will be the topic of the present section. The following discussion will be short and very elementary. The reader particularly interested in an in-depth exposition of Coulomb blockade and related effects is referred to the existing excellent reviews on this subject (see, e.g., [160–162]).

The Coulomb blockade effect in semiconductor nanostructures was first demonstrated and subsequently extensively studied on planar quantum dot devices, defined by properly designed split-gate geometries. Because the particular nature of the Coulomb blockade is most easily understood for these planar devices, we make a short digression from our discussion of vertical transport. The typical features of a planar quantum dot are depicted in Figure 55. The two constrictions formed by the gates G0, G1, and G2 define together with the independently biased plunger gate GP a small electron island within the underlying

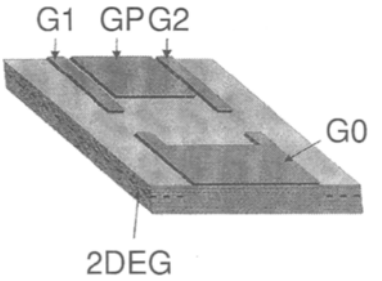


Fig. 55. Typical planar quantum dot geometry, which consists of the metallic gate areas G0, . . . , G2, GP, and the two-dimensional electron gas underneath. (Source: Reprinted with permission from [161].)

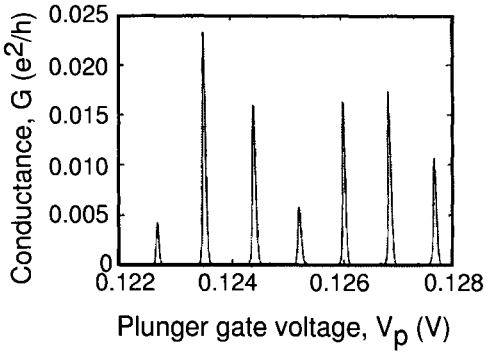


Fig. 56. Typical data showing the conductance of a planar quantum dot as a function of the plunger gate voltage V_p. The measurement was carried out at a temperature of $T = 100$ mK. (Source: Reprinted with permission from [161].)

2DEG. The point contacts between G0, G1, and G2 can be narrowed until they form low-energy barriers, through which electrons can be transferred by tunneling processes. Detailed information on the potential distribution and the corresponding electron energy spectrum can be obtained from self-consistent calculations [171]. It is also worth noting that, if the narrow constrictions are operated below pinch-off voltage, the planar dot structure of Figure 55 can be regarded as a short quantum wire, displaying transport properties characteristic of ballistic transport, such as, for example, quantized conductance (for details, see [160, 161]).

The plunger gate GP is a very common feature of all planar quantum dot structures [172–174]. It is coupled capacitively to the electron island and is used to change the electron concentration in the dot as well as the confinement strength. The relation between the plunger gate voltage V_p and the electron concentration is found to be linear. In a properly designed planar structure, the tunneling barriers at the entrance and exit of the dot are not influenced by the plunger voltage.

If the current through the dot is measured as a function of the plunger voltage at low temperatures (usually below 0.5 K) and a given source drain bias V_{DS}, the conductance $G = I/V_{DS}$ displays a series of sharp spikes, as shown in Figure 56. These spikes are called *Coulomb blockade oscillations* and they occur whenever an additional electron is added to a low-capacitance, few-electron system. Coulomb blockade oscillations were first observed in a system of metallic junctions [175]. For the case of semiconductor quantum dots, they were theoretically explained by Beenakker and van Houten [176, 177] as single-electron charging of the dot.

For an elementary explanation of the basic physics of the Coulomb blockade effect, we assume that N electrons are present in the dot, leading to a total charge of $Q = Ne$. Because the plunger is capacitively coupled to the dot, Q can be varied by varying V_p. However, owing to the discrete nature of the electron charge, Q must increase in discrete steps when the plunger gate voltage is swept continuously. The electrostatic energy of the dot is given by

$$E(N) = \frac{(Ne)^2}{2C} - \varphi Ne \tag{104}$$

where the first term represents the capacitive charging of the dot and the second term is the potential energy. C is the total capacitance of the dot with respect to its surroundings and φ is the electrostatic potential. If the plunger gate is assumed to be the only gate with significant capacitive coupling to the dot, one has $C = C_p$ and $\varphi = V_p$.

The previous equation can be easily solved for those integer values of N minimizing $E(N)$ for a given value of V_p, which immediately leads to the staircase relationship

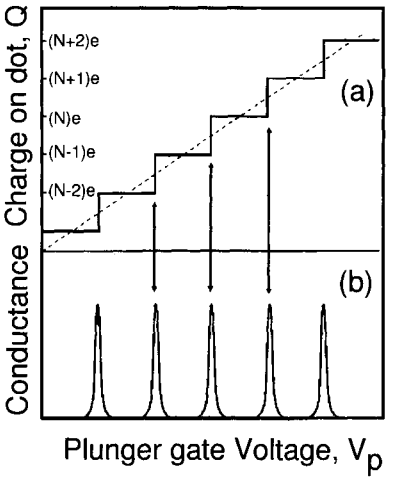


Fig. 57. (a) Charge on the quantum dot according to the relation $Q = CV_p$ (dashed line) and single electron charging (solid line). (b) Schematic plot of the conductance showing peaks each time an electron is added to the system. (Source: Reprinted with permission from [161].)

depicted in Figure 57a. The situation where a new electron is added to the dot corresponds to $E(N) = E(N+1)$. This occurs periodically at plunger gate voltages given by

$$V_p = \frac{e(N+1/2)}{C_p} \tag{105}$$

If V_p is adjusted according to this relation, the corresponding charge on the dot would be given by a half-integer multiple of e. Because half-integer values of e cannot occur, this means, of course, that the actual lowest energy state is degenerate and corresponds to either N or $N+1$ electrons. At the gate voltage given by Eq. (105), the dot is thus free to fluctuate between the N or $N+1$ electron state.

If a current flows through the dot, an electron must cross the barrier at the entrance and be able to stay inside the dot for a finite amount of time before exiting it through the other barrier. It is clear that this can happen only for those values of V_p where charge in the dot can fluctuate between Ne and $(N+1)e$, that is, where electron transfer into the dot is possible for constant energy. Away from these so-called charge degeneracy points, the electron transfer is suppressed by the Coulomb charging energy. This explains the occurrence of the Coulomb blockade oscillations shown in Figure 56.

The electrostatic charging energy necessary to add another electron to the dot is equal to e times the voltage spacing between two neighboring charge degeneracy points: $e(V_p^{N+1} - V_p^N) = e^2/C$. The resonances in the conductance are periodic and have a voltage separation of $\Delta V_p = e/C_p$. A detailed theoretical explanation of the exact shape of Coulomb blockade resonances and also of some additional fine structure observed in the experiment is rather complex and takes tunneling rates, bias voltages, and temperature effects into account [178, 179]. Coulomb blockade effects completely disappear if the temperature exceeds the Coulomb charging energy, that is, for $k_B T \approx e^2/C$.

7.2.2. Excitation Spectrum

Consider a situation where the plunger gate voltage and, hence, the electron concentration in the dot are kept constant. Electrons can now be injected into the dot by sweeping the voltage V_{DS} applied across the dot [180–182]. The schematic band diagram in Figure 58 is intended to illustrate this situation. Because of 0D confinement, a series of

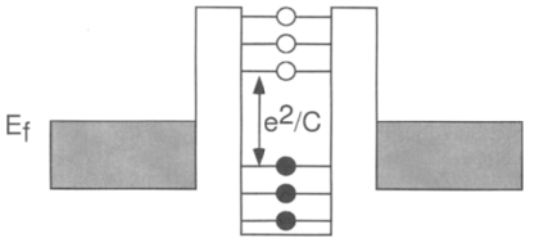


Fig. 58. Conduction band profile of a quantum dot, showing both occupied and empty levels in the dots having a Coulomb gap in between. (Source: Reprinted with permission from [161].)

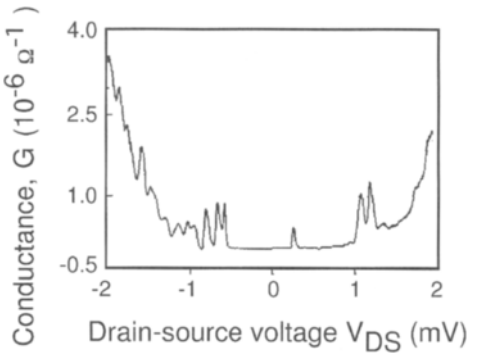


Fig. 59. Differential conductance dI/dV_{DS} as a function of V_{DS}. The flat region at zero bias reflects the Coulomb gap. The peaks are due to higher energy states in the dot. (Source: Reprinted with permission from [181]. © 1993 American Physical Society.)

equidistant electron levels exists in the dot. Occupied and unoccupied levels are separated by the Coulomb blockade gap e^2/C.

As long as the applied voltage is so small that the corresponding electron energy is below the electrostatic charging energy, electrons are not allowed to tunnel into the dot and the conductance is zero. With increasing Fermi level on the left-hand side, current begins to flow as soon as the Coulomb gap is overcome and E_F is aligned with the lowest empty level of the dot. The differential conductance dI/dV_{DS}, plotted as a function of the source drain bias, therefore, displays a flat region around $V_{DS} = 0$, which is a direct consequence of the Coulomb gap, followed by a number of resonant structures associated with the quantized levels of the dot. An example of this so-called *excitation spectrum* of the dot is shown in Figure 59.

Although it is clear from the preceding arguments that the peaks in dI/dV_{DS} are associated with higher energy levels inside the dot, a quantitative analysis of the peak positions is nevertheless difficult because of the interplay between resonant and Coulomb blockade effects. There will be a one-to-one correspondence between the peaks in the excitation spectrum and the quantum dot levels only if just one electron at a time is allowed to tunnel through the dot. Even if there are many empty states available, an additional electron will be able to enter the dot only if it has enough energy to overcome the additional Coulomb barrier of the first electron *and* if it is in resonance with an empty state of the dot. The same arguments are valid for all other electrons that could enter the dot at sufficiently high bias voltages. Taking into account that the tunneling rates and dwell times will be different for electrons in different 0D states, it is easy to imagine that a quantitative analysis of the subband energies in the presence of Coulomb blockade effects will not be a straightforward matter.

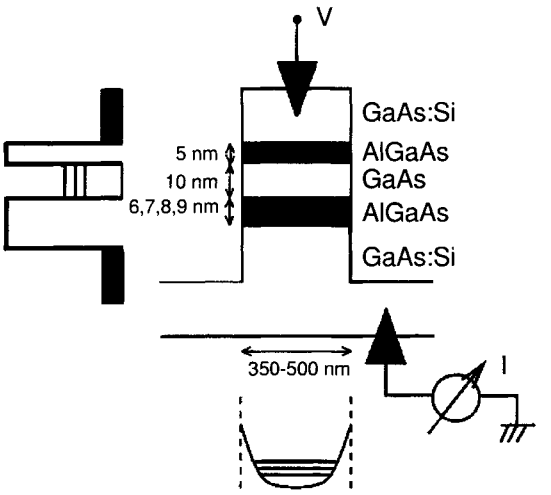


Fig. 60. Cross section of a double-barrier tunneling device used for single-electron tunneling spectroscopy. (Source: Reprinted with permission from [185].)

7.2.3. Tunneling and Coulomb Blockade Effects in Vertical Quantum Dots

Coulomb blockade effects in vertical transport through quantum dots were first demonstrated by capacitance spectroscopy on strongly asymmetric double-barrier structures [183, 184]. In vertical tunneling experiments, it is possible to detect them also if samples with a relatively wide central well and asymmetric barriers are used [185, 186]. A cross section of such a double-barrier tunneling device is shown in Figure 60. For the depicted sample structure, the emitter and collector electrodes are degenerate at low temperatures and, therefore, contain no quantized states. This is an important point concerning the interpretation of the resulting tunneling spectra because 0D states in the emitter electrode would cause a multitude of additional structure in the corresponding $I-V$ curves in zero [187] as well as in nonzero magnetic fields [167, 188]. Some theoretical considerations concerning this topic are found in [168, 169, 189–191].

Owing to the asymmetric conduction band profile of this 3D–0D–3D tunneling structure, the $I-V$ characteristics exhibit an asymmetric bias voltage dependence, because completely different physical processes dominate the measured $I-V$ curves, depending on the polarity of the bias voltage. A schematical view of the band diagram under bias and the corresponding $I-V$ curves are shown in Figure 61. For positive bias direction (Fig. 61a), the emitter barrier is thicker than the collector barrier, and, as a consequence, the tunneling rate through the emitter barrier will be low compared to the tunneling rate out of the central well. It is, therefore, reasonable to expect that the electrons will be transferred through the central well one by one and all structures in the measured $I-V$ curves are due to new channels for tunneling electrons, which open as soon as the emitter Fermi level matches their energetic position.

For opposite bias, the collector barrier is thick and the tunneling rate out of the dot is small. Thus, charge will accumulate inside the dot and Coulomb blockade effects can be expected. As shown in Figure 61b, one indeed observes a Coulomb staircase, which is shifted in voltage because of the confinement energy inside the dot [192–194]. Note that the step height is dominated by the transmission coefficient of the collector barrier. Systematic studies of devices with different barrier thickness have shown that the step height increases exponentially with increasing barrier thickness [195].

As shown by Nomoto et al. [196] for a vertical double-dot system [197], both the excitation spectrum and the Coulomb staircase can be used to extract some information on the

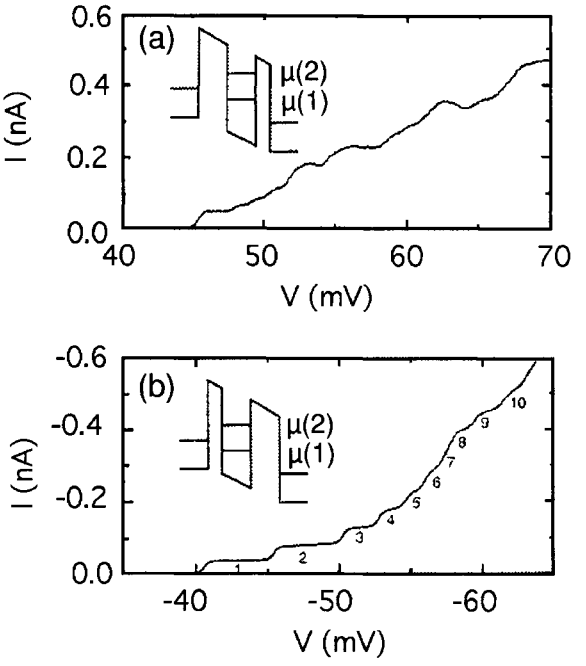


Fig. 61. I–V curves measured on vertical quantum dots with asymmetric barriers. (a) Situation for positive bias and thick emitter barrier (excitation spectrum); (b) situation for the thick collector barrier (charging regime). (Source: Reprinted with permission from [185].)

confining potential in the dot. We outline the underlying ideas in the following considerations, which refer to an asymmetric tunneling system similar to that shown in Figure 60. Assume a cylindrical symmetric confinement whose radial part is given by a harmonic oscillator potential: $V(r) = m\omega_0^2 r^2/2$. Here, r is the radial coordinate, $\omega_0 = 1/R\sqrt{2\Phi/m^*}$, $\Phi = 0.7$ eV is the Fermi level pinning at the surface, and R is the lithographically defined radius of the diode. As mentioned earlier, this approximation will give a fairly correct description only for a certain range of dot radii R. In the limit of very small R, the diode will be totally depleted, whereas for relatively large values of R the potential will not be parabolic but rather exhibit a flat center part. For a parabolic potential, the eigenstates can be easily calculated, and, provided the scaling factor between electron energy and sample bias is known, it should yield the peak positions in the excitation spectrum correctly. For the forward bias situation of Figure 61a, a direct comparison of the outlined simple calculation with the experimental excitation spectrum is feasible and can be used to determine the strength of the confinement potential. From the latter, the radial extension of an electron in the ground state can be estimated according to $r_{\text{wave}} = [\hbar/(m^*\omega_0)]^{1/2}$.

As shown by Nomoto et al. [196], this value is in good agreement with the radius of the internal capacitor, which can be estimated from the (reverse bias) Coulomb staircase as follows. The dot is considered as a planar capacitor with circular electrodes. The corresponding capacitance is simply given by $C = \varepsilon\varepsilon_0\pi r_{\text{cond}}^2/d$, where ε is the permittivity of the AlGaAs barrier and d is the corresponding thickness. The radius r_{cond} of this capacitor is defined as the radius of the conducting area in the dot. According to the orthodox theory of Coulomb blockade, the width of a current step, ΔV, is always equal to $\Delta V = e/C$, which offers the possibility of determining the junction capacitance directly from the voltage positions of current steps. By inserting the preceding expression for the capacitance and solving for the radius r_{cond}, good agreement with the radius of the wave function in the ground state r_{wave} is obtained.

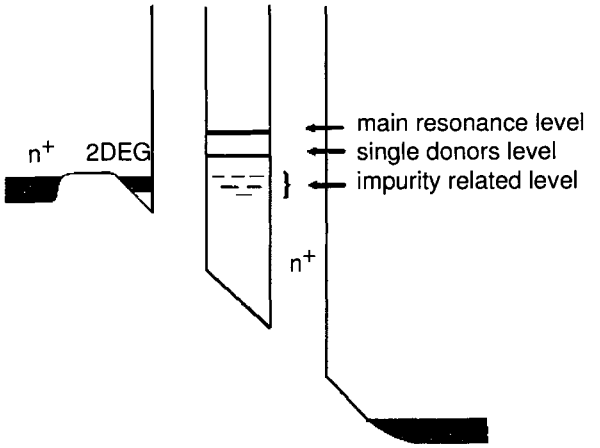


Fig. 62. Energy band diagram of a resonant tunneling device, where a layer of donors was incorporated between the barriers. Tunneling occurs from the two-dimensional electron gas via the main resonance level and also via single-donor and impurity-related levels. (Source: Reprinted from [199]. © 1994 American Institute of Physics.)

7.3. Tunneling via Zero-Dimensional Donor States

Besides quantized states and Coulomb blockade effects, tunneling processes through single impurities can also result in additional resonance structures in the measured I–V curves of a quantum dot. Although tunneling through donor states is not at all restricted to 0D systems, it is treated here in the framework of quantum dot tunneling for two reasons. First, the donors themselves can be considered to be natural 0D systems, giving rise to a set of localized states that can serve as some kind of collector in tunneling experiments. Second, as will be shown that the natural way to achieve a better understanding of the tunneling through donor states is to reduce the number of donors involved. This can be attained by reducing the lateral dimensions of the underlying tunneling devices, thereby entering the quantum dot regime.

The first detailed investigations on this subject, which we will discuss briefly at the beginning of this section, were performed on large-area double-barrier resonant tunneling diodes (DBRTDs). As mentioned earlier, DBRTDs are often equipped with undoped GaAs spacer layers in front of the barriers in order to enhance the resolution of the tunneling experiments. Provided the GaAs spacer is sufficiently thick, a triangular well is formed in front of the barriers under bias, leading to a two-dimensional accumulation layer of electrons as shown in Figure 62. Because the electron wavevector parallel to the barrier is conserved during a tunneling process, the transmission coefficient of the barrier only depends on the electron wavevector component k_z perpendicular to the barrier. The wavevector components parallel to the barrier do not influence the transmission coefficient at all. For the sample structure under consideration, this means that resonances in the I–V curves are only expected when the edge of the 2D subband in the emitter (and *not* the Fermi level as in similar samples used, e.g., by Reed et al. [163]; see Section 7.1) is in exact coincidence with the main resonance levels within the double barrier. Because the linewidth of the resonances in a tunneling I–V curve is limited only by the natural width of the 2D subband, the resolution of fine structure in the I–V curves is enhanced compared to those cases where the linewidth is determined by the distribution of electrons at the Fermi energy. By proper design, it can be achieved that only one subband is occupied in the 2D emitter, leading to an almost perfectly monoenergetic energy distribution in tunneling direction. Note that for a tunneling process starting from a 2D emitter the shape of the resonance is to first order independent of the temperature. This is easily understood from the fact that the main effect

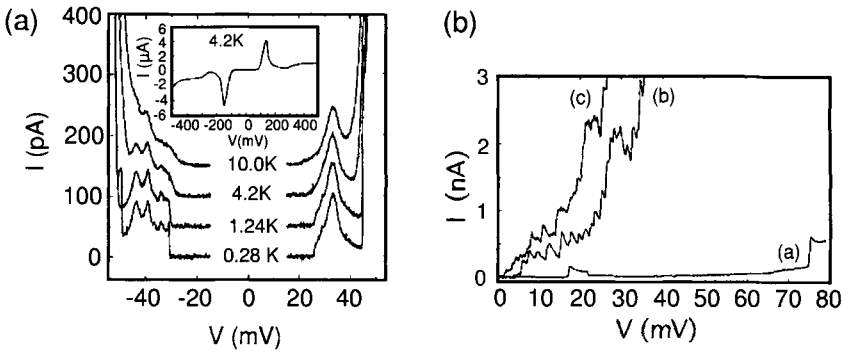


Fig. 63. Left: $I-V$ curves of a DBRT device as a function of temperature. Right: $I-V$ curves of a DBRT device as a function of doping level: (a) undoped device, (b) 4×10^{13} m^{-2}, and (c) 8×10^{13} m^{-2}. (Source: Reprinted from [199]. © 1994 American Institute of Physics.)

of temperature is to broaden the Fermi distribution function. For a 2D emitter, this only changes the momentum distribution parallel to the barriers in the emitter, which obviously has no influence on the transmission coefficient in the tunneling direction.

The strongly enhanced energy resolution obtained for samples with a 2D emitter was exploited by Geim and co-workers [198–200] to investigate tunneling processes through single-donor related states on *large-area* DBRTDs with a delta-doped layer incorporated between the double barriers. Figure 63 shows typical data. As seen from the inset of Figure 63 (left) the main resonance of the $I-V$ curve has the commonly expected form. Note that because of the two-dimensional emitter electrode the peak-to-valley ratio of the main resonances is much larger than for the samples used by Reed et al. [163], where the electrons in the emitter showed 3D behavior. In the low-bias region of the $I-V$ curve, pronounced additional fine structure is revealed, which is temperature dependent and which can unambiguously be demonstrated to be impurity related. Consider Figure 63 (right), where the $I-V$ curves of three different samples are plotted. Curve a corresponds to an undoped sample and exhibits no fine structure. This is in contrast to curves b and c, which correspond to two different donor concentrations in the δ-doping layer.

It was shown by Geim and co-workers that the observed effects can be quantitatively explained if donor pairs of random separation ("donor molecules") are made responsible for the fine structure in the tunneling $I-V$. Because of the relatively low donor concentration in the well, the average donor separation is in the range of 0.1 to 0.5 μm. Consequently, only a small number of donor molecules will exist in a tunneling device with a mesa diameter of typically 10 μm. As shown by Geim and co-workers [198], only donor molecules formed by nearest-neighbors will play a role at the used doping level. Larger clusters would lead to binding energies too small to account for the observed peak positions. The multitude of fine structures in the tunneling characteristics then originates from the random distribution of the relative nearest-neighbor donor separation and the corresponding multitude of possible energy states. Although the model is relatively simple, quantitative simulations showed excellent agreement with the measured tunneling current in the low-bias regime.

The next step toward a more advanced investigation of impurity-related tunneling was initiated by the introduction of "squeezable" quantum dot structures with side-gate geometry. The sample design, originally developed by Kinard et al. [201] and used later on by Eaves and co-workers [202–204] for detailed studies of tunneling via single-donor states, is shown in the inset of Figure 64. The lithographically defined width of the active device region is 1 μm^2. In contrast to the previously discussed sample structures, the well enclosed by the AlAs barriers is *not* intentionally doped. The lateral confinement, that is, the effective width of the current path can be controlled by the electrically tunable side-wall depletion. By determining the current density in the device, the scaling factor of the actual

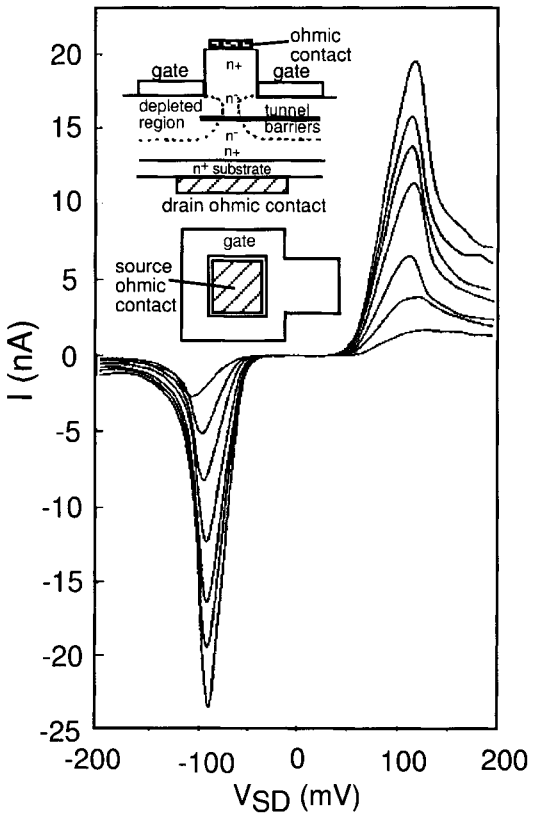


Fig. 64. I–V curves of a squeezable quantum dot structure. The different curves show the influence of the applied side-gate voltage. (Source: Reprinted with permission from [202].)

conducting area as a function of the side-gate voltage can be obtained. The conducting area is found to decrease down to 0.1 μm^2 for a gate bias of -5 V.

Figure 64 shows the I–V curves obtained for various values of the side-gate voltage. The main resonance peak current is seen to decrease when the conducting channel is narrowed. An interesting feature is the asymmetry between the forward and the reverse bias region which is induced when the tunneling region is squeezed. This behavior can be explained in terms of a lateral variation of the potential drop across the AlGaAs barriers. To see this, consider the schematic view of the sample cross section shown in Figure 65. Figure 65a refers to zero side-gate voltage. The point of maximum depletion is seen to be slightly above the tunnel barriers. Parts b and c of Figure 65 show the equipotential lines for forward ($V > 0$) and reverse bias ($V < 0$), respectively. The solid circles represent the electron accumulation layer from which the electrons are injected into the double barrier. The important point is that for positive bias the equipotential lines converge in the direction of the electron flow upwards in Figure 65b, implying that the voltage drop between the accumulation layer and the quantum well is larger at the center of the device than at the edge. In reverse bias, the equipotential lines diverge in the direction of the current flow and the potential difference between the accumulation layer and the quantum well does not vary over the width of the accumulation layer. The lateral variation of the voltage drop in forward bias means that the edge of the device goes on resonance at a higher bias than the center of the device (see Fig. 65b). As a consequence, the main resonance is smeared out and the peak-to-valley ratio decreases faster for positive side-gate voltages.

The second main feature of these squeezable dots is revealed when the I–V curves close to threshold are considered as they are plotted in Figure 66. A series of peaks is clearly

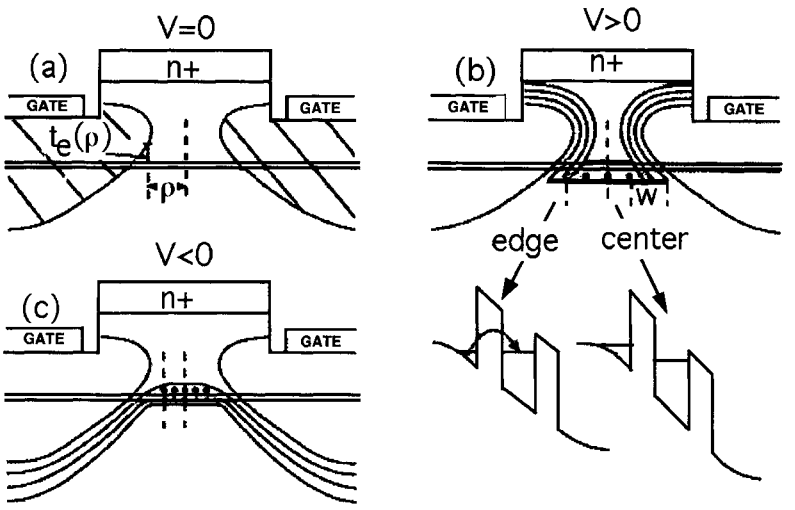


Fig. 65. Schematic diagram of the equipotential lines and depletion regions for a side-gated double-barrier resonant tunneling diode. (a) $V = 0$, (b) $V > 0$, and (c) $V < 0$. In (a), the cross-hatched area represents the region that is depleted by the gate. In (b), the conduction band profile indicates how the device can be on resonance at the edge, but not at the center. (Source: Reprinted with permission from [202].)

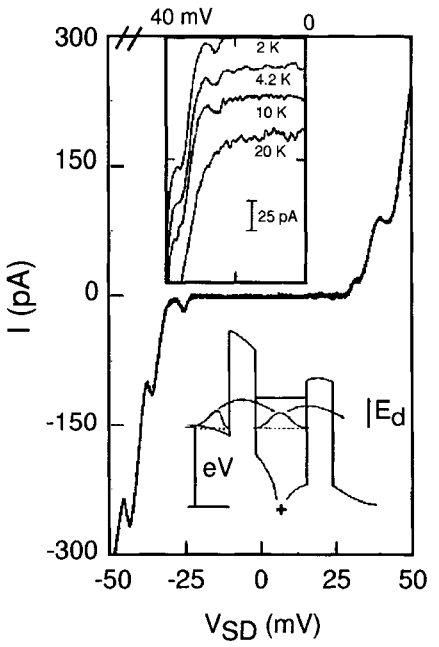


Fig. 66. I–V curve close to threshold for $V_g = 0$ V measured at $T = 39$ mK. The inset shows I–V in reverse bias for temperatures of $T = 2$, 4.2, 10, and 20 K. (Source: Reprinted with permission from [202].)

observed for both bias directions although for reverse bias the peaks are better resolved. These peaks are a universal feature and also occur for different samples at similar voltage positions, but always below the onset of the main resonance. They are attributed to energy levels lying below the first confined state in the well. The striking feature of these peaks is, however, that their position is independent of the side-gate voltage and, as can be seen in the inset of Figure 66, they are also relatively insensitive to temperature. Thus, quantum

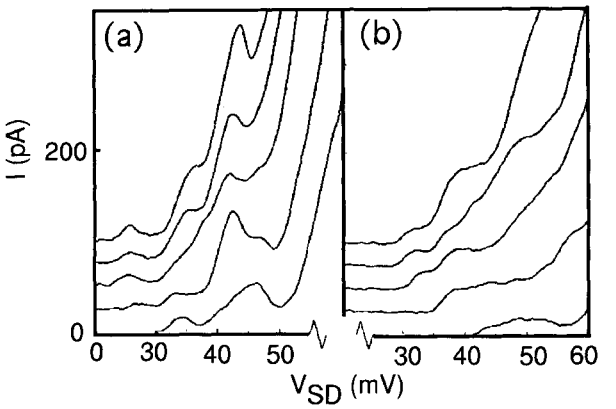


Fig. 67. Dependence of $I(V)$ on the applied side-gate voltage in reverse bias (a) and forward bias (b) for voltages of $V_g = 0$, 1, 1.5, 2.25, and 3 V from top to bottom. (Source: Reprinted with permission from [202].)

confined states or Coulomb blockade effects cannot be made responsible for the structures in the low-bias range; otherwise, they would occur at a position above the main resonance and show a distinct voltage dependence.

Tunneling via a local inhomogeneity, such as a donor impurity unintentionally incorporated in the well between the AlAs barriers, provides a possible explanation for the observed behavior. In contrast to the large-area DBRTDs considered previously, the gated structures now offer the possibility of probing the spatial extent of these donor states using the following considerations. A peak in the I–V curves will be unaffected until the depletion edge impinges on the region of the corresponding localized state, through which the electrons tunnel. If the depletion zone moves across the active area of the localized state, the amplitude of the corresponding resonance peak will decrease, because electrons are prohibited from entering the depletion zone. Thus, the current path for electrons flowing through this impurity state becomes smaller. If the side-gate voltage becomes large enough, the localized states will lie totally within the depletion region and the corresponding resonance will be quenched. This is shown in Figure 67, where the near-threshold I–V curves are given for various side-gate voltages. If the effective diameter d of the resonant tunneling device as a function of the side-gate voltage is known, the spatial extent Δx of such an impurity-related level can be determined. If V_{g1} is the highest voltage for which the resonance peak is still unaffected and V_{g2} is the lowest voltage, where the peak is totally suppressed, one estimates $\Delta x = \frac{1}{2}[d(V_{g1}) - d(V_{g2})]$. For the lowest peak in the I–V curves of Figure 67, one obtains, for example, a spatial extension of approximately 30 nm, which is close to the value for a single-donor bound state, expected from a simple first-principles calculation.

In the preceding experiment, donor-related tunneling was investigated using squeezable quantum dot devices, which, however, showed no sign of resonant tunneling via 0D states. It was shown by Blanc et al. [205], however, that the inverse situation can be achieved by some modifications of the device design. By growing a larger spacer layer in front of the double barrier (7 nm instead of 3.4 nm in the case of Eaves and co-workers [202]), the unintentional incorporation of shallow donors in the quantum well region is largely suppressed. A reduction of the mesa size down to 0.1 μm leads to relatively high 0D quantization energies, which facilitates the observation of resonant tunneling via quantized states.

With increasing side-gate voltage, the main resonance peak current is reduced in analogy to the previously discussed experiment, but no asymmetry is observed for forward and reverse bias. In contrast to the previous experiment, no evidence of donor-related tunneling processes is found. The low-temperature conductance exhibits a series of well-resolved

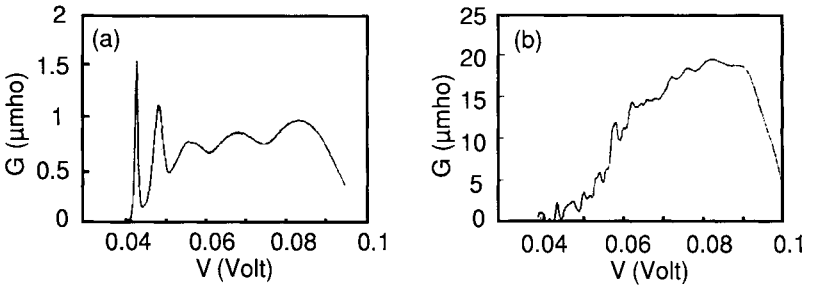


Fig. 68. Conductance measured at 40 mK for a device with a diameter of 0.2 μm ($V_g = -0.2$ V) (a) and a device with a nominal diameter of 0.8 μm and $V_g = 0$ V (b). The resonance structures are due to resonant tunneling via 0D states. For the smaller device (curve a), the energy spacing of the quantized states is considerably enhanced compared to the larger device (curve b). (Source: Reprinted from [205], with permission of Elsevier Science.)

peaks (Fig. 68), which are attributed to resonant tunneling via 0D states. This is confirmed by the observed dependence of the I–V characteristics on gate voltage as well as magnetic field.

7.4. 0D–2D Tunneling

So far, the presented experiments on quantum dot tunneling were not or only superficially analyzed in terms of the properties of the confinement potential defining the dot. Whenever an attempt of a quantitative comparison between experiment and calculation was made, the confinement was assumed to be parabolic and subband energies or the spatial extent of electronic wave functions were calculated within this assumption. The transfer Hamiltonian formalism, which was introduced in Section 6.2, can also be employed to gain more detailed information on the shape of the quantum dot potential from 0D–2D tunneling processes. This will be discussed in the following for tunneling experiments performed using the double-heterostructure layout already treated in Sections 6.1 and 6.3 in the context of 1D–2D tunneling. The same sample structure turned out to be also suitable for the fabrication of a 0D–2D tunneling device [206]. For this purpose, the upper (emitter) channel is nanostructured into quantum dots as schematically depicted in Figure 69. The dot array can be fabricated by laser holography using a double-exposure technique. In order to deplete the accumulation layer between the dots, the structures were wet chemically etched 300 Å deep into the GaAs cap layer. An ohmic contact to the dots is obtained by evaporating a Au/Ge electrode covering the dot array. The experimental data shown in Figure 70 were obtained for a period of the dot array of $a = 350$ nm. The corresponding dot diameter was estimated to be approximately $a/2$.

As discussed in Section 6.1, the applied bias voltage can be assumed to drop exclusively across the potential barrier separating the 2D collector from the 0D islands. A bias voltage ΔV_b is, thus, equivalent to a relative energetic shift of the 0D states by $\Delta E = e\Delta V_b$. A negative bias voltage $V_b < 0$ corresponds to tunneling processes from a 0D state into a 2D subband of the inversion channel. The band structure of the biased sample is shown in Figure 69b for both the etched and the nonetched regions (upper and lower parts, respectively).

Some experimental results are plotted in Figure 70. Part a of this figure shows the dI/dV_b characteristics of the nanostructured (0D–2D) sample for various temperatures in the range between $T = 1.7$ K (curve 1) and $T = 40$ K (curve 12). For reference purposes, the dI/dV_b characteristics of an unstructured sample are plotted in part b of the figure for two temperature values $T = 1.7$ K (curve 1) and $T = 40$ K (curve 2). All resonance peaks of the (0D–2D) dI/dV_b characteristics show a strong dependence on temperature.

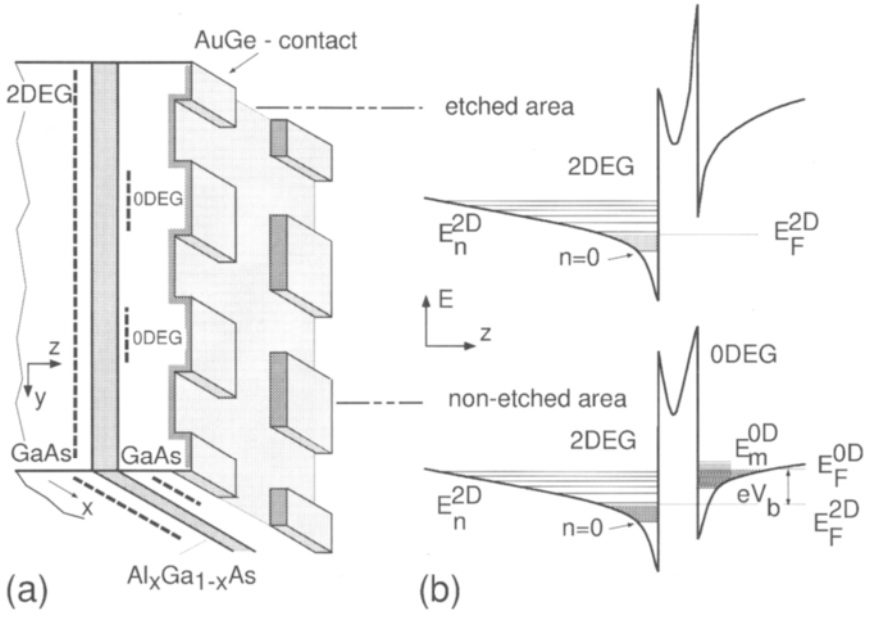


Fig. 69. (a) Schematic view of a 0D–2D sample. (b) The corresponding conduction band profile for the etched and nonetched areas of the sample. (Source: Reprinted with permission from [24].)

Above $T = 4.2$ K (part a, curve 2), the number of resolved resonance structures is already considerably reduced. A further increase in temperature results in a monotonic broadening of the resonance structures, accompanied by a decrease in the peak amplitudes. Generally, the resonance positions observed for $V_b < 0$ are slightly shifted toward more negative bias voltages. This behavior, which also occurs for the subband resonances of the (2D–2D) tunneling characteristics, is due to the thermally activated occupation of the first excited subband in the inversion channel causing a modification of the self-consistent potential profile. In both parts a and b of Figure 70, the positions of the (2D–2D) subband resonances are denoted by arrows.

Similar to the 1D–2D tunneling processes discussed in Section 6.3 it can be shown that the structures in the measured tunneling characteristics can be traced back to the form of the overlap integral formed by the initial and final states. To see this, we introduce cylinder coordinates and write the wave functions for the collector and the emitter system in the form

$$\begin{aligned} \text{2DEG}: \quad & \Psi_{\mathrm{I},\nu}^{\mathrm{2D}} = \frac{1}{\sqrt{A_{\rho\varphi}}}\psi_{\mathrm{I},\nu}(z)\frac{1}{\sqrt{2\pi}}\exp(im_{\mathrm{I}}\varphi)J_{m_{\mathrm{I}}}(k_{\parallel}\rho) \\ \text{0DEG}: \quad & \Psi_{\mathrm{A}}^{\mathrm{0D}} = \frac{1}{\sqrt{A_{\rho\varphi}}}\psi_{\mathrm{A}}(z)\frac{1}{\sqrt{2\pi}}\exp(im_{\mathrm{A}}\varphi)\varphi_{n_{\mathrm{A}},m_{\mathrm{A}}}(\rho) \end{aligned} \tag{106}$$

In the expression for $\Psi_{\mathrm{A}}^{\mathrm{1D}}$, n_{A} represents the radial and m_{A} the azimuthal quantum number. Because prior to the nanofabrication process the upper 2DEG (accumulation layer, index A) contains only one occupied subband in the z direction, these two quantum numbers are sufficient to describe the 0D states of the quantum dot system. The wave functions of the subbands in the lower 2DEG (inversion layer, index I) are given by $\Psi_{\mathrm{I},\nu}^{\mathrm{2D}}(\rho, \varphi, z; m_{\mathrm{I}})$. Here, ν is the 2D subband index and m_{I} takes the degeneracy of $E_{\parallel}$ (energy of the motion parallel to the interface) into account. $A_{\rho\varphi}$ represents the normalization area in both systems.

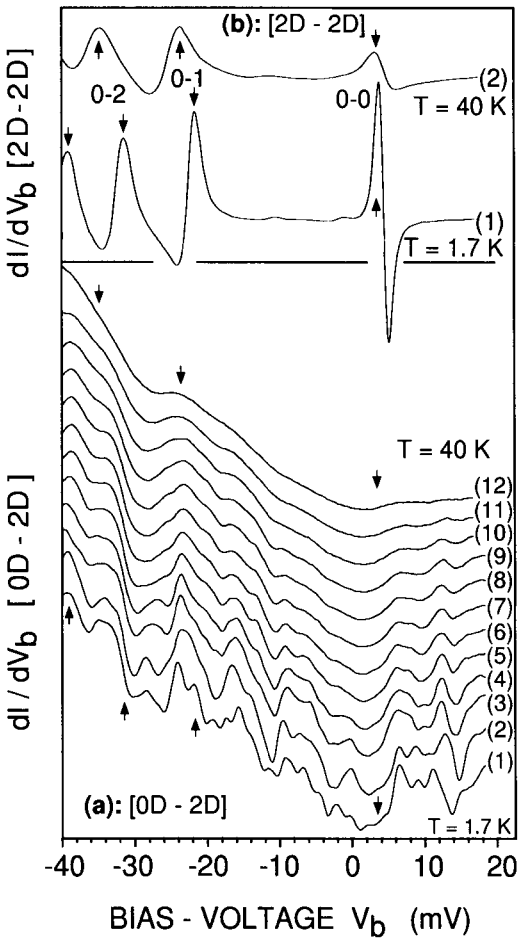


Fig. 70. (a) Measured dI/dV_b curves in the temperature range between 1.7 and 40 K. (b) For comparison, dI/dV_b curves of an unstructured sample are also shown. The corresponding temperatures are 1.7 K (curve 1), 4.2 K (2), 6.5 K (3), 9.5 K (4), 11.7 K (5), 13.9 K (6), 15.7 K (7), 18.5 K (8), 22.7 K (9), 29.0 K (10), 35.5 K (11), and 40 K (12). (Source: Reprinted with permission from [24].)

The matrix element M_{AI} [Eq. (81)], which is governed by the overlap of the single wave functions, now has the following form:

$$M_{AI} = -\frac{\hbar^2}{2m^*}\int\int_S dx\,dy\left(\Psi_I^*\frac{\partial\Psi_A}{\partial z} - \Psi_A\frac{\partial\Psi_I^*}{\partial z}\right)$$

$$= \underbrace{-\frac{\hbar^2}{2m^*}\left[\psi_{I,\nu}^*\frac{\partial\psi_A}{\partial z} - \psi_A\frac{\partial\psi_{I,\nu}^*}{\partial z}\right]_{z=z_b}}_{t_B} \times \delta_{m_I,m_A} \times \underbrace{\int d\rho\,\rho J_{m_I}(k_\parallel\rho)\varphi_{n_A,m_A}(\rho)}_{\langle J_m(k_\parallel\rho)|\varphi_{n_A,m}(\rho)\rangle} \quad (107)$$

The first term in this equation, t_B, represents the transmission coefficient of the barrier. The Kronecker symbol guarantees the conservation of the angular momentum (quantum number m) during the tunneling process. The matrix element is nonzero only if $m_I = m_A \equiv m$.

The value of the corresponding matrix element is a function of the radial quantum number n_A, the (common) azimuthal quantum number m, and the wavevector $\mathbf{k}_\parallel$ which depends on the applied bias voltage. Its value, however, is completely determined by the

requirement of total energy conservation:

$$\tilde{k}_{\parallel}(V_b) = \sqrt{\frac{2m^*}{\hbar^2}[E_{n_A,m} - E_{\nu_I} - eV_b]} \tag{108}$$

As in the case of 1D–2D tunneling, the (0D–2D) matrix element M_{AI} not only depends on the quantum numbers n_A and m and on the bias voltage V_b, but also on the particularities of the potential profile. Considering the multitude of resonant structures in the tunneling differential conductance, a strictly rectangular potential profile can be excluded, because just as in the 1D–2D case it would lead only to weak fine structure (cf. Section 6.3). As in the case of shallow etched quantum wires, one obtains a relatively realistic description of the situation by assuming a cosine-shaped radial part of the quantum dot potential profile:

$$V_{dot}(\rho) = V_{mod}\left[\frac{1}{2} + \frac{1}{2}\cos\left(\frac{\pi}{R_{dot}}(\rho - R_{dot})\right)\right] \qquad \text{with } \rho \leqslant R_{dot} \tag{109}$$

In Figure 71, the tunneling probability, calculated from this potential profile, is compared to the measured dI/dV_b at $T = 1.7$ K. The parameters of the model potential were adjusted to obtain the best possible agreement with the experimental results. Again, an energy (i.e., bias voltage) independent transmission coefficient of the tunnel barrier was assumed for this calculation. Hence, the model is, just as in the 1D–2D case, unable to reproduce the monotonic background in the experimental tunneling characteristics. It should be noted that the tunneling probability is proportional to the tunneling current, so that, to be rigorous, one has to compare the calculated curve directly with the measured tunneling current. Because the resonant structure is too weak to be observed in $I(V_b)$ directly and because a numerical derivative of the calculated results would somewhat obscure their structure, a direct comparison is not feasible in this case. Nevertheless, good agreement between the experimental results and the calculated peak positions is immediately obvious. The parameter values used in the calculation are $R_{dot} = 62.5$ nm and $V_{mod} = 38$ meV.

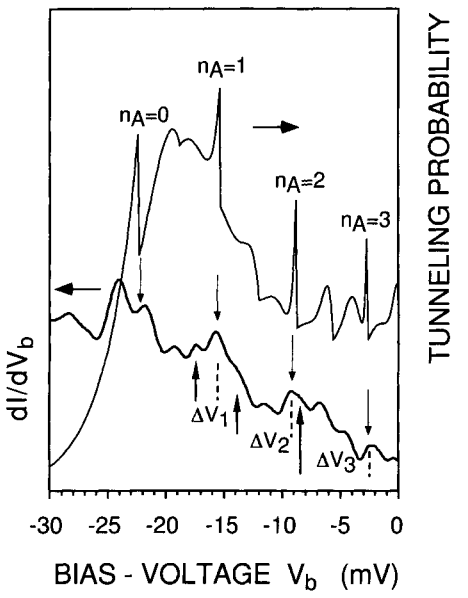


Fig. 71. Comparison between the calculated tunneling probability and the measured dI/dV_b curve at 1.7 K. The downward arrows denote the $n = 0, \ldots, 3$ resonance peaks. The upward arrows denote the peak positions where individual 0D and 2D subbands are exactly aligned. As for 1D–2D tunneling, ΔV_n denotes the distance between the resonance maximum and those positions. (Source: Reprinted with permission from [24].)

The sharp structures in the total tunneling probability are due to sharp peaks in the wave function overlap integrals for $n_A = 0, 1, 2, 3$ and can, therefore, be assigned to single peaks in the measured tunneling characteristics (denoted by downward arrows). In this way, the energy spacings of the lowest three 0D subbands in the quantum dot can be determined. If one takes into account that the relative energy shift of the 2D and 0D states is approximately equal to $e\Delta V_b$, these subband spacings are given by $\Delta E_{01} \approx 7$ meV, $\Delta E_{12} \approx 6$ meV, and $\Delta E_{23} \approx 5$ meV. ΔE_{ij} is, thus, found to decrease with increasing subband index, which is consistent with the assumption of a cosine-shaped dot potential.

Finally, it is worth noting that Coulomb charging effects will play no significant role in the discussed experiment. This is mainly due to the particular sample layout. As discussed earlier in the context of an asymmetric double-barrier tunneling device (cf. Fig. 61), Coulomb blockade effects are not observed, if the emitter barrier is less transmissive than the collector barrier. This picture is valid for *forward bias* also in the present situation, if one identifies the emitter barrier with the AlGaAs layer separating the two electron systems and the collector barrier with the broad but low barrier between the dot and the alloyed AuGe contact. Because the collector barrier is then clearly much more transmissive than the emitter barrier, Coulomb blockade is not expected for positive sample bias. For negative bias, Coulomb charging effects could, in principle, play a role. In practice, however, the sample design leads to a large capacitance between the dot and its surroundings: Each dot is capacitively coupled vertically to two large electrodes covering the whole area of the quantum dot array, namely, the underlying 2DEG and the top electrode. A rough estimate shows that this leads to an effective "capacitive" radius of the dot on the order of 150 nm. The corresponding Coulomb charging energy is far below 1 meV and, therefore, an order of magnitude smaller than the average subband spacing of the dot. This means that in the temperature range of the preceding experiments quantization effects are dominant.

Acknowledgments

The authors are grateful to G. Berthold, W. Demmerle, and F. Hirler for their substantial contribution to the scientific part of this work and N. Reinacher for solving the numerical problems. The excellent samples used in our experiments were grown by G. Böhm, W. Schlapp, G. Strasser, and G. Weimann. Valuable technical help during the sample preparation process was provided by C. Eder, C. Gmachl, M. Hauser, R. Maschek, and V. Rosskopf. The authors also acknowledge numerous fruitful discussions with W. Boxleitner, C. Hamaguchi, M. Heiblum, Y. Levinson, U. Meirav, J. C. Portal, D. Schneider, F. Stern, P. Streda, and P. Vogl. Financial support was obtained through the Gesellschaft für Mikroelektronik (GMe) and the Jubiläumsfonds der Oesterreichischen Nationalbank (OENB). Finally, we wish to thank E. Gornik for his help and continuous support during the past years.

References

1. Y. Arakawa, K. Vahala, and A. Yariv, *Appl. Phys. Lett.* 45, 950 (1984).
2. Y. Arakawa, H. Sakaki, and M. Nishioka, *Oyo Buturi* 52, 852 (1983).
3. Y. W. Lai and S. DasSarma, *Phys. Rev. B* 33, 8874 (1986).
4. S. Luryi and F. Capasso, *Appl. Phys. Lett.* 47, 1347 (1985).
5. K. Tsubaki, T. Fukui, Y. Tokura, H. Saito, and N. Susa, *Electron. Lett.* 24, 1267 (1988).
6. W.-Y. Wu, N. J. Schulmann, Y. T. Hsu, and E. Uzi, *Appl. Phys. Lett.* 51, 710 (1987).
7. T. Takagahra, *Phys. Rev. B* 36, 9293 (1987).
8. L. Wolf, "Principles of Tunneling Spectroscopy." Oxford University Press, New York, 1985.
9. D. C. Tsui, in "Handbook of Semiconductors" (T. W. Moss and W. Paul, eds.), Vol. 1, p. 662. North-Holland, Amsterdam, 1982.
10. M. Boero and J. C. Inkson, *Phys. Rev. B* 50, 2479 (1994).
11. B. J. van Wees, H. van Houten, C. W. J. Beenakker, G. J. Williamson, L. P. Kouwenhoven, D. van Marel, and C. T. Foxon, *Phys. Rev. Lett.* 60, 848 (1988).

12. D. A. Wharam, T. J. Thornton, R. Newbury, M. Pepper, H. Ahmed, J. E. F. Frost, D. G. Hasko, D. C. Peacock, D. A. Ritchie, and G. A. C. Jones, *J. Phys. C* 21, L209 (1988).
13. C. W. J. Beenakker and H. van Houten, *Phys. Rev. Lett.* 60, 2406 (1988).
14. F. M. Peeters, *Phys. Rev. Lett.* 61, 589 (1988).
15. R. K. Reich, D. K. Ferry, R. O. Grondin, and G. J. Iafrate, *Phys. Lett.* 91, 28 (1982).
16. D. R. Hofstadter, *Phys. Rev. B* 14, 2239 (1976).
17. A. Lorke, J. P. Kotthaus, and K. Ploog, *Phys. Rev. B* 44, 3447 (1991).
18. K. Ensslin and P. M. Petroff, *Phys. Rev. B* 41, 12307 (1990).
19. D. Weiss, K. von Klitzing, K. Ploog, and G. Weimann, *Europhys. Lett.* 8, 179 (1989).
20. H. Fang and P. J. Stiles, *Phys. Rev. B* 41, 10171 (1990).
21. E. S. Alves, P. H. Beton, M. Henini, L. Eaves, P. Main, O. H. Hughes, G. A. Toombs, S. P. Beaumont, and C. C. W. Wilkinson, *J. Phys. C* 1, 8257 (1989).
22. B. Kardynal, C. H. W. Barnes, E. H. Linfield, D. A. Ritchie, K. M. Brown, G. A. C. Jones, and M. Pepper, in "Proceedings of NANOMES 96," Santa Fe, NM, 1996.
23. W. Demmerle, J. Smoliner, E. Gornik, G. Böhm, and G. Weimann, *Phys. Rev. B* 47, 13574 (1993).
24. J. Smoliner, W. Demmerle, E. Gornik, G. Böhm, and G. Weimann, *Semicond. Sci. Technol.* 9, 1925 (1994).
25. C. W. J. Beenakker and H. van Houten, in "Solid State Physics" (H. Ehrenreich and D. Turnbull, eds.), Vol. 44. Academic Press, New York, 1991.
26. H. van Houten, C. W. J. Benakker, and B. J. van Wees, in "Semiconductors and Semimetals" (R. K. Willardson, A. C. Beer, and E. R. Weber, eds.), Vol. 35. Academic Press, New York, 1992.
27. A. Yacoby, U. Sivan, C. P. Umbach, and J. M. Hong, *Phys. Rev. Lett.* 66, 1938 (1991).
28. A. Yacoby, M. Heiblum, H. Shtriktman, V. Umansky, and D. Mahalu, *Semicond. Sci. Technol.* 9, 907 (1994).
29. R. Schuster, E. Buks, M. Heiblum, D. Mahalu, V. Uhansky, and H. Shtrikman, *Nature* 385, 417 (1997).
30. A. Yacoby, M. Heiblum, D. Mahalu, and H. Shtriktman, *Phys. Rev. Lett.* 74, 4047 (1995).
31. L. Pfeiffer, H. L. Stormer, K. W. Baldwin, K. W. West, A. R. Goni, A. Pinczuk, R. C. Ashoori, M. M. Dignam, and W. J. Wegscheider, *J. Cryst. Growth* 127, 849 (1993).
32. W. Wegscheider, G. Schedelbeck, G. Abstreiter, M. Rother, and M. Bichler, *Phys. Rev. Lett.* 79, 1917 (1997).
33. A. Yacoby, H. L. Stormer, K. W. Baldwin, L. N. Pfeiffer, and K. W. West, *Solid State Commun.* 101, 77 (1997).
34. T. Honda, S. Tarucha, T. Saku, and Y. Tokura, *Jpn. J. Appl. Phys.* 34, L72 (1995).
35. A. Yacobi, H. L. Stormer, N. S. Wingreen, L. N. Pfeiffer, K. W. Baldwin, and K. W. West, *Phys. Rev. Lett.* 77, 4612 (1996).
36. S. Tarucha, T. Honda, and T. Saku, *Solid State Commun.* 94, 413 (1995).
37. K. J. Thomas, M. Y. Simmons, J. T. Nicholls, D. R. Mace, M. Pepper, and D. A. Ritchie, *Appl. Phys. Lett.* 67, 109 (1995).
38. A. Gold and L. Calmels, *Philos. Mag. Lett.* 74, 33 (1966).
39. K. J. Thomas, J. T. Nicholls, M. Y. Simmons, M. Pepper, D. R. Mace, and D. A. Ritchie, *Phys. Rev. Lett.* 77, 135 (1996).
40. M. J. Kelly, "Low Dimensional Semiconductors." Clarendon Press, Oxford, U.K., 1995.
41. D. K. Ferry et al., eds., "NATO ASI Series B," Vol. 342. Plenum, New York, 1995.
42. R. D. Woods and D. S. Saxon, *Phys. Rev. B* 95, 577 (1954).
43. C. W. J. Beenakker, H. van Houten, and B. J. van Wees, *Superlattices Microstruct.* 5, 127 (1989).
44. S. E. Laux, D. J. Frank, and F. Stern, *Surf. Sci.* 196, 101 (1988).
45. S. E. Laux and A. C. Warren, in "Proceedings of the 1986 Int. Electron. Dev. Meeting," 1986, p. 576.
46. S. E. Laux and F. Stern, *Appl. Phys. Lett.* 49, 91 (1986).
47. S. E. Laux, in "Proceedings of NASECODE V Conference" (J. J. H. Miller, ed.), p. 270. Boole Press, 1987.
48. A. C. Warren and A. D. Antoniadis, *IEEE Electron Device Lett.* 7, 413 (1986).
49. J. H. Davies, *Semicond. Sci. Technol.* 3, 995 (1988).
50. T. Kerkhoven, A. T. Galick, and Y. Saad, *J. Appl. Phys.* 68, 3461 (1990).
51. B. S. Garbow, J. M. Boyle, J. J. Dongara, and B. B. Moler, *Lecture Notes Comput. Sci.* 51 (1977).
52. J. H. Luscombe, *Nanotechnology* 4, 1 (1993).
53. J. H. Luscombe and W. R. Frensley, *Nanotechnology* 1, 131 (1990).
54. J. H. Luscombe and A. M. Bouchard, *Phys. Rev. B* 46, 10262 (1992).
55. J. H. Luscombe, in "Proceedings of the International Symposium on Nanostructures and Mesoscopic Systems, Santa Fe, 1991" (W. P. Kirk and M. A. Reed, eds.), p. 357. Academic Press, Boston, 1992.
56. J. H. Luscombe, J. N. Randall, and A. M. Bouchard, *Proc. IEEE* 79, 1117 (1991).
57. A. M. Bouchard, J. H. Luscombe, A. C. Seabaugh, and J. N. Randall, in "Nanostructured and Mesoscopic Systems" (W. P. Kirk and M. Reed, eds.), p. 393. Academic Press, New York, 1992.
58. J. H. Luscombe and M. Luban, *Appl. Phys. Lett.* 57, 61 (1990).
59. J. M. Bigelow and J. P. Leburton, *J. Appl. Phys.* 76, 2887 (1994).
60. D. Jovanovic and J. P. Leburton, *Phys. Rev. B* 49, 7474 (1994).
61. J. Smoliner, G. Berthold, F. Hirler, and N. Reinacher, *Semicond. Sci. Technol.* 6, 642 (1991).
62. W. H. Press, B. P. Flannery, S. A. Teukolsky, and W. T. Vettering, "Numerical Recipes." Cambridge University Press, Cambridge, U.K., 1986.

63. D. D. Johnson, *Phys. Rev. B* 38, 12807 (1988).
64. G. P. Srivastava, *J. Phys. A: Math. Gen.* 17, L317 (1984).
65. M. Luban, J. H. Luscombe, M. A. Reed, and D. L. Pursey, *Appl. Phys. Lett.* 54, 1997 (1989).
66. A. Kumar, S. E. Laux, and F. Stern, *Phys. Rev. B* 42, 5166 (1990).
67. S. Udipi, D. Vasileska, and D. K. Ferry, *Superlattices Microstruct.* 20, 3 (1996).
68. A. Scholze, A. Wettstein, A. Schenk, and W. Fichtner, in "Proceedings of IWCE-5," Notre Dame, IN, 1996.
69. G. Klimek, R. Lake, R. C. Bowen, W. R. Frensley, and T. S. Moise, *Appl. Phys. Lett.* 76, 2539 (1995).
70. W. R. Frensley, *Rev. Mod. Phys.* 62, 745 (1990).
71. M. Luban and J. H. Luscombe, *Phys. Rev. B* 35, 9045 (1987).
72. M. Reed, in "Semiconductors and Semimetals" (R. K. Willardson, A. C. Beer, and E. R. Weber, eds.), Vol. 35. Academic Press, New York, 1992.
73. S. Datta, in "Cambridge Studies in Semiconductor Physics and Microelectronic Engineering" (H. Ahmed, M. Pepper, and A. Broers, eds.), Vol. 3. Cambridge University Press, 1995.
74. K. F. Berggren, T. J. Thornton, D. J. Newson, and M. Pepper, *Phys. Rev. Lett.* 57, 1769 (1986).
75. K. F. Berggren, G. Roos, and H. van Houten, *Phys. Rev. B* 37, 10118 (1988).
76. K. F. Berggren and D. J. Newson, *Semicond. Sci. Technol.* 1, 327 (1986).
77. A. A. Abrikosov, "Fundamentals of the Theory of Metals." North-Holland, Amsterdam, 1988.
78. F. Hirler, J. Smoliner, E. Gornik, G. Weimann, and W. Schlapp, *Appl. Phys. Lett.* 57, 16 (1990).
79. F. Brinkop, W. Hansen, J. P. Kotthaus, and K. Ploog, *Phys. Rev. B* 37, 6517 (1988).
80. V. Gudmundsson, A. Brataas, P. Grambow, B. Meurer, T. Kurth, and D. Heitmann, *Phys. Rev. B* 51, 17744 (1995).
81. H. J. Rundquist, *Semicond. Sci. Technol.* 4, 455 (1989).
82. T. J. Thornton, M. L. Roukes, A. Scherer, and P. P. Van de Gaag, *Phys. Rev. Lett.* 63, 2128 (1989).
83. H. Akera and T. Ando, in "Proceedings of the 20th International Conference on the Physics of Semiconductors" (E. M. Anastassakis and J. D. Joannopoulos, eds.), Vol. 3. World Scientific, Singapore, 1990.
84. W. Hansen, "Semiconductors and Semimetals" (R. K. Willardson, A. C. Beer, and E. R. Weber, eds.), Vol. 35. Academic Press, New York, 1992.
85. Y. Imry, in "Directions of Condensed Matter Physics" (G. Grinstein and G. Mazenko, eds.), Vol. 2. World Scientific, Singapore, 1986.
86. G. Bergmann, *Phys. Rev. B* 2, 2914 (1983).
87. S. Chakravarty and A. Schmid, *Phys. Rep.* 140, 193 (1986).
88. B. L. Altshuler and A. G. Aronov, *Pis'ma Zh. Eksp. Teor. Fiz.* 33, 499 (1981).
89. C. W. J. Beenakker and H. van Houten, *Phys. Rev. B* 38, 6544 (1988).
90. C. W. J. Beenakker and H. van Houten, *Phys. Rev. B* 38, 3232 (1988).
91. T. J. Thornton, M. Pepper, H. Ahmed, D. Andrews, and G. J. Davies, *Phys. Rev. Lett.* 56, 1198 (1986).
92. H. van Houten, C. W. J. Beenakker, B. J. van Wees, and J. E. Mooij, *Surf. Sci.* 196, 144 (1988).
93. B. L. Altshuler and A. G. Aronov, in "Electron–Electron Interactions in Disordered Systems" (A. L. Efros and M. Pollak, eds.). North-Holland, Amsterdam, 1985.
94. H. van Houten, B. J. van Wees, M. G. J. Heijman, and J. P. André, *Appl. Phys. Lett.* 49, 1781 (1986).
95. V. L. Gurevich and Y. A. Firsov, *Zh. Eksp. Teor. Fiz.* 40, 198 (1961) [*Sov. Phys. JETP* 13, 137 (1961)].
96. R. L. Peterson, in "Semiconductors and Semimetals" (R. K. Willardson and A. C. Beer, eds.), Vol. 10, p. 221. Academic Press, New York, 1975.
97. R. A. Stradling and R. A. Wood, *Solid State Commun.* 6, 701 (1968).
98. P. G. Harper, J. W. Hodby, and R. A. Stradling, *Rep. Prog. Phys.* 37, 1 (1973).
99. D. Schneider, D. Rürup, B. Schönfelder, and A. Schlachetzki, *Z. Phys. B* 100, 33 (1996).
100. D. Schneider, K. Fricke, J. Schulz, G. Irmer, and M. Wenzel, in "Proceedings of the 23rd International Conference on the Physics of Semiconductors" (M. Scheffler and R. Zimmermann, eds.), Vol. 1, p. 221. World Scientific, Singapore, 1996.
101. D. C. Tsui, T. Englert, A. Y. Cho, and A. C. Gossard, *Phys. Rev. Lett.* 44, 341 (1980).
102. M. A. Brummell, R. J. Nicholas, M. A. Hopkins, J. J. Harris, and C. T. Foxon, *Phys. Rev. Lett.* 58, 77 (1987).
103. M. A. Brummell, D. R. Leadley, R. J. Nicholas, J. J. Harris, and C. T. Foxon, *Surf. Sci.* 196, 451 (1988).
104. D. R. Leadley, R. J. Nicholas, J. Singleton, W. Xu, F. M. Peeters, J. T. Devreese, J. A. Perenboom, L. van Bockstal, F. Herlach, J. J. Harris, and C. T. Foxon, *Phys. Rev. Lett.* 73, 589 (1994).
105. P. Vasilopoulos, P. Warmenbol, F. M. Peeters, and J. T. Devreese, *Phys. Rev. B* 40, 1810 (1989).
106. P. Vasilopoulos, *Phys. Rev. B* 33, 8587 (1986).
107. J. R. Barker, *J. Phys. C* 5, 1657 (1972).
108. N. Mori, H. Murata, K. Taniguchi, and C. Hamaguchi, *Phys. Rev. B* 38, 7622 (1988).
109. N. Mori, H. Momose, and C. Hamaguchi, *Phys. Rev. B* 45, 4536 (1992).
110. J. Y. Ryu and R. F. O'Connell, *Phys. Rev. B* 48, 9126 (1993).
111. J. Y. Ryu and R. F. O'Connell, *Phys. Rev. B* 49, 10437 (1994).
112. J. Y. Ryu and S. D. Choi, *Phys. Rev. B* 44, 11328 (1991).

113. G. Ploner, J. Smoliner, G. Strasser, and E. Gornik, in "Proceedings of the 23rd International Conference on Physics of Semiconductors" (M. Scheffler and R. Zimmermann, eds.), Vol. 2, p. 1245. World Scientific, Singapore, 1996.

114. G. Ploner, J. Smoliner, G. Strasser, and E. Gornik, *Superlattices Microstruct.* 22, 249 (1997).

115. G. Ploner, J. Smoliner, G. Strasser, M. Hauser, and E. Gornik, *Phys. Rev. B* 57, 3966 (1998); G. Ploner, PhD thesis, Tu Vienna (1998).

116. G. Berthold, J. Smoliner, C. Wirner, E. Gornik, G. Böhm, G. Weimann, M. Hauser, C. Hamaguchi, N. Mori, and H. Momose, *Semicond. Sci. Technol.* 8, 735 (1993).

117. C. W. J. Beenakker, *Phys. Rev. Lett.* 62, 2020 (1989).

118. R. R. Gerhardts, D. Weiss, and K. von Klitzing, *Phys. Rev. Lett.* 62, 1173 (1989).

119. R. W. Winkler, J. P. Kotthaus, and K. Ploog, *Phys. Rev. Lett.* 62, 1177(1989).

120. P. Vasilopoulos and F. M. Peeters, *Phys. Rev. Lett.* 63, 2120 (1989).

121. P. H. Beton, E. S. Alves, P. C. Main, L. Eaves, M. W. Dellow, M. Henini, and O. H. Hughes, *Phys. Rev. Lett.* 42, 9229 (1990).

122. P. H. Beton, M. W. Dellow, P. C. Main, E. S. Alves, L. Eaves, S. P. Beaumont, and C. D. Wilkinson, *Phys. Rev. B* 43, 9980 (1991).

123. J. Kucera, P. Streda, and R. R. Gerhardts, *Phys. Rev. B* 55, 14439 (1997).

124. P. Streda and J. Kucera, *Superlattices Microstruct.* 22 (1997).

125. P. Streda and A. H. MacDonald, *Phys. Rev. B* 41, 11892 (1990).

126. A. Soibel, U. Meirav, D. Mahalu, and H. Shtriktman, *Phys. Rev. B* 55, 4482 (1997).

127. Y. Paltiel, D. Mahalu, H. Shtriktman, G. Bunin, and U. Meirav, *Semicond. Sci. Technol.* 12, 987 (1997).

128. J. H. Davies and I. A. Larkin, *Phys. Rev. B* 49, 4800 (1994).

129. G. Müller, P. Streda, D. Weiss, K. von Klitzing, and G. Weimann, *Phys. Rev. B* 50, 8938 (1994).

130. C. C. Eugster and J. A. del Alamo, *Phys. Rev. Lett.* 67, 3586 (1991).

131. C. C. Eugster, J. A. del Alamo, M. R. Melloch, and M. J. Rooks, *Phys. Rev. B* 48, 15057 (1993).

132. S. Luryi and F. Capasso, *Appl. Phys. Lett.* 47, 1347 (1985).

133. A. Zaslavsky, D. C. Tsui, M. Santos, and M. Shayegan, *Appl. Phys. Lett.* 58, 1440 (1991).

134. M. M. Dignam, R. C. Ashoori, H. L. Stoermer, L. N. Pfeiffer, K. L. Baldwin, and K. W. West, *Phys. Rev. B* 49, 3369 (1994).

135. S. Tarucha, Y. Hirayama, T. Saku, and T. Kimura, *Phys. Rev. B* 41, 5459 (1990).

136. S. Tarucha, Y. Hirayama, and Y. Tokura, *Appl. Phys. Lett.* 58, 1623 (1991).

137. G. W. Bryant, *Phys. Rev. B* 39, 3145 (1989).

138. G. W. Bryant, *Phys. Rev. B* 44, 3782 (1991).

139. J. Smoliner, E. Gornik, and G. Weimann, *Appl. Phys. Lett.* 52, 2136 (1988).

140. J. Smoliner, F. Hirler, E. Gornik, G. Weimann, M. Hauser, and W. Schlapp, *Semicond. Sci. Technol.* 6, 389 (1991).

141. J. Smoliner, W. Demmerle, G. Berthold, E. Gornik, G. Weimann, and W. Schlapp, *Phys. Rev. Lett.* 63, 2116 (1989).

142. W. Demmerle, J. Smoliner, G. Berthold, G. Weimann, and W. Schlapp, *Phys. Rev. B* 44, 3090 (1991).

143. L. Wang, P. H. Beton, N. Mori, L. Eaves, H. Buhmann, L. Mansouri, P. C. Main, T. J. Foster, and M. Henini, *Phys. Rev. Lett.* 73, 1146 (1994).

144. P. H. Beton, J. Wang, N. Mori, L. Eaves, P. C. Main, T. J. Foster, and M. Henini, *Phys. Rev. Lett.* 75, 1996 (1995).

145. N. Mori, P. H. Beton, J. Wang, and L. Eaves, *Phys. Rev. B* 51, 1735 (1995).

146. N. Mori, P. H. Beton, J. Wang, and L. Eaves, *Phys. Rev. B* 52, 1505 (1995).

147. B. Kardynal, E. H. Linfield, D. A. Ritchie, K. M. Brown, C. H. W. Barnes, G. A. C. Jones, and M. Pepper, *Appl. Phys. Lett.* 68, 826 (1996).

148. B. Kardynal, C. H. W. Barnes, E. H. Linfield, D. A. Ritchie, K. M. Brown, G. A. C. Jones, and M. Pepper, *Phys. Rev. Lett.* 76, 3802 (1996).

149. B. Kardynal, C. H. W. Barnes, E. H. Linfield, D. A. Ritchie, T. J. Nicholls, K. M. Brown, G. A. C. Jones, and M. Pepper, *Phys. Rev. B* 55, R1966 (1997).

150. J. P. Eisenstein, L. N. Pfeiffer, and K. W. West, *Phys. Rev. Lett.* 69, 3804 (1992).

151. J. P. Eisenstein, L. N. Pfeiffer, and K. W. West, *Surf. Sci.* 305, 393 (1994).

152. K. M. Brown, N. Turner, J. T. Nicholls, E. H. Linfield, M. Pepper, D. A. Ritchie, and G. A. C. Jones, *Phys. Rev. B* 50, 15465 (1994).

153. J. R. Oppenheimer, *Phys. Rev.* 13, 66 (1928).

154. J. Bardeen, *Phys. Rev. Lett.* 6, 57 (1961).

155. W. A. Harrison, *Phys. Rev.* 123, 85 (1961).

156. J. Smoliner, W. Demmerle, F. Hirler, E. Gornik, G. Weimann, M. Hauser, and W. Schlapp, *Phys. Rev. B* 43, 7358 (1991).

157. J. Wang, P. H. Beton, N. Mori, H. Buhmann, L. Mansouri, L. Eaves, P. C. Main, T. J. Foster, and M. Henini, *Appl. Phys. Lett.* 65, 1124 (1994).

158. G. D. Mahan, "Many Particle Physics," 2nd ed. Plenum Press, New York, 1990.

159. L. Zheng and A. H. MacDonald, *Phys. Rev. B* 47, 13547 (1993).

160. H. Grabert and M. Devoret, eds., "Single Charge Tunneling." Plenum Press, New York, 1991.
161. U. Meirav and E. B. Foxman, *Semicond. Sci. Technol.* 10, 255 (1996).
162. L. P. Kouwenhoven, C. M. Marcus, P. L. McEuen, S. Tarucha, R. M. Westervelt, and N. S. Wingreen, in "Mesoscopic Electron Transport" (L. L. Sohn, L. P. Kouwenhoven, and G. Schön, eds.). Kluwer Academic, Dordrecht, The Netherlands, 1997.
163. M. A. Reed, J. N. Randall, R. J. Aggarwal, R. J. Matyi, T. M. Moore, and A. E. Wetsel, *Phys. Rev. Lett.* 60, 535 (1988).
164. J. N. Randall, M. A. Reed, R. J. Matyi, and T. M. Moore, *J. Vac. Sci. Technol. B* 6, 1861 (1988).
165. J. N. Randall, M. A. Reed, and Y. C. Kao, *J. Vac. Sci. Technol. B* 8, 348 (1990).
166. K. Y. Lee, T. P. Smith III, H. Arnot, C. M. Knoedler, J. M. Hong, D. P. Kern, and S. E. Laux, *J. Vac. Sci. Technol. B* 6, 1856 (1988).
167. N. Kamata, K. Yamada, N. Miura, and L. Eaves, *J. Phys. Soc. Jpn.* 2120 (1993).
168. M. Boero and J. C. Inkson, *Phys. Rev. B* 50, 2479 (1994).
169. A. Sa'ar, J. Feng, I. Grave, and A. Yariv, *J. Appl. Phys.* 72, 3598 (1992).
170. S. Tarucha, Y. Hirayama, T. Saku, and T. Kimura, *Phys. Rev. B* 41, 5459 (1990).
171. A. Kumar, *Surf. Sci.* 263, 335 (1992).
172. D. C. Glattili, C. Pasquier, U. Meirav, F. I. B. Williams, Y. Jin, and B. Etienne, *Z. Phys. B* 85, 367 (1991).
173. L. P. Kouwenhoven, N. C. van der Maart, C. J. P. M. Harmans, and C. Foxon, *Adv. Solid State Phys.* 31, 329 (1991).
174. A. A. M. Staring, J. G. Williamson, H. van Houten, C. W. J. Beenakker, L. P. Kouwenhoven, and C. T. Foxxon, *Physica B* 175, 226 (1991).
175. T. A. Fulton and G. A. Dolan, *Phys. Rev. Lett.* 59, 109 (1987).
176. H. van Houten and C. W. J. Beenakker, *Phys. Rev. Lett.* 63, 1893 (1989).
177. C. W. J. Beenakker, *Phys. Rev. B* 44, 1646 (1991).
178. D. V. Averin and K. K. Likharev, in "Mesoscopic Phenomena in Solids" (B. L. Altshuler et al., eds.). Elsevier, Amsterdam, 1991.
179. L. G. Ingold and Y. V. Nazorov, in "Single Charge Tunneling and Coulomb Blockade Phenomena in Nanostructures" (H. Grabert and M. H. Devoret, eds.), p. 21. Plenum, New York, 1992.
180. A. T. Johnson, L. P. Kouvenhoven, W. Dejong, C. C. van der Maart, C. J. P. M. Harmans, and C. T. Foxxon, *Phys. Rev. Lett.* 69, 1592 (1992).
181. E. B. Foxman, L. P. McEuen, U. Meirav, N. S. Wingren, Y. Meir, P. A. Belk, N. R. Belk, M. A. Kastner, and S. J. Wind, *Phys. Rev. B* 47, 10020 (1993).
182. J. Weis, R. J. Haug, K. von Klitzing, and K. Ploog, *Phys. Rev. Lett.* 71, 4019 (1993).
183. R. C. Ashoori, H. L. Stormer, J. S. Weiner, L. N. Pfeiffer, S. J. Pearton, K. W. Baldwin, and K. W. West, *Phys. Rev. Lett.* 68, 3088 (1992).
184. R. C. Ashoori, H. L. Stormer, J. S. Weiner, L. N. Pfeiffer, S. J. Pearton, K. W. Baldwin, and K. W. West, *Phys. Rev. Lett.* 62, 2168 (1989).
185. R. H. Blick, T. Schmidt, R. Haug, and K. von Klitzing, *Semicond. Sci. Technol.* 11, 1506 (1996).
186. Y. G. Gobato, J. M. Berroir, and Y. Gouldner, *Solid State Commun.* 87, 513 (1993).
187. M. Tewordt, L. Martin-Moreno, T. J. Nicholls, M. Pepper, M. J. Kelly, V. J. Law, D. A. Ritchie, J. E. F. Frost, and G. A. C. Jones, *Phys. Rev. B* 46, 3948 (1992).
188. J. W. Sleight, E. S. Hornbeck, M. R. Desphande, R. G. Wheeler, M. A. Reed, R. C. Bowen, W. R. Frensley, J. N. Randall, and R. J. Matyi, *Phys. Rev. B* 53, 15727 (1996).
189. Z.-L. Ji, *Phys. Rev. B* 50, 4658 (1994).
190. H. C. Liu and G. C. Aers, *Solid State Commun.* 67, 1131 (1988).
191. S. Y. Chou, E. Wolak, and J. S. Harris, *Appl. Phys. Lett.* 52, 657 (1988).
192. B. Su, V. J. Goldmann, and J. E. Cunningham, *Phys. Rev. B* 46, 7644 (1992).
193. T. Schmidt, M. Tewordt, R. H. Blick, R. J. Haug, D. Pfannkuche, K. von Klitzing, A. Foster, and A. Luth, *Phys. Rev. B* 51, 5570 (1995).
194. M. Tewordt, L. M. Moreno, J. T. Nicholls, M. Pepper, M. J. Kelly, V. Law, D. A. Ritchie, J. E. F. Frost, and G. A. C. Jones, *Phys. Rev. B* 45, 14407 (1992); M. J. Kelly, V. Law, D. A. Ritchie, J. E. F. Frost, and G. A. C. Jones, *Phys. Rev. B* 45, 14407 (1992).
195. T. Schmidt, R. J. Haug, K. von Klitzing, A. Föster, and H. Lüth, *Phys. Rev. B* 55, 2230 (1997).
196. K. Nomoto, T. Suzuki, K. Taira, and K. Hase, *Phys. Rev. B* 55, 2523 (1997).
197. M. Tewordt, R. J. F. Hughes, L. Martin-Moreno, T. J. Nicholls, H. Asahi, M. J. Kelly, V. J. Law, D. A. Ritchie, J. E. F. Frost, G. A. C. Jones, and M. Pepper, *Phys. Rev. B* 49, 8071 (1994).
198. A. K. Geim, T. J. Foster, A. Nogaret, N. Mori, P. J. McDonnel, N. La Scala, P. C. Main, and L. Eaves, *Phys. Rev. B* 50, 8074 (1994).
199. J. W. Sakai, P. C. Main, P. H. Beton, N. La Scala Jr., A. K. Geim, L. Eaves, and H. Henini, *Appl. Phys. Lett.* 64, 2563 (1994).
200. P. H. Beton, H. Buhmann, L. Eaves, T. J. Foster, A. K. Geim, N. La Scala Jr., P. C. Main, L. Mansouri, N. Mori, J. W. Sakai, and J. Wang, *Semicond. Sci. Technol.* 9, 1912 (1994).
201. W. B. Kinard, M. H. Weichold, G. F. Spencer, and W. P. Kirk, *J. Vac. Sci. Technol. B* 8, 393 (1991).
202. L. Eaves, in "Physics of Nanostructures" (J. H. Davies and A. R. Long, eds.), p. 149. IOP Publishing, 1992.

203. P. C. Main, P. H. Beton, M. W. Dellow, L. Eaves, T. J. Foster C. J. G. M. Langerak, M. Henini, and J. W. Sakai, *Physica B* 189, 125 (1993).
204. M. W. Dellow, P. H. Beton, M. Henini, P. C. Main, L. Eaves, S. P. Beaumont, and C. D. W. Wilkinson, *Electron. Lett.* 27, 134 (1991).
205. N. Blanc, P. Gueret, R. Germann, and H. Rothuizen, *Physica B* 189, 135 (1993).
206. J. Smoliner, *Semicond. Sci. Technol.* 11, 1 (1996).

This Page Intentionally Left Blank

Chapter 2

ELECTRONIC TRANSPORT PROPERTIES OF QUANTUM DOTS

M. A. Reed, J. W. Sleight*, M. R. Deshpande†

Departments of Physics, Applied Physics, and Electrical Engineering, Yale University, New Haven, Connecticut, USA

Contents

1. Introduction 93
   1.1. Fabricated Quantum Dots: Vertical and Horizontal Systems 93
   1.2. Impurity Dot System: Coulomb Potential Confinement 95
2. Theory 96
   2.1. Energy States of a Fabricated Quantum Dot 96
   2.2. Energy States of the Impurity Dot 97
   2.3. Current–Voltage Characteristics of Vertical Dot: Fabricated and Impurity Systems 100
3. Sample Growth and Fabrication 101
4. Experimental Results 101
   4.1. Current–Voltage Characteristics 101
   4.2. Variable-Temperature Measurements 103
   4.3. Magnetotunneling Measurements: Diamagnetic Shifts and Current Suppression 106
   4.4. Magnetotunneling Measurements: Fine Structure 113
   4.5. Magnetotunneling Measurements: Spin Splitting and g^* Factor 117
   4.6. Magnetotunneling Measurements: Electron Tunneling Rates 121
5. Conclusions 128
   Acknowledgments 129
   References 129

1. INTRODUCTION

1.1. Fabricated Quantum Dots: Vertical and Horizontal Systems

Tunneling in low-dimensional semiconductor structures has been a very active research field, both experimentally [1–10] and theoretically [11–19]. Traditionally, there have been two different approaches to achieving a three-dimensionally confined system (Fig. 1).

In one approach, horizontal dots [7–10], electrons are first confined to a two-dimensional (2D) electron layer formed at the interface of GaAs/$Al_xGa_{1-x}As$. Band bending

*Present address: IBM Semiconductor Research & Development Center, New York.
†Current affiliation: Motorola Corporate Research Laboratories, 2100 East Elliot Road, Tempe, AZ 85284.

Handbook of Nanostructured Materials and Nanotechnology, edited by H.S. Nalwa
Volume 3: Electrical Properties
Copyright © 2000 by Academic Press
All rights of reproduction in any form reserved.
ISBN 0-12-513763-X/$30.00

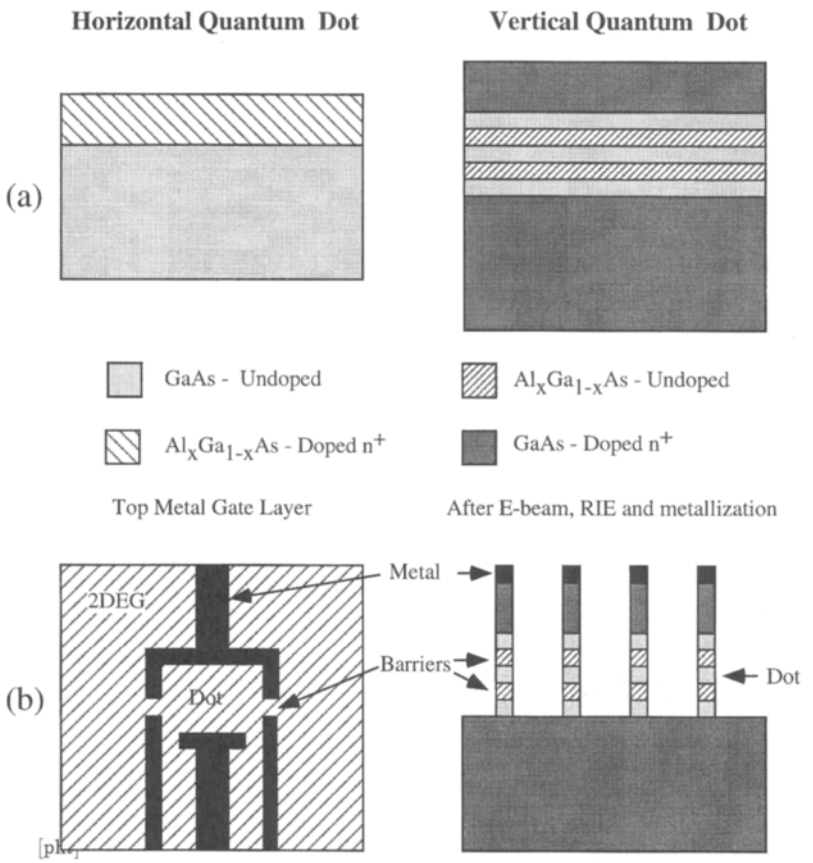


Fig. 1. (a) Comparison of the starting epitaxially grown material for a horizontal quantum dot structure (left) to a vertical structure (right). (b) Same structures after the fabrication that forms the quantum dot showing the top view of the horizontal dot and the side view of the vertical dot.

at the interface results in the formation of a triangular potential well in the GaAs region. Electrons are confined in this well and their motion in the direction perpendicular to the interface (z direction) is restricted. The number of electrons in the well can be controlled by suitably doping the barrier $Al_xGa_{1-x}As$ material sufficiently far from the interface. The electrons released by these donors accumulate in the well formed in the GaAs. These electrons are free to move in the lateral 2D plane and, therefore, this system is called a 2D electron gas. One can also control the density of the electrons by putting a gate electrode on top of the $Al_xGa_{1-x}As$ barrier and applying a suitable bias to it. A negative voltage applied to the gate repels electrons from underneath it. A suitable pattern of gate electrodes will electrostatically confine the electrons in a small area of the 2D layer. A full three-dimensional confinement is achieved as a result of the interface band bending and electrostatics. The electronic states of this confined dot can be probed by the tunneling of electrons into and out of the dot from the 2D electron gas surrounding the dot. The barrier between the dot and the 2D electron gas is due to the electrostatic potential of the fringing electric field of the patterned gate electrodes. The transport in this system is thus within the interface plane and, hence, this system is known as a horizontal quantum dot.

Another approach, vertical dots [1–6], starts with a double-barrier resonant tunneling structure consisting of heterostructure layers such as, GaAs/$Al_xGa_{1-x}As$/GaAs/$Al_xGa_{1-x}As$/GaAs. In this system, electrons are confined along one direction, the z direction, in the quantum well region (GaAs) in between the two barriers ($Al_xGa_{1-x}As$).

Reactive ion etching is used to physically reduce the lateral size of the device (Fig. 1), thus confining electrons along the remaining two (x and y) dimensions. The electronic states of this confined dot can be probed by tunneling of electrons into and out of the dot from the GaAs electrodes on either side of the device. The barrier between the dot and the GaAs electrodes is composed of the $Al_xGa_{1-x}As$ layers. The transport in this system is thus perpendicular to the interface and, therefore, this system is known as the vertical quantum dot.

In both techniques, the confinement potential spatially localizes electrons in a region, and quantizes the allowed energy levels in this region. However, there are major differences between the two systems. The barriers in the vertical dot system are well defined, atomically precise, and rigidly formed during growth of the layers. In contrast, the barriers in the horizontal dot are electrostatically defined and are soft barriers as they are ill defined, smooth, and flexible. The vertical dot is essentially a two-terminal system, whereas in the horizontal dot system it is easily possible to incorporate a gate electrode that makes it a three-terminal system. Usually, the total number of electrons residing in a vertical dot is very small (from 0 up to approximately 10), while that number is typically much larger in the horizontal dot system. In the case of horizontal dots, the single-electron charging energy, U_C, is usually much greater than δE, the spacing between single-particle states in the dot. In the case of vertical dots, δE and U_C are of the same order [2], or U_C can be less than δE. In the regime where they are on the same order, it is difficult to distinguish between the transport phenomena caused by each of these effects [2, 17] and proper modeling [15] is required to appropriately assign the observed structure to either spatial quantization or single-electron charging.

In this chapter, we restrict ourselves to the discussion of vertical quantum dots only. The vertical quantum dots described previously were the first structures where the effects of fully three-dimensionally confined electron states were observed [3]. These devices are small in size and, hence, have potential for high-density device applications. It is thus important to fully understand and characterize this and similar systems.

1.2. Impurity Dot System: Coulomb Potential Confinement

There is another way in which one can create a three-dimensionally confined experimental system consisting of discrete, single-electron states. This is by having a small number of donor impurities in the quantum well regions of large-area resonant tunneling diodes [20–23, 38]. The Coulomb potential of the ionized donor atoms gives rise to shallow, hydrogenic bound states (Fig. 2).

These localized states are physically similar to discrete quantum dot states. The $I(V)$ characteristics of this system are similar to those of a quantum dot system. The impurity system has certain advantages over the quantum dot system. It is a truly 3D–0D–3D

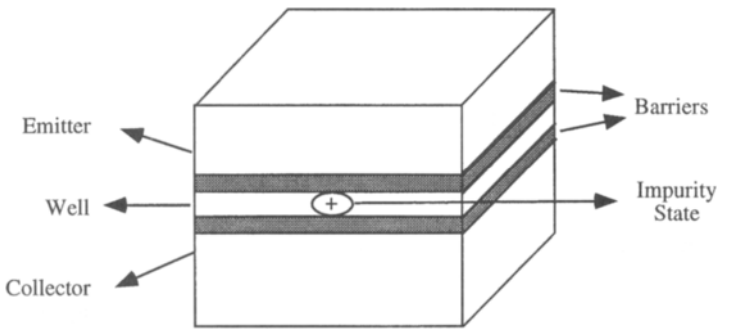


Fig. 2. Schematic of an impurity system showing an impurity state in the quantum well.

tunneling system unlike a 1D–0D–1D system of the fabricated quantum dot. There is no fabrication-imposed unknown potential in the emitter and collector regions. The Coulomb potential experienced by the electron resulting from the impurity is a known potential and the impurity states and energies are better characterized. It is possible to get devices with only a few isolated impurities and thus investigate the basic properties of a single, discrete state without having to worry about other states and their occupancy. The physical extent of the impurity state in a GaAs quantum well is on the order of 10 nm, which is smaller than the lateral extents of fabricated quantum dot eigenstates. An understanding of the basic physics of this impurity system is thus valuable for the understanding of the fabricated quantum dot system.

In Section 2, we first discuss the theory of the quantum dot eigenstates, the charging energy, and the effect of a magnetic field. We then discuss the eigenstates of the impurity potential. In Section 3, we discuss growth and fabrication details and, in Section 4, we present experimental results and, finally, conclude in Section 5.

2. THEORY

2.1. Energy States of a Fabricated Quantum Dot

2.1.1. Quantum Size Confinement Effects

In a fabricated quantum dot as described previously, the potential an electron experiences along the z direction is due to the semiconductor heterostructure band alignments and is modeled as a finite square well potential as in a quantum well. The potential the electron experiences along the lateral (x–y) directions depends critically on the highly anisotropic reactive ion etching process. This confinement potential, which is enhanced because of Fermi-level pinning on the side walls [2, 3], may be modeled in a few different ways.

If the lateral shape of the dot is asymmetric, then each eigenstate of the system is, in general, nondegenerate (except for the spin degeneracy). If the dot has cylindrical symmetry, then the various eigenstates reflect that symmetry. An additional effect to be considered is the Fermi-level pinning of the exposed side walls of the device. The Fermi level in the exposed semiconductor material gets pinned at a fixed value near the midgap. This induces bending of the bands and depletion of carriers from the region near the surface. The effective lateral size of the electrically active device is thus smaller than its physical dimensions. The potential an electron experiences along the lateral directions because of band bending and depletion is often modeled as a cylindrically symmetric parabolic potential [2, 3] as

$$\Phi(r) = \Phi_T\left[\frac{1-(R-r)}{W}\right]^2 \tag{1}$$

where Φ_T is the Fermi-level pinning energy at the side walls, R is the lateral physical dimension, r is the radial coordinate, and W is the depletion depth.

Schrödinger's equation for such a structure is best expressed in cylindrical coordinates. There is no θ dependence, and, because the potential is separable along the radial and the z directions, $\Phi(r, z) = \Phi(r) + \Phi(z)$, separation of variables is possible. The single-electron eigenenergies are given by $E_N = E_z + E_{n,l}$. E_z comes from the vertical quantization, and this will almost always be E_0, the quantum well ground state in the vertical direction. $E_{n,l}$ are the eigenenergies that result from the parabolic potential. $E_{n,l} = (2n + |l| + 1)\hbar\omega_0$ where the radial quantum numbers $n = 0, 1, 2, \ldots$ and the azimuthal quantum numbers $l = 0, \pm 1, \pm 2, \ldots$. If we assume that we are in the first vertical subband, E_0, and that the lateral dimension is reduced to $2W$ or less, then the energy spacing between states is

$$\Delta E = \hbar\omega_0 = \left(\frac{2\Phi_T}{m^*}\right)^{1/2}\frac{\hbar}{R} \tag{2}$$

For a GaAs well, with AlGaAs barriers, typical values for energy state separation are on the order of 25 meV, for $\Phi_T = 0.8$ eV and $R \approx 500$ Å.

2.1.2. *Magnetic Field Effects*

The dependence of electronic transport on magnetic field is a valuable tool in understanding the nature of localized states in semiconductor nanostructures. If a magnetic field oriented parallel to the current direction (perpendicular to the heterointerfaces) is applied, according to first-order perturbation theory, the shift of the energy levels is given by

$$\delta E_{B\|I} = \left(\frac{e\hbar}{2m^*}\right)\ell B + \frac{e^2B^2\langle r_0^2\rangle}{8m^*} \tag{3}$$

Note that spin is neglected in Eq. (3), as the spin splitting energy, $ge\hbar B/2m$, is only 0.25 meV at 10 T. The shift for a localized level with $\ell = 0$ is *entirely* due to the diamagnetic term, $\delta E_{\text{diamagnetic}} = e^2B^2\langle r_0^2\rangle/8m^*$, where $\langle r_0^2\rangle$ is the spatial extent of the localized wave function. Therefore, the observation of an experimental diamagnetic shift is a *direct measure* of $\langle r_0^2\rangle$.

For a magnetic field oriented perpendicular to the current, the first-order perturbation term is more difficult to evaluate, and numerical methods are required [24, 25]. Numerical results indicate an increase in dot energy states by a diamagnetic shift term, which is predicted to be less than 0.5 meV at 10 T for a GaAs/AlGaAs quantum dot system with the same well width (50 Å) as in this study. The small value for the state energy shift in this field orientation is due to the interaction of a relatively weak magnetic potential with the much stronger confinement potential in the epitaxial confinement (z) direction.

2.1.3. *Charging Effects*

Charging effects become important as the lateral device area is scaled down. Charging can be introduced into the usual single-electron model by modeling the Coulomb charging energy of the quantum dot as arising from a single effective capacitance C [1]. This approach uses the semiclassical geometric capacitance (the sum of an emitter capacitance C_e and a collector capacitance C_c):

$$C = C_e + C_c \approx \frac{\varepsilon\varepsilon_0\pi a^2}{4}\left(d_e^{-1} + d_c^{-1}\right) \tag{4}$$

where d_e and d_c are the thicknesses of the emitter and collector barriers, respectively, and a is the dot effective electrical diameter. For the structures in this paper, $C \approx 2.6 \times 10^{-16}$ F using $\varepsilon_{\text{AlGaAs}} \approx 11.6$, and $a \approx 800$ Å. The value a is the electrical diameter, which is the extrapolated value determined from current density measurements on large-area samples. In this case, the estimated charging energy, $E_C = e^2/2C$, is approximately 0.31 meV.[1] More generally, $E_{C,N} = e^2/C(N - \frac{1}{2})$ is the Coulomb charging energy for N electrons residing on the dot [1, 26].

2.2. Energy States of the Impurity Dot

2.2.1. *Energy of a Donor Impurity in Bulk GaAs*

In GaAs, a group IV atom (such as Si) at the Ga site acts as an electron donor. Upon ionization, the impurity site has an unbalanced positive charge, which introduces a Coulomb potential that is screened by the available free carriers in the semiconductor. The attractive Coulomb potential gives rise to hydrogen-like energy states that can bind free carriers.

[1] In [1], the expression for capacitance incorrectly includes a factor of 4π in the denominator. E_C is given as e^2/C, whereas it should be $e^2/2C$.

To determine the energy states of such a semiconductor hydrogenic atom, we follow the treatment of Bastard [28].

The wave function of a donor state in a semiconductor can be expressed in the form (from Kohn [29])

$$\psi(\mathbf{r}) = \sum_{i=1}^{N} \alpha_i F_i(\mathbf{r}) \phi_i(\mathbf{r}) \tag{5}$$

where N is the number of equivalent conduction band minima, $\phi_i(\mathbf{r})$ are the Bloch wave functions, and $F_i(\mathbf{r})$ are the envelope functions. In GaAs for the conduction band that is nondegenerate and isotropic with parabolic dispersion relations ($N = 1$ and single effective mass m^*), the envelope functions, $F(r)$, of the impurity states fulfill the equation

$$\left[\frac{p^2}{2m^*} - \frac{e^2}{4\pi\varepsilon_0 k r}\right] F(\mathbf{r}) = E F(\mathbf{r}) \tag{6}$$

where p is the momentum, m^* is the carrier effective mass, k is the dielectric constant of the semiconductor, e is the electronic charge, ε_0 is the permittivity of space, and E is the energy of the impurity state. The ground bound state of this system is the 1S hydrogenic wave function:

$$F_{1S}(\mathbf{r}) = \frac{1}{(\pi a_b^3)^{1/2}} \exp\left(-\frac{r}{a_b}\right) \tag{7}$$

where a_b is the effective three-dimensional Bohr radius of the semiconductor hydrogenic impurity:

$$a_b = \frac{4\pi\varepsilon_0 k \hbar^2}{m^* e^2} = 0.53 \times k \times \frac{m_0}{m^*} \text{ Å} \tag{8}$$

The binding energy of this 1S state, R_b, is given by

$$R_b = \frac{m^* e^4}{32\pi^2 \varepsilon_0^2 k^2 \hbar^2} = \frac{1}{k^2} \times \frac{m^*}{m_0} \times 13.6 \text{ eV} \tag{9}$$

In GaAs, $k = 12.85$ and $m^*/m_0 = 0.067$ giving us $a_b \approx 101$ Å and $R_b \approx 5.5$ meV.

We can see that the binding energy of hydrogenic donors in bulk GaAs has a very small energy compared to its band gap of 1.5 eV. Therefore, this state is called a shallow donor state. An electron occupying this state has an energy of -5.5 meV as measured from the bottom of the conduction band.

2.2.2. Energy of a Donor Impurity in a Quantum Well

In contrast to the bulk material, the binding energy of an impurity in a quantum well depends on the properties of the well, in particular, its width L and its barrier height V_0. The impurity binding energy increases as the well width decreases as long as the penetration of the quantum well wave function [$\chi(z)$] in the barriers remains small. This seems surprising at first because we intuitively associate higher kinetic energy (and, hence, lower binding energy) with the localization of a particle in a finite region of space. This is true of the energy value of the ground state of the quantum well, $E_1(L)$, and so also of the ground state of the impurity, $\varepsilon(L)$, when measured with respect to some fixed reference such as the bottom of the well. But the binding energy of the impurity $E_b(L) = E_1(L) - \varepsilon(L)$ actually increases as L decreases because for the impurity state the confinement causes the electron to stay near the attractive center, thus experiencing a higher potential energy. In the limiting case of an infinite barrier ($V_0 = \infty$) and zero well width ($L = 0$), we reach the two-dimensional limit when the ground state binding energy of a hydrogenic impurity is $4R_b = 22$ meV.

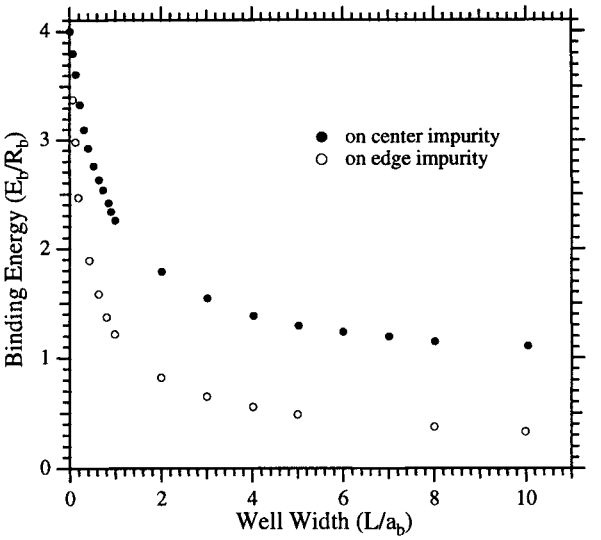


Fig. 3. Calculated dependences of the on-center and on-edge hydrogenic donor binding energies versus the well thickness L in a quantum well with an infinite barrier height ($V_0 = \infty$). R_b and a_b are the bulk effective Rydberg and Bohr radius, respectively. (Source: Adapted from [30].)

Another important feature of impurities in quantum wells is that the impurity binding energy explicitly depends on the precise location of the impurity along the growth axis (z direction) as there is no translational invariance along that axis. This energy depends on whether the impurity is at the center of the well or at the edge of the well or within the barrier. The wave function for an impurity at the center of the well ($z = 0$) approaches the 1S wave function of the bulk. But the wave function for an impurity at the edge of the well ($z = L/2$) approaches a truncated $2p_z$ wave function as the barrier potential forces the impurity wave function to almost vanish at the interface. The edge impurity has a lower binding energy than the center impurity. If the impurity is located within the barrier, it is still able to bind an electron in the well. The electron is physically separated from the impurity charge and such a system has lower binding energy than even an impurity at the edge.

The impurity binding energy in a quantum well can be obtained numerically as has been done by Bastard [28]. The results of such a calculation for an infinite barrier quantum well ($V_0 = \infty$) are shown in Figure 3 for an impurity located at the center and for an edge impurity. The binding energy is in the units of the bulk impurity Rydberg ($R_b = 5.5$ meV for GaAs) and the well width is in the units of the bulk impurity Bohr radius ($a_b = 101$ Å for GaAs).

For our experimental system where the well width is 44 Å, this figure gives us a binding energy for center impurity of approximately 16 meV and a binding energy for edge impurity of approximately 10 meV.

Because the impurities are randomly distributed in the well, it is statistically possible to have two impurities close to each other particularly in large-area samples. If the separation between the two impurities is on the order of the Bohr radius of a single impurity (100 Å), then the energy state of the electron is substantially modified. This is analogous to a hydrogen molecular ion problem. These impurity pairs give rise to higher binding energy states with the energy depending on the impurity separation. In the limiting case when the two impurities overlap, the situation is similar to a He^+ system with the resulting binding energy of the electron being four times as much as the single impurity binding energy.

So far, we have assumed that the barriers are infinite. For real systems, this is not true and the binding energy of an impurity does depend on the barrier height V_0. For finite barriers, as the well width decreases beyond a certain limit ($\approx 0.2a_b$), the impurity energy

becomes comparable to the barrier height and the impurity wave function gets more and more delocalized. The effect of the Coulomb potential gets smaller and, hence, the binding energy decreases for L less than approximately $0.2a_b$ (unlike the trend observed in Fig. 3). For the samples under study where $L = 44$ Å, an infinite barrier approximation is shown to be a reasonable approximation [31].

2.2.3. Coulomb Charging Energy in the Impurity System

In the impurity system, the lateral size of the device is large (a few micrometers) and the charging energy of one electron is negligible. If the impurity concentration in the device is low and the impurities are separated by a large distance (in the micrometer range), then we can assume that each impurity channel is independent of the others as the presence or absence of an electron in one would not have any effect on the others. A given hydrogenic impurity has many eigenstates. In particular, the ground state of the impurity is spin degenerate in zero magnetic field. Although we have two states with the same energy, only one of them can be occupied by an electron at a given time because of charging effects. This has important consequences on the $I(V)$ characteristics as will be discussed later.

2.3. Current–Voltage Characteristics of Vertical Dot: Fabricated and Impurity Systems

The electronic structure of the dots can be probed by studying the two-terminal current–voltage [$I(V)$] characteristics as in a quantum well resonant tunneling diode. If the heterostructure barriers along the z direction have finite thickness, then the dot eigenstates (localized states) couple to the electronic states in the emitter and the collector regions on either side of the dot along the z direction.

Let us first consider the simple case when the Coulomb charging energy of the dot is small compared to the size quantization energy. Any electron incident on such a structure at an energy equal to one of the localized state energies will see an increased transmission probability as it is able to couple to the eigenstate and tunnel through the structure. As bias is applied across the device, the localized states are pulled down in energy toward the emitter Fermi level. As a level crosses the Fermi energy, electrons in the emitter having the same energy as the localized state experience an enhanced transmission probability and thus there is a sharp increase in current. This current is due to single electrons tunneling one at a time through the quantum dot eigenstate and it can be written as

$$\Delta I \approx \frac{e}{\tau} \tag{10}$$

where e is the electronic charge and τ is the lifetime of the dot state. The lifetime (τ) depends on the heterostructure barrier thicknesses, the bias, and the density of available, occupied electronic states in the emitter. As the bias increases slightly, to first order, the current through a given localized state remains the same and, therefore, causes a current plateau or step in the $I(V)$ characteristics. A further increase in bias brings another localized state below the Fermi level in the emitter introducing another channel for electrons to tunnel through. The $I(V)$ characteristics of the device thus resemble a staircase structure. In the case of the fabricated dot, the bias locations of the steps correspond to the energy spectrum of the quantum dot. In the case of the impurity dot, the bias locations of the steps are random as each step is attributed to a separate impurity and the impurities are randomly distributed. This simple picture gets modified when the Coulomb charging energy becomes comparable to the size quantization energy. An additional bias, corresponding to the charging energy of a single electron, is necessary for the threshold of conduction. The energy spectrum of the dot also depends on the number of electrons occupying the dot states. The staircase structure of the $I(V)$ characteristics is modified and the bias locations of the steps no longer just correspond to the energy spectrum of the uncharged dot but also depend on the occupancy of the dot.

3. SAMPLE GROWTH AND FABRICATION

Samples are grown using molecular beam epitaxy on a Si-doped (100) GaAs substrate [32]. For the resonant tunneling diodes of the impurity system, the epitaxial layers consist of a 1.8×10^{18}-cm^{-3} Si-doped GaAs contact, a 150-Å undoped GaAs spacer layer, an undoped $Al_{0.27}Ga_{0.73}As$ bottom barrier of width 85 Å, a 44-Å undoped GaAs quantum well, an undoped $Al_{0.27}Ga_{0.73}As$ top barrier of the same width 85 Å, a 150-Å undoped GaAs spacer layer, and a 1.8×10^{18}-cm^{-3} Si-doped GaAs top contact. Square mesas with lateral dimensions ranging from 2 to 64 μm are fabricated using standard photolithography techniques.

In the case of the fabricated quantum dots, the active region consists of a 50-Å $In_{0.1}Ga_{0.9}As$ quantum well, enclosed by a pair of 40-Å-thick $Al_{0.25}Ga_{0.75}As$ barriers. This region, along with 100-Å spacer layers of GaAs that contact the barriers, is undoped. The spacer layers are contacted by GaAs doped with Si at a density of 3×10^{18}-cm^{-3}. Small ($\sim$100 nm) AuGe/Ni/Au ohmic top-contact dots are defined by electron beam lithography on the surface of the grown resonant tunneling structure. A bilayer polymethylmethacrylate (PMMA) resist and lift-off method are used. The metal dot ohmic contact serves as a self-aligned etch mask for highly anisotropic reactive ion etching (RIE) using BCl_3 as an etch gas. The resonant tunneling structure is etched through to the bottom n^+ GaAs contact. Contact to the top of the structures is achieved through a planarizing/etch-back process employing polyimide and an O_2 RIE [3]. A gold contact pad is then evaporated over the columns. Bottom contact is achieved through the conductive substrate.

Note that in the fabricated quantum dot samples $In_{0.1}Ga_{0.9}As$ is used as the well material rather than the standard GaAs, although the contact electrodes are still GaAs. $In_{0.1}Ga_{0.9}As$ has a lower band gap than GaAs. The quantum eigenstates in the $In_{0.1}Ga_{0.9}As$ well thus have lower energies (measured from the bottom of the contact electrodes) as opposed to a conventional sample, which would have GaAs well material with the same well width. By using an InGaAs well, the equilibrium dot quantum states are brought down closer to, or below, the Fermi level. Lower quantum levels in the well imply longer lifetimes (i.e., less intrinsic energy broadening). Additionally, because this reduces the resonant bias voltage far less distortion of the emitter/dot/collector potential occurs while examining the density of states of the dot as compared to a conventional GaAs vertical quantum dot. Owing to the lower applied bias required, there is far less power dissipation and local electron heating in the dot region.

Two-terminal direct-current (dc) $I(V)$ characteristics are measured in a dilution refrigerator with a mixing chamber temperature (T_{mix}) of 35 mK.

4. EXPERIMENTAL RESULTS

4.1. Current–Voltage Characteristics

4.1.1. Fabricated Quantum Dots

Several different types of transport measurements were performed to investigate the electronic properties of the vertical InGaAs quantum dot structures.

Large-area resonant tunneling diodes (RTDs) are fabricated to examine the peak positions and current densities for the epitaxial material. Figure 4a shows a current versus voltage trace for a 1024-μm^2 sample measured at 4 K. A symmetric response is observed that is consistent with the symmetric epitaxial structure. The negative differential resistance (NDR) occurs at $\pm$23 mV with a peak current density of 56 A/cm^2. The low bias conductance is 25 mS for the 1024-μm^2 device, and this value is observed to scale linearly with device area, as expected, providing a means of extrapolating the upper limits for the electrical sizes of the smaller devices.

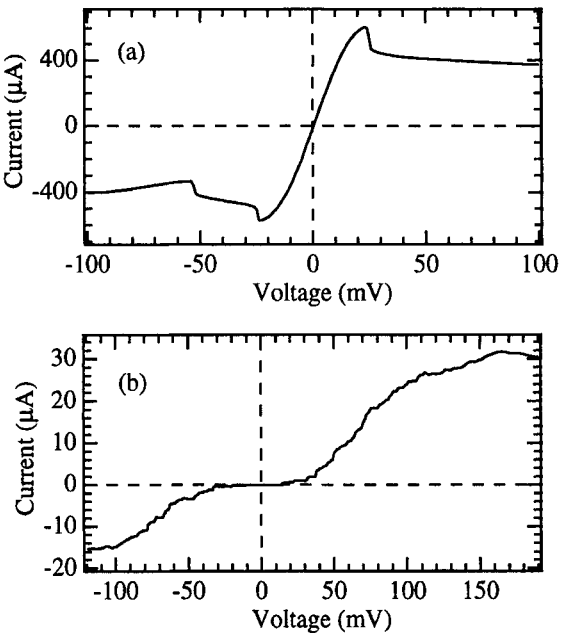


Fig. 4. (a) Current versus voltage for a large-area (1024 μm^2) sample fabricated from the same epitaxial material used for the small-area quantum dots ($T = 4.2$ K). (b) Current versus voltage for an $In_{0.1}Ga_{0.9}As$ quantum dot. Note the steplike structure in current near zero bias ($T = 50$ mK, mixing chamber).

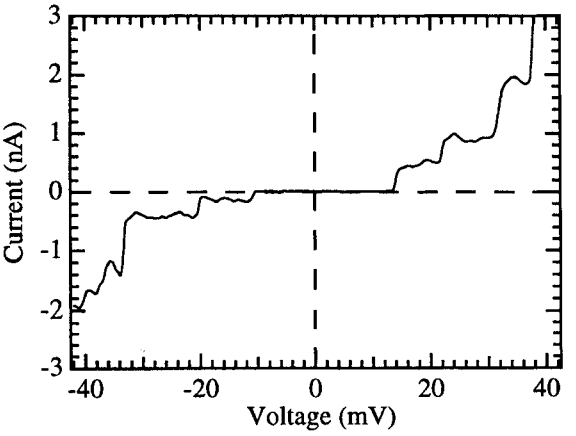


Fig. 5. Expansion of the low-bias regime of Figure 4b.

The small-area quantum dot samples are measured at millikelvin temperatures in a dilution refrigerator. Figure 4b shows a current versus voltage [$I(V)$] curve for a sample ($R \approx 100$ nm) under zero magnetic field, at a mixing chamber temperature of 50 mK. Figure 5 shows an expansion of the zero-bias region. The conductance for this sample ($\sim$0.4 μS) yields a value of approximately 800 Å for the electrical diameter, a. A staircase structure in current is observed in Figures 4b and 5 in both bias directions, especially at low biases.

A similar structure in the low-bias regime for double-barrier resonant tunneling structures (DBRTS) has been previously reported by other groups [2, 27]. The major difference in our work is the use of an InGaAs dot, as well as the use of a symmetric epitaxial

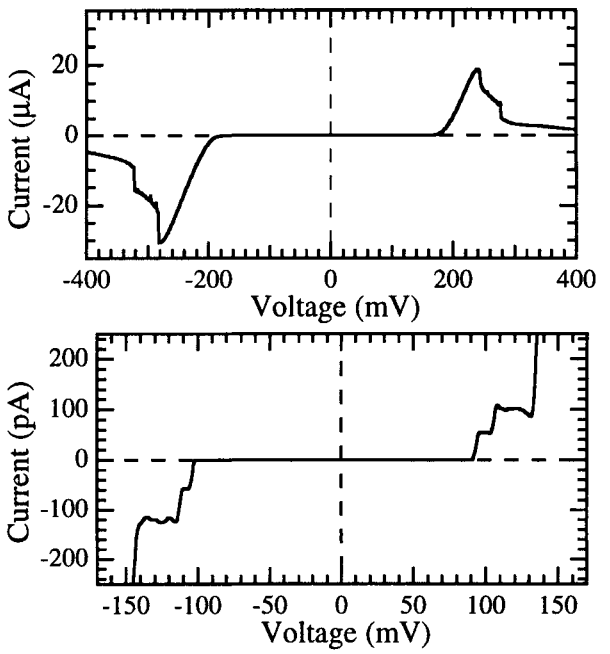


Fig. 6. $I(V)$ characteristics (zero magnetic field) at 1.4 K of the quantum well device showing the main resonance peaks (top). The magnified prethreshold region shows two steplike structures resulting from two isolated impurities (bottom).

structure. The current steps are relatively flat at low bias, where the transmission coefficient is not a strong function of applied bias.

We also note that there is an oscillatory structure on the current steps. This structure appears random but is very reproducible even after thermal cycling of the device. We will refer to this structure as the "fine structure" and discuss it in detail later.

4.1.2. Impurity Quantum Dot

Figure 6 shows the $I(V)$ characteristics for a typical resonant tunneling diode of the impurity system, (64 μm^2, 1.4 K), showing the main quantum well resonance peaks (top). Magnification of the current in the prethreshold region (bottom) shows two sharp current steps for both forward- and reverse-bias directions. This step structure is observed to be sample specific, but for a given sample it is exactly reproducible from one voltage sweep to another and independent of the voltage sweep direction. The steps are reproduced even after thermal cycling of the sample, except for slight threshold voltage shifts (<1 mV). Similar steps are observed in other devices with different barrier thickness. These steps look similar to the steps in Figure 5 and are attributed to tunneling through single impurity states. Note that these steps also show an oscillatory fine structure on the current plateaus.

To analyze the electron spectroscopy of the dot systems in greater detail, we need to determine the bias-to-energy conversion factor, α. The value of α is a measure of the amount of voltage that is actually dropped between the emitter and the quantum dot state. As will be shown, α can be determined from the temperature dependence of the plateau edges.

4.2. Variable-Temperature Measurements

As expressed in Eq. (10), the magnitude of the current step is given by $\Delta I = e/\tau$, where τ is the lifetime of the 0D state. This τ depends, among other factors, on the available

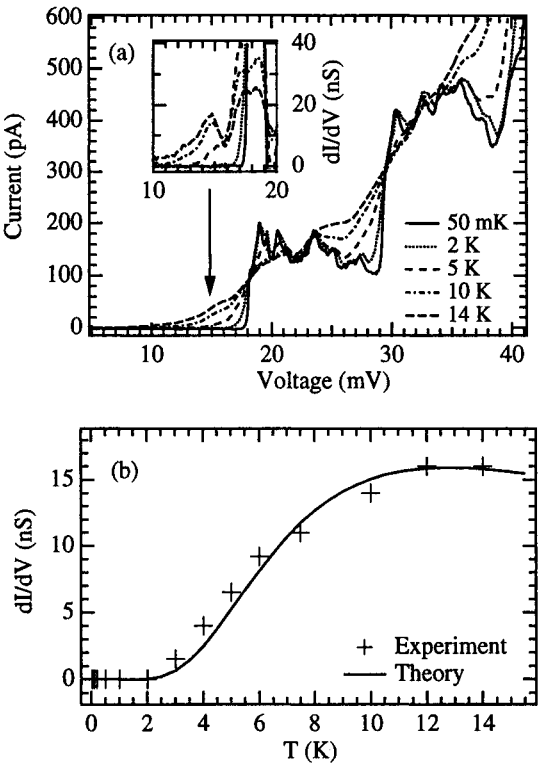


Fig. 7. (a) Reverse bias $I(V)$ characteristics of the fabricated quantum dot at different temperatures. The inset shows the subthreshold peak (in conductance) that arises as temperature is increased. (b) Experimental conductance (crosses) versus temperature [for the peak in the inset of (a)] and the theoretical fit (solid line).

and occupied density of states in the emitter. The occupancy of the electronic states in the emitter is determined by the Fermi distribution function and thus we expect the current ΔI to be proportional to the Fermi function. The sharpness of the current plateau edges is expected to broaden as the temperature increases, because of the broadening of the emitter Fermi distribution function. The $I(V)$ characteristics as a function of temperature for the fabricated quantum dot in reverse bias are shown in Figure 7a.

The voltage-to-energy conversion factor, α, is calculated by fitting the Fermi function to the first current plateau (I_0 is the value of the current on the plateau) in the variable-temperature data, that is,

$$I(V,T) = I_0 f(\alpha V) = \frac{I_0}{1+\exp[-e\alpha(V-V_{\text{th}})/(kT)]} \tag{11}$$

Here, V_{th} is the threshold voltage for the current plateau and can be accurately determined from the intersection point of the $I(V,T)$ curves in Figure 7a, because the current given by Eq. (11) does not depend on the temperature for $V = V_{\text{th}}$. The value of α is determined to be 0.37 in the forward-bias direction and 0.50 in the reverse-bias direction for the fabricated quantum dot. The different α values imply an asymmetry in the emitter and collector contacts of the quantum dot device (either in doping or in the barrier or spacer layer thickness) in contrast to the symmetric response seen in the large-area device (Fig. 4a). This is not surprising as we are now probing a very localized region instead of averaging over nonuniformities in barriers or series doping, as in the large-area device.

The current plateau edges of the impurity system also exhibit characteristic Fermi-level thermal broadening (Fig. 8). From a Fermi function fit for this device, we get $\alpha = 0.48 \pm 0.02$ for forward bias and 0.42 ± 0.02 for reverse bias. Once again, the fits are done for the

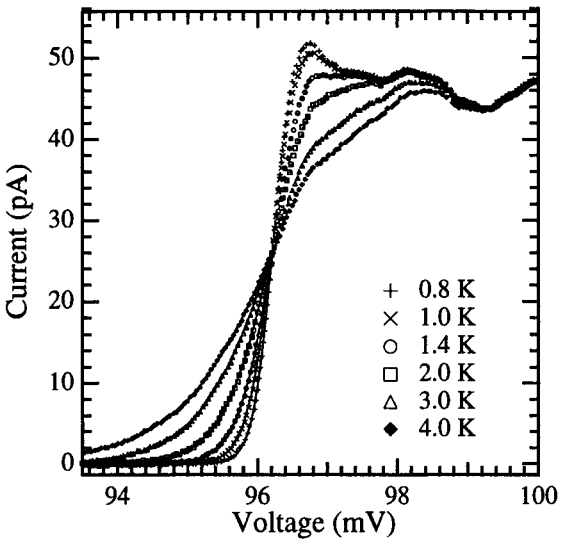


Fig. 8. $I(V)$ characteristics of the first impurity current step edge of the impurity device at different temperatures showing the Fermi-level broadening and the Fermi fit to these $I(V)$ traces.

region $V \leqslant V_{\text{th}}$ when the current is small and not affected by the occupancy of the impurity state.

We note the presence of an oscillatory, reproducible fine structure on the current plateaus in both the impurity and the fabricated quantum dot systems. Recently, it has also been investigated in detail by Schmidt et al. [38]. This structure (Figs. 7a and 8) exhibits significantly less dependence on temperature, especially for those regions located far away from the plateau edges. This indicates that the structure is not due to other states in the quantum dot or the quantum well itself, as current associated with tunneling through those states would exhibit Fermi broadening. The temperature insensitivity indicates that the current under consideration is from tunneling of the electrons from below the emitter Fermi level, where the emitter state occupation is not a function of temperature. Therefore, the fine structure is attributed to emitter states below the Fermi level, which pass into and out of resonance with the narrow 0D dot levels, as the applied bias is varied. At very low temperatures, only states in the emitter at or below the Fermi level, E_{F}, are occupied. These are the only emitter states available for tunneling. Electrons in the states nearest to the Fermi level will tunnel into the dot state first. States below the Fermi level then contribute to the tunneling as the bias is increased. If this model is correct, we expect that, as the sample temperature is increased, states above the Fermi level in the emitter will be populated. Figure 9 schematically shows how the occupation of discrete emitter levels (depicted as black lines in parts a and b of Fig. 9) is affected by increasing temperature.

At finite temperature, occupation of the emitter states above the Fermi level is possible and, therefore, thermally activated resonances *below* the first plateau should be observed. The inset of Figure 7a shows such a resonance effect, resulting in a subthreshold thermally activated conductance peak. Because $I(V) = I_0 f(\alpha V)$, where I_0 is a constant prefactor dependent on the transmission coefficient and $f(\alpha V)$ is the Fermi function, the conductance, $dI/dV = I_0\, df(\alpha V)/dV$. A fit of this to the subthreshold conductance peak strength (inset Fig. 7a), assuming an emitter state above the Fermi level becomes thermally activated, is shown in Figure 7b. The energy difference between the thermally activated emitter state and Fermi level (1.7 meV) is known from measuring the difference between the plateau threshold voltage at low temperatures (which determines the emitter Fermi-level position) and the thermally activated conductance peak position at higher temperatures. The *only* fitting parameter is I_0, which is within 5% of the value used for the first

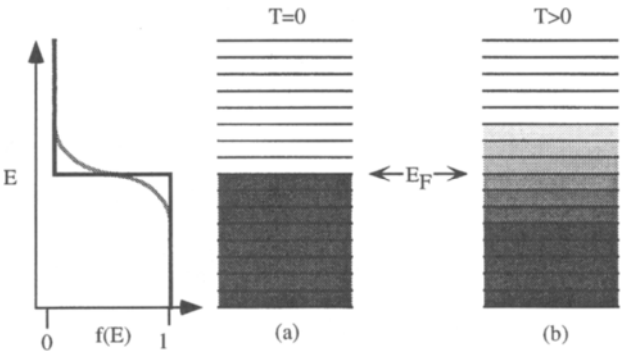


Fig. 9. (a) At $T = 0$, the Fermi function, $f(E)$, is a step function (black line) that results in a very sharp transition from occupied to unoccupied discrete emitter states. (b) At finite temperature, $f(E)$ becomes rounded near the Fermi energy, E_F, causing a gradual transition from states that are mostly occupied to states that are mostly unoccupied.

reverse-bias current plateau (at $V = V_{th}$). A similar thermally activated subthreshold peak is observed in the forward-bias direction as well. Similar thermally activated, prethreshold peaks are not observed in the impurity system. We will discuss the fine structure in more detail after investigating its magnetic field properties.

4.3. Magnetotunneling Measurements: Diamagnetic Shifts and Current Suppression

In addition to variable-temperature measurements, magnetic field is a valuable spectroscopy tool to examine bound states. Figures 10 and 11 show the forward-bias $I(V)$ characteristics in magnetic field parallel to current ranging from 0 to 9 T for the fabricated quantum dot and the impurity system, respectively. The traces are offset by a constant current value for clarity.

Note that there is a diamagnetic movement of all steps to higher bias with the magnetic field parallel to the current. This movement can be better observed in the fan diagrams shown in Figures 19 and 21. Plots of the plateau energy shift versus magnetic field squared (not shown) yield straight lines for all plateaus. At 9 T, the diamagnetic shift is approximately 1.4 to 2.6 meV (2–4 mV), depending on the current step/dot level for the fabricated quantum dot system, while it is about 0.4 meV (0.9 mV) for the current steps in the impurity system, implying that the impurity states are more localized. In the case of the fabricated quantum dot, different current steps are due to different energy eigenstates of the quantum dot. We expect these different eigenstates to show different shifts in a magnetic field and, hence, for the rest of this section we would concentrate on the diamagnetic shift of the fabricated dot only.

Table I lists the values for the diamagnetic shifts and current plateau widths for the first six steps in the reverse- and forward-bias directions of the fabricated quantum dot. From Eq. (3) ($\ell = 0$) and slope of the experimentally measured diamagnetic energy shift versus B^2 (accounting for α), the radial wave function extent is determined to be approximately 100 Å for the ground state in both bias directions. The implications of the radial wavefunction extent on the dot electron spectroscopy will be elaborated on after discussing the results for the magnetic field oriented perpendicular to the current.

It should be noted here that all resonances shift to *higher* bias with *only* a diamagnetic trend. This is in contrast to the single-electron theories for two-dimensionally and three-dimensionally confined, nearly cylindrical quantum dots in a magnetic field [36]. These theories show that some states increase in energy with magnetic field, while other states decrease in energy. Starting from zero field, the ground state *always* shifts upward

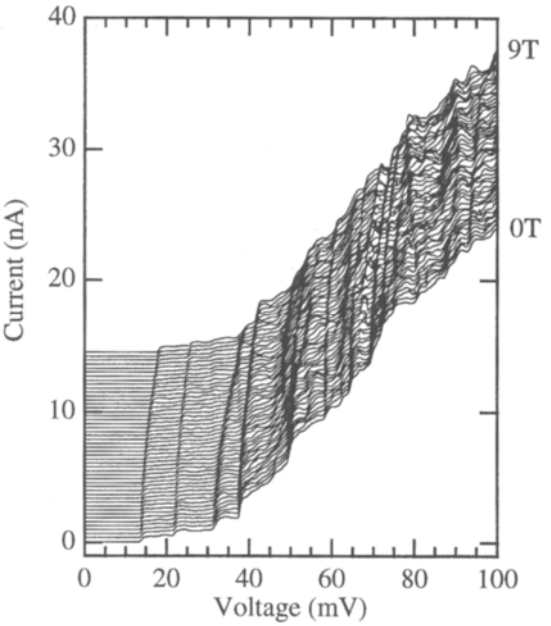


Fig. 10. Current–voltage characteristics in a dilution fridge with a mixing chamber temperature of 35 mK, in a magnetic field (0–9 T in 0.1875-T increments) parallel to the current for the forward-bias direction of the fabricated quantum dot. Traces are offset by a constant current value for clarity.

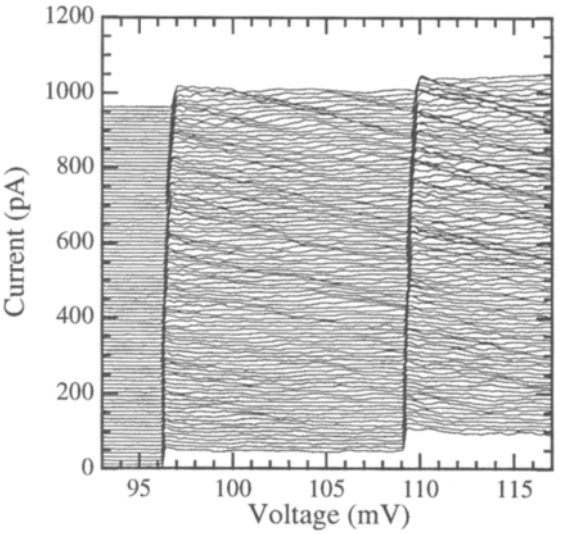


Fig. 11. Current–voltage characteristics in a dilution fridge with a mixing chamber temperature of 35 mK, in a magnetic field (0–9 T in 0.094-T increments) parallel to the current for the forward-bias direction of the impurity system. Traces are offset by a constant current value for clarity.

in energy, while the second state *always* shifts downward (ignoring spin). This is due to the Zeeman term (the term linear in B) in Eq. (3). The absence of Zeeman effects in the experimental data (i.e., peaks splitting and shifting in energy with a linear term) implies that either we cannot probe $\ell > 0$ states, possibly because of orthogonality between the emitter wave functions and $\ell > 0$ dot levels, or this simply tells us that ℓ is not a good quantum number for this system. This implies that the assumed cylindrical symmetry has

Table I. Experimentally Observed Diamagnetic Shifts and Current Plateau Widths for the Reverse- and Forward-Bias Directions for the Fabricated Quantum Dot Structure

Plateau index (N)	$\delta E_{\text{diamagnetic}}$ (meV, $B = 9$ T) (reverse, forward bias)	Plateau width (meV) (reverse, forward bias)
1	1.4, 1.6	5.0, 3.3
2	1.5, 1.6	6.5, 3.3
3	1.9, 2.6	6.5, 2.6
4	2.0, 1.6	9.0, 4.4
5	2.1, 1.6	1.1, 3.0
6	2.1, 1.0	3.5, 2.2

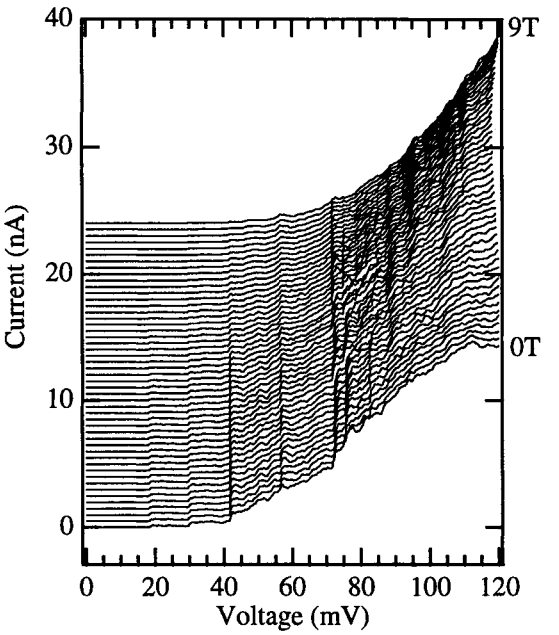


Fig. 12. Current–voltage characteristics in a magnetic field (0–9 T in 0.1825-T steps) perpendicular to the current for the fabricated quantum dot in the reverse-bias direction.

been distorted significantly. It should be noted that other groups [1, 2, 37] investigating similar systems also observe a diamagnetic dependence only.

Figures 12 and 13 show the $I(V)$ characteristics in the perpendicular magnetic field, for the fabricated quantum dot (reverse bias) and the impurity system (forward bias) at a mixing chamber temperature of 35 mK. As expected, the bias locations of all the current steps attributed to 0D dot states are not greatly affected by the perpendicular field, in contrast to the diamagnetic movement observed in the parallel field. This is confirmation that the current steps are the result of tunneling through the laterally localized dot states that reside in the strong confinement of the quantum well.

In addition to the difference in the response of the dot energy levels (i.e., the current plateau edges) to parallel and perpendicular magnetic fields, suppression of the plateau

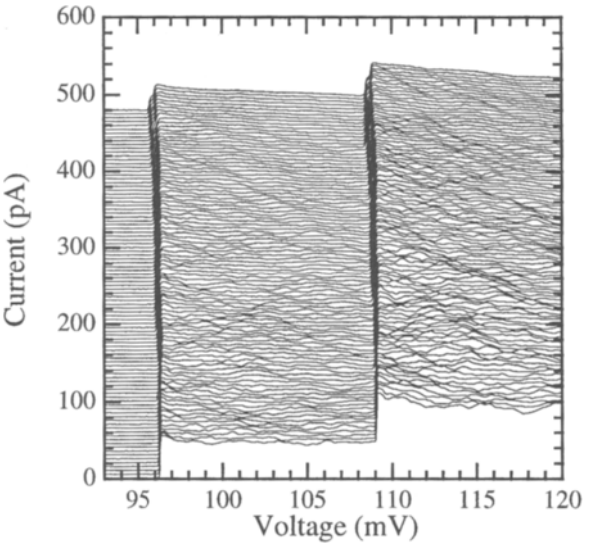


Fig. 13. Current–voltage characteristics in a magnetic field (0–9 T in 0.094-T steps) perpendicular to the current for the impurity system in the forward-bias direction.

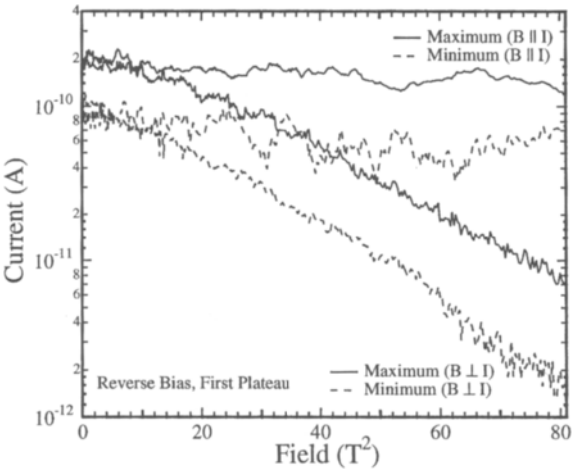


Fig. 14. Maximum (solid) and minimum (dashed) current values for the first current plateau of the fabricated quantum dot in reverse bias as a function of perpendicular and parallel magnetic fields.

current is observed for both bias directions in magnetic field oriented perpendicular to the current for both dot systems. Especially noteworthy are the lower plateaus of the fabricated dot system (Fig. 12), which appear to vanish because of the current scale. Figure 14 shows how dramatic these effects are. Current versus magnetic field squared is shown for the maximum and minimum current observed on the first plateau in the reverse-bias direction, in both parallel and perpendicular field orientations. In parallel field, the difference between the current minimum and maximum remains constant on a logarithmic scale over the field range in both bias directions, and only slight suppression is observed at 9 T. The current suppression for perpendicular field at 9 T is very large for the reverse bias (a factor of 100 for the plateau current minimum and 25 for the current maximum). In forward bias, a factor of approximately 10 is observed for both the current plateau minimum and the current plateau maximum.

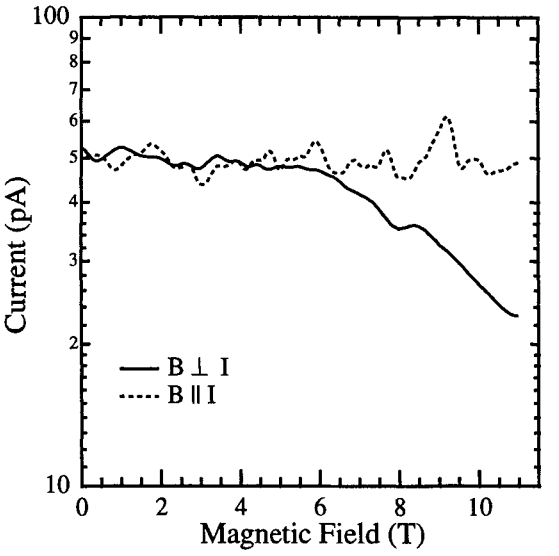


Fig. 15. Maximum current values for the first current step of the impurity system in forward bias as a function of perpendicular and parallel magnetic fields.

A similar current suppression is also observed in the case of the impurity system, although the effect is less dramatic (Fig. 15). In forward bias, the current gets suppressed by a factor slightly larger than 2 and, in reverse bias, by a factor slightly smaller than 2 when the field is perpendicular to the current. In parallel field, the current is approximately of the same field range except for some fluctuations. These fluctuations are attributed to the fine structure on the current plateaus and its movement in a magnetic field.

The current suppression has been observed previously in a coupled-dot system [24], and was attributed to a decreasing 0D–0D transition probability between the coupled dots. In our case, for the fabricated quantum dot, because there is one quantum well, the perpendicular field can *only* be decreasing the 1D emitter to a 0D dot transition probability. If the emitter and dot lateral wave functions are modeled as Gaussian functions, the observed linear Log(I) versus B^2 trend can be accounted for. The current is proportional to the overlap between the emitter and the dot wave functions

$$I \propto \int \psi_{\text{Emitter}} \psi_{\text{Dot}}\, dy = \lambda \sqrt{\frac{\pi}{2}} \tag{12}$$

where both the emitter and the dot wave functions are assumed to have a Gaussian wave function, $\psi \propto \exp(-y^2/\lambda^2)$. Under the application of a perpendicular magnetic field that shifts the emitter wave function with respect to the dot wave function by a displacement y_0,

$$\psi_{\text{emitter}} \propto \exp\left[-\frac{(y - y_0)^2}{\lambda^2}\right] \tag{13}$$

In this case,

$$\int \psi_{\text{Emitter}} \psi_{\text{Dot}}\, dy = \left(\lambda \sqrt{\frac{\pi}{2}}\right) \exp\left(-\frac{y_0^2}{2\lambda^2}\right) \tag{14}$$

As current is proportional to this overlap, Log(I) $\propto y_0^2$. If $y_0 \propto B$, we have the Log(I) $\propto B^2$ behavior observed experimentally.

To consider whether this trend is reasonable, note that coupling to the strong epitaxial dot potential in the z direction prevents a substantial shift of the dot wave function center.[2] The shift of the emitter wave function, y_0, may be estimated using a parabolic lateral potential approximation in magnetic field and assuming that in magnetic field this potential is offset by y_0, that is,

$$V = \frac{1}{2}\omega_c\left(y^2 - y_0^2\right) \tag{15}$$

As a result of introducing the potential into the Hamiltonian and applying Schrödinger's equation in Cartesian coordinates, the displacement y_0 is given by

$$y_0 = \frac{p_z\omega_c}{m^*(\omega_c^2 + \omega_0^2)} \tag{16}$$

For $\omega_0 > \omega_c$, this term varies as B, as required.

4.3.1. Spectroscopic Analysis of Fabricated Dot States

The wide-bias magnetotransport studies point out some clear inconsistencies with the expected quantum dot system. The magnitude of the diamagnetic shift implies a dot wave function spatial extent of approximately 200 Å in diameter. For this dimension, a charging energy of 5 meV is expected,[3] and a quantization energy, E_Q, of 35 to 45 meV between the ground state and the first excited state is expected (the lower limit is the parabolic result; the upper limit is the hard-wall result). While the charging seems reasonable to account for the observed plateau edge–to–plateau edge separations (see Table I), the quantization energy is *far* too large to account for the spacing from the second to the third plateau. As the ground state is only doubly degenerate because of spin, we expect to observe only two plateaus, separated by 5 meV/α. Subsequent plateaus in the $I(V)$ should then not be observed until at least 70 mV higher in bias. Clearly, a model beyond simple charging and quantization is required to explain the experimental data.

To explain similar diamagnetic shifts in previous work, a model of conducting filaments through the dot has been proposed by Tewordt and co-workers [1]. The filaments are assumed to be caused by the potential created by dopant atoms near or in the dot, which enhances the lateral quantization already present in the dot. Because, on average, all filament states are laterally localized by about the same amount, all of the peaks should exhibit similar diamagnetic shifts, which is observed. This also yields a more complicated density of states for the dot. However, transport through the system is still proceeding via tunneling through highly localized dot states. Note that this model also provides for the distortion of the cylindrical symmetry that is needed to prevent observation of $\ell > 0$ levels. Therefore, this model is consistent with our experimental data.

Applying this to our case, we expect to have a series of Coulomb-split plateau pairs with similar current step heights (ΔI_n), current suppression (for $B \perp I$), and diamagnetic shifts. Restated, the transport model is that conduction is proceeding through N dots in parallel with the emitter. For this specific sample, $N \approx 2$–3. In examining Table I, note that for reverse bias the diamagnetic shift is the same for $N = (1, 2)$ and for $N = (3, 4)$, and that the energy spacing between all of these is close to what is expected for the charging energy. For forward bias, a similar trend is observed for the $N = (1, 2)$ and $N = (4, 5)$ pairs. Figure 16 shows the conceptual energy ladder diagram for this transport process.

[2] If the wave function in the dot shifted significantly, the confinement energy would also change, which is not seen experimentally (i.e., no plateau shift for magnetic field perpendicular to current).

[3] In estimating the charging energy, E_C, the crucial parameter is the junction area. The geometrical capacitance argument assumes a metallic density of states, which is a questionable assumption in the emitter and collector electrodes, and certainly suspect in the dot. To provide a better estimate, a charging radius R_C is assumed. R_C is estimated from the wave function extent determined from the diamagnetic shift (100 Å), which results in $E_C \approx 5.0$ meV.

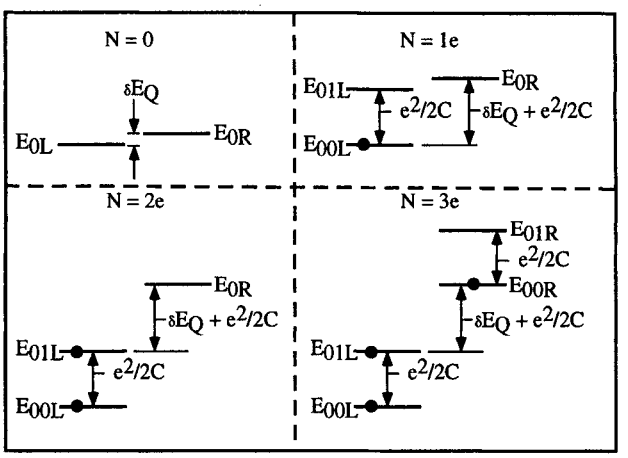


Fig. 16. Energy ladder diagram for the two-dot model. For no electrons in the dot ($N = 0$), there is a ground state spin-degenerate level for the left and right dot (E_{0L} and E_{0R}), separated by a small offset, δE_Q. When the dot is occupied by one electron ($N = 1$), it will occupy the lowest state available, E_{0L}, and the spin degeneracy of that state will be split by the Coulomb energy, $e^2/2C$, into E_{00L} and E_{01L}. The right state is also assumed to be lifted by the charging energy. The second electron ($N = 2$) will enter the next lowest energy state (E_{01L}). The third electron ($N = 3$) will then enter the ground state of the right dot.

Table II. Experimentally Observed Current Step Values in Zero Field and Also for $B = 9$ T ($B \perp I$). Suppression Values are the Ratio of $\Delta I_n(B = 0)/\Delta I_n(B = 9\text{ T})$

Plateau index (N)	ΔI_n (pA) 0 T (−, + bias)	ΔI_n (pA) $B = 9$ T (−, + bias)	Current suppression (−, + bias)
1	200, 600	8, 70	25, 8.6
2	200, 500	11, 60	18, 8.3
3	800, 1100	80, 240	10, 4.6
4	2300, 1600	500, 570	4.6, 2.8
5	2500, 2500	1400, 580	1.8, 4.3

The current suppression and current step height (ΔI_n) for these pairs should also track together. Table II lists the approximate ΔI_n at 0 and 9 T ($B \perp I$) and suppression values for reverse and forward bias for the first five plateaus. There is some degree of uncertainty in estimating ΔI_n, as the assumption is that each current plateau is independent of the others and that the background line shape (caused by the preceding plateaus) is flat. This approximation begins to break down around the fourth plateau in both bias directions. For the $N = (1, 2)$ pairs in both bias directions, there is good agreement between both the ΔI_n values and the suppression. For the $N = (3, 4)$ pair in reverse bias and the $N = (4, 5)$ pair in forward bias, the agreement is not as good, although, as previously mentioned, there is great uncertainty in estimating ΔI_n in this regime. However, it is interesting to note that the $N = 3$ plateau in forward bias (which exhibits a large diamagnetic shift compared to the other steps) exhibits a suppression value different from the other pairs. This could indicate that it is the result of a third dot; however, its absence in reverse bias cannot be explained. While the N-dot model cannot be proven conclusively with these data, it is consistent with

many of the features observed (i.e., state separation, magnetic field dependence, current suppression, and the lack of Zeeman shifts).

4.4. Magnetotunneling Measurements: Fine Structure

We mentioned earlier that we observe an oscillating, temperature-independent fine structure on the current plateaus of the $I(V)$ characteristics in both the fabricated dot and the impurity systems. A comparison between the observations of the two systems gives insight into the origin of the fine structure. To better characterize this, we investigate the effect of magnetic field on this structure. Figure 17 shows the evolution of the $I(V)$ characteristics of the fabricated quantum dot in forward bias. The magnetic field is parallel to the current and ranges from 0 T (bottom) to 2.25 T (top). The $I(V)$ traces have been vertically offset by a constant current value, so the movement of the fine structure in magnetic field is apparent. Similar fine-structure behavior is observed at higher magnetic fields (up to 9 T) and in a magnetic field perpendicular to the current. The fine-structure characteristics are reproducible, even after thermally cycling the sample to 300 K. It is apparent that the field dependence of the fine structure is different from that of the dot energy states (plateau edge behavior). Figure 18 shows the evolution of the $I(V)$ characteristics in a parallel magnetic field ranging from 6 to 9 T. Other groups [1, 2, 40, 41] have seen similar fine structure; however, their field steps were on the order of teslas, rather than 100 Gauss, so the dependence of this fine structure upon field appeared random.

To better view the data, fan diagrams are generated that plot the plateau edge and fine-structure peak voltage positions versus magnetic field. Figures 19 and 20 show fan diagrams for the fabricated quantum dot for the reverse bias in a parallel field ($B \parallel I$) and a perpendicular field ($B \perp I$), respectively. In a parallel field, three lines resulting from the current plateau edges at 10, 20, and 32 mV ($B = 0$ T) are clearly visible. Between plateau edges, the fine-structure motion clearly correlates with varying magnetic field. The fine-structure peaks form a complex lattice of crossing lines. From measuring the slope of these lines, we find that the fine structure typically moves at a rate of 2.5 mV/T (1.25 meV/T) in the reverse-bias direction and 5.0 mV/T (1.85 meV/T) in the forward bias direction. Both

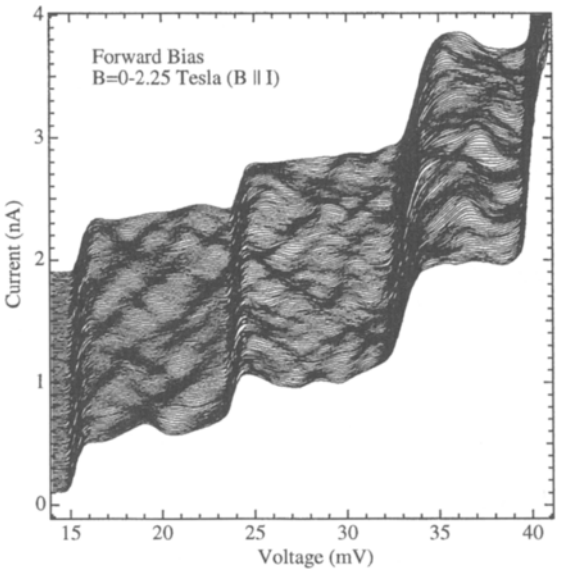


Fig. 17. $I(V)$ data for the fabricated quantum dot in parallel field, ranging from 0 T (bottom) to 2.25 T (top). Curves are vertically offset by a constant current value for clarity.

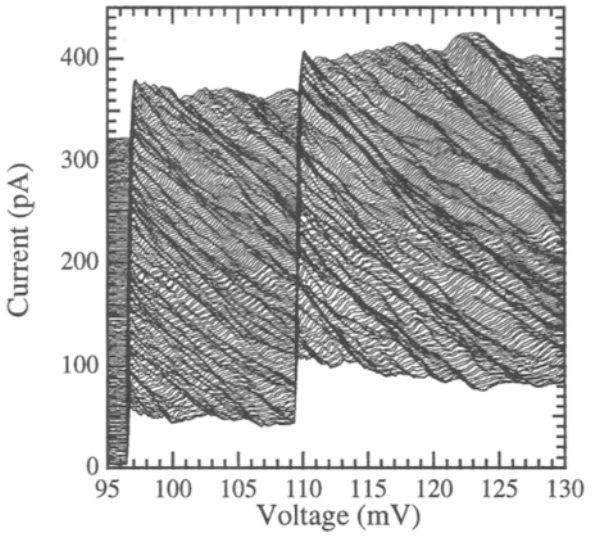


Fig. 18. $I(V)$ data for the impurity dot in parallel field, ranging from 6 T (bottom) to 9 T (top). Curves are vertically offset by a constant current value for clarity.

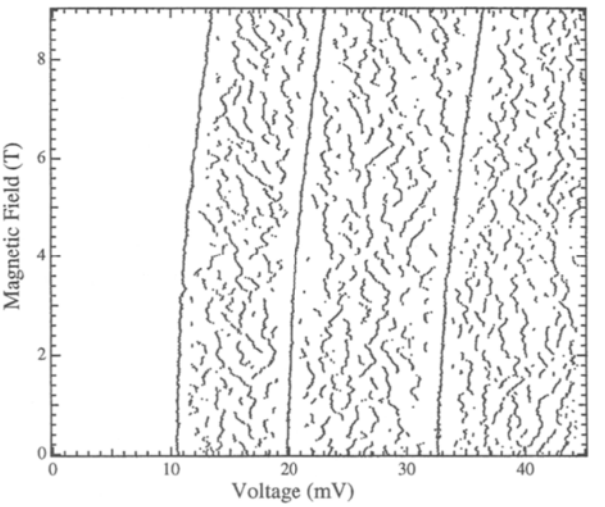


Fig. 19. Fan diagram showing peak voltage location versus magnetic field parallel to the current for the reverse-bias direction for the fabricated quantum dot.

of these values are on the order of the value for eB/m^* (1.8 meV/T in $In_{0.1}Ga_{0.9}As$ and 1.7 meV/T in GaAs). Similar field dependence of the fine structure is seen in the perpendicular orientation.

Figures 21 and 22 show fan diagrams for the impurity dot for the forward bias in a parallel field ($B \parallel I$) and a perpendicular field ($B \perp I$), respectively. Two lines resulting from the two current plateau edges are clearly visible and show only small movement with magnetic field. Between plateau edges, the fine-structure peaks show distinct movement to lower voltage as the field is increased. This movement is most prominent at fields greater than 2 T. The rate of this movement is approximately 5 meV/T for $B \parallel I$ and 3.5 meV/T for $B \perp I$. A similar shift is observed in reverse bias.

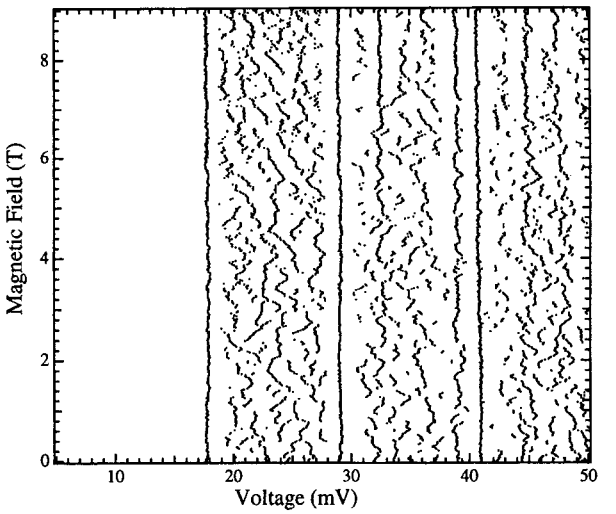


Fig. 20. Fan diagram showing peak voltage location versus magnetic field perpendicular to the current for the reverse-bias direction for the fabricated quantum dot.

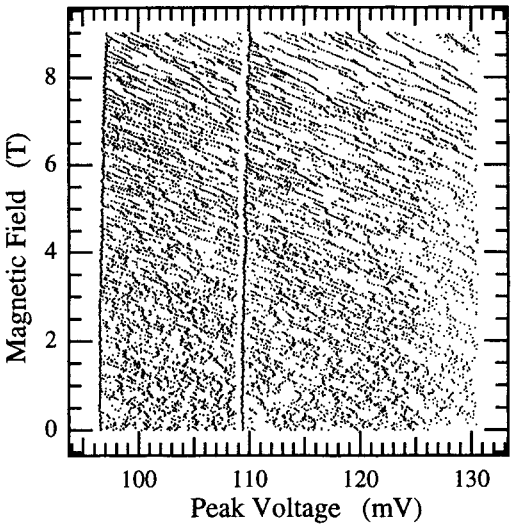


Fig. 21. Fan diagram showing peak voltage location versus magnetic field parallel to the current for the forward-bias direction for the impurity dot system.

While the fine structure, the number of plateaus observed, and the plateau widths are consistent through device thermal cycling, the spectra are sometimes offset in voltage. We believe this is due to the different donor charge distributions in the emitter and collector upon cool down, which may change from run to run. In contrast, dot state current plateau edges only shift in magnetic field parallel to current. This confirms that the source of the fine structure does not reside in the dot and implies the presence of emitter states.

The average energy separation between the fine-structure peaks on the first plateau in both bias and field directions has been calculated by performing a numerical Fourier transform upon the fan diagrams. Table III shows the values for the mean fine-structure separation, $\bar{x}$, and the standard deviation, σ. As expected, no dramatic change in the peak separation is observed when the field orientation is changed.

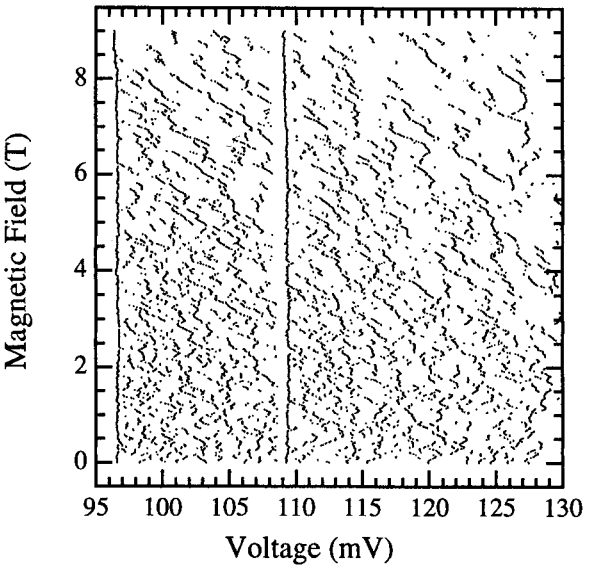


Fig. 22. Fan diagram showing peak voltage location versus magnetic field perpendicular to the current for the forward-bias direction for the impurity dot system.

Table III. Average Fine-Structure Peak-to-Peak Separation and Standard Deviation for the Fabricated Quantum Dot

Plateau (bias, field)	Fine-structure separation $\bar{x} \pm \sigma$ (meV)
Reverse, $B \perp I$	0.91 ± 0.4
Reverse, $B \| \| I$	0.83 ± 0.3
Forward, $B \perp I$	0.58 ± 0.2
Forward, $B \| \| I$	0.81 ± 0.3

In previous work by Su et al. [2, 40], the fine structure was observed to quench in magnetic field. This was viewed as evidence against the fine structure being attributed to a discrete density of states in the emitter. This is not the case observed for the samples studied in our work. Even at fields of up to 11 T the fine structure is still strong and clearly present. In a strong perpendicular field, the fine structure is observed to quench at the *same* rate as the current steps. Both are suppressed because of a decrease in the emitter–dot transition probability in a perpendicular field, and this is the expected result if the fine structure is due to the density of states in the emitter.

Several factors indicate that the fine structure results from the emitter contact. The weak temperature dependence shows that the fine structure is not due to states in the dot and is due to tunneling processes from states below the Fermi level in the emitter. The observation of thermally activated preresonant fine-structure peaks is consistent with this model. Also, other groups have shown that the fine structure is due to emitter states by studying transport in asymmetric quantum dots [37, 38]. The motion of the fine structure in magnetic field, which is on the order of $\hbar\omega_c$, is consistent with what one expects for states in GaAs when the confinement energy is weak. The lack of dependence upon magnetic field orientation excludes states localized in the dot, as states in the dot exhibit very different response

in parallel ($B \| I$) versus perpendicular ($B \perp I$) magnetic field orientations owing to the strong quantum well confinement. The observed fine-structure peak energy separations of 0.6–0.9 meV are too small to arise from 1D subbands in the leads. Other possible models that account for this close energy separation, including interference effects [42], universal conductance fluctuations (UCF) [43], or effects resulting from chaotic transport [44], can be individually excluded.

The small energy separation between the fine-structure peaks in conductance indicates that they may be due to the effect that individual donors have on the 1D density of states in the emitter. For the dopant levels used in this structure, there are approximately two impurities in a 100-Å cube in the emitter (the value of 100 Å is used as it is the mean free path in the doped lead at low temperature). This places about 100 dopant atoms with electrons contributing to the degenerate doping of the conduction band in this volume. For a calculated Fermi level of 80 meV, this results in level spacings that are approximately 0.8 meV in energy (2.2 mV in forward bias, 1.6 mV in reverse bias). This in good agreement with the observed 0.6–0.9-meV spacing.

4.5. Magnetotunneling Measurements: Spin Splitting and g^* Factor

So far in this chapter, we ignored the spin of the electron. We expect the ground states of the fabricated or the impurity dot systems to be spin degenerate. In a magnetic field, this degeneracy is lifted. The energy separation between these split states is given by $\Delta E = g^* \mu_b B$, where B is the magnetic field strength, μ_b is the Bohr magneton, and g^* is the effective spin (Landé g) factor of electrons in the semiconductor material. This g factor of electrons in a material depends on the band structure and is different from the free-electron value of 2. In bulk GaAs, it is -0.44. In a confined system, the g^* factor changes further as the confinement affects the band structure. Thus, an accurate experimental determination of the spin g^* factor of electrons in a confined region serves as an important test of the band theory of solids. In what follows, we present the observation of spin splitting in the impurity dot system only. A similar effect is not observed in the fabricated dot systems for the several following reasons. The spin splitting energy is very small ($\approx$150 μeV at 10 T). First, in order to observe this small splitting, we have to have sharp current steps and low temperatures. The observed spin splitting in the impurity dot system could not be resolved at a temperature above 300 mK (Fig. 28). It is possible that the electrons in the fabricated dot samples did not get as cold as those in the impurity dot samples. Second, the nature of the emitter in the two systems is different. In the impurity system, we have a 3D emitter with a continuum of density of states. Therefore, electrons of both spin orientations are available for tunneling at any energy even in a magnetic field. We do not have to worry about the spin splitting in the emitter if the emitter is 3D. On the other hand, the fabricated dot samples have a 1D emitter with a discrete density of states. The splitting of these 1D subbands would have to be taken into account as well and the net splitting would be a difference between the emitter subband splitting and the quantum dot state splitting. We will now discuss the observation of spin splitting in the impurity dot system and how it allows us to determine the spin g^* factor and the electron tunneling rates.

Figure 23 shows an expanded view of one such current step with and without a magnetic field when the sample is in a dilution fridge with the base temperature of the fridge (T_{mix}) at 35 mK.

At zero field, the ground state of the impurity is spin degenerate causing a single current step. Upon lifting of the degeneracy at finite field, a splitting of the current step is observed. Note that the splitting is not the same for the two different field orientations. This splitting is observed in all devices and for all the current steps in a given device investigated at low temperatures. Figure 24 depicts the $I(V)$ characteristics for the same device at higher bias showing six different current steps. Each of those steps are observed to split in a magnetic field in both forward and reverse bias.

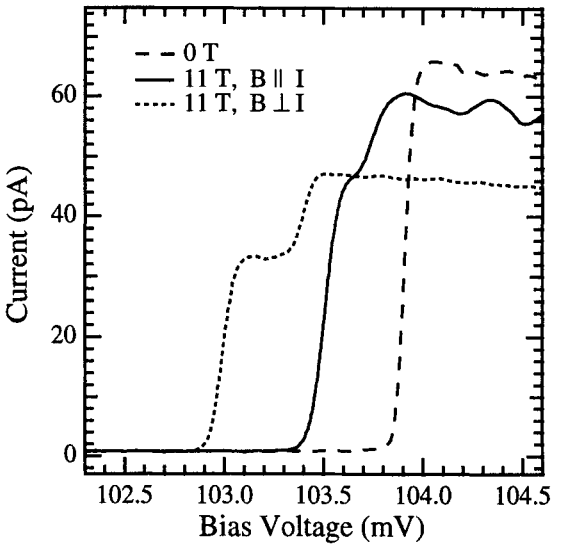


Fig. 23. $I(V)$ characteristics of the first current step edge ($T_{mix} = 35$ mK) in reverse bias at 0 T and at 11 T under both magnetic field orientations (field parallel to current and field perpendicular to current). The three curves are arbitrarily offset along the x axis for clarity.

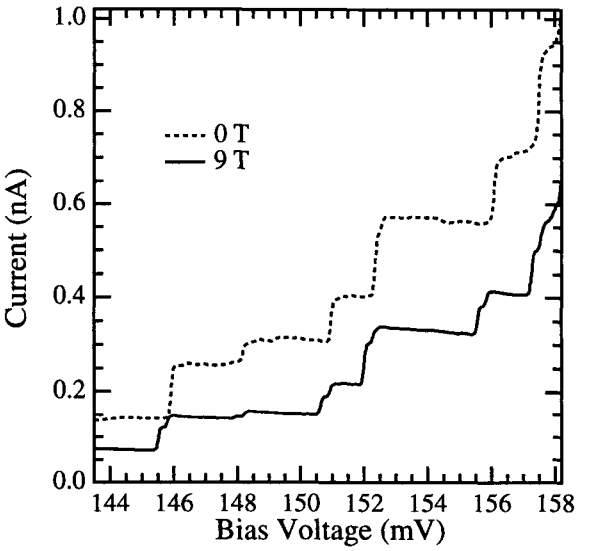


Fig. 24. $I(V)$ characteristics at $T_{mix} = 35$ mK showing six different current steps in zero field (dashed line) and with a field of 9 T oriented perpendicular to current (solid line).

Figure 25 shows the evolution of the $I(V)$ characteristics upon increasing magnetic field. Note that the spin splitting increases as the field is swept from 0 T (bottom) to 9 T (top).

Figure 26 shows the voltage separation between the corresponding two spin-split conductance peaks, which increases linearly with the magnetic field strength as expected. Because of the finite widths of the conductance peaks, it is not possible to resolve the splitting for magnetic fields less than 5.5 T. The best line fit to the data (Fig. 26) closely intersects $\Delta V = 0$ at $B = 0$ and has a slope of $g^*\mu_b/\alpha$, where μ_b is the Bohr magneton, g^* is the effective spin g factor of the impurity, and α is the voltage-to-energy conversion factor [2, 6, 34, 35]. The observed spin splitting is different for the two field orientations and we denote

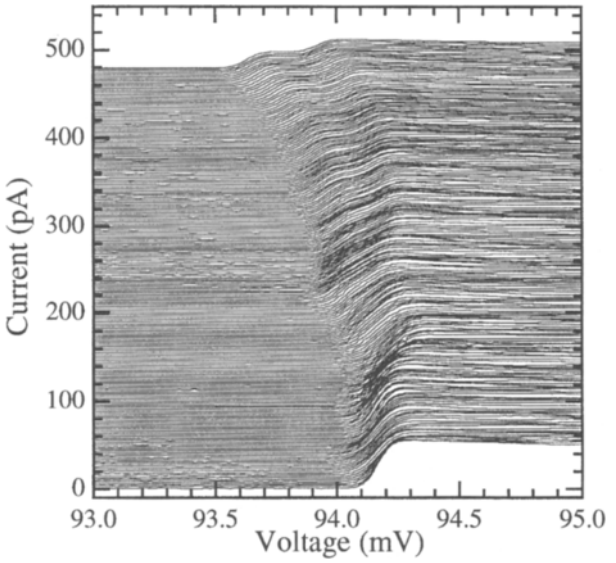


Fig. 25. $I(V)$ characteristics ($T_{\text{mix}} = 35$ mK) of the first current step edge in forward bias in increasing magnetic fields (field perpendicular to current) from 0 T (bottom) to 9 T (top). The successive field curves are offset a constant amount along the y axis for clarity.

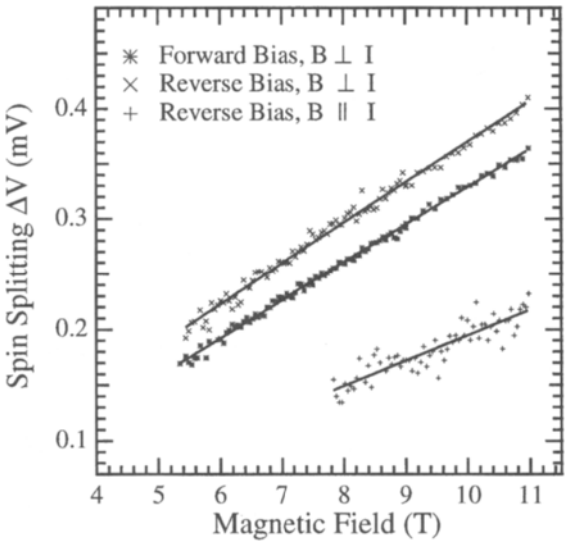


Fig. 26. Experimental spin splitting versus magnetic field for the first current step for the different bias and magnetic field orientations at $T_{\text{mix}} = 35$ mK. The solid lines are linear fits to the data.

$g^*_\perp$ and $g^*_\parallel$ to be the effective g factors for the field being perpendicular and parallel to the current flow direction, respectively.

To determine the spin g^* factor, it is necessary to know the voltage-to-energy conversion factor, α, which is accurately determined by studying the thermal broadening of the current steps as discussed earlier in Section 4.2.

From these values of α and the measured slopes of the fits in Figure 26, the absolute magnitude of the spin $g^*_\perp$ and $g^*_\parallel$ values of the impurities can be calculated. Table IV lists the measured g^* values for the various devices and current steps. For a given device, we

Table IV. α and g^* Values as Calculated for the Various Devices and Current Steps

	α		$g^*_\perp$		$g^*_\parallel$	
Current step	+bias	−bias	+bias	−bias	+bias	−bias
First step	0.48 ± 0.02	0.42 ± 0.02	0.28 ± 0.02	0.28 ± 0.02	0.14 ± 0.04	0.13 ± 0.04
Second step			0.28 ± 0.02	0.27 ± 0.02		

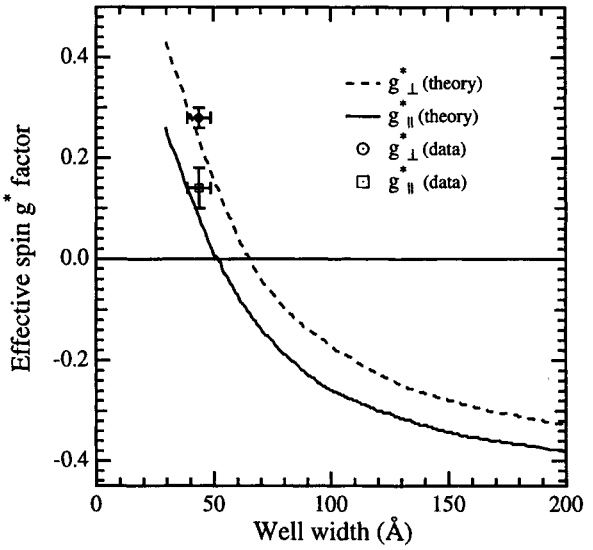


Fig. 27. Comparison of the measured g^* factors with the theoretical predictions of Ivchenko and Kiselev [45]. We assume that the sign of the measured quantities is positive.

determine the g^* factors in both the forward- and the reverse-bias directions. Note that the slopes of the two lines in Figure 26 for the first step in forward bias and reverse bias are different, but so are the corresponding α values, giving us the same g^* values. The α value in this device is not determined for the second current step independently. We assume that the α value for the second step is the same as that of the first step. This is a good assumption, as the α values are not very sensitive to small bias changes.

As discussed earlier, g^* is theoretically predicted to be a strong function of the quantum well width and is calculated to change from the bulk value of -0.44 to greater than $+0.4$ for well widths less than 30 Å and it also becomes asymmetric [45]. In Figure 27, we show our data with respect to the preceding theoretical predictions of Ivchenko and Kiselev [45].

Our measurements are consistent with this prediction and with recent experimental results [46, 48]. We cannot determine the sign of the g^* factors and we have assumed here that it is positive. Note that the predictions are made for quantum wells with $Al_xGa_{1-x}As$ barriers with $x = 0.35$, while our measured data are on quantum wells with $Al_xGa_{1-x}As$ barriers with $x = 0.27$. We expect the effect of this difference in Al concentration to be small. Also note that, strictly speaking, the measured g^* factor is that of an electron bound to a Coulomb potential in the quantum well and not that of free electrons in the quantum well. We expect this difference to be small, too, as the impurity state is a shallow impurity state.

So far, we have neglected the spin splitting of the electrons in the emitter. Naively, one may expect that observed splitting of the current steps is due to the difference in the spin

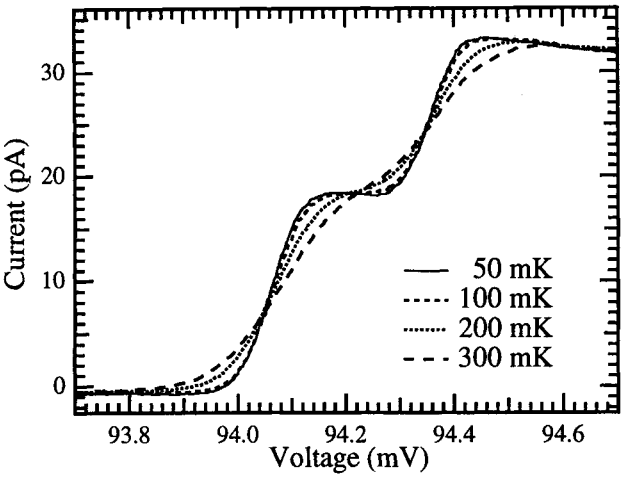


Fig. 28. $I(V)$ characteristics at 9 T showing the spin-split first current step edge in forward bias at different temperatures. Both fragments of the split edge exhibit Fermi broadening with the temperature.

splitting of the emitter electrons and the impurity state. This is not the case as the localized impurity state is an individual, isolated state, while the emitter is a 3D sea of electrons with a continuum of occupied electron states. All electron levels in the emitter split in an applied magnetic field but, owing to the continuum, at any given energy electrons of both spin orientations are available for tunneling. Because the spin splitting energy ($\approx$0.15 meV at 10 T) is much smaller than the Fermi energy in the emitter ($\approx$40 meV), we do not expect to observe any spin polarization effects in the emitter. Figure 28 shows thermal broadening of the first current step edge split at 9 T. Separate Fermi broadening of the two fragments of the split step indicates that in both cases electrons involved in tunneling are the Fermi electrons in the emitter. The observed experimental voltage difference is entirely due to the spin splitting of the impurity state only, and is not affected by the g^* factor of the electrons in the emitter.

If the Fermi energy in the emitter is small and weakly localized states are formed in the emitter, the g^* factor of these weakly localized states would have to be taken into account as reported by Sakai et al. [22, 49].

We also note that electron–electron interactions will not alter the relative energy of the two spin states and thus the measured g^* factor in this experiment. There are two possible mechanisms for electron–electron interactions. One is between the electrons in the well and the other is between the tunneling electron and the electrons in the emitter. The first mechanism can be ignored because, at the bias of interest, there is very little electron density in the well. It has been observed in transport studies of 2D electron gases that there is an enhancement in the g^* factor of electrons, which is attributed to electron–electron interactions; however, such an enhancement is not observed when single-electron energy levels of the 2D electron gas are probed (as shown by Dobers et al. [47]). In our experiment, we do not have a 2D electron gas in the quantum well, and we are probing single-electron states. The second mechanism, the Coulomb interaction between the tunneling electron and the electrons in the emitter, causes a rise in the step current near the threshold at low temperatures, which is observed (as first reported by Geim et al. [34]), but it should not affect the energy separation of the two spin states.

4.6. Magnetotunneling Measurements: Electron Tunneling Rates

Analysis of the tunneling current through a system yields information about the tunneling rates through the system. We now have a unique opportunity to investigate a two-state tun-

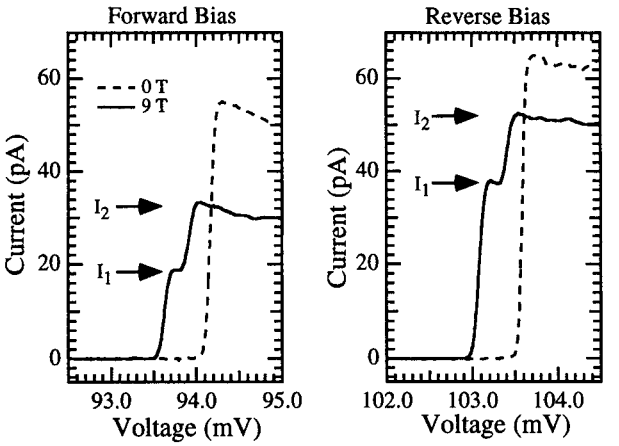


Fig. 29. $I(V)$ characteristics at $T_{mix} = 35$ mK of the first current step edge of the 85-Å-thick barrier device in forward bias (left) and reverse bias (right) at 0 T (dashed line) and 9 T (solid line). The magnetic field is oriented perpendicular to the current direction. I_1 and I_2 denote the current values at 9 T as shown. I_1 gives the current of the first fragment, while I_2 is the net current of both fragments of the split step edge.

neling system, which can give more information than just a single-state tunneling system. Figure 29 shows that the two fragments of the spin-split step at 9 T are observed *not* to have the same current magnitude, that is, $I_2 - I_1 \neq I_1$, where I_1 and I_2 denote the current values as shown. I_1 gives the current of the first fragment, while I_2 is the net current of both fragments of the split step edge. This difference is more prominent in reverse bias. An understanding of this asymmetry gives us the electron tunneling rates through each of the two barriers of the double-barrier heterostructure individually.

To analyze this, we define T_b and T_t to be the tunneling rates for an electron to tunnel through the bottom and the top (referred to as the growth direction) potential barriers, respectively, of the double-barrier heterostructure. We also define T_{cl} and T_{em} to be the electron tunneling rates through the collector (downstream) and the emitter (upstream) (referred to as the electron flow direction) potential barriers. In forward bias, electron injection is through the top barrier into the quantum well ($T_{em} \equiv T_t$, $T_{cl} \equiv T_b$), while, in reverse bias, electron injection is through the bottom barrier into the quantum well ($T_{em} \equiv T_b$, $T_{cl} \equiv T_t$). We also define p to be the occupation probability for an electron in a localized state in the quantum well. In the sequential tunneling picture, $p = f(E)T_{em}/(T_{em} + T_{cl}) = f(E)p_0$. Because the spin splitting energy ($\Delta E \leqslant 150$ μeV) is much smaller than the barrier potential energy ($\approx$300 meV), we assume that the tunneling rates are the same for electrons tunneling through the spin-up or the spin-down states irrespective of the slight energy difference. We also assume that the emitter electrons are not spin polarized, which is a good assumption because the Fermi energy ($\sim$40 meV) is much larger than the spin splitting energy even at 10 T.

In high magnetic fields and at low temperatures, when the Fermi level is sharp ($p = p_0$, Fig. 28), we can adjust the bias near a given impurity to obtain the following two conditions as noted schematically in Figure 30. At a lower bias, V_1, only the lower energy spin state channel is active for conduction, and the current is given by

$$I_1 = peT_{cl} \tag{17}$$

At a higher bias, V_2, the higher energy spin state channel is also active for conduction, and the current is given by

$$I_2 = p'eT_{cl} = \left(2p - p^2\right)eT_{cl} \tag{18}$$

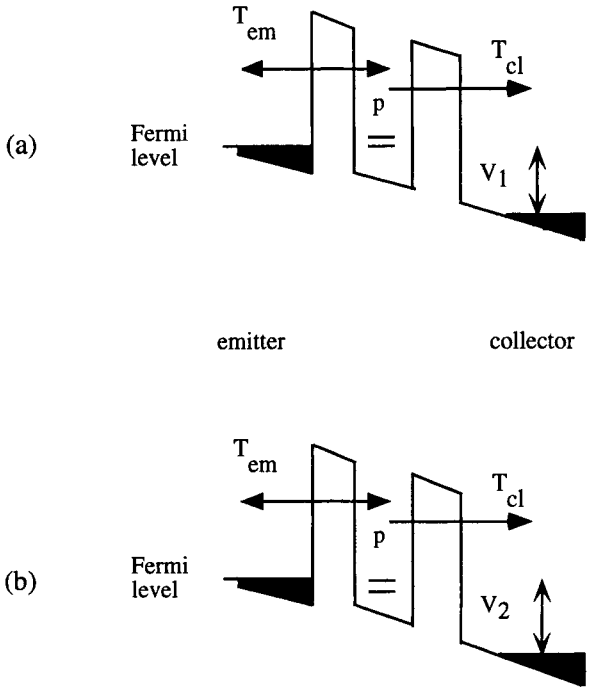


Fig. 30. Schematic of electron tunneling through the two-state system.

where $p' = (2p - p^2)$ is the probability of occupying either the lower or the higher state, but not both of them. Both states cannot be occupied at the same time because of the large Coulomb energy required for another electron to simultaneously occupy the second state. For this system, the single-electron Coulomb charging energy ($U_C = e^2/2C$, where C is the effective capacitance of the double-barrier device) is much larger than the spin splitting energy ΔE. We can estimate the capacitance of the system to be $C = (\varepsilon_0 k \pi r_0^2)(d_t^{-1} + d_b^{-1})$, where k is the dielectric constant, d_t and d_b are the top and bottom barrier thicknesses, and r_0 is the radius of the lateral region affected by the localized impurity state in the quantum well. We take r_0 as the Bohr radius of hydrogenic impurities in GaAs ($\approx$100 Å) and obtain $U_C \approx 9$ meV. Although taking r_0 as the Bohr radius is only an approximation, we obtain $U_C \geqslant \Delta E$ even for r_0 seven times larger.

In Eqs. (17) and (18), we have assumed that the tunneling rates are the same at the two different biases V_1 and V_2, which is a good assumption because the bias difference $(V_1 - V_2)$ is much smaller than the barrier potential. In the extreme limits, these equations indicate that, for $T_{cl} \gg T_{em}$, $p \approx 0$ and $I_2 \approx 2I_1$, while, for $T_{cl} \ll T_{em}$, $p \approx 1$ and $I_2 \approx I_1$. This qualitatively explains the behavior observed in Figure 29. To get a quantitative understanding, we solve Eqs. (17) and (18), using the experimentally measured I_1 and I_2, to determine p.

4.6.1. Effect of Spin Degeneracy at Zero Magnetic Field

The preceding analysis of the tunneling current through the two-state system is valid even at zero magnetic field when the two spin states are degenerate. We, hence, expect to observe some effect of the finite occupancy, p, of the impurity state. This effect is very nicely observed by investigating the thermal broadening of the current steps. In Section 4.2, we mentioned that current steps broaden as the temperature increases and this broadening was modeled by the Fermi equation [Eq. (11)]. A fit of this equation to the data is shown in Figure 8. This fit was done for a bias region $V \leqslant V_{th}$. If we extrapolate these fits to the

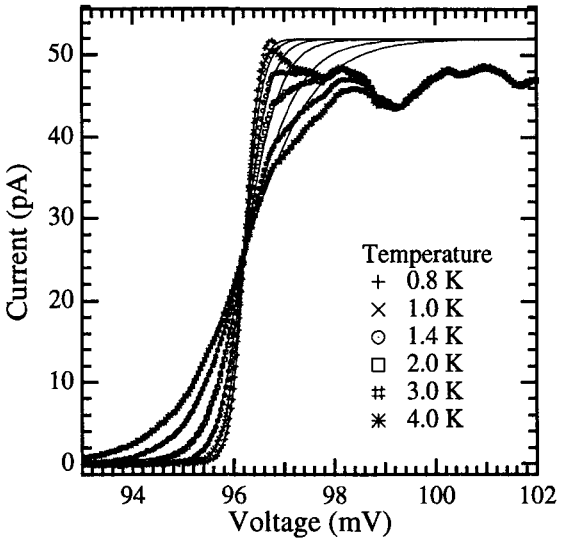


Fig. 31. $I(V)$ characteristics of the first current step edge in forward bias of the impurity system with 85-Å-thick barrier at different temperatures and the extrapolation of the Fermi fits [Eq. (11)] to these $I(V)$ traces as obtained in Figure 8 to voltages greater than the threshold ($V \geqslant V_{\text{th}}$). The experimentally measured current can be seen to be less than the theoretically expected current on the plateau.

region above the threshold (Fig. 31), we observe that the experimentally measured current is lower than the predicted value. We attribute this deviation to the Fermi behavior of the spin degeneracy of the localized state and Coulomb charging effects.

This fit is strictly valid for the case of tunneling through a single state only. The current in the case of tunneling through two degenerate states can be expressed as in Eq. (18) [assuming $p = p_0 f(E)$]:

$$\Delta I = A p_0 f(E)\big(2 - p_0 f(E)\big) \tag{19}$$

where A is a constant and $p_0 = T_{\text{em}}/(T_{\text{em}} + T_{\text{cl}})$ is the occupancy of the electron in either one of the two localized degenerate states when $f(E) = 1$. p_0 depends on the relative tunneling rates of the two potential barriers. Equation (19) can be fit to the data. Once again, the fits are done only for bias voltages $V \leqslant V_{\text{th}}$ because of the presence of the "fine structure" on the current plateaus for $V \geqslant V_{\text{th}}$. However, in Figure 32, we directly show the extrapolation of the corrected fits to all bias voltages. V_{th} is obtained from the common intersection point of the curves at different temperatures. A and p_0 are obtained from the measured current values of the plateau current (I_{plateau}) and the threshold current I_{th} in the following way. If $V \gg V_{\text{th}}$, then $f(E) = 1$ and

$$\Delta I = I_{\text{plateau}} = A p_0 (2 - p_0) \tag{20}$$

If $V = V_{\text{th}}$, then $f(E) = \frac{1}{2}$ and

$$\Delta I = I_{\text{th}} = A\left(\frac{p_0}{2}\right)\left(\frac{2 - p_0}{2}\right) \tag{21}$$

Solving these two equations simultaneously from the measured values of I_{plateau} and I_{th}, we get A and p_0. We get for the data shown in Figure 32, $A = 81.4$ pA and $p_0 = 0.35$. Thus, once again, the only free parameter in the fit is α, which then can be accurately determined. The α values obtained from this fit for this step is 0.5, which is within the experimental error of that obtained from the previous fit (0.48). This is consistent as both the fits are done at $V \leqslant V_{\text{th}}$ [$f(E) < \frac{1}{2}$], when the occupancy [$p = p_0 f(E)$] is small, and Eq. (19)

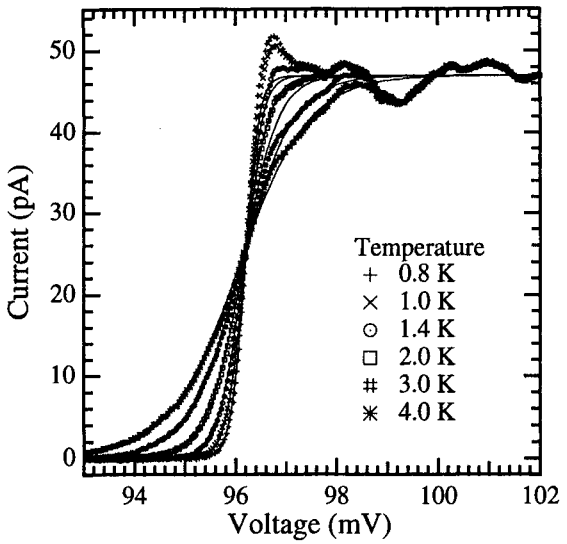


Fig. 32. $I(V)$ characteristics of the first current step edge in forward bias of the impurity system with 85-Å-thick barrier thickness at different temperatures and the extrapolation of the corrected fits [Eq. (19)] to these $I(V)$ traces to voltages greater than the threshold ($V \geqslant V_{th}$).

reduces to that of Eq. (11). These fits and their extrapolation to bias voltages $V \geqslant V_{th}$ now accurately determine the current plateau values as can be seen from Figure 32.

It is also possible to determine the occupancy for the localized states in reverse bias. For the same device in reverse bias, we obtain $p_0 = 0.57$ and $\alpha = 0.42$. This difference in forward and reverse bias is attributed to a slight asymmetry in the growth of the device and will be discussed in detail later.

The importance of this corrected fit becomes even more apparent while investigating the thermal broadening of current steps on which the fine structure is not very prominent. In such cases, the fit can be carried out over the entire range of the data unlike the earlier case where it was restricted to $V \leqslant V_{th}$. This is shown in Figure 33 for the 65-Å-thick barrier device in forward bias. From the fit, we obtain $p_0 = 0.57$, $A = 0.56$ nA, and $\alpha = 0.42$ for this particular step.

Note that doing a Fermi fit only [Eq. (11)] to the data of Figure 33 would be very inaccurate. The ratio of the current at the threshold, the common intersection point of all the curves, and the current on the plateau is $I_{th}/I_{plateau} = 0.275$ nA/0.458 nA $= 0.6$. This is much larger than 0.5 as one would have expected if one had a perfect Fermi function behavior.

From the experimental values of A and p_0, one can determine the electron tunneling rates T_{em} and T_{cl}. $p_0 = T_{em}/(T_{em} + T_{cl})$ and $A = eT_{cl}$. Thus, for the first current step in forward bias of the 85-Å-thick barrier device (Fig. 32), $T_{cl} = 509$ MHz and $T_{em} = 274$ MHz. Similarly, for the first current step in forward bias of the 65-Å-thick barrier device (Fig. 33), $T_{cl} = 3.6$ GHz and $T_{em} = 4.7$ GHz. Similar measurements of the tunneling rates can also be obtained from the magnetic field studies. Those measurements, however, require really low temperatures (less than 300 mK) and high magnetic fields. The calculation described here requires relatively moderate temperatures (greater than 1 K) and, hence, is important.

4.6.2. Tunneling Rates in a Magnetic Field

For the remainder of this chapter, we confine ourselves to a discussion of the results of only one device (the device with the 85-Å barrier and data from the first current step only).

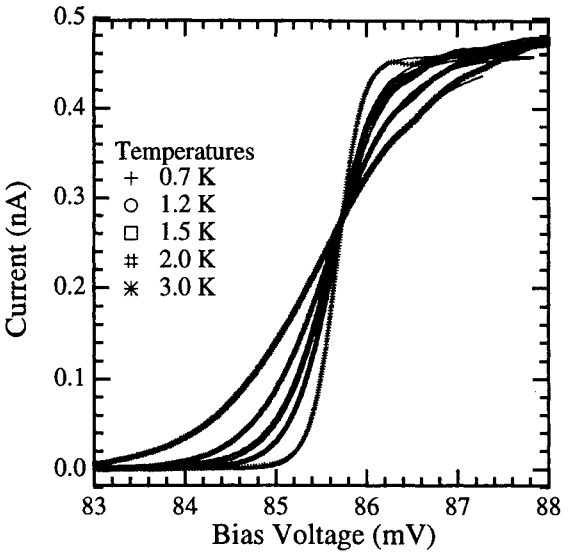


Fig. 33. $I(V)$ characteristics of the first current step edge in forward bias of the impurity system with 65-Å-thick barrier at different temperatures and the corrected fits [Eq. (19)] to these $I(V)$ traces. The fits are done over the entire bias range spanning the step.

The results of the other device (65-Å barrier) show similar trends. From the data shown in Figure 29 at 9 T (field perpendicular to current), we get $p = 0.21$ for forward bias and $p = 0.62$ for reverse bias. A high p value indicates that the electron tunneling rate through the collector (downstream) barrier (T_{cl}) is lower than that through the emitter (upstream) barrier (T_{em}), causing an accumulation in the well. A higher p value for reverse bias (as compared to forward bias) suggests an asymmetry in the heterostructure growth with one barrier being slightly thicker than the other barrier. In forward bias, the top barrier is the emitter barrier, while, in reverse bias, the top barrier is the collector barrier. This implies that the top barrier is slightly thicker than the bottom barrier. This is consistent with the difference in the measured α values, observed asymmetry in the $I(V)$ characteristics for this sample (the main resonance peak voltage and peak current values are higher for reverse bias as compared to forward bias), and is in agreement with previous characterization [32, 33].

We also obtain the absolute magnitude of the electron tunneling rates through the two potential barriers and study their dependence on the magnetic field. Figures 34 and 35 show the tunneling rates and the probability of occupation as a function of the magnetic field perpendicular to the current in the forward-bias and reverse-bias orientations, respectively. Note that T_{em} is smaller than T_{cl} in the forward-bias orientation, while T_{cl} is smaller than T_{em} in the reverse-bias orientation. This is because p is smaller than 0.5 in forward bias, while it is larger than 0.5 in reverse bias. As mentioned before, this asymmetry suggests that the top barrier of the heterostructure is slightly thicker than the bottom barrier.

Despite the asymmetry, we observe that, in either orientation, T_{em} (and p) decreases with field strength, while T_{cl} is approximately constant. T_{em} roughly decreases by a factor of 2 as the field increases from 6 to 11 T in both bias orientations. The probability of occupation p also decreases as the field strength increases. The oscillations in the tunneling rate are probably due to the fine structure observed on the current plateaus and its movement in magnetic field [38, 50]. The suppression of T_{em} results in the observed plateau current suppression with magnetic field.

Figures 34 and 35 and the previous discussion indicate that the magnetic field affects the emitter-to-well tunneling process (T_{em}) more than it affects the well-to-collector tunneling process (T_{cl}). We, therefore, expect more current suppression when the current is emitter

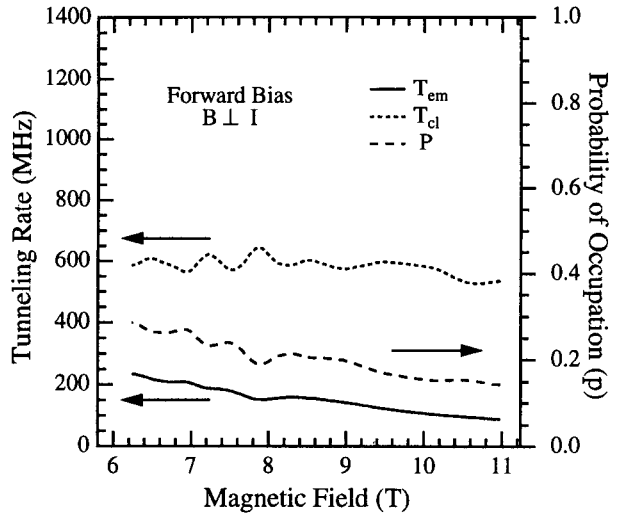


Fig. 34. Tunneling rates T_{em} and T_{cl} and the probability of occupation, p, as a function of the magnetic field strength perpendicular to current for the 85-Å-thick barrier device in forward-bias orientation.

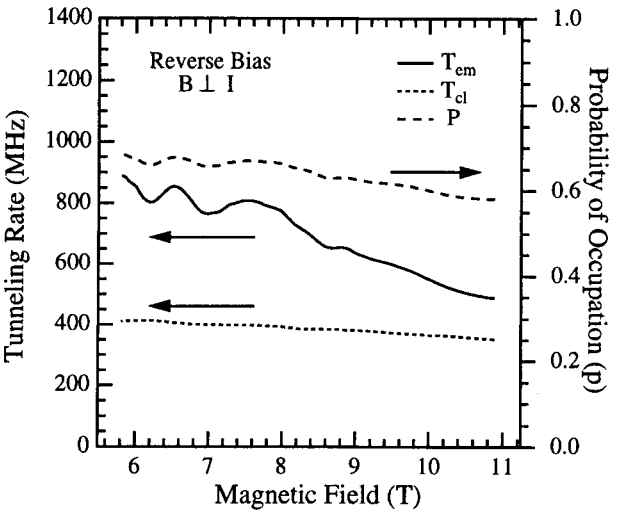


Fig. 35. Tunneling rates T_{em} and T_{cl} and the probability of occupation, p, as a function of the magnetic field strength perpendicular to current for the 85-Å-thick barrier device in reverse-bias orientation.

barrier limited than when it is collector barrier limited, which is observed (Fig. 29). For forward bias (thicker emitter), the current at 9 T is suppressed by a factor of 41% (as compared to 0 T), while the suppression is only 20% for reverse bias (thicker collector).

We can also study the effect on the tunneling rates of magnetic field parallel to current. Figures 36 and 37 show the tunneling rates and the probability of occupation, p, as a function of the magnetic field parallel to the current in forward bias. The oscillations observed in the tunneling rate and, hence, in p (Fig. 36) are due to the "fine structure" on the current plateaus and its movement in the magnetic field [38, 39, 50]. Nevertheless, it is possible to extrapolate the measured value of p to zero field and compare it with those obtained from the thermal broadening measurements.

For the data shown in this chapter for forward bias of the 85-Å-thick barrier device, we estimate the zero-field occupancy $p \sim 0.3$ from magnetic field studies. This is in good

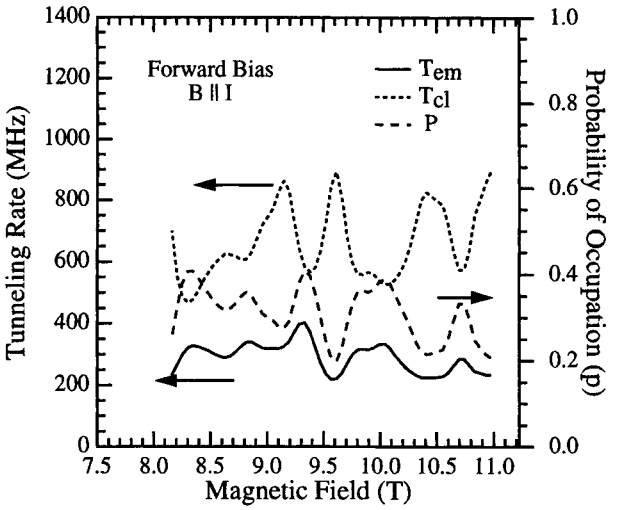


Fig. 36. Tunneling rates T_{em} and T_{cl} and the probability of occupation, p, as a function of the magnetic field strength parallel to current for the 85-Å-thick barrier device in forward-bias orientation.

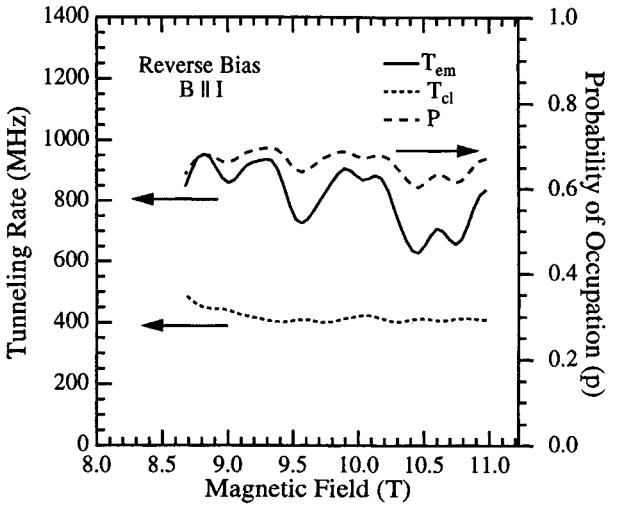


Fig. 37. Tunneling rates T_{em} and T_{cl} and the probability of occupation, p, as a function of the magnetic field strength parallel to current for the 85-Å-thick barrier device in reverse-bias orientation.

agreement with the measured value of $p = 0.35$ from the temperature studies. Similarly, in reverse bias, we get $p \sim 0.65$ from magnetic field measurements and $p = 0.57$ from temperature studies. A single parameter p, the occupancy of the impurity state, thus explains the non-Fermi thermal broadening and also the asymmetry in the magnetic field behavior. These two independent measurements thus give an added proof that the theory is correct.

5. CONCLUSIONS

In this chapter, we have presented both the basic theory and the experimental data for the electron spectroscopy as a function of magnetic field and temperature for two vertical quantum dot systems, the fabricated quantum dot and the impurity quantum dot. Current steps in the $I(V)$ characteristics are observed in both systems. In the fabricated quantum dot, these steps are due to the discrete nature of the 0D dot density of states. In the impurity system,

these steps are attributed to the discrete 0D states resulting from the Coulomb potential of a single or a pair of impurities in the quantum well region. In both systems, in magnetic fields parallel to the current, the step edges exhibit a diamagnetic shift as expected, while a suppression of the current plateaus is observed in magnetic fields perpendicular to the current, which is attributed to the decreasing overlap between emitter and dot wave functions. In the impurity system, we also investigate the Zeeman splitting of these current steps and determine the effective spin g^* factor of electrons in the quantum well region, which is observed to be asymmetric. An analysis of the tunneling current through the two-state spin system allows us to determine the tunneling rate across each of the two barriers of the device individually. In the case of the fabricated quantum dot, the inconsistencies in the step spacings, the diamagnetic shifts, and the lack of Zeeman splittings indicate that transport is proceeding through more than one channel in parallel (i.e., two dots or more). A model incorporating this type of transport is proposed and found to be consistent with the first few plateaus.

Using the highly localized dot states as spectroscopic probes, the electronic structure of the emitter electrode is measured through the oscillatory fine structure observed on top of the normal current plateaus of both systems. The fine structure is observed to be reproducible, both upon repeated traces and upon thermal cycling. Variable-temperature results indicate that this fine structure originates from below the Fermi level in the emitter. In both parallel and perpendicular magnetic field orientations, the fine structure peaks are observed to shift to lower bias, which is, again, consistent with emitter states. With increasing temperature, states *above* the Fermi level are populated. In the case of the fabricated dot, we observe a preresonant thermally activated peak as temperature increases, which is in excellent agreement with the emitter discrete-state model.

Acknowledgments

We would like to thank Professor R. G. Wheeler and Ellen S. Hornbeck for experimental assistance and many useful discussions; W. R. Frensley, C. L. Fernando, and R. C. Bowen for help with the modeling of the devices; and J. N. Randall and R. J. Matyi for growth and fabrication. This work was supported by NSF DMR-9112497 and 9216121 and the Office of Naval Research.

References

1. M. Tewordt, L. Martin-Moreno, M. Pepper, J. E. F. Frost, V. J. Law, M. J. Kelly, R. Newbury, D. A. Ritchie, and G. A. C. Jones, *Phys. Rev. B* 46, 3948 (1992).
2. B. Su, V. Goldman, and J. Cunningham, *Phys. Rev. B* 46, 7644 (1992).
3. M. Reed, J. N. Randall, R. J. Aggarwal, R. J. Matyi, T. M. Moore, and A. E. Wetsel, *Phys. Rev. Lett.* 60, 535 (1988); M. Reed, J. N. Randall, J. H. Luscombe, W. R. Frensley, R. J. Aggarwal, R. J. Matyi, T. M. Moore, and A. E. Wetsel, *Festköperprobleme* 29, 267 (1989).
4. M. Dellow, P. H. Beton, M. Henini, P. C. Main, and L. Eaves, *Electron. Lett.* 27, 134 (1991).
5. S. Tarucha, Y. Hirayama, T. Saku, and T. Kimura, *Phys. Rev. B* 41, 5459 (1990); S. Tarucha and Y. Hirayama, *Phys. Rev. B* 43, 9373 (1991).
6. J. W. Sleight, E. S. Hornbeck, M. R. Deshpande, R. G. Wheeler, M. A. Reed, R. C. Bowen, W. R. Frensley, J. N. Randall, and R. J. Matyi, *Phys. Rev. B* 53, 15727 (1996).
7. U. Meirav, M. Kastner, and S. Wind, *Phys. Rev. Lett.* 65, 771 (1990).
8. P. McEuen, E. B. Foxman, U. Meirav, M. A. Kastner, Y. Meir, and N. S. Wingreen, *Phys. Rev. Lett.* 66, 1926 (1991).
9. L. P. Kouwenhoven, N. C. van der Vaart, A. T. Johnson, W. Kool, C. J. P. M. Harmans, J. G. Williamson, A. A. M. Staring, *Z. Phys. B* 85, 367 (1991); L. P. Kouwenhoven, A. T. Johnson, N. C. van der Vaart, A. van der Enden, C. J. P. M. Harmans, and C. T. Foxon, *Z. Phys. B* 85, 381 (1991).
10. A. Ramdane, G. Faini, and H. Launois, *Z. Phys. B* 85, 389 (1991).
11. J. H. Luscombe, *Nanotechnology* 4, 1 (1993).
12. H. Liu and G. Ayers, *J. Appl. Phys.* 65, 4908 (1989).
13. G. Bryant, *Phys. Rev. B* 39, 3145 (1989).
14. H. van Houten and C. Beenakker, *Phys. Rev. B* 63, 1893 (1989).

15. D. Averin, A. Korotkov, and K. Likharev, *Phys. Rev. B.* 44, 6199 (1991).
16. Y. Meir, N. Wingreen, and P. Lee, *Phys. Rev. Lett.* 66, 3048 (1991).
17. A. Groshev, T. Ivanov, and V. Valtchinov, *Phys. Rev. Lett.* 66, 1082 (1991).
18. L. Chen and C. Ting, *Phys. Rev. B* 44, 5916 (1991).
19. N. Johnson and M. Payne, *Phys. Rev. Lett.* 67, 9 (1991).
20. M. W. Dellow, P. H. Beton, C. J. G. M. Langerak, T. J. Foster, P. C. Main, L. Eaves, M. Henini, S. P. Beaumont, and C. D. W. Wilkinson, *Phys. Rev. Lett.* 68, 1754 (1992).
21. M. R. Deshpande, N. H. Dekker, J. W. Sleight, J. L. Huber, E. S. Hornbeck, M. A. Reed, R. J. Matyi, Y. C. Kao, C. J. L. Fernando, and W. R. Frensley, in "Proceedings of the IEEE/Cornell Conference on Advanced Concepts in High Speed Semiconductor Devices and Circuits," 1993, p. 177.
22. J. W. Sakai, P. C. Main, P. H. Beton, N. LaScala Jr., A. K. Geim, L. Eaves, and M. Henini, *Appl. Phys. Lett.* 64, 2563 (1994).
23. M. R. Deshpande, E. S. Hornbeck, P. Kozodoy, N. H. Dekker, J. W. Sleight, M. A. Reed, C. L. Fernando, and W. R. Frensley, *Semicond. Sci. Technol.* 9, 1919 (1994).
24. M. Tewordt, R. J. F. Hughes, L. Martin-Moreno, J. T. Nicholls, H. Asghi, M. J. Kelly, V. J. Law, D. A. Ritchie, J. E. F. Frost, M. Pepper, and G. A. C. Jones, *Phys. Rev. B* 49, 8071 (1994).
25. G. M. G. Oliveira, V. M. S. Gomes, A. S. Chaves, and J. R. Leite, *Phys. Rev. B* 35, 2896 (1987).
26. V. Goldman, D. Tsui, and J. Cunningham, *Phys. Rev. B* 35, 9387 (1987).
27. M. Tewordt, V. J. Law, R. T. Syme, M. J. Kelly, R. Newbury, M. Pepper, J. E. F. Frost, D. A. Ritchie, and G. A. C. Jones, in "Proceedings of the 20th International Conference on the Physics of Semiconductors," (J. Joannopoulos, Ed.), p. 2455. World Scientific, Singapore, 1991.
28. G. Bastard, "Wave Mechanics Applied to Semiconductor Heterostructures." Halsted Press, New York, 1988.
29. W. Kohn, in "Solid State Physics" (F. Seitz and D. Turnbull, Eds.), Vol. 5, p. 258. Academic Press, New York, 1957.
30. G. Bastard, *Phys. Rev. B* 24, 4714 (1981).
31. C. Priester, G. Bastard, G. Allan, and M. Lannoo, *Phys. Rev. B* 30, 6029 (1984).
32. M. A. Reed, W. R. Frensley, R. J. Matyi, J. N. Randall, and A. C. Seabaugh, *Appl. Phys. Lett.* 54, 1256 (1989).
33. M. A. Reed, W. R. Frensley, W. M. Duncan, R. J. Matyi, A. C. Seabaugh, and H.-L. Tsai, in "Proceedings of the International Symposium on GaAs and Related Compounds," Atlanta, GA, 1988, p. 587.
34. A. K. Geim, P. C. Main, N. LaScala Jr., L. Eaves, T. J. Foster, P. H. Beton, J. W. Sakai, and F. W. Sheard, *Phys. Rev. Lett.* 72, 2061 (1994).
35. M. R. Deshpande, J. W. Sleight, M. A. Reed, R. G. Wheeler, and R. J. Matyi, *Phys. Rev. Lett.* 76, 1328 (1996).
36. V. Fock, *Z. Phys.* 47, 446 (1928); C. Silorski and U. Merkt, *Phys. Rev. Lett.* 62, 2164 (1989); W. Hansen, T. P. Smith III, K. Y. Lee, J. A. Brum, C. M. Knoedler, J. M. Hong, and D. P. Kern, *Phys. Rev. Lett.* 62, 2168 (1989).
37. T. Schmidt, M. Tewordt, R. H. Blick, R. J. Haug, D. Pfannkuche, and K. von Klitzing, *Phys. Rev. B* 51, 5570 (1995).
38. T. Schmidt, R. J. Haug, V. I. Fal'ko, K. von Klitzing, A. Forster, and H. Luth, *Europhys. Lett.* 36, 61 (1996).
39. T. Schmidt, R. J. Haug, V. I. Fal'ko, K. von Klitzing, A. Forster, and H. Luth, *Phys. Rev. Lett.* 78, 1540 (1997).
40. V. Goldman, B. Su, and J. Cunningham, in "Nanostructures and Mesoscopic Systems," pp. 173–182. Academic Press, San Diego, 1992.
41. M. Tewordt, V. J. Law, T. J. Nicholls, L. Martin-Moreno, D. A. Ritchie, M. J. Kelly, M. Pepper, J. E. F. Frost, R. Newbury, and G. A. C. Jones, *Solid-State Electron.* 37, 793 (1994).
42. G. Bryant, *Phys. Rev. B* 44, 12837 (1991); A. Szafer and A. D. Stone, *Phys. Rev. Lett.* 62, 300 (1989).
43. A. D. Stone, in "Physics and Technology of Submicron Structures," p. 108. Springer-Verlag, Berlin, 1988.
44. R. A. Jalabert, H. Baranger, and A. D. Stone, *Phys. Rev. Lett.* 65, 2442 (1990); T. M. Fromhold, M. L. Leadbeater, L. Eaves, T. J. Foster, P. C. Main, and F. W. Sheard, *Surf. Sci.* 305, 511 (1994); T. Fromhold, L. Eaves, F. W. Sheard, M. L. Leadbeater, T. J. Foster, and P. C. Main, *Phys. Rev. Lett.* 72, 2608 (1994).
45. E. L. Ivchenko and A. A. Kiselev, *Sov. Phys. Semicond.* 26, 827 (1992).
46. M. J. Snelling, G. P. Flinn, A. S. Plaut, R. T. Harley, A. C. Tropper, R. Eccleston, and C. C. Phillips, *Phys. Rev. B* 44, 11345 (1991).
47. M. Dobers, K. von Klitzing, and G. Weimann, *Phys. Rev. B* 38, 5453 (1988).
48. R. M. Hannak, M. Oestreich, A. P. Heberle, W. W. Rühle, and K. Köhler, *Solid State Commun.* 93, 313 (1995).
49. J. W. Sakai, T. M. Fromhold, P. H. Beton, L. Eaves, M. Henini, P. C. Main, and F. W. Sheard, *Phys. Rev. B* 48, 5664 (1993).
50. M. R. Deshpande, J. L. Huber, N. H. Dekker, P. Kozodoy, J. W. Sleight, M. A. Reed, C. L. Fernando, W. R. Frensley, R. J. Matyi, and Y. C. Kao, in "Proceedings of the 2nd International Conference on the Physics of Semiconductors" (D. J. Lockwood, Ed.), p. 1899. World Scientific, Singapore, 1995.

Chapter 3

ELECTRICAL PROPERTIES OF CHEMICALLY TAILORED NANOPARTICLES AND THEIR APPLICATION IN MICROELECTRONICS

U. Simon, G. Schön

Institute of Inorganic Chemistry, University of Essen, 45127 Essen, Germany

Contents

1. Introduction 131
   1.1. Physical Background 132
2. Preparation Techniques and Classification of Chemically Tailored Nanoparticles 139
   2.1. Ligand-Stabilized Nanoparticles 139
   2.2. Nanoparticles in Block Copolymers 141
   2.3. Host/Guest Composites 142
   2.4. Electrochemical Composition of Nanoparticles 143
3. Arrangements and Deposition Techniques 143
   3.1. Three-Dimensional Arrangements 144
   3.2. Two-Dimensional Arrangements 145
   3.3. One-Dimensional Arrangements 149
4. Electrical Properties of Zero- to Three-Dimensional Arrangements of Nanoparticles 154
   4.1. Single-Particle Properties 154
   4.2. One-Dimensional Arrangements 158
   4.3. Two-Dimensional Arrangements 159
   4.4. Three-Dimensional Arrangements 162
5. Working Principles of Single-Electron Tunneling Devices and the Use of Chemically Built Nanoparticles 165
   5.1. Single-Electron Tunneling Devices and Circuits 165
   5.2. Metal Nanoparticles as Elements for Single-Electron Devices 169
   5.3. Time Scales of Recharging, Charge Relaxation, and Tunneling 172
6. Applications and Concluding Remarks 174
   Acknowledgments 175
   References 175

1. INTRODUCTION

Modern microelectronics strongly tends to miniaturization of the circuit elements and to a larger degree of integration. Because of shorter distances between the elements on the chip, it leads to an increase in the performance speed and, therefore, to smaller delay times in the information exchange. The availability of nanolithographic fabrication techniques realizes

Handbook of Nanostructured Materials and Nanotechnology, edited by H.S. Nalwa
Volume 3: Electrical Properties
Copyright © 2000 by Academic Press
All rights of reproduction in any form reserved.
ISBN 0-12-513763-X/$30.00

scaling down to 0.1 μm, which has already had a great impact on the performance of traditional semiconductor circuits as well as opened up new possibilities based on quantum effects. However, the same has also become true of the so-called "metallic" electronics. At present, because of exploitation of charging effects, or so-called Coulomb effects, in metallic circuits comprising tunnel junctions with submicrometer sizes individual charge carriers can be manipulated. In metals, these carriers are electrons and, in the case of superconducting materials at low temperature, they can be Cooper pairs of electrons. This field is referred to as single electronics (SE) [1].

Although charging effects were observed earlier in granular thin metal films [2, 3], SE as a field in its own right was born more than one decade ago, when ultrasmall metal–insulator–metal sandwich structures (tunnel junctions) and simple systems of those were begun to be intensively studied both theoretically and experimentally [4]. It was demonstrated that under certain conditions the discreteness of the electric charge becomes essential and a quantum mechanical tunneling of electrons in the systems of such junctions can be affected by the Coulomb interaction of electrons, which can be varied by an externally applied voltage or by injected charges. Since that time, a profound understanding of this phenomenon, the so-called single-electron tunneling (SET), was developed; however, during that time interest in this field was not only a pure academic one. For example, very early a circuit was realized that can operate as an electrometer, capable of sensing a charge that is a small part of the elementary charge [5]. Later, another device was fabricated that can pass a well-defined number of electrons per second when alternating gate voltage drives it, that is, a so-called single-electron turnstile [6]. Although a lot of work has to be done in order to improve their operation, even these functions create great possibilities for precise electric measurements and for realizing the quantum standard of electric current [1]. Besides, there are attracting ideas on how to exploit the principles of SE for the development of logic and memory cells, which, in perspective, could lead to assembling a computer working "on single electrons," realizing a so-called "single-electron logic" (SEL). A comprehensive collection of leading reports on SET and related subjects was edited by Devoret and Grabert in 1992 [1].

The aim of the present review is, on the one hand, to acquaint the reader with the physical principles of SET and with basic SE structures where charging effects occur in the intended way. On the other hand, it will be shown that, in further development of the ideas of SE, ligand-stabilized nanoparticles of noble metals have been recognized to be suitable building blocks for single-electron devices [7, 8]. These nanoparticles consist of a metal core with a defined size that is surrounded by a dielectric ligand shell that acts as an insulating barrier (see Fig. 1).

Because the progress of lithographic methods guided by the miniaturization of conventional electronic circuits fails at present to satisfy the requirements arising from SE even at elevated temperatures, a requirement that extends the size range of a few nanometers or less [9, 10], chemically prepared nanoparticles can replace the islands of conventional tunnel junctions in SET arrangements.

1.1. Physical Background

1.1.1. Quantum Size Effect

The availability of small solids like transition metal clusters [11] offers a field of research that raises basic questions: How small a number of atoms is necessary until the properties of the original metal are lost? How does an ordered accumulation of atoms behave, when it is no longer under the influence of its ambient bulk matter? And perhaps most important for "nanoscientists": What are the future directions for nanotechniques and the applications of the new materials, for example, in microelectronic devices?

An increasing number of scientific groups is engaged in achieving the latter goal. However, until recently—besides more exotic applications such as reflecting surfaces—

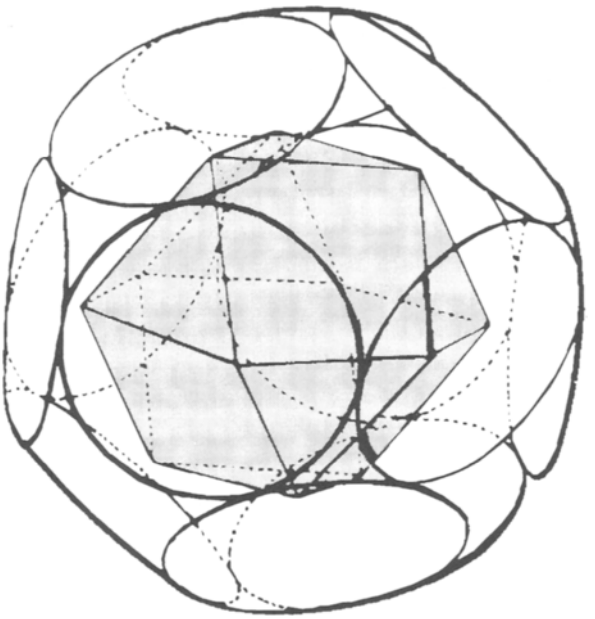


Fig. 1. Scheme of a nanoparticle $Au_{55}(PPh_3)_{12}Cl_2$ surrounded by a ligand shell. The metal core, which is typically a regular polyhedron, has a diameter of 1.4 nm and is dressed by umbrella-shaped ligands like PPh_3 to give a total diameter of 2.1 nm. (Source: Reprinted with permission from [7].)

chemists have been mainly interested in their potential in heterogeneous catalysis. This field of application for metal colloids and stable metal nanoparticles will not be treated in this chapter. However, we would like to point out that for this use, in the range between metal and molecule, size and shape play a more important role than the problem of uniform size distribution.

If a metal particle, initially having bulk properties, is reduced in size to a few hundred or dozen of atoms, the density of states in the valence and conductivity bands decreases to such an extent (Fig. 2a–c) that the electronic properties change dramatically; that is, conductivity, magnetism, and so on begin to disappear. The quasicontinuous density of states is replaced by a discrete energy level structure, with a level spacing, for example, larger than the characteristic thermal energy k_BT (Fig. 2b). The situation in molecular clusters is simple. Three metal atoms, for instance, form energetically well-defined bonding and antibonding molecular orbitals (Fig. 2c). With respect to the size-dependent decreasing electrical conductivity, in 1986 Nimtz et al. [12–14] spoke of the so-called size-induced metal–insulator transition (SIMIT). This refers to the transition caused by a geometrical limitation of extended states with a corresponding De Broglie wavelength when the volume of metallic particles is strongly reduced by fractionation, beginning with a diameter of 1 μm, down to an experimental limit of less than 20 nm. This effect was detected by measuring the microwave absorption of small particles of solid or liquid indium metal dispersed in oil. Its explanation claims that the boundaries of these particles are potential walls between which the electrons are localized, and that the conduction electrons form standing waves with multiples of half of the De Broglie wavelength $\lambda/2$, thus leading to the picture of "particles in a box." But the corresponding level spacings of these electron states in the preceding size regime are still smaller than k_BT, so that the temperature dependence of the conductivity of these particles is very weak. This means that the particles are still metallic, but with a size-determined limited number of electrons. The first attempts to take advantage of this effect was the design of so-called cutoff wavelength (COW) transistors [14].

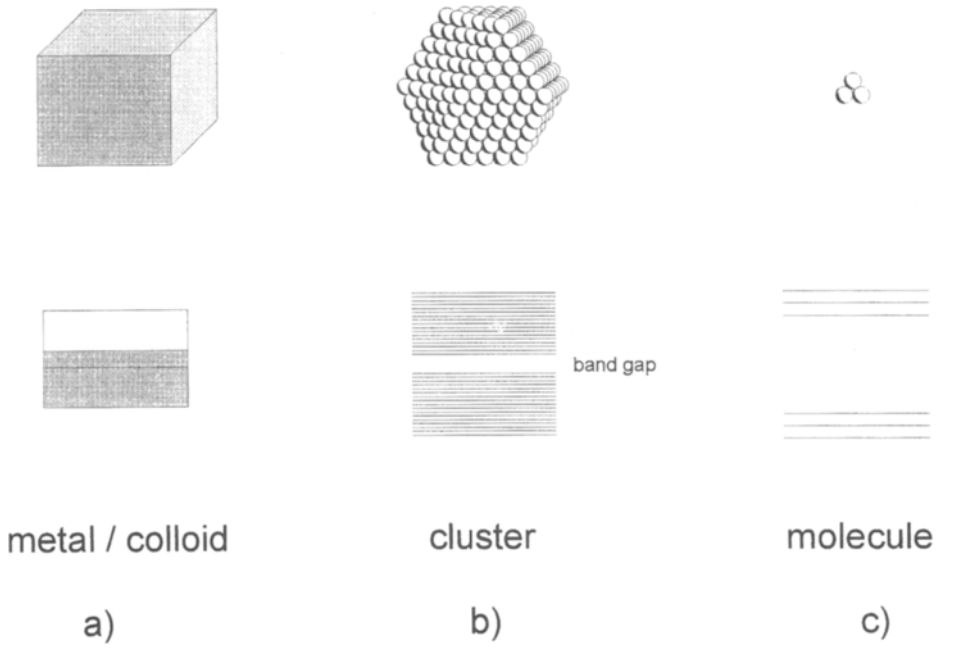


Fig. 2. Illustration of (a) a bulk metal or colloid with typical band structure, (b) a large metal cluster, and (c) a triatomic cluster with bonding and antibonding orbitals. (Source: Reprinted with permission from [7].)

This "size quantization" effect may be the onset of the metal–semiconductor transition at the very end of metallic behavior of much smaller particles. The size at which the transition occurs depends on the type of metal and the criterion chosen for metallicity as well as the method of investigation. Keeping this in mind, the term SIMIT should not be fixed to the change in the electrical conductivity, but generalized by means of additional indicators. Indeed, the results of a number of recent physical investigations on ligand-stabilized transition metal clusters, which are metal nanoparticles consisting of a defined number of atoms surrounded by a dielectric ligand shell, lead to the conclusion that, coming from the molecular state, metal particles with about 50–100 metal atoms and a diameter between 1 and 2 nm are just barely showing metallic behavior [15].

Why are these metallic nanoparticles expected to reveal new electronic properties as soon as the boundary conditions given by their dimensions (e.g., diameter) reach the order of magnitude of the De Broglie wavelength of the "valency" electrons? The answer is given by quantum mechanics with Heisenberg's uncertainty relation. The position and momentum of an electron cannot be determined with the same accuracy. The more one electron is spatially confined, the broader its range of momentum. Hence, its average energy will no longer be determined by its chemical origin but only by the dimension. Electrons localized as "particles in a box" within zero-dimensional quantum dots lose their freedom in all three dimensions, leading to discrete energy states, as long as their energy is not great enough to break out of this confinement. Whenever it is in the magnitude of the electron wavelength $\lambda/2$ or even smaller, quantum effects govern the wave propagation of the system. This effect is called the quantum size effect QSE). So, by nature, metal clusters of the preceding diameter seem to be chemically size tailored quantum dots in which some few electrons can be localized, both in terms of geometry and quantum mechanics.

To distinguish the common features of the previously described metallic quantum dots and to separate them from semiconductor materials, one should note the following: Principally, semiconductors in the macroscopic bulk state, already have a band gap. The size-dependent change in nanoparticles by the QSE can be observed simply and precisely

by optical absorption spectroscopy [16]. On the other hand, a dot made from a metallic nanoparticle has many more conductance electrons than a dot made from a semiconductor material of the same size and yet has no band gap. For this, the dot should actually be much smaller. For instance, the wavelengths of metallic electrons can reach up to 0.5 nm (in comparison, the wavelengths of semiconductors, because of the effective mass, can be as long as 1 μm). In contrast, based on the Fermi energy of bulk gold, the wavelength of the valency electrons at the Fermi level for a Au_{55} cluster, as shown in Figure 1, with $\lambda/2$ would be approximately 0.1 nm. This wavelength is too small to be affected in a particle of 1.4 nm diameter. So far, the influence of size quantization with metal clusters seems to be much less than with semiconductor nanoparticles and possibly undetectable because the metal dot would have to be reduced to such a small size that it would be only a small molecular object. On the other hand, according to SIMIT, the metal dot will turn out to be a "semiconductor." Consequently, it seems appropriate to postulate the existence of formerly metallic "valency" electrons with an effective mass. Assuming an effective mass of 10%, the previously cited boundary condition could be reached. Within dots of the same small size built of semiconductor materials, this "size effect" would have already taken place, converting them to insulators.

The latter more speculative considerations are less important, because now the small metal clusters can, for certain, be called "quantum dots," as they are mesoscopic confinements characterized by a set of discrete energy levels according to the predictions for a possible level splitting in gold nanoparticles consisting of 55 gold atoms [$Au_{55}(PPh_3)_{12}Cl_6$] [11, 15, 17, 18]. The not yet finally evaluated scanning tunnel spectra (STS) of these Au_{55} clusters, which was examined at room temperature [19], reveal fine structures with oscillation intervals of about 100 mV. Furthermore, it was recently found at 4.2 K with the same method that even the larger $Pt_{309}phen_{36}O_{20}$ metal cluster (2.2 nm) reveals a level splitting of 25–50 meV by an additional structure in the Coulomb staircase [20]. This spacing is more pronounced than expected based on the predictions of Halperin [21]. However, because the outer shell of the five-shell Pt cluster is not typically metallic (as in any ligand-stabilized metal nanoparticle, the electrons of the outer shell bond more strongly), only the diameter of the inner metallic core ($\sim$1.6 nm) consisting of only 147 Pt atoms should be taken into consideration [7]. Furthermore, the high symmetry of the cluster might cause some degeneration, leading to a larger level splitting [22].

1.1.2. Physical Principles of Single-Electron Tunneling

The transfer of electric charges, or, in other words, electric current, in a metal conductor is associated with the motion of a huge amount of free electrons over the whole volume. Because of electron–electron interaction and the interaction of electrons with the crystal lattice, the effective charge that passes a cross section of the wire per second is a result of the displacement of charges in the respective conductor. As a result, in spite of the discrete nature of the charge constituents, the current flow in a metal is averaged over a huge amount of charge carriers and because of this is continuous. On the contrary, if one deals with an isolated nanoscaled piece of metal, the number of electrons is always integer. The number of electrons can be changed, for example, by means of direct connection and then disconnection of that nanoparticle to another charged object or a lead with an applied voltage and the resulting change of the number of electrons, which is on the macroscopic scale large and uncontrollable, obviously is also integer. Therefore, the question arises whether it is possible to transfer electrons in a circuit that is built up by nanoscaled metallic objects strictly one by one in a controlled way.

Physically, such a transfer of electrons can be realized by means of quantum mechanical tunneling (see Fig. 3) as the probability of such a tunneling event depends on the driving voltage and current applied to the circuit as well as on the distribution of excess electrons over the constituting sites. Therefore, an SET circuit should present a number of reservoirs

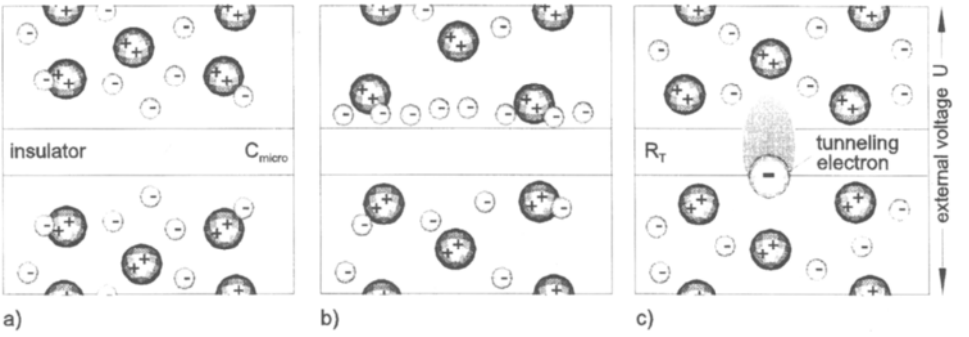


Fig. 3. Tunneling of a single electron between two metal electrodes through a small insulating barrier. (a) At the beginning, the junction is uncharged, then (b) by external voltage U the charge carriers are gathering at the tunnel junction, and (c) finally, one single charge "drips" through the insulating layer. (Source: Reprinted with permission from [7].)

for free electrons, which should be small well-conducting islands separated by poorly permeable tunneling barriers. The size of these so-called mesoscopic islands is much larger than the atomic scale and, hence, they certainly comprise a huge amount of free charge carriers. However, handling of individual charges is possible if the characteristic electric capacitance of the islands C is small enough. It works in such a way that the presence of only one excess electron changes the electric potential of the island considerably, that is, $\Delta V = e/C$. Then the control of single tunneling events could be realized in the following scenario: The enhanced voltage V could prevent further charging of the island, reducing essentially the probability of corresponding tunneling since it increases the energy of the whole system. If the potential of the neighbor islands and/or gates is changed, the probability of tunneling could be restored and then the tunneling of strictly one electron occurs. Thus, one can say that SE deals with a small amount of excess electrons on islands changing their distribution over the islands in time in a desirable way. To realize this, the following two principal conditions must be fulfilled.

First, the insulating barriers separating the conducting islands from each other should be rather opaque. The barrier properties determine the transport of electrons, which are microparticles that obey the rules of quantum mechanics and, therefore, are described by wave functions. The coordinate dependence of a wave function depends on the energy profile of the barrier. If the energy barrier separating the islands is high and thick enough (e.g., 1 eV and 2 nm, respectively), it provides an essential decay of the electron wave function outside the island and, as a result, only a weak overlapping of the wave functions of the neighbor islands occurs within the interisland space. If, besides this, the number of electronic states contributing to tunneling is small enough, then the total exchange of electrons between the islands becomes negligibly small. This situation is often referred to in the case of small quantum fluctuations of charge. In spite of relatively complex rigorous quantum mechanical considerations, quantitatively this condition can be clearly formulated using the tunneling resistance R_T as a characteristic of the tunneling junction. It should be much higher than the characteristic resistance expressed via fundamental constants, the so-called resistance quantum, $R_q = h/e^2 = 25.8\ \mathrm{k}\Omega$. Then the electrons in the island can be considered to be localized and their number already behaves classically, although they undergo thermodynamic fluctuations as does every statistical variable.

Second, to ensure that these thermal fluctuations are small enough and, consequently, to make the exchange of electrons controllable, the Coulomb energy associated with charging by one extra electron should be essential with respect to the characteristic thermal energy $k_B T$. The Coulomb, or electrostatic, energy E_C of a charged conductor depends on its charge Q, on its size, and on the charge of eventually surrounding conductors (capacitances of junctions, gates, etc.). As long as the size of an island exceeds the electric

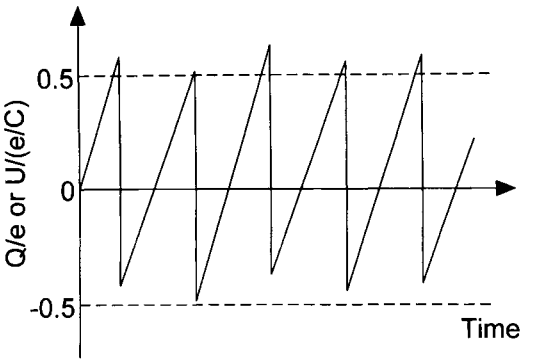


Fig. 4. A constant current I leads to oscillation of charge and voltage on a junction, whereas the oscillation frequency ν_{SET} is determined by $I = \nu_{SET} e$.

screening length (which is a few tenths of a nanometer), the geometrical dependence of the charging energy is simply incorporated into the parameter C, that is, the total island capacitance, and the energy takes the simple form $E_C = Q^2/2C$. Then the condition of prevailing Coulomb energy over the thermal one is quantitatively expressed by $E_C = e^2/2C \gg k_B T$.

To satisfy the aforementioned condition for a system with characteristic capacitances of 10^{-15}–10^{-16} F, which are typical values for present-day lithographically made metallic circuits, one has to cool down the sample to a few tens of millikelvins. Because this, of the present-day SE, although it is characterized even by sub-100-nm patterning, still deals with very low temperatures.

When the previously mentioned conditions are satisfied, the system is characterized by a set of configurations with various distributions of a small integer number of excess charges over the islands. These configurations, or states, of the system can be switched by means of tunneling of individual electrons and the characteristic time scale of single-electron transitions in lithographically fabricated arrays, which depend on the temperature and the resulting changes of the energy in time of the whole system; that is, the so-called recharging time ranges from about 10^{-11} s for typical values of $R_T = 100$ kΩ and $C = 10^{-16}$ F up to several hours with extremely large R_T owing to the relation $\tau = R_T \cdot C$. Furthermore, there exists a fundamental relationship for correlated tunneling through an SET array:

$$\nu_{SET} = \frac{I}{e}$$

This means that, with a constant current I, charge and voltage are oscillating with the so-called SET frequency ν_{SET}; that is, the driving current source acts as an external "clock" (see Fig. 4).

Thus, as soon as the changes in energy can be calculated for any charge configuration, the transitions of individual electrons at low temperature can be well predicted. This gives rise to the manipulation of charges in the circuit on the single-electron level and, therefore, to the utilization this for the creation of, for example, sensitive amplifiers and electrometers, switches, current standards, transistors, ultrafast oscillators, or, generally, digital electronic circuits with single electrons [1].*

* The idea of SET and its simple principles were somewhat surprising for our progressive era in which immense research expenditures are customary. Besides, dealing with single electrons was not completely new, but had only sunk into oblivion. In 1909, Millikan succeeded in finding the elementary charge e of a single electron with his famous oil-droplet experiment [23]. Furthermore, people have made use of the tunnel effect since the invention of electrical switches in which on the nanometer scale, the metal contacts never actually touch; that is, electrons must bridge the last nanometer by tunneling. As for the QSE and the pieces of matter that today are called quantum dots, in 1938, Fuchs pointed out that electrons, if enclosed in small structures of some few nanometers, should show extraordinary quantum mechanical properties [24].

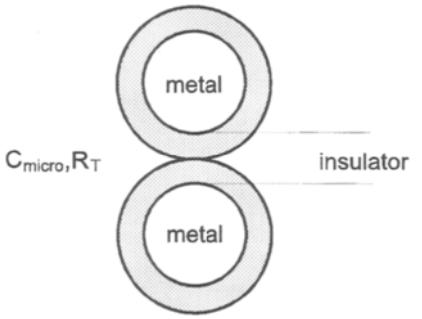


Fig. 5. Tunnel junction consisting of two ligand-stabilized nanoparticles in direct contact. (Source: Reprinted with permission from [7].)

1.1.3. Single-Electron Tunneling in Nanoparticles

The fact that lithographically fabricated tunnel junctions with a typical size of e.g. 100 nm × 100 nm have to be cooled down to the millikelvin range turns out to be a toilsome work. The utilization of the SET events for applications up to the range of room temperature leads to the necessary condition of decreasing the junction capacitance by at least two orders of magnitude. As we already predicted, this can be realized by the use of chemically tailored ligand-stabilized metal nanoparticles in a size range of a few nanometers [7, 8]. Among these, the most promising candidates are the ligand-stabilized metal clusters for two reasons [11]. On the one hand, they contain a selected "magic" number of metal atoms, 13, 55, 147, 309, 561, ..., and perfect polyhedral shapes with a high degree of symmetry. On the other hand, these clusters are stabilized by organic molecules, the ligands, that surround the metal cores and play the role of a separating layer in contacts with neighboring clusters as well as with conducting objects (see Fig. 5).

Obviously, the sizes of the cluster cores depend on the material and the number of atoms contained therein. For example, the diameter (we call it diameter because its shape is close to spherical) of the core for the cluster $Au_{55}(PPh_3)_{12}Cl_6$ is about 1.4 nm and for the cluster $Pd_{561}phen_{30}O_{200}$ it is about 2.5 nm, which is merely one order larger than the sizes of the constituent atoms. Therefore, the space volume for electrons is restricted and the number of electrons is already countable, which makes the physics of such systems more complicated requiring a slight modification of the two principal conditions for "classical" SET.

First, the standard (macroscopic) electrostatic approach, when a conductor is treated as a continuous body with infinitely thin screening depth, already fails, as the latter almost reaches the size of the object. Moreover, the number of conductance electrons in the object becomes small. As a result, the electron–electron interaction is not completely screened out, so that the concept of electric capacitances does not strictly work anymore. In this case, the calculation of the charging energy should be done by counting directly the energy of the interacting charges. However, the Coulomb energy can be still described roughly with the same elementary formula for the charging energy of a capacitor. Then the symbol C already denotes an amount that generally depends on the total number of interacting electrons occupying the cluster.

The second point is that the small size of a cluster changes its energy spectrum essentially because of the aforementioned quantum size effect. In contrast to a bulk piece of metal having a quasicontinuous electron energy spectrum (this was assumed when we discussed charging effects in larger structures), a metal cluster presents for electrons a small potential energy well, which in accordance with quantum mechanical laws, has a set of distinctly discrete energy levels. Their density and distribution depend on the size and shape of the cluster and, consequently, the tunnel junctions, where one of its elec-

trodes is a small cluster can hardly be described by such a simple parameter as constant tunneling resistance R_T (such an approximation is valid when the densities of the levels in both electrodes are high and independent of the energy). For the case of the clusters under consideration, the average level splitting is already well noticeable on the scale of Coulomb energy. The already mentioned measurements on the Pt_{309} cluster exhibit 25–50 meV for the level splitting and 50 meV or more for the characteristic charging energy (see Section 4.1.2).

The previously discussed two peculiarities of metal nanoparticles do not, however, eliminate charging effects. Theory and experiment show that the basic results of single-electron tunneling still qualitatively remain and take on new features. For example, the current–voltage characteristic of a double-barrier junction with a quantum dot possesses at low temperature, in addition to the Coulomb staircase, the fine structure resulting from energy quantization inside the dot. Futhermore, the description of the effect will be complicated when the characteristic time R_TC becomes as short as the characteristic time of the energy relaxation inside the dot (see [25]) and, consequently, the distribution of electrons is no longer a pure Fermi one. However, the single-electron charging effect and quantum size effect do not contradict each other, and can coexist. Thus, the tunneling characteristics of single clusters provide information on their electron energy spectrum, particularly the density of levels, their degeneracy, and so on. We will discuss this further in Section 4.

2. PREPARATION TECHNIQUES AND CLASSIFICATION OF CHEMICALLY TAILORED NANOPARTICLES

In the following, a brief overview will be given about the different types and preparation techniques of stabilized metal and semiconductor nanoparticles. In addition, several methods are known for the synthesis of naked or bare metal clusters, that is, molecular beam techniques [26] or matrix techniques [27]. Although the bare, nonprotected clusters (so-called physical sub-10-nm nanostructures) are also excellent objects for studying the evolution of metallicity, the main difficulty is their very short life time and their high reactivity. Furthermore, most cluster samples prepared by these techniques reveal a more or less broad size distribution, a problem that has not been solved. Because there exists a comprehensive literature [27] detailing the techniques, possibilities, and frontiers in the field of bare clusters, they will be excluded from consideration here. Instead, the focus here will be on so-called chemical sub-10-nm nanostructures such as stabilized nanoparticles. Because the problem of size distribution has partially been solved with the latter, ligand-stabilized nanoparticles especially are for the first time ideal objects for studying the properties of uniform particles and they are shown to be suitable building blocks for microelectronic devices, as we will see later.

2.1. Ligand-Stabilized Nanoparticles

The preparation of ligand-stabilized nanoparticles is based on the classical routes of colloid or organometallic chemistry. These are suitable for various metals, usually transition metals, and for many semiconductors that have technological applications in the bulk state [11, 16]. In addition to [28–30] and photochemical [31] techniques, the typical methods of preparation are (i) in the case of metals the reduction of soluble metal salts or complexes by suitable reductive agents, such as hydrogen, borhydride, methanol, citric acid, and so on and (ii) in the case of semiconductors the reaction of metal ions or complexes with group V–VII anions. To control the particle size, typical colloid chemical stabilizers or electron donor ligands, such as phosphine or thiol, are added to saturate the free valences on the surface of the particle and to give an electrostatic or steric stabilization. These routes are illustrated in Figures 6 and 7.

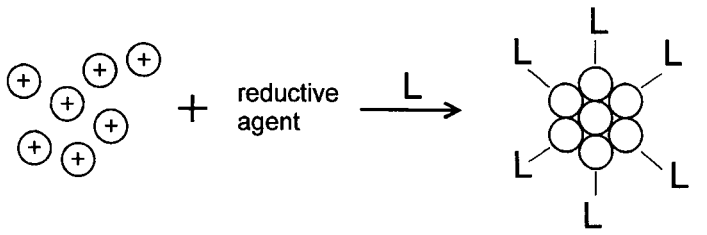


Fig. 6. Formation of metal nanoparticles by reduction of metal ions in the presence of ligands L.

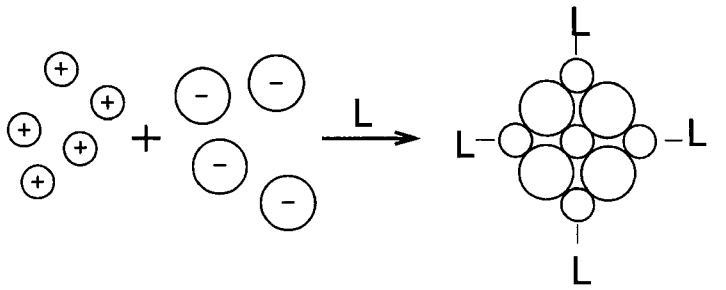


Fig. 7. Formation of semiconductor nanoparticles by reaction of metal ions with group V–VII anions in the presence of ligands L.

The size of most transition metal nanoparticles, which are obtained by the methods described previously, is well defined and is, in some cases, even determined by the so-called geometric magic numbers. This model is developed from a simple geometric consideration and it explains the formation of the well-defined size and stability of many nanoparticles [32–36]. According to this model, the metal atoms tend to form a closed geometry of densest sphere packings, where one central atom is surrounded by a closed shell of atoms as next neighbors, whereas a second shell of 42 atoms surrounds this 13-atom arrangement to give altogether 55 atoms and so on. Examples of ligand-stabilized metal nanoparticles or clusters are $Au_{55}(PPh_3)_{12}Cl_6$, $Pt_{309}phen^*_{36}O_{30}$, and $Pd_{561}phen_{36}O_{200}$, where phen* is bathophenantroline and phen is 1,10-phenantroline. A comprehensive review of the synthetic aspects, structure, and characterization of these highly developed materials is given in [11]. Another example of a gold nanoparticle with a defined number of atoms is the Au_{459} cluster, introduced by Whetten and co-workers [37]. Further examples, especially for larger nanoparticles up to the range of 10 nm, which do not consist of a defined number of metal atoms, are based mainly on the use of gold as the metal and alkanethiols or -dithiols as the ligands [39–43].

Most of these materials are stable in air and can be compacted to solids with a dense but mostly disordered packing. In these solids, which in the case of the previously mentioned ligand-stabilized metal clusters have been the objects of intensive studies of the electrical properties [7, 8, 44], the nanoparticles are spatially separated by the molecules of the surrounding ligand shell. As proposed before in [7], it was demonstrated in a recent paper that (i) gold nanoparticles have been connected by dithiol molecules [10, 40] and (ii) the well-defined Pd_{561} clusters have been connected with 4,4′-diamino-1,2-diphenyl [45] to form three-dimensional networks. Here, the larger bifunctional molecules connect the particles and act as dielectric spacers to increase the volume of the quasicontinuous phase between the particles, that is, to decrease the filling metal factor and, therefore, the interparticle spacing. This directly affects the activation energy of the charge transport between the nanoparticles; that is, the charging energy increases as the interparticle capacitance decreases. We will discuss this in Section 4.4.

In addition to pure metals, nanoparticles of metals connected with group V–VII elements can also be synthesized following similar routes. These compounds are usually semiconductors in the bulk and they can also be obtained in well-defined sizes over a broad size scale. Various examples have been developed within the last decade [16, 38, 46–54] (and the references cited therein) and the numerous reports about these preparation routes indicate the great interest in these materials, as the quantum size effect can directly be studied by means of ultraviolet–visual (UV–vis) spectroscopy, owing to the size-induced blue shift of the absorption edge in band gap semiconductors [55]. Although efforts have been made to obtain monodisperse nanoparticles and to arrange them in solids, just a few examples are known of crystallized superlattices of semiconductor nanoparticles [38, 52, 56–59], which are of enormous academic and technical interest [60]. The most prominent examples are given by Fenske and co-workers, who described large single crystals of small chalcogenide clusters, such as $Cu_{20}Se_{13}(PR_3)_{12}$, that may include up to 146 Cu atoms [61–65]. In high nuclear clusters, such as $Cu_{70}Se_{35}(PR_3)_{22}$, the structural principle of bulk Cu_2Se dominates. The lateral size of the Cu_2Se core in the Cu_{70} cluster is approximately 2.5 nm. Of particular interest for further developments is the fact that with the CuSe clusters even quantum dots with nonspherical shape can be generated. Furthermore—in contrast to the pure metal clusters—these semiconductor clusters can be crystallized to form solids with a superstructure upon removing the solvent. However, quite disadvantageous for possible applications is the fact that most of these cluster compounds are not stable in air.

2.2. Nanoparticles in Block Copolymers

Besides using interconnecting bifunctional molecules, more or less equidistant spatial separation of metal and semiconductor nanoparticles can be realized by the use of reverse micelles or block copolymer micelles [66, 67]. Micelles have been employed as "nanoscopic reactors" in which single nanoparticles could be formed. After forming in a selective solvent, a soluble metal salt can be transferred to the core of the micelles, which then can be assembled to defined films. Analogously to the formation of the previously mentioned route, the ions are transformed, for example, by reduction, to give one single nanoparticle per micelle. Naturally, the size of the nanoparticles depends on the size of the micelle as well as on the number of metal ions that were provided to the micelle's core.

As most impressively demonstrated by Möller and co-workers, Au nanoparticles in polystyrene–block–polyethyleneoxide (PS–B–PEO) hexagonally assembled micelles with rather regularly arranged particles of 2.5, 4, or 6 nm in diameter could be obtained [66, 68] (see Fig. 8). In this work, the association of PS–B–PEO for the formation of micelles in a nonpolar solvent like toluene was utilized. After adding $LiAuCl_4$ to this solution, the salt was slowly solubilized as the Li^+ ions formed a complex with the polyethylene oxide. Thus, the $AuCl_4$ anions were incorporated as counterions into the inner core of the micelles where the nanoparticles are formed by reduction. From this mixture, thin films and at least monolayers of micelles could be obtained. Because of the large kinetic stability of the

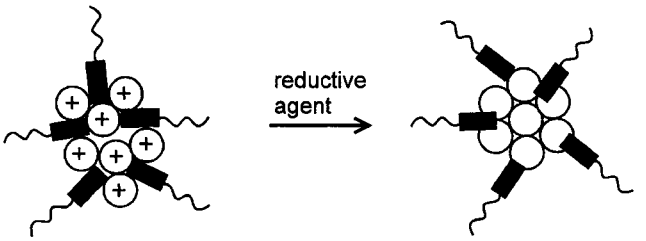


Fig. 8. Formation of nanoparticles in a block copolymer micelle. (Source: Adapted from [68].)

block ionomer micelles, they did not transform to cylindrical domains, which is the bulk equilibrium structure of the block copolymers employed. In the samples described here, the interparticle spacing is expected to be large enough to exclude electronic interaction, but electrical investigations on these materials are still lacking.

2.3. Host/Guest Composites

2.3.1. Nanoparticles in Porous Solids

Instead of covering the surface by ligands, nanoparticles can also be synthesized and protected in porous amorphous or crystalline solids. To control the size and dispersion of the particles, crystalline host lattices with well-defined pore and channel structures are expected to be promising. Therefore, molecular sieves such as zeolites or related mesoporous phases are often used to accommodate particles in colloidal dispersion [69–79]. The interest in these materials results from the principal possibility of synthesizing monodisperse nanoparticles in the confinement of the cages and herewith arranging them with defined interparticle spacing at the same time. Ideally, this would also lead to an ordered arrangement of identical nanoparticles that is an inverse lattice or superlattice similar to the crystallized, ligand-stabilized semiconductor clusters described in Section 2.1.

The preparation of nanoparticles inside a host lattice can be realized for various transition metals such as Pt, Pd, Ag, or Ni [72, 80, 81] as well as for semiconductors such as sulfides or selenides of Zn, Cd, or Pb [82, 83]; ZnO [84–88]; CdO [89], or SnO_2 [90]. Here, the host lattice acts as a solid electrolyte. In solution or in melts, the mobile charge compensating cations (usually Na^+) are exchanged by mono- or multivalent cations, which than can be reduced by suitable agents such as hydrogen or alkali metal vapor.

This process, which is illustrated in Figure 9 in a simplified manner, also requires the migration and agglomeration of the metal atoms, which, before reduction, are spatially separated, as they are located on well-defined cation sites. The formation of the nanoparticles leads, in most cases, to a local degradation of the host lattices, for example, by partial hydrolysis of the zeolite. As a consequence, the advantage of the defined pore size, which is likely to be used as a size controlling confinement, is usually deleted by this effect. Furthermore, the migration leads, in some cases, to the formation of nanoparticles or microcrystallites on the crystallite surface of the matrix.

Another route, that is, the preparation of nanoparticles via decomposition of organometallic or metal carbonyl precursors, starts with the loading of the dehydrated zeolite via the gas phase or from solution. Thermal treatment then leads to ligand desorption and decomposition, which enables the metals to aggregate. Comprehensive reviews on this method are given in [69, 72].

Finally, the inclusion of ligand-stabilized nanoparticles into the channels of a porous solid has recently been demonstrated [91] and seems to be a promising approach to realize one-dimensional arrays of nanoparticles. We will discuss this in Section 3.3.1.

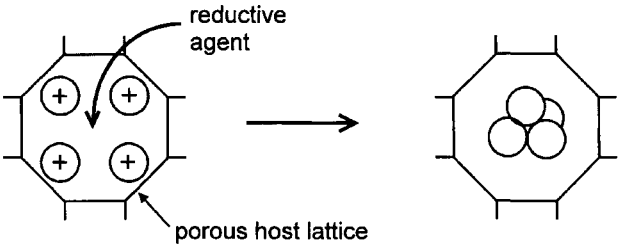


Fig. 9. Formation of metal nanoparticles by reduction in a porous inorganic host lattice.

2.3.2. Nanoparticles in Polymer Matrices

The preparation of nanoparticles in an organic or inorganic polymer matrix is a well-established technique for obtaining thin films of nanoparticle composites with high optical quality [92–95]. Already electroluminescent devices have been developed [51] taking advantage of the specific electronic and optical properties of ZnS nanoparticles and the excellent film processability, that is, typically a spin coating technique. Yang et al. [51] described the synthesis of a ZnS nanoparticle/polymer composite, which was obtained from the reaction of styrene, zinc oxide, azoisobutyronitrile, methacrylic acid (MA), methanol, and tetrahydrofuran, via the intermediate reaction of ZnO and MA to $Zn(MA)_2$, where the two C=C bonds in each $Zn(MA)_2$ are copolymerized with styrene, which acts like a cross-linking agent. The particle size, which is approximately 3 nm, and crystallinity were deduced from UV–vis and transmission electron microscopy (TEM) including electron diffraction, respectively.

The use of plasma polymers for metal nanoparticles is described by Kay et al. [96] and Davis and Klabunde [97], and later, in a more sophisticated technique, by Lamber et al. [98]. This technique is based on the simultaneous plasma polymerization of a fluorocarbon monomer and deposition of a metal by sputtering. Using this technique, different noble metal particles with sizes of a few nanometers and a considerable broad size distribution could be obtained [99]. In a modified technique, they introduced a metal source spatially separated from the plasma discharge region. Shown by the example of gold, nanoparticles with a size of 1.4 nm in a narrow size distribution embedded in the plasma polymer film could be synthesized. Depending on the filling factor, the composites are electrical insulators or electron hopping conductors [100], as might be expected from a highly disordered arrangement of metallic conductors in an insulating matrix [101].

2.4. Electrochemical Composition of Nanoparticles

In 1994, Reetz and Helbig [102] reported on a new approach for obtaining certain transition metal nanoparticles from Pd or Ni and even from superparamagnetic Co by the use of electrochemical methods [102, 103]. The process, in which the particle size (with a certain size distribution) can be controlled in a simple manner by adjustment of the current density, makes use of a simple two-electrode setup, in which the sacrificial anode consists of the bulk metal to be transferred into the nanoparticles. The supporting electrolyte contains tetraalkylammonium salts, which serve as stabilizing ligands in the aforementioned way. Thus, in the overall process, the bulk metal is oxidized at the anode, the metal cations migrate to the cathode, and a consecutive reduction takes place, resulting in the formation of ligand-stabilized nanoparticles (see Fig. 10).

Using this technique, particle sizes in the range of 1.4 to 4.8 nm (and above), with a considerable size distribution in comparison to the chemically tailored nanoparticles, can be obtained. The most striking advantage seems to be the broad variation range of the corresponding ligand shell. Because the tetraalkylammonium ions are simply added to the reaction mixture, the thickness of the ligand shell can easily be varied by changing the length of the alkyl chain [104].

3. ARRANGEMENTS AND DEPOSITION TECHNIQUES

The main difficulty in using chemically prepared nanoparticles as quantum dots or tunnel junctions in microelectronics is the simultaneous interconnection and isolation of the dots to allow a single-electron transport between them controlled by external bias. In three-dimensional arrangements of ligand-stabilized clusters, this problem is solved in an ideal way: During deposition from solution, during pressing to condensed solid, or during crystallization, the ligand shells prevent the clusters from coalescence, acting at the same time

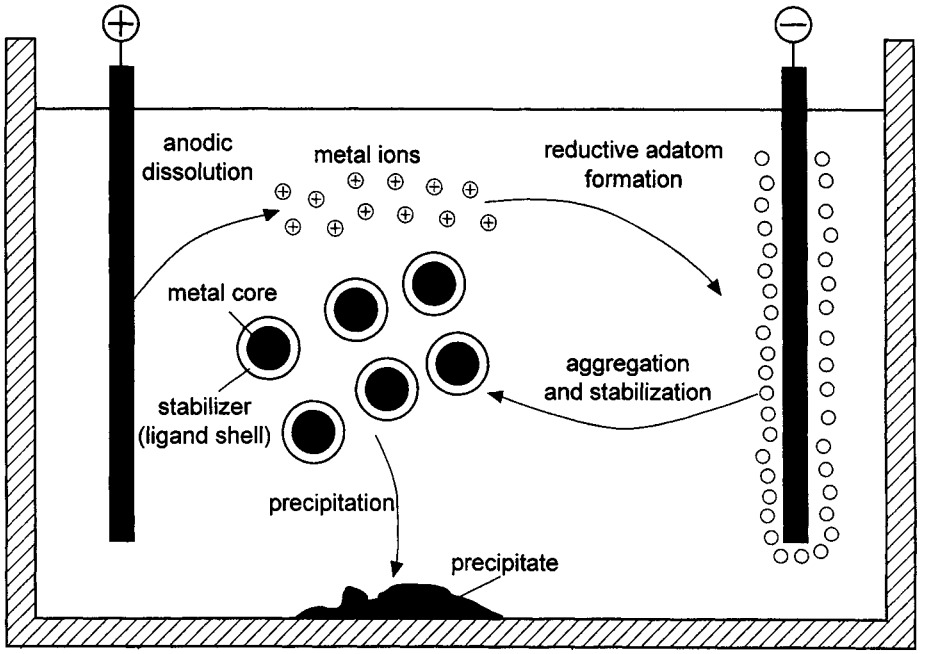


Fig. 10. Electrochemical composition of tetraalkylammonium-stabilized metal nanoparticles. (Source: Adapted from [102].)

as a lubricant and as a "glue." Thus, three-dimensional interconnected arrangements result. In contrast, the preparation of one- or two-dimensional cluster arrangements requires the development of some new deposition techniques such as Langmuir–Blodgett or self-assembly techniques. Fendler reviewed these in [105, 106]. Depending on the special requirements, suitable ligand-stabilized nanoparticles need to be synthesized and modified.

As mentioned previously, in crystals as well as in compressed pellets, the ligand-stabilized particles arrange themselves following the principles of closest packing. The "tunneling distance" for charge carriers is the barrier determined by the thickness and chemical nature of the ligand shell. The same situation results if the nanoparticles are attached to each other in one or two dimensions.

3.1. Three-Dimensional Arrangements

3.1.1. Condensed Cluster Solids

As mentioned previously, condensed solids with perfect arrangements of the nanoparticles are realized in some semiconductor superlattices that are of technical as well as academic interest [60]. The structures are suitable for X-ray structure determination and are often referred to as solids consisting of artificial atoms, that is, the nanoparticles. Although examples are given for uniform ligand-stabilized metal clusters [32–35, 107, 108], crystals have not been found up to now. Therefore, size and structure determination has been performed by different techniques such as Mössbauer [109], high-resolution transmission electron microscopy (HRTEM) [11], or extended X-ray absorption fine structure (EXAFS) [110] instead of X-ray diffraction. Similar to crystallized semiconductor nanoparticles, the attractive interparticle interaction resulting from van der Waals forces or ionic coupling depends on the chemical nature of the protecting ligands and should be sufficient to grow a crystal, but, this problem has not been solved up to now.

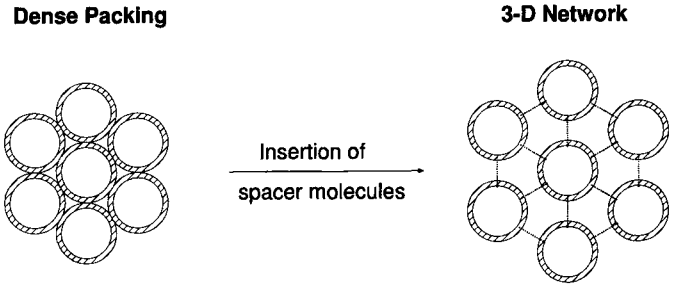


Fig. 11. Scheme of insertion on bifunctional spacer molecules into a dense packing of ligand-stabilized nanoparticles. The stretching of the packing results in a three-dimensional (3D) network.

3.1.2. Cluster Networks

A promising alternative for obtaining three-dimensional quasi-ordered solids of metallic nanoparticles is the interconnection of suitable metal clusters or colloids by identical bifunctional spacer molecules [8, 105] (see Fig. 11). Accordingly, Schiffrin and co-workers reported on a new preparative technique for obtaining this new class of nanomaterials, which comprises gold nanoparticles of 2.2 and 8.0 nm self-assembled into a three-dimensional network by means of organic dithiols [40]. The approach involves the preparation of Au nanoparticles in a two-phase liquid–liquid system [39], where organic dithiols are used as bifunctional interconnecting ligands. This procedure leads directly to the formation of an insoluble precipitate of cross-linked nanoparticles. The existence of self-assembled nanoparticles is deduced from TEM micrographs.

Using ligand-stabilized metal clusters with a defined number of atom, we actually [45] reported the insertion of bifunctional amines into a three-dimensional arrangement of $Pd_{561}phen_{36}O_{200}$, clusters. The spread of the cluster packing, that is, the insertion of the spacer molecules, starts with the deoxygenation of the clusters by hydrogen. The oxygen-free cluster $Pd_{561}phen_{36}$ provides free metal surface sites that can be coordinated by the NH_2 groups of 4,4′-diamino-1,2-diphenyl-ethane. As the free cluster surface is oriented in all directions, the spacing procedure also leads to an insoluble precipitate with three-dimensional cluster linkage. This network exhibits an increased interparticle spacing with respect to the closed sphere packing such as in a pressed pellet or a thick film obtained from solution of the nonmodified cluster.

In both examples, the insertion of large spacer molecules is reflected by an increase in the activation energy of electron transport through the material (see Section 4.4).

3.2. Two-Dimensional Arrangements

The preparation of highly ordered planar arrays of metal or semiconductor nanoparticles isolated from each other by defined tunnel barriers is one of the greatest challenges in the fabrication of microelectronic devices based on chemical nanostructures. To achieve this goal, the principles of molecular self-organization of surfactant monolayers—Langmuir–Blodgett (LB) and self-assembled films—have to be combined with colloid chemistry, which is the backbone of highly developed cluster preparation techniques. Fendler reviewed self-assembled nanostructured materials [106] developed from "wet" colloid chemistry, which was inspired by biomineralization (the *in vivo* formation of inorganic crystals and/or amorphous particles in biological systems [111–113]). A comparison of LB and self-assembled films is given therein and the most crucial step, that is, the deposition of pre-organized layers onto solid surfaces, is emphasized. For a detailed discussion, the reader may be guided by the previously mentioned review as well as by a recently published

review by Ulman [114], while in this section examples of two-dimensional arrangements of ligand-stabilized nanoparticles will be given.

3.2.1. Self-Assembled Monolayers

Schmid et al. [115] reported the formation of two-dimensional arrangements of ligand-stabilized gold clusters and gold colloids on various inorganic conducting and insulating surfaces. For this purpose, oxidized silicon as well as quartz glass surfaces were treated with (3-mercaptopropyl) trimethoxysilane to generate monolayers of the SH-functionalized silane. Dipped into an aqueous solution of 13-nm gold colloids, stable S–Au bonds were formed to fix the colloids in a highly disordered arrangement. The coating of the surface was visualized by atomic force microscopy (AFM). Following a similar route, gold colloids of the same size stabilized by water-soluble $P(C_6H_5SO_3H)$ ligands were deposited two dimensionally on a poly(ethyleneimine)-coated mica surface. The driving force for the deposition of the colloids on the surface is the acid–base interaction between the SO_3H group of the ligand and the NH group of the imine. This procedure leads to a more close packing, which was also visualized by AFM. Deposition of ligand-stabilized Au_{55} clusters on a conducting substrate, that is, a gold (111) surface, was realized by the initial coating of the surface by 2-mercaptoethylamine and a subsequent reaction with the water-soluble cluster $Au_{55}(Ph_2PC_6H_4SO_3H)_{12}Cl_6$ (see Fig. 12). A close coverage of the gold surface results, which, however, is still highly disordered. The conducting substrate enables the characterization of the cluster monolayer by scanning tunneling microscopy (STM), but, unfortunately, no electrical characteristics have been obtained by these investigations besides the imaging of the surface topography.

The most promising results with respect to possible utilization of the size-determined electrical properties were reported by Andres et al. [43, 116, 117]. Close-packed planar

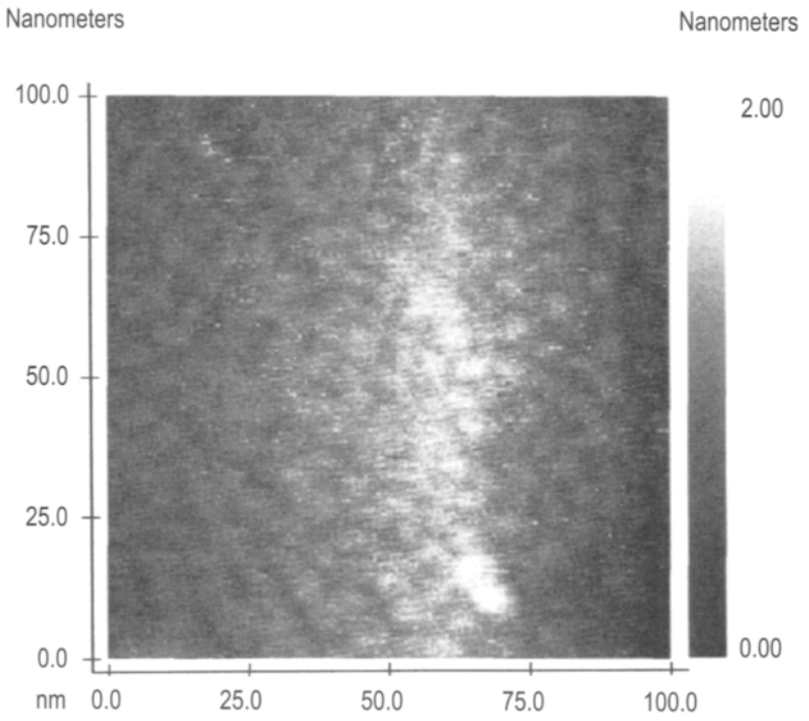


Fig. 12. $Au_{55}(Ph_2PC_6H_4SO_3H)_{12}Cl_6$ clusters on Au(111) fixed on a layer of mercaptomanine molecules via $NH_2\ldots HO_3S$ interactions imaged by STM. (Source: Reprinted with permission from [115].)

arrays of gold nanoparticles 3.7 nm in diameter stabilized by alkylthiol molecules were cast from solution onto a flat MoS_2 substrate. By adding aryldithiols or aryl di-isonitriles, the monofunctional alkylthiols are displaced, leading to a covalent linkage of adjacent nanoparticles in two dimensions. Following the same idea, Reetz et al. [118] realized self-assemblies of palladium clusters stabilized by tetraalkylammonium salts. In accordance with the results obtained on three-dimensional networks, a two-dimensional structure of metal nanoparticles coupled by uniform tunnel junctions could be realized. The electrical properties will be summarized in Section 4.3.

Likewise regular and uniform were the two-dimensional arrangements of gold nanoparticles incorporated into micelles of A–B diblock polymers described by Möller et al. [66, 68], as discussed in Section 2.2.

As an intermediate between two- and three-dimensional arrangements, Decher and coworkers [119] recently reported the fabrication of metal nanoparticle/polymer superlattice films. These film architectures were prepared by first depositing alternating poly(styrene sulfonate sodium salt) (PSS) and poly(allylaminehydrochloride) (PAH) onto a poly(ethyleneimine) (PEI) modified substrate. The uppermost layer of PAH provides a positively charged surface for subsequent self-assembly of a monolayer of gold nanoparticles of 15 nm diameter (see Fig. 13). From this state, the deposition procedure can be repeated to realize multilayer arrangements. Electrical investigations are also lacking in this case, but, because of its unique structure, for example highly anisotropic transport properties may be expected.

3.2.2. Langmuir–Blodgett Films

Just recently, Chi et al. [120] reported access to monolayers of ligand-stabilized Au_{55} clusters via the Langmuir–Blodgett (LB) technique. Two different ligands, which make the cluster water insoluble, were used to spread the clusters on an air/water interface, where they could be compressed to form a closed monolayer. These could be transferred to different solid surfaces, for example, mica, silicon, and evaporated and anealed gold. From the latter, current–voltage characteristics have been recorded by STS, which will be discussed in Section 4.1.2. Close-packed monolayers with a few well-ordered arrays with partially two-dimensional crystallization were illustrated by AFM (see Fig. 14). These results are the first examples of the fabrication of ordered arrangements that fulfill the requirements of periodicity in two dimensions, for example, to enable ballistic or highly correlated electron transport. In any case, however, the method described here, by nature, does not yield sufficient sample qualities to be a routine manufacturing method.

3.2.3. Deoxyribonucleic Acid–Based Method of Self-Assembly

A promising approach, which is, from the point of view of colloid chemistry, strongly related to the methods described in Sections 3.1.2 and 3.2.2, was demonstrated by Mirkin et al. [121], who developed a deoxyribonucleic acid (DNA)–based method to assemble gold nanoparticles in two dimensions. The method starts with the preparation of 13-nm gold particles, using the well-known method of synthesis [122, 123]. In a second step, the gold particles are modified by oligonucleotides, which are functionalized with alkane thiols at their 3′ termini (see Fig. 15, which shows the assembly strategy).

One part of the nanoparticle solution was treated with 3′-thiol-TTTGCTGA, while a second part was treated with 3′-thiol-TACCGTTG, so that the oligonucleotides are noncomplementary. The resulting solutions of oligonucleotide-stabilized Au nanoparticles can be combined, and no reaction takes place because of the noncomplementarity. In a third step, the assembly of the particles results from the addition of a duplex containing 8-base-pair sticky ends, which are complementary to the 8-base-pair oligonucleotides, which are the ligands of the Au particles. Evidence of the polymerization/assembly process is given

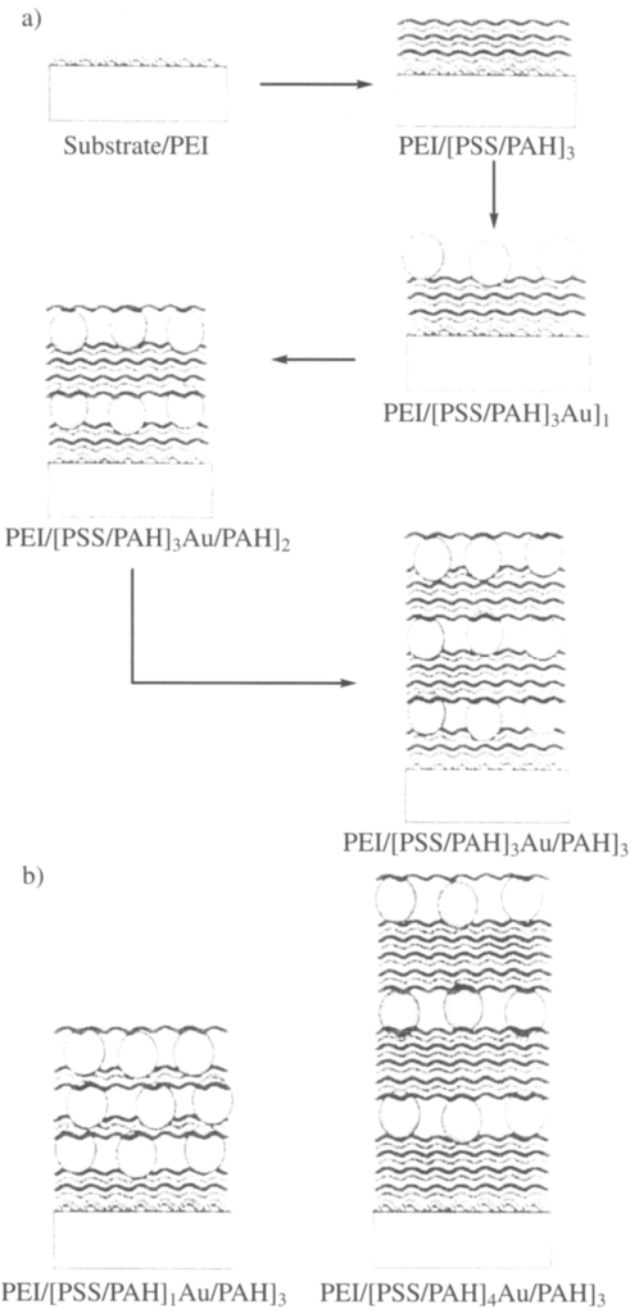


Fig. 13. (a) Process for fabricating colloidal gold/PE multilayers to a final structure with $m = 3$ and $n = 2$. (b) Schematic representation of increased gold particle layer separation achieved by changing the interlayer spacing from $m = 1$ (left) to $m = 4$ (right). On top is the PEI layer. PSS is the light-shaded layer and the PAH layer is shaded dark. Note that this drawing is an oversimplification of the actual layer structure. (Source: Reprinted with permission from [119].)

by TEM images (see Fig. 16). Although it was difficult to obtain any information about the degree of order for three-dimensional aggregates, two-dimensional aggregates provide evidence of the self-assembly process in small-scale images. Close-packed assemblies of uniform particles and uniform particle separation of 6 nm results, whereas the interparti-

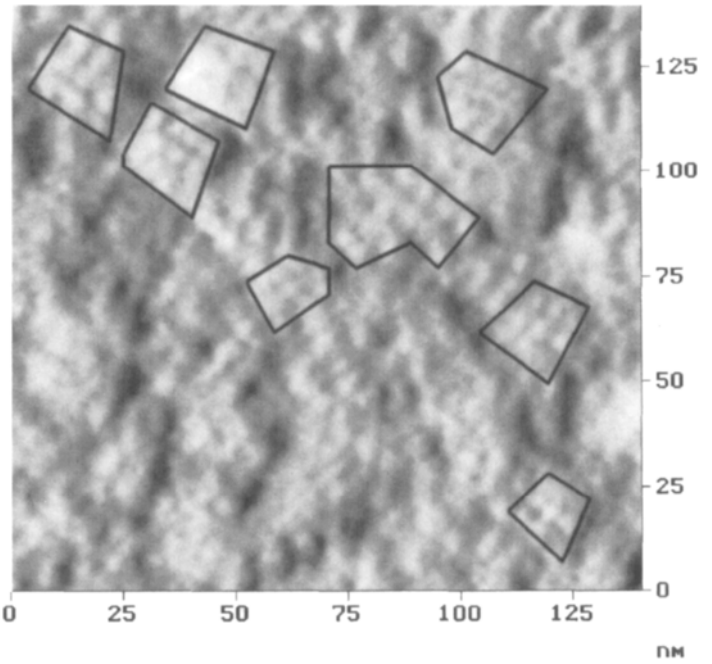


Fig. 14. Single $Au_{55}(PPh_3)_{12}Cl_6$ clusters resolved by noncontact AFM on mica. The black lines indicate the ordered cluster arrays with partial crystallization.

cle distance of slightly smaller, as might be expected from the length of the DNA spacer molecules, that is, 9.5 nm if they are regarded as be rigid. This approach provides a promising way of controlling the particle topology in nanoparticle assemblies, as it allows control of the particle size as well as the spacer length by defining the oligonucleotide sequence and length.

3.3. One-Dimensional Arrangements

The formation of one-dimensional (1D) arrangements of nanoparticles is, in a practical sense, the most common step toward the fabrication of single-electron devices. To realize one-dimensional arrays, which may act as multiple tunnel junctions or quantum wires, different methods are now in progress. Generally, the formation in just one dimension requires the steering influence of a substrate or a matrix, which may be chainlike molecules, linear displacements on solid surfaces, or one-dimensional channels in a, at least, "physically inert" matrix. In the following, actual examples of the development of these different techniques are given.

3.3.1. Intercalation of Ligand-Stabilized Metal Clusters into Solids with One-Dimensional Channel Structures

Crystalline nanoporous solids that perform as 1D channel structures have been recognized as supports for the assembly of ligand-stabilized nanoparticles. The most prominent compounds are zeolites and related structures, which are strongly bounded open-framework aluminosilicates, wherein pores or channels of nanometer lateral extension are formed. Because of their chemical composition, these nanoporous solids have wide electronic band gaps, making these materials optically transparent as well as electrical insulators (whereas ionic conductivity is not taken into account); that is, they are physically inert. Besides this, efforts have been made to synthesize nanoporous semiconductors, as many new physical

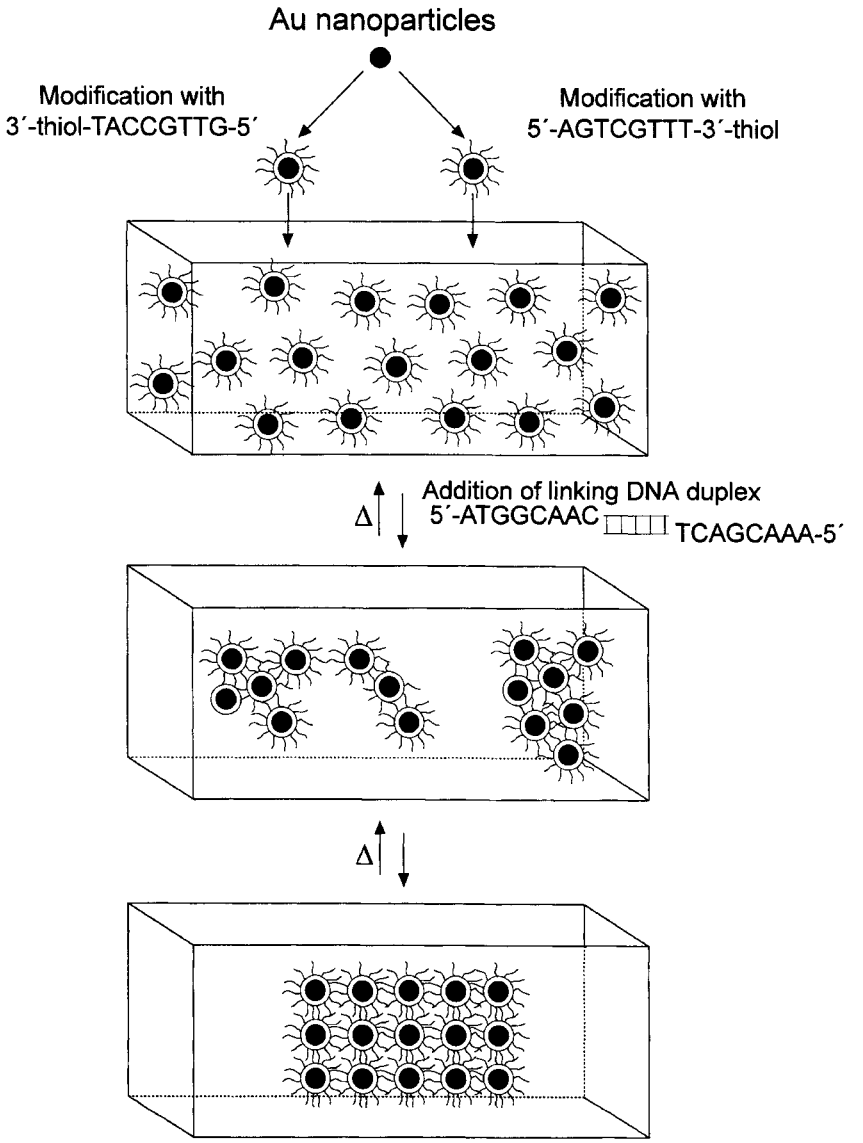


Fig. 15. DNA-based colloidal nanoparticle assembly strategy. If a duplex with a 12-base-pair overlap but with "sticky ends" with four base mismatches (5′-AAGTCAGTTATACGCGCTAG and 2′-ATATGCGC-GATCAAATCACA) is used in the second step, no reversible particle aggregation is observed. The scheme is not meant to imply the formation of a crystalline lattice but rather an aggregate structure that can be reversibly annealed. Δ is the heating above the dissociation temperature of the duplex. (Source: Adapted from [121].)

properties are expected from these "quantum antidot" solids, but, up to now, just a few examples are known [124]. By inclusion of nanoscaled guests inside the defined void spaces of the matrix, new nanocomposites can be obtained with tunable optical, magnetic, or electrical properties.

In the case of one-dimensional structures, it was illustrated recently that, in principle, one-dimensional bundles of metallic wires can be realized by loading the uniaxial channels of zeolite L with potassium via the gas phase. The presence of conducting paths was deduced from alternating-current (ac) measurements at 3 GHz [125]. Numerical calculations on this material suggest that the spatial separation between neighboring metallic channels

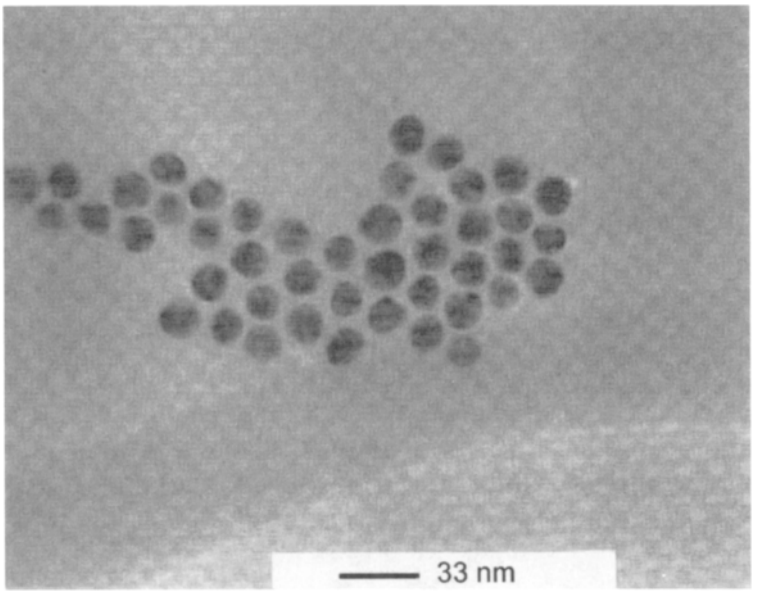


Fig. 16. TEM image of a two-dimensional colloidal aggregate showing the ordering of the DNA-linked Au nanoparticles. (Source: Reprinted with permission from [121].)

is not sufficient to give an electrical and optical anisotropy perpendicular to the orientation of the channels because of pronounced electronic coupling [126].

To avoid this problem, it might be useful to fill the channels with preformed and stabilized metal clusters. In this arrangement, the metallic core and its surrounding insulating shell replace the islands and tunnel junctions, respectively, of conventional single-electron tunneling (SET) arrangements. In practice, although these particles are labeled as uniform, certain statistical fluctuations in the atom numbers forming the core by nature have to be taken into account, leading to a finite size distribution. These deviations will directly affect the self-capacitance C_0 of the particles and by this the electrical properties of such an arrangement. Furthermore, it is a difficult, if not an imposible, task to avoid disorders along the array, when filling the channels with clusters, which will modify the interparticle capacitance C.

A discussion of the effect of disorder on the potential distribution in such arrangements has recently been given by Simon and Gasparian [127, 128] and will be discussed in Section 4.2.1.

In spite of large experimental efforts, up to now the ordered inclusion of ligand-stabilized metal clusters into a zeolite or related crystalline matrix has not been realized. Besides, even examples are known about the intercalation of C_{60} fullerenes via the gas phase [129] as well as the random inclusion of $Au_{55}(PPh_3)_{12}Cl_6$ into MCM 41 for catalytic prospects. An alternative route has recently been suggested by Schmid and co-workers, who used the quasi-parallel channels of anodically generated porous alumina as a matrix for cluster inclusion [91] (see Fig. 17).

The diameter of the quasi-parallel, penetrating channels can be controlled and varies from 2 to 100 nm and thus exhibits a complementary size for the inclusion compounds. Because the arrangement of the channels exhibits nonperiodicity in a strict sense, that is, diameter and parallelism do not fulfill the requirements for X-ray diffraction patterning, a priori, even here the problems of disorder cannot be avoided.

Clusters and colloids of a corresponding size could be introduced into the channels by vacuum induction, capillary action, and electrophoretic or chemisorption/immersion

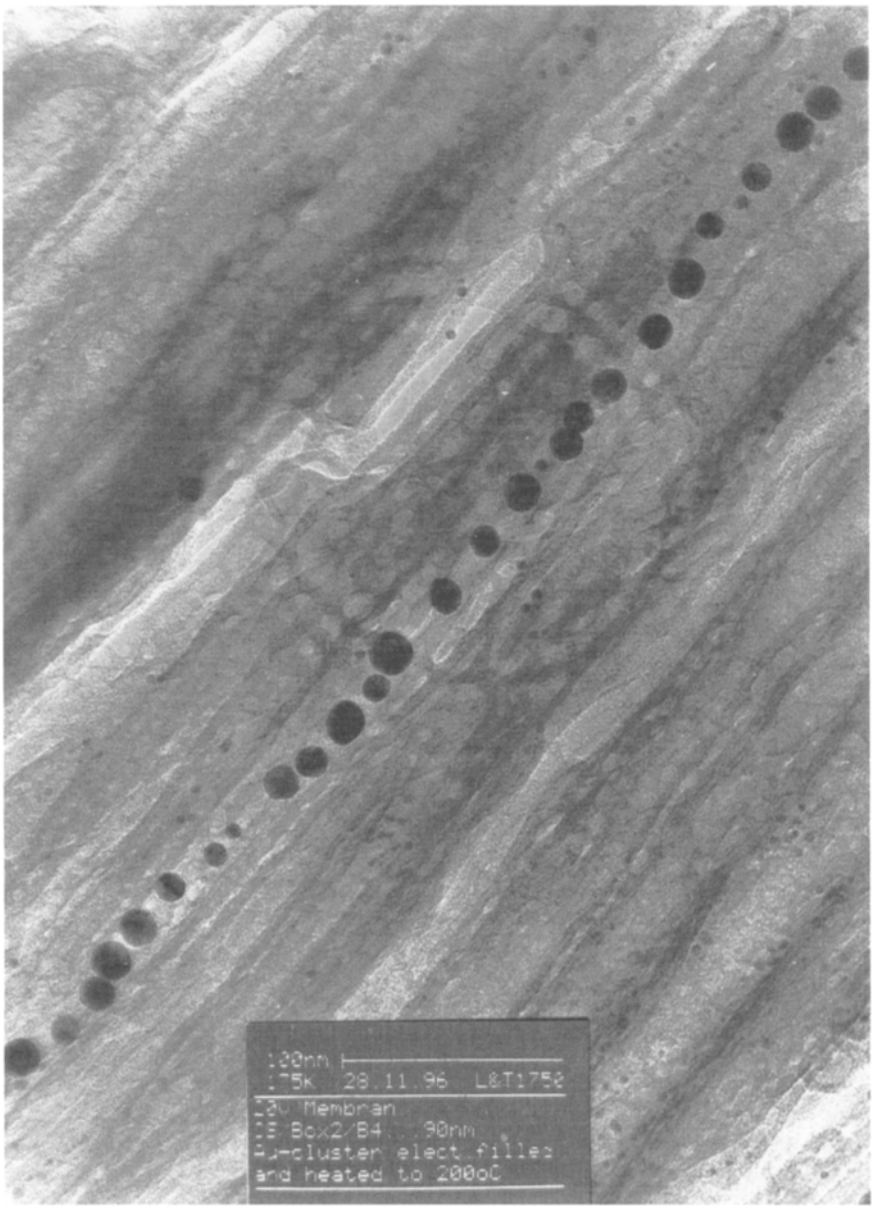


Fig. 17. Pore channel of an alumina membrane field with ligand-stabilized gold nanoparticles. (Source: Reprinted with permission from [91].)

mechanisms. The results of initial experiments have been illustrated by means of TEM images, which proved that the arrangement of the particles inside the channels is far from being strictly one-dimensional. But, in any case, the principle developed seems to be promising and deserves to be developed.

3.3.2. Deposition on Crystalline Surfaces

First attempts have been made to deposit ligand-stabilized metal clusters one dimensionally aligned on the surface of crystalline [15] or preformed solids [8], which may result from the enhanced surface energy. "String of pearls"-like alignments of superclusters consisting

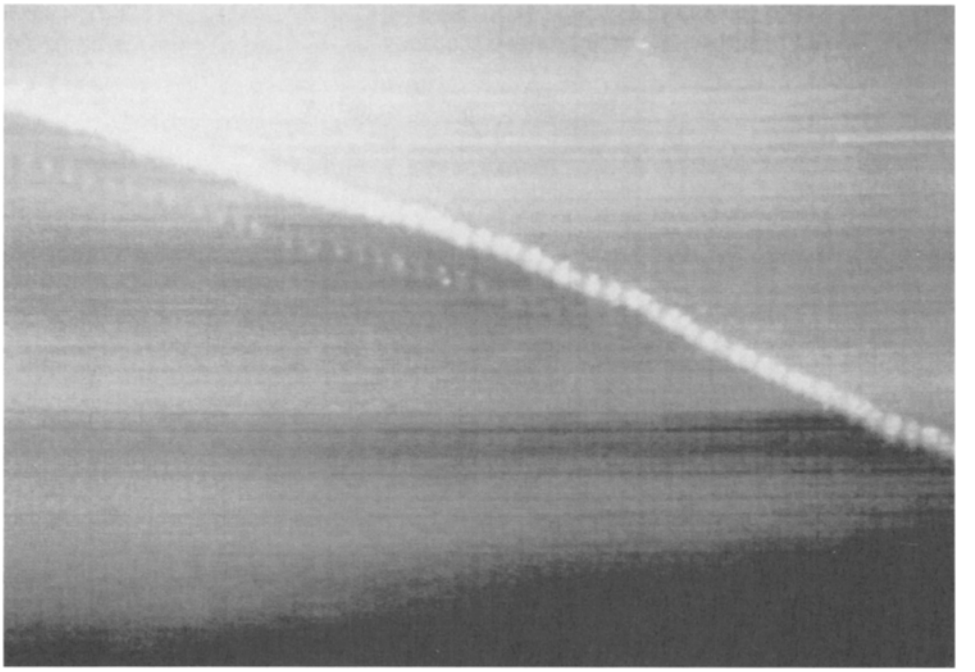


Fig. 18. String-of-pearl-like arrangement of $(Au_{55})_{13}$ superclusters on HOPG. (Source: Reprinted with permission from [15].)

of 13 Au_{55} self-assembled particles are known [15] (see Fig. 18). However, up to now, this technique has not been developed to give reproducible results with a high standard degree of order. Alternatively, although no nanoparticles with a defined insulating barrier are used, the deposition of metal nanoparticles from the vapor phase leads to encouraging results. Francis et al. [130] reported the deposition and growth of noble metal clusters on highly oriented pyrolytic graphite (HOPG). On this support, clusters of Au and Ag formed quasi-one-dimensional chains along the surface steps, resulting in a similar string-of-pearls alignment.

3.3.3. Organization along Single-Stranded Deoxyribonucleic Acid Oligonucleotides

The use of chainlike molecules as organizing agents to obtain linear arrangements of nanoparticles was introduced by Alivisatos et al. [131], who described a strategy for the synthesis of "nanocrystal molecules," in which discrete numbers of defined gold nanoparticles are organized into spatially defined DNA-like structures. In contrast to the two-dimensional (2D) assembly described in Section 3.2.3, in this approach parallel and antiparallel homodimer oligonucleotides react with 1.4-nm, water-soluble Au clusters. One N-propylmalinide ligand per cluster couples selectively to a sulfhydryl group incorporated into the single-stranded DNA (see Fig. 19).

Oligonucleotides, modified at either the 3′ or the 5′ terminus with a free sulfhydryl group, were coupled with an excess of the nanoparticles. After combining with suitable oligonucleotide templates, parallel and antiparallel dimers as well as parallel trimers could be obtained. The linear alignment of the clusters, the center-to-center distance of which ranges from 2 to 6 nm, respectively, was illustrated by means of TEM images.

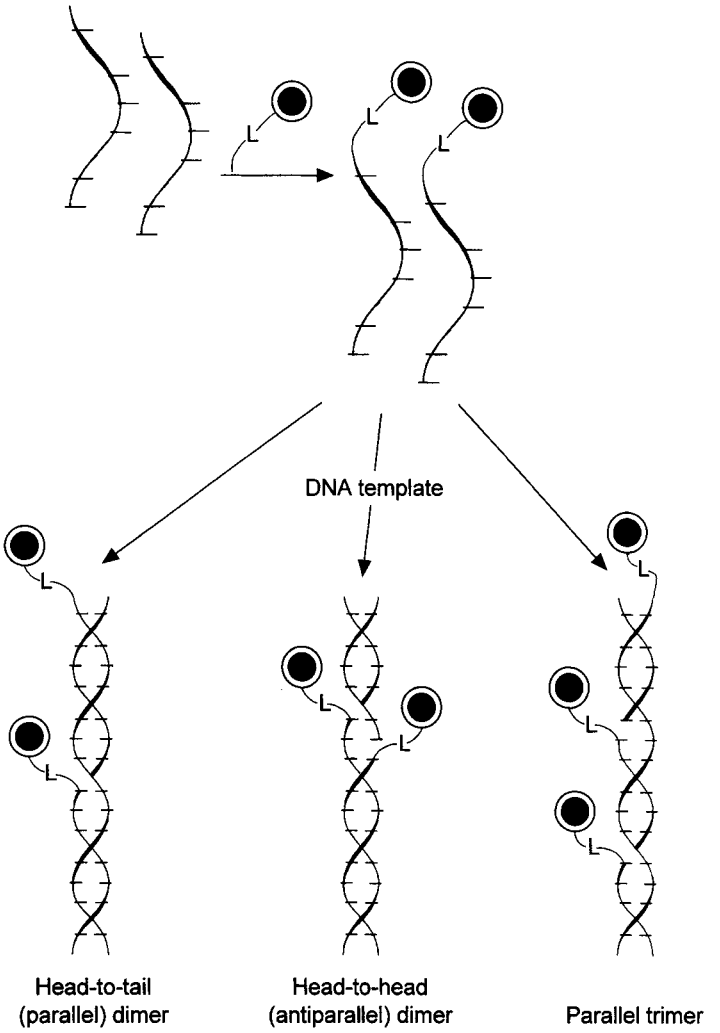


Fig. 19. Nanocrystal assembly based on Watson–Crick base-pairing interactions. Attachment of the inorganic nanoparticles (black) to either the 3′ or the 5′ terminus of the oligonucleotide "codon" by the linker L permits the preparation of head-to-head dimers, head-to-tail dimers, and trimers. (Source: Adapted from [131].)

4. ELECTRICAL PROPERTIES OF ZERO- TO THREE-DIMENSIONAL ARRANGEMENTS OF NANOPARTICLES

4.1. Single-Particle Properties

4.1.1. Thin-Film Structures and Scanning Tunneling Microscopy Single-Electron Systems

At present, the fabrication of "traditional" single-electron circuits, such as transistors or pumps, is carried out by the evaporation of metal (usually Al) films through a fine-pattern mask, which is often made of polymer resist by means of an electron beam lithographic process [132]. The mask presents a number of thin splits, determining the sizes and shapes of resulting islands, and the bridges interrupting them determine the position of the future tunnel junctions and gates. Because of the composite polymer resist layer, which is chemically undercut, the resulting mask is rigidly fixed above the substrate and its bridges

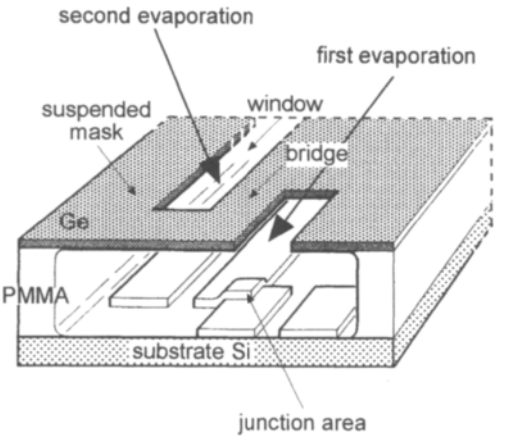


Fig. 20. Evaporation of metal through windows of a suspended mask to fabricate tunnel junctions. (Source: Adapted from [132].)

become suspended above it. Such arrangements of splits and bridges allow the evaporation of metals onto substrates from various angles, which allows different positions of the resulting evaporated layer (see Fig. 20).

To form a set of islands connected by tunnel junctions, the evaporation is usually made from two different angles in two steps with an oxidation process in between, when aluminum is used. By adjusting the angles, the linear sizes of the resulting overlapping area of the first and the second metallic layers can be even smaller than the width of the strips, that is, somewhat less than 0.1 μm. At the same time, a gate electrode coupled to the islands only capacitively should not overlap them, which is taken into account in the mask pattern design. After double evaporation, the mask and the supporting layer are lifted off.

The resulting barrier of Al_2O_3 with a desirable thickness of a few nanometers is mechanically and chemically stable. The height of the corresponding energy barrier is about 1 eV and it readily provides a tunnel resistance in the range of 50 to 500 kΩ for junctions of the aforementioned size. The resulting capacitance of such tunnel junctions is in the range of 10^{-16} to 10^{-15} F, which corresponds to a Coulomb energy E_C expressed in terms of temperature units, E_C/k_B, of approximately 1 K. This means that such circuits operate correctly only at temperatures well below 1 K, that is, at 10–100 mK, which is just attainable with immense technical effort.

Thus, the junction size and, correspondingly, the energy and temperature scale are finally restricted by resolution of the resist and critically depend on the performance of electron beam writing of the mask pattern. At present, in order to approach finer structures and, therefore, smaller sizes of tunnel junctions, the search for new materials both for resist and for metal circuits is in progress. Furthermore, efforts are also being made to improve the etching and underetching technique of the bridges. These will probably extend the operation temperature up to the routinely achievable temperature of liquid helium at 4.2 K. Nevertheless, this technique has its own natural size limit.

To increase the operating temperature essentially more sophisticated technologies for the fabrication of SE structures are definitely needed. One of the most promising alternatives in metallic single-electron structures is the use of ligand-stabilized metal nanoparticles as building blocks.

The drastic reduction of the sizes and, therefore, of the capacitances of tunnel junctions can be made, for example, in a single-electron structure comprising small metallic particles and the tip of the scanning tunneling microscope (STM). It is known that this instrument can probe a conducting surface with even atomic resolution because of electron tunneling through the energy barrier between the tip and the surface. The resulting tunneling space

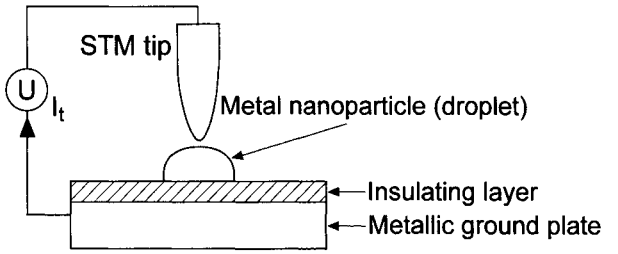


Fig. 21. Single-electron, two-junction system consisting of an STM tip and a metallic nanoparticle as a central electrode on a ground plane.

can also be filled with a thin dielectric, for example, oxide, covering the metal surface. If a nanoparticle is embedded into an oxide layer or if it is fixed somehow onto an oxide surface, then the tunneling current predominantly goes through the particle. Such an arrangement presents a typical single-electron, two-junction system. One of the junctions, which is between the ground plane and the grain, is mechanically fixed, while another one, which is between the grain and the STM tip, is tunable because of displacement of the latter (see Fig. 21).

The structures described previously were successfully and repeatedly realized in practice. The one-dimensional arrangement in a double-barrier tunnel junction working at room temperature has been realized by an STM tip above Au particles of approximately 4 nm in diameter obtained by metal evaporation on a 1-nm-thick layer of ZrO_2 (tunnel barrier) on a flat Au substrate. The experimentally determined capacitance of the nanoparticle–substrate junction is approximately 0.8×10^{-18} F. This value is in good agreement with the theoretically estimated capacitance of 1×10^{-18} F based on the model of a parallel-plate capacitor with ZrO_2 as a defined dielectric [133]. This example shows that, by means of metal nanostructures, SET in the range of room temperature is accessible, but for SET devices particle size distribution has to be avoided, which is not possible when metal evaporation is used as the nanoparticle source.

Of course, although such a procedure makes possible the fabrication of structures that are, in fact, double-junction systems with very small capacitances, the controllable gating of current seems to be practically impossible. Instead, the tunneling current is strongly affected by random charge trapped in the underlying oxide. Moreover, the size and shape of the grains are very random and are not predictable, which ruins any hopes of fabricating a system with well-defined parameters. On the other hand, the very small capacitances of such structures extend the range of observability of Coulomb blockade above helium and even up to room temperature. To take advantage of the minute grain size and to avoid the problems caused by size distribution, the use of ligand-stabilized nanoparticles seems to be a suitable method.

4.1.2. Single-Electron Tunneling on Single Chemically Tailored Nanoparticles

The first results obtained on single chemically tailored nanoparticles have been reported by van Kempen et al. [20, 134]. They reported scanning tunneling spectroscopy on a $Pt_{309}phen_{36}O_{20}$ cluster at 4.2 K, which was deposited from a droplet of an aqueous solution of the clusters on a Au(111) facet (see Fig. 22).

The $I(U)$ characteristics exhibit clear charging effects, which indicates that the ligands are sufficient electrical insulators, as they act like tunnel barriers between the cluster and the substrate. The experimentally observed charging energy ranges from 50 to 500 meV, while a value of 140 meV would be expected, assuming a continuous density of states in

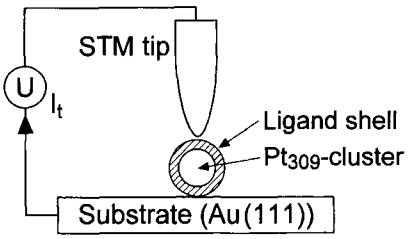


Fig. 22. Single ligand-stabilized Pt_{309} cluster between STM tip and a Au(111) facet. The junction between the cluster and the substrate is built up by the ligand shell.

the particles and a dielectric constant $\varepsilon_r = 10$ for the ligand molecules, when the "classical" formula $E_C = e^2/4\pi\varepsilon_0\varepsilon_r R$ (where R is the radius of the particle) is applied.

There are different factors affecting the variation in E_C, which have been taken into account: Because the clusters have different facets (squares and triangles), E_C will depend on the exact way in which the cluster lies on the substrate. Furthermore, the ligands, which, for simplification, have been assumed to be a spherical dress for the cluster, may have different orientations varying from cluster to cluster with respect to the underlying substrate, thus causing a different tunnel barrier between the cluster and the ground and, therefore, a different capacitance. Finally, the effect of residual water molecules from the solvent may be physically or chemically bound on the cluster surface or on the ligand shell and, therefore, the tunnel junction between the cluster and the substrate may differ for different clusters.

Additional structures on the charging characteristics have been observed in some cases, which might be expected from a discrete electron level spectrum in the cluster caused by the quantum size effect. The effect of discrete levels on the charging characteristics has been treated theoretically by Averin and Korotkov [25], who extended the existing "orthodox" theory of correlated SET in a double normal-metal tunnel junction to the case of a nanoscaled central electrode. According to this, the $I(U)$ characteristics should exhibit small-scale singularities reflecting the structure of the energy spectrum of the central electrode, that is, the nanoparticle. Furthermore, the energy relaxation rate becomes evident because of the small recharging time τ, resulting from the small junction capacitance according to $\tau = R \cdot C$, where R is the resistance of the tunnel barrier and C is the capacitance of the junction. Although the theoretical prediction for the level splitting Δ according to $\Delta = 4E_F/3N$ or to a refined approach by Halperin [21] leads to an assumed splitting of approximately 8 meV (E_F is the Fermi energy of the metal and N is the number of free electrons), the fit of the spectra lies between 20 and 50 meV. Although different reasons are discussed in the cited paper, the measurements reflect the discreteness of the level spectrum in the clusters as large as 2.2-nm Pt_{309} clusters.

On smaller ligand-stabilized metal clusters of 1.4 nm, for example, $Au_{55}(PPh_3)_{12}Cl_6$, scanning tunneling spectroscopy (STS) has been performed up to the range of room temperature. Already from cluster pellets, that is, three-dimensional compacts of the clusters, single-electron transfer has clearly been observed in the $I(U)$ curves [19] taken at room temperature. In these investigations, however, neither the vertical nor the lateral arrangement of the clusters is well defined, as would be the case in a one-, two-, or three-dimensional superlattice. As a consequence, the charging energy has a wider spread, as would be expected from the estimation of the charging energy of a single cluster according the formula mentioned previously.

Excluding this problem, Chi et al. [135] reported STS on Au_{55} monolayers prepared on various technically relevant substrates. The samples could be obtained utilizing a two-step self-assembly (SA) process and by a combined Langmuir–Blodgett/SA process, which, in principle, have been described in Section 3.2. The spectroscopy gives clear evidence of the

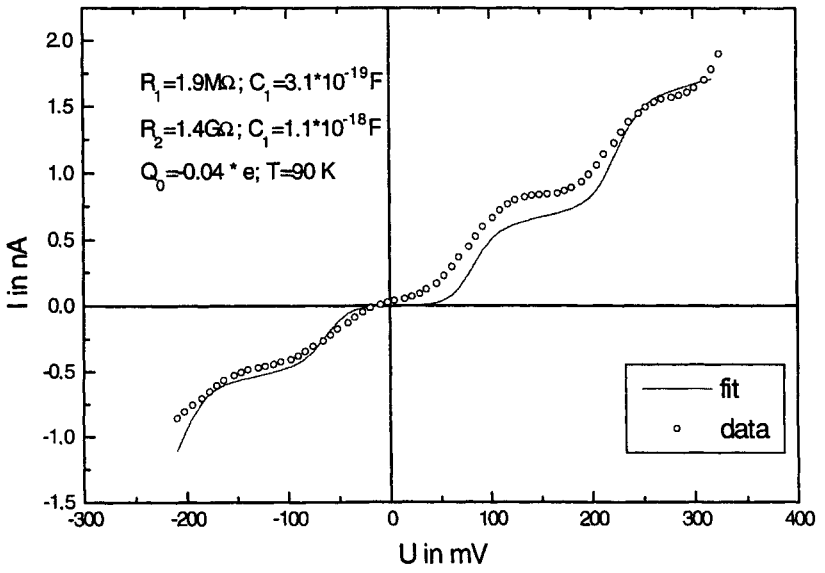


Fig. 23. SET on a single ligand-stabilized Au_{55} cluster at 90 K. The junction capacitance was calculated to be 3×10^{-19} F by fitting.

Coulomb blockade originating from the double barrier at the ligand-stabilized cluster as the central electrode up to the range of room temperature. By a fit of the experimental data at 90 K, the capacitance of the cluster was calculated to be 3.9×10^{-19} F (see Fig. 23). This value is in agreement with the value of the microscopic capacitance determined earlier by temperature-dependent impedance measurements [7]; see Section 4.4.1.

Furthermore, these results are in good agreement with the capacitance data obtained from self-assembled gold nanoparticles on a dithiol-modified Au [111] surface [136, 137]. Here STS has been performed on 1.8-nm Au particles that were grown in the gas phase with a multiple expansion cluster source. Deposited on a suitable surface, Coulomb staircases at room temperature associated with a cluster/substrate capacitance of 1.7×10^{-19} F could be obtained.

4.2. One-Dimensional Arrangements

To the authors' knowledge, at present no experimental data about electrical properties exist from 1D arrays consisting of chemically tailored nanoparticles. In spite of the efforts to get experimental access to these most interesting structures (see Section 3.3), the electrical properties of 1D arrays have been studied theoretically up to now.

4.2.1. Potential Distribution in Nanoparticle Arrays

In 1D arrays of mesoscopic tunnel junctions, time and space correlations between tunneling events may appear because of the Coulomb blockade effect [4, 138]. The time oscillations of correlated single-electron tunneling events, for example, the so-called charge soliton, can be counted very precisely in such arrangements and can be used in practice for possible metrological applications as well as for digital devices [138–141]. These arrays are usually fabricated by lithographic techniques in which the typical size of the junction is a few tens of nanometers. If chemical nanostructures are used to build up these kinds of devices, they tend to a length scale of 1–2 nm, where deviations in the number of atoms, which form the metal cluster core, influence their size and shape and have to be taken into account. Furthermore, packing defects may not be avoided on the molecular scale so that both kinds

of disorders will affect the form of the charge soliton and, therefore, the electrical properties of the array.

Originally, charge soliton propagation would take place in a homogeneous 1D and infinitely long array of identical junctions, where the potential distribution does not change its form when an electron tunnels from one electrode to another [4, 138, 142, 143]. This means that in an infinite-chain approximation the potential profile $\phi_i^{(0)}$ does not depend on the number N of junctions in the array. On the other hand, in some devices such as the "SET turnstile" and the "SET pump" [138, 139], the soliton can extend over approximately 6–10 tunnel junctions and, therefore, enters the same scale as the array itself. In this situation, the main condition of the infinite-array approach is not fulfilled. Then the finite number of junctions becomes crucial and starts to play an important role in the formation of the potential profile.

The limits of the validity of the infinite-chain approximation have been discussed by Hu and O'Connell [144, 145]. They found an exact solution for the charge soliton in the case of a finite 1D array of N gated junctions with equal junction capacitances C and equal gate capacitances C_0 as well as for a single-electron multijunction trap. The key to the approach was, on the one hand, to adopt the semiclassical model to describe the 1D array [142] and, on the other hand, to rewrite the charge conservation law and Kirchhoff's laws as equations for the island potentials $\{\phi_i^{(0)}\}$, instead of the island voltages $\{V_i\}$.

Most recently, Gasparian and Simon [127, 128] found an exact analytical solution in terms of the Green's function (GF) for the potential distribution in a finite 1D array consisting of N small ligand-stabilized metal nanoparticles with a finite size distribution, which are arranged in series. The GF approach enabled them to formulate the so-called partial "solitary" problem of small mesoscopic tunnel junctions similarly to the problem of the behavior of an electron in a 1D tight binding and in a set of random delta-function models.

With regard to metal nanoparticle arrays, it has been assumed that either (i) the capacitance C is the same for all junctions, whereas the self-capacitance C_0 can fluctuate from site to site because of the finite size distribution; or (ii) C_0 is the same, whereas C can fluctuate from site to site because of packing defects. Furthermore, it has been assumed that the metal nanoparticles have a continuous density of states, that is, quantum size effects, and its influence on the capacitance has been excluded from consideration. Generally, these simplifications are not necessary assumptions for the method discussed there, as such a general expression takes all these effects into account.

The main results are that a decrease of the particle size at one position of the array (denoted as impurity in Fig. 24) increases the potential at this point, which may lead, at least, to localization; that is, the single excess electron in the array may be trapped.

A packing defect, which affects the interparticle capacitance at one point, acts as an inhomogeneity, where the soliton will interact with its mirror-image soliton (or antisoliton) and, therefore, will be attracted. For more practical use of this method, it was pointed out that the total reflection amplitude, which was obtained by these calculations, is directly related to the Landauer resistance [10], which reflects the electrical characteristics of such multijunction arrays.

4.3. Two-Dimensional Arrangements

4.3.1. Electronic Conduction through Coupled Nanoparticle Networks

Janes et al. [117] reported the electronic conduction across a network of 4-nm gold nanoparticles interconnected by di-isonitrile ligands [1,4-di(4-isocynaophenylethynyl)-2-ethylbencene], which is a conjugated, rigid molecule, to give an interparticle spacing of approximately 2.2 nm. The two-dimensional assembly results from the deposition of the nanoparticles from a colloidal solution, followed by reactive addition of the linking molecules. To allow for electrical characterization, the layers were deposited on a SiO_2-supported GaAs wafer with gold contacts separated by 500 and 450 nm, respectively.

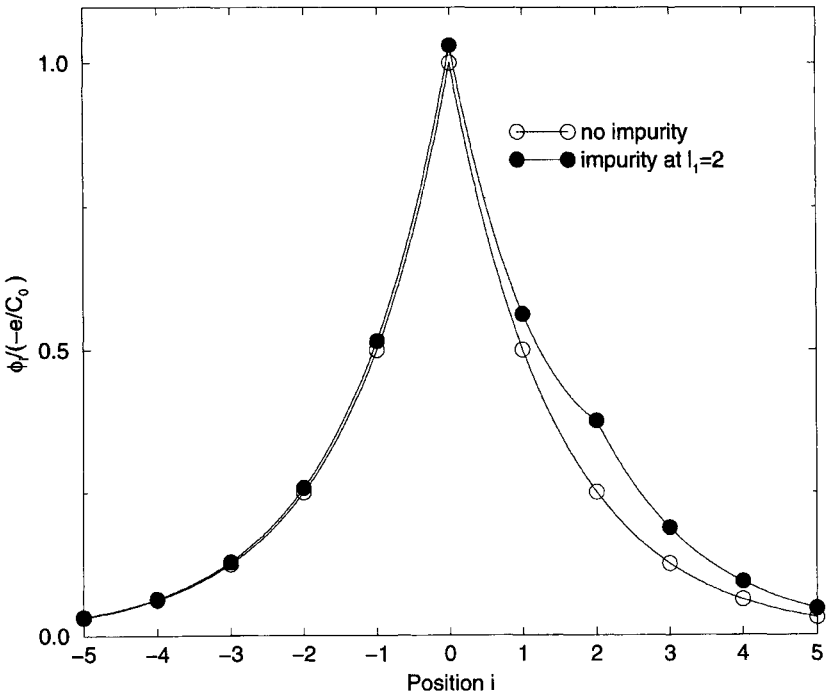


Fig. 24. Potential distribution in a 1D array of ligand-stabilized nanoparticles. A size fluctuation at $i = 2$ (decrease of the self-capacitance) leads to an increase of the potential (black circles). (Source: Reprinted from V. Gasparian and U. Simon, *Physica B* 240, 289 (1997) with the kind permission of Elsevier Science–NL, Sara Burgerhartstraat 25, 1055 KV Amsterdam, The Netherlands.)

The $I(U)$ characteristic of the arrays is linear over a broad voltage range. Because a dot-to-dot capacitance of 2×10^{-19} F might be assumed, the total dot capacitance will be 1.2×10^{-18} F, if each cluster is assumed to have six nearest neighbors. The corresponding charging energy thus will be approximately 11 meV, which is only about half of the characteristic thermal energy at room temperature. Therefore, a Coulomb gap at room temperature is not apparent.

On the other hand, the charging energy of the nanoparticles has been obtained from comparable samples with two-dimensional cluster linkage by Andres et al. [43] from temperature direct-current (dc) measurements. According to the Arrhenius relationship $G_0 = G_\infty \exp(-E_A/k_B T)$, where G_∞ is the conductance as $T \to \infty$, E_A is the activation energy, and k_B is Boltzmann's constant, a Coulomb charging behavior with a charging energy (which corresponds to the activation energy) of $E_A = 97$ meV was indicated. The interparticle resistance was revealed to be 0.9 MΩ, from which a single molecule resistance of 29 MΩ is predicted. This value is in considerable agreement with the prediction of 43 MΩ obtained from Hückel molecular orbital (MO) calculations.

A two-dimensional tunnel junction array has also been realized by Nejoh and Aono [146] by using liquid crystal molecules (4′-n-heptyl-4-cyanobiphenyl) as tunnel junctions between Pt and Pd nanoparticles deposited on a quartz substrate by dc sputtering (see Fig. 25).

The average size of the particles is 1 nm and the average spacing ranges from 0.2 to 0.5 nm. This arrangement has been contacted by an STM tip and a directly connected outer electrode. The $I(U)$ characteristics of the arrays indicate a Coulomb blockade at approximately 100 mV at room temperature with an interdroplet capacitance of 5×10^{-18} F.

Because the spatial distance between the STM tip and the outer electrode is about 5 mm, the number of particles participating in the charge transport is approximately 2.5×10^6. To

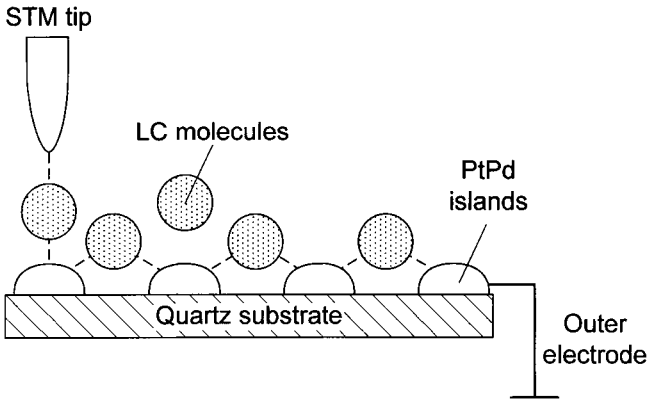


Fig. 25. Schematic picture of PtPd nanoparticles deposited on a SiO_2 substrate. Liquid crystal (LC) molecules occupy the positions between the islands and support the tunneling process. (Source: Adapted from [146].)

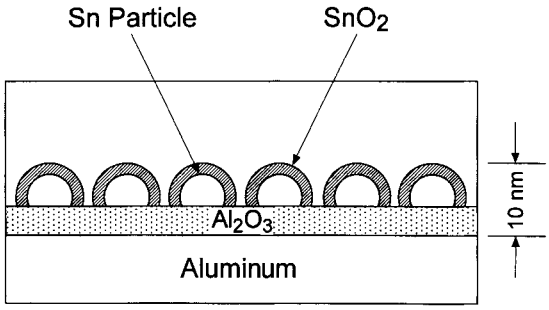


Fig. 26. Schematic representation of a Giaever–Zeller system for tunneling in parallel into a system of small metal particles. Here, both barriers are created by the oxidation of metal layers/surfaces. The basic barrier is formed by the oxidation of Al and the barrier over the particles is formed by the oxidation of the Sn droplets themselves. (Source: Adapted from [147].)

calculate the $I(U)$ characteristic of this kind of long array, a 1D array of 14 junctions—just for simplicity—has been assumed and qualitative agreement of the calculated curve (calculated with a capacitance of 5×10^{-18} F) with the measured curve was found. Although these results are regarded as a step forward in realizing single-electron devices, the mechanism on how the liquid crystal molecules participate in the charge transport needs to be clarified.

Although the former examples referred to an in-plane charge transport, electrical transport perpendicular to the orientation of a two-dimensional array has also been investigated. The most famous measuring arrangement was developed by Giaever and Zeller [2, 3], who performed tunneling experiments on 10-nm Sn particles in the 1960s.

Figure 26 shows a schematic presentation of the Giaever–Zeller system for tunneling in parallel through a two-dimensional layer of small metal particles. The two tunnel barriers are formed by oxide layers on the substrate and surrounding the particles. Recent work by Ruggiero and Barner [147, 148] took advantage of this and examined layers of Ag, Pb, and Cu nanoparticles in an Al_2O_3 matrix with a considerable size distribution ranging from 3 to more than 100 nm. The $I(U)$ characteristic gave evidence of the size distribution, as significant conductance peak spacing, determined by the capacitance of the particles, has been observed. By making the assumption that the nanoparticles are embedded in a uniform dielectric medium of constant $\varepsilon = 8$ for Al_2O_3, they gave an expression for the conductance peak spacing $\Delta V = e/C$, where C is the junction capacitance, approximated

by $2\pi\varepsilon_0\varepsilon d$ and d is the particle diameter. To take into account also the self-capacitance C_0 of the particles, which feel the proximity of the base and outer electrode, the expression had to be extended to a model according to which a particle under consideration is surrounded by a sphere of metal and separated from it by thickness s of the barrier material, that is, Al_2O_3 in this case. According to this, they found a good correlation, when the average peak spacing is plotted as a function of diameter, for a variety of samples. What is most important to emphasize from these investigations is that obviously the information on the size distribution of nanoparticles in these arrangements is completely represented by the conductance data, implying that tunneling occurs from particles representing all size scales in the tunnel system.

4.4. Three-Dimensional Arrangements

4.4.1. Solids and Networks

Various dc and ac measurements on compacts of ligand-stabilized transition metal clusters have been performed. Measurements on compressed powder samples of $Au_{55}(PPh_3)_{12}Cl_6$ as well as $Pd_{561}(phen)_{36}O_{200}$ indicated that the temperature dependence of the dc conductivity σ_{dc} follows over a wide range of temperatures (70–350 K) the exponential law $\sigma \sim (T/T_0)^{-1/2}$ [44]. The frequency dependence of the ac conductivity as well as the nonohmic behavior at strong electric fields discloses a pronounced similarity to different heterogeneous materials, like cermets, doped and amorphous semiconductors, or metal– and carbon–insulator composites. This "universal response" [149] was carefully analyzed by different physical models of hopping conductivity with the conclusion that the experimental data can be best fitted with a thermally activated stochastic multiple-site hopping process, whereas at high temperatures around room temperature nearest-neighbor hops dominate. Unfortunately, these models [44] do not allow any distinction between different local transport mechanisms (tunneling or hopping) or between the chemical nature of the sites (e.g., energy levels in atoms, molecules, clusters, ligand shells, aggregates of clusters, or metal particles). Hence, no principal difference was found between different cluster sizes or between the comparative substances.

With respect to the application of single ligand-stabilized nanoparticles or collectives of them in SE, the authors reported temperature-dependent impedance measurements to explain or to predict local microscopic behavior. The experiments were performed on different types of ligand-stabilized clusters and have been conducted in the high-temperature range from ambient temperatures up to the respective limit of chemical stability from 253 to 333 K [7, 8, 15, 17, 107, 108].

The samples investigated by this method were pressed into disks with controlled high pressure in steps to maximum 1 GPa. Well-prepared disks revealed a gravimetrical defined density of more than 90% of the theoretical closest sphere packing of the spherical particles. By redissolution in appropriate solvents, chemical and spectroscopic analysis, and STM [19], it was verified that the protecting ligand shells were not destroyed and that the metal cores did not reveal any noticeable aggregation via coalescence.

Impedance measurements on these highly compressed, close-packed samples of ligand-stabilized Au_{55} clusters reveal in every case two relaxation domains in the kilohertz or megahertz region caused by coupled processes with macroscopic relaxation times. In contrast, samples diluted with unpolar polystyrene did not show either relaxation process.

The most striking feature observed for all samples investigated was the appearance of a Debye-like relaxation as well as a Cole–Cole-like relaxation, both in the low-frequency range. Both processes, which could be resolved from the spectra by mathematical fitting of a circuit equivalent consisting of a Debye R, C link and a Cole–Cole R, CPE link, are thermally activated and follow the Arrhenius relationship, where the conductivity is $\sigma \sim \exp(-E_A/k_BT)$. It should be pointed out here that the same experimental evidence of

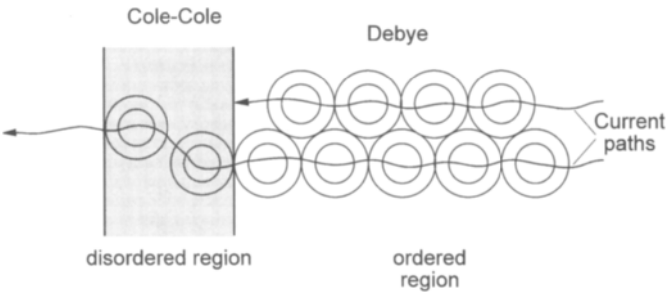


Fig. 27. Illustration of ordered and disordered regions of a compact cluster sample. While the ordered region gives a Debye response, the Cole–Cole element reflects the disordered regions with packing defects.

simple thermal activation has been observed in self-assembled two- and three-dimensional nanoparticle networks [40, 43, 45].

Taking into account structural details such as packing defects or the formation of superclusters, that is, superstructures consisting of several clusters in crystalline order, the authors applied a well-established physical model to a cluster solid with an inhomogeneous partially disordered system. To describe the charge transport and to explain both low-frequency relaxations, they used the so-called brick-layer model [150]. Whereas the Cole–Cole process was interpreted as an "intercluster" process resulting from the transport of electrons between nearest-neighboring clusters by consecutive transitions, the Debye-like process was identified as an "intracluster" process, which denotes electron transport in a band structure of cluster superstructures (see Fig. 27).

The existence of the latter has been proved by STM investigations on the cluster pellets used for impedance measurements. The topography of the pellet surface showed a dense packing of the clusters with inclusions of such superstructures which have been identified to be superclusters consisting mainly of 13 Au_{55} clusters in a crystalline arrangement. In addition, 13-member "superclusters" of 6-nm diameter have been identified to be the building blocks of a "quantum wire," as shown in Section 3.3.2.

The main advantage of the performance of temperature-dependent impedance measurements reveals that the microscopic properties of the nanoparticles could be deduced from two different measured quantities. From the temperature dependence of the conductivity of the Cole–Cole process, the height of the barrier between clusters in the disordered regions of the samples could be determined. Transferred into the "language" of SET, the activation energy is directly connected to the charging energy of two attached clusters along a current path through the sample, as it reflects the energy that has to be overcome to transfer a single electron between two initially neutral clusters and to create a charged pair. In the "language" of chemistry, this is so-called "disproportionation." In this situation, the total dot capacitance is equivalent to the dot-to-dot capacitance of two attached clusters, while the neighboring clusters in a disordered hemisphere have a minor influence. Because the activation energy E_A, which is assumed to be equivalent to the charging energy E_C, is for all Au_{55} cluster samples between 0.15 and 0.19 eV, the dot-to-dot capacitance is in the range of $1–5 \times 10^{-18}$ F or less, deduced from a simple electrostatic approach. This value shows that the transport mechanism between the clusters even up to room temperature may be attributed to an SET mechanism. In accordance with this, Brust et al. [40], Andres et al. [43], and Terrill et al. [42] deduced single-particle properties in three-dimensional arrangements of gold nanoparticles from temperature-dependent dc measurements.

The second quantity obtained from impedance measurements was the capacitance of the Debye process. Because of its attribution to a charge transport and polarization process inside crystalline-ordered grains of nanoparticle arrangements, the total or macroscopic capacitance C_{macro} could be assumed to be constituted from a three-dimensional network

of microscopic capacitors with capacitance C_{micro}, each reflecting the capacitance of a single nanoparticle in a close sphere packing according to Kirchhoff's laws. Following this argument, the "intracluster" process, which is more precisely an "intra"-ordered cluster region process, reflects the single-particle capacitance C_{micro} of a $Au_{55}(PPh_3)_{12}Cl_6$ cluster even in the same range mentioned previously, that is, $1–5 \times 10^{-18}$ F.

Because the charge transport is attributed to consecutive single-electron transitions between attached clusters along single or multiple current paths, the quantity of the microscopic capacitance C_{micro} allows the calculation of the characteristic time constant for the singular process τ_{micro} from the estimation of the tunneling resistance R_T between the nanoparticles, when an electron passes the potential barrier.

According to Kirchhoff's laws,

$$C_{macro} = |n|C_{micro}$$

Thus,

$$\tau_{macro} = R_T \cdot C_{macro} = R_T \cdot |n|C_{micro}$$

Because $|n| = 10^5$ in the samples investigated and the macroscopic relaxation time τ_{macro} is measured in the range of some 100 kHz, R_T is approximately 100 MΩ. This rough estimation allows the calculation of τ_{micro} according to

$$\tau_{micro} = R_T \cdot C_{micro}$$

that is, 10^{-12} s, where this quantity denotes the so-called recharging time. Correspondingly, τ_{macro} is the operating time needed to transport an electron from one electrode to the other, while passing $|n|$ junctions in series.

4.4.2. Tailoring of the Charging Energy

The chemical tailoring of the charging energy in three-dimensional arrangements of metallic nanoparticles has been reported in recent work [40, 45]. The basic idea is to stretch the close cluster package in comparison to the densest sphere packing described before and thereby increase the interparticle spacing. This should lead to an increase of the charging energy, that is, a decrease of the electrical capacitance between the clusters. Following this idea, Simon et al. [45] reported the insertion of bifunctional amines into arrangements of $Pd_{561}phen_{36}O_{200}$ clusters. The spacing started with deoxygenation of the cluster by hydrogen in a water–pyridine solution at room temperature with the formation of H_2O_2. The oxygen-free cluster $Pd_{561}phen_{30}$ then offers active surface sites that can be coordinated by the NH_2 groups of 4,4′-diamino-1,2-diphenyl ethane, which was used as the spacer molecule. As the naked cluster surface sites are oriented in all directions, the spacing procedure leads to an insoluble precipitate with three-dimensional cluster linkage. This network exhibits an increased interparticle spacing with respect to the closest sphere packing of the unmodified cluster, as in the pressed pellets described previously.

The charging energy E_C is dependent on the interparticle capacitance C and can be determined directly from the temperature dependence of the dc conductivity of the cluster arrangements. Earlier investigations on the electrical properties of these clusters have shown that even at high temperatures thermally activated electron hops instead of hops of variable range dominate the charge transport through the samples [44]. This was confirmed in [45] because the activated behavior over a temperature range of 80 to 300 K was found. Figure 28 shows the Arrhenius plot, in which the slope of the straight lines corresponds to the activation energy of the charge transport, that is, the charging energy of the particles in the three-dimensional arrangement.

Whereas the close packing of the cluster material shows an activation energy of 0.02 eV, the insertion of the spacer molecules increases the value up to 0.05 eV. Correspondingly, the capacitance decreased from 4.0×10^{-18} F initially to 1.6×10^{-18} F. The specific

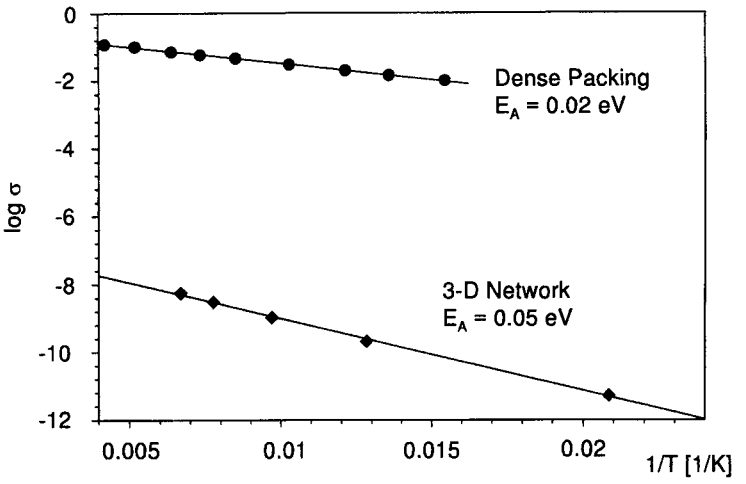


Fig. 28. Arrhenius plot of $Pd_{561}phen_{36}O_{200}$ cluster in (a) densest arrangement and (b) a stretched packing due to insertion of spacer molecules.

conductivity follows the same trend as might be expected because of the decrease of the volume fraction of the metal in the volume of the sample. Comparable results were found by Brust et al. [40], who investigated 2.2- and 8.8-nm colloidal gold nanoparticles with interconnecting alkyldithiols of different length.

These examples show that the electrical capacitance between metal nanoparticles in a three-dimensional arrangement and thus the charging energy can be tailored chemically by the use of bifunctional spacer molecules, and thus prove the chemical control of the physical properties of cluster arrangements, which contributes to an understanding of the structure–property relationships in nanomaterials.

5. WORKING PRINCIPLES OF SINGLE-ELECTRON TUNNELING DEVICES AND THE USE OF CHEMICALLY BUILT NANOPARTICLES

5.1. Single-Electron Tunneling Devices and Circuits

5.1.1. Metal-Based Single-Electron Transistor

The simplest circuit that reveals the peculiarities of single-electron tunneling comprises only one Coulomb island with two leads (electrodes) attached to it. In other words, this geometry presents the double tunnel junction system. If besides these parts one attaches a so-called gate electrode, which is capacitively coupled to the island, then such a system has a control and this geometry is often called a single-electron transistor (see Fig. 29). Applying a dc voltage to the outer (drain) electrodes of this circuit either may cause sequential transfer of electrons into and out of the central island or may lead to no charge transport; that is, the transistor remains in a nonconductive state. The result depends on the voltage U applied to the drain electrodes, as well as on the voltage U_g applied to the gate.

Because of the small total capacitance of the island, $C = C_1 + C_2 + C_0 + C_{0'}$ ($C_{1,2}$ are the capacitances of the junctions, which, for the sake of simplicity, we shall assume to be equal, $C_1 = C_2 = C_J$, while C_0, the capacitance with respect to the gate, and $C_{0'}$, the capacitance of other remote conducting objects, will both be assumed to be much less than C_J), the island has a large Coulomb energy, and $E_C \gg k_B T$. The total change of energy of the system ΔE while one electron is tunneling in one of the junctions consists of

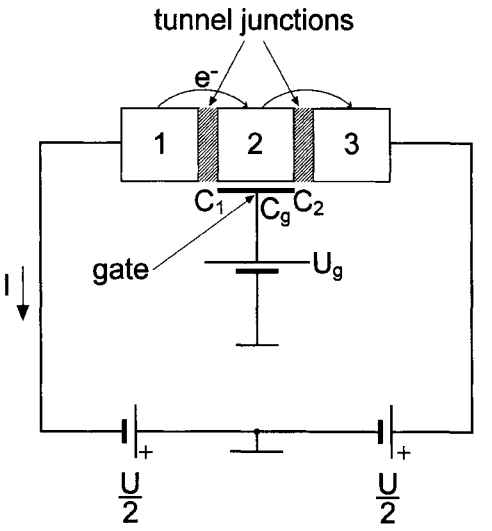


Fig. 29. Illustration of a simple single-electron transistor, consisting of a two-junction arrangement and a gate electrode coupled capacitively to the central island.

the charging energy of the island itself as well as of the work done by the voltage source. For $U_g = 0$, this is simply expressed by

$$\Delta E = \frac{Q_f^2}{2C} - \frac{Q_i^2}{2C} - qU$$

where Q_i and Q_f are the initial and final charges of the island, respectively, and q is the charge (not necessarily an integer) which passed the drain voltage source. From elementary reasoning, it is clear that if, say, $Q_i = 0$ and $Q_f = e$, then $q \pm e/2$ (depending on the direction of electron tunneling) and, therefore, $\Delta E = e^2/2C \pm eU/2$. This means that $-e/C$, the change of energy, is always positive when $-e/C \leqslant U \leqslant e/C$. Hence, electron tunneling could only increase the energy of the system and this transition does not occur if the system cannot "borrow" some energy from its environment, when the temperature is assumed to be low enough. Therefore, there is a Coulombically blocked state of the single-electron transistor when the voltage U is within the interval given previously and U_g is zero. Outside this range, the device conducts current by means of sequential tunneling of electrons.

When the gate voltage U_g is finite, the calculation of the energy change resulting from one electron tunneling gives another value, because of the additional polarization of the island electrostatically induced by the gate. The result of this consideration is illustrated in Figure 30, where the U versus U_g diagram of the Coulomb blockade is shown. The diagram reflects an interesting feature; it is periodic with respect to the voltage U_g with a period of e/C_0. This results from the fact that every new "portion" of the gate voltage of e/C_0 is compensated by one extra electron on the island and it returns to the previous conditions for electron tunneling. Therefore, at constant bias U, the current through the device is alternatively turning on and off with a sweep of voltage U_g.

The behavior of the transistor outside the Coulomb blockade region also shows the single-electron peculiarities, especially for the case of a highly asymmetrical junction, where $R_1 \gg R_2$ and $C_1 \gg C_2$. In Figure 31, one can see the $I(U)$ characteristics with a steplike structure fading with decreasing U. This so-called Coulomb "staircase" results from the fact that an increase in U increases the number of channels for tunneling in a steplike manner, allowing an increasingly larger number of electrons to be present on the island. Another manifestation of charging effects in the SE transistor is the offset of the linear asymptotes by e/C.

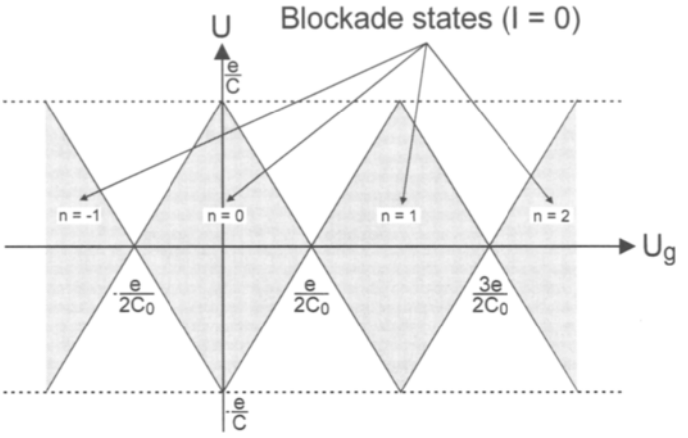


Fig. 30. Periodic rhomb pattern showing the Coulomb blockade region on the plane of voltages U and U_g. The value of the number n is the number of extra electrons trapped in the island in the blocked state.

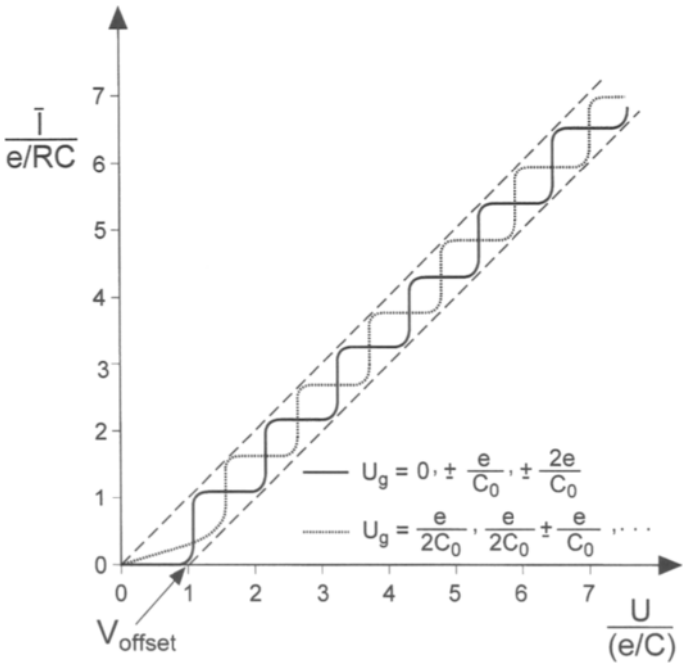


Fig. 31. Dependence of the time-averaged current I versus U for asymmetrical single-electron transistor.

The dependence of the transistor current on the gate voltage opens up the opportunity to fabricate a sensitive device that measures directly either an electric charge on the island or a charge induced on the island by the charges collected at the gate, that is, a highly sensitive electrometer. The sensitivity of such an electrometer, which has already been reached in practice, is on the level of 10^{-4}–10^{-5} parts of electronic charge and thus exceeds the charge sensitivity of conventional devices by several orders of magnitude.

5.1.2. Traps and Turnstiles

The idea of effectively controling the tunneling current by means of electrostatic gating has been developed further in multiisland systems and has opened new possibilities for SE. An

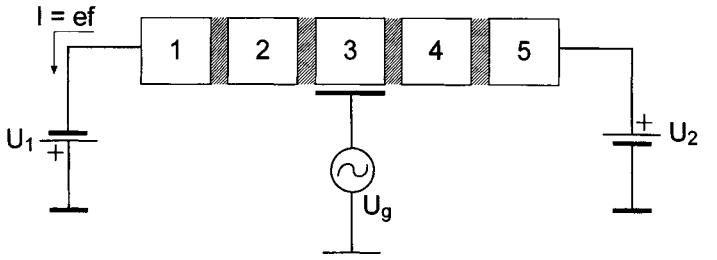


Fig. 32. Four-junction (three-island) single-electron turnstile. The alternating voltage applied to the gate is $U_g = U_{amp}\sin(\omega t)$ and at its rise an electron makes a transition. The electron remains trapped in the central island until the negative half-wave of U_g is diminished.

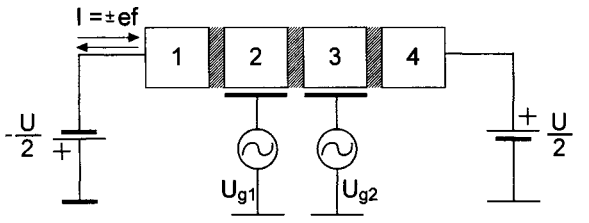


Fig. 33. Three-junction single-electron pump. The two sinus-waveform voltages U_{g1} and U_{g2} have the phase difference, whose value can determine at small bias U the direction of single-electron current $I = ev_{SET}$.

example of such a circuit is the so-called single-electron turnstile. In its simplest version, it consists of three islands aligned between two outer electrodes, as shown in Figure 32, and can be considered as two double junctions connected in series. The very central island of this chain is supplied with the capacitively connected gate, which controls electron tunneling in all four junctions. However, in contrast to the operation of the single-electron transistor, the additional two islands allow the realization of this condition. The central island works as a controllable trap for electrons, endowing the turnstile with its unique properties.

If the entire chain of islands is initially blocked for small bias voltage U and the gate voltage U_g is swept, the central island first attracts one electron from the left arm. This is possible because the Coulomb blockade in the left double junction is lifted as a result of the gate voltage applied. The blockade is automatically restored after that tunneling even when U_g is increased. Hereby the electron remains trapped in the central island. Then if the voltage U_g diminishes the blockade in the right double junction, the electron sequentially passes two right junctions, completing its course through the whole array. Hence, if one applies an alternating voltage, for example, sinusoidal, to the gate of the turnstile, it should transfer exactly one electron during a period of the signal.

The idea of the turnstile has been developed further in the single-electron pump device shown in Figure 33. This is a two-island (or, in other terms, a three-junction) circuit that is supplied by two sinusoidal signals applied via two gates to both of the islands. In contrast to a turnstile, this circuit can operate even at zero drain voltage U. The phase difference between these signals is 90° and during one cycle exactly one electron sequentially tunnels from the left drain electrode to the left and then to the right island and, finally, to the right drain. Such pumping of individual electrons has been likened to the mechanical pumping of a liquid. Moreover, in a similar manner, the direction of transferred matter depends on which of two oscillations is ahead of another, so the direction is changed by changing the phase from $+90°$ to $-90°$.

Frequency-controlled single-electron tunneling opens an opportunity to maintain a dc current in a lead, the value of which is determined by the frequency of an ac signal by means of the fundamental relation $I = ev_{SET}$. This is of great importance for modern quantum metrology, which could then determine the unit of dc current via the unit of frequency using one universal constant, that is, the electronic charge. In that case, taking into account the very high accuracy of the atomic standard of frequency, the accuracy of this current standard would be basically limited by the accuracy of the electron transfer cycle. At present, it is on the level of parts of 1% for currents of several picoamperes, caused by a number of factors that make the operation of the devices far from being as ideal as described previously. Among these factors are (i) the influence of thermal fluctuations, (ii) uncontrollable higher-order tunneling of an electron through all the junctions of the circuit at the same time, and (iii) rare intermittence of tunneling events in spite of their statistical character. The solution of this problem, which necessarily involves a decrease in structure size and thus an increase of the Coulomb charging energy, seems clear when taking chemical nanostructures into consideration. Accordingly, at present, ligand-stabilized metal nanoparticles with this well-defined structure, seem to be the most promising candidates.

5.2. Metal Nanoparticles as Elements for Single-Electron Devices

As discussed previously, the progress of lithographic methods guided by the miniaturization of conventional electronic circuits fails to satisfy the requirements arising from single electronics even operating at room temperature, a requirement that extends to a size range of a few nanometers or less [7–10].

Consequently, the use of ligand-stabilized metal nanoparticles, as it was supposed by the authors, should solve the problem and embody suitable building blocks for a new nanoscale architecture. Furthermore, in general, new techniques for a defined organization of such nanoparticles have to be developed to build up single-electron circuits of different complexity. So far, it has become evident that utilizing the principles of self-assembly by controlling intermolecular interaction, which is one of the main interests of supermolecular chemistry, will be a key feature in this development.

In addition, the relatively simple theory of tunneling successfully applied to larger SE objects might now be applied with much caution and should be certainly revised for nanoparticles, where quantum size effects appear for the reasons explained in Section 1.1.3. In particular, depending on the cluster type and its bonding of the nanoparticles, the standard diffusive single-electron transport that arises from the particle nature of electrons could be converted into ballistic transport or even into resonant tunneling reflecting the wave nature of electrons. These could drastically modify the Coulomb blockade, but still leave the important role of Coulomb repulsion.

Summarizing these problems, it should be noted that transition to nanoparticle SE promises incredibly high density of the elements on a chip, which is extremely important for computer-like circuits [138]. Thus, assuming a "three-nanometer design rule" (the nanoparticle size including its ligand shell) and the necessity of 10 by 10 clusters for every reliable gate, then for a two-dimensional architecture the number of gates on a 1-cm^2 chip might be about 10^{11}. The extension of such a friable structure into the third dimension could result in an even larger number of about 10^{16}.

This is a rather conservative estimate based on the traditional paradigm for information processing. On the other hand, for nanoparticle networks, the locally interconnected architecture, such as cellular automata with neural networks, seems to be more adequate. This points out new problems in design and operation principles, the solving of which could lay a bridge to structures on the true atomic scale.

5.2.1. Mesoscopic Arrays with Nanoparticles and First Devices

It is not the purpose of this review to detail concrete microelectronic circuits. This would exceed the knowledge of the authors, and here the reader's attention should be drawn to other reviews [132, 151–153]. It should be pointed out, however, that most suggestions deal with much larger devices based on semiconductor materials, even though in the last 10 years a general understanding of the fundamental principles of conventional SET junctions between metals has been developed by extensive theoretical and experimental work. Conventional SET junctions show the SET effect only at temperatures near absolute zero and they are much larger than single nanoparticles, which show the SET at room temperature. One example of the smallest subunit of an SE device working at room temperature may be the "smallest switch with electrons" [7].

Such a switch consists of two ligand-stabilized nanoparticles and, in the ideal case, of two $Au_{55}(PPh_3)_{12}Cl_6$ clusters where the ligand shells keep the cluster cores at a distance of 0.7 nm, a barrier that can be passed by tunneling (see also Fig. 5). The electrical capacitance of this junction determines the Coulomb or switching offset as well as the temperature at which this quantum device can be used. Regarding this, it becomes clear that the fundamental principle of SET can be directly transferred to a digital technology developing more complex devices, where the information can be transported or stored by means of one electron (at a defined time and a special place) in a single nanoparticle [4].

The most detailed and concrete work utilizing the SET effect has been done in a so-called SET transistor based an metal nanoparticles. In general, this simple circuit reveals the peculiarities of SE because it includes the usual three junctions but, at least, only one metallic particle. Most recently, Sato et al. [10] reported detailed electrical characteristics of the first SET transistor utilizing charging effects on single chemically tailored gold nanoparticles. They developed a device as a hybrid system; that is, it was fabricated by means of metal electrodes formed by electron beam lithography to which a self-assembled chain of colloidal gold particles was connected. The interparticle connection as well as the connection to the electrodes results from a linkage by bifunctional organic molecules, which present the tunnel barriers, and the authors clearly demonstrated that the self-assembling nature of the gold nanoparticles helped in overcoming the size limitations of lithography.

The fabrication is described as follows and is illustrated schematically in Figure 34: Gold nanoparticles with an average diameter of 10 nm were deposited on a thermally grown SiO_2 surface on a Si substrate by using alkanesiloxane molecules as an adhesion agent. After formation of the Si–O–Si bond by thermal treatment, terminal amino groups of the silane attach to gold nanoparticles in an appropriate gold particle solution to form a submonolayer. Because the gold particles were obtained by the citrate method [154], they

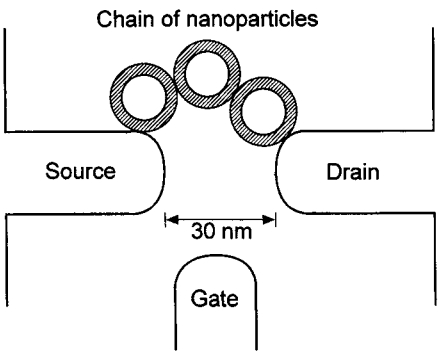


Fig. 34. SET transistor based on self-assembling of gold nanoparticles on electrodes fabricated by electron beam epitaxy. (Source: Adapted from [10].)

retain their ionic charges on the surface. Therefore, the nanoparticle deposition stopped automatically before it reached a close-packing density leaving an interparticle spacing of 10–50 nm. After the submonolayer coating, 1,6-hexanedithiol was added to interconnect the particles with a more defined spacing, as described before in Sections 2 and 3. Then a second immersion into a gold particle solution increased the coverage where, again, the dithiol molecules maintained the distance between the particles. While the second layer filled the gaps between the particles of the first layer, however, chains of 2–4 particles were formed. When this procedure was performed on a SiO_2 substrate, equipped with source, drain, and gate metal electrodes defined by electron beam lithography, the particles formed a chain of at least three particles bridging the gap between the outer driving electrodes.

Because all steps of this procedure could not be controlled in detail, the number of nanoparticles in the bridge chain differed from device to device, but, in any case, electron conduction dominated by single-electron charging indicated by a Coulomb gap could be observed up to 77 K, whereas the nonlinearity is smeared out at room temperature. Simulation and fitting of the data with a model circuit for a three-dot (four-junction) SET transistor indicated that the capacitance of all junctions in the chain was $1.8–2 \times 10^{-18}$ F and the calculated Coulomb gap was in reasonably good agreement with the value of 150 mV obtained from the measured $I(U)$ characteristic, which was systematically squeezed, when a gate voltage of $-0.4–0.4$ V was applied. The plot of the current through the device was clearly dependent on the gate voltage showing the typical current oscillations, proving the desired function of the single-electron transistor. According to a Green's function–based method, which was proposed by Samanta et al. [155], the transmission function of electrons across the dithiol ligands was calculated from which the resistance R per molecule was obtained by the Landauer formula, $R = (h/2e^2)/T(E_g)$, where $T(E_F)$ is the transmission function, that is, $T \sim \exp[2(mE_g)^{1/2}/\hbar]$. Assuming a barrier height $E_g \simeq 2.8$ in the dithiol molecules, the resulting resistance was estimated to be $R \simeq 30$ GΩ.

Instead of chemically tailored metal nanoparticles, however, even cluster-like molecules of the same size seem to be suitable building blocks in the fabrication of SET devices. Soldatov et al. [156] reported the fabrication of an SET transistor on the base of a carborane cluster, which is also a spherical-shaped molecule, working at room temperature (see Fig. 35).

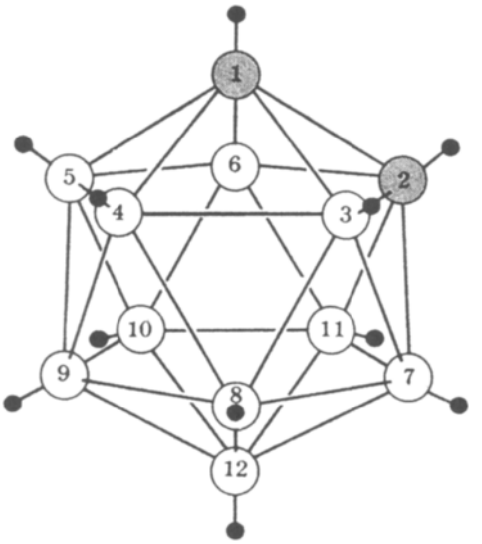


Fig. 35. Closo-1,2-$C_2B_{10}H_{12}$ (o-carborane), which was used as the central electrode in the experiment described. The organic substituents are left out for simplification.

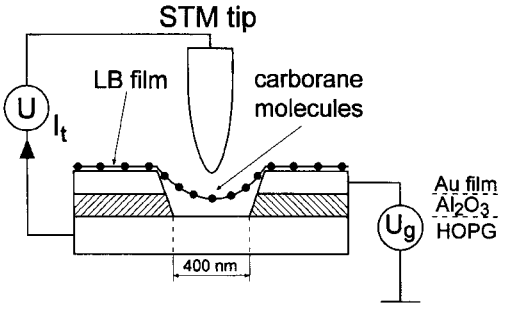


Fig. 36. SET transistor based on carborane molecules in an LB film on a gold electrode array deposited on graphite (HOPG). (Source: Adapted from [156].)

They deposited LB monolayers of the carborane 1,7-$(CH_3)_2$-1,2-$C_2B_{10}H_9Tl$ $(OCOCF_3)_2$ in a mixture with stearic acid dissolved in tetrahydrofuran on a preformed gate electrode system (see Fig. 36). The electrode system was formed by a conventional electron lithography technique and consisted of thin and narrow bilayer strips, where 50-nm gold on 50-nm Al_2O_3 was deposited on a graphite substrate (HOPG) with a strip width and distance of approximately 400 nm. The strips were connected in series and had the same potential. The electron transport through the layers was probed by an STM tip at room temperature. When the tip was positioned above the single carborane molecules, a transistor, consisting of a double junction (tip/molecule/HOPG) and closely situated gate electrodes (Au strips), was realized. In this arrangement, the junction capacitance was estimated to be 1×10^{-19} F.

In the discussion of their results, the authors pointed out that the explanation of the experimental data they obtained has to involve the discreteness of the electronic structure of the carborane molecules, which act as the central electrode. This was already emphasized in Section 4.1.2 and, furthermore, we will see in Section 5.3 that even the charge relaxation in the nanoparticles or molecular particles becomes a relevant quantity.

5.3. Time Scales of Recharging, Charge Relaxation, and Tunneling

Apart from the fundamental questions in the quantum mechanical (QM) concept of time and concepts of tunneling times, which are discussed in detail by Gasparian et al. [157], practical questions arise when time-related quantities such as current determine the performance of microelectronic devices, as is the case in SE.

Before dealing with time in these ultimate structures, we have to recall some facts from Section 1.1.2 about SET: SE deals with small amounts of excess electrons on islands changing their distribution over the islands in time in a desirable way. In spite of relatively complex rigorous quantum mechanical considerations, quantitatively this situation can be clearly formulated using a characteristic of the tunneling junction such as its tunneling resistance R_T, which necessarily must be larger than the so-called resistance quantum R_q. Then electrons in the island can be considered to be localized and classical electrodynamics can be applied, although their number is undergoing thermodynamic fluctuations as does every statistical variable.

Second, to minimize these fluctuations and, consequently, to make the exchange of electrons controllable, the Coulomb energy of an extra charge $E_c = e^2/2C$ has to be sufficiently larger than k_BT. Thus, SET at ambient temperature can only be achieved with capacitances between 10^{-18} and 10^{-19} F, which can be realized by the use of sub-10-nm chemical nanoparticles.

If the preceding conditions are met, the transfer of single electrons can be realized by means of QM tunneling if the probability of such tunneling depends on current biasing and driving voltages applied to the circuit.

Starting outside the Coulomb blockade region, time-dependent recharging of the junction occurs with $Q = \int j_y\,dt - Q_T$, where the first term is the charge supplied by a current source j_y and the second term is the charge transferred through the barrier junction by tunneling, which is regulated by the tunneling rate. Because in metallic tunnel junctions a tunneling time of 10^{-15} s is very short, external recharging of the junction in time-correlated SET will be periodic with the so-called single-electron tunneling frequency $\nu_{SET} = j_y/e$. The smaller the current, the more regular are the SET oscillations, but generally with an inherent noise component because of the stochastic nature of the tunneling process.

Although charge transport through an SET device is determined by the transit time τ_T [158], which refers to the "external" system around the single tunnel junction, supplying its current bias j_y, the tunnel junction itself is characterized by "recharging time" $\tau_r = R_T \cdot C$. Depending on the approach to recharging time, it may be defined

- either as a "decay time" of an excess charge that appears on one of the barriers after a fast tunneling step (with finite but ultrashort traversal time on the order of 10^{-15} s), forming a polaron-like state together with the "hole" it left on the other side,
- or as a "relaxation time" that the junction system needs to return to equilibrum, ready for a new cycle of external recharging.

Thus, recharging time and the much faster tunneling time are additive in SET systems.

As pointed out in Section 4.1.1, in nanostructured arrays with the smallest possible conventional chip architecture, the single tunnel junction comes up to a tunneling resistance of $R_T \approx 10^5\ \Omega$ and with a barrier length of $L \approx 1$–2 nm a capacitance $C \geqslant 10^{-16}$ F is feasible. Thus, the recharging time with $\tau \approx 10^{-11}$ s is still much larger than the tunneling time τ_T. An intermediate time scale is the "uncertainty time" $\tau = R_q \cdot C$, where R_q is the resistance quantum. In the theory of SET, a clear separation of time scales $\tau_T \ll \tau_q \ll \tau_r$ is assumed, where the first inequality states that the tunneling time is negligible and the second one states the classical nature of recharging by single charge tunneling [1].

With the availability of chemically tailored ligand-stabilized nanoparticles, the junction capacitance and with it the Coulomb barrier $e^2/2C$ can be controlled by the thickness of the ligand shell and by the diameter of the metallic (or semiconductor) core and can roughly be estimated by geometrical considerations. More complicated is the estimation or the measurement of the junction resistance R, which may have very small values on the order of magnitude of quantum resistance R_q up to typical tunneling resistances R_T.

With respect to the small capacitances of $C = 10^{-19}$ F, which can be realized by use of chemical sub-10-nm nanostructures, we look again to the relevant time scales:

- The tunneling time τ_T from theory, as mentioned previously, is
$$\tau_T \approx 10^{-15}\ \text{s}$$
- The recharging time $\tau_r = R_T \cdot C$, again, may be the longest time. However, for nanoparticles with very low $R_T \leqslant 10^5\ \Omega$, we get
$$\tau_r \leqslant 10^{-14}\ \text{s}$$
- The "uncertainty time" $\tau_q = R_q \cdot C = \hbar C/e^2$ associated with the Coulomb energy, a quantity for the electron fluctuations of any electrons involved in the recharging and tunneling mechanism, is
$$\tau_q \approx 10^{-14}\ \text{s}.$$

Now, with approximately 10^{-14}–10^{-15} s, all three times are in the same order of magnitude with $\tau_r \approx \tau_q \approx \tau_T$. For nanoparticle SET junctions the question arises which time scale is relevant for the charge transport, that is, the tunneling rates through an array. This

is not only of theoretical interest but also very important for practical application of chemically tailored nanoparticles in SET devices. Because, if we disregard the transit time of the environment, for simplicity, within an array of nanoparticles, we should know whether, and in which time, a single-electron signal starting at $t = 0$ arrives at a receiver, if this receiver is one nearest-neighboring nanoparticle unit.

We recall the suggestions of Averin and Korotkov [25], who emphasized that the discrete energy spectrum of sub-10-nm nanoparticles needs an extension of the "orthodox theory" of SET, particularly in view of possible applications in molecular electronics (see Section 4.1.2). Because just a little is known about the energy relaxation rate in small metallic particles, it seems reasonable to approximate the bulk value for metals, that is, on the order of 10^{12} s^{-1}, which is definitely increasing with decreasing particle size. Affecting the charge distribution on the electrodes or islands of the arrays, it will strongly influence the tunneling (or even recharching) probability.

Of course, the preceding simple considerations are not adequate to replace the still missing theoretical work and analytical calculations of fast charge distribution and of tunneling problems with possible superluminal speed in periodic chemical nanostructures [159–161]. They clearly point out, however, that an ultimate miniaturization, which will bring the future chip architecture to the true atomic scale, will raise new questions concerning the physical limits of miniaturization.

6. APPLICATIONS AND CONCLUDING REMARKS

According to the present state of knowledge, chemically tailored nanoparticles in the sub-10-nm range are suitable building blocks for SE devices. Their minute size combined with the well-defined insulation barrier, which is determined by the size and nature of the stabilizing ligand shell, opens access to ultrasmall electrical capacitances in the range of 10^{-19} F, a value that cannot be reached by classical techniques such as lithography because of their physical limits. The small capacitance increases the charging energy, thus raising the molecular SE to the level of room temperature.

This opens a broad field of possible applications of these structures. According to the ideas that have already been developed for physically fabricated nanostructures and that are restricted to an operation temperature in the millikelvin range, the following applications seem to be most probable.

Fabrication of a current standard using with the elementary charge e only one universal constant. This is of major imprtance for modern quantum metrology and could close the so-called "quantum metrology triangle," enabling one to find possible quantum-electrodynamical corrections to the corresponding fundamental relations among frequency, current, and voltage [4].

The most remarkable opportunities for SE will occur in the field of digital circuits. We believe that the unique properties of chemical nanostructures can develop a new single electronics. According to Averin and Likharev [138], it will provide the first available realistic physical basis for devices that perform digital information processing on the molecular scale. Further applications might include high-frequency devices or cellular automata [162].

In spite of these promising ideas, which imply the use of the chemical nanostructure as a "minimum working unit," one has to be aware that the utilization of the minute size requires generally new and comprehensive fabrication and addressing techniques. An extension of the present-day technologies to smaller structures or the development of techniques that treat chemical nanostructures with conventional technologies [163] will not reach the molecular size scale and, therefore, will waste many of the advantages of these structures. However, even in arrays that are preformed by lithographic techniques, the self-assembling nature of chemical nanostructures helps to overcome the size limitation of the present-day technology.

Besides SE, the following applications should be mentioned:

- Electrochromic arrays [8]
- Photovoltaic devices [107, 108]
- Quantum lasers [164]
- Magnetorisistive materials
- Nonlinear optics [78]

These examples might show that the use of chemically tailored nanoparticles for SE devices promote the strong claim of Averin and Likharev [138] that "single charge tunneling is the only evident basis for future nanoelectronics."

Acknowledgments

This review was completed during a current national research project founded by the Bundesminister für Bildung, Wissenschaft und Forschung (BMBF) under Contract 03N 1012A7 which is gratefully acknowledged. We thank A. Thöneböhn and J. Jockel for all their extensive work in typesetting the manuscript and preparing the graphs.

References

1. M. H. Devoret and H. Grabert, in "Single Charge Tunneling Coulomb Blockade Phenomena in Nanostructures," (H. Grabert and M. H. Devoret, eds.), Nato ASI Series, Vol. 294, pp. 1–20. Plenum Press, New York, 1992.
2. I. Giaever and H. R. Zeller, *Phys. Rev. Lett.* 20, 1504 (1968).
3. I. Giaever, *Phys. Rev.* 181, 789 (1969).
4. K. K. Likharev, *IBM J. Res. Develop.* 32, 144 (1988).
5. L. S. Kuzmin and K. K. Likharev, *Jpn. J. Appl. Phys.* 26, 1387 (1987).
6. C. J. Geerlings, V. F. Anderegg, P. S. M. Holweg, J. E. Mooig, H. Portier, D. Esteve, C. Urbania, and M. H. Devorit, *Phys. Rev. Lett.* 64, 2691 (1990).
7. G. Schön and U. Simon, *Colloid Polym. Sci.* 273, 101 (1995).
8. G. Schön and U. Simon, *Colloid Polym. Sci.* 273, 202 (1995).
9. K. K. Licharev and A. Korotkov, in "Proceedings of the 190th Electrochemical Society," San Antonio, TX, 1996, Vol. 96, Chap. 2, p. 563.
10. T. Sato, H. Ahmed, D. Brown, and B. F. H. Johnson, *J. Appl. Phys.* 82, 696 (1997).
11. G. Schmid, *Chem. Rev.* 92, 1709 (1992).
12. P. Marquardt, L. Börngen, G. Nimtz, H. Gleiter, R. Sonnberger, and J. Zhu, *Phys. Lett. A* 114, 39 (1986).
13. G. Nimtz, P. Marquardt, and H. Gleiter, *J. Cryst. Growth* 86, 66 (1988).
14. P. Marquardt and G. Nimtz, *Festkörperprobleme* 29, 317 (1989).
15. U. Simon, G. Schön, and G. Schmid, *Angew. Chem., Int. Ed. Engl.* 32, 250 (1993).
16. H. Weller, *Angew. Chem.* 105, 43 (1993).
17. D. Fenske, G. Longoni, and G. Schmid, in "Clusters and Colloids," (G. Schmid, ed.). VCH, Weinheim, Germany, 1994.
18. O. D. Häberlen, S.-C. Chung, and N. Rösch, *Ber. Bunsen-Ges. Phys. Chem.* 98, 882 (1994).
19. R. Houbertz, T. Feigenspan, F. Mielke, U. Memmert, U. Hartmann, U. Simon, G. Schön, and G. Schmid, *Europhys. Lett.* 28, 641 (1994).
20. H. van Kempen, J. G. A. Dubois, J. W. Gerritsen, and G. Schmid, *Physica B* 204, 51 (1995).
21. W. P. Halperin, *Rev. Mod. Phys.* 58, 533 (1986).
22. K. Kimura, *Z. Phys. D* 11, 327 (1989).
23. R. A. Millikan, in, for example, "Lehrbuch der Physikalischen Chemie," (G. Wedler, ed.). VCH, Weinheim, Germany, 1982.
24. K. Fuchs, *Proc. Cambridge Philos. Soc.* 34, 100 (1938).
25. D. V. Averin and A. N. Korotkov, *J. Low Temp. Phys.* 3/4, 173 (1990).
26. O. Echt, K. Sattler, and E. Recknagel, *Phys. Rev. Lett.* 47, 1127 (1981).
27. G. A. Ozin and S. A. Mitchell, *Angew. Chem.* 95, 706 (1983).
28. A. Henglein and J. Lille, *J. Phys. Chem.* 85, 1246 (1981).
29. A. Henglein, M. Guttierez, E. Janata, and B. G. Ershov, *J. Phys. Chem.* 96, 4598 (1992).
30. J. L. Marignier, J. Belloni, M. O. Decourt, and J. P. Chevalier, *Nature* 317, 344 (1985).
31. B. G. Ershov, E. Janata, M. Michaelis, and A. Henglein, *J. Phys. Chem.* 95, 8996 (1991).

32. G. Schmid, R. Boese, R. Pfeil, F. Bandermann, S. Meyer, G. H. M.Calis, and J. W. A. van der Velden, *Chem. Ber.* 114, 3634 (1981).
33. G. Schmid, B. Morun, and J.-O. Malm, *Angew. Chem., Int. Ed. Engl.* 28, 778 (1989).
34. G. Schmid and A. Lehnert, *Angew. Chem., Int. Ed. Engl.* 28, 780 (1989).
35. G. Schmid, A. Lehnert, U. Kreibig, Z. Adamczyk, and P. Belouschek, *Z. Naturforsch., B* 45, 989 (1990).
36. G. Schmid, A. Lehnert, J.-O. Malm, and J.-O. Bovin, *Angew. Chem.* 103, 852 (1991); *Angew. Chem., Int. Ed. Engl.* 30, 874 (1991).
37. R. L. Whetten, J. T. Khoury, M. M. Alvarez, S. Murthy, I. Vezmar, Z. L. Wang, P. W. Stephens, Ch. L. Cleveland, W. D. Luedtke, and U. Landman, *Adv. Mater.* 8, 428 (1996).
38. H. Weller, *Angew. Chem.* 108, 1159 (1996).
39. L. E. Brus, *J. Chem. Phys.* 79, 5566 (1983).
40. M. Brust, D. Bethell, D. J. Schiffrin, and Ch. J. Kiely, *Adv. Mater.* 7, 795 (1995).
41. J. I. Henderson, S. Feng, G. M. Ferrence, Th. Bein, and C. P. Kubiak, *Inorg. Chim. Acta* 242, 115 (1996).
42. R. H. Terrill, T. A. Postlethwaite, Ch. Chen, Ch.-D. Poon, G. Wignall, J. D. Londono, R. Superfine, M. Falvo, Ch. S. Johnson, Jr., E. T. Samulski, and R. W. Murray, *J. Am. Chem. Soc.* 117, 12537 (1995).
43. R. P. Andres, J. D. Bielefeld, J. I. Henderson, D. B. Janes, V. R. Kolagunta, C. P. Kubiak, W. J. Mahoney, and R. G. Osifchin, *Science* 273, 1690 (1996).
44. M. P. J. van Staveren, H. B. Brom, and L. J. de Jongh, *Phys. Rep.* 208, 1 (1991).
45. U. Simon, R. Flesch, H. Wiggers, G. Schön, and G. Schmid, *J. Mater. Chem.* 8, 517 (1998).
46. M. T. Reetz, St. A. Quaiser, M. Winter, J. A. Becker, R. Schäfer, and U. Stimming, *Angew. Chem.* 108, 2228 (1996).
47. D. L. Klein, P. L. McEuen, J. E. B. Katari, R. Roth, and A. P. Alivisatos, *Appl. Phys. Lett.* 68, 2574 (1996).
48. M. Ohtaki, K. Oda, K. Eguchi, and H. Arai, *J. Chem. Soc., Chem. Commun.* 1209 (1996).
49. T. Abe, Y. Tachibana, T. Uematsu, and M. Iwamoto, *J. Chem. Soc., Chem. Commun.* 1617 (1995).
50. H. Yoneyama and T. Torimoto, *Adv. Mater.* 7, 492 (1995).
51. Y. Yang, J. Huang, Sh. Liu, and J. Shen, *J. Mater. Chem.* 7, 131 (1997).
52. L. Cusack, R. Rizza, A. Gorelov, and D. Fitzmaurice, *Angew. Chem.* 109, 887 (1997).
53. T. Trinade and P. O'Brien, *Chem. Mater.* 9, 523 (1997).
54. A. P. Alivisatos, *J. Phys. Chem.* 100, 13226 (1996).
55. L. E. Brus, *J. Chem. Phys.* 79, 5566 (1983).
56. C. B. Murray, C. R. Kagan, and M. G. Bawendi, *Science* 270, 1335 (1995).
57. T. Voßmeier, G. Reck, L. Katsikas, E. T. K. Haupt, B. Schulz, and H. Weller, *Science* 267, 1476 (1995).
58. N. Herron, J. C. Calabrese, W. E. Farneth, and Y. Wang, *Science* 259, 1426 (1993).
59. T. Voßmeier, G. Reck, B. Schulz, L. Katsikas, and H. Weller, *J. Am. Chem. Soc.* 117, 12881 (1995).
60. A. A. Demkov and O. F. Sankey, *Chem. Mater.* 8, 1793 (1996).
61. J. F. Corrigan, S. Balter, and D. Fenske, *J. Chem. Soc., Dalton Trans.* 729 (1996).
62. S. Dehnen and D. Fenske, *Angew. Chem., Int. Ed. Engl.* 33, 2287 (1994).
63. D. Fenske and H. Krautscheid, *Angew. Chem., Int. Ed. Engl.* 29, 1452 (1990).
64. D. Fenske and J.-Ch. Steck, *Angew. Chem., Int. Ed. Engl.* 32, 238 (1993).
65. H. Krautscheid, D. Fenske, G. Baum, and M. Semmelmann, *Angew. Chem.* 105, 1364 (1993).
66. J. P. Spatz, A. Roescher, S. Sheiko, G. Krausch, and M. Möller, *Adv. Mater.* 7, 731 (1995).
67. R. S. Kane, R. E. Cohen, and R. Silbey, *Chem. Mater.* 8, 1919 (1996).
68. J. P. Spatz, A. Roescher, and M. Möller, *Adv. Mater.* 8, 337 (1996).
69. G. A. Ozin, *Adv. Mater.* 10, 612 (1992).
70. G. A. Ozin, *Adv. Chem. Ser.* (1992).
71. G. A. Ozin and S. Özkar, *Chem. Mater.* 4, 551 (1992).
72. S. Kawi and B. C. Gates, in "Clusters and Colloids," (G. Schmid, ed.). VCH, Weinheim, Germany, 1994.
73. D. W. Breck, ed., "Zeolite Molecular Sieves." Wiley, New York, 1974.
74. D. Exner, N. I. Jaeger, A. Kleine, and G. Schulz-Ekloff, *J. Chem. Soc., Faraday Trans.* 84, 4097 (1988).
75. F. Blatter and K. W. Blazey, IBM Research Report, Zurich, 1990.
76. V. I. Sradanov, K. Haug, H. Metiu, and G. D. Stucky, *J. Phys. Chem.* 96, 9039 (1992).
77. P. P. Edwards, L. J. Woodall, P. A. Anderson, A. R. Armstrong, and M. Slaski, *Chem. Soc. Rev.* 305 (1993).
78. Y. Wang, N. Herron, W. Mahler, and H. Suna, *J. Opt. Soc. Am. B* 6, 808 (1989).
79. G. A. Ozin, A. Kupermann, and A. Stein, *Angew. Chem., Int. Ed. Engl.* 28, 359 (1989).
80. P. A. Jacobs, N. I. Jaeger, P. Jiru, and G. Schulz-Ekloff, eds., "Metal Microstructures in Zeolites." Elsevier, Amsterdam, 1982.
81. U. Simon, C. Möhrke, and G. Schön, *Chem.-Ing.-Tech.* 67, 583 (1995).
82. N. Herron, Y. Wang, M. M. Eddy, G. D. Stucky, D. Cox, K. Möller, and T. Bein, *J. Am. Chem. Soc.* 111, 530 (1989).
83. K. L. Moran, W. T. A. Harrison, I. Kamben, T. E. Gier, X. Bu, D. Herren, P. Behoens, H. Eckert, and G. D. Stucky, *Chem. Mater.* 8, 1930 (1996).
84. V. B. Kazansky, L. M. Kustov, and A. Yu. Khodakov, *Stud. Surf. Sci. Catal.* 49b, 1173 (1989).
85. F. Roessner, A. Hagen, U. Mroczek, H. G. Karge, and K.-H. Steinberg, *Stud. Surf. Sci. Catal.* 75, 1707 (1993).

86. T. Türk, F. Sabin, and A. Vogler, *Mater. Res. Bull.* 27, 1003 (1992).
87. C. Henning, F. Thiel, K.-H. Hallmeier, R. Szargam, A. Hagen, and F. Roessner, *Spectrochim. Acta* 49a, 1495 (1993).
88. S. Yamamuchi, A. Satsuma, S. Komai, T. Asakawa, T. Hattori, and Y. Murakawi, *Stud. Surf. Sci. Catal.* 84, 1571 (1994).
89. M. Wark, H. Kessler, and G. Schulz-Ekloff, *Microporous Mater.* 8, 241 (1997).
90. H. J. Schwenn, M. Wark, G. Schulz-Ekloff, H. Wiggers, and U. Simon, *Colloid Polym. Sci.* 275, 91 (1997).
91. G. Hornyak, M. Kröll, R. Pugin, Th. Sawitowski, G. Schmid, J.-O. Bovin, G. Karsson, H. Hofmeister, and S. Hopfe, *Chem.—Eur. J.* 3, 1951 (1997).
92. M. Y. Gao, Y. B. Yang, F. L. Bian, and J. C. Shen, *J. Chem. Soc., Chem. Commun.* 2777 (1994).
93. M. Y. Gao, Y. B. Yang, F. L. Bian, and J. C. Shen, *J. Chem. Soc., Chem. Commun.* 2229 (1994).
94. M. Y. Gao, X. G. Peng, and J. C. Shen, *Thin Solid Films* 248, 106 (1994).
95. J. M. Huang, Y. Yang, B. Yang, S. Y. Liu, and J. C. Shen, *Polym. Bull.* 36, 337 (1996).
96. E. Kay, A. Dilks, and U. Hetzler, *J. Macromol. Sci., Chem. A* 12, 1393 (1978).
97. S. C. Davis and K. Klabunde, *J. Chem. Rev.* 82, 153 (1982).
98. R. Lamber, A. Baalmann, N. I. Jaeger, G. Schulz-Ekloff, and St. Wetjen, *Adv. Mater.* 6, 223 (1994).
99. J. Perrin, B. Despax, and E. Kay, *Phys. Rev. B* 32, 719 (1985).
100. U. Simon, R. Lamber, and G. Schulz-Ekloff, unpublished results.
101. H. Böttger and V. V. Bryksin, eds., "Hopping Conduction in Solids." VCH, Weinheim, Germany, 1985.
102. M. T. Reetz and W. Helbig, *J. Am. Chem. Soc.* 116, 7401 (1994).
103. J. A. Becker, R. Schäfer, R. Festag, W. Ruland, and J. H. Wendorff, *J. Chem. Phys.* 103, 2520 (1995).
104. M. T. Reetz, W. Helbig, St. A. Quaiser, U. Stimming, N. Breuer, and R. Vogel, *Science* 267, 367 (1995).
105. J. H. Fendler and F. C. Meldrum, *Adv. Mater.* 7, 607 (1995).
106. J. H. Fendler, *Chem. Mater.* 8, 1616 (1996).
107. G. Schmid, G. Schön, and U. Simon, German Patent 402-12220, 1992.
108. G. Schmid, G. Schön, and U. Simon, U.S. Patent 08/041,239, 1992.
109. H. H. A. Smit, P. P. Nugteren, R. C. Thiel, and L. J. de Jongh, *Physica B* 153, 33 (1988).
110. M. C. Fairbanks, R. E. Benfield, R. J. Newport, and G. Schmid, *Solid State Commun.* 74, 431 (1990).
111. S. Mann, *Nature* 365, 499 (1993).
112. L. Addadi and S. Weiner, *Angew. Chem., Int. Ed. Engl.* 31, 153 (1992).
113. B. R. Heywood and S. Mann, *Adv. Mater.* 6, 9 (1994).
114. A. Ulman, *Chem. Rev.* 96, 1533 (1996).
115. G. Schmid, St. Peschel, and Th. Sawitowski, *Z. Anorg. Allg. Chem.* 623, 719 (1997).
116. R. G. Osifchin, W. J. Mahoney, J. D. Bielefeld, and R. P. Andres, *Superlattices Microstruct.* 18, 283 (1995).
117. D. B. Janes, V. R. Kolagunta, R. G. Osifchin, J. D. Bielefeld, R. P. Andres, J. I. Henderson, and C. P. Kubiak, *Superlattices Microstruct.* 18, 275 (1995).
118. M. T. Reetz, M. Winter, and B. Tesche, *Chem. Commun.* 147 (1997).
119. J. Schmitt, G. Decher, W. J. Dressick, S. L. Brandow, R. E. Geer, R. Shashidhar, and J. M. Calvert, *Adv. Mater.* 9, 61 (1997).
120. L. F. Chi, S. Rakers, T. Drechsler, M. Hertig, H. Fuchs, and G. Schmid, unpublished manuscript.
121. Ch. A. Mirkin, R. L. Letsinger, R. C. Mucic, and J. J. Storhoff, *Nature* 382, 607 (1996).
122. M. A. Hayat, ed., "Gold: Principles, Methods, and Applications." Academic Press, San Diego, 1991.
123. K. C. Grabar, R. G. Freeman, M. B. Hommer, and M. J. Natan, *Anal. Chem.* 67, 735 (1995).
124. U. Simon, F. Schüth, S. Schunk, X. Wang, and F. Liebau, *Angew. Chem., Int. Ed. Engl.* 36, 1121 (1997).
125. P. A. Anderson, R. G. Bell, S. R. A. Catlow, F. L. Chang, A. J. Dent, P. P. Edwards, I. Gameson, I. Hussain, A. Porch, and J. M. Thomas, *Chem. Mater.* 8, 2114 (1996).
126. M. J. Kelly, *J. Phys.: Condens. Matter* 7, 5507 (1995).
127. U. Simon and V. Gasparian, *Phys. Status Solidi B* 205, 223 (1998).
128. V. Gasparian and U. Simon, *Physica B* 240, 289 (1997).
129. A. Gügel, K. Müllen, H. Reichert, W. Schmidt, G. Schön, F. Schüth, J. Spikermann, J. Titmann, and H. Unger, *Angew. Chem.* 105, 618 (1993).
130. G. M. Francis, I. M. Goldby, L. Kuipers, B. von Issendorff, and R. E. Palmer, *J. Chem. Soc., Dalton Trans.* 665 (1996).
131. A. P. Alivisatos, K. P. Johnsson, X. Peng, T. E. Wilson, C. J. Loweth, M. P. Bruchez, Jr., and P. G. Schultz, *Nature* 382, 609 (1996).
132. (a) H. Grabert, *Z. Phys. B* 85, 319 (1991). (b) M. H. Devoret, *Bull. Bur. Nat. Métrol* 22, 7 (1991).
133. D. Anselmetti, D. Richmont, A. Baratoff, G. Borer, M. Dreier, M. Bernasconi, and H.-J. Güntherodt, *Europhys. Lett.* 25, 297 (1994).
134. J. G. A. Dubois, J. W. Gerritsen, S. E. Shafranjuk, E. J. G. Boon, G. Schmid, and H. van Kempen, *Europhys. Lett.* 33, 279 (1996).
135. L. F. Chi, M. Hartig, T. Drechsler, Th. Schaak, C. Seidel, H. Fuchs, and G. Schmid, *Appl. Phys. Lett. A* 66, 187 (1998).
136. R. P. Andres, Th. Bein, M. Dorogi, S. Feng, J. I. Henderson, C. P. Kubiak, W. Mahoney, R. G. Osifchin, and R. Reifenberger, *Science* 272, 1323 (1996).

137. M. Dorogi, J. Gomez, R. Osifchin, R. P. Andres, and R. Reifenberger, *Phys. Rev. B* 52, 9071 (1995).
138. D. V. Averin and K. K. Likharev, in "Single Charge Tunneling Coulomb Blockade Phenomena in Nanostructures," (H. Grabert and M. H. Devoret, eds.), Nato ASI Series, Vol. 294, pp. 311–332. Plenum Press, New York, 1992.
139. D. Esteve, in "Single Charge Tunneling Coulomb Blockade Phenomena in Nanostructures," (H. Grabert and M. H. Devoret, eds.), Nato ASI Series, Vol. 294, pp. 109–137. Plenum Press, New York, 1992.
140. A. B. Zorin, *Phys. Rev. Lett.* 76, 4408 (1996).
141. A. B. Zorin et al., *Phys. Rev. B* 53, 13682 (1996).
142. K. K. Likharev, N. S. Bakhvalov, G. S. Kazacha, and S. I. Serdyukova, *IEEE Trans. Magn.* 25, 1436 (1989).
143. P. Delsing, in "Single Charge Tunneling Coulomb Blockade Phenomena in Nanostructures," (H. Grabert and M. H. Devoret, eds.), Nato ASI Series, Vol. 294, pp. 249–274. Plenum Press, New York, 1992.
144. G. Y. Hu and R. F. O'Connell, *Phys. Rev. B* 49, 16773 (1994).
145. G. Y. Hu and R. F. O'Connell, *Phys. Rev. Lett.* 74, 1839 (1995).
146. H. Nejoh and M. Aono, *Jpn. J. Appl. Phys.* 32, 532 (1993).
147. J. B. Barner and S. T. Ruggiero, *Phys. Rev. Lett.* 59, 807 (1989).
148. S. T. Ruggiero and J. B. Barner, *Z. Phys. B: Condens. Matter* 85, 333 (1991).
149. A. K. Jonscher, "Dielectric Relaxation in Solids." Chelsea Dielectric Press, London, 1983.
150. J. R. Macdonald, ed., "Impedance Spectroscopy." Wiley, New York, 1987.
151. A. Gladun and A. B. Zorin, *Phys. Z.* 23, 159 (1992).
152. K. K. Likharev and T. Claeson, *Spektr. Wiss.* 8, 62 (1992).
153. H. Koch and H. Lübbig, eds., "Single-Electron Tunneling and Mesoscopic Devices." Springer-Verlag, Berlin/Heidelberg, 1992.
154. M. Mabuchi, T. Takenaka, Y. Fujiyoshi, and N. Ugeda, *Surf. Sci.* 119, 150 (1982).
155. M. P. Samanta, W. Tian, and S. Datta, *Phys. Rev. B* 53, R7626 (1996).
156. E. S. Soldatov, V. V. Khanin, A. S. Trifonov, S. P. Gubin, V. V. Kolesov, D. E. Presnov, S. A. Iakovenko, and G. B. Khomutov, Moscow State University, 1996.
157. V. Gasparian, M. Ortuno, G. Schön, and U. Simon, in "Handbook of Nanostructured Materials and Nanotechnology," (H. S. Nalwa, ed.), Chap. X, p. X. Academic Press, Boston, 1999.
158. Y. P. Tsividis, ed., "Operation and Modeling of the MOS Transistor," p. 439. McGraw-Hill, New York, 1987.
159. A. Enders and G. Nimtz, *Phys. Rev. B* 47, 9605 (1993).
160. A. M. Steinberg, P. G. Kwiat, and R. Y. Chiao, *Phys. Rev. Lett.* 71, 708 (1993).
161. Ch. Spielmann, R. Szipöcs, A. Stingl, and F. Krausz, *Phys. Rev. Lett.* 73, 708 (1994).
162. A. O. Orlov, I. Amloni, G. H. Bernstein, C. S. Lent, and G. L. Smider, *Science* 277, 928 (1997).
163. M. T. Reetz, M. Winter, G. Dumpich, J. Lohau, and St. Friedrichowski, *J. Am. Chem. Soc.* (1996).
164. E. Corcoran, *Spektr. Wiss.* 11, 76 (1992).

Chapter 4

THE DESIGN, FABRICATION, AND ELECTRONIC PROPERTIES OF SELF-ASSEMBLED MOLECULAR NANOSTRUCTURES

R. P. Andres, S. Datta, D. B. Janes, C. P. Kubiak, R. Reifenberger
Purdue University, West Lafayette, Indiana, USA

Contents

1. Introduction . . . 180
2. Molecular Wire Synthesis . . . 181
   2.1. Overview . . . 181
   2.2. Recent Advances in the Synthesis of Molecular Wires . . . 181
   2.3. The Chemistry of Self-Assembled Monolayers . . . 184
   2.4. Chemical Self-Assembly of Aryl Dithiol Monolayers on Gold . . . 185
   2.5. Self-Assembly of "Chemically Sticky" Surfaces . . . 189
   2.6. Concluding Remarks . . . 189
3. Metal Cluster Synthesis . . . 189
   3.1. Overview . . . 189
   3.2. Gas Phase Synthesis . . . 190
   3.3. Capture of Clusters as Bare Metal Particles . . . 193
   3.4. Capture of Clusters as Colloidal Particles . . . 193
   3.5. Precipitation of Colloidal Networks from Solution . . . 194
   3.6. Formation of an Unlinked Cluster Array . . . 195
   3.7. Formation of a Linked Cluster Network . . . 197
   3.8. Concluding Remarks . . . 199
4. Theory of Electronic Conduction through Organic Molecules . . . 200
   4.1. Overview . . . 200
   4.2. Theoretical Model . . . 200
   4.3. Factors Affecting the Current–Voltage Characteristics . . . 203
   4.4. Concluding Remarks . . . 206
5. Electronic Properties of Molecular Nanostructures . . . 207
   5.1. Overview . . . 207
   5.2. Experimental Considerations . . . 207
   5.3. Electronic Properties of Individual Molecules . . . 209
   5.4. Electronic Conduction through Supported Clusters . . . 209
   5.5. Electronic Properties of Encapsulated Gold Clusters . . . 211
   5.6. Electronic Properties of Tethered Gold Clusters . . . 212
   5.7. Estimating the Electrical Resistance of a Molecule . . . 215
   5.8. Concluding Remarks . . . 216
6. Electronic Properties of Cluster Arrays and Networks . . . 216
   6.1. Overview . . . 216
   6.2. Sample Preparation . . . 217

Handbook of Nanostructured Materials and Nanotechnology, edited by H.S. Nalwa
Volume 3: Electrical Properties
Copyright © 2000 by Academic Press
All rights of reproduction in any form reserved.
ISBN 0-12-513763-X/$30.00

6.3. Electrical Measurements 220
6.4. Conduction Model 221
6.5. Concluding Remarks 224
7. Summary 225
Acknowledgments 226
References 226

1. INTRODUCTION

The ability to design, fabricate, and test a well-characterized, molecular-based nanoelectronic device is a challenging and important problem. The ability to controllably self-organize a collection of atoms and molecules to function in a desired way will form the basis of future technologies as fundamental limits governing the conventional fabrication of increasingly smaller devices are reached. Many groups are now taking the first steps to demonstrate this capability by assembling useful molecular nanostructures from the "ground up." It is likely that the electronic properties of these nanostructures will be quite different from the silicon-based devices in production today, and that the architecture and function of these nanoelectronic devices will find their own special niche over time. Part of this evolutionary process will surely require a duplication of accepted microelectronic functions by nanoelectronic prototypes.

In the rush to participate in this exciting, emerging field, there is a need to perform systematic prototype experiments that determine the relevant properties of molecular nanostructures. New techniques must be developed and, more often than not, we must learn to reformulate many traditional questions. To guide us through the early stages of this journey, it is useful to have a few well-characterized, versatile systems capable of providing answers to fundamental questions in a systematic and convincing fashion.

Crucial issues limiting design, fabrication, and performance can only be solved if the nanostructure is thermally and chemically stable and well defined. A successful program in this area requires careful attention to a number of important issues. It should be reasonably evident that progress will require the following:

1. A multidisciplinary approach, because often the expertise required is not confined to one or two related disciplines
2. Advances in theory to understand what interesting properties a molecular nanostructure might possess
3. The ready availability of well-characterized, stable, nanometer-size "building blocks" having sufficient uniformity that can be manipulated and controlled in a straightforward and robust way
4. A skillful combination of self-assembly techniques and high-resolution lithography, because only a marriage of these two approaches will provide the necessary flexibility to ensure success
5. Advanced characterization techniques with nanometer resolution that are capable of asking and answering important questions about the nanostructure's properties

An effort at Purdue University during the past 5 years has focused on these five important issues. This effort has taken an approach that exploits the unique size-dependent electronic properties of ultrasmall metallic clusters (containing a few hundred atoms) interconnected by molecular wires to produce novel molecular nanostructures. A course has been set that requires a tailoring of the properties of both the individual clusters and the molecules. Relying heavily on self-assembly techniques, a number of molecular nanostructures have been designed and fabricated [1–3] and their electronic properties have been measured [4–8] and compared to theoretical expectations [9–11].

In what follows, we review important aspects regarding the synthesis and characterization of the fundamental building blocks we have used—the molecular wires and nanoscale metallic clusters. We also present a theory for electronic conduction in a molecular wire and review the scanning tunneling microscopy (STM) studies of cluster-based nanostructures that support this theory. A periodic structure of particular interest for developing nanoscale electronics is a planar array of metal clusters separated from each other and from external contact pads by controlled tunnel barriers. Developing techniques for synthesizing and characterizing such a linked cluster network (LCN) would open up the possibility of fabricating novel linear and nonlinear electronic and optoelectronic devices. The electronic properties of such a quantum superlattice could be tailored to specific applications by controlling the size of the clusters and the strength of the coupling between them. We discuss the techniques for synthesizing such LCNs and review the interesting electronic properties that they possess.

This chapter is organized in the following way. First, we discuss relevant issues regarding the fabrication of molecular nanostructures. Such issues as the synthesis of molecular wires and nanoscale clusters, their characterization and self-assembly, and relevant processing issues are presented. A section is devoted to the theory of electronic conduction through molecular wires. Important aspects of this problem such as the location of the Fermi level of a molecule when attached to a surface, the location of potential drops when current flows through the molecule, and the electrical resistance of a single molecule are discussed. The experimental work involving STM studies of a "unit cell" nanostructure is then reviewed, including evidence for room temperature single-electron effects. The electronic transport properties of cluster arrays and linked cluster networks are then discussed. By connecting the clusters together in ordered two-dimensional networks, a novel nanostructured material with a promising future is formed. An analysis of the measured temperature dependence of the electronic conductivity of such an LCN indicates that current flow is governed by single-electron effects. Finally, a summary is included that provides a synopsis of the chapter.

2. MOLECULAR WIRE SYNTHESIS

2.1. Overview

One paradigm shift envisioned for computational devices involves the assembly of the device from molecular scale components [12–15]. Many groups have discussed the possibility of using single or small bundles of molecules as wires in such devices [16, 17]. The term "molecular wire" has been widely used within the past few years. The use of the term is highly varied and ambiguous. For the purpose of the present work, the term molecular wire will be used to describe any molecule used to pass current. The electrons in question may be transported through molecular orbitals, or the electrons may tunnel through the molecule. Until recently, few groups have been able to predict or even measure the resistance of a single molecule [6, 9, 18–20]. To study this phenomenon, it is important to find a system where the length of the molecules and the functional end groups can be varied systematically. It is also desirable to have molecules that are rigid and that remain in a near-linear conformation. In what follows, a review of recent advances in the synthesis of molecules used as molecular wire interconnects and the chemistry of the self-assembly of these molecules on metal clusters and surfaces is presented.

2.2. Recent Advances in the Synthesis of Molecular Wires

Before describing the synthesis of molecular wires, a few words about chemical nomenclature and our choice of molecules are in order. Different types of molecules are required depending on their intended use or function. For nanostructures constructed from molecules

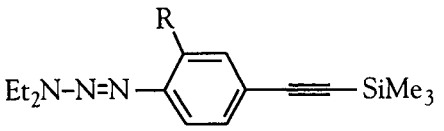
connecting metal clusters to surfaces, both the nature of the "ligand" group at the end of the molecule that contacts the metal and the internal electronic structure of the molecule are important. Most earlier work on self-assembled monolayers of thiol molecules (organic molecules containing a terminal –SH group) on gold have involved *n*-alkyl chain (CH_3–$(CH_2)_{n-1}$–) molecules. These molecules have flexible chains that pack well into a dense, ordered monolayer film. The alkyl chains also possess tightly localized electronic structures with large (6–8 eV) gaps between filled and vacant levels. Thus, alkyl thiols are useful for forming insulating films and for passivating colloidal gold clusters from aggregating into larger crystallites. For other applications, we have developed the chemistry of aryl thiols. The aryl molecules contain planar phenyl groups or chains of phenyl groups. The poly(phenyl) chains are rigid and possess delocalized π-electron systems. Thus, aryl and poly(phenyl) thiols are interesting for use as electronic interconnects or when a structurally rigid connection is needed between cluster/surface or cluster/cluster. One particularly interesting class of molecules is that containing alkynyl phenyl chains based on rigid phenyl groups alternating with alkyne (acetylene) groups. These offer similar functional uses as the the purely aryl systems, but also allow an entire family of related molecules of systematically different lengths to be prepared by a general strategy with an additional flexibility in the choice of the end group. One scheme adopted by our group to synthesize these molecules is based on a divergent/convergent synthetic strategy.

Whiting et al. [21, 22] originally described a synthetic method for doubling monomeric units. Later, Moore et al. [23] used Whiting's method to prepare oligo(1,3-phenylacetylenes). Recently, Tour et al. [24, 25] used the same method as well as a solid support to synthesize molecular wires greater than 10 nm in length based on 1,4-substituted phenylene units. It is clearly desirable to develop a strategy for the synthesis of systematically longer molecules based on a repeating unit. One such approach is divergent/convergent synthesis. The divergent/convergent approach to doubling monomeric units hinges on the synthesis of the starting material, or "building block." The synthesis of the alkyl-substituted monomer **1** shown in Figure 1 has been reported and used to make some impressive molecular wires [24, 25].

Because the previous synthesis of **1** is very tedious and time consuming, a new synthesis was developed. The previous reported synthesis of **1** involved five steps and an overall yield of 21% [24]. The new synthesis of **1** involved only three steps with an overall yield of 74% (see Fig. 2). The alkyl substituent can be varied easily to allow for greater product solubility.

Once the starting monomer **1** or "building block" is synthesized, only three different reactions are needed at each stage to double the molecular length as shown in Figure 3. The number of times this divergence/convergence can be used is presently limited by the solubility of the products [25, 26]. The final steps involve the replacement of the terminal triazide and iodo groups with thiol or other functional groups appropriate for binding to a metal surface.

This approach has been used by us to prepare several long-chain alkynyl phenyl molecules with both thiol (–SH) and isocyanide (–NC) groups. Some of the molecules employed in our studies of self-assembled molecular nanostructures are given in Figure 4.



1

Fig. 1. Alkynyl phenyl "building block" for the divergent/convergent synthesis of a family of systematically longer oligomers.

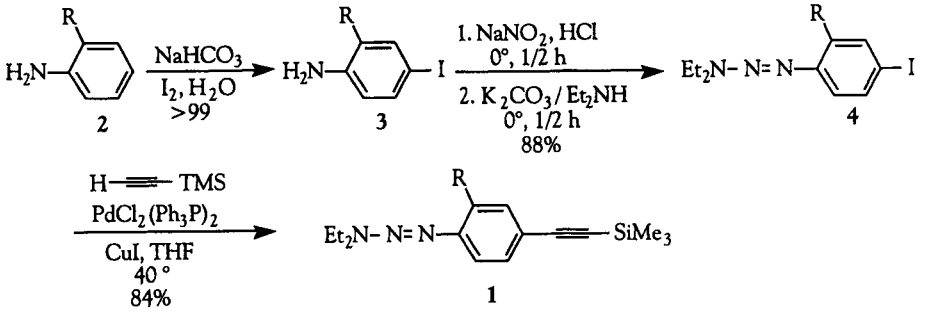


Fig. 2. New and improved synthesis of an alkynyl phenyl "building block" for the divergent/convergent synthesis of longer oligomers.

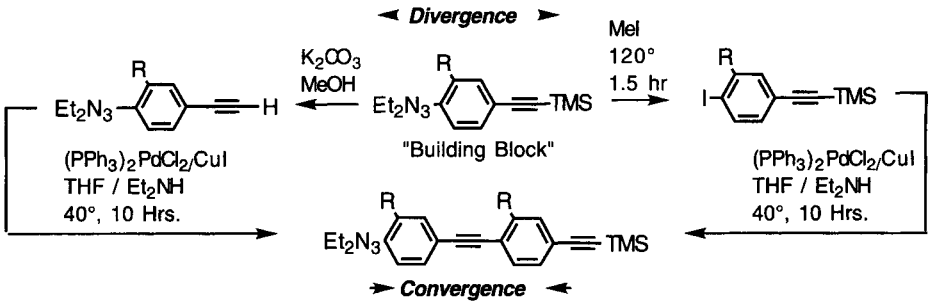


Fig. 3. Divergent/convergent synthesis doubling the length of **1**. The presentation of the original end groups allows the length to be doubled again.

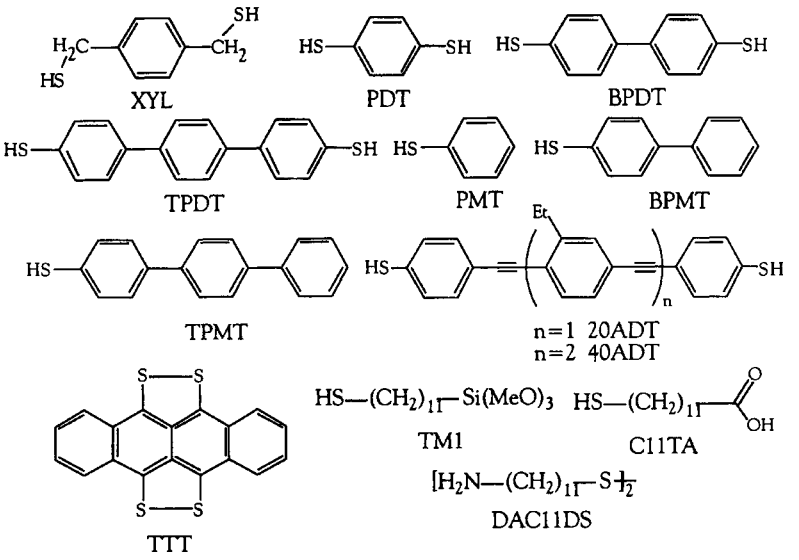


Fig. 4. Thiol and dithiol molecules used in preparing chemically self-assembled nanostructures.

Two of the molecules used extensively in our studies are 1,4-di(4-thiophenylacetylynl)-2-ethylbenzene and 1,4-di(4-isocyanophenylacetylynl)-2-ethylbenzene, which we call 20ADT and 22ADI. In a highly interdisciplinary project such as this, it has been necessary to use the abbreviated names of these molecules. In some cases, the abbreviated names are

chosen to reflect important physical attributes, namely, the length of the molecule. Here 20ADT is a 2-nm-long dithiol, whereas 22ADI is a 2.2-nm-long di-isocyanide. In other cases, these names follow conventional chemical nomenclature, for example, xylyl dithiol (XYL), phenyl dithiol (PDT), biphenyl dithiol (BPDT), and terphenyl dithiol (TPDT).

2.3. The Chemistry of Self-Assembled Monolayers

It has been known for a long time that certain molecules will spontaneously adsorb onto a metal surface to form monolayer films [27, 28]. It is now widely recognized that an appropriate molecule/substrate combination will lead to the formation of highly organized monolayer films. These films are prepared by immersing a clean substrate into a neat sample of the molecule or a solution (ca. 1 mM) of the molecule. The monolayer forms spontaneously and is referred to as a self-assembled monolayer (SAM). SAMs, however, are only one example of the general phenomenon of self-assembly. In nature, self-assembly results in supermolecular hierarchical organizations of interlocking components that produce very complex systems [29].

Among the several different types of molecules that have been studied, alkyl thiols and disulfides adsorbed on the coinage metals, predominately gold, have been studied most [30–82]. Other sulfur-containing species have also been shown to form SAMs on gold. These include, among others, mercaptopyridines [83], thiophenes [84], cysteines [85, 86], xanthates [87], di-*n*-alkyl sulfides [88, 89], and thiocarbamates [90]. Organosulfur compounds also have been shown to form SAMs on InP [91], GaAs [92–96], $YBa_2Cu_3O_{7-\delta}$ [97], TlBaCaCuO [98], silicon [99], iron [52, 100–102], mercury [103–107], nickel [47], and platinum [46, 106–111].

Other types of molecules have been shown to form SAMs including silanes adsorbed on Al_2O_3 [112] or on silicon or glass [66, 113–129]. Alkylphosphines on gold and the triphenyl compounds of the group 15 elements on gold and copper have also been shown to form different types of monolayers and even "multilayers" [130]. Alkyl phosphonic acids have also been used to grow SAMs on ZrO_2, TiO_2, and zirconated silica powders [131]. Fatty acids have been shown to form SAMs on aluminum oxide [132, 133], silver [134], and silver oxide [135, 136]. Molecules with α, ω functional groups have also been studied and shown to adsorb on various metals, including gold [3, 6, 137, 138]. Complex molecules like calix[4]resorcinarene [139] and coordination compounds of rhenium [69] have also been shown to form SAMs on Au(111).

Interestingly, SAMs provide excellent protection of the metal surface against oxidation and this is one reason for industrial interest in the subject. For example, silver surfaces with octadecanethiolate monolayers can be kept in ambient conditions without tarnishing for many months [140], and copper surfaces coated with the same monolayer resisted degradation in nitric acid [141].

Most studies on SAMs have been done with *n*-alkyl thiols on Au(111) surfaces. Kinetic studies of alkanethiol adsorption onto Au(111) surfaces have shown that at relatively dilute concentrations (10^{-3} M), two distinct adsorption kinetics can be observed [142]. Second-harmonic generation and X-ray photoelectron spectroscopy (XPS) [143, 144] as well as near edge X-ray absorption fine structure (NEXAFS) studies [145] have confirmed this two-step kinetic process. The first step only takes a few minutes, and, by the end, the water contact angle is near its limiting value and the ellipsometry-determined film thickness is about 80% to 90% of its maximum. This first step, which can be described by diffusion-controlled Langmuir adsorption, was found to depend strongly on thiol concentration. The kinetics are governed by the surface-head group reaction, and the activation energy may depend on the electron density of the adsorbing sulfur atom.

The second step is slower, lasting several hours, and brings the SAM to the limiting film thickness and water contact angles [142]. This step can be described as a surface crystallization process, where the alkyl chains order themselves, forming a two-dimensional

crystal. Badia et al. [80] have shown that the melting point of a well-ordered SAM scales with the melting point of the bulk solid. The kinetics of the second step can depend on chain disorder (i.e., gauche defects), the different components of chain–chain interactions (van der Waals, dipole–dipole interactions, etc.), and the surface mobility of the chains. It was also found that this kinetics is dependent on alkyl chain length, such that the longer the chain the faster the second step [142], possibly as a result of van der Waals interactions.

SAMs formed from *n*-alkanethiols or di-*n*-alkane disulfides on clean gold surfaces are indistinguishable [146]. This may be because of the formation of Au(I) thiolate species. A simple oxidative addition of the S–S bond to the gold surface is a possible mechanism in the disulfide case. The rates of SAM formation were also indistinguishable for the two species. However, the rate of displacement of an SAM by another alkyl thiol was much faster for thiols than for disulfides [147].

Evidence for the disulfide oxidative addition to the surface comes from the work done by Biebuyck and Whitesides [146]. This study showed that the reaction of unsymmetrical disulfide ($HO(CH_2)_{10}S$–$S(CH_2)_3CF_3$) with a clean gold surface gave SAMs containing roughly equal amounts of the two thiolate groups. However, when these SAMs were exposed to a solution of $HS(CH_2)_{10}CN$, the displacement of the CF_3-terminated thiol was about 10^3 times faster than the hydroxyl-terminated thiol. This is strong evidence that the disulfide bond is cleaved upon adsorption on the surface.

Fenter et al. [148] reported evidence that the disulfide bond may, in fact, still be present at the surface. However, their evidence was secondary and no further direct evidence supporting their assertions have been made [141].

In the case of alkyl thiols, the reaction at the surface may be considered formally as an oxidative addition of the S–H bond to the gold surface. There have been no direct measurements, but the proton probably ends as a H_2 molecule. This can be deduced from the reports that SAMs can be formed from the gas phase in the complete absence of oxygen [149–151]. The combination of hydrogen atoms at the metal surface yielding molecular hydrogen may be an important step in the overall thermodynamics. The bonding of the thiolate group to the surface has been estimated to have a bond strength of 40 kcal mol^{-1} [152]. Using accepted bond energies of RS–H and molecular hydrogen (87 and 104 kcal mol^{-1}), the net energy of a thiol adsorbing onto the surface is about -5 kcal mol^{-1}, exothermic. Schlenoff and co-workers, using electrochemical data, calculated the net energy of the reaction to be -5.5 kcal mol^{-1} [108]. The adsorbed species has been demonstrated by XPS [153–156], Fourier transform mass spectroscopy [157], electrochemistry [158], Fourier transform infrared (FTIR) spectroscopy [154], and Raman spectroscopy [84, 159, 160] to be the thiolate species (RS^-).

Electron diffraction (both high and low energy), helium diffraction, and atomic force microscopy (AFM) suggest that SAMs of alkyl thiols (chain length longer than 10 carbons) form with the sulfur atoms having hexagonal symmetry and a S...S distance of approximately 0.5 nm and a tilt angle of approximately 26°–28°. The SAM structure is commensurate with the underlying gold lattice and is a simple $\sqrt{3} \times \sqrt{3}$ R 30° [161–165]. More recent STM studies suggest that the SAM structure is a c(4 × 2) superlattice of a $\sqrt{3} \times \sqrt{3}$ R 30° lattice [55, 166–170]. Despite the thousands of studies done on SAMs, particularly SAMs on gold surfaces, there is still much work to be done.

2.4. Chemical Self-Assembly of Aryl Dithiol Monolayers on Gold

We now consider the use of thiol and dithiol molecules for the self-assembly of several interesting nanostructures: first, as chemically sticky surfaces for the anchoring of gold clusters; second, as molecular interconnects to form two- and three-dimensional arrays of gold clusters.

Although SAMs of alkyl thiols on gold have been studied intensively, *vide infra*, studies of SAMs of aryl thiols, and particularly aryl dithiols, had not been reported prior to our

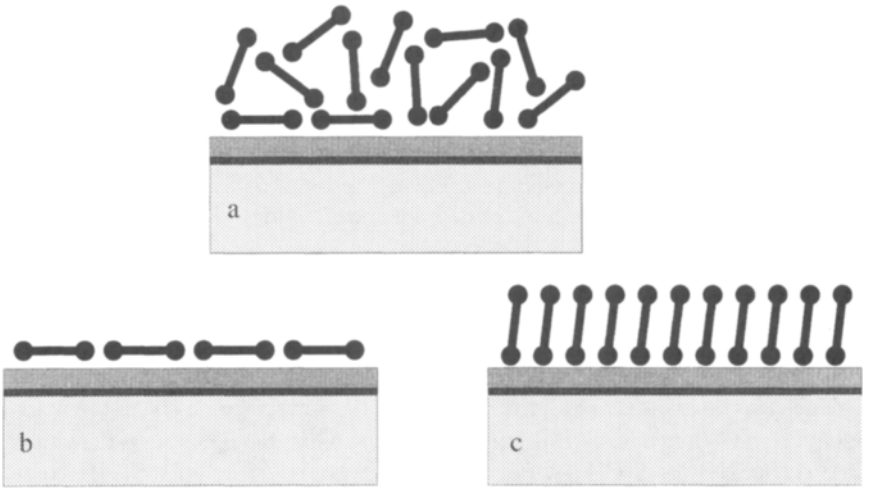


Fig. 5. Three possible orientations that bifunctional dithiols may adopt. The possibilities are (a) a disordered arrangement, (b) parallel to the surface, and (c) normal to the surface.

work. Some of the dithiols and difunctionalized thiols we have studied appear in Figure 4. There are three possible orientations a bifunctional molecule may adopt in forming an SAM (Fig. 5). We find that SAMs of aryl dithiols form in the "stand up" vertical orientation shown in Figure 5c.

SAMs of the aliphatic thiol, 1-octadecanethiol, $CH_3(CH_2)_{17}SH$ (ODT), were prepared according to procedures previously described. SAMs of the dithiols 4,4′-biphenyldithiol (BPDT) and α, α'-xylyldithiol (XYL) on gold were prepared two separate ways: first, from CH_2Cl_2 solutions following procedures described for SAMs of ODT on gold, and, second, by displacement of preexisting SAMs of ODT. The gold surfaces were prepared on Si(100) wafers precoated with a 10-nm Cr layer followed by a 200-nm Au layer, then precleaned with air plasma. Adsorption times of 2–4 h for ODT and 15 h for BPDT and XYL are sufficient to form ordered films. These SAMs were characterized by reflection absorption infrared (RAIR) spectroscopy, surface-enhanced Raman spectroscopy (SERS), optical ellipsometry, and measurement of advancing contact angle (Θ_a) to determine which of the three orientations (Fig. 5) were dominant.

A comparison of reflection absorption infrared (RAIR) spectra of BPDT and XYL SAMs on gold with the corresponding infrared (IR) spectra of bulk solid samples in KBr reveal similar band energies but different relative intensities, consistent with metal surface adsorption. Assignments for the observed RAIR bands for BPDT on gold were made following the system of substituted benzene normal modes, **1–20a, b**, with symmetry labels appropriate for the local symmetry ($C2v$) of the ring system [171]: 3045 cm^{-1} (**2** a_1), 3021 cm^{-1} (**7b** b_2), 1592 cm^{-1} (**8a** a_1), 1474 cm^{-1} (**19a** a_1), 1406 cm^{-1} (**19b** b_2), 1387 cm^{-1} (**19b** b_2), 1106 cm^{-1} (**18b** b_2), and 1000 cm^{-1} (**18a** a_1). The RAIR spectra did not display the expected ν(S–H) mode, observed at 2555 cm^{-1} in a bulk solid spectrum of BPDT. One possible explanation for the absence of this mode is that this mode would be nearly parallel to the surface and, hence, forbidden by surface selection rules if the molecules are oriented normal to the surface. This is even true using the 6°–7° tilt angle reported for aryl mono thiols [141, 172, 173]. Another explanation is that the thiols oxidized to disulfides when the samples were transferred from the inert atmosphere where the SAMs were prepared to the RAIR chamber.

Close inspection of the RAIR spectra (Fig. 6) of adsorbed BPDT molecules provides evidence for the SAM alignment with the long molecular axis oriented nearly normal to the surface.

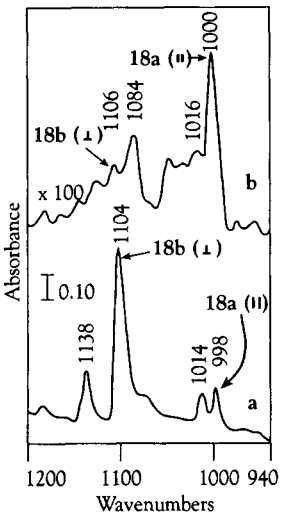


Fig. 6. (a) Bulk sample of biphenyldithiol (BPDT) as a KBr pellet. (b) Reflectance absorption infrared (RAIR) spectrum of BPDT on gold. (Source: Reprinted from [6]. © 1996 American Association for the Advancement of Science.)

In particular, the bands at 998 and 1104 cm^{-1} in the bulk spectrum of BPDT (curve a) are assigned to the **18a** and **18b** normal modes of the phenyl rings, respectively. The net dipole moment changes associated with the **18a** and **18b** modes are parallel and perpendicular, respectively, to the long molecular axis. The relative intensities of these modes for adsorbed BPDT are enhanced (**18a**) and decreased (**18b**) (curve b) relative to the intensities of the bulk spectrum and are consistent with surface selection rules for molecules oriented normal to the gold surface as shown in Figure 5c.

In the case of XYL, the observed IR absorptions for films of XYL on gold also agreed well with the bulk solid spectrum. Assignments, again, follow the system of substituted benzene normal modes, **1–20a, b**, with symmetry labels appropriate for the local symmetry (*D2h*) of the ring system [171]: 3022 cm^{-1} (**20b** b_{2u}), 2921 cm^{-1} (ν_{as}, CH_2), 1511 cm^{-1} (**19a** b_{1u}), 1423 cm^{-1} (**19b** b_{2u}), and 1263 cm^{-1} (**13** b_{1u}). No significant changes in relative band intensities compared to the bulk spectrum of XYL were observed.

Ellipsometric data gave an experimental film thickness for BPDT of 1.22 nm, in reasonable agreement with the expected film thickness (1.3 nm) for a normal to surface orientation. (A refractive index of 1.5 was used in the ellipsometric calculation.) Using the 6°–7° tilt angle suggested by Ulman [141], Sabatani et al. [172], and Chang et al. [173], this agreement is even closer. The experimental film thickness for XYL was 0.83 nm, consistent with a tilted molecular orientation. The tilt (~24°) is not quite as much as that generally accepted for alkyl thiol SAMs, *vide infra*, but is apparently caused by the presence of the methylene carbon atoms in the XYL molecule.

Advancing water contact angle measurements also indicate that the aryl dithiols form SAMs with only one thiol attached to the surface. The advancing contact angle of water droplets on SAMs of XYL and BPDT on gold were 69°–71°. By comparison, Wasserman et al. [174] found contact angles on a $HS(CH_2)_{11}SiCl_3$-modified Si–SiO_2 substrate to be 72°–74°.

Exposure of a preexisting SAM of ODT to either XYL or BPDT leads to complete displacement of ODT and to the formation of SAMs of XYL or BPDT, which are spectroscopically similar to SAMs of XYL and BPDT prepared on freshly cleaned gold substrates. Figure 7 shows the development of the RAIR spectra of an SAM of ODT after its immersion into a 1.0-mM CH_2Cl_2 solution of BPDT.

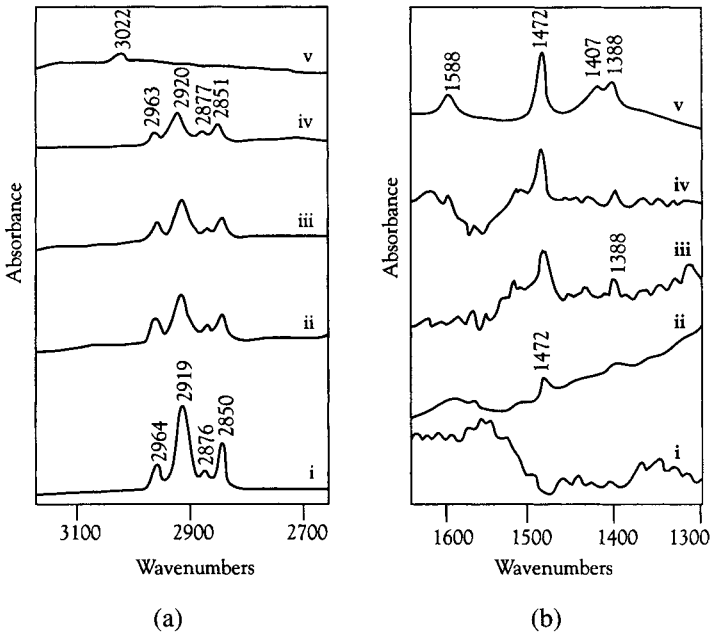


Fig. 7. Reflectance absorption infrared (RAIR) spectra following the displacement of octadecylthiol (ODT) by biphenyldithiol (BPDT) in the C–H stretching region at (i) $t = 0$, (ii) $t = 15$ min, (iii) $t = 1.5$ h, (iv) $t = 4.0$ h, and (v) $t = 15$ h. (b) RAIR spectra of the same sample at the same time intervals in the phenyl ring C–C stretching region.

Table I. Film Thicknesses (D_{exp}) and Contact Angles (Θ_a) of Water for Self-Assembled Monolayers of Octadecylthiol (ODT), Biphenyldithiol (BPDT), and Xylyldithiol (XYL). D_{calc} is the Expected Length of the Molecules

Molecule	D_{exp}	D_{calc}	Θ_a
ODT	2.6 nm	2.7 nm	111°
BPDT	1.2 nm	1.3 nm	70°
XYL	0.83 nm	0.92 nm	70°

A continued decrease in intensity of the IR bands attributed to ODT at 2964 cm^{-1} [CH_3, ν_a, (ip)] 2919 cm^{-1} (CH_2, ν_a), 2876 cm^{-1} [CH_3, ν_s (FR)], and 2850 cm^{-1} (CH_2, ν_s) is accompanied by the appearance of IR bands attributed to BPDT at 3022 cm^{-1}, 1588 cm^{-1}, 1472 cm^{-1}, 1407 cm^{-1}, and 1388 cm^{-1}. After 15 h, complete displacement of ODT by BPDT is effected.

Table I summarizes film thicknesses determined by optical ellipsometry and contact angles when an SAM of ODT is exposed to XYL or BPDT compared to experiments where SAMs of XYL or BPDT are exposed to ODT. These studies establish that an SAM of a particular long-chain aliphatic thiol, for example, octadecane thiol, can be displaced upon exposure to a solution containing the dithiols XYL or BPDT. The formation of an SAM of XYL or BPDT by displacement of ODT was found to be irreversible. The SAMs formed by direct adsorption or by displacing a preexisting SAM of ODT were spectroscopically indistinguishable.

2.5. Self-Assembly of "Chemically Sticky" Surfaces

A longstanding problem in the use of scanning probe microscopy to study supported metallic clusters is the tip–cluster interaction that results in unwanted motion of the nanocluster [175]. If clusters are supported on chemically similar surfaces, wetting is often observed [176]. Only careful work utilizing noncontact scanning techniques allowed detailed scanning probe studies of supported clusters [177]. However, another solution to this problem is at hand when it is realized that the "stand up" structure of SAMs of the dithiols XYL and BPDT (see Fig. 5c) can be exploited to tether a gold cluster to a gold substrate that has been covered with a dithiol SAM.

A set of experiments to demonstrate this capability was carried out by depositing nanocrystalline gold clusters onto dithiol SAMs by two methods. First, a gold substrate covered with a dithiol SAM was exposed in vacuum to a molecular beam of bare gold clusters using the techniques discussed in Section 3.3. Second, a similar Au(111) substrate was exposed to approximately three drops of gold colloid containing gold clusters encapsulated by dodecanethiol, $CH_3(CH_2)_{11}SH$. The cluster/dithiol/Au(111) nanostructure assemblies were then studied using ultrahigh vacuum (UHV) STM [4–6, 8].

The positions of the clusters remained constant for repeated scans of the same region of surface. In contrast, gold clusters deposited on highly oriented pyrolytic graphite (HOPG) surfaces or on SAMs of ODT did not produce stable images. This indicates that the exposed thiol from the dithiol molecule reacts with the gold cluster forming a covalent S–Au bond. Additionally, when the gold colloid is used, the aryl thiol displaces the alkyl thiol on the gold cluster and forms a bond to the cluster.

2.6. Concluding Remarks

Aryl dithiols have been shown to form SAMs on Au(111) with the long molecular axis perpendicular to the surface. These SAMs form with only one thiol bound to the gold surface. The second thiol end group can act as a chemically sticky surface for immobilizing a gold cluster. SAMs of aryl dithiols can be formed in two ways: first, by direct adsorption onto a clean gold surface, and, second, by displacing a previously formed SAM of octadecanethiol. Gold clusters, both naked and encapsulated with dodecanethiol, have been immobilized on SAMs of aryl dithiols.

3. METAL CLUSTER SYNTHESIS

3.1. Overview

Over the last decade, there has been a wealth of experimental and theoretical studies of nanometer-scale metal particles or clusters. The focus of much of this research is to understand and predict the size-dependent evolution of the solid-state properties of ultrasmall particles in which chemical bonding and electron delocalization are strong. This literature is too large and too varied to review in the context of the present contribution. However, a few general conclusions from this research are relevant. Metal clusters with diameters in the 1–20-nm range have hybrid properties characteristic of neither the atomic nor bulk solid-state limits. Because of this, there is substantial interest in developing methods for producing significant quantities of such clusters and assembling them in a controlled manner to produce bulk materials with novel properties.

Techniques exist for the gas phase synthesis of metal clusters containing from only a few atoms up to many hundreds of atoms and for their physical characterization with exquisite precision. However, it is one thing to identify a cluster species with desirable physical or chemical properties in a cluster beam experiment, and quite another to devise a practical process by which these clusters can be synthesized and assembled into a macroscopic film or solid material. It is this latter problem that will be the focus of the present section.

To synthesize a nanostructured material consisting of ultrasmall metal clusters linked to each other by organic molecules in such a way that the resulting network is a uniform superlattice with controllable electronic transport characteristics, several criteria must be satisfied:

- The process must be capable of producing macroscopic numbers of clusters.
- The clusters must have a controlled atomic composition to be nearly identical.
- The clusters must be chemically and thermally stable.
- The clusters must have a controlled mean size and a reasonably narrow size distribution.
- The clusters must have a stable atomic configuration.
- The process must be capable of capturing and manipulating the clusters to form the desired superlattice.

The techniques we have developed that satisfy these criteria include:

- An aerosol synthesis of metal clusters of controlled size and composition
- The gas phase melting and recrystallization of the clusters to produce single crystals
- The capture of these nanocrystals either by expanding them through a capillary leak into a vacuum chamber to form a molecular beam or by scrubbing them from the gas phase with a solvent spray
- Soft landing the molecular beam clusters onto flat solid substrates
- Encapsulating the clusters captured in a solvent by means of reactive molecules that form a self-assembled monolayer around each cluster and transform the bare metal particles into stable colloidal species.

In what follows we will briefly outline these techniques.

3.2. Gas Phase Synthesis

Figure 8 is a schematic diagram of a source developed at Purdue University for the synthesis of nanometer diameter metal clusters as aerosol particles suspended in a low-pressure inert-gas stream. A detailed description of this multiple expansion cluster source (MECS) can be found elsewhere [178, 179]. Single-component and two-component metal clusters that are crystalline and that have a controlled mean diameter in the range from 1 to 20 nm and a size distribution characterized by a full width at half-maximum of approximately 0.5 nm at the low end of this range and approximately 5 nm at the high end can be synthesized in this source at total production rates of approximately 100 mg/h.

The MECS consists of four main regions: (1) a resistively heated carbon oven, (2) a small quench region in which room temperature inert gas is mixed with the hot flow coming from the oven, (3) a tubular laminar flow reactor in which metal vapor condensation and cluster aggregation occur, and (4) an annealing reactor in which the clusters can be thermally annealed in the gas phase.

The metal of interest is placed inside a closed crucible, which is located inside the oven. The evaporation rate from the crucible is controlled by varying the oven temperature, the oven pressure, and the size of the crucible aperture. Superheated metal vapor consisting of single atoms and diatoms diffusing from the crucible is entrained in a helium gas flow and expanded through a sonic orifice in the oven wall. The resulting free jet is mixed with room temperature quench gas (either He or Ar) and the supersaturated mixture is expanded into the condensation reactor. The clusters grow initially by accretion of single atoms onto particles that originate as diatoms present in the oven. The concentration of single metal atoms is rapidly depleted as the aerosol flows through the condensation reactor, and eventually

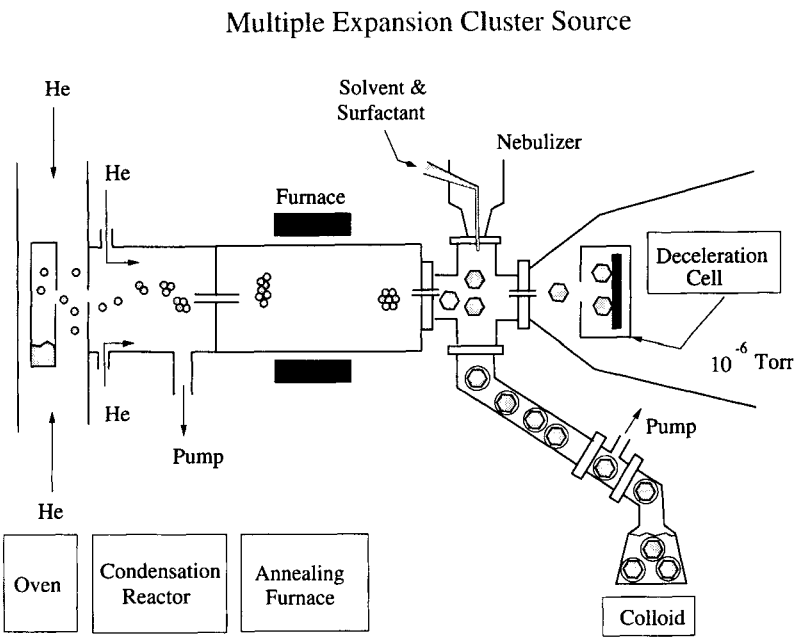


Fig. 8. Schematic diagram of the multiple expansion cluster source (MECS) used to make na size clusters.

Table II. MECS Operating Conditions

Physical variable	Typical operating range
Oven gas	He
Oven pressure	100–150 torr
Oven temperature	1200–1600 °C
Quench gas	He or Ar
Moles quench gas/moles oven gas	2–4
Condensation reactor pressure	20–50 torr
Vacuum chamber pressure	10^{-6} torr
Deceleration cell pressure	10^{-3} torr

cluster–cluster agglomeration becomes the dominant mode of cluster growth. The size is controlled by varying the ratio of quench gas flow to oven gas flow, the re time in the reactor, and the type of quench gas used. The residence time in the conde reactor is controlled by passing the entire flow through a throttle valve into a mec pump. Typical operating conditions are shown in Table II. Typical residence time condensation reactor are on the order of 1–10 ms.

A portion of the cluster aerosol is passed through a capillary leak into a vacuum c to form a molecular beam. Cluster samples are obtained by decelerating the cluster beam in a low-pressure gas cell and depositing the decelerated clusters onto thin amc carbon films supported on 400-mesh nickel or copper grids. Information about the structure and size distribution of the bare metal clusters is obtained by analyzin samples using transmission electron microscopy (TEM).

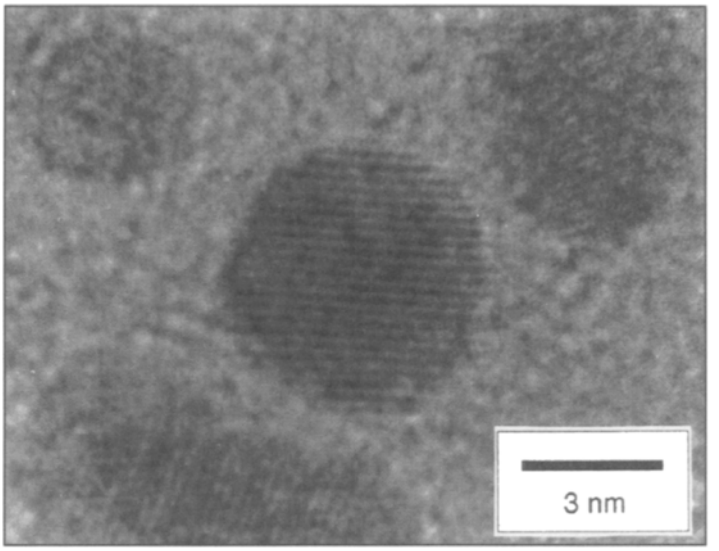


Fig. 9. High-resolution TEM of Au clusters. The Au clusters are supported on an amorphous carbon substrate. The clusters are all single fcc crystals with a lattice spacing between (111) equal to that of bulk gold.

Gold clusters formed in the MECS are typically multiply twinned polycrystals with face-centered cubic (fcc) domains 1–2 nm in size [180]. These ultrafine particles are nearly spherical in shape. Their polycrystallinity is revealed by performing electron microdiffraction or high-resolution transmission electron microscopy (HRTEM) on single clusters. To transform these multiply twinned clusters into single crystals, they are thermally annealed in the gas phase. The annealing reactor (see Fig. 8) consists of an alumina tube placed inside a Lindburg furnace. A portion of the cluster aerosol formed in the condensation reactor is expanded into this tube. Additional inert gas is added to decrease the cluster concentration and to forestall cluster–cluster collisions. As the clusters pass down the tube, they are first heated to the temperature of the furnace and then cooled to room temperature. The typical residence time in the annealing reactor is about 1 s.

When nanometer-scale gold clusters are heated in the gas phase above their melting temperature and then cooled, they are transformed into single fcc crystals [181]. The most stable shape for these fcc crystals appears to be that of a truncated octahedron with eight hexagonal (111) faces and six square (100) faces. Figure 9 is a HRTEM micrograph of bare gold clusters produced via the procedure described previously. Clusters grown in the MECS have an inherent size distribution; thus, there are nearly always adatoms decorating the facets of the underlying closed-shell crystal. However, if the cluster in the center of the TEM micrograph in Figure 9 were a perfect truncated octahedron, it would contain 2406 Au atoms.

A source like the MECS, capable of synthesizing clusters in the gas phase and of producing a molecular beam of these clusters, is the experimental workhorse of cluster science. It makes possible detailed studies of the size-dependent properties of clusters as free particles and (when combined with the ability to soft-land the clusters) as supported particles [182–188].

The MECS differs from most other molecular beam cluster sources in that it operates with a relatively high partial pressure of inert gas (20–50 torr in the condensation region), which allows gas phase annealing. The MECS can produce macroscopic numbers of clusters (up to 0.1 g/h). It has been used to synthesize single-component clusters of Al, Sn, Au, Ag, Cu, Si, and Fe, and two-component clusters involving combinations of these atoms. In what follows, we shall limit our discussion to single-component gold clusters.

3.3. Capture of Clusters as Bare Metal Particles

One way to study the electronic behavior of a molecular wire linking two metal surfaces is to assemble a molecular nanostructure by depositing gold clusters onto a "chemically sticky" surface made by an aryl dithiol monolayer on a gold substrate. When performing such a deposition, it is important to control the impact energy of the clusters. The ability to slow clusters before deposition has been addressed by recent molecular dynamics calculations, which have shown that clusters deposited onto a substrate at high kinetic energies can suffer damage upon impact [189, 190]. Cheng and Landman [189] considered Cu_{147} clusters incident on a (111)-oriented Cu surface. They found that significant damage (cluster deformation and mixing of surface and cluster atoms) occurred for impacts where the kinetic energy was greater than approximately 1 eV/atom or for cluster speeds greater than 2 km/s. Betz and Husinsky [190] studied Al and Pb clusters impinging on Cu surfaces, with similar results. Minimal damage occurred for collisions with an average kinetic energy less than 1 eV/atom.

Because the clusters formed in the MECS are accelerated by collisions with inert carrier gas molecules to a velocity of approximately 500 m/s or a kinetic energy of approximately 0.25 eV/Au atom during beam formation, it is important to reduce this velocity before directing them onto a substrate. A "soft landing" is accomplished by placing the substrate inside a closed box placed inside the MECS vacuum system and bleeding inert gas into this box so that the incoming cluster beam is completely decelerated or thermalized via collisions with background gas molecules before the clusters reach the surface of the substrate. Such a deceleration cell is illustrated in Figure 8.

Cluster-based nanostructures designed to have a weak coupling between cluster and substrate were fabricated by first preparing an ultraflat gold substrate (see the discussion in Section 5.2) and then coating the substrate with an aryl dithiol SAM. This SAM-covered substrate was then placed in the deceleration cell within the MECS vacuum chamber and exposed to a beam of single-crystal gold clusters. The substrate was then removed from the MECS system and transported in a desiccator to a separate UHV chamber in which the electronic properties of the nanostructure were studied by STM (see Section 5).

3.4. Capture of Clusters as Colloidal Particles

Once crystalline clusters of a desired size are synthesized, the problem still remains of how to assemble them into a useful material. This is complicated in the case of gold by the fact that at room temperature gold clusters agglomerate upon contact. We have found that efficient cluster collection and elimination of cluster agglomeration can be achieved by contacting the cluster aerosol with a fine mist of organic solvent containing surfactant molecules and then collecting the solvent drops in a liquid receiver (Fig. 8). A detailed description of this technique can be found elsewhere [191].

The critical ingredient in successful operation of this technique is finding a surfactant molecule that rapidly adsorbs onto the surface of the clusters to encapsulate them in an SAM. We have found a number of surfactant species to be effective for stabilizing 1–5-nm-diameter metal clusters. These include fatty acids, alkyl amines, alkyl thiols, alkyl disulfides, and alkyl isonitriles. The key requirements seem to be an end group that covalently attaches to the metal of interest and a methylene chain 8–12 units long for steric repulsion. With the proper surfactant, it is possible to capture nanometer diameter metal clusters from the gas phase and transform them into stable colloidal particles without altering their size distribution.

Using alkyl thiols and alkyl disulfides, we have been able to capture nanometer diameter gold clusters as stable colloids in mesitylene (C_9H_{12}) and decane ($CH_3(CH_2)_8CH_3$) with no observable change in the cluster size distribution except a sharpening of the surface facets caused by removal of gold adatoms decorating the surface of the underlying closed-shell crystal. We find that dodecanethiol is a particularly effective surfactant for this system.

A 25-ppm colloidal suspension of 3.7-nm-diameter gold clusters (passivated by an SAM of dodecanethiol) in either decane or mesitylene is stable with no observable cluster growth, dissolution, or precipitation for months at a time. The self-assembly of alkyl thiols on Au(111) has been studied in UHV [192]. This study documents the ability of alkyl thiols to reconstruct the Au(111) surface and lends credibility to our observation that alkyl thiol–encapsulated gold clusters appear to have cleaner facets than bare gold clusters.

The facile adsorption of alkyl thiols on gold forms the basis of a novel direct colloidal synthesis for thiol–encapsulated gold clusters proposed by Brust et al. [150]. Leff et al. [193] have shown that cluster size can be controlled in this synthesis by simply varying the gold-to-thiol ratio. They concluded that the gold nanocrystals are obtained as equilibrium products in this room temperature liquid phase synthesis. This conclusion is disproved by our experiments in which preformed gold clusters are encapsulated using excess thiol with no observable size change. Thus, the mechanism for size control in the Brust synthesis must be a kinetic one.

The availability of a simple method for synthesizing alkanethiol-encapsulated gold clusters of controlled size has generated a lot of interest in these nanoparticles. In particular, Whetten et al. [194] have shown that these encapsulated clusters seem to exist in preferred closed-shell configurations and that these "molecular" nanocrystals can be considered to be stable chemical species. Whetten [195] has made use of fractional precipitation to separate the smallest nanocrystal species formed via the Brust method and has studied their properties in some detail.

Direct solution phase synthesis of surfactant-encapsulated metal particles has the great advantage of simplicity. The Brust synthesis seems to produce encapsulated gold nanocrystals of equivalent quality to those produced by the two-step process developed at Purdue. Nevertheless, gas phase synthesis of bare clusters followed by solution phase encapsulation provides advantages over direct solution phase synthesis. Ultrafine particles containing practically any atomic species can be grown in the gas phase and these particles can be encapsulated by a wide variety of surfactant molecules. Separation of the particle synthesis and particle passivation steps also permits thermal annealing of the particles prior to encapsulation, and this can lead to unique structures [196].

3.5. Precipitation of Colloidal Networks from Solution

The gold clusters encapsulated by an alkyl thiol, such as dodecanethiol, are stable in aliphatic solvents for over a year [197]. However, if a small amount of a dithiol or a solution of the same is added to a sample of the gold colloid, a three-dimensional (3D) cluster network precipitates out of solution. This process is rather rapid and is dependent on the amount of dithiol added. The normally red-to-pink gold colloid solution, upon addition of the dithiol, turns purple and then a black precipitate forms and the solution becomes clear and colorless. A TEM of a sample of the precipitate suggests that the dithiol molecule links the gold clusters to each other, until the supramolecular structure becomes insoluble.

Conceptually, the process of forming these three-dimensional networks is thought to begin by an aryl dithiol molecule displacing an alkane thiol on the gold cluster surface as shown schematically in Figure 10. Once a dithiol is attached to a gold cluster, there is a pendant thiol that can displace an alkane thiol on a different gold cluster. If the displacement occurs, then a dimer of gold clusters is formed. These steps can be repeated, forming trimers, tetramers, and so on. Finally, a random three-dimensional network of interconnected clusters forms, becomes insoluble, and precipitates out of solution.

To understand this linking better, an ultraviolet–visible (UV–vis) analysis was undertaken. The UV–vis spectrum of the gold colloid has an absorption at $\lambda_{max} = 520$ nm. This absorption is caused by the plasmon excitation of the gold clusters and is at a slightly higher wavelength compared to the bulk gold plasmon energy. This plasmon absorption band is predicted to be near Lorentzian in shape. The position (λ_{max}), full width at half-maximum (FWHM), and height (A_{max}) of the absorbance peak are related to the particle

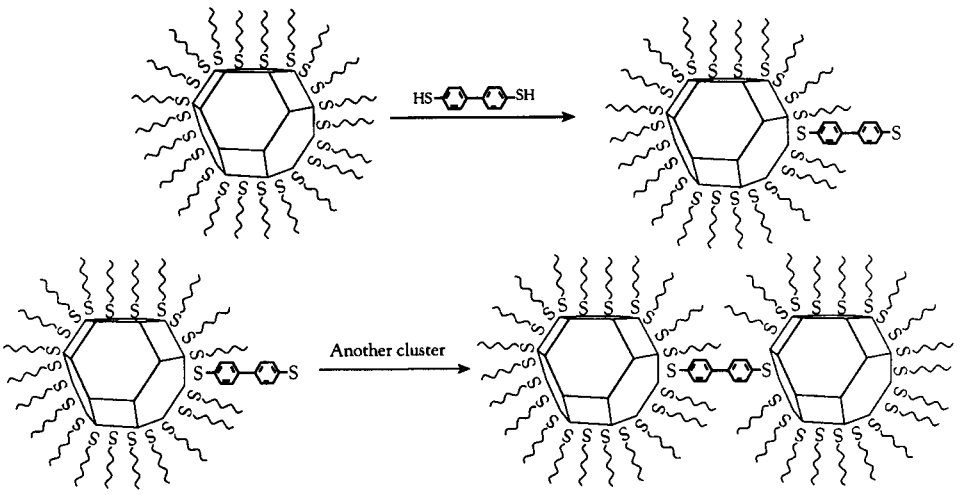


Fig. 10. Possible mechanism for two-dimensional and three-dimensional linked cluster network (LCN) formation.

size [198–202]. A sample of the colloid solution (mesitylene was used because the dithiols are not soluble in decane) was first analyzed by UV–vis. Dithiol was then added and UV–vis spectra were taken at approximately 30-min intervals until no more absorbance was observed.

The UV–vis data are different for different dithiol molecules. For example, the data using XYL is different from those using BPDT. In the case of BPDT, the UV–vis spectrum shows a definite red-shifting plasmon peak along with a quenching of absorbance as three-dimensional aggregates precipitate from solution. The total red shift is a little more than 30 nm as opposed to less than 10 nm for XYL as shown in Figure 11.

This red-shift spectral phenomenon can be explained by considering the molecular orbitals of the respective molecules and the effect of conjugation length on optical absorption spectra. BPDT has fully conjugated π electrons from end to end and is expected to be able to delocalize charge better than the more localized π electrons of the XYL molecule. The methylene carbons of XYL are sp^3 hybridized and thus prevent charge delocalization from end to end. When BPDT absorbs on a cluster or links two clusters together in solution, the electronic conjugation length is longer and the species absorbs a longer-wavelength light.

3.6. Formation of an Unlinked Cluster Array

Once a colloidal solution of encapsulated clusters is obtained, several techniques exist for depositing the clusters onto a flat substrate. The simplest method is to spin-cast a dilute solution of the clusters onto the substrate. In order for this technique to be successful, the solvent must completely wet the substrate. In this case, the liquid forms a thin planar film that covers the entire surface. This liquid film shrinks in thickness as the solvent evaporates. As the film shrinks, the clusters are forced to the surface of the substrate where they coalesce into a uniform close-packed array. Depending on the original cluster concentration and initial thickness of the film, one can achieve monolayer or multilayer arrays with this technique.

The biggest drawback of the spin-casting technique is that it is difficult when working with nanoscale clusters to obtain uniform coverage of the entire substrate. As the liquid film shrinks, it resists becoming too thin because of the disjoining pressure contribution to its free energy and below a critical "equilibrium thickness," which is generally greater than the diameter of the clusters, holes form in the film [203]. As a hole grows in size,

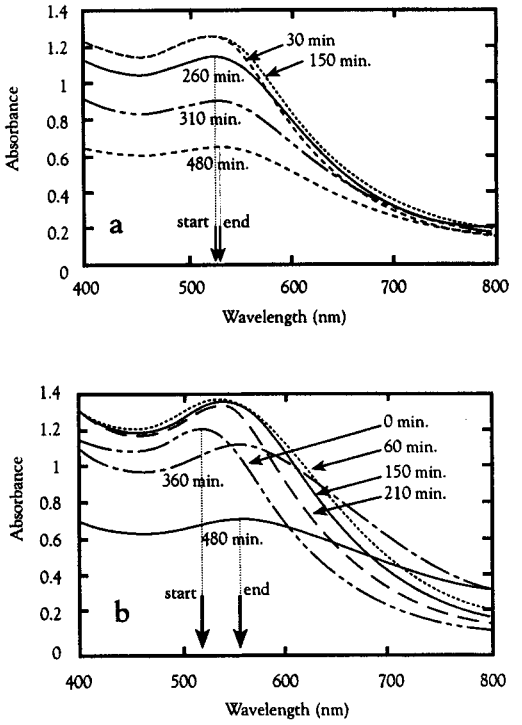


Fig. 11. Time-elapsed UV–vis electronic absorption spectra of dodecanethiol-encapsulated gold clusters dissolved in mesitylene and cross-linked by reaction with (a) xylyldithiol (XYL) and (b) biphenyldithiol (BPDT).

the liquid/gas interface at its edge tends to sweep the clusters from the dewetted area of the substrate. This leaves areas of the substrate that are not covered by clusters and either produces rings of clusters [204] or compact islands. Thus, it is difficult to achieve uniform coverage using spin casting; however, within the covered areas, the clusters self-assemble into close-packed monolayer or multilayer arrays.

Figure 12 is a TEM micrograph of a monolayer array fabricated by the spin-casting technique. This array consists of 3.7-nm-diameter gold clusters encapsulated using dodecanethiol. The micrograph shows a small section of an array containing approximately 5×10^4 clusters covering an approximately 1×10^6-nm^2 area. The clusters were cast from a mesitylene solution onto an electron transparent sheet of MoS_2. The average center-to-center separation in Figure 12 is 5 nm. This yields an average gap between clusters of 1.3 nm. This is less than expected if the clusters are each surrounded by a monolayer film of dodecanethiol. Laibinis et al. [205] determined the thickness of a self-assembled monolayer of dodecanethiol on Au(111) to be 1.2 nm, yielding a gap of $2 \times 1.2 = 2.4$ nm. Thus, the alkyl thiols attached to adjacent clusters likely interpenetrate in the region between the clusters.

The arrays have been imaged using STM techniques as shown in Figure 13, which is a top-view STM image showing the edge of a two-dimensional array of approximately 3.5-nm-high Au clusters on a MoS_2 substrate. The Au clusters are coated by a dodecanethiol surfactant to prevent agglomeration. Because the clusters are encapsulated by dodecanethiol molecules, STM images must be taken at a low-set-point current (~50 pA or less) to reduce the interaction force between the STM tip and the molecules.

Both a wide first layer [labeled (a)] on the MoS_2 substrate and a few clusters forming the second layer [labeled (b)] on top of the first layer can be observed. The relative orientation between the first and the second layer shows that the encapsulated cluster system has a hexagonal closed-packed structure.

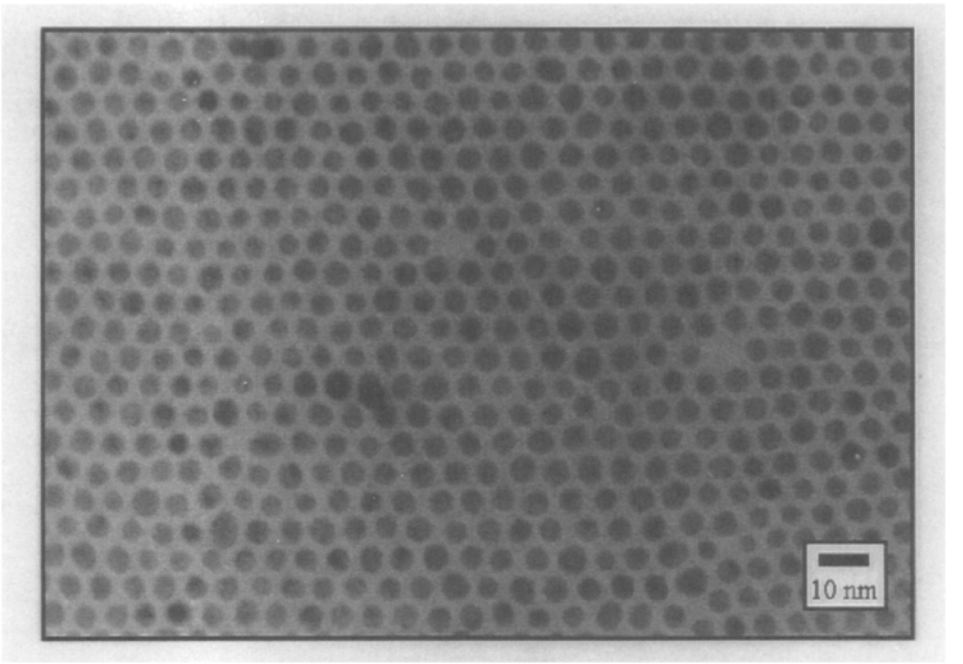


Fig. 12. TEM of unlinked cluster array. The Au clusters in this array have a 3.7-nm diameter and are encapsulated by dodecanethiol. (Source: Reprinted from [7]. © 1996 American Association for the Advancement of Science.)

Two other methods have been proposed for fabricating ordered two-dimensional colloid lattices that cover an entire substrate. Both of these techniques show promise and are being studied in several laboratories including our own. The first of these is the technique of electrophoretic deposition [206, 207]. The second method is the Langmuir–Blodgett technique in which a monolayer of clusters is formed at an air/water interface and transferred to the substrate as a Langmuir–Blodgett film [208].

3.7. Formation of a Linked Cluster Network

Self-assembled arrays of encapsulated gold clusters are not very robust. They are destroyed by scanning electron microscopy (SEM) imaging or by immersing the substrate in various solvents. To produce a network that is chemically and thermally stable, it is necessary to interconnect the clusters in the array by displacing the single-ended alkyl thiol molecules by double-ended molecules such as dithiols or di-isonitriles, which bridge the gap between adjacent clusters in the array and form strong bonds that chemically link the clusters to each other. This interconnection step produces a stable linked cluster network (LCN).

We have used a number of conjugated dithiol and di-isonitrile molecules to chemically bind gold clusters to each other and to bulk gold surfaces. Two kinds of structures have been fabricated. The first is produced by preparing a flat gold surface by evaporating gold atoms onto a mica substrate in a vacuum chamber. The Au(111) surface is then immersed in a solvent containing the dithiol or di-isonitrile molecule of interest and the molecule is allowed to form an SAM on the substrate. This organic-covered sample is then mounted in the MECS vacuum chamber and exposed to a submonolayer flux of bare gold clusters. The resulting sample is ideal for studying electronic transport through organic molecules bridging two gold surfaces [6].

The second structure is obtained by interconnecting the clusters in a close-packed unlinked array. Henderson et al. [3] showed that aryl dithiols and di-isonitriles completely displace alkyl thiols from a Au(111) surface to form a dithiol or di-isonitrile SAM in which

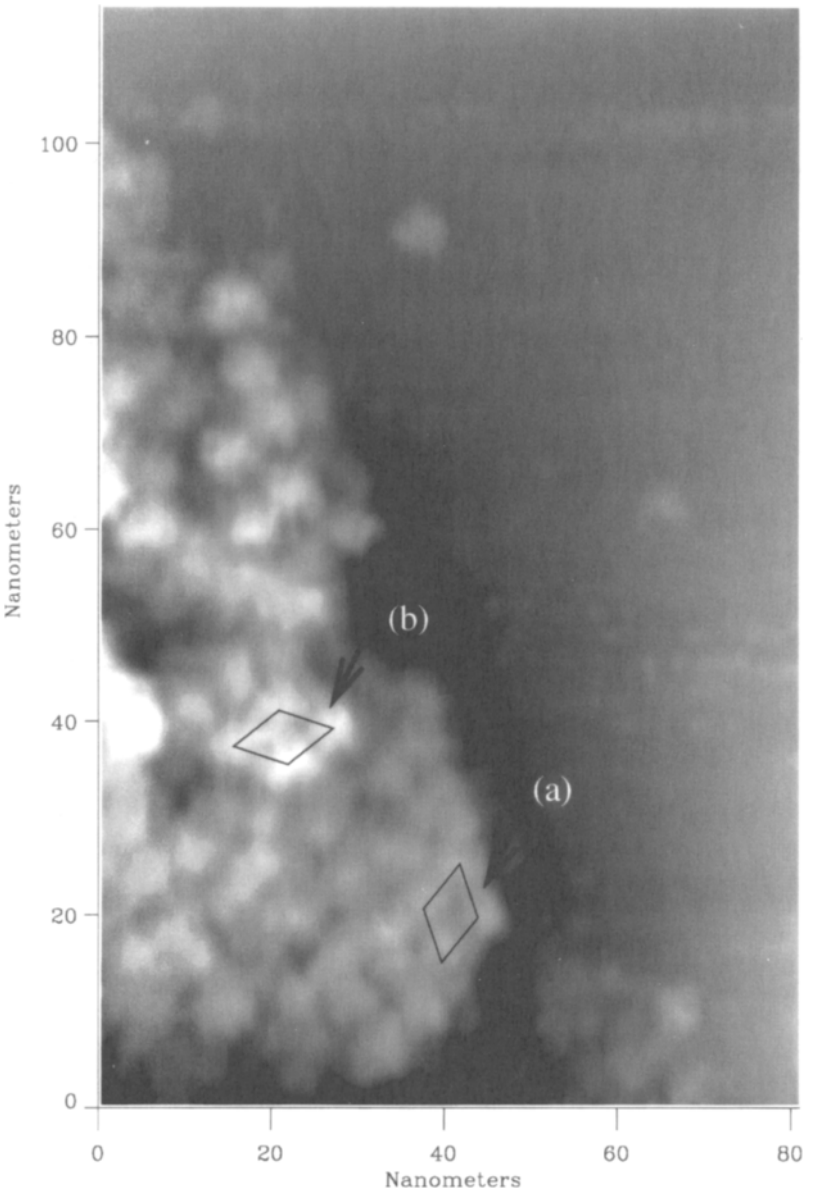


Fig. 13. Unfiltered STM image of dodecanethiol-coated Au clusters on a MoS_2 substrate. The imaging conditions are $I_t = 50$ pA and $V_t = -1.6$ V. At location (a), the 3.5-nm-diameter clusters self-assemble into a hexagonal network on MoS_2. In (b), the start of a second cluster layer is observed. The unit cells for the first and second layers are indicated. (Source: Reprinted from [8] with kind permission from Kluwer Academic Publishers.)

only one end of the molecule is attached to the gold surface. Thus, it was expected that immersing an array of clusters that have been encapsulated with an alkyl thiol molecule in a solvent containing an aryl dithiol or di-isonitrile would result in displacement of the alkyl thiol molecules and hopefully interconnection of the clusters into a linked cluster network [6].

Unlinked arrays of gold clusters that are encapsulated in dodecanethiol can be immersed in acetonitrile (CH_3CN) without affecting the structure of the array or its stability. If the same array is immersed in a solution of aryl dithiol or di-isonitrile in acetonitrile, however, the spacing between the clusters and the stability of the array are altered. In particular, the

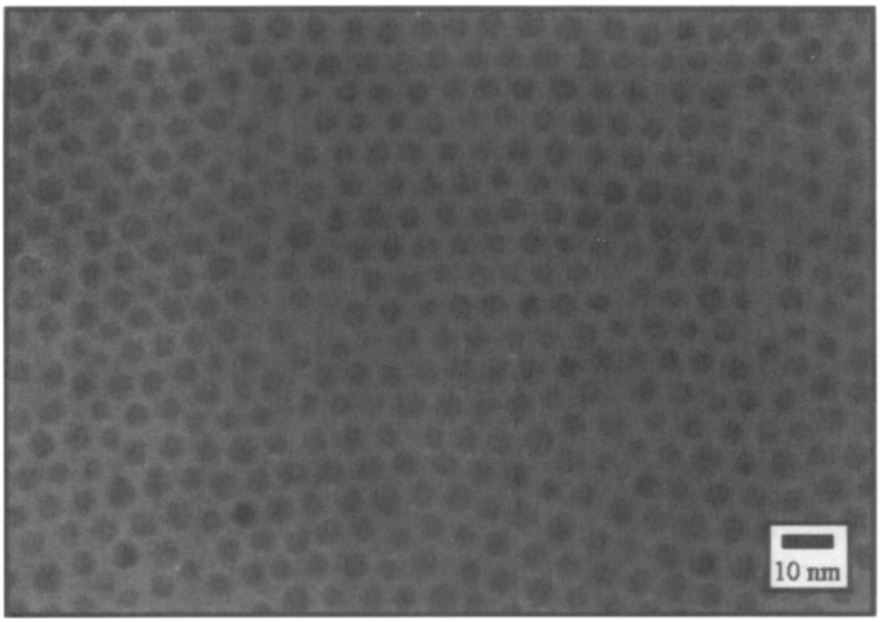


Fig. 14. TEM of linked cluster network (LCN). This LCN was prepared by immersing the cluster array shown in Figure 12 in a solution of 20ADT (see Fig. 4) in acetonitrile. The 3.7-nm-diameter Au clusters are linked together by the 20ADT molecules. (Source: Reprinted from [7]. © 1996 American Association for the Advancement of Science.)

chemical and thermal stability of the array is dramatically increased. The observations that there is a structural change induced by the linking molecule and that there is a dramatically increased chemical and thermal stability lead us to hypothesize that the clusters are indeed interconnected. This process is reproducible; however, we have no proof to date that the displacement of the alkyl thiol molecules is complete or that the molecular interconnections between the clusters are uniform.

Figure 14 is a TEM micrograph of a monolayer of clusters that was linked using a 2-nm-long aryl dithiol 1,4-di(4-isocyanophenylethynyl)-2-ethylbenzene (20ADT) shown in Figure 4. The clusters in this micrograph are 3.7 nm in diameter. Their unlinked array was fabricated in the same way as the array shown in Figure 12. The unlinked array was then immersed for 12 h in a millimolar solution of 20ADT in acetonitrile, followed by a 20-min rinse in acetonitrile. The average center-to-center distance between clusters in Figure 14 is 5.4 nm, which yields an average gap between clusters of 1.7 nm. This is an increase of 0.4 nm over the 1.3-nm gap of the unlinked array.

3.8. Concluding Remarks

Gold clusters with diameters in the 2–5-nm size range have been synthesized in the gas phase as single crystals. These bare metal clusters have been deposited on SAM-covered gold substrates to produce well-characterized molecular nanostructures and captured in mesitylene as stable colloidal particles in which the individual gold clusters are encapsulated by an SAM of dodecanethiol molecules. Aryl dithiols have been used to precipitate gold clusters by linking the clusters in solution. Uniform close-packed monolayer arrays of encapsulated clusters have been deposited on a variety of smooth surfaces by spin casting a dilute colloidal solution of the uniform-size clusters produced in the MECS onto the substrate. Finally, these unlinked cluster arrays have been successfully transformed into linked cluster networks by immersing them in an acetonitrile solution containing an aryl dithiol or aryl di-isonitrile molecular wire.

4. THEORY OF ELECTRONIC CONDUCTION THROUGH ORGANIC MOLECULES

4.1. Overview

Organic molecules display a rich variety in their electrical conducting properties [209]. On the one hand, we have insulating molecules based on alkane chains with large band gaps in excess of 6–8 eV. On the other hand, we have conjugated polymers such as polyparaphenylene that behave like semiconductors with moderate band gaps on the order of 2–4 eV. In bulk form, they have been doped to attain near metallic levels of conductivity. Finally, we have carbon nanotubes that are semimetallic (e.g., graphite) and can conduct well even in intrinsic form without any doping. Organic molecular wires with high conductivity could, in principle, find use in constructing self-assembled interconnection networks for ultrasmall electronic devices, which is a truly intriguing possibility. Two leading candidates for the construction of such molecular wires are nanotubes [210] and doped conjugated polymers.

Conjugated polymers in bulk form have been used to demonstrate transistors and light-emitting devices [211]. However, the conduction process in such solidified polymers is a complex process dominated by interchain hopping and hopping from one domain to another. By contrast, electrical conduction through SAMs of these molecules is determined by the intrinsic conduction properties of individual molecules. Indeed, we have had considerable success in explaining our measurements of the current–voltage $[I(V)]$ characteristics of such molecular monolayers in terms of a theoretical model that computes the current through an individual organic molecule connected to two contact pads across which a voltage is applied [10, 11]. This is the model that we will describe.

4.2. Theoretical Model

Molecular monolayers generally attach strongly to a gold surface through thiol (–S) end groups [212–214], giving a strong chemical bond with good orbital overlap. The other contact, typically an STM probe (see Fig. 15a), is usually coupled weakly to the molecule, but, in principle, could also be coupled just as strongly, as is the case when a gold cluster is attached to the free thiol group of an aryl dithiol molecule. The problem is calculating the current–voltage $I(V)$ characteristics of this system. In mesoscopic physics, this is usually done using the transmission formalism, which is based on the following expression for the current–voltage relation [215]:

$$I = \frac{2e}{h} \int_{-\infty}^{+\infty} dE\, T(E)\big[f(E-\mu_1) - f(E-\mu_2)\big] \tag{1}$$

Here, $T(E)$ is the transmission function from one contact to the other, $f(E)$ is the Fermi function, and μ_1 and μ_2 are the electrochemical potentials in the two contacts. We can write [216, 217]:

$$I = \frac{2e}{h} \int_{\mu_1}^{\mu_2} dE\big[T(E) \otimes F_{\mathrm{T}}(E)\big] \simeq \frac{2e}{h} \int_{\mu_1}^{\mu_2} dE\, T(E) \tag{2}$$

where $F_{\mathrm{T}}(E)$ is the thermal broadening function and the symbol $\otimes$ denotes convolution. Because $k_{\mathrm{B}}T = 26$ meV is relatively insignificant on our energy scale, we can neglect it as indicated. A number of groups have recently applied this approach to molecular nanostructures [9, 19, 20, 218, 219].

Figure 15b shows the calculated transmission function for the structure shown in Figure 15a. As we might expect, it has peaks at energies corresponding to the molecular energy levels. The peak resulting from the highest occupied molecular orbital (HOMO) is separated from that resulting from the lowest unoccupied molecular orbital (LUMO) by the

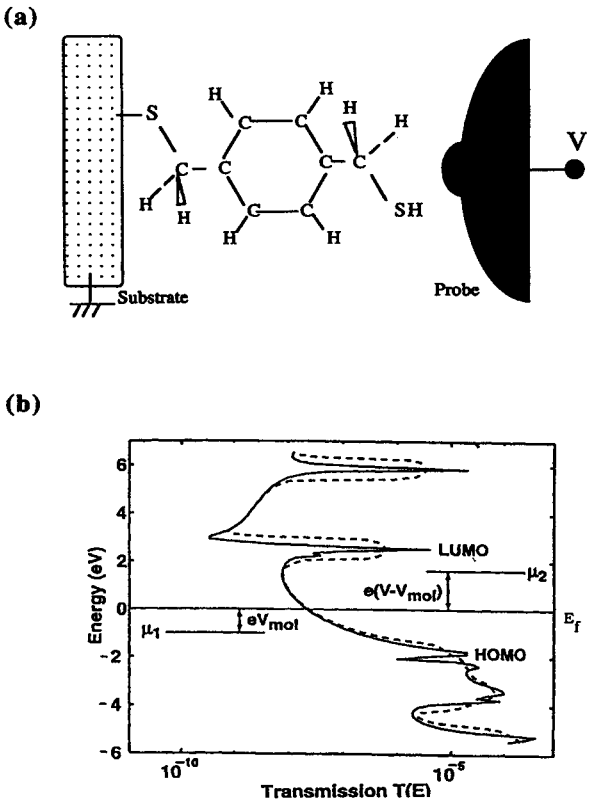


Fig. 15. (a) Self-assembled monolayer of α, α'-xylyldithiol on a gold substrate (only one molecule of the monolayer is shown for clarity). Also shown schematically is an STM probe used to measure the current–voltage characteristics. (b) Transmission function, $T(E)$, through the molecule from the tip to the substrate neglecting (solid) and including (dashed) scattering. Taking the molecular Fermi energy E_f as our reference, μ_1 moves down by eV_{mol} while μ_2 moves up by $e(V - V_{mol})$ where V_{mol} is the average electrostatic potential in the molecule (Source: Reprinted with permission from [10]. © 1997 American Physical Society.)

band gap of the molecule (~4 eV). The peaks are broadened by the coupling to the contacts and by scattering processes in the molecule. The transmission function, of course, plays a central role in determining the conduction properties of the molecule. However, it is evident from Eq. (2) that the location of μ_1 and μ_2 relative to the molecular energy levels is also crucial. Their location is determined by the equilibrium Fermi energy E_f and a voltage division factor $\eta \equiv V_{mol}/V$ $(0 \leqslant \eta \leqslant 1)$, which describes how the overall applied bias eV is divided between the two junctions:

$$\mu_1 = E_f - eV_{mol} \qquad \text{and} \qquad \mu_2 = E_f + eV - eV_{mol} \tag{3}$$

where E_f is the equilibrium Fermi energy and eV is the applied bias (note that $e = -1.6 \times 10^{-19}$ C) . As we will see, the factor η has a significant effect on the shape of the overall $I(V)$ characteristics.

The low bias resistance R of the molecule is determined solely by the transmission at the equilibrium Fermi energy [9]:

$$R^{-1} = \left[\frac{\partial I}{\partial V}\right]_{V=0} = \frac{2e^2}{h} T(E_f) \tag{4}$$

As we will see later, experimental estimates of R for an XYL dithiol molecule agree reasonably well with experimental measurements [4]. The advantage of this theoretical approach is that estimates for the resistance of a molecule are now possible. An example is

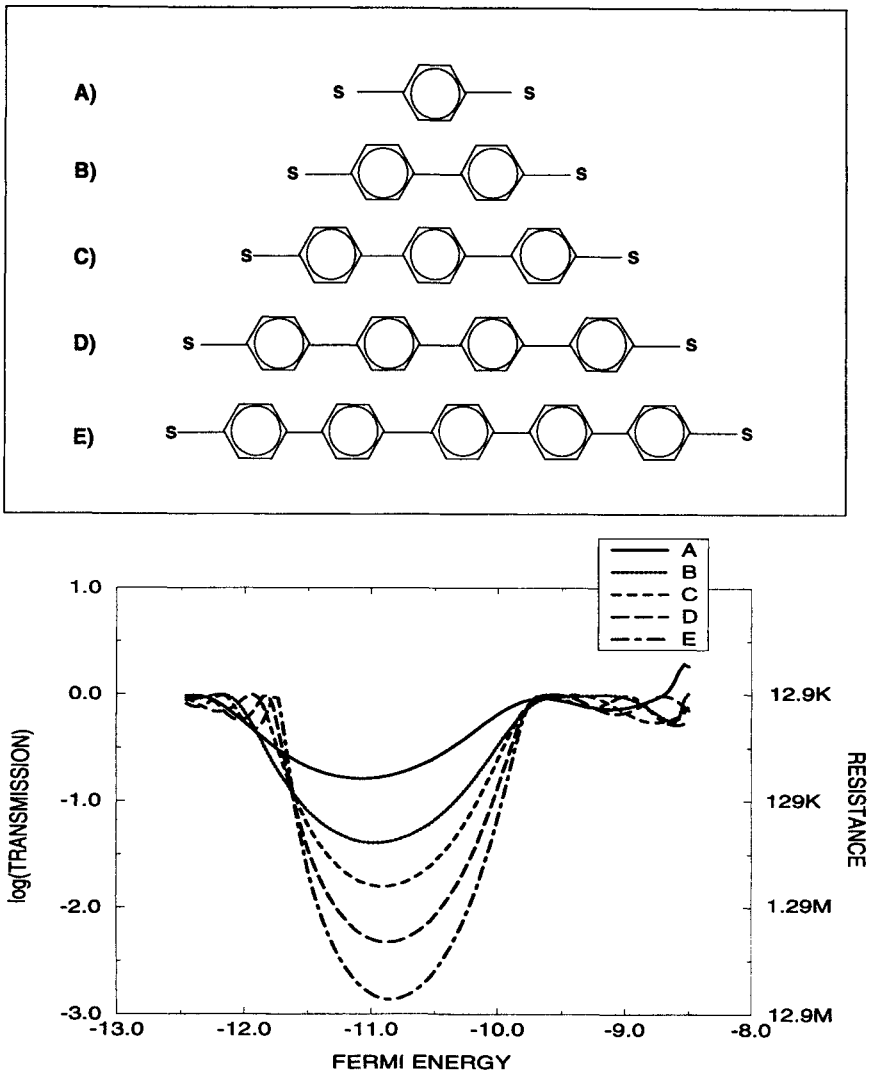


Fig. 16. Calculations for the resistance of different molecules as a function of the molecular Fermi energy. The resistance can be obtained by locating the position of the Fermi level on this graph for each molecule. (Source: Reprinted with permission from [9]. © 1996 American Physical Society.)

shown in Figure 16, which predicts how the resistance of a family of aryl dithiol molecules should vary as a function of overall length. Note, however, that the resistance is strongly dependent on the location of the Fermi energy, which can be very different for molecules of different lengths. This variation of the Fermi energy has to be taken into account when comparing the resistance of molecules of different lengths.

The transmission formalism is intuitively appealing because it seems reasonable to expect that the current flow through any conductor should be determined by the ease with which an electron can transmit from left to right. The main limitation of this point of view is that we have to assume that the molecule is short enough that an electron is not inelastically scattered within the molecule—that is, it exits the molecule with essentially the same energy with which it is incident. To account for inelastic effects properly, more sophisticated techniques are required [220]. This does not seem warranted at this stage when we are trying to understand the broad features qualitatively with a minimum number of fitting parameters. Some broadening of the energy levels by molecular vibrations can be included

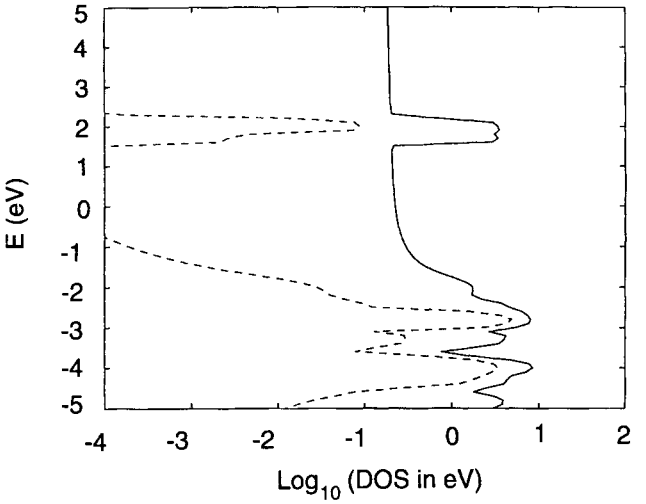


Fig. 17. Density of states versus energy for the structure shown in Figure 15a. The solid line indicates the total DOS, while the dashed line represents the LDOS on the sulfur atom at one end.

approximately within the transmission formalism as described previously [11]. This rounds out sharp features in the transmission function and smooths out cusps in the $I(V)$ characteristics. The results we present here are based on the transmission formalism, with the transmission function calculated using an extended Hückel model for the molecule [220] taking proper account of the metal–molecule bonding. We are assuming that the molecular chains are short enough that polaronic effects are not significant. Also, we assume that the level broadening caused by the coupling to the contacts is larger than the single-electron charging energy so that any charging effects can be accounted for with a self-consistent field approach.

We will not go into the detailed techniques used for calculating the transmission function, which has been described elsewhere [10, 9]. However, there are a couple of important factors that we would like to point out. First, the chemical structure of the metal–molecule bond is extremely important in determining the transmission. For example, the states near the Fermi energy of gold are largely derived from s orbitals. If the sulfur atom were to sit directly on top of a gold atom, its p_z orbitals (which form the HOMO and LUMO levels around the band gap) would not couple to the gold s orbitals because of symmetry considerations. However, in practice, it has been established that the sulfur atom sits at the center of an equilateral triangle of gold atoms leading to good coupling. Second, the transmission corresponding to the HOMO levels is much stronger than that for the LUMO levels. This is because the HOMO levels are largely sulfur based and couple well to the contacts, while the LUMO levels are largely ring based. This is evident from Figure 17, where we compare the total density of states (DOS) with the local density of states (LDOS) on the sulfur atom as a function of energy.

4.3. Factors Affecting the Current–Voltage Characteristics

Given a transmission function $T(E)$, there are two factors that determine the $I(V)$ characteristics: the equilibrium Fermi energy, E_f, and the voltage division factor, η. This is evident from parts a–c of Figure 18, which show the $I(V)$ characteristics corresponding to the same transmission function (shown in Fig. 15b) for different values of E_f and η. Let us discuss the factors that determine these two parameters.

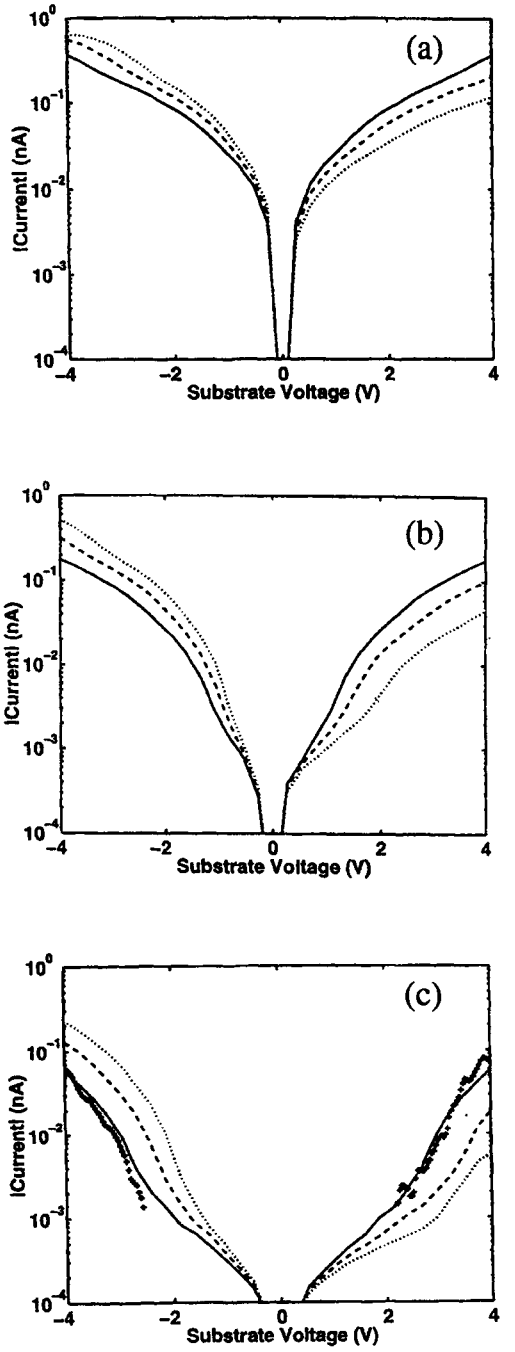


Fig. 18. Theoretical current–voltage characteristics for the molecule shown in Figure 15 with $\eta = 0.5$ (solid), 0.4 (dashed), and 0.3 (dotted): (a) $E_f - E_{HOMO} = 0.5$ eV, (b) $E_f - E_{HOMO} = 1$ eV, and (c) $E_f - E_{HOMO} = 1.8$ eV. The crosses in (c) show a typical experimental curve. (Source: Reprinted from [11], with permission from Elsevier Science.)

4.3.1. Where Is the Fermi Energy?

Basically, the equilibrium Fermi energy is determined by counting the number of electrons: the number of states below the Fermi energy must be equal to the number of electrons in the molecule. One point to remember is that the molecule on connecting to the contacts

does not remain exactly neutral. It can and does pick up a fractional charge, depending on the work function of the metal. However, the charge transferred for most metal–molecule combinations is usually much less than one electronic charge. It is easy to see that if the charge transferred (δn) is less than one, then the equilibrium Fermi energy must be located in the HOMO–LUMO gap. Indeed, if δn were equal to $+1$, the Fermi energy would lie on the LUMO, while, if δn were -1, it would lie on the HOMO. Clearly, for values in between, it should lie in the gap.

We can locate the Fermi energy quantitatively from the requirement that the total number of electrons in the molecule, n_T, must be given by

$$n_T = \int_{-\infty}^{E_f} dE\, N(E) \tag{5}$$

where $N(E)$ is the density of states. As explained previously, n_T is fractional if we consider the density of states just for the molecule. A better approach is to include a few gold atoms at each end as part of the molecule; this "extended molecule" then has an integer number of electrons that can be obtained just by counting. For example, for the molecule shown in Figure 15a, we add six gold atoms at each end to form an "extended molecule." The molecular density of states is then calculated using a total of 61 orbitals: four orbitals each for the eight carbon atoms and two sulfur atoms (40) plus one orbital each for the nine hydrogen atoms and twelve gold atoms (21). Note that we use only one s orbital for each of the gold atoms, because it is known that the DOS around the Fermi energy is dominated by the s band. An imaginary self-energy term is added to the gold atoms to account for the coupling to the infinite gold contacts whose density of states is known from the band structure calculations for bulk gold [221]. This imaginary term is responsible for converting the discrete energy levels of the isolated molecule into a continuous density of states appropriate for an open system. The total number of electrons, n_T, that go into these states is obtained easily by counting the electrons that each atom provides: four electrons each for the eight carbon atoms (32), six electrons each for the two sulfur atoms (12) plus one electron each for the nine hydrogen atoms and twelve gold atoms (21), making a total of $n_T = 65$ electrons.

It is evident from parts a–c of Figure 18 that the shape of the $I(V)$ data is affected significantly by the location of E_f. However, it should be noted that the DOS inside the HOMO–LUMO gap is quite small making the precise location of the Fermi energy very sensitive to small amounts of charge transfer from any ambient species. As such, it seems advisable to treat E_f as a "fitting parameter" within reasonable limits when trying to explain experimental $I(V)$ data.

4.3.2. How Does the Voltage Drop?

It is common to assume that the voltage division factor η is zero; that is,

$$\mu_1 = E_f \qquad \text{and} \qquad \mu_2 = E_f + eV \tag{6}$$

However, if we make this assumption, then the resulting $I(V)$ characteristic is extremely asymmetric. This is because the molecule conducts strongly as the electrochemical potential in the tip, μ_2, approaches the LUMO (for negative substrate voltage) or the HOMO (for positive substrate voltage). This leads to a strongly asymmetric $I(V)$ characteristic because the HOMO is a sulfur-based level that couples strongly to the gold, while the LUMO is a ring-based level that couples only weakly. Experimentally, however, we observe fairly symmetric $I(V)$ characteristics that can be explained quite easily if we recognize that the voltage division factor need not be zero.

The assumption that $\eta = 0$ implies that the molecular potential is fixed with respect to the substrate. This is usually justified by arguing that the substrate–molecule resistance R_1 is much smaller than the tip–molecule resistance R_2. Because the current I is the same

across either junction, one can write

$$I = \frac{\mu_{\text{mol}} - \mu_1}{R_1} = \frac{\mu_2 - \mu_{\text{mol}}}{R_2} \rightarrow \frac{\mu_{\text{mol}} - \mu_1}{\mu_2 - \mu_1} = \frac{R_1}{R_1 + R_2} \rightarrow 0 \tag{7}$$

as $R_2/R_1 \rightarrow \infty$. However, what this argument proves is that the electrochemical potential in the molecule (μ_{mol}) is the same as that of the substrate (μ_1) [222]. It says nothing about the electrostatic-potential, $\phi(\mathbf{r})$, which can vary spatially in inhomogeneous conductors even when no current is flowing. A p–n junction in equilibrium, for example, has an electrostatic potential difference of nearly 1 eV. Such equilibrium variations in $\phi(\mathbf{r})$ are already included in the calculation of the molecular energy levels. What we need to know is the change, $\delta\phi(\mathbf{r})$, in the electrostatic potential under bias that enters the molecular Hamiltonian and affects the molecular energy levels (the electrochemical potential enters only indirectly through charging effects). As long as the bias is small enough that μ_1 and μ_2 both lie in the gap, there is no significant transfer of charge into or out of the molecule. The molecule then behaves much like an insulator and the electrostatic potential divides according to the ratio of the capacitances rather than the resistances. Because capacitances vary only linearly with distance, the average electrostatic potential in the molecule V_{mol} is fairly close to half the applied voltage, V. Taking the molecular energy levels as a fixed reference, we can let the substrate float down by $eV/2$ to yield

$$\mu_1 = E_{\text{f}} - \frac{eV}{2} \qquad \text{and} \qquad \mu_2 = E_{\text{f}} - \frac{eV}{2} \tag{8}$$

corresponding to a voltage division factor of $\eta = 0.5$. With $\eta = 0.5$, the $I(V)$ data turn out to be fairly symmetric. This is because the molecule can now conduct through the HOMO for either polarity of the bias. For smaller values of η, the $I(V)$ data become more asymmetric with less current for positive substrate voltages than for negative substrate voltages.

We have measured a few hundred $I(V)$ data at different locations within an XYL SAM with different tips. A vast majority of these curves are reasonably symmetric: The currents for equal values of positive and negative bias are within an order of magnitude (or less) of each other. Slight asymmetries can be explained in terms of a small decrease in the value of η from the perfectly symmetric case ($\eta = 0.5$). Another consistent trend that we find is that as the tip is moved away from the molecule, the current for positive bias decreases much faster than that for negative bias. This is consistent with our theoretical predictions, because we expect η to decrease as the tip is withdrawn. It is evident from the theoretical plots in Figure 18 that for each value of E_{f}, the $I(V)$ data are symmetric for $\eta = 0.5$. With smaller values of η, however, the current for positive bias is reduced far more than that for negative bias, as observed experimentally with increasing tip–molecule distance. Smaller current for positive bias than for negative bias has also been reported elsewhere [222]. It should be noted that although η decreases as the STM tip is moved away from the sample, the decrease is linear (not exponential) with probe distance. Because the probe has to be within a few angstroms from the end of the molecule in order for the current to be measurable, the factor η remains as large as 0.4 for most measurements. We have obtained similar results for a series of molecules with thiol and isocyanide end groups with different numbers of phenyl rings. These results will be discussed in more detail elsewhere.

4.4. Concluding Remarks

We have shown that the current–voltage characteristics of self-assembled monolayers of conjugated organic molecules can be understood quantitatively in terms of the intrinsic properties of the molecule and the nature of its coupling to the contacts. We have described a theoretical model for computing the current through an individual organic molecule connected to two contact pads across which a voltage is applied.

The theoretical model has been tested in two separate ways. First, it has been used to predict the resistance of individual molecules that tether Au clusters to substrates and/or link Au clusters together when forming an LCN. Second, the model has been used to interpret experimental $I(V)$ data from an XYL SAM. In both cases, the model agrees fairly well with data.

The model shows that the $I(V)$ characteristics depend crucially on two parameters: the voltage division factor, η, and the equilibrium Fermi energy, E_f. The former is largely set by the geometry and remains close to 0.5. But the latter is very sensitive to charge transfer from ambient species, raising the possibility of doping through the formation of charge transfer complexes as well as the prospect of extremely sensitive chemical sensors.

5. ELECTRONIC PROPERTIES OF MOLECULAR NANOSTRUCTURES

5.1. Overview

To study the electronic properties of molecular nanostructures successfully, considerable attention must be devoted to scanning probe microscopy. This is one of the few techniques that probes the local electronic properties with sufficient spatial resolution to answer questions of fundamental importance. It is no accident that the rapid increase in the study of nanostructures has closely followed the widespread use of scanning probe microscopes. The electronic properties of a variety of different nanostructures have been studied, mostly using STM and scanning tunneling spectroscopy (STS) [223–225].

The different nanostructures under investigation in the present study are shown schematically in Figure 19. STM studies of individual molecules have been undertaken, with those molecules forming an SAM either on the substrate or around a Au cluster receiving special attention. Au clusters *encapsulated* by alkyl thiol molecules offer advantages for studying the electronic properties of self-assembled nanostructures. The encapsulating molecules serve two purposes. First, they prevent the Au clusters from forming into large aggregates. Second, they provide a convenient way to isolate the cluster from the substrate, allowing for the possibility of weak coupling and single-electron tunneling (SET) phenomena. Studies of bare Au clusters supported on different organic molecules have also been undertaken. A variety of different molecules have been studied, with dithiol molecules having a number of advantages.

For the molecular nanostructures shown in Figure 19, we have found that reliable SET effects can be observed from molecular nanostructures prepared in one laboratory, transported between laboratories under controlled conditions inside a desiccator, and briefly exposed to air during insertion into our load-locked UHV STM chamber for analysis.

5.2. Experimental Considerations

The STM imaging and spectroscopy system used in our studies is a home-built microscope with a computer-controlled digital feedback system for imaging [226] and spectroscopy [227]. The STM is housed in a UHV chamber with a base pressure of 3×10^{-10} torr. The UHV chamber is equipped with a load lock to allow insertion of samples and tips without the need to vent the entire chamber. Typically, STM tips were prepared by cutting 0.25-mm-diameter Pt/Ir wire. Usually, the tip was cleaned by extracting a field emission current of approximately 1 μA at a tip bias of approximately -100 V just prior to use. With this system, tunnel currents down to approximately 5 pA could be routinely measured.

The advent of fast digital signal processors (DSPs) has extended the capabilities of this instrument, allowing real-time calculations of important physical properties. For this reason, recent studies have been augmented by using the NanoDigital software, which

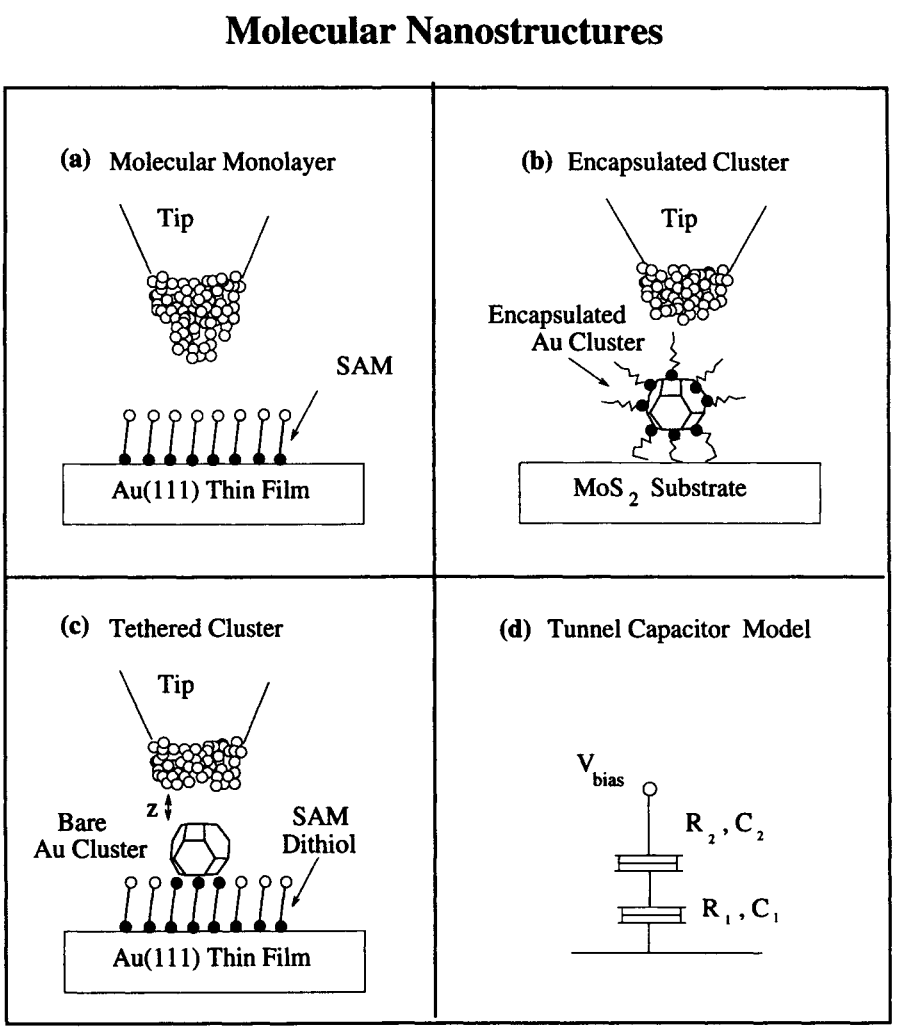


Fig. 19. Schematic diagrams of the nanostructures studied. In (a), the STM is used to study the electronic properties of individual molecules forming an SAM. In (b), the Au cluster is encapsulated by alkyl thiol molecules and isolated from the MoS_2 substrate. In this case, a chemical bond only forms between the alkyl thiol and the Au cluster. In (c), the Au cluster is tethered to the Au(111) substrate by an aryl dithiol SAM. A chemical bond is formed between both the dithiol and the Au cluster as well as between the dithiol and the Au substrate. In (d), the double-junction model used to analyze the $I(V)$ data from the cluster-based nanostructures is shown.

has been retrofitted to our instrument, allowing for such features as current-imaging spectroscopy (CITS), $I(V, z)$ studies, and better real-time control of the experiments.

Two different atomically flat substrates were employed in these studies:

1. Atomically flat, semiconducting substrates were achieved by using high-quality, single-crystal MoS_2 grown by vapor phase transport using Br_2 as the transport agent [228, 229]. The material was found to be n type from prior photocurrent measurements. High-quality, clean surfaces were routinely obtained by cleaving MoS_2 before use.
2. Initially, atomically flat Au(111) films were prepared by evaporating high-purity Au shot onto a heated mica surface. This practice has given way to a procedure for producing ultraflat, template-stripped Au(111) surfaces as described by Wagner et al. [230]. The preparation of a template-stripped surface begins by heating freshly cleaved ruby muscovite mica for 12 h at 330 °C at a pressure of approximately

10^{-6} torr. Then, gold films are formed by vapor depositing Au at 320 °C in two steps: (i) first a 5-nm-thick Au layer is deposited at an approximately 0.5 nm/s rate, followed by annealing for 6 h at the same temperature; and (ii) depositing an approximately 200-nm-thick layer with an approximately 1 nm/s rate. The gold-covered mica samples are then glued gold face down onto a flat Si(100) wafer using Epo-tek 377 [231] and cured by heating to 150 °C for 1–2 h. Before use as an ultraflat substrate, these Si/Au/mica samples are soaked in tetrahydrofuran (THF), leading to a complete detachment of the mica layer, thereby exposing the ultraflat gold film. The quality of the gold films prepared in this way was checked by STM before molecular deposition. STM scans showed an atomically flat surface over dimensions of a few micrometers with step edges clearly visible. The template-stripped gold films typically showed a dramatic improvement in surface roughness when compared to those films made by the thermal evaporation method initially employed.

5.3. Electronic Properties of Individual Molecules

As shown schematically in Figure 19a, an STM tip is ideal for determining the electronic properties of individual molecules self-assembled onto an atomically flat substrate. The key to successfully performing a meaningful STM $I(V)$ experiment is to maintain a controlled vacuum tunnel gap between the tip and the molecular layer. Burying the tip in the molecular monolayer produces data that are not particularly meaningful. In practice, this means using small tunnel currents at high bias voltages.

Work on the STM characterization of SAMs can be illustrated by reviewing typical data taken from an XYL dithiol SAM. Representative $I(V)$ data from this molecule when supported on a Au(111) surface is shown in Figure 20. Calculations of the HOMO and LUMO for this molecule reveal an energy gap $\Delta E_G = E_{LUMO} - E_{HOMO} \simeq 4.5$ eV, leading one to believe that an asymmetric $I(V)$ characteristic should result, with the degree of asymmetry depending on the position of the Fermi level of the molecule. Instead, the measured $I(V)$ data in Figure 20 are reasonably symmetric and show significant conductance within the region of the anticipated band gap. Only by properly taking into account the potential drop across the molecule can the details of the measured $I(V)$ characteristic be understood (see the discussion in Section 4).

In addition to explaining the overall shape of the $I(V)$ data, the model presented in Section 4 predicts a threshold for conduction when the bias voltage eV is greater than $\Delta = \pm(E_F - E_{HOMO})/\eta$, where E_F is the Fermi energy of the molecule and η is the voltage division factor defined in Section 4.2. Such a conductance onset is, in fact, observed and is often accompanied by a distinct feature in the conductance data (dI/dV). This feature is evident in Figure 20 and is attributed to conduction through the HOMO level of the molecule. Assuming $\eta = 0.5$, this would imply a value for $E_F - E_{HOMO} \simeq 1.7$ eV for the XYL dithiol SAM on Au.

More systematic measurements of $I(V)$ for a variety of SAMs are underway in our laboratory, employing a series of molecules to learn more about the overall validity of the electronic conduction through individual molecules. How the parameter η depends on bias voltage and its polarity should provide considerable insight into the polarization response of any molecules employed in a molecular nanostructure.

5.4. Electronic Conduction through Supported Clusters

While conduction through an individual molecule is clearly an evolving story, electronic conduction through a molecular nanostructure involving a nanometer Au cluster supported by molecules is somewhat better understood. For sufficiently small nanoclusters weakly coupled to substrates, Coulomb charging effects can be anticipated if the charging energy

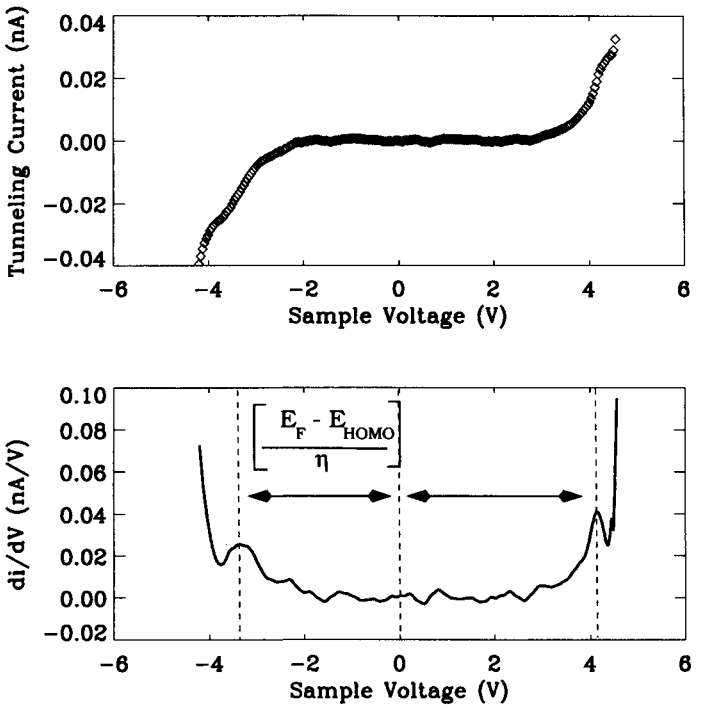


Fig. 20. Current–voltage (top) and conductance data (dI/dV) (bottom) for a Pt/Ir tip over an XYL dithiol SAM. The two features in the conductance spectrum are attributed to conduction through the HOMO states of the XYL molecule.

is greater than the thermal energies. In the semiclassical model of Coulomb blockade [232, 233], the two tunnel capacitors shown schematically in Figure 19d are biased by applying a voltage V_{bias} between the tip and the substrate. Each junction has a capacitance (C_i), an effective resistance (R_i), and a tunneling rate (Γ_i; $i = 1, 2$) associated with it. In principle, an offset charge Q_o may exist on the center electrode, allowing for asymmetry in the $I(V)$ data.

For the double junction in Figure 1c to show single-electron tunneling, it must satisfy two basic criteria. First, the Coulomb charging energy ($e^2/2C$) for one electron must be much greater than the thermal energy $k_B T$, where C is $C_1 + C_2$:

$$k_B T \ll \frac{e^2}{2C} \tag{9}$$

Under this condition, an electron cannot tunnel through the center electrode unless the bias voltage exceeds $e/2C$.

The second condition requires that, for excess charge on the center electrode, the energy uncertainty $\hbar/\tau_j$ associated with the lifetime $\tau_j = R_j C$ caused by tunneling through the jth junction be much smaller than the Coulomb charging energy $e^2/2C$. This consideration requires that

$$R_K \ll R_j \tag{10}$$

where R_K is the resistance quantum $h/e^2 \simeq 25.8$ KΩ.

A detailed semiclassical theory for single-electron tunneling is now well established and revolves around four basic principles. The theory relies on the existence of a steady-state distribution function $\sigma(n)$, which characterizes the excess number n of electrons on the center electrode and the tunneling probability $\Gamma_j^{\pm}$ for an electron to tunnel from/to ($\pm$) the center electrode through the jth junction. The theory also allows for a residual charge

Q_o on the center electrode. These considerations allow for the definition of four important quantities [233]:

1. A steady-state condition expressed by a rate equation

$$\sigma(n)\left[\Gamma_1^+(n)+\Gamma_2^+(n)\right]=\sigma(n+1)\left[\Gamma_1^-(n+1)+\Gamma_2^-(n+1)\right]$$

where the distribution function $\sigma(n)$ satisfies the normalization condition

$$\sum_{n=-\infty}^{\infty}\sigma(n)=1$$

2. A steady-state current expressed by

$$I(V)=e\sum_{n=-\infty}^{\infty}\sigma(n)\left[\Gamma_2^+(n)-\Gamma_2^-(n)\right]=e\sum_{n=-\infty}^{\infty}\sigma(n)\left[\Gamma_1^-(n)-\Gamma_1^+(n)\right]$$

3. Quantization of the energy. Because charge is quantized, the energy change by adding or subtracting one electron to or from the center electrode having a charge Q is given by

$$\Delta E_1^{\pm}=\Delta U^{\pm}\pm\frac{eC_2}{C_1+C_2}V=\frac{e}{C_1+C_2}\left[\frac{e}{2}\pm(ne-Q_o)\pm C_2V\right]$$

$$\Delta E_2^{\pm}=\Delta U^{\pm}\mp\frac{eC_1}{C_1+C_2}V=\frac{e}{C_1+C_2}\left[\frac{e}{2}\pm(ne-Q_o)\mp C_1V\right]$$

where

$$\Delta U^{\pm}=\frac{(Q\pm e)^2}{2(C_1+C_2)}-\frac{Q^2}{2(C_1+C_2)}$$

4. 1D semiclassical tunneling at each junction. If D_j is the density of states and E_j is the Fermi energy of the jth electrode, D_c and E_c are the density of states and Fermi energy of the center electrode, and $|\tau(E)|^2$ is the tunneling matrix element coupling the initial and final states at energy E, then a standard expression for the tunneling rate can be written as

$$\Gamma_j^{\pm}=\int_{-\infty}^{\infty}\frac{2\pi}{\hbar}|\tau(E)|^2D_j(E-E_j)f\left(\mp(E-E_j)\right)\times D_c(E-E_c)f\left(\pm(E-E_c)\right)dE$$

In the simple case when $D_j(E)=D_{j0}$, $D_c(E)=D_{c0}$, and $|\tau(E)|^2=|\tau_{j0}|^2$, then the tunneling rate acquires the simple form:

$$\Gamma_j^{\pm}=\frac{1}{R_je^2}\left[\frac{-\Delta E_j^{\pm}}{1-\exp(\Delta E_j^{\pm}/k_BT)}\right]$$

where $R_j=\hbar/(2\pi e^2D_{j0}D_{c0}|\tau_{j0}|^2)$ is now the resistance of the jth junction.

These four assumptions provide a nonanalytic expression for $I(V)$ in terms of the temperature, tunnel resistance, and tunnel capacitance of any two-junction network.

5.5. Electronic Properties of Encapsulated Gold Clusters

Recent work indicates that the capture of clusters in a colloidal solution followed by wet-chemical deposition onto atomically flat substrates allows for the fabrication of molecular nanostructures that are stable enough for STM study at room temperature. As an example, Au clusters have been encapsulated in dodecanethiol and supported on a semiconducting

MoS_2 substrate as shown schematically in Figure 19b. Experiments indicate that this protocol provides a viable strategy for reproducibly isolating nanometer-size clusters from substrates in such a way as to achieve SET effects at room temperature, provided care is taken to ensure high-quality sample preparation. The degree of coupling in this situation is not as well defined as in Figure 19c, but presumably can be adjusted by changing the length of the alkyl thiol molecules.

Within this context, a semiconducting substrate such as MoS_2 has a number of advantages. The study of MoS_2 by STM began during the early stages of the STM era [234]. Because MoS_2 has a layered structure with a chemically inert basal plane, atomically flat surfaces for STM study can be easily obtained by cleaving. Systematic STM studies of the electronic properties of the MoS_2 substrate have also recently been completed [235]. Within the context of single-electron tunneling, it is interesting to compare $I(V)$ data with the tip positioned over (i) an island formed by the evaporation of Au atoms vacuum-deposited on MoS_2 (strong coupling limit) with (ii) an encapsulated Au cluster supported on MoS_2 (weak coupling limit).

For the case when Au atoms are deposited on heated MoS_2, nanometer-size, triangular-shaped, single-crystal islands of Au form. This interesting morphology has already been reported using STM [236] and is noteworthy because the triangular-shaped single crystals were determined to have a preferred orientation [237]. Ichinokawa et al. [238] studied Au islands using STM and also found a preferred orientation of the islands with respect to the MoS_2 substrate. A similar epitaxial orientation is found when bare, nanometer-size Au clusters are soft landed onto MoS_2 substrates [239]. No single-electron effects are observed in $I(V)$ data from such structures (see Fig. 21a), presumably because of the strong electronic coupling between the Au island and the MoS_2 substrate.

When encapsulated Au clusters are deposited on MoS_2 substrates, the coupling between the cluster and substrate is reduced by the intervening dodecanethiol coat and single-electron effects are observed as shown in parts b and c of Figure 21. The data in Figure 21b were obtained when the tip was positioned over an isolated cluster with an apparent height of 0.8 nm. Data obtained from clusters with this size show evidence for SET about 90% of the time.

As the cluster size increases, the number of clusters exhibiting SET behavior is found to decrease. This is illustrated in Figure 21c, which shows $I(V, z)$ data for a cluster with a nominal height of approximately 2.4 nm. About 20% of the clusters in this size range show evidence for SET behavior (see Fig. 21c), while the remaining 80% or so show quasilinear $I(V)$ behavior. The data in Figure 21c illustrate the SET behavior typically observed.

The data in Figure 21c show interesting trends when compared to the data in Figure 21b for similar values of the tunnel resistance between tip and cluster. For example, as the cluster size increases, the capacitance should also increase and a narrower Coulomb blockade step should result as calculated from the conduction model outlined in Section 5.4. This trend is, in fact, observed in the data, providing good evidence that the SET effects are scaling as expected with cluster size. It is important to use the same tip when making such comparisons, a condition that was easily achieved by the stability of the samples prepared for this study.

5.6. Electronic Properties of Tethered Gold Clusters

The weak electronic coupling between a preformed, metallic nanocluster and an underlying substrate could potentially form the basis for many useful nanoelectronic devices. It is advantageous to explore as many ways as possible to reliably achieve this condition. A promising way to realize this situation is to coat a Au(111) substrate with a double-ended thiol, such as XYL dithiol. By covering the substrate with a dithiol SAM before exposure to clusters, it is possible to produce the isolated cluster/dithiol/substrate structures shown schematically in Figure 19c. The double-ended thiol "tethers" the cluster to the substrate, allowing reproducible scans of the supported cluster by an STM tip.

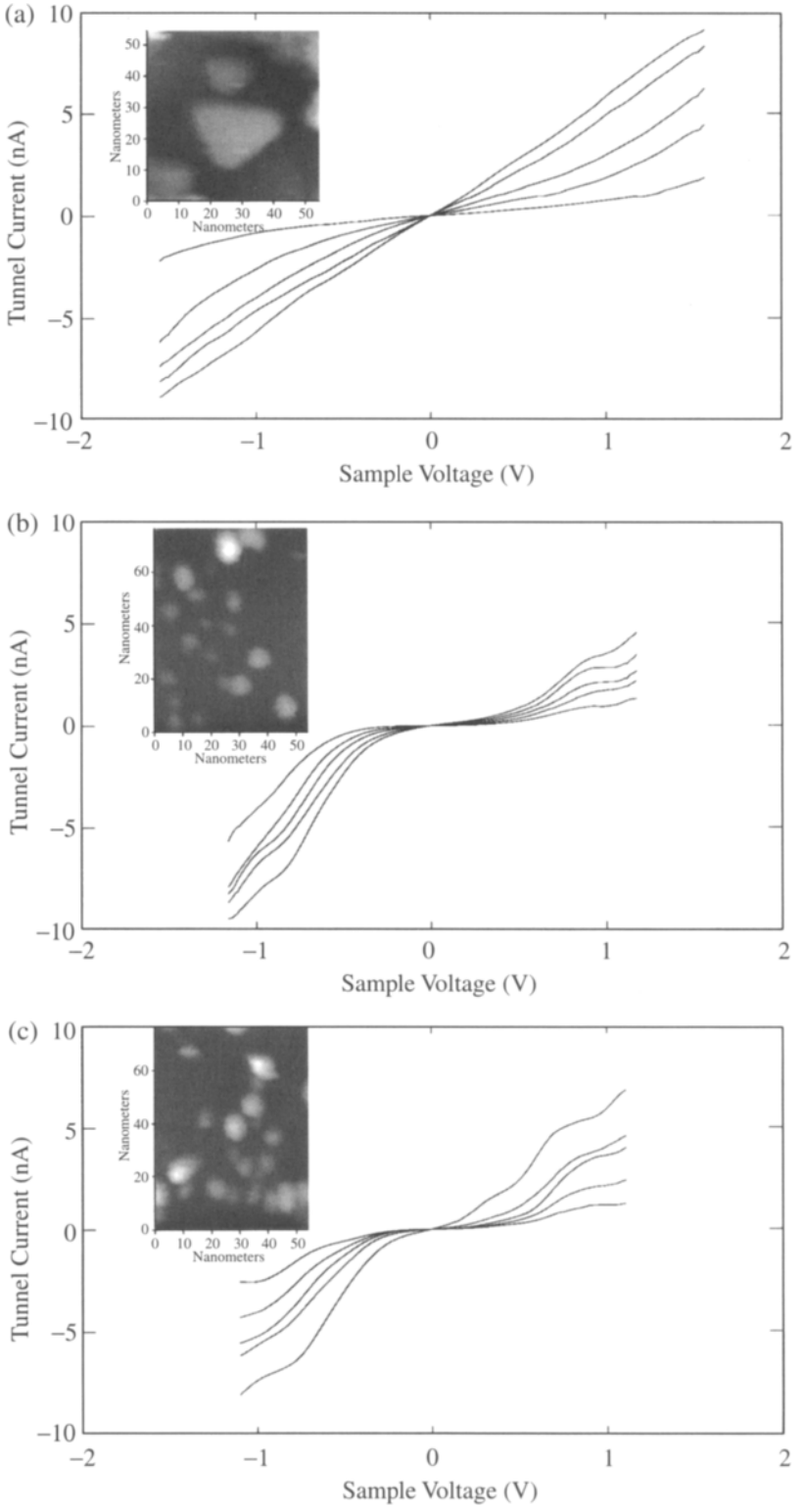


Fig. 21. $I(V)$ data taken when the tip is positioned over (a) a Au island formed by evaporating Au atoms onto MoS_2, (b) a small dodecanethiol-coated Au cluster (0.8 nm height), and (c) a large dodecanethiol-coated Au cluster (2.4 nm height). (b) and (c) show SET effects. The substrate supporting the Au clusters is freshly cleaved MoS_2. (Source: Reprinted from [8] with kind permission of Kluwer Academic Publishers.)

The well-characterized nature of the STM tip/vacuum/Au cluster/XYL SAM/Au(111) substrate allows a systematic study of $I(V)$ characteristics for different tip–cluster separations. For a typical STM scan encompassing approximately 10 clusters, $I(V, z)$ data with the STM tip positioned over each cluster indicated Coulomb blockade behavior for about 8 of the 10 clusters observed [4]. In addition to Coulomb blockade behavior, $I(V, z)$ data from these molecular nanostructures were also found to exhibit distinct, reproducible steps, suggesting the presence of a Coulomb staircase at room temperature [5, 6]. Typical $I(V, z)$ data obtained from a tethered cluster having a nominal height of approximately 1.8 nm as determined from the STM image are shown in Figure 22a. A representative fit to one of these data curves using the standard semiclassical model for Coulomb blockade (two tunnel capacitors in series) is shown in Figure 22b.

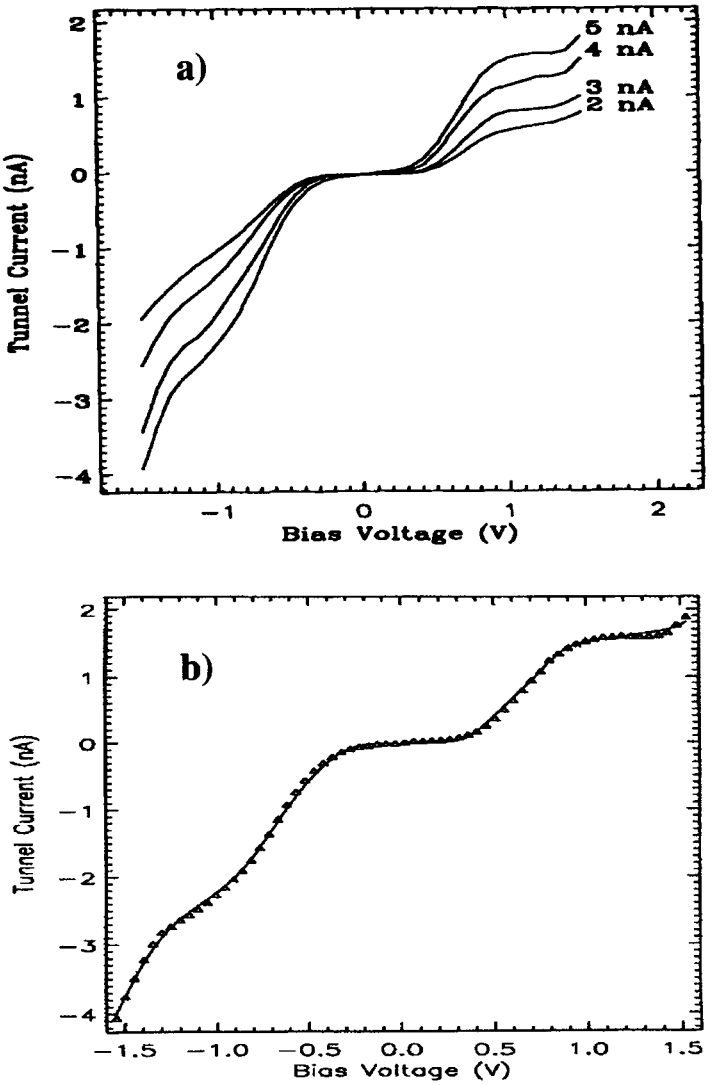


Fig. 22. (a) $I(V, z)$ data obtained at room temperature with the tip positioned over 1.8-nm-high Au cluster resting on an SAM of XYL dithiol. Each curve is the sum of 100 separate $I(V)$ sweeps. The different data sets illustrate how the $I(V, z)$ characteristics change as the specified set point tunneling current (i.e., the tip–cluster separation) is systematically varied. The reproducible nonlinearities in the $I(V)$ data indicate a Coulomb staircase behavior at room temperature. In (b), a typical fit to one of the $I(V)$ data. (Source: Reprinted from [6]. © 1996 American Association for the Advancement of Science.)

We find that the $I(V)$ data become more asymmetric as the tip–cluster separation increases and, for this reason, the data for positive and negative bias voltages were fit separately. The rapid, almost exponential drop in the tip–cluster resistance R_2 with a decrease in the tip–cluster distance was recovered from this fitting procedure. The other parameters (R_1, C_1, C_2 and Q_0) obtained by fitting the data were reasonably constant as the tip–cluster separation was systematically changed with C_2 increasingly slightly as the tip–cluster distance decreased. Average values required to fit all the data in Figure 22a are $C_1 = 0.8 \pm 0.5 \times 10^{-19}$ F, $C_2 = 1.3 \pm 0.3 \times 10^{-19}$ F, $R_1 = 1.8 \pm 1.2$ MΩ, and $Q_0/e = -0.20 \pm 0.17$.

Because of the well-characterized nature of this molecular nanostructure, it is possible to compare the capacitances obtained from fitting the $I(V, z)$ data to capacitances estimated using the geometry of the cluster and the approximate STM tip dimensions inferred from STM images. For a cluster with a diameter (i.e., height) of approximately 1.8 nm and a tip diameter estimated from the lateral dimension of the STM cluster image to be approximately 7.2 nm, the relevant capacitances can be calculated. If the cluster and tip are treated as spheres, estimates of C_1 and C_2 can be made using the method of image charges. These calculations give a tip–cluster capacitance C_2 of 1.4×10^{-19} F, which is close to the average parameter value of 1.3×10^{-19} F required to fit the data. In the same way, assuming a dielectric constant of 1.5, the cluster–substrate capacitance C_1 is estimated to be 1.7×10^{-19} F. This is about a factor of 2 larger than the average fitting parameter for C_1.

A nonzero average value for Q_0 of -0.20 ± 0.17 is necessary to fit the data. At the present time, it is not clear whether the nonzero value of Q_0 is related to work function differences between tip and cluster or related to the local chemical environment of the XYL/Au cluster nanostructure. The negative value for Q_0 seems consistent with the direction of the dipole moment formed for alkanethiol monolayers on Au [240]. More work will be required before the origin of the nonzero Q_0 and the asymmetry of the $I(V, z)$ data can be discussed further.

5.7. Estimating the Electrical Resistance of a Molecule

Bare nanocrystalline gold clusters tethered to a dithiol SAM and supported on Au(111) provide a reasonably well-characterized system for the estimation of the electrical resistance of a single molecule. Because the clusters have a truncated octahedron structure and realizing that the clusters orient with their (111) facets parallel to atomically flat substrates [239], it is possible to estimate the resistance of a single XYL molecule from measurements of R_1. This technique was first discussed in [4].

An estimate of the resistance of an individual molecule relies on the shape of the Au nanocluster. A relation between the area of the hexagonal [111] facet and cluster height can be obtained by considering the geometry of a perfect truncated octahedron. For the case of Au clusters containing 38, 201, 586, 1289, and so on atoms, the area of the (111) facet can be analytically related to the distance between two opposite facets. For clusters not described by a perfect truncated octahedron, an approximate hexagonal area can be inferred by interpolation. For example, from these considerations, a Au cluster approximately 1.8 nm high having a truncated octahedral structure has a (111) face with a surface area of approximately 2.1 nm^2. Electron diffraction studies of alkanethiolates on Au(111) show that the symmetry of the sulfur atoms is hexagonal with an area per molecule of 0.214 nm^2 [161, 165, 164]. Assuming the XYL dithiol molecules order in a way similar to the alkanethiolates, it follows that a 1.8-nm-high cluster is supported by about 10 XYL dithiol molecules.

Once the resistance between the cluster and the substrate (R_1 in Fig. 19d) has been determined, an estimate for the resistance of *one* XYL dithiol molecule can be made by

assuming that the molecules supporting the Au cluster conduct in parallel. This gives

$$\frac{N}{R_{\text{molecule}}} = \frac{1}{R_1} \tag{11}$$

where N is the number of molecules supporting the cluster. From fits to the Coulomb staircase data, an estimate for R_1 can be experimentally made. For the data in Figure 22 ($R_1 = 1.8 \pm 1.2\ \text{M}\Omega$), it follows from Eq. (11) that the resistance of a single XYL molecule is about $18 \pm 12\ \text{M}\Omega$. From similar data taken from an approximately 1.2-nm-high cluster, a value of about $8.8 \pm 1.2\ \text{M}\Omega$ is obtained.

These results can be compared with a theoretical calculation for the resistance of an XYL molecule bonded between two gold surfaces, in which R_{XYL} was calculated from Eq. (4). The low bias assumption is valid here because the majority of the voltage is dropped between the tip and the cluster. Samanta et al. [9] have calculated this resistance using an extended Hückel molecular orbital description of the molecule. Calculations give a mid gap resistance for the XYL molecule of $R_{\text{XYL}} \simeq 4.5 \pm 0.5\ \text{M}\Omega$. This is within a factor of 2–4 of that measured experimentally.

5.8. Concluding Remarks

UHV STM techniques have been successfully used to characterize the room temperature electronic properties of three interesting nanostructures: (i) SAMs of XYL dithiol molecules on Au(111), (ii) individual Au clusters encapsulated by dodecanethiol, and (iii) bare Au clusters tethered to flat Au(111) substrates using SAMs of XYL dithiol molecules. These studies permit an estimate for the resistance of individual molecules that is reasonably close to predictions of a theory for molecular conduction outlined in Section 4. Furthermore, the electronic properties of molecular nanostructures fabricated using isolated Au clusters are found to exhibit reproducible single-electron effects at room temperature. The nanostructure formed by combining molecular wires with a nanoscale cluster forms an interesting "unit cell" for the cluster arrays and linked cluster networks discussed in Section 6.

6. ELECTRONIC PROPERTIES OF CLUSTER ARRAYS AND NETWORKS

6.1. Overview

One- and two-dimensional arrays of quantum dots coupled by tunnel junctions are interesting both for their conduction characteristics and for their potential applications in nanometer-scale computational or memory devices [241]. Conduction in two-dimensional arrays of coupled tunnel junctions has been modeled in the regimes of strong and weak gate coupling [242–244]. Conduction through one- and two-dimensional arrays of Al dots separated by Al_2O_3 tunnel barriers has been demonstrated [245]. In experiments conducted at temperatures below 0.1 K, a conduction gap is observed near zero bias and conduction beyond threshold is found to behave as $I = (V/V_T - 1)^\gamma$ [245]. The measured values of γ range between 1 and 2 depending on whether the array is one or two dimensional and are consistent with theoretical predictions [243]. Higher-temperature studies using Al islands and Al_2O_3 tunnel junctions with weak coupling to a gate have demonstrated subthreshold conduction with an exponentially activated dependence [246]. These effects are attributed to Coulomb charging in the array, which dominates when the charging energy of an island is larger than the thermal energy. Several factors, including relatively large capacitances and the presence of random offset charge in the array, make lithographically defined tunnel junction arrays utilizing materials such as Al/Al_2O_3 unsuitable for room temperature

computational or memory applications. Random offset charge can have a serious impact on the conduction characteristics of tunnel junction arrays [247].

To see significant Coulomb charging effects in arrays of metallic dots at a temperature T, it is necessary to reduce the dot capacitance, C_D, that is, the total capacitance between a dot and all other nodes, to the point where $e^2/2C_D \gg k_B T$, where e is the electronic charge and k_B is Boltzmann's constant. For operation at $T = 300$ K, the corresponding C_D is substantially less than 1×10^{-18} F and corresponds to metallic dots with diameters less than approximately 5 nm. It is unlikely that low-cost, high-throughput lithographic techniques will be able to provide controlled features in this size range in the near future. However, techniques that exploit chemical self-assembly might be suitable for defining and connecting metallic islands on this size scale. A promising technique for the synthesis of controlled-size, nanometer diameter metal clusters is a gas aggregation cluster source such as the MECS [181, 191].

This section describes a study of the in-plane electronic conduction through two-dimensional arrays of uniform-size Au clusters interconnected to each other by means of conjugated organic molecules that bridge a gap between two gold contact pads separated by approximately 500 nm. These linked cluster networks (LCNs) were composed of single-crystal gold clusters with diameters of approximately 3.7 nm. Room temperature current–voltage relationships have been measured at various stages of the synthesis process to confirm the structural observations of deposition and linking. The conductance characteristics have been studied at various temperatures and models based on single-electron charging effects have been developed. The contact pad and array fabrication are described briefly, and a simple model for the conduction characteristics is presented.

6.2. Sample Preparation

To allow electrical characterization and nondestructive TEM observation of the LCN, a substrate was developed that provided lithographically defined contacts on a freestanding insulator film. This substrate allows both measurement of the in-plane conduction properties of the LCN and structural observation of the LCN, at various stages of preparation. A cross-sectional view of the substrate developed to meet these requirements is shown in Figure 23. The substrate consisted of two thin metal contacts fabricated on a TEM-transparent, freestanding SiO_2 film supported on a GaAs wafer. The thin SiO_2 film (40–70 nm) was deposited by thermal evaporation on a clean GaAs wafer. The metal contacts were 30–40-nm-thick gold contacts separated by 500 nm and were patterned by liftoff using a Cambridge EBMF-2 electron beam lithography system [1]. Contacts to external leads

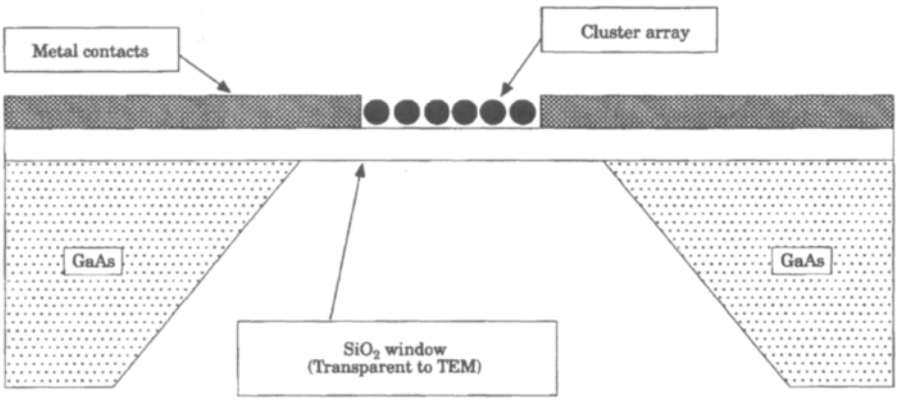


Fig. 23. Cross-sectional view of substrate used for electrical characterization and imaging of clusters. (Source: Reprinted from [1].)

were made by 300–500-nm-thick gold pads patterned using conventional UV lithography and liftoff. Freestanding SiO_2 windows aligned to the gap between the two metal contacts were formed by back etching the GaAs wafer. Details of the back etching and cleaning procedures required to prepare the substrate for LCN deposition are presented elsewhere [1].

Large close-packed arrays of encapsulated clusters spanning a micrometer or more have been fabricated on MoS_2 substrates [2, 7]. On such atomically flat substrates, two-dimensional, ordered, hexagonal arrays with relatively few defects can be realized by self-assembly.

To make useful substrates for electrical measurements, it is necessary to use lithographically defined contact structures on dielectric layers. Semiconductor materials such as Si or GaAs are preferable to materials such as MoS_2 or graphite (HOPG), because large-area samples are readily available and because conventional semiconductor processing techniques can be exploited. In this case, two issues are of critical concern for the development of high-quality LCNs: (i) surface flatness and (ii) possible molecular-level contamination of the surface resulting from photolithography and related processing techniques. To obtain continuous close-packed arrays of clusters, the root mean square (RMS) roughness of the surface on which these arrays are formed must be less than the diameter of the clusters. Atomic force microscopy (AFM) studies of thin evaporated SiO_2 films comparable to those used in this study indicated an RMS surface roughness of approximately 1 nm, with features that vary slowly on the scale of a cluster diameter. The residue from photoresist processing is thoroughly removed before LCN formation by a combination of solvent treatments and oxygen plasma cleaning. The current SiO_2 substrates provide a surface that is suitable for deposition of large-area arrays, but the quality of the array is limited by residual contaminants and imperfections on the surface, along with the chemistry of the SiO_2 surface.

The LCNs were formed using procedures comparable to those employed for deposition on MoS_2 substrates; that is, they were cast from colloidal suspensions of encapsulated clusters. The current–voltage relationships between the contact pads were measured (i) before array deposition (to verify the substrate leakage characteristics), (ii) in the "as-deposited" cluster arrays, and (iii) following linking by conjugated organic molecules. The clusters had an average diameter of 3.7 nm and a size distribution with a half-width of approximately 0.5 nm, determined using TEM imaging. During synthesis, the clusters are encapsulated by a monolayer of dodecanethiol molecules to prevent the clusters from coalescing during storage or array formation. The suspension spreads over both gold and silica surfaces. As the solvent evaporates, the encapsulated clusters form two-dimensional rafts on the surface. To form a relatively continuous monolayer of clusters in the gap, this procedure is repeated several times. Dodecanethiol encapsulation prevents the clusters from aggregating to form larger particles and produces a fairly uniform spacing between adjacent clusters, but does not provide strong mechanical tethering or reliable electrical coupling. Most often, the clusters deposit as a single monolayer; however, occasionally multilayer islands have been observed by TEM. A TEM micrograph of an LCN between contact pads is shown in Figure 24.

To stabilize the cluster network and to control the electron tunneling resistance between adjacent clusters, the clusters are covalently linked by immersing the unlinked array of encapsulated clusters in a solvent solution containing a double-ended linking molecule. Two conjugated linking molecules were used in this study.

The first is a di-isonitrile molecule synthesized at Purdue, namely, 1,4-di(4-isocyanophenylethynyl)-2-ethylbenzene (22ADI). This conjugated molecule, shown in the inset of Figure 25, has a relatively rigid backbone with isocyanide groups at both ends and is 2.2 nm in length. For the linking process, the sample is exposed to the 22ADI molecule by immersion in a 1 mM solution of the molecule dissolved in acetonitrile (CH_3CN) for 12–14 h followed by a 20-min rinse in acetonitrile. It has been found that 22ADI displaces dodecanethiol from Au(111) by dislodging the sulfur atom of the dodecanethiol molecule

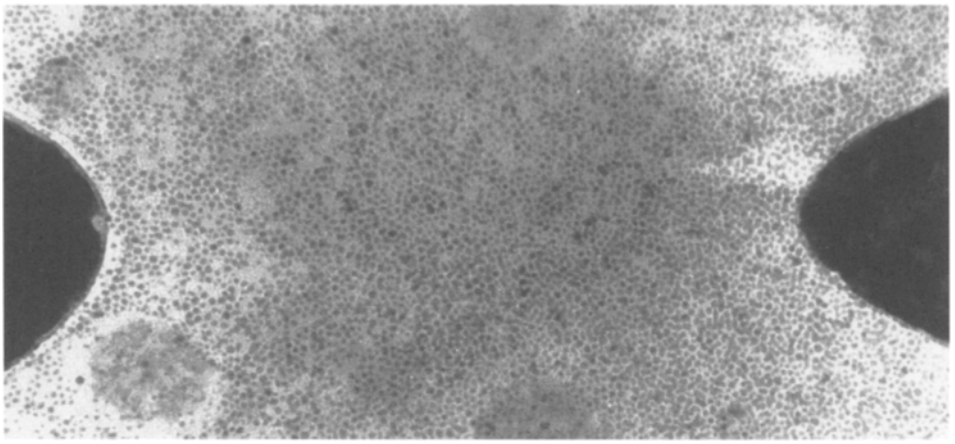


Fig. 24. Transmission electron micrograph of cluster array (sample A) deposited between Au contacts on a SiO_2 substrate for electrical characterization. (Source: Reprinted from [1].)

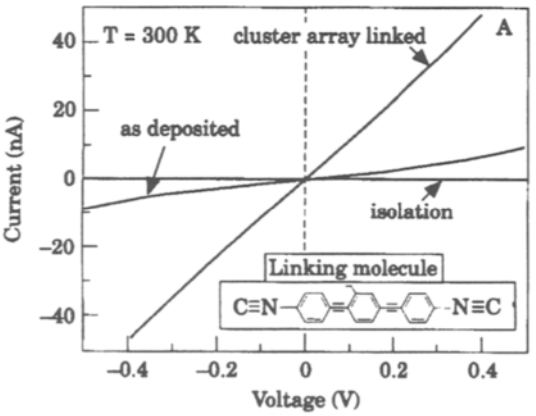


Fig. 25. Measured room temperature current–voltage characteristic for conduction in the cluster array denoted by sample A. The data show how the electronic conductivity changes as the array is linked to form a linked cluster network. Inset shows the structure of the linking molecule 22ADI. (Source: Reprinted from [1].)

bonded to the gold surface [3]. Because the 22ADI molecule has an isonitrile group at each end and a rigid backbone, it is expected that this molecule will similarly displace the dodecanethiol surrounding the clusters and bond together adjacent gold clusters, if conditions such as spacing between clusters are conducive for such linking. Structural evidence for such cross-linking on MoS_2 substrates is presented by Osifchin et al. [2].

The second linking molecule employed is 4,4′-biphenyldithiol (BPDT). This molecule has a thiol group at each end and is also believed to displace the single-ended thiol molecules on the Au surfaces. As will be shown in the next section, changes in the electrical conductivity following linking indicate that the 22ADI and BPDT molecules attach themselves between nearest-neighbor clusters to form LCNs.

Three-cluster network samples were characterized in this study. LCN samples, denoted as samples A and B, consisted of single-layer arrays and were linked with 22ADI and BPDT, respectively. Sample C was a multilayer array and was characterized in the as-deposited state; that is, the encapsulating molecules of dodecanethiol were not displaced by a conjugated linking molecule. The contact spacing (~500 nm) and contact geometry

were comparable in all samples. Before array deposition, the leakage resistances between contacts on the bare substrates were greater than 10 GΩ at room temperature, indicating that parasitic leakage paths were insignificant over the range of LCN resistances measured.

6.3. Electrical Measurements

Direct-current (dc) $I(V)$ measurements and TEM images were made on the samples deposited on SiO_2 substrates at various stages of sample preparation, namely, (i) before cluster array deposition (to confirm good isolation between the pads), (ii) after array deposition, and (iii) after linking. Although the TEM images indicate the presence of continuous conduction paths in these samples, most samples contain voids and other minor defects that are believed to be related to residual surface contamination and other imperfections. Figure 25 shows the measured $I(V)$ data corresponding to in-plane conduction in sample A between two contact pads separated by 500 nm at the various stages of the array preparation.

The isolation between pads, measured before cluster array deposition, corresponded to a leakage resistance in excess of 10 GΩ. The "as-deposited" cluster array, that is, following deposition from colloidal suspension but before linking, exhibits an $I(V)$ curve with an average resistance of 35 MΩ. At this stage of preparation, the conductivity properties of an LCN are associated with both the overall array structure and the local spacing of the encapsulated clusters, which is uncontrolled. The measured $I(V)$ curve for the linked LCN, that is, following exposure to the linking molecule (22ADI), is also presented. Following linking, the sample exhibits a linear $I(V)$ curve near zero bias with an average resistance of approximately 8.5 MΩ. The 22ADI molecule provides a local reordering of the array and controls the tunneling resistance between adjacent clusters. As is evident in Figure 25, the conduction between the pads shows a distinct change at each stage of the array formation and linking process, indicating that the conduction is through the cluster array and that the LCN conductance can be varied significantly by the introduction of an appropriate linking molecule. Measurements on control samples indicate that the processes of imaging and linking the cluster array do not cause molecular contamination of the surface, which would result in the formation of parasitic conduction paths between the two contact pads.

To characterize the conduction mechanism in an LCN, the $I(V)$ relationship for a linked LCN was measured versus temperature. Figure 26 shows the measured $I(V)$ for various temperatures between 80 and 210 K. The low-field conductance follows the relationship

$$G_0 = G_\infty \exp\left(\frac{-E_A}{k_B T}\right) \tag{12}$$

The measured values of E_A and G_∞ for sample A are 97 meV and 1.1 μS, respectively.

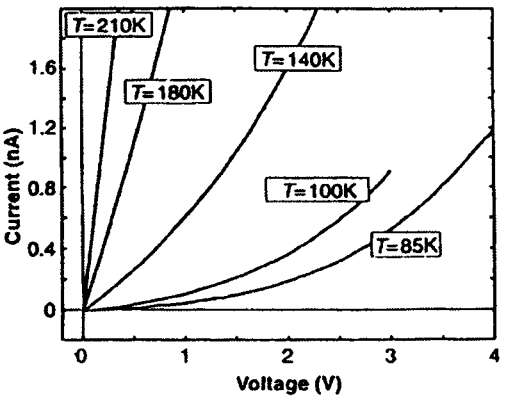


Fig. 26. Measured current–voltage relationship for an LCN versus temperature. (Source: Reprinted from [7]. © 1996 American Association for the Advancement of Science.)

6.4. Conduction Model

A model for an ideal hexagonal array of single-crystal gold clusters is shown in Figure 27. In this model, uniform intercluster resistive linking is provided by the conjugated organic molecules that bridge the gaps between clusters and bond to Au(111) facets on the clusters. Each resistor in the figure represents a number of linking molecules, with their end groups bonded to the cluster facet. Although LCNs fabricated to date do not show the perfect ordering depicted in this figure, this model provides a reasonable description of the local ordering within the array. The hexagonal symmetry depicted in this figure is observed in cluster arrays deposited on atomically flat MoS_2, as described earlier. The clusters also tend to align as shown in Figure 27; that is, they rest with Au(111) facets flat on the substrate and aligned with those of the nearest neighbors.

Detailed models of the conduction properties of one- and two-dimensional arrays of coupled tunnel junctions have been described in several papers [242–246]. In general, these analyses consider the behavior of solitary electrons within rectangular arrays of tunnel junctions, as depicted in Figure 28. Most of the modeling specifically considers the types of geometries generally employed in experimental work, namely, structures consisting of lithographically defined arrays where the islands are large compared to the dimensions of the tunnel junctions and there is a well-defined island-to-gate capacitance (C_G). In this regime, direct coupling between elements beyond nearest neighbors can be ignored, and the capacitance from island-to-island (C_D) corresponds to the capacitance of a single tunnel junction. The published models have considered various regimes of gate coupling (various ratios of C_G to C_D), operating temperature, voltage, and array uniformity.

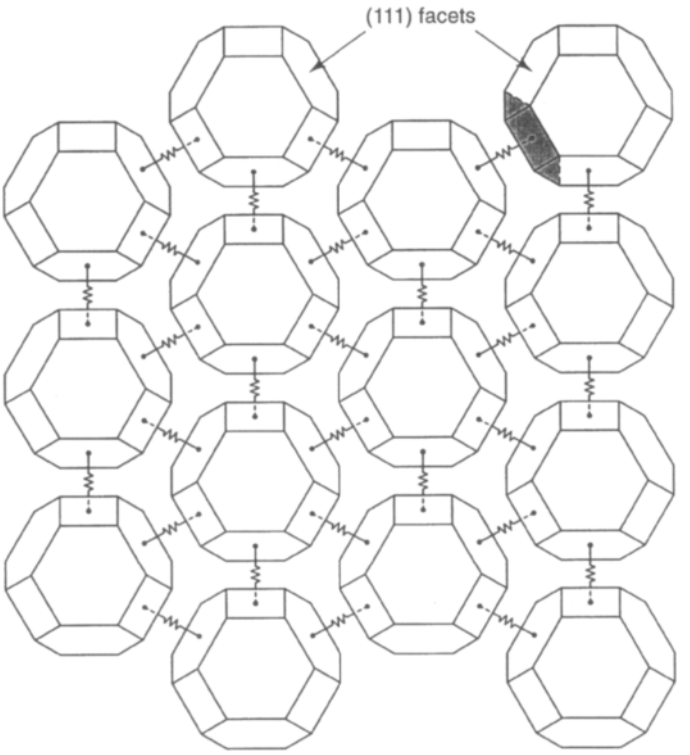


Fig. 27. Ideal hexagonal array of single-crystal gold clusters with uniform intercluster resistive linking. Surfaces shown on clusters represent crystal facets; shaded area on cluster at top right depicts one of three hidden Au(111) facets in this view. Each intercluster resistor represents a number of linking molecules spanning the gap between adjacent clusters.

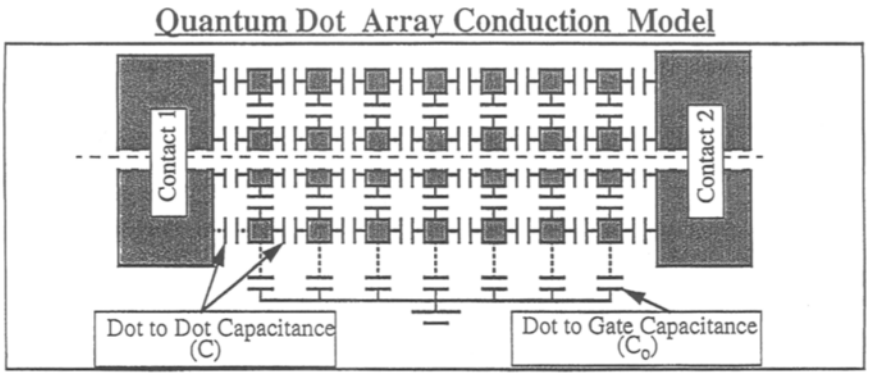


Fig. 28. Rectangular array of tunnel junctions used in various models to discuss conduction in two-dimensional networks. The horizontal dashed line indicates a symmetry plane for the array, which is usually much wider than shown in this figure.

In this work, we will present a simple picture of the conduction properties, along with comparisons between measured values and those calculated from the sample geometries and material characteristics. This picture incorporates the concepts outlined in published models on rectangular arrays, with the conductive islands consisting of the metal clusters and the tunnel junctions realized by the organic linking molecules between clusters. The qualitative picture should be applicable, although several details of the LCN structure are somewhat different from the typical models. In the LCNs used in this study, the resistive coupling is primarily between nearest-neighbor clusters, but significant capacitative coupling exists over longer ranges. Because the dimensions of the clusters are comparable to those of the tunnel junctions and because the clusters are very weakly coupled to the back gate in the LCNs studied to date, the appropriate value for effective dot capacitance must consider how the excess charge on an individual cluster is screened by surrounding clusters beyond the nearest neighbors. There is a metallic gate present on the back of the SiO_2 substrate during electrical characterization, but weak gate coupling is expected because the thickness of the SiO_2 layer is significantly larger than the cluster spacing. For the LCNs reported in this study, negligible gating action was observed over the gate voltage range where gate current was insignificant. Finally, the local structure within an LCN is hexagonal, rather than rectangular, so each cluster within an ideal single-layer array has six nearest neighbors.

A two-dimensional array is expected to undergo a conductor-to-insulator transition in the region where the Coulomb charging energy is approximately 10 times the thermal energy [244, 247], but a sharp threshold is not expected until the thermal energy is reduced significantly beyond this point. For the measurements presented in Figure 26, the temperature equivalent of the charging energy is approximately 1000 K; therefore, significant Coulomb charging effects are expected at room temperature and below, but a sharp threshold is not expected. Significant subthreshold conduction, that is, conduction in the voltage regime below the Coulomb blockade threshold voltage, is made possible in this regime by the presence of multiple paths through the LCN. The nonlinearity in the $I(V)$ data can be described by a relationship where the current is proportional to $V^{a(T)}$, where $a(T)$ is a temperature-dependent exponent. As the temperature is reduced, the value of $a(T)$ changes from approximately 1 to a value greater than 2 relatively rapidly. Although data at temperatures significantly below the transition temperature are not yet available, this behavior appears to follow the predicted behavior for arrays in that random offset charges do not play a major role [247]. In early LCN samples, fluctuations between two states of different average conductance were observed as the bias voltage was swept. It is believed that this behavior was due to areas within the array that were weakly coupled to the rest

of the array. The addition of an electron to this weakly coupled area shifted the threshold voltage for the main conduction paths through the array. As array fabrication procedures have improved, the uniformity of the clusters and the linking have improved, and charge trapping effects are no longer observed.

For a two-dimensional array with relatively uniform cluster sizes, locations, and spacings, that is, uniformly arranged islands with uniform tunnel junctions, the conductance can be modeled by a single-electron charging picture in which the characteristic energy is the Coulomb charging energy of an isolated island in the interior of the array, that is, the system energy acquired by moving an electron from a contact pad to an island well spaced from the contacts. In LCNs studied to date, the clusters are very weakly coupled to the gate, that is, $C_D \ll C_G$. In this case, excess electrons on clusters within the LCN are screened largely through a redistribution of charge in nearby clusters. The screening length, λ, is typically a few cluster periods, or two to three normalized spacings. The appropriate Coulomb charging energy, E_C, is dominated by the capacitance from the dot to the neutral portion of the array. The capacitance can be roughly modeled as that of concentric rings with an inner ring radius equal to the cluster radius and an outer ring diameter equal to the cluster radius plus λ. The low-field conductance behavior is somewhat analogous to the behavior of an intrinsic semiconductor. At $T = 0$ K, there is no thermal energy to excite carriers, so a Coulomb blockade is present for low biases, and no current flows until the bias voltage is sufficient to inject carriers into the array. For the regime where T is nonzero, but where E_C is much larger than $k_B T$, the sharp Coulomb blockade threshold becomes more rounded, until the $I(V)$ curve becomes nearly linear as $k_B T$ becomes comparable to E_C. For voltages below the Coulomb blockade threshold, the subthreshold conduction takes on the form of a power law, where the low-field conductance is determined by the thermal excitation of carriers and the conductance at moderate fields is determined by thermal excitation and bias-dependent injection of carriers. The LCN is sparsely populated for voltages near or below the threshold voltage and temperatures in these regimes. The assumption of isolated carriers is, therefore, valid.

The measured activation energy for the low-field conductance in sample A (97 meV) is consistent with the calculated Coulomb charging energy for an isolated electron in the interior of the LCN. A calculation using the FASTCAP program [248] for a 4-nm cluster embedded in a close-packed array with 1-nm space between clusters, relative dielectric constant of 1 in the surrounding media, and considering four nearest neighbors yields an estimated cluster capacitance of 0.38 aF, corresponding to a charging energy of 200 meV. The conjugated organic molecules are thought to have relative dielectric constants in the range of 1.5 to 2, which would lower the predicted activation energy to the range of 100 to 130 meV. The measured activation energy for sample B is comparable, as expected for a monolayer LCN with comparable cluster dimensions. For sample C, the measured E_A is 30 meV, which is consistent with the larger capacitance expected for a multilayer array. In this case, each cluster would have 12 nearest neighbors, as opposed to 6 in the monolayer case, and the three-dimensional screening would result in shorter screening lengths. The measured activation energies are, therefore, in good agreement with the values estimated from the geometry and material parameters.

The average resistance between each adjacent pair of clusters, R_D, can be estimated from the measured conductance versus temperature and compared with the value calculated from simulations of the conduction properties of the linking molecule. The high-temperature limit of the conductance, G_∞, should represent the properties of the resistive network alone, because Coulomb charging plays a negligible role in the high-temperature regime. In this case, the resistance of the array can be calculated by multiplying the sheet resistance of an array of resistors with resistance R_D by an effective number of squares. Using a calculation incorporating an ideal hexagonal two-dimensional array of linked resistors, each with value R_D, and the contact geometry of this sample, we calculate that the reciprocal of G_∞ is approximately equal to R_D. For sample A, the measured value of

G_∞ is 1.1 μS, corresponding to a value of approximately 0.9 MΩ for R_D. The resistance of a single linking molecule can be determined from the value of R_D and an estimate of the number of linking molecules present between each adjacent pair of metal clusters. Because the packing density of the double-ended linking molecules on Au is not known, the reported value for single-ended thiol molecules (such as dodecanethiol), chemisorbed from solution on large-area Au(111), namely, approximately one thiol molecule for every four gold atoms [249], was assumed to hold in this case.

Assuming that each Au(111) facet is covered at this density, this corresponds to approximately 32 linking molecules between each nearest neighbor pair of clusters. The resistance of each 22ADI molecule determined from the experimental result on sample A is, therefore, approximately 30 MΩ. The resistance per molecule of 22ADI molecules between gold surfaces has been independently predicted using a molecular orbital calculation to be 43 MΩ [250]. Because of the imperfections in the present cluster arrays and the simplifications inherent in the simulation, neither value of molecular resistance can be considered to be highly accurate. However, the reasonable agreement between the two values indicates that the interpretation of electrical linking between clusters through the 22ADI molecules is reasonable. The measured results from other samples are consistent with this picture. The resistance per molecule inferred from G_∞ for sample B is 90 MΩ; the BPDT linking molecule used in this sample is predicted to be less conductive than the 22ADI linker used in sample A [250]. For sample C, the measured G_∞ is 0.06 μS, which would correspond to an effective resistance per molecule of approximately 800 MΩ. In this sample, the intercluster resistance is provided by the single-ended thiol molecules, which do not provide well-controlled links between the clusters. This configuration is expected to be much less conductive than the conjugated linking molecules, as is observed in the measured characteristics.

6.5. Concluding Remarks

The conduction properties of linked two-dimensional cluster networks are reasonably explained by models employing single-electron charging effects, as expected from the nanometer dimensions of the clusters and the corresponding calculated capacitances. Although single-electron charging effects have been observed in numerous systems, several features of the LCNs stand apart from the majority of reported work. First, the effects of single-electron charging are clearly evident up to room temperature, which is rare in structures for which the structure can be stated with relatively exact dimensions and shapes. There is also evidence that random offset charge does not play a major role in the conduction properties, a feature that may make this technology suitable for certain applications in single-electron tunneling electronics. One of the key features of LCNs is the ability to control the intercluster resistance (the junction resistance) via the choice of linking molecule. This resistive control is enabled by the use of alkane thiols to initially encapsulate the clusters prior to array formation in which these alkane thiols are subsequently displaced by conjugated linking molecules. The molecular resistance values inferred from the low-field conductance properties of the LCNs agree well with the low-field resistances predicted for the molecules and those measured in the STM experiments, using the techniques discussed in Section 5. This agreement provides an indication that the linking molecules are strongly bonded to the surfaces of adjacent gold clusters. Because good electrical contact requires the linking molecules to locate properly on a flat gold surface, the use of single-crystal gold clusters with well-resolved facets is probably an essential component of the system. The capabilities to link LCNs with various molecules, along with the insights provided by the molecular modeling and characterization efforts, should provide the means to design and synthesize networks with interesting properties. For example, LCNs with spatially nonuniform resistances, such as low-resistance linking molecules in certain regions and higher-resistance molecules in other regions, could be realized by lithographic patterning or by means of an external stimulus applied during the linking process.

7. SUMMARY

This review summarizes the design, fabrication, and electronic properties of cluster-based molecular nanostructures. Details regarding the synthesis and characterization of both molecular wires and nanoscale metallic clusters have been discussed from a perspective that emphasizes the self-assembly of these nearly identical "building blocks" into interesting molecular nanostructures. The important steps in this cluster-based nanofabrication scheme are summarized in Figure 29, which schematically shows the self-assembly process for LCNs. This achievement was made possible by the combined efforts of an interdisciplinary team of researchers from chemistry, chemical engineering, electrical engineering, and physics.

A theory related to electronic conduction through individual molecular wires, attached at one end to a substrate and probed at the other end by an STM tip, has also been presented. This theory predicts the resistance of a molecular wire, and, more generally, the $I(V)$ characteristics of any molecule. The importance of the coupling between the molecule and substrate was found to be crucial in this analysis. Comparison of this theory to a limited $I(V)$ data set obtained from a variety of different molecules is encouraging.

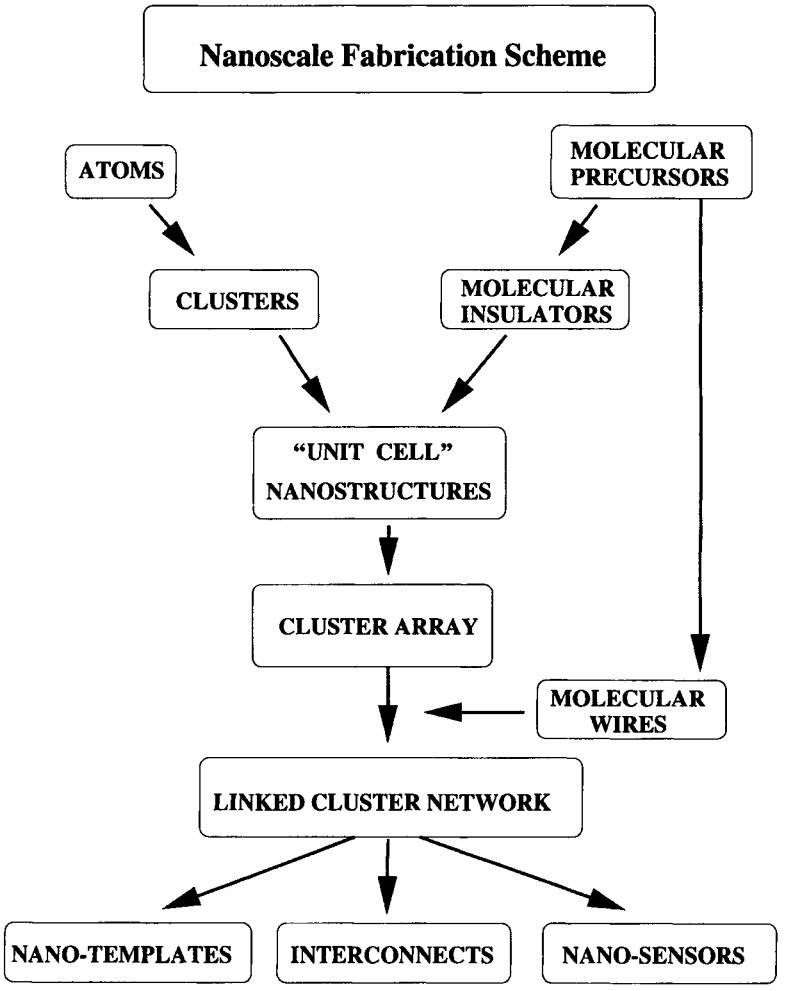


Fig. 29. Cluster-based nanofabrication scheme for self-assembly of linked cluster networks (LCNs). A few of the anticipated end uses of LCNs are indicated.

Well-characterized, "unit cell" molecular nanostructures have been fabricated from molecular wires and nanoscale clusters. The $I(V)$ characteristics of a number of these self-assembled molecular nanostructures show compelling evidence of semiclassical Coulomb blockade and Coulomb staircase phenomena at room temperature. A novel method for measuring the electrical resistance of individual molecules has also emerged from this work.

Finally, the self-assembly of these "unit cell" nanostructures into highly ordered two-dimensional cluster networks has also been described. Each individual cluster in the network is electronically linked to its nearest neighbor by bridging molecular wires. We have dubbed this interesting nanostructured material a linked cluster network (LCN). So far, we have fabricated LCNs up to 1 μm $\times$ 1μm in area and have studied the $I(V)$ characteristics of these LCNs at different temperatures. These measurements correlate well with a theoretical model for conduction, giving us confidence that we understand the factors that influence the resistance of LCNs.

It is hoped that the limited successes we have achieved offer a tantalizing view of the future that might emerge. As our ability to understand and control the assembly of molecular nanostructures continues to advance, not only will new and exciting avenues for practical applications continue to evolve, but also new disciplines devoted to furthering these efforts will develop.

Acknowledgments

This work was funded by the Army Research Office under University Research Initiative Grant DAALO3-G-0144. The authors are indebted to Dr. H. Everitt for his support of this work. During the past five years, we have greatly benefited from the diligent work of a number of graduate students. Without the efforts of Jeff Bielefeld, Matt Dorogi, Jason Henderson, Seunghun Hong, Venkat Kolagunta, Bill Mahoney, Richard Osifchin, Manoj Samanta, and Weidong Tian this work could not have advanced to its present stage.

References

1. D. Janes, V. Kolagunta, R. Osifchin, J. Bielefeld, R. Andres, J. Henderson, and C. Kubiak, *Superlattices Microstruct.* 18, 275 (1995).
2. R. Osifchin, W. Mahoney, R. Andres, J. Henderson, C. Kubiak, and R. Dominey, *Superlattices Microstruct.* 18, 283 (1995).
3. J. Henderson, G. Ferrence, S. Feng, T. Bein, and C. Kubiak, *Inorg. Chim. Acta* 242, 115 (1996).
4. M. Dorogi, J. Gomez, R. Oschifin, R. Andres, and R. Reifenberger, *Phys. Rev. B* 52, 9071 (1995).
5. R. Andres, S. Datta, M. Dorogi, J. Gomez, J. Henderson, D. Janes, V. Kolagunta, C. Kubiak, W. Mahoney, R. Osifchin, R. Reifenberger, M. Samanta, and W. Tian, *J. Vac. Sci. Technol., A* 14, 1178 (1996).
6. R. Andres, T. Bein, M. Dorogi, S. Feng, J. Henderson, C. Kubiak, W. Mahoney, R. Osifchin, and R. Reifenberger, *Science* 272, 1323 (1996).
7. R. Andres, J. Bielefeld, J. Henderson, D. Janes, V. Kolagunta, C. Kubiak, W. Mahoney, and R. Osifchin, *Science* 273, 1690 (1996).
8. S. Hong, J. Bielefeld, R. Andres, and R. Reifenberger, in "Nanowires" (P. Serena and N. Garcia, eds.), pp. 351–372. Kluwer Academic, Dodrecht, The Netherlands, 1997.
9. M. Samanta, W. Tian, S. Datta, J. Henderson, and C. Kubiak, *Phys. Rev. B* 53, 7626 (1996).
10. S. Datta, W. Tian, S. Hong, R. Reifenberger, J. Henderson, and C. Kubiak, *Phys. Rev. Lett.* 79, 2530 (1997).
11. W. Tian, S. Datta, S. Hong, R. Reifenberger, and J. Henderson, *Physica E* 1, 304 (1997).
12. A. Aviram, ed., "Molecular Electronics—Science and Technology," Vol. 262. American Institute of Physics, New York, 1992.
13. W. Tolles, ed., "Nanotechnology," Vol. 622. American Chemical Society, Washington, DC, 1996.
14. D. Waldeck and D. Beratan, *Science* 261, 576 (1993).
15. G. J. Ashwell, ed., "Molecular Electronics." Wiley, New York, 1992.
16. W. Kirk and M. Reed, eds., "Nanostructures and Mesoscopic Systems." Academic Press, New York, 1992.
17. R. Birge, ed., "Molecular and Biomolecular Electronics," Vol. 240. American Chemical Society, Washington, DC, 1991.

18. W. Tian, M. Samanta, J. Henderson, C. Kubiak, and S. Datta, in "Proceedings of the Third International Symposium on Quantum Confinement," Vol. 95-17, pp. 70–77. Electrochemical Society, 1995.
19. V. Mujica, M. Kemp, A. Roitberg, and M. Ratner, *J. Chem. Phys.* 104, 7296 (1996).
20. C. Joachim and J. Vinuesa, *Europhys. Lett.* 33, 635 (1996).
21. I. Bidd, D. Kelly, P. Ottley, O. Paynter, D. Simmonds, and M. Whiting, *J. Chem. Soc. Perkin Trans.* 1, 1369 (1983).
22. E. Igner, O. Paynter, D. Simmonds, and M. Whiting, *J. Chem. Soc. Perkin Trans.* 1, 2447 (1987).
23. J. Zhang, J. Moore, Z. Xu, and R. Aguirre, *J. Am. Chem. Soc.* 114, 2273 (1992).
24. J. Schumm, D. Pearson, and J. Tour, *Angew. Chem., Int. Ed. Engl.* 33, 1360 (1994).
25. L. Jones, J. Schumm, and J. Tour, *J. Org. Chem.* 62, 1388 (1997).
26. D. Pearson and J. Tour, *J. Org. Chem.* 62, 1376 (1997).
27. W. Zisman, *Adv. Chem. Ser.* 43, 1 (1964).
28. W. Bigelow, D. Pickett, and W. Zisman, *J. Colloid Interface Sci.* 1, 513 (1946).
29. H. Kuhn and A. Ulman, "Thin Films," Vol. 20. Academic Press, 1995.
30. D. Yang, H. Almaznai, and M. Morin, *J. Phys. Chem. B* 101, 1158 (1997).
31. D. Yang, C. Wilde, and M. Morin, *Langmuir* 12, 6570 (1996).
32. T. Wooster, P. Gamm, W. Geiger, A. Oliver, A. Black, D. Craig, and M. Paddonrow, *Langmuir* 12, 6616 (1996).
33. L. Williams, S. Evans, T. Flynn, A. Marsh, P. Knowles, R. Bushby, and N. Boden, *Langmuir* 13, 751 (1997).
34. K. Truong and P. Rowntree, *J. Phys. Chem.* 100, 19917 (1996).
35. J. Trevor, L. Hanley, and K. Lykke, *Rapid Commun. Mass Spectrom.* 11, 587 (1997).
36. D. Tobias, W. Mar, J. Blasie, and M. Klein, *Biophys. J.* 71, 2933 (1996).
37. K. Tamada, M. Hara, H. Sasabe, and W. Knoll, *Langmuir* 13, 1558 (1997).
38. V. Silin, H. Weetall, and D. Vanderah, *J. Colloid Interface Sci.* 185, 94 (1997).
39. H. Schonherr, F. Kremer, S. Kumar, J. Rego, H. Wolf, H. Ringsdorf, M. Jaschke, H. Butt, and E. Bamberg, *J. Am. Chem. Soc.* 118, 13051 (1996).
40. J. Schoer and R. Crooks, *Langmuir* 13, 2323 (1997).
41. C. Sayre and D. Collard, *Langmuir* 13, 714 (1997).
42. G. Poirier, *Langmuir* 13, 1145 (1997).
43. M. Ohtani, S. Kuwabata, and H. Yoneyama, *Anal. Chem.* 69, 1045 (1997).
44. S. Murthy, T. Bigioni, Z. Wang, J. Khoury, and R. Whetten, *Mater. Lett.* 30, 321 (1997).
45. A. Moore, E. Katz, and I. Willner, *Electroanalysis* 8, 1092 (1996).
46. R. Michalitsch, P. Lang, G. Nauer, and F. Garnier, *Adv. Mater.* 9, 3 (1997).
47. Z. Mekhalif, J. Riga, J. Pireaux, and J. Delhalle, *Langmuir* 13, 2285 (1997).
48. M. McDermott, J. Green, and M. Porter, *Langmuir* 13, 2504 (1997).
49. T. McCarley and R. McCarley, *Anal. Chem.* 69, 130 (1997).
50. H. Maeda, M. Itami, Y. Yamauchi, and H. Ohmori, *Chem. Pharm. Bull.* 44, 2294 (1996).
51. J. Madoz, B. Kuznetzov, F. Medrano, J. Garcia, and V. Fernandez, *Am. Chem. Soc.* 119, 1043 (1997).
52. D. Lowy and H. Finklea, *Electrochim. Acta* 42, 1325 (1997).
53. J. Li, J. Yan, Q. Deng, G. Cheng, and S. Dong, *Electrochim. Acta* 42, 961 (1997).
54. J. Li, G. Cheng, and S. Dong, *Thin Solid Films* 293, 200 (1997).
55. N. Larsen, H. Biebuyck, E. Delamarche, and B. Michel, *J. Am. Chem. Soc.* 119, 3017 (1997).
56. T. Kim, K. Chan, and R. Crooks, *J. Am. Chem. Soc.* 119, 189 (1997).
57. G. Jennings and P. Laibinis, *Langmuir* 12, 6173 (1996).
58. T. Ishida, N. Nishida, S. Tsuneda, M. Hara, H. Sasabe, and W. Knoll, *Jpn. J. Appl. Phys., Part 2* 35, L1710 (1996).
59. A. Heise, H. Menzel, H. Yim, M. Foster, R. Wieringa, A. Schouten, V. Erb, and M. Stamm, *Langmuir* 13, 723 (1997).
60. B. Heinz and H. Morgner, *Surf. Sci.* 372, 100 (1997).
61. P. He, Y. Ye, Y. Fang, I. Suzuki, and T. T. Osa, *Electroanalysis* 9, 1455 (1997).
62. W. Hayes, H. Kim, X. Yue, S. Perry, and C. Shannon, *Langmuir* 13, 2511 (1997).
63. U. Grummt, M. Geissler, and T. Schmitzhuebsch, *Chem. Phys. Lett.* 263, 581 (1996).
64. M. Fritz, G. Hahne, N. Spencer, R. Burli, and A. Vasella, *Langmuir* 12, 6074 (1996).
65. Z. Feng, S. Imabayashi, T. Kakiuchi, and K. J. Niki, *Chem. Soc. Faraday Trans.* 251, 633 (1997).
66. X. Feng, G. Fryxell, L. Wang, A. Kim, J. Liu, and K. Kemner, *Science* 276, 923 (1997).
67. I. Engquist and B. Liedberg, *Phys. Chem.* 100, 20089 (1996).
68. E. Eliadis, R. Nuzzo, A. Gewirth, and R. Alkire, *J. Electrochem. Soc.* 144, 96 (1997).
69. T. Ehler, N. Malmberg, K. Carron, B. Sullivan, and L. Noe, *J. Phys. Chem. B* 101, 3174 (1997).
70. M. Dishner, J. Hemminger, and F. Feher, *Langmuir* 13, 2318 (1997).
71. M. Dishner, J. Hemminger, and F. Feher, *Langmuir* 2, 6176 (1996).
72. W. Deng, D. Yang, Y. Fang, and C. Bai, *Sci. China, Ser. B* 39, 225 (1996).
73. S. Creager and G. Rowe, *J. Electroanal. Chem.* 420, 291 (1997).
74. J. Cheng and C. Miller, *J. Phys. Chem. B* 101, 1058 (1997).
75. G. Che and C. Cabrera, *J. Electroanal. Chem.* 417, 155 (1996).

76. O. Cavalleri, S. Gilbert, and K. Kern, *Chem. Phys. Lett.* 269, 479 (1997).
77. M. Browningkelley, K. Wadumesthrige, V. Hari, and G. Liu, *Langmuir* 13, 343 (1997).
78. M. Beulen, B. Huisman, P. Vanderheijden, F. Vanveggel, M. Simons, E. Biemond, P. Delange, and D. Reinhoudt, *Langmuir* 12, 6170 (1996).
79. K. Bandyopadhyay, M. Sastry, V. Paul, and K. Vijayamohanan, *Langmuir* 13, 866 (1997).
80. A. Badia, L. Cuccia, L. Demers, F. Morin, and R. B. Lennox, *J. Am. Chem. Soc.* 119, 2682 (1997).
81. M. Bader, *Phosphorus, Sulfur, Silicon Relat. Elem.* 116, 77 (1996).
82. R. Andreu, J. Calvente, W. Fawcett, and M. Molero, *J. Phys. Chem. B* 101, 2884 (1997).
83. M. Bryant, S. Joa, and J. Pemberton, *Langmuir* 9, 753 (1992).
84. T.-T. Li, H. Liu, and M. Weaver, *J. Am. Chem. Soc.* 106, 1233 (1984).
85. J. Cooper, K. Greenough, and C. McNeil, *J. Electroanal. Chem.* 347, 267 (1993).
86. K. Uvdal, P. Bodo, and B. Liedberg, *J. Colloid Interface Sci.* 149, 162 (1992).
87. A. Ihs, K. Uvdal, and B. Liedberg, *Langmuir* 9, 733 (1993).
88. E. Katz, N. Itzhak, and I. Willner, *J. Electroanal. Chem.* 336, 357 (1992).
89. E. Troughton, C. Bain, G. Whitesides, D. L. Allara, and M. Porter, *Langmuir* 4, 365 (1988).
90. J. Mielczarski and R. Yoon, *Langmuir* 7, 101 (1991).
91. Y. Gu, Z. Lin, R. Butera, V. Smentkowski, and D. Waldeck, *Langmuir* 11, 1849 (1995).
92. S. Lunt, P. G. Santangelo, and N. Lewis, *J. Vac. Sci. Technol., B* 9, 2333 (1991).
93. J. Martensson and D. Allara, *Jpn. J. Appl. Phys.* 30, 3759 (1991).
94. H. Ohno, M. Motomatsu, W. Mizutani, and H. Tokumoto, *Jpn. J. Appl. Phys.* 34, 1381 (1995).
95. C. W. Sheen, J.-X. Shi, J. Martensson, A. Parikh, and D. Allara, *J. Am. Chem. Soc.* 114, 1514 (1992).
96. R. Tiberio, H. Craighead, M. Lercel, T. Lau, C. Sheen, and D. Allara, *Appl. Phys. Lett.* 62, 476 (1993).
97. K. Chen, C. Mirkin, R.-K. Lo, J. Zhao, and J. McDevitt, *Appl. Phys. Lett.* 117, 6374 (1995).
98. K. Chen, F. Xu, C. Mirkin, R.-K. Lo, K. Nanjundaswamy, J.-P. Zhou, and J. McDevitt, *Langmuir* 12, 2622 (1996).
99. M. Linford and C. Chidsey, *J. Am. Chem. Soc.* 115, 12631 (1993).
100. S. Palacin, P. Hidber, J. Bourgoin, C. Miramond, C. Fermon, and G. Whitesides, *Chem. Mater.* 8, 1316 (1996).
101. Q. X. Liu and Z. Xu, *Langmuir* 11, 4617 (1995).
102. G. Katabi, Y. Koltypin, X. Cao, and A. Gedanken, *J. Cryst. Growth* 166, 760 (1996).
103. N. Muskal, I. Turyan, and D. Mandler, *J. Electroanal. Chem.* 409, 131 (1996).
104. O. Magnussen, M. Regan, E. Kawamoto, B. Ocko, P. Pershan, N. Maskil, M. Deutsch, S. Lee, K. Penanen, and L. E. Berman, *Physica B* 221, 257 (1996).
105. O. Magnussen, B. Ocko, M. Deutsch, M. Regan, P. Pershan, D. Abernathy, G. Grubel, and J. Legrand, *Nature* 384, 250 (1996).
106. R. Forster, *Analyst* 121, 733 (1996).
107. H. Yu, Y. Wang, J. Cheng, J. Zhao, S. Cai, H. Inokuchi, A. Fujishima, and Z. Liu, *Langmuir* 12, 2843 (1996).
108. J. Schlenoff, M. Li, and H. Ly, *J. Am. Chem. Soc.* 117, 12528 (1995).
109. T. Sagara, H. Kawamura, and N. Nakashima, *Langmuir* 50, 4253 (1996).
110. R. Forster, *J. Inorg. Chem.* 35, 3394 (1996).
111. R. Bretz and H. Abruna, *J. Electroanal. Chem.* 408, 199 (1996).
112. W. Thompson and J. Pemberton, *Langmuir* 11, 1720 (1995).
113. H. Liu, T. Tsong, Y. Liou, R. Nuzzo, B. Zegarski, L. H. Dubois, M. Walczak, C. Chung, S. Stole, C. Widrig, M. Porter, A. Abdelghani, J. Chovelon, N. Jaffrezicrenault, C. Veilla, and H. Gagnaire, *Anal. Chim. Acta* 337, 225 (1997).
114. M. Elking, G. He, and Z. Xu, *J. Chem. Phys.* 105, 6565 (1996).
115. G. Fryxell, P. Rieke, L. Wood, M. Engelhard, R. Williford, G. Graff, A. Campbell, R. Wiacek, L. Lee, and A. Halverson, *Langmuir* 12, 5064 (1996).
116. S. Gauthier, J. Aime, T. Bouhacina, A. Attias, and B. Desbat, *Langmuir* 12, 5126 (1996).
117. F. Linseisen, M. Hetzer, T. Brumm, and T. Bayerl, *Biophys. J.* 72, 1659 (1997).
118. W. Miller, N. Abbott, J. Paul, and M. Prentiss, *Appl. Phys. Lett.* 69, 1852 (1996).
119. J. Moon, J. Shin, S. Kim, and J. Park, *Langmuir* 12, 4621 (1996).
120. A. Nechifor, A. Philipse, F. Dejong, J. Vanduynhoven, R. Egberink, and D. Reinhoudt, *Langmuir* 12, 3844 (1996).
121. R. Opila, J. Legrange, J. Markham, G. Heyer, and C. Schroeder, *J. Adhes. Sci. Technol.* 11, 1 (1997).
122. R. Rye, *Langmuir* 13, 2588 (1997).
123. W. Thompson, M. Cai, M. Ho, and J. Pemberton, *Langmuir* 13, 2291 (1997).
124. P. Vandervoort and E. Vansant, *J. Liq. Chromatogr.* 19, 2799 (1996).
125. M. Wirth and R. Fairbank, *J. Liq. Chromatogr.* 19, 2799 (1996).
126. M. Wirth, R. Fairbank, and H. Fatunmbi, *Science* 275, 44 (1997).
127. L. Xing and W. Mattice, *Langmuir* 12, 3024 (1996).
128. X. Zhao and R. Kopelman, *J. Phys. Chem.* 100, 11014 (1996).
129. Y. Zhou, M. Bruening, Y. Liu, R. Crooks, and D. Bergbreiter, *Langmuir* 12, 5519 (1996).

130. U. Steiner, P. Neuenschwander, W. Caseri, U. Suter, and F. Stucki, *Langmuir* 8, 90 (1992).
131. W. Gao, L. Dickinson, C. Grozinger, F. Morin, and L. Reven, *Langmuir* 12, 6429 (1996).
132. H. Ogawa, T. Chihera, and K. Taya, *J. Am. Chem. Soc.* 107, 1365 (1985).
133. D. Allara and R. Nuzzo, *Langmuir* 1, 52 (1985).
134. N. Schlotter, M. Porter, T. Bright, and D. Allara, *Chem. Phys. Lett.* 132, 93 (1986).
135. A. Soundag, A. Tol, and F. Touwslager, *Langmuir* 8, 1127 (1992).
136. M. Samart, C. Brown, and J. Gordon, *Langmuir* 9, 1082 (1993).
137. U. Steiner, W. Caseri, and U. Suter, *Langmuir* 8, 2771 (1992).
138. J. Tour, L. Jones, D. Pearson, J. Lamba, T. Burgin, G. Whitesides, D. Allara, A. Parikh, and S. Atre, *J. Am. Chem. Soc.* 117, 9529 (1995).
139. H. Schonherr, G. Vancso, B. Huisman, F. Vanveggel, and D. Reinhoudt, *Langmuir* 13, 1567 (1997).
140. P. Laibinis and G. Whitesides, *J. Am. Chem. Soc.* 114, 9022 (1992).
141. A. Ulman, *Chem. Rev.* 96, 1533 (1996).
142. C. Bain, E. Troughton, Y. Tao, J. Evall, G. Whitesides, and R. Nuzzo, *J. Am. Chem. Soc.* 111, 321 (1989).
143. M. Buck, F. Eisert, J. Fischer, M. Grunze, and F. Träger, *Appl. Phys. A* 53, 552 (1991).
144. M. Buck, F. Eisert, and M. Grunze, *Ber. Bunsen-Ges. Phys. Chem.* 97, 399 (1993).
145. G. Hähner, C. Wöll, M. Buck, and M. Grunze, *Langmuir* 9, 1955 (1993).
146. H. Biebuyck and G. Whitesides, *Langmuir* 9, 1766 (1993).
147. H. Biebuyck, C. Bain, and G. Whitesides, *Langmuir* 10, 1825 (1994).
148. P. Fenter, A. Eberhardt, and P. Eisenberger, *Science* 266, 1216 (1994).
149. O. Chailapakul, L. Sun, C. Xu, and R. Crooks, *J. Am. Chem. Soc.* 115, 12459 (1993).
150. M. Brust, M. Walker, D. Bethell, D. Schiffrin, and R. Whyman, *J. Chem. Soc., Chem. Commun.* 802 (1994).
151. R. Thomas, L. Sun, and M. Crooks, *Langmuir* 7, 620 (1991).
152. L. Dubois and R. G. Nuzzo, *Ann. Phys. Chem.* 43, 437 (1992).
153. M. Porter, T. Bright, D. Allara, and C. Chidsey, *J. Am. Chem. Soc.* 109, 3559 (1987).
154. R. Nuzzo, F. Fusco, and D. Allara, *J. Am. Chem. Soc.* 109, 2358 (1987).
155. M. Walczak, C. Chung, S. Stole, C. Widrig, and M. Porter, *J. Am. Chem. Soc.* 113, 2370 (1991).
156. C. Bain, H. Biebuyck, and G. Whitesides, *Langmuir* 5, 723 (1989).
157. R. Nuzzo, L. Dubois, and D. Allara, *J. Am. Chem. Soc.* 112, 558 (1990).
158. Y. Li, J. Huang, J. R. T. McIver, and J. Hemminger, *J. Am. Chem. Soc.* 114, 2428 (1992).
159. M. Bryant and J. Pemberton, *J. Am. Chem. Soc.* 113, 3630 (1991).
160. C. Widrig, C. Chung, and M. Porter, *J. Electroanal. Chem.* 310, 335 (1991).
161. C. Chidsey and D. Loiacono, *Langmuir* 6, 709 (1990).
162. C. Chidsey, G.-Y. Liu, P. Rowntree, and G. Scoles, *J. Chem. Phys.* 91, 4421 (1989).
163. C. Alves, E. Smith, and M. Porter, *J. Am. Chem. Soc.* 114, 1222 (1992).
164. L. Dubois, B. Zegarski, and R. Nuzzo, *J. Chem. Phys.* 98, 678 (1993).
165. L. Strong and G. Whitesides, *Langmuir* 3, 546 (1988).
166. T. Nakamura, H. Kondoh, M. Matsumoto, and H. Nozoye, *Langmuir* 12, 5977 (1996).
167. E. Delamarche, B. Michel, H. A. Biebuyck, and C. Gerber, *Adv. Mater.* 8, 719 (1996).
168. G. Poirier and M. Tarlov, *Langmuir* 10, 2859 (1994).
169. P. Fenter, P. Eisenberger, and K. Liang, *Phys. Rev. Lett.* 70, 2447 (1993).
170. N. Camillone, C. Chidsey, G.-Y. Liu, and G. G. Scoles, *J. Phys. Chem.* 98, 3503 (1993).
171. G. Varsanyi, "Assignments for Vibrational Spectra of Seven Hundred Benzene Derivatives," Vol. 1. Wiley, New York, 1974.
172. E. Sabatani, J. Cohen-Boulakia, M. Bruening, and I. Rubinstein, *Langmuir* 9, 2874 (1993).
173. S.-C. Chang, I. Chao, and Y.-T. Tao, *J. Am. Chem. Soc.* 116, 4598 (1994).
174. S. Wasserman, H. Biebuyck, and G. Whitesides, *J. Mater. Res.* 4, 886 (1989).
175. A. Baro, A. Bartolome, L. Vazquez, N. Garcia, R. Reifenberger, E. Choi, and R. Andres, *Appl. Phys. Lett.* 51, 1594 (1987).
176. Y. Li, R. Reifenberger, E. Choi, and R. Andres, *Surf. Sci.* 250, 1 (1991).
177. D. Schaefer, A. Ramachandra, R. Andres, and R. Reifenberger, *Z. Phys. D* 26, S249 (1993).
178. R. Bowles, J. Kolstad, J. Calo, and R. Andres, *Surf. Sci.* 106, 117 (1981).
179. S. B. Park, Optimal Design for a Reactor for Gas-Phase Generation of Metal Microcluster, Ph.D. Thesis, Purdue University, 1988.
180. A. N. Patil, Synthesis and Characterization of Structured One and Two Component Clusters, Ph.D. Thesis, Purdue University, 1994.
181. A. Patil, D. Paithankar, N. Otsuka, and R. Andres, *Z. Phys. D* 26, 135 (1993).
182. T. Castro, Y. Li, R. Reifenberger, E. Choi, S. Park, and R. Andres, *J. Vac. Sci. Technol., A* 7, 2845 (1989).
183. T. Castro, R. Reifenberger, E. Choi, and R. Andres, *Phys. Rev. B* 42, 8548 (1990).
184. M. Lin, R. Andres, and R. Reifenberger, *Phys. Rev. Lett.* 67, 477 (1991).
185. M. Lin, R. Reifenberger, and R. Andres, *Phys. Rev. B* 46, 15490 (1992).
186. M. Lin, R. Reifenberger, A. Ramachandra, and R. Andres, *Phys. Rev. B* 46, 15498 (1992).
187. D. Schaefer, A. Patil, R. Andres, and R. Reifenberger, *Appl. Phys. Lett.* 63, 1492 (1993).
188. D. Schaefer, R. Andres, and R. Reifenberger, *Phys. Rev. B* 51, 5322 (1995).

189. H.-P. Cheng and U. Landman, *Science* 260, 1304 (1993).
190. G. Betz and W. Husinsky, *Nucl. Instrum. Methods Phys. Res., Sect. B* 122, 311 (1997).
191. L. C. Chao and R. P. Andres, *J. Colloid Interface Sci.* 165, 290 (1994).
192. G. Poirier and E. Pylant, *Science* 272, 1145 (1996).
193. D. Leff, P. Ohara, J. Heath, and W. Gelbart, *J. Phys. Chem.* 99, 7036 (1995).
194. R. Whetten, J. Khoury, M. Alvarez, S. Murthy, I. Vezmar, Z. Wang, P. Stephens, C. Cleveland, W. Luedtke, and U. Landman, *Adv. Mater.* 8, 428 (1995).
195. R. Whetten, in "Handbook of Nanostructured Materials and Nanotechnology" (H. S. Nalwa, ed.), Vol. xx, p. xx. Academic Press, Boston, 1998.
196. A. Patil, R. Andres, and N. Otsuka, *J. Phys. Chem.* 98, 924 (1994).
197. R. Osifchin, Ph.D. Thesis, Purdue University, 1994.
198. G. Mie, *Ann. Phys.* 152, 9 (1908).
199. U. Kreibig and C. Z. Fragstein, *Z. Phys.* 224, 307 (1969).
200. S. Tohno and M. Itoh, *J. Aerosol Sci.* 24, 339 (1993).
201. G. Schmid, ed., "Clusters and Colloids, From Theory to Applications." VCH Press, Berlin, 1994.
202. T. Jarosch, Ph.D. Thesis, Purdue University, 1989.
203. P. de Gennes, *Rev. Mod. Phys.* 57, 827 (1985).
204. P. Ohara, J. Heath, and W. Gelbart, *Angew. Chem., Int. Ed. Engl.* 36, 1078 (1997).
205. P. Laibinis, R. Nuzzo, and G. Whitesides, *J. Phys. Chem.* 96, 5097 (1992).
206. M. Giersig and P. Mulvaney, *Langmuir* 9, 3408 (1993).
207. M. Giersig and P. Mulvaney, *J. Phys. Chem.* 97, 6334 (1993).
208. J. Heath, C. Knobler, and D. Leff, *J. Phys. Chem. B* 101, 189 (1997).
209. D. J. Walton, *Mater. Design* 11, 142 (1990).
210. L. Chico, L. Benedict, S. Louie, and M. Cohen, *Phys. Rev. B* 54, 2600 (1996).
211. See, for example, articles in *MRS Bull.* 22 (1997) and in *Science* 273 (1996).
212. J. Swalen et al., *Langmuir* 3, 932 (1987).
213. G. Whitesides and P. Laibinis, *Langmuir* 6, 87 (1990).
214. Y. Xia and G. Whitesides, *Adv. Mater.* 7, 471 (1995).
215. S. Datta, "Electronic Transport in Mesoscopic Systems." Cambridge University Press, Cambridge, U.K., 1995.
216. W. Tian and S. Datta, *Phys. Rev. B* 49, 5097 (1994).
217. P. Bagwell and T. Orlando, *Phys. Rev. B* 40, 1456 (1989).
218. M. Kemp, A. Roitberg, V. Mujica, T. Wanta, and M. Ratner, *J. Phys. Chem.* 100, 8349 (1996).
219. C. Tsu and R. Marcus, *J. Chem. Phys.* 106, 584 (1997).
220. R. Hoffman, *J. Chem. Phys.* 39, 1937 (1963).
221. D. Papaconstantopoulos, "Handbook of the Band Structure of Elemental Solids." Plenum Press, New York, 1996.
222. A. Dhirani, P.-H. Lin, P. Guyot-Sionnest, R. Zehner, and L. Sita, *J. Chem. Phys.* 106, 5249 (1997).
223. H.-J. Guntherodt and R. Wiesendanger, eds., "Scanning Tunneling Microscopy I." Springer-Verlag, Berlin, 1992.
224. H.-J. Guntherodt and R. Wiesendanger, eds., "Scanning Tunneling Microscopy II." Springer-Verlag, Berlin, 1992.
225. R. Wiesendanger, "Scanning Probe Microscopy and Spectroscopy." Cambridge University Press, Cambridge, U.K., 1994.
226. R. Piner and R. Reifenberger, *Rev. Sci. Instrum.* 60, 3123 (1989).
227. T. Miller, M. McElfresh, and R. Reifenberger, *Phys. Rev. B* 48, 7499 (1993).
228. C. P. Kubiak, L. F. Schneemeyer, and M. S. Wrighton, *J. Am. Chem. Soc.* 102, 6898 (1980).
229. J. A. Baglio, G. S. Calabrese, E. Kamieniecki, R. Kershaw, C. P. Kubiak, A. J. Ricco, A. Wold, M. S. Wrighton, and G. D. Zoski, *J. Electrochem. Soc.* 129, 1463 (1982).
230. P. Wagner, M. Hegner, H.-J. Guntherodt, and G. Semenza, *Langmuir* 11, 3867 (1995).
231. Available from Epoxy Technologies, 14 Fortune Drive, Billerica, MA 01821-0567.
232. A. Hanna and M. Tinkham, *Phys. Rev. B* 44, 5919 (1991).
233. M. Amman, R. Wilkins, E. Ben-Jacob, P. Maker, and R. Jaklevic, *Phys. Rev. B* 43, 1146 (1991).
234. M. Weimer, J. Kramar, C. Bai, and J. Baldeschwieler, *Phys. Rev. B* 37, 4292 (1988).
235. S. Hong, J. Bielefeld, R. Andres, and R. Reifenberger, (unpublished).
236. D. Abraham, K. Sattler, E. Ganz, H. Mamin, R. Thomson, and J. Clark, *Appl. Phys. Lett.* 49, 853 (1986).
237. Y. Tanishiro, H. Kanamori, K. Takayanagi, K. Yagi, and G. Honjo, *Surf. Sci.* 111, 395 (1981).
238. T. Ichinokawa, T. Ichinose, M. Tohyama, and H. Itoh, *J. Vac. Sci. Technol., A* 8, 500 (1990).
239. W. Mahoney, S. Lin, and R. Andres, *Mater. Res. Soc. Symp. Proc.* 355, 83 (1995).
240. S. Evans and A. Ulman, *Chem. Phys. Lett.* 170, 462 (1990).
241. V. P. Roychowdhury, D. Janes, S. Bandyopadhyay, and X. Wang, *IEEE Trans. Electron Devices* 43, 1688 (1996).
242. N. S. Bakhvalov, G. S. Kazacha, K. K. Likharev, and S. I. Serdyokova, *Physica B* 173, 319 (1991).
243. A. Middleton and N. Wingreen, *Phys. Rev. Lett.* 71, 3198 (1993).

244. U. Geigenmuller and G. Schon, *Europhys. Lett.* 10, 765 (1989).
245. A. J. Rimberg, T. R. Ho, and J. Clarke, *Phys. Rev. Lett.* 74, 4714 (1995).
246. T. S. Tighe, M. T. Touminen, J. M. Hergenrother, and M. Tinkham, *Phys. Rev. B* 47, 1145 (1993).
247. H. Grabert and M. H. Devoret, eds., "Single Charge Tunneling: Coulomb Blockade Phenomena in Nanostructures." Plenum Press, New York and London, 1992.
248. K. Nabors and J. White, *IEEE Trans. Computer Aided Design Integrated Circuits Systems* 10, 1447 (1991).
249. A. Ulman, "An Introduction to Ultrathin Organic Films: From Langmuir Blodgett to Self-Assembly." Academic Press, Boston, 1991.
250. M. Samanta, Master's Thesis, Purdue University, 1995.

This Page Intentionally Left Blank

Chapter 5

SILICON-BASED NANOSTRUCTURES

Tamim P. Sidiki, Clivia M. Sotomayor Torres

Institute of Materials Science and Department of Electrical Engineering, University of Wuppertal, 42097 Wuppertal, Germany

Contents

1. Introduction 233
2. Optical Properties of Silicon and Related Materials 235
   2.1. General Remarks 235
   2.2. Group IV Heterostructures: Electronic Zone Folding 236
   2.3. The Direct-Gap Material $FeSi_2$ as a Silicon-Based Light Emitter 238
   2.4. Erbium-Doped Silicon Light Emitters 240
3. Quantum Confinement 242
   3.1. Two-, One-, and Zero-Dimensional Confinement 242
   3.2. Si–SiGe Quantum Wells 244
   3.3. Porous Silicon 246
   3.4. Postgrowth Nanofabrication by Lithography and Etching 249
   3.5. Self-Organized Growth 258
   3.6. Selective Epitaxial Growth 262
   3.7. V-Groove Growth 265
   3.8. Local Growth of Dots and Wires through Shadow Masks 266
   3.9. Silicon Nanocrystallites 270
   3.10. Si/III–V Light-Emitting Nanotips 275
4. Single-Electron Electronics 278
5. Tips for Atomic Force Microscopy and Field Emission 282
6. Conclusions 284
   Acknowledgments 284
   References 285

1. INTRODUCTION

Well-defined nanostructures are fabricated in a variety of materials to modify material properties. The laws of quantum mechanics determine that reducing the dimensions of an electronic system to something comparable to the De Broglie wavelength, that is, the nanometer scale, will modify the electronic states because of confinement and will thus lead to different properties compared to those of the bulk material, such as optical absorption, electrical conductivity, or mechanical properties. In the last 15 years, progress in scanning probe microscopy techniques opened the way to visualizing single atoms and manipulating them. As a result, the concept of atomic engineering of mate-

Handbook of Nanostructured Materials and Nanotechnology, edited by H.S. Nalwa
Volume 3: Electrical Properties
Copyright © 2000 by Academic Press
All rights of reproduction in any form reserved.
ISBN 0-12-513763-X/$30.00

rials has become a real technological method that has attracted much scientific and engineering effort. In parallel, several different methods were developed to fabricate and characterize structures with nanometer scales and clusters with a well-defined number of atoms.

The search for suitable device and systems applications of nanostructures is an ongoing process. In this respect, the driving force to fabricate nanostructure devices can be split into three different aspects: speed, versatility, and increased integration. An important point in fabricating nanometer active areas is the opportunity to fabricate electronic devices operating at frequencies in the 100 GHz up to the terahertz range. In optoelectronics, the realization of structures on the submicrometer scale, where quantum effects become more interesting, enables new material properties to be investigated making use of exciton confinement in a three-dimensional (3D) quantum box with distinct energy levels and their associated optical transitions yielding distinct emission lines. Furthermore, nanometer-sized active regions in electronic components could allow an increase of integration in circuits up to 10^{10} elements/cm^2.

The vast knowledge about silicon together with existing production lines makes silicon the most favored material for many potential applications of nanostructures. The efforts in nanoelectronics are to be understood in the context of future possible needs of the silicon industry. These are well documented in a number of journals, conference proceedings, and patents. In the optoelectronics area, research progress is driven by, for example, the demand to address the electrical wire bottleneck and the exploration of using Si for optoelectronic devices integrated into a Si platform. In this chapter, we focus mainly, but not exclusively, on research results aimed at fabricating Si-based nanostructures with improved optical properties.

The need for faster and more complex microelectronic devices leads unavoidably to an increase in miniaturization of devices and, consequently, to higher packing densities in integrated circuits (ICs). Current feature sizes are about 250 nm and are expected to reach 70 nm by the year 2007. However, this trend brings with itself a design problem because the density of aluminum wires connecting the various ports of the microchips increases dramatically, too, leading to what is called an "electrical wire bottleneck" in the microelectronics industry. One strategy is to replace electrical interconnects with optical interconnects between chips and between circuit boards for ultrafast connection with the expectation of overcoming the bottleneck problem. Many research teams worldwide are looking at the hybrid gallium arsenide on silicon technology. An alternative is to investigate optical interconnects based on silicon technology. Several optical components based on silicon and silicon oxide already exist, such as photodetectors and waveguides. However, for a realistic approach, it is necessary to address two basic devices: (1) a silicon-based light emitter and (2) a silicon-based detector.

Despite their indirect band gap, silicon-based structures continue to be intensively investigated for direct integration of a light-emitting diode onto chips. There are two main geometries considered for potential silicon-based optoelectronic devices: vertical structures, such as top- or bottom-emitting devices, suitable for interplane connections, and edge-emitting devices potentially suitable for in-plane optical connections. Some device ideas are based on laterally structured quantum wires and quantum dots. However, the fabrication of one- or quasi-zero-dimensional devices for device research, as opposed to physics research, remains a significant challenge mainly because of the strong device specifications expected.

Since 1990, porous silicon has evoked great interest because it shows a bright luminescence in the visible. Porous silicon is fabricated by electrochemical etching of crystalline silicon, which leads to the creation of quantum wirelike structures with modified electronic states. This has stimulated many different approaches for realizing nanostructures. A review of silicon-based optoelectronics has been published in the April 1998 issue of the *Materials Research Society Bulletin.*

This chapter is organized as follows: A brief overview of the relevant optical properties of Si and Si-based materials is given in Section 2 to lay down some of the terminology, concepts, and phenomena to be discussed later. In Section 3, we focus on structures exhibiting quantum confinement. Surfaces are intrinsically two-dimensional systems and thus constitute a good starting point. However, given that there are some excellent reviews about two-dimensional Si-based structures, we focus mainly on one- and zero-dimensional nanostructures. Much of the work referred to here aims at realizing a light-emitting device. We discuss hybrid integration of direct-gap alloys with silicon for optical as well as electronic devices. The electronic properties of nanostructures are treated in other chapters of this book; thus, our review of them will be a brief mention of the single-electron transistor in the context of Si nanostructures in Section 4. This chapter would not be complete without considering the progress made in microtechnologies; therefore, in Section 5 we discuss as a special example atomic force microscopy and field emission tips. Although not yet on the nanometer scale, it is instructive to realize how micromechanical devices are fabricated with high throughput.

2. OPTICAL PROPERTIES OF SILICON AND RELATED MATERIALS

2.1. General Remarks

Lasers and light-emitting diodes are used, for example, in optoelectronics, display devices, printers, and image processing and information storage on compact discs. Except for various kinds of silicon-based detectors, most optoelectronic devices are made of III–V compounds.

The development of modern optoelectronics and optical communications has been made possible by the outstanding light-emitting properties of III–V semiconductor compounds combined with efficient waveguiding by optical fibers. On the other hand, current microelectronic technology relies almost entirely on the use of silicon, which requires a different processing technology making the integration of optoelectronics (III–V) and microelectronic silicon devices at best cumbersome and at worst very expensive. However, bulk silicon being an indirect-band-gap semiconductor, is known to be a poor light emitter. The advent of a suitable Si-based light emitter could change this, particularly if the fabrication method of such a light emitter is compatible with silicon industry production lines. A comprehensive summary of optical and other properties of silicon can be found in the EMIS data review series volume on Si and in [1].

During the last few years, enormous progress has been made in the development of SiGe-based devices, such as double heterostructure bipolar transistors (HBTs), optical detectors, and many other devices. Good control in the preparation of this lattice-mismatched material by sophisticated growth techniques, such as molecular beam epitaxy (MBE), metallorganic chemical vapor deposition (MOCVD), and chemical vapor deposition (CVD), enables specific engineering of the desired semiconductor properties. One example is band gap engineering, realized by controlling the layer thickness and composition, resulting in a well-controlled strained or strain-symmetrized heterostructure. Although the use of SiGe strained layers has increased the electrical speed of p and n logics by means of the SiGe heterobipolar transistor, there is still no useful optical device based on Si because its indirect band gap.

Before summarizing the different approaches to realizing nanostructures, a brief overview of the optical properties of silicon is essential to understanding the effort put into silicon-based light emitters. Silicon crystallizes in the diamond structure, which consists of two face-centered cubic lattices (fcc) shifted by a quarter of the body diagonal of the unit cell. By contrast, GaAs crystallizes in the zincblende structure and, therefore, it differs from Si because Ga and As atoms each occupy a separate sublattice. This leads

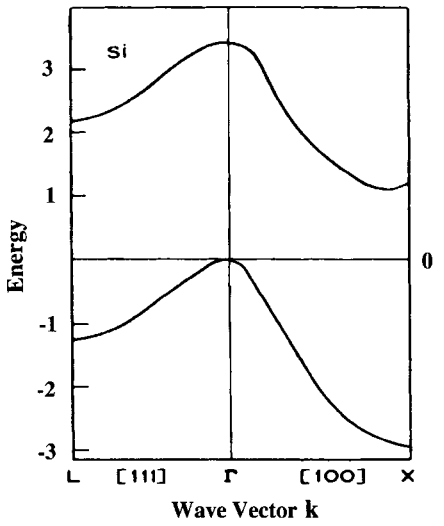


Fig. 1. Schematic band structure of Si. The top of the valence band lies at $k = 0$ and the minimum of the conduction band is at approximately $0.85X$ along the (001) direction. Thus, a phonon is involved in the recombination process.

to a break in the inversion symmetry of the GaAs lattice, which is not the case in Si [2]. The different electronic and optical properties of Si and GaAs can be derived from this structural difference, which is reflected in their respective band structure. The band structure is determined by the crystal structure, the bond type between the atoms, their bond lengths, the chemical species, the electronegativity, the stiffness, and the elasticity [3]. The band structure is the key to the dispersion relation of the charge carriers. Figure 1 shows a schematic dispersion relation for electrons and holes in Si within the first Brillouin zone. For a detailed calculation, see [4].

Note that positive and negative energies refer to electrons and holes, respectively. The valence band structure exhibits a maximum at $k = 0$ known as the Γ-symmetry point. Optical transitions are divided into direct and indirect ones, depending on whether conduction band minimum and valence band maximum occur at the same k value. Restricting the reciprocal space to the first Brillouin zone, Figure 1 shows that the conduction band minimum does not occur at $k = 0$ but at $k \approx 0.85X$ along the (001) direction. In a direct-band gap semiconductor, exciting an electron from the top of the valence band to the bottom of the conduction band, leaving a hole in the valence band, will lead to the emission of a photon upon recombination of these two carriers. The energy of this photon is the same as that of the band gap. In the case of indirect semiconductors, for example, Si, owing to translational symmetry such direct recombination is not possible because the bulk selection rule $\Delta k = 0$ has to be fulfilled. The transition from the highest occupied level of the valence band to the lowest unoccupied level of the conduction band is forbidden unless a momentum-conserving phonon participates. Such a three-body interaction is less likely than a two-body interaction. Thus, the recombination rate in pure Si is much slower compared to GaAs [5]. Therefore, the main drawback concerning Si as a light emitter is its extremely low efficiency of only 1 photon emitted per 10^7 generated electron–hole pairs.

2.2. Group IV Heterostructures: Electronic Zone Folding

One method to overcome the poor luminescence of bulk silicon was proposed in 1974 by Gnutzmann and Clausecker [6]. By building an artificial order perpendicular to the surface, a new potential term is introduced in the Hamiltonian for electron motion in the semiconductor material. The idea was to introduce this extra periodicity by growing superlattices

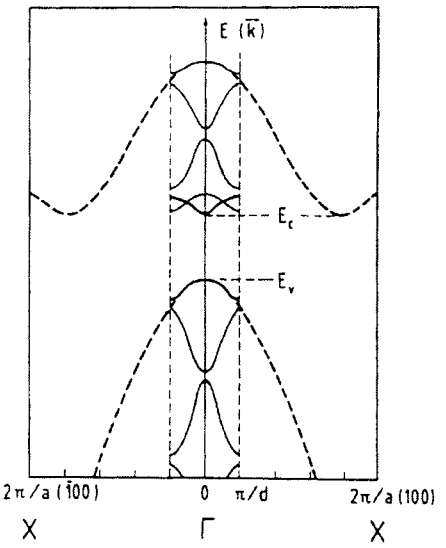


Fig. 2. Schematic illustration of the effect of Brillouin zone folding of the Si band dispersion induced by a superlattice period of about 10 monolayers of Si. The conduction band minimum near the X point is folded back onto the Γ point. (Source: Reprinted with permission from [7].)

of Si and Ge, the period d of which is given by the sum of the thickness of each layer. If the period of the superlattice is smaller than the electron mean free path, "minizones," not observed in the bulk crystal, are formed in momentum space as shown in Figure 2.

The idea of zone folding is based on an increase of the coupling of the conduction band minimum with the valence band maximum at the Γ point, resulting from the superperiodicity of the superlattice. Choosing the superlattice period as $d \approx 5/2a$, where a is the crystal lattice, one can fold the conduction band minimum onto the valence band maximum, resulting in a quasi-direct band structure (see Fig. 2). In a rigorous treatment, the presence of interfaces and the effect of strain as well as band offsets would have to be considered.

The hydrostatic pressure within the strained layers leads to a splitting of the sixfold conduction band X into two degenerate longitudinal states $X_c^{\perp}$ and four degenerated states $X_c^{\parallel}$, which show different folding behavior. The strain-induced tetragonal distortion permits the folding of the $X_c^{\perp}$ states, whereas the $X_c^{\parallel}$ states do not fold onto the Γ point [8]. For Si_nGe_n grown on Si(001), $X_c^{\perp}$ is shifted above the nonfolding $X_c^{\parallel}$ band and thus the alignment is indirect. However, Froyen et al. [8] have calculated that, using a substrate with a larger lattice constant than Si, such as $Si_{0.5}Ge_{0.5}$, will produce a nearly direct-band-gap superlattice. In this case, the Ge layers are less strained and the tetragonal distortion can be neglected. As the system Si/Ge is of type II, the transition will remain indirect in real space, even if a direct band alignment is achieved via zone folding in reciprocal space. Because increasing the superlattice period would lead to a decrease of the optical matrix element, zone folding tends to be restricted to ultrashort-period superlattices.

The first observation of superlattice-induced interband transitions was reported by Pearsall et al. [9] using electroreflectance spectroscopy of Si_4Ge_4 superlattices grown on Si(001). This observation stimulated a great deal of interest based on theoretical band structure calculations [8, 10]. Menczigar et al. [11, 12] have grown Si_mGe_n superlattices on step-graded 650-nm-thick alloy buffers followed by a 500-nm $Si_{0.6}Ge_{0.4}$ alloy film. Figure 3 shows photoluminescence spectra of Si_9Ge_6, Si_6Ge_4, Si_3Ge_2, and the $Si_{0.6}Ge_{0.4}$ alloy. The inset shows the effective mass calculations of the energy positions of the no-phonon (NP) peak. The two lines observed from the superlattices are attributed to the NP line and the transverse optical (TO) phonon-assisted interband transitions of excitons

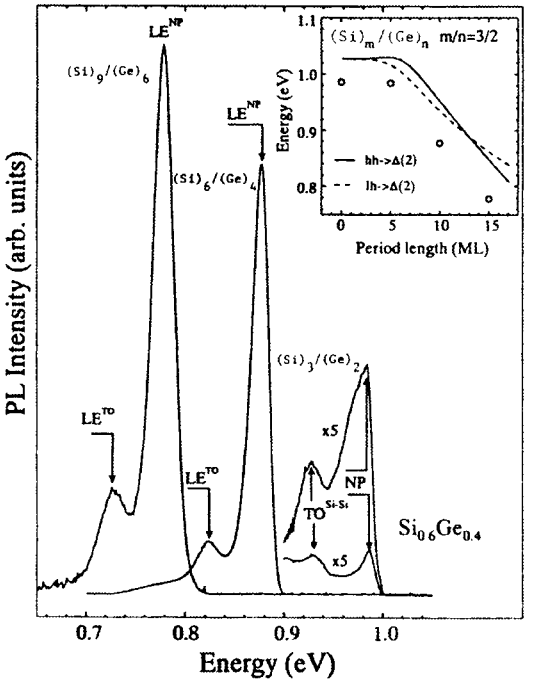


Fig. 3. Photoluminescence spectra of Si_9/Ge_6, Si_6/Ge_4, Si_3/Ge_2 superlattices and a $Si_{0.6}Ge_{0.4}$ alloy. The inset shows the energy positions of the NP lines compared to effective mass calculations. (Source: Reprinted with permission from [12]. © 1993 American Physical Society.)

localized at alloy fluctuations. The systematic blue shift of the peak positions with increasing superlattice period length fits well with the effective mass calculations, indicating the superlattice modifications of the luminescence transitions observed by Pearsall et al. [9].

Although the high luminescence intensity and the promising emission wavelength range suggested the use of Si/Ge superlattices as light emitters, the extremely low luminescence quenching temperature of about 30 to 50 K hindered applications. Afterwards, these authors also reported a reduction in luminescence intensity as well as an increased superlattice band gap after thermal annealing, which led to interdiffusion of the Si and Ge layers. Engvall et al. [13] attributed their TO Ge luminescence to Si–Ge modes originating from the interface. Their annealed samples luminesced up to about 200 K. This provided a hint that further structural improvements could eventually lead to room temperature luminescence. Two recent reviews of the properties of SiGe have appeared [7, 14] and the reader is encouraged to consult them.

2.3. The Direct-Gap Material $FeSi_2$ as a Silicon-Based Light Emitter

Whereas alloying Si with Ge or more recently also with C [15, 16] has led to modified optical and electrical properties, the fundamental band gap remained indirect. The situation changes significantly if Si or Ge is alloyed with Sn [3, 17] or if Si is alloyed with Fe to form $FeSi_2$. Both materials are predicted to exhibit a direct band alignment.

Although $NiSi_2$ and $CoSi_2$ are metallic in their stable fluorite structure, $FeSi_2$ has a 0.85-eV direct gap at room temperature in its stable structure. Hence, there is significant technological interest evoked by this feature [18, 19] as the observed band gap matches quite well with the absorption minimum of optical fibers at 1.5 μm. Because of a local Jahn–Teller distortion, determined by electron–lattice coupling, the cubic fluorite structure is modified to acquire the stable orthorhombic configuration [20]. This deformation, which is responsible for the direct gap, breaks the symmetry and, unfortunately, the

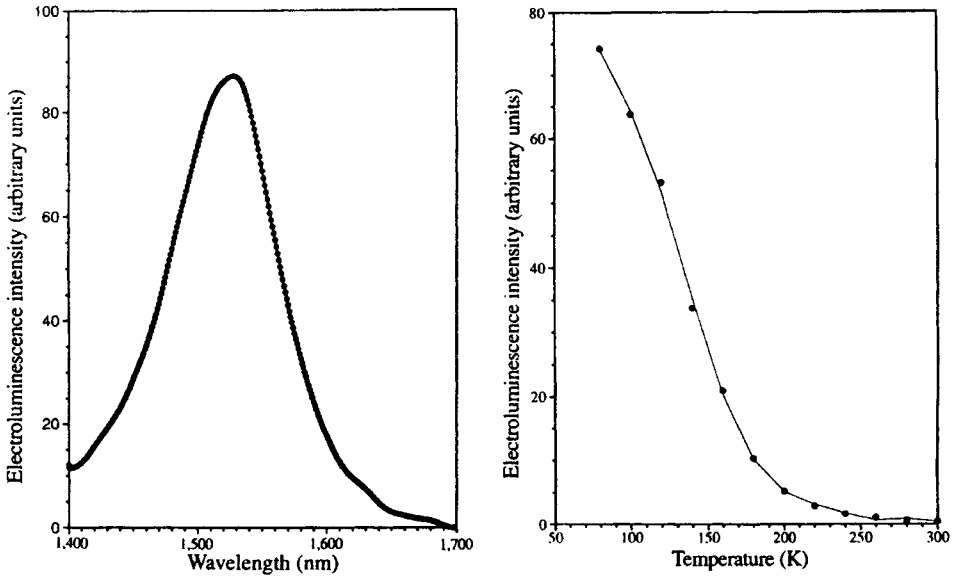


Fig. 4. Electroluminescence spectrum of a β-iron disilicide–based LED recorded at $T = 80$ K under 15 mA of forward current (left). Temperature dependence of the electroluminescence intensity, still detectable at room temperature (right). (Source: Reprinted by permission from [22]. © 1997 Macmillan Magazines Ltd.)

lattice matching to silicon (001) substrates. Thus, the crystalline quality of experimentally achieved $FeSi_2$ films is so far rather low. A possible solution would be a suitable tailoring of the Si(001) surface in analogy to graded SiGe buffer layers leading to coherent epitaxial growth.

Leong et al. [21, 22] have demonstrated a β-iron disilicide-based light-emitting diode (LED) operating at 1.54 μm that incorporates β-$FeSi_2$ into a conventional silicon bipolar junction. The silicon p–n junction was grown by molecular beam epitaxy and consisted of a 1.0-μm-thick B-doped p-type region (1×10^{17} cm^{-3}) grown on a 0.4-μm-thick Sb-doped n^+-type region (5×10^{18} cm^{-3}). The substrate was n^+-Si(001) with a resistivity of 0.008–0.02 Ω cm. The direct-gap iron disilicide is incorporated into the recombination region at the p side of the depletion region by ion beam synthesis with an implant dose of 2×10^{16} cm^{-2} and an ion energy of 960 keV. The implantation produces isolated single-crystalline precipitates after annealing at 900 °C for 18 h with typical sizes of several tens of nanometers. Because of the large size of the crystallites, there are no quantum confinement effects involved in this process. The onset of room temperature electroluminescence was determined to be around 0.8 V.

Figure 4 (left) shows the electroluminescence spectrum of a β-iron disilicide-based LED obtained at $T = 80$ K under a forward current $I = 15$ mA. The luminescence peaks at 1.54 μm with a full width at half-maximum (FWHM) of 50 meV. Figure 4 (right) shows the temperature quenching of the electroluminescence. Besides the decrease by nearly a factor of 70 from 80 to 300 K, there is still some luminescence observable at room temperature. A red shift of the electroluminescence with temperature (50 meV between 80 and 300 K) indicates a band edge–related emission and follows the band gap shift determined from optical absorption studies [23]. The external quantum efficiency of the LED was estimated to be approximately 0.1%. The LED shows no deterioration after several hundred hours of operation under continuous-wave mode at various temperatures.

The possibility of increasing the quantum efficiency of the device, the compatibility with conventional microelectronics processing technologies, and the direct-gap nature of β-$FeSi_2$ make this material system very promising for the integration of a light-emitting diode or an injection laser with an integrated circuit.

2.4. Erbium-Doped Silicon Light Emitters

Because of its potential application in Si-based optoelectronics, Er doping of amorphous and crystalline Si has recently attracted much interest. An intra-4f shell transition between the first excited state ($^4I_{13/2}$) and the ground state ($^4I_{15/2}$) of Er in its trivalent charge state (Er^{3+}) arises from a host electron–hole-mediated excitation when Er is inserted in a Si matrix [24]. The free Er ion intra-4f transitions are forbidden because of the parity selection rules. However, when Er is incorporated into a host matrix, the Er states are mixed, leading to a relaxation of the selection rule. The deexcitation process, with its sharp atomlike light emission at 1.54 μm, is of special interest as it corresponds to the minimum absorption in silica optical fibers. Ennen et al. [25] reported electroluminescence from Er-doped Si diodes at 77 K. However, because of the strong temperature quenching and the absence of luminescence at room temperature, the Er:Si system was not seriously considered for optoelectronics until very recently. Additionally, Xie et al. [40] reported a very low modulation speed of about 1 kHz resulting from the long lifetime of Er in Si ($\sim$1 ms). Owing to this long lifetime, nonradiative competing processes, that is, energy back transfer to the Si host and Auger deexcitation, strongly reduce the luminescence intensity and the quenching temperature.

Several groups have shown sharp photoluminescence [26–28] and electroluminescence [29, 30] up to room temperature. The use of Er:Si in optoelectronics was limited by the strong temperature quenching of three orders of magnitude between 77 K and room temperature [31]. Polman et al. [31] reported a very weak low-temperature luminescence of Er-implanted float-zone Si, indicating that a very small fraction of Er is in the optical active 3+ state or that only a small fraction can be pumped through electron–hole recombination. Codoping Er with C, F, O, and N modifies the Er surrounding, enhancing the Er luminescence [32] and increasing the quenching temperature [27]. Priolo et al. [33] reported a detailed analysis on the erbium–impurity interaction and its effects on the 1.54-μm luminescence in crystalline silicon and concluded that O or F codoping modifies the chemical environment of Er in a way that increases the temperature quenching and enhances the luminescence intensity owing to the enhanced donor behavior of Er.

Franzò et al. [30] fabricated p^+–n^+ room temperature silicon LEDs by erbium ion implantation. An Er concentration of 1×10^{19} cm^{-3} was implanted into the n^+ active region at 0.5–5 MeV. 1×10^{20} cm^{-3} O or F were then implanted at 0.15–1.4 MeV to modify the chemical environment of the Er ions. To recrystallize the approximately 2.3-μm-thick amorphous layer after ion implantation, the samples were annealed at 620 °C for 3 h in a N_2 atmosphere. To activate the dopants and to passivate the Si surface by an approximately 50-nm oxide, the samples were then annealed for 30 min at 900 °C in N_2. The electroluminescence intensity under reverse bias in the breakdown regime was reported to be about 20 times higher than under forward bias. Measuring the electroluminescence intensity as a function of current density reveals a linear increase without any saturation for both forward and reverse bias, the slope of the reverse-biased curve being larger. Increasing the temperature from 100 K to room temperature decreases the electroluminescence intensity in forward bias and the photoluminescence intensity for both O and F doping by a factor of 30 to 50. Recalling the three-orders-of-magnitude decrease reported by Michel et al. [26] and Polman et al. [31] codoping Er has drastically increased the quenching temperature, an effect that was also reported by Ni et al. [34].

Coffa et al. [27] suggested that the electron–hole-mediated recombination process for photoluminescence, which excites the Er^{3+} ion, is due to the recombination of excitons bound to the neutral donor level of the Er ions. Ren et al. [35] alternatively suggested that Auger recombination of a hole in the valence band with an electron in an Er-related trap level transfers energy to the intra-4f Er^{3+} shell. However, only those Er^{3+} ions, which introduce deep levels in the silicon band gap, at which electron–hole (e–h) recombination can transfer energy to the Er ion, can contribute to efficient luminescence. Owing to the similarity in intensity and temperature quenching of photo- and electroluminescence under

forward bias, these authors conclude that a similar process must be responsible for the electroluminescence.

Under reverse bias, the temperature is quenched only by a factor of 7 between 77 K and room temperature. The authors attribute the luminescence process under reverse bias to the impact excitation of Er^{3+} ions from the $^4I_{15/2}$ to the $^4I_{13/2}$ level. Here band-to-band tunneling produces carriers that can be accelerated in the electric field over the depletion region to gain the required energy of approximately 0.8 eV, necessary for impact excitation. Coffa et al. [36] reported an internal electroluminescence quantum efficiency of 1.5×10^{-5} under forward bias and 5×10^{-4} under reverse bias at room temperature. Owing to its impact excitation origin, the quantum efficiency is higher under reverse bias, as Auger processes are strongly reduced because of a lower free-carrier concentration in the depletion regime. In the case of ion implantation, a subsequent annealing step is necessary to remove induced lattice damage and to activate optically the Er atoms. Enhancement of the Er incorporation in high-quality crystalline Si is one of the main targets concerning this issue. Stimmer et al. [37] and Sterna et al. [38] have reported low-temperature MBE growth of Er-doped Si layers in an oxygen ambient. Matsuoka and Tohno [39] achieved an Er concentration of 10^{19} cm^{-3} by ion beam epitaxy.

Ni et al. [34] have investigated the luminescence properties of Er/O and Er/F in MBE-grown silicon Schottky diodes. An advantage of Schottky-type LEDs is that electro- and photoluminescence can both be obtained from the same sample, enabling a direct comparison and a better understanding of the excitation and deexcitation mechanisms of Er^{3+} ions. In this work, Er was directly incorporated together with oxygen and fluorine during MBE growth by evaporating Er_2O_3 and ErF_3. Structural properties were characterized *in situ* by reflection high-energy electron diffraction, low-energy electron diffraction, and Auger electron spectroscopy; the *ex situ* characterization was performed by secondary ion mass spectroscopy, photoluminescence, electroluminescence, and cross-sectional transmission electron microscopy. The epitaxial growth was performed at a growth rate of 0.5–1 Å s^{-1} with substrate temperatures varying between 350 and 600 °C. The authors could increase the concentration of Er incorporation to 5×10^{19} cm^{-3} without Er-related precipitates. This is already more than one order of magnitude higher than the solid-state solubility limit for Er in Si reported by Xie et al. [40]. A strong Er luminescence at 1.54 μm was detected for Er/O- and Er/F-doped layers.

Figure 5 shows a comparison of the low-temperature photoluminescence with the room temperature electroluminescence spectra recorded on the same sample. At elevated temperatures, the photoluminescence is seen to decrease strongly. In contrast to the relative broad photoluminescence peak (FWHM $\approx$ 4.5 meV) from Er/O-doped samples, the Er/F samples show a number of very fine lines in the spectrum. A few of these fine lines remain with higher intensity especially after annealing. From X-ray diffraction studies, the authors concluded that Er/O doping destroys the lattice more efficiently than Er/F.

The authors have demonstrated that the very thin emission lines from Er/F-doped samples disappear both in the photo- and electroluminescence spectra of samples with high F concentration ($0.5–2 \times 10^{20}$ cm^{-3}). Furthermore, the authors found, by electrical characterization, that F-related complexes act as acceptors in Si, leading to p-type material [42]. In this kind of diode, driven in reverse bias, holes would be accelerated as hot carriers. Because of the four times lower mobility of holes in contrast to electrons, the kinetic energy that the holes could gain crossing the depletion region, is lower, leading to a more difficult excitation of the Er atoms and thus to a strong-intensity quenching already at temperatures less than 200 K. Thus, for impact excitation, Er/O doping is usually favored. Franzò et al. [30] found relatively strong electroluminescence from reverse-biased Schottky diodes at room temperature. As in the case of p^+–n^+ diodes [30], the origin of the luminescence in Schottky diodes is also ascribed to electron impact excitation. The electroluminescence line width is comparable to that from a reverse-biased Er-doped Si p^+–n^+

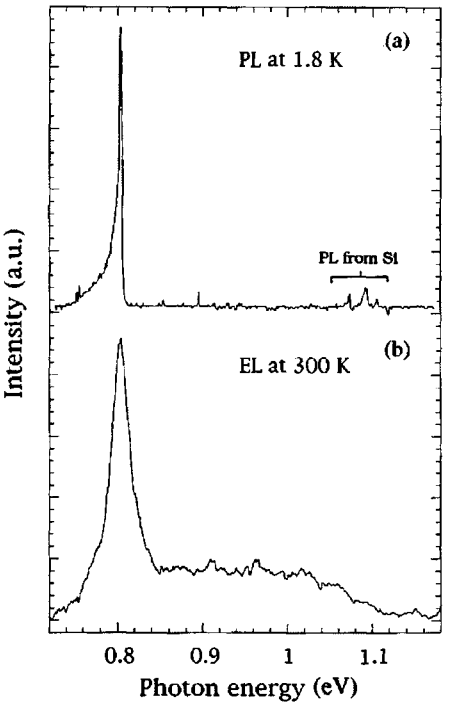


Fig. 5. (a) Low-temperature photoluminescence spectrum of an Er/O-doped sample grown at 420 °C showing intense Er luminescence compared to silicon-related emission. (b) Room temperature electroluminescence of the same sample excited by electron impact. (Source: Reprinted with permission from [34]. © 1997 American Institute of Physics.)

structure (24 meV) [37]. The broad bump at higher energies (see Fig. 5) is related to hot carrier transitions [41].

Time-dependent electroluminescence experiments on forward-biased Er-doped Si p–i–n LEDs at 30 K have revealed a slow component (~700 μs) and a fast component (~4 μs). By increasing the driving current, the fraction of the fast decay can be increased. The long decay can be attributed to the spontaneous Er emission. Ni et al. [42] fabricated a novel Er-doped edge-emitting LED with a SiGe waveguide. A B-doped p-SiGe layer acts as a waveguide for this edge-emitting device. The Er and the O concentrations were both 1×10^{20} cm^{-3}. Additionally, approximately 1% C was incorporated, which resulted in the narrowing of the band gap. Although these are recent developments, the external quantum efficiency could be increased to about 5×10^{-5}. The efficiency remains rather low for applications as a light emitter. However, work is in progress to fabricate a lasing structure, which would increase the intensity by several orders of magnitude and would open the field of real applicable optical interchip connects for Er-doped emitters.

3. QUANTUM CONFINEMENT

3.1. Two-, One-, and Zero-Dimensional Confinement

The particle–wave duality allows us to regard electrons and holes as waves. This situation is extended to other excitations in the crystal such as phonons and excitons. The wave description allows us to associate a De Broglie wavelength to charge carriers and these excitations. Quantum confinement (see Fig. 6) of charge carriers or phonons or excitons occurs when the sizes of the volume where these waves are found is comparable to the De Broglie wavelength.

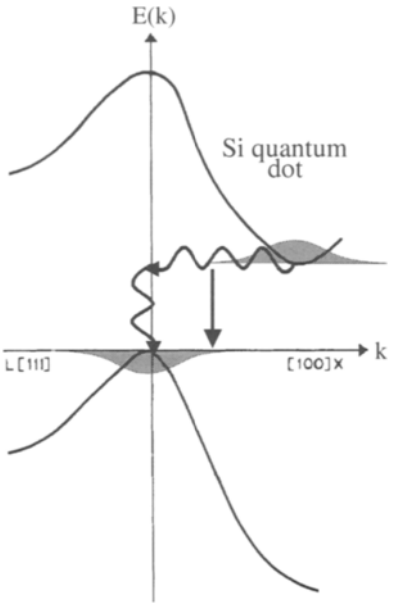


Fig. 6. Schematic illustration of the effect of spatially confining electrons and holes leading to an enhanced overlap of the carriers wave functions as discussed in the text.

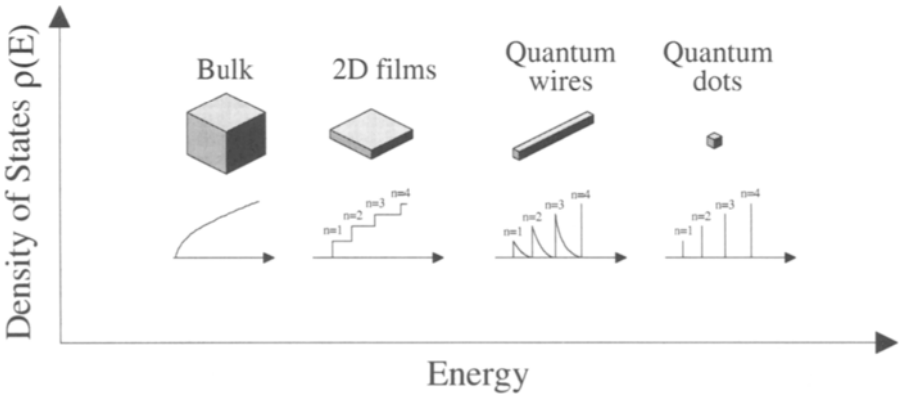


Fig. 7. Change in the idealized density of states $\rho(E)$ while reducing the system dimensionality from a three-dimensional bulk crystal to a two-dimensional layer and, finally, via a one-dimensional wire to a zero-dimensional quantum box.

The physics of low-dimensional semiconductors has been treated by several authors and the reader is pointed to some of these works [43, 44]. A key aspect of semiconductor nanostructures is the modification of the energy levels and the density of states owing to the confinement of charge carriers (see Fig. 7). The carriers behave as the well-known quantum mechanical particle in a box. Thus, only discrete energy levels are allowed, leading to a higher density of states and, theoretically, in the context of this chapter, to well-defined emission lines.

The overlap of the electron and hole wave functions plays an essential role in the radiative recombination efficiency. Because confining these quasiparticles leads to an increased overlap of wave functions in real space, there is also a concentration of the oscillator strength into the few optical transitions allowed in a quantum-confined electronic system. In addition, the recombination probability via nonradiative channels decreases

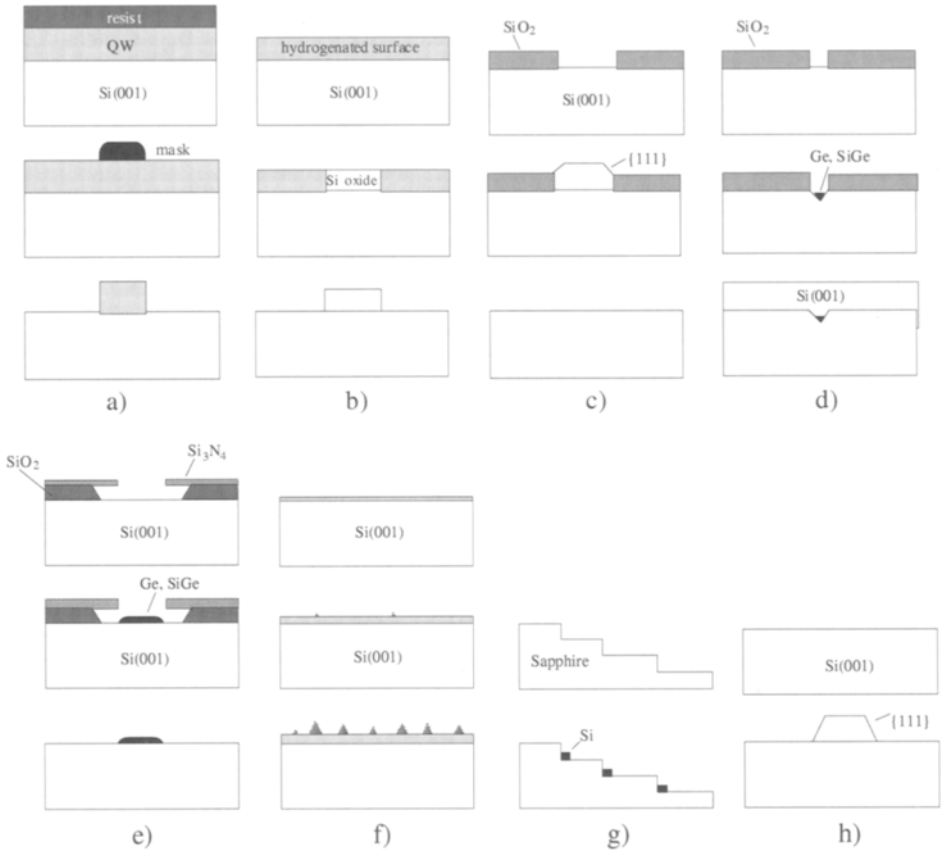


Fig. 8. Sketch of different techniques to fabricate local nanostructures: (a) electron beam or other lithography and reactive ion etching; (b) scanning probe lithography by, for example, using a scanning tunneling microscope; (c) selective epitaxy; (d) growth in V grooves; (e) growth through shadow masks; (f) self-organized growth; (g) growth on structured surfaces; and (h) anisotropic wet etching.

simply because of the lower probability of the carriers reaching nonradiative centers. However, as confinement of many particles leads to Auger nonradiative recombination processes, ideally one wants only one carrier per quantum dot. One practical approach is to use low-excitation-power densities in the case of photoluminescence experiments or lower applied current densities in the case of current injection to create fewer electrons and holes per dot and thus keep the Auger recombination probability small.

Figure 8 shows a sketch of the different fabrication processes for nanostructures. Local growth techniques are of special interest because of the possibility of achieving defect-free strain relaxation and avoiding the introduction of defects through reactive ion etching (RIE). Later in this section, we discuss these techniques and present some experimental results.

3.2. Si–SiGe Quantum Wells

Before turning to one-dimensional (1D) and zero-dimensional (0D) structures, some aspects of two-dimensional (2D) systems have to be discussed. The five group IV elements C, Si, Ge, Sn, and Pb are characterized by their large lattice mismatch resulting from the large difference in their covalent radii. This lattice mismatch leads to strain fields in the heterostructures, which, in turn, determines many characteristics such as the effective mass, the dielectric constant, and the band gap. The lattice mismatch restricts the realization of

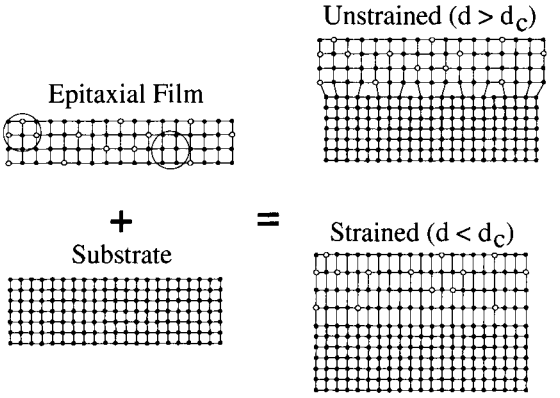


Fig. 9. Schematics of two different natural ways to accommodate lattice mismatch. The full circles denote Si atoms; the open circles represent Ge atoms. The translational symmetry is broken because of compositional disorder (e.g., in the circled regions).

high-quality heterostructures to short-period Si/Ge or to Si/SiGe superlattices. For a detailed review on the Si/SiGe system, we refer to the extensive literature [7, 14, 45]. Some promising progress has been reported on band gap engineering of SiC/Si and SiCGe/SiGe heterostructures [16].

Despite the 4.17% lattice mismatch between Si and Ge, the growth of $Si/Si_{1-x}Ge_x$ heterostructures is possible with a very high epitaxial quality. The in-plane stress is compensated by a tetragonal distortion of the lattice. There is a crossover from this elastic mismatch compensation to a plastic accommodation, if the layer thickness exceeds the critical thickness. In this case, misfit dislocations are created at the interface or threading dislocations can pass through the whole layer, leading to a relaxation of the stored elastic energy. Figure 9 illustrates these two fundamental mismatch accommodation modes.

The rapid development of Si/SiGe heterostructures, relying mainly on improved growth techniques such as MBE or CVD, enabled precise band gap engineering in epitaxially grown wafers. This feature has been used effectively in electronic applications to realize new high-speed devices such as modulation-doped field effect transistors (MODFETs) or heterojunction bipolar transistors (HBTs). Top values for f_{max} reported by IBM and Daimler Benz [46] are well in the range of 160 GHz and are comparable to state-of-the-art GaAs transistors. As many of the following Si-based nanostructures discussed in this chapter are characterized optically, we briefly discuss the major parts of the photoluminescence (PL) spectrum of Si and SiGe. Photoluminescence is very sensitive to nonradiative defects and thus it is used, in general, to probe the quality of undoped or low-doped semiconductors. The use of photoluminescence to characterize 3D and 2D semiconductors has been reviewed by Perkowitz [47]. There are a number of delicate issues such as exciton localization, exciton confinement, and their roles in the emission process. Such themes are the subject of many international conferences (e.g., the conference series "Optics of Excitons in Confined Systems") and will not be treated here.

Figure 10 shows a typical low-temperature band edge–resolved PL spectrum of a $Si/Si_{0.7}Ge_{0.3}/Si$ multiple quantum well recorded under an excitation power $P = 60$ mW. At $\lambda = 1089.9$ and 1107.7 nm, Si substrate emission lines are observed originating from the no-phonon (NP) bound-exciton (BE) recombination (Si_{BE}^{NP}) and the transverse acoustical (TA) phonon–assisted exciton emission (Si_{BE}^{TA}). The strong emission at 1128.7 nm is due to the transverse optical (TO) phonon–assisted bound-exciton recombination (Si_{BE}^{TO}), which is commonly observed in Si crystals [1]. At 1147.7 nm, the Si electron–hole droplet (EHD), emission (Si^{EHD}) is observed under higher excitation power densities. Intense luminescence lines labeled $SiGe^{NP}$ (1219.9 nm) and $SiGe^{TO}$ (1290.3 nm) are the no-phonon

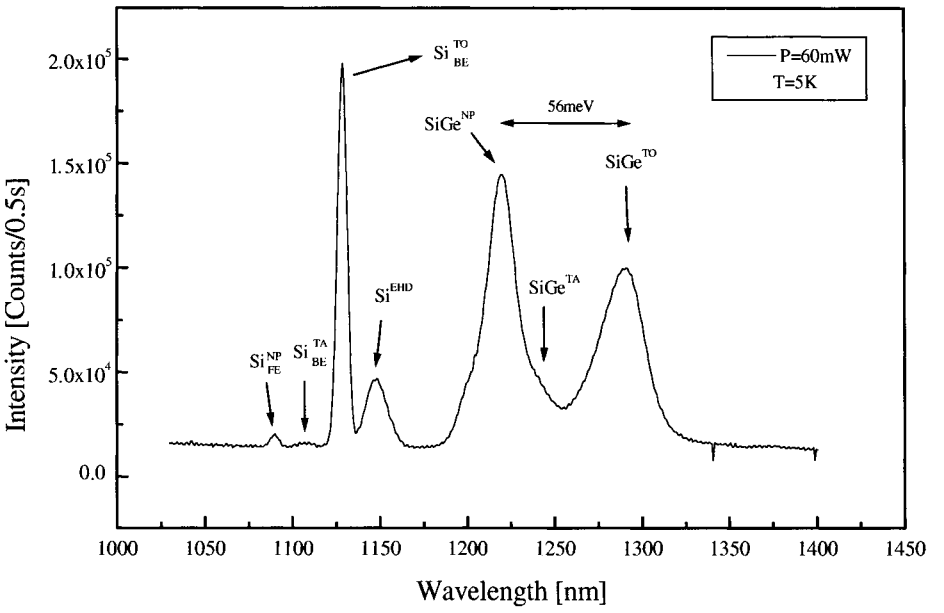


Fig. 10. 5-K PL spectrum of a 15-period Si(3nm)/$Si_{0.7}Ge_{0.3}$(3nm)/Si(3nm) multiple quantum well structure recorded under an excitation power of 60 mW.

and the transverse optical phonon–assisted emission, respectively, originating from SiGe layers, as shown by several authors. Note that the energy difference of 56 meV between the NP and TO lines closely matches the Si–Si TO phonon energy as expected. The Si–Ge and Ge–Ge TO lines are not resolved in this spectrum. Transverse acoustical phonons are also observed in the same spectrum between the NP and TO emission lines.

The strong no-phonon emission is a manifestation of the broken translational symmetry within the SiGe layers, as has already been reported by Weber and Alonso [48]. This occurs via scattering because of compositional disordering (Fig. 9) in the SiGe well layer, leading to a momentum-conserving transition. However, the emission intensity from SiGe quantum wells is still too low for use in LEDs.

Nanofabrication of these two-dimensional systems is under investigation to confine the excitons further and in more dimensions in an attempt to increase the emission intensity.

3.3. Porous Silicon

Current interest in porous silicon was initiated by the demonstration that a simple electrochemical etching process leads to intense luminescence from silicon in the visible region of the spectrum even at room temperature [49]. As the fabrication by an anodic dissolution in a HF-based electrolyte is very simple, porous silicon has been intensely investigated. The structural characteristics of porous silicon exhibit extremely fine tubular structures, viewed as a mesh of wires or dots, which are small enough to exhibit some quantum confinement effects.

Transmission electron microscopy (TEM) studies [50] have demonstrated that under suitable conditions this etching process can generate isolated columns of width less than 5 nm (see Fig. 11). With such small sizes, quantum size effects are expected, which Canham [49] has suggested are responsible for the higher luminescence intensity and emission energy of porous Si in contrast to bulk silicon. The small cross section of the wires also means that the number of nonradiative centers per unit length of wire is very small, irrespective of these centers being distributed over the surface or throughout the bulk [3]. Migration of excitons to these nonradiative defects is suppressed by exciton localization [49].

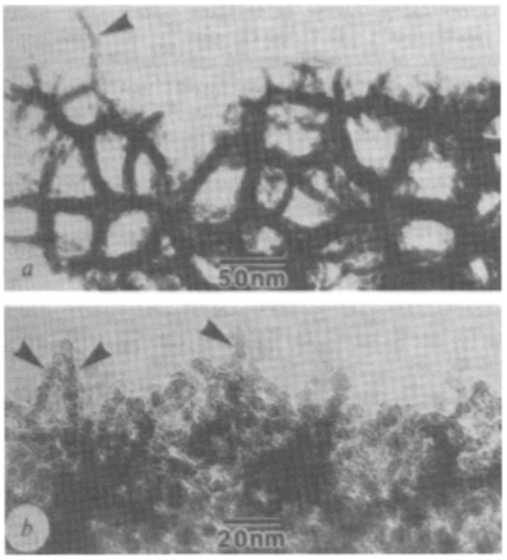


Fig. 11. Transmission electron micrographs of thin Si layers with 80% porosity. The narrow Si columns within the irregular matrix are marked with arrows. (a) Sample with weak luminescence and (b) sample with strong luminescence. (Source: Reprinted by permission from [50]. © 1991 Macmillan Magazines Ltd.)

The assignment of the visible photoluminescence of porous silicon to quantum-confined carriers in crystalline silicon was controversial for a long time but is now generally accepted. Alternative suggestions were, for example, that the photoluminescence was due to siloxene [51], a silicon-based polymer ($Si_6O_3H_6$), or due to polysilanes or hydrates at the surface [52]. The problem with these models was the experimental result that the material exhibited intense red photoluminescence even after high oxidation temperatures, which modified the silicon surface. Other groups agree with the quantum confinement model, but propose quantum dot structures [53] instead of Canham's quantum wires. Detailed characterization by several researchers has confirmed that the filaments are single-crystallites. Bassous et al. [54] have demonstrated a clear quantum confinement effect as there is a blue shift of the photoluminescence signal with reduction of the porous silicon features sizes caused by subsequent HF etching.

The width of the rather broad luminescence peaks ($\approx$0.4–0.6 eV) results from quantum size fluctuations. It is quite possible that the luminescence is at least partly surface defect related, as hydrogen passivation leads to an enhancement of the luminescence. This point is backed up by the observation that high annealing temperatures cause a strong quenching of the luminescence as hydrogen is desorbed. To reduce the surface recombination velocity and thus to keep the radiative lifetime long in comparison with the lifetime of nonradiative channels, it is necessary to terminate the dangling bonds at the silicon surface with hydrogen [49]. The temperature dependence of the photoluminescence intensity hints at some interesting possibilities to explain the luminescence process in more detail. The maximum in the photoluminescence intensity at $T = 200\,^{\circ}\mathrm{C}$ [55] and the fact that the luminescence is completely quenched at low temperatures indicate the possibility of a defect level quenching or an interplay of radiative and nonradiative channels, where the latter is dominant at low temperatures.

However, it is more likely that the still indirect character of the radiative transition involves additional phonons for momentum conservation reasons and that these phonons are depopulated at low temperatures. Using PL spectroscopy under resonant photoexcitation, Calcott et al. [56] showed that phonons are involved in the luminescence process and that porous silicon thus remains an indirect band gap material. From the experimental

point of view, the origin of the luminescence can be traced to the existence of quantum size crystalline structures. Detailed theoretical studies have been carried out to identify the confinement character of the luminescence.

Based on experimental results, Buda et al. [57] have performed first-principle calculations of the electronic properties of (001)-oriented silicon quantum wires with diameters $d = 0.76$, 1.14, and 1.56 nm using the density functional theory within the local-density approximation for the exchange correlation energy. As in the experimental case, they have assumed the silicon dangling bonds to be passivated at the surface by hydrogen atoms. In contrast to bulk silicon with its indirect gap of 1.17 eV, here a direct gap of 1.84 eV appears at $k = 0$. For the external field polarized in the direction of the axis of the wires, calculations of the imaginary part of the dielectric function $\varepsilon_2(\omega)$ exhibit a peak in the range of visible light. This feature cannot be identified with any bulklike electronic state of crystalline silicon. The dependence of this peak on the wire size was correlated with the behavior of the luminescence peak in porous silicon. Moreover, the extrapolation of the luminescence energy as a function of the wire thickness covers the energy range in which porous silicon is seen to luminesce.

Although the breakdown of the momentum selection rule enhances the interband optical matrix element, this is not the main reason for the radiative efficiency of porous silicon. Read et al. [58] have calculated the radiative lifetime of localized excitons in quantum wires to be in the range of 380 μs, which is much longer than the lifetime of 1 ns for bound excitons in GaAs [58, 59]. Here the enhancement of the exciton binding and localization energies by confinement and the low rate of nonradiative recombination are considerable. However, the luminescence behavior of porous silicon does depend strongly on the exact sample treatment during sample preparation. In the case of an array of quantum wires in porous silicon, samples etched for a shorter time should have a distribution of larger wire diameters. However, Pearsall et al. [60] did not identify any red shift of the luminescence peak with decreasing etch time. Instead, they only measured a decrease in the luminescence intensity as the etch time decreases. The results of this group suggested that a film of strained [61] luminescent material such as a fractal phase of silicon or a silicon complex [62] is created or redeposited on the surface during etching.

Quantum confinement effects in porous silicon are no longer disputed. The simple etching of silicon does not work if using n-doped silicon as the required holes for the etching process are no longer available. To fabricate porous silicon out of an n-doped wafer, one has to illuminate the sample with light to create electron–hole pairs. Among others, Eisebitt et al. [63] have prepared porous silicon under different wavelengths of illumination. Using soft X-ray emission, absorption spectroscopy, and X-ray fluorescence measurements, they could selectively probe the silicon core of oxidized nanostructures by suitable choice of the excitation wavelength. The changes in the valence and conduction bands could be explained by the changes in the electronic structure associated with quantum confinement in silicon nanostructures.

The interpretation of the luminescence from porous Si is made more difficult by the presence of defects in the silicon oxide that act as radiative centers. To analyze this, Ge nanoparticles were fabricated by Nozaki et al. [64] using the cluster beam evaporation technique. These nanoparticles have the same diamond structure and they also have an indirect band gap. In contrast to Si, however, Ge shows a less natural oxidation. Saito [65] has reported a mixture of diamond and tetragonal structure in Ge nanoparticles when their size is smaller than 20 nm. This phase transition occurs due to a minimization of the surface energy, as the diamond structure is less closely packed [64, 65]. Nozaki et al. [64] attributed the blue luminescence ($E = 2.9$ eV) of the Ge nanoparticles to defect centers in the Ge oxide formed by photooxidation. In addition, quantum confinement could be excluded as there was no energy shift with adjacent photooxidation.

Although some progress has been made concerning the potential integration of porous silicon–based light emitters with microelectronics, two fundamental problems affecting

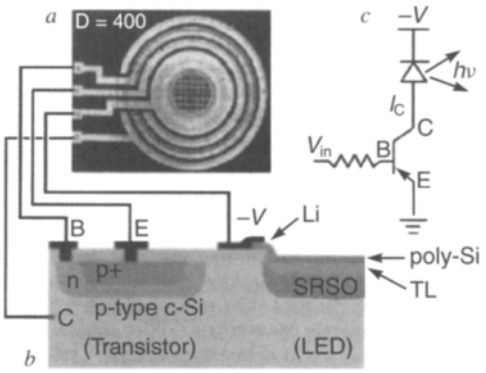


Fig. 12. Sketch of the integrated porous silicon–based LED with the driving bipolar transistor. (a) Top view of the structure with a 400-μm active light-emitting area. (b) Cross section from the center of the LED at the right side to the transistor at the left side. (c) Electronic circuit. (Source: Reprinted by permission from [68]. © 1996 Macmillan Magazines Ltd.)

porous silicon are its extreme fragility, which leads to a degradation of the more than 5% PL quantum efficiency in about 1 h under ambient conditions [66], and the relative low modulation speed. Moreover, the reported values of electroluminescence (EL) efficiency were more than 100 times smaller than that of PL, with even faster degradation times. The reason behind this is inefficient carrier transport through the irregularly built structure of porous silicon. The lack of robustness during high-temperature cycles may seriously limit the potential use of this material. However, Loni et al. [67] enhanced the room temperature EL efficiency to more than 10^{-3}.

First Integration of a Porous Silicon–Based Light-Emitting Diode with a Conventional Bipolar Transistor. Despite its fragility and low-temperature resistivity, the integration of porous silicon with conventional silicon technology was recently demonstrated. Hirschman et al. [68] demonstrated the integration of a porous silicon–based LED with a conventional bipolar transistor as a driving transistor. They enhanced the thermal ($\sim$1000 °C) and chemical stability of porous silicon by partial oxidation [69]. With this silicon-rich silicon oxide (SRSO) process, the light emission and electrical characteristics still retain the desirable device stability, which is higher than that of porous silicon [68]. Figure 12 shows the optoelectronic circuit that integrates the SRSO-based LED with a surrounding bipolar driver transistor. In an emitter configuration, a base input signal is amplified by the transistor and controls the current flow through the diode. Thus, the diode can be directly modulated.

These authors integrated several diodes with active areas ranging from 0.005 to 2 mm^2. Typical of porous silicon is the rather broad electroluminescence ranging from 1.4 to 2.3 eV. The luminescence onset lies at 2 V. The highest noted external power efficiency is 0.1%. Although the device stability has been tested over several weeks without any degradation, the modulation bandwidth of 1 MHz still remains extremely low.

3.4. Postgrowth Nanofabrication by Lithography and Etching

The feature size limit set by current lithography is well within the quantum size regime using state-of-the-art pattern transfer sizes down to a few 10 nm. At present, nanostructure devices are fabricated by a pattern definition technique, for example, electron beam lithography, followed by a pattern transfer using an etching technique such as reactive ion etching. An outline of this process is shown in Figure 13. Considering a positive resist such as polymethylmethacrylate (PMMA), the fabrication process basically consists of (a) spinning the resist on the as-grown 2D substrate, for example, a multiple quantum well. A pattern consisting of wires and or dots can be written on the resist with a focused

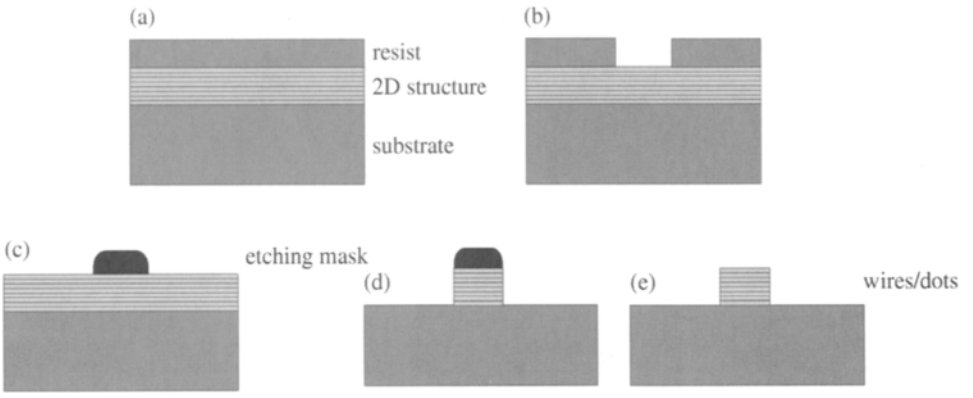


Fig. 13. Schematic view of the nanofabrication process used for fabricating quantum wires or quantum dots in the range of approximately 50 nm (see text).

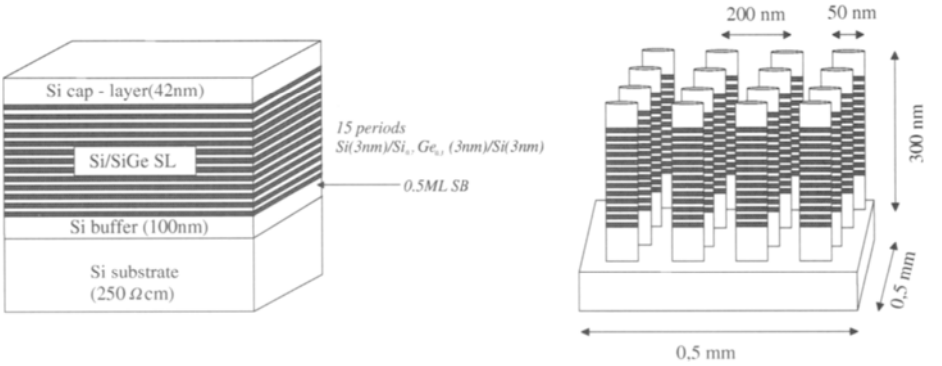


Fig. 14. Sketches of the as-grown $Si_{1-x}Ge_x$ multiple quantum wells and the dot array.

electron beam and then undergo development in a solvent (b). After depositing an etching mask, the resist is lifted off (c). A highly anistropic reactive ion etch process is then used to transfer the pattern onto the as-grown wafer (d). In the final step, the etch mask is removed if necessary. The advantage of this technique is the good size control of the nanostructures and flexibility in the nanostructure pattern design. However, the nonnegligible damage introduced by the etching procedure could alter dramatically the electrical and optical characteristics of the material. Even with an optimized low-damage RIE recipe, damage, such as an amorphous layer on the surface of the nanostructures, will persist along with possible point defects inside the semiconductor.

Tang et al. [70, 71] reported an increase in the electroluminescence properties of reactive ion-etched $Si/Si_{1-x}Ge_x$ quantum dots by a factor of 100. For this work, the structures shown in Figures 14 to 18 were used. Figure 14 illustrates the as-grown wafer and nanostructured dots. The highest luminescence intensity was observed for wafers consisting of a 15-period $Si/Si_{0.7}$(3 nm)$Ge_{0.3}$(3 nm) multiple quantum well structure. The pitch size of the dots was about 200 nm and each dot had a diameter of 50–70 nm and a height of 300 nm. Thus, very dense dot arrays could be fabricated. The single-array areas with a high dot density were about $500 \times 500\ \mu m^2$.

Figure 15 shows a scanning electron microscopy (SEM) micrograph of Si/SiGe dots fabricated by electron beam lithography and RIE in $SiCl_4$. At this stage, photoluminescence experiments can be performed to characterize the dot array, provided the patterned sample is nominally undoped. In several samples grown by MBE on Si(001) and on strain

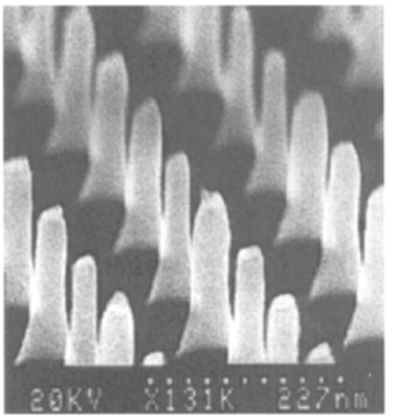


Fig. 15. SEM micrograph of a $Si/Si_{1-x}Ge_x$ quantum dot array.

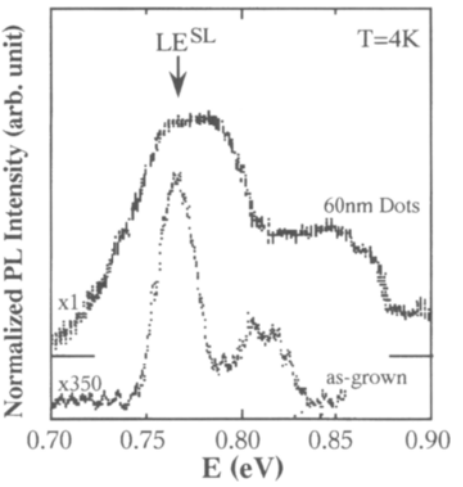


Fig. 16. Comparison of 4-K photoluminescence spectra from an as-grown Si_9/Ge_6 superlattice and a 60-nm dot array from the same sample.

symmetrized substrates of Si with a SiGe superlattice, a similar observation was made: The 4-K photoluminescence intensity of samples patterned into dot arrays is 100–200 times stronger than that of the as-grown samples. One example is shown in Figure 16, which shows a photoluminescence increase of more than two orders of magnitude of photoluminescence from 60-nm dots compared to the as-grown sample. The lower curve is the reference spectrum. The intense peak at 0.7654 eV is attributed to the localized intrinsic exciton from the superlattice (LE^{SL}) as already reported by Menczigar et al. [12]. The broadening of this peak after nanofabrication is explained as an effect of process-induced strain.

For electroluminescence, electrical contacts on the top and at the bottom are needed. Prior to depositing the top contact, the dots have to be planarized with a suitable low-stress insulator. Tang et al. [72] have reported the crucial role of strain on the observed enhanced light emission. A 3-nm-thick $Si_{0.78}Ge_{0.22}$ quantum well was grown on float-zone (FZ) Si and capped by 120-nm Si. After nanofabrication into 50-nm dots, different dot arrays were coated with amorphous SiN_x by PECVD at 300 °C. The built-in stress of the SiN_x coating was varied by changing the radio frequency (rf) power, and measured by laser interferometry on a simultaneously codeposited SiN_x film on a glass substrate.

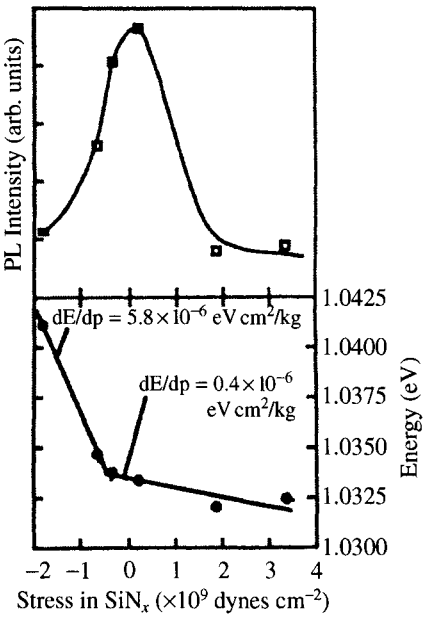


Fig. 17. Photoluminescence intensity and peak energy of the SiN_x-coated dots as a function of the stress in the planarizing layer.

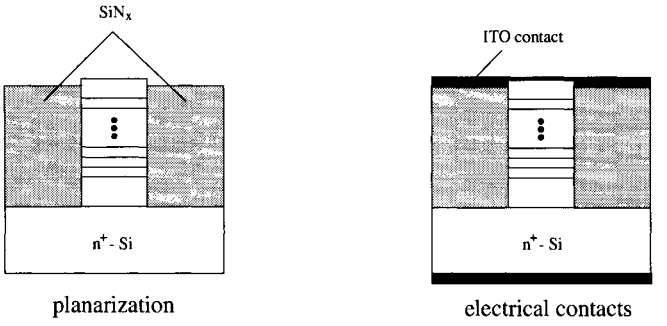


Fig. 18. Planarization of the dot array with SiN_x (left) and electrical contacts with ITO (right).

Figure 17 shows the photoluminescence intensity of the dot arrays recorded at 6 K together with the peak energy as a function of the corresponding stress of the SiN_x film. When the stress in the SiN_x is nearly zero, the spectrum shows the maximum photoluminescence efficiency, close to that of uncoated dots. External induced tensile as well as compressive strain drastically decreases the luminescence intensity. Thus, there is an optimum regime for the SiN_x deposition with respect to maximum luminescence yield. These experiments on the stress of the SiN_x coating were very important, as in previous tests polyimide had led to unstable and shifted current–voltage (I–V) characteristics because of a leakage current under bias. Using high-stress PECVD SiN_x removed these problems, but decreased the emission. On the other hand, stress-free SiN_x reported in [72] did not alter the light emission strength and exhibited acceptable I–V characteristics. Figure 18 (left) shows a schematic of the planarized structure.

Finally, a 70-nm NiCr layer was deposited as electrical top contact. Experiments are in progress to replace NiCr by an optically transparent and conducting indium tin oxide (ITO), to be used as a mask and ohmic contact in future tests. In Figure 18, NiCr has already been replaced by ITO. Figure 19 shows the electroluminescence intensity of the

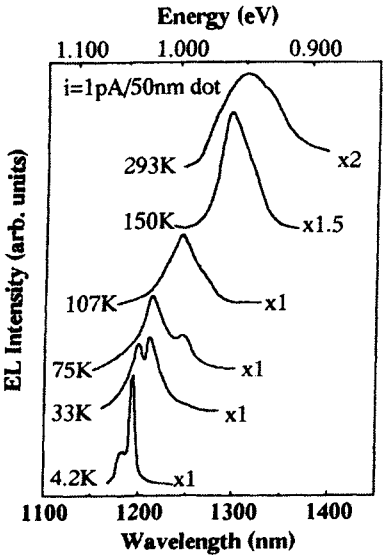


Fig. 19. Electroluminescence spectrum of the $Si/Si_{1-x}Ge_x$ dot array at different temperatures. This array had polyimide as the insulating material and a 70-nm NiCr top contact. For reference, the spectrum of a large mesa structure is also shown.

dots at different temperatures, compared to a low-temperature spectrum of the as-grown wafer. These spectra were recorded at an injection current of 1 pA/dot under reverse bias, 0.5 V at 293 K and 2.0 V at 4.2 K. At room temperature, an external quantum efficiency of 0.14% was estimated [70].

The results of the luminescence data have shown the crucial role of strain during the fabrication of low-dimensional structures. Tang et al. [73] found that the smaller the nanostructures, the bigger is the strain relaxation. This observation was deduced from the Raman shift of the Ge–Ge, Si–Ge, and Si–Si modes of 50-nm dots with different Ge concentration, which were accounted for by a 50% strain relaxation.

Figure 20 shows the Ge content–dependent Raman shifts of the Si–Si, Si–Ge, and Ge–Ge modes for different dot arrays of similar size. The solid line is the calculation of a corresponding unstrained pseudomorphic structure; the dashed line is the calculation with a 50% strain relaxation [74]. The solid circles represent the experimental data. In addition to the strain relaxation resulting from material removal through etching, a thin SiGe layer, redeposited on the walls of the dots, may force the atoms to rearrange and induce a lattice distortion inside the dots [75]. This hypothesis is supported by Raman spectra from etched regions away from the dot arrays pointing to the existence of a thin SiGe alloy being redeposited all over the remaining silicon substrate.

To investigate the effect of size reduction on strain relaxation inside the Si/SiGe nanostructures, a series of 2.5-μm-long and 10-to-500-nm-wide wires were fabricated of a modulation-doped p^+-$Si/Si_{1-x}Ge_x$ heterojunction structure [76]. Figure 21 shows room temperature photoreflectance spectra for wires with different widths compared to a mesa control sample. In this spectrum, $11h$ represents Γ-like 2D interband transitions between the first electron subband and the first heavy-hole subband. On reducing the wire width down to about 100 nm, the $11h$ transition is red-shifted, indicating a strain relaxation of the original comprehensive strain in the SiGe layer of the heterostructure during wire fabrication. Further reduction of the wire width to 40 and 15 nm leads to a blue shift because of lateral confinement effects, indicating a clear 2D–1D transition [77]. Similar phenomena were also observed in wires cut from $Si–Si_{1-x}Ge_x$ multiple quantum wells [78]. However, a quantitative analysis of the strain and confinement shifts was not carried out.

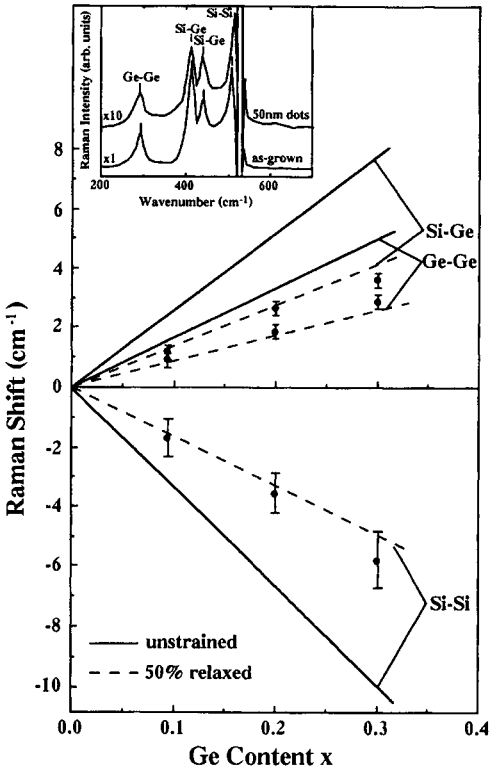


Fig. 20. Ge content dependence of the Raman peak shift of the dot arrays compared to the as-grown superlattice. The inset on the top left shows the Raman spectra of a dot array and the corresponding as-grown samples cut from a Si–$Si_{0.7}Ge_{0.3}$ superlattice. The sharp features at around 521 cm^{-1} are due to the removal of the Si TO phonon peak from the substrate.

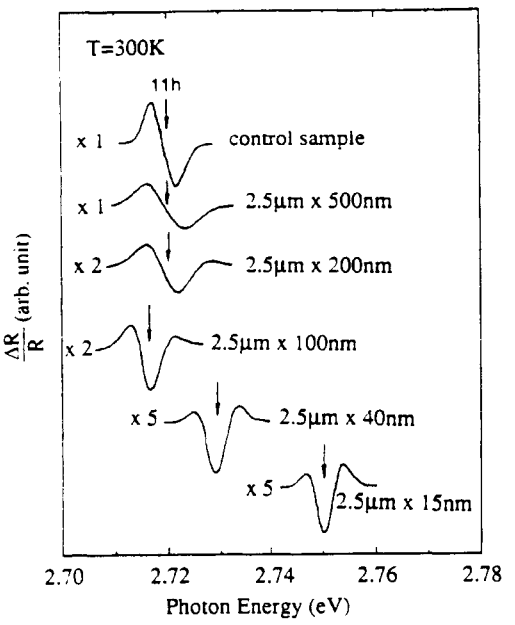


Fig. 21. Photoreflectance spectra of a control sample and etched wires with different widths. The top spectrum corresponds to the control sample. Wire widths range from 500 nm (second scan from top) to 15 nm (bottom spectrum).

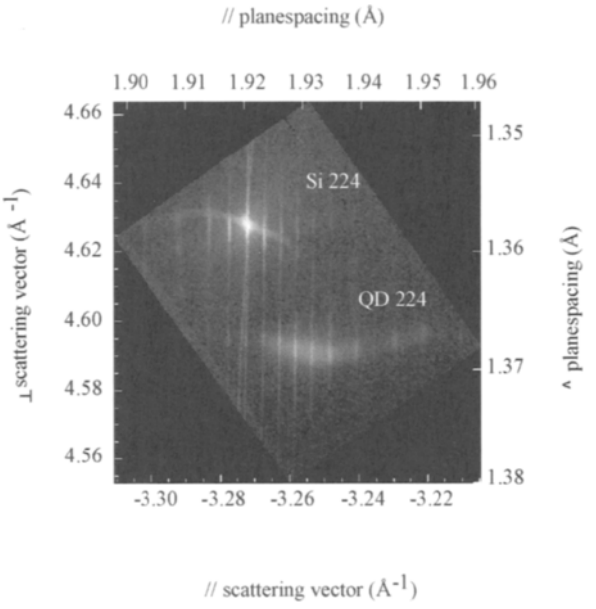


Fig. 22. Intensity distribution of a 2D RSM obtained around the (224) reflection from an array consisting of 50-nm dots. (Source: Courtesy of W.-X. Ni and J. Birch.)

Generally, the smaller the nanostructure, the more the strain relaxes in strained-layer heterostructures.

Nondestructive X-ray diffraction is widely used to map the two-dimensional reciprocal space to characterize ordering, crystallinity, or layer sequence in superlattices. However, the relatively low diffraction intensity from low-dimensional structures makes necessary the use of synchrotron radiation for structural analysis. In comparison to reciprocal space mapping (RSM) of two-dimensional superlattices, which shows satellites resulting from the periodicity of the superlattice in the q_z direction, in the case of quantum dot arrays additional satellites are found in the $q_{\|}$ direction, which originate from the periodicity of the dots within the array. Figure 22 shows the 2D reciprocal space maps around the Si(224) reflection recorded at the European Synchrotron Radiation Facility. The spacing of these satellites is, as usual, related to the inverse of the dot distance in real space. Ni et al. [79] have found a reduction of the mean lattice mismatch of the dots to the substrate in the growth direction from 0.0113 for a fully strained 30-period Si(3 nm)/$Si_{0.7}Ge_{0.3}$(3 nm) 2D superlattice to 0.0070 caused by strain relaxation after structuring the sample into 50-nm dots with a height of 300 nm and a pitch size of 130 nm. Such a lattice relaxation was only detected within dot structures compared to an approximately 0.1×1 mm^2 reference 2D Si/SiGe area. From 2D RSM around an asymmetric reflection, the authors also determined a mean in-plane lattice mismatch of 0.0059 to the substrate.

A partial strain relaxation consistent with the previously mentioned Raman experiments led to the difference between these two values. The clear observation of higher-order satellites of the superlattice within the dots indicates that the superlattice layers are still well ordered after the partial strain relaxation. However, the existence of some weak diffuse scattering in between the superlattice reflections raises the possibility of the presece of amorphous layers surrounding the dots. This may be the result of crystal damage caused by the rather crucial reactive ion etching or from a redeposited SiGe alloy surrounding the dots.

Using bulk elastic theory for a homogeneous deformation, the authors found a partial relaxation in the SiGe layers, whereas the Si layers are biaxially expanded. This strain

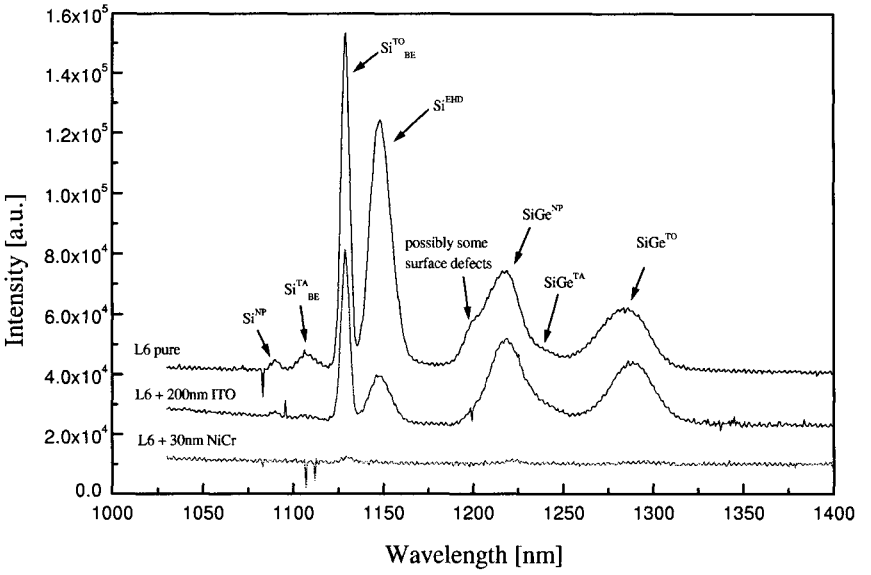


Fig. 23. Photoluminescence spectra of a $Si/Si_{1-x}Ge_x$ mesa structure (top curve) and of the same structure coated with 200-nm ITO (middle curve) and 30 nm NiCr (bottom curve).

symmetrization affects the band offsets at the heterointerfaces in becoming type II. The strain induces a splitting of the sixfold degenerated conduction band. Edge electrons in a $\Delta(2)$ band located near $k_{\|} \approx 0$ can recombine with holes located at $k_{\|} \approx 0$ across the interface without additionally involving a phonon for the required momentum conservation. This is probably a reason for the reported enhanced luminescence properties of Si/SiGe quantum dots.

Considering the almost 94% absorption of infrared photons in the top NiCr layer, the luminescence intensity could potentially be increased by a factor of 10 by replacing NiCr with ITO. Figure 23 shows a 5-K PL spectrum of a $Si/Si_{1-x}Ge_x$ mesa structure and of the same structure coated with ITO and NiCr. The low absorption of about 5% with a still good sheet resistance of 2000 $\mu\Omega$/square is noteworthy. An additional advantage of this layer is also pointed out in Figure 23. Higher excitation powers revealed surface defects, which are visible in the PL spectrum as a small shoulder at the smaller wavelength side of the $SiGe^{NP}$ line. The shoulder, which is only observed at higher excitation powers, is not detectable when the ITO layer is deposited. This is possibly due to oxygen absorption out of the ITO layer, which passivates the Si surface.

Lithographic techniques combined with reactive ion etching provide well-defined spatial structures. However, lateral dimensions at which quantum confinement effects are observed at room temperature (~5–10 nm) cannot directly be generated. An additional thinning of the structures by dry oxidation at elevated temperatures leads to much smaller structures.

Nassiopoulos et al. [80] have used deep ultraviolet (UV) lithography and reactive ion etching in a mixture of SF_6 and CHF_3 to fabricate Si nanopillars (see Fig. 24). Their intention was to relate the red photoluminescence observed from porous silicon to the quantum confinement model. PMMA and Cr were both used as a mask layer. In both cases, a remarkable aspect ratio of height to diameter greater than 40:1 was achieved. The diameter of the pillars was in the range of 20 to 40 nm and could be reduced to below 10 nm by thermal oxidation at 900–950 °C followed by a dip in HF to remove the oxide layer.

From these vertical nanowires, photoluminescence in the visible was obtained at room temperature. The peak position was between 580 and 650 nm, depending on the chemical

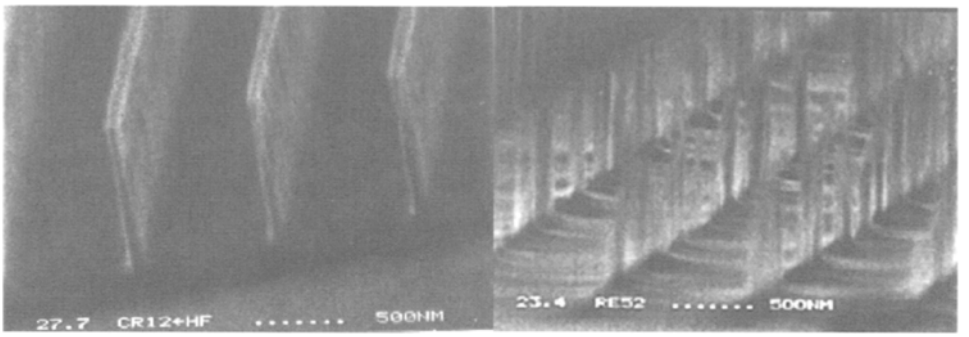


Fig. 24. SEM micrographs of Si pillars (right) and ridges (left) fabricated by high-resolution deep-UV lithography and highly anisotropic silicon etching based on fluorine chemistry. (Source: Reprinted with permission from [81].)

preparation and the exposure to ambient conditions [81]. In a next step, the pillars were planarized and etched back by an oxygen plasma in order to set free the pillar tops. A thin (150 Å) Au layer was deposited as the top ohmic contact. The electroluminescence spectrum under forward bias peaks at approximately 650 nm and is visible to the naked eye. The onset bias voltage for electroluminescence was determined to be 12–14 eV. The luminescence is attributed to electrons injected from the n-type substrate into the wires. During the drift in the electric field to the metal electrode, some of these electrons can recombine radiatively.

Chen and Ahmed [82] have used electron beam (e-beam) lithography and reactive ion etching in $SiCl_4$ and CF_4 to fabricate Si nanocolumns with an aspect ratio of height to diameter of about 7:1. The tip diameters of the approximately 40-nm-high dots were between 5 and 7 nm, the bottom diameters were 9 to 11 nm. However, no luminescence of the dots was reported. Liu et al. [83] have fabricated 50-nm-wide and 0.6-μm-high Si columns by e-beam lithography and NH_3 reactive ion etching. To remove the reactive ion etch damage, the samples were oxidized in dry O_2 at 800 °C and then dipped in HF. The oxidation process was monitored by transmission electron microscopy over a temperature range from 800 to 1200 °C. At oxidation temperatures below 950 °C, a self-limiting oxidation process was found. Thus, a silicon core remained even after 10 h of oxidation. The vertical Si nanowire depicted in Figure 25 was oxidized for 10 h at 875 °C. The inner Si core is reduced to its limiting dimension $2r_c = 2$ nm.

With increasing oxidation time, the Si core diameter decreased, whereas the oxide thickness increased until both reached saturation after a few hours. This saturation, which was absent for planar oxides, depends on the starting column diameter. The limiting Si core diameter had a stronger dependence on the starting column diameter at lower temperatures. The authors attributed this saturation effect to a diffusion-limited oxidation. During the oxidation process, the oxygen diffuses to the Si/SiO_2 interface and new oxide is formed. The previously formed oxide is thus pushed to the surface, creating stress. The counterplay of diffusion and stress can lead to an equilibrium state where diffusion stops. At high temperatures, the viscous flow of the oxide diminishes all stress. Therefore, at temperatures higher than 950 °C, there is no self-limiting oxidation observed.

As vertical nanopillars require additional, challenging technology for contacting, Kedzierski et al. [84] have fabricated planar silicon nanowires down to 10 nm in diameter using self-limited oxidation. The 30–40-nm-wide wires were defined on silicon-on-insulator (SOI) with electron beam lithography followed by a nichrome liftoff process and a silicon plasma etch. These lines were then oxidized at a low temperature (875 °C for 5–7 h) to thin the silicon core. As reported by Liu et al. [83], the stress created at the Si/SiO_2 interface slows down and eventually stops further oxidation. In this way, wires

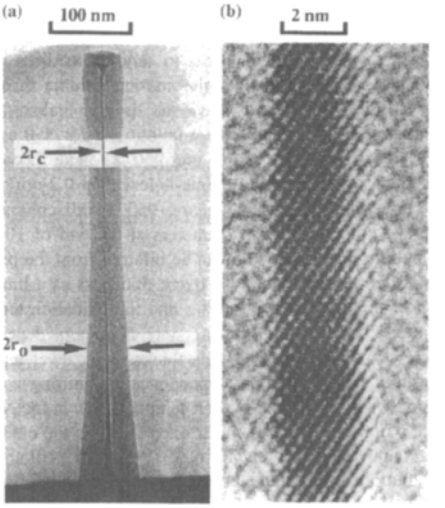


Fig. 25. (a) Transmission electron micrograph of an oxidized Si nanocolumn. The inner silicon core has reached its limiting dimensions. (b) High-resolution image of the inner 2-nm-thick Si core. (Source: Reprinted from [83]. © 1994 American Institute of Physics.)

with 25-nm-high and 5-nm-wide Si cores were fabricated along the ⟨110⟩ direction and annealed afterwards to improve the interface quality between the Si and the oxide. The shape of the oxidized structures strongly depends on the crystal orientation. The oxide growth rate for (111) planes is greater than for (110) planes. (100) planes have the lowest growth rate. From TEM cross sections of ⟨110⟩ oriented wires, the authors reported a factor of 2 higher oxidation rate for the (110) planes as compared to the (100) planes. They concluded a stronger (100) linear oxidation rate dependence on stress.

Reactive ion etching suffers from contamination effects and crystal damage. Therefore, it is worthwhile investigating appropriate direct epitaxial growth techniques for the realization of silicon-based nanostructures, which are discussed next.

3.5. Self-Organized Growth

Considerable efforts are in progress to produce quantum wires and dots from crystalline Si and crystalline $Si_{1-x}Ge_x$, as has been done for GaAs-based systems, but, to date, the available lithographic and etching techniques have not been able to produce nanostructures small enough to observe substantial confinement effects [85]. In c-Si, dimensions much smaller than the free-exciton Bohr radius of approximately 5 nm are required for such effects [86].

Another approach to obtain confinement is by appropriate epitaxial growth, such as quantum wire formation along wafer edge steps or by self-organized dot growth [87]. Most of the reported studies of Ge and SiGe islands on Si use physically determined deposition methods such as solid source MBE [88, 89]. Few reports describe the growth by chemical vapor deposition at pressures lower than about 0.1 torr such as gas source MBE [87, 90], ulrahigh vacuum (UHV) CVD [91], and low-pressure CVD [92]. Other reports describe the formation of islands by liquid phase epitaxy [93, 94]. Yanagiya et al. [95] have grown self-organized Si(110) wires on ultrasmooth sapphire $(01\bar{1}2)$ substrates by disilane (Si_2H_6) gas source MBE. The original sapphire surface has been imaged by AFM image and is shown in Figure 26a. After annealing the substrate at 1400 °C for 1 h and cleaning the surface in order to remove carbon contamination, atomic steps were obtained as depicted in Figure 26b. The distance between the flat terraces was 350 nm and the step height was 0.5 nm. The Si growth was performed at 700 °C at a Si_2H_6 pressure of 7×10^{-3} Pa.

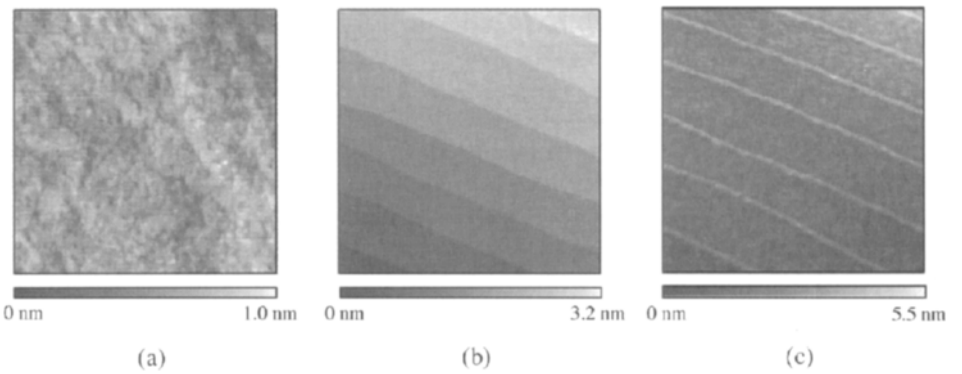


Fig. 26. AFM images (2 μm × 2 μm) of (a) as-supplied sapphire substrate, (b) substrate after 1 h annealing at 1400 °C showing approximately 350-nm-wide and 0.5-nm-high terraces, and (c) 50-nm-wide and 1-nm-high Si wires grown at 700 °C for 2 min. (Source: Reprinted from [95]. © 1997 American Institute of Physics.)

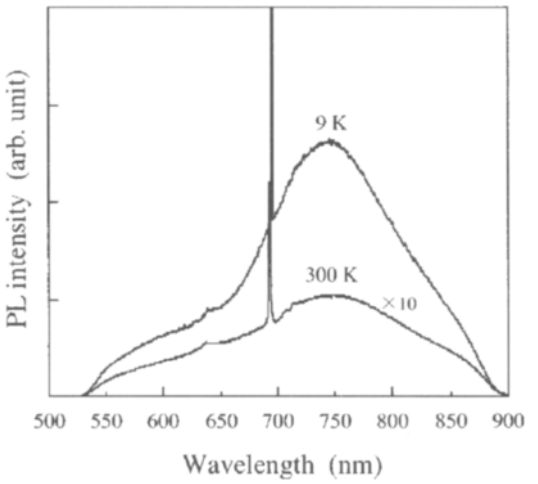


Fig. 27. Photoluminescence spectra at 9 and 300 K of self-organized silicon nanowires on the ultra smooth annealed sapphire substrate. (Source: Reprinted from [95]. © 1997 American Institute of Physics.)

Figure 26c shows the obtained Si wires aligned along the steps and oriented along the (110) direction. The width of the uniformly shaped wires was 50 nm and the height was 1 nm.

From X-ray diffraction, it could be concluded that the wires were monocrystalline. The sapphire surface could be modified by altering the annealing conditions [96]. Thus, in combination with the growth temperature, the size of the Si wires could be controlled. The wires grew according to the step-flow mode. Figure 27 shows photoluminescence signals at 9 and 300 K. At room temperature, the luminescence is quenched by more than a factor of 20. Both spectra peak at 750 nm with an FWHM of about 100 nm. The luminescence is quite similar to that of porous Si. The authors explain the broad luminescence band by the three-region model proposed by Kanemitsu et al. [97] that explains the luminescence of Si nanocrystallites in the system Si/SiO_2. According to this model, the electron–hole pairs are excited in the Si wires. The photons are emitted through radiative recombination centers that exist in the disordered localized state in the Si/Al_2O_3 interface region. As the distribution of the localized states is broad, this also leads to a broad luminescence signal. The sharp feature at 695 nm does not originate from the wires and is attributed

to a chromium ion in ruby, which is also seen in the spectrum of porous Si formed on sapphire [98].

Besides the fabrication of quantum dots by lithographic tools and the growth on patterned substrates, *in situ* self-organized growth of islands has recently attracted much interest. Here the Stranski–Krastanow growth mode in the heteroepitaxy was used. We will only briefly discuss this technique. A detailed review is given in the chapter by Weinberg in this Handbook. The main advantage of self-organization is the process simplicity, the possibility of growing defect-free structures with dot sizes well below 100 nm. A drawback of this approach is making the dots conducting. A further problem is the rather large size and distance fluctuation between the dots compared to those fabricated by lithographic means. Therefore, the major application envisaged at the moment is restricted mainly to optical devices. We will see later on that, under certain conditions, quantum dot superlattices will point to some possible solutions to overcome these problems and to use the strain created by embedded islands to enhance the self-organization and to obtain more homogeneous islands with respect to size and spacing.

The driving force for nucleation of self-assembled islands is the strain resulting from the lattice mismatch between the substrate and the epilayer. According to the Stranski–Krastanow mode, the growth first starts in the layer-by-layer mode. If the thickness of this wetting layer exceeds a certain critical value (typically 4–6 monolayers), the strain will relax either through misfit dislocations or, under appropriate growth conditions, by a 2D $\rightarrow$ 3D transition. Because of to the relatively high misfit, the systems Ge or SiGe on Si and InAs on GaAs are the most investigated ones showing this effect. The strain depends on both the thickness of the layer and the alloy composition. Schittenhelm et al. [88, 99] have grown self-assembled $Si_{1-x}Ge_x$ dots on Si(001) by molecular beam epitaxy. The size, areal density, and homogeneity of the dots were investigated by varying several parameters including the growth temperature, the growth rate, the composition of the dots, and the thickness of the deposited layer. The authors found an increase of the dot height (8–33 nm) with increasing Ge concentration x while the areal density and the diameter remained nearly unchanged. They attributed this effect to the reduced strain with reduced Ge concentration. As the total amount of material is the same, the dots will automatically become smaller if the wetting layer becomes thicker because of the smaller strain.

With increasing coverage, the authors reported an increased formation of dots until the areal density starts to saturate for layers with more than 7 monolayers (ML). After this stage, the dots start to grow in height and diameter. Increasing the growth temperature also increases the surface diffusion length of the incoming atoms. As already existing islands represent a region of lower strain [100], the atoms nucleate preferentially at these islands, which leads to fewer but larger islands at higher growth temperatures. Darhuber et al. [101] determined the 2D $\rightarrow$ 3D transition for Ge on Si(001) to be between 5.33 and 5.67 ML by performing X-ray reflectivity experiments, which are in good agreement with photoluminescence experiments on the same samples [88, 89].

For electronic applications, uniformly sized quantum dots are needed. Therefore, there has been a growing interest in self-organized three-dimensional stacking of self-assembled dots. For technological applications, besides the size homogeneity, a high spatial density as well as spatial homogeneity is also required. Several groups [102–106] have grown quantum dot superlattices of InAs dots embedded in GaAs. They reported a spatial correlation in the following layers. The strain field at the surface arising from the underlying embedded dot makes the new dot nucleate directly above the embedded island. Yao et al. [104] suggested that such an alignment of the islands in the growth direction results if the spacer layers are not thick enough, and they associated the alignment with a lattice strain relaxation. Thus, one can conclude from the alignment that the island is a region of lower strain. Xie at al. [106] considered the effect of strain on the surface diffusion of incoming atoms to explain the island distribution. Tersoff and Le Goues [107] considered the exponential dependence of the nucleation rate on the nucleation barrier, which, in turn, depends on the

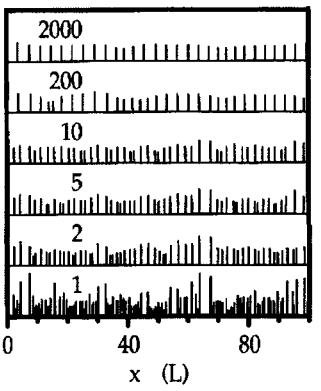


Fig. 28. Calculated island position and size for different layers of a dot stack. The island distance and size becomes more homogeneous in subsequent layers. (Source: Reprinted with permission from [108]. © 1996 American Physical Society.)

strain. Therefore, an island nucleates most favorably at those positions where the strain at the surface reduces the mismatch between surface and island to a local minimum.

However, a detailed analysis is rather complex and many parameters such as flux, temperature, and strain field must be known. Tersoff et al. [108], therefore, developed a generic model based on the continuum elastic theory considering Ge dots embedded in Si, which is also valid for SiGe, GaAs, or InAs islands. The buried dots are treated as spherical inclusions in an isotropic elastic matrix. Their size is assumed to be small relative to their lateral and vertical separation. The nucleation only occurs at each local misfit minimum. Following experimental results [103, 105], they assumed a nearly flat Si layer covering the Ge islands. Only some local strain resulting from the buried islands is present. Figure 28 shows the calculated position and the height of the Ge islands. At the beginning (layer 1), the islands are randomly distributed on the Si, substrate. After covering the islands by Si, new Ge islands are assumed to form at local strain minima. The development of a vertical correlation is clearly visible. By changing the spacer layer thickness L and the starting distribution of the islands, one can tune the resulting height and spatial homogeneity of the islands. After several layers are grown, the final lateral island spacing is about $3.5L$. Thus, the spacer thickness allows direct control of the final island spacing. If the initial island spacing is larger than $3.5L$, the new islands will also nucleate in the space between the prior islands. If the initial spacing is smaller than $3.5L$, the strain minimum will not be distinct and several islands will be replaced by a single new island. This explains the better homogeneity of the following layers. It must be mentioned that for real systems the model may only be applicable in certain growth regimes as parameters such as the surface diffusion length are not taken into account. Furthermore, for three-dimensional real systems, the strain minima at the surface may be too weak or may vanish. However, the surface diffusion length can be manipulated by varying the substrate temperature and the molecular flux during growth.

Figure 29 shows a $Si_{0.25}Ge_{0.75}$ dot layer deposited on (001)Si (part a) and the surface of a 20-period superlattice (part b). It is obvious that the islands at the top are more uniform in size and space. Qualitatively, this rather simple model can describe the experimental case even if many parameters are not yet taken into account.

Following prior experimental work on the vertical stacking of SiGe dots [105] and the theoretical modeling of Tersoff et al. [108], Schittenhelm et al. [99] have grown a 10-period Si(30 nm)/5–6-ML Ge multiple-dot layer at 670 °C at a growth rate of 0.075 Å s^{-1}. These parameters were chosen according to results from single layers to get an optimum size and spatial homogeneity already in the first layer. Atomic force microscopy analysis of the height distribution of the dots at the topmost uncapped layer revealed a variation of only

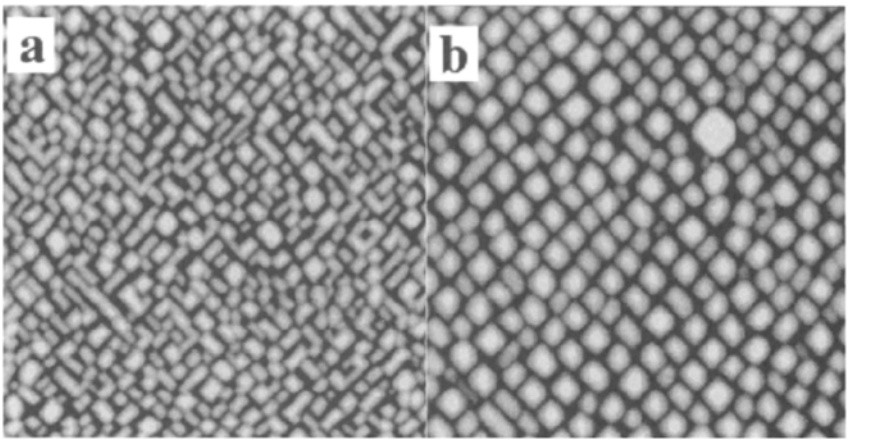


Fig. 29. AFM images of SiGe dot layers: (a) single layer and (b) topmost dot layer of a 20-period dot stack. (Source: Reprinted with permission from [108]. © 1996 American Physical Society.)

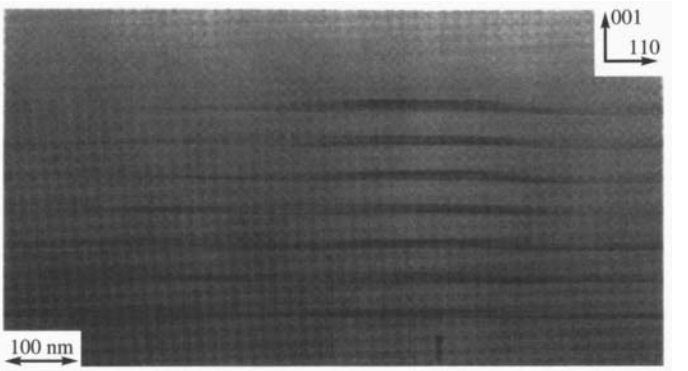


Fig. 30. Cross-sectional transmission electron micrograph of a seven-period 35-nm Si/12-ML Ge stack. The dots are seen to exhibit vertical order. (Source: Reprinted from [99], with permission from Elsevier Science.)

6% for the 5-ML sample and 8% for the 6-ML sample. Figure 30 shows a cross-sectional transmission electron micrograph of a Si(35 nm)/12-ML Ge multiple dot layer. The strong vertical correlation of the dots as simulated by Tersoff et al. [108] is clearly visible.

3.6. Selective Epitaxial Growth

Vescan et al. [105, 109–111] have grown strained SiGe/Si quantum well dots and wires by the selective epitaxial growth technique using low pressure chemical vapor deposition (LPCVD). They grew an approximately 500-Å-thick thermal oxide on 2000-Ω cm p-type Si(001) wafers and patterned them into arrays of rectangular holes parallel to the ⟨100⟩ or ⟨110⟩ direction by optical lithography. Figure 31 shows the process schematically. The 5-mm-long wires had a width between 0.4 and 300 μm; the square holes had a similar sizerange. The growth was performed at 700 °C using $SiCl_2H_2$ and GeH_4 as the source gases, and the carrier gas was H_2. The schematic structure is shown in Figure 31.

Here the basic idea is to form a facet of the selective epitaxial growth (SEG) area as narrow as possible. During SEG, facets usually form at the edges of the growth area. For the surface energies of the different Si crystallographic planes, one obtains $E_{001} > E_{110} > E_{311} > E_{111}$ [112, 113] . In the case of SiGe, one gets the same relations [114]. Therefore, the {111}, {110}, and {311} facets are favored during growth. Figure 32 shows a TEM

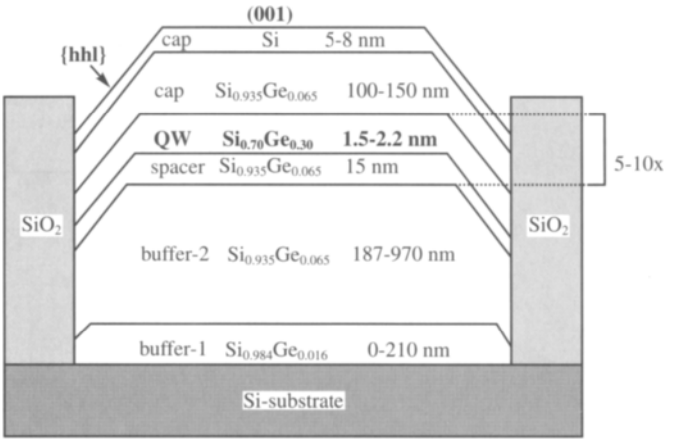


Fig. 31. Schematics of the QW structure within the oxide window. (Source: Reprinted from [110], with permission from Elsevier Science.)

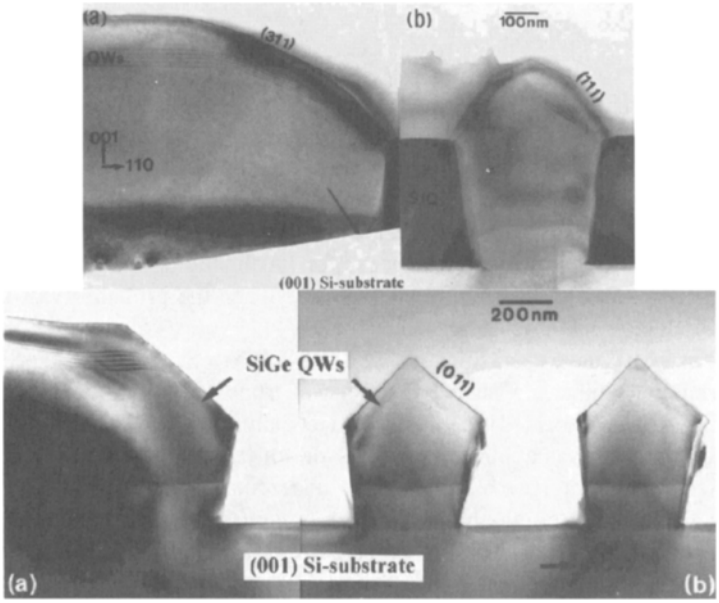


Fig. 32. Transmission electron micrograph cross section of wires with ⟨110⟩ side-wall orientation: (a) edge of a 10-μm wire and (b) 400-nm wire. (Source: Reprinted from [110], with permission from Elsevier Science.)

micrograph of the cross section of 10-μm (part a) and 400-nm (part b) wires with side-wall orientations of ⟨110⟩. The (001) quantum wells are planar and the {311} and (111) facets are also flat. In contrast to the wires, the dots all show the facets during growth, because the holes in the SiO_2 do not have perfect square shapes. Facet formation in this growth technique is needed to reduce the lateral dimensions of the quantum wells. However, to realize these facets, structures much thicker than the critical thickness are needed.

Stoica and Vescan [115] attributed this higher critical thickness to an eventually hindered defect multiplication in the local structures. For $x = 0.065$, the size reduction leads to an increase in the critical thickness of approximately 700 nm for 30-μm-wide wires and to even more than 1 μm for 300-μm dots. The characterization of the grown structures

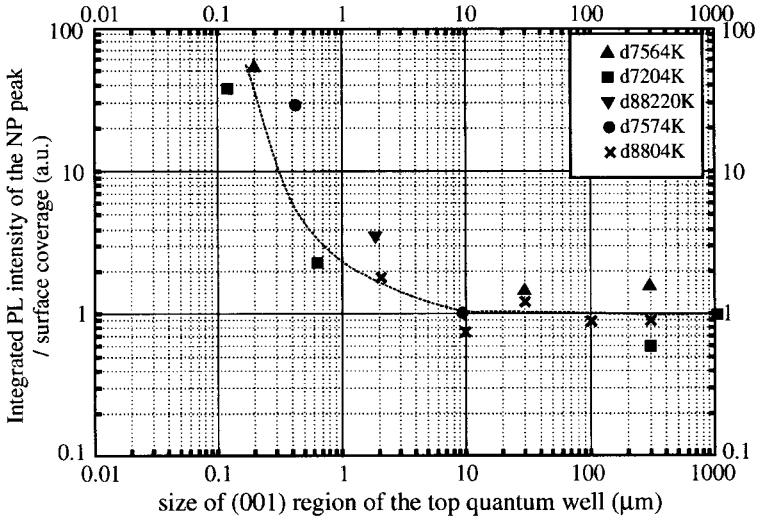


Fig. 33. Integrated intensity of the $SiGe^{NP}$ line, normalized to the surface of the dots, for different dot samples against the size of the (001) region of the top quantum well in the dots. (Source: Reprinted from [110], with permission from Elsevier Science.)

was performed optically by photoluminescence. From the presence of dislocation-related emission lines, the authors concluded that wires remain strained for sizes less than or equal to 30 μm, whereas dots are strained for diameters less than or equal to 300 μm. The photoluminescence intensity normalized to the patterned area increased by a factor of 50 for the dots less than or equal to 400 nm (see Fig. 33). This is attributed to the reduced role of nonradiative recombination channels by exciton localization. This suggests a further increase of intensity through fabricating smaller dots when the probability of the excitons reaching nonradiative center is decreased.

Hobart et al. [116] have used solid-source MBE to grow Si on nonplanar Si substrates. The prestructured Si substrate surface consisted of truncated pyramids with {111} sides and (100) tops that were formed by anisotropic wet etching in KOH or EDA solutions. The height of the pyramids was about 1 μm; the width of the tops ranged from 0.4 to 1 μm. The pitch size was about 10 μm. Because of undercutting of the SiO_2 layer used as a mask for the anisotropic etching, the mesa structure typically also had {331} facets. Si was deposited on such templates at various temperatures and growth rates. The authors found no structural change for temperatures between 470 and 550 °C. In a temperature range between 650 and 700 °C, {113} facets formed that laterally reduced the (100) tops of the pyramids to less than 20 nm. At higher temperatures around 800 °C, only {113} and {100} facets were formed. {113} facets have also been observed by Booker and Joyce [117] and Yang and Williams [118] during CVD deposition of Si, whereas the Si surface was carbon contaminated. Hirayama et al. [119] have observed {113} facets during selective epitaxial growth through a patterned SiO_2 mask. The occurrence of {113} facets was explained by pinning of the step flow at defect sites [120] or at the edges of the SiO_2 mask used for the selective growth [119]. Hirayama et al. [119] and Oshiyama [121] attributed the formation of {113} facets on Si(001) to bunching of double height steps. Thus, during chemical vapor deposition, surface orientation–dependent growth rates occur because of different silane and disilane deposition rates, whereas for MBE growth dynamical processes determine the facet growth.

Hobart et al. [116] have used the previously described Si templates to fabricate $Si_{1-x}Ge_x$ quantum dots. Thus, a 20-period Si(20 nm)/$Si_{0.8}Ge_{0.2}$(4 nm) multiple quantum well was grown at 550 °C on top of a mesa with a Si(100) surface reduced by the {113} facets to 10 nm. Although no optical or electrical characterization was performed

to confirm low dimensionality, transmission electron micrographs indicated that quantum boxes may be realized on the top as the SiGe growth rate on the {113} facets was 85% of that on the (100) facets for geometrical reasons.

3.7. V-Groove Growth

Kapon et al. [122] have demonstrated the growth of quantum wire arrays on V-groove-patterned GaAs substrates by MOCVD. Performing cathodoluminescence (CL), they showed the existence of quantized states resulting from the quantum wires at the bottom of the grooves. Tsukamoto et al. [123] fabricated GaAs "arrowhead-shaped" quantum wires by selective growth using MOCVD.

Usami et al. [124] were the first to demonstrate SiGe/Si quantum wires on V-groove-patterned Si substrates. They have grown Si/SiGe/Si double-heterostructure quantum wires on V-groove-patterned p-Si(001) wafers (resistivity 5–10 Ω) by gas source MBE at 740 °C using silane and germane. Using thermal oxidation, a SiO_2 film was first grown as a mask layer for the chemical etching and for the subsequent selective epitaxial growth. The fabrication process is depicted in Figure 34.

With electron beam lithography and wet chemical etching in a N_2H_4-based solution, line patterns along the ⟨110⟩ direction with a period of 0.6 μm were fabricated. Because of the directional selectivity of wet etching, the V grooves have {111} side facets (Fig. 34a). The SiO_2 mask layer was then removed by a HF dip (Fig. 34c) and subsequently the whole structure was overgrown by a thick Si overlayer (Fig 34d). Figure 35 shows a TEM micrograph of a 15-nm-high SiGe/Si crescent-shaped quantum wire revealing no misfit dislocations. The shape and the vertical height, which is higher than the nominal one, are due to anisotropy in the different orientations during gas source Si MBE. As the surface migration of adatoms on (111) surfaces is higher than on (100) surfaces, one gets an enhanced mass transport from Si(111) toward the bottom of the V grooves.

The SiGe transverse optical phonon–assisted transition and the no-phonon line are clearly visible in low-temperature photoluminescence spectra, indicating a high crystalline structure in the wires. The broadening of these two peaks in the case in the wires in comparison with spectra of a two-dimensional reference structure results from the SiGe width and Ge compositional variations. The SiGe luminescence quenching temperature was determined to be 70 K. The electroluminescence spectrum is comparable to the photoluminescence spectrum, indicating that the recombination process is identical in both cases.

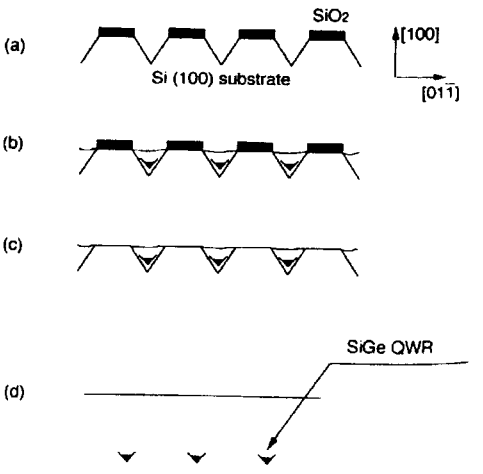


Fig. 34. Schematics of the processing steps of SiGe quantum wires by selective epitaxial growth. (Source: Reprinted from [125]. © 1994 American Institute of Physics.)

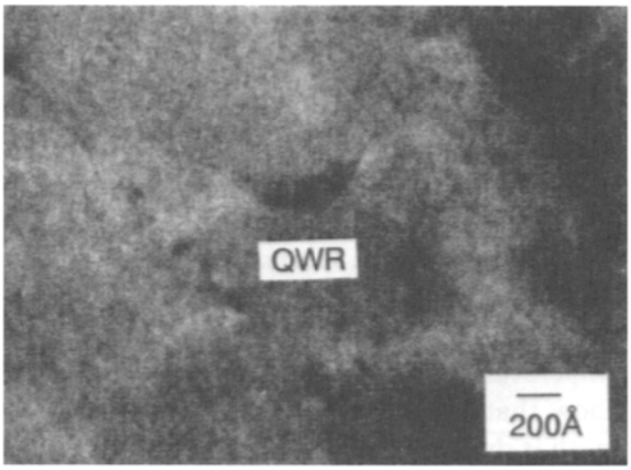


Fig. 35. Transmission electron micrograph of a Si/SiGe/Si wire grown on a V-groove patterned substrate. (Source: Reprinted from [124]. © 1993 American Institute of Physics.)

Polarized electroluminescence was obtained in the direction of the cross section of the wires and in the growth direction. Although the wires do not show any polarization in the cross section, the single quantum well shows a strong in-plane polarization as expected from the selection rule of the $hh1$–$e1$ transition. In the direction perpendicular to the sample surface, the situation changes to the opposite. Here the quantum well is optically isotropic and the wires show strong anisotropy. The polarization experiments clearly indicate successfully realized luminescent SiGe wires of high crystalline quality. From TEM micrographs, the lateral and vertical wire widths were determined to be 30 and 8 nm. However, the peak positions do not fit these dimensions as the distribution of strain and the Ge atomic fluctuations lead to a shift of these peaks.

A main disadvantage of the V-groove growth technique is its limit for further reduction to quantum dots. From a scientific point of view, this method seems to be an elegant way to produce quantum wires 30–40 nm in width with high crystallinity.

3.8. Local Growth of Dots and Wires through Shadow Masks

The method of local epitaxial growth through shadow masks for the homoepitaxy of Si epilayers was reported by Hammerl et al. in 1991 [126]. Brunner et al. [127] used this technique to grow directly wires and dots with SiGe quantum wells through a patterned SiO_2/Si_3N_4 shadow mask. The dots and wires were physically detached from the surrounding material and after overgrowth they were completely embedded in Si. The dots and wires were grown on (100) Si wafers with a resistivity of 1200 Ω cm. Figure 36 shows the schematics of this growth technique.

After fabrication of the LPCVD-deposited Si_3N_4 100-nm-thick shadow mask [126], the opened window is cleaned and the wafer transferred to the MBE reactor. The thickness of the SiO_2 spacer layer is 1 μm. The nitride is underetched up to 5 μm. The shape of the wires and dots is determined by the growth parameters and by the angle of the incident beam with respect to the sample surface as shown in parts b and c of Figure 36. Finally, the SiO_2 layer is lifted off by selective wet etching (part d).

The structures mentioned here were grown at 720 °C under an incident angle of 20°, consisting of a 140-nm Si buffer layer, a Ge concentration of 25% in the quantum well, and a 160-nm-thick Si cap layer. The minimum lateral dimension was 200 nm [128]. An SEM cross-sectional micrograph of a dot array is shown in Figure 37. The mask layer is not yet removed and it can be clearly seen that there is no direct contact of the structures with

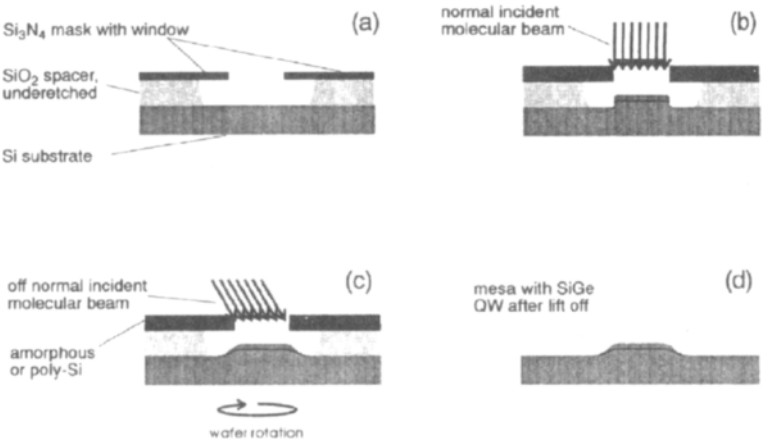


Fig. 36. Schematics of the local MBE growth through micro shadow masks: (a) underetched SiO_2 with the patterned silicon nitride, (b, c) local epitaxy with normal and off-normal incident molecular beams, and (d) mesa with smooth side walls after liftoff. (Source: Reprinted with permission from [127]. © 1994 American Institute of Physics.)

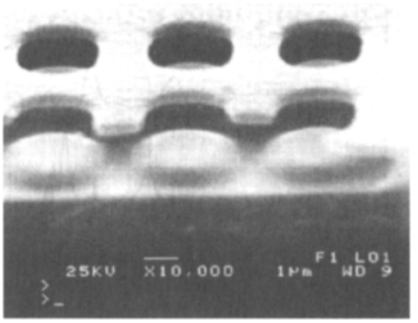


Fig. 37. Scanning electron micrograph of locally grown Si/SiGe/Si 2-μm × 5-μm mesas. Note that there is no pillar support of the nitride mask over the whole dot group. (Source: Reprinted with permission from [127]. © 1994 American Institute of Physics.)

the walls; thus, structural imperfections can be avoided during growth. Figure 38 shows a TEM micrograph of the edge of a wire with the embedded SiGe quantum well [129]. As the quantum well is completely buried in silicon, the potential problem of surface states at the side walls is eliminated.

The thickness of the quantum well (QW) decreases toward the edge of the mesa; thus, the energy gap increases toward the edges confining carriers in the middle part of the mesa structure. This results in an effective passivation of the side walls without mediation of surface states. Photoluminescence experiments excited with 457 nm reveal the typical SiGe TO phonon–assisted and no-phonon lines and reflect the high structural quality of these dots and wires. The exact shape of the side walls can be controlled by the growth conditions to be nearly vertical or smoothly ascending [130]. Rotating the substrate during growth and positioning the e-beam evaporator off axis leads to smoothly ascending side walls as shown in Figure 36c.

Figure 39 shows the peak intensities of the SiGe TO phonon replica as a function of wire width normalized to the fractional coverage of the mesa islands [131]. For comparison, the intensity of a homogeneously grown quantum well reference sample is also included. The increasing luminescence intensity with decreasing wire width from 1 μm to 200 nm has been attributed to an effective passivation of the side walls and to confinement of excitons

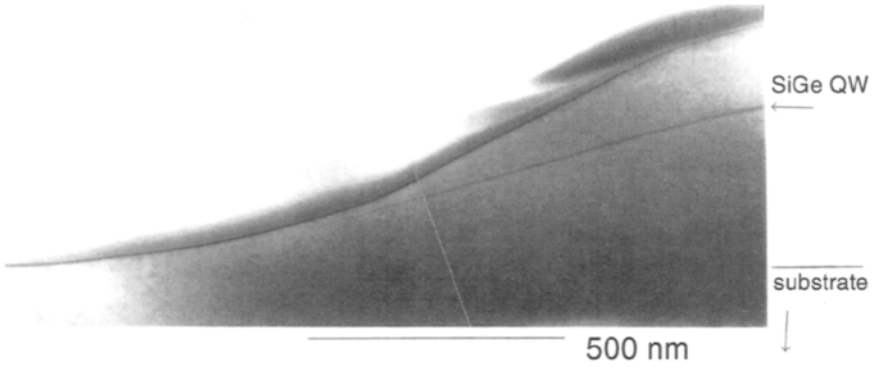


Fig. 38. Cross-sectional transmission electron micrograph of a SiGe QW completely embedded in silicon. (Source: Reprinted from [129], with permission from Elsevier Science.)

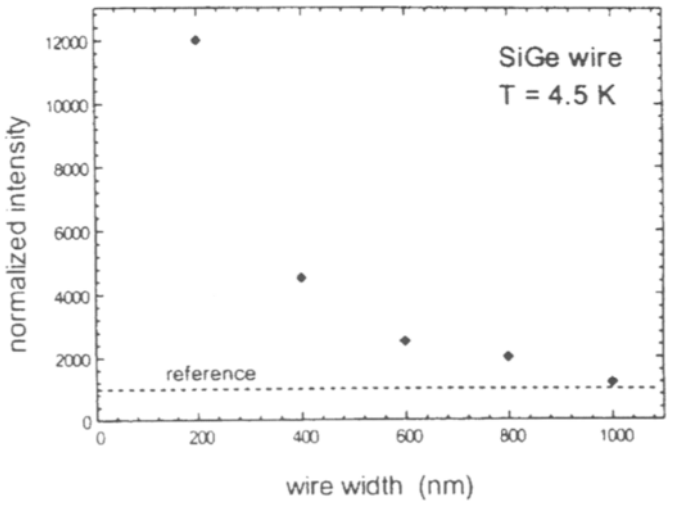


Fig. 39. Normalized TO phonon–assisted luminescence transition intensity of locally grown SiGe wires as a function of wire width. The reference line is the intensity of a homogeneously grown quantum well. (Source: Reprinted from [131], with permission from Elsevier Science.)

within the mesa structure and thus to a smaller probability of reaching nonradiative channels. This trend is similar to observations made in GaAs–GaAlAs wires [132].

However, as in the case of all normalized spectra of this type, one has to keep in mind that excitons in silicon have a diffusion length of about 400 μm. Thus, once generated, they can diffuse to the SiGe wires and recombine there. This effect will always contribute to an increase in intensity unless the SiGe layer is excited with light below the Si absorption edge. Some simulations to investigate this effect may be helpful to estimate the general relevance. Spatially resolved photoluminescence was used to investigate the luminescence intensity distribution and thus the exciton density distribution along a 1-μm-long wire. From fitting the data to an exponential decay, a decay length of about 10 μm could be estimated.

If growth is carried out with the incident beam parallel to the mask normal direction, one obtains faceted side walls [129]. In the case of (100) substrates, the slightly lower (111) surface energy leads to {111} facet formation. Eisele et al. [129] have grown wires and pyramidal dots through submicrometer masks with the edges oriented in the ⟨110⟩ direction. Figure 40 shows SEM micrographs of this facet formation for a cleaved wire

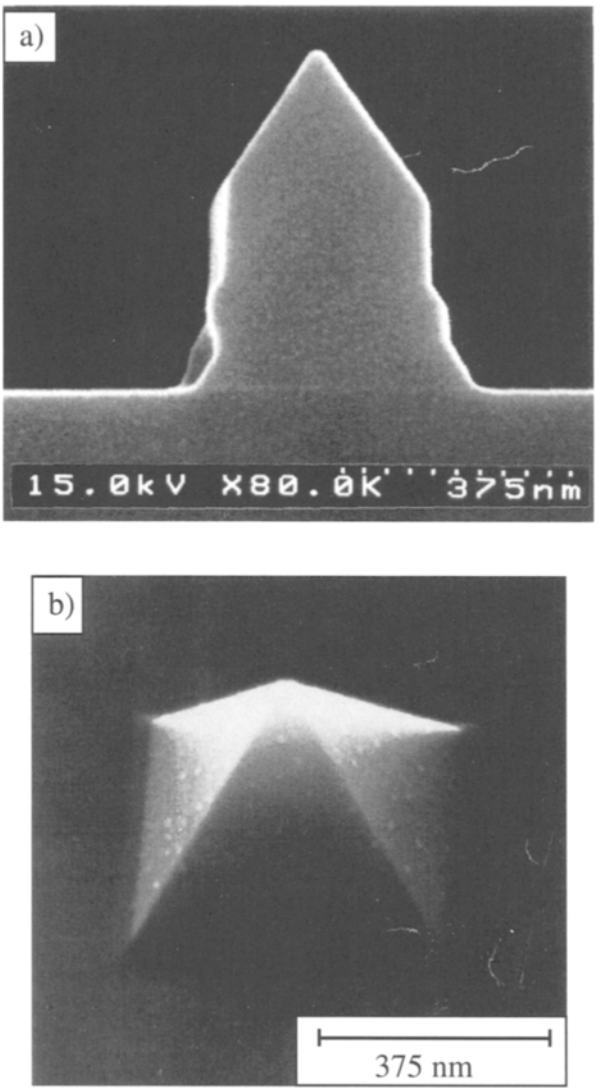


Fig. 40. Scanning electron micrographs of {111} facet formation in (a) a wire structure grown at 500 °C through a 310-nm mask and (b) a pyramidal dot structure grown at 500°C through a 350-nm square mask. (Source: Reprinted from [129], with permission from Elsevier Science.)

(part a) and a dot structure (part b). Both structures were grown at 500 °C with a rate of 0.1 nm/s. In the case of the wire, a 310-nm mask was used, and a 350-nm square mask was used for the dot. The radius of the dot tip was estimated to be less than 5 nm. The maximum length of the {111} facets is diffusion limited. When impinging atoms have reached their diffusion limit underneath the mask, vertical (011) side walls grow as can be seen in Figure 40a. Neither thermal oxidation at 800 °C nor thermal annealing at 1000 °C under nitrogen atmosphere led to any facet degradation. From capacitance–voltage characteristics of metal-on-silicon (MOS) capacitors, the presence of a dense oxide with negligible leakage could be deduced.

Using the same technique, Gossner et al. [133] grew silicon nanostructures through micro shadow masks. Figure 41 shows the patterned nitride film and the Si mesa structures grown through this mask. At a growth temperature of 500 °C, {111} facets formed on the side walls. Wedge-like mesas with a top radius of about 5 nm with perfect {111}

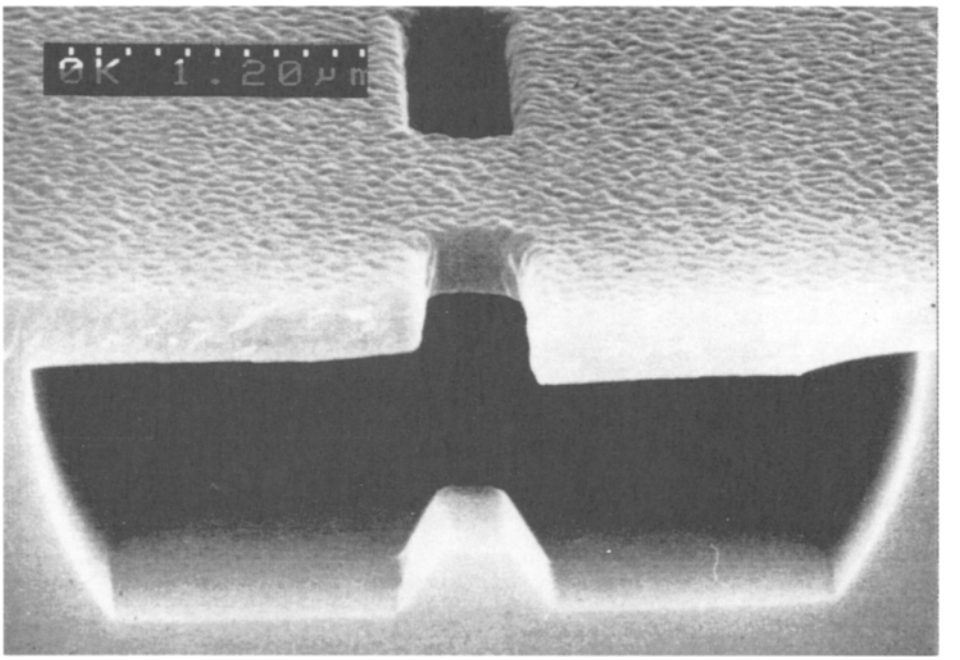


Fig. 41. Scanning electron micrograph of a Si mesa grown through a nitride micro shadow mask at 500 °C. (Source: Reprinted from [133], with permission from Elsevier Science.)

facets were grown through ⟨110⟩-oriented line-shaped masks. The formation of a perfect pyramidical shape was independent of the orientation and shape of the mask aperture.

The technique of local growth through a mask allows a variety of nanostructures to be grown, as well as the realization of laboratory-scale devices as, for example, a field effect transistor with built-in one- and zero-dimensional electrical confinement (see Section 4), ultrathin tips for scanning probe microscopy and direct nanostructuring of surfaces.

3.9. Silicon Nanocrystallites

3.9.1. General Remarks

Another way of realizing nanostructures is forming nanocrystallites in, for example, a matrix. Nanocrystallites are made up of one or more clusters. A cluster consists of agglomerations of up to 10^5 atoms, which, in conventional terms, can be regarded as neither a bulk material nor as atoms or molecules. Clusters in the size range of 1 to 1000 nm exhibit new physical and chemical properties, which can be directly modified by controlling the cluster size. In the limit of very small clusters, the addition of a single atom can drastically modify electronic, magnetic, and other physical properties. To investigate cluster properties as a function of cluster size, it is necessary to separate the cluster by its mass. Electronic and optical properties can be probed by photoelectron, absorption, fluorescence, or photoluminescence spectroscopy, among other techniques. Chemical reactions of clusters with surfaces can be studied by depositing the cluster onto different substrates.

Clusters can be classified according to their chemical bonding. For example, in a van der Waals cluster, the induced dipole–dipole interaction is the force keeping the cluster together. The stability and structure of the cluster is driven by geometric packing effects leading to closed packages with 12 nearest neighbors. Group IV semiconductor clusters, especially C, Si, and Ge, are extensively investigated. Their bonding is covalent and the clusters are not closely packed. Instead, the coordination number is given by the number

of valence electrons or by the degree of hybridization. A prediction of the cluster structure is very difficult because of the spatially oriented bondings. Different hybridization of the valence orbitals leads to single, double, or triple bonding, forming carbon chains, rings, or nanotubes [134]. In semiconductors, II–VI and III–V compounds have been widely investigated [135, 136] and silver halides have been widely used in the photography industry [137].

Silicon nanoparticles are found to luminesce in the red and blue region of the visible spectrum when illuminated by ultraviolet radiation or when a current is passed through them [138, 139]. The origin of the red luminescence is generally accepted to be due to a quantum confinement shift of the bulk silicon band gap, whereas the blue emission is not yet fully understood.

Since the discovery of porous Si [49] and the interpretation of its luminescence originating from quantum confinement in nanostructures, different methods have been used to synthesize nanostructures. In the reduction of $SiCl_4$, $HSiCl_3$, or octyl $SiCl_3$ by Na [140] in nonpolar organic solvents, the synthesis is performed at temperatures around 385 °C at relatively high pressures of around 100 atm for several days. After cooling and washing out the Na, NaCl, and hydrocarbon residue, the product is dried in vacuum. Analysis mainly reveals single crystals of 5–3000 nm with a hydrogen-terminated surface. Using octyl $SiCl_3$, one can achieve a size distribution of only 2–9 nm. Other groups have separated nanocrystals from a porous Si sample [141–144]. Here the porous silicon layer on top of the single crystalline wafer is removed mechanically. After ultrasonic agitation within a solvent for several days, one gets a colloid with particles ranging from 1 to 10 nm and some agglomerates up to 50 nm. The disadvantage of this method is the lack of size control. Thermal evaporation [145] and decomposition of silanes have also been used to fabricate silicon nanoclusters [146–148]. Well-controlled silicon nanopowder with particle sizes varying between less than 10 and 200 nm can be synthesized from gas phase reactions in a radio frequency discharge in silane. The size of the particles can be controlled by the gas flow, gas composition, and plasma characteristics, as reported by Kobayashi et al. [149] and Yasuda [150]. Dutta et al. [151] have published a review article on this technique. In the following, we describe some of the recently reported techniques with a high potential for crystallite size control.

3.9.2. Silicon Nanocrystals Produced by a Laser Vaporization Technique

Li et al. [152] have produced weblike aggregates of coalesced Si nanoparticles on glass through laser vaporization and subsequent controlled condensation. A pulsed Nd:YAG laser with 15–30 mJ/pulse and 10^{-8} s pulses evaporates Si in a chamber consisting mainly of two metal plates facing each other at different temperatures. The chamber is filled with different carrier gases such as Ar. The temperature gradient between the two metal plates leads to a strong convection. Nucleation of the Si vapor leads to the growth of Si nanoparticles, which are driven to the cold plate by convection. The temperature gradient between the two plates controls the convection and the supersaturation of the Si vapor. High supersaturation leads to smaller nuclei, which are required for the condensation of nanoparticles. The convection drives away the small nanoparticles before they can grow further.

Although SEM analysis revealed spherical particles of about 10 nm in diameter connected by a weblike structure with a wall thickness of 10–20 nm, the Raman shift suggested an average particle size of approximately 4 nm. X-ray powder diffraction of these samples revealed distinct Si(111), (220), and (311) reflections, but, as the powder sample was not rotated during the scan, a possible texturing of the nanoparticles cannot be ruled out. Fourier transform infrared (FTIR) spectroscopy indicated an oxidized surface layer after exposing the nanoparticles to air consisting of SiO_x with $x < 2$. The thickness of this SiO_x was estimated to be 1–2 nm. Annealing the particles at 300 °C in air leads to $x = 2$. The freshly deposited particles do not show any luminescence until they are exposed to

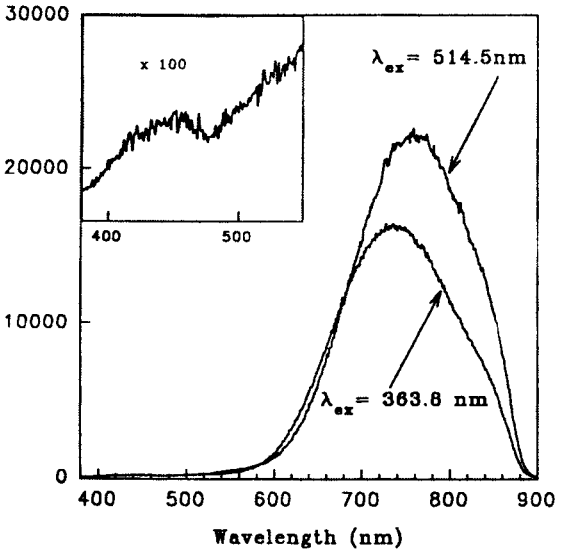


Fig. 42. Photoluminescence spectrum of Si nanocrystals excited with 363.8- and 415.5-nm radiation. The inset shows the weak blue luminescence excited with a 363.8-nm wavelength similar to the luminescence of SiO_2 nanoparticles. (Source: Reprinted with permission from [152]. © 1997 American Chemical Society.)

air and their surface is passivated by SiO_x. The luminescence, which shows a peak in the red and a smaller one in the blue, was excited with 363.8- and the 514.5-nm laser lines, respectively. The quantum efficiency of the red line is about 1.3%. Based on a quantum confinement model [153], the authors concluded that the longer wavelength excitation selects the larger particle resulting in a stronger emission to the red. The inset of Figure 42 shows a weak blue emission at 450 nm using an excitation wavelength of 363.8 nm, which is quite similar to the emission of SiO_2 nanoparticles and is related to the oxidized surface layer of Si nanoparticles [154].

Based on the results of the FTIR experiments and bearing in mind the approximately 8-eV band gap of SiO_2, this surface layer was said to be nonstoichiometric SiO_x with x between 1.4 and 1.6, resulting in a band gap of around 3–4 eV, corresponding well to the blue emission [155]. Defects in SiO_2 cannot be ruled out because they luminesce in the red and blue spectral regions [156]. In contrast to this, pure SiO_2 does not show red luminescence. Its absorption spectra in the range of 200 to 800 nm suggest that the radiative transitions are indirect. From fitting the data with the relation $(\alpha h\nu)^{1/2} = B(h\nu - E_g)$, the authors obtained a band gap of 1.78 eV, corresponding well to the 700-nm red luminescence. The blue shift compared to the 1.1 eV of bulk Si is attributed to quantum confinement. The great potential of this technique lies in the good size control through a simple technique. Applications such as Si powders seem reasonable. However, for any device application, the integration into the Si circuit remains an open question.

3.9.3. Si/SiO₂/Si Multilayers

Abeles and Tiedje [157] demonstrated the first amorphous semiconductor/insulator superlattices. In contrast to porous silicon, these regular periodic structures do not show a size distribution and suffer minimal contamination effects. Growing Si nanostructures by MBE enables a detailed study of the correlation of luminescence properties to crystallinity, interface chemistry, and nanostructure size. The commonly used insulators are SiO_2, CaF_2, and Al_2O_3.

Lockwood et al. [86, 158, 159] fabricated a number of Si/SiO_2 superlattices with a silicon layer thickness d_{Si} = 1–30 nm. The samples were grown by solid-source MBE and

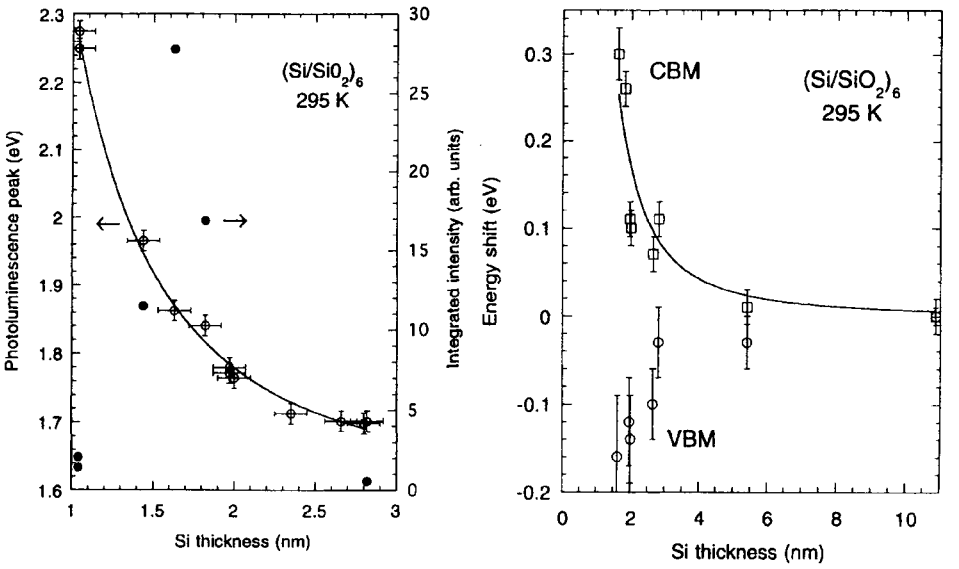


Fig. 43. Photoluminescence energy (open circles) and integrated intensity (full circles) for different Si layer thicknesses (left) and shift of the conduction and valence band of Si/SiO_2 superlattices at room temperature for different Si layer thicknesses. The solid line in both pictures is the best fit using effective mass theory. (Source: Reprinted with permission from [159]. © 1996 American Physical Society.)

characterized by Auger electron spectroscopy (AES), X-ray photoelectron spectroscopy (XPS), photoluminescence (PL), Raman scattering, soft X-ray Si–$L_{2,3}$ near-edge absorption spectroscopy (XANES), TEM, and X-ray reflectivity. The density ratio of the amorphous Si layers to c-Si was found to be 0.97, indicating little film porosity and low contamination level. Visible-to-near-infrared PL was observed at 295 K in all superlattices with $d_{Si} < 3$ nm, with the maximum of the emission peak at 665 nm (1.86 eV) with a full width at half-maximum (FWHM) of 0.38 eV.

The dependence of the PL peak energy and intensity on d_{Si} is shown on the left-hand side of Figure 43, indicating a clear blue shift with decreasing Si layer thickness. The PL signal is attributed to the Si layers as the SiO_2 layer thickness remains constant. The blue shift and the increasing intensity with decreasing d_{Si} indicates quantum confinement effects [57, 58]. Using effective mass theory together with the assumption of infinite potential barriers, this energy gap dependency on layer thickness is fitted to

$$E = E_g + \frac{\pi^2 h^2}{2d^2}\left(\frac{1}{m_e^*} + \frac{1}{m_h^*}\right) \tag{1}$$

where E_g is the bulk material energy gap and m_e^* and m_h^* are the electron and hole effective masses. The band edge E_g obtained from fitting is in good agreement with the bulk value for amorphous Si (1.5–1.6 eV at 295 K). To obtain the shift of the conduction and valence band, XANES and XPS measurements were performed. Figure 43 (right) shows the conduction band minimum upshifted by approximately 0.3 eV and the valence band maximum downshifted by approximately 0.1 eV when the Si layer thickness is reduced to $d_{Si} = 1.5$ nm. These results are consistent with the band gap shift obtained from PL experiments (Fig. 43, left) and for the first time demonstrate unambiguously quantum confinement and direct band-to-band transitions.

Figure 44 shows a photo of the National Research Council logo made of a Si/SiO_2 superlattice. To obtain the PL image, the mesa structure was excited from the back by a laser. The red luminescence is visible to the naked eye. The complete integrability with conventional silicon-based technology and the good size controllability makes this technique a strong candidate for the realization of a silicon-based light-emitting diode. Quantum



Fig. 44. Visible photoluminescence from a Si/SiO_2 superlattice mesa structure excited from the back. (Source: Reprinted from [160]. © 1996 American Institute of Physics.)

efficiency values, not published up to now, would be very desirable to gauge the technological potential of Si/SiO_2 superlattices.

3.9.4. Nanocrystalline Si/CaF_2 Multilayers

D'Avitaya et al. [161, 162] have grown nanocrystalline Si/CaF_2 multilayers with periods ranging from 50 to 100 by solid-source MBE at room temperature on CaF_2 and Si(111) substrates. CaF_2 was chosen as the barrier layers because of its large band gap of about 12 eV and its small lattice mismatch of 0.6% to Si. For a review of Si/CaF_2 superlattices, see [163]. As the nanocrystallinity of the whole multilayer is driven by the ionic character of CaF_2 and the low growth temperature, the authors expect no effect of the substrate. However, to date, there are no published results on the growth of nanocrystalline Si/CaF_2 on technologically relevant Si(100) surfaces. Whereas the CaF_2 layer thickness is kept constant at 3 nm, the Si layer thickness is varied between 0.3 and 5 nm. From extended X-ray absorption fine structure (EXAFS) experiments on Si(2 nm)/CaF_2(3 nm) multilayers, the Si grain size of the multilayers could be determined to be smaller than 1.5 nm. Schuppler et al. [164] have reported the same upper limit for the grain size in porous Si also determined by EXAFS experiments.

After allowing hydrogen and oxygen to passivate the dangling bonds of the Si nanostructures, intense PL was observed at room temperature, with a peak maximum at approximately 1.65 eV and an FWHM of approximately 0.4 eV, very similar to the observed spectra of porous Si. The luminescence could be observed only if the Si layer thickness was less than 2.5 nm, similar to the 3-nm-thick Si layer reported by Lockwood et al. [159] for Si/SiO_2 multilayers. Thus, in combination with the observed blue shift as the Si layer thickness decreased, the authors attributed the luminescence to a quantum confinement effect. Optical absorption measurements made on the same structures gave a corresponding gap value of 2.4 eV. This energy difference between the absorption and emission was ascribed to the Stokes shift. Time-resolved photoluminescence experiments revealed a slow ($t > 1$ μs) and a fast ($t < 1$ μs) component [165]. These two emission bands, their lifetime, and their spectral positions are very similar to porous silicon, although the monotonic temperature dependence of PL intensity differs from that of porous silicon. Moreover, Vervoort et al. [165] have reported a significant increase of the PL intensity upon aging of the multiple quantum wells of Si/CaF_2 in air, again an effect also observed in porous silicon. This effect was attributed to a possible oxygen saturation of Si dangling bonds migrating along the grain boundaries, which most likely led to the passivation of nonradiative centers.

A mesa light-emitting diode was fabricated with a transparent indium tin oxide (ITO) ohmic contact. Under forward bias (7–8 V), room temperature EL was observed. It was

also reported that ITO deposition has a strong effect on the luminescence. First, the PL peak position is shifted to lower energies, then the line width decreases to 100 nm, and, finally, the luminescence intensity is higher by a factor of 3. These effects are attributed to the absorption of oxygen out of the ITO layer, which modifies the surface passivation and also affects the size of the Si crystallites. This could correspond to the reported aging effect. In the case of EL, the authors attribute the excitation to tunneling of carriers through the dielectric under the high applied electric field.

Bassani et al. [166] have reported a more pronounced blue shift of the optical absorption edge with decreasing Si layer thickness, adding support to the interpretation of the emission being determined by quantum confinement of carriers within Si nanocrystallites. The CaF_2 thickness for all these samples is kept constant. Nevertheless, the nanocrystalline Si layers are assumed to have an indirect band gap. From Tauc's relationship $(\alpha h\nu)^{1/2} = B(h\nu - E_g)$, the optical pseudogap could be obtained by extrapolating the experimental data to $\alpha = 0$. The dependence of the optical band gap on the Si layer thickness is consistent within the effective mass theory. The huge Stokes shift of 1 eV observed for the thinnest Si layer (1.2 nm) was attributed to relaxation of the Si atoms near the surface forming a deep luminescent center. Numerical simulations by Allan et al. [167] and Baierle et al. [168] have predicted a Stokes shift of approximately 1 eV for crystalline diameters of 1.5 nm, which agrees well with that reported by Bassani et al. [166]. The smaller blue shift of photoluminescence compared to the absorption spectrum was related to near-surface localized states, which are less influenced by the silicon grain sizes [166]. However, quantum confinement remains a necessary condition for luminescence. Borisenko et al. [169] have used an improved self-consistent linear combination of atomic orbitals (LCAO) method with the extended Huckel Hamiltonian to calculate the electronic band structure of nanometer-thick (111) monocrystalline and nanocrystalline freestanding silicon films.

These structures are very similar to the Si/CaF_2 system. The Si dangling bonds are passivated by hydrogen. Figure 45 shows the evolution from a monocrystalline film to a "pseudofilm" and finally to a "pseudowire" and a "pseudodot" structure. On the right-hand side of Figure 45, the corresponding electronic band structure is depicted, showing the transition from an indirect to direct band gap resulting from silicon grains being formed. The calculated band gap of 2.07 eV of the "pseudodot" grain can be considered as a lower limit. For an isolated grain, the calculated band gap is 4.61 eV, which can be considered as an upper limit. Thus, the value of 2.4 eV for the gap in Si/CaF_2 multiple quantum wells with grain size in the range of 0.5 to 1.5 nm would fall within the likely band gap energies in this material.

3.10. Si/III–V Light-Emitting Nanotips

So far, the route favored by industry to solve temporarily the electrical wire bottleneck is to combine III–V direct band gap materials with indirect band gap silicon complementary metal on silicon (CMOS) platforms. This approach explores the excellent optical properties of III–V compounds and combines them with the existing technology of the silicon microelectronics industry. There are essentially two different ways to realize a hybrid Si/III–V device. The first is to grow directly GaAs or GaAs-based structures on Si. The second is to fabricate first the III–V-based optoelectronic circuit and to mount it by wafer bonding, fusion, epitaxial liftoff, or flip-chip bonding on the Si wafer. The first approach faces three different fundamental challenges [3]:

1. The high lattice mismatch of 3.88% between GaAs and Si leads to a high density of misfit dislocations and to relaxed GaAs layers.
2. There is also a polar–nonpolar surface mismatch. Whereas III–V compounds are polar, different sides of the nonpolar silicon crystal cannot be distinguished. This

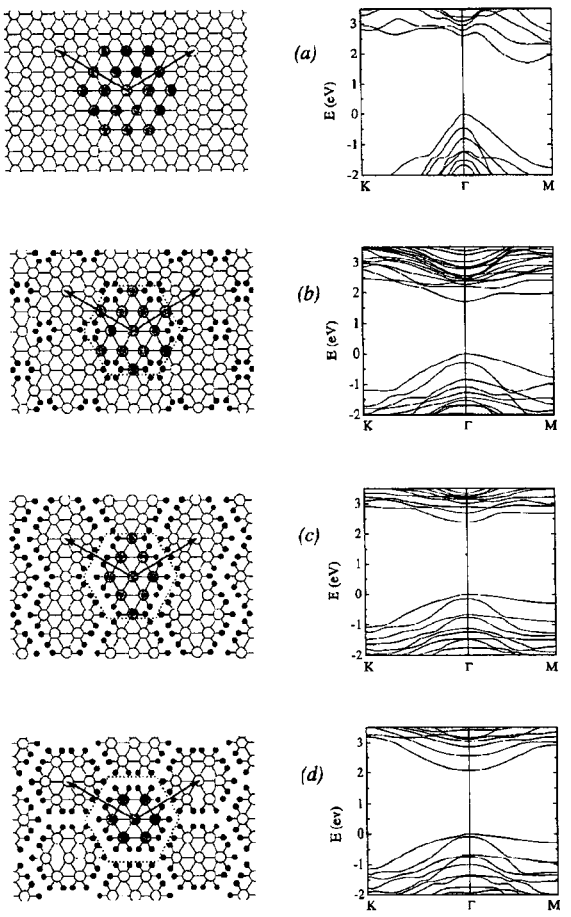


Fig. 45. The evolution from a monocrystalline film (a) to a pseudodot structure (d) is shown on the left-hand side. The corresponding electronic band structure is shown on the right-hand side. The small circles represent H atoms; the large circles represent Si atoms. The unit cell is denoted by a dotted line. (Source: Reprinted from [169]. © 1997 American Institute of Physics.)

mismatch leads to the growth of antiphase boundaries, as there are always atomic steps on the silicon wafer. Thus, during growth, a phase difference occurs in the stacking of GaAs between domains on opposite sites of the silicon steps, leading to Ga–Ga and As–As bonds at the so-called antiphase boundary in contrast to the Ga–As bonds.

3. Finally, there is the problem of charging of the interface. An interface that is abruptly terminated between a polar and a nonpolar semiconductor results in a heavily charged plane modifying strongly the electronic characteristics of a device.

There are several groups exploring these two approaches and the reader is referred to [170–174] for recent progress in this area. One novel approach, though not specific for optical interconnects, has been proposed by Shealy et al. [175], who selectively grew a III–V alloy (GaInP) by organometallic vapor phase epitaxy on sharp silicon tips. As the thin tip behaves as a compliant substrate, the creation of misfit dislocations can be avoided as the authors showed by photoluminescence studies. The basic idea was to fabricate field-emitting devices for high-resolution-color flat panels without the need of phosphorous

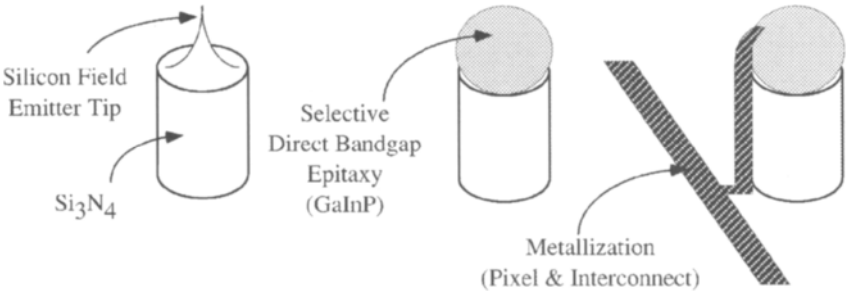


Fig. 46. Schematics of the fabrication process of a single pixel of Si–GaInP field-emitting tip proposed for flat panel display. (Source: Reprinted with permission from [175]. © 1997 American Institute of Physics.)

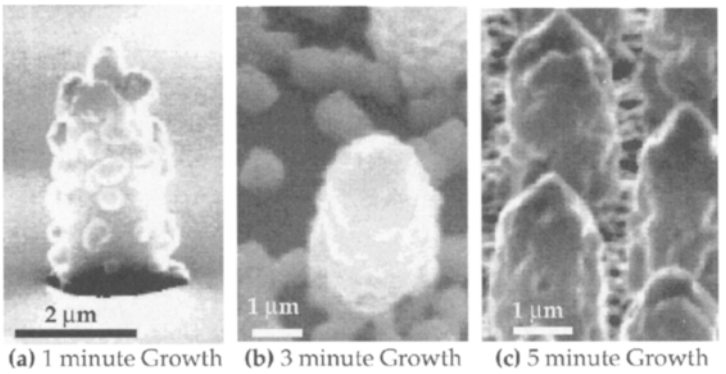


Fig. 47. SEM micrographs of submicrometer silicon tips coated by GaInP after (a) 1 min, (b) 3 min, and (c) 5 min. At the beginning, growth takes place only on top of the tip, but, at longer deposition times, material is also deposited in between the tips. (Source: Reprinted with permission from [175]. © 1997 American Institute of Physics.)

screens and vacuum conditions. The silicon tip can thus directly field emit electrons into the conduction band of the direct band gap material. Figure 46 shows schematically the pixel fabrication process. More details on the fabrication of the silicon tips with an onset voltage of 30 V for field emission into a vacuum are given elsewhere [176, 177].

It is important to cover all the bare silicon surrounding the sharp tips with Si_3N_4 to avoid nucleation of the III–V material. After growth of the direct gap material, the metallization is performed to connect each single pixel of the array. Fabrication of silicon field emission arrays proceeded by selective lateral thermal oxidation, which is described in more detail in [177]. A tip-to-tip distance of 3 μm for the tips with a radius of curvature of 10–20 nm was thus achieved. Figure 47 shows an SEM micrograph of a silicon tip after different GaInP coating times.

Photoluminescence in the visible consisted of single-peak spectra and a peak shift to higher wavelengths as compared to a GaInP reference layer grown on GaAs, indicating at least different alloy composition. Other effects may also contribute to this red shift. Both photoluminescence and cathodoluminescence images showed luminescence from the area between the tips for longer deposition times, probably coming from III–V material deposited between the tips as shown in the SEM micrographs. Thus, short deposition times, of around 1 min, have to be chosen to realize spatially well-defined tip luminescence. As the widths of the cathodoluminescence image have nearly the same dimensions as the SEM features, the authors excluded surface recombination processes.

4. SINGLE-ELECTRON ELECTRONICS

An electrically isolated nanostructure, such as a quantum dot, can be charged by electrons tunneling into the dot, which then become localized if the tunnel resistance is larger than the resistance quantum h/e^2 and if the energy level separation $e^2/2C$ within the dot is bigger than the thermal energy kT [178]. The second condition requires nanostructures less than or equal to 5 nm to reduce the total capacitance C of the island if Coulomb blockade effects are to be observed at room temperature. The charging energy $e^2/2C$ blocks further electrons from tunneling into the dot until the applied voltage exceeds the critical value $e/2C$ and the energy is higher than the next energy level in the dot. Thus, between $-e/2C$ and $+e/2C$, the energy level separation of $e^2/2C$ within the dot blocks any carrier transport and steplike I–V characteristics are obtained. Extending the device structure to a single-electron transistor (SET) by applying a gate voltage V to the dot via a capacitance C to modulate the field leads to oscillations of the current through the dot as a function of the applied gate voltage. Thus, if $CV/e = n$ is an integer value, the current is blocked. For $CV/e \pm \frac{1}{2} = n$, the current can flow through the dot [178].

Silicon-based SETs are regarded as particularly important because of their potential role in future electronic circuits. Single-electron electronics based on silicon-on-insulator (SOI) SETs have been discussed first by Ali and Ahmed [179] and Takahashi et al. [180]. Kurihara et al. [181] reduced the size of the islands to obtain Coulomb oscillations at nearly room temperature. Yano et al. [182] used a thin polysilicon film with small islands and demonstrated a room temperature operating single-electron memory device. Carrier transport through double-barrier structures has been demonstrated with SiO_2 barriers and well layers of amorphous Si [183], single-crystalline Si [184], microcrystalline Si [185, 186], and polycrystalline Si [187]. However, evidence of room temperature Coulomb blockade was not given in these tunneling studies.

Matsumoto et al. [188] used scanning tunneling microscopy (STM) lithography to fabricate a room temperature operating SET with a Coulomb staircase of approximately 150 mV. The width of the 30–50-nm-long TiO_x lines was 15–25 nm. The island size was 30–50 × 30–50 nm^2. The relevant tunnel junction area was only 2–3 nm (the thickness of the Ti film) × 30–50 nm (the length of the TiO_x line). For such small sizes, the tunnel capacitance is about 10^{-19} F, which enables room temperature operation of SETs with well-defined size.

Possible applications of SETs, such as very accurate current standards, sensitive electrometers [189], and single-electron memories [190, 191], have been demonstrated. For a detailed review of single-electron devices, we refer to the chapter by Chou on quantum dot transistors and memories in this book.

Eisele et al. [129] realized the use of Si wires and dots grown through micro shadow masks (see Section 3.8) for field-effect-controlled one- and zero-dimensional electronic confinement.

Figure 48 shows the schematics of a MOS device on a nonplanar silicon surface. No dry etching is used in this process. The (111) faceted silicon side walls are formed by a self-assembling process. In this structure, the nonplanar surface regions exhibit different threshold voltages for inversion, where the surface potential is larger than the difference between the intrinsic semiconductor Fermi level E_i and the gate material Fermi level. By solving Poisson's equation numerically for p-type silicon, the authors showed that the surface potential is lowered at convex edges, thus forming a quasi-one-dimensional wire before the side walls start to invert. Eisele et al. [1129] fabricated vertical MOS transistors with 85-nm channel lengths but different planar geometries as shown in the inset of Figure 49. Thus, they realized two or four edges within the width of the transistor. Figure 49 shows the conductance against applied gate voltage for both transistors. Although the wide transistor ($W = 80$ μm) shows a steplike behavior, it is not possible to resolve the structures because of the relatively large subthreshold current. Decreasing the width to 9 μm results in smaller

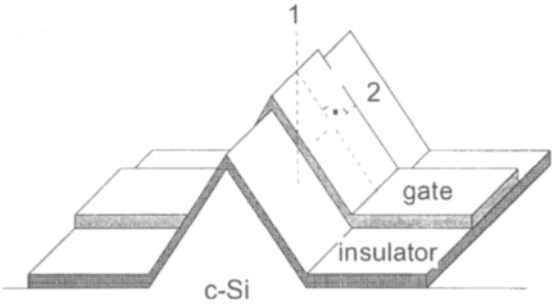


Fig. 48. Schematical cross section of the self-assembled growth mechanism on a nonplanar surface for 1D and 0D silicon devices. (Source: Reprinted from [129], with permission from Elsevier Science.)

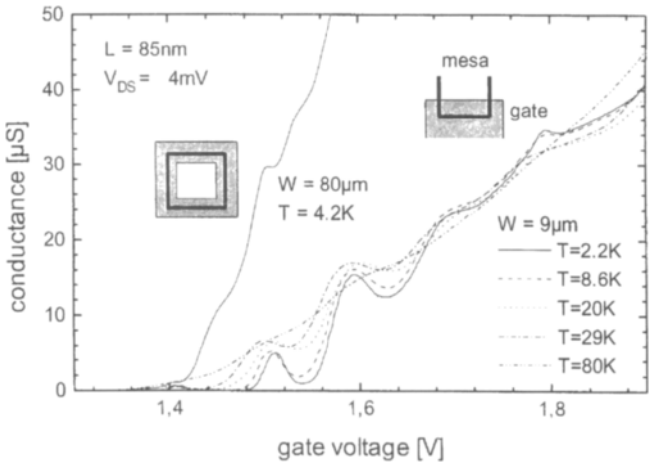


Fig. 49. Conductance versus varying gate voltage for two different gate configurations ($W = 80$ μm and $W = 9$ μm). The temperature dependence is related to the narrow device. The applied source–drain voltage was 4 meV. (Source: Reprinted from [129], with permission from Elsevier Science.)

parasitic 2D current, allowing resolution of these conductance oscillations, which are not observed for transistors without edges. The authors explained the observed steplike conductance as arising from the 1D subband crossing of the Fermi level with increasing gate voltage. The mobility near the subband edges is reduced because of carrier intersubband scattering into the next subband. From the presence of the oscillations up to about 80 K, the authors deduced an energy level separation corresponding to kT of 6 meV.

Coulomb staircases in the I–V characteristics [192] and Coulomb blockade effects [193, 194] were observed at room temperature owing to the strong confinement in silicon quantum dots. Fukuda et al. [193] fabricated self-assembled Si quantum dots by LPCVD on native and thermally grown SiO_2 that had been etched back to a thickness of 1 nm. The height and diameter of the dots varied between 1.5 to 8 nm and 10 to 20 nm, respectively. A top barrier layer of 1 nm thickness was achieved by the same means. The I–V characteristics were measured on a single dot using AFM with a conductive cantilever. The dots had a height of 2.7 and 2.8 nm. The I–V characteristics were also simulated using the well-known transfer matrix approach [102, 195]. Some clear discrepancies were attributed to a possible leakage current through the SiO_2 barrier and to Si/SiO_2 interface states and traps, which smear out the resonance current.

As a quantum dot is a three-dimensional confined electronic system, its discrete energy spectrum potentially permits the storage of single electrons. Nakajima et al. [194, 196]

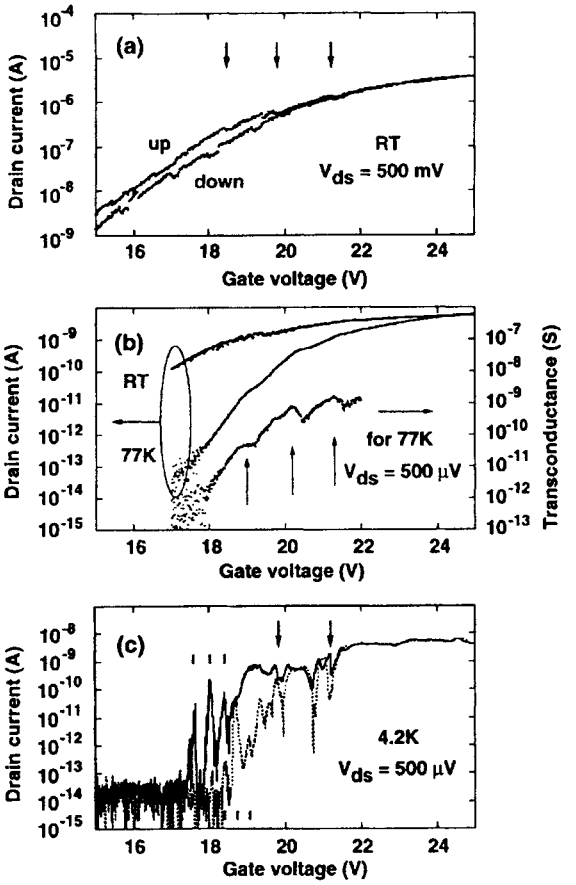


Fig. 50. Drain current versus gate voltage of a single-electron tunneling transistor at (a) room temperature (V_{DS} = 500 mV), (b) room temperature and 77 K with transconductance versus gate voltage (V_{DS} = 500 μV), and (c) 4.2 K with down sweeps represented by the dotted line. The Coulomb oscillation peaks are denoted by the arrows. (Source: Reprinted from [194]. © 1997 American Institute of Physics.)

realized a Si single-electron tunneling transistor with a nanoscale floating dot stacked on a Coulomb island by a self-aligned process as a possible electron memory device. The control gate consisted of polysilicon. The Coulomb island had a width of about 40–50 nm and a length of 50–60 nm. The floating dot on top of the Coulomb island had a side length of about 20–30 nm.

Figure 50 shows the drain current versus the control gate voltage at 4.2 K, 77 K, and room temperature. The drain current exhibits oscillations, denoted by the arrows, because of the Coulomb blockade effect. Sweeping the voltage up and down in parts a and c of Figure 50, denoted by the dotted line for down sweeping, leads to a hysteresis effect. The oscillations in the drain current do not occur at the same voltages. Nakajima et al. [194, 196] demonstrated the Coulomb blockade effect via tunneling of a single electron from the channel to the floating dot gate. If one can control the device design such that the drain current change from a valley to a peak is influenced by only a single electron, this device could be used to detect single electrons and, because of the hysteresis effect in the I–V characteristics, as an ultralow-power-consumption memory.

Guo et al. [197–199] fabricated a silicon SET memory that operates at room temperature and is suitable for ultralarge-scale integration (ULSI). A conventional floating-gate MOS memory was scaled down in order to realize a single-electron MOS memory (SEMM).

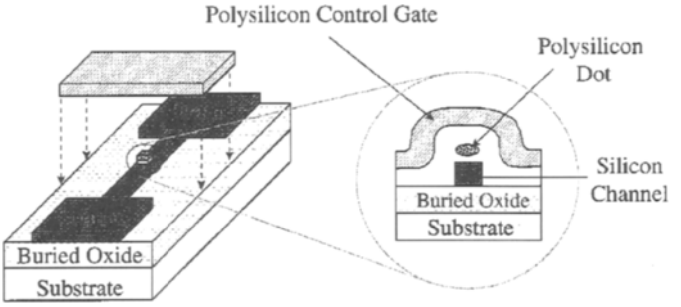


Fig. 51. Schematic drawing of a single-electron MOS memory using single-electron charging of a polysilicon nanodot to switch the gate threshold. (Source: Reprinted from [197]. © 1997 American Institute of Physics.)

However, the channel width was narrower than the Debye screening length of a single electron and the floating gate was a nanoscale square dot. Figure 51 shows a schematic view of this SEMM. As a floating gate, Guo et al. deposited an 11-nm-thick polysilicon film on top of the 35-nm-thick crystalline silicon layer of the SOI wafer. In between the crystalline silicon and the polysilicon, there was an approximately 1-nm-thick native oxide layer. No additional tunnel oxide was formed to enable fast charging of the dot through the channel. Furthermore, the number of electrons stored on the dot was regulated by the Coulomb blockade mechanism, as the potential difference between the channel and the dot is minimized for a given charging voltage. In a two-level step using electron beam lithography and reactive ion etching, the widths of the floating gate and the silicon channel were patterned first; then patterning in the perpendicular direction was carried out to form the squarelike polysilicon dot.

For the smallest device, the width of the channel was roughly estimated at approximately 10 nm. The approximately 7-nm × 7-nm square dot had a height of about 2 nm. To determine the electrical properties of the smallest device, a source–drain voltage of 50 meV was applied. Despite a continuous charging voltage, the threshold voltage of the device made discrete shifts of 55 meV, corresponding to a charging voltage interval of approximately 4 V. Because of the very thin native oxide in between the channel and the floating dot, the charge could be stored for about 5 s after setting the gate potential to ground. This shifted the threshold voltage to its original value. The calculated capacitance for an approximately 7-nm × 7-nm square dot is about 4.4×10^{-20} F, giving a single-electron charging voltage of 3.6 V, which corresponds well to the experimental value of about 4 V. The shift of the threshold voltage was estimated from the single-electron Debye screen length (~70 nm) and the channel thickness (~26 nm) to be approximately 64 meV, also corresponding well with the experimental value of 55 meV.

For single-electron computing, many interesting circuits have been proposed setting up Boolean logic circuits using Coulomb interactions between bistable charge polarization states [200, 201]. The main drawback of most of the proposed schemes is the missing isolation between the input and output terminals so that the input can thus drive the output but not vice versa. As the Coulomb interaction between two identical charge polarizations is reciprocal, the output can also drive the input, violating the necessity of unidirectionality and thus leading to the so-called "catastrophic failure" [202, 203].

To realize von Neumann computing architectures, proposals for dissipationless computing [204] have been made. The drawback of this scheme is the fault tolerance. Bandyopadhyay and Roychowdhury [203, 205, 206] have proposed a nanoelectronic architecture to overcome these drawbacks. However, it is still too early to comment on the chances of success of any given approach for logic operations.

5. TIPS FOR ATOMIC FORCE MICROSCOPY AND FIELD EMISSION

The displacement of single atoms on a surface is already possible using scanning probe techniques allowing, for example, new molecular arrangements to be realized for a variety of purposes. Some of these include integrated microscopic gears, pumps, motors, membranes, and nanotweezers. Whereas silicon-based microelectronic devices switch electron fluxes through thin metallic wires, micromechanical devices could establish the contact between microelectronics and the physical world. Because of the predominance of silicon-based microelectronics, this material is favored in micromechanics research and development. For a comprehensive overview, we refer the reader to *Scientific American, Special Dossier: Microsystem Technology 1996.*

Silicon is also the favored material for cold field emitter devices for nanolithography and for flat panel devices. Recent studies [207–210] have shown that miniaturization of the electron beam column leads to a well-focused and bright electron beam source. Such microcolumns can be used for scanning electron microscopy and electron beam lithography with high resolution [210, 211]. The main disadvantage of electron beam lithography having a low throughput could potentially be overcome, using arrays of electron beam microcolumns. The tip sharpness, gate diameter, and gate-to-tip distance influence the turn-on voltage and the emission current of field emission devices. Thus, very sharp tips with a small gate diameter and a small gate–tip distance are desired. Rakhshandehroo and Pang [212] have fabricated 100 single Si tip arrays with a spacing of 1 μm. Using dry etching and low-temperature plasma oxidation led to a sharpening of the tips with radius from 67 down to 8 nm, leading, in turn, to a lower turn-on voltage and to a higher emission current because of the higher electric field at the tip apex.

To reduce further the voltage applied to the anode, Jung et al. [213] fabricated nanosize Si tips with a tip diameter smaller than 20 nm. After reactive ion etching, a tip radius of about 300 nm was determined. To sharpen the tip to 20 nm, a low-temperature oxidation at 900 °C with a subsequent dip in BHF was carried out. Low-temperature oxidation leads to an enhanced oxide growth in the regions with high curvature. The diameter of the tip was reduced in this fashion to less than 20 nm. A 30-nm amorphous hydrogen free diamond-like carbon (DLC) film was deposited on top of this structure by PECVD. The film is composed of a diamond-like sp^3 and a graphite-like sp^2 phase.

The emission current of the DLC film is twice as high as the pure Si tip, and the onset of the field emission is shifted to smaller voltages from 700 to 600 V. At higher voltages, the emission current of the pure Si tip was zero because of deterioration, whereas the DLC-coated tip exhibited an emission current of approximately 100 μA at 1.5 kV.

Figure 52 shows a silicon tip with a silicon cantilever used in atomic force microscopy (AFM) fabricated by Dr. O. Wolter GmbH in Germany. The pyramidal tip points to the ⟨100⟩ direction. The tips have a radius less than or equal to 15 nm and are 10–15 μm high. The thickness of the cantilever with a trapezoidal cross section ranges from 0.3 to 8, 20, 60, 125, and 450 μm, depending on the specific applications. A sharp tip of 2 nm radius has been achieved (see the right-hand side of Fig. 52). The half cone angle is better than 10° at the last 200 nm of the tip and its mechanical robustness permits fast scan rates. The ability to control single atoms could potentially enable the storage of 10^{12} GB/cm^2 on a silicon chip. Such a data storage system would beat all conventional systems because of its increased capacity and lack of movable parts such as a rotating disk.

MacDonald et al. [214] have fabricated an STM tip with a diameter of 20 nm mounted on a floating frame with four motors, each 400 μm in diameter. These motors can pull or push the tip vertically and horizontally up to one million times per second and even tilting of the tip is possible. With a matrix of several hundred tips, a direct surface structuring in a parallel and thus a very fast process could be realized.

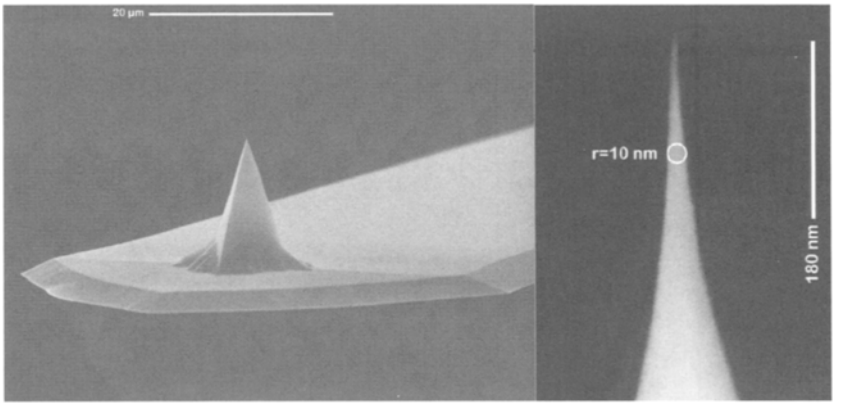


Fig. 52. Silicon tip together with a monolithic cantilever used in atomic force microscopy (left). Super-sharp silicon tip for high-resolution imaging of nanostructures and microroughness. The tip radius is only 2 nm (right). (Source: Reprinted with permission from NANOSENSORS.)

The use of Si tips in scanning probe–based lithography is increasing fast although formally still an the laboratory scale. Madsen et al. [215] wrote patterns with feature sizes down to 50 nm with a scanning near-field optical microscope (SNOM) using Al-coated fiber probes. Nagahara et al. [216] used the tip to expose a resist to extremely low energy electrons. Minne et al. [217] used a mix-and-match lithography to fabricate a metal oxide semiconductor field effect transistor (MOSFET). The electrodes at the gate were defined by atomic force microscopy (AFM), whereas the remaining levels were defined by optical lithography. Line widths between 60 and 700 nm were achieved. Abeln et al. [218] used STM lithography to fabricate structures smaller than 10 nm. Using STM, Matsumoto et al. [188] fabricated an SET with line widths of 15–25 nm.

Field-enhanced oxidation as a lithographic tool was first introduced by Dagata et al. [219]. They used a 5–10-V negatively charged STM tip under ambient air conditions. The huge electric field beneath the tip selectively desorbs passivating hydrogen atoms and molecules from the silicon surface, allowing bare silicon to oxidize under the influence of ambient air in the presence of huge fields generated at the tip. Lyding et al. [220] wrote 1.5-nm line widths in an UHV system pushing the resolution of this approach. During pattern transfer, by wet or dry etching, a high etch selectivity is essential as the oxide thickness is less than 5 nm.

In many cases, AFM tips consist of Si_3N_4 coated with a thin layer such as Ti to lengthen its lifetime. Birkelung et al. [221] have used Ni tips coated with a 5-nm Ti adhesion layer and a 100-nm Au cap layer as a plating base between the Ni and Si. They achieved 80-nm line widths writing over 1000 lines before the tip degraded. The partial Au deposition during the first few scans onto the surface had to be removed by etching.

Snow et al. [222] used AFM for local oxidation and subsequent RIE to fabricate approximately 10-nm-wide lines with a height of 30 nm. They used an n-type Si wafer hydrogen passivated in 10% aqueous solution after ozone treatment. Using a Si_3N_4 AFM tip coated with 30-nm Ti, they oxidized locally the Si surface by applying a negative voltage between 4 and 7 V under a scanning speed of 1–10 μm/s. To obtain fine patterns, they worked with low voltages and used slow scanning speeds. The ambient humidity was kept constant to 50% as this is a key process parameter.

The addition of oxygen has been found to increase the etch selectivity to more than 20. Figure 53 shows an AFM image of several lines of varying width after dry etching to a depth of 30 nm. The two lines marked by arrows in Figure 53 have a width between 25 to 30 nm (right) and 35 and 40 nm (left), respectively. Subtracting the convolution with the 20-nm tip diameter, a real line width for the smallest line of less than 10 nm is obtained.

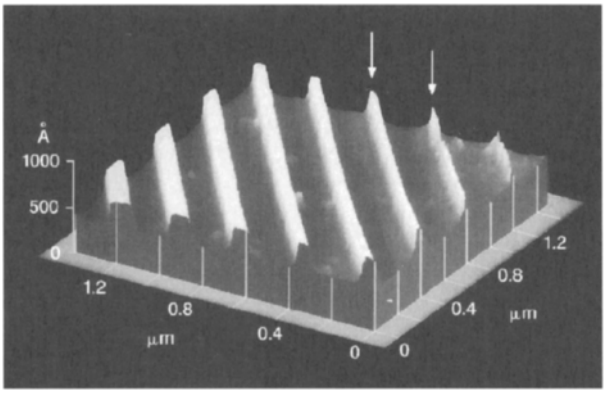


Fig. 53. AFM image of dry-etched Si nanowires of varying width etched to a depth of 30 nm. The arrows indicate two lines with widths between 25–30 nm and 35–40 nm. The real line widths are about 20 nm less because of a convolution effect with the tip diameter of the AFM. (Source: Reprinted from [222]. © 1995 American Institute of Physics.)

Snow et al. [223] demonstrated the use of silicon as a resist material for patterning GaAs using scanning probe lithography. Thus, combining this technique with an UHV system, true nanostructures may be realized in Si as well as in III–V wafers.

6. CONCLUSIONS

We have attempted to provide an overview concerning recent developments involving silicon-based nanostructures. It is almost certain we have not done justice to the many scientists and engineers who have contributed to the field. This is mainly a representive list of examples determined by the usual constraints of space, time, and energy.

In the quest to realize a variety of nanostructures using silicon and silicon-related semiconductors, the trend to miniaturization in electronics plays an overwhelming role. To some degree, this places an enormous burden on other developments that could potentially make use of nanostructures for other applications. The range of other applications comes under the umbrella of nanotechnology as demonstrated by the work on nanotips. It is clear that extension of the use of Si nanostructures into the biological and environmental areas has begun; however, this has not been touched upon here. The scientific and technological challenges are still formidable and there are no clear winners yet in, for example, a silicon-based light emitter suitable for optical interconnects. Our understanding is still too incomplete and we continue to learn about the impact of the local environment, in the nanometer scale, of optically active centers in silicon. On the other hand, the wealth of technological expertise developed collectively in silicon electronics ensures that any relevant scientific development in this area, which survives the acid test of industrial suitability and device specifications, could be made available to potential users because the connections to the outside world are provided by existing input and output Si-based circuitry and technology. Whereas this may well be the case in sensors and optical devices, there are significant challenges remaining in the area of quantum nanoscale electronic circuits, which is bound to keep the Si nanoelectronics community very active for years to come.

Acknowledgments

We are indebted to the many authors and colleagues who kindly provided us with photos and figures of their work as well as authors who gave permission to reproduce their published figures. Of course, any misinterpretation is our sole responsibility. The dry-etched

Si–SiGe dot work reviewed here was mostly carried while one of the authors (CMST) was at the University of Glasgow jointly with Y.-S. Tang and C. D. W. Wilkinson and G. V. Hansson and W.-X. Ni of Linköping University. Samples for the work at Glasgow University were also kindly provided by E. H. C. Parker of Warwick University and H. Presting of Daimler-Benz Research Laboratories in Ulm. The more recent work on deep-etched Si–SiGe dots has been supported by the European Commission ESPRIT Project 22644 SIBLE. We thank T. Maka, T. Köpke and our colleagues for their help with the preparation of this chapter. This work was partially supported by the University of Wuppertal.

References

1. G. Davies, *Phys. Rep.* 176, 83 (1989).
2. D. J. Lockwood, in "Semiconductors and Semimetals" (R. K. Williardson and E. R. Weber, eds.), Vol. 49, p. 1. Academic Press, San Diego, 1997.
3. S. S. Iyer and Y.-H. Xie, *Science* 260, 40 (1993).
4. J. R. Chelikowsky and M. L. Cohen, *Phys. Rev. B* 14, 556 (1976).
5. L. C. Kimberling, K. D. Kolenbrander, J. Michel, and J. Palm, *Solid State Phys.* 50, 333 (1997).
6. U. Gnutzmann and K. Clausecker, *Appl. Phys.* 3, 9 (1974).
7. E. Kasper and F. Schäffler, in "Semiconductors and Semimetals" (T. P. Pearsall, ed.), Vol. 33, p. 223. Academic Press, Boston, 1991.
8. S. Froyen, D. M. Wood, and A. Zunger, *Phys. Rev. B* 36, 4547 (1987).
9. T. P. Pearsall, J. Bevk, L. C. Feldman, J. M. Bonar, J. P. Mannaerts, and A. Ourmazd, *Phys. Rev. Lett.* 58, 729 (1987).
10. R. J. Turton and M. Jaros, *Mater. Sci. Eng., B* 7, 37 (1990).
11. U. Menczigar, J. Brunner, E. Friess, M. Gail, G. Abstreiter, H. Kibbel, H. Presting, and E. Kasper, *Thin Solid Films* 222, 227 (1992).
12. U. Menczigar, G. Abstreiter, J. Olajos, H. Grimmeiss, H. Kibbel, H. Presting, and E. Kasper, *Phys. Rev. B* 47, 4099 (1993).
13. J. Engvall, J. Olajos, G. Grimmeiss, H. Kibbel, and H. Presting, *Phys. Rev. B* 51, 2001 (1995).
14. S. C. Jain, in "Germanium–Silicon Strained Layers and Heterostructures." Academic Press, Boston, 1994.
15. K. Brunner, K. Eberl, and W. Winter, *Phys. Rev. Lett.* 76, 303 (1996).
16. K. Brunner, W. Winter, and K. Eberl, *Appl. Phys. Lett.* 69, 1279 (1996).
17. S. Oguz, W. Paut, T. F. Deutsch, B.-Y. Tsaur, and D. V. Murphy, *Appl. Phys. Lett.* 43, 848 (1983).
18. J. Derrien, J. Chevrier, V. Le Thanh, T. E. Crumbaker, J. Y. Natoli, and I. Berbezier, *Appl. Surf. Sci.* 70–71, 546 (1993).
19. M. C. Bost and J. E. Mahan, *J. Appl. Phys.* 58, 2696 (1996).
20. L. Miglio, F. Tarazza, and G. Malegori, *Appl. Phys. Lett.* 67, 1 (1995).
21. D. N. Leong, M. A. Harry, K. J. Reeson, and K. P. Homewood, *Appl. Phys. Lett.* 68, 1649 (1996).
22. D. Leong, M. Harry, K. J. Reeson, and K. P. Homewood, *Nature* 387, 686 (1997).
23. Z. Yang, K. P. Homewood, M. S. Finney, M. Harry, and K. J. Reeson, *J. Appl. Phys.* 78, 1958 (1995).
24. H. Ennen, J. Schneider, G. Pomrenke, and A. Axmann, *Appl. Phys. Lett.* 43, 943 (1983).
25. H. Ennen, G. Pomrenke, A. Axmann, K. Eisele, W. Haydl, and J. Schneider, *Appl. Phys. Lett.* 46, 381 (1985).
26. J. Michel, J. L. Benton, R. F. Ferrante, D. C. Jacobson, D. J. Eaglesham, E. A. Fitzgerald, Y.-H. Xie, J. M. Poate, and L. C. Kimerling, *J. Appl. Phys.* 70, 2672 (1991).
27. S. Coffa, G. Franzò, F. Priolo, A. Polman, and A. Serna, *Phys. Rev. B* 49, 16313 (1994).
28. G. N. van den Hoven, J. H. Shin, A. Polman, S. Lombardo, and S. U. Campisano, *J. Appl. Phys.* 78, 2642 (1995).
29. B. Zheng, J. Michel, F. Y. G. Ren, L. C. Kimerling, D. C. Jacobson, and J. Poate, *Appl. Phys. Lett.* 64, 2842 (1994).
30. G. Franzò, F. Priolo, S. Coffa, A. Polman, and A. Carnera, *Nucl. Instrum. Methods Phys. Res., Sect. B* 96, 374 (1995).
31. A. Polman, J. S. Custer, E. Snoeks, and G. N. van den Hoven, *Nucl. Instrum. Methods Phys. Res., Sect. B* 80/81, 653 (1993).
32. D. C. Adler, D. C. Jacobson, D. J. Eaglesham, M. A. Marcus, J. L. Benton, J. M. Poate, and P. H. Citrin, *Appl. Phys. Lett.* 61, 2181 (1992).
33. F. Priolo, G. Francò, S. Coffa, A. Polman, S. Libertino, R. Barklie, and D. Carey, *J. Appl. Phys.* 78, 3874 (1995).
34. W.-X. Ni, K. B. Joelsson, C.-X. Du, I. A. Buyanova, G. Pozina, W. M. Chen, G. V. Hansson, B. Monemar, J. Cardenas, and B. G. Svensson, *Appl. Phys. Lett.* 70, 3383 (1997).

35. F. Y. G. Ren, J. Michel, Q. Sun-Paduano, B. Zheng, H. Kitagawa, D. C. Jacobson, J. M. Poate, and L. C. Kimerling, *Mater. Res. Soc. Symp. Proc.* 301, 87 (1993).
36. S. Coffa, G. Franzò, and F. Priolo, *MRS Bull.* 23, 25 (1998).
37. J. Stimmer, A. Reittinger, J. F. Nützel, G. Abstreiter, H. Holzbrecher, and C. Buchal, *Appl. Phys. Lett.* 68, 3290 (1996).
38. R. Sterna, J. H. Shin, M. Lohmeier, E. Vlieg, A. Polman, and P. F. A. Alkemade, *J. Appl. Phys.* 79, 2658 (1996).
39. M. Matsuoka and S.-I. Tohno, *Appl. Phys. Lett.* 66, 2751 (1995).
40. Y.-H. Xie, E. A. Fitzgerald, and Y. J. Mii, *J. Appl. Phys. Lett.* 70, 3223 (1990).
41. S. Coffa, F. Priolo, G. Franzò, A. Polman, S. Libertino, M. Saggio, and A. Carnera, *Nucl. Instrum. Methods Phys. Res., Sect. B* 106, 386 (1995).
42. C.-X. Du, W.-X. Ni, K. B. Joelsson, F. Duteil, and G. V. Hansson, Proc. of E-MRS'98 Spring Symposium "Light Emission from Silicon: Progress towards Si-Based Optoelectronics" (in press).
43. C. Weisbuch and B. Vinter, in "Quantum Semiconductor Structures." Academic Press, Boston, 1991.
44. J. H. Davies and A. R. Long, in "Proceedings of the 38th Scottish Universities Summer School in Physics" (P. Osborne, ed.), Vol. 38. SUSSP, 1991.
45. E. Kasper, in "EMIS Datareviews," Vol. 12. INSPEC, London, 1988.
46. A. Schuppen, U. Erben, A. Gruhle, H. Kibbel, H. Schumacher, and U. Konig, *Tech. Digest Int. Electron Device Meeting* 743 (1995).
47. S. Perkowitz, in "Optical Characterization of Semiconductors: Infrared, Raman and Photoluminescence Spectroscopy" (N. H. March, ed.). Academic Press, London, 1993.
48. J. Weber and I. Alonso, *Phys. Rev. B* 40, 5683 (1989).
49. L. T. Canham, *Appl. Phys. Lett.* 57, 1046 (1990).
50. A. G. Cullis and L. T. Canham, *Nature* 353, 335 (1991).
51. M. S. Brandt, H. D. Fuchs, M. Stutzmann, J. Weber, and M. Cardona, *Solid State Commun.* 81, 307 (1992).
52. S. M. Prokes, O. J. Glembocki, V. M. Bermudez, R. Kaplan, L. E. Friedersdorf, and P. C. Perason, *Phys. Rev. B* 45, 13788 (1992).
53. Y.-H. Xie, W. L. Wilson, F. M. Ross, J. A. Mucha, E. A. Fitzgerald, and J. M. Macaulay, *J. Appl. Phys.* 71, 2403 (1992).
54. E. Bassous, M. Freeman, J.-M. Halbout, S. S. Iyer, V. P. Kesan, P. Munguia, S. F. Pesarcik, and B. L. Williams, *Mater. Res. Soc. Symp. Proc.* 256, 23 (1992).
55. V. P. Kesan, E. Bassous, P. Munguia, S. F. Pesarcik, M. Freeman, and S. S. Iyer, *J. Vac. Sci. Technol., A* 11, 1736 (1993).
56. P. D. G. Calcott, K. J. Nash, L. T. Canham, M. J. Kane, and D. Brumhead, *J. Phys.: Condens. Matter* 5, 91 (1993).
57. F. Buda, J. Kohanoff, and M. Parrinello, *Phys. Rev. Lett.* 69, 1272 (1992).
58. A. J. Read, R. J. Needs, K. J. Nash, L. T. Canham, P. D. J. Calcott, and A. Qteish, *Phys. Rev. Lett.* 69, 1232 (1992).
59. C. J. Hwang, *Phys. Rev. B* 8, 646 (1973).
60. T. P. Pearsall, J. C. Adams, J. N. Kidder, Jr., P. S. Williams, S. A. Chambers, J. Lach, D. T. Schwartz, and B. Z. Nosho, *Thin Solid Films* 222, 200 (1992).
61. G. Bai, K. H. Kim, and M.-A. Nicolet, *Appl. Phys. Lett.* 57, 2247 (1990).
62. T. P. Pearsall, J. C. Adams, J. E. Wu, B. Z. Nosho, C. Aw, and J. C. Patton, *J. Appl. Phys.* 71, 4470 (1992).
63. S. Eisebitt, J. Luning, J.-E. Rubensson, T. Van Buuren, S. N. Patitsas, T. Tiedje, M. Berger, R. Arens-Fischer, S. Frohnhoff, and W. Eberhardt, *Solid State Commun.* 97, 549 (1996).
64. S. Nozaki, S. Sato, H. Ono, H. Morisaki, and M. Iwase, *Nucl. Instrum. Methods Phys. Res., Sect. B* 121, 455 (1997).
65. Y. Saito, *J. Cryst. Growth* 47, 61 (1979).
66. M. A. Tischler, R. T. Collins, J. H. Stathis, and J. C. Tsang, *Appl. Phys. Lett.* 60, 639 (1992).
67. A. Loni, A. J. Simons, T. I. Cox, P. D. J. Calcott, and L. T. Canham, *Electron. Lett.* 31, 1288 (1995).
68. K. D. Hirschman, L. Tsybeskov, S. P. Duttagupta, and P. M. Fauchet, *Nature* 384, 338 (1996).
69. L. Tsybeskov, S. P. Duttagupta, K. D. Hirschman, and P. M. Fauchet, *Appl. Phys. Lett.* 68, 2058 (1996).
70. Y.-S. Tang, W.-X. Ni, C. M. Sotomayor Torres, and G. V. Hansson, *Electron. Lett.* 31, 1385 (1995).
71. Y. S. Tang, C. M. Sotomayor Torres, W. X. Ni, and G. V. Hansson, *Superlattices Microstruct.* 20, 505 (1996).
72. Y.-S. Tang, S. E. Hicks, C. M. Sotomayor Torres, C. D. W. Wilkinson, W.-X. Ni, and G. V. Hansson, in "23rd International Conference on the Physics of Semiconductors, Berlin, 1996," p. 1628. World Scientific, Singapore, 1996.
73. Y. S. Tang, C. M. Sotomayor Torres, S. Nilsson, B. Dietrich, W. Kissinger, T. E. Whall, E. H. C. Parker, H. Presting, and H. Kibbel, *Solid State Electron.* 40, 383 (1996).
74. Y.-S. Tang, C. M. Sotomayor Torres, B. Dietrich, W. Kissinger, T. E. Whall, and E. H. C. Parker, *Solid State Commun.* 94, 369 (1995).
75. Y.-S. Tang, C. D. W. Wilkinson, D. W. Smith, T. E. Whall, and E. H. C. Parker, *J. Appl. Phys.* 33, 2348 (1994).

76. Y.-S. Tang, C. D. W. Wilkinson, C. M. Sotomayor Torres, D. W. Smith, T. E. Whall, and E. H. C. Parker, *Solid State Commun.* 85, 199 (1993).
77. Y.-S. Tang, *J. Appl. Phys.* 69, 8289 (1991).
78. Y.-S. Tang, C. D. W. Wilkinson, C. M. Sotomayor Torres, D. W. Smith, T. E. Whall, and E. H. C. Parker, *Appl. Phys. Lett.* 63, 497 (1993).
79. W.-X. Ni, J. Birch, Y.-S. Tang, K. B. Joelsson, C. M. Sotomayor Torres, Å. Kvick, and G. V. Hansson, *Thin Solid Films* 294, 300 (1997).
80. A. G. Nassiopoulos, S. Grigoropoulos, and D. Papadimitriou, *Appl. Phys. Lett.* 69, 2267 (1996).
81. A. G. Nassiopoulos, S. Grigoropoulos, D. Papadimitriou, and E. Gogolides, *Phys. Status Solidi B* 190, 91 (1995).
82. W. Chen and H. Ahmed, *Appl. Phys. Lett.* 63, 1116 (1993).
83. H. I. Liu, D. K. Biegelsen, F. A. Ponce, N. M. Johnson, and R. F. W. Pease, *Appl. Phys. Lett.* 64, 1383 (1994).
84. J. Kedzierski, J. Bokor, and C. Kisielowski, *J. Vac. Sci. Technol., B* 15, 2825 (1997).
85. A. S. Chu, S. H. Zaidi, and S. R. J. Brueck, *Appl. Phys. Lett.* 63, 905 (1993).
86. D. J. Lockwood, *Solid State Commun.* 92, 101 (1994).
87. H. Sunamura, N. Usami, Y. Shiraki, and S. Fukatsu, *Appl. Phys. Lett.* 66, 3024 (1995).
88. P. Schittenhelm, M. Gail, and G. Abstreiter, *J. Cryst. Growth* 157, 260 (1995).
89. P. Schittenhelm, M. Gail, J. Brunner, J. F. Nützel, and G. Abstreiter, *Appl. Phys. Lett.* 67, 1292 (1995).
90. H. Sunamura, S. Fukatsu, N. Usami, and Y. Shiraki, *J. Cryst. Growth* 157, 265 (1995).
91. B. Cunningham, J. O. Chu, and S. Akbar, *Appl. Phys. Lett.* 59, 3574 (1991).
92. A. Hartmann, L. Vescan, C. Dieker, and H. Lüth, *Mater. Sci. Technol.* 11, 410 (1995).
93. P. O. Hansson, M. Albrecht, W. Dorsch, H. P. Strunk, and E. Bauser, *Phys. Rev. Lett.* 73, 444 (1994).
94. M. Albrecht, S. Christiansen, J. Michler, W. Dorsch, and H. P. Strunk, *Appl. Phys. Lett.* 67, 1232 (1995).
95. S.-I. Yanagiya, S. Kamimura, M. Fujii, M. Ishida, Y. Moriyasu, and M. Matsui, *Appl. Phys. Lett.* 71, 1409 (1997).
96. M. Yoshimoto, T. Maeda, T. Ohnishi, H. Koinuma, O. Ishiyama, M. Shinohara, M. Kubo, R. Minra, and A. Miyamoto, *Appl. Phys. Lett.* 67, 2615 (1995).
97. Y. Kanemitsu, *Phys. Rev. B* 49, 16845 (1994).
98. W. B. Dubbelday, D. M. Szaflarski, R. L. Shimabukuro, S. D. Russel, and M. J. Sailor, *Appl. Phys. Lett.* 62, 1694 (1993).
99. P. Schittenhelm, G. Abstreiter, A. Darhuber, G. Bauer, P. Werner, and A. Kosogov, *Thin Solid Films* 294, 291 (1997).
100. J. Eaglesham and M. Cerullo, *Phys. Rev. Lett.* 64, 1943 (1990).
101. A. A. Darhuber, J. Stangl, G. Bauer, P. Schittenhelm, and G. Abstreiter, *Thin Solid Films* 294, 296 (1997).
102. T. M. Kalotas and A. R. Lee, *Am. J. Phys.* 59, 48 (1991).
103. T. S. Kuan and S. S. Iyer, *Appl. Phys. Lett.* 59, 2242 (1991).
104. J. Y. Yao, T. G. Andersson, and G. L. Dunlop, *J. Appl. Phys.* 69, 2224 (1991).
105. L. Vescan, W. Jäger, C. Dieker, K. Schmidt, A. Hartmann, and H. Lüth, *Mater. Res. Soc. Symp. Proc.* 263, 23 (1992).
106. Q. Xie, A. Madhukar, P. Chen, and N. P. Kobayashi, *Phys. Rev. Lett.* 75, 2542 (1992).
107. J. Tersoff and F. K. Le Goues, *Phys. Rev. Lett.* 72, 3570 (1994).
108. J. Tersoff, C. Teichert, and M. G. Lagally, *Phys. Rev. Lett.* 76, 1675 (1996).
109. L. Vescan, C. Dieker, A. Hartmann, and A. van der Hart, *Semicond. Sci. Technol.* 9, 387 (1994).
110. L. Vescan, *Thin Solid Films* 294, 284 (1997).
111. L. Vescan, C. Dieker, A. Souifi, and T. Stoica, *J. Appl. Phys.* 81, 6709 (1997).
112. A. Aoyama, T. Ikarashi, K. Miyanaga, and T. Tatsumi, *J. Cryst. Growth* 136, 349 (1994).
113. P. Rai-Choudhury and D. K. Schroeder, *J. Electrochem. Soc.* 120, 664 (1973).
114. L. Vescan, W. Jäger, C. Dieker, K. Schmidt, A. Hartmann, and H. Lüth, *Mater. Res. Soc. Symp. Proc.* 263, 23 (1992).
115. T. Stoica and L. Vescan, *J. Cryst. Growth* 131, 32 (1993).
116. K. D. Hobart, F. J. Kub, H. F. Gray, M. E. Twigg, D. Park, and P. E. Thompson, *J. Cryst. Growth* 157, 338 (1995).
117. G. R. Booker and B. A. Joyce, *Philos. Mag.* 14, 301 (1969).
118. Y.-N. Yang and E. D. Williams, *J. Vac. Sci. Technol., A* 8, 2481 (1990).
119. H. Hirayama, M. Hiroi, and T. Ide, *Phys. Rev. B* 48, 17331 (1993).
120. Y.-N. Yang and E. D. Williams, *J. Vac. Sci. Technol., A* 8, 2481 (1990).
121. A. Oshiyama, *Phys. Rev. Lett.* 74, 130 (1995).
122. E. Kapon, K. Kash, E. M. Clausen, Jr., D. M. Hwang, and E. Colas, *Appl. Phys. Lett.* 60, 477 (1992).
123. S. Tsukamoto, Y. Nagamune, M. Nishioka, and Y. Arakawa, *Appl. Phys. Lett.* 62, 49 (1993).
124. N. Usami, T. Mine, S. Fukatsu, and Y. Shiraki, *Appl. Phys. Lett.* 63, 2789 (1993).
125. N. Usami, T. Mine, S. Fukatsu, and Y. Shiraki, *Appl. Phys. Lett.* 64, 1126 (1994).
126. E. Hammerl, F. Wittmann, J. Messarosch, I. Eisele, V. Huber, and H. Oppolzer, *Mater. Res. Soc. Symp. Proc.* 220, 27 (1991).
127. J. Brunner, T. S. Rupp, H. Gossner, R. Ritter, I. Eisele, and G. Abstreiter, *Appl. Phys. Lett.* 64, 994 (1994).

128. J. Brunner, W. Jung, P. Schittenhelm, M. Gail, G. Abstreiter, J. Gonderman, B. Hadam, T. Koester, B. Spangenberg, H. G. Roskos, H. Kurz, H. Gossner, and I. Eisele, *J. Cryst. Growth* 157, 270 (1995).
129. I. Eisele, H. Baumgärtner, and W. Hansch, *J. Cryst. Growth* 157, 248 (1995).
130. H. Gossner, G. Fehlauer, W. Kiunke, I. Eisele, M. Stolz, M. Hintermaier, and E. Knapek, *Mater. Res. Soc. Symp. Proc.* 351, 393 (1994).
131. J. Brunner, P. Schittenhelm, J. Gonderman, B. Spangenberg, B. Hadam, T. Köster, H. G. Roskos, H. Kurz, H. Gossner, I. Eisele, and G. Abstreiter, *J. Cryst. Growth* 150, 1060 (1995).
132. W. E. Leitch, C. M. Sotomayor Torres, D. Lootens, S. Thoms, P. van Daele, C. R. Stanley, P. Demeester, and S. P. Beaumont, *Surf. Sci.* 263, 622 (1992).
133. H. Gossner, T. Rupp, and I. Eisele, *J. Cryst. Growth* 157, 308 (1995).
134. R. O. Jones and G. Seifert, *Phys. Rev. Lett.* 79, 443 (1997).
135. M. L. Steigerwald and L. B. Brus, *Ann. Rev. Mater. Sci.* 19, 471 (1989).
136. A. Henglein, *Chem. Rev.* 89, 1861 (1989).
137. T. Takagaharar and K. Takeda, *Phys. Rev. B* 46, 15578 (1992).
138. L. Brus, *J. Phys. Chem.* 98, 3575 (1994).
139. Ö. Dag, A. Kuperman, and G. A. Ozin, *Adv. Mater.* 7, 72 (1995).
140. J. R. Heath, *Science* 258, 1131 (1992).
141. J. L. Heinrich, C. L. Curtis, G. M. Credo, K. L. Kavanagh, and M. J. Sailor, *Science* 255, 66 (1992).
142. S. Berhane, S. M. Kauzlarich, K. Nishimura, R. L. Smith, J. E. Davis, H. W. H. Lee, M. L. S. Olson, and L. L. Chase, *Mater. Res. Soc. Symp. Proc.* 298, 99 (1993).
143. R. A. Bley, S. M. Kauzlarich, H. W. H. Lee, and J. E. Davis, *Mater. Res. Soc. Symp. Proc.* 351, 275 (1994).
144. R. A. Bley, S. M. Kauzlarich, J. E. Davis, and H. W. H. Lee, *Chem. Mater.* 8, 1881 (1996).
145. A. Matsunawa, S. Katayama, and Y. J. Arata, *J. High Temp. Soc.* 13, 69 (1987).
146. D. Zhang, R. M. Kolbas, P. Mehta, A. K. Singh, D. J. Lichtenwalner, K. Y. Hsieh, and A. I. Kingon, *Mater. Res. Soc. Symp. Proc.* 256, 35 (1992).
147. K. A. Littau, P. J. Szajowshki, A. J. Muller, A. R. Kortan, and L. E. Brus, *J. Phys. Chem.* 97, 1224 (1993).
148. A. Fojtik and A. Henglein, *Chem. Phys. Lett.* 221, 363 (1994).
149. H. Kobayashi, A. T. Bell, and M. Shen, *Macromolecules* 7, 277 (1974).
150. H. K. Yasuda, in "Plasma Polymerization." Academic Press, Orlando, 1985.
151. J. Dutta, H. Hofmann, C. Hollenstein, and H. Hofmeister, in "Nanoparticles and Nanostructured Films" (J. H. Fendler, ed.). Wiley–VCH, Weinheim, Germany, 1998.
152. S. Li, S. J. Silvers, and M. S. El-Shall, *J. Phys. Chem. B* 101, 1794 (1997).
153. L. J. Brus, P. F. Szajowski, W. L. Wilson, T. D. Harris, S. Schuppler, and P. H. Cirtin, *J. Am. Chem. Soc.* 117, 2915 (1995).
154. M. S. El-Shall, S. Li, T. Turkki, D. Graiver, U. C. Pernisz, and M. E. Baraton, *J. Phys. Chem.* 99, 17805 (1995).
155. R. A. Bley and S. M. Kauzlarich, in "Synthesis of Silicon Nanoclusters" (J. H. Fendler, ed.). Wiley–VCH, Weinheim, Germany, 1998.
156. L. N. Skuja, A. N. Streletsky, and A. B. Pakovich, *Solid. State Commun.* 150, 1069 (1994).
157. B. Abeles and T. Tiedje, *Phys. Rev. Lett.* 51, 2003 (1983).
158. D. J. Lockwood, G. C. Aers, L. B. Allard, B. Bryskiewicz, S. Charbonneau, D. C. Houghton, J. P. McCaffrey, and A. Wang, *Can. J. Phys.* 70, 1184 (1992).
159. D. J. Lockwood, Z. H. Lu, and J.-M. Baribeau, *Phys. Rev. Lett.* 76, 539 (1996).
160. B. T. Sullivan, D. J. Lockwood, H. J. Labbé, and Z.-H. Lu, *Appl. Phys. Lett.* 69, 3149 (1996).
161. F. A. d'Avitaya, L. Vervoort, F. Bassani, S. Ossicini, A. Fasolino, and F. Bernadini, *Europhys. Lett.* 31, 25 (1995).
162. F. A. d'Avitaya, F. Bassani, I. Mihalcesu, and A. G. Nassiopoulos, in "Physics, Chemistry and Application of Nanostructures," p. 3. World Scientific, Singapore, 1997.
163. S. Sinharoy, *Thin Solid Films* 187, 231 (1990).
164. S. Schuppler, S. L. Friedman, M. A. Marcus, D. L. Adier, Y.-H. Xie, F. M. Ross, Y. J. Chabal, T. D. Harris, W. L. Brown, E. E. Chaban, P. F. Szajowski, S. B. Christman, and P. H. Citrin, *Phys. Rev. B* 52, 4910 (1995).
165. L. Vervoort, F. Bassani, I. Mihalcescu, J. C. Vial, and F. A. d'Avitaya, *Phys. Status Solidi B* 190, 123 (1995).
166. F. Bassani, S. Ménard, and F. A. d'Avitaya, *Phys. Status Solidi A* 165, 49 (1998).
167. G. Allan, C. Delerue, and M. Lanoo, *Phys. Rev. Lett.* 76, 2961 (1996).
168. R. J. Baierle, M. J. Caldas, E. Molinari, and S. Ossicini, *Solid State Commun.* 102, 545 (1997).
169. A. B. Filonov, A. N. Kholod, V. A. Novikov, V. E. Borisenko, L. Vervoort, F. Bassani, A. Saul, and F. A. d'Avitaya, *Appl. Phys. Lett.* 70, 744 (1997).
170. K. Maehashi, H. Nakashima, F. Bertram, P. Veit, and J. Christen, *Jpn. J. Appl. Phys.* 37, 39 (1998).
171. M. Tachikawa, T. Yamada, T. Sasaki, and H. Mori, in "Proceedings of the 24th State-of-the-Art Program on Compound Semiconductors," Los Angeles, 1996, p. 115.
172. J. M. Kuo, Y. C. Wang, K. W. Goossen, L. M. F. Chirovsky, S. P. Hui, B. T. Tseng, J. Walker, A. L. Lentine, R. E. Leibenguth, G. Livescu, W. Y. Jan, J. E. Cunningham, L. A. D'Asaro, A. Ron, D. Dahringer, D. Kossives, D. D. Bacon, R. L. Morrison, R. A. Novotny, D. B. Buchholz, and W. E. Mayo, *J. Cryst. Growth* 175–176, 971 (1997).
173. M. J. Jurkovic, J. Alperin, Q. Du, W. I. Wang, and M. F. Chang, *Electron. Lett.* 33, 1658 (1997).

174. J. Liang, P. Li, Y. Gao, and J. Zhao, *J. Mater. Sci.* 32, 4377 (1997).
175. J. R. Shealy, N. C. Macdonald, Y. Xu, K. L. Whittingham, D. T. Emerson, and B. L. Pitts, *Appl. Phys. Lett.* 70, 3458 (1997).
176. Z. L. Zhang and N. C. Macdonald, *J. Vac. Sci. Technol., B* 11, 437 (1993).
177. J. P. Spallas, J. H. Das, and N. C. Macdonald, *J. Vac. Sci. Technol., B* 11, 2538 (1993).
178. H. Ahmed, *J. Vac. Sci. Technol., B* 15, 2101 (1997).
179. D. Ali and H. Ahmed, *Appl. Phys. Lett.* 64, 2119 (1994).
180. Y. Takahashi, M. Nagase, H. Namatsu, K. Kurihara, K. Iwdate, Y. Nakajima, S. Horiguchi, K. Murase, and M. Tabe, *Electron. Lett.* 31, 136 (1995).
181. K. Kurihara, H. Namatsu, M. Nagase, and T. Takino, *Microelectron. Eng.* 35, 261 (1997).
182. K. Yano, T. Ishii, T. Hashimoto, T. Kobayashi, F. Murai, and K. Seki, *Techn. Digest Int. Electron Device Meeting* 541 (1993).
183. A. C. Seabaugh, C.-C. Cho, R. M. Steinhoff, T. S. Moise, S. Tang, R. M. Wallace, E. A. Beam, and Y.-C. Kao, in "2nd International Workshop on Quantum Functional Devices," Tokyo, 1995, p. 32.
184. K. Yuki, Y. Hirai, K. Morimoto, K. Inouse, M. Niwa, and J. Yasui, *Jpn. J. Appl. Phys.* 34, 860 (1995).
185. S. Y. Chou and A. E. Gordon, *Appl. Phys. Lett.* 60, 1827 (1992).
186. Q. Ye, R. Tsu, and E. H. Nicollian, *Phys. Rev. B* 44, 1806 (1991).
187. M. Hirose, M. Morita, and Y. Osaka, *Jpn. J. Appl. Phys.* 16, 561 (1977).
188. K. Matsumoto, M. Ishii, K. Segawa, Y. Oka, B. J. Vartanian, and J. S. Harris, *Appl. Phys. Lett.* 68, 34 (1996).
189. L. J. Geerlings, V. F. Anderegg, P. A. M. Holweg, J. E. Mooij, H. Pothier, D. Esteve, C. Urbina, and M. H. Devoret, *Phys. Rev. Lett.* 64, 2691 (1990).
190. K. Nakazato, R. J. Blaikie, J. R. A. Cleaver, and H. Ahmed, *Electron. Lett.* 29, 384 (1993).
191. K. Yano, T. Ishii, T. Hashimoto, T. Kobayashi, F. Murai, and K. Seki, *IEEE Trans. Electron Devices* ED4, 1628 (1994).
192. A. Dutta, M. Kimura, Y. Honda, M. Otobe, A. Itoh, and S. Oda, *Jpn. J. Appl. Phys.* 36, 4038 (1997).
193. M. Fukuda, K. Nakagawa, S. Miyazaki, and M. Hirose, *Appl. Phys. Lett.* 70, 2291 (1997).
194. A. Nakajima, T. Futatsugi, K. Kosemura, T. Fukano, and N. Yokoyama, *Appl. Phys. Lett.* 71, 353 (1997).
195. R. Tsu and L. Esaki, *Appl. Phys. Lett.* 22, 562 (1973).
196. A. Nakajima, T. Futatsugi, K. Kosemura, T. Fukano, and N. Yokoyama, *Appl. Phys. Lett.* 70, 1742 (1997).
197. L. Guo, E. Leobandung and S. Y. Chou, *Appl. Phys. Lett.* 70, 850 (1997).
198. L. Guo, E. Leobandung, L. Zhuang, and S. Y. Chou, *J. Vac. Sci. Technol., B* 15, 2840 (1997).
199. L. Guo, E. Leobandung, and S. Y. Chou, *Science* 275, 649 (1997).
200. C. S. Lent, P. D. Tougaw, W. Porod, and G. H. Bernstein, *Nanotechnology* 4, 49 (1993).
201. T. Tanamoto, R. Katoh, and Y. Naruse, *Jpn. J. Appl. Phys.* 33, 1502 (1994).
202. A. N. Korotkov, *Appl. Phys. Lett.* 67, 2412 (1995).
203. S. Bandyopadhyay, B. Das, and A. E. Miller, *Nanotechnology* 5, 113 (1994).
204. S. Lloyd, *Science* 261, 1569 (1993).
205. S. Bandyopadhyay and V. Roychowdhury, *Phys. Low Dimension. Syst.* 8/9, 29 (1995).
206. S. Bandyopadhyay and V. Roychowdhury, *Jpn. J. Appl. Phys.* 35, 3350 (1996).
207. T. H. P. Chang, L. P. Muray, U. Staufer, and D. P. Kern, *Jpn. J. Appl. Phys.* 31, 4232 (1992).
208. T. H. P. Chang, D. P. Kern, and L. P. Muray, *J. Vac. Sci. Technol., B* 6, 2743 (1992).
209. J. Y. Park, H. J. Choi, Y. Lee, S. Kang, K. Chun, S. W. Park, and Y. Kuk, *J. Phys. IV* C5, 258 (1996).
210. J. Y. Park, H. J. Choi, Y. Lee, S. Kang, K. Chun, S. W. Park, and Y. Kuk, *J. Vac. Sci. Technol., A* 15, 1499 (1997).
211. T. H. P. Chang, M. G. R. Thomson, E. Kratschmer, H. S. Kim, M. L. Yu, K. Y. Lee, S. A. Rishton, and B. W. Hussey, *J. Vac. Sci. Technol., B* 14, 3774 (1996).
212. M. R. Rakhshandehroo and S. W. Pang, *J. Vac. Sci. Technol., B* 15, 2777 (1997).
213. M.-Y. Jung, D. W. Kim, S. S. Choi, Y.-S. Kim, Y. Kuk, K. C. Park, and J. Jang, *Thin Solid Films* 294, 157 (1997).
214. G. Stix, *Scientific American* 77 (February 1995).
215. S. Madsen, S. I. Bozhevolvyi, K. Birkelund, M. Müllenborn, J. M. Hvam, and F. Grey, *J. Appl. Phys.* 82, 493 (1997).
216. L. A. Nagahara, P. I. Oden, A. Majumdar, J. P. Carrejo, J. Graham, and K. Alexander, *Proc. SPIE* 1639, 171 (1992).
217. S. C. Minne, H. T. Soh, P. Flueckiger, and C. F. Quate, *Appl. Phys. Lett.* 66, 703 (1995).
218. G. C. Abeln, T. C. Shen, J. R. Tucker, and J. W. Lyding, *Microelectron. Eng.* 27, 23 (1995).
219. J. A. Dagata, J. Scheir, H. H. Harary, C. J. Evans, M. T. Postek, and J. Bennett, *Appl. Phys. Lett.* 56, 2001 (1990).
220. J. W. Lyding, T.-C. Shen, J. S. Hubacek, T. R. Tucker, and G. C. Abeln, *Appl. Phys. Lett.* 64, 2010 (1994).
221. K. Birkelung, E. V. Thomsen, J. P. Rasmussen, O. Hansen, P. T. Tang, P. Møller, and F. Grey, *J. Vac. Sci. Technol., B* 15, 2912 (1997).
222. E. S. Snow, W. H. Juan, S. W. Pang, and P. M. Campbell, *Appl. Phys. Lett.* 66, 1729 (1995).
223. E. S. Snow, P. M. Campbell, and B. V. Shanabrook, *Appl. Phys. Lett.* 63, 3488 (1993).

This Page Intentionally Left Blank

Chapter 6

SEMICONDUCTOR NANOPARTICLES

Prashant V. Kamat

Notre Dame Radiation Laboratory, Notre Dame, Indiana, USA

Kei Murakoshi, Yuji Wada, Shizo Yanagida

Chemical Process Engineering, Faculty of Engineering, Osaka University, Suita, Osaka, Japan

Contents

1. Introduction 292
2. Preparation and Characterization 293
   2.1. Size Control 293
   2.2. Crystalline Phase Control 294
   2.3. Size Quantization Effects 296
   2.4. Nonlinear Optical Properties 297
   2.5. Emission Characteristics 297
   2.6. Trapping of Charge Carriers 298
3. Interfacial Charge Transfer Processes in Colloidal Semiconductor Systems 299
   3.1. Reductive Process 300
   3.2. Oxidative Process 300
   3.3. Kinetics of Interfacial Electron Transfer 301
4. Photocatalytic Applications 303
   4.1. Organic Synthesis 304
   4.2. Fixation of Carbon Dioxide into Organic Compounds 304
   4.3. Reduction of Nitrogen 308
   4.4. Decomposition of Nitrogen Oxides and Their Anions 308
   4.5. Photocatalytic Degradation of Organic Contaminants 308
5. Surface Modification of Semiconductor Colloids 309
   5.1. Deposition of Metals on Semiconductors 309
   5.2. Capping with Organic and Inorganic Molecules 310
   5.3. Surface Modification with Sensitizing Dyes 312
   5.4. Ultrafast Charge Injection into Semiconductor Nanocrystallites 314
   5.5. Designing Multicomponent Semiconductor Systems 315
6. Ordered Nanostructures using Semiconductor Nanocrystallites and Their Functionality 318
   6.1. Preparation and Characterization of Nanostructured Semiconductor Films 319
   6.2. Electron Storage and Photo- and Electrochromic Effects 322
   6.3. As a Photosensitive Electrode 323
   6.4. Sensitization of Large-Band-Gap Semiconductors 325
   6.5. Single-Electron Tunneling Devices 327
7. Concluding Remarks 329
   Acknowledgments 329
   References 329

Handbook of Nanostructured Materials and Nanotechnology, edited by H.S. Nalwa
Volume 3: Electrical Properties
Copyright © 2000 by Academic Press
All rights of reproduction in any form reserved.
ISBN 0-12-513763-X/$30.00

1. INTRODUCTION

The multidisciplinary research of semiconductor nanoclusters has witnessed exceptional growth during the past decade. A basic understanding of the photophysical and photochemical properties gained from colloidal semiconductor research is beneficial in the design and development of nanostructured semiconductor materials for practical applications. A great deal of attention has been focused on understanding the properties of nanostructured semiconductor systems because of their practical applications in solar energy conversion and photocatalytic degradation of organic contaminants. Some other applied areas, which can benefit from nanostructured semiconductor technology, are chemical sensors, electrooptics, microelectronics, imaging science, and photovoltaics. Possible applications that make use of the unique properties of semiconductor nanoclusters are illustrated in Figure 1.

By making use of the principles of photoelectrochemistry, several semiconductor systems comprised of native and surface-modified semiconducor nanoparticles have been employed in the direct conversion of light energy into chemical or electrical energy [1–5]. The term colloid refers to ultrasmall particles with a particle diameter less than 100 nm with the ability to suspend in an aqueous or nonaqueous medium. These are also referred as Q particles, nanoclusters, nanoparticles, or nanophase materials. Under band gap excitation, these semiconductor nanoparticles act as short-circuited microelectrodes and initiate the oxidation and reduction processes of the adsorbed substrate. Alternatively, an adsorbed molecule can inject charge from its excited state into the semiconductor particle and the sensitizer can be regenerated with a redox couple. This process, which is commonly referred to as photosensitization, is extensively used in photoelectrochemistry and imaging science. The application of semiconductor systems in initiating and controlling various photocatalytic processes has been reviewed recently by several researchers [5–18]. Elucidation of the photophysical properties of the semiconductor colloids and the dynamics of the interfacial processes at the semiconductor–electrolyte interface has also been reviewed by many researchers [11, 19–46].

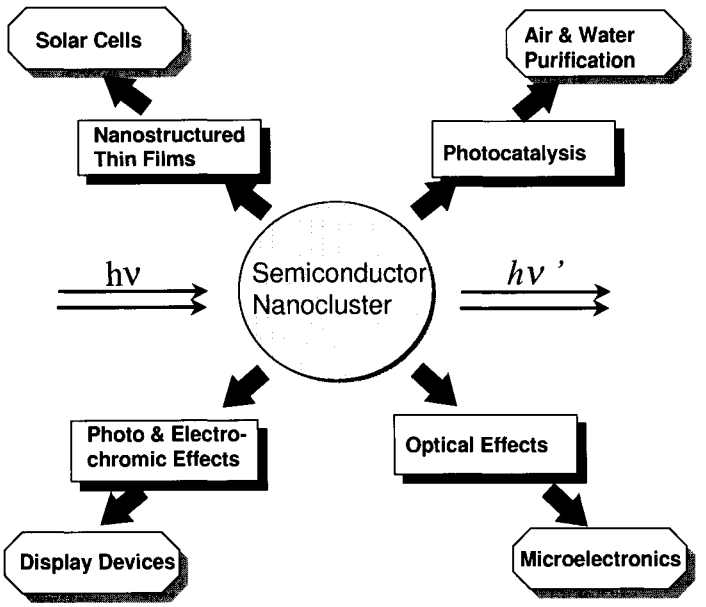


Fig. 1. A diversifying area of semiconductor nanocluster research.

2. PREPARATION AND CHARACTERIZATION

2.1. Size Control

Several approaches have been considered to prepare size-controlled semiconductor nanocrystallites with narrow size distribution. Many of these preparation methods of the size-controlled nanocrystallites control the growth process by using stabilizers such as thiols [47–65], phosphate [22, 66], and phosphine oxide [67] and restricting the reaction space in matrices such as zeolites [68–76], glasses [71, 77–79], polymers [70, 80–84], reverse micelles [85–92], vesicles [93–102], LB films [103–112], multilayer film [113, 114], xerogels [115], β-cyclodextrin [116, 117], and silica [118, 119]. Each step in the growth process, for example, nucleation, growth (propagation), and ripening, can be controlled by changing the preparation conditions, such as the choice of the starting materials and media (solvents), composite ratios of the reactants, and preparation temperature and time. These synthetic methods for the smaller nanocrystallites (clusters) were much more successful in the preparation and characterization of thiol-capped CdS clusters. Highly purified clusters form single crystals of $(Cd_{10}S_4(SC_6H_5)_{16})^{4-}$ [120], $(Cd_{17}S_4(SC_6H_5)_{28})^{2-}$ [121], $Cd_{17}S_4(SCH_2CH_2OH)_{26}$ [122], $Cd_{32}S_{14}(SCH_2CH(OH)CH_3)_{36}\cdot 4H_2O$ [123], and $Cd_{32}S_{14}(SC_6H_5)_{24}\cdot 4DMF$ [124], which can be used as model compounds of the smallest CdS nanocrystallites. Nosaka et al. [49] reported size control of colloidal CdS nanocrystallites by changing concentration of the surface stabilizer (C_2H_5SH) in a reaction bath. Henglein and co-workers also reported the dependence of CdS size on concentration of long-chain alkanethiols at the stage of nucleation and growth of the nanocrystallites [52].

Apart from chemical precipitation and hydrolysis of suitable precursors, several other methods have also been considered in the synthesis of semiconductor colloids by chemical methods [11, 125–127]. Electrochemical and photoelectrochemical etching of silicon wafers can yield porous film composed of nanostructured silicon [128, 129]. Some other techniques such as radiolysis [11, 45, 51, 130–136] and sonolysis [137] have also been employed. Sonochemical formation of Q-CdS colloids and dissolution of larger colloidal CdS particles has also been attempted by Grieser and co-workers [138].

Despite these various attempts to control the size and shape of the nanoclusters, two crucial problems still remain as challenging issues. (i) The size distributions of nanocrystallites prepared by the previous methods are not monodisperse (standard deviation more than 10%). A relatively narrow size distribution (standard deviation ~8%) has been achieved in the preparation of CdS nanocrystallites in vesicles of phosphatidylcholine [101]. (ii) The use of stabilizers or confined matrices often yield byproducts, such as metal–thiolate complexes, which makes it difficult to quantitatively assess the microscopic structure of nanocrystallites.

Efforts have been made to narrow the size distribution by size fractionation using exclusion chromatography [139–141] and capillary zone electrophoresis [141–144]. The separation in electrophoresis is based on the fact that the charge-to-size ratios are different for different size particles. Size-selective precipitation [48, 67] or photocorrosion has also been considered to minimize the dispersity in particle size [145, 146]. Yoneyama et al. [145] applied the method of size-selective photocorrosion using monochromatic light irradiation. Narrower size distribution of CdS nanoparticles was achieved by irradiating light whose wavelength was close to the absorption onset of nanocrystallites in air-saturated sodium hexametaphosphate solution [145]. Photocorrosion of CdS nanocrystallites using Ar ion laser irradiation was also useful in preparing smaller nanocrystallites [146]. Recently, Murakoshi et al. [147] reported the size control of CdS nanocrystallites over the range from 1.8 to 4.2 nm while keeping the *hexagonal* crystalline structure by varying the sulfur source (H_2S and Na_2S) and by regulating the preparation temperature. Strongly terminating sulfur species stabilize the nanocrystallites, thus leading to the formation of smaller size particles even in the absence of any stabilizers or matrices. Bawendi and co-workers [67] have recently adopted a novel approach of synthesizing size-controlled CdSe nanocrystallites of

highest monodispersity (standard deviation less than 5%). Although these methods are useful for the size control of semiconductor nanocrystallites, further development of a novel and simple preparation method that excludes chemical capping or host matrices would be the topic of future research efforts.

2.2. Crystalline Phase Control

II–VI semiconductor bulk materials, such as CdS and ZnS, are well known to have two crystalline structures, cubic (zincblende) and hexagonal (wurtzite) types. For the bulk materials, CdS has highly stable hexagonal phase from room temperature to the melting point (1750 °C) [148], while bulk ZnS has the cubic structure. Because the difference in the crystalline structure of the bulk semiconductor materials leads to considerable change in the effective masses of e and h in their electronic bands [149], the crystalline structure of semiconductor nanocrystallites should play a dominant role in determining their photochemical, photocatalytic, and photophysical properties.

The crystalline structure of nanocrystallites is largely influenced by the preparation conditions. Although the hexagonal phase is the most stable phase of CdS, for example, only a few reports on the preparation of *hexagonal* CdS nanocrystallites have been published [48, 67, 150–153]. *Hexagonal* CdS nanocrystallites can be prepared by reacting Cd^{2+} and S^{2-} (H_2S or Na_2S) in *N,N*-dimethylformamide (DMF) without using any surface stabilizers [147]. The mean diameter of CdS nanocrystallites can be rigorously controlled over the range from 1.8 to 4.2 nm by varying the sulfur source (H_2S and Na_2S) and by controlling the reacton temperature (Figs. 2 and 3). In these studies, the use of Na_2S as a sulfur source produces smaller CdS nanocrystallites than those prepared using H_2S. The size control and stability of CdS nanocrystallites are discussed in terms of the surface structures that were elucidated using *in situ* Cd K-edge extended X-ray absorption fine structure (EXAFS) analysis. The strong terminal binding of the sulfur atoms to the surface cadmium atoms resulted in the weaker solvation of DMF molecules and the controll of their size and crystalline phase.

Phase transformation of semiconductor nanocrystallites can be used to obtain a desirable crystalline structure [44]. The phase transition of semiconductor nanocrystallites can

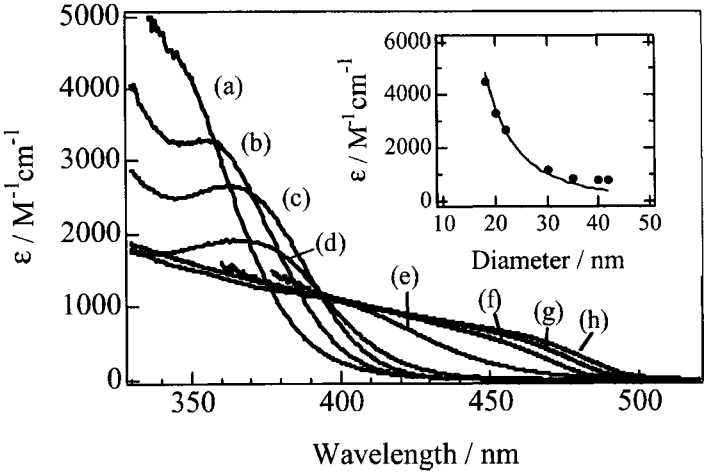


Fig. 2. Room temperature absorption spectra of CdS–Na_2S, which were prepared at (a) −40 °C, (b) −20 °C, (c) 0 °C, (d) 30 °C, and (e) 60 °C. Those of CdS–H_2S were prepared at (f) 0 °C, (g) 30 °C, and (h) 60 °C. The inset shows the dependence of the molar extinction coefficient on the size of CdS–H_2S and CdS–Na_2S. The experimental data were fitted in proportion to the inverse cube of the Bohr radius divided by the CdS radius $(a_B/R)^3$, $a_B = 26$ Å). (Source: Reprinted with permission from [147].)

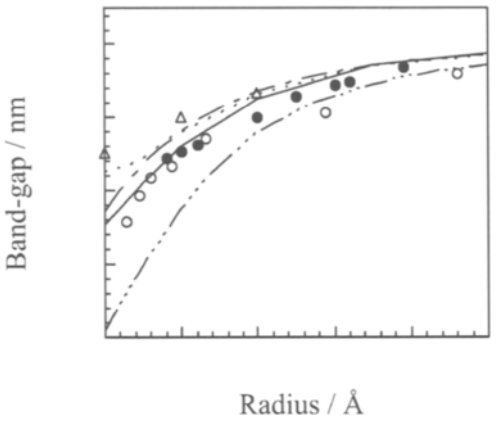


Fig. 3. Band gap dependence on the CdS radius. The experimental data are from this study (•), from Vossmeyer et al. (○), and from Herron et al. (△). The curves are predicted by the effective mass approximations with infinite (–···–) and finite potential well (–··–), and the pseudopotential calculations for hexagonal (—) and cubic CdS lattice (···). (Source: Reprinted with permission from [147].)

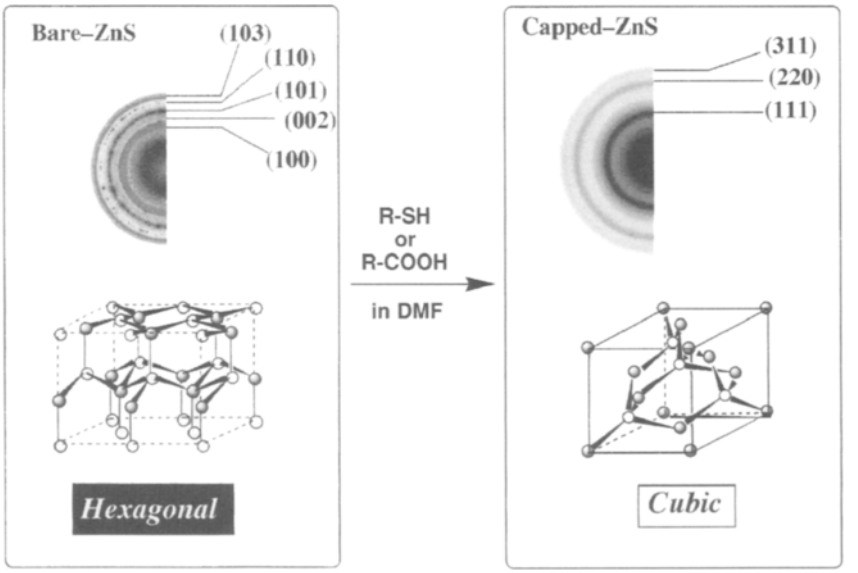


Fig. 4. Electron diffraction patterns of (a) ZnS–DMF and (b) ZnS–DMF combined with C_6F_5SH. (Source: Reprinted with permission from [158].)

be achieved under high temperature [154] and pressure [155–157]. Unfortunately, these extreme conditions often cause unexpected structural deformations, such as the growth of nanocrystallites and change of their chemical composition [154]. Alivisatos and co-workers carried out a four- to six-coordinate phase transformation of CdS [155] and CdSe [156, 157] nanocrystallites without altering their size or their chemical composition. The control of crystalline structures of quantum-confined semiconductor nanocrystallites was achieved at ambient temperature and pressure through the chemical modification of the ZnS nanocrystallite surface with organic molecules (Fig. 4) [158]. Pentafluorothiophenol, thiophenol, 1-decanethiol, 1-hexanethiol, benzoic acid, and cyanoacetic acid, which chemically bind to the surface of ZnS nanocrystallites, are capable of changing the hexagonal phase of ZnS nanocrystallites to the cubic. On the other hand, similar phase transitions

could not be observed with unreactive octanoic acid, acetic acid, and phenol, which do not bind to ZnS. The formation of the chemical bonding between surface zinc atoms of ZnS nanocrystallites and the added thiolate or carboxylate anion should lead to a change in the surface energy of ZnS nanocrystallites. This change in the surface energy could induce the phase transition from the metastable phase (hexagonal) to the stable phase (cubic) at ambient temperature and pressure. [The difference in the internal energy of ZnS between the hexagonal and the cubic phase is quite small (3.2 kcal mol^{-1})].

2.3. Size Quantization Effects

A great deal of attention has been focused on the transformation from solid-state electronic properties to molecular properties of various semiconductor nanoparticles [11, 34, 35, 39–41, 74, 149, 159–167]. These crystallites are molecular clusters in which complete electron delocalization has not yet occurred. Quantization in these ultrafine particles arises from the confinements of charge carriers in semiconductors with potential wells of small dimensions (less than the De Broglie wavelength of the electrons and holes). Under these conditions, the energy levels available for the electrons and holes in the conduction and valence bands become discrete. In addition to the very large effects on optical properties, size quantization also leads to major changes in the effective redox potential of the photogenerated carriers. Semiconductor particles that exhibit size-dependent optical and electronic properties are termed quantized particles (or Q particles) or semiconductor clusters. The particles with diameters greater than 150 Å typically behave as bulk semiconductors. However, similarly prepared crystallites of approximately 15–50 Å diameter that possess a bulk lattice structure differ considerably in electronic properties.

Size quantization effects have been experimentally demonstrated in various laboratories around the world by controlling the synthetic procedure and monitoring the size-dependent optical effects. A few representative examples include [11, 24, 25, 34–36, 40, 42, 49, 51, 52, 79, 133, 137, 139, 160–162, 164, 165, 168–207]. Optical effects caused by size quantization in layered-type semiconductors have also been reported [131, 170, 199, 200, 208, 209]. The absorption spectra of CdS colloids of various particle size are compared in Figure 5 [173]. The onset of absorption for larger colloids closely matches the absorption edge of bulk CdS. The absorption edge shifts to blue for smaller size particles as a result of the increase in the effective band gap.

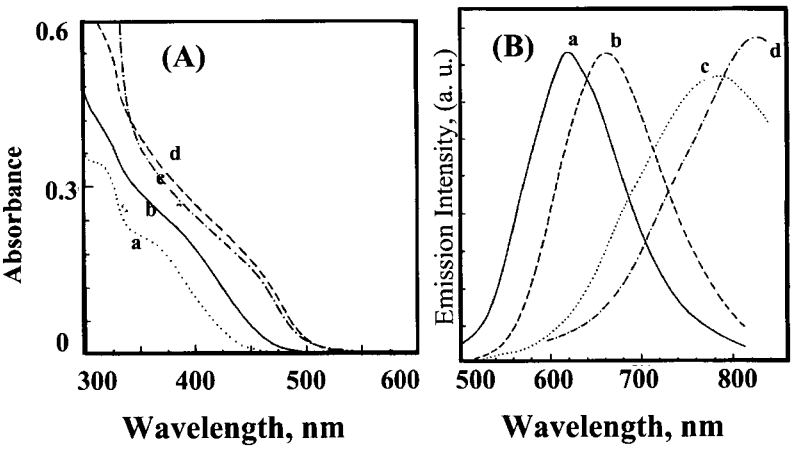


Fig. 5. (A) Absorption and (B) emission spectra of colloidal CdS in acetonitrile. The average particle diameters were, respectively, (a) <25, (b) 30, (c) 37, and (d) >42 Å. (Source: Reprinted with permission from [173]. © 1987 American Chemical Society.)

Brus [210, 211], Henglein [22, 24], Anderson [212], and Friesner [149] and co-workers have modified the quantum mechanical treatment to explain the various experimental results of wavelength threshold as a function of the diameter of CdS particles. A comparison of various models and the experimental results has been established. A plot of the wavelength of the onset of absorption versus the function of particle diameter seems to agree well with the proposed model [22, 24].

Size quantization effects on the optical properties of nanocrystalline silicon have been discussed by Brus and co-workers [36, 188, 213]. A comparison is made to explain the behavior of porous Si that is prepared from electrochemical etching. Nanocrystalline Si and porous Si are indirect-gap-type materials with oscillator strengths that are not markedly increased with respect to bulk Si. The indirect gap in these Si nanocrystallites can be as high as 1.0 eV. An enhanced luminescence is seen in these materials because of the spatial confinement of electrons and holes. Zunger and co-workers [214–217] have carried out theoretical modeling to elucidate the electronic structure of Si quantum dots and wires. The published work related to porous Si is quite vast and readers may refer to a recently published review article [218].

2.4. Nonlinear Optical Properties

Semiconductor nanoparticles as materials for generating nonlinear optical effects have drawn the attention of many researchers [219–227]. Photoinduced blue shifts in the absorption have been reported for the colloids of CdS [228–239], Cd_3P_2 [234], In_2S_3 [240], PbS [84, 171, 197, 241], CdSe [83, 242, 243], In_2Se_3 [244], FeS_2 [233], TiO_2 [177], and ZnO [206, 245, 246]. Such photoinduced blue shifts appear as a bleaching in the transient absorption spectrum. Transient absorption spectroscopy has been employed to probe the transient bleaching in CdS [236, 237, 247] and GaAs [248] colloids. Subpicosecond events in colloidal $Zn_{1-x}Cd_xS$ have been characterized by Ernsting et al. [247]. In the case of CdS/HgS/CdS colloids with a quantum dot–quantum well structure, the transient photobleaching follows spectrally the newly evolving 1s–1s electronic transition of the composite particles [249].

The observed transient bleaching in these nanoclusters was attributed to photophysical processes, such as the dynamic Burstein effect, increase in excitonic energy due to surface-trapped electrons, or Coulombic screening by photogenerated free carriers [230–232, 235–237, 250]. An alternate explanation based on the Stark effect has also been proposed recently. Charge separation occurs when semiconductor colloids are subjected to band gap excitation with a laser pulse. The intense electric field created as a result of photoinduced charge separation is likely to cause a blue shift in the band edge of these colloids. This effect has also been observed by depositing excess charge on CdS colloids or by applying an electric field to CdSe film [251, 252].

Third-harmonic generation in CdS-doped poly(vinyl alcohol) (PVA) film has also been investigated [253]. Wang and co-workers have extensively investigated the third-order optical nonlinearity in quantum-confined CdS clusters [219, 220]. They have demonstrated nonresonant third-order optical nonlinearity using third-harmonic generation from 1.91–0.64 μm. The nonlinearity increased with increasing cluster size. The intrinsic, nonresonant $\chi^{(3)}$ for 30- and 15-Å-diameter CdS clusters were 3.3×10^{-10} and 2.5×10^{-11} esu, respectively. The nonlinearity can be controlled by passivating the CdS surface with ammonia.

2.5. Emission Characteristics

Considerable attention has been given in recent years to the study of the emission behavior of various semiconductor colloids: ZnO [191, 206, 254–257], ZnS [98, 168, 258–260], CdSe [83, 243, 261–265], CdS [22, 57, 66, 71, 96, 98, 150, 173, 207, 229, 231, 238, 253,

257, 259, 260, 266–287], and MoS_2 [288]. Luminescence of porous silicon has also been the theme of a number of recent studies [36, 289–301]. Photoluminescence in semiconductors occurs when a photogenerated minority carrier recombines with a previously existing majority carrier. Hence, emission measurements give valuable information regarding the nature of surface states and the recombination of charge carriers. The analysis of luminescence decay gives important information on the kinetic and mechanistic details of charge carrier recombination in colloidal semiconductors. The photophysical properties of II–VI semiconductor nanoclusters have been extensively investigated in this regard. The emission spectra of CdS colloids recorded under steady-state irradiation excitation are shown in Figure 5. Under steady-state irradiation conditions, red emission appears as a result of sulfur vacancies. The emission maximum is dependent on the particle size and is blue-shifted in smaller size particles. The short-lived excitonic emission can be seen when a high concentration of charge carriers is attained with laser excitations. The excitonic emission has been considered to arise via detrapping of electrons. The traps work as a reservoir for electrons and thus contribute to the delayed emission [143]. With decreasing temperature, an increase in the intensity and a blue shift in the maximum have been observed for the Q-CdS excitonic band. A thermal repopulation phenomenon is also investigated by monitoring band edge luminescence in CdS Q-particles [276, 277, 302]. A similar size-dependent shift in the excitonic emission band at 77 K has been observed for quantized PbI_2 particles embedded in porous silica films [209]. Emission spectroscopy has also been used to resolve the spectra of quantization effects in CdS- [303] and CdTe-doped glasses [304].

A model that involves strong resonance between three-dimensional quantized internal states and the intrinsic surface states because of reconstruction has also been outlined by Brus and co-workers [262, 305]. Time, wavelength, and polarization resolution of the emission indicate a complex kinetics for the band edge luminescence in 32-Å-diameter CdSe particles. A strong resonant mixing between the standing wave molecular orbital delocalized inside the crystallite and the intrinsic surface Se lone pair states has been postulated.

2.6. Trapping of Charge Carriers

Semiconductor nanoclusters synthesized from a common bench top recipe contain a high density of defect sites, usually at the semiconductor surface, and the nature of these defect sites depends strongly on the method of chemical synthesis. Upon optical excitation, the free carriers get trapped at the defect sites and these trapped charge carriers undergo further radiative and radiationless recombination:

$$TiO_2 + h\nu \rightarrow TiO_2\left(e^-_{CB} + h^+_{VB}\right) \quad (1)$$

$$e^-_{CB} \rightarrow e^-_{tr} \quad (2)$$

$$h^+_{VB} \rightarrow h_t \quad (3)$$

where e_{CB} and h_{VB} are the free charge carriers in the conduction and valence bands and e_t and h_t are the trapped electrons and holes, respectively. Such an accumulation of charges in the minute reaction space of a semiconductor colloid is important in improving the efficiency of interfacial redox reactions.

Bard and co-workers [306–308] demonstrated the effect of charge trapping on the photoelectrochemical properties of TiO_2 particles under illumination. They carried out electrophoretic and photocurrent measurements in the presence and absence of electron acceptors. A buildup of negative charge on the TiO_2 particles under illumination was observed when reducible species were excluded. The dynamics of charge carrier trapping, recombination, and photophysical processes have been studied by several researchers [143, 236, 238, 268, 302, 309–334]. These trapped charge carriers exhibit characteristic absorption bands in the infrared (IR) and ultraviolet (UV) regions. These absorption bands have also been independently confirmed from radiolysis and electrochemical experiments [335].

By selectively scavenging the photogenerated holes in a semiconductor colloid, it is possible to monitor the behavior of trapped electrons. Electron paramagnetic resonance (EPR) studies of photoexcited anatase TiO_2 particles have shown that the photogenerated electrons are trapped at Ti^{4+} sites within the bulk [336–338]. Electron trapping in ZnO [206], WO_3 [183], and SnO_2 [339] colloids has been investigated by laser flash photolysis. Similarly, trapped electrons in colloidal metal chalcogenides such as CdS undergo chemical changes by reacting with Cd^{2+} sites. Zhang and co-workers [326, 340] and Bowman and co-workers [332] have concluded that the electron trapping in TiO_2 and CdS colloids occurs in the range of 90 to 180 fs. A mechanism that allows for slower electron transport via surface trap-to-trap hopping has been considered in these studies.

The basic hydroxide groups at the surface of TiO_2 can be considered deep traps for valence band holes. Although the majority of these trapped holes recombine with conduction band and trapped electrons, a small fraction of O^- undergoes dimerization at the surface to form stable titanium peroxide. An indirect method of hole trapping was achieved in this study by reacting TiO_2 colloids with pulse radiolytically generated $OH^\bullet$ radicals. The transient spectrum recorded after irradiation of aqueous colloidal TiO_2 suspension with electron pulse showed an absorption band with onset at 470 nm and a maximum around 350 nm. A slightly red-shifted band ($\lambda_{max} = 420$ nm) has also been observed in UV-irradiated TiO_2 colloids [309, 323]. Electron spin resonance studies have identified these trapped holes as oxygen anion radicals covalently bound to titanium ions, Ti^{IV}–O–Ti^{IV}–$O^\bullet$ [338, 341–344]. Time-resolved microwave conductivity measurements have also been carried out to probe the electronic processes in semiconductor materials [315, 330, 345–351]. Based on the analysis of luminescence decay, Brus has estimated that hole localization on the CdSe surface occurs within 150 fs [305].

The chemical changes associated with trapping of charge carriers in CdS, PbS, and CdSe have also been time resolved [238, 241, 268, 318, 352]. The observed growth in the absorption band at wavelengths greater than 460 nm is attributed to the formation of S^- at the CdS surface, the identity of which has been confirmed earlier by pulse radiolysis measurements [192].

3. INTERFACIAL CHARGE TRANSFER PROCESSES IN COLLOIDAL SEMICONDUCTOR SYSTEMS

The principle of electron and hole transfer at the photoexcited semiconductor particle has already been described in Figure 6. Both free and trapped charge carriers participate in these interfacial redox processes. By decreasing the particle size, it is possible to shift the conduction band to more negative potentials and the valence band to more positive

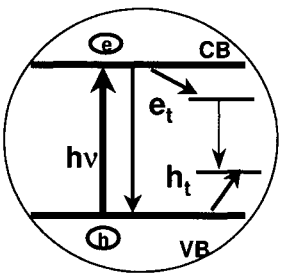


Fig. 6. Photoinduced charge transfer processes in a semiconductor particle. E_{CB} and E_{VB} correspond to the conduction and valence bands, and e_t and h_t correspond to trapped electrons and trapped holes, respectively. These charge carriers are responsible for the interfacial redox processes.

potentials as a result of quantization effects. Hence, redox processes that cannot occur in bulk materials can be facilitated in quantized semiconductor particles.

3.1. Reductive Process

In the early years, semiconductor nanoparticles were extensively employed in water-splitting reactions [7, 353–357]. Although this area still continues to draw the attention of several scientists [358–364], recent studies have focused on the mechanistic and kinetic study of the interfacial charge transfer processes. Laser flash photolysis has been extensively employed to probe the reduction of viologen in colloidal TiO_2 [23, 75, 309, 354, 365–377] and metal chalcogenide [62, 173, 195, 240, 242, 378–386] systems. The reduction of several organic dyes in various colloidal semiconductor systems has also been investigated. Some of these dye reductions include thiazine [387], oxazine [388], phenoxazine [389], squaraine [390], and azo [391, 392] dyes. Band gap excitation of the semiconductor leads to one-electron reduction of the dye to yield a semireduced dye, which then disproportionates to yield a two-electron reduction product (leuco dye). Recently, one-electron reduction of fullerenes (C_{60} and C_{70} [393–396], C_{76} and C_{78} [397], and C_{84} [398]) has been carried out in ZnO and TiO_2 colloidal suspensions. The anion formed as a result of direct reduction of fullerene at the excited semiconductor colloid surface has been monitored with both steady-state and laser flash photolysis experiments. The energetics of the conduction band and the redox couple act as a driving force for heterogeneous electron transfer at the semiconductor colloid.

The reduction of oxygen in a semiconductor suspension plays an important role in photocatalytic applications [399]. The formation of $O_2^{-\bullet}$ has recently been confirmed from chemiluminescence measurements [400]. $O_2^{-\bullet}$ was deactivated mainly by an electron transfer to surface defects or vacancy sites on the TiO_2 surface.

The simple double and triple bonds can be photocatalytically hydrogenated with Pt-loaded TiO_2 using alcohol as an electron donor [401]. TiO_2 can be also used as an electron donor for asymmetric reduction of carbonyl compounds with chiral Rh(I) complexes as an electron mediator [402]. Photoreduction of aldehydes [403], and Shiff bases [404] in TiO_2 suspensions have also been reported. Photolysis of dimethyl maleate in deuterated methanol revealed that CdS nanocrystallites catalyze sequential two-electron-transfer photoreduction, affording deuterated dimethyl succinate [405].

Under visible-light-induced photolysis, the methanolic CdS suspension becomes brown owing to the reduction of lattice Cd^{2+} to Cd^0 (metallic Cd). The effective formation of alcohols from ketones and dihydro compounds from alkenes has been observed as a result of this reduction step. The presence of excess sulfide ions (S^{2-}) in the CdS nanocrystallite system, however, suppresses the formation of lattice Cd^0. The photogenerated lattice Cd^0 can also function as the active site for the two-electron reduction [406]. The relationship between light intensity and product distribution has been investigated in the case of the photocatalytic reduction of nanoscale CdS nanocrystallites. The yield of one-electron reduction products increases with decreasing light intensity. Cd^0 formation is proportional to the square of the relative light intensity. Consequently, the chemoselectivity in the photocatalysis using nanoscale CdS depends on the amount of Cd^0 formation, which, in turn, is controlled by the excitation light intensity [407].

3.2. Oxidative Process

Photogenerated holes can be utilized to oxidize adsorbed substrates at the semiconductor surface. The oxidation of halide ions has been investigated in various colloidal semiconductor suspensions by laser flash photolysis [173, 240, 367, 408, 409]. The energetics of the semiconductor valence band and the oxidation potential of the redox couple influence the photocatalytic oxidation. For example, the enhancement in the efficiency of halide oxidation at TiO_2 follows the sequence $Cl^- < Br^- < I^-$, correlating with the decrease in the

oxidation potential [367, 408]. Shifting the valence band of TiO_2 shifts to more positive potentials, by decreasing the pH and thus results in the enhancement of quantum efficiency of halide oxidation. The femtosecond dynamics of the oxidation of SCN^- has been investigated recently in a colloidal TiO_2 system [410]. These studies confirm the previous finding that the surface complexation between SCN^- and TiO_2 plays an important role in the efficient charge transfer at the semiconductor interface.

The oxidation of several other organic compounds such as 2-propanol [388, 411], diethyldithiocarbamate [412], and methyl orange [413] in colloidal semiconductor suspensions has also been investigated. The oxidation of the N_3^- to the $N_3^\bullet$ radical in CdS and ZnO suspensions has been investigated by the ESR spin-trapping the technique using phenyl-tert-butylnitrone (PBN) as a spin trap [414]. Draper and Fox [372, 415] have employed a diffuse reflectance laser flash photolysis technique to elucidate the mechanism of oxidation of several inorganic and organic compounds in TiO_2 particulate systems. Becker and co-workers [416] have discussed the factors that control the photocatalytic oxidations in nonaqueous media.

By simultaneously capturing holes and electrons at the semiconductor surface, it is possible to decrease the charge recombination and thus enhance the quantum yield of the charge transfer process [367, 417]. The importance of back reaction suppression for improving the quantum efficiency of charge transfer has been illustrated by Curran and Lamouche [418]. They have presented a kinetic model to derive the quantum efficiency based on the particle radius, the Faradaic rate constants, and the diffusion length in the semiconductor.

3.3. Kinetics of Interfacial Electron Transfer

The kinetic analysis of heterogeneous electron transfer in colloidal semiconductor systems is often complex and it is difficult to apply a generalized kinetic expression for these photocatalytic reactions. Lewis [419] has used both steady-state (equilibrium) and pulsed (nonequilibrium) experimental data to propose a unified kinetic model for heterogeneous electron transfer at the semiconductor interface. A more detailed discussion on the kinetic aspects of interfacial electron transfer has been presented in a recent review article [167]. Apart from the energetics of the conduction band of the semiconductor and the redox potential of the acceptor, factors such as the surface charges of the colloids, adsorption of the substrates, participation of surface states, and competition with charge recombination influence the rate of heterogeneous charge transfer at the semiconductor interface. This fact is evident from the widely differing rates of experimentally observed charge transfer in various colloidal semiconductor systems. (The time scale reported for charge transfer varies from picoseconds to milliseconds under different experimental conditions in various laboratories.) In general, interfacial charge transfer can be classified into two categories: static and dynamic quenching processes.

The static process dominates when the electron acceptor (or donor) substrate is adsorbed strongly on the semiconductor surface. Electron transfer under these conditions is rapid and directly competes with charge recombination. Both the adsorption equilibrium and the quick removal of the product from the surface is important in controlling the efficiency of charge transfer. Laser flash photolysis has been employed to probe the ultrafast charge transfer between an excited semiconductor colloid and the adsorbed substrate [310, 318, 323, 420–423]. The time-resolved transient absorption spectra recorded in a picosecond laser flash photolysis of a CdS–ZV system have indicated the rise time of $ZV^{\bullet -}$ formation to be less than 20 ps. The rate constant for the interfacial electron transfer is thus expected to be greater than $5 \times 10^{10}\ s^{-1}$. This estimate is in good agreement with the value ($k = 2$–$5 \times 10^{10}\ s^{-1}$) proposed by Rossetti and Brus [424] in their picosecond resonance Raman experiments. Such a large value of the rate constant indicates the interfacial electron transfer from the photoexcited CdS to the adsorbed viologen as rapid. Strong adsorbate–adsorbent interaction is essential to carry out the reduction process.

A major fraction of $ZV^{\bullet -}$ decayed within 500 ps as a result of its reaction with trapped holes (or S^{-}_{surf}). A fraction of $ZV^{\bullet -}$ survives as it diffuses away from the surface. Negatively charged Nafion, which is used to stabilize the colloids, drives away $ZV^{\bullet -}$ from the particle surface by electrostatic repulsion. The role of the ionic charge of the polymeric stabilizer in influencing the rate of heterogeneous electron transfer has been studied recently [385, 425–427]. The influence of electrostatic interaction on the stabilization of the viologen radical in negatively charged TiO_2-coated SiO_2 colloids [426] and functionalized polymeric systems [428] has also been discussed. The conditions for carrying out efficient redox processes on a semiconductor particle have been discussed by Gerischer [429, 430]. A large increase in the reduction efficiency can be achieved by locally contacting the particles with suitable metals, owing to the formation of an accumulation layer at this contact.

Similar static processes can also be observed in hole transfer processes. For example, the formation of $(SCN)^{\bullet -}_2$ was completed within the laser pulse duration as a result of the association of SCN^- with TiO_2 [417]. Scavenging of holes by SCN^- had a marked effect on the reduction of tetranitromethane [367] and oxazine dyes [417] at the TiO_2 colloidal particle. Simultaneous capture of holes and electrons at the TiO_2 surface with suitable scavengers enhanced the efficiency of interfacial charge transfer by a factor of 2. The holes trapped at the TiO_2 surface have been shown to survive for a long duration [309, 310, 343, 344, 394]. Surface complexation of colloidal TiO_2 by monodentate and bidentate benzene derivatives can enhance the interfacial electron transfer to methyl viologen [431]. The oxidation of diethyldithiocarbamate anion ($NCEt_2S^-_2$) in colloidal CdS suspension has been investigated [318, 412] to resolve the kinetic components arising from the reactions of the valence band and trapped holes.

The formation of $Et_2NCS^{\bullet}_2$ following the laser pulse excitation of CdS colloids was monitored from its absorption band at 600 nm. The rate constants for these two processes were estimated to be greater than 5×10^{10} s^{-1} and approximately 10^{10} s^{-1}, respectively. Only a small fraction (~15%) of $NCEt_2S^{\bullet}_2$ decayed during the time period of 1 ns probably by reacting with trapped electrons, and the rest underwent dimerization as it diffused away from the CdS surface ($k = 4.6 \times 10^9$ M^{-1} s^{-1}) [412].

Dynamic electron transfer is observed when the adsorption between the electron acceptor (or donor) molecules and the semiconductor colloid is poor. Under these conditions, the substrate molecules have to diffuse from solution to the semiconductor surface to accept the charge. Because photogenerated charge carriers undergo rapid charge recombination, it is necessary to accumulate one of the charges (electrons or holes) within the semiconductor particle. By employing sacrificial electron donors (e.g., alcohols) or electron acceptors (O_2), it is possible to accumulate electrons or holes within the semiconductor particles as trapped charge carriers. The kinetics of dynamic charge transfer is controlled by factors such as particle size, surface charge, and the thermodynamic driving force for the charge transfer.

One of the initial demonstrations, of dynamic charge transfer involved the reduction of tetranitromethane [367] and methyl viologen [354] in aqueous TiO_2 sols stabilized with polyvinyl alcohol. Recently, it has been possible to carry out a systematic kinetic study of heterogeneous electron transfer to several dyes from excited WO_3 colloids [183]. The efficiency of electron trapping in these colloids was very high ($\phi = 0.5$) as the holes were quickly scavenged by a sacrificial electron donor, oxalic acid. Dyes such as thionine could easily be reduced in excited WO_3 suspension. The bimolecular rate constants were determined by monitoring the pseudo-first-order growth of the dye anion radical, k_d, at various dye concentrations and by the expression

$$k_d = k_0 + k_{et}\,(\text{dye}) \tag{4}$$

The rate constants for the heterogeneous electron transfer, k_{et}, can be obtained from the slope of a straight-line plot of k_d versus dye concentration. The rate constants, k_{et}, which

vary from 0.7–2.4 $\times$ 10^9 M^{-1} s^{-1}, are close to the value for a diffusion-controlled electron transfer reaction. Because the reduction potential of these dyes is positive compared to the flat band potential of WO_3, we expect ΔG to be sufficiently negative to drive the electron transfer by a diffusion-controlled process.

Albery and Bartlett [432, 433] and Grätzel and Frank [434] have shown that the effective second-order rate constant, k_E (cm^3 mol^{-1} s^{-1}), was related to the electrochemical rate constant, k_{et}, as follows:

$$k_E = 4\pi r^2 N k_{et} \tag{5}$$

where r is the radius and N is Avagadro's number. The larger particles are expected to react faster than the smaller particles because of the dependence of the electron transfer rate constant on the surface area. Thus, the discrete range of particle sizes in a colloidal semiconductor system leads to the multiexponential kinetic behavior of the heterogeneous electron transfer because k_{et} is dependent on the particle size. Albery and co-workers [433, 435–437] have proposed a general model that considers a Gaussian distribution of the logarithm of the rate constant about some mean and the width of the distribution as an additional parameter. In the case of colloidal semiconductors, the dispersion in the kinetic transients is caused by the dispersion in the radii. Good agreement for the radial dispersion between the value found from dynamic light scattering and the value found from kinetic analysis has been demonstrated for colloidal semiconductor systems.

However, Darwent and co-workers [23] and Meisel and co-workers [438] have shown that the potential distribution around colloidal oxides coupled with the charge of the reducing species could significantly affect the rate of electron transfer to and from the colloid. Thus, while investigating pH dependence, it is necessary to consider both the thermodynamic driving force and the electrostatic effects. The observed electrochemical rate constant, k_{et}, can be related to the surface charge by the expression,

$$\log k_{et} = \log k_{et}^0 + \alpha n(\text{pH–PZZP}) \tag{6}$$

where k_{et}^0 is the electrochemical rate constant when the surface charge is zero and PZZP is the point of zero ζ potential. Such a model can explain the deviation of results from monoexponential kinetic behavior in several other studies. Good agreement between the calculated rate constants based on electrophoretic data and the experimentally obtained rate constant for the electron transfer between $ZV^{\bullet -}$ (and $MV^{+\bullet}$) and iron (III) oxide colloids at various pH values has been demonstrated in these studies. The manipulation of the surface potential by control of the pH and ionic strength can improve the efficiency of charge transfer processes.

4. PHOTOCATALYTIC APPLICATIONS

In one of the early articles in 1955, Markham [439] pointed out the photocatalytic properties of zinc oxide, titanium oxide, and antimony trioxide with UV irradiation [439]. In aqueous solutions, the holes are scavenged by surface hydroxyl groups to generate $^{\bullet}OH$ radicals that then promote the oxidation of organics [338, 341–344]. The $^{\bullet}OH$ radical–mediated oxidation has been successfully employed in the mineralization of several hazardous chemical contaminants. Interestingly, the electron scavenging becomes a rate limiting factor in such oxidation processes [399, 440–445]. As described in an earlier section, failure to scavenge electrons with a sacrificial electron acceptor results in the promotion of charge recombination. Alternative methods have also been suggested to promote the charge separation by applying an electrochemical bias to a TiO_2 particulate film electrode [444]. On the other hand, both reductive and oxidative steps can be beneficially used to degrade aromatic compounds such as trinitrophenol [446].

4.1. Organic Synthesis

Early contributions in the area of organic phototransformation came from Kato and Masuo [447, 448], who carried out photocatalyzed oxidation of tetralin in UV-irradiated TiO_2 suspensions. Bard and co-workers [341, 449, 450] demonstrated that photocatalytic processes such as the photo-Kolbe reaction and amino acid synthesis can be readily performed with platinized TiO_2 under band gap excitation. Developments in this area have been extensively reviewed by Fox [8, 448, 451–453].

CdS-mediated cis–trans isomerization of several derivatives of styrene have been reported by de Mayo and co-workers [454, 455]. The conversion of cis to trans isomer proceeded via the olefin radical cation intermediate, which was formed at the photoexcited CdS surface. The mechanism of cis–trans photoisomerization of electron-deficient alkenes on CdS has also been investigated in the presence of electron donors [456]. The reaction accompanies the formation of the dihydro compound as a two-electron reduction product. The photoisomerization does not occur at all in the absence of triethylamine (TEA). Two pathways involving the photoreduction of alkenes have been proposed. One is through the back electron transfer from the radical anion of the alkene toward the radical cation of TEA, both formed by photoexcited conduction band electrons and holes of CdS, respectively. The other is the reoxidation of a radical intermediate, formed by protonation of alkenes by the TEA cation radical.

Recently, Li and co-workers [457] have initiated reduction of nitro compounds for synthesizing specialty chemicals. The role of various semiconductors in initiating and controlling organic reactivity has been explored by several research workers. Such transformations on photoexcited semiconductor surfaces include oxidation of olefins, arenes, alkanes, amines, and alcohols; cycloadditions and retrocycloadditions; and geometric isomerizations. For example, double and triple bonds can be photocatalytically hydrogenated by Pt-loaded TiO_2 in the presence of alcohol as an electron donor [401]. Addition reaction of polychlorocompounds to carbon–carbon bonds catalyzed by TiO_2 under photoirradiation is considered to proceed through photoreduction [458]. TiO_2 can also be used as an electron supplier for asymmetric reduction of carbonyl compounds in the presence of chiral Rh(I) complexes as an electron mediator [402]. Photoreduction of aldehydes [403], azo dyes [391, 392], and Shiff bases [404] was observed by TiO_2. The developments in this area have been extensively reviewed by Fox [8, 451, 452].

Freshly prepared CdS suspensions consisting of quantized particles and their loose aggregation catalyze photoreduction of aromatic ketones and olefins in methanol under visible light irradiation using triethylamine as a sacrificial electron donor, yielding alcohols and dihydro compounds, respectively, which are more selective than photocatalysis of commercially available crystalline CdS [405]. Deuterium incorporation experiments in the photolysis of dimethyl maleate in methanol-O-D revealed that CdS^- nanocrystallites catalyze sequential two-electron-transfer photoreduction, affording deuterated dimethyl succinate.

4.2. Fixation of Carbon Dioxide into Organic Compounds

Photoreduction of carbon dioxide (CO_2) to organic compounds is an important topic for fuel production and resolving the greenhouse effect. The development of artificial photosynthetic systems is one of the ultimate goals in the reduction of CO_2. Photoassisted reductions of CO_2 in semiconductor particulate systems have been studied, since Inoue et al. [459] first reported photoreduction of CO_2 with suspensions of particulate semiconductors such as WO_3, TiO_2, ZnO, CdS, GaP, and SiC. However, most semiconductor-catalyzed photoreduction of CO_2 using water as the electron donor suffers from very low photoconversion efficiency and poor selectivity of reduction products. Until now, semiconductor particulate systems have been used to reduce CO_2 to a small range of compounds such as formic acid, CO, methanol, or methane. Photofixation of CO_2 into large organic substrates will be a challenging topic that needs to be tackled in the future.

Photocatalytic fixation of CO_2 into organic compounds can also be achieved using visible light ($\lambda > 400$ nm) irradiation of CdS nanocrystallites suspended in CO_2-saturated DMF solutions and using triethylamine as a sacrificial electron donor [152, 460]. Benzilic acid (BPCOOH), atrolactic acid (APCOOH), and phenylacetic acid (BZCOOH) were produced from benzophenone (BP), acetophenone (AP), and benzyl halides. The formation of a CO_2 anion radical ($CO_2^{-\bullet}$) was confirmed by EPR measurements using DMPO as a spin-trapping agent. Both the formation of $CO_2^{-\bullet}$ and the concurrent one-electron reduction of the organic substrates were evident in the photofixation process. This suggests that the photofixation proceeds via their (bimolecular) coupling on the surface of CdS nanocrystallites. The photocatalytic fixation of CO_2 of pyruvic acid to malic acid is achieved in TiO_2 or CdS particle suspensions using malic enzyme as the catalyst and methyl viologen as the electron mediator [461].

4.2.1. Photocatalytic Reduction of Carbon Dioxide with Metal Oxides

Among the many metal oxides examined as photocatalysts, TiO_2 is most commonly used as a photocatalyst for the reduction of CO_2 in combination with metal complexes working as photosensitizers [462–464]. Ru(II) complexes along with EDTA-bipyridine or EDTA-o-phenanthroline are useful as photosensitizers as they inject electrons from the excited state into the conduction band of TiO_2. These photoinjected electrons further lead to the reduction of CO_2 into HCOOH and HCHO [465]. Similar photosensitization experiments have also been reported in the photocatalytic reduction of CO_2 using chemically bonded eosin on the TiO_2 surface [464]. In the system consisting of TiO_2 and immobilized Pd, the photogenerated conduction band electrons reduce HCO_3^- to formate [466]. However, the fate of the photoproduced holes in these experiments is unclear. A possibility exists for these holes to react with various organic compounds contained as ligands of the complexes or stabilizers such as cyclodextrin. In a recent work, Anpo and co-workers [467, 468] report a Ti–mesoporous zeolite system in which CO_2 is reduced to methanol under UV irradiation. Photocatalyzed CO_2 reduction over pure oxide or oxides doped with other transition metal oxides have also been reported [362, 469, 470]. The production of CO in the system containing ZrO_2 as a photocatalyst and $NaHCO_3$ as an efficient promoter should be interesting because of the stoichiometric evolution of oxygen with respect to reduction products, namely, H_2 and CO [362].

4.2.2. Photocatalytic Reduction of Carbon Dioxide with Metal Sulfides

Metal chalcogenides, especially metal sulfides, constitute another class of the photocatalysts used for CO_2 reduction [471–474]. Although they are attractive as visible light catalysts, metal sulfides suffer from the problem of photocorrosion. Photogenerated holes if not scavenged efficiently induce anodic corrosion. Efforts have been made to overcome this problem using electron donors and/or organic reaction media [475–480]. The colloidal ZnS suspensions effectively catalyze photoreduction of CO_2 in Na_2S solution (pH 7 buffer) [475, 476]. The evolution of H_2 as well as the formation of formate and a very small quantity of CO were observed. An apparent quantum yield of $\Phi_{1/2}(HCOO^-) = 0.24$ was observed at 313 nm, where $H_2PO_2^-$ was quantitatively photooxidized to HPO_3^{2-}. The high efficiency of this system was attributed to the low density of surface defects on quantized ZnS crystallites.

Another system uses ZnS and CdS nanocrystallites prepared in *N*,*N*-dimethylformamide (DMF) at 0 °C [151, 479–481]. CO_2 undergoes effective photoreduction in the presence of triethylamine as a sacrificial electron donor. These systems show high quantum efficiency for the reduction of CO_2 under UV light ($\lambda > 290$ nm) irradiation, giving formate and CO. The formation of formate is observed when ZnS–DMF is prepared stoichiometrically [479, 481]. These colloids show a blue emission at approximately 325 nm arising from the conduction band or the shallow electron trap sites of ZnS–DMF. The yield and

the lifetime of the blue emission are enhanced by the addition of CO_2 to the system. This enhancement has been explained on the basis of stabilization of photogenerated electrons in the conduction band or at trap sites via the adsorptive interaction with CO_2 molecules on the ZnS–DMF surface. The addition of a zinc ion to this system changes the product distribution without a significant decrease in the photoconversion efficiency or the emission behavior. The competitive formation of CO with formate and the appearance of red emission at approximately 460 nm under continuous light excitation could also be seen. The selectivity of the two products, formic acid and CO, in the photocatalytic reduction of CO_2 can be controlled by the introduction of In^{3+} cations in the CdS colloidal system [153].

CO_2 is reduced to CO on hexagonal CdS nanocrystallites (mean diameter of 4 nm) in DMF under visible light irradiation. A quantum yield of 0.098 at $\lambda = 405$ nm has been observed using triethylamine as a sacrificial electron donor [151, 479, 480]. Solvation of the surface of CdS nanocrystallites by DMF or related amide molecules should control the crystalline growth and stabilize the favorable morphology with a size quantization effect. Addition of Cd^{2+} or H_2S influences the emission behavior and CO production, thereby suggesting the important role that surface structures of CdS–DMF plays in the photocatalytic reduction of CO_2.

One of the important aspects of understanding photocatalytic properties of semiconductor nanoclusters is to establish the surface active sites. Stable suspension of colloidal CdS (CdS–DMF) [152] and ZnS (ZnS–DMF) [476] nanocrystallites showed a relatively high catalytic activity for the photoreduction of CO_2 [151–153, 460, 476, 481–483]. The stability of the metal chalcogenide nanocrystallites prepared in DMF was found to be higher than those prepared in other solvents such as acetonitrile, methanol, and water. This observation supports the fact that adsorbed DMF molecules stabilize the nanocrystallites via effective binding to the semiconductor surface. In the case of CO_2 reduction by metal complexes and electrodes, the adsorptive interaction between CO_2 molecules and the metal center strongly depends on their orbital parentage, the charge of the metal atoms, and the microscopic structures of neighboring molecules. The adsorptive interaction of CO_2 molecules with the surface of semiconductor nanocrystallites also plays a crucial role in determining their photocatalytic activity.

The effect of the surface sulfur vacancy on photocatalytic activity has been examined thoroughly for the CdS nanocrystallites [460]. A remarkable increase in the photocatalytic activity of CdS was achieved by the addition of excess Cd^{2+} to the colloidal system (Fig. 7). The emission behavior, which depends on the amount of excess Cd^{2+} in the system, suggests the formation of sulfur vacancies on the surface of nanocrystallites because of the adsorption of excess Cd^{2+} to the surface. The formation of the sulfur vacancies on the surface was supported by *in situ* Cd K-edge EXAFS analysis of the nanocrystallites in

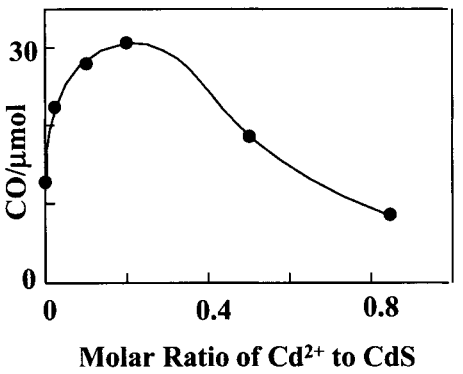


Fig. 7. Effect of the addition of excess Cd^{2+} on the efficiency of CdS–DMF-catalyzed CO formation. (Source: Reprinted with permission from [460]. © 1994 American Chemical Society.)

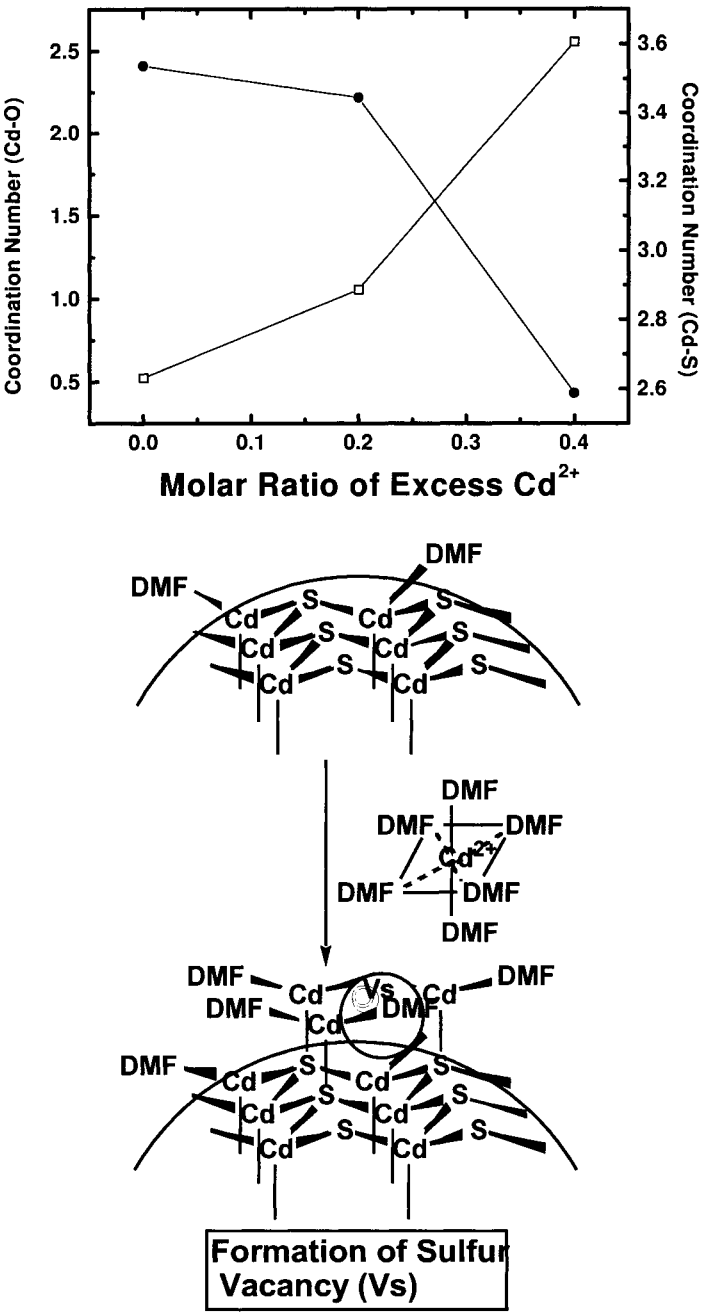


Fig. 8. Effect of the excess Cd^{2+} addition on the coordination number of the Cd–O (•) and Cd–S (○) shell obtained by EXAFS measurement. (Source: Reprinted with permission from [460]. © 1994 American Chemical Society.)

solution as changes in the coordination numbers of cadmium–sulfur and cadmium–oxygen (Fig. 8). Theoretical molecular orbital calculations using a density-functional method support the preferential adsorptive interaction of a CO_2 molecule with a Zn atom in the vicinity of a sulfur vacancy on hexagonal ZnS. Furthermore, the calculations for CdS models suggest the preferential bidentate-type absorption of CO_2 with the Cd atom in the vicinity of the sulfur vacancy.

4.3. Reduction of Nitrogen

Nitrogen fixation with irradiated TiO_2 semiconductor nanoparticles in aqueous solution was confirmed from the production of NH_3 [484]. The hydrous oxides of samarium(III) and europium(III) are found to catalyze the photoreduction of dinitrogen in aqueous suspensions [485]. The chemisorption of nitrogen and the sufficiently negative flat band potential of oxides were found to play an important role in determining the efficiency of photocatalytic reduction for TiO_2 systems. Photosensitized reduction of nitrogen to ammonia in the presence of sacrificial electron donors has been attempted by Taqui-Khan and co-workers [463] using a Ru(II) complex–TiO_2 system. The complex containing nitrogen as a ligand has also been reduced by the photogenerated electrons in Pt/Cd, giving ammonia [486]. This is another approach for nitrogen fixation using semiconductors.

4.4. Decomposition of Nitrogen Oxides and Their Anions

Conversion of nitrogen oxides to less toxic compounds is also important from the viewpoint of global environmental pollution. Nitrogen oxides can be converted to N_2 and other nitrogen compounds by reduction. CdS catalysts can reduce nitrite to ammonia using sodium sulfate and sodium sulfite as sacrificial agents in the photoefficiency of 2.6% [487]. The activity is enhanced by loading noble metals, such as Ru, Pd, or Ir, or by the use of hole-transferring agents, such as RuO_2. TiO_2 prepared by the sol–gel method also reduces nitrate and nitrite ions to ammonia at higher activity than TiO_2 prepared by other conventional methods [488].

Anpo and Yamashita [468, 489, 490] discovered that TiO_2-loaded zeolites and the vanadium silicalite-1 decompose NO under irradiation. Although the vanadium silicalite-1 requires propane as a reducing reagent [490], TiO_2 included in zeolite cavities results in complete decomposition into N_2 and O_2 without any reducing reagent [468]. Both the nitrogen fixation and the decomposition of nitrogen oxides have just appeared on the scene as a new aim for research in the field of semiconductor photocatalysis. Accumulation of much knowledge will promote the application of semiconductors to new reaction systems.

4.5. Photocatalytic Degradation of Organic Contaminants

The photocatalytic properties of anatase TiO_2 particles in degrading undesirable organics from air and water are well documented [15, 17, 18, 491–494]. Organic materials such as hydrocarbons, haloaromatics, phenols, halogenated biphenyls, surfactants, and textile dyes in TiO_2 slurries have been successfully mineralized. For reactor applications, it is convenient to immobilize the semiconductor particles on a suitable substrate. Several studies have been reported with TiO_2 particles immobilized on glass substrates [492, 495–498].

The oxidation reactions are usually initiated by the hydroxyl groups generated at the semiconductor surface. The reaction mechanism leading to mineralization of aromatic molecules is a multistep process and the pathways are often complex to analyze. A detailed discussion on this topic is beyond the scope of the present chapter. The reader can refer to recent review articles for the developments in this area [1, 6, 12, 14–18, 491–493, 495, 499–511].

In a single-crystal semiconductor (n-type)-based photoelectrochemical cell, the problem of charge recombination is easily overcome by applying an anodic bias as was first demonstrated by Fujishima and Honda [512]. Using a single crystal of TiO_2, they were able to carry out the photoelectrolysis of water under the influence of an anodic bias. Thin semiconductor particulate films coated on a conducting surface provide a convenient way of manipulating the photocatalytic reaction by electrochemical methods [444, 492]. We have thus succeeded in achieving better charge separation by applying an anodic bias to the immobilized semiconductor nanocrystallites [444, 513, 514]. In an electrochemically assisted photocatalytic process (ECAP), the externally applied anodic bias greatly improves

the efficiency of charge separation by driving the photogenerated electrons via the external circuit to the counterelectrode compartment.

The photocatalytic studies of 4-chlorophenol degradation provide a representative example of the use of ECAP in elucidating the mechanism of degradation [444, 513]. By controlling the applied bias potential, it is possible to control the degradation rate. The photocatalytic degradation occurs at a faster rate when the applied potential is maintained at +0.6 V, while little degradation is seen when the potential is maintained at −0.6 V versus saturated calomel electrode (SCE). Because the charge separation in the TiO_2 particulate film increases when an anodic bias is applied to the optically transparent electrode (OTE)/TiO_2 electrode, one observes a higher efficiency for photocatalytic degradation. At potentials close to the flat band potential (−0.6 V versus SCE), all the electron–hole pairs are lost in the recombination process and, hence, it is not possible to carry out the oxidation of 4-chlorophenol. In a slurry system, the irradiated particles behave as short-circuited microelectrodes and thus the interfacial charge transfer competes with the charge recombination process. This situation closely resembles the experimental conditions in which the OTE/TiO_2 is maintained at 0.0 V. Thus, nanostructured semiconductor films are useful in carrying out electrochemically assisted photocatalysis and overcome the limitation of electron scavenging, which one encounters in the slurry system. A similar technique has also been extended to several other systems [446, 515–517].

The advantage of using the ECAP technique is not just limited to the faster degradation rates. The use of an anodic bias to separate the charge carriers obviates the need for oxygen as an electron scavenger and makes it possible to carry out the photocatalytic reaction in anaerobic conditions. The electrochemical arrangement also provides unique opportunity to separate the anodic and cathodic processes and thereby isolate the various reactions occurring in photocatalytic systems.

5. SURFACE MODIFICATION OF SEMICONDUCTOR COLLOIDS

5.1. Deposition of Metals on Semiconductors

The selectivity and efficiency of a photoelectrochemical reaction can be improved by modifying the surface of the semiconductor particle with a suitable noble metal. For example, an order of magnitude enhancement in the efficiency of photocatalytic hydrogen production from water has been achieved upon platinization of semiconductor particles. The metal deposit on the semiconductor acts as a sink for the photogenerated electron and catalyzes the production of hydrogen. Platinization can be done either by direct photoreduction of $PtCl_6^{2-}$ on the semiconductor or particle [518, 519] or by stirring the suspensions of semiconductor colloids and platinum colloids together [256, 520–524]. The effect of platinum loading on the photocatalytic activity of semiconductor particles has also been investigated [525]. Photoinduced oxidation of bromide to bromine on irradiated platinized TiO_2 powders and platinized TiO_2 particles supported in Nafion films has also been carried out [526].

Other noble metals and metal oxides (e.g., RuO_2) have also been deposited on semiconductor particles to improve the efficiency of the photocatalytic reaction [527–534]. The effect of various transition metal ion doping on the dynamics of photoinduced charge transfer processes in colloidal semiconductor systems has been probed [535–539]. RuO_2 clusters in the native form [540–543] and deposited on semiconductor particles [465, 527, 529, 530, 533, 534, 544–546] improve the efficiency of photocatalytic redox processes such as H_2 production from water or H_2S and fixation of nitrogen and carbon dioxide. Similarly, In_2O_3 particles have also been found to be useful for oxygen generation [547]. Efforts have been made to bind semiconductor nanoclusters to metal surfaces using a self-assembled monolayer approach [58] or to synthesize multilayered metal nanoclusters [548]. Recently, an

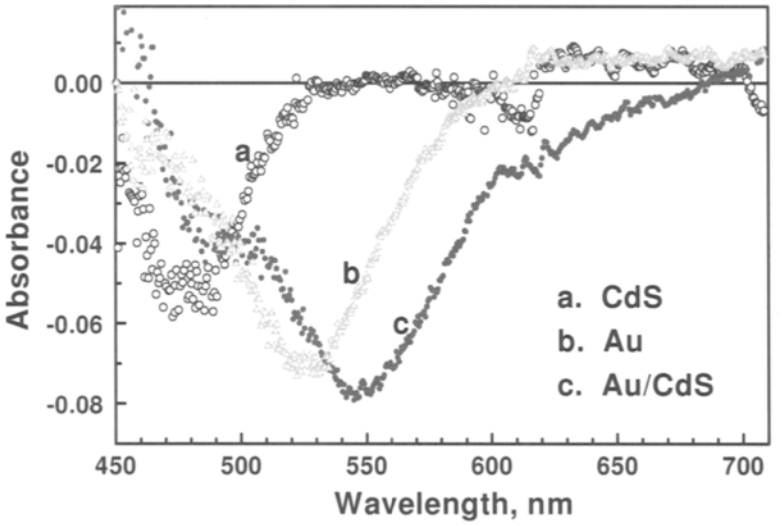


Fig. 9. Plasmon bleach of the CdS/Au system. (Source: Reprinted with permission from [460]. © 1994 American Chemical Society.)

attempt has been made to investigate the optical properties of gold-capped CdS composite nanoclusters [549]. The photophysical study of metal clusters continues to reveal new interesting properties and the reader is refered to some of the recently published articles [11, 45, 222, 550–563].

The kinetics and the mechanism of interparticle electron transfer between semiconductor and metal nanocrystallites were elucidated using picosecond laser flash photolysis. Capping of gold colloids with ultrasmall CdS nanoclusters (particle diameter ~4 nm) significantly alters the picosecond dynamics of the gold core. The bleaching of the surface plasmon absorption of the gold core is achieved by exciting the CdS shell (Fig. 9). The major fraction of the interparticle electron transfer between CdS and Au nanoclusters is completed within the laser pulse duration of 18 ps.

5.2. Capping with Organic and Inorganic Molecules

Redox species that strongly interact with a semiconductor surface are of great interest in improving the performance of photoelectrochemical activity of the semiconductor system [564, 565]. Such interactions are also useful in controlling the size of the colloidal particle as observed for the colloidal CdSe and CdS. Steigerwald et al. [50] have monitored the CdSe nanocrystal growth in the presence of added reagents and passivation by the addition of organoselenides. Similarly, surface-capped CdS colloids have been prepared in the presence of various thiols [62, 63, 133, 142, 566–569]. For example, Herron et al. [54] have shown that CdS clusters in the quantum confinement regime (particle diameter <50 Å) can be prepared by adjusting the ratio of sulfide to thiophenol during synthesis. The competitive reaction chemistry between the growth of the CdS core and the surface capping by thiophenolate leads to a CdS core whose surface has been passivated by covalently attached phenyl groups. Figure 10 shows the absorption spectra of CdS colloids prepared with and without a surface-capping procedure. Fox and co-workers have investigated the optical and electrochemical properties of cadmium benzenethiolate clusters as a function of cluster size [570, 571]. These clusters, which show structured absorption, represent molecular models for metal chalcogenides. Similarly, amorphous polysilsesquioxanes [115], aminocalixarenes [184], charged polymers [83, 207, 229, 425, 427, 572, 573], and surfactants [574] have also been employed to control the particle size in the quantum

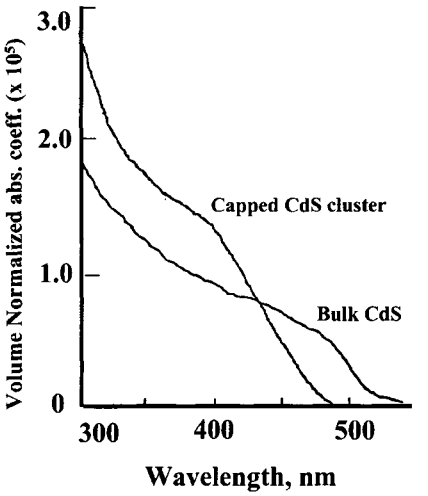


Fig. 10. Absorption coefficients of 30-Å CdS/SPh cluster solid. Also shown is the coefficient of bulk CdS in a medium of dielectric constant 30, calculated with the Lorentz–Mie formula. (Source: Reprinted with permission from [54]. © 1990 American Chemical Society.)

size regime. The preparation of MoS_2 nanoclusters has also been facilitated by capping with a layer of dialkylthiophosphate [575].

Significant efforts have also been made to functionalize CdS colloids with electron donors and acceptors. These include viologen derivatives [62, 385], ferrocene [576], amines [172, 577, 578], and diethyldithiocarbamate anion [412]. A bifunctional mercaptocarboxylic acid has also been employed to bridge CdS and TiO_2 particles [65]. The interaction between the semiconductor surface and the surface modifier often alters their absorption characteristics. These spectral changes include the displacement or broadening of the absorption bands, the appearance of new charge transfer bands, and changes in the extinction coefficient of absorption. For example, surface complexation of a TiO_2 colloid with SCN^- results in the appearance of a new absorption band at 285 nm [417]. Recently, Lauerhaas and Sailor [297] have investigated the effect of adsorbates on the quenching of porous silicon luminescence. The visible luminescence from porous silicon has been found to be highly surface sensitive, and the surface interactions can be tuned by specific chemical transformations.

Enhancement in the emission yield has been achieved by modifying the colloidal CdS surface with triethylamine [172, 578, 579], indole [286], and mercaptoethylamine [567] or by activation of the surface with Ag_2S or Cd^{2+} ions [66, 269]. Similarly, coating the CdS particles with a $Cd(OH)_2$ layer resulted in a strong enhancement of the emission yield and stabilized against photocorrosion. Surface defects, which promote radiationless recombination of the charge carriers, can be blocked upon such modifications.

A decrease in the emission lifetime of semiconductor colloids observed when an electron acceptor or a surface modifier is adsorbed onto the semiconductor surface. For example, the average emission lifetime of CdS colloids in acetonitrile at 640 nm decreased from 156 to 26 ns when the semiconductor surface was modified with the diethyldithiocarbamate anion [412]. It has also been shown that viologen compounds, thiazine dyes, or ethylenediaminetetraacetate [375] can efficiently quench the emission of CdS colloids, and by using Poisson statistics one can determine the number of molecules aggregated in the CdS colloid [150, 173, 196, 580]. A decrease in the emission lifetime observed upon adsorption of Cu^{2+}, I_3^-, and S^{2-} ions on a CdS surface has been explained on the basis of increased surface recombination velocity [312, 581–583]. However, in the case of ZnO colloids, hole scavengers such as I^- and SCN^- quenched the green emission as they interacted with the surface anionic vacancies [206].

5.3. Surface Modification with Sensitizing Dyes

Another important aspect of surface modification of a semiconductor colloid is to extend its response toward low-energy excitations. This is often achieved by attaching sensitizer molecules by direct adsorption or covalent linkage. The interaction between the sensitizer and the semiconductor surface can be probed with the electronic absorption and emission spectra of the sensitizer as the energetics of its ground and excited states are altered.

Extensive efforts have been made in various laboratories to modify the semiconductor surface with various dyes. The process of charge injection from the excited state into the conduction band of the semiconductor has been studied with respect to extending the photoresponse of large-band-gap semiconductor materials and has applications in imaging science and solar energy conversion [39, 584–589]. The energy level diagram, which compares the band energies of semiconductors and the oxidation potentials of excited states, is illustrated in Figure 11. Spectroscopic techniques such as emission, resonance Raman, diffuse reflectance, microwave absorption, and nanosecond and picosecond laser flash photolysis are often employed to probe the interfacial charge transfer between an excited sensitizer and the semiconductor particle.

Dyes such as erythrosin B [590], eosin [464, 591–594], rose bengal [389, 595], rhodamines [596–600], cresyl violet [601–603], thionine [604], chlorophyllin [605, 606], anthracene-9-carboxylate [607], 8-hydroxyquinoline [608], porphyrins [609], phthalocyanines [423, 610], perylenes [611–613], transition metal cyanides [614, 615], $Ru(bpy)_3^{2+}$ and its analogs [38, 339, 377, 465, 588, 616–621], cyanines [587, 622–629], squaraines [352, 630, 631], and phenylfluorone [632], which have high extinction coefficients in the visible, are often employed to extend the photoresponse of the semiconductor in photoelectrochemical systems. Visible light sensitization of platinized TiO_2 photocatalyst by surface-coated polymers derivatized with ruthenium tris(bipyridyl) complex has also been attempted [633, 634]. Because the singlet excited state is short lived, it becomes essential

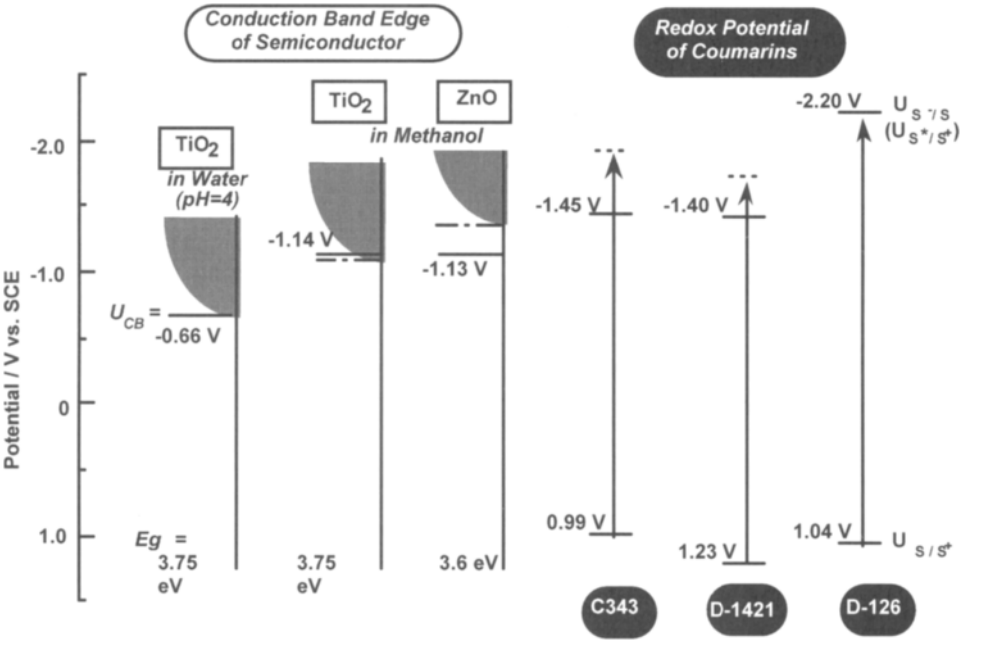


Fig. 11. Energy diagram of TiO_2 and ZnO nanocrystallites in methanol or water. Redox potentials of coumarin dyes, C343, D-1421, and D-126, are also shown. Absorption coefficients of 30-Å CdS/SPh cluster solid. Also shown is the coefficient of bulk CdS in a medium of dielectric constant 30, calculated with the Lorentz–Mie formula. (Source: Reprinted with permission from [612]. © 1996 American Chemical Society.)

to adsorb these dyes on the semiconductor surface with an electrostatic, hydrophobic, or chemical interaction so that electron transfer can occur within the lifetime of the singlet excited state. The sensitization of semiconductor crystallites (e.g., silver halides) by dye aggregates has important applications in imaging science. The charge injection from an excited dye aggregate into the semiconductor crystallite is an important step in latent image formation. Internal reflection spectroscopy has been employed by Natoli et al. [625] to probe the mechanism of sensitization of a ZnO single-crystal electrode with *J* aggregates of cyanine dyes. Quantum efficiencies up to 0.2 were observed for sensitized photocurrent generation in these systems. Similarly, the interaction between *J* aggregates of squaraine dyes and semiconductor nanocrystallites has been probed by both spectral and photocurrent measurements [630, 631]. The dependence of quantum efficiency (ϕ_{et}) of photoinduced electron transfer from sensitizing dyes (cyanine dyes) to silver bromide microcrystals on the sensitizer reduction potential has been discussed [627, 635, 636]. The dependence of ϕ_{et} on the reduction potential of the dye has been explained on the basis of Marcus theory with a small rearrangement energy (0.05 eV) and without the inverted region. Spitler [636] has employed a quantitative photoconductive model to explain the data of Tani et al. [627]. The model predicts an energetic threshold for spectral sensitization, correlating a high speed of spectral sensitization of a dye with a highly negative electrochemical reduction potential. Temperature-independent heterogeneous electron transfer reactions in the inverted Marcus region have been reported for the interfacial electron transfer between the conduction band of a TiO_2 nanocrystallite and an oxidized sensitizer [637]. Recently, efforts have also been made to understand the role of *H* aggregates of cresyl violet [638–643] and rhodamine 6G [644] in sensitizing SnO_2 colloids and thin films. The efficiency of net charge transfer was significantly lower than that observed for corresponding monomers. This was attributed to fast intersystem crossing of the excited singlet state and back electron transfer processes.

Coadsorption of a photosensitizer, such as ruthenium(II) trisbipyridyl complex, $Ru(bpy)_3^{2+}$, and an electron transfer on the colloid surface opens up the possibility of initiating semiconductor-mediated electron transfer. For example, optical excitation of $Ru(bpy)_3^{2+}$ results in the population of a relatively long-lived metal-to-ligand charge transfer (MLCT) excited state ($\tau = 580$ ns in aqueous solution at room temperature), which is simultaneously more reducing and more oxidizing than the precursor ground state [645–651]. On a semiconductor surface, electrons are injected from the excited $Ru(bpy)_3^{2+}$ and subsequently transferred to an electron acceptor such as an *H* aggregate of cresyl violet [639]. A similar strategy of using a semiconductor nanoparticle as a mediator for transporting electrons between an electron donor and acceptor has been demonstrated in several other systems [607, 652, 653].

Other techniques have also been employed to obtain mechanistic information on the interfacial charge transfer process. The mechanism of cation radical formation in the colloidal TiO_2–eosin system has also been established by time-resolved resonance Raman spectroscopy [592, 594]. Diffuse reflectance laser flash photolysis [389, 654–658] and microwave absorption [351, 595, 605] studies have also been carried out in our laboratory to probe the charge injection process. The net charge transfer efficiency in the case of the eosin–TiO_2 system is approximately 38% [591]. However, much smaller (<1%) efficiencies have been observed when anthracene-9-carboxylic acid [607] or chlorophyllin [605] is chosen as a sensitizer.

Very few examples of a triplet excited state being the electron donor in the charge injection process exist in the literature. These include eosin (EO)–TiO_2 [593], thionine (TH^+)–ZnO [604], chlorophyllin–TiO_2 [606], cresyl violet aggregate–TiO_2 [659], and squaraine–TiO_2 [641] systems. The difference in reactivity of the singlet and triplet excited states in different colloidal semiconductor systems depends on the interaction between the sensitizer and the semiconductor [641, 659, 660]. When the sensitizer is strongly bound to the semiconductor with a strong electronic coupling (e.g., charge transfer complexation), the

singlet excited state dominates the charge injection process. And when the interaction between the sensitizer and the semiconductor is very weak, one can expect the triplet excited state to participate in a diffusion-controlled charge injection process.

The sensitizer molecules adsorbed on the TiO_2 surface have a significantly shorter fluorescence lifetime than in the homogeneous solution and this decrease in lifetime has been attributed to the charge injection process [339, 597–599, 601–603, 606, 621, 628, 661–664]. Heterogeneous electron transfer rate constants in the range of 10^7 to 10^{11} have been reported in these studies. Microwave absorption and luminescence decay measurements have been independently carried out to monitor the charge injection from excited $Ru(bpy)_2(dcbpy)^{2+}$ into SnO_2, ZnO, and TiO_2 nanocrystallites [351]. Because microwave conductivity arises as a result of mobile charge carriers within semiconductor particles, it is possible to probe the charge injection process by monitoring the growth in the microwave absorption [595].

5.4. Ultrafast Charge Injection into Semiconductor Nanocrystallites

Excitation of sensitizing dyes adsorbed on semiconductor nanoclusters results in the production of a dye cation radical ($S^{\bullet+}$). Picosecond and femtosecond laser flash photolysis experiments have shown that the formation of the dye cation is an ultrafast process and occurs within a few hundred femtoseconds to several picoseconds. Recently, the dynamics of charge injection from an excited sensitizer into semiconductor nanoclusters has been characterized by femtosecond laser flash photolysis and emission experiments [612, 643, 665–669]. Ford and Rodgers have elucidated the kinetics of nitroxyl radical oxidation by the oxidized sensitizer $Ru(bpy)_3^{3+}$ following photosensitization of antimony-doped tin oxide colloidal particles [670].

Dye sensitization from photoexcited strongly anchored dye molecules on the semiconductor surface often achieve a quantum efficiency close to unity [671]. Theories have been developed to explain the ultrafast rate and the mechanism of the phenomenon at the interfaces [419, 671, 672]. It was proposed that the description for the process at the heterogeneous interface is directly related to Fermi's golden rule when nuclear degrees of freedom are neglected. The rate of electron transfer can be related to the electronic density of states and the electronic coupling of the system. The quasicontinuum electronic states in the semiconductor conduction band accept electrons from excited dye molecules and thus contribute to delocalization of the electronic wave function via electronic dephasing. The electronic dephasing that occurs within a sub-50-fs time scale is significantly faster than the typical relaxation of the nuclear degrees of freedom for most molecular species (~100 fs) in a homogeneous system. A time scale of 10–50 fs was suggested in the theoretical estimation for electron transfer at a heterogeneous interface [673]. In spite of the advantage of providing a well-defined, flat, and smooth surface, the optical signals of time-correlated single-photon counting from an ordered monolayer of oxazine SnS_2 led to a relatively low signal-to-noise ratio. Direct determination of the electron transfer time as well as characterization of the adsorbed structure seems to be difficult in this system. Recent progress in femtosecond laser spectroscopy has allowed us and others to observe such a fast electron transfer event on the semiconductor surface [673]. McLendon et al. [666] reported a charge injection time of less than 200 fs for a coumarine dye, C343, adsorbed on TiO_2 nanocrystallites. Willig et al. [612] showed that the perylene dye adsorbed on a TiO_2 porous electrode had a time of less than 190 fs in ultrahigh vacuum (UHV). They minimized the dye aggregation on the semiconductor surface by functionalizing the dye with phosphonate groups. Durrant et al. [667] reported a lifetime of less than 150 fs for the Ru complex (*cis*-di(thiocyanato)-*N,N'*-bis(2,2'-bipyridyl-4,4'-dicarboxylicacid)-ruthenium(II)dihydrate, $\{RuL_2(NCS)_2\}\cdot 2H_2O$) on a TiO_2 porous electrode. Fast injection from a natural dye of blackberries exceeding 100 fs was also reported by Zhang and co-workers [674].

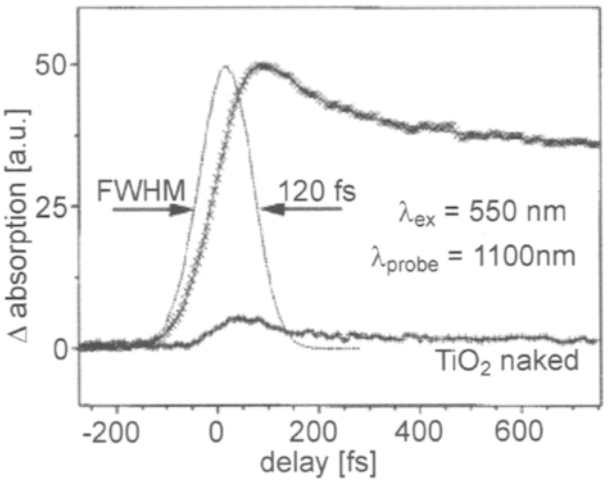


Fig. 12. Transient absorption signal detected at 1100 nm for the Ru-dye–covered colloidal TiO_2 electrode mounted in ultrahigh vacuum. This signal is due to light absorption by the injected electrons. The instrumental function is shown with 120 fs half-width. (Source: Reprinted with permission from [669]. © 1997 American Chemical Society.)

In a recent study, Willig et al. [669] observed a transient absorption signal of the injected hot electron with a rise time less than 25 fs for the system of ruthenium(II) *cis*-di(isothochanato)-bis(2,2′-bipyridyl-4,4′-dicarboxylate)/TiO_2 porous nanocrystalline electrode in ultrahigh vacuum (Fig. 12). They have used the UHV condition to measure the temperature dependence on the rate of the charge injection process. A fast charge injection on the time scale of 10–50 fs was also available for the system involving several coumarine dyes on TiO_2 and ZnO nanocrystallites. Murakoshi et al. [675, 676] also observed a charge carrier injection rate of less than 20 fs for the coumarine 343 adsorbed on 53-Å-diameter TiO_2 nanocrystals that were suspended in water. The dependence of the band energies of semiconductor nanocrystallites on the solvents and redox potential of excited dye molecules indicated that the ultrafast electron transfer injection rate should not only occur because of the strong adsorption, but also because of large overlap between the conduction band levels and the donor states of the excited dye molecules.

Based on the fact that injection at TiO_2 is relatively slower than that at ZnO in methanol, the effect of the density of states of the conduction band as well as the conduction band edge due to proton concentration was considered (see Fig. 11 for an energy level diagram). The density of states for the conduction band of TiO_2, originating from high-density d orbitals, is larger than that of ZnO, originating from relatively simple s orbitals, by more than two orders of magnitude. Such a high density of states of TiO_2 should increase the states overlapping for electron transfer. They concluded that the electronic orbital character of the semiconductor is also an essential factor in determining the efficiency of dye sensitization.

5.5. Designing Multicomponent Semiconductor Systems

The feasibility of coupling a metal oxide nanocrystallite with one or more semiconductors by chemical precipitation or electrochemical deposition opens up a wide array of possibilities in utilizing these materials for microelectronics. For example, in a recent study, we have shown that it is possible to rectify the flow of electrons in nanostructured TiO_2 film by coating a thin CdSe film [677]. Uekawa et al. [678] have also succeeded in developing a p–n junction diode. The advantage of using coupled semiconductor films in photoelectrochemical cells is twofold: (i) to extend the photoresponse by coupling a large-band-gap

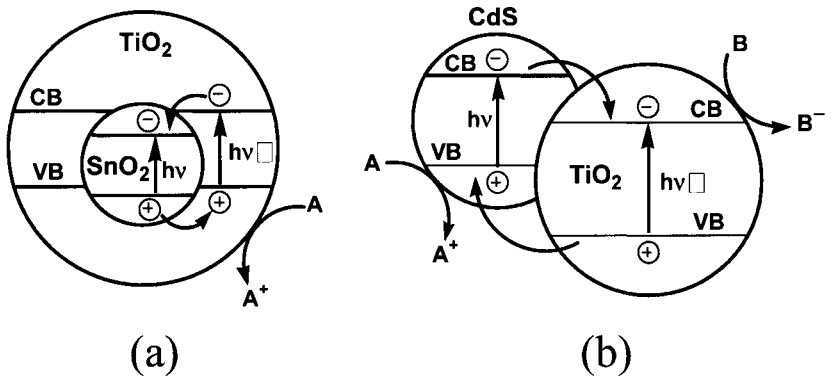


Fig. 13. Photoinduced charge separation in semiconductor heterostructures: (a) coupled and (b) capped semiconductor nanocrystallites. Photogenerated charge carriers move in the opposite directions, thus facilitating charge rectification.

semiconductor with a short-band-gap semiconductor and (ii) to retard the recombination of photogenerated charge carriers by injecting electrons into the lower-lying conduction band of the large-band-gap semiconductor.

Both capped and coupled geometries have been employed to develop semiconductor heterostructures. The principle of charge separation in coupled and capped semiconductor systems is illustrated in parts a and b of Figure 13, respectively. While the mechanism of charge separation in a capped semiconductor system is similar to that in coupled semiconductor systems, the interfacial charge transfer or charge collection at this multicomponent semiconductor system is significantly different. In coupled semiconductor systems, the two particles are in contact with each other and both holes and electrons are accessible for selective oxidation and reduction processes on different particle surfaces. On the other hand, capped semiconductors have a core–shell geometry. If the shell is relatively thick, a charge rectification occurs and only one of the charge carriers is accessible at the surface. This makes selective charge transfer possible at the semiconductor electrolyte interface. The other charge carrier (i.e., the electron in Fig. 13b) gets trapped within the inner semiconductor particle and is not readily accessible.

5.5.1. Coupling of Two Semiconductor Colloids

A variety of interesting properties of such coupled semiconductor systems have recently been reported by several researchers (see, e.g., [679, 680]). Evidently, the rectification properties of these coupled semiconductor systems are attractive enough to explore their feasibility in designing molecular devices and integrated chemical systems for solar energy conversion. Use of coupled semiconductor particles in improving the photocurrent generation in TiO_2–CdS [680–683], ZnO–CdS [257], TiO_2/CdSe [677, 679], and SnO_2/CdSe [684] systems has been demonstrated. Such coupled semiconductor thin films not only extend the photoresponse of large-band-gap semiconductors but also rectify the flow of photogenerated charge carriers [679] and improve the efficiency of dye sensitization [685].

Electron transfer between two different semiconductor colloids can be achieved by coupling them with or without surface modification. For example, in a colloidal CdS–TiO_2 system, a photogenerated electron can be injected from CdS into a TiO_2 particle while the holes remain in the CdS particle (Fig. 13b). The difference in the energy levels of the two semiconductor systems plays an important role in achieving such a charge separation. The feasibility of sensitizing large-band-gap semiconductor ZnO with a deposit of CdS film has been demonstrated by Gerischer and Lübke [681].

One of the early demonstrations of this concept came from Nozik and co-workers [686], who developed a simple photochemical diode by sandwiching p- and n-type semiconductors. Recently, considerable interest has focused on studying coupled semiconductor systems. These include CdS–TiO_2 [274, 681, 687, 688], SnO_2/TiO_2 [684], CdS–PbS [689], CdS–ZnO [257, 688], CdS–AgI [274], Cd_3P_2–TiO_2 and Cd_3P_2–ZnO [255], ZnO–ZnS [254], ZnO–ZnSe [206], AgI–Ag_2S [195], and CdS/HgS [690]. In our earlier studies, we have shown that excitation of CdS colloids coupled with a metal oxide colloid such as TiO_2 [274] or ZnO [257] results in the injection of electrons into the lower-lying conduction band of the metal oxide.

The charge injection process in a coupled semiconductor system was further demonstrated by carrying out methyl viologen reduction at a TiO_2 semiconductor, but with excitation of a CdS semiconductor in the CdS–TiO_2 system [688]. The efficient quenching of CdS emission and high quantum yield for reduction of MV^{2+} in the presence of colloidal TiO_2 indicated an efficient charge injection process with a quantum efficiency of 100%. Similarly, enhanced efficiency of SCN^- oxidation has been observed in a ZnO–ZnSe coupled semiconductor system [206].

The primary photochemical events associated with the charge separation in CdS–TiO_2 and ZnO systems were also probed with transient absorption measurements [257, 274]. The transient absorption spectra recorded immediately after the laser pulse excitation of CdS in a CdS–TiO_2 system are shown in Figure 14. The broad absorption in the region of 500–760 nm corresponds to the charge trapped at the Ti^{4+} site of a TiO_2 colloid. This transient formation was completed within the laser pulse duration of 18 ps. Recent studies have indicated that such an inter-particle electron transfer occurs within 500 fs to 2 ps [320, 691]. This suggests that the rate constant for the charge injection process is greater than 5×10^{11} s^{-1}.

The improved charge separation in the coupled semiconductor system also enhances the process of hole trapping. This process can be followed by monitoring the absorbance of $S^{\bullet-}_{surf}$. The photocatalytic applications of coupled semiconductor systems have yet to be explored fully. But it is evident that the rectification properties of these coupled semiconductor systems are attractive enough to explore their feasibility in designing molecular devices and integrated chemical systems for solar energy conversion. Use of coupled semiconductor particles for improving the photocurrent generation of thin TiO_2–CdS [682, 683]

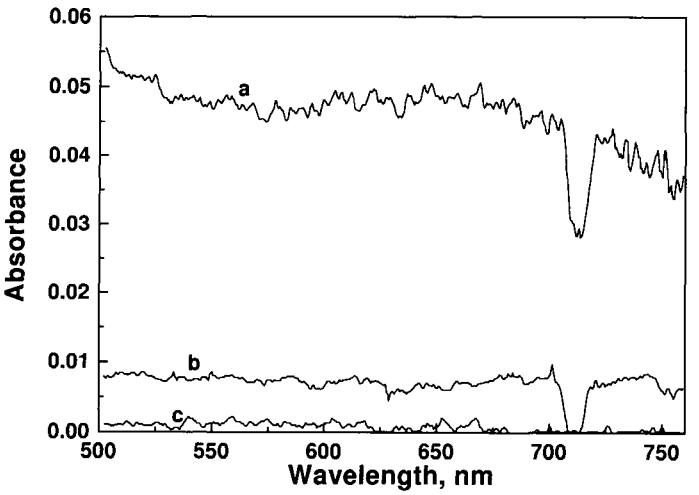


Fig. 14. Transient absorption spectra recorded after 355-nm laser pulse excitation of colloidal suspension ($\Delta t = 0$ ps): (a) 0.75 mM CdS + 1.15 mM TiO_2, (b) 0.75 mM CdS, and (c) 1.5 mM TiO_2. (Source: Reprinted with permission from [274]. © 1990 American Chemical Society.)

and ZnO–CdS [257] films and photocatalytic degradation of an azo dye with TiO_2–SnO_2 film [514] has been demonstrated recently.

5.5.2. Capped Semiconductor Colloids

Capped semiconductor particles facilitate an interesting way to change electronic structure by combining the properties of two semiconductor materials. Recently, Brus and co-workers [53] have synthesized and characterized composite semiconductor crystallites involving CdSe grown on a ZnS seed, and vice versa. They have demonstrated nucleation and partial growth of composite particles despite the fact that the two materials have bond lengths differing by 13%. Eychmüller and co-workers [249, 690] have demonstrated interesting fluorescence properties of CdS colloids capped with HgS. Elucidation of the energetic structure and charge carrier dynamics of this system led to the conclusion that its electronic properties are significantly different from the sum of the separate particles. Haus and co-workers [692] have modeled quantum confinement effects in nanometer-size semiconductor particles coated with another semiconductor. By using the band offsets and effective masses, the overlap of electron and hole functions can be altered by changing the core radius of the particles. Development of such semiconductor heterostructures are considered to be interesting because by changing the thickness of the shell and particle radius the overlap of the wave functions and band gap can be altered.

Matijevic and co-workers [693] have prepared spherical ZnO particles coated with uniform layers of TiO_2. By making use of the principle described in Figure 13a, it was possible to enhance the efficiency of SCN^- oxidation in a ZnSe-capped ZnO system [206]. Such a capping process is not only convenient to build tandem semiconductor structures but also provides an economical way to deposit expensive semiconductor material on an inexpensive support.

Charge transfer processes in a TiO_2-capped SnO_2 (TiO_2@SnO_2) and TiO_2-capped SiO_2 (TiO_2@SiO_2) colloids have also been investigated [684]. The effectiveness of SnO_2@TiO_2 colloids as an improved oxidative photocatalyst was demonstrated by oxidizing I^- in a laser flash photolysis experiment. Upon excitation with a 308-nm laser pulse, the photogenerated electrons accumulate at the inner core of SnO_2 and holes at the outer TiO_2 shell. Surface-adsorbed scavengers such as I^- can quickly scavenge away the holes at the interface and forms $I_2^{\bullet -}$ (reaction 7):

$$TiO_2(h_t) + I^- \rightarrow TiO_2 + I^{\bullet}\text{—}(I^-) \rightarrow I_2^- \tag{7}$$

The absorption bands observed at 380 and 700 nm confirmed the formation of $I_2^{-\bullet}$. The relative quantum efficiency for I^- oxidation at a SnO_2@TiO_2 colloid was two- to threefold higher than SiO_2@TiO_2 or TiO_2 colloid alone (Fig. 15). These results further demonstrate the usefulness of SnO_2@TiO_2 colloids in carrying out photocatalytic oxidation reactions. A simple variation in the synthetic procedure results in significant changes in the photoelectrochemical properties of the multicomponent semiconductor system. If employed in a suitable configuration, multicomponent semiconductor systems can pave the way toward developing materials for microelectronics or photosensitive devices. It should be noted that the capping layer of TiO_2 studied in these experiments is relatively thick and does not exhibit size quantization effects. Such systems differ from other systems [53, 249, 689, 690] in which the capping layer was size quantized (4–5 Å thick).

6. ORDERED NANOSTRUCTURES USING SEMICONDUCTOR NANOCRYSTALLITES AND THEIR FUNCTIONALITY

Considerable effort has been made in recent years to synthesize and characterize the properties of thin semiconductor films prepared from colloidal semiconductor suspensions [694–697]. This method of preparation is relatively simpler and inexpensive compared

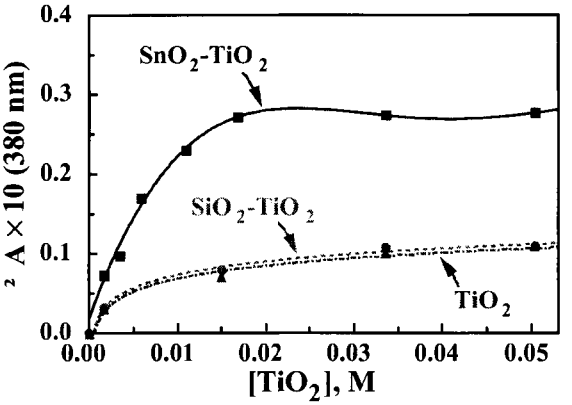


Fig. 15. Dependence of $I_2^{-\bullet}$ yield on the concentration of TiO_2: The maximum absorbance at 380 nm was monitored following the 308-nm excitation of (a) SnO_2@TiO_2, (b) SiO_2@TiO_2, and (c) TiO_2 colloidal suspension containing 0.05 M KI (deaerated with N_2). The concentrations of SnO_2 (29 mM) and SiO_2 (15 mM) were kept constant in the corresponding set of experiments. (Source: Reprinted with permission from [684]. © 1995 American Chemical Society.)

to the other existing methods such as chemical vapor deposition or molecular beam epitaxy. By controlling the preparative conditions of the semiconductor colloid precursors, it is possible to tailor the properties of these semiconductor films. These thin metal oxide films exhibit interesting photochromic, electrochromic, and photocatalytic and photoelectrochemical properties that are inherited from the native colloids.

Preparation of semiconductor nanoclusters in polymer films [80, 83, 84, 203, 227, 229, 532, 572, 698–703] and Langmuir Blodgett films [94, 103, 105, 108, 110, 111, 704–711] have also been considered. The sol-gel technique has been found useful in developing nanostructured semiconductor membranes with either a 2D [712] or a 3D configuration [180, 224, 620, 712–723]. Organic template mediated synthesis has been employed to develop nanoporous tin(IV) sulfide materials [724]. Fabrication and characterization of CdS-nanoparticle mono- and multilayers on a self-assembled monolayer of alkanedithiols on gold has also been reported recently [725].

The nanostructured films are highly porous and can easily be surface modified with sensitizers, redox couples, and other nanostructured semiconductors [143, 257, 339, 513, 629, 630, 638, 677–680, 685, 694, 696, 704, 711, 726–747]. Attempts have been made to sensitize large-band-gap semiconductors such as TiO_2 and SnO_2 with short-band-gap semiconductors [679, 680, 682, 685] and composite semiconductor films with Ru(II) polypyridyl complex [742]. Photoconversion efficiencies in the range of 11% to 15% in diffuse daylight are obtained for the sensitized photocurrent generation using nanostructured TiO_2 films modified with a ruthenium polypyridyl complex [588, 748]. Recent efforts have also focused on utilizing nanostructured semiconductor materials for sensors and microelectronic, photovoltaic, and electrooptic devices. Examples include a p–n junction rectifier using metal oxide films [678], gas sensors using SnO_2 films [749], a Schottky barrier solar cell fabricated from chemically deposited CdSe and Sb_2S_3 films [750], and a light-emitting diode developed from CdSe nanocrystalline film and a semiconducting polymer [751].

6.1. Preparation and Characterization of Nanostructured Semiconductor Films

6.1.1. From Preformed Colloidal Suspensions

The synthetic procedure involves preparation of ultrasmall semiconductor particles (particle diameter 2–10 nm) in aqueous or ethanolic solutions by controlled hydrolysis. A con-

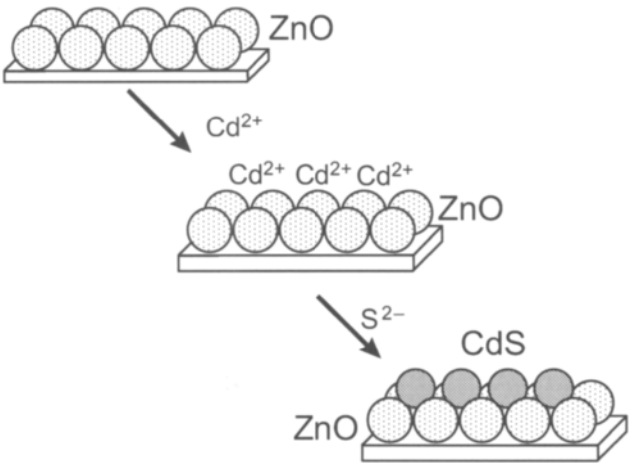


Fig. 16. Designing semiconductor heterostructures with selective adsorption of ions from solution.

centrated TiO_2 is one of the most commonly used semiconductor suspensions for casting thin nanostructured films. A colloidal suspension of SnO_2 (particle diameter 5–15 nm) is also commercially available (Johnson Matthey). The colloidal suspension of the metal oxide semiconductor is coated onto a conducting glass plate [also referred to as an optically transparent electrode (OTE)], and dried on a warm plate. The film is then annealed at 200–400 °C in air for about 1–2 h. This simple approach of coating preformed colloids on a desired surface and annealing produces a thin semiconductor film that is robust with excellent stability in both acidic and alkaline media (pH range 1–13). Usually, one can achieve a thickness in the range of 0.1 to 10 μm. It may be necessary to optimize the concentration of precursor colloid for a particular application because higher colloid concentrations lead to cracking of the film. This procedure can be repeated several times to cast thicker films. (For example, see the references for the methodology of preparing SnO_2 [339], ZnO [257], TiO_2 [444], and WO_3 [752] films.)

Transmission electron micrographs of nanostructured films prepared from colloidal suspensions show a three-dimensional network of SnO_2 nanocrystallites of particle diameter less than 5 nm [339]. All these particles are in direct contact with each other, often resembling a *grape-bunch* type of assembly. No significant particle growth or sintering effects could be seen during the annealing process. X-ray diffraction (XRD) analysis has also confirmed the crystallinity of these nanostructured films.

6.1.2. Chemical Precipitation

Chemical precipitation of the semiconductor directly on the surface of a desired substrate is another convenient approach to growing thin films of II–VI compound semiconductor nanocrystallites (Fig. 16) [257, 682]. For example, by successively dipping the ZnO film in Cd^{2+} and S^{2-} solutions, one can cast a thin film of CdS nanocrystallites. The yellow coloration of the film indicates the formation of CdS on the ZnO surface. Such a chemical precipitation technique is especially useful for designing coupled or multicomponent semiconductor films. The scanning electron microscope picture (Fig. 17) shows the formation of uniform size CdS clusters of diameter approximately 20 nm.

Electrochemical deposition is also a convenient technique for casting thin films of II–VI compound semiconductors, namely, CdS, CdSe, CdTe, and several mixed semiconductor films. Quantum size TiO_2 crystallites have also been deposited on conductive surfaces by anodic oxidative hydrolysis of $TiCl_3$ [753]. The details of the synthesis of electrochemically deposited semiconductor films are discussed elsewhere [679, 694, 726, 754]. Elec-

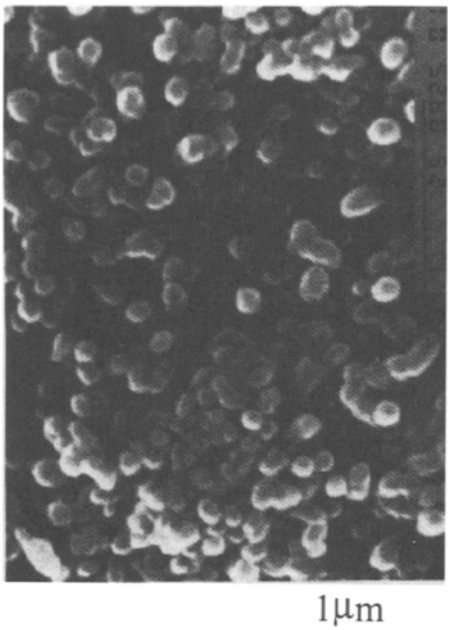


Fig. 17. Scanning electron micrograph of CdS nanocrystallites deposited on a ZnO thin film. The chemical precipitation was carried out by dipping ZnO film in $Cd(ClO_4)_2$ and Na_2S solutions successively. (Source: Reprinted from [685], with permission of Elsevier Science B.V.)

trochemically deposited films are strongly adherent to the substrate and are composed of aggregated nanocrystallites. The nanocrystal size distribution (isolated or aggregated) can be controlled by the deposition current and temperature. Recently, a new hybrid electrochemical/chemical (E/C) method has been employed to synthesize β-CuI nanocrystallites (10–180 Å) on an atomically smooth graphite basal plane surface [755]. The method consists of electrochemical deposition of copper nanocrystallites onto an electrode surface followed by their oxidation to Cu_2O and then displacement of oxygen in Cu_2O by iodide in aqueous solution. A similar method has also been employed to synthesize CdS nanocrystalline thin films [756].

6.1.3. Self-Organized Ordered Structure

Three- or two-dimensional periodic superstructures formed by colloidal crystals can be applied to important technological fields for optical filters [757, 758], switches [118], and photonic band gap materials [759–761]. Recently, methods have been developed for self-assembly of nanocrystal superlattices or nanocrystallite arrays of metal [710, 762–764], semiconductors [110, 765–769], oxides [770, 771], and sulfide clusters [725, 772, 773]. A highly ordered structure of nanometer-sized nanocrystallites is expected to induce collective excitation in ordered superlattice structures, possibly leading to unusual electronic interactions between the adjacent quantum dots [774]. Bawendi et al. [765] reported the self-organization of CdSe nanocrystallites capped with trialkylphosphine chalcogenide into a three-dimensional superlattice. They successfully prepared ordered thin films at solid and liquid interfaces using CdSe quantum dots with diameters of 63, 54, 47, 39, and 35 Å. The distance between the quantum dots was controlled with near atomic precision using various capping reagents. Capping reagents of tributylphosphine oxide (four carbons per chain), trioctylphosphine chalcogenide (eight carbons per chain), and trihexadecylphosphate (16 carbons per chain) gave separation distances of 7, 11, and 17 Å, respectively. Their preparation method onto solid surfaces can be applied to the integration of dot superlattice

structures into existing Si-based microelectronic architectures. Nanometer-size templates, such as the liquid-crystalline phase formed from nonionic organic amphiphiles [775] and the bacterial S layer, have also been found useful for the synthesis of superlattices [766]. Use of molecular templates seems to be a promising method to fabricate "tailored" superlattice structures, because the template can be synthesized or modified with a desirable structure using a cell protein monomer via an ordinary organic synthetic method. Fabrication for a scale larger than nanometer size was also achieved using nanotubes of chrysotile asbestos [776], porous aluminum oxide films [777], and commercially available membrane filter [778]. In the near future, novel superlattice structures using colloidal semiconductor nanocrystallites will be synthesized or fabricated for optical/magnetic/electronic devices with ultrasmall ordered structure.

6.1.4. Surface Modification

The porous metal oxide semiconductor films prepared from colloidal suspensions have a great affinity for interaction with organic dyes, redox couples, and organometallic complex molecules. This technique is especially convenient for extending the photoresponse of large-band-gap semiconductors with sensitizing dye molecules or for making the nanostructured films electrochemically active [339, 638, 748]. Because of the high porosity of the nanocrystalline film, large amounts of the sensitizing molecules (up to 0.1 M) can be incorporated in a nanocrystalline film of thickness of approximately 1 μm. Significant interaction between the adsorbed molecules leads to the aggregation effects. Similarly, deposition of monomer and aggregate forms of chlorophyll and chlorophyllin on ZnO, TiO_2, and SnO_2 films has been carried out [685, 728, 779]. A monolayer of aromatic amines anchored on nanocrystalline metal oxide films has been used to investigate the lateral electron transport in nanostructured materials [780].

6.2. Electron Storage and Photo- and Electrochromic Effects

Thin films made from metal oxide colloids such as WO_3, SnO_2, and TiO_2 exhibit reversible electrochromic and photochromic effects [183, 752, 781–784]. A blue coloration quickly develops as a result of electron storage at the trap sites when these films are subjected to UV irradiation or to an electrochemical (cathodic) bias. The electrons injected into the conduction band of the semiconductor get quickly trapped at the surface defects. Excess metal ions (e.g., Ti^{4+} in TiO_2) present at these defect sites accept the electrons and the reduced metal ions give rise to the blue coloration.

The changes in the absorption observed in a WO_3 nanostructured film at different applied potentials are shown in Figure 18. The film turns blue as we increase the applied bias. This is indicated by the increase in the absorption at wavelengths greater than 500 nm. The original color of the film can be restored by reversing the applied potential. The onset potential at which the electrochromic effect is observed corresponds to the flat band potential of the corresponding semiconductor and is dependent on the pH of the medium. By monitoring the optical absorbance, Fitzmaurice and co-workers [782, 785–788] have determined the flat band potentials of nanostructured films of TiO_2 and GaAs and the extinction coefficient of the trapped electrons. On the other hand, ZnO [246] and CdS [232] films exhibit bleaching at potentials more negative than the flat band potential. The accumulation of electrons in the conduction band results in the blue shift of the absorption edge (Burstein–Moss shift).

When dry films of WO_3 and TiO_2 were subjected to UV irradiation, they turned blue as a result of electron trapping. Spectrochemical and microwave absorption experiments suggest that trapped electrons are the major species responsible for the blue coloration of the film [729, 752]. Because the trapped electrons have a long lifetime, they provide a convenient method of storing electrons. Investigations of the trapping process by picosecond laser flash photolysis indicate this trapping process occurs on a subnanosecond

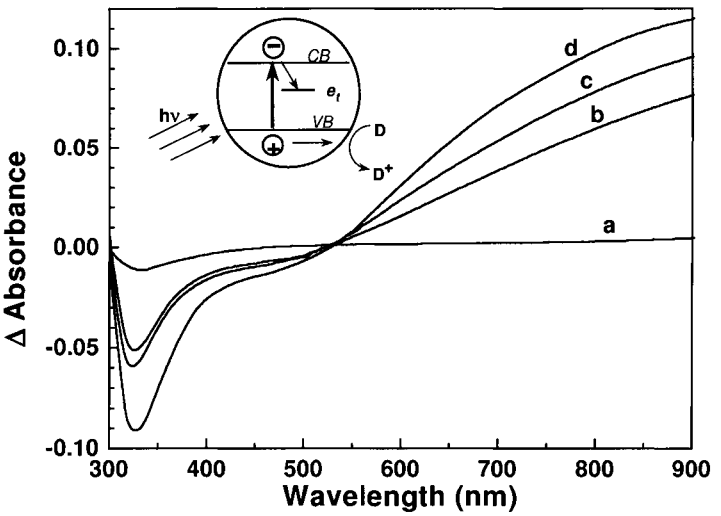


Fig. 18. Photoelectrochromic effect at WO_3 particulate films. (Source: Reprinted with permission from [752]. © 1994 American Chemical Society.)

time scale [183]. Annealing at higher temperature (>473 K) destroys the surface traps that are responsible for trapping photogenerated electrons [718, 752]. The electron storage effects in such semiconductor nanostructures have potential applications not only in electrochromic devices, but also in building electronic devices such as microcapacitors.

6.3. As a Photosensitive Electrode

A nanostructured semiconductor film is capable of generating photocurrent when employed as an electrode in a photoelectrochemical cell. The operation of a photoelectrochemical cell employing nanostructured semiconductor film as a photoanode is shown in Figure 19. The nanostructured semiconductor films exhibit photoelectrochemical characteristics similar to those of a polycrystalline semiconductor material. Under illumination with UV light, these metal oxide films undergo charge separation to form electron–hole pairs. Because the formation of an ideal space charge layer in semiconductor nanocrystallites with particle diameters less than 10 nm is less likely, the differing rates of electron or hole transfer into the electrolyte results in the accumulation of one of the charge carriers within the film [339, 444, 679, 726, 731, 789]. For example, one can accumulate electrons in a nanocrystalline TiO_2 film if photogenerated holes are scavenged by hydroxide ions. The varying degree of electron accumulation changes the pseudo-Fermi level and creates a potential gradient to drive away the electrons toward the collecting surface. The photocurrent generation as represented by IPCE (incident photon-to-current efficiency) in SnO_2, TiO_2, and SnO_2/TiO_2 films is compared in Figure 20. The onset of photoresponse in these films corresponds to the band gap energy of respective semiconductors.

The photoelectrochemical properties of these films are susceptible to surface adsorbed species such as oxygen [444], charge recombination at the grain boundaries [339, 731], and leakage of electrons into the solution instead of generating photocurrent [679]. However, a properly designed semiconductor particulate system and a suitably matched redox couple can greatly improve the efficiency of charge separation and thus the photoelectrochemical performance of the nanostructured semiconductor film.

The generation of photocurrent as a result of charge separation is strongly dependent on the applied potential. The applied anodic bias shifts the pseudo-Fermi level in such a way that it creates a potential gradient within the nanocrystalline film and drives away the photogenerated electrons and holes in opposite directions. With increasing negative

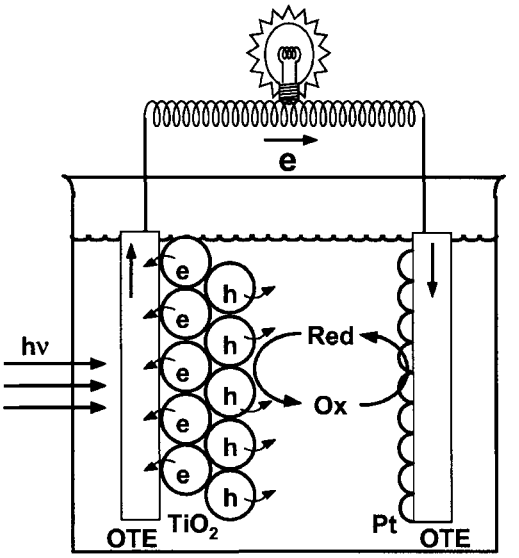


Fig. 19. Mechanism of photocurrent generation in a nanostructured semiconductor film. The electrons accumulated in TiO_2 nanocrystallites are collected at the optically transparent electrode surface and are transferred to the counterelectrode via the external circuit.

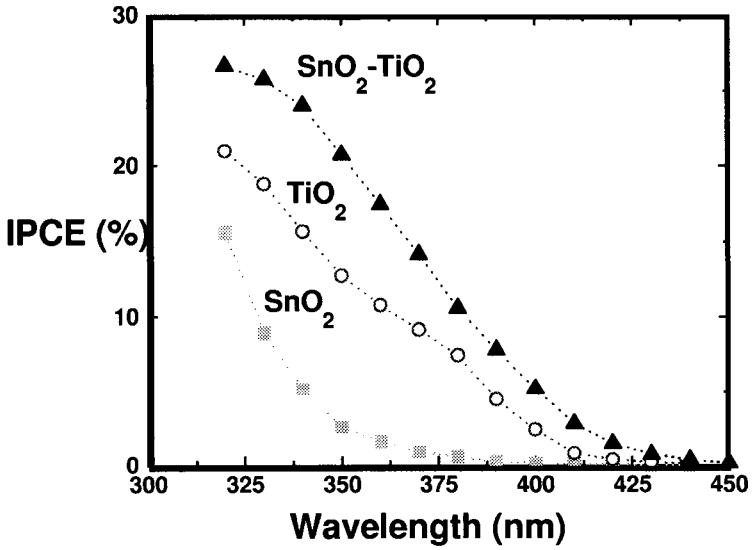


Fig. 20. Photocurrent action spectra of SnO_2, TiO_2, and SnO_2/TiO_2 composite films. (Source: Reprinted with permission from [814]. © 1996 American Chemical Society.)

potential, the pseudo-Fermi level increases, resulting in the accumulation of electrons. At a potential corresponding to the flat band potential, the photocurrent drops to zero as all the photogenerated charge carriers are lost in recombination.

A Schottky barrier model has been employed to analyze photovoltage and photocurrent results [257, 727]. For a photoelectrochemical cell operating on a Schottky barrier principle, V_{oc} can be related to i_{sc} by the following expression [10]:

$$V_{oc} = \frac{nkT}{q} \ln \left\{ \frac{i_{sc}}{i_0} + 1 \right\} \tag{8}$$

where k, T, and q are, respectively, the Boltzmann constant, absolute temperature, and electric charge, and n and i_0 are the diode quality factor and the reverse saturation current, respectively.

Efforts have also been made to understand the role of surface traps in influencing the photocurrent generation. For example, time-resolved photovoltage measurements carried out with a 337-nm laser pulse excitation indicate fast and slow growth components. The initial rise in photovoltage, which is completed within the time constant of the apparatus (500 ns), is attributed to the photoinduced charge separation between the conduction and valence bands. The slow growth was attributed to the existence of trapped charge carriers that exist in equilibrium with the charge carriers in the conduction and valence bands. Both fluorescence [83, 191, 302, 790] and microwave absorption [173, 315, 345, 347, 349, 605, 791] measurements have shown the importance of surface states in extending the lifetime of charge carriers.

One can observe novel effects from the thin films consisting of semiconductor structures in the form of multiple quantum wells (MQWS) or superlattices (SLS). Nozik and co-workers [792–795] have carried out a photoelectrochemical study on a 250-Å-thick $GaAs/GaAs_{0.5}P_{0.5}$ superlattice film. The photocurrent action spectra of lattice-matched superlattice electrodes in photoelectrochemical cells show structure with stepped waves that correspond to the quantum states in the quantum wells of the superlattice. The question regarding the hot-electron transfer from upper quantum states into solution has also been addressed with both a kinetic model and experimental results [795–797]. The flat band potential and photocurrent spectra of a single quantum well was also investigated in these studies.

6.4. Sensitization of Large-Band-Gap Semiconductors

The nanostructured films of metal oxides respond only in the UV region because they are large-band-gap semiconductors ($E_g > 3.0$ eV). One way to extend their photoresponse is to modify the semiconductor surface with sensitizing dyes that absorb strongly in the visible. The process of utilizing sub-band-gap excitations with dyes is referred to as photosensitization and conveniently employed in color photography and other imaging science applications. This approach of light energy conversion is similar to plant photosynthesis, in which chlorophyll molecules act as light-absorbing antenna molecules. In other words, the dye-modified semiconductor films provide an efficient method to mimic the photosynthetic process. Bignozzi et al. [798] have presented a supramolecular approach for designing photosensitizers. By optimizing the molecular design, it should be possible to suppress the interfacial charge recombination and improve the cross section for light absorption.

The high porosity and strong surface bonding property of the nanostructured semiconductor films facilitate surface modification with organic dyes and organometallic complexes such as bis(2,2′-bipyridine)(2,2′-bipyridine-4,4′dicarboxylic acid)ruthenium(II). The nanostructured TiO_2 films modified with a ruthenium complex exhibit photoconversion efficiencies in the range of 10% to 15% in diffused daylight [748], which is comparable to that of amorphous silicon-based photovoltaic cells.

The photocurrent response evaluated in terms of the photon-to-current efficiency (IPCE) of SnO_2 film with and without surface modification is shown in Figure 21 [339]. The IPCE maximum of the surface-modified SnO_2 film closely matches the absorption maximum of the sensitizer. The SnO_2 film, which is sensitive only to UV excitation prior to surface modification, responds to the visible light (wavelengths greater than 400 nm) as a result of surface modification. This shows that a photosensitization mechanism is operative in extending the photocurrent response of the SnO_2 film. When the electrode is illuminated with visible light, the sensitizer molecules absorb light and inject electrons into the SnO_2 particles. These electrons are then collected at the conducting glass surface to generate anodic photocurrent. The redox couple (e.g., I_3^-/I^-) present in the electrolyte quickly regenerates the sensitizer. By choosing an appropriate sensitizer, it is possible to tune the

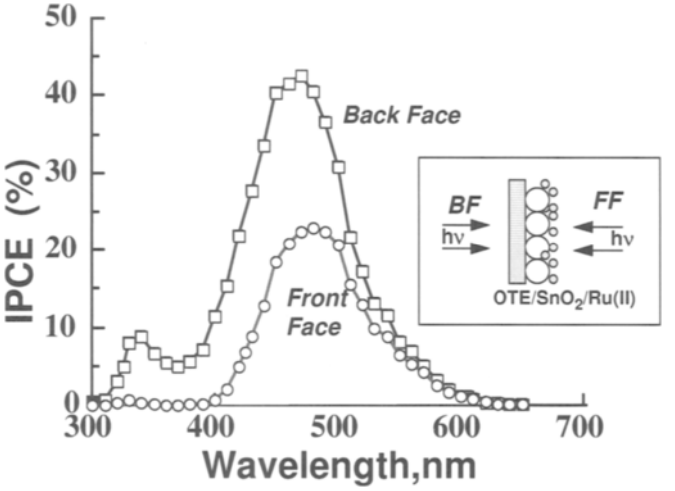


Fig. 21. Sensitized photocurrent generation at a SnO_2 nanocrystalline semiconductor film modified with a ruthenium complex in a photoelectrochemical cell containing 0.04 M I_2 and 0.5 M LiI in acetonitrile as electrolyte. (a) SnO_2 film before modification and (b) after modification with a ruthenium complex. (Source: Reprinted with permission from [339]. © 1994 American Chemical Society.)

photoresponse of these nanostructured semiconductor films. For example, sensitizing dyes such as chlorophyll a and b [685, 728], squaraines [630], and oxazines [638] can extend the photoresponse of SnO_2 films to the red-infrared region. The maximum IPCE in the example discussed in Figure 24 (around 50%) shows that nearly half of the injected charge from the excited sensitizer is lost as a result of recombination with the oxidized sensitizer. By optimizing the operating conditions, it is possible to improve the performance of the IPCE of the sensitizer-based cells. Ru complex–modified TiO_2 nanostructured films exhibit an IPCE of nearly 90% under optimized light-harvesting conditions [748]. Both experimental and theoretical evaluations of these cells have been carried out and the efficiency limiting factors have been identified [799, 800].

The varying degree of electron accumulation within the semiconductor particles alters the energetics of the quasi-Fermi level and creates a potential gradient within the thin film (Fig. 22). The formation of such a potential gradient provides the necessary driving force for the electron transport to the collecting surface of OTE. Although it is difficult to establish the exact nature of this overall potential gradient, the experimental results indicate it to be qualitatively similar to that of the Schottky barrier observed in a single-crystal semiconductor system [339, 629, 728]. Because this potential gradient is not an ideal type of Schottky barrier, significant loss of electrons is encountered during the transit because of recombination at the grain boundaries. This is evident from the relatively high reverse saturation photocurrents observed in these examples.

The excited state lifetime of the sensitizer adsorbed on semiconductor films is significantly lower than that adsorbed on an insulator surface such as alumina. The kinetic evaluation of the multiexponential luminescence decay of the excited Ru complex adsorbed on SnO_2 suggests that multiple injection/adsorption sites exist on the surface of a semiconductor nanocrystallite. The rate constants for heterogeneous electron transfer between excited Ru complex and semiconductor crystallites such as SnO_2, TiO_2, and ZnO are in the range of 10^7 to 10^9 s^{-1} [339, 621, 658]. Independent microwave absorption and luminescence measurements have been carried out to monitor the charge injection from excited $Ru(bpy)_2(dcbpy)^{2+}$ into SnO_2, ZnO, and TiO_2 nanocrystallites [351]. The growth of microwave absorption was delayed from the laser pulse by a process showing a similar rate constant to the fast decay portion of the luminescence. The appearance of microwave

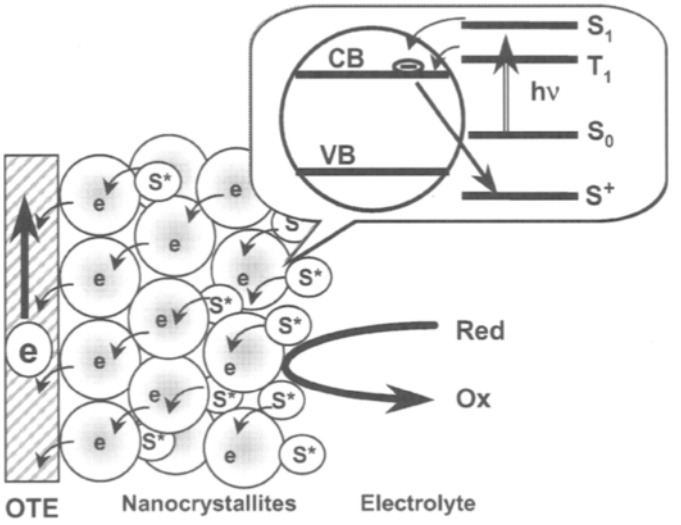


Fig. 22. Mechanism of sensitized photocurrent generation in a nanocrystalline semiconductor film.

conductivity at rates corresponding to the luminescence directly confirms the fast component of the heterogeneous electron rate constant to be in the range of 1 to 3×10^8 s^{-1}.

The charge injection from a singlet excited sensitizer into the conduction band of a large-band-gap semiconductor is usually considered to be an ultrafast process occurring in the picosecond time domain. The charge injection process in the case of organic dyes such as anthracene carboxylate [801], squaraines [802], and cresyl violet [602, 603] has been shown to occur within 20 ps. Similar fast electron transfer has also been noted for $Ru(H_2O)_2^{2-}$ on a TiO_2 surface at very low coverage [603]. On the contrary, relatively smaller charge injection rate constants (10^8–10^9 s^{-1}) have been reported by several research groups investigating the photophysical behavior of ruthenium complexes adsorbed on various semiconductor surfaces [339, 621, 658, 662, 663, 803, 804]. It has been suggested that electron trapping at surface defects may be a contributing factor in controlling the heterogeneous electron transfer at the semiconductor surface [805]. Similarly, the charge injection from the triplet excited dyes into TiO_2 [593] and ZnO [604] colloids has also been shown to occur on a slower time scale. The results presented here suggest that the electron transfer from the excited $Ru(bpy)_2(dcbpy)^{2+}$ occurs with a relatively slower rate than the singlet excited organic dyes but is comparable to the triplet excited dyes. It should be noted that the excited state of $Ru(bpy)_2(dcbpy)^{2+}$ involves metal-to-ligand charge transfer state and the implications are that such an electronic configuration of the excited state plays an important role in controlling the electron injection rates. The possibility of a connection between the multiplicity of the excited sensitizer and the rate constant for charge injection deserves more careful study.

6.5. Single-Electron Tunneling Devices

Controlling single-electron tunneling (SET) phenomena in nanostructured materials is gaining interest, because of its importance in developing extremely small electronic devices with high speed and low power consumption. When the size of the junction becomes small enough to have extremely small capacitance, C, the charging energy resulting from a single electron at the junction, $W = q^2/2C$, becomes larger than the thermal energy, kT, thus preventing additional electron injection to the junction (Fig. 23) [806]. Assembling a semiconductor junction using 1–2-nm nanoparticles results in the construction of single-electron devices that can be operated at room temperature [807, 808]. The charging energy

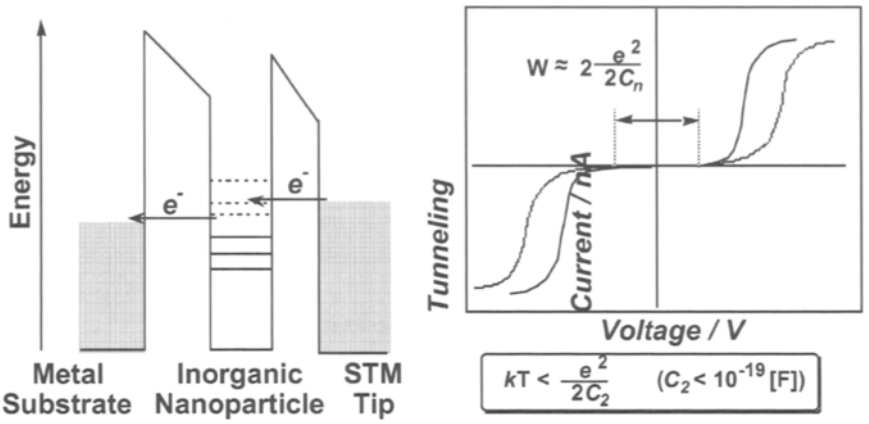


Fig. 23. Energy diagram of single-electron tunneling junction and typical voltage–current characteristics. (Source: Reprinted with permission from [806].)

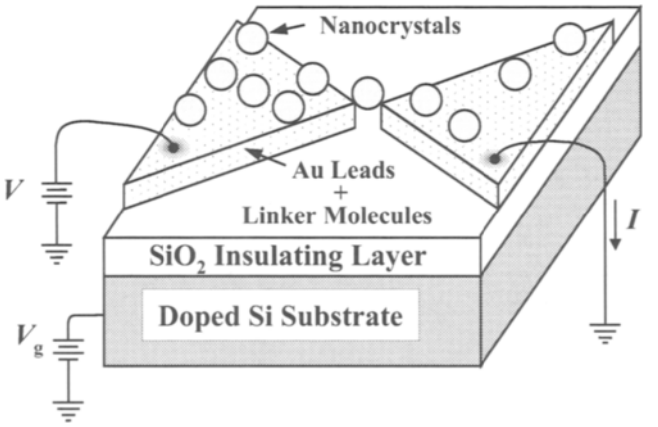


Fig. 24. Diagram of single-electron tunneling device. The electrochemical potential of the nanocrystallites between bridges can be tuned by applying a gate voltage to the substrate. (Source: Reprinted with permission from [813]. © 1997 Macmillan, Magazines Limited.)

of the junction, which consists of metal nanoparticles in the size range of 1 to 2 nm, becomes larger than the thermal energy at room temperature because of the extremely small capacitance of the metal nanoparticle ($C < 10^{-19}$ F). Several reports are available for the observation of the Coulomb blockade phenomenon at room temperature using systems of small gold nanoparticles on self-assembled organic monolayers [807, 808], polysilicon dots [809], small gold nanoparticles sandwiched by lamellar inorganic solids [810], and ultrasmall microelectrodes [811].Efforts have now gradually become to be focused on the development of techniques to construct such ultrasmall junctions with organized structure, because generally their dimensions are much smaller than those using ordinary lithographic techniques at the present. The techniques of colloidal chemistry could be a promising way to construct/synthesize/assemble such ultrasmall junctions. Controlling the size, crystalline structure, and structure anisotropy should be applied to this field. The use of various organic surface-modified reagents should also be helpful in controlling the nature of junction gap characteristics.

Alivisatos et al. [812, 813] reported interesting results showing the future possibility of applying colloidal semiconductors to single-electron transistors. Electrical transport properties of a single-electron transistor using 5.5-nm CdSe nanocrystallines was investigated

at 77 K (Fig. 24). They observed clearly the Coulomb oscillation spacing at 30–60 meV using the devices. The observed values correspond to estimated energy values of 50 meV for a 5.5-nm-diameter metallic sphere. The number of charges on the nanocrystallites was tuned precisely by the gate voltage, and changed the blockade energy reflecting their degeneration of the state. They pointed out the possibility of the device application for the measurement of energy level spectra of small electronic systems [813]. Their reports on CdSe nanocrystallites are the first examples of applying semiconductor nanocrystallites for ultrasmall devices using single-electron phenomenon. In the near future, smaller nanocrystallites with well-defined crystalline structure could be applied to the devices and operated at room temperature.

7. CONCLUDING REMARKS

The ability of semiconductor nanoclusters to carry out redox processes with greater efficiency and selectivity than in homogeneous solutions has made them potential candidates for the conversion and storage of solar energy and environmental remediation. The future challenge lies in designing novel microheterogeneous assemblies for artificial photosynthesis. The possibility of casting thin nanostructured semiconductor films on conducting glass plates has brought us new opportunities to explore their properties and novel applications.

Acknowledgments

PVK acknowledges the support of the Office of Basic Energy Sciences of the U.S. Department of Energy. This is contribution 4068 from the Notre Dame Radiation Laboratory. PVK also acknowledges the Japan Society for Promotion of Science for the award of JSPS fellowship, which made the visit to Osaka University possible.

References

1. A. J. Bard, *J. Photochem.* 10, 59 (1979).
2. A. J. Nozik, *Faraday Discuss. Chem. Soc.* 17 (1980).
3. A. J. Bard, *J. Phys. Chem.* 86, 172 (1982).
4. Y. Y. Gurevich and Y. V. Pleskov, *Russ. Chem. Rev.* 52, 563 (1983).
5. P. V. Kamat and N. M. Dimitrijevic, *Sol. Energy* 44, 83 (1990).
6. M. A. Fox, *Acc. Chem. Res.* 16, 314 (1983).
7. K. Kalyanasundaram, M. Grätzel, and E. Pelizzetti, *Coord. Chem. Rev.* 69, 57 (1986).
8. M. A. Fox, *Top. Curr. Chem.* 142, 72 (1987).
9. A. Heller, *New J. Chem.* 11, 187 (1987).
10. R. Memming, *Top. Curr. Chem.* 143, 79 (1988).
11. A. Henglein, *Chem. Rev.* 89, 1861 (1989).
12. M. Anpo, *Res. Chem. Intermed.* 11, 67 (1989).
13. E. N. Savinov, Y. A. Gruzdkov, and V. N. Parmon, *Int. J. Hydrogen Energy* 14, 1 (1989).
14. N. Serpone and E. Pelizzetti, "Photocatalysis Fundamentals and Applications." Wiley, New York, 1989.
15. M. A. Fox, *CHEMTECH* 22, 680 (1992).
16. D. F. Ollis and H. Al Ekâbi, "Photocatalytic Purification of Water and Air." Elsevier Science, Amsterdam, 1993.
17. M. R. Hoffmann, S. T. Martin, W. Choi, and D. W. Bahnemann, *Chem. Rev.* 95, 69 (1995).
18. U. Stafford, K. A. Gray, and P. V. Kamat, *Heterogeneous Chem. Rev.* 3, 77 (1996).
19. M. Grätzel, "Energy Resources through Photochemistry and Catalysis." Academic Press, New York, 1983.
20. A. Henglein, *Pure Appl. Chem.* 56, 1215 (1984).
21. G. Hodes and M. Grätzel, *Nouv. J. Chim.* 8, 509 (1984).
22. A. Fojtik, H. Weller, U. Koch, and A. Henglein, *Ber. Bunsen-Ges. Phys. Chem.* 88, 969 (1984).
23. G. T. Brown, J. R. Darwent, and P. D. I. Fletcher, *J. Am. Chem. Soc.* 107, 6446 (1985).
24. H. Weller, H. M. Schmidt, U. Koch, A. Fojtik, S. Baral, A. Henglein, W. Kunath, K. Weiss, and E. Dieman, *Chem. Phys. Lett.* 124, 557 (1986).
25. A. Henglein, *Prog. Colloid Polym. Sci.* 73, 1 (1987).

26. J. J. Ramsden, *Proc. R. Soc. London, Ser. A* 410, 89 (1987).
27. M. Grätzel and K. Kalyanasundaram, "Kinetics and Catalysis in Microheterogeneous Systems." Marcel Dekker, New York, 1991.
28. M. Grätzel, "Heterogeneous Photochemical Electron Transfer." CRC Press, Boca Raton, FL, 1989.
29. N. S. Lewis, *Acc. Chem. Res.* 23, 176 (1990).
30. M. D. E. Forbes and N. S. Lewis, *J. Am. Chem. Soc.* 112, 3682 (1990).
31. L. M. Peter, *Chem. Rev.* 90, 753 (1990).
32. P. V. Kamat, in "Kinetics and Catalysis in Microheterogeneous Systems" (M. Grätzel and K. Kalyanasundaram, eds.), p. 375. Marcel Dekker, New York, 1991.
33. C. A. Koval and J. N. Howard, *Chem. Rev.* 92, 411 (1992).
34. L. Brus, *J. Phys. Chem.* 90, 2555 (1986).
35. M. L. Steigerwald and L. E. Brus, *Acc. Chem. Res.* 23, 183 (1990).
36. L. Brus, *J. Phys. Chem.* 98, 3575 (1994).
37. L. Brus, *Colloid Interface Sci.* 1, 197 (1996).
38. Y. I. Kim, S. J. Atherton, E. S. Brigham, and T. E. Mallouk, *J. Phys. Chem.* 97, 11802 (1993).
39. P. V. Kamat, *Chem. Rev.* 93, 267 (1993).
40. H. Weller, *Adv. Mater.* 5, 88 (1993).
41. H. Weller, *Angew. Chem. Int. Ed. Engl.* 32, 41 (1993).
42. O. I. Micic, T. Rajh, J. M. Nedeljkovic, and M. I. Comor, *Isr. J. Chem.* 33, 59 (1993).
43. G. N. Ryba, C. N. Kenyon, and N. S. Lewis, *J. Phys. Chem.* 97, 13814 (1993).
44. P. Alivisatos, *J. Phys. Chem.* 100, 13226 (1996).
45. J. Belloni, in "Homogeneous Photocatalysis" (M. Chanon, ed.), p. 170. Wiley, New York, 1997.
46. P. V. Kamat and D. Meisel, in "Studies in Surface Science and Catalysis," p. 474. Elsevier Science, Amsterdam, 1997.
47. T. Rajh, O. I. Micic, and A. J. Nozik, *J. Phys. Chem.* 97, 11999 (1993).
48. T. Vossmeyer, L. Katsikas, M. Giersig, I. G. Popovic, K. Diesner, A. Chemseddine, A. Eychmüller, and H. Weller, *J. Phys. Chem.* 98, 7665 (1994).
49. Y. Nosaka, K. Yamaguchi, H. Miyama, and H. Hayashi, *Chem. Lett.* 605 (1988).
50. M. L. Steigerwald, A. P. Alivisatos, J. M. Gibson, T. D. Harris, R. Kortan, A. J. Muller, A. M. Thayer, T. M. Duncan, D. C. Douglass, and L. E. Brus, *J. Am. Chem. Soc.* 110, 3046 (1988).
51. D. Hayes, O. I. Micic, M. T. Nenadovic, V. Swayambunathan, and D. Meisel, *J. Phys. Chem.* 93, 4603 (1989).
52. C. H. Fischer and A. Henglein, *J. Phys. Chem.* 93, 5578 (1989).
53. A. R. Kortan, R. Hull, R. L. Opila, M. G. Bawendi, M. L. Steigerwald, P. J. Carroll, and L. E. Brus, *J. Am. Chem. Soc.* 112, 1327 (1990).
54. N. Herron, Y. Wang, and H. Eckert, *J. Am. Chem. Soc.* 112, 1322 (1990).
55. V. Swayambunathan, D. Hayes, K. H. Schmidt, Y. X. Liao, and D. Meisel, *J. Am. Chem. Soc.* 112, 3831 (1990).
56. S. Yanagida, T. Enokida, A. Shindo, T. Shiragami, T. Ogata, T. Fukumi, T. Sakaguchi, and T. Sakata, *Chem. Lett.* 1773 (1990).
57. U. Resch, A. Eychmueller, M. Haase, and H. Weller, *Langmuir* 8, 2215 (1992).
58. V. L. Colvin, A. N. Goldstein, and A. P. Alivisatos, *J. Am. Chem. Soc.* 114, 5221 (1992).
59. S. Mahamuni, A. A. Khosravi, M. Kundu, A. Kshirsagar, A. Bedekar, D. B. Avasare, P. Singh, and S. K. Kulkarni, *J. Appl. Phys.* 73, 5237 (1993).
60. T. Torimoto, H. Uchida, T. Sakata, H. Mori, and H. Yoneyama, *J. Am. Chem. Soc.* 115, 1874 (1993).
61. T. Torimoto, T. Sakata, H. Mori, and H. Yoneyama, *J. Phys. Chem.* 98, 3036 (1994).
62. T. Torimoto, K. Maeda, J. Maenaka, and H. Yoneyama, *J. Phys. Chem.* 98, 13658 (1994).
63. H. Inoue, N. Ichiroku, T. Torimoto, T. Sakata, H. Mori, and H. Yoneyama, *Langmuir* 10, 4517 (1994).
64. S. Yanagida, H. Kawakami, Y. Midori, H. Kizumoto, C. Pac, and Y. Wada, *Bull. Chem. Soc. Jpn.* 68, 1811 (1995).
65. D. Lawless, S. Kapoor, and D. Meisel, *J. Phys. Chem.* 99, 10329 (1995).
66. L. Spanhel, M. Haase, H. Weller, and A. Henglein, *J. Am. Chem. Soc.* 109, 5649 (1987).
67. C. Murray, D. Norris, and M. Bawendi, *J. Am. Chem. Soc.* 115, 8706 (1993).
68. T. L. Pettit and M. A. Fox, *J. Phys. Chem.* 90, 1353 (1986).
69. Y. Wang and N. Herron, *J. Phys. Chem.* 91, 257 (1987).
70. M. A. Fox, *Res. Chem. Intermed.* 15, 153 (1991).
71. R. D. Stramel, T. Nakamura, and J. K. Thomas, *J. Chem. Soc., Faraday Trans.* 84, 1287 (1988).
72. N. Herron, Y. Wang, M. M. Eddy, G. D. Stucky, D. E. Cox, K. Moller, and T. Bein, *J. Am. Chem. Soc.* 111, 530 (1989).
73. K. Moller, M. M. Eddy, G. D. Stucky, N. Herron, and T. Bein, *J. Am. Chem. Soc.* 111, 2564 (1989).
74. Y. Wang and N. Herron, *Res. Chem. Intermed.* 15, 17 (1991).
75. X. Liu, K. K. Iu, and J. K. Thomas, *J. Chem. Soc., Faraday Trans.* 89, 1861 (1993).
76. A. Jentys, R. W. Grimes, J. D. Gale, and C. R. A. Catlow, *J. Phys. Chem.* 97, 13535 (1993).
77. A. I. Ekimov, A. L. Efros, and A. A. Onushchenko, *Solid State Commun.* 56, 921 (1985).

78. J. Kuczynski and J. K. Thomas, *J. Phys. Chem.* 89, 2720 (1985).
79. T. Rajh, M. I. Vucemilovic, N. M. Dimitrijevic, O. I. Micic, and A. J. Nozik, *Chem. Phys. Lett.* 143, 305 (1988).
80. M. Krishnan, J. R. White, M. A. Fox, and A. J. Bard, *J. Am. Chem. Soc.* 105, 7002 (1983).
81. N. Kakuta, J. M. White, A. Campion, A. J. Bard, M. A. Fox, and S. E. Webber, *J. Phys. Chem.* 89, 48 (1985).
82. Y. Wang, A. Suna, W. Mahler, and R. Kasowski, *J. Chem. Phys.* 87, 7315 (1987).
83. K. R. Gopidas and P. V. Kamat, *Mater. Lett.* 9, 372 (1990).
84. R. Tassoni and R. R. Schrock, *Chem. Mater.* 6, 744 (1994).
85. P. Lianos and J. K. Thomas, *Chem. Phys. Lett.* 125, 299 (1986).
86. C. Petit and M. P. Pileni, *J. Phys. Chem.* 92, 2282 (1988).
87. C. Petit, P. Lixon, and M. P. Pileni, *J. Phys. Chem.* 94, 1598 (1990).
88. L. Motte, F. Billoudet, and M. P. Pileni, *J. Phys. Chem.* 99, 16425 (1995).
89. J. Cizeron and M. P. Pileni, *J. Phys. Chem.* 99, 17410 (1995).
90. L. Levy, J. F. Hochepied, and M. P. Pileni, *J. Phys. Chem.* 100, 18322 (1996).
91. S. Modes and P. Lianos, *J. Phys. Chem.* 93, 5854 (1989).
92. E. Stathatos, P. Lianos, F. Del Monte, D. Levy, and D. Tsiourvas, *Langmuir* 13, 4295 (1997).
93. Y. M. Tricot and J. H. Fendler, *J. Am. Chem. Soc.* 106, 7359 (1984).
94. R. Rafaeloff, Y. M. Tricot, F. Nome, and J. H. Fendler, *J. Phys. Chem.* 89, 533 (1985).
95. Y. M. Tricot, A. Emeren, and J. H. Fendler, *J. Phys. Chem.* 89, 4721 (1985).
96. Y. M. Tricot and J. H. Fendler, *J. Phys. Chem.* 90, 3369 (1986).
97. H. J. Watzke and J. H. Fendler, *J. Phys. Chem.* 91, 854 (1987).
98. H. C. Youn, S. Baral, and J. H. Fendler, *J. Phys. Chem.* 92, 6320 (1988).
99. A. C. Chang and J. H. Fendler, *J. Phys. Chem.* 93, 2538 (1989).
100. M. I. Khramov and V. N. Parmon, *J. Photochem. Photobiol., A* 71, 279 (1993).
101. B. A. Korgel and H. G. Monbouquette, *J. Phys. Chem.* 100, 346 (1996).
102. B. A. Korgel and H. G. Monbouquette, *J. Phys. Chem.* 100, 346 (1996).
103. X. Zhang and A. J. Bard, *J. Phys. Chem.* 92, 5566 (1988).
104. R. Zhu, G. Min, Y. Wei, and H. J. Schmitt, *J. Phys. Chem.* 96, 8210 (1992).
105. K. C. Yi and J. H. Fendler, *Langmuir* 6, 1519 (1990).
106. J. H. Fendler, in "Electrochemistry in Colloids and Dispersions" (R. A. Mackay and J. Texter, eds.), p. 475. VCH Publishers, New York, 1992.
107. J. H. Fendler, *Isr. J. Chem.* 33, 41 (1993).
108. N. J. Geddes, R. S. Urquhart, D. N. Furlong, C. R. Lawrence, K. Tanaka, and Y. Okahata, *J. Phys. Chem.* 97, 13767 (1993).
109. X. Peng, R. Lu, Y. Y. Zhao, L. H. Qu, H. Y. Chen, and T. J. Li, *J. Phys. Chem.* 98, 7052 (1994).
110. J. H. Fendler, *Chem. Mater.* 8, 1616 (1996).
111. J. H. Fendler, in "Semiconductor Nanoclusters—Physical, Chemical and Catalytic Aspects" (P. V. Kamat and D. Meisel, eds.), p. 261. Elsevier Science, Amsterdam, 1997.
112. J. Yang, F. C. Meldrum, and J. H. Fendler, *J. Phys. Chem.* 99, 5500 (1995).
113. I. Ichinose, N. Kimizuka, and T. Kunitake, *J. Phys. Chem.* 99, 3736 (1995).
114. I. Ichinose, T. Asai, S. Yoshimura, N. Kimizuka, and T. Kunitake, *Chem. Lett.* 1837 (1994).
115. K. M. Choi and K. J. Shea, *J. Phys. Chem.* 98, 3207 (1994).
116. I. Willner and Y. Eichen, *J. Am. Chem. Soc.* 109, 6862 (1987).
117. I. Willner, Y. Eichen, and A. J. Frank, *J. Am. Chem. Soc.* 111, 1884 (1989).
118. S. Y. Chang, L. Liu, and S. A. Asher, *J. Am. Chem. Soc.* 116, 6745 (1994).
119. S. Y. Chang, L. Liu, and S. A. Asher, *J. Am. Chem. Soc.* 116, 6739 (1994).
120. I. G. Dance, A. Choy, and M. L. Scudder, *J. Am. Chem. Soc.* 106, 6285 (1984).
121. G. S. Lee, D. C. Craig, I. Ma, M. L. Scudder, T. D. Bailey, and I. G. Dance, *J. Am. Chem. Soc.* 110, 4863 (1988).
122. T. Vossmeyer, G. Reck, L. Katsikas, E. T. K. Haupt, B. Schulz, and H. Weller, *Science* 267, 1476 (1995).
123. T. Vossmeyer, G. Reck, B. Schulz, L. Katsikas, and H. Weller, *J. Am. Chem. Soc.* 117, 12881 (1995).
124. N. Herron, J. C. Calabrese, W. E. Farneth, and Y. Wang, *Science* 259, 1426 (1993).
125. D. M. Wilhelmy and E. Matijevic, *J. Chem. Soc., Faraday Trans. 1* 80, 563 (1984).
126. E. Matijevic, *Langmuir* 2, 12 (1986).
127. C. Hayashi, *Phys. Today* 44 (1987).
128. C. Levy-Clement, A. Lagoubi, D. Ballutaud, F. Ozanam, and J.-N. Chazalviel, *Appl. Surf. Sci.* 65/66, 408 (1993).
129. C. Levy-Clement, A. Lagoubi, and M. Tomkiewicz, *J. Electrochem. Soc.* 141, 958 (1994).
130. T. Rajh, O. I. Micic, and A. J. Nozik, *Langmuir* 2, 477 (1986).
131. O. I. Micic, L. Zongguan, G. Mills, J. C. Sullivan, and D. Meisel, *J. Phys. Chem.* 91, 6221 (1987).
132. Y. Haruvy, M. Grätzel, and L. A. Rajbenbach, *Radiat. Phys. Chem.* 31, 843 (1988).
133. D. Hayes, D. Meisel, and O. I. Micic, *Colloids Surf.* 55, 121 (1991).
134. D. Hayes, K. H. Schmidt, and D. Meisel, *J. Phys. Chem.* 93, 6100 (1989).

135. D. Meisel, in "Radiation Research, A Twentieth Century Perspective," Proceedings of the 9th International Congress Radiation Research, Vol. 2, p. 121. Academic Press, New York, 1992.
136. J. Khatouri, M. Mostafavi, and J. Belloni, in "Photochemistry and Radiation Chemistry. Complementary Methods for Studying Electron Transfer" (J. Wishart and D. Nocera, eds.), p. XX. American Chemical Society, Washington, DC, 1997.
137. R. A. Hobson, P. Mulvaney, and F. Grieser, *J. Chem. Soc., Chem. Commun.* 823 (1994).
138. J. Z. Sostaric, R. A. Caruso-Hobson, P. Mulvaney, and F. Grieser, *J. Chem. Soc., Faraday Trans.* 93, 1791 (1997).
139. C. H. Fischer, H. Weller, A. Fojtik, P. C. Lume, E. Janata, and A. Henglein, *Ber. Bunsen-Ges. Phys. Chem.* 90, 46 (1986).
140. C. H. Fischer, J. Lilie, H. Weller, L. Katsikas, and A. Henglein, *Ber. Bunsen-Ges. Phys. Chem.* 93, 61 (1989).
141. C. H. Fischer, H. Weller, L. Katsikas, and A. Henglein, *Langmuir* 5, 429 (1989).
142. Y. Wang, M. Harmer, and N. Herron, *Isr. J. Chem.* 33, 31 (1993).
143. H. Weller, A. Eychmuller, R. Vogel, L. Katsikas, A. Hasselbarth, and M. Giersig, *Isr. J. Chem.* 33, 107 (1993).
144. H. Matsumoto, H. Uchida, T. Matsunaga, K. Tanaka, and T. Sakata, *J. Phys. Chem.* 98, 11549 (1994).
145. H. Matsumoto, T. Sakata, H. Mori, and H. Yoneyama, *J. Phys. Chem.* 100, 13781 (1996).
146. T. Torimoto, H. Nishiyama, T. Sakata, H. Mori, and H. Yoneyama, *J. Electrochem. Soc.* 145, 1964 (1998).
147. K. Murakoshi, H. Hosokawa, M. Saito, Y. Wada, T. Sakata, H. Mori, and S. Yanagida, *J. Chem. Soc., Faraday Trans.* 4, 579 (1998).
148. D. R. Lide, in "CRC Handbook of Chemistry and Physics," 75th ed., p. 4. CRC Press, Boca Raton, FL, 1995.
149. M. V. Ramakrishna and R. A. Friesner, *J. Chem. Phys.* 95, 8309 (1991).
150. J. J. Ramsden, S. E. Webber, and M. Grätzel, *J. Phys. Chem.* 89, 2740 (1985).
151. M. Kanemoto, K. Ishihara, Y. Wada, T. Sakata, H. Mori, and S. Yanagida, *Chem. Lett.* 835 (1992).
152. M. Kanemoto, H. Ankyu, Y. Wada, and S. Yanagida, *Chem. Lett.* 2113 (1992).
153. M. Kanemoto, M. Nomura, Y. Wada, T. Akano, and S. Yanagida, *Chem. Lett.* 1687 (1993).
154. R. J. Bandaranayake, G. W. Wen, J. Y. Lin, H. X. Jiang, and C. M. Sorensen, *Appl. Phys. Lett.* 67, 831 (1995).
155. M. Haase and A. P. Alivisatos, *J. Phys. Chem.* 96, 6756 (1992).
156. S. H. Tolbert and A. P. Alivisatos, *Science* 265, 373 (1994).
157. S. H. Tolbert and A. P. Alivisatos, *J. Chem. Phys.* 102, 4642 (1995).
158. K. Murakoshi, H. Hosokawa, N. Tanaka, M. Saito, Y. Wada, T. Sakata, H. Mori, and S. Yanagida, *Chem. Commun.* 3, 321 (1998).
159. L. Brus, in "Photoinduced Electron Transfer. Part B: Experimental Techniques and Medium Effects" (M. A. Fox and M. Chanon, eds.), p. 314. Elsevier, Amsterdam, 1988.
160. L. Brus, *New J. Chem.* 11, 123 (1987).
161. A. Henglein, *Top. Curr. Chem.* 143, 113 (1988).
162. A. Henglein and H. Weller, in "Photochemical Energy Conversion" (J. R. Norris, Jr. and D. Meisel, eds.). Elsevier, New York, 1989.
163. A. I. Ekimov, A. L. Efros, T. V. Shubina, and A. P. Skvortsov, *J. Lumin.* 46, 97 (1990).
164. Y. Wang and N. Herron, *J. Phys. Chem.* 95, 525 (1991).
165. Y. Wang, in "Photochemical Conversion and Storage of Solar Energy" (E. Pelizzetti and M. Schiavello, eds.). Kluwer Academic, Dordrecht, The Netherlands, 1991.
166. L. Banyai and S. W. Koch, "Semiconductor Quantum Dots." World Scientific, River Edge, NJ, 1993.
167. P. V. Kamat, *Prog. React. Kinet.* 19, 277 (1994).
168. H. Weller, U. Koch, M. Gutierrez, and A. Henglein, *Ber. Bunsen-Ges. Phys. Chem.* 88, 649 (1984).
169. R. Rossetti, R. Hull, J. M. Gibson, and L. E. Brus, *J. Chem. Phys.* 83, 1406 (1985).
170. A. J. Nozik, F. Williams, M. T. Nenadovic, T. Rajh, and O. I. Micic, *J. Phys. Chem.* 89, 397 (1985).
171. O. I. Micic, M. T. Nenadovic, T. Rajh, N. M. Dimitrijevic, and A. J. Nozik, *NATO ASI Ser. C* 26 (1986).
172. T. Dannhauser, M. O'Neil, K. Johansson, D. Whitten, and G. McLendon, *J. Phys. Chem.* 90, 6074 (1986).
173. P. V. Kamat, N. M. Dimitrijevic, and R. W. Fessenden, *J. Phys. Chem.* 91, 396 (1987).
174. T. Rajh, M. W. Peterson, J. A. Turner, and A. J. Nozik, *J. Electroanal. Chem. Interfacial Electrochem.* 228, 55 (1987).
175. A. Fojtik and J. Jirkovsky, *Chem. Phys. Lett.* 137, 226 (1987).
176. H. Weller, M. Haase, L. Spanhel, and A. Henglein, *Prog. Colloid Polym. Sci.* 76, 24 (1988).
177. C. Kormann, D. W. Bahnemann, and M. R. Hoffmann, *J. Phys. Chem.* 92, 5196 (1988).
178. D. Meisel and W. A. Mulac, *Colloids Surf.* 35, 179 (1989).
179. H. Yoneyama, S. Haga, and S. Yamanaka, *J. Phys. Chem.* 93, 4833 (1989).
180. L. Spanhel and M. A. Anderson, *J. Am. Chem.* Soc. 112, 2278 (1990).
181. H. Weller, *Ber. Bunsen-Ges. Phys. Chem.* 95, 1361 (1991).
182. M. P. Pileni, L. Motte, and C. Petit, *Chem. Mater.* 4, 338 (1992).
183. I. Bedja, S. Hotchandani, and P. V. Kamat, *J. Phys. Chem.* 97, 11064 (1993).

184. J. L. Coffer, R. R. Chandler, C. D. Gutsche, I. Alam, R. F. Pinizzotto, and H. Yang, *J. Phys. Chem.* 97, 696 (1993).
185. A. Mews, A. Eychmuller, M. Giersig, D. Schooss, and H. Weller, *J. Phys. Chem.* 98, 934 (1994).
186. R. Rossetti, J. L. Ellison, J. M. Gibson, and L. E. Brus, *J. Chem. Phys.* 80, 4464 (1984).
187. D. W. Banemann, *Isr. J. Chem.* 33, 115 (1993).
188. K. A. Littau, P. J. Szajowski, A. J. Muller, A. R. Kortan, and L. E. Brus, *J. Phys. Chem.* 97, 1224 (1993).
189. H. Weller, A. Fojtik, and A. Henglein, *Chem. Phys. Lett.* 117, 485 (1985).
190. A. Fojtik, H. Weller, and A. Henglein, *Chem. Phys. Lett.* 120, 552 (1985).
191. U. Koch, A. Fojtik, H. Weller, and A. Henglein, *Chem. Phys. Lett.* 122, 507 (1985).
192. S. Baral, A. Fojtik, H. Weller, and A. Henglein, *J. Am. Chem. Soc.* 108, 375 (1986).
193. A. Henglein, *J. Chim. Phys. Phys.-Chim. Biol.* 84, 1043 (1987).
194. A. Henglein, A. Fojtik, and H. Weller, *Ber. Bunsen-Ges. Phys. Chem.* 91, 441 (1987).
195. A. Henglein, M. Gutierrez, H. Weller, A. Fojtik, and J. Jirkovsky, *Ber. Bunsen-Ges. Phys. Chem.* 93, 593 (1989).
196. P. Lianos and J. K. Thomas, *J. Colloid Interface Sci.* 117, 505 (1987).
197. J. M. Nedeljkovic, M. T. Nenadovic, O. I. Micic, and A. J. Nozik, *J. Phys. Chem.* 90, 12 (1986).
198. O. I. Micic, M. T. Nenadovic, M. W. Peterson, and A. J. Nozik, *J. Phys. Chem.* 91, 1295 (1987).
199. M. W. Peterson, O. I. Micic, and A. J. Nozik, *J. Phys. Chem.* 92, 4160 (1988).
200. M. W. Peterson, M. T. Nenadovic, T. Rajh, R. Herak, O. I. Micic, J. P. Goral, and A. J. Nozik, *J. Phys. Chem.* 92, 1400 (1988).
201. D. W. Bahnemann, C. Kormann, and M. R. Hoffmann, *J. Phys. Chem.* 91, 3789 (1987).
202. E. S. Smotkin, C. Lee, A. J. Bard, A. Campion, M. A. Fox, T. E. Mallouk, S. E. Webber, and J. M. White, *Chem. Phys. Lett.* 152, 265 (1988).
203. Y. Nosaka, K. Yamaguchi, H. Yokoyama, and H. Miyama, in "Photoresponsive Materials," MRS International Meeting on Advanced Materials, Vol. 12, p. 155. Materials Research Society, 1989.
204. Y. Nosaka, N. Ohta, and H. Miyama, *J. Phys. Chem.* 94, 3752 (1990).
205. M. Grätzel, in "Electrochemistry in Colloids and Dispersions" (R. A. Mackay and J. Texter, eds.), p. 333. VCH Publishers, New York, 1992.
206. P. V. Kamat and B. Patrick, *J. Phys. Chem.* 96, 6829 (1992).
207. K. R. Gopidas and P. V. Kamat, *Proc. Ind. Acad. Sci. (Chem. Sci.)* 105, 505 (1993).
208. Y. Nosaka, T. Fukuyama, M. Horiuchi, and N. Fujii, *Isr. J. Chem.* 155, 71 (1993).
209. E. Lifshitz, M. Yassen, L. Bykov, and I. Dag, *J. Phys. Chem.* 99, 1245 (1995).
210. L. E. Brus, *J. Chem. Phys.* 80, 4403 (1984).
211. L. E. Brus, *J. Chem. Phys.* 79, 5566 (1983).
212. V. Mohan and J. B. Anderson, *Chem. Phys. Lett.* 156, 520 (1989).
213. W. L. Wilson, P. F. Szajowski, and L. E. Brus, *Science* 262, 1242 (1993).
214. L.-W. Wang and A. Zunger, *J. Chem. Phys.* 100, 2394 (1994).
215. L.-W. Wang and A. Zunger, *Phys. Rev. Lett.* 73, 1039 (1994).
216. S. B. Zhang, C.-Y. Yeh, and A. Zunger, *Phys. Rev. B* 48, 11204 (1993).
217. C.-Y. Yeh, S. B. Zhang, and A. Zunger, *Appl. Phys. Lett.* 64, 3545 (1994).
218. M. J. Sailor, J. L. Heinrich, and J. M. Lauerhaas, in "Semiconductor Nanoclusters—Physical, Chemical and Catalytic Aspects" (P. V. Kamat and D. Meisel, eds.), p. 209. Elsevier Science, Amsterdam, 1997.
219. L.-T. Cheng, N. Herron, and Y. Wang, *J. Appl. Phys.* 66, 3417 (1989).
220. Y. Wang, N. Herron, W. Mahler, and A. Suna, *J. Opt. Soc. Am. B* 6, 808 (1989).
221. L. Brus, *Appl. Phys. A* 53, 465 (1991).
222. O. A. Aktsipetrov, P. V. Elyutin, A. A. Fedyanin, A. A. Nikulin, and A. N. Rubtsov, *Surf. Sci.* 325, 343 (1995).
223. Y. Wang, *Adv. Photochem.* 19, 179 (1995).
224. Y. Nosaka, N. Tohriiwa, T. Kobayashi, and N. Fujii, *Chem. Mater.* 5, 930 (1993).
225. E. J. Heilweil and R. M. Hochstrasser, *J. Chem. Phys.* 82, 179 (1985).
226. L. L. Beecroft and C. K. Ober, *Chem. Mater.* 9, 1302 (1997).
227. Y. Wang, in "Semiconductor Nanoclusters—Physical, Chemical and Catalytic Aspects" (P. V. Kamat and D. Meisel, eds.), p. 277. Elsevier Science, Amsterdam, 1997.
228. W. J. Albery, G. T. Brown, J. R. Darwent, and E. Saivar-Iranizad, *J. Chem. Soc., Faraday Trans. 1* 81, 1999 (1985).
229. J. P. Kuczynski, B. H. Milosavljevic, and J. K. Thomas, *J. Phys. Chem.* 88, 980 (1984).
230. A. Henglein, A. Kumar, E. Janata, and H. Weller, *Chem. Phys. Lett.* 132, 133 (1986).
231. M. Haase, H. Weller, and A. Henglein, *J. Phys. Chem.* 92, 4706 (1988).
232. C. Liu and A. J. Bard, *J. Phys. Chem.* 93, 3232 (1989).
233. C. Liu and A. J. Bard, *J. Phys. Chem.* 93, 7047 (1989).
234. M. Haase, H. Weller, and A. Henglein, *Ber. Bunsen-Ges. Phys. Chem.* 92, 1103 (1988).
235. P. V. Kamat, N. M. Dimitrijevic, and A. J. Nozik, *J. Phys. Chem.* 93, 2873 (1989).
236. E. F. Hilinski, P. A. Lucas, and Y. Wang, *J. Chem. Phys.* 89, 3435 (1988).

237. Y. Wang, A. Suna, J. McHugh, E. F. Hilinski, P. A. Lucas, and R. D. Johnson, *J. Chem. Phys.* 92, 6927 (1990).
238. T. Rajh, O. I. Micic, D. Lawless, and N. Serpone, *J. Phys. Chem.* 96, 4633 (1992).
239. A. V. Barzykin and M. A. Fox, *Isr. J. Chem.* 33, 21 (1993).
240. P. V. Kamat, N. M. Dimitrijevic, and R. W. Fessenden, *J. Phys. Chem.* 92, 2324 (1988).
241. M. T. Nenadovic, M. I. Comor, V. Vasic, and O. I. Micic, *J. Phys. Chem.* 94, 6390 (1990).
242. N. M. Dimitrijevic and P. V. Kamat, *J. Phys. Chem.* 91, 2096 (1987).
243. N. M. Dimitrijevic, *J. Chem. Soc., Faraday Trans. 1* 83, 1193 (1987).
244. N. M. Dimitrijevic and P. V. Kamat, *Langmuir* 3, 1004 (1987).
245. M. Haase, H. Weller, and A. Henglein, *J. Phys. Chem.* 92, 482 (1988).
246. G. Redmond, A. O'Keeffe, C. Burgess, C. MacHale, and D. Fitzmaurice, *J. Phys. Chem.* 97, 11081 (1993).
247. N. P. Ernsting, M. Kaschke, H. Weller, and L. Katsikas, *J. Opt. Soc. Am. B* 7, 1630 (1990).
248. H. Uchida, C. J. Curtis, P. V. Kamat, K. M. Jones, and A. J. Nozik, *J. Phys. Chem.* 96, 1156 (1992).
249. A. Eychmüller, T. Vobmeyer, A. Mews, and H. Weller, *J. Lumin.* 58, 223 (1994).
250. L. Banyai and S. W. Koch, *Phys. Rev. Lett.* 57, 2722 (1986).
251. C. Luangdilok, D. Lawless, and D. Meisel, in "Fine Particles Science and Technology" (E. Pelizzatti, ed.), p. 457. Kluwer Academic, Boston, 1996.
252. V. L. Colvin and A. P. Alivisatos, *J. Chem. Phys.* 97, 730 (1992).
253. Y. Nosaka, K. Tanaka, and N. Fujii, *J. Appl. Polym. Sci.* 47, 1773 (1993).
254. J. Rabani, *J. Phys. Chem.* 93, 7707 (1989).
255. L. Spanhel, A. Henglein, and H. Weller, *Ber. Bunsen-Ges. Phys. Chem.* 91, 1359 (1987).
256. M. Anpo, K. Chiba, M. Tomonari, S. Coluccia, M. Che, and M. A. Fox, *Bull. Chem. Soc. Jpn.* 64, 543 (1991).
257. S. Hotchandani and P. V. Kamat, *J. Phys. Chem.* 96, 6834 (1992).
258. W. G. Becker and A. J. Bard, *J. Phys. Chem.* 87, 4888 (1983).
259. M. F. Finlayson, K. H. Park, N. Kakuta, A. J. Bard, A. Campion, M. A. Fox, S. E. Webber, and J. M. White, *J. Lumin.* 39, 205 (1988).
260. Z. Alfassi, D. Bahnemann, and A. Henglein, *J. Phys. Chem.* 86, 4656 (1982).
261. S. A. Empedocles, D. K. Norris, and M. G. Bawendi, *Phys. Rev. Lett.* 77, 3873 (1996).
262. M. G. Bawendi, P. J. Carroll, W. L. Wilson, and L. E. Brus, *J. Chem. Phys.* 96, 946 (1992).
263. B. O. Dabbousi, M. G. Bawendi, O. Onitsuka, and M. F. Rubner, *Appl. Phys. Lett.* 66, 1316 (1995).
264. J. S. Massa, G. S. Buller, A. C. Walker, G. Horsburgh, J. T. Mullins, K. A. Prior, and B. C. Cavenett, *Appl. Phys. Lett.* 66, 1346 (1995).
265. M. A. Hines and P. Guyot-Sionnest, *J. Phys. Chem.* 100, 468 (1996).
266. R. Rossetti and L. Brus, *J. Phys. Chem.* 86, 4470 (1982).
267. A. Cornet, J. Collet, T. Amand, M. Pugnet, B. S. Razbirin, and G. Michailov, *J. Phys. Chem. Solids* 44, 53 (1983).
268. W. J. Albery, G. T. Brown, J. R. Darwent, and I. E. Saievar, *J. Chem. Soc., Faraday Trans. 1* 81, 1999 (1985).
269. L. Spanhel, H. Weller, A. Fojtik, and A. Henglein, *Ber. Bunsen-Ges. Phys. Chem.* 91, 88 (1987).
270. M. Hiramoto, K. Hashimoto, and T. Sakata, *Chem. Phys. Lett.* 133, 440 (1987).
271. Y. Wang and N. Herron, *J. Phys. Chem.* 92, 4988 (1988).
272. M. I. Vucemilovic, N. Vukelic, and T. Rajh, *J. Photochem. Photobiol., A* 42, 157 (1988).
273. Y. Y. Aaviksoo, Y. E. Lippmaa, A. M. Freiberg, and S. F. Savikhin, *Sov. Phys. Solid State* 31, 462 (1989).
274. K. R. Gopidas, M. Bohorquez, and P. V. Kamat, *J. Phys. Chem.* 94, 6435 (1990).
275. A. I. Ekimov, I. A. Kudryavtsev, M. G. Ivanov, and A. L. Efros, *J. Lumin.* 46, 83 (1990).
276. A. Eychmueller, A. Haesselbarth, L. Katsikas, and H. Weller, *Ber. Bunsen-Ges. Phys. Chem.* 95, 79 (1991).
277. A. Eychmueller, A. Haesselbarth, L. Katsikas, and H. Weller, *J. Lumin.* 49, 745 (1991).
278. M. Hiramoto, K. Hashimoto, and T. Sakata, *Chem. Phys. Lett.* 182, 139 (1991).
279. K. Misawa, H. Yao, T. Hayashi, and T. Kobayashi, *Chem. Phys. Lett.* 183, 113 (1991).
280. A. Kumar and S. Kumar, *J. Photochem. Photobiol., A* 69, 91 (1992).
281. A. Eychmueller, A. Haesselbarth, and H. Weller, *J. Lumin.* 53, 113 (1992).
282. S. R. Bigham and J. L. Coffer, *J. Phys. Chem.* 96, 10581 (1992).
283. O. Horvath and J. H. Fendler, *J. Phys. Chem.* 96, 9591 (1992).
284. T. Miyoshi, *Jpn. J. Appl. Phys.* 31, 375 (1992).
285. A. Haesselbarth, A. Eychmueller, and H. Weller, *Chem. Phys. Lett.* 203, 271 (1993).
286. A. Kumar and S. Kumar, *J. Photochem. Photobiol., A* 83, 251 (1994).
287. H. S. Zhou, H. Sasahara, I. Honma, H. Komiyama, and J. W. Haus, *Chem. Mater.* 6, 1534 (1994).
288. F. Parsapour, D. F. Kelley, S. Craft, and J. P. Wilcoxon, *J. Chem. Phys.* 104, 4978 (1997).
289. C. Delerue, M. Lannoo, and G. Allan, *J. Lumin.* 57, 249 (1993).
290. P. M. Fauchet, *J. Lumin.* 70, 294 (1996).
291. M. Ben-Chorin, A. Kux, and I. Schechter, *Appl. Phys. Lett.* 64, 481 (1994).
292. L. Brus, *Jpn. J. Appl. Phys.* 2, 34, Suppl. 34-1 (1994).
293. L. Brus, *Phys. Rev. B* 53, 4649 (1996).

294. A. Bsiesy, F. Muller, M. Ligeon, F. Gaspard, R. Herino, R. Romestain, and J. Vial, *Phys. Rev. Lett.* 71, 637 (1993).
295. A. Bsiesy, F. Muller, M. Ligeon, F. Gaspard, R. Herino, R. Romestain, and J. Vial, *Appl. Phys. Lett.* 65, 3371 (1994).
296. E. Kooij, R. Despo, and J. Kelly, *Appl. Phys. Lett.* 66, 2552 (1995).
297. J. M. Lauerhaas and M. J. Sailor, *Science* 261, 1567 (1993).
298. K. Li, C. Tsai, J. Sarathy, and J. Campbell, *Appl. Phys. Lett.* 62, 3192 (1993).
299. H. Noguchi, T. Kondo, and K. Uosaski, *J. Phys. Chem. B* 101, 4978 (1997).
300. K. Uosaki, H. Noguchi, K. Murakoshi, and T. Kondo, *Chem. Lett.* 667 (1995).
301. K. Uosaki, H. Noguchi, K. Murakoshi, and T. Kondo, *J. Phys. Chem.* 100, 4564 (1996).
302. M. O'Neil, J. Marohn, and G. McLendon, *J. Phys. Chem.* 94, 4356 (1990).
303. J. Warnock and D. D. Awschalom, *Appl. Phys. Lett.* 48, 425 (1986).
304. C. R. M. de Oliveira, A. M. de Paula, F. O. P. Filho, J. A. Medeiros Neto, L. C. Barbosa, O. L. Alves, E. A. Menezes, J. M. M. Rios, H. L. Fragnito, and C. H. Brito Cruz, *Appl. Phys. Lett.* 66, 439 (1995).
305. L. Brus, *Isr. J. Chem.* 33, 9 (1993).
306. W. W. Dunn, Y. Aikawa, and A. J. Bard, *J. Am. Chem. Soc.* 103, 3456 (1981).
307. M. D. Ward and A. J. Bard, *J. Phys. Chem.* 86, 3599 (1982).
308. M. D. Ward, J. R. White, and A. J. Bard, *J. Am. Chem. Soc.* 105, 27 (1983).
309. D. Bahnemann, A. Henglein, J. Lilie, and L. Spanhel, *J. Phys. Chem.* 88, 709 (1984).
310. G. Rothenberger, J. Moser, M. Grätzel, N. Serpone, and D. K. Sharma, *J. Am. Chem. Soc.* 107, 8054 (1985).
311. C. Arbour, D. K. Sharma, and C. H. Langford, in "Photochemistry and Photophysics of Coordination Compounds." Springer-Verlag, Berlin, 1987.
312. D. Benjamin and D. Huppert, *J. Phys. Chem.* 92, 4676 (1988).
313. J. J. Kasinski, J. L. A. Gomez, L. Min, Q. Bao, and R. J. D. Miller, *J. Lumin.* 41, 555 (1988).
314. K. Bitterling, F. Willig, and F. Decker, *J. Electroanal. Chem. Interfacial Electrochem.* 228, 29 (1987).
315. J. M. Warman, M. P. de Haas, S. W. F. M. van Hovell tot Westerflier, J. J. M. Binsma, and Z. I. Kolar, *J. Phys. Chem.* 93, 5895 (1989).
316. J. R. Morgan and L. V. Natarajan, *J. Phys. Chem.* 93, 5 (1989).
317. G. J. Meyer, L. K. Leung, J. C. Yu, G. C. Lisensky, and A. B. Ellis, *J. Am. Chem. Soc.* 111, 5146 (1989).
318. P. V. Kamat, T. W. Ebbesen, N. M. Dimitrijevic, and A. J. Nozik, *Chem. Phys. Lett.* 157, 384 (1989).
319. M. O'Neil, J. Marohn, and G. McLendon, *Chem. Phys. Lett.* 168, 208 (1990).
320. R. Kietzmann, F. Willig, H. Weller, R. Vogel, D. N. Nath, R. Eichberger, P. Liska, and J. Lehnert, *Mol. Cryst. Liq. Cryst.* 194, 169 (1991).
321. Y. Rosenwaks, B. R. Thacker, A. J. Nozik, Y. Shapira, and D. Huppert, *J. Phys. Chem.* 97, 10421 (1993).
322. Y. Rosenwaks, B. R. Thacker, R. K. Ahrenkiel, and A. J. Nozik, *J. Phys. Chem.* 96, 10096 (1992).
323. G. P. Lepore, C. H. Langford, J. Vichova, and A. J. Vlcek, *J. Photochem. Photobiol., A* 75, 67 (1993).
324. C. Liu, H. Pan, M. A. Fox, and A. J. Bard, *Science* 261, 897 (1993).
325. M. P. Cantao, J. I. Cisneros, and R. M. Torresi, *J. Phys. Chem.* 98, 4865 (1994).
326. J. G. Zhang, R. H. O'Neil, and T. W. Roberti, *J. Phys. Chem.* 98, 3859 (1994).
327. X. Marguerettaz and D. Fitzmaurice, *J. Am. Chem. Soc.* 116, 5017 (1994).
328. X. Liu, G. Zhang, and J. K. Thomas, *J. Phys. Chem.* 99, 10024 (1995).
329. N. Serpone, D. Lawless, and R. Khairutdinov, *J. Phys. Chem.* 99, 16646 (1995).
330. H. Herrmann, S. Martin, and M. Hoffmann, *J. Phys. Chem.* 99, 16641 (1995).
331. N. Serpone, D. Lawless, R. Khairutdinov, and E. Pelizzetti, *J. Phys. Chem.* 99, 16655 (1995).
332. D. E. Skinner, D. P. J. Colombo, J. J. Cavaleri, and R. M. Bowman, *J. Phys. Chem.* 99, 7853 (1995).
333. G. K. Boschloo and A. Goossens, *J. Phys. Chem.* 100, 19489 (1996).
334. P. V. Kamat and K. Vinodgopal, in "Fine Particles Science and Technology: From Micro to Nanoparticles" (E. Pelizzetti, ed.), p. 303. Kluwer Academic, Dordrecht, The Netherlands, 1996.
335. M. T. Nenadovic, T. Rajh, O. I. Micic, and A. J. Nozik, *J. Phys. Chem.* 88, 5827 (1984).
336. E. Serwicka, M. W. Schlierkamp, and R. N. Schindler, *Z. Naturforsch.* 32 (1981).
337. R. F. Howe and M. Grätzel, *J. Phys. Chem.* 91, 3906 (1987).
338. R. F. Howe and M. Grätzel, *J. Phys. Chem.* 89, 4495 (1985).
339. I. Bedja, S. Hotchandani, and P. V. Kamat, *J. Phys. Chem.* 98, 4133 (1994).
340. J. Z. Zhang, R. H. O'Neil, T. W. Roberti, J. L. McGowen, and J. E. Evans, *Chem. Phys. Lett.* 218, 479 (1994).
341. B. Kraeutler, C. D. Jaeger, and A. J. Bard, *J. Am. Chem. Soc.* 100, 4903 (1978).
342. M. Anpo, T. Shima, and Y. Kubokawa, *Chem. Lett.* 1799 (1985).
343. O. I. Micic, Y. Zhang, K. R. Cromack, A. D. Trifunac, and M. C. Thurnauer, *J. Phys. Chem.* 97, 13284 (1993).
344. O. I. Micic, Y. Zhang, K. R. Cromack, A. D. Trifunac, and M. C. Thurnauer, *J. Phys. Chem.* 97, 7277 (1993).
345. J. M. Warman, M. P. de Haas, M. Grätzel, and P. P. Infelta, *Nature* 310, 306 (1984).
346. J. M. Warman, M. P. de Haas, and H. M. Wentinck, *Radiat. Phys. Chem.* 34, 581 (1989).

347. J. M. Warman, M. P. de Haas, P. Pichat, T. P. M. Koster, A. E. A. van der Zouwen, A. Mackor, and R. Cooper, *Radiat. Phys. Chem.* 37, 433 (1991).
348. J. M. Warman, M. P. de Haas, P. Pichat, and N. Serpone, *J. Phys. Chem.* 95, 8858 (1991).
349. S. T. Martin, H. Herrmann, W. Choi, and M. R. Hoffmann, *Faraday Trans.* 90, 3315 (1994).
350. S. T. Martin, H. Herrmann, and M. R. Hoffmann, *Faraday Trans.* 90, 3323 (1994).
351. R. W. Fessenden and P. V. Kamat, *J. Phys. Chem.* 99, 12902 (1995).
352. P. V. Kamat, K. R. Gopidas, and N. M. Dimitrijevic, *Mol. Cryst. Liq. Cryst.* 183, 439 (1990).
353. A. Henglein, *J. Phys. Chem.* 86, 2291 (1982).
354. D. Duonghong, J. Ramsden, and M. Grätzel, *J. Am. Chem. Soc.* 104, 2977 (1982).
355. T. Watanabe, A. Fujishima, and K. Honda, in "Energy Resour. Photochem. Catal." (M. Grätzel, ed.). Academic Press, New York, 1983.
356. N. Serpone, E. Pelizzetti, and M. Gratzel, *Coord. Chem. Rev.* 64, 225 (1985).
357. M. Grätzel, *NATO ASI Ser. C* 174, 91 (1986).
358. V. N. Parmon, *Adv. Hydrogen Energy* 8, 801 (1990).
359. Z.-C. Bi, Y.-Y. Qian, J. Huang, Z. Xiao, and J.-Y. Yu, *J. Photochem. Photobiol., A* 77, 37 (1994).
360. K. Sayama and H. Arakawa, *J. Photochem. Photobiol., A* 77, 243 (1994).
361. K. Sayama and H. Arakawa, *Chem. Lett.* 6 (1992).
362. K. Sayama and H. Arakawa, *J. Phys. Chem.* 97, 531 (1993).
363. E. Amouyal, *Sol. Energy Mater. Sol. Cells* 38, 249 (1995).
364. A. J. Bard and M. A. Fox, *Acc. Chem. Res.* 28, 141 (1995).
365. M. A. Fox, B. Lindig, and C. C. Chen, *J. Am. Chem. Soc.* 104, 5828 (1982).
366. A. Harriman, G. Porter, and P. Walters, *J. Photochem.* 19, 183 (1982).
367. D. Bahnemann, A. Henglein, and L. Spanhel, *Faraday Discuss. Chem. Soc.* 78, 151 (1984).
368. K. Chandrasekaran and J. K. Thomas, *J. Colloid Interface Sci.* 106, 532 (1985).
369. J. R. Darwent and A. Lepre, *J. Chem. Soc., Faraday Trans. 1* 82, 2323 (1986).
370. N. Serpone, D. K. Sharma, J. Moser, and M. Grätzel, *Chem. Phys. Lett.* 136, 47 (1987).
371. N. Getoff, *Adv. Hydrogen Energy* 93, 383 (1990).
372. R. B. Draper and M. A. Fox, *Langmuir* 6, 1396 (1990).
373. O. Enea, P. Crouigneau, J. Moser, M. Grätzel, and S. Huenig, *New J. Chem.* 15, 267 (1991).
374. J. A. Navio, F. J. Marchena, M. Roncel, and M. A. De la Rosa, *J. Photochem. Photobiol., A* 55, 319 (1991).
375. T. Uchihara, T. Nakamura, and A. Kinjo, *J. Photochem. Photobiol., A* 66, 379 (1992).
376. T. Uchihara, Y. Asato, and A. Kinjo, *J. Photochem. Photobiol., A* 67, 101 (1992).
377. I. Willner, Y. Eichen, A. J. Frank, and M. A. Fox, *J. Phys. Chem.* 97, 7264 (1993).
378. J. R. Darwent, *J. Chem. Soc., Faraday Trans. 1* 80, 183 (1984).
379. J. J. Ramsden and M. Grätzel, *Chem. Phys. Lett.* 132, 269 (1986).
380. R. D. Stramel and J. K. Thomas, *J. Colloid Interface Sci.* 110, 121 (1986).
381. P. V. Kamat and N. M. Dimitrijevic, *Proc. Electrochem. Soc.* 6, 90 (1988).
382. S. Baral and J. H. Fendler, *J. Am. Chem. Soc.* 111, 1604 (1989).
383. A. Mills, P. Douglas, and G. Williams, *J. Photochem. Photobiol., A* 48, 397 (1989).
384. A. Green and A. Mills, *J. Photochem. Photobiol., A* 64, 211 (1992).
385. Y. Nosaka, K. Yamaguchi, A. Kuwabara, H. Miyama, R. Baba, and A. Fujishima, *J. Photochem. Photobiol., A* 64, 375 (1992).
386. H. Matsumoto, H. Uchida, T. Matsunaga, K. Tanaka, T. Sakata, H. Mori, and H. Yoneyama, *J. Phys. Chem.* 98, 11549 (1994).
387. P. V. Kamat, *J. Photochem.* 28, 513 (1985).
388. P. V. Kamat, *J. Chem. Soc., Faraday Trans. 1* 81, 509 (1985).
389. K. R. Gopidas and P. V. Kamat, *J. Phys. Chem.* 93, 6428 (1989).
390. B. Patrick, M. V. George, P. V. Kamat, S. Das, and K. G. Thomas, *J. Chem. Soc., Faraday Trans.* 88, 671 (1992).
391. K. Vinodgopal, I. Bedja, S. Hotchandani, and P. V. Kamat, *Langmuir* 10, 1767 (1994).
392. C. Nasr, K. Vinodgopal, S. Hotchandani, A. K. Chattopadhyay, and P. V. Kamat, *Res. Chem. Intermed.* 23, 219 (1997).
393. P. V. Kamat, *J. Am. Chem. Soc.* 113, 9705 (1991).
394. P. V. Kamat, I. Bedja, and S. Hotchandani, *J. Phys. Chem.* 98, 9137 (1994).
395. P. V. Kamat, I. Bedja, and S. Hotchandani, in "Recent Advances in the Chemistry and Physics of Fullerenes and Related Materials" (K. M. Kadish and R. S. Ruoff, eds.), Vol. 94-24, p. 964. Electrochemical Society, Pennington, NJ, 1994.
396. A. Stasko, V. Brezova, S. Biskupic, K.-P. Dinse, P. Schweitzer, and M. Baumgarten, *J. Phys. Chem.* 99, 8782 (1995).
397. D. Guldi, D. Liu, and P. V. Kamat, *J. Phys. Chem. A* 101, 6195 (1997).
398. G. Sauve, P. V. Kamat, and R. S. Ruoff, *J. Phys. Chem.* 99, 2162 (1995).
399. J. M. Kesselman, G. A. Shreve, M. R. Hoffmann, and N. S. Lewis, *J. Phys. Chem.* 98, 13385 (1994).
400. K. Ishibashi, Y. Nosaka, K. Hashimoto, and A. Fujishima, *J. Phys. Chem. B* 102, 2117 (1998).
401. H. Yamataka, N. Seto, J. Ihichara, T. Hanafusa, and S. Teratani, *J. Chem. Soc., Chem. Commun.* 788 (1985).

402. H. Wang, T. Sakata, M. Azumo, T. Ohta, and H. Takaya, *Chem. Lett.* 1331 (1990).
403. C. Joyce-Pruden, J. K. Pross, and Y. Li, *J. Org. Chem.* 57, 5087 (1992).
404. B. Ohtani, T. Goto, S. Nishimoto, and T. Inui, *J. Chem. Soc., Faraday Trans.* 92, 4291 (1996).
405. T. Shiragami, C. Pac, and S. Yanagida, *J. Phys. Chem.* 94, 504 (1990).
406. T. Shiragami, H. Ankyu, S. Fukami, C. Pac, S. Yanagida, H. Mori, and H. Fujita, *J. Chem. Soc., Faraday Trans.* 88, 1055 (1992).
407. T. Shiragami, S. Fukami, Y. Wada, and S. Yanagida, *J. Phys. Chem.* 97, 12882 (1993).
408. J. Moser and M. Grätzel, *Helv. Chim. Acta* 65, 1436 (1982).
409. D. J. Fitzmaurice, M. Eschle, H. Frei, and J. E. Moser, *J. Phys. Chem.* 97, 3806 (1993).
410. D. P. J. Colombo and R. M. Bowman, *J. Phys. Chem.* 100, 18445 (1996).
411. A. Henglein, *Ber. Bunsen-Ges. Phys. Chem.* 86, 241 (1982).
412. P. V. Kamat and N. M. Dimitrijevic, *J. Phys. Chem.* 93, 4259 (1989).
413. G. T. Brown and J. R. Darwent, *J. Phys. Chem.* 88, 4955 (1984).
414. R. Amadelli, A. Maldotti, C. Bartocci, and V. Carassiti, *J. Phys. Chem.* 93, 6448 (1989).
415. R. B. Draper and M. A. Fox, *J. Phys. Chem.* 94, 4628 (1990).
416. W. G. Becker, M. M. Truong, C. C. Ai, and N. N. Hamel, *J. Phys. Chem.* 93, 4882 (1989).
417. P. V. Kamat, *Langmuir* 1, 608 (1985).
418. J. S. Curran and D. Lamouche, *J. Phys. Chem.* 87, 5405 (1983).
419. N. Lewis, *Ann. Rev. Phys. Chem.* 42, 543 (1991).
420. N. Serpone, D. K. Sharma, M. A. Jamieson, M. Grätzel, and J. J. Ramsden, *Chem. Phys. Lett.* 115, 473 (1985).
421. Y. Nosaka, H. Miyama, M. Terauchi, and T. Kobayashi, *J. Phys. Chem.* 92, 255 (1988).
422. Y. Nosaka and M. A. Fox, *J. Phys. Chem.* 92, 1893 (1988).
423. C. Arbour, D. K. Sharma, and C. H. Langford, *J. Phys. Chem.* 94, 331 (1990).
424. R. Rossetti and L. E. Brus, *J. Phys. Chem.* 90, 558 (1986).
425. Y. Nosaka and M. A. Fox, *Langmuir* 3, 1147 (1987).
426. A. J. Frank, I. Willner, Z. Goren, and Y. Degani, *J. Am. Chem. Soc.* 109, 3568 (1987).
427. T. Rajh and J. Rabani, *Langmuir* 7, 2054 (1991).
428. T. Nakahira and M. Grätzel, *J. Phys. Chem.* 88, 4006 (1984).
429. H. Gerischer, *J. Phys. Chem.* 88, 6096 (1984).
430. H. Gerischer, in "Photocatalytic Purification and Treatment of Water and Air" (D. F. Ollis and H. Al-Ekabi, eds.), p. 1. Elsevier Science, Amsterdam, 1993.
431. J. Moser, S. Punchihewa, P. P. Infelta, and M. Grätzel, *Langmuir* 7, 3012 (1991).
432. W. J. Albery and P. N. Bartlett, *J. Electroanal. Chem. Interfacial Electrochem.* 131, 137 (1982).
433. W. J. Albery and P. N. Bartlett, *J. Electrochem. Soc.* 131, 315 (1984).
434. M. Grätzel and A. J. Frank, *J. Phys. Chem.* 86, 2964 (1982).
435. P. Lemasson, J. Gautron, W. J. Albery, P. N. Bartlett, E. M. P. Dare, and A. Hammett, *J. Electrochem. Soc.* 129, 1269 (1982).
436. W. J. Albery, *J. Electrochem. Soc.* 131, 2896 (1984).
437. W. J. Albery, P. N. Bartlett, C. P. Wilde, and J. R. Darwent, *J. Am. Chem. Soc.* 107, 1854 (1985).
438. P. Mulvaney, V. Swayambunathan, F. Grieser, and D. Meisel, *J. Phys. Chem.* 92, 6732 (1988).
439. S. M. C. Markham, *J. Chem. Ed.* 32, 540 (1955).
440. H. Gerischer and A. Heller, *J. Phys. Chem.* 95, 5261 (1991).
441. C. M. Wang, A. Heller, and H. Gerischer, *J. Am. Chem. Soc.* 114, 5230 (1992).
442. H. Gerischer and A. Heller, *J. Electrochem. Soc.* 139, 113 (1992).
443. M. W. Peterson, J. A. Turner, and A. J. Nozik, *J. Phys. Chem.* 95, 221 (1991).
444. K. Vinodgopal, S. Hotchandani, and P. V. Kamat, *J. Phys. Chem.* 97, 9040 (1993).
445. J. M. Kesselman, A. Kumar, and N. S. Lewis, in "Photocatalytic Purification and Treatment of Water and Air" (D. F. Ollis and H. Al-Ekabi, eds.), p. 19. Elsevier Science, Amsterdam, 1993.
446. D. Schmelling, K. A. Gray, and P. V. Kamat, *Environ. Sci. Technol.* 30, 2547 (1996).
447. S. Kato and F. Masuo, *Kogyo Kagaku Zasshi (Ind. Chem. J.)* 67, 1136 (1964).
448. K. Tokumaru, H. Sakuragi, T. Kanno, T. Oguchi, H. Misawa, Y. Shimamura, and Y. Kuriyama, *ACS Symp. Ser.* 55, 43 (1985).
449. B. Kraeutler and A. J. Bard, *J. Am. Chem. Soc.* 100, 2239 (1978).
450. B. Kraeutler and A. J. Bard, *Nouv. J. Chim.* 3, 31 (1979).
451. M. A. Fox, in "Topics in Organic Electrochemistry," p. 177. Plenum Press, New York, 1986.
452. M. A. Fox, in "Advances in Electron Transfer Chemistry" (P. S. Mariano, ed.), Vol. 1, p. 1. Jai Press, Greenwich, CT, 1991.
453. Y. Li and L. Wang, in "Nanocrystalline Semiconductor Materials" (P. V. Kamat and D. Meisel, eds.), p. 391. Elsevier Science, Amsterdam, 1997.
454. H. Al-Ekabi and P. de Mayo, *J. Phys. Chem.* 89, 5815 (1985).
455. T. Hasegawa and P. de Mayo, *Langmuir* 2, 362 (1986).
456. T. Shiragami, S. Fukami, C. Pac, Y. Wada, and S. Yanagida, *Bull. Chem. Soc. Jpn.* 66, 2461 (1993).
457. F. Madhavi, T. C. Burton, and Y. Li, *J. Org. Chem.* 58, 744 (1993).

458. M. Mitani, T. Kiriyama, and T. Kuratate, *J. Org. Chem.* 59, 1279 (1994).
459. T. Inoue, A. Fujishima, S. Konishi, and K. Honda, *Nature* 277, 637 (1979).
460. H. Fujiwara, H. Hosokawa, K. Murakoshi, Y. Wada, S. Yanagida, T. Okada, and H. Kobayashi, *J. Phys. Chem. B* 101, 8270 (1997).
461. H. Inoue, M. Yamachika, and H. Yoneyama, *J. Chem. Soc., Faraday Trans.* 88, 2215 (1992).
462. M. W. Rophael and L. B. Khalil, *Vacuum* 41, 143 (1990).
463. M. M. Taqui Khan, D. Chatterjee, M. Krishnaratnam, and M. Bala, *J. Mol. Catal.* 72, 13 (1992).
464. V. Heleg and I. Willner, *J. Chem. Soc., Chem. Commun.* 2113 (1994).
465. M. M. Taqui Khan, D. Chatterjee, A. Hussain, and M. A. Moiz, *J. Photochem. Photobiol., A* 76, 97 (1993).
466. Z. Goren, I. Willner, A. J. Nelson, and A. J. Frank, *J. Phys. Chem.* 94, 3784 (1990).
467. S. G. Zhang, H. Yamashita, K. Koano, T. Tatsumi, and M. Anpo, *Chem. Lett.* 659 (1997).
468. M. Anpo, H. Yamashita, Y. Ichihashi, Y. Fujii, and M. Honda, *J. Phys. Chem. B* 101, 2632 (1997).
469. K. M. Vijayakumar and N. N. Lichtin, *J. Catal.* 90, 173 (1984).
470. Y. Kohno, T. Tanaka, T. Funabiki, and S. Yoshida, *Chem. Lett.* 993 (1997).
471. S. M. Aliwi and J. K. F. Al, *Sol. Energy Mater.* 18, 223 (1989).
472. H. Kisch and G. Twadzik, *Chem. Ber.* 124, 1161 (1991).
473. T. S. Dzhabiev, B. B. Tarasov, and A. M. Uskov, *Catal. Today* 13, 695 (1992).
474. H. Inoue, H. Moriwaki, K. Maeda, and H. Yoneyama, *J. Photochem. Photobiol., A* 86, 191 (1995).
475. M. Kanemoto, T. Shiragami, C. Pac, and Y. Yanagida, *Chem. Lett.* 931 (1990).
476. M. Kanemoto, T. Shiragami, C. Pac, and Y. Yanagida, *J. Phys. Chem.* 96, 3521 (1992).
477. S. Yanagida, M. Kanemoto, T. Shiragami, and C. Pac, in "Proceedings of the IS&T 44th Annual Conference," 1991.
478. M. Kanemoto, K. Ishihara, Y. Wada, T. Sakata, H. Mori, and S. Yanagida, *Chem. Lett.* 6 (1992).
479. S. Yanagida, M. Kanemoto, H. Hosokawa, Y. Wada, and M. Ishikawa, *Trans. Mater. Res. Soc. Jpn., B* 16, 1575 (1994).
480. S. Yanagida, M. Kanemoto, K. Ishihara, Y. Wada, T. Sakata, and H. Mori, *Bull. Chem. Soc. Jpn.* 70, 2063 (1997).
481. M. Kanemoto, H. Hosokawa, Y. Wada, K. Murakoshi, S. Yanagida, T. Sakata, H. Mori, M. Ishikawa, and H. Kobayashi, *J. Chem. Soc., Faraday Trans.* 92, 2401 (1996).
482. H. Fujiwara, H. Hosokawa, K. Murakoshi, Y. Wada, S. Yanagida, T. Okada, and H. Kobayashi, *J. Phys. Chem. B* 101, 8270 (1997).
483. H. Fujiwara, M. Kanemoto, H. Ankyuu, M. Murakoshi, Y. Wada, and S. Yanagida, *J. Chem. Soc., Perkin Trans.* 2, 317 (1997).
484. G. N. Schrauzer and T. D. Guth, *J. Am. Chem. Soc.* 99, 7189 (1977).
485. K. Tennakone, O. A. Ileperuma, J. M. S. Bandara, and C. T. K. Thaminimulla, *Sol. Energy Mater.* 22, 319 (1991).
486. N. N. Rao, *J. Mol. Catal.* 93, 23 (1994).
487. K. T. Ranjit, R. Krishnamoorthy, T. K. Varadarajan, and B. Viswanathan, *J. Photochem. Photobiol., A* 86, 185 (1995).
488. K. T. Ranjit, B. Viswanathan, and T. K. Varadarajan, *J. Mater. Sci. Lett.* 15, 874 (1996).
489. H. Yamashita, Y. Ichihashi, M. Anpo, M. Hashimoto, C. Louis, and M. Che, *J. Phys. Chem.* 100, 16041 (1996).
490. S. Higashimoto, S. G. Zhang, H. Yamashita, Y. Matsumura, S. Souma, and M. Anpo, *Chem. Lett.* 1127 (1997).
491. D. F. Ollis, E. Pelizzetti, and N. Serpone, *Environ. Sci. Technol.* 25, 1523 (1991).
492. W. A. Zeltner, C. G. Hill, Jr., and M. A. Anderson, *CHEMTECH* 21 (1994).
493. K. Rajeshwar, *J. Appl. Electrochem.* 25, 1067 (1995).
494. P. V. Kamat and K. Vinodgopal, in "Organic and Inorganic Photochemistry" (V. Ramamurthy and K. Schanze, eds.), Vol. 2, p. 307. Marcel Dekker, New York, 1998.
495. R. W. Matthews, *Sol. Energy* 38, 405 (1987).
496. H. Al-Ekabi and N. Serpone, *J. Phys. Chem.* 92, 5726 (1988).
497. S. Yamagata, R. Baba, and A. Fujishima, *Bull. Chem. Soc. Jpn.* 62, 1004 (1989).
498. Y. Ohko, D. A. Tryk, K. Hashimoto, and A. Fujishima, *J. Phys. Chem. B* 102, 2699 (1998).
499. D. F. Ollis, *Environ. Sci. Technol.* 19, 480 (1985).
500. P. Pichat, *NATO ASI Ser. C* 174, 533 (1986).
501. D. F. Ollis, E. Pelizzetti, and N. Serpone, in "Photocatalysis. Fundamentals and Applications" (N. Serpone and E. Pelizzetti, eds.), p. 603. Wiley, New York, 1989.
502. M. Grätzel, in "Photocatalysis. Fundamentals and Applications" (N. Serpone and E. Pelizzetti, eds.). Wiley, New York, 1989.
503. P. Pichat, in "Photochemical Conversion and Storage of Solar Energy" (E. Pelizzetti and M. Schiavello, eds.). Kluwer Academic, Dordrecht, The Netherlands, 1991.
504. N. Serpone, D. Lawless, R. Terzian, C. Minero, and E. Pelizzetti, in "Photochemical Conversion and Storage of Solar Energy" (E. Pelizzetti and M. Schiavello, eds.). Kluwer Academic, Dordrecht, The Netherlands, 1991.

505. N. Serpone, D. Lawless, R. Terzian, and D. Meisel, in "Electrochemistry in Colloids and Dispersions" (R. A. Mackay and J. Texter, eds.), p. 399. VCH Publishers, New York, 1992.
506. J. M. Herrmann, C. Guillard, and P. Pichat, *Catal. Today* 17, 7 (1993).
507. M. A. Fox and M. T. Dulay, *Chem. Rev.* 93, 341 (1993).
508. O. Legrini, E. Oliveros, and A. M. Braun, *Chem. Rev.* 93, 671 (1993).
509. A. Wold, *Chem. Mater.* 5, 280 (1993).
510. D. Bahnemann, J. Cunningham, M. A. Fox, E. Pelizzetti, P. Pichat, and N. Serpone, in "Aquatic and Surface Chemistry" (G. R. Helz, R. G. Zepp, and D. G. Crosby, eds.), p. 261. Lewis Publishers, Boca Raton, FL, 1994.
511. N. Serpone, *J. Photochem. Photobiol., A* 104, 1 (1997).
512. A. Fujishima and K. Honda, *Nature* 238 (1972).
513. K. Vinodgopal, U. Stafford, K. A. Gray, and P. V. Kamat, *J. Phys. Chem.* 98, 6797 (1994).
514. K. Vinodgopal and P. V. Kamat, *Environ. Sci. Technol.* 29, 841 (1995).
515. D. H. Kim and M. A. Anderson, *Environ. Sci. Technol.* 28, 479 (1994).
516. N. Serpone, E. Borgarello, and E. Pelizzetti, *J. Electrochem. Soc.* 135, 2760 (1988).
517. I. U. Haque and J. F. Rusling, *Chemosphere* 26, 1301 (1997).
518. B. Kraeutler and A. J. Bard, *J. Am. Chem. Soc.* 100, 4317 (1978).
519. R. Palmans and A. J. Frank, *J. Phys. Chem.* 95, 9438 (1991).
520. D. Duonghong, E. Borgarello, and M. Grätzel, *J. Am. Chem. Soc.* 103, 4685 (1981).
521. A. Mills and G. Porter, *J. Chem. Soc., Faraday Trans. 1* 78, 3659 (1982).
522. T. Sakata, T. Kawai, and K. Hashimoto, *Chem. Phys. Lett.* 88, 50 (1982).
523. C. P. Lafrance, S. Kaliaguine, P. C. Roberge, and P. Pichat, *Stud. Surf. Sci. Catal.* 17, 309 (1984).
524. R. Baba, S. Nakabayashi, A. Fujishima, and K. Honda, *J. Phys. Chem.* 89, 1902 (1985).
525. T. Uchihara, M. Matsumura, A. Yamamoto, and H. Tsubomura, *J. Phys. Chem.* 93, 5870 (1989).
526. R. Dabestani, X. Wang, A. J. Bard, A. Campion, M. A. Fox, S. E. Webber, and J. M. White, *J. Phys. Chem.* 90, 2729 (1986).
527. D. H. M. W. Thewissen, R. M. Eeuwhorst, K. Timmer, A. H. A. Tinnemans, and A. Mackor, *Recl.: J. R. Neth. Chem. Soc.* 101, 79 (1982).
528. M. M. Taqui Khan, R. C. Bhardwaj, and C. M. Jadhav, *J. Chem. Soc., Chem. Commun.* 1690 (1985).
529. C. Minero, E. Lorenzi, E. Pramauro, and E. Pelizzetti, *Inorg. Chim. Acta* 91, 301 (1984).
530. K. Kalyanasundaram, E. Borgarello, and M. Grätzel, *Helv. Chim. Acta* 64, 362 (1981).
531. W. Gissler, A. J. McEvoy, and M. Grätzel, *J. Electrochem. Soc.* 129, 1733 (1982).
532. D. Gningue, G. Horowitz, J. Roncali, and F. Garnier, *J. Electroanal. Chem. Interfacial Electrochem.* 269, 337 (1989).
533. G. Blondeel, A. Harriman, G. Porter, D. Urwin, and J. Kiwi, *J. Phys. Chem.* 87, 2629 (1983).
534. E. Borgarello, K. Kalyanasundaram, M. Grätzel, and E. Pelizzetti, *Helv. Chim. Acta* 65, 243 (1982).
535. E. Serwicka and R. N. Schindler, *Z. Phys. Chem. (Wiesbaden)* 127, 79 (1981).
536. J. S. Thorp and H. S. Eggleston, *J. Mater. Sci.* 20, 2369 (1985).
537. Y. F. Lee, M. Olshavsky, and J. Chrysochoos, *J. Less-Common Met.* 148, 259 (1989).
538. S. C. Martin, C. L. Morrison, and M. R. Hoffmann, *J. Phys. Chem.* 98, 13695 (1994).
539. W. Choi, A. Termin, and M. R. Hoffmann, *J. Phys. Chem.* 98, 13669 (1994).
540. D. Duonghong, W. Erbs, L. Shuben, and M. Grätzel, *Chem. Phys. Lett.* 95, 266 (1983).
541. U. Resch and M. A. Fox, *J. Phys. Chem.* 95, 6316 (1991).
542. U. Resch and M. A. Fox, *J. Phys. Chem.* 95, 6169 (1991).
543. U. Resch and M. A. Fox, in "Electrochemistry in Colloids and Dispersions" (R. A. Mackay and J. Texter, eds.), p. 417. VCH Publishers, New York, 1992.
544. E. Borgarello, N. Serpone, P. Liska, W. Erbs, M. Grätzel, and E. Pelizzetti, *Gazz. Chim. Ital.* 115, 599 (1985).
545. K. Rajeshwar and M. Kaneko, *J. Phys. Chem.* 89, 3587 (1985).
546. M. M. Taqui Khan, R. C. Bhardwaj, and C. Bhardwaj, *Indian J. Chem., Sect. A* 25, 1 (1986).
547. W. Erbs, J. Kiwi, and M. Grätzel, *Chem. Phys. Lett.* 110, 648 (1984).
548. P. Mulvaney, M. Giersig, and A. Henglein, *J. Phys. Chem.* 97, 7061 (1993).
549. B. Shanghavi and P. V. Kamat, *J. Phys. Chem. B* 101, 7675 (1997).
550. A. Henglein, *J. Phys. Chem.* 97, 5457 (1993).
551. A. Henglein, *Ber. Bunsen-Ges. Phys. Chem.* 99, 903 (1995).
552. M. Mostafavi, N. Keghouche, M.-O. Delcourt, and J. Belloni, *Chem. Phys. Lett.* 167, 193 (1990).
553. J. Khatouri, M. Mostafavi, J. Amblard, and J. Belloni, *Chem. Phys. Lett.* 191, 351 (1992).
554. O. Platzer, J. Amblard, J. L. Marignier, and J. Belloni, *J. Phys. Chem.* 96, 2334 (1992).
555. T. S. Ahmadi, S. L. Logunov, and M. A. El-Sayed, *J. Phys. Chem.* 100, 8053 (1996).
556. S. L. Logunov, T. S. Ahmadi, M. A. El-Sayed, J. T. Khoury, and R. L. Whetten, *J. Phys. Chem. B* 101, 3713 (1997).
557. P. Mulvaney, in "Semiconductor Nanoclusters—Physical, Chemical and Catalytic Aspects" (P. V. Kamat and D. Meisel, eds.), p. 99. Elsevier Science, Amsterdam, 1997.
558. P. Mulvaney, *Langmuir* 12, 788 (1996).

559. U. Kreibig and M. Vollmer, "Optical Properties of Metal Clusters." Springer-Verlag, Berlin, 1995.
560. U. Kreibig, M. Gartz, A. Hilger, and H. Hovel, in "Fine Particles Science and Technology" (E. Pelizzatti, ed.), p. 499. Kluwer Academic, Boston, 1996.
561. I. Lisiecki, F. Billoudet, and M. P. Pileni, *J. Phys. Chem.* 100, 4160 (1996).
562. P. V. Kamat, M. Flumiani, and G. Hartland, *J. Phys. Chem. B* 101, 3123 (1997).
563. M. M. Alvarez, J. T. Khoury, T. G. Schaaff, M. N. Shafigullin, I. Vezmar, and R. L. Whetten, *J. Phys. Chem. B* 101, 3706 (1997).
564. J. W. Thackeray, M. J. Natan, P. Ng, and M. S. Wrighton, *J. Am. Chem. Soc.* 108, 3570 (1986).
565. M. J. Natan, J. W. Thackeray, and M. S. Wrighton, *J. Phys. Chem.* 90, 4089 (1986).
566. A. Fojtik, P. Mulvaney, T. Linnert, M. Giersig, and A. Henglein, *Ber. Bunsen-Ges. Phys. Chem.* 95, 770 (1991).
567. P. V. Kamat, M. de Lind, and S. Hotchandani, *Isr. J. Chem.* 33, 47 (1993).
568. D. Meisel, *Isr. J. Chem.* 33, 53 (1993).
569. R. R. Chandler and J. L. Coffer, *J. Phys. Chem.* 97, 9767 (1993).
570. T. Tuerk, U. Resch, M. A. Fox, and A. Vogler, *J. Phys. Chem.* 96, 3818 (1992).
571. R. Tuerk, U. Resch, M. A. Fox, and A. Vogler, *Inorg. Chem.* 31, 1854 (1992).
572. F. R. F. Fan, H. Y. Liu, and A. J. Bard, *J. Phys. Chem.* 89, 4418 (1985).
573. M. D. Butterworth, S. P. Armes, and A. W. Simpson, *J. Chem. Soc., Chem. Commun.* 2129 (1994).
574. J. Kuczynski and J. K. Thomas, *Langmuir* 1, 158 (1985).
575. Z. J. Zhang, J. Zhang, and Q. J. Xue, *J. Phys. Chem.* 98, 12973 (1994).
576. R. R. Chandler, J. L. Coffer, S. J. Atherton, and P. T. Snowden, *J. Phys. Chem.* 96, 2713 (1992).
577. G. C. Lisensky, R. L. Penn, C. J. Murphy, and A. B. Ellis, *Science* 248, 840 (1990).
578. C. J. R. Cowdery, D. G. Whitten, and G. L. McLendon, *Chem. Phys.* 176, 377 (1993).
579. K. Johansson, R. Cowdery, M. O'Neil, J. Rehm, G. McLendon, A. Marchetti, and D. G. Whitten, *Isr. J. Chem.* 33, 67 (1993).
580. J. J. Ramsden and M. Grätzel, *J. Chem. Soc., Faraday Trans.* 80, 919 (1984).
581. M. Evenor, S. Gottesfeld, Z. Harzion, D. Huppert, and S. W. Feldberg, *J. Phys. Chem.* 88, 6213 (1984).
582. Y. Rosenwaks, L. Burstein, Y. Shapira, and D. Huppert, *J. Phys. Chem.* 94, 6842 (1990).
583. P. P. Bessler, D. Huppert, Y. Rosenwaks, and Y. Shapira, *J. Phys. Chem.* 95, 4370 (1991).
584. H. Meier, *J. Photochem. Photobiol.* 16, 219 (1972).
585. H. Gerischer and F. Willig, *Top. Curr. Chem.* 61, 31 (1976).
586. M. Spitler and B. A. Parkinson, *Langmuir* 2, 549 (1986).
587. M. A. Ryan and M. T. Spitler, *J. Imaging Sci.* 33, 46 (1989).
588. B. O'Regan and M. Grätzel, *Nature (London)* 353, 737 (1991).
589. M. Grätzel, *Coord. Chem. Rev.* 111, 167 (1991).
590. P. V. Kamat and M. A. Fox, *Chem. Phys. Lett.* 102, 379 (1983).
591. J. Moser and M. Grätzel, *J. Am. Chem. Soc.* 106, 6557 (1984).
592. R. Rossetti and L. E. Brus, *J. Am. Chem. Soc.* 106, 4336 (1984).
593. M. A. Ryan, E. C. Fitzgerald, and M. T. Spitler, *J. Phys. Chem.* 93, 6150 (1989).
594. S. Umapathy, A. M. Cartner, A. W. Parker, and R. E. Hester, *J. Phys. Chem.* 94, 8880 (1990).
595. R. W. Fessenden and P. V. Kamat, *Chem. Phys. Lett.* 123, 233 (1986).
596. T. Takizawa, T. Watanabe, and K. Honda, *J. Phys. Chem.* 82, 1391 (1978).
597. K. Hashimoto, M. Hiramoto, and T. Sakata, *Chem. Phys. Lett.* 148, 215 (1988).
598. K. Hashimoto, M. Hiramoto, and T. Sakata, *J. Phys. Chem.* 92, 4272 (1988).
599. Y. Liang, P. F. Moy, J. A. Poole, and A. M. Ponte Goncalves, *J. Phys. Chem.* 88, 2451 (1984).
600. K. Bitterling and F. Willig, *J. Electroanal. Chem. Interfacial Electrochem.* 204, 211 (1986).
601. R. L. Crackel and W. S. Struve, *Chem. Phys. Lett.* 120, 473 (1985).
602. F. Willig, R. Eichberger, N. S. Sundaresan, and B. A. Parkinson, *J. Am. Chem. Soc.* 112, 2702 (1990).
603. R. Eichberger and F. Willig, *Chem. Phys. Lett.* 141, 159 (1990).
604. B. Patrick and P. V. Kamat, *J. Phys. Chem.* 96, 1423 (1992).
605. P. V. Kamat, J. P. Chauvet, and R. W. Fessenden, *J. Phys. Chem.* 90, 1389 (1986).
606. A. Kay, R. Humphry-Baker, and M. Grätzel, *J. Phys. Chem.* 98, 952 (1994).
607. P. V. Kamat, *J. Phys. Chem.* 93, 859 (1989).
608. V. H. Houlding and M. Grätzel, *J. Am. Chem. Soc.* 105, 5695 (1983).
609. K. Kalyanasundaram, N. Vlachopoulos, V. Krishnan, A. Monnier, and M. Grätzel, *J. Phys. Chem.* 91, 2342 (1987).
610. F. R. F. Fan and A. J. Bard, *J. Am. Chem. Soc.* 101, 6139 (1979).
611. J. D. Luttmer and A. J. Bard, *J. Electrochem. Soc.* 126, 414 (1979).
612. B. Burfeindt, T. Hannappel, W. Storck, and F. Willig, *J. Phys. Chem.* 100, 16463 (1996).
613. S. Ferrere, A. Zaban, and B. A. Gregg, *J. Phys. Chem. B* 101, 4490 (1997).
614. E. Vrachnou, N. Vlachopoulos, and M. Grätzel, *J. Chem. Soc., Chem. Commun.* 868 (1987).
615. E. Vrachnou, M. Grätzel, and A. J. McEvoy, *J. Electroanal. Chem. Interfacial Electrochem.* 258, 193 (1989).
616. P. K. Ghosh and T. G. Spiro, *J. Am. Chem. Soc.* 102, 5543 (1980).

617. D. A. Gulino and H. G. Drickamer, *J. Phys. Chem.* 88, 1173 (1984).
618. R. Dabestani, A. J. Bard, A. Campion, M. A. Fox, T. E. Mallouk, S. E. Webber, and J. M. White, *J. Phys. Chem.* 92, 1872 (1988).
619. M. K. Nazeeruddin, P. Liska, J. Moser, N. Vlachopoulos, and M. Grätzel, *Helv. Chim. Acta* 73, 1788 (1990).
620. B. O'Regan, J. Moser, M. Anderson, and M. Grätzel, *J. Phys. Chem.* 94, 8720 (1990).
621. W. E. Ford and M. A. J. Rodgers, *J. Phys. Chem.* 98, 3822 (1994).
622. T. Iwasaki, S. Oda, H. Kamada, and K. Honda, *J. Phys. Chem.* 84, 1060 (1980).
623. H. Hada, Y. Yonezawa, and H. Inaba, *Ber. Bunse-Ges. Phys. Chem.* 85, 425 (1981).
624. C. Kavassalls and M. T. Spitler, *J. Phys. Chem.* 87, 3166 (1983).
625. L. M. Natoli, M. A. Ryan, and M. T. Spitler, *J. Phys. Chem.* 89, 1448 (1985).
626. Y. Hayashi, S. Ogawa, M. Sanada, and R. Hirohashi, *J. Imaging Sci.* 33, 124 (1989).
627. T. Tani, T. Suzumoto, and K. Ohzeki, *J. Phys. Chem.* 94, 1298 (1990).
628. R. Kietzmann, A. Ehret, M. Spitler, and F. Willig, *J. Am. Chem. Soc.* 115, 1930 (1993).
629. C. Nasr, S. Hotchandani, P. V. Kamat, S. Das, K. George Thomas, and M. V. George, *Langmuir* 11, 1777 (1995).
630. S. Hotchandani, S. Das, K. G. Thomas, M. V. George, and P. V. Kamat, *Res. Chem. Intermed.* 20, 927 (1994).
631. Y.-S. Kim, K. Liang, K.-Y. Law, and D. G. Whitten, *J. Phys. Chem.* 98, 984 (1994).
632. H. Frei, D. J. Fitzmaurice, and M. Grätzel, *Langmuir* 6, 198 (1990).
633. T. Nakahira and M. Grätzel, *Makromol. Chem., Rapid Commun.* 6, 341 (1985).
634. T. Nakahira, Y. Inoue, K. Iwasaki, H. Tanigawa, Y. Kouda, S. Iwabuchi, K. Kojima, and M. Grätzel, *Makromol. Chem., Rapid Commun.* 9, 13 (1988).
635. T. Tani, T. Suzumoto, K. Kemnitz, and K. Yoshihara, *J. Phys. Chem.* 96, 2778 (1992).
636. M. T. Spitler, *J. Imaging Sci.* 35, 351 (1991).
637. J. E. Moser and M. Grätzel, *Chem. Phys.* 176, 493 (1993).
638. D. Liu and P. V. Kamat, *J. Electrochem. Soc.* 142, 835 (1995).
639. D. Liu, G. L. Hug, and P. V. Kamat, *J. Phys. Chem.* 99, 16768 (1995).
640. D. Liu and P. V. Kamat, *Langmuir* 12, 2190 (1996).
641. D. Liu and P. V. Kamat, *J. Chem. Phys.* 105, 965 (1996).
642. D. Liu, R. W. Fessenden, G. L. Hug, and P. V. Kamat, *J. Phys. Chem. B* 101, 2583 (1997).
643. I. Martini, G. Hartland, and P. V. Kamat, *J. Phys. Chem. B* 101, 4826 (1997).
644. C. Nasr, D. Liu, S. Hotchandani, and P. V. Kamat, *J. Phys. Chem.* 100, 11054 (1996).
645. D. M. Klassen and G. A. Crosby, *J. Chem. Phys.* 48, 1853 (1968).
646. C. Creutz and N. Sutin, *J. Am. Chem. Soc.* 98, 6384 (1976).
647. J. Van Houten and R. J. Watts, *J. Am. Chem. Soc.* 98, 4853 (1976).
648. D. Meisel, M. S. Matheson, W. A. Mulac, and J. Rabani, *J. Phys. Chem.* 81, 1449 (1977).
649. J. C. Casper and T. J. Meyer, *J. Am. Chem. Soc.* 105, 5583 (1983).
650. Y. Komada, S. Yamauchi, and N. Hirota, *J. Phys. Chem.* 92, 6511 (1988).
651. E. Krausz, *Comments Inorg. Chem.* 7, 139 (1988).
652. D. J. Fitzmaurice and H. Frei, *Langmuir* 7, 1129 (1991).
653. V. Kurshev and L. Kevan, *Langmuir* 13, 225 (1997).
654. P. V. Kamat, K. R. Gopidas, and D. Weir, *Chem. Phys. Lett.* 149, 491 (1988).
655. K. R. Gopidas, P. V. Kamat, and M. V. George, *Mol. Cryst. Liq. Cryst.* 183, 403 (1990).
656. K. Vinodgopal and P. V. Kamat, *J. Phys. Chem.* 96, 5053 (1992).
657. M. Gevaert and P. V. Kamat, *J. Chem. Soc., Chem. Commun.* 1470 (1992).
658. K. Vinodgopal, X. Hua, R. L. Dahlgren, A. G. Lappin, L. K. Patterson, and P. V. Kamat, *J. Phys. Chem.* 99, 10883 (1995).
659. D. Liu, P. V. Kamat, K. George Thomas, K. J. Thomas, S. Das, and M. V. George, *J. Chem. Phys.* 106, 6404 (1997).
660. P. V. Kamat and B. Patrick, in "Electrochemistry in Colloids and Dispersions" (R. A. Mackay and J. Texter, eds.), p. 447. VCH Publishers, New York, 1992.
661. K. Itoh, Y. Chiyokawa, M. Nakao, and K. Honda, *J. Am. Chem. Soc.* 106, 1620 (1984).
662. K. Hashimoto, M. Hiramoto, T. Kajiwara, and T. Sakata, *J. Phys. Chem.* 92, 4636 (1988).
663. K. Hashimoto, M. Hiramoto, A. B. P. Lever, and T. Sakata, *J. Phys. Chem.* 92, 1016 (1988).
664. K. Kemnitz, N. Nakashima, K. Yoshihara, and H. Matsunami, *J. Phys. Chem.* 93, 6704 (1989).
665. K. Misawa, K. Minoshima, and T. Kobayashi, *J. Raman Spectrosc.* 26, 553 (1995).
666. J. M. Rehm, G. L. McLendon, Y. Nagasawa, K. Yoshihara, J. Moser, and M. Grätzel, *J. Phys. Chem.* 100, 9577 (1996).
667. Y. Tachibana, J. E. Moser, M. Grätzel, D. R. Klug, and J. R. Durrant, *J. Phys. Chem.* 100, 20056 (1996).
668. I. Martini, J. Hodak, G. Hartland, and P. V. Kamat, *J. Chem. Phys.* 107, 8064 (1997).
669. T. Hannappel, B. Burfeindet, W. Storck, and F. Willig, *J. Phys. Chem. B* 101, 6799 (1997).
670. W. E. Ford and M. A. J. Rodgers, *J. Phys. Chem.* 101, 930 (1997).
671. F. Willig, in "Surface Electron Transfer Process" (R. J. Dwayne Miller, G. L. McLendon, A. J. Nozik, W. Scmickler, and F. Willig, eds.), p. 167. VCH Publishers, New York, 1995.

672. R. J. D. Miller, in "Surface Electron Transfer Process" (R. J. D. Miller, G. L. McLendon, A. J. Nozik, W. Scmickler, and F. Willig, eds.), p. 95. VCH Publishers, New York, 1995.
673. J. M. Lanzafame, R. J. D. Miller, A. A. Muenter, and B. A. Parkinson, *J. Phys. Chem.* 96, 2820 (1992).
674. N. J. Cherepy, G. P. Smestad, M. Grätzel, and J. Z. Zhang, *J. Phys. Chem. B* 101, 9342 (1997).
675. K. Murakoshi, S. Yanagida, M. Capel, and E. W. Castner, in "Nanostructured Materials: Clusters, Composites, and Thin Films" (M. Moskovits, ed.), p. 221. American Chemical Society, 1997.
676. J. Randy, R. J. Ellingson, J. B. Asbury, S. Ferrere, H. N. Ghosh, J. R. Sprague, T. Lian, and A. J. Nozik, *J. Phys. Chem. B* 102, 6455 (1998).
677. D. Liu and P. V. Kamat, *J. Electroanal. Chem. Interfacial Electrochem.* 347, 451 (1993).
678. N. Uekawa, T. Suzuki, S. Ozeki, and K. Kaneko, *Langmuir* 8, 1 (1992).
679. D. Liu and P. V. Kamat, *J. Phys. Chem.* 97, 10769 (1993).
680. R. Vogel, P. Hoyer, and H. Weller, *J. Phys. Chem.* 98, 3183 (1994).
681. H. Gerischer and M. Lübke, *J. Electroanal. Chem. Interfacial Electrochem.* 204, 225 (1986).
682. R. Vogel, K. Pohl, and H. Weller, *Chem. Phys. Lett.* 174, 241 (1990).
683. S. Kohtani, A. Kudo, and T. Sakata, *Chem. Phys. Lett.* 206, 166 (1993).
684. I. Bedja and P. V. Kamat, *J. Phys. Chem.* 99, 9182 (1995).
685. S. Hotchandani and P. V. Kamat, *Chem. Phys. Lett.* 191, 320 (1992).
686. A. J. Nozik, *Appl. Phys. Lett.* 30, 567 (1977).
687. N. Serpone, E. Borgarello, and M. Grätzel, *J. Chem. Soc., Chem. Commun.* 342 (1984).
688. L. Spanhel, H. Weller, and A. Henglein, *J. Am. Chem. Soc.* 109, 6632 (1987).
689. H. S. Zhou, I. Honma, and H. Komiyama, *J. Phys. Chem.* 97, 895 (1993).
690. A. Haesselbarth, A. Eychmüller, R. Eichberger, M. Giersig, A. Mews, and H. Weller, *J. Phys. Chem.* 97, 5333 (1993).
691. J. E. Evans, K. W. Springer, and J. Z. Zhang, *J. Chem. Phys.* 101, 6222 (1994).
692. J. W. Haus, H. S. Zhou, I. Honma, and H. Komiyama, *Phys. Rev.* 47, 1359 (1993).
693. M. Ocana, W. P. Hsu, and E. Matijevic, *Langmuir* 7, 2911 (1991).
694. G. Hodes, *Isr. J. Chem.* 33, 95 (1993).
695. G. J. Meyer and P. C. Searson, *Interface* 23 (1993).
696. P. V. Kamat, *CHEMTECH* 22 (1995).
697. A. Hagfeldt and M. Grätzel, *Chem. Rev.* 95, 49 (1995).
698. A. W. H. Mau, C. B. Huang, N. Kakuta, A. J. Bard, A. Campion, M. A. Fox, J. M. White, and S. E. Webber, *J. Am. Chem. Soc.* 106, 6537 (1984).
699. K. Honda, A. Kuwano, K. Chiba, A. Ishikawa, and H. Miyama, *Chem. Lett.* 195 (1988).
700. M. Kaneko, T. Okada, S. Teratani, and K. Taya, *Electrochim. Acta* 32, 1405 (1987).
701. O. V. Salata, P. J. Dobson, P. J. Hull, and J. L. Hutchison, *Thin Solid Films* 251, 81 (1994).
702. M. Gao, Y. Yang, B. Yang, F. Bian, and J. Shen, *J. Chem. Soc., Chem. Commun.* 2779 (1994).
703. Y. Wang and N. Herron, *J. Lumin.* 70, 48 (1996).
704. J. H. Fendler, *Chem. Rev.* 87, 877 (1987).
705. W. Kautek and H. Gerischer, *Electrochim. Acta* 27, 355 (1982).
706. D. V. Paranjape, M. Sastry, and P. Ganguly, *Appl. Phys. Lett.* 63, 18 (1993).
707. R. S. Urquhart, C. L. Hoffmann, D. N. Furlong, N. J. Geddes, J. F. Raboldt, and F. Grieser, *J. Phys. Chem.* 99, 15987 (1995).
708. L. Sereno, J. Silber, L. Otero, M. Bohorquez, A. L. Moore, T. A. Moore, and D. Gust, *J. Phys. Chem.* 100, 814 (1996).
709. F. Grieser, D. N. Furlong, R. S. Urquhart, and D. J. Elliot, in "Fine Particles Science and Technology" (E. Pelizzatti, ed.), p. 733. Kluwer Academic, Boston, 1996.
710. L. Motte, F. Billoudet, E. Lacaze, J. Douin, and M. P. Pileni, *J. Phys. Chem.* 101, 138 (1997).
711. S. G. Yan and J. T. Hupp, *J. Phys. Chem. B* 101, 1493 (1997).
712. I. Moriguchi, H. Maeda, Y. Teraoka, and S. Kagawa, *J. Am. Chem. Soc.* 1139 (1995).
713. Q. Xu and M. A. Anderson, *J. Mater. Res.* 6, 1073 (1991).
714. S. Tunesi and M. Anderson, *J. Phys. Chem.* 95, 3399 (1991).
715. J. Sabate, M. A. Anderson, M. A. Aguado, J. Gimenez, M. S. Cervera, and C. G. J. Hill, *J. Mol. Catal.* 71, 57 (1992).
716. G. Dagan and M. Tomkiewicz, *J. Phys. Chem.* 97, 12651 (1993).
717. M. N. Kamalasanan, N. D. Kumar, and S. Chandra, *J. Appl. Phys.* 74, 679 (1993).
718. S. Sakohara, L. D. Tickanen, and M. A. Anderson, *J. Phys. Chem.* 96, 11086 (1992).
719. D. Papoutsi, P. Lianos, P. Yianoulis, and P. Koutsoukos, *Langmuir* 10, 1684 (1994).
720. B. O'Regan and D. T. Schwartz, *Chem. Mater.* 7, 1349 (1995).
721. D. M. Antonelli and J. Y. Ying, *Angew. Chem., Int. Ed. Engl.* 34, 2014 (1995).
722. N. Negishi, T. Iyoda, K. Hashimoto, and A. Fujishima, *Chem. Lett.* 841 (1995).
723. C. Anderson and A. J. Bard, *J. Phys. Chem.* 99, 9882 (1995).
724. T. Jiang, A. L. Lough, G. A. Ozin, and D. Young, *Chem. Mater.* 7, 245 (1995).
725. T. Nakanishi, B. Ohtani, and K. Uosaki, *J. Phys. Chem. B* 102, 1571 (1998).
726. G. Hodes, I. D. J. Howell, and L. M. Peter, *J. Electrochem. Soc.* 139, 3136 (1992).

727. S. Hotchandani and P. V. Kamat, *J. Electrochem. Soc.* 139, 1630 (1992).
728. I. Bedja, S. Hotchandani, R. Carpentier, R. W. Fessenden, and P. V. Kamat, *J. Appl. Phys.* 75, 5444 (1994).
729. I. Bedja, S. Hotchandani, R. Carpentier, K. Vinodgopal, and P. V. Kamat, *Thin Solid Films* 247, 195 (1994).
730. U. Bjorksten, J. Moser, and M. Grätzel, *Chem. Mater.* 6, 858 (1994).
731. A. Hagfeldt, S. E. Lindquist, and M. Grätzel, *Sol. Energy Mater. Sol. Cells* 32, 245 (1994).
732. C. Nasr, S. Hotchandani, and P. V. Kamat, *Proc. Ind. Acad. Sci.* 107, 699 (1995).
733. P. V. Kamat, in "Nanoparticles and Nanostructural Films" (J. Fendler, ed.), p. 207. Wiley–VCH, New York, 1998.
734. I. Bedja, S. Hotchandani, and P. V. Kamat, *J. Electroanal. Chem.* 401, 237 (1996).
735. I. Bedja, P. V. Kamat, and S. Hotchandani, *J. Appl. Phys.* 80, 4637 (1996).
736. K. Vinodgopal, D. Wynkoop, and P. V. Kamat, *Environ. Sci. Technol.* 30, 1660 (1996).
737. H. Lindstrom, H. Rensmo, S. Sodergren, A. Solbrand, and S. Lindquist, *J. Phys. Chem.* 3084 (1996).
738. N. Papageorgiou, Y. Athanassov, M. Armand, P. Bonhote, H. Petterson, A. Azam, and M. Grätzel, *J. Electrochem. Soc.* 143, 3099 (1996).
739. S. G. Yan and J. T. Hupp, *J. Phys. Chem.* 100, 6867 (1996).
740. L. Kavan, M. Grätzel, J. Rathousky, and A. Zukal, *J. Electrochem. Soc.* 143, 394 (1996).
741. A. Zaban, S. Ferrere, J. Sprague, and B. A. Gregg, *J. Phys. Chem. B* 101, 55 (1997).
742. C. Nasr, S. Hotchandani, W. Y. Kim, R. H. Schmehl, and P. V. Kamat, *J. Phys. Chem. B* 101, 7480 (1997).
743. P. V. Kamat, in "Progress in Inorganic Chemistry Series" (J. Meyer, ed.), Vol. 44, p. 273. Wiley, New York, 1997.
744. J. J. Fang, J. X. Wu, X. Lu, S. Y., and Z. Lu, *Chem. Phys. Lett.* 270, 145 (1997).
745. C. Nasr, S. Hotchandani, and P. V. Kamat, in "Photoelectrochemistry" (K. Rajeshwar, ed.). Electrochemical Society, Pennington, NJ, 1997.
746. I. Bedja, P. V. Kamat, X. Hua, A. G. Lappin, and S. Hotchandani, *Langmuir* 13, 2398 (1998).
747. C. Nasr, S. Hotchandani, and P. V. Kamat, *J. Phys. Chem. B* 102, to appear.
748. M. K. Nazeeruddin, A. Kay, I. Rodicio, B. R. Humphry, E. Mueller, P. Liska, N. Vlachopoulos, and M. Grätzel, *J. Am. Chem. Soc.* 115, 6382 (1993).
749. R. Ionescu, C. Moise, and A. Vancu, *Appl. Surf. Sci.* 84, 291 (1995).
750. O. Savadogo and K. C. Mandal, *J. Electrochem. Soc.* 141, 2871 (1994).
751. V. L. Colvin, M. C. Schlamp, and A. P. Alivisatos, *Nature* 370, 354 (1994).
752. S. Hotchandani, I. Bedja, R. W. Fessenden, and P. V. Kamat, *Langmuir* 10, 17 (1994).
753. L. Kavan, T. Stoto, M. Grätzel, D. J. Fitzmaurice, and V. Shklover, *J. Phys. Chem.* 97, 9493 (1993).
754. K. Rajeshwar, R. O. Lezna, and N. R. deTacconi, *Anal. Chem.* 64, 429 (1992).
755. G. S. Hsiao, M. G. Anderson, S. Gorer, D. Harris, and R. M. Penner, *J. Am. Chem. Soc.* 119, 1439 (1997).
756. M. A. Anderson, S. Gorer, and R. M. Penner, *J. Phys. Chem. B* 101, 5895 (1997).
757. E. A. Kamenetzky, L. G. Mangliocco, and H. P. Panzer, *Science* 263, 207 (1994).
758. H. B. Sunkara, J. M. Jethmalani, and W. T. Ford, *Chem. Mater.* 6, 362 (1994).
759. W. L. Vos, R. Sprik, A. van Blaaderen, A. Imhof, A. Lagendijk, and G. H. Wegdam, *Phys. Rev. B* 53, 16231 (1996).
760. I. I. Tarhan and G. H. Watson, *Phys. Rev. Lett.* 76, 315 (1996).
761. C. R. Kagan, C. B. Murray, and M. G. Bawendi, *Phys. Rev. B* 54, 8633 (1996).
762. J. R. Heath, C. M. Knobler, and D. V. Leff, *J. Phys. Chem. B* 101, 189 (1997).
763. G. Chmanov, K. Sokolov, and T. M. Cotton, *J. Phys. Chem.* 100, 5166 (1996).
764. C. A. Mirkin, R. L. Letsinger, R. C. Mucic, and J. J. Storhoff, *Nature* 382, 607 (1996).
765. C. Murray, C. Kagan, and M. Bawendi, *Science* 270, 1335 (1995).
766. W. Shenton, D. Pum, U. B. Sleytr, and S. Mann, *Nature* 389, 585 (1997).
767. L. Cusack, X. Marguerettaz, S. N. Rao, J. Wenger, and D. Fitzmaurice, *Chem. Mater.* 9, 1765 (1997).
768. L. Cusack, R. Rizza, A. Gorelov, and D. Fitzmaurice, *Angew. Chem., Int. Ed. Engl.* 36, 848 (1997).
769. T. Moritz, J. Reiss, K. Diesner, D. Su, and A. Chemseddine, *J. Phys. Chem. B* 101, 8052 (1997).
770. J. S. Yin and Z. L. Wang, *J. Phys. Chem. B* 101, 8979 (1997).
771. J. S. Yin and Z. L. Wang, *Phys. Rev. Lett.* 79, 2570 (1997).
772. L. Motte, F. Billoudet, E. Lacaze, and M.-P. Pileni, *Adv. Mater.* 8 (1996).
773. S. Ogawa, K. Hu, F.-R. F. Fan, and A. J. Bard, *J. Phys. Chem. B* 101, 5707 (1997).
774. T. Takagahara, *Surf. Sci.* 267, 310 (1992).
775. P. V. Braun, P. Osenar, and S. I. Stupp, *Nature* 380, 325 (1996).
776. S. G. Romanv, C. M. Sotomayor Torres, H. M. Yates, M. E. Pemble, V. Butko, and V. Tretijakov, *J. Appl. Phys.* 82, 380 (1997).
777. R. Routkevitch, T. Bigioni, M. Martin, and J. M. Xu, *J. Phys. Chem.* 100, 14037 (1996).
778. J. D. Klein, R. D. Herrick, II, D. Palmer, and M. J. Sailor, *Chem. Mater.* 5, 902 (1993).
779. A. Kay and M. Grätzel, *J. Phys. Chem.* 97, 6272 (1993).
780. P. Bonhote, E. Gogniat, S. Tingry, C. Barbe, N. Vlachopoulos, F. Lenzmann, P. Comte, and M. Grätzel, *J. Phys. Chem. B* 102, 1498 (1998).
781. C. M. Lampert, *Solar Energy Mater.* 11, 1 (1984).
782. B. O'Regan, M. Grätzel, and D. Fitzmaurice, *Chem. Phys. Lett.* 183, 89 (1991).

783. A. Hagfeldt, N. Vlachopoulos, and M. Grätzel, *J. Electrochem. Soc.* 141, L82 (1994).
784. C. Bechinger, S. Ferrere, A. Zaban, J. Sprague, and B. A. Gregg, *Nature* 383, 608 (1996).
785. B. O'Regan, M. Grätzel, and D. Fitzmaurice, *J. Phys. Chem.* 95, 10525 (1991).
786. G. Redmond, D. Fitzmaurice, and M. Grätzel, *J. Phys. Chem.* 97, 6951 (1993).
787. G. Redmond and D. Fitzmaurice, *J. Phys. Chem.* 97, 1426 (1993).
788. L. Butler, G. Redmond, and D. Fitzmaurice, *J. Phys. Chem.* 97, 10750 (1993).
789. S. Sodergren, A. Hagfeldt, J. Olsson, and S.-E. Lindquist, *J. Phys. Chem.* 98, 5552 (1994).
790. N. Chestnoy, T. D. Harris, R. Hull, and L. E. Brus, *J. Phys. Chem.* 90, 3393 (1986).
791. H. Tributsch, G. Schlichthoerl, and L. Elstner, *Electrochim. Acta* 38, 141 (1993).
792. A. J. Nozik, B. R. Thacker, J. A. Turner, and J. M. Olson, *J. Am. Chem. Soc.* 107, 7805 (1985).
793. A. J. Nozik, B. R. Thacker, and J. M. Olson, *Nature* 316, 51 (1985).
794. A. J. Nozik, B. R. Thacker, J. A. Turner, J. Klem, and H. Morkoc, *Appl. Phys. Lett.* 50, 34 (1987).
795. A. J. Nozik, B. R. Thacker, J. A. Turner, and M. W. Peterson, *J. Am. Chem. Soc.* 110, 7630 (1988).
796. A. J. Nozik, J. A. Turner, and M. W. Peterson, *J. Phys. Chem.* 92, 2493 (1988).
797. C. A. Parsons, M. W. Peterson, B. R. Thacker, J. A. Turner, and A. J. Nozik, *J. Phys. Chem.* 94, 3381 (1990).
798. C. A. Bignozzi, R. Argazzi, T. Indelli, and F. Scandola, *Solar Energy Mater.* 32, 229 (1994).
799. G. Smestad, C. Bignozzi, and R. A. Argazzi, *Solar Energy Mater.* 32, 259 (1994).
800. G. Smestad, *Solar Energy Mater.* 32, 273 (1994).
801. P. V. Kamat, *Langmuir* 6, 512 (1990).
802. P. V. Kamat, S. Das, K. G. Thomas, and M. V. George, *Chem. Phys. Lett.* 178, 75 (1991).
803. H. Takemura, T. Saji, M. Fujihira, S. Aoyagui, K. Hashimoto, and T. Sakata, *Chem. Phys. Lett.* 122, 496 (1985).
804. K. Hashimoto, M. Hiramoto, T. Sakata, H. Muraki, H. Takemura, and M. Fujihira, *J. Phys. Chem.* 91, 6198 (1987).
805. K. Schwarzburg and F. Willig, *Appl. Phys. Lett.* 58, 2520 (1991).
806. H. Grabert and M. H. Devoret, "Single Charge Tunneling: Coulomb Blockade Phenomena in Nanostructures." Plenum Press, London, 1992.
807. R. P. Andres, T. Bein, M. Dorogi, S. Feng, J. I. Henderson, C. P. Kubiak, W. Mahoney, R. G. Osifchin, and R. Reifenberger, *Science* 272, 323 (1996).
808. R. P. Andres, S. Datta, M. Dorogi, J. Gomez, J. I. Henderson, D. B. Jones, V. R. Kolagunta, C. P. Kubiak, W. Mahoney, and R. G. Osifchin, *J. Vac. Sci. Technol., A* 14, 1178 (1996).
809. L. Guo, E. Leobandung, and S. Y. Chou, *Science* 275, 649 (1997).
810. D. L. Fedheim, K. C. Grabar, M. J. Natan, and T. E. Mallouk, *J. Am. Chem. Soc.* 118, 7640 (1996).
811. F. F. Fan and A. J. Bard, *Science* 277, 1791 (1997).
812. D. L. Klein, P. L. McEuen, J. E. B. Katari, R. Roth, and P. Alivisatos, *Appl. Phys. Lett.* 68, 2574 (1996).
813. D. L. Klein, R. Roth, A. K. L. Lim, P. Alivisatos, and P. L. McEuen, *Nature* 389, 699 (1997).
814. K. Vinodgopal, I. Bedja, and P. V. Kamat, *Chem. Mater.* 8, 2180 (1996).

Chapter 7

HYBRID MAGNETIC–SEMICONDUCTOR NANOSTRUCTURES

François M. Peeters
Departement Natuurkunde, Universiteit Antwerpen, Antwerpen, Belgium

Jo De Boeck
IMEC, Leuven, Belgium

Contents

1. Introduction 346
2. Electrons in Microscopically Inhomogeneous Magnetic Fields 347
3. Magnetic Field Profiles 348
   3.1. One-Dimensional Profiles 348
   3.2. Periodic Structures 351
4. Quantum Motion in Nonhomogeneous Magnetic Fields 353
   4.1. Magnetic Step 354
   4.2. Magnetic Barrier 356
   4.3. Magnetic Quantum Well 359
   4.4. Resonant Tunneling Structures 361
   4.5. Magnetic Dot 363
5. Diffusive Transport of Electrons through Magnetic Barriers 366
   5.1. Theoretical Formalism 367
   5.2. Single Magnetic Barrier 368
   5.3. Magnetic Barriers in Series 370
6. One-Dimensional Magnetic Modulation 371
   6.1. Weak Magnetic Modulation 372
   6.2. Electric and Magnetic Modulations 377
   6.3. Magnetic Minibands 380
7. Two-Dimensional Magnetic Modulation 386
   7.1. Periodic Two-Dimensional Modulation 386
   7.2. A Random Array of Identical Magnetic Disks 387
   7.3. Random Magnetic Fields 388
8. Hall Effect Devices 390
   8.1. Ballistic Hall Magnetometry 391
   8.2. Hall Magnetometry in the Diffusive Regime 395
   8.3. Hybrid Hall Effect Device 399
9. Nonpolarized Current Injection from Semiconductor into Ferromagnets 403
10. Spin Injection Ferromagnetic/Semiconductor Structures 404
   10.1. Spin-Polarized Electronic Current from Ferromagnets 404
   10.2. Optical Detection of Spin-Polarized Tunnel Current 404
   10.3. Spin-Polarized Electronic (Tunnel) Current from Optically Pumped Semiconductors 405
   10.4. Spin-Polarized Current from Magnetic Contacts to Semiconductors 406

Handbook of Nanostructured Materials and Nanotechnology, edited by H.S. Nalwa
Volume 3: Electrical Properties
Copyright © 2000 by Academic Press
All rights of reproduction in any form reserved.
ISBN 0-12-513763-X/$30.00

11. Ferromagnetic/Semiconductor Experimental Structures 408
11.1. The Need for Epitaxy 408
11.2. General Metal Epitaxy Criteria 409
11.3. Elemental Ferromagnetic Metal Epitaxy on Semiconductors 410
11.4. Magnetic and Electrical Properties of Ferromagnets at the Ferromagnetic/Semiconductor Interfaces 411
11.5. Properties of Manganese-Based Epitaxial Magnetic Layers on III–V Semiconductors 412
11.6. Semiconductor/Ferromagnetic/Semiconductor Multilayers 413
12. Nanoscale Magnets 414
12.1. Introduction 414
12.2. Self-Organized Magnetic Nanostructures in Semiconductor Thin Films 414
12.3. Experimental Conditions for Thin Films with Nanoclusters by Molecular Beam Epitaxy + Annealing 415
13. Superlattices of Nanoscale Magnet Layers and Semiconductors 418
13.1. Engineering Aspects of Superlattices of Nanoscale Magnet Layers and Semiconductors . . . 418
13.2. Structural and Magnetic Properties of the Superlattices 418
13.3. Current Perpendicular to the Plane Magnetotransport 418
13.4. Conclusions 419
Acknowledgments 420
References 420

1. INTRODUCTION

During the last half century, there has been a rapid development in the field of solid-state electronics, which started with the discovery of the transistor and subsequently was fueled by the integration of many circuit elements onto one semiconductor chip. Magnetic materials, on the other hand, have been developed separately, independently from the semiconductor systems. They have been very important for information storage (tape, disk, magnetooptic disk) and for magnetic circuits.

Recently, one started to incorporate magnetic materials into planar integrated electronic circuitry. In those integrated devices, the semiconductor properties are combined with and enhanced by the presence of magnetic elements. In a first level of integration, one fabricates on the same substrate a hybrid system consisting of separated magnetic and electronic components. A much higher level of integration is realized when the magnetic elements modify and enhance the behavior of the electronic devices by becoming part of them. This may ultimately lead to completely new classes and concepts of devices.

The outline of the present chapter follows the preceding division. In the first part (Sections 2–8), we consider systems consisting of a semiconductor [typically containing a two-dimensional electron gas (2DEG) as found, for example, in heterojunctions] with a patterned ferromagnetic material on top of it. The electrons move in local nonhomogeneous magnetic fields that alter the orbital motion of the electrons through the Lorentz force, that is, $\mathbf{F} = q\mathbf{v} \times \mathbf{B}$. Such a magnetic field will also induce a shift in the energy of the electrons. Because in typical III–V semiconductors the effective g factor is small, the spin will be of secondary importance in this case.

In the second part (Sections 9–12), structures are considered in which the electron (or hole) current passes through the ferromagnetic/semiconductor (FM/SC) interface. Here, one relies on spin-dependent scattering and the Zeeman spin splitting as the fundamental mechanisms on which the action of the device is based. Spin-up and spin-down electrons now become different types of carriers. Several device concepts have been proposed, including an all-metal spin transistor based on the accumulation of a spin-up or spin-down population, an analog of the electrooptic modulator based on a precession of the electron spin, and systems where one uses the FM/SC analog of the giant magnetoresistance.

As in semiconductor research and technology, in present-day magnetic thin-film research the technology to fabricate submicrometer structures is very important. Electron beam (e-beam) lithography and other techniques are used for fabricating submicrometer

features. The characterization of magnetic nanowires, magnetic dot arrays, and so forth will lead to an increased understanding of the physics of micromagnetism and magnetoelectronics. Small feature sizes will also be essential in applications such as magnetic random-access memory (MRAM) and intriguing device applications such as spin transport devices.

In the first part of this overview, we focus on the motion of two-dimensional (2D) electrons in nonhomogeneous magnetic fields. In Section 3, we show how such nonhomogeneous magnetic field profiles can be created experimentally and we calculate the perpendicular magnetic field component that is felt by the 2DEG. The ballistic motion of 2D electrons through different magnetic field profiles are studied in Section 4, while the diffusive regime is discussed in Section 5. Periodic magnetic structures are considered in Section 6 [one-dimensional (1D) magnetic modulation] and Section 7 (2D periodic and random modulation). Different devices based on the Hall effect in combination with nonhomogeneous magnetic fields are discussed in Section 8.

In the second part of this overview, we will focus on ferromagnetic/semiconductor (FM/SC) combinations that try to take advantage of the combination of the electronic transport of both materials for new device structures. The emphasis will be on technological issues for the fabrication of structures in which the electronic current is passing through at least one interface between the ferromagnetic and the semiconductor. In Section 10, a device structure exploiting spin-dependent scattering is briefly discussed. The next section deals with spin-polarized current in an FM/SC structure. The other sections are devoted to materials issues in trying to realize optimum FM/SC combinations for future spin-dependent transport devices. These issues include the control of the FM/SC interface and the fabrication of magnetic nanostructures.

2. ELECTRONS IN MICROSCOPICALLY INHOMOGENEOUS MAGNETIC FIELDS

The behavior of electrons in *macroscopically* homogeneous magnetic fields has been used extensively to obtain experimental information on the properties of charge carriers [1] such as, for example, their density and the Fermi surface [through the Shubnikov–de Haas (SdH) effect] and their mass (e.g., using cyclotron resonance). The scattering of electrons on magnetic impurities form the other limit in which electrons feel locally (on an angstrom scale) strong magnetic fields (i.e., *microscopically* inhomogeneous) that may act as scattering centers in, for example, diluted semimagnetic materials [2].

Between these limits lie inhomogeneous magnetic fields on the *nanometer* scale. They have been realized with the creation of magnetic dots, the integration of ferromagnetic materials with semiconductors where the patterning of such films was recently demonstrated experimentally. This new technology will add a new functional dimension to the present semiconductor technology and will open new avenues for new physics and possible applications such as switches based on the Lorentz force and nonvolatile memories based on the Hall voltage generated by a local magnetic field. A different route to create inhomogeneous magnetic fields is through the integration of superconducting materials with semiconductors. This was realized experimentally using type II superconductors, which were deposited on a metal-oxide-semiconductor field-effect transistor (Si-MOSFET) or a GaAs/AlGaAs heterojunction. Magnetic flux lines penetrate the two-dimensional electron gas (2DEG) that acts as nanoscale scattering centers for the electrons, offering the possibility of studying the weak localization and the dynamics of vortices. Using lithographic techniques, these superconducting films can be patterned into any desired form. The geometry of the patterning determines the geometry of the inhomogeneous magnetic field.

In general, the shape anisotropy of the magnetic film (or the stripes) will force the magnetization in the plane of the film. Other mechanisms can be active that can lead to

a magnetization vector perpendicular to the film, which is the situation we are mostly interested in. Out-of-plane magnetization has been realized in ultrathin layers of Fe on Ag or Cu; compounds such as MnAlGa, Co/Ni multilayers, and ultrathin MnGa films; and the metastable τ-MnAl phase, which can be grown epitaxially on GaAs/AlAs heterostructures using molecular beam epitaxy (MBE).

3. MAGNETIC FIELD PROFILES

3.1. One-Dimensional Profiles

As schematically illustrated in Figure 1, a one-dimensional magnetic barrier can be created by the deposition, on top of a heterostructure, of a ferromagnetic strip with magnetization (a) perpendicular and (b) parallel to the 2DEG, (c) of a conducting strip with a current driven through it, and (d) of a type I superconducting plate interrupted by a strip. In all cases, the 2DEG is situated at a distance z_0 below the strip whose thickness and height are d and h, respectively. The resulting magnetic field profile is obtained from the following Maxwell equation:

$$\begin{aligned} \operatorname{div}\mathbf{B} &= -4\pi \operatorname{div}\mathbf{M} = 4\pi\rho_{\mathrm{M}}(\mathbf{r}) \\ \mathbf{B} &= -\operatorname{grad}\Phi_{\mathrm{M}} \end{aligned} \tag{1}$$

which can be integrated and results in the magnetic potential

$$\Phi_{\mathrm{M}}(\mathbf{r}) = \int d^3r' \frac{\rho_{\mathrm{M}}(\mathbf{r}')}{|\mathbf{r}-\mathbf{r}'|} \tag{2}$$

For illustrative purposes, we consider perpendicular magnetization (Fig. 1a) in which the width of the magnetic strip d is small such that we can replace it by a dipole line with magnetic charge density $\rho_{\mathrm{M}}(\mathbf{r}) = -M_0\delta(x)(d/dz)\delta(z)$. Integrating (2) results in the magnetic potential $\Phi_{\mathrm{M}}(\mathbf{r}) = 2M_0 z/(x^2+z^2)$, which leads to the magnetic field distribution

$$B(x) = 2M_0 \frac{z_0^2 - x^2}{(z_0^2+x^2)^2} \tag{3}$$

and the vector potential $A(x) = 2M_0 x/(z_0^2+x^2)$. If we have strips of width d instead of wires, we have to integrate Eq. (2) numerically in the region $-d/2 \leqslant x' \leqslant d/2$. It turns out

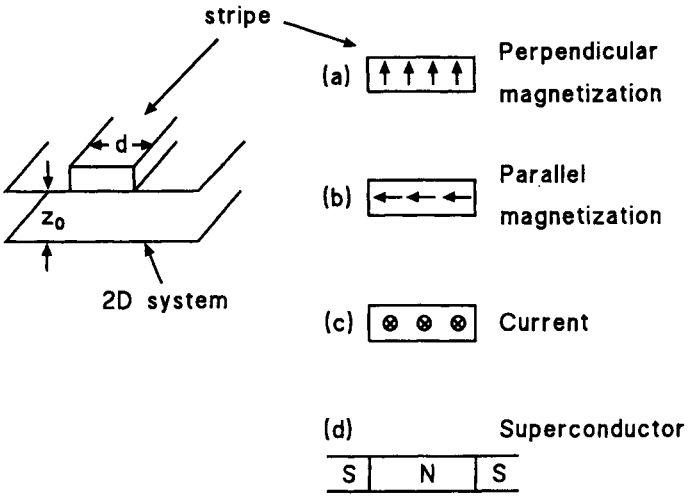


Fig. 1. Layout of the system for the creation of a one-dimensional magnetic field profile in a 2DEG.

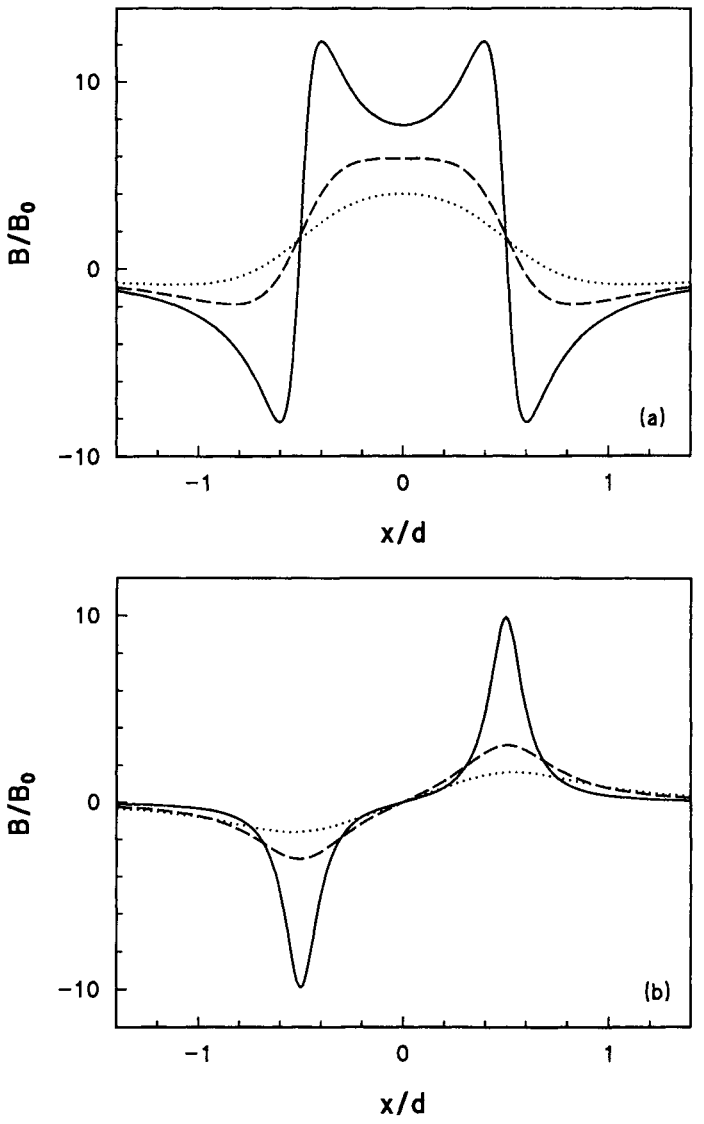


Fig. 2. Magnetic field under the strip corresponding to the four different configurations shown in Figure 1 for three different distances from the magnetic strip: $z_0 = 0.1$ (solid curve), $z_0 = 0.3$ (dashed curve), and $z_0 = 0.5$ (dotted curve).

that in the limit z_0, $h \ll d$, the magnetic field distribution takes the simple form (h is the height of the magnetic strip)

$$B(x, z_0) = B_0\big(K(x + d/2, z_0) - K(x - d/2, z_0)\big) \tag{4}$$

with $B_0 = Mh/d$ and $K(x, z) = 2xd/(x^2 + z^2)$, which is depicted in Figure 2a for three values of z_0. Similarly for parallel magnetization, we found $K(x, z) = -zd/(x^2 + z^2)$, which is depicted in Figure 2b for three values of z_0.

For completeness, we also calculate the magnetic field resulting from a finite size magnetic film of finite thickness that is located at $a < x < b$, $c < y < d$, $e < z < f$. The magnetization of such a ferromagnetic film is

$$\begin{aligned}\mathbf{M}(x, y, z) = {} & \theta(x)\big(1 - \theta_b(x)\big)\theta(y)\big(1 - \theta_c(y)\big)\theta(z)\big(1 - \theta_d(y)\big) \\ & \times (m_z\mathbf{e}_x + m_y\mathbf{e}_y + m_z\mathbf{e}_z)\end{aligned} \tag{5}$$

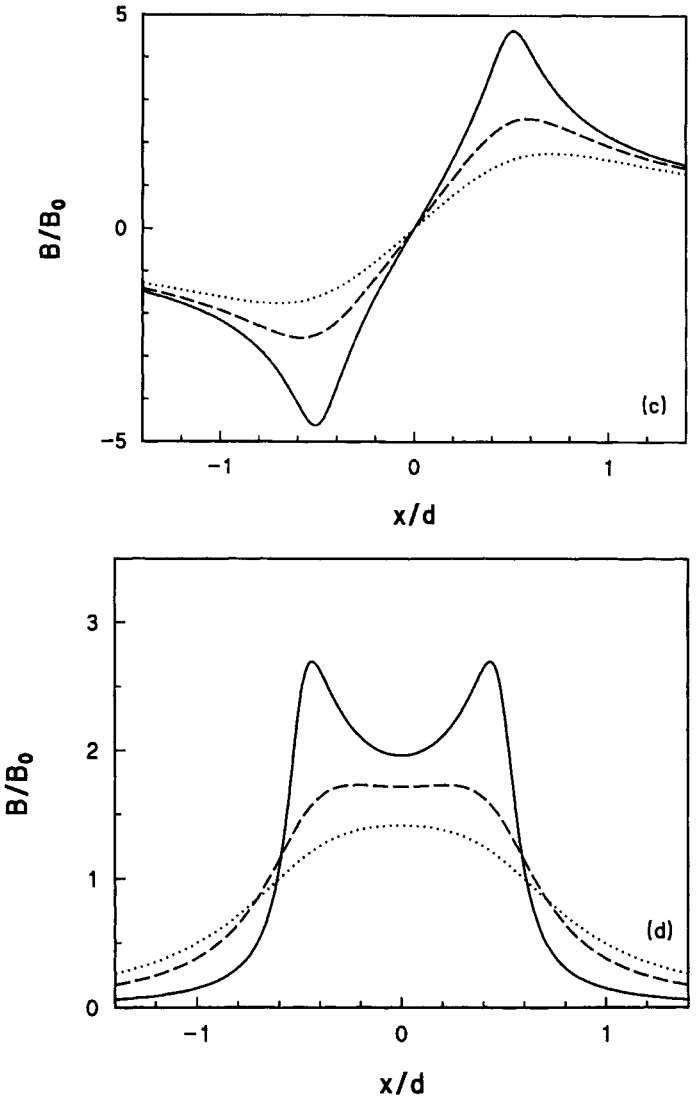


Fig. 2. (*Continued.*)

where $\theta_a(x) = \theta(a - x)$ and $\theta(x)$ is the Heaviside step function. We insert this expression into Eq. (2) and take as an example the magnetization along the x direction, that is, $m_y = m_z = 0$. After performing the differentiation and the integration, we obtain the following exact solution for the z component of the magnetic field [3]:

$$B_z(x, y, z) = m_x\big[-\big(f_{adf}(x, y, z) - f_{acf}(x, y, z)\big) + \big(f_{ade}(x, y, z) - f_{ace}(x, y, z)\big) + \big(f_{bdf}(z, y, z) - f_{bcf}(x, y, x)\big) - \big(f_{bde}(x, y, z) - f_{bcd}(x, y, x)\big)\big] \tag{6}$$

with $f_{\alpha\beta\gamma}(x, y, z) = \operatorname{arcsinh}((\beta - y)/\sqrt{(x - \alpha)^2 + (z - \gamma)^2})$.

For a wire with a current I going through it (Fig. 1c), the magnetic field is determined by the Maxwell equation $\operatorname{rot}\mathbf{B} = 4\pi\mathbf{j}/c$, which results in the angular magnetic field component $B_\phi = 2I/cr$ at a radial distance r from the wire. In the plane of the 2DEG a distance z_0 from the wire, this leads to the magnetic field profile

$$B(x) = B_z(x, z_0) = B_0 \frac{x}{z_0^2 + x^2} \tag{7}$$

with $B_0 = 2I/c$, which is depicted in Figure 2c. The vector potential is obtained by integrating the equation $\mathbf{B} = \mathrm{rot}\,\mathbf{A}$, which gives $A(x) = A_y(x, z_0) = \frac{1}{2}B_0 \ln((z_0^2 + x^2)/(z_0^2 + R^2))$, where R is some distance away from the wire where the opposite current is flowing. For a strip of finite width d such that $z_0, h \ll d$, we can cast the result in the form of Eq. (4) with $K(x, z) = \ln[(x^2 + z^2)/d^2]$. This magnetic field profile is shown in Figure 2c.

For a superconducting strip in a magnetic field, we have to solve the Maxwell equations in the superconductor: $\mathbf{j} = -(ne^2/mc)\mathbf{A}$ and $\nabla^2\mathbf{H} = (1/L_0^2)\mathbf{H}$, where $L_0^2 = mc^2/4\pi ne^2$ and we made use of $\mathrm{rot}\,\mathbf{H} = -(4\pi ne^2/mc^2)\mathbf{A}$. Outside the superconductor, we have the equation $\nabla^2\Phi_\mathrm{M} = 0$, with the boundary condition on the superconductor $B_n = -\partial\Phi_\mathrm{M}/\partial n = 0$. This 2D potential problem can be solved by the conformal mapping $x + iz = \sin(\pi w)$ where we introduce the complex potential $W = \Phi_\mathrm{m} + i\Psi$. The solution of the problem [4] is $W = iw$ and the magnetic potential is given by $\Phi_\mathrm{M} = \mathrm{Re}\,W = -\mathrm{Im}(\arcsin(x + iz))$, which results in the magnetic field

$$B = B_0\,\mathrm{Re}\left(\frac{1}{\sqrt{1 - (x + iz)^2}}\right) \tag{8}$$

which is depicted in Figure 1d.

3.2. Periodic Structures

As a last example, we consider a periodic structure and calculate the magnetic field resulting from a ferromagnetic thin film in which the magnetic domains are in the form of a periodic array of parallel strips (see Fig. 3a). The magnetization of each domain strip can be either in the plane of the film or perpendicular to it.

First, we consider the case depicted in Figure 3a but where we consider only a single magnetic domain strip with magnetization perpendicular to the (x, y) plane with boundaries $x \in (-a, a)$, $y \in (-\infty, \infty)$, $z \in (-d, d)$, which implies

$$\rho_\mathrm{m} = -\nabla \cdot \mathbf{M} = M\big[\delta(z - d) - \delta(z + d)\big]\big[\theta(x + a) - \theta(x - a)\big] \tag{9}$$

and the magnetic field at the point $\mathbf{r}$ is obtained from Eqs. (1) and (2) as [5]:

$$\mathbf{B}(\mathbf{r}) = \frac{\mu_0 M}{2\pi}\big[\mathbf{B}_*(x, y, z + d) - \mathbf{B}_*(x, y, z - d)\big] \tag{10}$$

where

$$\mathbf{B}_*(\mathbf{r}) = \frac{1}{2}\ln\left(\frac{(x + a)^2 + z^2}{(x - a)^2 + z^2}\right)\mathbf{e}_x + \left[\arctan\left(\frac{x + a}{z}\right) - \arctan\left(\frac{x - a}{z}\right)\right]\mathbf{e}_z \tag{11}$$

For in-plane magnetization, the solution can be obtained by simply rotating the magnetic strip by 90° about the y axis with the corresponding interchange of the x and z coordinates in the previous expression for the magnetic field. That is, Eqs. (10) and (11) become, respectively,

$$\mathbf{B}(\mathbf{r}) = \frac{\mu_0 M}{2\pi}\big[\mathbf{B}_*(x + a, y, z) - \mathbf{B}_*(x - a, y, z)\big] \tag{12}$$

where

$$\mathbf{B}_*(\mathbf{r}) = \frac{1}{2}\ln\left(\frac{x^2 + (z + d)^2}{x^2 + (z - d)^2}\right)\mathbf{e}_z + \left[\arctan\left(\frac{z + d}{x}\right) - \arctan\left(\frac{z - d}{x}\right)\right]\mathbf{e}_x \tag{13}$$

The magnetic field profile resulting from a periodic array of ferromagnetic domain strips is the superposition of the contributions of each of the individual domain strips at that point. In particular, for the situation of Figure 3a, we have

$$\mathbf{B}_\mathrm{total}(\mathbf{r}) = \sum_{n=-\infty}^{\infty} (-1)^n \mathbf{B}(x - nl/2, y, z) \tag{14}$$

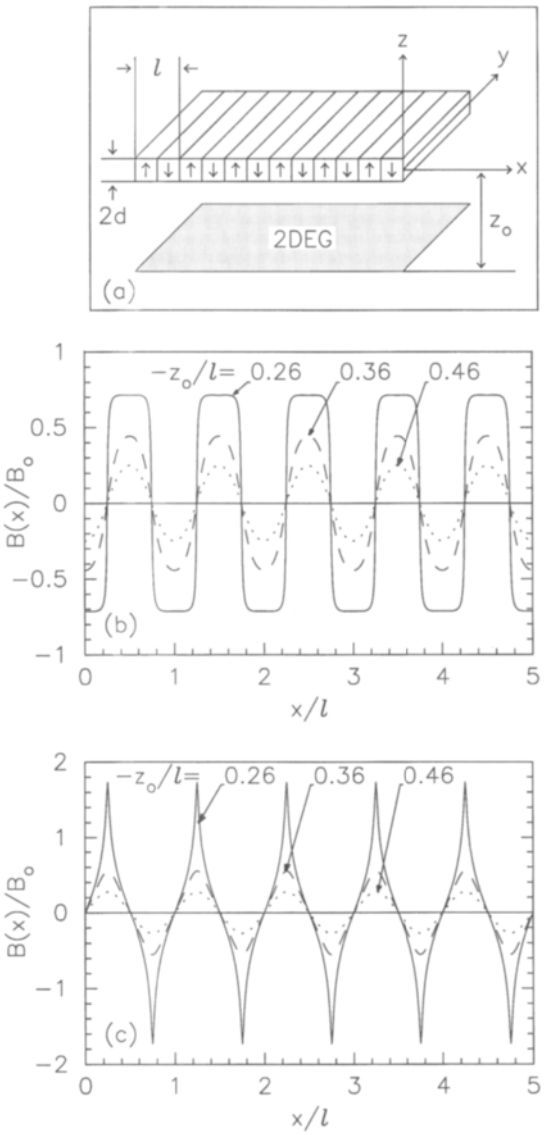


Fig. 3. (a) Superlattice of magnetic strips with alternating sign of magnetization above a 2DEG. (b) Resulting magnetic field in the plane of the 2DEG for three different values of the setback distance. (c) Magnetic field profile when the magnetization of the strips is in plane along the x direction with alternating sign.

where $\mathbf{B}(\mathbf{r})$ is given by Eq. (10) and the period $l = 4a$. Using Poisson's method for the summation of infinite series, we can write the z component of this expression also as

$$\mathbf{B}_z(\mathbf{r}) = \sum_{n=0}^{\infty} \mathbf{B}_n(kz)\cos(kx) \tag{15}$$

with

$$\mathbf{B}_n(kz) = \frac{(-1)^n}{(2n+1)}\left(e^{-kd} - e^{kd}\right)e^{-kz}\mathbf{e}_z \tag{16}$$

where $k = (2n+1)2\pi/l$. This result agrees with the solution obtained directly from Poisson's equation using the Fourier series expansion for ρ_m and the method of separation of

variables. The resulting magnetic field profile is shown in Figure 3b for different values of the distance z_0 from the area of the magnetic strips.

In the case the magnetic domains are aligned in the plane, but with alternating direction, we have

$$\mathbf{B}_{\text{total}}(\mathbf{r}) = \sum_{n=-\infty}^{\infty} (-1)^n \mathbf{B}(x - nl/2, y, z) \tag{17}$$

but where $\mathbf{B}(\mathbf{r})$ is now given by Eq. (12). Using Poisson's summation method, we find the z component to be

$$\mathbf{B}_z(\mathbf{r}) = \sum_{n=0}^{\infty} \mathbf{B}_n(kz) \sin(kx) \tag{18}$$

with k and $\mathbf{B}_n(kz)$ identical as given previously. The resulting magnetic field profile is shown in Figure 3c for different values of the distance z_0 from the area of the magnetic strips.

Similarly, one can study periodic two-dimensional magnetic strip structures. This was done by Van Roy et al. [6] in which only a numerical solution for the magnetic field profile can be obtained.

4. QUANTUM MOTION IN NONHOMOGENEOUS MAGNETIC FIELDS

First, we will show some remarkable aspects of the energy spectrum and the motion of electrons in nonhomogeneous magnetic fields. We consider a 2DEG moving in the (x, y) plane with a magnetic field $\mathbf{B}$ along the z direction. In the single-particle approximation, such a system is described by the Hamiltonian

$$H = \frac{1}{2m}\left(\mathbf{p} + \frac{e}{c}\mathbf{A}\right)^2 \tag{19}$$

For 1D nonhomogeneous magnetic field profiles, we take the vector potential in the Landau gauge $\mathbf{A} = (0, A, 0)$ and the magnetic field is uniform along the y direction but modulated along the x direction and thus $B_z = B(x) = dA(x)/dx$.

Let us introduce the following characteristic parameters [7]: (i) the frequency $\omega_c = eB_0/mc$ with B_0 some typical magnetic field, and (ii) the length $l_B = \sqrt{\hbar c/eB_0}$. For GaAs and an estimated $B_0 = 0.1$ T, we have $l_B = 813$ Å, $\hbar\omega_c = 0.17$ meV, and $l_B\omega_c = 1.4$ m/s. From now on, we will express all quantities in dimensionless units: (1) the magnetic field $B(x) \to B_0 B(x)$, (2) the vector potential $A(x) \to B_0 l_B A(x)$, (3) the time $t \to t/\omega_c$, (4) the coordinate $\mathbf{r} \to l_B\mathbf{r}$, (5) the velocity $\mathbf{v} \to l_B\omega_c\mathbf{v}$, and (6) the energy $E \to \hbar\omega_c E$.

In these dimensionless units, the two-dimensional (2D) Schrödinger equation becomes

$$\left\{\frac{\partial^2}{\partial x^2} + \left(\frac{\partial}{\partial y} + iA(x)\right)^2 + 2E\right\}\Psi(x, y) = 0 \tag{20}$$

Because of the special form of the gauge, the system is translational invariant along the y direction and, as a consequence, we can choose the following form for the wave function:

$$\Psi(x, y) = e^{-iqy}\psi(x) \tag{21}$$

where $-q = k_y$ is the wavevector of the electron in the y direction, which is a conserved quantity. This does *not* imply that v_y is conserved. The wave function $\psi(x)$ actually satisfies the following 1D Schrödinger equation:

$$\left\{\frac{d^2}{dx^2} - \big(A(x) - q\big)^2 + 2E\right\}\psi(x) = 0 \tag{22}$$

where the function

$$V(x) = \frac{1}{2}\big(A(x) - q\big)^2 \tag{23}$$

can be interpreted as a q-dependent electrical potential. Note that in the case of one-dimensional (1D) magnetic field modulation, there is an analogy between the magnetic field and the potential given by the following relation $B(x) = (1/\sqrt{2V(x)})(dV(x)/dx)$. A jump in the magnetic field will result in a discontinuity in the derivative of the potential $V(x)$.

4.1. Magnetic Step

First, let us consider the most simple shape for a nonhomogeneous magnetic field: the magnetic step. We will show that this leads to a *new type of bound state*. In this situation, the magnetic field fills the half space $x > 0$, which is described by $B(x) = \theta(x)$, with the corresponding vector potential $A(x) = x\theta(x)$, where $\theta(x) = 1$ $(x \geqslant 0)$, 0 $(x < 0)$ is the step function. A continuous version of this magnetic step profile was studied by Calvo [8]. There are two different cases that we have to consider.

In Case 1 $(q > 0)$, the potential $V(x) = \frac{1}{2}(x\theta(x) - q)^2$ has the form of an asymmetric quantum well that deepens with increasing q. It is well known that such a well can have a bound state if the well is sufficiently deep. Thus, we have to consider separately: (a) $E < q^2/2$ where bound eigenstates are expected to appear in the region $x \sim q$, and (b) $E > q^2/2$, which corresponds to scattered states, describing the electron reflection by the magnetic step. The appearance of bound states makes this system essentially different from the usual potential step problem where only scattered states exist.

In Case 2 $(q < 0)$, the equivalent potential is a constant $V(x) = q^2/2$ for $x < 0$, and a barrier $V(x) = \frac{1}{2}(x\theta(x) + |q|)^2$ in the region $x > 0$, which is unbounded for $x \to \infty$. In this case, there are only scattered states that correspond to electron reflection by the magnetic barrier.

For $x > 0$, the Schrödinger equation takes the form

$$\left\{\frac{d^2}{dz^2} - \frac{z^2}{4} + p + \frac{1}{2}\right\}\psi(z) = 0 \tag{24}$$

with $z = \sqrt{2}(x - q)$ and $p = E - 0.5$. The solutions are the Weber functions $D_p(z)$, which have the following asymptotic behavior: $D_p(z)|_{z\to+\infty} \to 0$. In the region $x > 0$, the wave function becomes $\psi(x) \sim D_{E-0.5}(\sqrt{2}(x - q))$, up to a normalization constant, while, for $x < 0$, there is no magnetic field and the wave function is proportional to $\psi(x) \sim \exp(x\sqrt{q^2 - 2E})$ when $E < q^2/2$. Matching the wave function and its first derivative at $x = 0$, we obtain the following equation:

$$\sqrt{q^2 - 2E} = \frac{d}{dx} \ln D_{E-0.5}\big(\sqrt{2}(x - q)\big)\bigg|_{x=0} \tag{25}$$

whose solutions lead to the electron eigenvalues $E = E_n(q)$ with the corresponding wave function $\psi_{nq}(x)$.

Once we know the eigenvalues and the corresponding wave function, we can obtain the other characteristics of the bound states. The average electron velocity of the bound state along the magnetic step (y direction)

$$-v_n(q) \equiv \int_{-\infty}^{\infty} dx\, \psi_{nq}^2(x)\big(q - A(x)\big) = \frac{d}{dq}E_n(q) \tag{26}$$

where the minus sign results from the definition $q = -k_y$. The mean electron position along the x axis $X_n(q)$ has the simple form

$$X_n(q) = \int_{-\infty}^{\infty} dx\, x\psi_{nq}^2(x) = q + \left(1 + \frac{1}{2q\sqrt{q^2 - 2E_n(q)}}\right) v_n(q) \tag{27}$$

The numerical results of the solution of Eq. (25) are depicted in Figure 4a by the solid curves, for the lowest three eigenvalues. These curves start at a certain q value (denoted by the solid dot in Fig. 4a), which is a function of n. The corresponding results for the average electron velocity $v_n(q)$ (solid curves) and mean electron position $X_n(q)$ (dashed curves) are shown in Figure 4b. Notice that the eigenvalues asymptotically, that is, $q \to \infty$, reach the values $(n + \frac{1}{2})$ for Landau levels in a homogeneous magnetic field as it should be. In this asymptotic limit, the mean electron position approaches $X_n(q) \sim q$ and the average

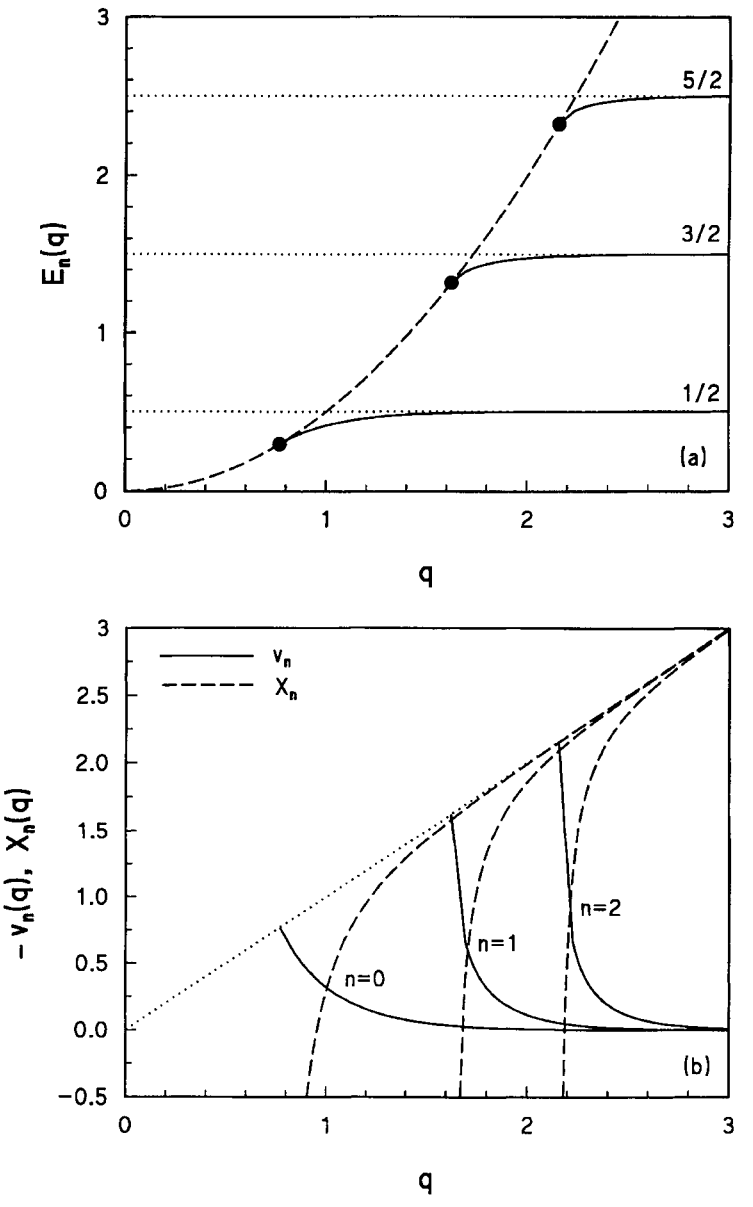


Fig. 4. (a) Energy spectrum for the bound states (solid curves) and (b) corresponding average velocity along the magnetic step $v_n(q)$ (solid curves) and the electron average position $X_n(q)$ along the x axis (dashed curves) for the magnetic step problem.

electron velocity tends to zero. In this limit, the electron is situated far from the magnetic step and is not influenced by the $x < 0$ region. With decreasing q, the electron wave function starts to feel the magnetic step: (1) Its energy decreases, because part of the wave function will be situated in a region with zero magnetic field where the electron will have a smaller kinetic energy; (2) its average position is less than q, because the wave function is sucked into the $x < 0$ region; and (3) its velocity increases and the electron runs along the step. From parts a and b of Figure 4, we notice that the width of the transition region, that is, the q region where $E_n < (n + \frac{1}{2})$, is narrower with increasing n. The preceding properties of these bound states force us to make the analogy with edge states [9]. Nevertheless, there are a number of differences: (1) The available q space for edge states increases with increasing Landau level number n, which is opposite to the behavior of the present bound states; (2) the direction of the velocity is opposite as compared to that of the usual edge states; and (3) the magnitude of the velocity satisfies $|v_n(q)| \leqslant q$, which is different from edge states that do not have an upper bound on their velocity.

From Figure 4, we notice that there exist critical values q_n^* such that for $q < q_n^*$ no bound states are found. These points are indicated by the dots in Figure 4a and are situated on the free-electron spectrum curve $E = q^2/2$ (dashed curve in Fig. 4a). For the plotted curves, we found the critical values $q_0^* = 0.768$, $q_1^* = 1.623$, $q_2^* = 2.155$ at which the eigenenergy curve $E_n(q)$ is tangent to the $E = q^2/2$ curve. At these points, the electron velocity equals the free-electron value $-v_n = q$ and $X_n(q) \to -\infty$.

Notice that in the present magnetic step case, the transmission coefficient is always zero. Independent of the strength of the magnetic field and the magnitude of the electron energy, an electron impeding on the magnetic barrier will always be reflected, which is a consequence of the Lorentz force acting on the electron. In this respect, this system is different from the textbook potential step problem in which the reflection coefficient becomes different from zero when the electron energy is larger than the potential barrier height.

4.2. Magnetic Barrier

The magnetic step can be used as a building block, from which more complicated structures can be built [4, 7, 10]. As a first example, we consider the magnetic barrier in which the magnetic field is different from zero in a strip of width d. In this case, the magnetic field has the following form in dimensionless units: $B(x) = \theta(d^2/4 - x^2)$, and we choose the vector potential as follows: $A(x) = -d/2$ $(x < -d/2)$, x $(|x| \leqslant d/2)$, $d/2$ $(x > d/2)$. The analogous potential $V(x)$ of (23) depends on the value of the wavevector q: When $|q| < d/2$, the potential consists of an asymmetric well of finite height; when $|q| > d/2$, it is a gradual step. The problem is symmetric under the substitution $q \to -q$ (and $x \to -x$) and, consequently, we may limit ourselves to the case $q \geqslant 0$.

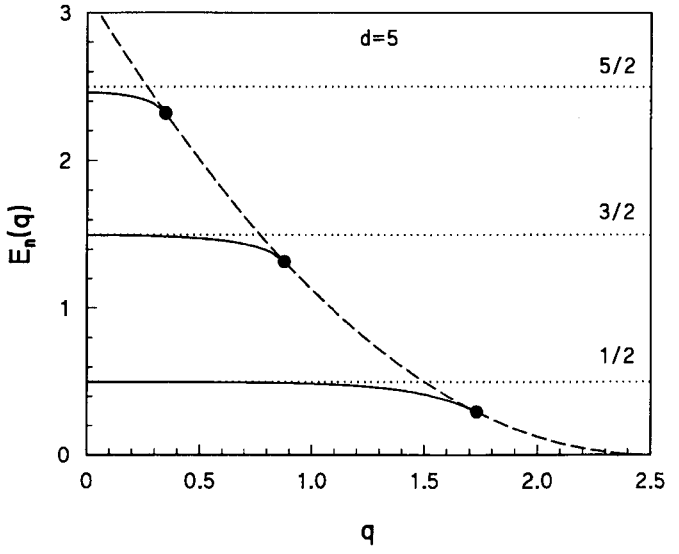
There are three different energy regions important to us: (1) $0 \leqslant E \leqslant (d/2 - q)^2/2$, where bound eigenstates can exist; (2) $(d/2 - q)^2/2 < E \leqslant (d/2 + q)^2/2$, which is the reflection region; and (3) $(d/2 + q)^2/2 < E$, where the electron is transmitted through the magnetic barrier.

First, let us concentrate on the situation in which we have bounded electron states. In this case, the electron wave function in the barrier region, that is, $|x| < d/2$, is a linear combination of Weber functions

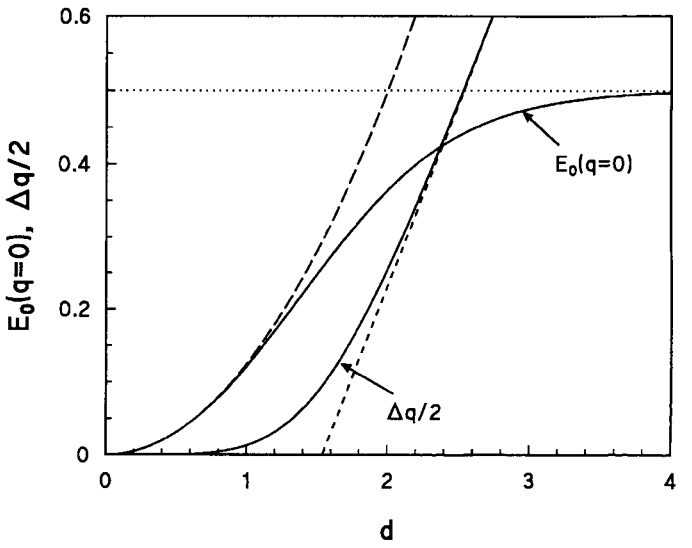
$$\psi(x) = aD_{E-0.5}\big(\sqrt{2}(x - q)\big) + bD_{E-0.5}\big(\sqrt{2}(q - x)\big) \tag{28}$$

which we must match (and its first derivative) to the free-electron wave functions at the points $x = \pm d/2$. This matching results in a nonlinear equation for the electron energy that was solved numerically. The results for a wide magnetic barrier ($d = 5$) are shown in Figure 5a by the solid curves that end at the solid dots. The latter are situated on the $E = (q - d/2)^2/2$ curve (dashed curve). Notice that the spectrum resembles the one of

the magnetic step case (see Fig. 4a) with the distinction that the latter has an infinite number of branches, while the one for a magnetic barrier has a finite number of bound states for each q. For $d = 5$, there are only three branches in the energy spectrum. The number of energy branches decreases with decreasing barrier width d. Irrespective of the value of d, there is always *at least one* discrete energy value for $q = 0$. This is a consequence of the fact that for $q = 0$ the potential $V(x)$ is one dimensional and symmetric. Such a potential is known [11] to have at least one discrete eigenvalue irrespective of the size of the potential well. The value of the lowest branch in the spectrum is plotted in Figure 5b for $q = 0$ as function of the barrier width d. Notice that when $d < 1$ (i.e., when



(a)



(b)

Fig. 5. (a) Energy spectrum for the bound states (solid curves) in a magnetic barrier. The dashed curve indicates the free-electron spectrum. (b) Lowest eigenvalue of the bound state in a magnetic barrier as function of the barrier width for $q = 0$ and the width Δq of the lowest energy branch in q space.

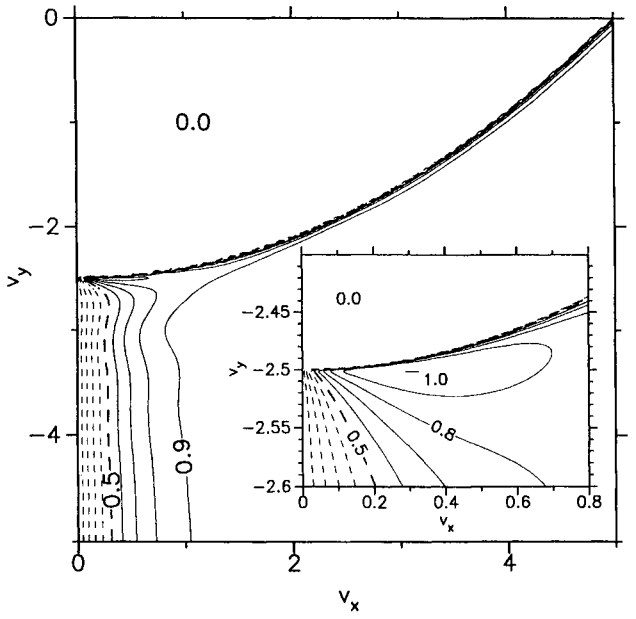


Fig. 6. Contour plot of the transmission coefficient through a magnetic barrier in the incident electron velocity space (v_x, v_y).

the magnetic barrier width is less than the magnetic length l_B) the eigenvalue approaches $E_0(q=0) \approx (d/2)^2/2$, which is shown by the long-dashed curve in Figure 5b. Although the electron is bound to the barrier, in the case of small d values the electron wave function is situated mainly outside the barrier and, consequently, its energy approaches the height of the potential well $V(d/2)$. The width in q space (Δq) of the lowest energy branch is also given in Figure 5b. It is seen that this width decreases rapidly to zero when $d < 1$ and in the opposite case (when $d \to \infty$) it asymptotically reaches the line $\Delta q/2 = d/2 - q_0^*$ (short-dashed line), where $q_0^* = 0.768$ is the value as obtained from the magnetic step spectrum. Another distinction as compared to the magnetic barrier spectrum (see Fig. 4a) is that the energy eigenvalues are smaller in magnitude than those in the magnetic step case.

For the unbounded states, we have calculated the transmission coefficient, which now depends not only on the electron energy but also on the electron wavevector q in the y direction. In the present case, tunneling is a two-dimensional process in which the total electron wavevector and the electron energy is conserved but the direction of the wavevector is altered. A contour plot of the transmission coefficient $T(q, E)$ versus the initial electron velocity components (v_x, v_y) is shown in Figure 6 for a magnetic barrier of width $d = 5$. The quantum transition coefficient is zero above the line $v_y = (v_x^2 - d^2)/2d$, which is the result one would obtain from classical mechanics and which defines a semiinfinite transmission window. Below this line, we have classically $T = 1$, but quantum mechanically $T(q, E)$ gradually increases with increasing electron energy. For rather thick barriers (as in the case of $d = 5$), there is some additional structure at low energy, which is enlarged in the inset of Figure 6. There is an additional peak around $(v_x, v_y) = (0.3, -2.5)$, which is a consequence of the presence of a resonant energy level above the quantum well $V_q(x)$.

The continuous magnetic barrier problem with magnetic field profile $\mathbf{B} = (0, 0, B/\cosh^2((x - x_0)/\delta))$ was discussed by Hudák [12], who was able to solve the single-particle problem for this case exactly. The same discussion was given later on by Calvo [8]. The situation of a magnetic barrier in a ballistic quantum wire was discussed in [13, 14], where the conductance was calculated and found to be quantized and to oscillate with changing magnetic field. Ramaglia and co-workers [15, 16] studied the related problem of quan-

tum tunneling of a 3DEG through a potential barrier in a transverse magnetic field where the magnetic field has the same extension as the barrier. They found that for sufficiently wide barriers the tunneling current and the differential conductivity exhibits steps and resonances as a function of the applied voltage. A model consisting of a continuous potential well together with a continuous magnetic barrier was discussed by Calvo [17, 18], who obtained exact expressions for the energy spectrum.

4.3. Magnetic Quantum Well

The inverse situation of the previous problem is the magnetic well case, which we will discuss now. Because of the essential 2D character of the electron motion in a magnetic field, we should rather speak of a magnetic wire. In dimensionless units, the magnetic field is given by $B(x) = 0$ ($|x| \leqslant d/2$), 1 ($|x| > d/2$), and the corresponding vector potential is $A(x) = x - d/2$ ($x > d/2$), 0 ($|x| \leqslant d/2$), $x + d/2$ ($x < -d/2$). The value of the vector potential is now unbounded, that is, $A(x)|_{x\to\pm\infty} \to \pm\infty$, and, as a consequence, the potential satisfies $V(x)|_{x\to\pm\infty} \to \infty$, which implies that the electron motion is confined in the x direction and *all the states are bound* at least in this direction.

The corresponding wave functions are constructed by matching the quasi-free-electron wave function in the region $|x| < d/2$ with the Weber functions $\psi(x) = D_{E-0.5}(\pm\sqrt{2}(x \mp d/2 - q))$, which are valid in the regions $|x| > d/2$. This matching of the wave function and its first derivative leads to a nonlinear algebraic equation for the eigenvalues that is solved numerically.

The results of the numerical solution of this equation are presented in Figure 7 for a wide well (i.e., $d = 5$). There are clearly two distinct regions that are separated by the free-electron energy $E = q^2/2$ curve (dashed curve in Fig. 7). For $E \ll q^2/2$, the energy spectrum consists of Landau levels. The electron is mainly located in the barrier where there exists a uniform magnetic field. For small q values, that is, $E \gg q^2/2$, the spectrum consists of bands with free-electron-like motion in the y direction. This is similar to the case of the well-known quantum wire with electrical potential barriers. When we decrease the width of the well, the two regions are less distinct. For example, for $d = 1$ the well is narrower than the width of the electron wave function and, consequently, there is always an appreciable overlap of the wave function with the magnetic barrier region and the energy

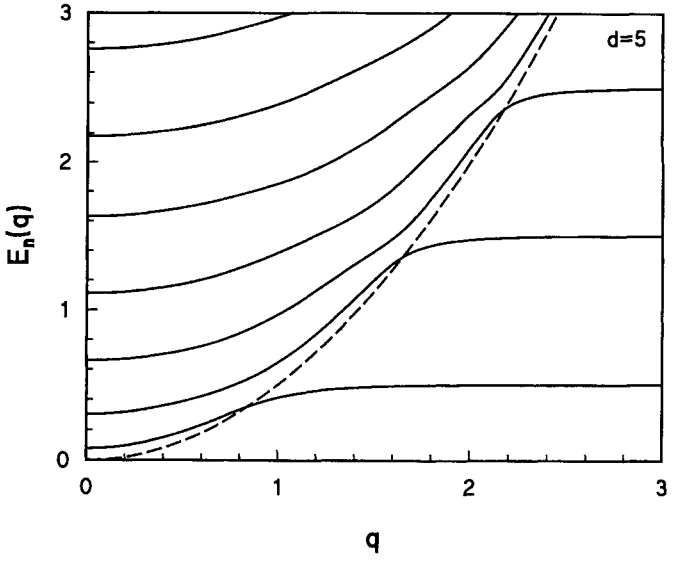


Fig. 7. Energy spectrum of a magnetic well of width $d = 5$.

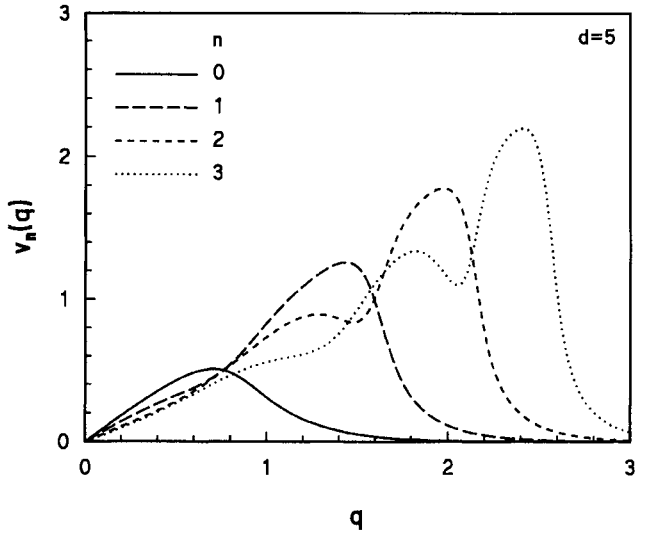


Fig. 8. Electron average velocity corresponding to the energy spectrum of Figure 7 for the different branches.

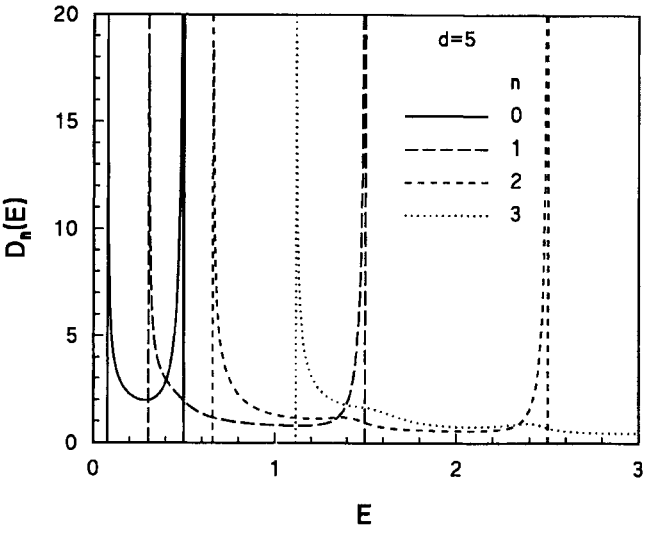


Fig. 9. Density of states of the one-electron states in the magnetic well corresponding to Figure 7.

levels will have almost no dispersion (see, e.g., [7]). The different behavior between the two cases is also illustrated in Figure 8 where the electron velocity is shown for the different states. Notice that the velocity exhibits a maximum near $E = q^2/2$ and it diminishes fast for $q \gg \sqrt{2E}$, which is the region where the electron is mainly located inside the magnetic barrier. For wide wells, the velocity curve $v_n(q)$ can have several local maxima, which is a consequence of the repulsion of the different energy levels as shown in Figure 7. In the case of the usual quantum wire constructed from walls consisting of potential barriers, the electron velocity is $v_n = \hbar k_y = -q$ and is independent of the energy level index n and is a uniform increasing function of the electron wavevector. The behavior of $v_n(q)$ as depicted in Figure 8 is also different from that of the edge states in which $v_n(q)$ is a uniform increasing function of q.

The density of states (DOS) is depicted in Figure 9. Notice that, as in the usual quantum wire case, the DOS exhibits singularities at the onset of each energy level. There is a

difference, however, in that the width in energy space of each level is finite and bounded by a singularity in the DOS. Suppose we have a system in which we are able to increase the Fermi energy gradually. Starting from zero, we first populate the quantum wire states; the electrons are mainly situated in the well region. Further increasing the Fermi energy, we see that for $d = 5$ we first start to populate the next energy level which consists initially of states located inside the well. For a narrower well, for example, $d = 1$, on the other hand, we start to populate states that are situated in the magnetic barrier region and that are nothing else then 2D Landau states. Thus, by changing the Fermi level, we are able to have 1D states or 2D states at the Fermi level, which will have considerable influence on the electrical properties of the system. The 1D states are quasi-free, while the 2D states are localized on Landau orbits and can only move if scattering is involved.

4.4. Resonant Tunneling Structures

In previous sections, we have made a detailed study of the nature of the electron states in different magnetic barrier and well structures. In this section, we will consider different tunneling structures where we will focus on the tunneling current going through them [10, 19].

For simplicity, we now consider electron tunneling through a magnetic barrier of constant height B_0 and width $d = x_+ - x_-$ surrounded by regions of zero magnetic field. The free-electron wave function on the left-hand side of the barrier ($x < x_-$) is $\psi_-(x) = A\exp[ik_-(x - x_-)] + B\exp[-k_-(x - x_-)]$ and on the right-hand side of it ($x > x_+$) $\psi_+(x) = \exp[ik_+(x - x_+)]$, where $k_\pm = \sqrt{2[E - V(\pm\infty)]}$ is the x component of the electron wavevector on the corresponding side of the barrier. Under the barrier, there are two solutions for $\psi(x)$ that can be written as a linear combination of the Weber function $D_p(x)$ and its derivative $D'_p(x)$. Next, we construct the transition matrix

$$T(x, x_0) = \begin{pmatrix} u(x) & v(x) \\ u'(x) & v'(x) \end{pmatrix} \tag{29}$$

where we defined the functions $u(x) = c\{D'_p(\sqrt{2q})D_p(z) + D'_p(-\sqrt{2q})D_p(-z)\}$ and $v(x) = c\{D_p(\sqrt{2q})D_p(z) - D_p(-\sqrt{2q})D_p(-z)\}$, with $p = E - \frac{1}{2}$ and $z = \sqrt{2}(x - q)$, which satisfies the boundary conditions $u(x_0) = 1$, $u'(x_0) = 0$, $v(x_0) = 0$, and $v'(x_0) = 1$. Matching the wave function at the edges of the barrier, $x_\pm$, by means of the preceding matrix, we obtain

$$A = T_{11}^{-1} + \frac{k_+}{k_-}T_{22}^{-1} + i\left(\frac{1}{k_-}T_{21}^{-1} - k_+T_{12}^{-1}\right) \tag{30}$$

The electron transmission through the barrier $t(E, q)$ is given by

$$t(E, q) = \frac{k_+}{k|A|^2} \tag{31}$$

where T^{-1} stands for the inverse of the matrix $T \equiv T(x_+, x_-)$. For complex structures involving several barriers of constant height, the total T matrix is a product of the T matrices that correspond to the separate barriers and the one describing the free-electron propagation between the barriers. As for the electron current through such a structure, it can be calculated, in the ballistic regime, by introducing the conductance G as the electron flow averaged over half the Fermi surface [20]:

$$G = G_0 \int_{-\pi/2}^{\pi/2} t\left(E_F, \sqrt{2E_F}\sin\phi\right)\cos\phi\, d\phi \tag{32}$$

where ϕ is the angle of incidence relative to the x direction. Furthermore, $G_0 = e^2 m v_F l/\hbar^2$, where l is the length of the structure in the y direction and v_F is the Fermi velocity.

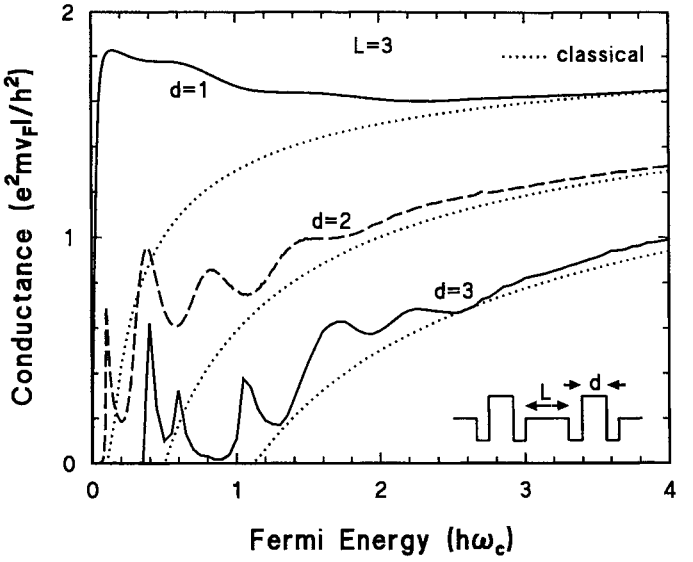


Fig. 10. Conductance through the barrier structure shown in the inset for different values of the barrier parameter. The dotted curves are the results from a classical calculation.

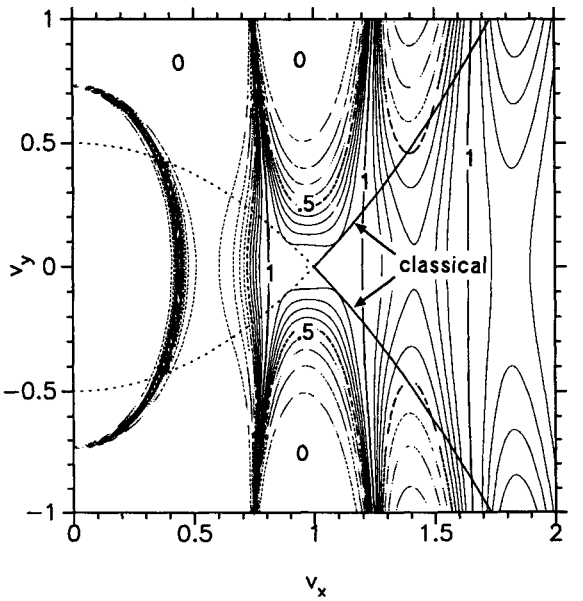


Fig. 11. Contour plot of the electron transmission probability in the (v_x, v_y) plane for the structure of Figure 10 with $d = 2$ and $L = 3$ together with the corresponding classical result.

To reveal the main qualitative features of tunneling through these barriers, we restrict ourselves to complex structures composed of rectangular magnetic barriers that are used as a building block to make a double-barrier-like structure. The contour plot of the transmission through a complex structure, shown in the inset of Figure 10, is presented in Figure 11 for $L = 3$ and $d = 1$. Notice that the quantum calculation and the classical calculation give drastically different results. In the classical calculation, the electrons satisfy Newton's equation, which is solved in the presence of the magnetic barriers, that is, for a spatially dependent magnetic field. Notice the sharp resonances in the velocity contour plot and the

strong transmission anisotropy. As can be seen, the system exhibits *wavevector filtering* properties.

Having seen the transmission results, one may wonder to what extent their structure is reflected in measurable quantities that involve some kind of averaging. In Figure 10, we show the conductance, as given by Eq. (32), for the previous tunneling structure shown in the inset of the figure, together with the corresponding classical result (dotted curves). Despite the averaging of $t(E, q)$ over half the Fermi surface, we have again a strong resonant structure. This structure will become sharper if one can select the wavevectors that give the sharpest resonance in the transmission. As for the classical result, we see again that they are determined only by the first barrier in each structure.

Although our consideration of electron tunneling through rectangular magnetic barrier structures gives only a qualitative picture, nevertheless these resonant tunneling spikes should be present in the more realistic cases with barriers of smooth shape. This was studied in [21]. The effect of spin, which was neglected here, on quantum tunneling was studied in [22] and the influence of the asymmetry of the magnetic barriers was investigated in [23]. Indeed, these resonant spikes do not depend on the actual shape of the magnetic barrier but only on the presence of barriers in the potential $V(x)$.

Other magnetic field profiles were studied by several groups. Vil'ms and Éntin [24] presented a theoretical analysis of the energy spectrum of 2D electrons near domain walls and near narrow parallel magnetic strips. The latter system is the continuous version of the single and multiple magnetic barrier system discussed here and in [4, 7]. Linear varying magnetic fields in one direction were studied in [25–27]. The energy spectrum and the transport properties of a parabolic varying magnetic field in a quantum wire and in a Hall cross were studied in [28]. A circular symmetric magnetic field profile was considered by Grosse et al. [29], who proved some general properties of the energy spectrum. A problem related to the motion of electrons in nonhomogeneous magnetic fields is the one of electrons moving on different topological surfaces in the presence of a homogeneous magnetic field. Electrons moving on a sphere in an axial magnetic field were studied in [30, 31]. Foden et al. [32] proved that a curved 2DEG in a uniform magnetic field induces quantum magnetic confinement.

4.5. Magnetic Dot

Microfabrication techniques have made it possible to further confine a 2DEG in a quantum dot through built-in electrostatic potentials. Such quantum dots have a discrete spectrum and because of their analogy with atoms are called artificial atoms. Using nonhomogeneous magnetic fields, it is also possible to confine electrons in a dot structure. One way to realize this is by considering a system consisting of a heterostructure with a superconducting disk on top of it. This new quantum dot system is fundamentally different from the usual quantum dot system because now (1) the electrons are confined magnetically, (2) the confinement potential is inherently nonparabolic, and (3) the filling of the dot with electrons is a discrete function of the strength of the confinement.

First, we consider the magnetic field profile around a superconducting disk with radius a. We solve Maxwell equations outside the disk: $\operatorname{div}\mathbf{B} = 0$ and $\operatorname{rot}\mathbf{B} = 0$. In analogy with the electric field case, we can introduce a magnetic potential $\Phi(x, y, z)$, which is related to the magnetic field through $\mathbf{B} = -\operatorname{div}\Phi$. This reduces the problem to the solution of the Poisson-like equation $\Delta\Phi = 0$ with the boundary condition $B_z = \partial\Phi/\partial z = 0$ taken at the surface of the disk. The resulting magnetic field profile is shown in Figure 12 for different values of the distance between the 2DEG and the superconducting disk. Notice that the magnetic field under the disk is very small because of the Meissner effect, while far from the disk it becomes equal to the external magnetic field strength B_0. At the edge of the disk, there is an overshoot of the magnetic field strength, which becomes larger with decreasing value of z/a. When the 2DEG is farther away from the superconducting disk, almost no overshoot appears and there is a gradual increase of B when we go away from the center.

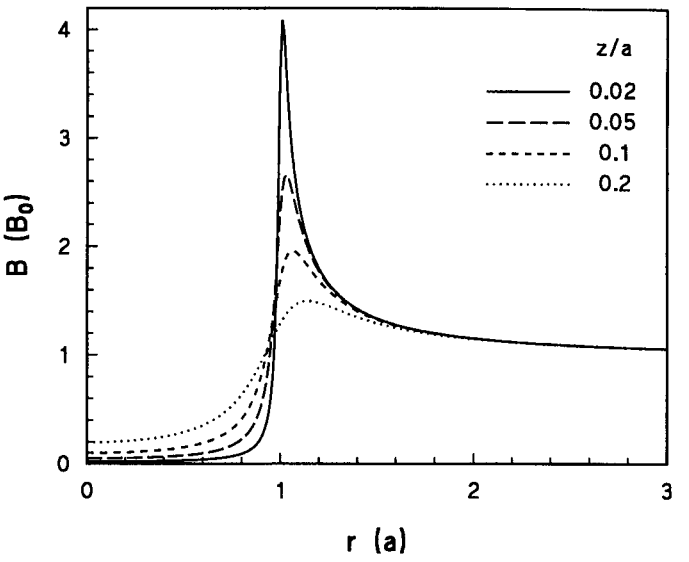


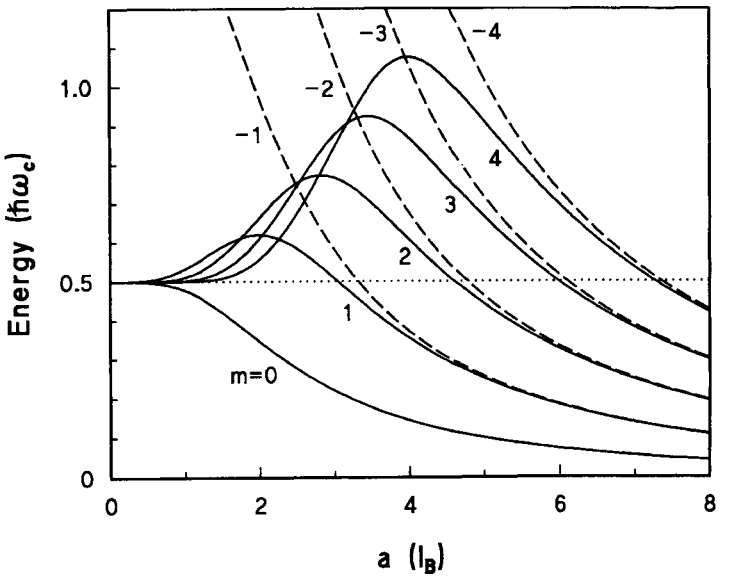
Fig. 12. Magnetic field profile at a distance z under a superconducting disk of radius a.

In principle, we can use the previous magnetic field profile, $\mathbf{B}(\rho = \sqrt{x^2 + y^2}, z)$, to determine the vector potential, $\mathbf{A}(\rho, z)$, which we have to insert into the Schrödinger equation $[-i(\hbar/m^*)\nabla - (e/c)\mathbf{A}(\mathbf{r})]^2\Psi = E\Psi$. The problem can only be solved numerically. Furthermore, we have an additional parameter in our problem: z/a, the distance between the superconducting disk and the 2DEG. Therefore, we found it more convenient to consider two-model systems, which correspond to two extreme situations but which contain the essential physics of the problem. Because of the cylindrical symmetry of the system, we introduce cylindrical coordinates (ρ, φ). The vector potential is given by $\mathbf{A} = \mathbf{B} \times \mathbf{r}/2$. In the cylindrical coordinate system, we have $\mathbf{A} = (A_r, A_\varphi)$ with $A_r = 0$ in case the magnetic field is directed along the z axis with $B_z = (\partial(\rho A_\varphi)/\partial\rho)/\rho$. The two models we consider [33] are defined by the following profiles: (1) $B_z = B(\rho) = B_0\theta(\rho - a)$, which is a limiting case for the situation that the distance between the 2DEG and the superconducting disk is large. It leads to the vector potential $A_\varphi = B_0 a^2/2\rho$ $(\rho < a)$, $B_0\rho/2$ $(\rho > a)$. The spectrum of this system was discussed in [33] and also in [34, 35] where the analogy with classical paths was pointed out; (2) $A_\varphi = (B_0\rho/2)\theta(\rho - a)$, which results in a magnetic field profile with a delta function overshoot: $B(\rho) = 0$ $(\rho < a)$, $(B_0\rho/2)\delta(\rho - a)$, B_0 $(\rho > a)$. In [33–35], one refers to the present system as the magnetic dot system, stressing the magnetic confinement in this quantum dot. From the magnetic field point of view, one has a circular hole inside a uniform magnetic field profile and, therefore, one can also call the present system a magnetic antidot.

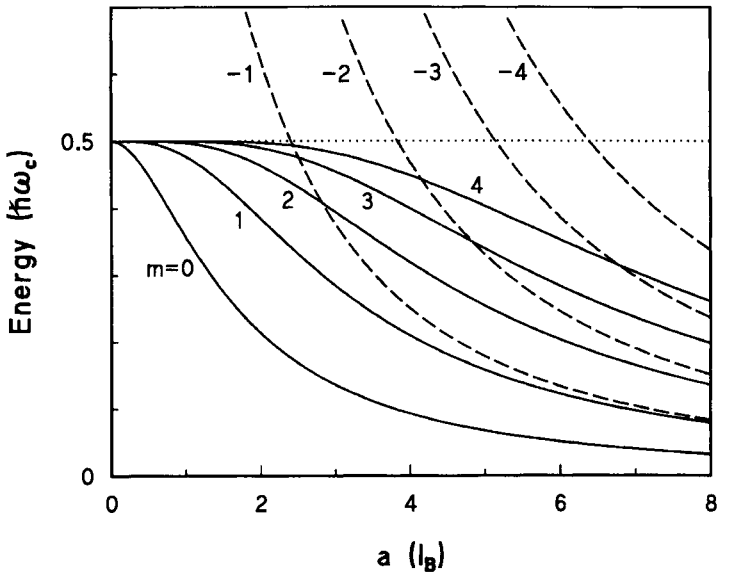
The wave function for the single-electron states can be written as $\Psi(\rho, \varphi) = e^{im\varphi}\psi(\rho)$ where the radial part is determined by the Schrödinger equation

$$\left(\frac{1}{\rho}\frac{d}{d\rho}\rho\frac{d}{d\rho} - V(m, \rho) + 2E\right)\psi(\rho) = 0 \tag{33}$$

with the angular momentum–dependent effective potential $V(m, \rho) = (A_\varphi(\rho) - m/\rho)^2$. The numerical results for the energy spectrum are shown in Figure 13a for the case with overshoot and in Figure 13b for the model without overshoot. Although the limiting behavior of the spectrum for $B_0 \to 0$ and $B_0 \to \infty$ is very similar for both models, the intermediate field behavior is very different. This distinct behavior is made more visible by plotting the energy in units of $\hbar\omega_c$ as a function of $a/l_B \sim \sqrt{B_0}$. This different behavior between the two models can be understood as follows. For $m > 0$, the electron wave func-



(a)



(b)

Fig. 13. One-electron energy levels in the magnetic quantum dot: (a) with magnetic field overshoot near the edge of the dot and (b) without overshoot.

tion exhibits a maximum at $\rho = \rho^* > 0$. With increasing a/l_B, this maximum shifts toward the center of the dot. In case there is an overshoot in the magnetic field profile, when the maximum of the electron wave function is situated near $\rho = a$, the electron energy will be increased, which results in a local maximum as shown in Figure 13a. From this interpretation, it is easy to understand that the maximum in $E_{n,m}/\hbar\omega_c$ shifts to larger a/l_B values with increasing angular momentum m. For large values of a/l_B, most of the wave function will be situated in the dot where there is no magnetic field and, consequently, the energy decreases.

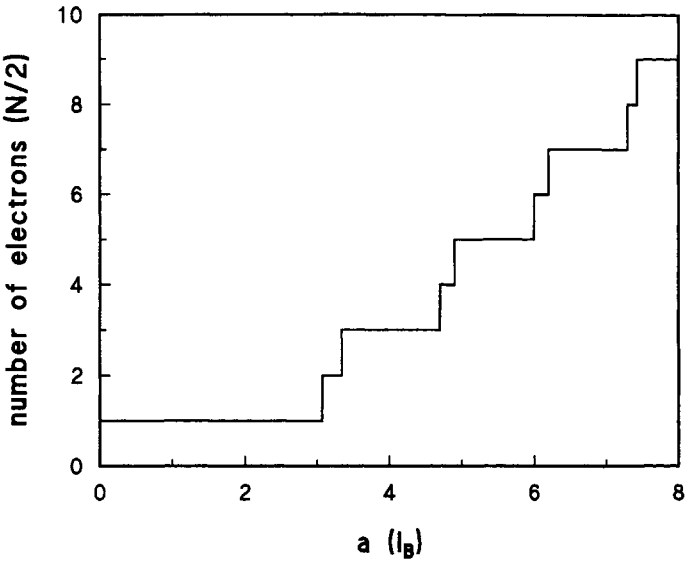


Fig. 14. Filling of the magnetic dot in case of magnetic field overshoot.

This behavior of the electron energy has important consequences for the filling of the dot. Outside the quantum dot, the magnetic field is B_0 and the electron lowest energy state is $\hbar\omega_c/2$. An electron will only be situated in the dot when its energy is lower than in the region outside the dot. For the moment, we will neglect the electron–electron interaction. From Figure 13b, we note that for a dot without magnetic field overshoot at its edges there are an infinite number of states, that is, the states with $m \geqslant 0$ for $n = 0$, which have an energy less than $\hbar\omega_c/2$ and, consequently, the electrons will be attracted toward the dot. For the system with magnetic overshoot, the situation is totally different. The $|0, 0\rangle$ state has energy below $\hbar\omega_c/2$ and two electrons (two because of spin) will be able to occupy the dot. When we add more electrons to the system, we see that for small a/l_B values, the electrons are repelled and are forced outside the dot. Only when a/l_B is sufficiently large will quantum dot states become available with energy less than $\hbar\omega_c$. Consequently, as a function of a/l_B, we observe a discrete filling of the dots. This is depicted in Figure 14 where we show the number of electrons in the dot as a function of $a/l_B \sim \sqrt{B_0}$.

Including the real magnetic profile as shown in Figure 12 will not alter our conclusions qualitatively. For example, the discrete filling of the dot as shown in Figure 14 will still be present. The exact position at which the number of electrons jump to higher values will be a function of the exact magnetic field profile, and, in particular, it will strongly depend on the sharpness of the magnetic overshoot.

5. DIFFUSIVE TRANSPORT OF ELECTRONS THROUGH MAGNETIC BARRIERS

In previous sections, it was assumed that the electron transport through the magnetic barriers was ballistic, and, consequently, the electrons exhibit quantum tunneling. This is valid when the width of the barriers (W) is much smaller than the mean free path (l_e) of the electrons and the cyclotron radius $R_c > W$. For wide magnetic field barriers, the charge transport is better described by a diffusive theory, which is also valid at higher temperature where the mobility is low and the electron motion is diffusive.

Until now, no experiments were available of quantum transport through single or multiple magnetic barriers. Recently, Leadbeater et al. [36] reported an alternative technique to

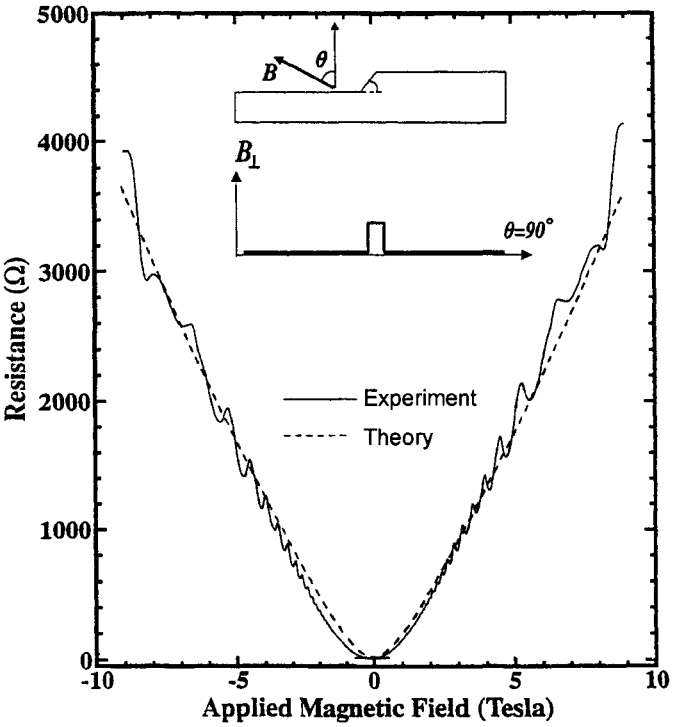


Fig. 15. Experimental (solid curve) and theoretical (dashed curve) results for the magnetoresistance as a function of the applied magnetic field. The magnetic barrier (inset) was created by faceting the 2DEG plane where the facet makes an angle of 20° to the substrate and the applied magnetic field is in the plane of the substrate (i.e., $\theta = 90°$).

produce effective spatially varying magnetic fields of much larger strength and gradients than could be obtained by lithographic patterned superconducting or ferromagnetic films. They constructed a nonplanar two-dimensional electron gas (2DEG) that was fabricated by growth of a GaAs/(AlGa)As heterojunction on a wafer prepatterned with facets at 20° to the substrate. Applying a uniform magnetic field (B) produces a spatially nonuniform field component perpendicular to the 2DEG (see inset of Fig. 15). With the field in the plane of the substrate, an effective magnetic barrier is created located at the facet. The resistance measured across such an etched facet showed oscillations that are periodic in $1/B$ and that are on top of a positive magnetoresistance background, which increases quadratically with the magnetic field for small B and quasi-linearly in B for large B (see full curve in Fig. 15).

5.1. Theoretical Formalism

To explain, quantitatively, the main features of the experimental measurements of [36–38], namely, the smooth background of the magnetic field dependence of the resistance, we will rely on a classical model for magnetotransport through such a wide (typically on the order of a micrometer) magnetic barrier. This theory is also valid for 2D diffusive transport in case magnetic barriers are created through the structuring of ferromagnetic material on top of a heterostructure. The 2DEG situated in the (x, y) plane is bounded by the edges of the Hall bar where a small part of the 2DEG is subjected to a perpendicular magnetic field in the z direction. The $B_z \neq 0$ region corresponds to the facet region in the experimental system, that is, $B_z = B\sin(\theta)$, $\theta = 20°$ is the facet angle, and B is the externally applied magnetic field in the plane of the substrate. To calculate the spatial distribution of the

electrostatic potential, the electric field, and the current density, we start from the stationary continuity equation, which expresses charge conservation

$$\nabla \cdot \mathbf{J} = 0 \tag{34}$$

which is supplemented by Ohm's law

$$\mathbf{J} = \sigma \mathbf{E} \tag{35}$$

In the steady state we have $\nabla \times \mathbf{E} = 0$ and the electric field can be written as the gradient of a potential, that is, $\mathbf{E} = -\nabla\phi$. The previous system of equations reduces to the following 2D elliptic partial differential equation for the electrical potential ϕ:

$$\nabla \cdot [\sigma(x, y)\nabla\phi(x, y)] = 0 \tag{36}$$

where $\sigma(x, y)$ is a spatially dependent conductivity tensor. For a homogeneous system and in the absence of a magnetic field $\sigma(x, y) =$ constant, we recover the Laplace equation. In our case, the conductivity tensor is no longer constant owing to the presence of the finite magnetic barrier:

$$\begin{aligned} \sigma(x, y) &= \begin{pmatrix} \sigma_{xx} & \sigma_{xy}(x, y) \\ \sigma_{yx}(x, y) & \sigma_{yy} \end{pmatrix} \\ &= \frac{\sigma_0}{1 + (\mu B_z(x, y))^2} \begin{pmatrix} 1 & \mu B_z(x, y) \\ -\mu B_z(x, y) & 1 \end{pmatrix} \end{aligned} \tag{37}$$

where $\sigma_0 = n_s e\mu$ is the Drude conductivity and $B_z = 0$ outside the facet. The 2D partial differential equation is cast into a finite-difference form and solved numerically [39] using the accelerated Gauss–Seidel iteration scheme with the boundary conditions $\phi(x, 0) = 0$ and $\phi(x, L) = V_0$ (L is the length of the sample and V_0 is the applied voltage) and the condition that no current can flow out the sides of the sample, that is, $j_x = 0$ for $x = 0$, and $x = W$. The distances are normalized by the width of the sample (typically $W = 40$ μm taken along the x axis) and the voltages are normalized by the total voltage drop between the current probes. The magnetoresistance between any two points a and b along one side of the sample is given by $R = V_{ab}/I_{cd}$, with the voltage drop $V_{ab} = \phi(x, b) - \phi(x, a)$, and the total current flowing normal to the facet is obtained through $I_{cd} = \int_c^d j_y(x, y)\, dx$, where c and d are any two points on the opposite sides of the sample. The Hall resistance at a distance y along the sample length is given by $R_H = V_H/I_{cd}$, where $V_H = \phi(W, y) - \phi(0, y)$.

There exist alternative approaches to solve the differential equation (36). Badalian et al. [40] used the conformal mapping method in order to find an analytic expression for the magnetic potential in an infinite long wire in the presence of a magnetic barrier. Jou and Kriman [41] developed a spectral expansion approach in which the magnetic potential was expanded into an orthogonal basis, which consisted of solutions of the Laplace equation in the different regions that satisfy the boundary conditions. Continuity of the magnetic potential at the boundary between the separate regions determined the expansion coefficients. In [41], this approach was applied to a single magnetic barrier and to a periodic array of them.

5.2. Single Magnetic Barrier

In Figure 15, we show both the experimental (solid curve) and the theoretical (dashed curve) traces for the magnetoresistance across a single facet of width 3 μm where the voltage probes are situated 10 μm apart across the facet and the current probes are more than 900 μm apart for a sample with width $W = 40$ μm. Notice that apart from the Shubnikov–de Haas (SdH) oscillations, which result from the quantizing effect of the magnetic field

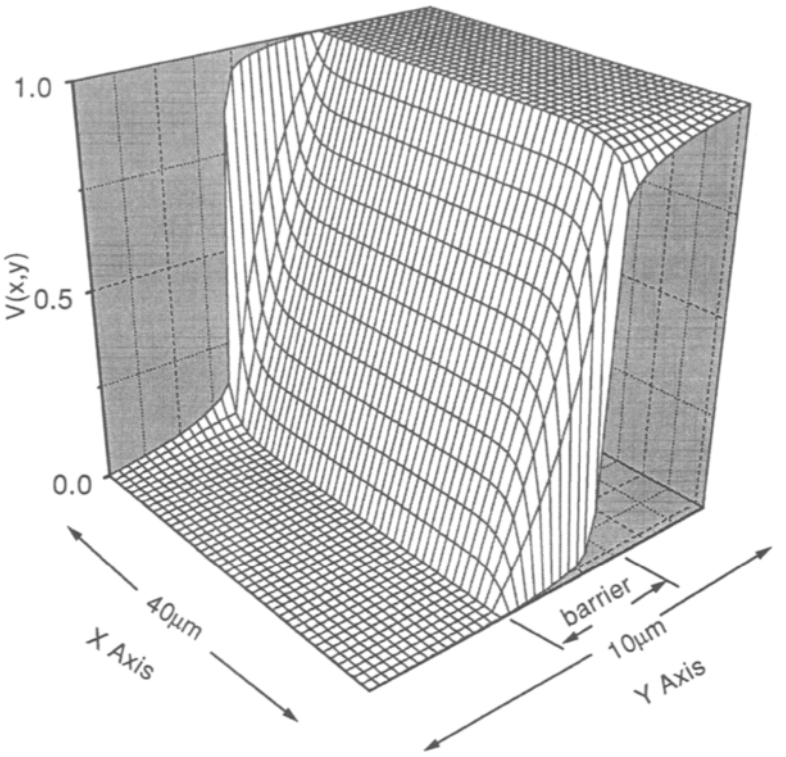


Fig. 16. Potential distribution in the sample for $B = -2$ T.

at low temperature, the theoretical curve accounts nicely for the overall behavior of the magnetoresistance. The experimental curve is slightly asymmetric around $B = 0$, which is due to the fact that the voltage probes are not exactly equidistant from the facet. The classical origin of the positive magnetoresistance was confirmed experimentally where it was found that it persists even for temperatures above 100 K. Note that the experimental configuration is effectively a two-terminal measurement where the measured resistance is determined by the Hall resistance as well as the magnetoresistance. For small B fields, the Hall resistance is small and thus the resistance is determined by the magnetoresistance and is, consequently, quadratic in B. For larger magnetic fields, a quasi-linear behavior of the resistance as a function of B is found, which is due to the fact that now the Hall resistance mainly limits the current.

The theoretical electric potential distribution in the sample is shown in Figure 16 for an applied magnetic field of $B = -2$ T, which gives $B_z = -2\sin(20°) = -0.6840$ T. Notice that almost all the potential drop takes place across the magnetic barrier. In the barrier region and just outside it, there is a voltage difference between the edges of the sample (i.e., across the x axis), which is nothing else than a spatially dependent Hall voltage. This is in accord with the concept that the ($B_z = 0$ regions) can be thought of as extended high mobility contacts to a short and wide Hall bar (the facet region) that tends to short out most of the voltage immediately outside the facet region. Particularly interesting is the development of the Hall voltage between the opposite edges of the facet. This becomes very small but nonzero outside the facet region and gives a steep increase of the Hall potential profile at the edges of the $B_z \neq 0$ region, which is reminiscent of the potential profile investigated experimentally and theoretically in [42, 43] in a conventional Hall bar under the conditions of the quantum Hall regime and in the middle of a plateau in the Hall resistance.

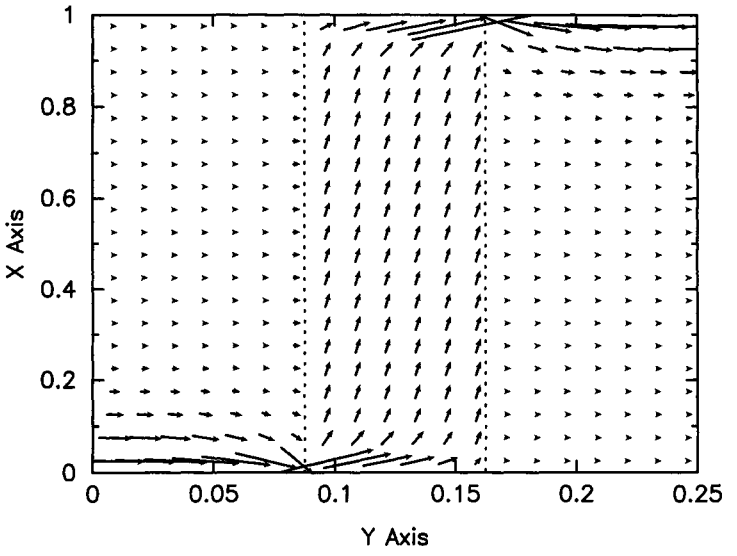


Fig. 17. Current flow in the sample for $B = -2$ T corresponding to the situation of Figure 16. The magnetic barrier region is delimited by the two dashed lines.

The spatial distribution of the components of the electric field are obtained as follows: $E_x = -\partial\phi(x, y)/\partial x$ and $E_y = -\partial\phi(x, y)/\partial y$. From Figure 16, it is clear that both components are very small outside the barrier region. Inside the magnetic barrier, E_x becomes very large close to the edges especially at the diagonally opposite corners and vanishingly small in the middle where E_y is finite and more uniform, singular at the diagonally opposite corners, and very small at the other two corners. Accordingly, the largest part of the current will enter the magnetic barrier region from the corner where both electric field components are large and exit the barrier from the diagonally opposite corner (see Fig. 17). Once inside the barrier region, the guiding center of the electron cyclotron orbits will drift along the equipotential lines (see Fig. 16) according to the $\mathbf{E} \times \mathbf{B}$ drift with velocity $\mathbf{v}_{\text{drift}} = -(\nabla\phi \times \mathbf{B})/B^2$. Electrons entering or exiting the small regions of the corners of the barrier will have large velocities, which are proportional to the electric field at these locations, to account for current conservation. There are larger number of electrons drifting with slow and uniform velocities in the middle of the barrier where the electric field is smaller and more uniform. This picture is graphically represented in Figure 17 where we show the calculated results for the current distribution $\mathbf{J}(x, y) = -\sigma(x, y)\nabla\phi(x, y)$ corresponding to the experimental situation of Figure 15. Notice that even well outside the barrier the current distribution is already modified by the presence of the magnetic field barrier in the facet region and it is concentrated closer to the edges of the sample. At the diagonally opposite corners, it is strongly peaked. These results for the field and current distribution are consistent with those of [44], which were calculated for a conventional Hall geometry in the case of very low-aspect-ratio. This problem of low-aspect-ratio Hall devices in a homogeneous magnetic field was studied earlier in the context of applications for magnetic sensors (see, e.g., [45] and the references therein).

5.3. Magnetic Barriers in Series

In [37], a ridge geometry (see top figure of the inset of Fig. 18) was fabricated resulting in two magnetic barriers in series (bottom figure of the inset of Fig. 18), each having the same B_z but with opposite sign. In Figure 18, both the experimental (solid) trace and the theoretical (dash-dotted and dashed) curves are shown. The experimental trace was claimed to be for $2S = 1$ μm base length of the ridge (in [37], it is noted that the etch depth for a

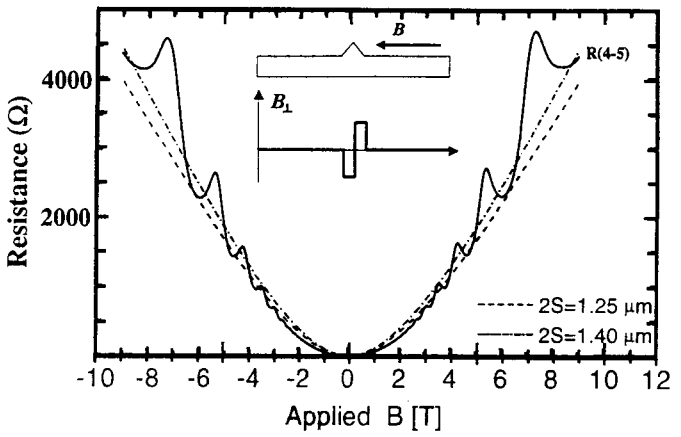


Fig. 18. Experimental (solid curve) and theoretical (dashed and dash-dotted curves) results for the magnetoresistance of the magnetic barrier created by the ridge (see inset).

ridge is less than the depth of the regrown material, which may produce some planarization during regrowth), while for the theoretical curves we found that a larger base length gives closer agreement with experiment. Notice that with this renormalization of the width of the magnetic barrier we obtain rather good agreement for the positive magnetoresistance part of the experimental curves. The oscillatory part in the experimental curves are again due to quantum effects.

The more general case of two magnetic barriers in series was studied in [39]. This can be realized experimentally by producing a ridge with a flat top, which is equivalent to introducing a zero magnetic field region between the two facets. It was shown that the relative sign of the magnetic field of the two magnetic barriers has important consequences for the magnetoresistance. For the case of two separate barriers with the same sign of B_z, the magnetoresistance at high magnetic fields is almost twice that of a single barrier and, consequently, classically the magnetoresistance of multiple barriers is additive. For not too large magnetic fields (the $R \sim B^2$ region), the current path spreads across the magnetic–nonmagnetic interface and, consequently, the current path is shorter, leading to a smaller magnetoresistance, and the simple rule of addition of resistances in series is no longer valid [38]. For barriers in series with opposite direction of the B_z field, the situation is different. The removal point of current from the first barrier is at the same side of the sample as the injection point of the current into the second barrier and, consequently, the resistance is not sensitive to the distance of separation between the two barriers.

6. ONE-DIMENSIONAL MAGNETIC MODULATION

The magnetoresistance oscillations of the two-dimensional electron gas (2DEG) subject to periodic *electric* (or potential) weak modulations, along one or two directions, also called *Weiss* oscillations, are now well established both experimentally [46–53] and theoretically [54–59]. The situation is mostly clear in the case of one-dimensional (1D) modulations where the oscillations reflect the commensurability between two length scales: the cyclotron diameter at the Fermi level, $2R_c = 2\sqrt{2\pi n_e} l^2$ (where n_e is the electron density and $l = \sqrt{\hbar/eB}$ is the magnetic length), and the period a of the modulation.

In this section, we consider electrical magnetotransport of a 2DEG in the presence of a weak 1D periodic modulation (of strength B_0) of the magnetic field and the extreme case of a strong magnetic modulation in which the average magnetic field is zero. We will show that both situations are essentially different from each other.

Different methods of establishing a periodic magnetic field on a micrometer or nanometer scale have been used: (i) using periodically arranged flux tubes in a type II superconductor (Abrikosov lattice) that penetrate the underlying 2DEG [60–63], (ii) using patterned superconducting gates that partially shield the external magnetic field [64–66], (iii) microfabricated ferromagnetic structures whose magnetic polarization adds to the external field [65–78], or (iv) nonplanar two-dimensional electron systems [36–38, 79, 80]. The first method is limited to low magnetic fields and, furthermore, a periodic flux lattice is, in practice, not achievable in an evaporated superconducting film because of the presence of pinning centra, which leads to a rather random array of flux lines. The last method of nonplanar 2D systems can result in large magnetic field modulations, the strength of which is determined by the external magnetic field. Also sign-alternating magnetic modulations are attainable. For the second method, different superconducting periodic arrays have been made using lead [64], and niobium [66]. Different ferromagnetic materials have been patterned on top of the 2DEG, for example, nickel [65, 66, 69–72, 74, 76, 81–83], dysprosium [67, 75, 77, 82], and cobalt [73, 83]. Alternatively, metal organic chemical vapor deposition with a tunneling microscopic tip [84] was used to deposit small magnetic particles.

The magnetic metallic strips also induce an electric modulation in the 2DEG and often also a strain-induced electric modulation at the 2DEG occurs because of the differential thermal contraction of the deposited magnetic material and the semiconductor. Initially [81], these built-in potential modulations dominated any effects caused by the magnetic modulation. By depositing a thin metallic film between the 2DEG and the magnetic strips, the electric modulation from the metallic strips can be shielded. For example, Weiss et al. [82] used a 10-nm thin NiCr film between the 2DEG and the magnetic strips in order to define an equipotential plane. The strain-induced modulation was removed [65, 72] by orienting the strips normal to the [100] direction of GaAs, which is nonpiezoelectric.

The magnetic metallic strips act as a periodic gate, which causes both scalar and vector potential modulation. By applying a bias to the ferromagnetic gates, the electric field modulation can be altered. In this way, one can drive the system from a predominantly electric-dominated modulation to a magnetic field–dominated modulation.

6.1. Weak Magnetic Modulation

There already exists a number of theoretical studies on the effect of a periodic magnetic modulation on the electrical transport properties of a 2DEG. Vasilopoulos and Peeters [85] predicted phase-shifted Weiss oscillations, which were later reobtained in [86]. This study was later extended [87] to the case of combined electric and magnetic 1D modulations (see also [88]). Li et al. [89] considered more general periodic magnetic field profiles by including several Fourier components in the expression for $\mathbf{B}(x)$. The corresponding quasiclassical band conductivity problem was studied by Gerhardts [90]. In [81], a numerical calculation of the energy spectrum for a 1D magnetic modulation of arbitrary strength was presented and the corresponding transport properties were discussed in [91]. Collective excitations of a 2DEG in a unidirectional magnetic field modulation were discussed by Wu and Ulloa [92–94].

Consider a 2DEG in the (x, y) plane, subject to the magnetic field $\mathbf{B} = (B + B_0 \cos Kx)\mathbf{e}_z$, where $K = 2\pi/a$, and a is the modulation period. Only the first Fourier component of the periodic magnetic field is retained, which is sufficiently accurate in most situations. Here we consider only the case of a weak modulation, that is, $B_0 \ll B$. In the Landau gauge, the vector potential $\mathbf{A}$ that describes this periodic magnetic field is $\mathbf{A} = (0, Bx + (B_0/K)\sin(Kx), 0)$ with $B_0 \ll B$. In the effective-mass (m^*) approximation, the corresponding one-electron Hamiltonian is given by $H = (\mathbf{p} + e\mathbf{A})/2m^*$ and can be written as

$$H = \frac{1}{2m^*}\left[p_x^2 + (p_y + eBx)^2\right] + \frac{\omega_0}{K}(p_y + eBx)\sin Kx + \frac{m^*\omega_0^2}{4K^2}(1 - \cos 2Kx) \quad (38)$$

where p_μ ($\mu = x, y$) is the momentum operator, $\omega_0 = eB_0/m^* \ll \omega_c = eB/m^*$, and ω_c is the cyclotron frequency. The first term on the right-hand side of Eq. (38) is the Hamiltonian of a free electron in a magnetic field. The corresponding normalized eigenvectors are $\psi_{nk_y} = \exp(ik_y y)\phi_n(x + x_0)/\sqrt{L_y}$, where $x_0 = -l^2 k_y = -\hbar k_y/eB$ is the center coordinate of the cyclotron orbit, L_y is the width of the sample in the y direction, and n is the Landau level index. $\phi_n(x)$ is the well-known harmonic oscillator wave function and the corresponding eigenvalues are $E_{nk_y} = (n + 1/2)\hbar\omega_c$ and are degenerate with respect to the wavevector k_y along the y direction.

Because of the inequality $B_0 \ll B$, we can consider the last two terms on the right-hand side of Eq. (38) as perturbation and evaluate the energy correction to E_{nk_y} given previously by first-order perturbation theory using the unperturbed eigenstates ψ_{nk_y}. The result is

$$E_{nk_y} = \left(n + \frac{1}{2}\right)\hbar\omega_c + \hbar\omega_0 G_n(u)\cos Kx_0 + \left(\frac{m^*\omega_0^2}{4K^2}\right)\left[1 - e^{-2u}L_n(4u)\cos 2Kx_0\right] \quad (39)$$

where $u = K^2 l^2/2$, $G_n(u) = e^{-u/2}[L_n(u)/2 + L_{n-1}^1(u)]$, and $L_n(z)$ is a Laguerre polynomial.

Because $x_0 = -l^2 k_y$, the k_y degeneracy of the energy levels is lifted and the energy levels broaden into bands. In the following, we will retain only terms of order ω_0 in the energy spectrum and neglect terms of higher order. Because a potential modulation can be present, we also consider the electric modulation problem. The correspondence with the *electric* case [54] for a modulation strength V_0 is as follows: $G_n(u) = -\partial F_n(u)/\partial u \rightarrow F_n(u) = \exp(-u/2)L_n(u)$. In a typical experiment, the magnetic field B is weak and many Landau levels are occupied. It then turns out that it is a good approximation to take the large n limit of the Laguerre polynomials that appear in $G_n(u)$ and $F_n(u)$. For the *electric* modulation, the width of the Landau level at the Fermi energy is given by [54]:

$$2V_0|F_n(u)| \approx 2V_0\left(\frac{2}{\pi K R_c}\right)^{1/2}\left|\cos\left(\frac{KR_c - \pi}{4}\right)\right| \quad (40)$$

whereas now V_0 is replaced by $\hbar\omega_0$ and $F_n(u)$ by $G_n(u)$. The resulting bandwidth for large n is

$$2\hbar\omega_0|G_n(u)| \approx 2\hbar\omega_0\left(\frac{ak_F}{2\pi}\right)\left(\frac{2}{\pi K R_c}\right)^{1/2}\left|\sin\left(\frac{KR_c - \pi}{4}\right)\right| \quad (41)$$

where $R_c = (n_F + \frac{1}{2})^{1/2} l$ is the cyclotron orbit at the Fermi energy and n_F is defined as the largest integer contained in $(E_F - \frac{1}{2})/\hbar\omega_c$. From Eq. (41), we obtain the flat-band condition as $2R_c/a = i + \frac{1}{4}$; the maximum bandwidth occurs for $2R_c/a = i + \frac{3}{4}$, with $i = 0, 1, 2, \ldots$.

Equations (40) and (41) were obtained using the asymptotic expressions for the Laguerre polynomials and are valid in the low-magnetic-field limit, typically $B \leqslant 1$ T, in which case $n \gg 1$. Comparing Eq. (40) with Eq. (41), we see that (1) the bandwidths are *out of phase*, and (2) the amplitude in the *magnetic* modulation case is larger by a factor of $ak_F/2\pi = \sqrt{n_e a^2/2\pi}$ ($= 8.6$ for $n_e = 3 \times 10^{11}$ cm^{-2} and $a = 3820$ Å) than the corresponding amplitude in the *electric* case for equal modulation strengths. This is illustrated in Figure 19 for the width of the Landau level at the Fermi energy. For the *magnetic* modulation, we show the result $2|G_n(u)|$ (solid curve) as well as the asymptotic expression Eq. (41) (dotted curve). The jumps in the solid curve are due to the fact that the integer n_F changes discontinuously with B. The bandwidth for the *electric* modulation, when $V_0 = \hbar\omega_0$, is shown as the short-dashed curve.

It is instructive to give a classical derivation of the energy correction resulting from the modulation because the magnetic field is weak and the quantum number n large. In classical mechanics, the electron motion along the x and y directions is described by $x(t) = x_0 + R_c\sin(\omega_c t + \varphi)$ and $y(t) = y_0 + R_c\cos(\omega_c t + \varphi)$, respectively, where x_0, y_0 are the center coordinates and φ is a phase factor. Without loss of generality,

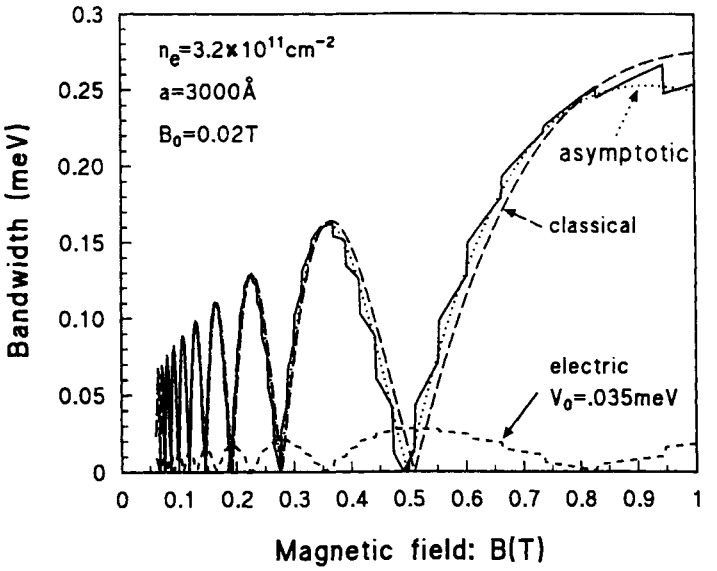


Fig. 19. Width of the Landau level at the Fermi energy as a function of the applied magnetic field. The solid curve is the exact numerical result for a constant magnetic field modulation of strength $B_0 = 0.02$ T. The dotted and long-dashed curves are the corresponding asymptotic and classical results. The short-dashed curve is the result for an electric modulation of equal strength, $V_0 = \hbar\omega_0$.

φ can be taken equal to zero. The contribution to the potential energy U caused by the modulation of the magnetic field is $U = -e\mathbf{A}_0 \cdot \mathbf{v}$, where $\mathbf{v}$ is the electron velocity and $\mathbf{A}_0 = (eB_0/K)\sin(Kx)\mathbf{e}_y$. The mean value $\langle U\rangle$ over the period t_0 of the cyclotron motion is

$$\langle U\rangle = \frac{1}{t_0}\int_0^{t_0} U(t)\,dt = eB_0\omega_c\left(\frac{R_c}{K}\right)\cos Kx_0\,\frac{1}{t_0}\int_0^{t_0}\sin\omega_c t\,\sin(KR_c\sin\omega_c t)\,dt$$
$$= \hbar\omega_0\left(\frac{R_c}{Kl^2}\right)J_1(KR_c)\cos Kx_0 \tag{42}$$

where $J_1(z)$ is the Bessel function of order one. In the limit $KR_c \gg 1$, that is, for weak magnetic fields, $\langle U\rangle$ becomes equal to the second term of Eq. (39), thus resulting in the bandwidth given by Eq. (41). The bandwidth resulting from Eq. (42), prior to taking the limit $KR_c \gg 1$, is shown in Figure 19 by the long-dashed curve and is indicated as "classical."

In the absence of modulation, we have $v_x = v_y = 0$ for all eigenstates. Because the modulation lifts the k_y degeneracy, we find, to order $\hbar\omega_0$,

$$v_y = \frac{1}{\hbar}\frac{\partial E_{n,k_y}}{\partial k_y} = -\frac{2\omega_0}{K}uG_n(u)\sin Kx_0 \tag{43}$$

while $v_x = 0$. The fact that v_y is no longer zero has important consequences for transport which will be detailed later.

For weak electrical fields, that is, for linear responses, and weak scattering, the conductivity tensor $\sigma_{\mu\nu}$ has been evaluated, for the case of *electric* modulations, in [54, 55]. In general, we have $\sigma^{\mathrm{I}}_{\mu\nu}(\omega) + \sigma^{\mathrm{II}}_{\mu\nu}(\omega)$, where ω is the frequency. The relevant quantity $\sigma^{\mathrm{I}}_{\mu\nu}(0) \equiv \sigma_{\mu\nu}$ for direct-current (dc) transport is, in general, the sum of a diffusive (dif)

$$\sigma^{\mathrm{dif}}_{\mu\nu} = \frac{\beta e^2}{\Omega}\sum_\zeta f_\zeta(1 - f_\zeta)\tau(E_\zeta)v^\zeta_\mu v^\zeta_\nu \tag{44}$$

and a collisional (col) contribution. The collisional contribution is the only contribution in the case of transport in a uniform 2DEG because $\mathbf{v}^{\zeta} = 0$ and leads to the well-known Shubnikov–de Haas (SdH) oscillations. Because in the modulated case $v_y \neq 0$, a new conduction channel opens up. In Eq. (44), we used the unperturbed one-electron states $|\,\zeta\rangle \equiv \psi_{nk_y}$ with the corresponding eigenvalue given by Eq. (39), $\tau(E_\zeta)$ is the relaxation time, f_ζ is the Fermi–Dirac function, and the velocity in the state $|\,\zeta\rangle$: $v_\mu^\zeta = \langle\zeta \mid v_\mu \mid \zeta\rangle$.

The dc component $\sigma_{\mu\nu}^{\mathrm{II}}$ is given by [54, 55]:

$$\sigma_{\mu\nu}^{\mathrm{II}} = i\hbar\frac{e^2}{\Omega}\sum_{\zeta\neq\zeta'} f_\zeta(1-f_{\zeta'})\langle\zeta \mid v_\mu \mid \zeta'\rangle\langle\zeta' \mid v_\nu \mid \zeta\rangle\frac{1-\exp[\beta(E_\zeta - E_{\zeta'})]}{(E_\zeta - E_{\zeta'})^2} \tag{45}$$

and is independent of scattering in the limits taken.

A detailed evaluation of formulas (44) and (45) has been carried out in [95] for scattering by randomly distributed impurities of density N_{I} and of interaction strength, in Fourier space, $U_q = (2\pi e^2/\epsilon)/\sqrt{q^2+k_{\mathrm{s}}^2} \approx (2\pi e^2/\epsilon)/k_{\mathrm{s}} = U_0$ in the limit $q \ll k_{\mathrm{s}}$; here k_{s} is the inverse screening length and ϵ the dielectric constant, which gives approximately $\tau(E_\zeta) \approx (\pi l^2\hbar^2/N_{\mathrm{I}}U_0^2)^{1/2}$.

In the absence of modulation, we have $v_x = v_y = 0$ and the diffusion contribution vanishes. In its presence, we have $v_x = 0$ but $v_y \neq 0$; cf. Eq. (43). Thus, $\sigma_{xx}^{\mathrm{dif}}(0) = 0$, whereas $\sigma_{yy}^{\mathrm{dif}}(0) \equiv \sigma_{yy}^{\mathrm{dif}} \neq 0$. To order B_0^2, we find

$$\sigma_{yy}^{\mathrm{dif}} = \frac{e^2}{h}\frac{2\pi^2\tau}{\hbar}\frac{l^2}{a^2}\sum_n [\hbar\omega_0 G_n(u)]^2\left(-\frac{\partial f(E)}{\partial E}\right)_{E=E_n} \tag{46}$$

where $E_n = (n+1/2)\hbar\omega_{\mathrm{c}}$. Comparing this result with that for *electric* modulation of strength V_0, Eq. (13) of [55], we see that it has the same structure: $V_0F_n(u)$ is replaced by $\hbar\omega_0 G_n(u)$. In either case, this contribution is proportional to the square of the bandwidth.

The resistivity tensor $\rho = \sigma^{-1}$ is evaluated from the conductivity tensor using the standard expressions $\rho_{xx} = \sigma_{yy}/S$, $\rho_{yy} = \sigma_{xx}/S$, and $\rho_{xy} = -\sigma_{yx}/S$ with $S = \sigma_{yy}\sigma_{xx} - \sigma_{xy}\sigma_{yx}$.

For $n \gg 1$, that is, when many Landau levels are occupied, the results of (46) can be cast into a form that exhibits explicitly both the Weiss (at low B) and the Shubnikov–de Haas (SdH) (at higher B) oscillations. The procedure has been detailed in [55, 87] and consists of using the asymptotic expressions for the Laguerre polynomials, for $n \gg 1$, and of the density of states $D(E) = D_0[1 - 2\exp(-\pi/\omega_{\mathrm{c}}\tau_{\mathrm{f}})\cos(2\pi E/\hbar\omega_{\mathrm{c}})]$ with the prescription $\sum_n \to 2\pi l^2\int D(E)\,dE$. The parameter τ_{f} is the electron quantum lifetime. Following verbatim this procedure and retaining only the leading terms, we obtain that Eq. (46) takes the form

$$\frac{\sigma_{yy}^{\mathrm{dif}}}{\sigma_0} = \frac{ak_{\mathrm{F}}}{2\pi^2}\frac{\hbar\omega_0}{\hbar\omega_{\mathrm{c}}}\frac{\hbar\omega_0}{E_{\mathrm{F}}}\left[G - 2\exp\left(\frac{-\pi}{\omega_{\mathrm{c}}\tau_{\mathrm{f}}}\right)A\left(\frac{T}{T_{\mathrm{c}}}\right)\cos\left(\frac{2\pi E_{\mathrm{F}}}{\hbar\omega_{\mathrm{c}}}\right)\sin^2\left(\frac{2\pi R_{\mathrm{c}}}{a} - \frac{\pi}{4}\right)\right] \tag{47}$$

where

$$G = \left[1 - A\left(\frac{T}{T_{\mathrm{a}}}\right)\right]\Big/2 + A\left(\frac{T}{T_{\mathrm{a}}}\right)\sin^2\left(\frac{2\pi R_{\mathrm{c}}}{a} - \frac{\pi}{4}\right) \tag{48}$$

Here $\sigma_0 = n_{\mathrm{e}}e^2\tau/m^*$ is the conductivity at zero magnetic field B and $A(x) = x/\sinh(x)$. The characteristic temperatures T_{a}, for the Weiss oscillations, and T_{c}, for the SdH oscillations, are defined by $k_{\mathrm{B}}T_{\mathrm{a}} = (\hbar\omega_{\mathrm{c}}/4\pi^2)ak_{\mathrm{F}}$ and $k_{\mathrm{B}}T_{\mathrm{c}} = \hbar\omega_{\mathrm{c}}/2\pi^2$, respectively, with k_{F} being the Fermi wavevector. In typical experiments, we have $T_{\mathrm{a}}/T_{\mathrm{c}} = ak_{\mathrm{F}}/2 \gg 1$; for example, for $n_{\mathrm{e}} = 3\times10^{11}$ cm^{-2} and $a = 3500$ Å, we have $ak_{\mathrm{F}} \approx 24$. As a result, the SdH oscillations disappear much faster with temperature than the Weiss oscillations. We further

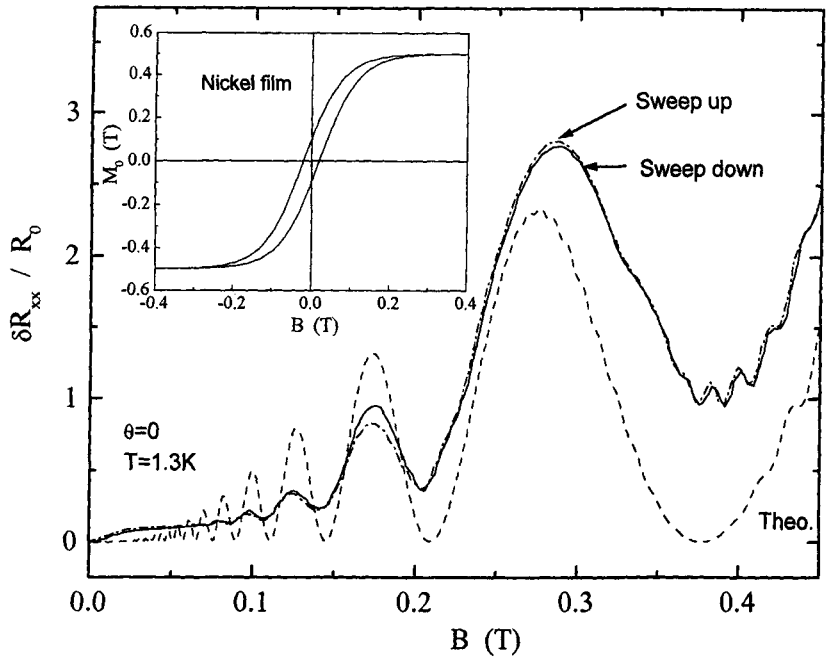


Fig. 20. Longitudinal magnetoresistance at 1.3 K for a 1D magnetic modulation of a 2DEG for "up" (dot-dashed curve) and "down" (solid curve) field sweeps as compared to the calculated behavior (dashed curve). The inset shows the magnetization of the Ni strips that is responsible for the magnetic modulation. (Source: Reprinted with permission from [72]. © 1997 American Physical Society.)

remark that in comparison with the *electric* case, cf. Eq. (34) of [55], the present result differs essentially by a term $(ak_F/2\pi)^2 \approx 60$ in the prefactor. Correspondingly, the amplitude will be larger in the *magnetic* case by this factor.

In Figure 20, the commensurability oscillations in the longitudinal magnetoresistance, $\delta R_{xx} = R_{xx}(B) - R_0$, of a 2DEG with mobility $\mu = 7 \times 10^5$ cm^2/V s (corresponding to a mean free path of $l_e = 7.7$ μm) that is subjected to a 2D magnetic modulation are shown. The 2D magnetic modulation was produced [72] by a periodic array ($a = 500$ nm) of Ni strips of width $d = 200$ nm and height $h = 100$ nm that are situated a distance of 35 nm from a 22-nm-wide GaAs/AlGaAs quantum well. These magnetoresistance oscillations result from the preceding commensurability effects between the diameter of the cyclotron orbit at the Fermi level $2R_c$ and the period of the magnetic modulation. Notice that these magnetoresistance oscillations are clearly visible and their position agrees very well with the previous theoretical result (dashed curve). For $B > 0.3$ T, small SdH oscillations are superimposed on top of the Weiss oscillations. Note that the experimental result exhibits a small hysteretic behavior that is associated with the hysteresis of the magnetization of the Ni strips (see inset of figure). In the calculation (dashed curve), the strength of the magnetic modulation (B_0) was taken from the magnetization (M_0) given by the model hysteresis curve shown in the inset of the figure. Note that there is not only a good agreement with the position of the oscillations, confirming that the oscillations originate from a predominantly magnetic modulation, but also the magnitude of the last commensurability peak at approximately 0.27 T is well reproduced. Above about 0.2 T, the theoretical prediction involves no free parameters so this agreement confirms the accuracy of the calculated saturation modulation amplitude. Below 0.2 T, the decrease in amplitude will depend on the exact form of the $M_0(B_{ext})$ curve and damping caused by scattering, which is not included in the theoretical curve, will be important.

6.2. Electric and Magnetic Modulations

Magnetic modulations are often accompanied by an electric modulation. Therefore, we have to study how the results of a pure magnetic modulation are modified when an electric modulation with the same period is present. Two cases are of interest: that where the two modulations are *in phase* and that where they are *out of phase*.

6.2.1. In-Phase Modulations

If a weak *electric* modulation described by the periodic potential $V_0\cos(Kx)$, which is *in phase* with the *magnetic* one, is present, Eq. (39) will have an additional term $V_0F_n(u)\cos(Kx_0)$. As a result, v_y, given by Eq. (43), will have an additional term $-(2V_0/\hbar K)uF_n(u)\sin(Kx_0)$. The bandwidth will be the sum of the two bandwidths. At the Fermi energy, the latter is given by the sum of those of Eqs. (40) and (41) and is equal to

$$2V_0\sqrt{\frac{2}{\pi KR_c}}\sqrt{1+\delta^{-2}}\left|\sin\left(\frac{2\pi R_c}{a}-\frac{\pi}{4}+\phi\right)\right| \tag{49}$$

where $\delta = 2\pi V_0/ak_F\hbar\omega_0 = \tan(\phi)$. Notice that the flat-band condition now reads $2R_c/a = i + 1/4 - \phi/\pi$ and depends on the relative strength of the two modulations.

The changes mentioned previously will be reflected in the transport coefficients as well. As an example, the diffusion contribution to the conductivity, Eq. (46), now takes the form

$$\sigma_{yy}^{\text{dif}} \approx \frac{e^2}{h}\frac{2\pi^2\tau}{\hbar}\frac{l^2}{a^2}\sum_n\left[\hbar\omega_0G_n(u)+V_0F_n(u)\right]^2\left(-\frac{\partial f(E)}{\partial E}\right)_{E=E_n} \tag{50}$$

and its asymptotic expression, obtained in the manner described earlier, reads

$$\begin{aligned}\frac{\sigma_{yy}^{\text{dif}}}{\sigma_0} \approx{}& \frac{ak_F}{2\pi^2}\frac{\hbar\omega_0}{\hbar\omega_c}\frac{\hbar\omega_0}{E_F}(1+\delta^2)\\ &\times\left\{1-A\left(\frac{T}{T_a}\right)+\left[A\left(\frac{T}{T_a}\right)-2\exp\left(\frac{-\pi}{\omega_c\tau_f}\right)A\left(\frac{T}{T_c}\right)\cos\left(\frac{2\pi E_F}{\hbar\omega_c}\right)\right]\right.\\ &\left.\times\sin^2\left(\frac{2\pi R_c}{a}-\frac{\pi}{4}+\phi\right)\right\}\end{aligned} \tag{51}$$

Notice that the influence of the combined effect of the two modulations is to introduce the phase factor ϕ in the Weiss oscillations.

In Figure 21, we plot $\Delta\rho$, that is, the change in resistance caused by the modulations, as a function of B (solid curve) for $B_0 = 0.02$ T and $V_0 = 0.2$ meV for a 2DEG with $n_e = 3\times10^{11}$ cm^{-2} at $T = 4.2$ K with a modulation period of $a = 3000$ Å. For comparison, we show the results when only the *magnetic* (dotted curve) or the *electric* (dashed curve) modulation is present. In line with Eq. (51) that was used for the evaluation of $\Delta\rho$, the solid curve is shifted from the other curves because of the phase factor ϕ. We also note the $\pi/2$ phase difference between the dashed and dotted curves, which reflects that of the corresponding bandwidths shown in Figure 19.

The dependence of $\Delta\rho$ on B and the phase factor ϕ is shown in Figure 22. B_0 is again kept constant ($B_0 = 0.02$ T) but V_0 is varied as indicated between positive and negative values; δ and ϕ change accordingly. We notice that (1) the position of the peaks depends on the specific value of δ, and (2) there is a π phase difference between large positive and large negative values of δ.

Such in-phase modulation of the electric and magnetic period was studied by Iye et al. [69]. In their experiment, a GaAs/AlGaAs heterojunction containing a 2DEG, with density $n_e = 4\times10^{11}$ cm^{-2} and mobility $\mu = 6\times10^5$ cm^2/V s at $T = 4.2$ K, was placed 75 nm below a periodic array ($a = 0.5$ μm) of Ni strips with height 150 nm. By changing the voltage on the gate consisting of the Ni strips, the strength of the electric field modulation is

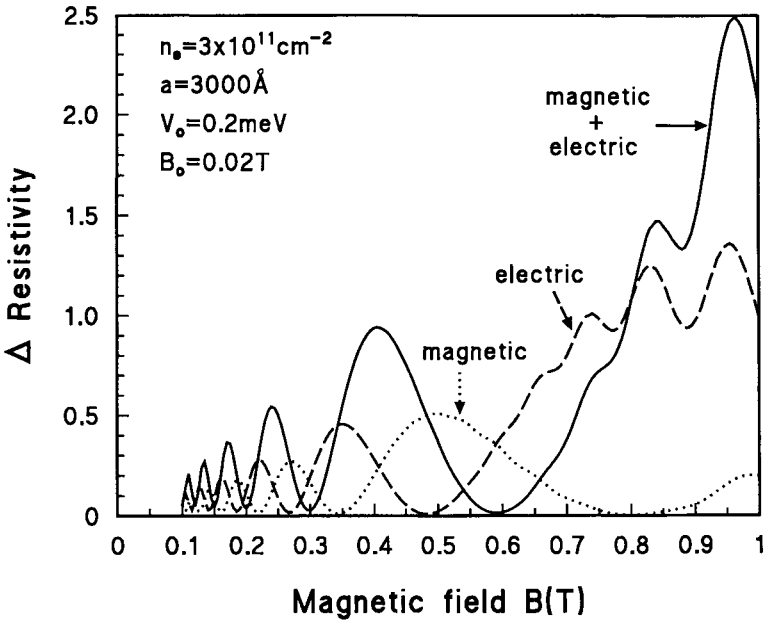


Fig. 21. Increase of the magnetoresistance (solid curve) resulting from magnetic and in-phase electric modulations with $B_0 = 0.02$ T and $V_0 = 0.2$ meV. The dotted and dashed curves represent the increase caused by the separate magnetic and electric modulation, respectively.

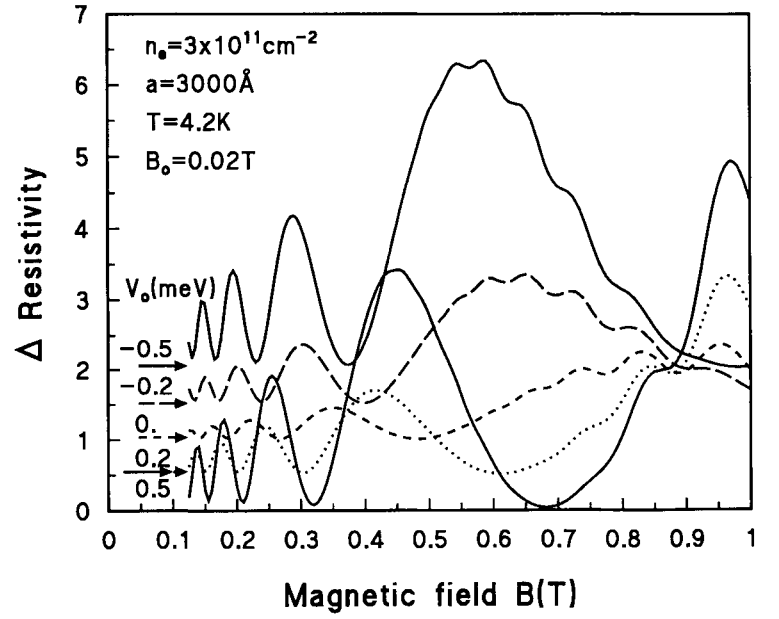


Fig. 22. Change of the magnetoresistance when magnetic and electric in-phase modulations are present for $B_0 = 0.02$ T and for different strengths of the electric modulation. The different curves are shifted upwards for clarity.

altered as shown in Figure 23. The positions of the two distinct minima shift to larger values of B/k_F (applying a gate voltage to the 2DEG changes the electron density, which is the reason why the result is plotted as a function of B/k_F). At $V_g = -250$ mV, the minima are almost at the positions with $\phi = -\frac{1}{4}$, and, consequently, the potential modulation is

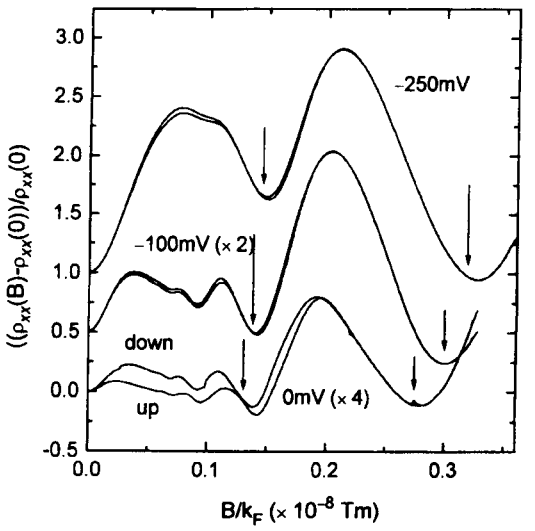


Fig. 23. Magnetoresistance for a 1D magnetic modulation for different values of the gate bias V_g. The arrows indicate the calculated positions of the minima. The curves are offset for clarity. (Source: Reprinted from [69], with permission from Elsevier Science.)

almost purely electric. Increasing the gate voltage shifts the position of the minima to a lower field because of the increase of the phase factor (ϕ) toward $\frac{1}{2}$, which is the value for the pure magnetic modulated case. Iye et al. [69] estimated that the magnetic modulation amplitude is $B_0 \approx 13$ mT at $B = 0.254$ T on the down-sweep. Similarly, they estimated that the electric potential modulation is 0.31, 0.85, and 1.8 meV for $V_g = 0$, -100, and -250 mV, respectively.

6.2.2. Out-of-Phase Modulations

If light is shined on top of a magnetically modulated heterostructure, the light pulses will ionize DX centers in the AlGaAs layer between the gates (e.g., strips of magnetic materials) where $B_0 = 0$. This will create an *electric* modulation $\pi/2$ *out of phase* with the *magnetic* one. Assuming that the *electric* modulation of the gates is much smaller than that due to the light, we are led to consider transport in the presence of the two modulations that are $\pi/2$ *out of phase* [87].

We take the same *electric* modulation $V_0 \cos(Kx)$ and assume a *magnetic* one given by $B(x) = B + B_0 \sin(Kx)$. To first order in V_0 and B_0, the eigenvalue E_{nk_y} and velocity v_y are given by

$$E_{nk_y} = \left(n + \frac{1}{2}\right)\hbar\omega_c + \hbar\omega_0 G_n(u)\sin(Kx_0) + V_0 F_n(u)\cos(Kx_0) \tag{52}$$

and

$$v_y = -\left(\frac{2u}{\hbar K}\right)\left[\hbar\omega_0 G_n(u)\cos(Kx_0) + V_0 F_n(u)\sin(Kx_0)\right] \tag{53}$$

respectively. These apparently smooth changes can have important consequences for transport. For instance, the combined bandwidth at the Fermi energy is now equal to

$$2V_0\sqrt{\frac{2}{\pi K R_c}}\sqrt{1 + \left(\delta^{-2} - 1\right)\sin^2\left(\frac{2\pi R_c}{a} - \frac{\pi}{4}\right)} \tag{54}$$

If $\delta = \pm 1$, the bandwidth no longer oscillates as a function of the magnetic field; that is, the Weiss oscillations are washed out.

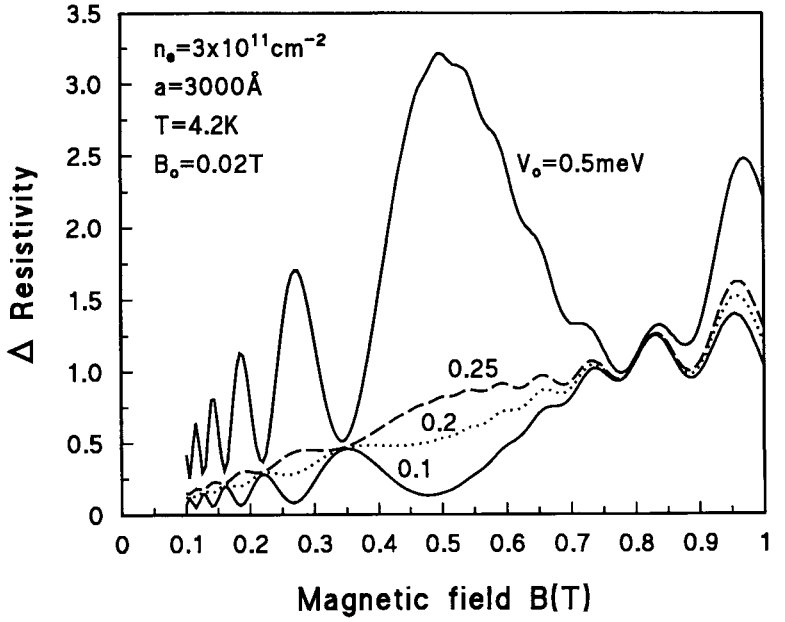


Fig. 24. Increase of the magnetoresistance when magnetic and electric out-of-phase modulations are present for different values of the strength of the electric modulation.

The result for the diffusion contribution reads

$$\sigma_{yy}^{\mathrm{dif}} = \frac{e^2}{h}\frac{2\pi^2\tau}{\hbar}\frac{l^2}{a^2}\sum_n \left\{\left[V_0 F_n(u)\right]^2 + \left[\hbar\omega_0 G_n(u)\right]^2\right\}\left(-\frac{\partial f(E)}{\partial E}\right)_{E=E_n} \tag{55}$$

There is no cross term involving the product $\hbar\omega_0 V_0$ in Eq. (55), as expected from Eqs. (44) and (53), because the integral over k_y vanishes for this term if we neglect the very weak k_y dependence of the argument of the Fermi functions.

The asymptotic expression for $\sigma_{yy}^{\mathrm{dif}}$ is

$$\frac{\sigma_{yy}^{\mathrm{dif}}}{\sigma_0} = \frac{\hbar\omega_0}{E_{\mathrm{F}}}\frac{\hbar\omega_0}{\hbar\omega_{\mathrm{c}}}\frac{ak_{\mathrm{F}}}{2\pi^2}\left\{G + \delta^2 F - 2\exp\left(\frac{-\pi}{\omega_{\mathrm{c}}\tau_{\mathrm{f}}}\right)A\left(\frac{T}{T_{\mathrm{c}}}\right)\cos\left(\frac{2\pi E_{\mathrm{F}}}{\hbar\omega_{\mathrm{c}}}\right)D\right\} \tag{56}$$

where

$$D = \delta^2 + \left(\delta^2 - 1\right)\sin^2\left(\frac{2\pi R_{\mathrm{c}}}{a} - \frac{\pi}{4}\right) \tag{57}$$

G is given by Eq. (48) and F by Eq. (48) after replacing $\sin^2(\,)$ by $\cos^2(\,)$. Comparing Eq. (56) with Eq. (51), we see that changing δ does not change the position of the extrema of $\Delta\rho$ as a function of B because the phase factor ϕ is absent from Eq. (56). This is illustrated in Figure 24 where $\Delta\rho$ is plotted as a function of B for $B_0 = 0.02$ T with variable V_0. For the upper two curves we have $\delta > 1$, whereas, for the lower two curves, δ is smaller than 1. This results in an *antiphase* between the two groups of curves and reflects the corresponding behavior of the bandwidth as given by Eq. (54).

6.3. Magnetic Minibands

The electronic band structure in a periodic magnetic field with zero average was investigated by several authors. Ibrahim and Peeters [96] calculated the energy spectrum of a periodic array of a delta function magnetic field oscillating in sign, which was generalized in [97] to an array with a more general unit cell. The energy spectrum and the conductivity

through sinusoidal [5, 98] and different periodic magnetic fields profiles was studied in [5]. Ballistic quantum transport through a periodic alternating step magnetic field profile and through a sinusoidal magnetic field structure was investigated in [99] and through a quasi-periodic magnetic superlattice in [100]. The surface states of a lateral magnetic superlattice were calculated in [101].

6.3.1. Periodic Sinusoidal Magnetic Fields

Directing the magnetic field more and more in plane reduces the background component (B) and enhances the modulation component (B_0). In the limit of $B = 0$, we have a pure periodic magnetic field with zero average. As an example of such a case, consider the physical system depicted in Figure 3. The magnetic field profile in the plane of the 2DEG is sinusoidal when the distance between the 2DEG and the ferromagnetic thin film is sufficiently large (see dotted curve in Fig. 3b). In such a case, only the first term of the Fourier series is important. In this subsection, we study the magnetic field profile [5, 98, 102]:

$$\frac{B(x)}{B_0} = \sin\left(\frac{2\pi x}{l}\right) \tag{58}$$

which has the corresponding vector potential (Fig. 25)

$$\frac{A(x)}{A_0} = -\frac{l}{2\pi}\cos\left(\frac{2\pi x}{l}\right) \tag{59}$$

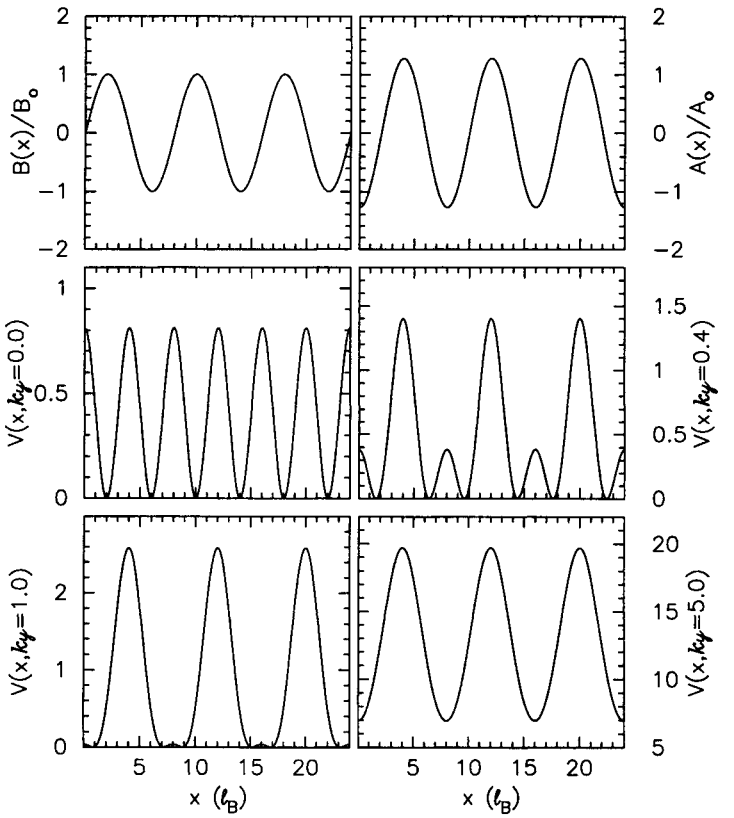


Fig. 25. Profiles for the magnetic field, the vector potential, and the effective potential for different values of k_y in the case of a sinusoidal magnetic field.

and which leads to the following Schrödinger equation:

$$\left\{\frac{d^2}{dx^2}+2E-\left[k_y-\frac{l}{2\pi}\cos\left(\frac{2\pi x}{l}\right)\right]^2\right\}\psi(x)=0 \tag{60}$$

The profiles for $B(x)$ and $A(x)$ are depicted in Figure 25 together with the effective potential for different k_y values. When solving the Schrödinger equation, we can restrict ourselves to one period and impose periodic boundary conditions. The potential profile $V(x,k_y)$ is shown in Figure 25 and satisfies the symmetry relation $V(x,k_y)=V(x+l/2,-k_y)$.

After making the substitutions $\theta=\pi x/l$, $\omega=(l/\pi)^2$, $\rho=lk_y/\pi$, and $\eta=(l/\pi)^2(2E-k_y^2-1/4)$, the preceding equation is cast into the following form:

$$\left\{\frac{d^2}{d\theta^2}+\left(\eta+\left(\frac{\omega^2}{8}\right)+\omega\rho\cos(2\theta)-\left(\frac{\omega^2}{8}\right)\cos(4\theta)\right)\right\}\psi(\theta)=0 \tag{61}$$

which is the Wittaker–Hill equation. It is interesting to note that, in the case $k_y=0$, Eq. (61) reduces to Mathieu's equation with period $l/2$.

The numerical solution of Eq. (61) for E versus k_y is shown in Figure 26 for $l=8$ and in the inset for a larger period $l=16$. To understand the energy spectrum, we show in Figure 9 the potential $V(x,k_y)$ for different k_y values. First, note that $V(x,k_y)=V(x+l/2,-k_y)$ results in spatially separated motions for the $+k_y$ and $-k_y$ electrons moving with $E<V_{\max}$. For $k_y=0$, the profile for $V(x,k_y)$ (see Fig. 25) is a periodic array of harmonic-like oscillators with finite depth and period $l/2$. In this case, the first Brillouin zone (FBZ) edge is at $k=2\pi/l$ and gaps in the spectrum appear only at $k=2n\pi/l$ where n is the band index. When k_y takes values different from zero, the periodicity of $V(x,k_y)$ becomes twice as large and equals l and, consequently, the FBZ edge becomes $k=\pi/l$ and the

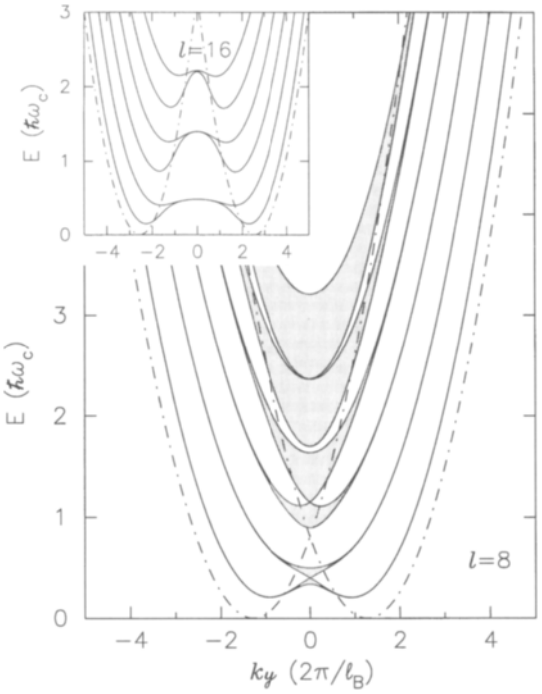


Fig. 26. Energy versus k_y dispersion relation for a single 2D electron in the presence of a sinusoidal magnetic field modulation with period $l=8$ and $l=16$ (inset). The shaded regions are the lowest six energy bands. The dash-dotted curves are the maximum and minimum values of the effective potential $V(x,k_y)$.

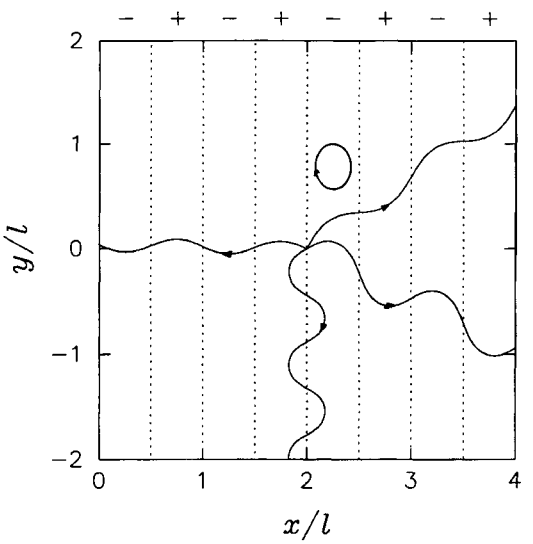


Fig. 27. Possible classical trajectories with the same initial position but different initial velocities for the magnetic field model of Figure 25.

number of energy bands and gaps doubles. The bands with energy below the barrier height (the dash-dotted curves in Fig. 26 indicate the bottom and top of the potential profile), that is, $E < V_{\max}$, correspond to open orbits traveling along the y direction and oscillating around the boundary separating the two magnetic strips, which are also called *snake orbits*. Electrons at adjacent boundaries move in the opposite y direction. The 1D states below $V_{\max}$ are similar to the so-called magnetoelectric states. Here, also, the electron motion along the $\pm y$ directions are spatially separated by half a period $l/2$.

In Figure 27, examples of the three kinds of possible classical orbits are given: (1) 0D cyclotron motion, which occurs when the electron energy is sufficiently small such that its cyclotron diameter is less than the width of the magnetic strip (because of the spatial variation of the magnetic field, the orbit in this case is not a circle); (2) 1D drift parallel to the magnetic strips for states with the center of their cyclotron orbit near the interface between the $+B_0$ and $-B_0$ regions, called snake orbits; and (3) 2D motion in the plane when the electron energy is larger than the magnetic field barriers, which results in a cyclotron diameter larger than the width of the magnetic strips.

The zero-temperature density of states (DOS) for the system considered is calculated by numerically integrating the inverse of the magnitude of the energy gradient in momentum space along the constant energy contours at the Fermi energy and within the first Brillouin zone

$$\frac{D(E)}{D_0} = \frac{1}{2\pi} \sum_n \int_{S_n} \frac{dS_n}{|\nabla E_n(k)|} \tag{62}$$

where $D_0 = m^*/\pi\hbar^2$ is the DOS of the free 2DEG, n is the band index, and S_n is the constant energy contour. Spin splitting of the energy levels is neglected. The spin degeneracy is taken into account and no scattering is assumed other than the interaction with the magnetic field.

The diagonal components of the electric conductivity tensor are calculated concurrently with the DOS and along the same constant energy contours where we used the expression

$$\frac{\sigma_{ii}}{\sigma_0} = \sum_n \int_{S_n} v_{n,i} v_{n,i} \, dS_n \tag{63}$$

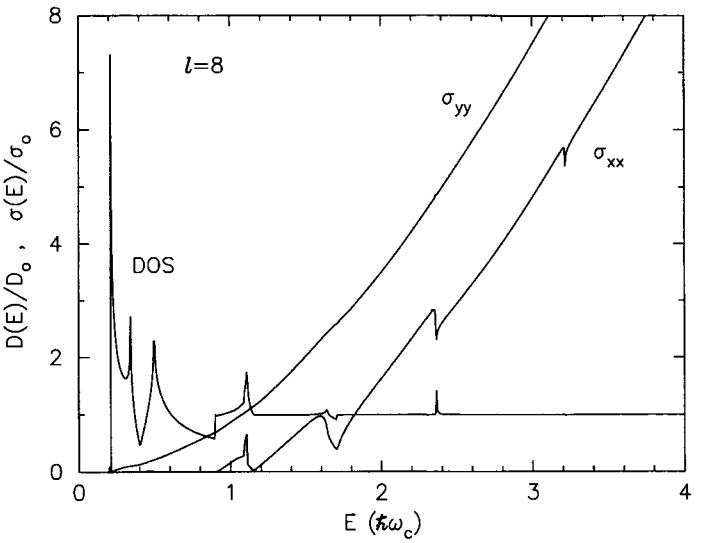


Fig. 28. Density of states (DOS) and the diagonal components of the electric conductivity tensor versus Fermi energy for 2D electrons moving in a sinusoidal magnetic field.

where $v_{n,i} = \partial E_n / \partial k_i$ is the drift velocity and σ_0 is the Drude conductivity of the free 2DEG. This formula is valid for a diffusive type of transport at zero temperature. Notice that because there is no net magnetic field, that is, $\langle B \rangle = 0$, we do not expect any Hall resistance and, consequently, $\sigma_{xy} = 0$.

The density of states (DOS) (Fig. 28) is on the average the one of a free 2DEG except for singular points (1) resulting from the edges of the minibands, which occur for $k_x = (2n+1)\pi/l, n = 0, 1, 2, 3, \ldots$; and (2) resulting from the local minima in the energy spectrum (see Fig. 26), which occur for small k_y values where $v_y = 0$. At these points in momentum space, the conditions for Bragg reflection are met for motion in the x direction and the average velocity in the y direction is zero. Electrons with these energies and wavevectors form standing waves with zero average velocity. This effect results in dips in the σ_{xx} conductivity (Fig. 28). Note that no such clear structure is apparent in the σ_{yy} conductivity because motion in the y direction does not exhibit this Bragg reflection. The σ_{yy} conductivity is obviously the least affected by the presence of the magnetic field modulations along the x direction, because there are always states available for motion along the y direction regardless of the value of the Fermi energy. Furthermore, the number of these states increases with increasing energy. In contrast, the miniband structure has a pronounced effect on the σ_{xx} component owing to the existence of energy gaps for motion along the x direction, where σ_{xx} shows downward dips corresponding to the edges of the Brillouin zone where $v_x \approx 0$. The magnitude of σ_{xx} does not become appreciable until the Fermi energy is near or above the magnetic potential barrier at $k_y = 0$. The σ_{xx} is always less than σ_{yy} even for high energies. The reason is that the effect of Bragg reflections, which does not influence σ_{yy}, persists up to high energies—a purely quantum mechanical effect.

6.3.2. Snakelike Orbits

The effects of these snake orbits on the magnetotransport were investigated experimentally in [72]. They measured the magnetoresistance for different angles θ between the external magnetic field and the 2DEG plane, which is shown in Figure 29. The results are plotted as a function of the z component of the applied field B_z, which is the component that affects the motion of the electrons in the 2DEG. The most striking feature is the appearance of

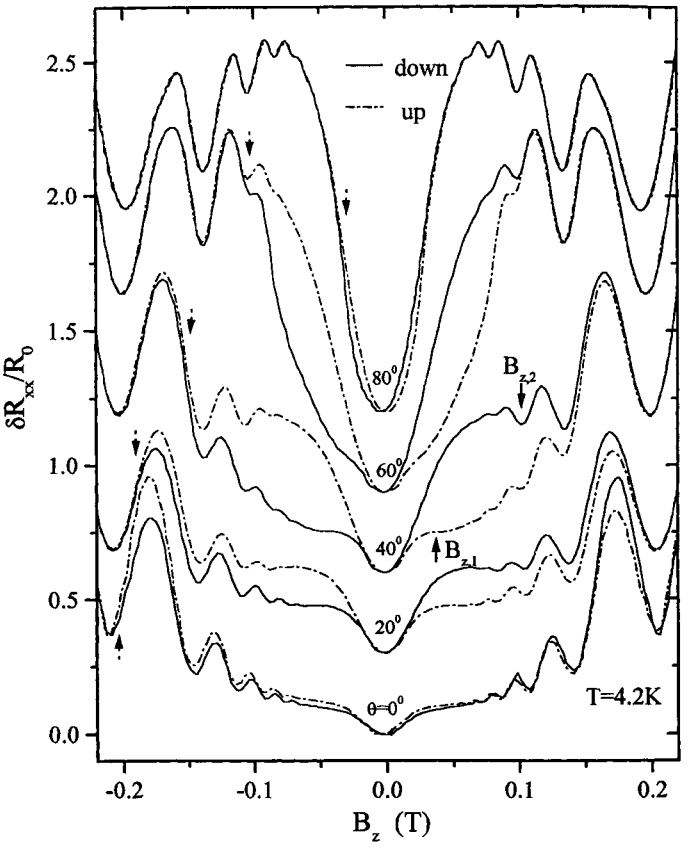


Fig. 29. Low-field magnetoresistance at 4 K as a function of the magnetic field component perpendicular to the 2DEG for different tilt angles θ of the magnetic field. (Source: Reprinted with permission from [72]. © 1997 American Physical Society.)

a positive low-field magnetoresistance that becomes much stronger and extends to larger B_z as θ increases. R_{xx} increases by a factor of up to approximately 2 on application of a B_z of only 50 mT. This can be understood from Figure 28 where increasing the magnetic field implies reducing $(E = E_F)/\hbar\omega_c$, which results in a decrease of the conductivity and, consequently, an increase of the resistance. The strong positive magnetoresistance is still observable well above 200 K, which suggests its semiclassical origin.

The observed low-field magnetoresistance can be understood in terms of channeling of electrons along lines of zero magnetic field within the sample. These are the so-called snake orbits discussed previously. In this situation, two kinds of electron states coexist. Electrons that have a sufficiently large initial velocity component perpendicular to the magnetic strips will propagate across the sample in the same direction they would have in the absence of the modulation. Electrons with smaller initial velocity components cannot pass through the magnetic barriers and will be channeled in the y direction along snakelike orbits centered on the lines of zero B.

The guiding center drift correction to the D_{yy} diffusion coefficient [58] leads to a magnetoresistance

$$\frac{\Delta R_{xx}}{R_0} = 2(\omega_c\tau)^2\frac{\langle v_d^2\rangle}{v_F^2} \tag{64}$$

where τ is the elastic scattering time and $\langle v_d^2\rangle$ is the appropriate average of the square drift velocity. This average was calculated [72] by numerically integrating the classical equation

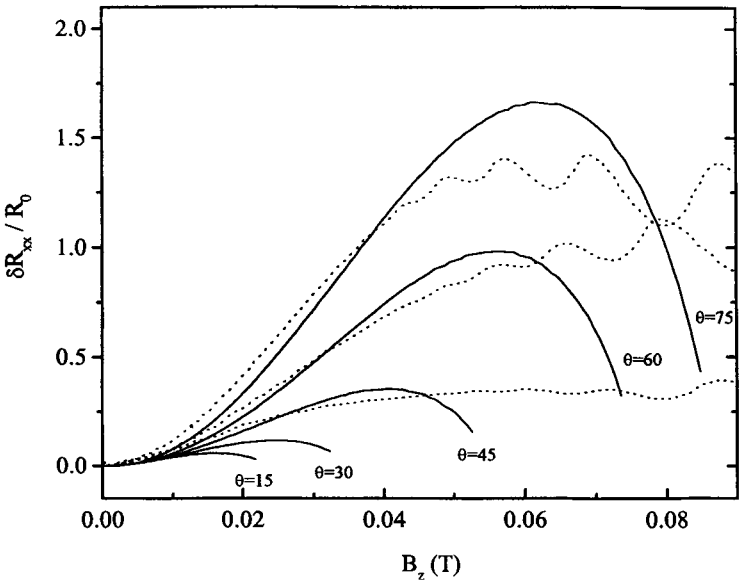


Fig. 30. Measured positive magnetoresistance (dotted curves) for different tilt angles of the magnetic field (see Fig. 29) as compared to the calculated contribution (solid curves) from the different classical orbits. (Source: Reprinted with permission from [72]. © 1997 American Physical Society.)

of motion for electrons traveling through the magnetic profiles. The numerical results are compared with the experimental results in Figure 30, and the dependence on the tilt angle is in good agreement with the experimental results, proving the existence of 1D electron states propagating along lines of zero magnetic field, that is, the snakelike orbits.

7. TWO-DIMENSIONAL MAGNETIC MODULATION

7.1. Periodic Two-Dimensional Modulation

The energy spectrum of electrons moving in a 2D lattice in the presence of a perpendicular homogeneous magnetic field is determined by fascinating commensurability effects. When the flux through a unit cell of the lattice $\Phi = Ba^2$ is a rational multiple of the flux quantum $\Phi_0 = ch/e$, that is, $\Phi/\Phi_0 = p/q$, then the resulting energy spectrum consists of broadened Landau levels, each having the same internal structure, which is called the Hofstadter butterfly [103] when plotted versus the inverse flux ratio. The width of the Landau bands oscillates as a function of the Landau quantum number and the flux ratio Φ/Φ_0. So far, this gap structure has not been observed directly in experiments. This band structure was investigated theoretically by several groups [104–108]. Recently, Gerhardts et al. [109] investigated this Hofstadter butterfly for the mixed 2D periodic electrostatic and magnetic modulation problem where they included higher harmonics and they found that the overall gap structure is similar to the one found in [103]. The classical dynamics was investigated in [110, 111]. The magnetoresitance of electrons in a periodic 2D magnetic field for different shapes of the magnetic field profile was investigated in [88, 90].

The experimental investigation of this system is still in its infancy. A 2D array of magnetic dysprosium dots on top of a GaAs/AlGaAs heterostructure was investigated in [74, 75]. The Dy micromagnets had a typical diameter of approximately 200 nm and a height of approximately 200 nm with a lattice period of $a = 500$ nm. No effects associated with the Hofstadter energy spectrum could be identified. The magnetoresistance was found [74] to exhibit commensurability oscillations very similar to those found in the case

of 1D modulation (see the previous section) with minima in the magnetoresistance occuring near $2R_c/a = n + \frac{1}{2}$ with n an integer. Also effects resulting from a strain-induced electrostatic periodic potential were observed [75]. By rotating the magnetization of the Dy dots, it was possible to induce a phase change of the magnetic stray field pattern with respect to the strain-induced electrostatic potential [75, 82].

7.2. A Random Array of Identical Magnetic Disks

Here we consider a new system in which electrons are scattered by a random array of identical circular magnetic field profiles that are created by magnetic disks located a certain distance from a 2DEG. This problem is different from the magnetic flux tube problem that is encountered when a type II superconducting film is deposited on top of a heterostructure [112]. The essential difference is that in the present problem the local inhomogeneous magnetic fields have zero average magnetic field strength. Here the circular magnetic field profiles have an inner core with a magnetic field that is opposite to the outer part in such a way that the average magnetic field strength is zero.

Recently, Van Roy et al. [6, 113] successfully fabricated a grating structure of magnetic material with a pattern of magnetic dots and antidots with period of about 600 nm. A similar structure with Dy micromagnets on top of a GaAs/AlGaAs heterostructure was realized by Ye et al. [82]. An alternative approach was demonstrated by McCord and Awschalom [114], who directly deposited nanometer-scale magnetic dots using a scanning tunneling microscope. They fabricated magnetic dots of diameter ranging from 10 to 30 nm and heights from 30 to 100 nm.

The perpendicular magnetic field component produced by such a ferromagnetic disk of radius R with magnetic moment along the z direction is shown in Figure 31a for different distances between the 2DEG and the ferromagnetic disk. The corresponding vector potential is inserted into the Schrödinger equation. The radial equation contains an effective potential $V(m, \rho)$ [see Eq. (33)], which is depicted in Figure 31b for the case of $z/R = 0.02$. It is clear that such a potential can only have scattered states. The scattering properties are described in terms of a phase shift δ_m, which is determined by solving the Schrödinger equation numerically. The zero-temperature magnetoresistance and Hall resistance are determined by (see, e.g., [115])

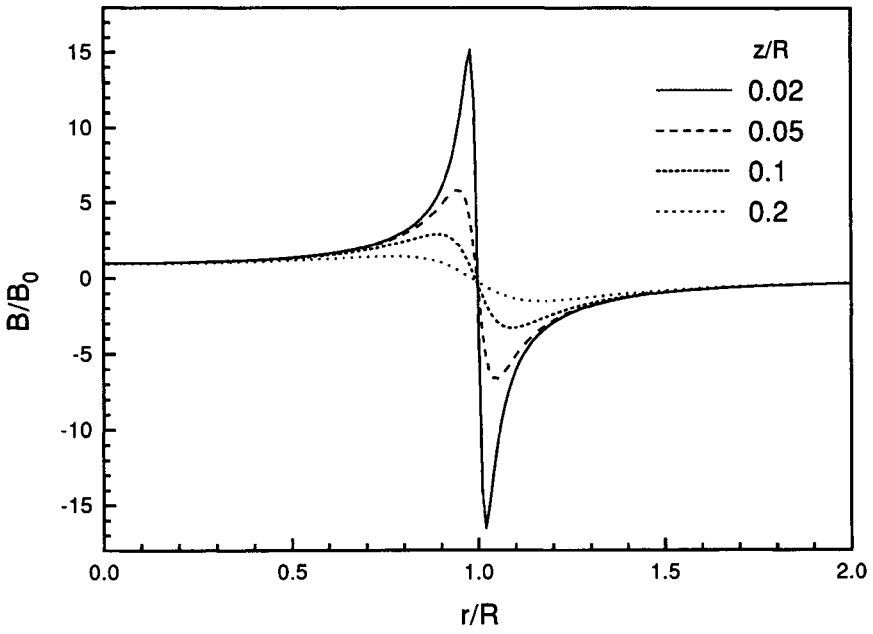
$$\frac{R_{xx}}{R_0} = 2\sum_m \sin^2(\delta_m - \delta_{m+1}) \tag{65}$$

and

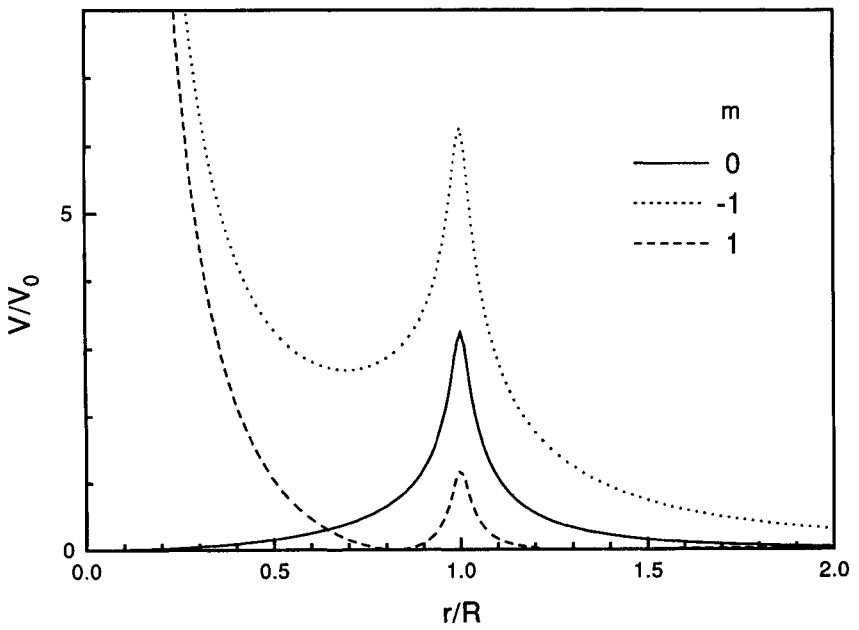
$$\frac{R_{xy}}{R_0} = \sum_m \sin\bigl(2(\delta_m - \delta_{m+1})\bigr) \tag{66}$$

where $R_0 = (\hbar/e^2)(n_0/n)$ with n_0 the density of ferromagnetic disks and n is the electron density. The numerical results are shown in Figure 32 for $b = (e/\hbar c)Ma\pi R = 2$, where M is the magnetization of the ferromagnetic disk and $z/R = 0.1$.

Notice that for small Fermi energies R_{xy} increases with k_F as is also the case when a constant magnetic field is present. This implies that the electrons are only able to probe the outer part of the magnetic field profile of the magnetic disk. For large k_F values, the electrons have sufficient energy such that they are able to penetrate the inner part of the magnetic field profile where the magnetic field is in the opposite direction. As a consequence, the average magnetic field felt by the electrons diminishes, which results in a reduction of R_{xy}. The oscillatory structure is a consequence of quantum mechanical resonances, which are a consequence of the quasi-bound states in the potential $V(m, \rho)$. Note also that at resonance R_{xy} is reduced while R_{xx} exhibits a local maximum. The reason for the different behavior is that R_{xx} measures the actual resistance while R_{xy} is a measure of the Lorentz force.



(a)



(b)

Fig. 31. (a) Magnetic field profile at a distance z under a ferromagnetic disk of radius R and (b) effective radial potential (in units of $V_0 = M/m_0h^2$) for $z/R = 0.02$ and different values of the angular momentum m.

7.3. Random Magnetic Fields

The problem of electrons moving in a 2D static random magnetic field has generated great experimental [60–63, 79, 80, 112, 116–120] and theoretical [121–123] interest. It is now understood to be distinctly different from transport in systems with ordinary potential dis-

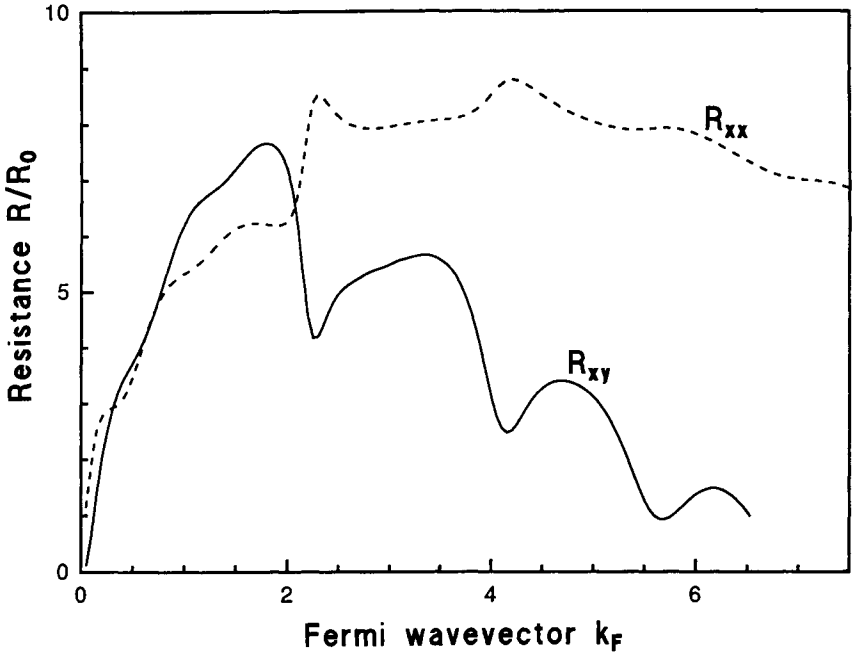


Fig. 32. Magnetoresistance and Hall resistance of a 2DEG under the influence of a random area of magnetic field profiles produced by ferromagnetic disks.

order. This problem is closely related to the 2D quantum Hall system near half integer filling factor [124–127] and the gauge field description of the high T_c superconductivity problem [128–131]. Both problems can be mapped into a system of charged particles moving in the background of a random magnetic field. The essential issue in the theoretical studies is to determine how the random magnetic field affects the transport properties. The localization of electrons in random magnetic fields is still a controversial issue. In principle, all states of a 2D system are exponentially localized according to the scaling theory of localization [132]. But the presence of a magnetic field that destroys time-reversal symmetry makes a stand against localization. Perturbation renormalization group calculations show that all states remain localized [133, 134] but numerical simulations have not led to a definite conclusion (see, e.g., [135, 136]). It is generally accepted that, except for weak localization effects [137] yielding small quantum corrections to the magnetoresistance at weak fields and at low temperatures, the semiclassical approach is an adequate framework when the typical length over which the random magnetic field varies is much larger than the Fermi wavelength of the electrons. In [138, 139], the effect of the random magnetic field was included in the collision term of the Boltzmann equation. A different approach in which the random magnetic field was included in the driving force of the transport equation was followed in [140] (see also [123]) using perturbation theory. Khveshchenko [141] analyzed the electron motion in a random magnetic field with long correlation length in the absence of impurities and derived a nonperturbative result based on an eikonal approximation. Calvo [122] used an ergodic hypothesis that allowed him to study the random magnetic field problem for arbitrary correlation length and in both the diffusive and ballistic regime.

Random magnetic fields in a 2DEG have been realized by using stochastically distributed vortices in a type II superconducting film [60–63, 112, 142–145], superconducting grains [118, 119], 2DEG grown on substrates with prepatterned submicrometer dimples [79, 80], rough macroscopic magnets [116, 117], and a random distribution of mesoscopic micromagnets [75]. The latter was achieved by depositing dysprosium dots

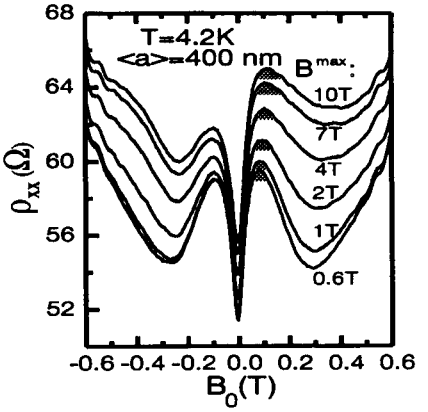


Fig. 33. Magnetoresistance of a 2DEG resulting from a random area of Dy disks with average separation $\langle a \rangle = 400$ nm as a function of the external magnetic field B_0 for different strengths of the magnetization of the disks that are determined by the conditioning field B_{max}. The asymmetry is due to the hysteresis loops of the micromagnets. (Source: Reprinted with permission from [75].)

with submicrometer diameters randomly on top of a high-mobility GaAs/AlGaAs heterojunction. This system is essentially different from the flux tube system because now the local inhomogeneous magnetic fields have zero average field strength. The circular magnetic field profiles of the dot have an inner core with a magnetic field that is opposite to the outer part in such a way that the average magnetic field strength is zero.

As a typical experiment, we consider the results of Ye et al. [75]. They started from a high-mobility GaAs/AlGaAs heterostructure ($\mu = 1.4 \times 10^6$ cm^2/V s, $n_e = 2.2 \times 10^{11}$ cm^{-2} at $T = 4.2$ K) in which the 2DEG was located approximately 100 nm underneath the sample surface. A 10-nm-thick NiCr film was evaporated on top of the device which defines an equipotential plane to the 2DEG. A random distribution of Dy dots with height 200 nm and with different density was defined by electron beam lithography on top of the NiCr gate. In Figure 33, the magnetoresistance of the 2DEG at 4.2 K is displayed for a random distribution of Dy dots with an average interparticle distance of $\langle a \rangle = 400$ nm. The different traces correspond to different magnitudes of the magnetization of the micromagnets. The random magnetic field is probably accompanied by a strain-induced electrostatic random potential as discussed before for the periodic modulated magnetic field case. These random magnetic fields give rise to (1) an increase of the zero magnetic field resistance and (2) a pronounced positive magnetoresistance, both of which increase with increasing strength of the magnetization of the micromagnets. Similar behavior has been found by others in other 2DEGs with random magnetic fields.

8. HALL EFFECT DEVICES

When a magnetic field is applied to a metallic system that carries a current, a Hall voltage develops in the direction perpendicular to the magnetic field and the current because of the Lorentz force. This phenomenon is called the Hall effect [146] and has been used very successfully to obtain information on the properties of the charge carriers, for example, the sign and the density of those carriers. In most previous investigations of the Hall effect, the applied magnetic field is uniform and its strength is known. In [112, 147–150], the Hall effect of a known 2DEG was used as a probe of the magnetic field. In such a case, the experimental system consists of a microfabricated Hall bar in which an inhomogeneous magnetic field is piercing through the Hall cross. This inhomogeneous magnetic

result, for example, from magnetic or superconducting clusters [112, 149] that are placed on top of the Hall bar.

Such Hall probes have become increasingly popular as local magnetometers for superconducting and ferromagnetic materials because of their (1) noninvasive nature; (2) high magnetic field sensitivity; (3) very small active region, that is, the cross region of the Hall bar, which, using modern microfabrication techniques, can be of submicrometer dimensions; and (4) broad temperature and magnetic field region over which they can be used.

In [151–153], a quantitative theory was presented that relates the measured Hall voltage to the local flux through the Hall probe. This is needed in order to interpret the experimental data obtained from the Hall magnetometer and to understand the mechanism behind the functioning of Hall devices. Such a theory was given in the ballistic regime [152], which is applicable at low temperatures (up to liquid nitrogen temperatures) and for small Hall probes, and in the diffusive regime [148, 153], which is more applicable for larger Hall crosses and/or for higher temperatures. We find that in the ballistic regime the relation between the measured Hall voltage and the probed inhomogeneous profile is able to provide much more detailed information than the equivalent system in the diffusive regime.

In this section, we investigate the effect of micrometer and submicrometer spatial variations of the magnetic field on a 2DEG. Knowing the response of a 2DEG to these magnetic field inhomogeneities is an important fundamental research problem in its own right but, in addition, has direct consequences on the development of microelectronic devices and applications that, in recent years, have witnessed a growing interest in exploiting the versatility and added functionality of the Lorentz force on a submicrometer scale. For instance, (i) a magnetoelectronic device in the shape of a Hall cross was recently shown to have the potential of operating as a bistable memory cell or logic gate component, (ii) with Hall probe microscopy it is possible to observe the dynamics of a single flux vortex and domain walls in superconducting films and magnetic materials, and (iii) Hall components are used as magnetic field sensors for distance and speed detection in brushless engines such as used in floppy and CD-ROM disc drives.

8.1. Ballistic Hall Magnetometry

In the inset of Figure 34a, we show the system under study, which consists of a Hall bar with four identical leads and a circular magnetic field profile situated in the middle of the cross junction. As an example, we consider two kinds of circular magnetic field profiles. The first profile is a superconducting disk in an external magnetic field. Because of the Meissner effect, the magnetic field will be expelled from the superconducting disk. We model the field distribution underneath the disk as zero inside a region of radius d, and constant outside it. In this way, we neglect the overshoot of the magnetic field at the edge of the disk, which is sensitive to several system parameters such as the thickness of the superconducting disk and the distance of the disk from the 2DEG. The second profile is a ferromagnetic disk that we model by a magnetic dipole placed a distance z_0 above the cross junction in the absence of an external magnetic field.

The Hall resistance is calculated numerically using the semiclassical formalism. The current in lead i is denoted by I_i, which can be expressed according to the Landauer–Büttiker formula as [20]:

$$I_i = \frac{2e}{h}\left[(N_i - R_i)\mu_i - \sum_{j\neq i} T_{ij}\mu_j\right] \tag{67}$$

where T_{ij} is the transmission probability for an electron from lead j to lead i and R_i is the reflection probability for returning back into the same lead i. In practice, these probabilities are calculated at the Fermi energy ϵ_F, and satisfy $\sum_{j\neq i} T_{ij} + R_i = N_i$, according to the condition of current conservation, where N_i is the number of propagating modes in lead i.

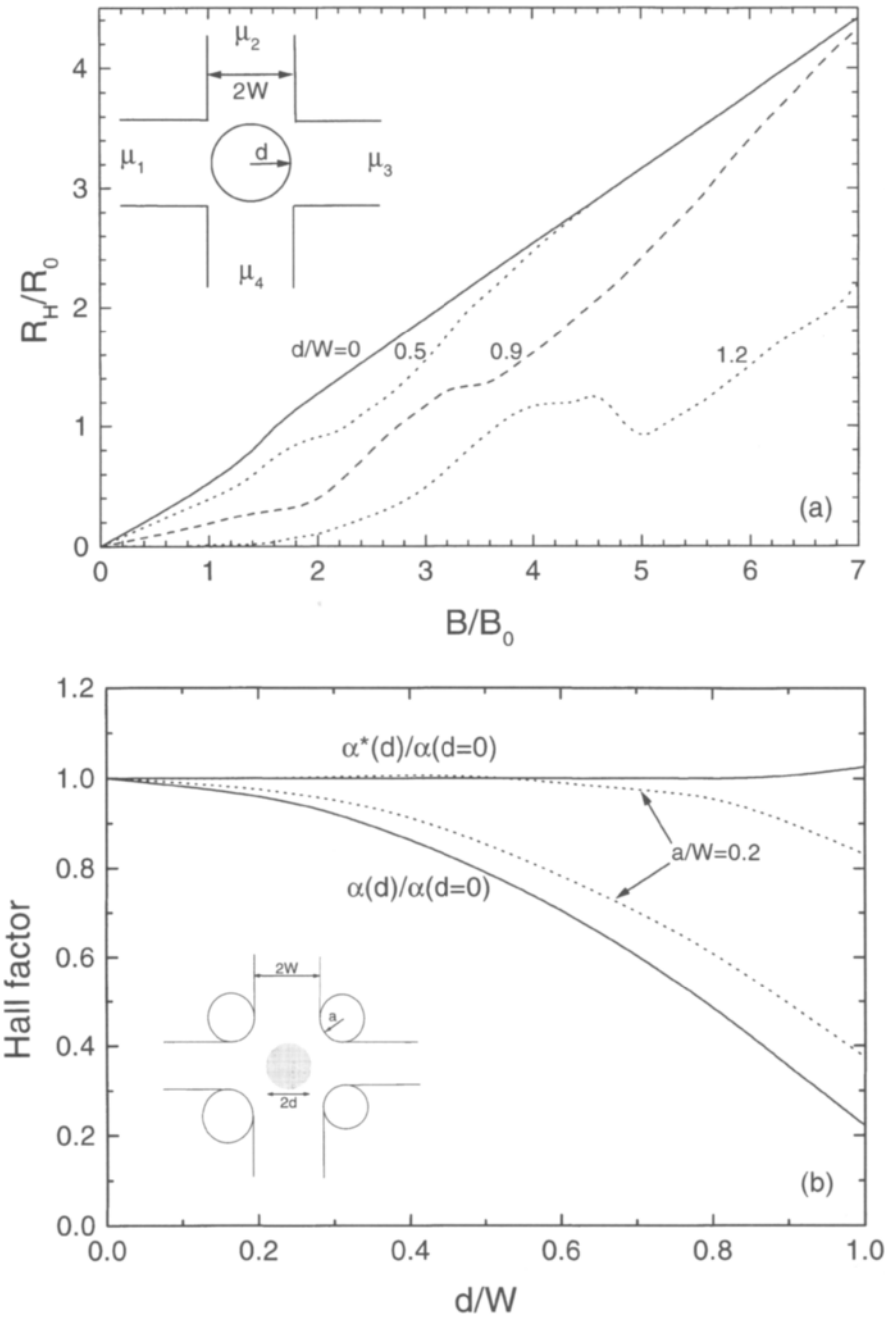


Fig. 34. (a) Hall resistance of the magnetic antidot configuration (see inset of figure) as a function of the magnetic field for different sizes (d) of the antidot. (b) Hall coefficient $\alpha = R_H/B$ in the low-magnetic-field region as a function of the disk radius (lower curves). The upper curves are obtained from $\alpha^* = R_H/\langle B\rangle$, where $\langle B\rangle$ is the average magnetic field in the junction. The dotted curves are the results for a cross with rounded corners (see inset of figure).

For the four-lead Hall geometry with identical leads, the Hall resistance R_H can be found from Eq. (67) by setting $I_1 = -I_3 = I$ and $I_2 = I_4 = 0$ and results in

$$R_H = \frac{(\mu_2 - \mu_4)/e}{I} = \frac{h}{2e^2}\frac{T_{21}^2 - T_{41}^2}{Z} \tag{68}$$

where $Z = [T_{21}^2 + T_{41}^2 + 2T_{31}(T_{31} + T_{21} + T_{41})](T_{21} + T_{41})$. For the asymmetric Hall system with either unidentical leads or asymmetric magnetic field in the cross junction, the simple formula (68) breaks down. In this case, the Hall and bend resistances should be solved from Eq. (67) by setting the same boundary conditions for the currents as used in the derivation of Eq. (68).

To obtain the probabilities T_{ij} and R_i, we follow the semiclassical approach developed by Beenakker and van Houten [154]. Thus, we neglect quantum interference effects, which are expected not to be important when $\lambda_F \ll d, W$, where λ_F is the Fermi wavelength, d the size of the magnetic field inhomogeneity, and W the width of the Hall probes. In our numerical simulation, we inject a large number of electrons ($N_e \geqslant 10^5$) toward the junction through lead 1, and follow their classical trajectories to determine the probabilities $T_{j1} = N_j/N_e$, where N_j is the number of electrons collected in lead j. Note that for the case of unidentical leads or asymmetric magnetic field profile, similar procedures should be followed for each of the four leads. The electrons are injected uniformly over lead 1, with a Fermi velocity $v_F = \sqrt{2\epsilon_F/m}$ and an angular distribution $P(\theta) = \frac{1}{2}\cos\theta$, where $\theta \in (-\pi/2, \pi/2)$ is the injecting angle with respect to the channel axis.

In the following, we will express the magnetic field in units of $B_0 = mv_F/2eW$ and the resistance in $R_0 = (h/2e^2)\pi/2k_FW$, where W is the half-width of the lead, m the mass of the electron, $k_F = (2m\epsilon_F/\hbar^2)^{1/2}$ the Fermi wavevector, and $v_F = \hbar k_F/m$ the Fermi velocity. For electrons moving in GaAs ($m = 0.067m_e$) and for a typical channel width of $2W = 1$ μm and a Fermi energy of $\epsilon_F = 10$ meV ($n_e = 2.8 \times 10^{11}$ cm^{-2}), we obtain $B_0 = 0.087$ T and $R_0 = 0.308$ kΩ.

First, we discuss the magnetic field profile that models the situation with a superconducting disk above the junction, which may be called a *magnetic antidot*. In Figure 34a, we show the Hall resistance as a function of the external applied magnetic field for different disk sizes. Notice that there exists a critical magnetic field $B_c = B_c(d)$, such that for $B > B_c$ the Hall resistance in the presence of the disk coincides with that for the homogeneous magnetic field case (i.e., $d = 0$). When $B < B_c$, the Hall resistance is sensitive to the presence of the disk. At this critical magnetic field B_c, the diameter of the cyclotron orbit, $2R_c = 2v_F/\omega_c$, equals the distance between the edge of the dot and the corner of the cross junction: $2R_c = \sqrt{2}W - d$. For $B > B_c$, the motion of the electron is determined by skipping orbits, located along the edge of the device, which do not feel the presence of the $B = 0$ region in the cross junction and the Hall resistance equals the classical 2D value: $R_H/R_0 = 2B/\pi$. We have $B_c/B_0 = 4.4, 7.8, 18.7$ for $d/W = 0.5, 0.9, 1.2$, respectively. Notice that in the absence of the magnetic antidot, that is, $d = 0$, we find $B_c/B_0 = \sqrt{2} = 1.41$, which is the field where the 2D Hall and bend resistance is recovered. For $B/B_0 \ll 1.4$, the Hall resistance is determined by the geometry of the cross [155] and for a cross with sharp corners is given by [156] $R_H/R_0 = B/2B_0$. The Hall resistance has a slope that is a factor $4/\pi = 1.27$ smaller than the classical 2D result. For $B < B_c$, the electron trajectories are only weakly bent and, consequently, they sample the $B = 0$ region.

Even in the presence of the magnetic antidot, the Hall resistance is linear for small magnetic fields (i.e., $B \ll B_c$), with a slope that decreases with the disk size, that is, with the amount of expelled magnetic flux. We analyzed the Hall factor $\alpha = R_H/B$, which is shown in Figure 34b, as a function of the disk radius (lower solid curve). α decreases with d because the average magnetic field in the cross junction decreases. Therefore, we calculate the average field in the cross junction $\langle B\rangle = [1 - \pi(d/2W)^2]B$, from which we define an effective Hall coefficient $\alpha^* = R_H/\langle B\rangle$, which is shown by the upper solid curve in Figure 34b. Notice that α^* is independent of d for $d/W < 1.0$, which indicates that for low magnetic fields the Hall resistance is completely determined by the average field in the cross region and is independent of the detailed distribution of the field. This conclusion is still true [152] (i) for a more continuous magnetic field profile such as, for example, a Gaussian; (ii) the case of asymmetric leads, that is, when the current and voltage leads have different widths; and (iii) for an off-center location of the magnetic antidot. The effect

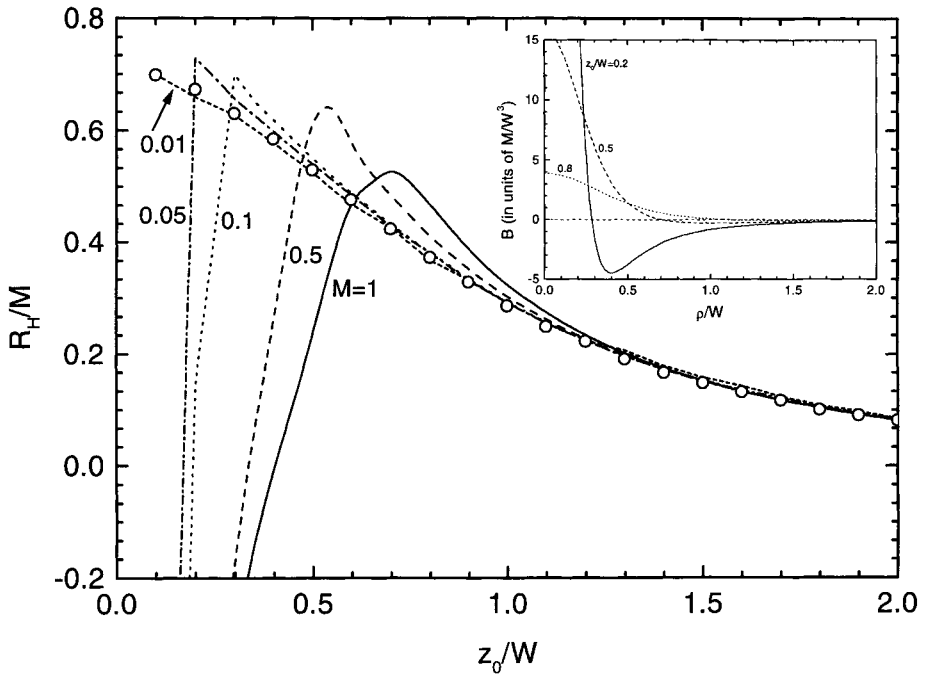


Fig. 35. Hall resistance resulting from a magnetic dipole in the center of the junction as a function of the distance (z_0) between the magnetic dipole and the 2DEG in the cross junction for different values of the magnetic moment. The dots are calculated using $R_H = \langle B \rangle / 2$ (see Fig. 34). The inset shows the magnetic field profile for the dipole for different values of z_0.

of rounding the corners of the cross junction on the Hall factor is illustrated by the dashed curves in Figure 34b. We considered circular rounded corners with radius $a/W = 0.2$. It is well known [155, 156] that rounding the corners has a very important effect on the low-magnetic-field Hall resistance but we found that even for a/W up to 0.2 the low-field Hall resistance is still determined by the average magnetic field for $d/W < 0.7$.

Next, we investigate the effect of the exact magnetic field profile on the Hall measurement. Therefore, we consider a magnetic dipole for which the component of the magnetic field perpendicular to the 2D plane is given by $B(\rho) = M(3\cos^2\theta - 1)/R^3$, where $R^2 = \rho^2 + z_0^2 = x^2 + y^2 + z_0^2$, $\cos^2\theta = z_0^2/R^2$, z_0 is the distance between the dipole and the 2D plane, and M is the dipole moment. In Figure 35, we show the scaled Hall resistance R_H/M as a function of the distance z_0 for different values of M, the strength of the dipole. Notice that, for large z_0, the Hall resistance R_H scales perfectly with M. This feature can be understood by the fact that the Hall resistance is proportional to the average magnetic field over the junction region. The result $R_H/R_0 = \langle B \rangle / 2B_0$ is shown by the open dots in Figure 35 and reproduces our numerical results. However, with decreasing z_0, the Hall resistance deviates from the preceding simple formula, because of the strongly nonuniform distribution of the magnetic field (see inset of Fig. 35). The validity range of the simple formula for R_H is determined by the maximum magnetic field in the cross junction, that is, $B(\rho = 0)$, such that the corresponding cyclotron diameter equals the width of the lead, that is, $R_c = W$, which leads to $z_0 = (2M)^{1/3}$. For $M = 0.01, 0.05, 0.1, 0.5, 1$, this gives, respectively, $z_0/W = 0.3, 0.5, 0.6, 1, 1.3$, which agrees with Figure 35. For small z_0, $B(\rho)$ has a large positive peak at the origin (see inset of Fig. 35) that is not sampled by the electrons and the Hall resistance is determined only by the negative magnetic field region, which results in a negative Hall resistance. In this regime, the Hall resistance is no longer determined completely by the average field in the cross junction.

8.2. Hall Magnetometry in the Diffusive Regime

In the diffusive regime, the approach outlined in Section 5 has to be used. Thus, the continuity equation is solved numerically using finite-difference methods subjected to the mixed boundary conditions $\phi(x, 0) = 0$ and $\phi(x, L) = V_0$ at the current contacts and the condition that the normal component of the current is zero (i.e., $\mathbf{J}_n = 0$) at all boundaries of the system other than the current contacts. In our numerical analysis, we took the length of the voltage leads to be the same as the length of the current leads of the Hall cross and each with aspect ratio one. We checked that our results are practically not altered by increasing the length of the voltage leads [153].

As in the previous subsection, we consider first a magnetic antidot with a magnetic field profile: $B(r) = B_0\theta(r - r_0)$, where r_0 is the radius of the antidot with origin at the geometrical center of the cross junction. In Figure 36, the steady-state equipotential contours in the cross-junction system for two magnetic field strengths are shown: (a) $\mu B_0 = 1$ and (b) $\mu B_0 = 10$ and for a disk radius of $r_0/W = 0.3$. The current is injected at $y/W = 0$ and leaves the system at $y/W = 3$. The zero magnetic field region (i.e., the antidot) is the white disk in the center of the Hall cross. Note that for $\mu B_0 = 10$ these contours are nearly the same as the current flow lines followed by the center coordinate of the cyclotron orbits while drifting according to the $\mathbf{E} \times \mathbf{B}$ force with drift velocity $v_d = E/B$. The Hall angle in the nonzero field region is $\theta_H = 84.3°$ owing to the finite mobility. There is a Hall voltage buildup between the voltage contacts at $x/W = 0$ and $x/W = 3$ and the potential inside the antidot region is flat; that is, the electric field inside the antidot is almost zero and, hence, there is no current inside the $B = 0$ antidot region. This flat potential region occurs because the zero field conductivity inside the antidot is larger than any of the components of the conductivity tensor outside the antidot. Consequently, the charges inside the antidot are more mobile and shorten out the potential difference inside the disk, resulting in nearly zero electric field in the antidot and a dipolar excess charge around the periphery of the antidot that screens the inside of the disk from the electric field. In Figure 36a, the Hall angle is 45° and there is still significant potential drop across the antidot, making charge flow possible through the antidot. There is an alternative physical explanation for the behavior of the equipotential contours in parts a and b of Figure 36. Because of the Lorentz force, the current flows along the edges of the 2DEG. This is more so the larger the magnetic field. At the cross junction, the current will prefer to flow along the edge of the voltage leads and in this way will avoid the central cross region and, consequently, the $B = 0$ region.

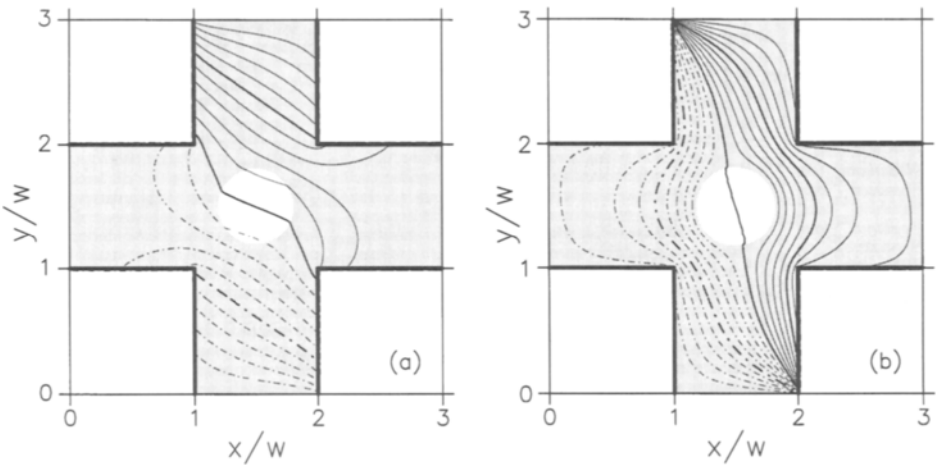


Fig. 36. Steady-state equipotential contours in the Hall junction with a magnetic antidot (white disk) in the center of the cross junction. The gray shaded region is the region of nonzero magnetic field. The radius is $r_0/W = 0.3$ and the magnetic field strength: (a) $\mu B_0 = 1$ and (b) $\mu B_0 = 10$.

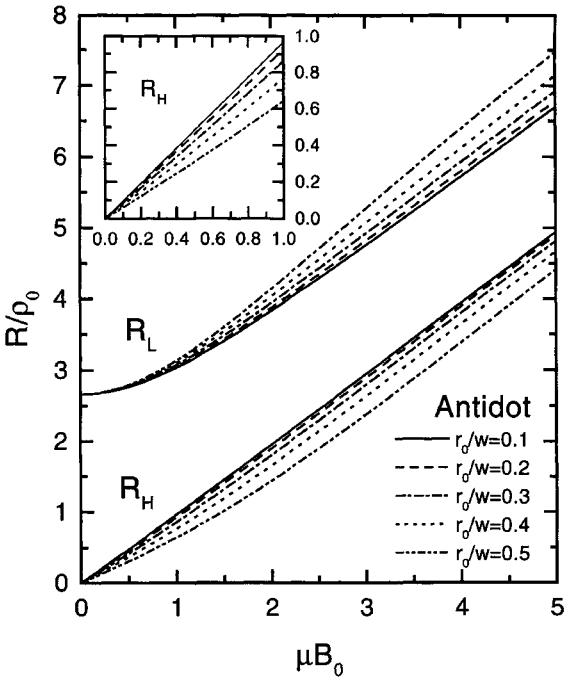


Fig. 37. Hall resistance and the longitudinal resistance versus μB_0 for the magnetic antidot. Inset shows the Hall resistance for small μB_0 values.

The Hall resistance and the longitudinal resistance are shown in Figure 36 as a function of μB_0 for different values of r_0/W. Notice that when $\mu B_0 < 1$ (see inset of Fig. 37) the Hall resistance is linear in μB_0 with a decreasing slope with increasing r_0. For $r_0 = 0$, we recover the well-known result $R_H = B/n_s e = \rho_0 \mu B$. The quenching of the Hall resistance increases as r_0 increases because the average magnetic field in the active area of the junction decreases as the magnetic flux is removed in proportion to the area of the antidot (i.e., πr_0^2). In contrast to the Hall resistance, the longitudinal resistance increases with increasing radius of the antidot, which can be explained by the fact that the contribution to the dissipative transport increases with the zero magnetic field area and the amount of transport current going through it, which is inversely proportional to the field strength. Another contribution to the longitudinal resistance is due to the fact that the current paths followed by the charge carriers become longer at high fields as the antidot radius is increased. To investigate how the Hall resistance changes with r_0, we plot the Hall factor $\alpha_H = R_H/(\rho_0 \mu B)$ for different values of B_0 as a function of r_0 in Figure 38. In general, the Hall factor is defined for $B_0 \to 0$, but we notice from Figure 38 that even for $\mu B_0 = 0.5$ the Hall factor is still very close to its $B_0 \approx 0$ result. Following [152], we calculate $\alpha_H^\circ = R_H/\langle B \rangle$ where the magnetic field is averaged over the cross junction (the cross junction has a unit area if expressed in units of W^2). We found that, in general, $\alpha_H^\circ \langle B \rangle / B \geqslant \alpha_H \geqslant \frac{1}{2} \alpha_H^\circ \langle B \rangle / B$, which is in contrast to the ballistic regime where it was found that $\alpha_H \approx \alpha_H^\circ \langle B \rangle / B$ for r_0/W up to almost 0.4–0.5. Therefore, in Figure 38, we also show another effective Hall factor defined as $\alpha_H^* = R_H/\langle B \rangle_2$ where now the magnetic field $\langle B \rangle_2$ is averaged over the region $W/2 < x < 5W/2$, $W < y < 2W$, which is twice the junction area of the cross. For the antidot system with $r_0/W \leqslant 0.5$, we have $\langle B \rangle = [1 - \pi (r_0/W)^2] B_0$, while $\langle B \rangle_2 = [1 - (\pi/2)(r_0/W)^2] B_0 \geqslant \langle B \rangle$. Notice that α_H^* is independent of the size of the disk for $r_0/W \leqslant 0.5$. Therefore, given the previous effective Hall factor, a measurement of the Hall resistance allows the experimentalist to obtain information on the size of the antidot.

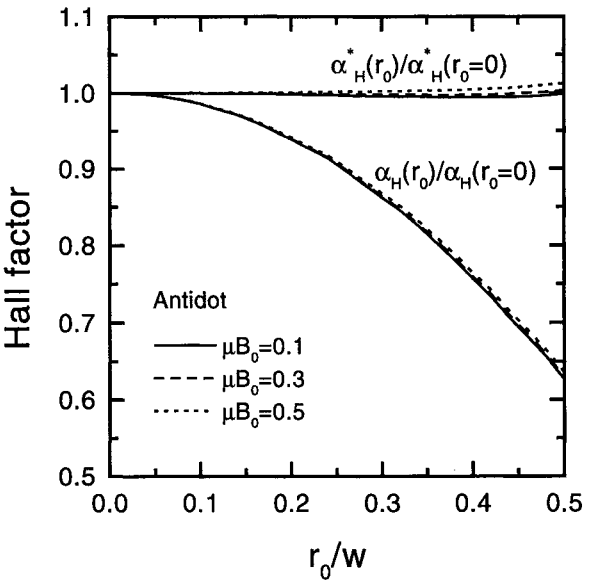


Fig. 38. Hall coefficient α_H and the effective Hall coefficient α_H^* for the magnetic antidot as a function of the antidot radius R_0 for different μB_0 values.

As compared to the ballistic regime, in the diffusive regime the Hall factor for the magnetic antidot system is larger, implying that in the diffusive regime the active area of the Hall cross is larger than in the ballistic regime. This is due to the spread of part of the transport current into the voltage probes, leading to an increased active area. We found numerically that the effective area in the diffusive regime is about two times larger than the cross area. A similar factor of 2 was recently found in [147, 148] for the case of a magnetic flux vortex penetrating a Hall junction.

The longitudinal resistance is found to be quadratic in B in the small B region and linear in B for large B values. Notice that at $B_0 = 0$ we have $R_L = 2.666\rho_0$. For a macroscopic sample, we have $R_L = (L/W)\rho_0$ with L the length and W the width of the 2DEG. Here $L = 3W$ and, consequently, one would expect $R_L = 3\rho_0$ at $B_0 = 0$. The presence of the voltage probes makes the 2DEG locally wider and, consequently, the effective width of the 2DEG is larger than W, resulting in a smaller longitudinal resistance. Furthermore, R_L increases with increasing disk radius r_0, which is opposite to the behavior of R_H. Notice that for large B values the slopes of R_L and R_H become equal because the longitudinal resistance includes contributions from both the magnetoresistance and the Hall resistance. At small magnetic fields, the magnetoresistance gives the dominant contribution and, consequently, R_L is quadratic in B. When B is large, the contribution from the magnetoresistance is less important and the Hall resistance becomes the dominant part of the longitudinal resistance and, consequently, R_L is linear in B. Notice that in the present units we have $dR_H/dB = dR_L/dB = 1$ for large magnetic fields, which implies that R_L and R_H are linear in B with coefficient $1/n_s e$. Notice also that $B/n_s e$ is nothing else than the classical 2D Hall resistance in the absence of the antidot. Both R_H and R_L are, for large B, shifted by a constant value that depends on r_0. The dependence of the Hall resistance on the position of the antidot was investigated in [148, 153].

As a last example, we studied the magnetic field profile resulting from a magnetic dipole placed above the junction and aligned perpendicular to the junction plane, that is, $B(r) = M(3\cos^2\theta - 1)/R^3$ where $R^2 = r^2 + z_0^2 = x^2 + y^2 + z_0^2$, $\cos^2\theta = z_0^2/R^2$, z_0 is the distance between the dipole and the plane of the junction, and M is the dipole moment. This system models the magnetic profile of a circular single-domain ferromagnetic cluster

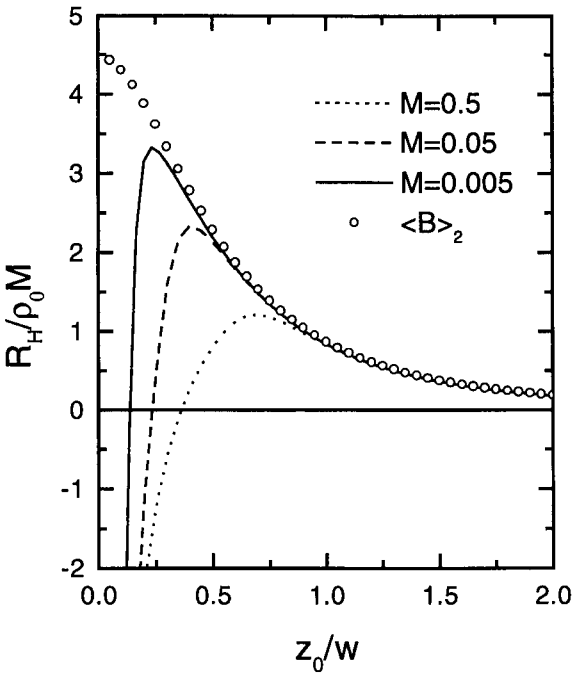


Fig. 39. Hall resistance versus the distance of the magnetic dipole from the Hall bar z_0 for different values of the strength of the dipole. The circles are obtained from $R_H = \langle B \rangle_2$.

that is placed above the Hall cross. Figure 39 shows the Hall resistance as a function of the perpendicular distance of the dipole above the junction z_0, where the Hall resistance is normalized by the magnetization M. For large z_0 values, the Hall resistance scales perfectly with the magnetization and is, to a good approximation, given by the average field in the effective area of the junction. This situation is valid up to smaller values of z_0 when the magnetization is decreased. Notice that for small z_0 values R_H is no longer related to the average field in the effective area of the junction and, in fact, it has even the opposite sign, which is the sign of the dipole field in the current and voltage probes. This implies that, as in the ballistic regime [152], the electrons do not sample the whole magnetic field profile in the junction. The reason is that they cannot penetrate into the strong magnetic field peak region in the center of the junction, which gives the dominant contribution to the average magnetic field in the active area. Consequently, $\langle B \rangle_2$ leads even to the wrong sign for R_H and, therefore, the simple expression $R_H = \langle B \rangle_2$ is valid only when z_0 is large or the magnetic dipole strength is weak.

Next, we discuss the effect of changing the relative ratio of the widths of the Hall voltage probes (W_y) to the current probes ($W_x = W$) on the Hall response of the cross-junction device. As an example of a magnetic field profile, we take the one of a magnetic dot, that is, $B(r) = B_0\theta(r_0 - r)$. In Figure 40, the Hall resistance and the effective Hall factor of the magnetic dot are shown as a function of the voltage probe width for $r_0/W = 0.25$ and $\mu B_0 = 0.3$. Notice that the effective Hall factor decreases with increasing deviation of the Hall probes from the symmetric case. For $W_y/W \leqslant 1.0$, this can be understood as being due to the decreasing averaging magnetic field in the Hall cross, that is, $\langle B \rangle = B_0\pi(r_0/W)^2/(W_y/W)$, with increasing W_y/W. Indeed, for $0.5 \leqslant W_y/W \leqslant 1.5$, we find $\alpha^\circ = R_H/\langle B \rangle \approx 0.35$–$0.5$ practically independent of W_y for $r_0/W < 0.5$. For Hall probes that are narrower than the current probes, the Hall resistance decreases faster with W_y/W than expected from $\langle B \rangle$. This implies that in such a case the effective area is smaller than twice the Hall cross region. The Hall factor is nearly half of the one given by the average

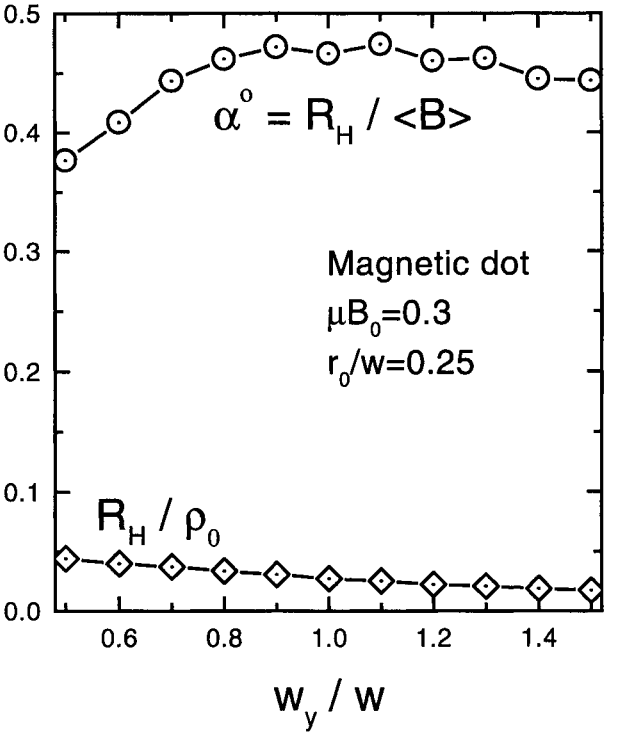


Fig. 40. Hall factor α_H° and the Hall resistance R_H as a function of $W_y/(W_x = W)$ for a magnetic dot with a radius of $r_0/W = 0.25$ and a magnetic field strength of $\mu B_0 = 0.3$.

magnetic field $\langle B \rangle$ when $W_y/W = 1$, but decreases slightly when the ratio of the width of the leads deviates from unity. This is different from the ballistic regime [152] where it was found that the small magnetic field Hall resistance is determined by the average magnetic field in the cross junction independent of the relative size of the Hall probes.

In the diffusive regime, the Hall resistance depends on the relative average velocity between the magnetic flux and the electric charges through the Lorentz expression of the induced electric field $\mathbf{E} = -\mathbf{v} \times \mathbf{B}(r)$, where the average velocity in this expression is influenced by the width of the Hall voltage probe (see also [153]). By changing the width of the voltage probe, we are also changing the average magnetic field in the junction area of the cross (i.e., the active area), and, therefore, the Hall resistance depends on both the average magnetic field and the average velocity in the active area.

8.3. Hybrid Hall Effect Device

As an example of the application of the Hall effect in novel magnetoelectronic devices, we consider the system recently proposed by Johnson et al. [157] and Monzon et al. [158]. They fabricated a new hybrid Hall device, incorporating a microstructured ferromagnetic film and a micrometer-scale Hall cross, which has potential applications as a magnetic field sensor, nonvolatile storage cell, or logic gate. Their experimental measurements showed this new device to have excellent scaling properties and output characteristics at room temperature.

The top view of the device configuration is shown in Figure 41. In [157], a thin metal ferromagnetic film F with thickness $d_f = 0.15\ \mu$m was deposited a distance $h = 0.076\ \mu$m above a Hall cross made from a high-mobility InAs film [157] (or a GaAs/AlGaAs heterostructure [158]) containing a 2DEG. F and the 2DEG are electrically isolated from each other. The ferromagnetic film has an in-plane magnetization in the x direction (taken

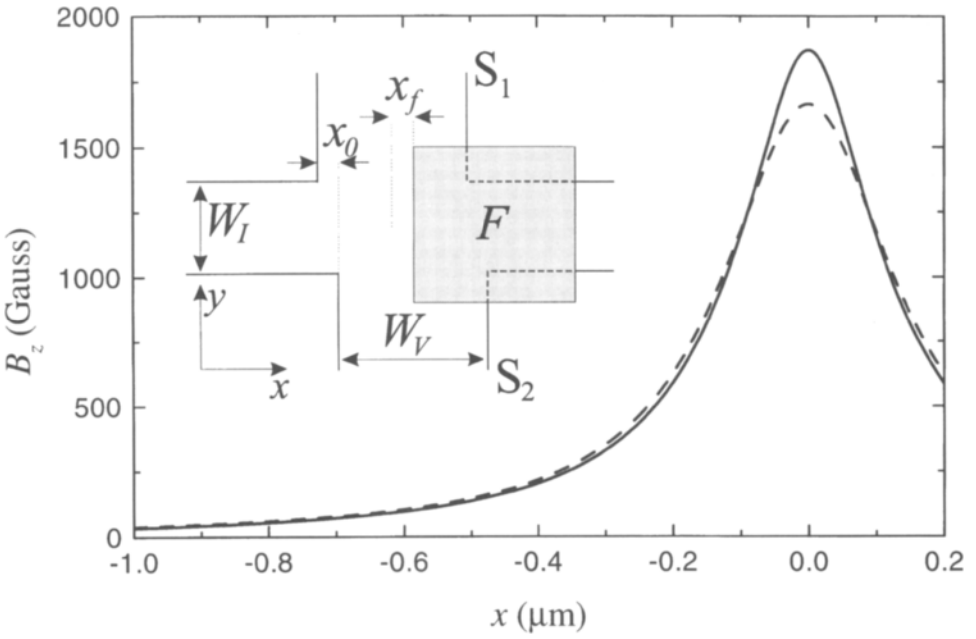


Fig. 41. Comparison between the analytical calculated magnetic field profile B_z in the 2DEG along the center of the current probe (solid curve) and the one based on the line charge model (dashed curve). The inset shows the top view of the configuration.

along the current direction), which will result in an inhomogeneous B_z profile in the 2DEG. When a voltage is applied in the x direction, a current will flow, and this will generate a measurable Hall voltage V_H over the voltage probes S_1 and S_2. An external applied magnetic field in the x direction sweeps the magnetization, resulting in changes in V_H. The current probes and the voltage probes of the Hall cross have, respectively, widths W_I and W_V, which are in the micrometer region. S_1 and S_2 may be shifted a distance x_0 from each other, for reasons described later. F is square shaped with typical dimension $W_I + 2$ μm and is located with one edge at distance x_f from the center of the Hall cross. In the y direction, the configuration is symmetric.

The experiments of [157] were done at room temperature and, consequently, our earlier approach [39, 153], which relies on a classical diffusive model to describe the electrical transport, is applicable. In the following, we restrict the calculations to a $(3W_V, 3W_I)$ region centered around $(0, 0)$, with the boundary conditions $\phi(-3W_V/2, y) = 0$ and $\phi(3W_V/2, y) = 1$, and the condition that no current can flow out of the sides of the sample, that is, $j_y(x, -3W_I/2) = j_y(x, 3W_I/2)$. We checked that our results were practically not altered by increasing the length of the voltage leads. The Hall resistance is given by $R_H = V_H/I$, where $V_H = \phi(x, -3W_I/2) - \phi(x, 3W_I/2)$, and $I = \int j_x(x, y)\, dy$ is the total current flowing in the direction of the applied field. In our numerical analysis, we used $\sigma_0 = 173.611\ \Omega$, which corresponds to the mobility $\mu = 20{,}000\ \text{cm}^2/\text{V s}$ and the electron density $n_s = 1.8 \times 10^{12}$ of the experimental system of [157] at $T = 300$ K.

The magnetic field profile in the 2DEG, resulting from the ferromagnetic film, was calculated (see Section 3) and is shown in Figure 41. We consider the situation of full saturation of the magnetization, which for the Permalloy material used in [157] yielded $m_x = 860 \pm 20\ \text{emu/cm}^3$ at room temperature. This result is compared with the line charge model used in [157, 158], which gives $B_z(x) = 2\lambda_m R/((x-a)^2 + R^2)$, where $\lambda_m = m_x d_f$ is the magnetic charge density, $x - a$ is the lateral distance to the edge of F, and $R = h + d_f/2$ is the distance of the approximated line of magnetic poles to the 2DEG. Note that

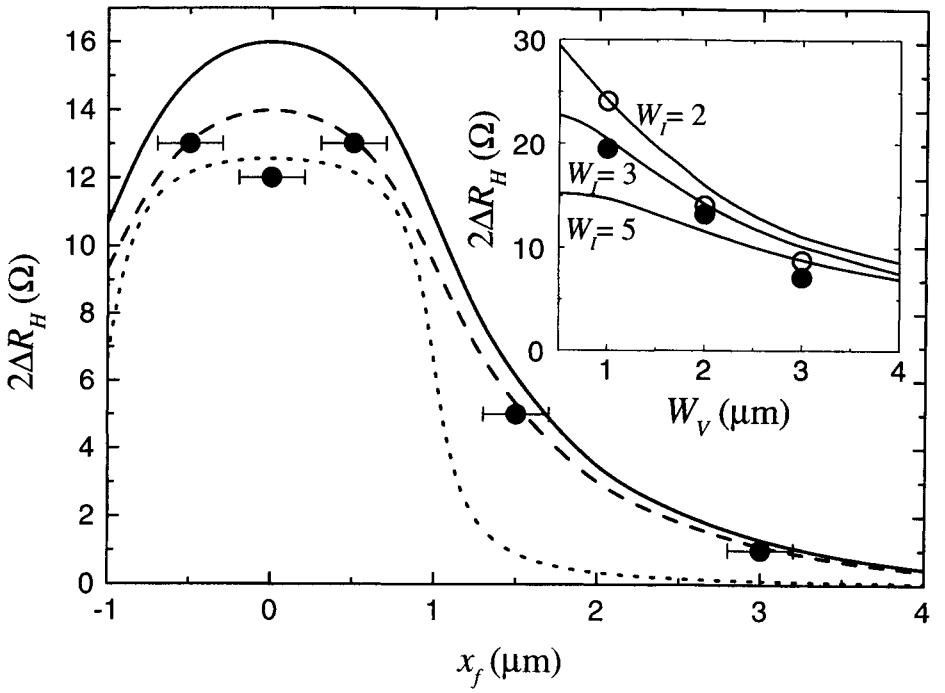


Fig. 42. Maximum change of the Hall resistance $2\Delta R_{\mathrm{H}}$ as a function of x_{f} for the $(W_V, W_I) = (2, 3)$-μm configuration at $T = 300$ K. The symbols are the experimental results and the theoretical results are given by the solid curve and the dashed curve when we alter the magnetic film thickness to $d_{\mathrm{f}} = 0.13$ μm. The dotted curve (which is reduced by a factor of 2) is based on the simple formula $2\Delta R_{\mathrm{H}} = 2\langle B_z\rangle/n_{\mathrm{s}}e$. The inset shows $2\Delta R_{\mathrm{H}}$ for various sizes of the current Hall probes W_I as a function of W_V (solid curves). The experimental values (solid dots) are compared with the calculated values (hollow dots).

there is good agreement between both curves (on a 10%–15% level), and using the line charge model was, at least in this case, justified.

Inserting this calculated magnetic profile in (37), we solve the partial differential equation (36) numerically. We only consider the case when the magnetization is saturated. First, we will study the symmetric configuration, where $x_0 = 0$. In Figure 42, the peak magnitude $2\Delta R_{\mathrm{H}}$ is plotted as a function of x_{f} using the parameters as given by Johnson et al. Our results (solid curve) slightly overestimate the experimental results (solid circles). Nevertheless, these calculations are in much better agreement than those based on the approximation that the Hall resistance is given by the average magnetic field in the cross region (dotted curve, which is reduced by a factor of 2), $2\Delta R_{\mathrm{H}} \approx 2\langle B_z\rangle/ne$. Note that the latter approach only works well in the ballistic regime [152]. Possible reasons for the discrepancy between experiment and theory are (1) it is possible that the magnetization of the film is not yet totally saturated, so $m_x < 860$ emu/cm^2; (2) the distance h between the magnetic film and the 2DEG or (3) the thickness d_{f} of the magnetic film can be different from that given in [157]. To find agreement, we have to increase h from 0.076 μm to 250 μm, which is unrealistically large, or we have to decrease the thickness of the magnetic film d_{f}. Decreasing this thickness to $d_{\mathrm{f}} = 0.13$ μm gives (see dashed curve in Fig. 42) excellent agreement with experiment. This also could be the reason why in the inset of Figure 42, where the experimental peak magnitudes $2\Delta R_{\mathrm{H}}$ (solid circles) for systems with different dimensions (1 μm, 2 μm), (2 μm, 3 μm), and (3 μm, 5 μm) are plotted, are theoretically (open circles) overestimated.

When the Hall cross is fabricated symmetrically, that is, $x_0 = 0$, the hybrid Hall device is characterized by a bipolar output $\pm\Delta R_{\mathrm{H}}$ as B is swept from positive to negative.

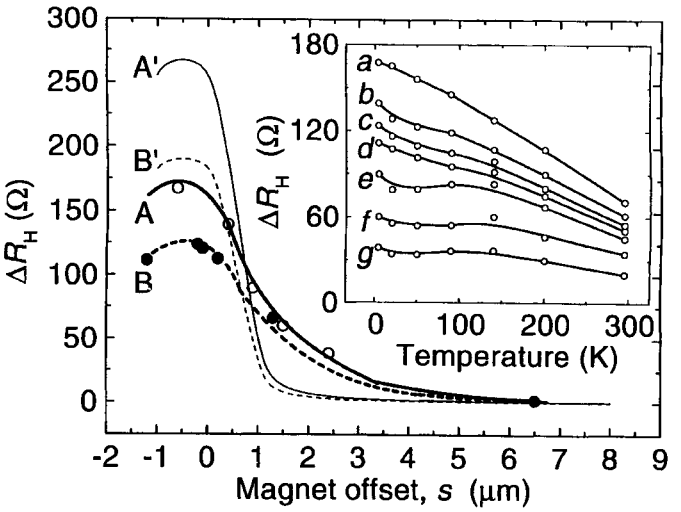


Fig. 43. Same as Figure 44 but now for $T = 4.2$ K. The experimental curves (A and B) are for two different thicknesses of the magnetic film. The theoretical results (A′ and B′) are obtained by averaging the magnetic field in the cross junction. The inset shows the temperature dependence of ΔR_H for devices with different values of the magnetic offset $s = x_f$: (a) $s = -0.6$, (b) 0.4, (c) -1.2, (d) -0.2, (e) 0.9, (f) 1.5, and (g) 2.4 μm. (Source: Reprinted with permission from [158]. © 1997 American Institute of Physics.)

Introducing a small asymmetry, a shift x_0 of voltage probes S_1 and S_2, results in a small offset resistance R_0. As shown in [157], this makes it possible to shift the output values and to obtain output characteristics varying, for example, between 0 Ω and $2\Delta R_H$.

The room temperature experiments of [157] were extended in [158] to liquid helium temperatures and the full temperature range of the output signal was investigated. They found that the magnitude of ΔR_H decreases with increasing temperature (see inset of Fig. 43). This can be attributed to (i) an increase of the electron density ($R_H \sim 1/n_e$) with increasing temperature, and (ii) the transition from the ballistic regime at low temperatures to the diffusive regime at high temperatures, which decreases the Hall resistance as discussed in the previous two subsections because of the larger effective area over which the magnetic field has to be averaged. The dependence of ΔR_H on the relative magnetic film position s (cf. Fig. 42 for $T = 300$ K) as obtained at $T = 4.2$ K ($n_e = 1.5 \times 10^{11}$ cm^{-2}, $\mu = 1.1 \times 10^6$ cm^2/V s) from ten devices on two separate chips (A and B, with five devices each) is shown in Figure 43. The overall behavior is similar to that seen at room temperature. The line charge model was used to obtain the magnetic field distribution inside the 2DEG and perpendicular to the 2DEG (see [158]). For chip A (B), they used for the saturation magnetization $m_x \approx 838$ emu/cm^3 (838), $d = 150$ nm (105) and for the position of the line charge above the 2DEG 152 nm (130). The curves labeled A′ and B′ are the theoretical results for ΔR_H obtained by averaging the magnetic field over the Hall cross region using the magnetic field distribution obtained from the line charge model in which the magnetic charge was distributed over a distance $\delta = 1$ μm. For $s < 1$ μm, the Hall resistance is overestimated by about a factor 1.5 for both cases. For $s > 1$ μm, the theoretical model predicts a substantially smaller output then found experimentally. The latter is more similar to the output found at room temperature [157] (see Fig. 42). This is surprising in view of the theoretical response of the ballistic Hall magnetometer discussed in [152] and in Section 8.1 where the response was found to be due to the average magnetic field in the cross. It is possible that the magnetic field strength is too large such that the electrons do not sample the complete magnetic field profile as discussed in Section 8.1 for the magnetic dipole profile. The discrepancy may also suggest that the local magnetic field profile is more complicated than the one given by the distributed line charge model.

9. NONPOLARIZED CURRENT INJECTION FROM SEMICONDUCTOR INTO FERROMAGNETS

Since the discovery of the so-called giant magnetoresistance (GMR) effect in metallic magnetic multilayers [159], a huge amount of research has been done on the properties of spin-dependent scattering in magnetic thin films and multilayers [160]. Device demonstrations where semiconductor and ferromagnetic layers are both in the current-carrying parts of solid-state devices are still very few.

One recently demonstrated device [161] is, in essence, a metal base hot-electron transistor and relies on the spin-dependent scattering of hot electrons in a magnetic metal multilayer [162, 163]. In this respect, the device structure is different from the standard all-metal GMR structures where conduction takes place at the Fermi level. The vertical spin valve transistor is a semiconductor-based device comprising a magnetic multilayer base, with a Si emitter and collector (Fig. 44). It was shown that this type of device structure can be fabricated successfully using low-temperature wafer bonding technology in a UHV sputter deposition chamber [164].

Let us take a closer look at the operation of this component. Hot electrons are launched by the Schottky barrier of the emitter into the base. In the base, the carriers are subject to spin-dependent scattering that determines their mean free path. The degree of this scattering will determine the collected carriers in the collector and can be controlled by controlling the magnetic state of the base. The combination of the perpendicular trajectory of the electrons and the exponential dependence of the collector current on the mean free path of the electrons in the multilayer is responsible for a very large change in collector current upon change of the magnetic state of the base. The metal base is typically a spin valve multilayer that is known to give relative resistance changes of 1% to 10% upon magnetization change. The spin valve transistor has been shown to give a collector current change of over 100%. Although the control of the magnetic base layer thickness is nanoscale, the lateral dimensions are currently technology limited to some tens of micrometers. In a new generation of such magnetic hot-electron devices, a metal–insulator tunnel emitter [165, 166] may replace the emitter semiconductor Schottky barrier, leading to a planar technology for the realization of this component, improving the application potential for integrated circuits (e.g., for MRAM).

The electrons arriving in the semiconductor collector of the structure may have a certain degree of spin polarization. The device operation, however, does not depend on the spin

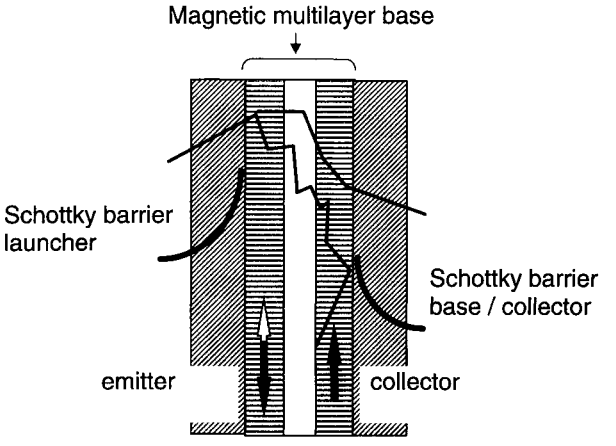


Fig. 44. Schematic cross section of a hot-electron spin valve transistor. Semiconductor emitter and collector are separated by a magnetic multilayer base.

polarization of this current. In the following sections, we will discuss device structures where spin-polarized electron transport across FM/SC interfaces is essential to their operation.

10. SPIN INJECTION FERROMAGNETIC/SEMICONDUCTOR STRUCTURES

10.1. Spin-Polarized Electronic Current from Ferromagnets

Because of the imbalance in spin population of a ferromagnetic metal, the electronic current emanating from a ferromagnetic electrode is spin polarized. This has been experimentally demonstrated in the pioneering work of Messervey et al., who injected current from a ferromagnetic into a superconductor (Al) across an Al_2O_3 barrier [167]. The degree of spin polarization was found to be 10% to 50% for Ni–Fe alloys in such a tunneling experiment with a superconductor/tunnel oxide/ferromagnetic metal trilayer [168]. The process of injecting an electric current with a spin imbalance is commonly referred to as spin injection.

A straightforward way to inject spin-polarized electrons in a nonmagnetic metal is to use a ferromagnetic contact and drive current through the interface [169]. For an ideal interface, this current would carry magnetization (spin information from the ferromagnetic): $\mathrm{Im} = \eta\beta I_e/e$. This formula simply states that with each electron crossing the interface (I_e/e), one Bohr magneton β is associated and that there will be an imbalance in the spin population of the current to a degree of η ($|\eta| \leqslant 1$). The (sign of the) coefficient η depends, in general, on the contributions from both spin bands, the hybridization of bands and interface effects. Associated with this magnetically polarized electric current is a spin accumulation and an induced nonequilibrium magnetization in the normal metal.

In principle, placing a second ferromagnetic contact to the nonmagnetic metal will enable one to probe (in an open-circuit voltage measurement) the polarization of the carriers at the position of that second ferromagnet [170]. The analysis of the coupling of the electron charge and the magnetization and the experimental demonstration of the injection/detection effect were reported by Johnson and Silsbee [171–173]. In this ferromagnetic/normal metal/ferromagnetic geometry, in which the current traverses the device's interfaces perpendicularly [so-called, current perpendicular to the plane (CPP) geometry], there are two approaches to theoretically explain the interface resistance associated with the spin-dependent signature of the transport measurements, based on thermodynamic arguments [174] and based on the theory and experiments of a spin scattering and relaxation in giant magnetoresistance multilayers [175]. The conclusion, however that the spin-polarized current can be used in electronic devices including ferromagnetic injectors is correct and exciting.

10.2. Optical Detection of Spin-Polarized Tunnel Current

The preceding experiments introducing spin injection are performed using either all-metal or metal/superconductor structures, but spin injection will also work in a semiconductor.

In fact, it was shown by optical means that a current from a magnetic (nickel) needle across a vacuum barrier into GaAs is spin polarized [176]. The geometry in this experiment, which makes use of scanning tunneling microscopy (STM), is as follows. The injector needle's magnetization is along its length axis, pointing perpendicular to the semiconductor surface. Carriers were injected from the tip over a vacuum barrier into the surface depletion zone of a GaAs wafer. The spin orientation direction of the injected electrons will also be perpendicular to the semiconductor surface. The ensemble of electrons injected in the semiconductor will have a net polarization, provided that the spin information is not lost while traversing the vacuum/semiconductor interface. Because of the spin polarization of the injected electrons, their radiative recombination in the depletion region results in

circularly polarized light emission from the semiconductor. The degree of polarization of the luminescence is a measure of the injected spin imbalance, taking into account the spin rotation processes and spin relaxation in the depletion region.

Note that in this experiment the sign of the polarization was found to be negative ($\eta = -0.31$). In another tunneling experiment involving Ni as a spin injector [177] into superconducting Al, the spin polarization was found to be positive. The latter result agrees with theoretical considerations [178–180] that in tunneling from a ferromagnetic transition metal alloy, the current is dominated by itinerant majority-spin carriers from the hybridized s–d band although around the Fermi level the minority spins have a higher density of available states. This contradicts the experimental results of Alvarado and Renaud [176], who showed that conduction from the 3d states at the Fermi level is dominant.

10.3. Spin-Polarized Electronic (Tunnel) Current from Optically Pumped Semiconductors

Also, the inverse configuration of the preceding experiment has received considerable attention: the emission of spin-polarized electrons from an optically pumped GaAs structure. Because of the spin–orbit splitting energies and the selection rules in GaAs, circularly polarized light induces electronic spin imbalance in GaAs.

The spin polarization of electrons photoemitted from negative-electron-affinity (NEA) thin GaAs photocathodes is well known. Highly doped p-type gallium arsenide with a thin surface coating of cesium with oxygen is used to create emitters with a negative electron affinity. Theoretical studies predict the intensity and spin polarization of photoelectrons excited by circularly polarized radiation from the GaAs(110) surface [181].

It has been demonstrated that these NEA (Al)GaAs sources [182] have a limited ($\approx$40% to 50%) but rather unstable polarization. To prevent the degradation of the electrode surface, oxide barrier films were suggested to protect the emitting surface [183]. The vacuum level and the surface potential barrier play a decisive role in the degree of spin polarization of the photoemission [184].

An increased polarization can be achieved by introducing strain in the semiconductor, affecting the energy band picture. The residual lattice misfit strain splits the degeneracy of the electron states in the valence band. The dependence of the amount of splitting on the strain was confirmed by the high spin polarization of photoelectrons [185]. Strained GaAs layers have been grown on GaAsP or InGaAsP [186] buffer layers, or vice versa [187]. Pseudomorphically strained epitaxial layers reveal a higher degree of polarization [188]. In the case of GaAs epilayers, a polarization of 85% could be obtained (at 866 nm wavelength) with a quantum efficiency of about 1.0%. Also, (strained) AlGaAs/GaAs superlattices reveal comparable numbers of polarization and quantum efficiency [189]. Further, structures have been proposed to increase the quantum efficiency at a predetermined wavelength, incorporating a distributed Bragg reflector [190] in the semiconductor structure. Strained GaAsP has been used to study the inverse photoemission from Fe(100) [191] and as a polarized electron source in microtron facilities [192].

Also, optically generated spin imbalance in an ultraclean cleaved GaAs tip leads to emission of spin-polarized electrons from the semiconductor tip [193]. Studies on the relation between the tunnel current, applied voltage, incident optical power, and tip–sample distance have been reported [194]. The experimental results are well described by the model that includes carrier capture in the semiconductor surface states.

Such a tip is considered very useful in spin-polarized scanning tunneling microscopy (SP-STM) [195] because an optically activated semiconductor spin source does not have difficulty controling the magnetic domain structure and would not alter the magnetic state of the sample under study through fringing fields. The construction of an SP-STM is being attempted and first results have been reported [196].

10.4. Spin-Polarized Current from Magnetic Contacts to Semiconductors

10.4.1. Spin Field Effect Transistor Concept

The next challenge is to inject spin-polarized electrons from a direct ferromagnetic contact into a semiconductor channel. It is clear that the semiconductor component would have a higher resistance than its all-metal counterparts. Also, the carrier density and mobility can be engineered in a semiconductor heterostructure. The combination of ferromagnetic and semiconductor structures in a single device will lead to possibilities of signal amplification and more exotic properties involving, for example, magnetooptic effects.

An FM/SC/FM device that resembles the structure of a field effect transistor (FET) has been proposed by Datta and Das [197]. Their spin FET is schematically represented in Figure 45. It relies on spin injection from a ferromagnetic source contact and detection at a ferromagnetic drain contact. A gate is present to impose a surface electric field that will cause a precession of the injected spins. The analysis of this mechanism is as follows.

10.4.2. Rashba Mechanism

An effective magnetic field is felt by a moving electron in a two-dimensional electron gas (2DEG, by convention in the x–y plane) when a perpendicular electric field E_z is present. The magnetic field is perpendicular to the electron motion and in the plane of the 2DEG. Assuming that the electrons are confined in one subband, the spin degeneracy of the subband can be lifted by a spin-splitting energy caused by the interaction of the electron with the effective magnetic field.

In InAs or InGaAs heterostructures [198–200], the main origin of the spin-splitting energy is the surface electric field in the heterostructure, referred to as the Rashba mechanism [201, 202]. This electric field can be modulated by an externally applied (gate) voltage, which can change the band-bending and carrier density in the heterostructure.

The spin–orbit interaction parameter α is proportional to the expectation value of the electric field $\langle E_z \rangle$ perpendicular to the 2DEG: $\alpha = b\langle E_z \rangle$. The energy associated with the Rashba mechanism is a linear function of this spin–orbit interaction parameter α and the Fermi wave number k_F:

$$\Delta R = 2\alpha k_F \tag{69}$$

The precession angle $\Delta\theta$ of the electron spin in semiconductor heterostructures is dependent on α and is a function of the length of the channel between source (injector) and drain (detector), L [197]:

$$\Delta\theta = \frac{2m^*\alpha L}{\hbar 2} \tag{70}$$

Experimentally, the spin–orbit interaction parameter for a 2DEG in a semiconductor heterostructure with sufficient mobility can be obtained from transverse magnetoresistance measurements. The experimental method relies on the occurrence of beat patterns in the Shubnikov–de Haas oscillations at moderate magnetic fields. In moderate fields, the Zeeman energy contribution is smaller than the effect of the Rashba mechanism.

10.4.3. Experimental Study to Support the Rashba Mechanism

In experiments by Heida et al. [203], it was found that the splitting energy δ_R in an AlSb/InAs heterostructure can be changed by an applied voltage. But the origin of the change was attributed to a change in k_F rather than a modulation of α by the voltage. In $In_{0.53}Ga_{0.47}As/In_{0.52}Al_{0.48}As$ heterostructures investigated by Nitta et al. [204], however, the parameter α was found to be modulated by the gate voltage V_g. A factor of 1.5 difference in α at $V_g = -1.0$ V and at $V_g = +1.54$ V was found. This would lead to a spin

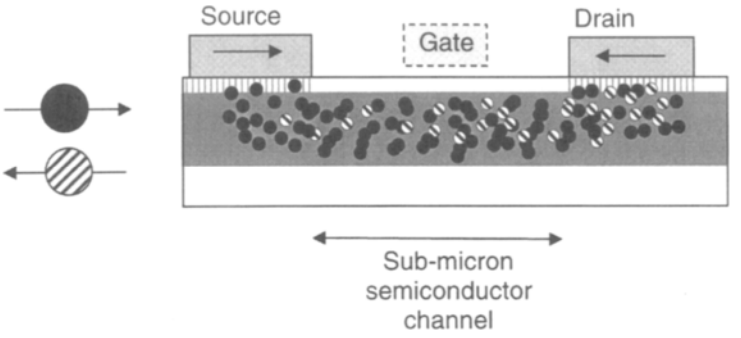


Fig. 45. Schematic representation of a lateral spin injection field effect transistor–like component with two ferromagnetic contacts and a gate (spin FET). (Source: Adapted from [197].)

precession change from π at the source to 1.5π at the drain for a gate length of 0.4 μm in a lateral spin transistor.

From this analysis, it is clear that the scattering events that change the direction of the electron motion will change the effective magnetic field for this electron. Hence, even if spin flip does not occur, scattering would disturb the coherent spin precession. Therefore, a ballistic device geometry would be ideal for the gated spin FET. In this respect, submicrometer structures fabricated from high-mobility one- or two-dimensional electron gas systems are desirable. The inverted $In_{0.53}Ga_{0.47}As/In_{0.52}Al_{0.48}As$ heterostructure and high-mobility near-surface InAs two-dimensional electron gas structures [205] are promising candidates for spin channels in the FET.

Associated with the gate electrode is the requirement of a stable insulator to separate it from the channel. In such metal–insulator–semiconductor (MIS) structures, the insulator is often a semiconductor layer with a larger band gap, while in some cases an SiO_x has been applied successfully [204, 206].

10.4.4. Spin Switch Concept

Making abstraction of the gate voltage–induced spin precession, a spin-dependent signature in the transport measurements is expected when the relative magnetization orientation of the source and drain is switched from parallel to antiparallel. Such a geometry is the equivalent of the all-metal spin switch discussed previously.

To make this spin switch work, the channel mobility requirement is somewhat more relaxed, as long as the spin diffusion length in the channel is sufficiently large. This is the case for appropriately designed semiconductor (hetero)structures (spin diffusion lengths of 1–10 μm). Nevertheless, devices with submicrometer channel length are desired to minimize the loss of spin coherence during channel transit. This spin disordering can be of particular importance for semiconductors with a large spin–orbit coupling, associated with the crystal asymmetry and in channels with a large number of magnetic scatterers where the number of spin-flip events is large.

The first data showing a "spin switch effect" have been reported [207] for a two-terminal device consisting of two sets of interdigitated Ni contacts on an n-type bulk Si wafer (three-dimensional channel). In this case, the change in relative orientation of the magnetization in the two sets of Ni electrodes is realized by making one set of the submicrometer Ni finger contacts narrower than the other set. As expected, the coercivity (or magnetic switching field) for the narrower one is larger. During the sweep of the magnetic field, an antiparallel magnetic situation will now appear when the softer contacts follow the external field, whereas the switching field of the harder contacts has not been attained.

Optical experiments are very useful to clarify the process of spin injection from a semiconductor into a ferromagnetic contact, for example, through an oxide tunnel barrier [208], or in the case of a direct contact interface [209]. In the latter experiment, the photoyield through a thin Fe overlayer on GaAs was found to be 1.7 times larger when the orientation of the Fe is parallel to the spin orientation of the optically generated polarized electrons from the GaAs, compared to the antiparallel orientation.

10.4.5. Technological Aspects of Ferromagnetic/Semiconductor Spin Injection Structures

As can be inferred from Figure 45, a respectable set of "show stoppers" for the realization of a spin FET or spin switch can be pictured. It has become clear from the previous description that the magnitude and the sign of the polarization of the injected current depend strongly on the detailed properties of the band structure and relative contributions to the conduction of carriers of the s, p, d (hybridized) bands [179], the ferromagnet's crystal orientation versus the current direction, and the spin transparency of the ferromagnetic/semiconductor interface. Therefore, the ideal ferromagnetic current injector is a single crystal with controllable crystal orientation, having a well-defined (single) magnetic domain structure. Clearly, these observations push the ideal contact size to the nanoscale regime, putting the same requirements on the lithographic tools as in other fields of microelectronics. Another reason for the ultrasmall contact sizes is the spin coherence of the injected current. For smaller contacts, however, it will become harder to switch the magnetization direction. The geometry and size difference in the source and drain contacts can actually be used to realize different coercive fields (see the preceding discussion on the Ni/Si injector geometry).

Moreover, instead of working with different size contacts, two ferromagnetic materials with different H_c may be a more desirable choice for realizing antiparallel alignment of the contact's magnetization. Such a requirement may be a tough challenge for lateral components in the nanoscale regime.

Magnetic contacts cause fringing fields either from edge states or from domain walls. Although it is unlikely that the ferromagnetic contacts will be in close enough proximity to suffer from magnetostatic coupling effects, the fringing fields close to the contacts may result in spin disorder of the injected current, through the Hanle effect.

As a final point, one has to consider the FM/SC interface. Given the importance of the control of the magnetic properties of the magnetic layers serving as contacts and the need for an extremely well controlled interface (structural, magnetic, and electrical), we will treat aspects of the FM/SC interface in a separate section later.

11. FERROMAGNETIC/SEMICONDUCTOR EXPERIMENTAL STRUCTURES

11.1. The Need for Epitaxy

Most metals used in semiconductor devices are polycrystalline. When the device dimensions shrink, these dimensions approach the grain size of the metals. In this case, the uniformity of the device characteristics is compromised. Inferior reliability and a variation in the physical properties of the device may also result. As an example of the latter, it was already mentioned that magnetic properties are strongly dependent on the crystal orientation (anisotropy, degree of spin polarization). Further, controlled deposition techniques are required to optimize the FM/SC interface properties.

Uniformity at nanoscale, single-crystalline structures and extremely well controlled interfaces are tough requirements to meet for most standard metal deposition methods. With the advent of epitaxial growth techniques such as molecular beam epitaxy, the preceding

requirements seem to be within reach. Epitaxy of metals on semiconductors has received considerable attention over the past decades. First, we will describe some general aspects of metal epitaxy on semiconductors. We continue with a review of the achievements of ferromagnetic/semiconductor epitaxial layered structures. In this case, control over the structural and magnetic properties (magnetization and magnetic anisotropy) is the focus.

11.2. General Metal Epitaxy Criteria

Many successful attempts have been made to deposit stable, single-crystal metallic thin films on semiconductor surfaces. An excellent review of this research for metal/III–V semiconductor combinations has been published by Sands et al. [210]. Because most of this chapter is related to III–V semiconductors, we will take this technology as an example to discuss the problems.

The items of concern are schematically shown in Figure 46. We finally want to arrive at a pinhole-free, monocrystalline metal. The interface should remain well defined after possible heat treatment during device fabrication or operation. Eventually, one may attempt to fabricate a metal/semiconductor/metal stack multilayer, in which case the epitaxy criterion is of importance to maintain good-quality semiconductor overgrowth.

The result after annealing under the conditions of case A of Figure 46 is the typical case for a metal contact to a semiconductor structure, in, for example, MESFET technology. After annealing, many phases may form and the metal layer is polycrystalline in nature. In the as-grown condition, there is no tendency to form a continuous layer because of failure to meet the epitaxy criterion.

In case B (Fig. 46), there exists some epitaxial relation to the semiconductor, which helps to stabilize the metal layer. After heat treatment, phase separation occurs because of thermodynamical instability. When solving both the epitaxy and the thermodynamical criteria, as in case C, the annealing will still cause problems as a result of insufficient morphological stability. The alloy phase that was deposited epitaxially as grown will ball up into a highly textured polycrystalline film. Notice that metal–III or metal–V alloys

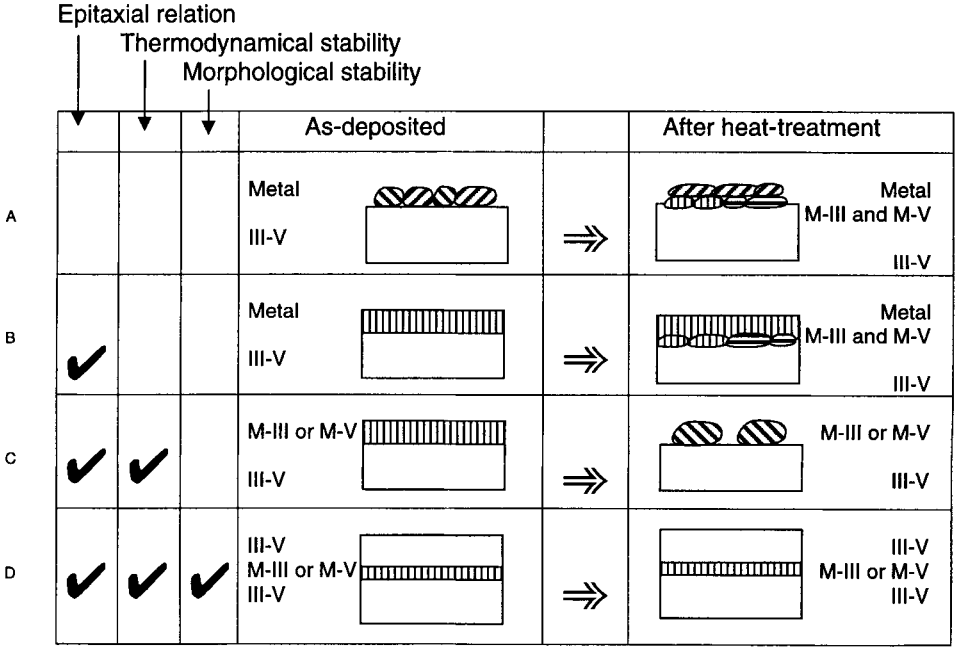


Fig. 46. Overview of the stability criteria of metal/semiconductor heterostructures. (Source: Adapted from [210].)

often have a higher chance of remaining thermodynamically stable. In the final case (D), all three criteria are fulfilled and a stable metal/III–V heterostructure results. In this case, semiconductor overgrowth can be attempted with a reasonable chance of success. Examples of the latter include GaAs/ErAs/GaAs resonant tunneling structures [211, 212] and GaAs/AlAs/NiAl/AlAs/GaAs [213]. In the case of the GaAs/ErAs/GaAs heterostructures [214, 215], a negative differential resistance was observed at room temperature for ErAs thicknesses in the range of 2.6 to 5 nm [216]. The success was attributed to the use of a Mn template monolayer deposited prior to ErAs deposition.

11.3. Elemental Ferromagnetic Metal Epitaxy on Semiconductors

The report on the epitaxy of Co on GaAs by Prinz [217] can be considered as the seed for research activity on magnetic/semiconductor epitaxy [218]. A large amount of research on metal/ferromagnet epitaxial superlattices on semiconductor substrates has been performed to clarify aspects of superlattice magnetism and giant magnetoresistance (GMR). In this section, we will limit the discussion to the recent studies of epitaxy of elemental Fe and Co on semiconductor substrates, in most cases GaAs. For spin injection devices, this material combination is an important test structure to gain understanding of the structural, magnetic, and electrical properties at a ferromagnetic/semiconductor interface. Figure 47 shows a set of examples of metallic and ferromagnetic structures that have been grown epitaxially on GaAs. In the case of Co, epitaxy on GaAs can lead to the body-centered cubic (bcc) phase; some aspects of this widely studied structure will be briefly discussed. At the end of this section, the Mn-based magnetic layers will be briefly discussed.

11.3.1. Epitaxial Layers of Iron and Cobalt on Gallium Arsenide

A few research groups have been very active in the study of the epitaxy of elemental magnetic thin films of Co and Fe on GaAs (for a review, see also [160]). Such studies have addressed in detail the evolution of the magnetic anisotropy of thin (a few monolayers) Fe [219] and Co films on GaAs. The substrate conditions prior to metal deposition are crucial in the control of this anisotropy because contributions to the net magnetic anisotropy arise from the formation of the interface and early stages of metal film growth. The determining factors are the initial metal adsorption sites and subsequent bond or site filling,

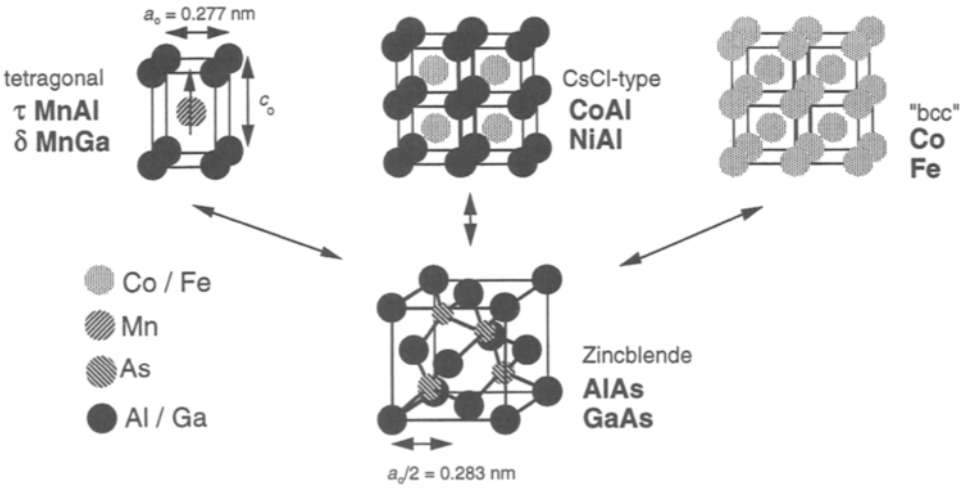


Fig. 47. Overview of some magnetic and compound metal structures suitable for growing epitaxially on GaAs (AlGaAs) semiconductors. The structural and magnetic properties of such epitaxial structures are determined by the epitaxial relationship and by the structure of the FM/SC interface.

and are strongly dependent on the semiconductor surface reconstruction [220, 221]. Also, anisotropies can be influenced by surface topography, as in the case of epitaxy on cross-hatched InGaAs epilayers [222], and by the early stages of the growth (e.g., step bunching and island formation). The domain structure and magnetization reversal processes, dictated by the induced magnetic anisotropy, have been studied *in situ* and *ex situ*. Such experiments are typically performed using (a combination of) the following characterization tools:

- Magnetoresistance measurements using anisotropic magnetoresistance (AMR) [223, 224]
- Kerr microscopy [225–228]
- Brillouin light scattering [229–231]
- Ferromagnetic resonance (FMR); sometimes photothermally modulated FMR to achieve lateral resolution [232, 233]
- Magnetic force microscopy (MFM) [234]
- Lorentz microscopy [235]

Almost all epitaxy experiments are performed under UHV deposition conditions using molecular beam epitaxy. However, sputter beam methods are occasionally reported. Examples are Fe(001) single-crystal films on GaAs(001) [236] and Fe(111) on GaAs(111) [237]. Also, electrodeposition has gained much interest in magnetic multilayer research [238] and the formation of FM/GaAs Schottky barriers [239] and single-crystal magnetic (NiCu) layers have been reported [240].

For device structures, it will be important to know the magnetic properties after patterning the films for contact formation into (sub-)micrometer or even nanoscale dimensions. Magnetic properties of arrays of submicrometer ferromagnetic lines have been studied using magnetoresistance measurements [241]. For lateral dimensions down to about 500 nm, far-field Kerr microscopy has been used to determine the magnetization reversal in arrays of magnetic wires [242].

11.3.2. Body-Centered Cubic Cobalt

In the case of cobalt epitaxy on GaAs, a forced phase [243] of Co, the bcc phase [217], can be realized because of the epitaxial relationship. This bcc Co phase has received a lot of attention over the past decade. A review of the bcc Co related work until 1991 was given by Prinz [244]. More recently, the study of bcc Co as seed layers for epitaxial metal structures on GaAs has been reported, as well as further studies on the structural [226] and magnetic properties [245] of bcc Co and CoFe alloys [246]. The appearance of bcc Co in superlattices of Co/Fe [247–249], Co/Pd(111) [250], and Co/τ-MnAl [251] has been demonstrated. In the case of Co/Fe superlattices, nuclear magnetic resonance (NMR) measurements on the short-range chemical order in combination with hyperfine field experiments have illustrated the limits of stability. In superlattices with Co thicknesses above 2 nm, alloy formation with Fe at the interfaces is responsible for the observation of the bcc phase. From reflection high-energy electron diffraction (RHEED) during the growth of the Co, it was concluded that the bcc phase is not sustained beyond about 1 nm. Oscillations of the Fe and Co magnetic moments at the (110) Fe/Co interfaces have recently been studied [252].

11.4. Magnetic and Electrical Properties of Ferromagnets at the Ferromagnetic/Semiconductor Interfaces

For spin injection experiments, it is essential to know the details of the interface, such as the formation of extra phases, the magnetic character of the first metal layers, the stability in time [253], and the electrical properties.

Sulfur passivation of GaAs surfaces has been employed to prevent As interdiffusion into Fe overlayers [254, 255]. It has been suggested that Au be used as an epitaxial barrier

for Fe on GaAs(110) [256]. The Au layer is lattice matched and does not suppress magnetism at the interface. It will also work as a surfactant to support layer-by-layer growth. Recent work by Filipe et al. [257] showed the existence of a nearly half-magnetized phase at the Fe/GaAs interface, which was suggested to be the Fe_3GaAs compound. For Co, an amorphous phase tends to occur at the Co/GaAs interface because of a solid phase regrowth [258]. The use of O_3 treatment of the GaAs surface prior to growth inhibits the As interdiffusion and results in bcc Fe overlayers that are ferromagnetic when thicker than 4 monolayers [259]. Another study reports the onset of ferromagnetism to be at a coverage of 4 to 8 monolayers of Fe on a GaAs(001)–2 × 4 reconstructed surface [260]. In these experiments, it was shown that the initial nucleation proceeds through 2D island formation along the [110] direction. The easy axis of such films turned out to be perpendicular to this direction, demonstrating the limited importance of shape anisotropy induced by the initial nuclei.

The interface properties will change the electrical behavior of the metal/semiconductor heterostructure. These electrical characteristics are normally designed by changing the electronic properties of the semiconductor using doping and band gap engineering such that a tunnel barrier, an ohmic contact, or a Schottky barrier is formed. An uncontrolled interface resulting from phase separation or severe intermixing leads to unpredictable changes in the device performance. The structural and magnetic information on the ferromagnetic/semiconductor interface is quite substantial, but detailed electrical characterization is rather limited. Recently, enhanced carrier lifetimes at room temperature and suppression of midgap states in GaAs were found at an Fe/GaAs interface [261]. This observation leads to the very promising conclusion that the epitaxial Fe film is a good ferromagnetic contact and an excellent choice as a surface passivation layer that does not pin the Fermi level. This was explained in terms of an atomic model of the Fe/GaAs interface in which the Fe is bonded to an As monolayer after dissolution of the As dimers of the GaAs(001)–2 × 4 surface [262].

11.5. Properties of Manganese-Based Epitaxial Magnetic Layers on III–V Semiconductors

When a metal alloy contains either a group III or a group V element, improved interface characteristics can be expected. MnAs is such an alloy that has been grown epitaxially on GaAs [263, 264], for which it was shown that the preparation of the semiconductor surface before growth changes the orientation of the epilayer with respect to the crystal orientation of the substrate. Another example of this class is MnSb epitaxy, which has been demonstrated recently [265, 266]. As in the case of elemental metals, the magnetization of these epitaxially grown alloys is in the plane of the film. Another interesting class of epitaxial magnetic films is that of Mn–III alloys, in which the magnetization is out of the plane. Examples of this class are Mn-based magnetic thin films such as τ-MnAl [267, 268] and δ-MnGa [269, 270] (see Fig. 47). In these cases, the epitaxial growth on a III–V semiconductor substrate (such as GaAs) is the key to obtaining the desired perpendicular magnetization. The metastable phase τ-MnAl can be stabilized by coherence to the semiconductor substrate, and because of the epitaxial relationship, the c axis of the tetragonal lattice is normal to the growth surface. As a consequence, the easy axis of the magnetization of the thin film points out of the plane. The flexibility in engineering new epitaxial multilayers and new magnetic properties using this class of ferromagnetic films has been demonstrated: MnGa/NiGa [269] with multistepped hysteresis loops and ferrimagnetic [271] τ-MnAl/Co superlattices on GaAs [272], in which both magnetic sublayers of the superlattice have a perpendicular magnetization, which are aligned antiparallel at zero field. Very large antiferromagnetic interface coupling strength is observed, together with a strong perpendicular magnetic anisotropy for both the τ-MnAl and the Co layers [271]. Kerr hysteresis loops of

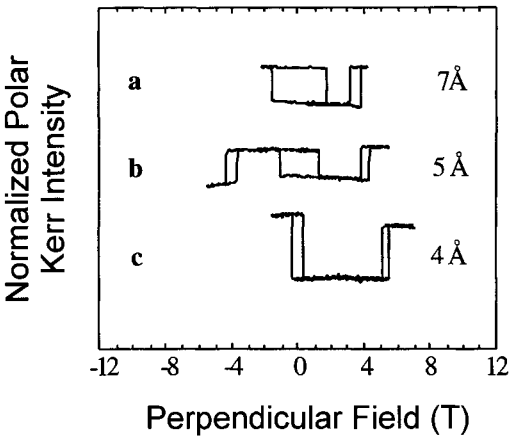


Fig. 48. Polar magneto-optic Kerr effect (MOKE) measurements with the field applied perpendicular to the sample surface of a wedged $6 \times \tau$-MnAl(20 Å)/Co(x Å) lattice grown on GaAs. For the curves in the figure, $x = 7$ (a), $x = 5$ (b), and $x = 4$ (c). (Source: Adapted from [272].)

τ-MnAl/Co superlattices showing the abrupt transitions from antialigned to aligned states are given in Figure 48. These Co layers are found to be partially in the bcc phase.

In alloys such as MnAl and MnGa, a large imbalance in the density of states for majority and minority spins exists about 1 eV above the Fermi level [273, 274]. This property makes them interesting for ballistic magnetotransport studies in ferromagnet/semiconductor hybrid devices. A drawback is the large coercive field in these magnetic films, which may limit their applicability in circuit applications such as magnetic random-access memory (MRAM) [275]. For a more complete review, see [276].

11.6. Semiconductor/Ferromagnetic/Semiconductor Multilayers

As the technology of building artificial structures improves, even more challenging structures may become possible such as epitaxial multilayers of magnetic metal and semiconductors (case D in Fig. 46). Van Roy et al. [277, 278] reported magnetoresistance and coupling effects as a function of the (Ga, Mn, As) thickness in MnGa/(Ga, Mn, As)/MnGa trilayers. When such structures are further optimized, control of the magnetic properties with external modulation sources, such as optical power, may become reality. Announcements of light- (or heat-) induced ferromagnetism [279] and antiferromagnetic coupling [280] in Fe/FeSi have been made recently. This FeSi/Si structure is still under extensive investigation; see, for example, [281].

Butler et al. [282] have performed calculations of the electronic structure of a Fe/GaAs/Fe structure. They conclude that the simple models relying on potential barriers or density of states from the bulk may not apply to such FM/SC/FM structures.

The magnetooptical properties of Co(100)/Ge/Co trilayers have been reported [238]. The coercivity and the anisotropy of these structures oscillate with the Ge thickness. CoPt/(Si, Ge)/Co trilayer and multilayer structures have been fabricated and analyzed using CPP magnetotransport [284]. In these structures, a small steep CPP resistance change has been found that was ascribed to the change in the relative spin orientation of the Co (magnetic soft) and the CoP (magnetic hard) layers.

Although these structures show promising results, often stability at higher temperatures (even room temperature) is a critical issue. In the following section, we discuss an alternative approach to fabricate intimate ferromagnetic/semiconductor hybrid structures, using nanoscale magnetic clusters.

12. NANOSCALE MAGNETS

12.1. Introduction

In all of the previously described structures, the nanoscale dimensions are either controlled in the vertical dimension by deposition or advanced lithography tools are required to realize the nanoscale in the lateral dimension. One alternative that deserves special attention is that of self-organization or self-assembly to realize nanoscale structured materials.

Also popular in semiconductor epitaxial technology is self-organization of nanostructures by growth on structured substrates, step-flow techniques, three-dimensional nucleation, and phase separation. Sort-like experiments in micromagnetics have been reported, nanowires of Co on stepped Cu surfaces [285], nanometer-scale needle-shaped magnetic multilayer wires [286, 287] fabricated using electrodeposition, and a variety of granular structures. Alternatives to incorporating nanoscale magnets in a III–V semiconductor matrix are described in the following discussion. The degrees of freedom in the design of structures incorporating such nanoscale magnets are discussed.

12.2. Self-Organized Magnetic Nanostructures in Semiconductor Thin Films

Self-assembly of nanoscale magnetic clusters in semiconductor materials has gained much interest recently as a route to fabricate magnetic/semiconductor structures that show spin-dependent transport.

Mn or Fe ion implantation in GaAs and subsequent annealing leads to phase separation and formation of magnetic precipitates: MnGa [288–290], MnAs by implantation in As-rich GaAs [291], and Fe_3GaAs [292, 293]. Typical annealing conditions are 600 to 920 °C, for a few seconds to 20 min for Mn-based structures, and 650 °C, 30 s for Fe-implanted layers.

In MBE-grown (Fe, Mn)(In, Ga)As structures, precipitation of FeAs [294, 295], MnAs [296–298], and ErAs [299] has been demonstrated.

Comparing these two techniques leads to the following advantages of ion implantation over MBE growth:

- Lateral dot, wire, or grating structures can be fabricated by "writing" a pattern with the ion beam or by deposition through a lithographically defined mask [289].
- There is no need for an epitaxial layer (unless a specially designed buffer layer is needed, e.g., low-temperature GaAs with an As-rich condition [291].
- Various cluster materials have been demonstrated, see MnGa, MnAs, and Fe_3GaAs mentioned previously.

On the other hand, an MBE process has the following interesting features:

- Buried layers (ferromagnetic/semiconductor) are easier because the epitaxy of the Mn-rich structures is compatible with the growth of III–V semiconductor structures.
- Extreme thickness control of the magnetic layers, down to thicknesses of 5 nm, is possible, and vertical magnet/semiconductor superlattices can be grown.
- The anealing temperatures are compatible with MBE growth (500–650 °C) and annealing can be performed *ex situ* or *in situ*.
- In both fabrication methods, the cluster sizes can be tailored, but, typically, larger near-surface clusters are formed when using ion implantation. Next, we will discuss some experimental data illustrating the flexibility of the MBE procedure.

12.3. Experimental Conditions for Thin Films with Nanoclusters by Molecular Beam Epitaxy + Annealing

12.3.1. Nanoscale Clusters by Molecular Beam Epitaxy: Fabrication and Magnetic Properties

In brief, the fabrication procedure to obtain MnAs precipitates in GaAs is as follows. It is well known that metallic arsenic precipitates form upon annealing of low-temperature grown GaAs (LT-GaAs) using MBE [300]. After the growth of an LT-GaAs buffer layer of typically 200 nm, a Mn flux is supplied to grow LT-$Ga_{1-x}Mn_xAs$. Annealing experiments are performed either *ex situ* or *in situ* while growing a III–V layer or held under As pressure. Under the proper conditions, magnetic particles are formed that are found to be MnAs. The α-MnAs [301] phase is a ferromagnetic phase with NiAs-type hexagonal structure ($a = 0.3724$ nm, $c = 0.5706$ nm). In the bulk, a reversible α-MnAs to β-MnAs (paramagnetic, orthorombic) phase transition takes place at 40 °C.

Magnetization measurements are performed for various annealing treatments. Figure 49 shows a compilation of alternating gradient force magnetometry data for a 0.72-μm-thick $Ga_{0.94}Mn_{0.06}As$ layer [276]. The evolution of the magnetization is described later, where the measured moment is divided by the total epilayer volume to obtain the magnetization value. The values of the saturation magnetization M_{sat} are measured at 796 kA/m (104 Oe).

The as-grown films (curve a in Fig. 49) show very little saturation magnetization, M_{sat} of 3 kA/m (3 emu/cc). Upon annealing at 625 °C for 10 s (curve b of Fig. 49), the M_{sat} rises to 22 kA/m, while the remanent magnetization M_r is only 0.8 kA/m and the coercive field $H_c = 0.96$ kA/m (12 Oe). This curve suggests a superparamagnetic behavior of ultrasmall magnetic particles dispersed in the semiconductor. Annealing at 650 °C for 30 s (curve c in Fig. 49) does not change M_{sat}, but M_r increases to 6 kA/m and H_c increases to 10.4 kA/m (131 Oe). The particle size has increased and the film shows remanence and a clear hysteretic behavior. The decrease of saturation magnetization with subsequent higher annealing is ascribed to the change in composition or phase in the coarsened metallic clusters.

Figure 50 illustrates the phase separation, comparing an as-grown $Ga_{0.94}Mn_{0.06}As$ (Fig. 50a) with the same layer after anneal (600 °C, 30 s, Figure 50b). For $Ga_{1-x}Mn_xAs$

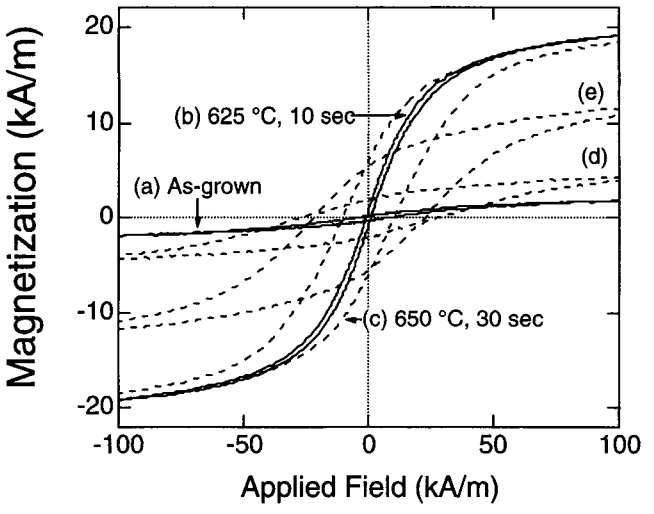


Fig. 49. Magnetization curves of a 0.72-μm-thick $Ga_{0.94}Mn_{0.06}As$ layer as grown and after annealing. The conditions for (a)–(c) are given in the figure. Subsequent annealing at higher tempertures leads to inferior magnetic properties (d) and (e). (Source: Adapted from [276].)

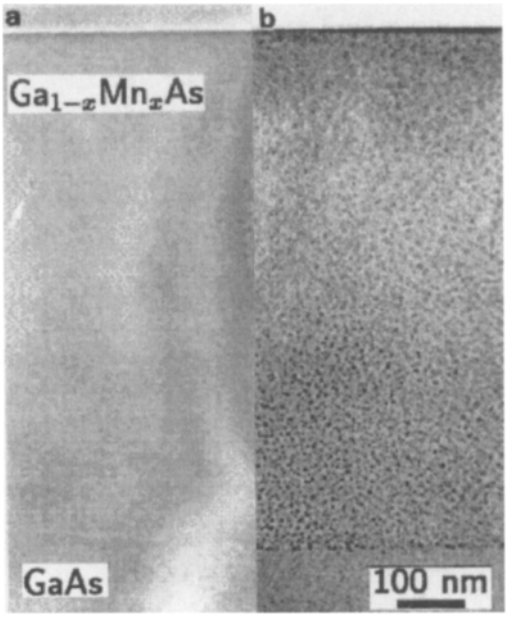


Fig. 50. TEM cross section, illustrating the phase separation in a $Ga_{0.94}Mn_{0.06}As$ layer. No particles are observed in the layer as grown (a) but after anneal (600 °C, 30 s) MnAs precipitates are present (b). (Source: Adapted from [276].)

($x = 0.06$) samples without high-temperature treatment, no particles can be observed using tunneling electron microscopy (TEM). After annealing, the size of the clusters varies with Mn concentration and annealing conditions. For $x = 0.06$, we observe diameters from 3 to 20 nm for heat treatments in the range of 600 to 625 °C (10–30 s, Fig. 50) to 30 nm for treatments exceeding 650 °C (30 s). The surrounding GaAs semiconductor crystal is found to be free of structural defects.

12.3.2. Good-Quality III–V Quantum Structures on Buried Magnetic Buffer Layers

Good-quality semiconductor heterostructures can be fabricated on top of the magnetic MnAs-rich buffers. This is demonstrated by a structure consisting of a 750-nm-thick $Ga_{0.94}Mn_{0.06}As$ buffer layer followed by a 10 × {GaAs(5 nm)/AlAs(5 nm)} multiquantum well (MQW). This sample was terminated by another LT-grown $Ga_{0.96}Mn_{0.04}As$ layer (300 nm thick). The substrate temperature for the epitaxy of the homogeneous $Ga_{0.96}Mn_{0.04}As$ buffer layer was 230 °C. The substrate temperature was then increased to 600 °C for the initiation of the MQW growth. During this growth, the LT-$Ga_{0.96}Mn_{0.04}As$ buffer experienced an *in situ* annealing of 90 min total at 600 °C and MnAs cluster formation occurred. Magnetization measurements on these samples show clear magnetic behavior.

Figure 51 shows the TEM cross-sectional images of this structure, as-grown and after annealing (650 °C, 30 s). The defects shown in Figure 51a are introduced because of improper growth parameters at the initiation of the LT-$Ga_{0.96}Mn_{0.04}As$ layer. They are mostly annealed out after the heat treatment (Fig. 51b). Figure 51c is a TEM closeup of the MQW after anneal Fig. 51(b). The MQW is of excellent structural quality and the magnetic precipitates are well confined in the original Mn-rich epilayers. TEM images reveal as-grown particle sizes of 25–30 nm diameter. Photoluminescence characterization demonstrated good optical quality of the MQW, illustrating the potential of vertically combining magnetic and semiconductor heterostructures using this technique.

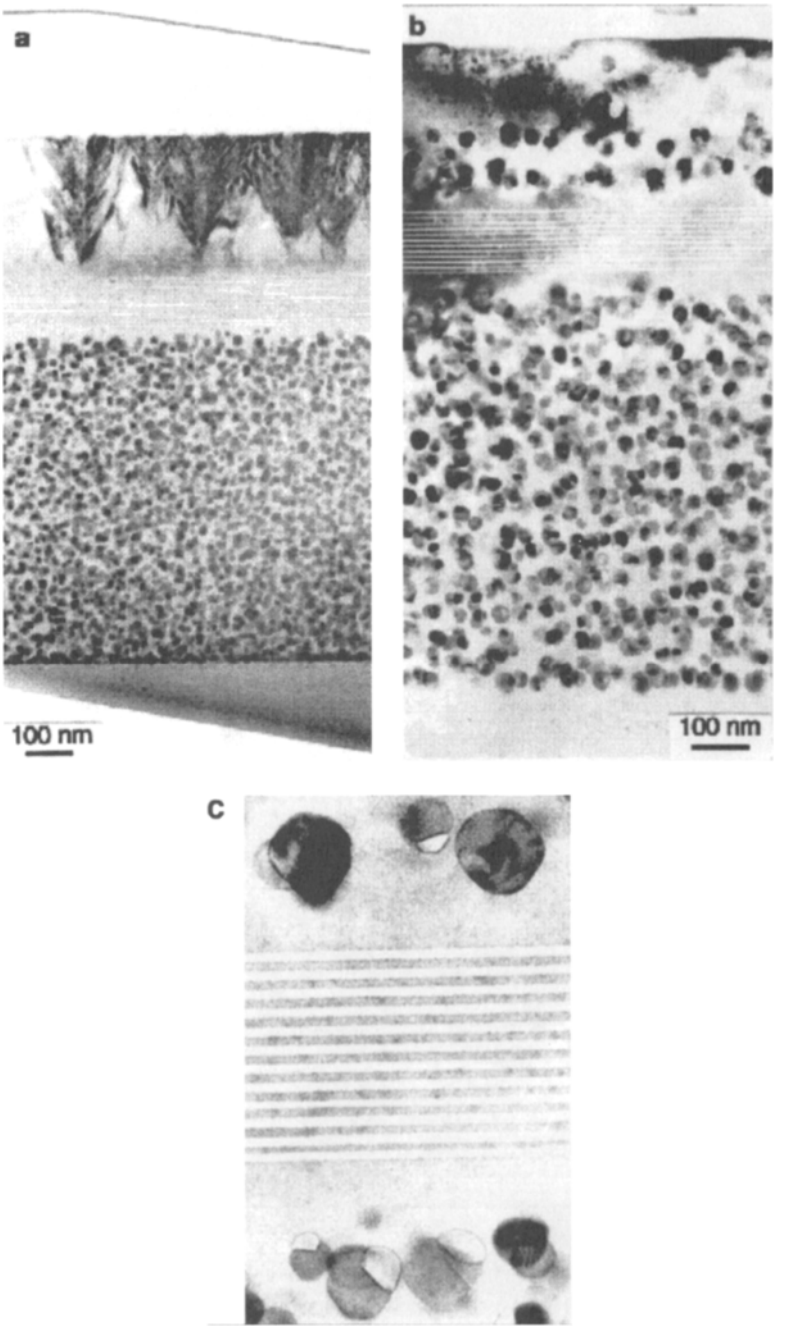


Fig. 51. TEM cross section of sample A (see text for description) (a) as grown and (b) after anneal (650 °C, 30 s). A high-resolution image of the MQW sandwiched by magnetic MnAs-rich layers (c). (Source: Adapted from [276].)

12.3.3. Magnetotransport in Thin Heterogeneous Films

ErAs clusters in GaAs grown by MBE have been recently reported to show large current in the plane (CIP) magnetoresistance (MR) at low temperature [299]. The magnetoresistance properties at low temperatures of clustered InGaAs/FeGaAs [302] and GaAs:MnAs [303] have been recently reported, for the current in the plane of the thin films (CIP geometry). In the case of FeGaAs, the spin transport signal can only be obtained after subtraction of

the MR of a reference InGaAs sample. In the GaAs:MnAs case, up to 1.5 negative MR was found at 30 K in a magnetic field of 1 T, which was attributed to spin-dependent transport properties caused by the presence of the MnAs precipitates [303]. The flexibility of the MBE procedure allows the fabrication of more complex structures such as magnet/semiconductor superlattices in which stronger MR effects may be demonstrated. Next, we will discuss the potential for fabricating superlattices with MnAs-rich heterogeneous layers.

13. SUPERLATTICES OF NANOSCALE MAGNET LAYERS AND SEMICONDUCTORS

13.1. Engineering Aspects of Superlattices of Nanoscale Magnet Layers and Semiconductors

For the realization of spin transport structures involving magnetic clusters, magnet/semiconductor superlattices are a possible candidate. Recently, the fabrication and characterization of magnetic {GaAs:MnAs}/{InGaAs} superlattices was described [304]. In such structures, magnetotransport phenomena can be studied with the current applied perpendicular to the plane (so-called CPP geometry). Such a structure may have many advantages: a vertical structure that is promising for future device applications, control over the vertical distance of the clusters, and the possibility of having a semiconductor spacer of different composition between the clusters, to act as a barrier or a conducting layer (using, e.g., delta-doping). This may help to overcome one of the prime problems in achieving interesting spin-dependent transport, namely, the high resistance of such layers owing to the presence of a Schottky barrier around the metallic precipitates.

The right choice of layer structure may enable modulation of the magnetoelectronic properties of the superlattice by electrically or optically varying the semiconductor properties. These degrees of freedom may be applied in novel device concepts. For clarity, in the text the term magnetic layer is used for the heterogeneous layers with the magnetic clusters {GaAs:MnAs}.

13.2. Structural and Magnetic Properties of the Superlattices

As an example of such superlattices, Figure 52 shows a TEM cross section of a superlattice consisting of 40 periods of {5 nm $In_{0.03}Ga_{0.97}As$/5 nm GaAs:MnAs} after a 500 °C anneal. The MnAs clusters have formed and they are nicely confined within the 5-nm-thick original GaMnAs layers. The clusters are arranged in a 2D sheet and they are spherical with a narrow diameter distribution around 5 nm. As grown, the sample shows negligible magnetization and, after annealing to 500 °C, the room temperature magnetization increases a little. Also, after a 550 °C anneal, superparamagnetic behavior occurs with an increased total moment. Annealing at 600 °C resulted in a ferromagnetic behavior at room temperature, a consequence of large cluster formation (15–30 nm in diameter).

13.3. Current Perpendicular to the Plane Magnetotransport

These superlattice samples are very well suited to test CPP magnetotransport in clustered structures. In a simple model, one can visualize the current in such CPP transport as in Figure 53. As grown (Fig. 53A), the superlattice consists of LT-grown InGaAs and the dilute magnetic semiconductor (DMS) GaMnAs, comparable to a recently reported structure by Shen et al. [305]. In this case, the MR will be dominated by the DMS behavior, which shows a ferromagnetic transition between 40 and 90 K depending on the Mn concentration. Below this transition temperature, hopping conductivity and large negative MR are observed [306].

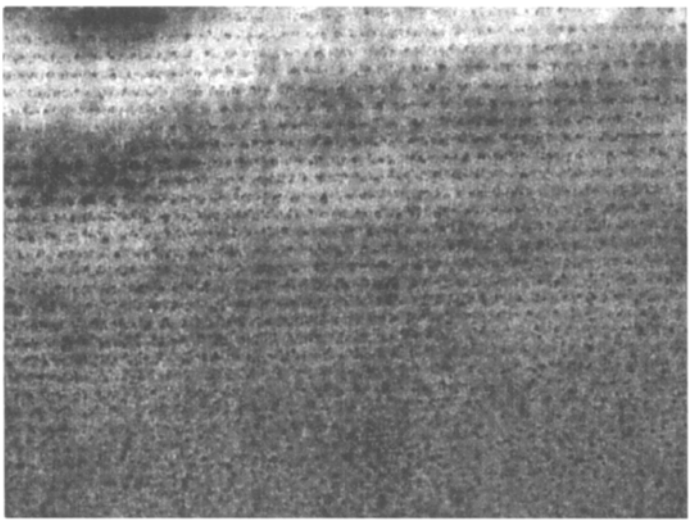


Fig. 52. High-resolution TEM image of an InGaAs(5 nm)/GaAs:MnAs(5 nm) superlattice. (Source: Adapted from [304].)

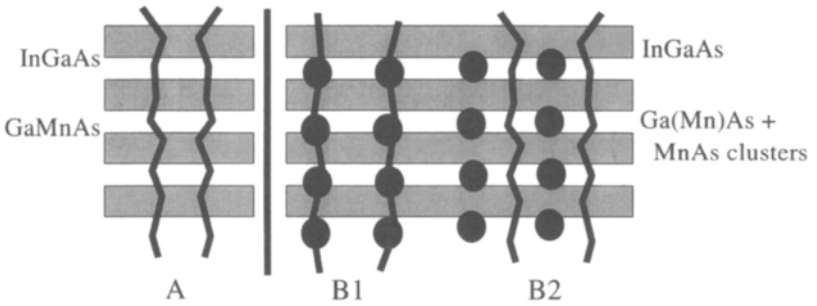


Fig. 53. CPP magnetotransport devices can be fabricated from magnet/semiconductor superlattices. The interpretation of the magnetotransport data is complicated because of the various possible contributions and current paths in the device structure (as grown, A; after anneal, B). (Source: Adapted from [304].)

When clusters are present (Fig. 53B), the idealized model shows two possible current paths in the CPP orientation: the path of interest in this study is B1 where the current samples the clusters and crosses the magnet/semiconductor interfaces, hence becoming dependent on the magnetic state of the clusters. In path B2, the situation is comparable to A, except for the much lower Mn concentration in the Ga(Mn)As layers of B2.

13.4. Conclusions

It is clear that self-assembled hybrid nanoscale magnetic/semiconductor heterostructures can be designed to show exciting new physical, electronic, and magnetooptical [307–312] properties. When the magnetic/semiconductor structures are reaching the nanoscale dimensions, effects such as Coulomb blockade may start to appear. First attempts are being made today in tunneling into magnetic clusters to observe a magnetotransport phenomenon in structures working in the Coulomb blockade regime [313]. It is to be expected that nanomagnet structures will become important in the demonstration of spin-dependent transport phenomena for device applications.

Acknowledgments

JDB would like to thank G. Borghs for his encouragement and many fruitful discussions and for a critical reading of the manuscript. FMP is supported as a Research Director with the Flemish Science Foundation. The following co-workers are kindly acknowledged for their important contribution to parts of the work described: H. Akinaga, K. Attenborough, M. Behet, H. Boeve, G. Borghs, C. Bruynseraede, K. Dessein, B. Dutta, I. S. Ibrahim, A. Matulis, J. Reijniers, V. Schweigert, A. Van Esch, W. Van Roy, P. Vasilopoulos, T. Sands, and M. Tanaka. This work was supported by the Interuniversity Micro-Electronics Center (IMEC), the Flemish Science Foundation (FWO-Vl), and IUAP-IV. JDB acknowledges the financial support of the European Commission through funding of the ESPRIT long-term research program SPIDER, Spin-dependent nanoelectronics (No. 23.307), in which ferromagnetic/semiconductor combinations are investigated.

References

1. D. Shoenberg, "Magnetic Oscillations in Metals." Cambridge University Press, Cambridge, U.K., 1984.
2. For a review, see, for example, J. K. Furdyna, *J. Appl. Phys.* 64, R29 (1988).
3. J. Reijniers and F. M. Peeters, *Appl. Phys. Lett.* 73, 357 (1998).
4. F. M. Peeters and A. Matulis, *Braz. J. Phys.* 24, 283 (1994).
5. I. S. Ibrahim and F. M. Peeters, *Phys. Rev. B* 52, 17321 (1995).
6. W. Van Roy, J. De Boeck, and G. Borghs, *Appl. Phys. Lett.* 61, 3056 (1992).
7. F. M. Peeters and A. Matulis, *Phys. Rev. B* 48, 15166 (1993).
8. M. Calvo, *Phys. Rev. B* 48, 2365 (1993).
9. J. Hajdu, in "Physics of the Two-Dimensional Electron Gas" (J. T. Devreese and F. M. Peeters, eds.), p. 27. Plenum Press, New York, 1987.
10. A. Matulis, F. M. Peeters, and P. Vasilopoulos, *Phys. Rev. Lett.* 72, 1518 (1994).
11. L. D. Landau and E. Lifshitz, "Quantum Mechanics," p. 66. Pergamon Press, Oxford, U.K., 1977.
12. O. Hudák, *Z. Phys.* 88, 233 (1992).
13. H. Yoshioka and Y. Nagaoka, *J. Phys. Soc. Jpn.* 59, 2884 (1990).
14. B. Y. Gu and X. D. Fan, *Z. Phys. B* 101, 527 (1996).
15. V. M. Ramaglia and F. Ventriglia, *J. Phys.: Condens. Matter* 3, 4881 (1991).
16. V. M. Ramaglia, A. Tagliacozzo, F. Ventriglia, and G. P. Zucchelli, *Phys. Rev. B* 43, 2201 (1991).
17. M. Calvo, *J. Phys.: Condens. Matter* 6, 3329 (1994).
18. M. Calvo, *Phys. Rev. B* 51, 2268 (1995).
19. A. Matulis, F. M. Peeters, and P. Vasilopoulos, *Surf. Sci.* 305, 434 (1994).
20. M. Büttiker, *Phys. Rev. Lett.* 57, 1761 (1986).
21. J. Q. You, L. Zhang, and P. K. Ghosh, *Phys. Rev. B* 52, 17243 (1995).
22. A. Majumdar, *Phys. Rev. B* 54, 11911 (1996).
23. Y. Guo, B. L. Gu, W. H. Duan, and Y. Zhang, *Phys. Rev. B* 55, 9314 (1997).
24. P. P. Vil'ms and M. V. Éntin, *Sov. Phys. Semicond.* 22, 1209 (1988) [*Fiz. Tekh. Poluporovodn.* 22, 1905 (1988)].
25. J. M. Repko, W. W. Repko, and A. Saaf, *Am. J. Phys.* 59, 652 (1991).
26. J. E. Müller, *Phys. Rev. Lett.* 68, 385 (1992).
27. E. Hofstetter, J. M. C. Taylor, and A. MacKinnon, *Phys. Rev. B* 53, 4676 (1996).
28. Y. Takagaki and K. Ploog, *Phys. Rev. B* 53, 3885 (1996).
29. H. Grosse, A. Martin, and J. Stubbe, *Phys. Lett. A* 181, 7 (1993).
30. D. Huang and G. Gumbs, *Phys. Lett. A* 167, 396 (1992).
31. C. L. Foden, M. L. Leadbeater, and M. Pepper, *Phys. Rev. B* 52, 8646 (1995).
32. C. L. Foden, M. L. Leadbeater, J. H. Burroughes, and M. Pepper, *J. Phys.: Condens. Matter* 6, L127 (1994).
33. (a) F. M. Peeters, A. Matulis, and I. S. Ibrahim, *Physica B* 227, 131 (1996); (b) J. Reijniers, F. M. Peeters, and A. Matulis, *Phys. Rev. B* 59, 2817 (1999).
34. L. Solimany and B. Kramer, *Solid State Commun.* 96, 471 (1995).
35. H. S. Sim, K. H. Ahn, K. J. Chang, G. Ihm, N. Kim, and S. J. Lee, *Phys. Rev. Lett.* 80, 1501 (1998).
36. M. L. Leadbeater, C. L. Foden, T. M. Burke, J. H. Burroughes, M. P. Grimshaw, D. A. Ritchie, L. L. Wang, and M. Pepper, *J. Phys.: Condens. Matter* 7, L307 (1995).
37. M. L. Leadbeater, C. L. Foden, J. H. Burroughes, M. Pepper, T. M. Burke, L. L. Wang, M. P. Grimshaw, and D. A. Ritchie, *Phys. Rev. B* 52, R8629 (1995).
38. M. L. Leadbeater, C. L. Foden, J. H. Burroughes, T. M. Burke, D. A. Ritchie, and M. Pepper, in "Proceedings of the 23rd International Conference on the Physics of Semiconductors" (M. Scheffler and R. Zimmermann, eds.), p. 2219. World Scientific, Singapore, 1996.

39. I. S. Ibrahim, V. A. Schweigert, and F. M. Peeters, *Phys. Rev. B* 56, 7508 (1997).
40. S. M. Badalian, I. S. Ibrahim, and F. M. Peeters, in "Proceedings of the 12th International Conference on High Magnetic Fields in the Physics of Semiconductors II" (G. Landwehr and W. Ossau, eds.), p. 327. World Scientific, Singapore, 1997.
41. H. Jou and A. M. Kriman, *Superlattices Microstruct.* 19, 203 (1996).
42. P. F. Fontein, J. A. Kleinen, P. Hendriks, F. A. P. Blom, J. H. Wolter, H. G. M. Lochs, F. A. J. M. Driessen, L. J. Giling, and C. W. J. Beenakker, *Phys. Rev. B* 43, 12090 (1991).
43. A. H. MacDonald, T. M. Rice, and W. F. Brinkman, *Phys. Rev. B* 28, 3648 (1983).
44. R. W. Rendell and S. M. Girvin, *Phys. Rev. B* 23, 6610 (1981).
45. J. Heremans, *J. Phys. D: Appl. Phys.* 26, 1149 (1993).
46. D. Weiss, K. von Klitzing, K. Ploog, and G. Weiman, *Europhys. Lett.* 8, 179 (1989).
47. R. R. Gerhardts, D. Weiss, and K. von Klitzing, *Phys. Rev. Lett.* 62, 1173 (1989).
48. R. W. Winkler, J. P. Kotthaus, and K. Ploog, *Phys. Rev. Lett.* 62, 1177 (1989).
49. E. S. Alves, P. H. Beton, M. Henini, L. Eaves, P. C. Main, O. H. Hughes, G. A. Toombs, S. P. Beaumont, and C. D. W. Wilkinson, *J. Phys.: Condens. Matter* 1, 8257 (1989).
50. P. H. Beton, E. S. Alves, P. C. Main, L. Eaves, M. W. Dellow, M. Henini, O. H. Hughes, S. P. Beaumont, and C. D. W. Wilkinson, *Phys. Rev. B* 42, 9229 (1990).
51. P. H. Beton, P. C. Main, M. Davison, M. Dellow, R. P. Taylor, E. S. Alves, L. Eaves, S. P. Beaumont, and C. D. W. Wilkinson, *Phys. Rev. B* 42, 9689 (1990).
52. H. Fang and P. J. Stiles, *Phys. Rev. B* 41, 10171 (1990).
53. A. Toriumi, K. Ismail, M. Burkhardt, D. A. Antoniadis, and H. I. Smith, *Phys. Rev. B* 41, 12346 (1990).
54. P. Vasilopoulos and F. M. Peeters, *Phys. Rev. Lett.* 63, 2120 (1989).
55. F. M. Peeters and P. Vasilopoulos, *Phys. Rev.* B 46, 4667 (1992).
56. C. T. Cui, V. Fessatidis, and N. J. M. Horing, *Phys. Rev. Lett.* 63, 2598 (1989).
57. P. Středa and A. H. MacDonald, *Phys. Rev. B* 41, 11892 (1990).
58. C. W. J. Beenakker, *Phys. Rev. Lett.* 62, 2020 (1989).
59. C. Zhang and R. R. Gerhardts, *Phys. Rev. B* 41, 12850 (1990).
60. G. H. Kruithof and T. M. Klapwijk, in "Proceedings of the 19th International Conference on the Physics of Semiconductors" (W. Zawadzki, ed.), p. 499. Polish Academy of Science, Wroclaw, Poland, 1988.
61. G. H. Kruithof, P. C. van Son, and T. M. Klapwijk, *Phys. Rev. Lett.* 67, 2725 (1991).
62. S. J. Bending, K. von Klitzing, and K. Ploog, *Phys. Rev. Lett.* 65, 1060 (1990).
63. A. K. Geim, S. J. Bending, I. V. Grigorieva, and M. G. Blamire, *Phys. Rev. B* 49, 5749 (1994).
64. H. A. Carmona, A. K. Geim, A. Nogaret, P. C. Main, T. J. Foster, M. Henini, S. P. Beaumont, and M. G. Blamire, *Phys. Rev. Lett.* 74, 3009 (1995).
65. S. Carlton, A. Nogaret, H. A. Carmona, B. L. Gallagher, P. C. Main, and S. P. Beaumont, in "Proceedings of the 23rd International Conference on the Physics of Semiconductors" (M. Scheffler and R. Zimmermann, eds.), p. 1537. World Scientific, Singapore, 1996.
66. P. D. Ye, D. Weiss, R. R. Gerhardts, K. von Klitzing, K. Eberl, H. Nickel, and C. T. Foxon, *Semicond. Sci. Technol.* 10, 715 (1995).
67. P. D. Ye, D. Weiss, R. R. Gerhardts, M. Seeger, K. von Klitzing, K. Eberl, and H. Nickel, *Phys. Rev. Lett.* 74, 3013 (1995).
68. H. A. Carmona, A. Nogaret, A. K. Geim, P. C. Main, T. J. Foster, M. Henini, S. P. Beaumont, H. McLelland, and M. G. Blamire, *Solid-State Electron.* 40, 217 (1996).
69. Y. Iye, A. Endo, S. Izawa, M. Kato, and S. Katsumoto, *Physica B* 227, 122 (1996).
70. S. I. Izawa, S. Katsumoto, A. Endo, and Y. Iye, *J. Phys. Soc. Jpn.* 64, 706 (1995).
71. S. I. Izawa, S. Katsumoto, A. Endo, and Y. Iye, *Jpn. J. Appl. Phys.* 34, 4306 (1995).
72. A. Nogaret, S. Carlton, B. L. Gallagher, P. C. Main, M. Henini, R. Wirtz, R. Newbury, M. A. Howson, and S. P. Beaumont, *Phys. Rev. B* 55, R16037 (1997).
73. N. Overend, A. Nogaret, B. L. Gallagher, P. C. Main, M. Henini, R. Wirtz, R. Newbury, M. A. Howson, and S. P. Beaumont, in "ICM'97."
74. P. D. Ye, D. Weiss, K. von Klitzing, and K. Eberl, *Appl. Phys. Lett.* 67, 1441 (1995).
75. P. D. Ye, D. Weiss, G. Lütjering, R. R. Gerhardts, K. von Klitzing, and K. Eberl, in "Proceedings of the 23rd International Conference on the Physics of Semiconductors" (M. Scheffler and R. Zimmermann, eds.), p. 1529. World Scientific, Singapore, 1996.
76. P. D. Ye, D. Weiss, R. R. Gerhardts, K. von Klitzing, K. Eberl, and H. Nickel, *Surf. Sci.* 361/362, 337 (1996).
77. P. D. Ye, D. Weiss, R. R. Gerhardts, G. Lütjering, K. von Klitzing, and H. Nickel, *Semicond. Sci. Technol.* 11, 1613 (1996).
78. P. D. Ye, D. Weiss, R. R. Gerhardts, K. von Klitzing, and S. Tarucha, in "Proceedings of the Electronic Properties of Two-Dimensional Systems," *Physica B* (1998).
79. G. M. Gusev, U. Gennser, X. Kleber, D. K. Maude, J. C. Portal, D. I. Lubyshev, P. Basmaji, M. de P. A. Silva, J. C. Rossi, and Yu. V. Nastaushev, *Superlattices Microstruct.* 18, 67 (1995).
80. G. M. Gusev, V. Gennser, X. Kleber, D. K. Maude, J. C. Portal, D. I. Lubyshev, P. Basmaji, M. de P. A. Silva, J. C. Rossi, and Yu. V. Nastaushev, *Phys. Rev. B* 53, 13641 (1996).

81. R. Yagi and Y. Iye, *J. Phys. Soc. Jpn.* 62, 1279 (1993).
82. D. Weiss, P. D. Ye, and R. R. Gerhardts, in "Proceedings of the 23rd International Conference on the Physics of Semiconductors" (M. Scheffler and R. Zimmermann, eds.), p. 2367. World Scientific, Singapore, 1996.
83. N. Overend, A. Nogaret, B. L. Gallagher, P. C. Main, M. Henini, C. H. Marrows, M. A. Howson, and S. P. Beaumont, *Appl. Phys. Lett.* 72, 1724 (1998).
84. D. D. Awschalom, M. A. McCord, and G. Grinstein, *Phys. Rev. Lett.* 65, 783 (1990).
85. P. Vasilopoulos and F. M. Peeters, *Superlattices Microstruct.* 7, 393 (1990).
86. D. P. Xue and G. Xiao, *Phys. Rev. B* 45, 5986 (1992).
87. F. M. Peeters and P. Vasilopoulos, *Phys. Rev. B* 47, 1466 (1993).
88. R. R. Gerhardts, in "Proceedings of the 12th International Conference on High Magnetic Fields in the Physics of Semiconductors II" (G. Landwehr and W. Ossau, eds.), p. 289. World Scientific, Singapore, 1997.
89. T. Z. Li, S. W. Gu, X. H. Wang, and J. P. Peng, *J. Phys.: Condens. Matter* 8, 313 (1996).
90. R. R. Gerhardts, *Phys. Rev. B* 53, 11064 (1996).
91. R. Menne and R. R. Gerhardts, *Phys. Rev. B* 57, 1707 (1998).
92. X. G. Wu and S. E. Ulloa, *Solid State Commun.* 82, 945 (1992).
93. X. G. Wu and S. E. Ulloa, *Phys. Rev. B* 47, 7182 (1993).
94. X. G. Wu and S. E. Ulloa, *Phys. Rev. B* 47, 10028 (1993).
95. F. M. Peeters and P. Vasilopoulos, *Phys. Rev. B* 42, 5899 (1990).
96. I. S. Ibrahim and F. M. Peeters, *Am. J. Phys.* 63, 171 (1995).
97. A. Krakovsky, *Phys. Rev. B* 53, 8469 (1996).
98. R. B. S. Oakeshott and A. MacKinnon, *J. Phys.: Condens. Matter* 5, 9355 (1993).
99. J. Q. You and L. Zhang, *Phys. Rev. B* 54, 1526 (1996).
100. Y. Guo, B. L. Gu, Z. Q. Li, J. L. Zhu, and Y. Kawazoe, *J. Phys.: Condens. Matter* 10, 1549 (1998).
101. A. Akjouj and B. Djafari-Rouhani, *Solid State Commun.* 103, 161 (1997).
102. I. S. Ibrahim and F. M. Peeters, *Surf. Sci.* 361/362, 341 (1996).
103. R. D. Hofstadter, *Phys. Rev. B* 14, 2239 (1976).
104. B. A. Dubrovin and S. P. Novikov, *Sov. Phys. JETP* 52, 511 (1980) [*Zh. Eksp. Teor. Fiz.* 79, 1006 (1980)].
105. D. Yoshioka and Y. Iye, *J. Phys. Soc. Jpn.* 56, 448 (1987).
106. A. Barelli, J. Bellissard, and R. Rammal, *J. Phys. France* 51, 2167 (1990).
107. P. Hedegård and A. Hoff, *Physica B* 194, 1075 (1994).
108. M. C. Chang and Q. Niu, *Phys. Rev. B* 50, 10843 (1994).
109. R. R. Gerhardts, D. Pfannkuche, and V. Gudmundsson, *Phys. Rev. B* 53, 9591 (1996).
110. G. J. O. Schmidt, *Phys. Rev. B* 47, 13007 (1993).
111. P. Schmelcher and D. L. Shepelyansky, *Phys. Rev. B* 49, 7418 (1994).
112. A. K. Geim, S. J. Bending, and I. V. Grigorieva, *Phys. Rev. Lett.* 69, 2252 (1992).
113. W. Van Roy, E. L. Carpi, M. Van Hove, A. Van Esch, R. Bogaerts, J. De Boeck, and G. Borghs, *J. Magn. Magn. Mater.* 121, 197 (1993).
114. M. A. McCord and D. D. Awschalom, *Appl. Phys. Lett.* 57, 2153 (1990).
115. M. Nielsen and P. Hedegård, *Phys. Rev. B* 51, 7679 (1995).
116. F. B. Mancoff, R. M. Clarke, C. M. Marcus, S. C. Zhang, K. Campman, and A. C. Gossard, *Phys. Rev. B* 51, 13269 (1995).
117. F. B. Mancoff, L. J. Zielinski, C. M. Marcus, K. Campman, and A. C. Gossard, *Phys. Rev. B* 53, R7599 (1995).
118. P. Omling, H. Linke, K. Deppert, L. Samuelson, L. T. Hansen, and P. E. Lindelof, *Jpn. J. Appl. Phys.* 34, 4575 (1995).
119. A. Smith, R. Taboryski, L. T. Hansen, C. B. Sørensen, P. Hedegård, and P. E. Lindelof, *Phys. Rev. B* 50, 14726 (1994).
120. D. F. Yue, G. Banerjee, A. E. Miller, and S. Bandyopadhyay, *Superlattices Microstruct.* 19, 191 (1996).
121. A. G. Aronov, E. Altshuler, A. D. Mirlin, and P. Wölfle, *Europhys. Lett.* 29, 239 (1995).
122. M. Calvo, *Phys. Rev. B* 57, R4241 (1998).
123. L. Zielinski, K. Chaltikian, K. Birnbaum, C. M. Marcus, K. Campman, and A. C. Gossard, *Europhys. Lett.* 42, 73 (1998).
124. B. I. Halperin, P. A. Lee, and N. Read, *Phys. Rev. B* 47, 7312 (1993).
125. V. Kalmeyer and S. C. Zhang, *Phys. Rev. B* 46, 9889 (1992).
126. W. Kang, H. L. Stormer, L. N. Pfeiffer, K. J. Boldwin, and K. W. West, *Phys. Rev. Lett.* 71, 3850 (1993).
127. R. L. Willet, R. R. Ruel, K. W. West, and L. N. Pfeiffer, *Phys. Rev. Lett.* 71, 3846 (1993).
128. P. W. Anderson, *Science* 235, 1196 (1987).
129. L. B. Ioffe and A. I. Larking, *Phys. Rev. B* 39, 8988 (1989).
130. N. Nagaosa and P. A. Lee, *Phys. Rev. Lett.* 64, 2450 (1990).
131. N. Nagaosa and P. A. Lee, *Phys. Rev. B* 46, 5621 (1992).
132. E. Abrahams, P. W. Anderson, D. C. Liciardello, and V. Ramakrishnan, *Phys. Rev. Lett.* 42, 673 (1979).
133. S. Hikami, *Prog. Theor. Phys. Suppl.* 107, 213 (1992).
134. A. G. Aronov, A. D. Mirlin, and P. Wölfle, *Phys. Rev. B* 49, 16609 (1994).

135. T. Sugiyama and N. Nagaosa, *Phys. Rev. Lett.* 70, 1980 (1993).
136. D. N. Sheng and Z. Y. Weng, *Phys. Rev. Lett.* 75, 2388 (1995).
137. J. Rammer and A. L. Shelankov, *Phys. Rev. B* 36, 3135 (1987).
138. L. Brey and H. A. Fertig, *Phys. Rev. B* 47, 15961 (1993).
139. A. Khaetskii, *J. Phys.: Condens. Matter* 3, 5115 (1991).
140. P. Hedegård and A. Smith, *Phys. Rev. B* 51, 10869 (1995).
141. D. Khveshchenko, *Phys. Rev. Lett.* 77, 1817 (1996).
142. A. K. Geim, *JETP Lett.* 50, 389 (1989) [*Pis'ma Zh. Eksp. Teor. Fiz.* 50, 359 (1989)].
143. A. K. Geim, S. V. Dubonos, and A. V. Khaetskii, *JETP Lett.* 51, 121 (1990) [*Pis'ma Zh. Eksp. Teor. Fiz.* 51, 107 (1990)].
144. A. K. Geim, *JETP Lett.* 50, 389 (1989) [*Pis'ma Zh. Eksp. Teor. Fiz.* 50, 359 (1989)].
145. A. K. Geim, V. I. Falko, S. V. Dubonos, and I. V. Grigorieva, *Solid State Commun.* 82, 831 (1992).
146. E. Hall, *Am. J. Math. II* 287 (1879).
147. A. Oral, S. J. Bending, and M. Henini, *Appl. Phys. Lett.* 69, 1324 (1996).
148. S. J. Bending and A. Oral, *J. Appl. Phys.* 81, 3721 (1997).
149. A. K. Geim, S. V. Dubonos, J. G. S. Lok, I. V. Grigorieva, J. C. Maan, L. T. Hansen, and P. E. Lindelof, *Appl. Phys. Lett.* 71, 2379 (1997).
150. A. K. Geim, I. V. Grigorieva, S. V. Dubonos, J. G. S. Lok, J. C. Maan, A. E. Filippov, and F. M. Peeters, *Nature (London)* 390, 259 (1997).
151. F. M. Peeters, X. Q. Li, and A. Matulis, in "Proceedings of the International Conference on Quantum Devices and Circuits" (K. Ismail, S. Bandyopadhyay, and J. P. Leburton, eds.), p. 253. World Scientific, Singapore, 1997.
152. F. M. Peeters and X. Q. Li, *Appl. Phys. Lett.* 72, 572 (1998).
153. I. S. Ibrahim, V. A. Schweigert, and F. M. Peeters, *Phys. Rev. B* 57, 15416 (1998).
154. C. W. J. Beenakker and H. van Houten, *Phys. Rev. Lett.* 63, 1857 (1989).
155. M. L. Roukes, A. Scherer, S. J. Allen, Jr., H. G. Craighead, R. M. Ruthen, E. D. Beebe, and J. Harbison, *Phys. Rev. Lett.* 59, 3011 (1987).
156. H. U. Baranger, D. P. DiVincenzo, R. A. Jalabert, and A. D. Stone, *Phys. Rev. B* 44, 10637 (1991).
157. M. Johnson, B. R. Bennett, M. J. Yang, M. M. Miller, and B. V. Shanabrook, *Appl. Phys. Lett.* 71, 974 (1997).
158. F. G. Monzon, M. Johnson, and M. L. Roukes, *Appl. Phys. Lett.* 71, 3087 (1997).
159. M. N. Baibich, J. M. Broto, A. Fert, F. Ngyuen van Dau, F. Petroff, P. Etienne, G. Creuzet, A. Friederich, and J. Chazelas, *Phys. Rev. Lett.* 61, 2472 (1988).
160. B. Heinrich and J. A. C. Bland, eds., "Ultrathin Magnetic Films I and II." Springer-Verlag, Berlin, 1994, and the many references therein.
161. D. J. Monsma, J. C. Lodder, Th. J. A. Popma, and B. Bieny, *Phys. Rev. Lett.* 74, 5260 (1995).
162. R. J. Celotta, J. Unguris, and D. T. Pierce, *J. Appl. Phys.* 75, 6452 (1994).
163. H. J. Drouhin, A. J. van der Sluijs, Y. Lassaly, and G. Lampel, *J. Appl. Phys.* 79, 4734 (1996).
164. D. J. Monsma, R. Vlutters, T. Shimatsu, E. G. Keim, R. H. Mollema, and J. C. Lodder, *IEEE Trans. Magn.* 33, 3495 (1997).
165. K. Mizuyama, T. Kinno, T. Yamauchi, and K. Tanaka, *IEEE Trans Magn.* 33, 3500 (1997).
166. T. Kinno, K. Tanaka, and K. Mizushima, *Phys. Rev. B* 56, R4391 (1997).
167. M. Messervey, P. M. Tedrow, and P. Fulde, *Phys. Rev. Lett.* 25, 1270 (1970).
168. R. Messervey, D. Paraskevopoulos, and P. M. Tedrow, *Phys. Rev. Lett.* 37, 858 (1976).
169. A. G. Aronov, *JETP Lett.* 24, 32 (1976) [*Pis'ma Zh. Eksp. Teor. Fiz.* 24, 37 (1976)].
170. R. H. Silsbee, *Bull. Magn. Reson.* 2, 284 (1980).
171. M. Johnson and R. H. Silsbee, *Phys. Rev. Lett.* 55, 17 (1985).
172. M. Johnson and R. H. Silsbee, *Phys. Rev. B* 37, 5312 (1988).
173. M. Johnson and R. H. Silsbee, *Phys. Rev. B* 37, 5326 (1988).
174. M. Johnson, *Phys. Rev. Lett.* 67, 3594 (1991), and references therein.
175. A. Fert and S. F. Lee, *J. Magn. Magn. Mater.* 165, 115 (1997), and references therein.
176. S. Alvarado and P. Renaud, *Phys. Rev. Lett.* 68, 1387 (1992).
177. P. M. Thedrow and R. Messervey, *Phys. Rev. Lett.* 26, 192 (1971).
178. J. A. Hertz and K. Aoi, *Phys. Rev. B* 8, 3252 (1973).
179. M. B. Stearns, *J. Magn. Magn. Mater.* 5, 167 (1977).
180. R. Messervey, *J. Appl. Phys.* 61, 3709 (1987).
181. J. Braun and G. Borstel, *Surf. Sci.* 307–309, 1118 (1994).
182. T. Maruyama, E. L. Garwin, R. A. Mair, R. Prepost, J. S. Smith, and J. D. Walker, *J. Appl. Phys.* 73, 5189 (1993).
183. G. K. Zyryanov, I. A. Pchelkin, and M. S. Lepestkina, *Techn. Phys. Lett.* 20, 122 (1994).
184. M. Tawada, T. Baba, Y. Kurihara, M. Mizuta, T. Nakanishi, K. Nishitani, S. Okumi, T. Omori, C. Suzuki, Y. Takeuchi, K. Togawa, and M. Yoshioka, *Jpn. J. Appl. Phys., Part 1* 36, 2863 (1997).
185. T. Saka, T. Kato, T. Nakanishi, H. Aoyagi, T. Kosugoh, S. Nakamura, M. Tawada, M. Tsubata, H. Horinaka, and Y. Kamiya, *J. Cryst. Growth* 124, 346 (1992).

186. W. G. Bi and C. W. Tu, *J. Vac. Sci. Techol., B* 14, 2282 (1996).
187. Yu. B. Bolkhovityanov, A. M. Gilinskii, N. V. Nomerotskii, E. M. Trukhanov, and A. S. Yaroshevich, *Techn. Phys. Lett.* 19, 399 (1993).
188. E. Pelucchi, S. De-Rossi, and F. Ciccacci, *J. Electron Spectrosc. Relat. Phenom.* 76, 505 (1995).
189. T. Nakanishi, H. Aoyagi, S. Nakamura, S. Okumi, C. Suzuki, C. Takahashi, Y. Tanimoto, M. Tawada, K. Togawa, M. Tsubata, Y. Kurihara, T. Omori, Y. Takeuchi, M. Yoshioka, T. Kato, T. Saka, T. Baba, and M. Mizuta, *AIP Conf. Proc.* 343, 622 (1995).
190. T. Saka, T. Kato, T. Nakanishi, M. Tsubata, K. Kishino, H. Horinaka, Y. Kamiya, S. Okumi, C. Takahashi, Y. Tanimoto, M. Tawada, K. Togawa, H. Aoyagi, S. Nakamura, *Jpn. J. Appl. Phys.* 32, L1837 (1993).
191. F. Ciccacci, S. De Rossi, E. Pelucchi, and A. Tagliaferri, *Rev. Sci. Instrum.* 68, 1841 (1997).
192. P. Drescher, H. G. Andresen, K. Aulenbacher, J. Bermuth, T. Dombo, H. Fischer, H. Euteneuer, N. N. Faleev, M. S. Galaktionov, D. von-Harrach, P. Hartmann, J. Hoffmann, P. Jennewein, K. H. Kaiser, S. Koebis, O. V. Kovalenkov, H. J. Kreidel, J. Langbein, Y. A. Mamaev, C. Nachtigall, M. Petri, S. Pluetzer, E. Reichert, M. Schemies, H. J. Schoepe, K. H. Steffens, M. Steigerwald, A. V. Subashiev, H. Trautner, D. A. Vinokurov, Y. P. Yashin, and B. S. Yavich, *Appl. Phys. A* 63, 203 (1996).
193. M. W. J. Prins, R. Jansen, and H. van Kempen, *Phys. Rev. B* 53, 8105 (1996).
194. M. W. J. Prins, R. Jansen, R. H. M. Groeneveld, A. P. van Gelder, and H. van Kempen, *Phys. Rev. B* 53, 8090 (1996).
195. R. Wiesendanger, H.-J. Güntherodt, G. Güntherodt, R. J. Gambina, and R. Ruf, *Phys. Rev. Lett.* 65, 247 (1990), and references therein on spin-polarized analysis.
196. Y. Suzuki, W. Habhan, and K. Tanaka, *Appl. Phys. Lett.* 71, 3153 (1997).
197. S. Datta and B. Das, *Appl. Phys. Lett.* 56, 665 (1990).
198. G. Lommer, F. Malcher, and U. Rössler, *Phys. Rev. Lett.* 60, 728 (1988).
199. J. Luo, H. Munekata, F. F. Fang, and P. J. Stiles, *Phys. Rev. B* 38, 10142 (1988).
200. J. Luo, H. Munekata, F. F. Fang, and P. J. Stiles, *Phys. Rev. B* 41, 7685 (1990).
201. E. I. Rashba, *Sov. Phys. Solid State* 2, 1109 (1960) [*Fiz. Tverd. Tela (Leningrad)* 2, 1224 (1960)].
202. Y. A. Bychov and E. I. Rashba, *J. Phys. C* 17, 6039 (1984).
203. J. P. Heida, B. J. van Wees, T. M. Klapwijk, and G. Borghs, in "Proceedings of the 23rd International Conference on the Physics of Semiconductors," p. 2467. World Scientific, Singapore, 1996.
204. J. Nitta, T. Akazaki, H. Takayanagi, and T. Enoki, *Phys. Rev. Lett.* 78, 1335 (1997).
205. M. Behet, S. Nemeth, J. De Boeck, G. Borghs, J. Tummler, J. Woitok, and J. Geurts, *Semicond. Sci. Technol.* 13, 428 (1998).
206. F. Rahman, B. L. Gallagher, M. Behet, and J. De Boeck, *Appl. Phys. Lett.* 72 (1998).
207. Y. Q. Jia, R. C. Shi, and S. Y. Chou, *IEEE Trans. Magn.* 32, 4707 (1996).
208. M. W. J. Prins, H. van Kempen, H. van Leuken, R. A. de Groot, W. Van Roy, and J. De Boeck, *J. Phys.: Condens. Matter* 7, 9447 (1995).
209. J. C. Grobli, D. Guarisco, S. Frank, and F. Meier, *Phys. Rev. B* 51, 2945 (1995).
210. T. Sands, C. J. Palmstrøm, J. P. Harbison, V. G. Keramidas, N. Tabatabaie, T. L. Cheeks, R. Ramesh, and Y. Silberberg, *Mater. Sci. Rep.* 5, 99 (1990), and references therein.
211. J. G. Zhu, C. B. Carter, C. J. Palmstrøm, and K. C. Garrison, *Appl. Phys. Lett.* 55, 39 (1990).
212. D. E. Brehmer, K. Zhang, Ch. J. Schwarz, S. P. Chau, S. J. Allen, J. P. Ibbetson, J. P. Zhang, C. J. Palmstrom, and B. Wilkens, *Appl. Phys. Lett.* 67, 1268 (1995).
213. T. Sands, J. P. Harbison, N. Tabatabaie, W. K Chan, H. L. Gilchrist, T. L. Cheeks, L. T. Florez, and V. G. Keramidas, *Surf. Sci.* 228, 1 (1990).
214. S. J. Allen, Jr., N. Tabatabaie, C. J. Palmstrøm, G. W. Hull, T. Sands, F. DeRosa, H. L. Gilchrist, and K. C. Garrison, *Phys. Rev. Lett.* 62, 2309 (1989).
215. J. G. Zhu, C. B. Carter, C. J. Palmstrom, and S. Mounier, *Appl. Phys. Lett.* 56, 1323 (1990).
216. M. Tanaka, M. Tsuda, T. Nishinaga, and C. J. Palmstrøm, *Appl. Phys. Lett.* 68, 84 (1996).
217. G. A. Prinz, *Phys. Rev. Lett.* 54, 1051 (1985).
218. G. A. Prinz, *Science* 250, 1092 (1990).
219. M. Gester, C. Daboo, R. J. Hicken, Sj. Gray, A. Ercole, and J. A. C. Bland, *J. Appl. Phys.* 80, 347 (1996).
220. B. T. Jonker, H. Abad, and J. J. Krebs, *J. Appl. Phys.* 76, 6294 (1994).
221. E. Kneedler, P. M. Thibado, B. T. Jonker, B. R. Bennett, B. V. Shanabrook, R. J. Wagner, and L. J. Whitman, *J. Vac. Sci. Technol.* 14, 3193 (1996).
222. J. M. Florczak, P. J. Ryan, J. N. Kuznia, A. M. Wowchak, P. I. Cohen, R. M. White, G. A. Prinz, and E. D. Dahlberg, *Mater. Res. Soc. Symp. Proc.* 300, 213 (1989).
223. D. K. Lottis, G. A. Prinz, and E. D. Dahlberg, *Mater. Res. Soc. Symp. Proc.* 300, 219 (1989).
224. K. T. Riggs, E. D. Dahlberg, and G. A. Prinz, *Phys. Rev. B* 41, 7088 (1990).
225. J. M. Florczak and E. D. Dahlberg, *J. Magn. Magn. Mater.* 104, 399 (1992).
226. S. J. Blundell, M. Gester, J. A. C. Bland, C. Daboo, E. Gu, M. J. Baird, and A. J. R. Ives, *J. Appl. Phys.* 73, 5948 (1993).
227. C. Daboo, R. J. Hicken, D. E. P. Fley, M. Gester, S. J. Gray, A. J. R. Ives, and J. A. C. Bland, *J. Appl. Phys.* 75, 5586 (1994).
228. U. Ebels, M. Gester, C. Daboo, and J. A. C. Bland, *Thin Solid Films* 275, 172 (1996).

229. A. Moghadam, J. G. Booth, D. G. Lord, J. Boyle, and A. D. Boardman, *IEEE Trans. Magn.* 30, 769 (1994).
230. E. Gu, M. Gester, R. J. Hicken, C. Daboo, M. Tselepi, S. J. Gray, J. A. C. Bland, L. M. Brown, T. Thomson, and P. C. Riedi, *Phys. Rev. B* 52, 14704 (1995).
231. R. J. Hicken, D. E. P. Eley, M. Gester, S. J. Gray, C. Daboo, A. J. R. Ives, and J. A. C. Bland, *J. Magn. Magn. Mater.* 145, 278 (1995).
232. R. Meckenstock, O. von Geisau, F. Schreiber, E. C. Da Silva, and J. Pelzl, *J. Phys. IV* 4, 663 (1994).
233. R. Meckenstock, O. von Geisau, J. Pelzl, and J. A. Wolf, *J. Appl. Phys.* 77, 6439 (1995).
234. M. Schneider, S. Muller-Pfeiffer, and W. Zin, *J. Appl. Phys.* 79, 8578 (1996).
235. E. Gu, J. A. C. Bland, C. Daboo, M. Gester, L. M. Brown, R. Ploessl, and J. N. Chapman, *Phys. Rev. B* 51, 3596 (1995).
236. S. Okamoto, O. Kitakami, and Y. Shimada, *Jpn. J. Appl. Phys.* 33, 6164 (1994).
237. Y. Endo, S. Okamoto, O. Kitakami, and Y. Shimada, *J. Appl. Phys.* 81, 344 (1997).
238. M. Alper, K. Attenborough, R. Hart, S. J. Lane, D. S. Lashmore, C. Younes, and W. Schwarzacher, *Appl. Phys. Lett.* 63, 2144 (1993).
239. P. Allongue and E. Souteyrand, *J. Vac. Sci. Technol., B* 5, 1644 (1987).
240. R. Hart, P. A. Midgley, A. Wilkinson, and W. Schwarzacher, *Appl. Phys. Lett.* 67, 1316 (1995).
241. C. Shearwood, S. J. Blundell, M. J. Baird, J. A. C. Bland, M. Gester, H. Ahmed, and H. P. Hughes, *J. Appl. Phys.* 75, 5249 (1994).
242. U. Ebels, O. Adeyeye, M. Gester, R. P. Cowburn, C. Daboo, and J. A. C. Bland, *Phys. Rev. B* 56, 5443 (1997).
243. A. Y. Liu and D. J. Singh, *Appl. Phys. Lett.* 73, 6189 (1993).
244. G. A. Prinz, *J. Magn. Magn. Mater.* 100, 469 (1991).
245. J. A. C. Bland, R. D. Bateson, P. C. Riedi, R. G. Graham, H. J. Lauter, J. Penfold, and C. Shackleton, *J. Appl. Phys.* 69, 4989 (1991).
246. C. J. Gutierrez, J. J. Krebs, and G. A. Prinz, *Appl. Phys. Lett.* 61, 2476 (1992).
247. C. J. Gutierrez, G. A. Prinz, J. J. Krebs, M. E. Filipkowski, V. G. Harris, and W. T. Elam, *J. Magn. Magn. Mater.* 126, 232 (1993).
248. J. Dekoster, E. Jedryka, C. Meny, and G. Langouche, *J. Magn. Magn. Mater.* 121, 69 (1993).
249. J. P. Jay, E. Jedryka, M. Wojcik, J. Dekoster, G. Langouche, and P. Panissod, *Z. Phys. B* 101, 329 (1996).
250. C. D. England, B. N. Engel, and C. M. Falco, *J. Appl. Phys.* 69, 5310 (1991).
251. J. De Boeck, W. Van Roy, C. Bruynseraede, A. Van Esch, H. Bender, and G. Borghs, *Microelectron. J.* 27, 383 (1996).
252. B. Swinnen, J. Dekoster, J. Meersschaut, S. Demuynck, S. Cottenier, G. Langouche, and M. Rots, *J. Appl. Phys.* 81, 4343 (1997).
253. J. Weissman, E. Zolotoyabko, L. Levin, and A. Ginzburg, *Mater. Chem. Phys.* 37, 175 (1994).
254. G. W. Anderson, R. C. Hanf, and P. R. Norton, *Phys. Rev. Lett.* 74, 2764 (1995).
255. G. W. Anderson, M. C. Hanf, X. R. Qin, P. R. Norton, K. Myrtle, and B. Heinrich, *Surf. Sci.* 346, 145 (1996).
256. F. J. Himpsel, W. Drube, A. B. McLean, and A. Santoni, *Appl. Surf. Sci.* 56–58, 160 (1992).
257. A. Filipe, A. Schuhl, and P. Galtier, *Appl. Phys. Lett.* 70, 129 (1997).
258. F. Y. Shiau, S. L. Chen, M. Loomans, and Y. A. Chang, *J. Mater. Res.* 6, 1532 (1991).
259. A. Filipe and A. Schuhl, *J. Appl. Phys.* 81, 4359 (1997).
260. E. M. Kneedler and B. T. Jonker, *J. Appl. Phys.* 81, 4463 (1997).
261. B. T. Jonker, O. J. Glembocki, R. T. Holm, and R. J. Wagner, *Phys. Rev. Lett.* 79, 4886 (1997).
262. B. T. Jonker, E. M. Kneedler, P. Thibado, O. J. Glembocki, L. J. Whitman, and B. R. Bennett, *J. Appl. Phys.* 81, 4362 (1997).
263. M. Tanaka, J. P. Harbison, M. C. Park, Y. S. Park, T. Shin, and G. M. Rothberg, *J. Appl. Phys.* 76, 6278 (1994).
264. M. Tanaka, J. P. Harbison, and G. M. Rothberg, *J. Cryst. Growth* 150, 1132 (1995).
265. H. Akinaga, Y. Suzuki, K. Tanaka, K. Ando, and T. Katayama, *Appl. Phys. Lett.* 67, 141 (1995).
266. H. Akinaga, S. Miyanishi, W. Van Roy, and L. H. Kuo, *Appl. Phys. Lett.* 70, 2472 (1997).
267. T. Sands, J. P. Harbison, M. L. Leadbeater, S. J. Allen, Jr., G. W. Hull, R. Ramesh, and V. G. Keramidas, *Appl. Phys. Lett.* 57, 2609 (1990).
268. W. Van Roy, J. De Boeck, H. Bender, C. Bruynseraede, A. Van Esch, and G. Borghs, *J. Appl. Phys.* 78, 398 (1995).
269. M. Tanaka, J. P. Harbison, J. De Boeck, T. Sands, B. Philips, T. L. Cheeks, and V. G. Keramidas, *Appl. Phys. Lett.* 62, 1565 (1993).
270. K. M. Krishnan, *Appl. Phys. Lett.* 61, 2365 (1992).
271. G. Lauhoff, C. Bruynseraede, J. De Boeck, W. Van Roy, J. A. C. Bland, and G. Borghs, *Phys. Rev. Lett.* 79, 5290 (1997).
272. J. De Boeck, C. Bruynseraede, H. Bender, A. Van Esch, W. Van Roy, and G. Borghs, *J. Cryst. Growth* 150, 1139 (1995).
273. H. van Leuken, A. Lodder, M. T. Czyzyk, F. Springelkamp, and R. A. de Groot, *Phys. Rev. B* 41, 5613 (1990).

274. A. Sakuma, *J. Phys. Soc. Jpn.* 63, 1422 (1994).
275. J. De Boeck, T. Sands, J. P. Harbison, A. Scherer, H. Gilchrist, T. L. Cheeks, M. Tanaka, and V. G. Keramidas, *Electron. Lett.* 29, 421 (1993).
276. J. De Boeck, W. Van Roy, C. Bruynseraede, A. Van Esch, H. Bender, C. Van Hoof, and G. Borghs, *Phys. Scr., T* 66, 183 (1996).
277. W. Van Roy, H. Akinaga, S. Miyanishi, K. Tanaka, and L. H. Kuo, *Appl. Phys. Lett.* 69, 711 (1996).
278. W. Van Roy, H. Akinaga, S. Miyanishi, K. Tanaka, and L. H. Kuo, *J. Magn. Magn. Mater.* 165, 149 (1997).
279. B. Briner and M. Landolt, *Z. Phys. B* 92, 137 (1993).
280. J. E. Mattson, S. Kumar, E. E. Fullerton, S. R. Lee, C. H. Sowers, M. Grimsditch, S. D. Bader, and F. T. Parker, *Phys. Rev. Lett.* 71, 185 (1993).
281. J. Dekoster, H. Bemelmans, S. Degroote, R. Moons, J. Verheyden, A. Vantomme, and G. Langouche, *J. Appl. Phys.* 81, 5349 (1997).
282. W. H. Butler, X. G. Zhang, X. Wang, J. van Eck, and J. M. MacLaren, *J. Appl. Phys.* 81, 5518 (1997).
283. S. S. Kang, G. J. Jin, X. N. Xu, A. Hu, H. R. Zhai, S. S. Jiang, Y. Chen, W. R. Zhu, G. S. Dong, S. M. Zhou, X. Jin, and J. W. Feng, *Appl. Phys. Lett.* 69, 3923 (1996).
284. K. Matsuyama, H. Asada, T. Saeki, Y. Sawamoto, and K. Taniguchi, *J. Appl. Phys.* 81, 5449 (1997).
285. J. de la Figuera, M. A. Huerta-Garnica, J. E. Prieto, C. Ocal, and R. Miranda, *Appl. Phys. Lett.* 66, 1006 (1995).
286. M. Blondel, J. P. Meyer, B. Doudin, and J. Ph. Ansermet, *Appl. Phys. Lett.* 65, 3019 (1994).
287. L. Piraux, J. M. George, J. F. Despres, C. Leroy, E. Ferain, and R. Legras, *Appl. Phys. Lett.* 65, 2484 (1994).
288. J. Shi, J. Kikkawa, R. Proksch, T. Schffer, D. Awschalom, G. Medeiros-Ribeiro, and P. Petroff, *Nature (London)* 377, 707 (1995).
289. J. Shi, D. D. Awschalom, P. M. Petroff, and K. Babcock, *J. Appl. Phys.* 81, 4331 (1997).
290. J. P. Zhang, A. K. Cheetham, K. Sun, J. S. Wu, K. H. Kuo, J. Shi, and D. D. Awschalom, *Appl. Phys. Lett.* 71, 143 (1997).
291. P. J. Wellmann, J. M. Garcia, J. L. Feng, and P. M. Petroff, *Appl. Phys. Lett.* 71, 2532 (1997).
292. J. C. P. Chang, N. Otsuka, E. S. Harmon, M. R. Melloch, and J. M. Woodall, *Appl. Phys. Lett.* 65, 2801 (1994).
293. T. M. Pekarek, B. C. Crooker, D. D. Nolte, J. Deak, M. McElfresh, J. C. P. Chang, E. S. Harmon, M. R. Melloch, and J. M. Woodall, *J. Magn. Magn. Mater.* 169, 261 (1997).
294. M. W. Bench, C. B. Carter, W. Feng, and P. I. Cohen, *Appl. Phys. Lett.* 66, 2400 (1995).
295. J. Katcki, M. Shiojiri, T. Isshiki, K. Nishio, Y. Yabuuchi, and N. Y. Jin-Phillipp, *Electron Technol.* 29, 393 (1996).
296. S. Guha and H. Munekata, *J. Appl. Phys.* 74, 2974 (1993).
297. J. De Boeck, R. Oesterholt, A. Van Esch, H. Bender, C. Bruynseraede, C. Van Hoof, and G. Borghs, *Appl. Phys. Lett.* 68, 2744 (1996).
298. J. De Boeck, R. Oesterholt, H. Bender, A. Van Esch, C. Bruynseraede, C. Van Hoof, and G. Borghs, *J. Magn. Magn. Mater.* 156, 148 (1996).
299. D. R. Schmidt, J. P. Ibbetson, D. E. Brehmer, C. J. Palmstrøm, S. J. Allen, Jr., *Mater. Res. Soc. Conf. Proc.* 475, 251 (1997).
300. See, for example, *Mater. Res. Soc. Proc.* 214 (1992) and *J. Electron. Mater.* 22 (1993).
301. H. Okamoto, *Bull. Alloy Phase Diagrams* 10, 549 (1989).
302. T. M. Pekarek, B. C. Crooker, S. Li, M. McElfresh, J. C. P. Chang, D. Mcinturff, E. S. Harmon, M. R. Melloch, and J. M. Woodall, *J. Appl. Phys.* 81, 4869 (1997).
303. H. Akinaga, J. De Boeck, G. Borghs, S. Miyanishi, A. Asamitsu, W. Van Roy, Y. Tomioka, and L. H. Kuo, *Appl. Phys. Lett.* 72 (1998).
304. J. De Boeck, H. Akinaga, C. Bruynseraede, H. Bender, and G. Borghs, *IEEE Trans. Magn.* (1998).
305. A. Shen, H. Ohno, F. Matsukura, Y. Sugawara, Y. Ohno, N. Akiba, and T. Kuroiwa, *Jpn. J. Appl. Phys.* 36, L73 (1997).
306. A. Van Esch, L. Van Bockstal, J. De Boeck, G. Verbanck, A. S. Van Steenbergen, P. J. Wellman, B. Grietens, R. Bogaerts, F. Herlach, and G. Borghs, *Phys. Rev. B* 56, 20 (1997).
307. A. Berkowitz, J. R. Mitchell, M. J. Carey. A. P. Young, S. Zhang, F. E. Spada, F. T. Parker, A. Hutten, and G. Thomas, *Phys. Rev. Lett.* 68, 3745 (1992).
308. J. Q. Xiao, J. S. Jiang, and C. L. Chien, *Phys. Rev. Lett.* 68, 3749 (1992); *Phys. Rev. B* 46, 9266 (1992).
309. F. W. Smith, H. W. Le, V. Diadiuk, M. A. Hollis, A. R. Calawa, S. Gupta, M. Frankel, D. R. Dykaar, G. A. Mourou, and T. Y. Hsiang, *Appl. Phys. Lett.* 54, 890 (1991).
310. A. C. Warren, N. Katzenellenbougen, D. Grischkowsky, J. M. Woodall, M. R. Melloch, and N. Otsuka, *Appl. Phys. Lett.* 58, 1512 (1991).
311. D. D. Nolte, M. R. Melloch, J. M. Woodall, and S. E. Ralph, *Appl. Phys. Lett.* 62, 1356 (1991).
312. D. D. Nolte, *J. Appl. Phys.* 76, 3740 (1991).
313. R. Desmicht, G. Faini, V. Cros, A. Fert, F. Petroff, and A. Vaurs, *Appl. Phys. Lett.* 72, 386 (1998).

Chapter 8

COLLOIDAL QUANTUM DOTS OF III–V SEMICONDUCTORS*

Olga I. Micić, Arthur J. Nozik

Center for Basic Sciences, National Renewable Energy Laboratory, Golden, Colorado, USA

Contents

1. Introduction 427
2. Synthesis of Colloidal Quantum Dots 429
   2.1. Synthesis of Colloidal InP Quantum Dots 430
   2.2. Etching of Colloidal InP Quantum Dots with HF 431
   2.3. Synthesis of Colloidal GaP Quantum Dots 431
   2.4. Synthesis of Colloidal $GaInP_2$ Quantum Dots 431
3. Properties of III–V Quantum Dots 432
   3.1. InP Quantum Dots 432
   3.2. GaP Quantum Dots 442
   3.3. $GaInP_2$ Quantum Dots 444
   3.4. GaAs Quantum Dots 446
4. Summary 447
   Acknowledgment 447
   References 447

1. INTRODUCTION

Quantization effects in semiconductor structures were first demonstrated in the early 1970s in III–V quantum wells [1, 2]; these structures consisted of a thin epitaxial film of a smaller band gap (E_g) semiconductor (e.g., GaAs, $E_g = 1.42$ eV) sandwiched between two epitaxial films of a larger band gap semiconductor (e.g., $Al_{0.3}Ga_{0.7}As$, $E_g = 2.0$ eV). The conduction and valence band offsets of the two semiconductor materials produce potential barriers for electrons and holes, respectively; the smaller band gap semiconductor constitutes the quantum well region and the larger band gap material the potential barrier region. If the film of the smaller band gap material is sufficiently thin (thickness less than the De Broglie wavelength of the charge carriers, which typically requires thicknesses less than about 300 Å for III–V semiconductors), then the charge carriers are confined in one dimension by the potential barriers and quantization of the energy levels for both electrons and holes can occur (Fig. 1).

*Parts of this manuscript have been excerpted with permission from [17] and [24]. © 1995 and 1997 American Chemical Society.

Handbook of Nanostructured Materials and Nanotechnology, edited by H.S. Nalwa
Volume 3: Electrical Properties
Copyright © 2000 by Academic Press
All rights of reproduction in any form reserved.
ISBN 0-12-513763-X/$30.00

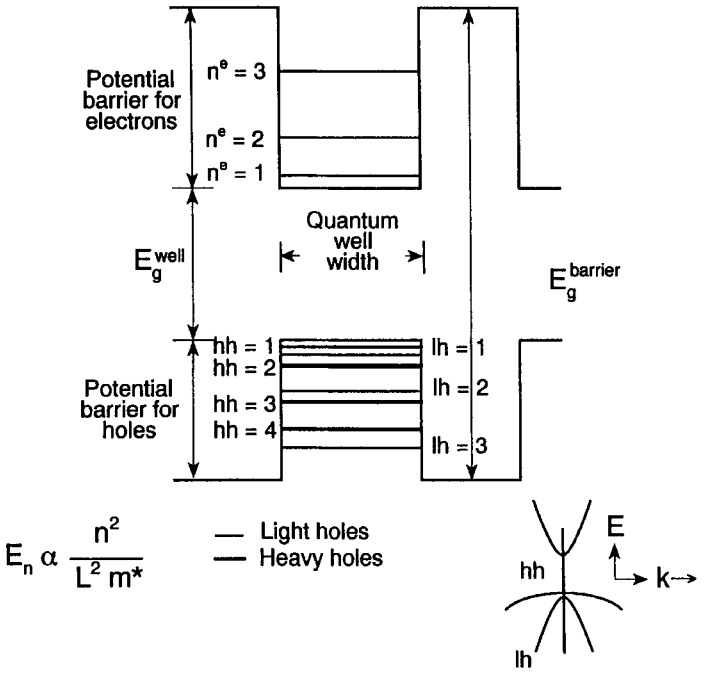


Fig. 1. Quantization in quantum wells (quantum films).

In general, three regimes of quantization can be defined depending on whether the charge carriers are confined in one, two, or three dimensions. Confinement in one dimension, described previously, creates structures that have been termed quantum wells; this is because the first such structures [1] could be described by the elementary quantum mechanics of a particle in a one-dimensional box; these structures have also been labeled as "quantum films." Carrier confinement in two dimensions produces "quantum wires," and confinement in three dimensions produces "quantum dots" (also called nanocrystals or quantum boxes). The dimensionality of confinement affects many aspects of quantization; Figure 2 shows the effect on the density of states. Many reviews of quantum wells or films [3–5], quantum wires [6–8], and quantum dots [6, 9–15] are available.

Quantum wells are produced by the growth of high-quality epitaxial layers of semiconductors by molecular beam epitaxy (MBE) or metallorganic chemical vapor deposition (MOCVD). Quantum dots (QDs) are usually produced by one of two approaches: (1) epitaxial growth and/or nanoscale patterning and (2) formation of nanosized semiconductor particles through colloidal chemistry. This chapter will deal only with the preparation, characterization, spectroscopy, and applications of QDs of III–V semiconductors produced via colloidal chemistry. Some important characteristics of the colloidal route to nanocrystalline QDs are: (1) very small sized QDs can be readily formed (20–100 Å); (2) colloidal QDs can be easily formed into closed-packed QD arrays to create either amorphous QD solids or crystalline QD solids (three-dimensional superlattices and opal-like structures); (3) QD size distributions can be made relatively narrow (5%–10% variation in average QD size); (4) high-quality QD nanocrystallites can be formed; and (5) colloidal QDs can be studied either in solution, as solid powders, or as solid QD arrays in films. These characteristics have been realized in II–VI [9–15] and III–V QDs [16–24]. Other semiconductors that have been prepared as colloidal QDs include groups I–VII, IV, IV–VI, and layered chalcogenides [6, 25].

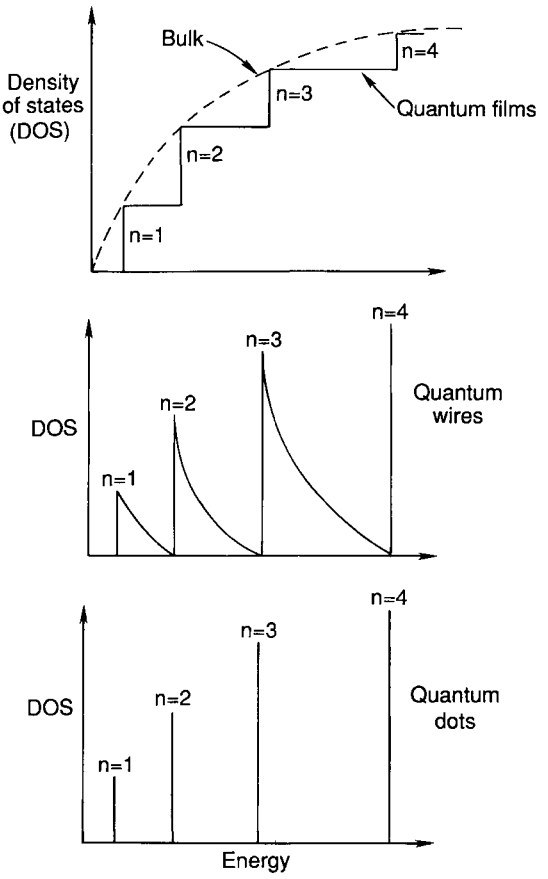


Fig. 2. Effects of dimensionality of quantization on the electronic density of states.

2. SYNTHESIS OF COLLOIDAL QUANTUM DOTS

The most common approach to the synthesis of colloidal QDs is the controlled nucleation and growth of particles in a solution of chemical precursors containing the metal and the anion sources (controlled arrested precipitation) [26–28]. The technique of forming monodisperse colloids is very old, and can be traced back to the synthesis of gold colloids by Michael Faraday in 1857. A common method for II–VI colloidal QD formation is to rapidly inject a solution of chemical reagents containing the group II and group VI species into a hot and vigorously stirred solvent containing molecules that can coordinate with the surface of the precipitated QD particles [26, 28, 29]. Consequently, a large number of nucleation centers are initially formed, and the coordinating ligands in the hot solvent prevent or limit particle growth via Ostwald ripening (the growth of larger particles at the expense of smaller particles to minimize the higher surface free energy associated with smaller particles). Further improvement of the resulting size distribution of the QD particles can be achieved through selective precipitation [28, 29], whereby the slow addition of a nonsolvent to the colloidal solution of particles causes precipitation of the larger-sized particles (the solubility of molecules with the same type of chemical structure decreases with increasing size). This process can be repeated several times to narrow the size distribution of II–VI colloidal QDs to a few percent of the mean diameter [28, 29].

The synthesis of colloidal III–V QDs is more difficult than that of II–VI QDs. The reason is that III–V semiconductors are more covalent compounds and high temperatures are required for their synthesis. In progressive, more covalent series of semiconductors,

the synthesis of QDs by colloidal techniques becomes increasingly difficult. To use the colloidal chemical method for the synthesis of QDs, it is important that the stabilizer and solvent do not decompose during the reaction time in order to ensure good solubility of QDs after synthesis and to avoid formation of different trapping states on the surface. The preparation method that we used is a compromise between these two requirements. One difference with the synthesis described previously for II–VI materials is that more than 1 day of heating at reaction temperature is required to form crystalline III–V QDs, whereas II–VI QDs form immediately upon injection of the reactants into the hot coordinating solution. The synthesis must be conducted in rigorously air-free and water-free atmospheres; it generally requires higher reaction temperatures. The best results to date have been obtained for InP QDs [17, 18, 20, 22–24].

2.1. Synthesis of Colloidal InP Quantum Dots

In this synthesis, an indium salt [$In(C_2O_4)_3$, InF_3, or $InCl_3$] is reacted with trimethylsilylphosphine [$P(Si(CH_3)_3)_3$] in a solution of trioctylphosphine oxide (TOPO) and trioctylphosphine (TOP) to form a soluble InP organometallic precursor species that contains In and P in a 1:1 ratio [17, 22]. The following procedure can be used: First, indium salts (oxalate, 1.15 g), tris(trimethylsilyl)phosphine (0.75 g), and a colloidal stabilizer (10 g of a mixture of trioctylphosphine oxide and trioctylphosphine in a TOPO:TOP ratio of 0.1:1) are mixed together at room temperature to form a transparent solution of an InP precursor; then, the precursor solution is heated at 250–290 °C for 1–6 days, depending on the desired QD properties. Use of TOPO/TOP as a colloidal stabilizer is based on the work of Murray et al. [29], who showed the remarkable ability of TOPO/TOP to stabilize semiconductor CdSe QDs at high temperature. Different particle sizes of InP QDs can be obtained by changing the temperature at which the solution is heated. The duration of heating only slightly affects the particle size, but does improve the QD crystallinity. The precursor has a high decomposition temperature (>200 °C); this is advantageous for the formation of InP quantum dots because the rate of QD formation is controlled by the rate of decomposition of the precursor. This slow process leads to InP QDs with a narrow size distribution. p-doped (InP:Zn), n-doped (InP:S), and undoped QDs of InP were synthesized as well-crystallized zincblende nanocrystals. For the synthesis of p-doped InP QDs, indium salt is first mixed with zinc acetate in a ratio such that the resulting QDs contain one Zn^{2+} ion per particle. For example, for 40-Å QDs, the ratio of In:Zn is 10^3:1. For n-doped InP QDs, $P(SiMe_3)_3$ is mixed with bis(trimethylsilyl)sulfide and then added to an indium salt solution. After heating, the clear reaction mixture contains InP QDs, byproducts of the synthesis, products resulting from TOPO/TOP thermal decomposition, and untreated TOP and TOPO. Anhydrous methanol is then added to the reaction mixture to flocculate the InP nanocrystals. The flocculate is separated and completely redispersed in the mixture of hexane (0.9) and 1-butanol (0.1) containing 1% TOPO to produce an optically clear colloidal solution. The process of dispersion in the mixture of hexane and 1-butanol and flocculation with anhydrous methanol is repeated several times to purify and isolate a pure powder of InP nanocrystals that are capped with TOPO. Repetitive selective flocculation by methanol gradually strips away the TOPO capping group; thus, TOPO (1%) is always included in the solvent when the QDs are redissolved in order to maintain the TOPO cap on the QDs.

Fractionation of the QD particles into different sizes was obtained by selective precipitation methods [29]. This technique will narrow the size distribution of the initial colloid preparation; the narrower the latter, the narrower will be the final size distribution.

The resulting InP QDs contain a capping layer of TOPO, which can be readily exchanged for several other types of capping agents, such as thiols, furan, pyridines, amines, fatty acids, sulfonic acids, and polymers. The size distribution of the InP QDs can be further narrowed to less than 10% through selective precipitation techniques. Finally, they can be studied in the form of colloidal solutions, powders, or dispersed in transparent polymers

or organic (for low-temperature studies) glasses; capped InP QDs recovered as powders can also be redissolved to form transparent colloidal solutions.

In addition to InP QDs, similar methods have been used to produce QDs of GaP [16, 17], $GaInP_2$ [16, 17], GaAs [16, 17, 21, 30, 31], and InAs [19]; higher temperatures (400 °C) are required for GaP and $GaInP_2$ QDs. However, the quality (especially narrow size distributions) of these other III–V QDs is not yet as high as that obtained for InP QDs; this is primarily because less effort has been spent thus far on these other QD preparations.

2.2. Etching of Colloidal InP Quantum Dots with HF

Intense band edge emission from InP QDs can be achieved after etching the particles with a dilute alcoholic solution of HF [23]. The method described by Waldeck et al. [32] was adapted for etching InP QD colloidal solutions; in the former work, HF was used to remove the surface native oxide from single-crystal InP to obtain a clean surface. For colloidal solutions of InP QDs with a diameter of 20–40 Å, about 1–10 μL of methanolic solution was used; it contained 5% HF and 10% H_2O, which was added to 4 mL of a mixture of 2,2,4-trimethylpentane and acetonitrile (1:1) that also contains InP QDs and 2–5% oleyamine or dodecanethiol. Two liquid phases are formed and the dots are dispersed in the upper nonpolar phases of 2,2,4-trimethylpentane, while HF, methanol, and H_2O are in the acetonitrile phase. The mixture is shaken and left overnight and then the 2,2,4-trimethylpentane phase with the colloids is separated and used. For fresh colloidal InP QDs solutions, lower amounts of HF are required than for solutions that were exposed in air or stored for a long period of time. Freshly prepared solutions give the best quantum yields, and adsorption spectra only slightly shift to the ultraviolet (UV). It was also noticed that etching of smaller particles with a diameter of 25–35 Å is much faster than etching of particles larger than 50 Å. After etching, solutions were stored in an air-free atmosphere. The solution slowly loses emission intensity with time. Solid samples are more stable in air. Solid samples are prepared after drying etched InP QD solutions in vacuum and dissolving the residue in toluene and 5% polyvinyl butyryl under vacuum. Alternatively, after etching the QDs can be treated with octanethiol, and the QDs (now capped with octanethiol) can be redissolved in tetrahydrofuran to produce a colloidal QD solution that is stable in air and that shows intense band edge emission after a month in contact with air.

2.3. Synthesis of Colloidal GaP Quantum Dots

Quantum dots of GaP were synthesized by mixing $GaCl_3$ and $P(SiMe_3)_3$ in a molar ratio of Ga:P of 1:1 in toluene at room temperature to form a GaP precursor species and then heating this precursor in a high-boiling solvent. Wells et al. [33–35] first synthesized and characterized the yellow GaP precursor, $[Cl_2GaP(SiMe_3)_2]_2$, that is formed from $GaCl_3$ and $P(SiMe_3)_3$. The GaP precursor solution is then added to a toluene solution of TOPO, stirred for 1 h, and then transferred to a high-boiling solvent; toluene was removed using vacuum and the resulting transparent viscous solution was slowly heated. The colloidal 30 Å GaP QDs reported here were prepared by first mixing 0.18 g of $GaCl_3$ with 0.25 g of $P(SiMe_3)_3$ in 0.1 g of TOPO and 2 g of TOP and heating to 270–320 °C. At this stage, the GaP is amorphous. To prepare crystallized QDs, the amorphous material is mixed with 10 g of TOPO (or 5 g of triphenylphosphine) and heated at 360 °C for 3 days. The GaP QDs were precipitated with CH_3OH, separated, washed with CH_3OH, and redissolved in toluene; when triphenylphosphine or tris(2-diphenylphosphinoethyl) phosphine were used instead of TOPO, the QD precipitate only partially dissolved in toluene.

2.4. Synthesis of Colloidal $GaInP_2$ Quantum Dots

Quantum dots of $GaInP_2$ were synthesized by mixing chlorogallium oxalate and chloroindium oxalate complexes and $P(SiMe_3)_3$ in a molar ratio of Ga:In:P of 1:1:2.6 in toluene

at room temperature, followed by heating. The specific conditions for the 25-Å QDs were to heat 0.19 g of chlorogallium oxalate and 0.23 g of chloroindium oxalate with 0.52 g of $P(SiMe_3)_3$ in 0.1 g of TOPO and 0.4 g of diphenyltetraphosphine at 400 °C for 3 days. The $GaInP_2$ QDs were separated, purified with CH_3OH, and partially redissolved in a 0.1% solution of TOPO in toluene. The larger, more crystalline 65-Å sample was obtained by heating a flask containing the isolated material in a yellow flame and redissolving in a similar manner.

3. PROPERTIES OF III–V QUANTUM DOTS

3.1. InP Quantum Dots

3.1.1. X-Ray Diffraction and Transmission Electron Microscopy

X-ray diffraction patterns of 26-, 35-, and 46-Å InP QD particles formed into a film by drying the colloids are shown in Figure 3. Powder X-ray diffraction spectra were collected on a Rigaku 300 Rotaflex diffractometer operating in the Bragg configuration using Cu Kα radiation. Samples for X-ray diffraction were prepared from approximately 50–100 mg of thoroughly washed and dried nanocrystalline powder. Diffraction peaks from the $\langle 111 \rangle$, $\langle 220 \rangle$, and $\langle 311 \rangle$ planes of crystalline zincblende InP are seen at 2θ of $26.2 \pm 0.2°$, $46.3 \pm 0.2°$, and $51.7 \pm 0.2°$, respectively. The mean particle diameter can be estimated from the broadening of the diffraction peaks using the Debye–Scherer formula. These diameters are in agreement with the values obtained from transmission electron microscopy (TEM)

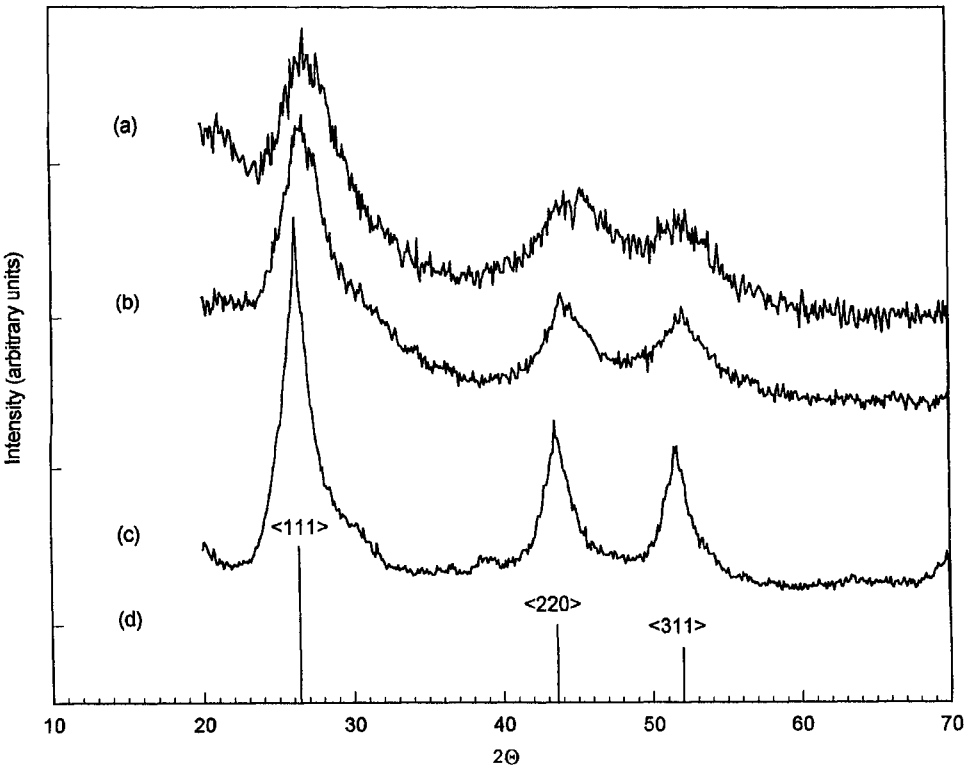


Fig. 3. X-ray diffraction of dried colloidal InP QDs with diameters (a) 25 Å, (b) 35 Å, and (c) 45 Å compared with bulk zincblende InP. (Source: Reprinted with permission from [17]. © 1995 American Chemical Society.)

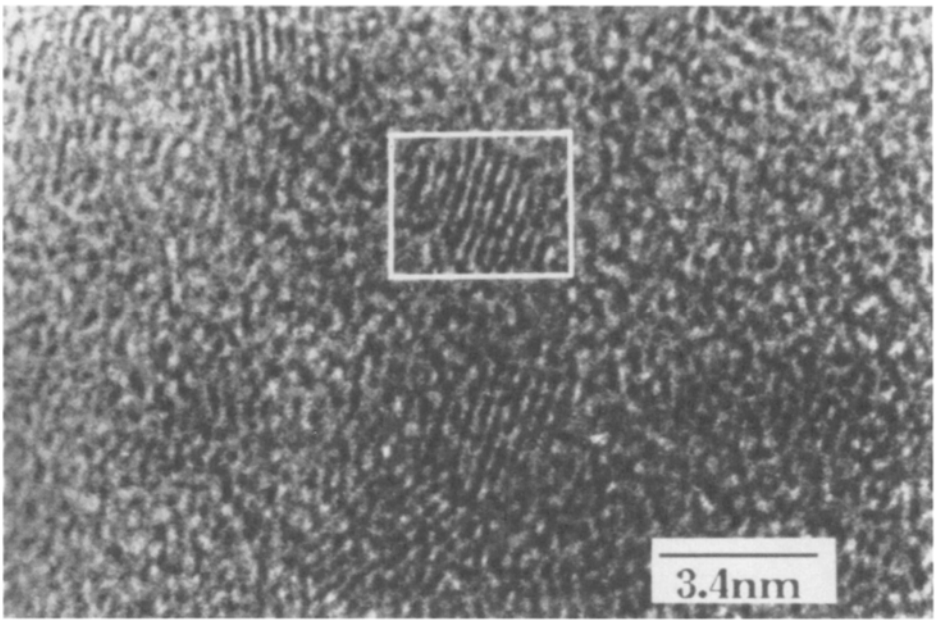


Fig. 4. TEM of InP QD. (Source: Reprinted with permission from [22]. © 1994 American Chemical Society.)

and from small-angle X-ray scattering (SAXS) data [17, 22]. In the absence of the TOPO stabilizer, the particles grow large and the sharp peaks of bulk InP are obtained.

The shape and size distribution of the InP QDs can be determined by TEM [22]. A Philips CM-30 electron microscope operating at 200 kV was used for TEM. Imaging was carried out in bright field with an objective aperture selected to permit lattice imaging of the ⟨111⟩ zincblende plane. TEM pictures of InP preparations with TOPO that were only heated to 220 °C for 3 days do not show the formation of either amorphous or crystalline InP. Upon heating to 240 °C for three days, the formation of zincblende nanocrystallites becomes evident, but the product is primarily amorphous. However, when the preparation is heated at 270 °C for 2 days, electron diffraction patterns show the ⟨111⟩, ⟨220⟩, and ⟨311⟩ planes of zincblende InP [17, 22]. The InP QDs generally show an elliptical shape (see Fig. 4).

3.1.2. Absorption and Luminescence Spectroscopy

3.1.2.1. Absorption and Global Photoluminescence

The absorption and emission spectra of initially prepared InP QDs with a mean diameter of 32 Å are shown in Figure 5. Optical absorption spectra were collected at room temperature using a Cary 5E UV-VIS-NIR spectrophotometer with 0.2-cm quartz cuvettes. Samples were prepared by dispersing washed QDs in toluene. Photoluminescence spectra were obtained at room temperature using a SPEX Fluorolog-2 spectrometer.

The absorption spectrum shows an excitonic peak at about 590 nm. The photoluminescence (PL) spectrum (excitation at 500 nm) shows two emission bands: a weaker one near the band edge with a peak at 655 nm and a second, stronger, broader band that peaks above 850 nm. The PL band with deep red-shifted subgap emission peaking above 850 nm is attributed to radiative surface states on the QDs produced by phosphorous vacancies [23]. These surface defects and the accompanying red-shifted emission can be completely removed by etching the InP QDs with HF. Intense band edge emission from our InP QDs can be achieved after etching the particles with a diluted methanolic solution of HF [23].

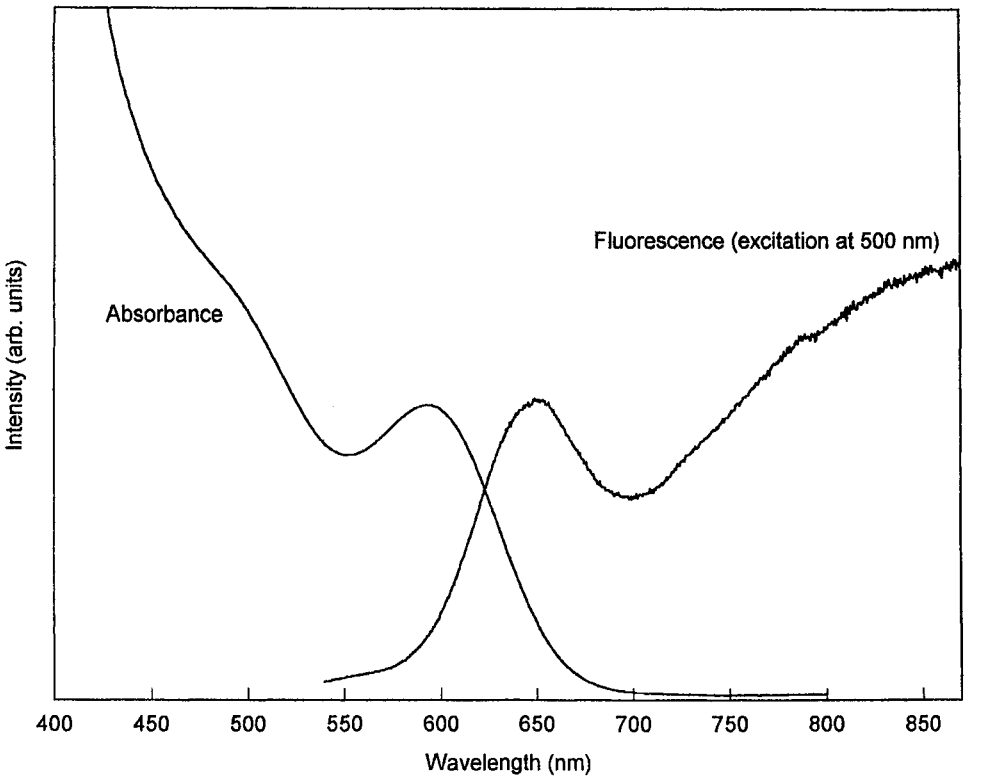


Fig. 5. Absorption and emission spectra of InP QDs as initially prepared. (Source: Reprinted with permission from [23].

After the etching of fresh solution, the PL intensity increases by a factor of 10, and the near-infrared emission produced by deep surface traps is completely removed [23]. The near–band edge quantum yield increases from 30% to 60% as the temperature decreases from 300 to 10 K [23].

The room temperature absorption spectra as a function of QD size ranging from 25 to 54 Å (measured by TEM) are shown in Figure 6. The absorption spectra show one or more broad excitonic peaks that reflect substantial inhomogeneous line broadening arising from the QD size distribution; as expected, the spectra shift to higher energy as the QD size decreases [24]. The color of the InP QD samples changes from deep red (1.7 eV) to green (2.4 eV) as the diameter decreases from 60 to 26 Å. Bulk InP is black with a room temperature band gap of 1.35 eV and an absorption onset at 918 nm. Higher energy transitions above the first excitonic peak in the absorption spectra can also be easily seen in QD samples with mean diameters equal to or greater than 30 Å. The spread in QD diameters is generally about 10% and is somewhat narrower in samples with larger mean diameters; this is why higher energy transitions can be resolved for the larger-sized QD ensembles. All of the prepared QD nanocrystallites are in the strong confinement regime because the Bohr radius of bulk InP is about 100 Å. Figure 7 shows typical room temperature absorption and global emission spectra of the InP colloids with mean particle diameters ranging from 26 to 60 Å as measured by TEM; the excitation energy for all QD sample ensembles in Figure 7 was 2.48 eV, well above their absorption onset in each case.

The global emission peaks in Figure 7 show an increasing red shift from the first excitonic absorption peak as the mean QD size decreases from 60 to 26 Å; the results are summarized in Figure 7. The global ("nonresonant") red shift is as large as 300 meV for samples with the smallest mean diameter [24]. We define global PL as that observed when

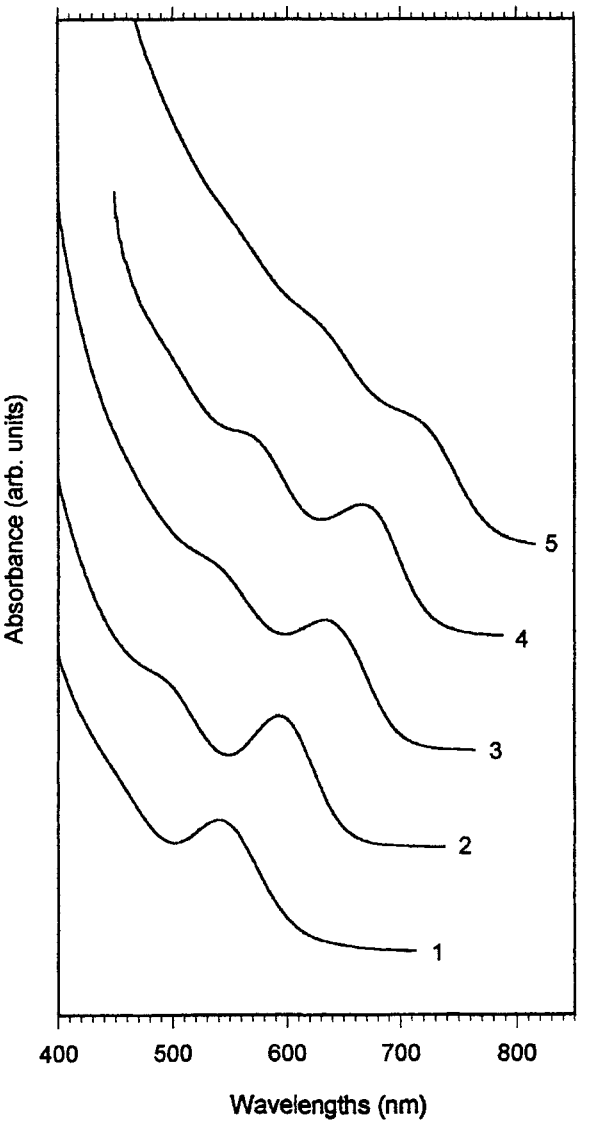


Fig. 6. Absorption spectra for InP QD colloids with different diameters (1) 25 Å, (2) 30 Å, (3) 35 Å, (4) 45 Å, and (5) 55 Å.

the excitation energy is much higher than the energy of the absorption threshold exhibited in the absorption spectrum produced by the ensemble of QDs in the sample. That is, the excitation wavelength is well to the blue of the first absorption peak for the QD ensemble, and, therefore, a large fraction of all the QDs in the sample are excited. The particle diameters that are excited range from the largest in the ensemble to the smallest, which has a diameter that produces a blue-shifted band gap equal to the energy of the exciting photons. The resulting global PL shows a very broad peak (line width of 175–225 meV) that is red-shifted by 100–300 meV from the first absorption peak (Figs. 7 and 8). The broad PL line width is caused by inhomogeneous line broadening arising from the approximately 10% size distribution sampled in the global PL experiment. The large global red shift is caused by the volume dominance of the larger particles in the size distribution; the larger QDs will absorb most of the incident photons and will also show large red shifts because the PL excitation energy is well above their lowest transition energy.

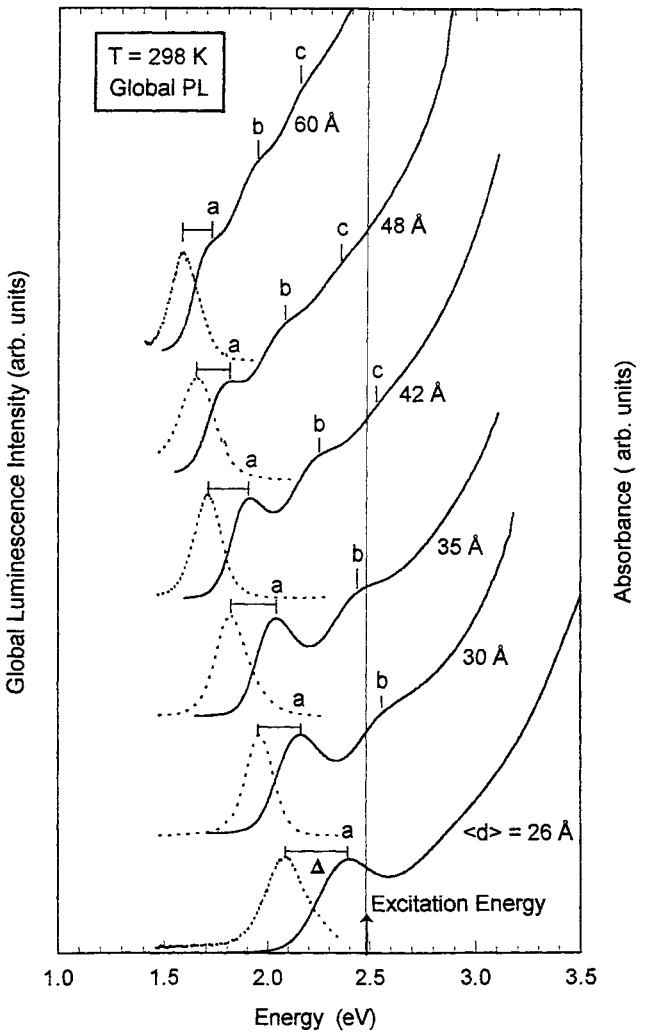


Fig. 7. Absorption and emission spectra of InP QDs as a function of QD size after treatment with HF. (Source: Reprinted with permission from [24]. © 1997 American Chemical Society.)

3.1.2.2. Size-Selected Photoluminescence

If the excitation energy is restricted to the onset region of the absorption spectrum of the QD ensemble, then a much narrower range of QD sizes is excited; these QDs will have the larger particle sizes in the ensemble. Consequently, the PL spectra from this type of excitation show narrower line widths and smaller red shifts with respect to the excitation energy. This technique is termed fluorescence line narrowing (FLN)—the resulting PL spectra being considerably narrowed.

FLN spectra at 10 K are shown in parts a–e of Figure 9 for InP QDs with a mean diameter of 32 Å. FLN/PL spectra are shown for a series of excitation energies (1.895–2.07 eV) spanning the absorption tail near the onset of absorption for this sample [24]. Also shown is the global PL spectrum produced when the excitation energy (2.41 eV) is deep into the high energy region of the absorption spectrum (Fig. 9f).

FLN spectra can be combined with photoluminescence excitation (PLE) spectra to determine the resonant red shift [24]. The experiment is done as follows: (a) first, a photon energy is selected in the onset region of the absorption spectrum of the QD ensemble spectrum, and this energy is set as the detected photon energy in the PLE; (b) the PLE spectrum

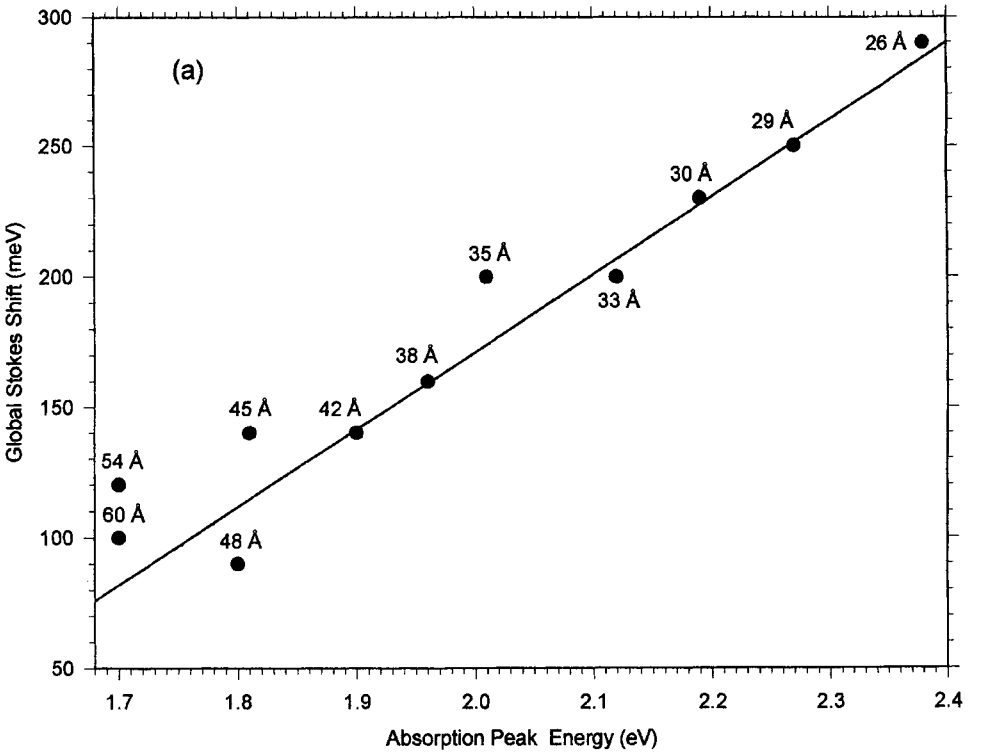


Fig. 8. The global red shift for different colloidal ensembles of InP QDs as a function of the position of the first peak in their absorption spectra. (Source: Reprinted with permission from [24]. © 1997 American Chemical Society.)

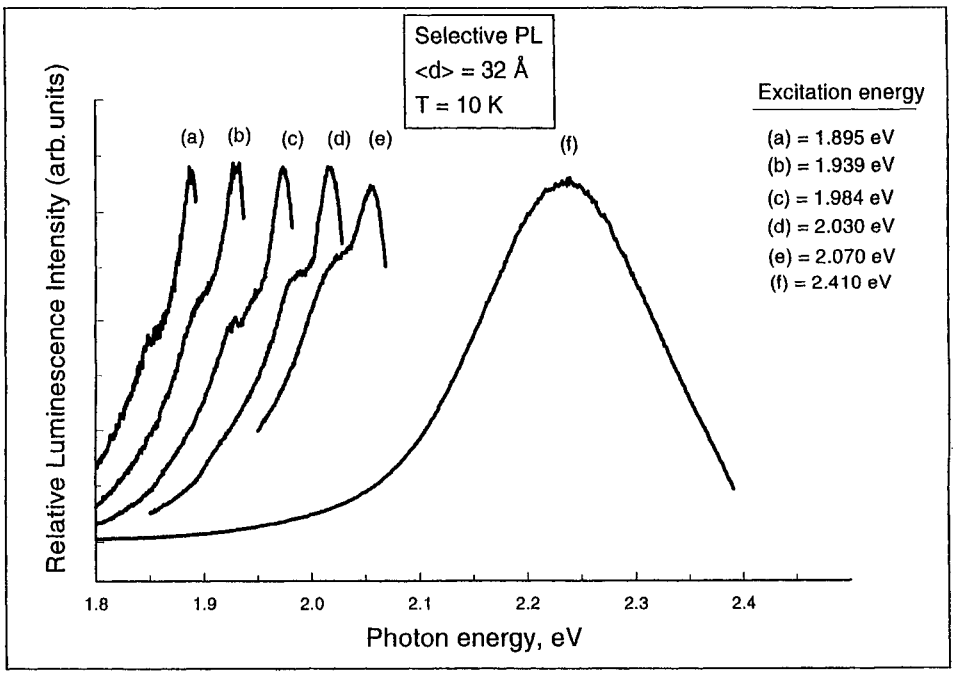


Fig. 9. PL spectra at 10 K for an ensemble of InP QDs with a mean diameter of 32 Å for different excitation energies. PL curves (a)–(e) result from excitation (1.895–2.070 eV) in the red tail of the onset region of the absorption spectrum; curve (f) is a global PL spectrum. (Source: Reprinted with permission from [24]. © 1997 American Chemical Society.)

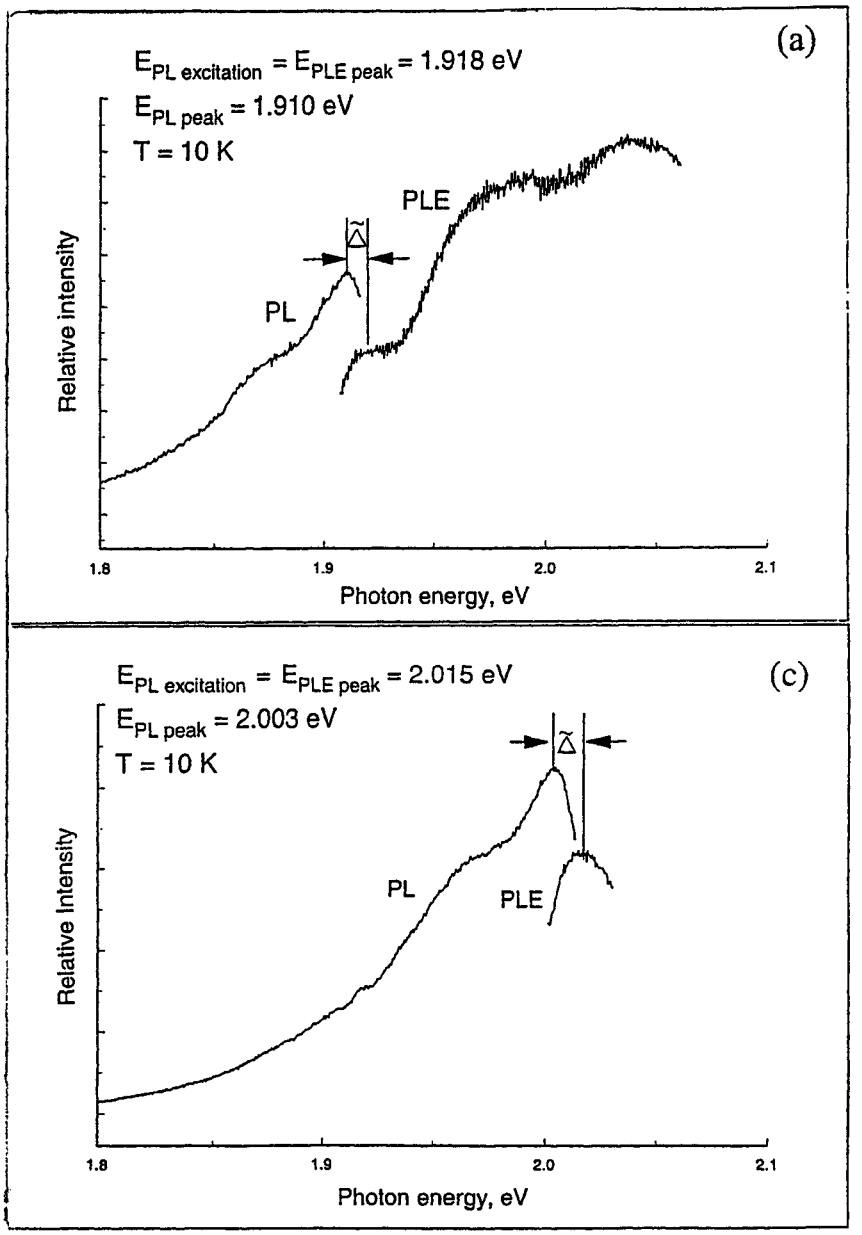


Fig. 10. Representative pairs of PL (FLN) and PLE spectra for the InP ensemble with a mean diameter of 32 Å. (Source: Reprinted with permission from [24]. © 1997 American Chemical Society.)

is then obtained, and the first peak of the PLE spectrum is taken to be the lowest energy excitonic transition for the QDs capable of emitting photons at the selected energy; and (c) an FLN spectrum is then obtained with excitation at the first peak of the PLE spectrum. The energy difference between the first FLN peak and the first PLE peak is then defined as the resonant red shift for the ensemble of QDs represented by the selected PL excitation energy. This process is repeated across the red tail of the absorption onset region of the absorption spectrum to generate the resonant red shift as a function of QD size. Typical FLN and PLE spectra are shown in Figure 10 for InP QDs with a mean diameter of 32 Å. The resultant $T = 11$ K resonant red shift as a function of PL excitation energy is presented in Figure 11 and ranges from 6 to 16 meV.

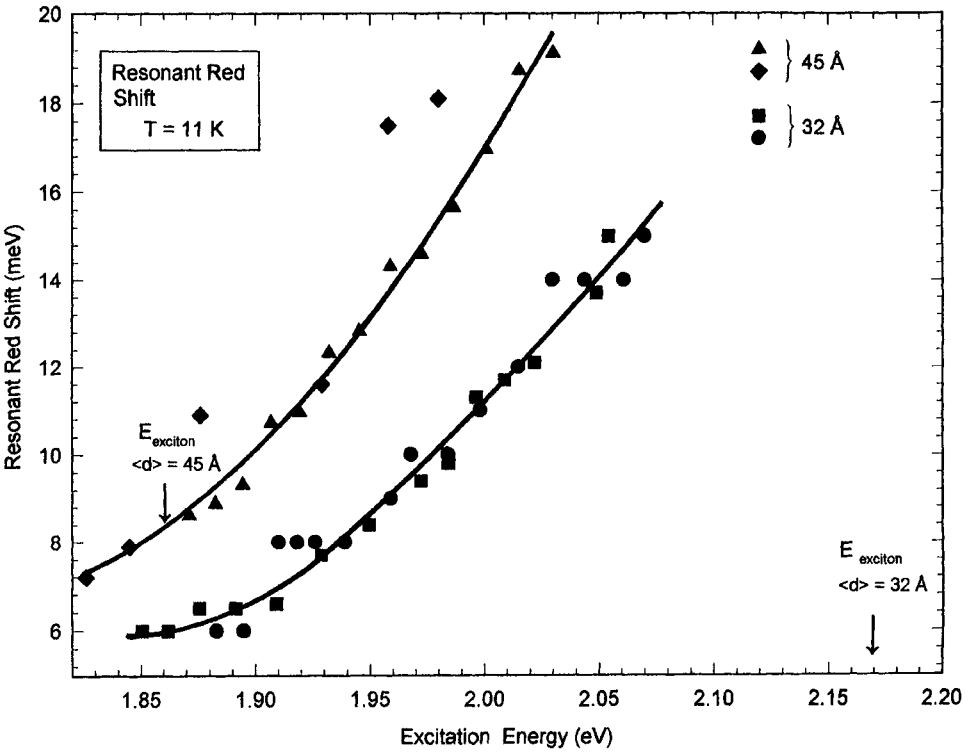


Fig. 11. The red shift for InP QD ensembles at 10 K for 32 Å and 45 Å QDs. (Source: Reprinted with permission from [24]. © 1997 American Chemical Society.)

As shown in Figures 9 and 10, the PL obtained by exciting into the red tail of the QD absorption spectrum, and thereby selectively exciting only the largest particles in the distribution, shows much smaller line widths (15–30 meV) and smaller red shifts compared to the global PL (compare Figs. 8 and 11). However, as our analysis shows, even the size-selected PL/FLN spectra contain effects caused by a residual size distribution. We have extracted the resonant red shifts for QDs of a single size from the experimental PL/FLN spectra [24]. The results of this analysis [24] show that the effective single-dot resonant red shift at 10 K exhibited by InP quantum dots that have been etched in HF to passivate surface states ranges from 4 meV for an excitation energy of 1.85 eV (corresponding to a QD size of 53 Å) to 9.7 meV for an excitation energy of 2.06 eV (corresponding to a QD size of 34 Å).

Our results show that for InP QDs formed via colloidal chemical processes, very large effects caused by a residual QD size distribution remain manifested in the photoluminescence spectroscopy of QD ensembles even after the colloidal samples have been subjected to size-selective precipitation techniques and size-selective photoexcitation. This behavior is similar to that reported for colloidal CdSe QD ensembles [36–46].

3.1.2.3. Photoluminescence Lifetime

The PL lifetimes were measured in a sample of HF-treated InP QDs immobilized in a PVB film at 298 and 13 K; the mean QD diameter was 30 Å. The emission lifetimes were determined by time-correlated single-photon counting. A cavity-dumped synchronously pumped dye laser (Spectra-Physics 3500) operating at 585 nm provided pump pulses of 10 ps. A Hamamatsu microchannel plate detector provided a typical instrument response function of 70 ps. The PL decay as a function of time for this sample is shown in Figure 12;

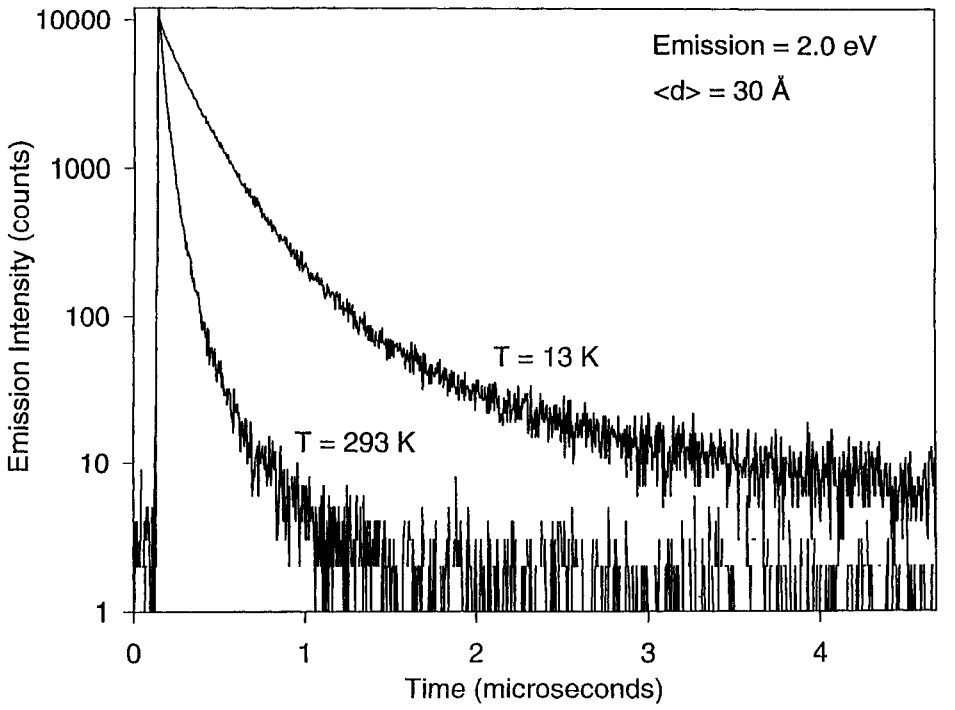


Fig. 12. PL decay for HF-treated InP QDs at 298 and 13 K. (Source: Reprinted with permission from [24]. © 1997 American Chemical Society.)

the excitation was at 585 nm and the emission was monitored at 620 nm. The decay is multiexponential and the data were fit to three exponentials. At 298 K, most of the decay (91%) can be described by two time constants of 28 and 73 ns; at 13 K, most of the decay (98%) can be described by two time constants of 173 and 590 ns.

3.1.2.4. Origin of Resonant Red Shift

The origin of the resonant red shift in InP has been recently analyzed theoretically [47, 48]. The methodology used was to treat a passivated quantum dot as a "giant molecule" in its own right, rather than an object drawn from an infinite crystal surrounded by an infinite potential barrier [36, 37, 39–43]. To this end, infinite-barrier k·p approaches [36, 37, 39–43] were avoided in favor of a pseudopotential supercell approach [47, 48], in which a dot of any selected shape and size is modeled explicitly, and passivating atoms decorate all surface sites. To examine possible surface effects, cation passivants and anion passivants were selectively removed, and the electron structure was recalculated. Four possible models have been examined as to their ability to explain the resonant red shift: (1) emission from an intrinsic, spin-forbidden state, split from its singlet counterpart because of screened electron–hole exchange; (2) emission from an intrinsic, orbitally forbidden conduction band state, for example, X_{1c} (rather than Γ_{1c}); (3) emission to an intrinsic, orbitally forbidden valence band state (e.g., p-like); and (4) emission from extrinsic surface defects (e.g., surface vacancies). The experimental results reported here are quantitatively consistent with model 1 when the exchange interactions are screened by a distance-dependent dielectric function [24]. In model 1, an enhanced (relative to bulk) electron–hole exchange interaction splits the exciton state into a lower-energy spin-forbidden state (triplet) and a higher-energy spin-allowed singlet. Absorption occurs into the upper state, followed by relaxation to and emission from the lower state; the difference between these two states is

the resonant red shift [30, 31, 36–42, 47–49]. The value of the single-dot resonant red shift (as a function of QD size) derived from the experimental data is in excellent agreement with the theoretical predictions [48].

Model 2 was rejected [48] because it was shown that the conduction band minimum in InP dots is not derived from an indirect X_{1c}-like state as in small GaAs particles [48], and model 3 was rejected [48] because the symmetry of the envelope function of the valence band maximum was found to be 1s-like and not 1p-like as expected from simple k·p models. Model 4 shows that *fully* passivated QDs have no surface states, despite the large surface-to-volume ratio. However, in the event that some of the surface atoms were not capped by a passivant (because of, e.g., steric hindrance by large passivating molecules), model 4 shows that surface *defect states* (caused by surface-uncapped In or surface-uncapped P) could appear inside the QD band gap. These surface defects lead to large red shifts extending from 100 to a few hundred meV depending on the surface conditions; such large red shifts are observed in unetched InP QDs but are removed upon HF etching [23]. The magnitude of the observed resonant red shifts reported here after etching is not consistent with the surface defects present in the initial QD synthesis; these are removed or passivated and do not affect the PL. Although surface defect states do not explain the less than 10 to 7 meV *resonant* red shift, direct theoretical modeling of such states [48] shows that they (i) affect the quantum efficiency (through nonradiative recombination) and (ii) lead to a significant hybridization with the ordinary, corelike band edge states, thus affecting the radiative emission rate from these states. Furthermore, because these hybridized states reflect the properties of the uncapped site (i.e., P or In "dangling bond") rather than those of the passivating molecules around this site, it was predicted [48] that surface defect states are mostly independent of the passivant and have size-dependent lifetimes. The degree of mixing of surface defect wave functions with the ordinary corelike band edge states remains unknown at this time.

The relatively long lifetimes of InP QDs with a mean diameter of 30 Å (28–73 ns at 298 K and 173–590 ns at 13 K) are also consistent with model 1 because the spin-forbidden lowest excitonic state has a small probability for radiative transitions to the ground state.

Additional experiments that can be done for InP QDs to check the validity of model 1 include measuring the PL lifetime as a function of magnetic field [36, 37, 40, 41], measuring the intensity ratio of the zero-phonon PL line to its replica as a function of magnetic field [37], and measuring the degree of linear polarization of the PL [40, 41]. In model 1, the PL lifetime should decrease with increasing magnetic field, the zero-phonon PL line intensity should increase relative to the one-phonon replica with magnetic field, and the degree of linear polarization should be negative. These experiments will be done in the future.

The preceding technique does not directly produce the *single-dot* resonant red shift as a function of QD size because the data still reflect the effects of a finite size distribution. The line widths of our FLN spectra are typically 15–30 meV; although these line widths are significantly narrower than the 175–225-meV line widths typically obtained from global (nonresonant) PL excitation, they are still much broader than the line widths reported from PL measurements on single dots. For a variety of II–VI and III–V QDs, single-dot PL line widths have been reported to range from 40 to 1000 μeV [35, 50–54]. The broader line widths in our FLN spectra are attributed to the significant QD size and shape distribution that still remains in the FLN experiment; this is evident in Figure 9 from the decreasing FLN line widths obtained as the excitation energy is moved to lower energies and, hence, to narrower QD size distributions (and also to larger QD diameters). Also, from Figure 6 it can be seen that the absorption peak moves about 35–45 meV for every 1-Å change in QD diameter. Thus, the PL line width of 15–30 meV for our FLN spectra reflects a QD diameter variation of less than 1 Å! It is apparent that the PL line width is extremely sensitive to the spread in QD diameters and that true line widths require PL data obtained from single dots. The experimental PL line widths observed for single QDs are smaller than a line widths of

we used by a factor of about 2 to 50. However, this does not affect the extracted red shifts we report here for single dots because the additional PL line broadening represented by a line width of about 2 meV reflects a variation in the single-dot diameter of less than 0.1 Å.

The FLN spectra show a shoulder that is displaced from the highest-energy PL peak by 30–35 meV; this is attributed to replicate PL lines caused by phonon emission. However, the bulk LO phonon energy for InP is 43 meV; further work is required to understand this difference.

3.1.3. InP Quantum Dots Arrays

Arrays of close-packed InP QDs can be formed by slowly evaporating colloidal solutions to form solid films [55]. It is known that monodispersed colloidal solutions have a natural tendency to self-organize to form colloidal crystal. Recently, Bawendi and co-workers [28, 43] fabricated rather perfect three-dimensional (3D) superlattices of CdSe QDs that are size selected to 3% to 4%. This is a novel quantum dot configuration where QDs form a crystal lattice similar to atoms in a solid. III–V QD preparations have a size distribution of about 10%, and, with such a size distribution, it is possible to prepare short-range two-dimensional (2D) ordered arrays [55].

Close-packed glass solid films of InP QDs can also be also fabricated that are completely optically transparent. In the films, the QDs are randomly ordered.

3.1.4. Applications in Solar Cells

Photosensitization of nanocrystalline TiO_2 semiconductor electrodes by adsorbed dyes has been extensively studied recently because of potential application as a new type of solar cell [44]. The key feature of this system is the use of nanocrystalline TiO_2 films that have extremely large surface-to-volume ratios because they are formed from nanocrystallites. This allows for greatly increased dye coverage in the TiO_2 film and produces very high quantum yields for photon-to-electronic current flow (above 80%) and solar conversion efficiencies above 10% [44, 45].

The band edge offset between InP QDs and TiO_2 allows for efficient photoinduced electron transfer from InP to TiO_2 because the conduction band of InP QDs can be 0.1–0.5 eV above that for TiO_2, depending on the degree of quantization. It has been found that InP QDs adsorb strongly on nanocrystalline TiO_2 electrode films and that InP QD particles can be utilized for photosensitization of nanocrystalline TiO_2 electrodes in solar cells [46]. The potential attraction of InP QDs for this application is that they can have a high absorption coefficient over a larger region of the solar spectrum, and they are photochemically stable.

3.2. GaP Quantum Dots

Quantum dots of GaP can be synthesized by mixing $GaCl_3$ (or the chlorogallium oxalate complex) and $P(Si(CH_3)_3)_3$ in a molar ratio of Ga:P of 1:1 in toluene at room temperature to form the GaP precursor species and then heating this precursor in TOPO at 400 °C for 3 days [17]. The mean particle diameters of our GaP QD preparations were estimated from the line broadening of their X-ray diffraction patterns and from TEM. Figure 13 shows the X-ray diffraction patterns for GaP QD samples that were heated at different temperatures. For diffraction pattern d, the temperature was 400 °C and the size was estimated to be about 30 Å; for diffraction pattern c, the temperature was 360 °C and the size was estimated to be about 20 Å. The diffraction patterns for the lower-temperature preparations (a and b) were too broad and ill defined to permit an estimate of the particle size.

The absorption spectrum in Figure 14 of the 30-Å-diameter GaP QD colloid (heated at 400 °C) exhibits a shoulder at 420 nm (2.95 eV) and a shallow tail that extends out to about 650 nm (1.91 eV) [17]. For 20-Å-diameter GaP QDs (heated at 370 °C), the shoulder is at 390 nm (3.17 eV) and the tail extends to about 550 nm.

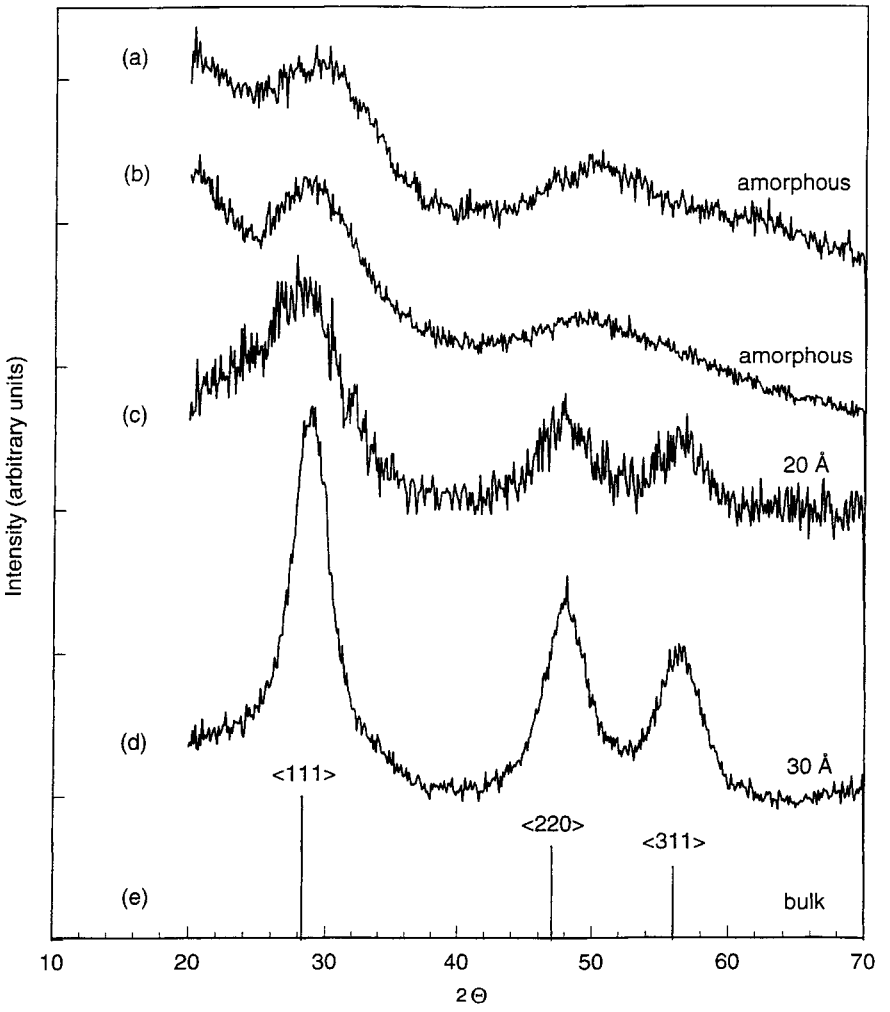


Fig. 13. X-ray diffraction of GaP QDs prepared at different temperatures: (a) 270 °C, (b) 320 °C, (c) 360 °C, and (d) 400 °C. (Source: Reprinted with permission from [17]. © 1995 American Chemical Society.)

Bulk GaP is an indirect semiconductor with an indirect band gap of 2.22 eV (559 nm) and a direct band gap of 2.78 eV (446 nm). Theoretical calculations [56] on GaP QDs show that the increase of the indirect band gap with decreasing QD size is much less pronounced than that for the direct gap; for 30-Å-diameter GaP QDs, the direct and indirect band gaps are predicted to be 3.35 eV and 2.4 eV, respectively. Below 30 Å, the direct band gap is predicted to *decrease* with decreasing size while the indirect band gap continues to increase. As a result, GaP is expected to undergo a transition from an indirect semiconductor to a direct semiconductor below about 20 Å.

The steep rise in absorption and the shoulder at 420 nm in the absorption spectrum of GaP QDs [17] is attributed to a direct transition in the GaP QDs; the shallow-tail region above 500 nm is attributed to the indirect transition. Also, the absorption tail extends below the indirect band gap of bulk GaP [17]. The origin of this subgap absorption is not understood at the present time; it could be caused either by a high density of subgap states in the GaP QDs, by impurities created by the high decomposition temperature, or by Urbach-type band tailing produced by unintentional doping in the QDs [57]. We note that such subgap absorption below the band gap was also observed in GaP nanocrystals that were prepared in zeolite cavities by the gas phase reaction of trimethylgallium and phosphine

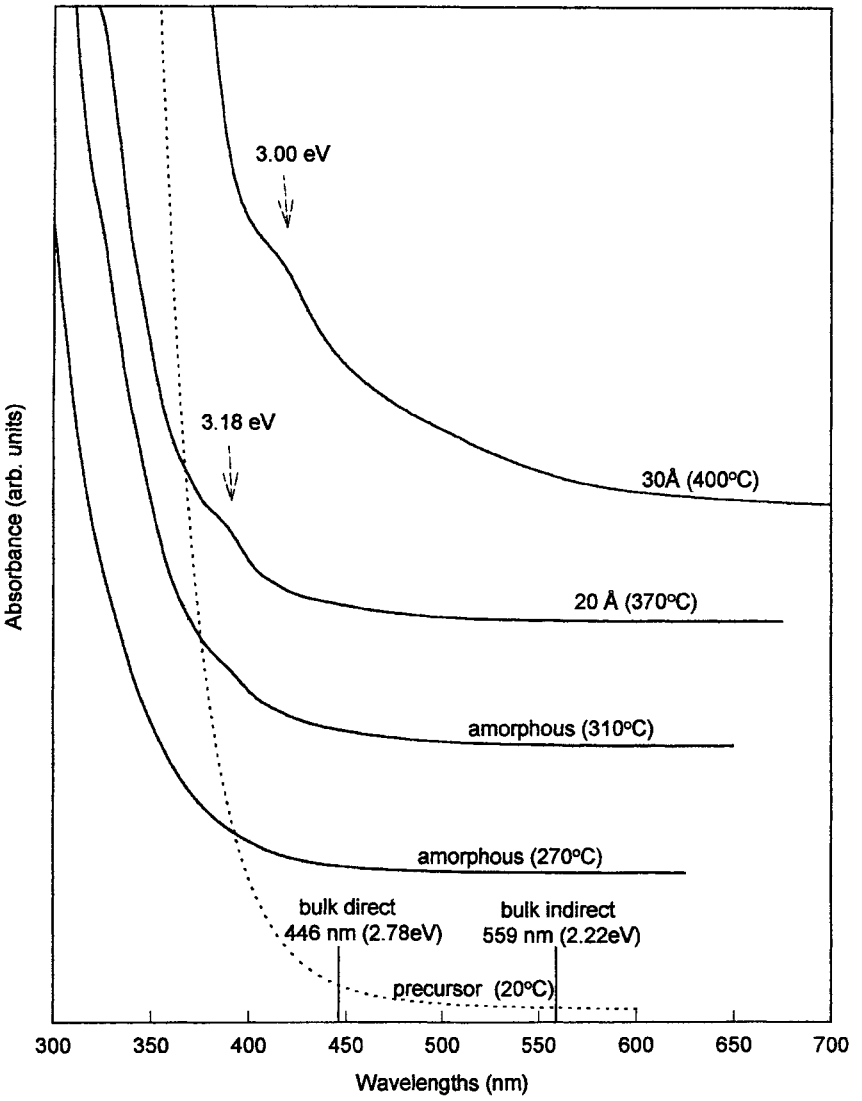


Fig. 14. Optical absorption spectra at room temperature of GaP QDS heated at different temperatures and dissolved in toluene; also shown (dotted line) is the absorption spectrum of the GaP precursor $\{[Cl_2GaP(SiMe_3)_2]_2\}$. The direct and indirect band gaps of bulk GaP are indicated by the vertical line markers on the abscissa. (Source: Reprinted with permission from [17]. © 1995 American Chemical Society.)

at temperatures above 225 °C [58]. This latter result implies that the subgap absorption in GaP QDs is related to their intrinsic behavior and is not caused by synthetic byproducts or impurities.

3.3. $GaInP_2$ Quantum Dots

Quantum dots of $GaInP_2$ can be synthesized by mixing chlorogallium oxalate and chloroindium oxalate complexes and $P(Si(CH_3)_3)_3$ in the molar ratio of Ga:In:P of 1:1:2.6 in toluene at room temperature, followed by heating in TOPO [17]. Heating at 400 °C for 3 days was required to form 25-Å QDs. An X-ray diffraction pattern for a 65-Å sample is shown in Figure 15 along with that of the GaP and InP QDs. As expected for $GaInP_2$, the lattice spacings of these QDs are approximately the average of that of GaP and InP.

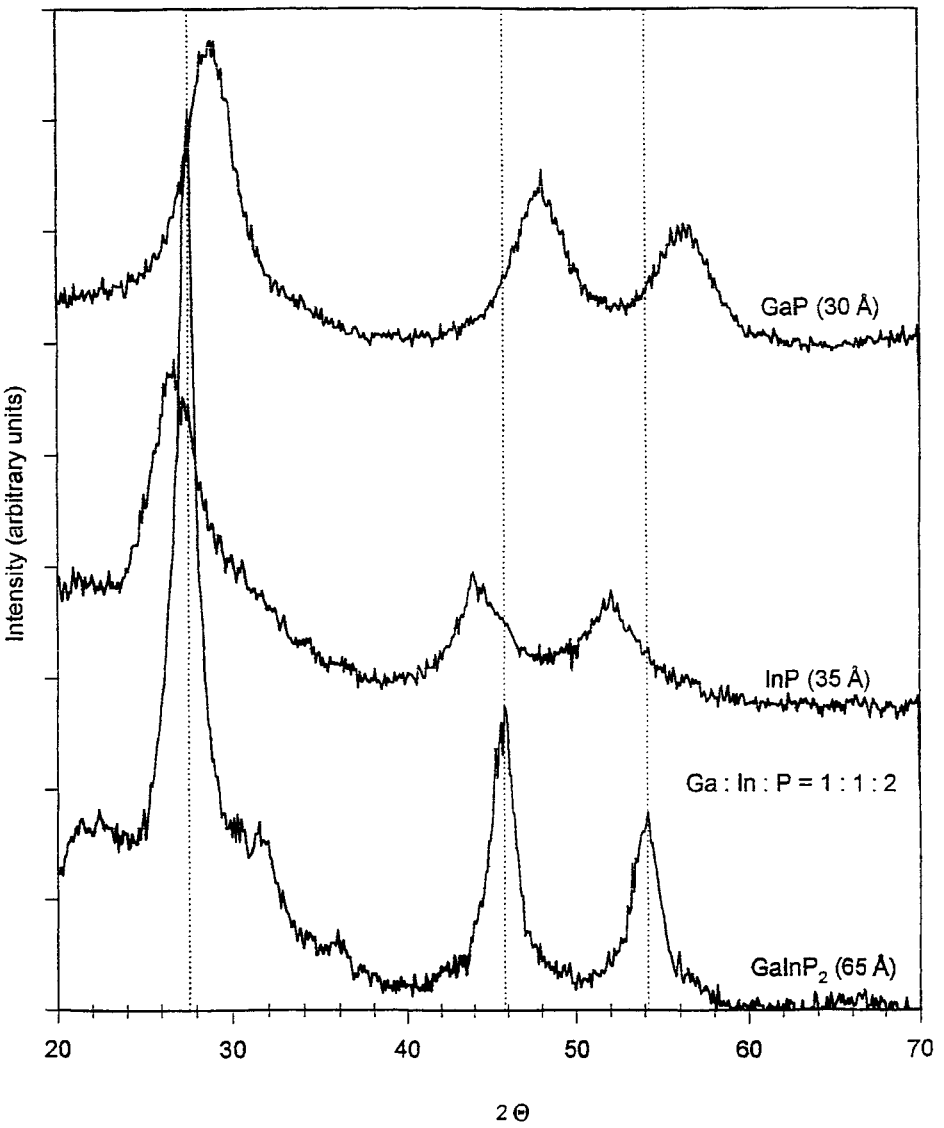


Fig. 15. X-ray diffraction of $GaInP_2$ QDs compared to InP and GaP QDs. (Source: Reprinted with permission from [17]. © 1995 American Chemical Society.)

The ternary Ga–In–P system forms solid solutions that can exhibit direct band gaps ranging from 1.7 to 2.2 eV, depending on the composition and growth temperature [59–65]. At the composition $Ga_{0.5}In_{0.5}P$, the structure can be either atomically ordered or disordered (random alloy) [59–65]; the band gap is direct, but it can range from about 1.8 to 2.0 eV, depending on the degree of atomic ordering. Although one issue of interest is how size quantization will affect the dependence of band gap on atomic ordering, at the present time it is not possible to specify the degree of atomic order in the $GaInP_2$ QDs.

The absorption spectrum of 25-Å $GaInP_2$ QDs does not show any excitonic structure (Fig. 16) [17]; this is caused by a wide size distribution that masks the excitonic peaks. An estimate of the direct band gap of the $GaInP_2$ QDs from a plot of the square of the absorbance times photon energy versus photon energy indicates a value of about 2.7 eV; this value is blue-shifted from the bulk value of 1.8–2.0 eV.

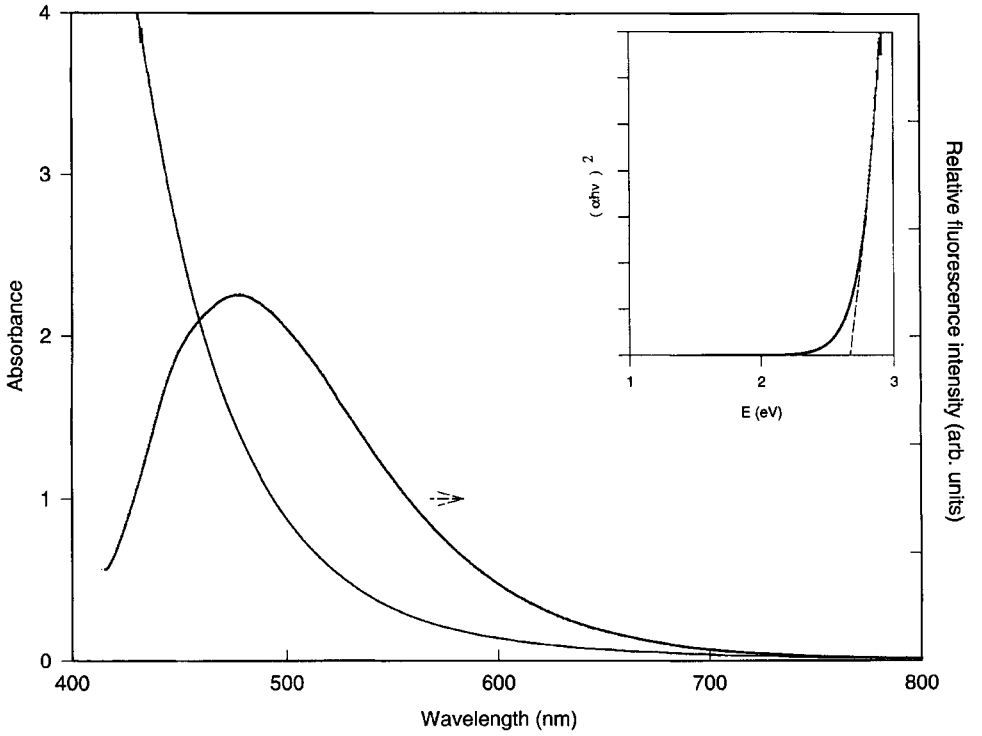


Fig. 16. Absorption spectra for 25-Å $GaInP_2$ colloids; insert shows that the colloid exhibits a direct band gap of 2.7 eV. (Source: Reprinted with permission from [17]. © 1995 American Chemical Society.)

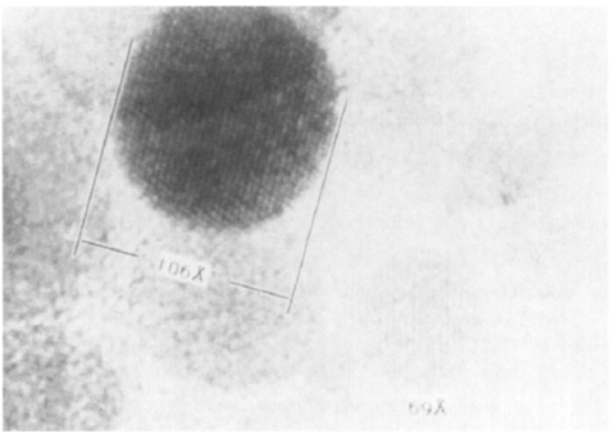


Fig. 17. TEM of GaAs QDs. (Source: Reprinted with permission from [30]. © 1992 American Chemical Society.)

3.4. GaAs Quantum Dots

GaAs quantum dots can be formed by first reacting Ga(III) acetylacetonate and As(Si $(CH_3)_3)_3$ at reflux (216 °C) in triethylene glycol dimethyl ether (triglyme) [16, 21, 30, 31]. This produces an orange-brown turbid slurry that can be filtered through a 700-Å ultrafilter to produce the GaAs colloidal QD solution. A TEM image of GaAs QDs prepared in this way, except that quinoline was used instead of triglyme, is shown in Figure 17. Electron diffraction data show clear *hkl* zincblende GaAs patterns of (111), (220), (311), and (422).

The observed lattice plane spacing of 3.2 Å in TEM images corresponds to the d(111) of GaAs.

A series of ultrafiltrations through 700-, 100-, and 15-Å pore-size filters can be performed to separate particles with different sizes. The optical absorption spectra of the GaAs colloid passed through the 700- and 100-Å pore-size filters exhibit similar absorption spectra: The onset of absorption occurs at about 600 nm; a shallow rise with decreasing wavelength steepens at about 470 nm and peaks at about 440 nm [16, 21, 30, 31]. The absorbance of the 100-Å filtrate was slightly less than that of the 700-Å filtrate. The spectrum for the 15-Å filtrate was similar to that of the blank sample consisting of Ga acetylacetonate refluxed in triglyme. The absorbance begins at about 525 nm and rises very weakly without any peaks.

The particle size distribution of the GaAs QDs was not sufficient to observe excitonic transitions in the absorption or emission spectra [16, 21, 30, 31]. Therefore, more detailed studies of these GaAs QDs were not conducted.

4. SUMMARY

Quantum dots of the III–V semiconductors InP, GaP, $GaInP_2$, InAs, and GaAs can be prepared by nonaqueous colloidal chemical synthesis at temperatures ranging from about 250 to 400 °C, depending on the specific compound and the desired QD size. The QD size for the synthesis can range from about 20 to 100 Å, and the size distribution around the mean diameter can be typically from about 5% to 10%. The synthesis requires capping the quantum dots with a stabilizing molecular species, such as, for example, trioctylphosphine oxide, to control the QD size and the size distribution. The capping species can be subsequently replaced with different molecules of varying length and type, or eliminated completely. As a result, the QDs can be formed into powders or suspended in various liquids or solids (such as polymers or organic and inorganic glasses); they can be studied at low or high temperatures.

The best colloidal III–V QDs synthesized to date are InP QDs; treatment with HF results in the elimination of deep surface traps and produces band edge emission with very high quantum yields (60% at 10 K). The color of these dots ranges from deep red (band gap = 1.7 eV) to green (band gap = 2.4 eV), corresponding to a size range of 60 to 26 Å, respectively. Structure in the absorption and emission spectra reflects the existence of quantized energy levels in the QDs. Size-selective spectroscopy (fluorescence line narrowing and photoluminescence excitation spectroscopy) has been done to help determine the energy level structure in the QDs. Solid arrays of close-packed InP QDs have been prepared; ordered hexagonal packing occurs in some regions.

Acknowledgment

This work was supported by the U.S. Department of Energy, Office of Basic Energy Sciences, Division of Chemical Sciences.

References

1. R. Dingle, W. Wiegmann, and C. H. Henry, *Phys. Rev. Lett.* 33, 827 (1974).
2. R. Dingle, *Feskörperprobleme* 15, 21 (1975).
3. C. Weisbuch and B. Vinter, "Quantum Semiconductor Structures." Academic Press, New York, 1991.
4. G. Bastard, "Wave Mechanics Applied to Semiconductor Heterostructures." Halsted Press, New York, 1988.
5. M. Jaros, "Physics and Applications of Semiconductor Microstructures." Oxford University Press, Oxford, U.K., 1989.
6. A. D. Yoffe, *Adv. Phys.* 42, 173 (1993).
7. K. Kash, *J. Lumin.* 46, 69 (1990).

8. S. P. Beaumont and C. M. Sotomayor Torres, *NATO ASI Ser. B* 1 (1990).
9. P. V. Kamat and D. Meisel, in "Studies in Surface Science and Catalysis," Vol. 103. Elsevier, Amsterdam, 1997.
10. A. P. Alivisatos, *Science* 271, 933 (1996).
11. A. P. Alivisatos, *J. Phys. Chem.* 100, 13226 (1996).
12. M. G. Bawendi, *NATO ASI Ser. B* 339 (1995).
13. L. Brus, *Appl. Phys. A* 53, 465 (1991).
14. Y. Wang, in "Advances in Photochemistry" (D. C. Neckers, D. H. Volman, and V. Bünau, eds.), Vol. 19, p. 179. Wiley, New York, 1995.
15. L. E. Brus, A. L. Efros, and T. Itoh, *J. Lumin.* 70, 1 (1996).
16. O. I. Mićić and A. J. Nozik, *J. Lumin.* 70, 95 (1996).
17. O. I. Mićić, J. R. Sprague, C. J. Curtis, K. M. Jones, J. L. Machol, and A. J. Nozik, *J. Phys. Chem.* 99, 7754 (1995).
18. U. Banin, G. Cerullo, A. A. Guzelian, C. J. Bardeen, A. P. Alivisatos, and C. V. Shank, *Phys. Rev. B* 55, 7059 (1997).
19. A. A. Guzelian, U. Banin, A. V. Kadavanich, X. Peng, and A. P. Alivisatos, *Appl. Phys. Lett.* 69, 1432 (1996).
20. A. A. Guzelian, J. E. B. Katari, A. V. Kadavanich, U. Banin, K. Hamad, E. Juban, A. P. Alivisatos, R. H. Wolters, C. C. Arnold, and J. R. Heath, *J. Phys. Chem.* 100, 7212 (1996).
21. M. A. Olshavsky, A. N. Goldstein, and A. P. Alivisatos, *J. Am. Chem. Soc.* 112, 9438 (1990).
22. O. I. Mićić, C. J. Curtis, K. M. Jones, J. R. Sprague, and A. J. Nozik, *J. Phys. Chem.* 98, 4966 (1994).
23. O. I. Mićić, J. R. Sprague, Z. Lu, and A. J. Nozik, *Appl. Phys. Lett.* 68, 3150 (1996).
24. O. I. Mićić, H. M. Cheong, H. Fu, A. Zunger, J. R. Sprague, A. Mascarenhas, and A. J. Nozik, *J. Phys. Chem. B.* 101, 4904 (1997).
25. M. Peterson and A. J. Nozik, in "Photoelectrochemistry and Photovoltaics of Layered Semiconductors" (A. Aruchamy, ed.), p. 297. Kluwer Academic, Boston, 1992.
26. H. Weller and A. Eychmüller, in "Semiconductor Nanoclusters" (P. V. Kamat and D. Meisel, eds.), Vol. 103, p. 5. Elsevier Science B.V., Amsterdam, 1996.
27. J. T. G. Overbeek, *Adv. Colloid Interface Sci.* 15, 251 (1982).
28. C. B. Murray, Synthesis and Characterization of II–VI Quantum Dots and Their Assembly into 3D Quantum Dot Superlattices, Ph.D. Thesis, Massachusetts Institute of Technology, 1995.
29. C. B. Murray, D. J. Norris, and M. G. Bawendi, *J. Am. Chem. Soc.* 115, 8706 (1993).
30. H. Uchida, C. J. Curtis, P. V. Kamat, K. M. Jones, and A. J. Nozik, *J. Phys. Chem.* 96, 1156 (1992).
31. A. J. Nozik, H. Uchida, P. V. Kamat, and C. Curtis, *Isr. J. Chem.* 33, 15 (1993).
32. Y. Gu, Z. Lin, V. Smetkowski, R. Butera, and D. H. Waldeck, *Langmuir* 11, 1849 (1995).
33. S. R. Aubuchon, A. T. McPhail, R. L. Wells, J. A. Giambra, and J. R. Browser, *Chem. Mater.* 6, 82 (1994).
34. R. L. Wells, M. F. Self, A. T. McPhail, S. R. Aubuchon, R. C. Wandenberg, and J. P. Jasinski, *Organometallics* 12, 2832 (1993).
35. S. A. Empedocles, D. J. Norris, and M. G. Bawendi, *Am. Phys. Soc.* 77, 3873 (1996).
36. M. Nirmal, D. J. Norris, M. Kuno, M. G. Bawendi, A. L. Efros, and M. Rosen, *Phys. Rev. Lett.* 75, 3728 (1995).
37. A. L. Efros, M. Rosen, M. Kuno, M. Nirmal, D. J. Norris, and M. Bawendi, *Phys. Rev. B* 54, 4843 (1996).
38. D. J. Norris and M. G. Bawendi, *Phys. Rev. B* 53, 16338 (1996).
39. D. J. Norris, A. L. Efros, M. Rosen, and M. G. Bawendi, *Phys. Rev. B* 53, 16347 (1996).
40. M. Chamarro, C. Gourdon, P. Lavallard, O. Lublinskaya, and A. I. Ekimov, *Phys. Rev. B* 53, 1336 (1996).
41. M. Chamarro, C. Gourdon, and P. Lavallard, *J. Lumin.* 70, 222 (1996).
42. U. Woggon, F. Gindele, O. Wind, and C. Klingshirn, *Phys. Rev. B* 54, 1506 (1996).
43. C. B. Murray, C. R. Kagan, and M. G. Bawendi, *Science* 270, 1335 (1995).
44. B. O'Regan and M. Grätzel, *Nature* 353, 737 (1991).
45. M. K. Nazeeruddin, A. Kay, I. Rodicio, R. Humphry-Baker, E. Müller, P. Liska, N. Vlachopoulos, and M. Grätzel, *J. Am. Chem. Soc.* 115, 6382 (1993).
46. A. Zaban, O. I. Mićić, B. A. Gregg, and A. J. Nozik, *Langmuir* 14, 3153 (1998).
47. H. Fu and A. Zunger, *Phys. Rev. B* 55, 1642 (1997).
48. H. Fu and A. Zunger, *Phys. Rev. B* 56, 1496 (1997).
49. A. Resta, *Phys. Rev. B* 16, 2717 (1977).
50. A. Forchel, R. Steffen, T. Koch, M. Michel, M. Albrecht, and T. L. Reinecke, *Semicond. Sci. Technol.* 11, 1529 (1996).
51. D. Gammon, E. S. Snow, and D. S. Katzer, *Appl. Phys. Lett.* 67, 2391 (1995).
52. M. Grundmann, J. Christen, N. N. Ledentsov, J. Bohrer, D. Bimberg, S. S. Ruvimov, P. Werner, U. Richter, U. Gosele, J. Heydenreich, V. M. Ustinov, A. Y. Egorov, A. E. Zhukov, P. S. Kop'ev, and Z. I. Alferov, *Phys. Rev. Lett.* 74, 4043 (1995).
53. L. Samuelson, N. Carlsson, P. Castrillo, A. Gustafsson, D. Hessman, J. Lindahl, L. Montelius, A. Petersson, M.-E. Pistol, and W. Seifert, *Jpn. J. Appl. Phys.* 34, 4392 (1995).
54. Y. Nagamune, H. Watabe, M. Nishioka, and Y. Arakawa, *Appl. Phys. Lett.* 67, 3257 (1995).
55. O. I. Mićić, K. M. Jones, A. Cahill, and A. J. Nozik, *J. Phys. Chem. B* 102, 9791 (1998).

56. M. V. Rama Krishna and R. A. Friesner, *J. Chem. Phys.* 95, 525 (1991).
57. J. I. Pankove, "Optical Processes in Semiconductors." Dover, New York, 1971.
58. J. E. MacDougall, H. Eckert, G. D. Stucky, N. Herron, Y. Wang, K. Moller, T. Bein, and D. Cox, *J. Am. Chem. Soc.* 111, 8006 (1989).
59. M. C. DeLong, W. D. Ohlsen, I. Viohl, P. C. Taylor, and J. M. Olson, *J. Appl. Phys.* 70, 2780 (1991).
60. S.-H. Wei and A. Zunger, *Phys. B* 39, 3279 (1989).
61. S.-H. Wei, L. G. Ferreira, and A. Zunger, *Phys. Rev. B* 41, 8240 (1990).
62. S. Froyen and A. Zunger, *Phys. Rev. Lett.* 66, 3132 (1991).
63. A. Mascarenhas and J. M. Olson, *Phys. Rev. B* 41, 9947 (1990).
64. G. S. Horner, A. Mascarenhas, S. Froyen, R. G. Alonso, K. A. Bertness, and J. M. Olson, *Phys. Rev. B* 47, 4041 (1993).
65. J. M. Olson, S. R. Kurtz, A. E. Kibbler, and P. Faine, *Appl. Phys. Lett.* 56, 623 (1990).

This Page Intentionally Left Blank

Chapter 9

QUANTIZATION AND CONFINEMENT PHENOMENA IN NANOSTRUCTURED SUPERCONDUCTORS

V. V. Moshchalkov, V. Bruyndoncx, L. Van Look, M. J. Van Bael, Y. Bruynseraede

Laboratorium voor Vaste-Stoffysica en Magnetisme, Katholieke Universiteit Leuven, Leuven, Belgium

A. Tonomura

Advanced Research Laboratory, Hitachi, Ltd., Hatoyama, Saitama, Japan

Contents

1. Introduction 452
   1.1. Quantization and Confinement 452
   1.2. Nanostructuring 452
   1.3. Confining the Superconducting Condensate 454
   1.4. Vortex Lattice in a Type II Superconductor 457
2. Individual Nanostructures 464
   2.1. Line 464
   2.2. Loop 465
   2.3. Dot 468
3. Clusters of Loops and Antidots 473
   3.1. One-Dimensional Clusters of Loops 473
   3.2. Two-Dimensional Clusters of Antidots 477
4. Huge Arrays of Nanoscopic Plaquettes in Laterally Nanostructured Superconductors 479
   4.1. The $T_c(H)$ Phase Boundary of Superconducting Films with an Antidot Lattice 480
   4.2. Pinning in Laterally Nanostructured Superconductors 482
   4.3. Regular Pinning Arrays with $n_s = 1$ 485
   4.4. Multiquanta Vortex Lattices ($n_s > 1$) 505
   4.5. Crossover from a Pinning Array to a Network ($n_s \gg 1$) 517
5. Conclusions 520
   Acknowledgments 521
   References 522

Handbook of Nanostructured Materials and Nanotechnology, edited by H.S. Nalwa
Volume 3: Electrical Properties
Copyright © 2000 by Academic Press
All rights of reproduction in any form reserved.
ISBN 0-12-513763-X/$30.00

1. INTRODUCTION

1.1. Quantization and Confinement

"Confinement" and "quantization" are two closely related definitions: If a particle is "confined" then its energy is "quantized," and vice versa. According to the dictionary, to "confine" means to "restrict within limits," to "enclose," and even to "imprison." A typical example, illustrating the relation between confinement and quantization, is the restriction of the motion of a particle by enclosing it within an infinite potential well of size L_A. Because of the presence of an infinite potential $U(x)$ (Fig. 1) for $x < 0$ and $x > L_A$, the wave function $\Psi(x)$ describing the particle is zero outside the well: $\Psi = 0$ for $x < 0$ and $x > L_A$ and, in the region with $U(x) = 0$ ($0 \leqslant x \leqslant L_A$), the solutions of the one-dimensional Schrödinger equation correspond to standing waves with an integer number n of half wavelengths λ along L_A: $n\lambda_n/2 = L_A$. This simple constraint results in the well-known quantized energy spectrum

$$E_n = \frac{\hbar^2 k_n^2}{2m} = \frac{\hbar^2 (2\pi/\lambda_n)^2}{2m} = \frac{\hbar^2 \pi^2}{2mL_A^2} n^2 \tag{1}$$

Here k_n is the wave number and m is the free electron mass. To have an idea about the characteristic energy scales involved and their dependence on the confinement length L_A, the energies E_1 [Eq. (1)] for electrons confined by an infinite potential well with sizes 1 Å, 1 nm, and 1 μm are given in Table I [1–5].

1.2. Nanostructuring

Recent impressive progress in nanofabrication has made it possible to realize the whole range of confinement lengths L_A: from 1 μm (photo- and e-beam lithography), via 1 nm to 1 Å (single-atom manipulation) and, through that, to control the confinement energy (temperature) from a few millikelvins higher up to far above room temperature (Table I).

This progress has stimulated dramatically the experimental and theoretical studies of different nanostructured materials and individual nanostructures. The interest toward such

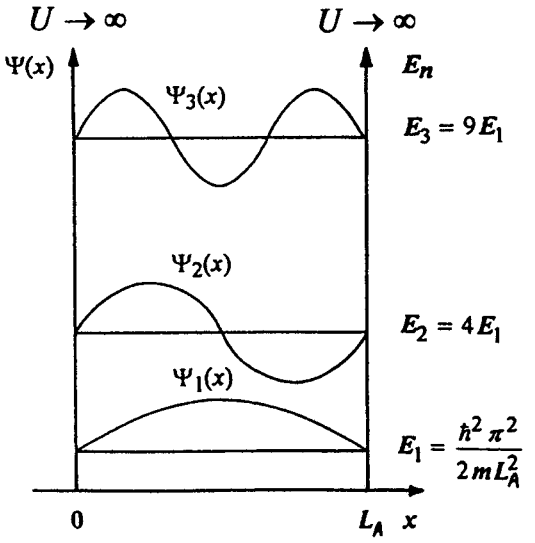


Fig. 1. Confinement and quantization of the motion of a particle by an infinite potential well applied on the length scale L_A for $n = 1, 2$, and 3. (Source: Reprinted with permission from [5]. © 1998 American Institute of Physics.)

Table 1. Confinement by the Infinite Potential Well

Confinement length L_A	Energy E_1	Temperature T
1 Å	40 eV	4×10^5 K
1 nm	0.4 eV	4×10^3 K
1 μm	0.4 μeV	4 mK

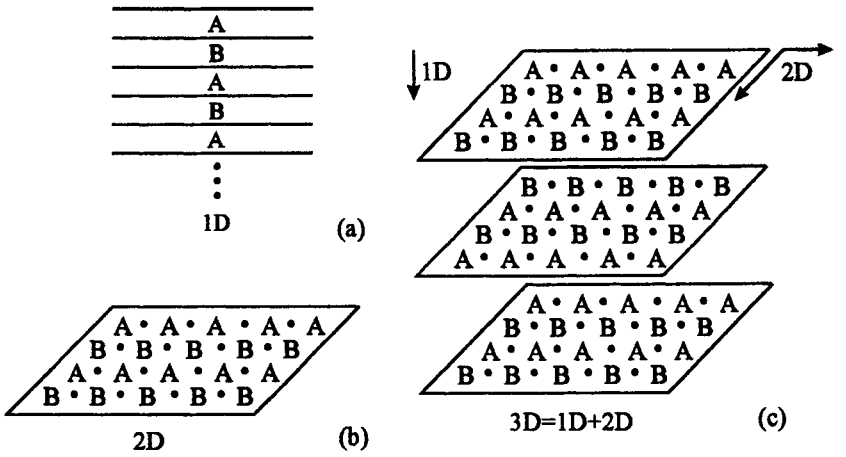


Fig. 2. Schematic presentation of the vertical modulation in superlattices or multilayers (a) of the horizontal modulation achieved by a lateral repetition of elements A and B (b) and of the 1D + 2D = 3D artificial modulation (c). (Source: Reprinted with permission from [5]. © 1998 American Institute of Physics.)

structures arises from the remarkable principle of "quantum design," when quantum mechanics can be efficiently used to tailor the physical properties of nanostructured materials.

Nanostructuring can also be considered as a sort of artificial modulation. We can identify then the main classes of nanostructured materials using the idea of their modification along one, two or three axes, thus introducing one-dimensional (1D), 2D or 3D artificial modulation (Fig. 2). The 1D or "vertical" modulation represents then the class of superlattices or multilayers (Fig. 2a) formed by alternating individual films of two (A, B) or more different materials in a stack. Some examples of the different types of multilayers are superconductor/insulator (Pb/Ge, WGe/Ge, ...), superconductor/metal (V/Ag, ...), superconductor/ferromagnet (Nb/Fe, V/Fe, ...), ferromagnet/metal (Fe/Cr, Cu/Co, ...), and so on [6–17].

The "horizontal" (lateral) superlattices (Fig. 2b) correspond to the 2D artificial modulation achieved by a lateral repetition of one (A), two (A, B), or more elements ("elementary plaquettes"). As examples, we should mention here antidot arrays or antidot lattices, when A = microhole ("antidot"), or arrays and lateral superlattices consisting of magnetic dots.

If the 2D lateral modulation is applied to each individual layer of a multilayer or superlattice, then we deal with the 1D + 2D = 3D artificial modulation (Fig. 2c). For example, if arrays of antidots are made in a multilayer, then we have a system with 3D artificial modulation that combines the 2D lateral "horizontal" with the 1D "vertical" modulation.

Finally, macroscopic nanostructured samples, with a huge number N of repeated elementary nanoplaquettes (A, B, ...), are examples of very complicated systems if the confined charge carriers or flux lines are strongly interacting with each other and the relevant interaction is of a long range. In this case, the essential physics of such systems can be

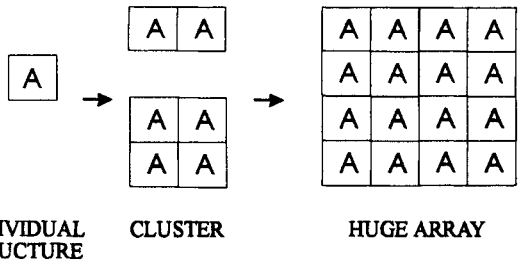


Fig. 3. Schematic presentation of an individual structure (A = nanoplaquette), a cluster of nanoplaquettes, and a huge array of nanoplaquettes. (Source: Reprinted with permission from [5]. © 1998 American Institute of Physics.)

understood much better if one uses *clusters* of elements ($N \simeq 10$), instead of their *huge arrays* ($N \to \infty$) (Fig. 3). These clusters, occupying an intermediate place between individual nanostructures ($N = 1$) and nanostructured materials ($N \to \infty$), are very helpful model objects to study the interactions between flux lines or charge carriers confined by finite arrays (clusters) of elements A. The "growth" of clusters on the way from an individual object A to a huge array of A's can be done either in a 1D or 2D fashion (Fig. 3), thus realizing 1D chains or 2D-like clusters of elements A.

1.3. Confining the Superconducting Condensate

The nanostructured materials and individual nanostructures, introduced in the previous section, can be prepared using modern facilities for nanofabrication. It is worth, however, first asking ourselves a few simple questions like: Why is it important to make such structures, what kind of new physics should be expected, and why is it of interest to focus on superconducting (and not, for example, normal metallic) nanostructured materials?

First, *by making nanostructured materials, one creates an artificial potential in which charge carriers or flux lines are confined.* The size L_A of an elementary "plaquette" A gives roughly the expected energy scale in accordance with Table I, while the positions and topology of the elements A determine the pattern of the potential modulation. The concentration of charge carriers or flux lines can be controlled by varying a gate voltage (in 2D electron gas systems) [18] or the applied magnetic field (in superconductors) [19]. In this situation, different commensurability effects between the fixed number of elements A in an array and a tunable number of charge or flux carriers are observed.

Second, *modifying the sample topology in nanostructured materials creates a unique possibility to impose the desired boundary conditions, and through that to change the properties of the sample.* A Fermi liquid or a superconducting condensate confined within such materials will be subjected to severe constraints and, as a result, the properties of these materials will be strongly affected by the boundary conditions.

While a normal metallic system should be considered quantum mechanically by solving the Schrödinger equation:

$$\frac{1}{2m}(-i\hbar\nabla - e\mathbf{A})^2\Psi + U\Psi = E\Psi \tag{2}$$

a superconducting system is described by the two coupled Ginzburg–Landau (GL) equations:

$$\frac{1}{2m^*}(-i\hbar\nabla - e^*\mathbf{A})^2\Psi_s + \beta|\Psi_s|^2\Psi_s = -\alpha\Psi_s \tag{3}$$

$$\mathbf{j} = \nabla \times \mathbf{h} = \frac{e^*}{2m^*}\left[\Psi_s^*(-i\hbar\nabla - e^*\mathbf{A})\Psi_s + \Psi_s(i\hbar\nabla - e^*\mathbf{A})\Psi_s^*\right] \tag{4}$$

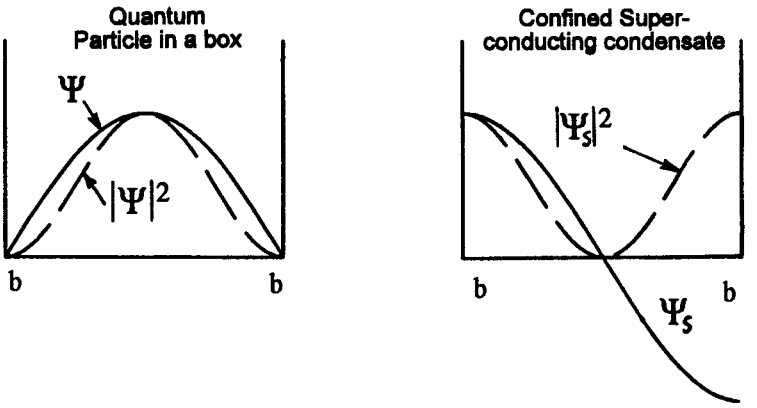


Fig. 4. Boundary conditions for normal metal–vacuum (quantum particle in a box) and superconductor–vacuum (confined superconducting condensate) interfaces. (Source: Reprinted with permission from [5]. © 1998 American Institute of Physics.)

with $\mathbf{A}$ the vector potential that corresponds to the microscopic field $\mathbf{h} = \mathrm{rot}\,\mathbf{A}/\mu_0$, U the potential energy, E the total energy, α a temperature-dependent parameter changing sign from $\alpha > 0$ to $\alpha < 0$ as T is decreased through T_c, β a positive temperature-independent constant, and m^* the effective mass, which can be chosen arbitrarily and is generally taken as twice the free electron mass m.

Note that the first GL equation [Eq. (3)], with the nonlinear term $\beta|\Psi_s|^2\Psi_s$ neglected, is the analog of the Schrödinger equation [Eq. (2)] with $U = 0$, when making a few substitutions: $\Psi_s \leftrightarrow \Psi$, $e^* \leftrightarrow e$, $-\alpha \leftrightarrow E$, and $m^* \leftrightarrow m$. The superconducting order parameter Ψ_s corresponds to the wave function Ψ in Eq. (2). The effective charge e^* in the GL equations is $2e$, that is, the charge of a Cooper pair, while the temperature-dependent GL parameter α

$$-\alpha = \frac{\hbar^2}{2m^*\xi^2(T)} \tag{5}$$

plays the role of E in the Schrödinger equation. Here $\xi(T)$ is the temperature-dependent coherence length:

$$\xi(T) = \frac{\xi(0)}{\sqrt{1 - T/T_{c0}}}. \tag{6}$$

The boundary conditions for normal metal–vacuum and superconductor–vacuum interfaces are, however, different (Fig. 4):

$$\Psi\Psi^*|_b = 0 \tag{7}$$

$$(-i\hbar\nabla - e^*\mathbf{A})\Psi_s|_{\perp,b} = 0 \tag{8}$$

that is, for normal metallic systems *the density* is zero (Dirichlet boundary condition), while for superconducting systems, *the gradient* of Ψ_s (Neumann boundary condition) has no component perpendicular to the boundary. As a consequence, the supercurrent cannot flow through the boundary. The nucleation of the superconducting condensate is favored at the superconductor/vacuum interfaces, thus leading to the appearance of superconductivity, at the third critical field $H_{c3}(T)$, in a surface sheet with a thickness $\xi(T)$ (Fig. 5).

For bulk superconductors, the surface-to-volume ratio is negligible and, therefore, superconductivity in the bulk is not affected by a thin superconducting surface layer. For nanostructured superconductors with antidot arrays, however, the boundary conditions [Eq. (8)] and the surface superconductivity introduced through them become very important if $L_A \leqslant \xi(T)$. The advantage of superconducting materials in this case is that it is not even necessary to go to the nanometer scale (as for normal metals), because for L_A on the

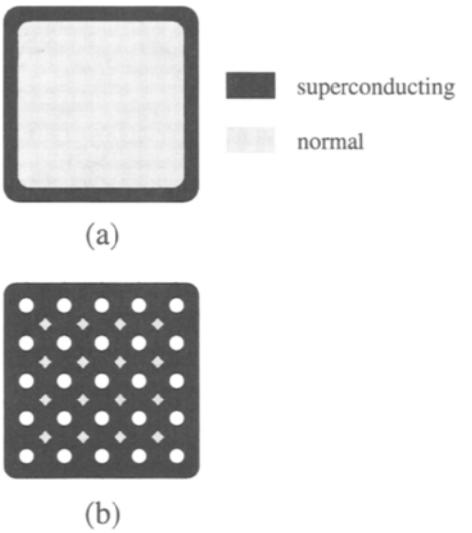


Fig. 5. Schematic illustration of the surface superconductivity nucleated at the third critical field $H_{c3}(T)$. (a) In a bulk superconductor, the surface superconducting sheet appears only at the external sample boundary, (b) while, in a laterally nanostructured superconductor the surface superconductivity appears around each antidot, thus covering the whole sample interior. In the latter case, the role of $H_{c2}(T)$ is played by $H_{c3}(T)$.

order of 0.1 to 1.0 μm the temperature range where $L_A \leqslant \xi(T)$ spreads over 0.01 to 0.1 K below T_c as a result of the divergence of $\xi(T)$ at $T \to T_{c0}$ (Eq. (6)).

In principle, the mesoscopic regime $L_A \leqslant \xi(T)$ [and $L_A \leqslant \lambda(T)$, with λ the magnetic penetration depth] can eventually be reached even in bulk superconducting samples with $L_A \sim 1$ cm–1 m, because $\xi(T)$ [and $\lambda(T)$ as well] diverges at $T \to T_{c0}$. However, the temperature window where $L_A \leqslant \xi(T)$ is so narrow, not more than approximately 1 nK below T_{c0}, that one needs ideal sample homogeneity and perfect temperature stability.

In the mesoscopic regime $L_A \leqslant \xi(T)$, which is quite easily realized in nanostructured materials, the surface superconductivity can cover the whole available space occupied by the material, thus spreading superconductivity all over the sample. It is then evident that in this case the surface effects play the role of bulk effects (see Fig. 5).

Using the similarity between the linearized GL equation [Eq. (3)] and the Schrödinger equation [Eq. (2)], the approach to determine $T_c(H)$ can be formalized as follows: Because the parameter $-\alpha$ [Eqs. (3) and (5)] plays the role of energy E [Eq. (2)], then *the highest possible temperature $T_c(H)$ for the nucleation of the superconducting state in the presence of the magnetic field H always corresponds to the lowest Landau level $E_{LLL}(H)$* found by solving the Schrödinger equation [Eq. (2)] with "superconducting" boundary conditions [Eq. (8)].

Figure 6 illustrates the application of this basic rule to the calculation of the upper critical field $H_{c2}(T)$: Indeed, if the well-known classical Landau solution for the lowest level in a bulk sample $E_{LLL}(H) = \hbar\omega/2$, where $\omega = e^*\mu_0 H/m^*$ is the cyclotron frequency, is taken, then, from $-\alpha = E_{LLL}(H)$, we have

$$\frac{\hbar^2}{2m^*\xi^2(T)} = \frac{\hbar\omega}{2}\bigg|_{H=H_{c2}} \tag{9}$$

with the help of Eq. (5). We obtain

$$\mu_0 H_{c2}(T) = \frac{\Phi_0}{2\pi\xi^2(T)} \tag{10}$$

with $\Phi_0 = h/e^* = h/2e$ the superconducting flux quantum.

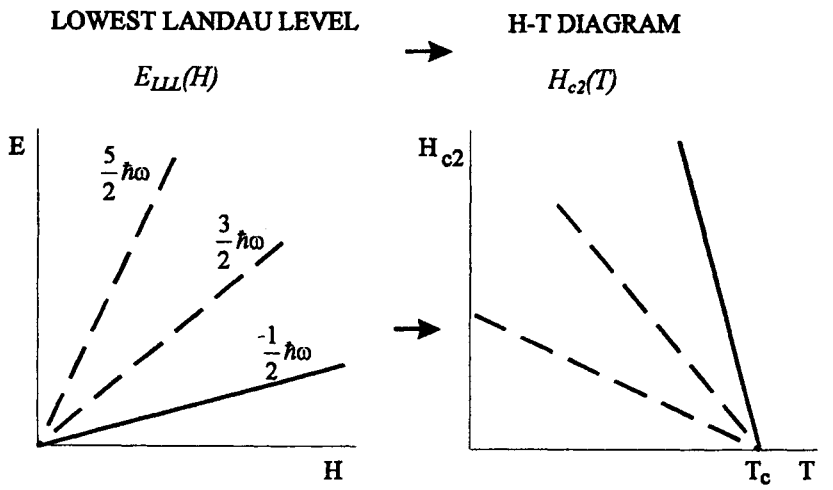


Fig. 6. Landau level scheme for a particle in a magnetic field. From the lowest Landau level $E_{\mathrm{LLL}}(H) = \hbar\omega/2$, the second critical field $H_{c2}(T)$ is derived (solid line). (Source: Reprinted with permission from [5]. © 1998 American Institute of Physics.)

In nanostructured superconductors, where the boundary conditions [Eq. (8)] strongly influence the Landau level scheme, $E_{\mathrm{LLL}}(H)$ has to be calculated for each specific confinement geometry. By measuring the shift of the critical temperature $T_c(H)$ in a magnetic field, one can compare the experimental phase boundary $T_c(H)$ with the calculated level $E_{\mathrm{LLL}}(H)$ and thus check the effect of the confinement topology on the superconducting phase boundary for a series of nanostructured superconducting samples. The transition between normal and superconducting states is usually very sharp and therefore, the lowest Landau level can be easily traced as a function of the applied magnetic field. The midpoint of the resistive transition from the superconducting to the normal state is usually taken as the criterion to determine $T_c(H)$.

1.4. Vortex Lattice in a Type II Superconductor

The value of the GL parameter $\kappa = \lambda(T)/\xi(T)$ determines the behavior of a bulk superconductor in a magnetic field. Depending on the κ values, a distinction can be made between type I ($\kappa < 1/\sqrt{2}$) and type II ($\kappa > 1/\sqrt{2}$) superconductors.

The two types of superconductors are characterized by their different behavior in a magnetic field (H) as function of temperature (T). The H–T phase diagram for a bulk type I and a type II superconductor is presented in parts a and b of Figure 7, respectively. A type I superconductor in a field smaller than the thermodynamical critical field $H_c(T)$ is in the Meissner state, where the magnetic flux is completely expelled ($B = 0$). Above $H_c(T)$, superconductivity is destroyed and the sample is in the normal state.

The H–T phase diagram of a type II superconductor is given in Figure 7b. At fields below the first critical field [$H < H_{c1}(T)$], the superconductor is in the Meissner state. In the mixed state between the first and the second critical field [$H_{c1}(T) < H < H_{c2}(T)$], magnetic flux is able to partially penetrate the superconductor in quantized units, which are called flux lines or vortices [20]. In the field and temperature region $H_{c2}(T) < H < H_{c3}(T) \simeq 1.69 H_{c2}(T)$, superconductivity only exists in a thin sheet at the surface (see Fig. 5a), while the rest of the material is in the normal state. Finally, above the third critical field [$H > H_{c3}(T)$], superconductivity is completely destroyed and the whole sample is in the normal state. The corresponding magnetization curves [$-M(H)$] for ideal homogeneous type I and type II superconductors (without demagnetization effects) are shown in Figure 8. The magnetization M can be written in terms of the applied field H and the flux

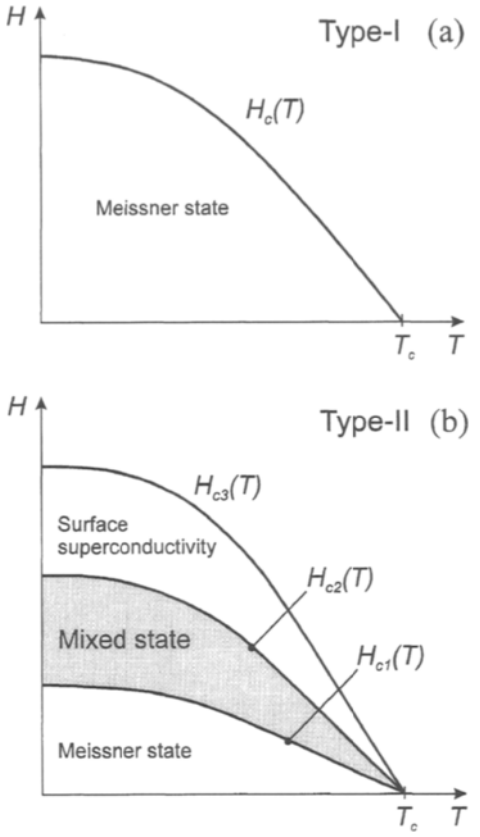


Fig. 7. $H-T$ phase diagram of (a) a type I and (b) a type II superconductor.

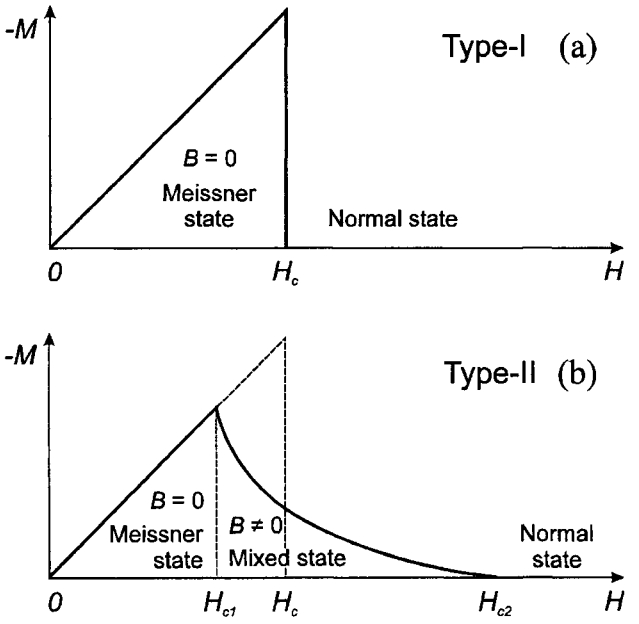


Fig. 8. Reversible magnetization as a function of the applied field $[-M(H)]$ for a long cylinder of an ideal homogeneous type I (a) and type II (b) superconductor.

density B in the sample:

$$\mu_0 M = B - \mu_0 H \tag{11}$$

The various critical fields of a type II superconductor can be expressed in terms of the characteristic length scales. $H_c(T)$ is the thermodynamic critical field, given by

$$\mu_0 H_c(T) = \frac{\Phi_0}{2\sqrt{2}\pi\lambda(T)\,\xi(T)} \tag{12}$$

The first and second critical fields of a type II superconductor can be written as

$$\mu_0 H_{c1}(T) = \frac{\ln(\kappa)}{\sqrt{2}\kappa}\mu_0 H_c(T) = \frac{\ln(\kappa)\Phi_0}{4\pi\lambda^2(T)} \tag{13}$$

and [see also Eq. (10)]

$$\mu_0 H_{c2}(T) = \frac{\Phi_0}{2\pi\xi^2(T)} = \sqrt{2}\kappa\mu_0 H_c(T) \tag{14}$$

For thin type II superconducting films, in a perpendicular field, the first critical field can be extremely small as a result of strong demagnetizing effects [21].

1.4.1. Structure of a Single Vortex

The amount of flux carried by a single vortex equals to one flux quantum Φ_0. A single vortex consists of a normal core of radius ξ, around which shielding currents are circulating. In Figure 9, a schematic presentation of a vortex is given, showing the local field h and the superconducting electron density n_{SC} as a function of the distance r from the vortex center. The superconducting order parameter vanishes in the center of the vortex core. The local field h is highest in the normal core and decays, due to the screening currents, over a distance given by the penetration depth λ.

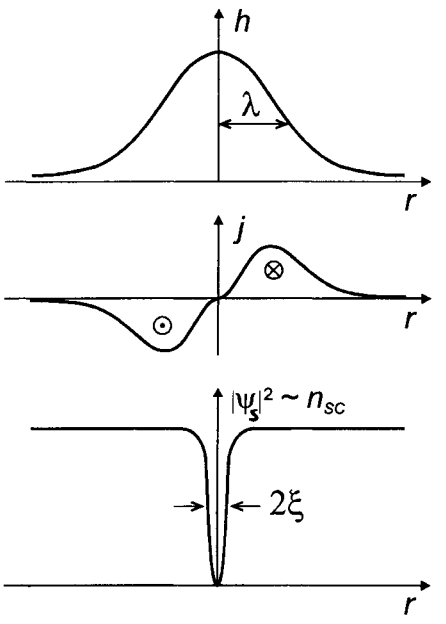


Fig. 9. Structure of a single vortex, showing the radial distribution of the local field $h(r)$, the circulating supercurrents $j(r)$, and the density of superconducting electrons $n_{SC}(r)$.

1.4.2. The London Limit

The local field and current distribution in the mixed state ($H_{c1} < H < H_{c2}$) of a type II superconductor with $\kappa \gg 1$, can be calculated in the framework of the London model [22], which is valid provided that $\kappa \gg 1$ and that the order parameter (Ψ_s or n_{SC}) is nearly constant in space. In the London limit, the free energy per unit length (the line energy) can be expressed as [23]:

$$E_l = \frac{1}{2\mu_0} \int \left(\mathbf{h}^2 + \lambda_L^2 |\nabla \times \mathbf{h}|^2\right) d\mathbf{r} \tag{15}$$

where the first and second terms are the magnetic and the kinetic energy, respectively, λ_L is the London penetration depth, and the integration volume does not include the hard cores of the vortices. Minimization of E_l with respect to the local field $\mathbf{h}$ yields the London equation for the local field distribution outside the vortex core:

$$\mathbf{h} + \lambda_L^2 \nabla \times \nabla \times \mathbf{h} = 0 \tag{16}$$

This equation can also be derived from the GL theory by setting $\nabla \Psi_s(\mathbf{r})$ equal to zero. To include the vortex core, Eq. (16) may be adjusted to

$$\mu_0\left(\mathbf{h} + \lambda_L^2 \nabla \times \nabla \times \mathbf{h}\right) = \Phi_0 \delta_2(\mathbf{r}) \tag{17}$$

where the small core is represented by a two-dimensional delta function and with Φ_0 along the local field direction. By combining this equation with the Maxwell equations, the local field and current distribution of a vortex can be calculated.

1.4.3. Local Field and Current Distribution around a Vortex

The local field is given by [23]:

$$\mu_0 h(r) = \frac{\Phi_0}{2\pi\lambda^2} K_0\left(\frac{r}{\lambda}\right) \tag{18}$$

where K_0 is the zero-order modified Bessel function. The asymptotic expressions are

$$\mu_0 h(r) = \frac{\Phi_0}{2\pi\lambda^2} \ln\left(\frac{\lambda}{r}\right) \tag{19}$$

for $\xi < r \ll \lambda$, and

$$\mu_0 h(r) = \frac{\Phi_0}{2\pi\lambda^2} \sqrt{\frac{\pi\lambda}{2r}} \exp\left(-\frac{r}{\lambda}\right) \tag{20}$$

for $r \gg \lambda$.

From the radial dependence of the local field, the current distribution of a single vortex can be calculated [24]:

$$j(r) = \frac{\Phi_0}{2\pi\mu_0\lambda^2} K_1\left(\frac{r}{\lambda}\right) \tag{21}$$

K_1 is the first-order modified Bessel function for which the asymptotic behavior is used to obtain expressions for the current very close to the normal core and at large distance:

$$j(r) = \frac{\Phi_0}{2\pi\mu_0\lambda^2 r} \tag{22}$$

for $\xi < r \ll \lambda$, and

$$j(r) = \frac{\Phi_0}{2\pi\mu_0\lambda^2} \sqrt{\frac{\pi\lambda}{2r}} \exp\left(-\frac{r}{\lambda}\right) \tag{23}$$

for $r \gg l$.

The line energy is the sum of the field and the kinetic energy of the currents and a small core contribution, and reads [23]:

$$E_l = \frac{1}{4\pi\mu_0}\left(\frac{\Phi_0}{\lambda}\right)^2\left(\ln\left(\frac{\lambda}{\xi}\right)+\epsilon\right) \tag{24}$$

The numerical constant $\epsilon \simeq 0.12$ describes the contribution of the normal core. Because E_l is a quadratic function of the magnetic flux, it is energetically unfavorable in a homogeneous superconductor to form multiquanta vortices, carrying more than one flux quantum. For example, when comparing E_l for a $2\Phi_0$ vortex and two Φ_0 vortices, one gets $(2\Phi_0)^2 > 2\Phi_0^2$, and, therefore, $E_l(2\Phi_0) > 2E_l(\Phi_0)$. In this simple consideration, however, the vortex–vortex interaction has been completely ignored. The line energy becomes definitely larger if one takes the lattice consisting of $2\Phi_0$ vortices instead of single Φ_0 vortices. At the same time, however, the vortex–vortex interaction energy will be reduced if $2\Phi_0$ vortices are formed, because the distance a_v between them increases: $a_v(2\Phi_0) > a_v(\Phi_0)$. Under certain conditions (see [25] and also Section 4), multiquanta vortex lattices have a lower energy than a conventional Φ_0 flux line lattice.

1.4.4. Vortex Lattice

Because of the repulsive electromagnetic interaction between vortices, they tend to occupy positions as far away from each other as possible, resulting in the well-known Abrikosov vortex lattice [20]. The repulsive interaction energy per unit length between two vortices i and j at a mutual distance r_{ij} is given by [23]:

$$U_{ij}(r_{ij}) = \frac{\Phi_0^2}{2\pi\mu_0\lambda^2}K_0\left(\frac{r_{ij}}{\lambda}\right) \tag{25}$$

which decreases exponentially at large distances, $r_{ij} \gg \lambda$, as

$$U_{ij}(r_{ij}) = \frac{\Phi_0^2}{2\pi\mu_0\lambda^2}\sqrt{\frac{\pi\lambda}{2r_{ij}}}\exp\left(-\frac{r_{ij}}{\lambda}\right) \tag{26}$$

and diverges at short distances, $\xi < r_{ij} \ll \lambda$, as

$$U_{ij}(r_{ij}) = \frac{\Phi_0^2}{2\pi\mu_0\lambda^2}\ln\left(\frac{\lambda}{r_{ij}}\right) \tag{27}$$

The repulsive force between two vortices can be calculated from the energy U_{ij}:

$$f_{ij}(r_{ij}) = -\frac{\partial U_{ij}}{\partial r_{ij}} = \frac{\Phi_0^2}{2\pi\mu_0\lambda^3}K_1\left(\frac{r_{ij}}{\lambda}\right) \tag{28}$$

For a given vortex density, the maximum mutual distance between the vortices is obtained for a triangular arrangement, which is the most favorable vortex configuration (Fig. 10a). The density of the vortices n_v increases with increasing field. The distance a_v between nearest-neighbor vortices in the triangular lattice is related to the induction B through the relation:

$$B(\triangle) = \Phi_0 n_v = \frac{2}{\sqrt{3}}\frac{\Phi_0}{a_v^2} \tag{29}$$

The second most favorable configuration, with only a slightly higher energy, is a square vortex lattice (Fig. 10b). The distance between nearest-neighbor vortices in a square lattice depends on the induction B as follows:

$$B(\square) = \Phi_0 n_v = \frac{\Phi_0}{a_v^2} \tag{30}$$

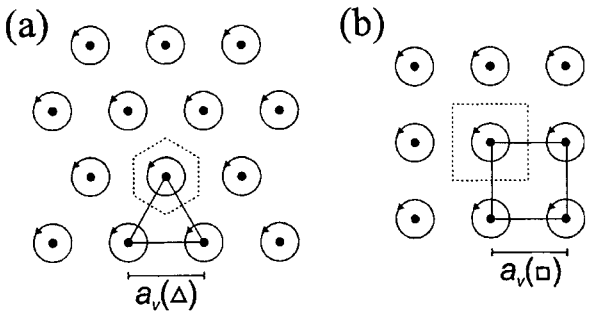


Fig. 10. Schematic diagram of (a) a triangular and (b) a square vortex lattice with period a_V. The dashed lines indicate the unit cell.

1.4.5. Thin Superconducting Film in a Perpendicular Field

In continuous and nonperforated thin films [thickness $\tau \ll \lambda(T)$] and with the field perpendicular to the film plane, the vortex lattice is quasi two dimensional. The small film thickness has important consequences for the vortex structure:

(i) The screening currents are restricted to the thickness τ of the film, resulting in a larger effective penetration depth $\Lambda(T)$ [23]:

$$\Lambda(T) = \frac{\lambda(T)^2}{\tau} \tag{31}$$

(ii) The field around a single vortex in a thin film is less effectively screened at larger distances. The radial distribution of the local field around a vortex is given by

$$\mu_0 h(r) = \frac{\Phi_0}{4\pi\Lambda(T)r} \tag{32}$$

for $\xi < r \ll \Lambda$, and

$$\mu_0 h(r) = \frac{2\Phi_0\Lambda(T)}{\pi r^3} \tag{33}$$

for $r \gg \Lambda$. Instead of an exponential screening at large distances [Eq. (20)], the field only falls off as $1/r^3$ in a thin film.

(iii) The current decreases within Λ as $1/r$, but even at large distances it decays only as $1/r^2$:

$$j(r) = \frac{\Phi_0}{2\pi\Lambda(T)r} \tag{34}$$

for $x < r \ll \Lambda$, and

$$j(r) = \frac{\Phi_0}{\pi r^2} \tag{35}$$

for $r \gg L$.

(iv) The repulsive energy between two vortices decreases as $1/r$, similar to a Coulomb repulsion between two electric charges [23]. This implies that the repulsive interaction between vortices in a thin film is of longer range than in a bulk superconductor.

1.4.6. Flux Pinning

A superconductor can carry a direct current without losses if the current density is smaller than the superconducting critical current density j_c of the material [23]. Reasonable values for the critical current density in an applied field can be obtained if the flux lines are

prevented from moving, because a moving vortex induces an electric field parallel to the current density j and hence dissipates energy. The origin of the flux motion and the associated dissipation is the Lorentz force from the current density j acting on the flux lines, which is per unit length and for one vortex given by

$$\mathbf{f}_L = \mathbf{j} \times \mathbf{\Phi}_0 \tag{36}$$

The Lorentz force tends to move the vortices transverse to the current. To suppress the motion of the vortices, the Lorentz force should be counteracted by a pinning force $\mathbf{f}_P$. The total force acting on a flux line per unit length is the sum of several contributions [26]:

$$\mathbf{f} = \mathbf{f}_L - \mathbf{f}_P - \eta \mathbf{v}_v - \mathbf{f}_M \tag{37}$$

with $\eta \mathbf{v}_v$ a small friction-like contribution proportional to the vortex velocity $\mathbf{v}_v$, and $\mathbf{f}_M$ the Magnus force, which usually is negligible. A general formula for $\mathbf{f}_P$ cannot be given, because it strongly depends on the specific type of pinning center.

The average macroscopic pinning force per unit volume (f_P) is linked to the critical current density by the expression:

$$f_P = j_c B \tag{38}$$

The theoretical upper limit for the critical current is determined by the depairing critical current $I_c^{GL}(T)$ at which the superconducting Cooper pairs are destroyed, and is given by the following expression [27]:

$$I_c^{GL}(T) = \frac{4}{3\sqrt{6}} \frac{H_c(T)}{\lambda(T)} \tag{39}$$

1.4.7. Pinning Mechanisms

A vortex can be trapped or pinned because of the presence of spatial variations in the free energy of the flux line lattice. Almost any kind of defect can create local minima in the free energy landscape (e.g., crystalline imperfections, columnar defects, grain boundaries, thickness variations of a film, etc.). Depending on the interaction between the vortex and the pinning center, a distinction can be made between two contributions to the pinning mechanism: core pinning and electromagnetic pinning [28].

Core pinning is the origin of flux pinning at most point defects, and refers to the local variation of T_c or κ, which reduces the free energy if the vortex core is located at the position of the (normal) defect.

Electromagnetic pinning is due to the kinetic energy of the confined screening currents around the defect and the perturbation of the magnetic field of a vortex. Theoretically, it can be described by assuming an antivortex image, in analogy with electrostatics. Thickness variations of a film can lead to the presence of the admixture of this type of pinning. The vortices are pinned at locations of smallest thickness where their energy is lowest [Eqs. (24) and (31)]. The typical length scale for this kind of pinning is the penetration depth λ. Both the core and the electromagnetic contributions define the pinning, which eventually controls the critical current density j_c.

After a brief introduction into the problem of optimizing the two critical parameters—$T_c(H)$ and $j_c(H)$—we are now ready to formulate the layout of this chapter. We present the systematic analysis of the influence of the confinement geometry on the superconducting phase boundary $T_c(H)$ in a series of nanostructured samples. We start with individual nanostructures of different topologies (lines, loops, dots) (Section 2) and then focus on "intermediate" systems: clusters of loops fabricated in the form of a 1D chain of loops (Section 3.1) or 2D antidot clusters (Section 3.2). Huge arrays of antidots are considered in Section 4 where we deal, first of all, with the $T_c(H)$ boundary for superconducting films with antidot lattices. Having demonstrated the importance of the confinement geometry of the superconducting condensate for the optimization of the critical parameter $T_c(H)$, we

move on, further in Section 4, to flux confinement phenomena in superconductors with an antidot lattice. We discuss the novel flux phases that can be stabilized by introducing regular pinning arrays. We show that lateral nanostructuring can lead to a substantial enhancement of the critical current density $j_c(H)$ (up to the depairing current) and to the appearance of a variety of commensurability effects between the periodic pinning potential and the vortex lattice.

2. INDIVIDUAL NANOSTRUCTURES

To begin this section, we present the experimental results on the $T_c(H)$ phase boundary of *individual superconducting mesoscopic structures of different topology*. It is important to keep other parameters of these structures the same, such as the material from which they are made (Al), the width of the lines ($w = 0.15$ μm), and the film thickness $\tau = 25$ nm, thus directly relating the differences in $T_c(H)$ to *topological effects*. The magnetic field H is always applied perpendicular to the structures.

2.1. Line

In Figure 11a, the phase boundary $T_c(H)$ of a mesoscopic line [29] is shown. The solid line gives the $T_c(H)$ calculated from the well-known formula [30]:

$$T_c(H) = T_{c0}\left[1 - \frac{\pi^2}{3}\left(\frac{w\xi(0)\mu_0 H}{\Phi_0}\right)^2\right] \tag{40}$$

which, in fact, describes the parabolic shape of $T_c(H)$ for a thin film of thickness w in a parallel magnetic field. Because the cross section, exposed to the applied magnetic field, is the same for a film of thickness w in a parallel magnetic field and for a mesoscopic line of width w in a perpendicular field, the same formula can be used for both [29]. Indeed, the solid line in Figure 11a is a parabolic fit of the experimental data with Eq. (40) where $\xi(0) = 110$ nm was obtained as a fitting parameter. The coherence length obtained using this method coincides reasonably well with the dirty limit

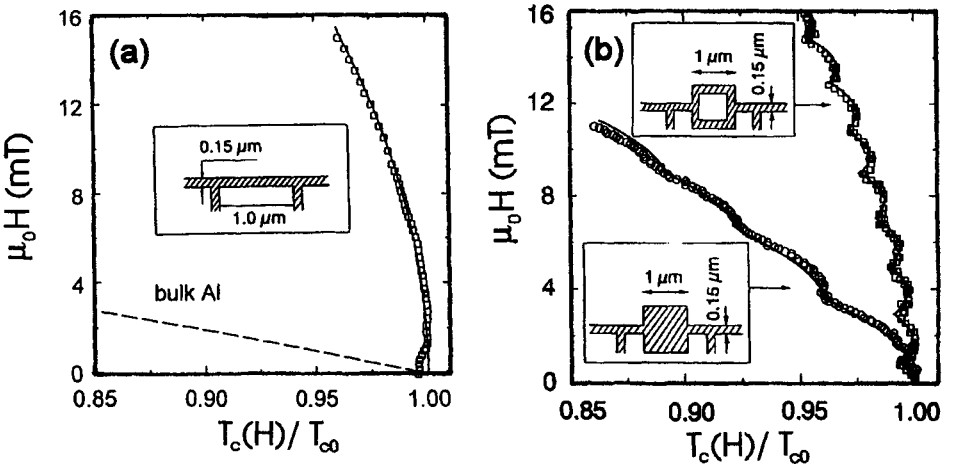


Fig. 11. Measured superconducting/normal phase boundary as a function of the reduced temperature $T_c(H)/T_{c0}$ for (a) the line and (b) the loop and the dot. The solid line in (a) is calculated using Eq. (40) with $\xi(0) = 110$ nm as a fitting parameter. The dashed line represents $T_c(H)$ for bulk Al. Comparing $T_c(H)$ for these three different mesoscopic structures, made of the same material, one clearly sees the effect of topology on $T_c(H)$. (Source: Reprinted with permission from [5]. © 1998 American Institute of Physics.)

value $\xi(0) = 0.85(\xi_0 l)^{1/2} = 132$ nm calculated from the known BCS coherence length $\xi_0 = 1600$ nm for bulk Al [23] and the mean free path $l = 15$ nm, estimated from the normal state resistivity ρ at 4.2 K [31].

Another simple argument can be used as well to explain the parabolic relation $T_c(H) \propto H^2$. The expansion of the energy $E(H)$ in powers of H, as given by the perturbation theory, is [32]:

$$E(H) = E_0 + A_1 L H + A_2 S_e H^2 + \cdots \tag{41}$$

where A_1 and A_2 are constant coefficients, the first term E_0 represents the energy level in zero field, the second term is the linear field splitting with the orbital quantum number L, and the third term is the diamagnetic shift, with S_e the area exposed to the applied magnetic field.

Now, for the topology of the line with a width w much smaller than the Larmor radius $r_H \gg w$, any orbital motion is impossible because of the constraints imposed by the boundaries onto the electrons inside the line. Therefore, in this particular case, $L = 0$ and $E(H) = E_0 + A_2 S_e H^2$, which immediately leads to the parabolic relation $T_c \propto H^2$. This diamagnetic shift of $T_c(H)$ can be understood in terms of a partial screening of the magnetic field H caused by the nonzero width of the line [27].

2.2. Loop

The $T_c(H)$ of the mesoscopic loop [29], shown in Figure 11b, demonstrates very distinct Little–Parks (LP) oscillations [33] superimposed on a monotonic background. A closer investigation leads to the conclusion that this background is very well described by the same parabolic dependence as the one discussed for the mesoscopic line [29] (see the solid line in Fig. 11a). As long as the width of the strips w, forming the loop, is much smaller than the loop size, the total shift of $T_c(H)$ can be written as the sum of an oscillatory part and the monotonic background given by Eq. (40) [29, 34]:

$$T_c(H) = T_{c0}\left[1 - \frac{\pi^2}{3}\left(\frac{w\xi(0)\mu_0 H}{\Phi_0}\right)^2 - \frac{\xi^2(0)}{R^2}\left(n - \frac{\Phi}{\Phi_0}\right)^2\right] \tag{42}$$

where $R^2 = R_1 R_2$ is the product of the inner and outer loop radius, and the magnetic flux threading the loop $\Phi = \pi R^2 \mu_0 H$. The integer n has to be chosen so as to maximize $T_c(H)$ or, in other words, selecting the lowest Landau level $E_{LLL}(H)$.

The LP oscillations originate from the fluxoid quantization requirement, which states that the complex order parameter $\Psi_s = |\Psi_s| \exp(i\varphi)$ should be a single-valued function when integrating along a closed contour

$$\oint \nabla\varphi \cdot dl = n2\pi \qquad n = \ldots, -2, -1, 0, 1, 2, \ldots \tag{43}$$

Fluxoid quantization gives rise to a circulating supercurrent in the loop when $\Phi \neq n\Phi_0$, which is periodic with the applied flux Φ/Φ_0.

Using the sample dimensions and the value for $\xi(0)$ obtained before for the mesoscopic line (with the same width $w = 0.15$ μm), the $T_c(H)$ for the loop can be calculated from Eq. (42) without any free parameter. The solid line in Figure 11b shows indeed good agreement with the experimental data [29]. It is worth noting here that the amplitude of the LP oscillations is about a few millikelvins—in qualitative agreement with the simple estimate given in Table I for $L_A \simeq 1$ μm.

The susceptibility of a single mesoscopic Al ring, showing LP oscillations, has been studied recently by Zhang and Price [35], who found an excellent agreement with the GL theory for the susceptibility below T_c.

The lower critical field of a loop is found from the condition that half a flux quantum is applied, thus giving [36]:

$$\mu_0 H_{c1}^{loop} = \frac{1}{2}\frac{\Phi_0}{\pi R^2} \tag{44}$$

which is totally different from the H_{c1} value of a bulk superconductor [see Eq. (13)].

The superconducting loop (Fig. 11b) nicely demonstrates the classical Little–Parks oscillatory $T_c(H)$ phase boundary [33], related to the quantization of the total flux threading the loop area. Moreover, in this simple homogeneous superconducting loop, the two supercurrents I_1 and I_2 flowing in the different branches of the loop gain *opposite* phases $\pm\pi\Phi/\Phi_0$ from the perpendicular applied field [37, 38]:

$$I_1 \propto \sin\left(\beta - \alpha - \pi\frac{\Phi}{\Phi_0}\right) \tag{45}$$

$$I_2 \propto \sin\left(\beta - \alpha + \pi\frac{\Phi}{\Phi_0}\right) \tag{46}$$

The interference of the currents flowing through the two branches of the loop produces an oscillatory dependence of the total current $I = I_1 + I_2$:

$$I \propto \sin(\beta - \alpha)\cos\left(\pi\frac{\Phi}{\Phi_0}\right) \tag{47}$$

The current amplitude in Eq. (47) is determined by the phase difference $\Delta\varphi = \beta - \alpha$ (as in the first Josephson equation $I \propto \sin\Delta\varphi$) [23, 39]. The critical current I_c for the homogeneous loop is obtained by taking $\sin\Delta\varphi = 1$ in Eq. (47) [37]:

$$I_c \propto \cos\left(\pi\frac{\Phi}{\Phi_0}\right) \tag{48}$$

Equation (48) implies that the critical current of a mesoscopic superconducting loop without artificial Josephson weak links oscillates with the applied magnetic field in the same way as it does in a classical SQUID with extrinsic weak links. The existence of these oscillations, predicted by Fink et al. [37, 38], has been confirmed experimentally by Moshchalkov et al. [40] and is shown in Figure 12.

Another interesting feature of a mesoscopic loop and other mesoscopic structures is the unique possibility they offer for studying nonlocal effects [41]. In fact, a single loop

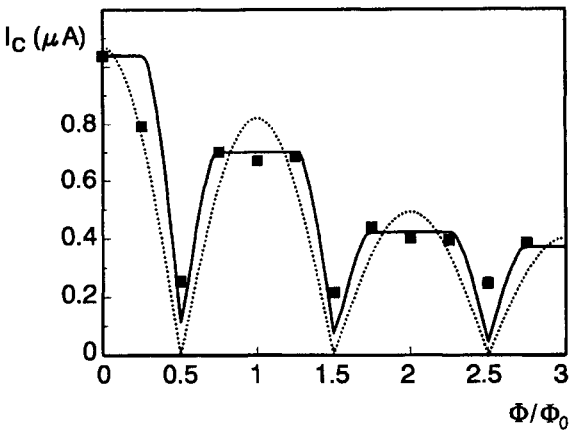


Fig. 12. Oscillations of the critical current I_c of a 1 μm × 1 μm square Al loop as a function of the normalized flux Φ/Φ_0. The solid line corresponds to the calculations based on the theory of Fink et al. [38], while the dashed line is the sinusoidal variation of I_c in a conventional SQUID with two Josephson junctions. (Source: Adapted from [40].)

can be considered as a 2D artificial quantum orbit with a *fixed radius*, in contrast to Bohr's description of flexible atomic orbitals. In the latter, the stable radii are found from the quasiclassical quantization rule, stating that only an integer number of wavelengths can be set along the circumference of the allowed orbits. For a superconducting loop with an arbitrary fixed circumference, however, supercurrents must flow, in order to fulfill the fluxoid quantization requirement [Eq. (43)], thus causing oscillations of the critical temperature T_c versus the magnetic field H.

To measure the resistance of a mesoscopic loop, electrical contacts have, of course, to be attached to it, and, as a consequence, the confinement geometry is changed. *A loop with attached contacts and the same loop without any contacts are, strictly speaking, different mesoscopic systems*. This "disturbing" or "invasive" aspect ("Schrödinger cat") of probing a quantum object can now be exploited for the study of nonlocal effects [41]. Because of the divergence of the coherence length $\xi(T)$ at $T = T_{c0}$ [Eq. (6)], the coupling of the loop with the attached leads is expected to be very strong for $T \to T_{c0}$.

Figure 13 shows the results of these measurements [41]. Both "local" (potential probes across the loop V_1/V_2) and "nonlocal" (potential probes aside of the loop V_1/V_3 or V_2/V_4) LP oscillations are clearly observed. For the "local" probes, there is an unexpected and pronounced increase of the oscillation amplitude with increasing field, in disagreement with previous measurements on Al microcylinders [34]. In contrast to this, for the "nonlocal" LP effect, the oscillations rapidly vanish when the magnetic field is increased.

When increasing the field, the background suppression of T_c [Eq. (40)] results in a decrease of $\xi(T)$. Hence, the change of the oscillation amplitude with H is directly related to the temperature-dependent coherence length. As long as the coherence of the superconducting condensate protuberates over the nonlocal voltage probes, the nonlocal LP oscillations can be observed.

On the other hand, the importance of an "arm" attached to a mesoscopic loop, was already demonstrated theoretically by de Gennes in 1981 [42]. For a perfect 1D loop

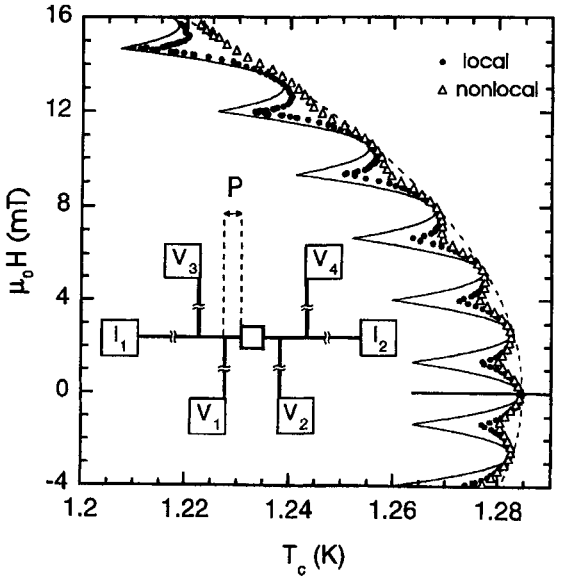


Fig. 13. Local (V_1/V_2) and nonlocal (V_1/V_3 or V_2/V_4) phase boundaries $T_c(H)$. The measuring current is sent through I_1/I_2. The solid and dashed lines correspond to the theoretical $T_c(H)$ of an isolated loop and a one-dimensional line, respectively, both made of strips of width w. The inset shows a schematic of the structure, where the distance $P = 0.4$ μm. (Source: Reprinted with permission from [5]. © 1998 American Institute of Physics.)

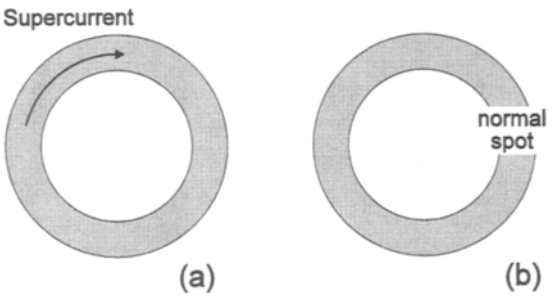


Fig. 14. Schematic view of a mesoscopic loop in (a) the multiply connected state and (b) the singly connected state, where a normal spot is spontaneously created and consequently no supercurrent flows.

(vanishing width of the strips), adding an "arm" will result in a decrease of the LP oscillation amplitude, which was observed indeed at low magnetic fields where $\xi(T)$ is still large. With these experiments, it has been proved that adding probes to a structure considerably changes both the confinement topology and the phase boundary $T_c(H)$.

The effect of topology on $T_c(H)$, related to the presence of the sharp corners in a square loop, has been considered by Fomin et al. [43]. In the vicinity of the corners, the superconducting condensate sustains a higher applied magnetic field because at these locations the superfluid velocity is reduced, in comparison with the ring. Consequently, in a field-cooled experiment, superconductivity will nucleate first around the corners [43]. Eventually, for a square loop, the introduction of a *local* superconducting transition temperature seems to be needed. As a result of the presence of the corner, the $H_{c3}(T)$ of a wedge with an angle θ [44] will be strongly enhanced at the corner.

Another interesting possibility for a superconducting ring has been analyzed [45–49]: Under certain conditions, superconductivity spontaneously breaks at some spot along the perimeter of the ring, so that the *superconducting area changes from multiple to single connectivity*. The physics behind this interesting theoretical prediction is the following. The oscillatory $T_c(\Phi)$ phase boundary is caused by a periodic variation of a circular supercurrent (when the applied flux Φ/Φ_0 is not integer; see Fig. 14a), which is induced in a ring in order to fulfill fluxoid quantization. The highest current [and, therefore, the strongest reduction of $T_c(\Phi)$] is realized for half integer flux when $\Phi/\Phi_0 - n = 1/2$ (see Figs. 11b and 13). In this situation, it may turn out, however, that somewhere in the ring the order parameter Ψ_s is spontaneously suppressed and a sort of "normal core" is created somewhere along the ring circumference (see Fig. 14b). The energy of this normal state core, below the $T_c(\Phi)$ line, is, of course, higher than the energy corresponding to a superconducting state everywhere in the ring, but, at the expense of that, the circular supercurrent is interrupted, thus effectively opening the ring for entrance and removal of flux. While Horane et al. [45] predicted the existence of the singly connected state for rings made of "1D" strips, Berger and Rubinstein [48] showed that the temperature region where the singly connected state exists can be enhanced by proper tuning of the nonuniform "strip width" profiles along the ring.

2.3. Dot

For a cylindrical symmetry, the choice of the coordinates (r, φ, z) and the gauge $\mathbf{A} = (Hr/2)\mathbf{e}_\varphi$, where $\mathbf{e}_\varphi$ is the tangential unit vector, is well suited. The solution of the Hamiltonian [Eq. (3) with the nonlinear term neglected] in cylindrical coordinates has the following form [50]:

$$\Psi_s(r, \varphi) = \exp(\pm i L\varphi) r^L \gamma^{(L+1)/2} \exp\left(-\frac{\gamma r^2}{2}\right) M\left(-N, L+1, \gamma r^2\right) \tag{49}$$

Here $\gamma = e^*\mu_0 H/\hbar$ and the energy $E_\perp$ of the motion in the plane perpendicular to H is determined by the orbital quantum number L and parameter N, *which is not necessarily an integer number*, as we shall see later:

$$E_\perp = \frac{e^*\hbar\mu_0 H}{2m^*}(2N \pm L + L + 1) \tag{50}$$

The function M is the Kummer function defined as

$$M(a, c, y) = 1 + \frac{a}{c}y + \frac{a(a+1)}{c(c+1)}\frac{y^2}{2!} + \frac{a(a+1)(a+2)}{c(c+1)(c+2)}\frac{y^3}{3!} + \cdots \tag{51}$$

where $a = -N$, $c = L + 1$, $y = \gamma r^2$. Introducing the dimensionless radius $R = \sqrt{\gamma r^2} = \Phi/\Phi_0$, the superconducting order parameter can be written in the form

$$\Psi_L(R, \varphi) = \exp(\pm iL\varphi)R^L \exp\left(-\frac{R^2}{2}\right)M\left(-N, L+1, R^2\right) \tag{52}$$

The representation of the order parameter $\Psi_s = \sum_L c_L \Psi_L$ as an expansion over states with different L for infinite samples has been analyzed in [51], where $M(0, L+1, R^2) = 1$ has been taken. Under these conditions, the functions $|\Psi_L|$ have their maxima at $R^2 = L$; that is, the area enclosed by the circle with radius corresponding to the $|\Psi_L|$ maximum is always penetrated by an integer number L of the flux quanta: $\Phi/\Phi_0 = L$. In this chapter, we shall analyze the case of *finite* samples, where the N value has to be found from the boundary condition [Eq. (8)]. It is very important to note that in the general form (Eqs. (49) and (50)) there are no limitations on the parameter N. It is not necessarily an integer number. The only argument, which is usually given in favor of taking integer N, is a possibility to get a cut off in the summation [Eq. (51)]. Indeed, if one inserts an integer N into the summation, then by adding 1 to N in each new term one eventually comes to the situation where $-N + N = 0$ and all subsequent terms in the summation will be equal to zero. Thus, by the cutoff we just use a finite number of terms in the summation [Eq. (51)] and, of course, M is finite in this case. We should keep in mind, however, that any converging, but infinite row also gives a finite solution for M. Therefore, not only positive integers N in Eq. (50), but also noninteger and even negative N values are possible. In finite size samples, the N value, which we further denote as $N(L, R_0)$, has to be found from the boundary condition at $R = R_0$ [Eq. (8)], where R_0 is the normalized disk radius:

$$\left.\frac{\partial|\Psi_s(R)|}{\partial R}\right|_{R=R_0} \tag{53}$$

Because we are looking for the lowest possible energy state, we should take the minus sign in the argument of the exponent $\exp(-iL\varphi)$ in the solution given by Eq. (51). In this case $-L$ and $+L$ in Eq. (50) cancel and for any L the energy levels are given by

$$E_\perp = \hbar\omega\left(N + \frac{1}{2}\right) \tag{54}$$

where $\omega = e^*\mu_0 H/m^*$ is the cyclotron frequency.

This result coincides with the well-known Landau quantization, but now N is *any real number, including negative real number*, which is to be calculated from Eq. (53). Using the expression

$$\frac{dM(a, c, y)}{dy} = \frac{a}{c}M(a+1, c+1, y) \tag{55}$$

for the derivative of the Kummer function, we can find the $N(L, R_0)$ value, which obeys the boundary condition [Eq. (53)], from the equation:

$$\left(L - R_0^2\right)M\left(-N, L+1, R_0^2\right) - \frac{2NR_0^2}{L+1}M\left(-N+1, L+2, R_0^2\right) = 0 \tag{56}$$

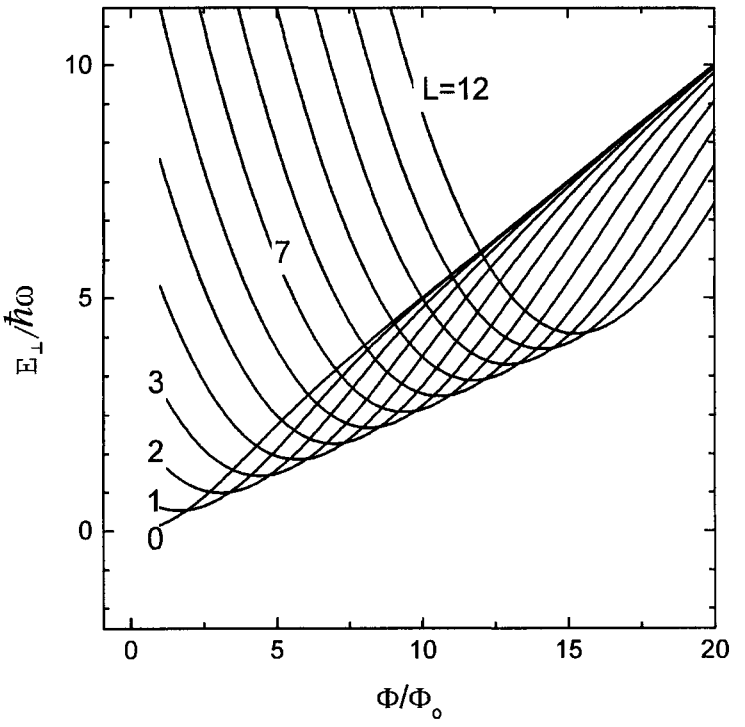


Fig. 15. Energy levels versus normalized flux Φ/Φ_0 for a superconducting cylinder in a parallel magnetic field. The lowest-lying cusplike $H_{c3}(T)$ line is formed because of the change of the orbital quantum number L. (Source: Reprinted with permission from [53]. © 1996 American Physical Society.)

The remarkable thing about the $N(L, R_0)$ values, found from the solutions of Eq. (53), is that they are negative, which immediately gives the energy $E_\perp$ in Eq. (54) lower than $\hbar\omega/2$. *As a result of the confinement with the superconducting boundary conditions, the energy levels in finite samples lie below the classical value $\hbar\omega/2$ for infinite samples* [52]. The whole energy level scheme (Fig. 15), found by Saint-James [52], can be reconstructed by calculating $E_\perp$ versus R_0^2 for different L values. From this diagram, one can easily go to the field versus temperature plot, using the relation $E_\perp = -\alpha$. The corresponding values of the Abrikosov parameter β_A, giving an idea about the flatness of $|\Psi_s|$ [39], are plotted in Figure 16. It should be noted that β_A for certain L and H (see the levels below the dashed line in Fig. 16) is smaller than the well-known minimum possible value $\beta_A = 1.16$ for the triangular Abrikosov vortex lattice.

To conclude this discussion, we note that in finite samples N is a bad quantum number. It is rather a parameter that has to be found from the boundary condition. A good quantum number for the problem is L. By forming a superconducting condensate with a proper finite L and $N(L, R_0) < 0$, we conserve the rotational momentum and, at the same time, reduce the energy below $\hbar\omega/2$ [53].

As shown previously, because of the onset of surface superconductivity at $H_{c3}(T)$, corresponding to negative N in Eq. (54), the superconductivity can appear at magnetic fields well above the $H_{c2}(T)$ line (found for $N = 0$). By changing the variable $E_\perp$ in Figure 15 into T, we obtain the cusplike phase boundary $H_{c3}(T)$ as shown in Figure 17, which is due to switching between different orbital momenta L. The phase boundary of the superconducting disk (Fig. 17) has been observed experimentally by Buisson et al. [52] and by Moshchalkov et al. [29]. It should be emphasized here that the presence of the oscillations in the $H_{c3}(T)$ curve is crucially dependent on the imposed Neumann boundary conditions [36]. Contrary to that, the equivalent eigenvalue spectrum with Dirichlet

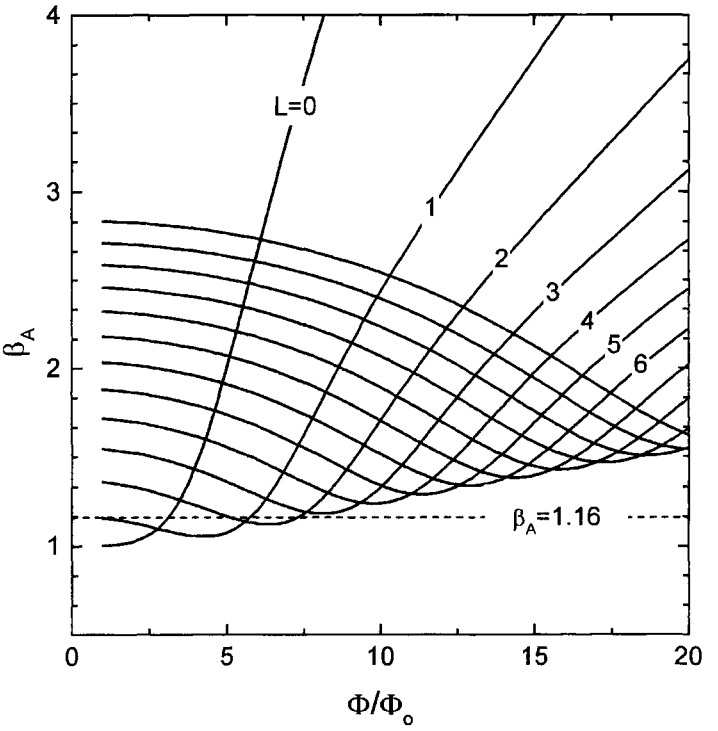


Fig. 16. Field dependence of the Abrikosov parameter β_A for different angular momenta L. (Source: Reprinted with permission from [53]. © 1996 American Physical Society.)

boundary conditions does not show any oscillations, if one follows the lowest Landau level $E_{LLL}(H)$ [54].

The Landau level scheme for a cylindrical dot with "superconducting" boundary conditions [Eq. (8)] is presented in Figure 15. Each level is characterized by a certain orbital quantum number L where $\Psi_s = |\Psi_s| \exp(\mp i L\varphi)$ [53]. The levels, corresponding to the sign "+" in the argument of the exponent are not shown because they are situated at energies higher than the ones with the sign "−." The lowest Landau level in Figure 15 represents, in fact, a cusplike envelope, obtained from the switching between different L values with changing magnetic field. Following our main guideline that $E_{LLL}(H)$ determines $T_c(H)$, for the dot, a cusplike superconducting phase boundary with nearly perfect linear background is expected. The measured phase boundary $T_c(H)$, shown in Figure 11b, can be nicely fitted by the calculated one (Fig. 15), thus proving that $T_c(H)$ of a superconducting dot indeed consists of cusps with different L's [52]. Each fixed L describes a giant vortex state that carries L flux quanta Φ_0. The linear background of the $T_c(H)$ dependence is very close to the third critical field $H_{c3}(T) \simeq 1.69 H_{c2}(T)$, which is obtained in the $L \to \infty$ limit [23, 55]. Contrary to the loop, where the LP oscillations are perfectly periodic, the dot demonstrates a certain aperiodicity [56], in very good agreement with the theoretical calculations [36, 52]. For the flux trapped inside the giant vortex, unusual *paramagnetic Meissner effect* has been predicted by Moshchalkov et al. [53], who found pronounced flux compression effects from the self-consistent solutions of the coupled GL equations (Eqs. (3) and (4)).

The lower critical field of a cylindrical dot H_{c1}^{dot} corresponds to the change of the orbital quantum number from $L = 0$ to $L = 1$, that is, to the penetration of the first flux line [36]:

$$\mu_0 H_{c1}^{dot} = 1.924 \frac{\Phi_0}{\pi R^2} \tag{57}$$

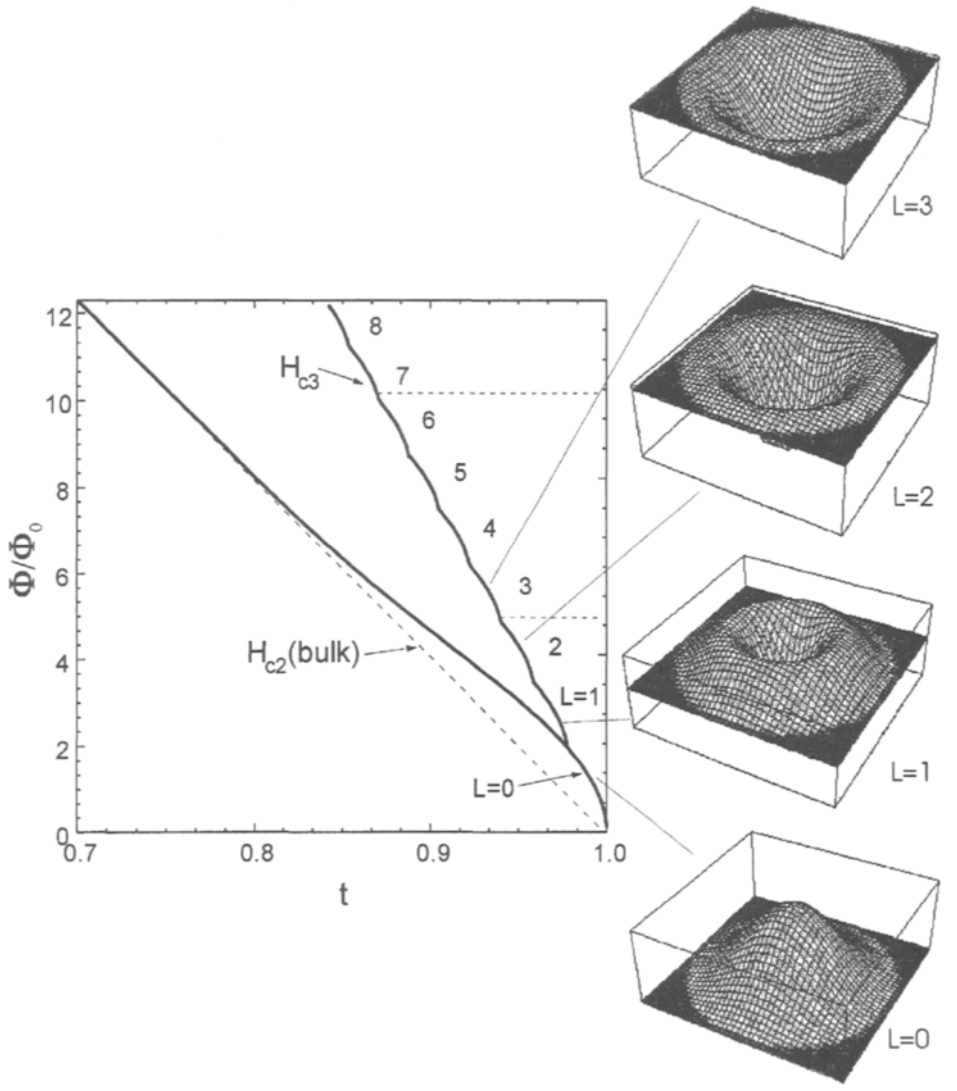


Fig. 17. Third critical field H_{c3} (theory) and the bulk upper critical field H_{c2} (dashed line) versus normalized temperature $t = T/T_{c0}$ for a superconducting disk. The cusplike $H_{c3}(T)$ line is formed because of the change of the orbital quantum number L. In the three-dimensional plots, $|\Psi_s|$ is depicted as a function of the spatial coordinates for several L values. (Source: Reprinted with permission from [53]. © 1996 American Physical Society.)

For the long mesoscopic cylinder described previously, demagnetization effects can be neglected. On the contrary, for a thin superconducting disk, these effects are quite essential [57–59]. For a mesoscopic disk, made of a type I superconductor, the phase transition between the superconducting and the normal state is of second order if the expulsion of the magnetic field from the disk can be neglected, that is, when the disk thickness is comparable with ξ and λ. When the disk thickness is larger than a certain critical value, first-order phase transitions should occur. The latter has been confirmed in ballistic Hall magnetometry experiments on individual Al disks [60–62]. A series of first-order transitions between states with different orbital quantum numbers L have been seen in magnetization curves $M(H)$ [60] in the field range corresponding to the crossover between the Meissner and the normal states. Besides the cusplike $H_{c3}(T)$ line, found earlier in transport measurements [29, 52], transitions between the $L = 2$ and $L = 1$ states have been observed [60]

by probing the superconducting state below the $T_c(H)$ line with Hall micromagnetometry. Still deeper in the superconducting area, the recovery of the normal Φ_0 vortices and the decay of the giant vortex state might be expected [51, 59]. The former has been considered [63] in the London limit, by using the image method. Magnetization and stable vortex configurations have been recently analyzed in mesoscopic disks [57–59].

3. CLUSTERS OF LOOPS AND ANTIDOTS

3.1. One-Dimensional Clusters of Loops

After a description of the confinement effects of several individual superconducting structures (A = line, loop, dot), we are ready to move further on to clusters of elements A (Fig. 3) on our way from "single plaquette" samples to materials nanostructured by introducing huge arrays of plaquettes A. First, we take A = loop and consider one-dimensional multiloop structures: "bola," double-, and triple-loop Al structures. Figure 18 shows an atomic force microscopy (AFM) image of the structures. For these geometries, some interesting theoretical predictions have been made, for which no experimental verification has been carried out up to now (see more [64]). The loops in all three structures have the same dimensions, thus leading to the same magnetic field period $\mu_0 \Delta H = 1.24$ mT. The strips forming the structures are 0.13 μm wide and the film thickness $\tau = 34$ nm. In all the experimental data shown here, the parabolic background [Eq. (40)] is already subtracted in order to allow a direct comparison with the theory. In the temperature interval where the $T_c(H)$ boundary was measured, the coherence length $\xi(T)$ is considerably larger than the width w of the strips. This makes it possible to use the one-dimensional models for the calculation of $E_{LLL}(H)$ and thus $T_c(H)$. The basic idea is to consider $|\Psi_s|$ = constant across the strips forming the network and to allow a variation of $|\Psi_s|$ only along the strips. In the simplest approach, $|\Psi_s|$ is assumed to be spatially constant (London limit) [65, 66], in contrast to the de Gennes–Alexander (dGA) approach [37, 42, 67], where $|\Psi_s|$ is allowed to vary along the strips. In the latter approach, one imposes

$$\sum_n \left(i \frac{\partial}{\partial x} + \frac{2\pi}{\Phi_0} A_{\parallel}(x) \right) \Psi_s(x) = 0 \tag{58}$$

at the points where the current paths join. The summation is taken over all strips connected to the junction point. Here, x is the coordinate defining the position on the strips, and $A_{\parallel}$ is the component of the vector potential along x. Equation (58) is often called the generalized first Kirchhoff law, ensuring current conservation [37]. The second Kirchhoff law for voltages in normal circuits is now replaced by the fluxoid quantization requirement [Eq. (43)], which should be fulfilled for each closed contour in the superconducting network (around each loop).

In Figures 19 to 21, the $T_c(H)$ boundaries of the three structures are shown. The dashed lines are the phase boundaries calculated in the London limit, while the solid lines give

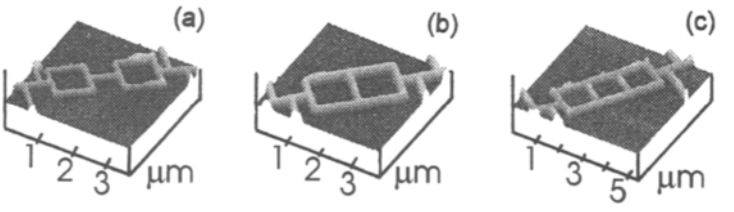


Fig. 18. AFM micrographs of the studied structures: (a) the bola, (b) the double loop, and (c) the triple loop. (Source: Adapted from [64].)

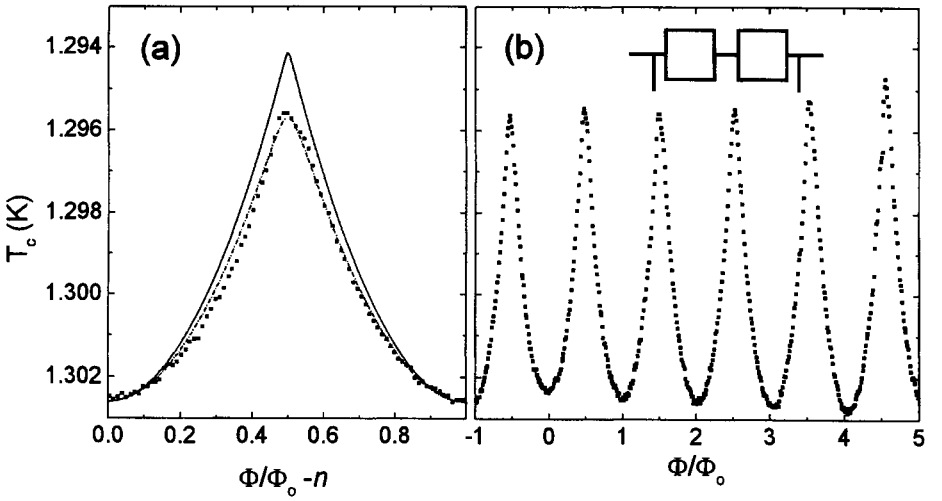


Fig. 19. Experimental $T_c(\Phi)$ data for the bola with the parabolic background [Eq. (40)] subtracted. The dots are the experimental data points, while the lines correspond to the different theoretical results as explained in the text. (a) Single period of $T_c(\Phi)$ and (b) a few periods of the experimental $T_c(\Phi)$ curve. (Source: Reprinted with permission from [5]. © 1998 American Institute of Physics.)

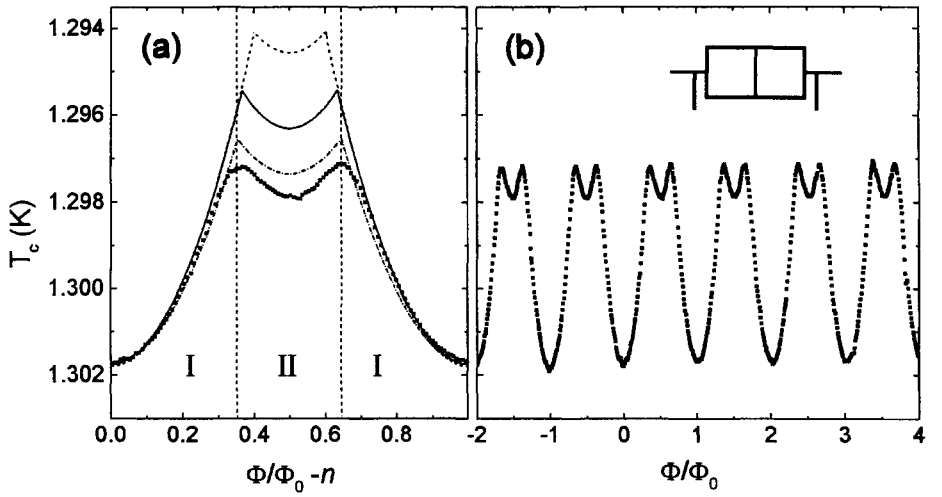


Fig. 20. Experimental $T_c(\Phi)$ data for the double loop with the parabolic background [Eq. (40)] subtracted. The dots are the experimental data points, while the lines correspond to the different theoretical results as explained in the text. (a) Single period of $T_c(\Phi)$ and (b) a few periods of the experimental $T_c(\Phi)$ curve. (Source: Reprinted with permission from [5]. © 1998 American Institute of Physics.)

the results from the dGA approach. As we discussed in Section 2.2 for a mesoscopic loop, attaching contacts modifies the confinement topology, so that the amplitude of the local LP oscillations is reduced at low magnetic fields. Here also the leads decrease the amplitude of the oscillations. The dash-dotted lines in Figures 19 to 21 give the results of the dGA calculation where the presence of the leads has been included. The values for $\xi(0)$ obtained from the fits agree within a few percent with the $\xi(0)$ values found independently from the monotonic background of $T_c(\Phi)$ [see Eq. (40)].

First, in Figure 19, we consider the mesoscopic "bola"—two loops connected by a wire. Fink et al. [37] showed that, in the complete magnetic flux interval, the spatially symmetric

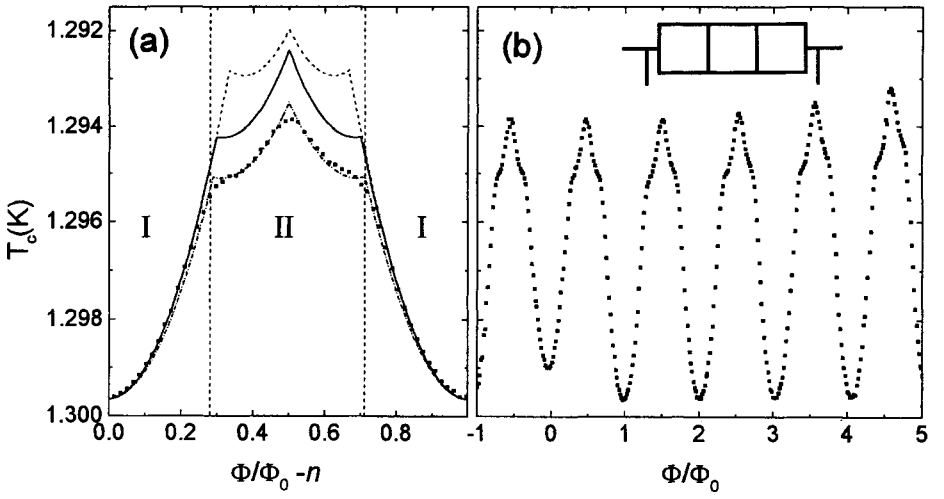


Fig. 21. Experimental $T_c(\Phi)$ data for the triple loop with the parabolic background [Eq. (40)] subtracted. The dots are the experimental data points, while the lines correspond to the different theoretical results as explained in the text. (a) Single period of $T_c(\Phi)$ and (b) a few periods of the experimental $T_c(\Phi)$ curve. (Source: Reprinted with permission from [5]. © 1998 American Institute of Physics.)

solution, with equal orientation of the supercurrents in both loops, has a lower energy than the antisymmetric solution. Coming back to the similarity between a mesoscopic loop and a hydrogen atom, which we discussed in Section 2.2, we can then compare the bola with a H_2 molecule, where the symmetric and the antisymmetric solutions correspond to singlet and triplet states, respectively. In fact, $T_c(\Phi)$ of the bola is the same as for a single loop provided that the length of the strip connecting the two loops is short, as confirmed by the LP oscillations observed in the experimental $T_c(\Phi)$ (Fig. 19).

In what follows, we will focus on the results obtained by Bruyndoncx et al. [64] on the phase boundaries of the double (Fig. 20) and the triple loop (Fig. 21). To facilitate the discussion, we divide the flux period in two intervals: flux regime I for $\Phi/\Phi_0 < g$ or $\Phi/\Phi_0 > (1-g)$ and flux regime II for $g < \Phi/\Phi_0 < (1-g)$. In flux regime I, the phase boundaries, predicted by the different models, are nearly identical. Near $\Phi/\Phi_0 = 1/2$ (flux regime II), however, clear differences are found between the dGA approach and the London limit. The dGA result fits better the experimental data with respect to the crossover point g between regimes I and II and the amplitude of the T_c oscillations. Using the dGA approach, the spatial modulation of $|\Psi_s|$ and the supercurrents for different values at the $T_c(\Phi)$ boundary has been calculated. In flux regime I, $|\Psi_s|$ varies only slightly and, therefore, the results of the London limit and the dGA models nearly coincide. The elementary loops have an equal fluxoid quantum number (and, consequently, an equal supercurrent orientation) for both the double- and the triple-loop geometry. For the double loop, this leads to a cancellation of the supercurrent in the middle strip, while for the triple loop the fluxoid quantization condition [Eq. (43)] results in a different value for the supercurrent in the inner and the outer loops. As a result, the common strips of the triple-loop structure carry a finite current.

In flux regime II, qualitatively different states are obtained from the London limit and the dGA approach. The states calculated within the dGA approach have strongly modulated $|\Psi_s|$ along the strips. This is most severe for the double loop: Ψ_s shows a node ($|\Psi_s| = 0$) in the center of the common strip, the phase φ having a discontinuity of π at this point. This node is a one-dimensional analog of the core of an Abrikosov vortex, where the order parameter also vanishes and the phase shows a discontinuity. In Figure 22, the spatial variation of $|\Psi_s|$ along the strips is shown for $\Phi/\Phi_0 = 0.36$ close to the crossover

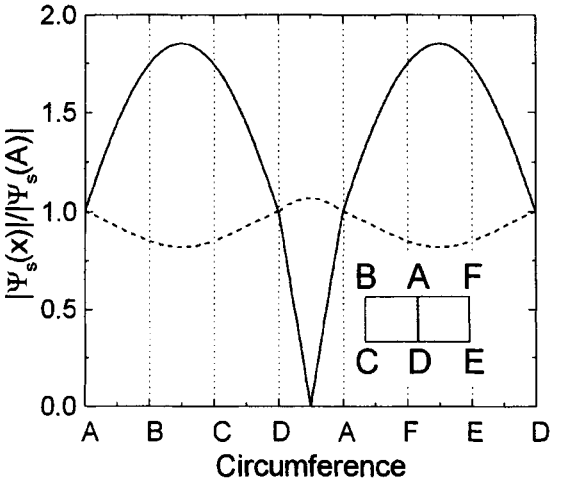


Fig. 22. Calculated variation of $|\Psi_s|$ along the circumference of the double loop, at the phase boundary ($\Phi/\Phi_0 = 0.36$). The dashed line is the solution with $|\Psi_s|$ nearly spatially constant, while the solid line is the state with a node in the center of the strip connecting points A and D. (Source: Reprinted with permission from [5]. © 1998 American Institute of Physics.)

point g. The dashed curve gives $|\Psi_s|$ in flux regime I, which is quasi-constant. The strongly modulated solution, which goes through zero in the center, is indicated by the solid line. Although there exists a finite phase difference across the junction points of the middle strip, no supercurrent can flow through the strip because of the presence of the node. This node is predicted to persist when moving below the phase boundary into the superconducting state [68, 69]. Already, in 1964, Parks [70] anticipated that, in a double loop, "a part of the middle link will revert to the normal phase," and that "this in effect will convert the double loop to a single loop," giving an intuitive explanation for the maximum in $T_c(\Phi)$ at $\Phi/\Phi_0 = 1/2$. Such a modulation of $|\Psi_s|$ is obviously excluded in the London limit, where the loop currents have an opposite orientation and add up in the central strip, thus giving rise to a rather high kinetic energy. An extra argument in favor of the presence of the node is given by the much better agreement for the crossover point g when the presence of the leads is taken into account in the calculations (see dash-dotted line in Fig. 20).

For the triple loop (Fig. 21a), the modulation of $|\Psi_s|$ is still considerable in flux regime II, but it does not show any nodes. Therefore, the supercurrent orientations can be found from the fluxoid quantum numbers $\{n_i\}$, obtained from integrating the phase gradients along each individual loop. When passing through the crossover point between flux regime I and regime II only the supercurrent in the middle loop is reversed, while increasing the flux above $\Phi/\Phi_0 = 1/2$ implies a reversal of the supercurrent in all loops.

Surprisingly, the behavior of a microladder with a linear arrangement of m loops appears to be *qualitatively different for even and for odd m* in the sense that m determines the presence or absence of nodes in the common strips. For an infinitely long microladder, $|\Psi_s|$ was found to be spatially constant below a certain $\Phi < \Phi_c$ [71], which is analogous to the states in flux regime I. For fluxes $\Phi > \Phi_c$, modulated $|\Psi_s|$ states, with an incommensurate fluxoid pattern, were found. At $\Phi/\Phi_0 = 1/2$, nodes appear at the center of every second common (transverse) branch.

A variety of other structures (micronets, coupled rings, bolas, a yin-yang, infinite microladders, bridge circuits, such as a Wheatstone bridge, wires with dangling branches, etc.) formed by 1D wires have been analyzed in a series of publications [37, 42, 68, 69, 71–81] using the approach initiated in 1981 by de Gennes [42] and further developed by Alexander [67] and Fink et al. [37]. For all these structures, very pronounced effects of topology on $T_c(\Phi)$ and critical current have been predicted.

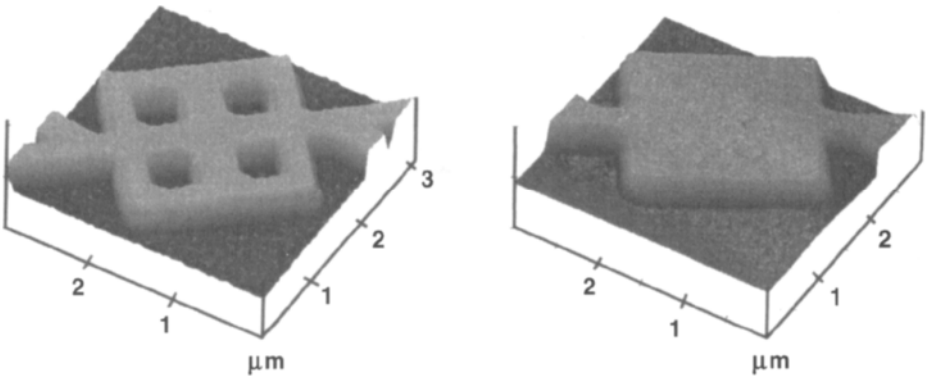


Fig. 23. AFM image of the Pb/Cu 2×2 antidot cluster (on the left) and the reference sample (on the right). (Source: Adapted from [82].)

3.2. Two-Dimensional Clusters of Antidots

As a 2D intermediate structure between individual elements A and their huge arrays (Fig. 3), we shall consider the superconducting microsquare with a 2×2 antidot cluster [82, 83]. In this case, the symbol A from Figure 2 indicates an "antidot." This microsquare with the 2×2 antidot cluster consists of a 2×2 μm^2 superconducting square with four antidots (i.e., square holes of 0.53×0.53 μm^2). A Pb/Cu bilayer with 50 nm of Pb and 17 nm of Cu was used as the superconducting film for the fabrication of this structure [83]. The thin Cu layer was deposited on the Pb to protect it from oxidation and to provide a good contact layer for wire bonding to the experimental apparatus. An AFM image of the Pb/Cu 2×2 antidot cluster is shown in Figure 23 together with a reference sample (i.e., a Pb/Cu microsquare of 2×2 μm^2 without antidots). The Pb(50 nm)/Cu(50 nm) bilayer behaves as a type II superconductor with a $T_{c0} = 6.05$ K, a coherence length, $\xi(0) \approx 35$ nm, and a dirty limit penetration depth, $\lambda(0) \approx 76$ nm. The $T_c(H)$ measurements on the reference sample [82] revealed characteristic features originating from the confinement of the superconducting condensate by the dot geometry (see Section 2.3). The additional features observed in the $T_c(H)$ phase boundary of the antidot cluster can, therefore, be attributed to the presence of the antidots.

The experimental $T_c(H)$ phase boundary is shown in Figure 24. It was measured by keeping the sample resistance at 10% of its normal state value and varying the magnetic field and temperature [82]. Strong oscillations are observed with a periodicity of 2.6 mT and, in each of these periods, smaller dips appear at approximately 0.75 mT, 1.3 mT, and 1.8 mT. The parabolic background superimposed on $T_c(H)$ can again be described by Eq. (40).

Defining a flux quantum per antidot as $\Phi_0 = h/2e = BS$, where $B = \mu_0 H$ and S is an effective area per antidot cell ($S = 0.8$ μm^2), the minima observed in the magnetoresistance and the $T_c(H)$ phase boundary at integer multiples of 2.6 mT can be correlated with a magnetic flux quantum per antidot cell, $\Phi = n\Phi_0$. Those observed at 0.75 mT, 1.3 mT, and 1.8 mT correspond to the values $\Phi/\Phi_0 = 0.3$, 0.5, and 0.7.

The solutions obtained from the London model define a phase boundary that is periodic in Φ with a periodicity of Φ_0. Within each parabola $\Delta T_c = \gamma(\Phi/\Phi_0)^2$, where the coefficient γ characterizes the effective flux penetration through the unit cell. The γ value is determined by the combination of λ and the effective size of the current loops. In Figure 25, the first period of this phase boundary, $\Delta T_c(\Phi) = T_{c0} - T_c(\Phi)$ versus Φ/Φ_0, is shown. There are six parabolic solutions given by a different set of flux quantum numbers $\{n_i\}$, each one defining a specific vortex configuration. In Figure 25a, this is indicated by the numbers shown inside the schematic drawings of the antidot cluster. Note that some vortex configurations are degenerate.

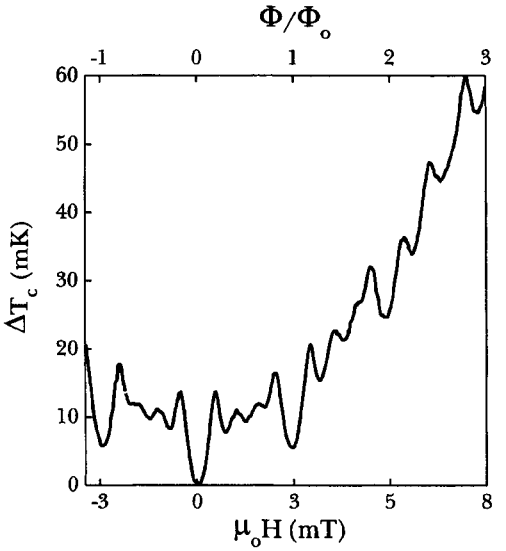


Fig. 24. Experimental phase boundary, $\Delta T_c(H)$, for the Pb/Cu 2×2 antidot cluster. (Source: Adapted from [82].)

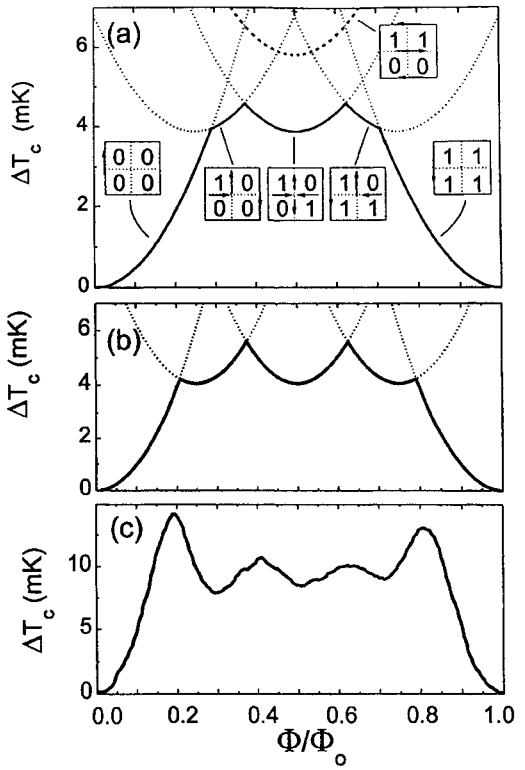


Fig. 25. (a) Theoretical phase boundary, $T_c(\Phi/\Phi_0)$, calculated in the London limit of the Ginzburg–Landau theory without any fitting parameter (solid line). All possible parabolic solutions are represented by dotted lines. The dashed line indicates the nonstable *parallel* configuration. The schematic representation of the $\{n_i\}$ quantum numbers at the antidots and characteristic current flow patterns for each parabolic branch are also sketched. (b) The $T_c(\Phi/\Phi_0)$ phase boundary, calculated as in (a), but with the curvature "γ" of the parabolas taken as a free parameter. The γ value was increased by a factor of 2 with respect to its calculated value used in (a). (c) First period of the measured phase boundary shown in Figure 24 after subtraction of the parabolic background. (Source: Adapted from [82].)

From all these possible solutions, for each particular value of Φ/Φ_0, only the branch with a minimum value of $\Delta T_c(\Phi)$ is stable (indicated with a solid line in Fig. 25a). For the phase boundary, calculated within the 1D model of four equivalent and properly attached squares, no fitting parameters were used because the variation of $T_c(\Phi)$ was calculated from the known values for ξ and the size. One period of the phase boundary of the antidot cluster is composed of five branches and in each branch a different stable vortex configuration is permitted. For the middle branch ($0.37 < \Phi/\Phi_0 < 0.63$), the stable configuration is the *diagonal* vortex configuration (antidots with equal n_i at the diagonals) instead of the *parallel* state (dashed line in Fig. 25a).

The net supercurrent density distribution circulating in the antidot cluster for different values of Φ/Φ_0 has been determined using the same approach. Circular currents flow around each antidot. For the states $n_i = 0$ and $n_i = 1$, currents flow in the opposite direction, because currents corresponding to $n_i = 0$ must screen the flux to fulfill the fluxoid quantization condition [Eq. (43)], whereas for $n_i = 1$ they have to generate flux. At low values of Φ/Φ_0, currents are canceled in the internal strips and screening currents only flow around the cluster. When the field range corresponding to the second branch of the phase boundary is entered, a vortex ($n_i = 1$) is pinned around one antidot of the cluster (see Fig. 25a). At the third branch, the second vortex enters the structure and is localized in the diagonal. In the fourth branch of the phase boundary, the third vortex is pinned in the antidot cluster. And, finally, the current distribution for the fifth branch is similar to that of the first branch although currents flow in opposite direction [83].

Figure 25c shows the first period of the measured phase boundary $T_c(\Phi)$ after subtraction of the parabolic background. The first period of the experimental phase boundary is composed of five parabolic branches with minima at $\Phi/\Phi_0 = 0, 0.3, 0.5, 0.7, 1$. If we compare it with the theoretical prediction given in Figure 25a, the overall shape can be reproduced although the experimental plot has two major peaks at $\Phi/\Phi_0 = 0.2$ and 0.8, whereas the theoretical curve only predicts cusps around these positions.

The agreement between the measured and the calculated $T_c(\Phi)$ is improved if we assume that the coefficient γ can be considered as a fitting parameter. This seems to be feasible if we take into account the simplicity and limitation of the used 1D model. Owing to the relatively large width of the strips forming the 2×2 cluster, the sizes of the current loops can change because they are "soft" in this case and not defined very precisely.

As a result, the coefficient γ cannot be treated as a known constant. If we use it as a free parameter (Fig. 25b), then the curvature of all parabolas forming $T_c(H)$ can be changed and the calculated $T_c(H)$ curve becomes closer to the experimental one though the amplitude of the maxima at $\Phi/\Phi_0 = 0.2$ and 0.8 is still lower than in the experiment (Fig. 25c). The discrepancy in the amplitude of the maxima at $\Phi/\Phi_0 = 0.2$ and 0.8 could also be related to the pinning of vortices by the antidot cluster when potential barriers between different vortex configurations may appear. At the same time, the achieved agreement between the positions of the measured and calculated minima of the $T_c(H)$ curves confirms that the observed effects are due to fluxoid quantization and the formation of certain stable vortex configurations at the antidots [82, 83].

An extrapolation of the results obtained from small to larger 2D antidot clusters (3×3, 4×4, etc.) gives an idea about possible vortex configurations, which can be expected in superconductors with huge regular arrays of antidots (antidot lattices) (see Fig. 27).

4. HUGE ARRAYS OF NANOSCOPIC PLAQUETTES IN LATERALLY NANOSTRUCTURED SUPERCONDUCTORS

The periodic repetition of a certain nanoscopic plaquette A over a macroscopic area makes it possible to implement the idea of an artificial lateral modulation in nanostructured superconductors. Several different types of elementary cells A have been used for that: antidots

[1–3, 56, 84–87] (complete microholes in a film), blind holes [4, 88] (no perforation but a thickness modulation at the sites of the blind holes), magnetic [89, 90], normal metallic [89], or insulating dots [89] covered by (or grown on top of) a superconducting film. These huge regular arrays of nanoscopic plaquettes can be used for systematic studies of the confinement and quantization phenomena in the presence of a 2D artificial periodic pinning potential. We begin in this section with the effect of lateral nanostructuring on the $T_c(H)$ phase boundary and then move on to the pinning phenomena, focusing on commensurability effects between the flux line lattice and a periodic pinning array in superconductors with an antidot lattice.

4.1. The $T_c(H)$ Phase Boundary of Superconducting Films with an Antidot Lattice

Superconducting films with a regular array of antidots are convenient models to study the effects of the confinement topology on the $T_c(H)$ phase boundary in two different regimes [88]:

(i) The first or "collective" regime corresponds to the situation where all elements A, forming an array, are coupled. From the experimental $T_c(H)$ data on antidot clusters, we expect for films with an antidot lattice higher critical fields at $\Phi = n\Phi_0$, which is in agreement with the appearance of the $T_c(H)$ cusps at $\Phi = n\Phi_0$ in superconducting networks [91]. Here, the flux Φ is calculated per unit cell of the antidot lattice.

(ii) On the other hand, by applying sufficiently high magnetic fields, the individual circular currents flowing around antidots can be decoupled and the crossover to a "single object" behavior could be observed. In this case, the relevant area for the flux is the area of the antidot itself and we deal with surface superconductivity around an antidot.

Figure 26 shows the critical field for a Pb(50 nm) sample with a square antidot lattice (period $d = 1$ μm and the antidot radius $r_a = 0.24$ μm). The $T_c(H)$ boundary is

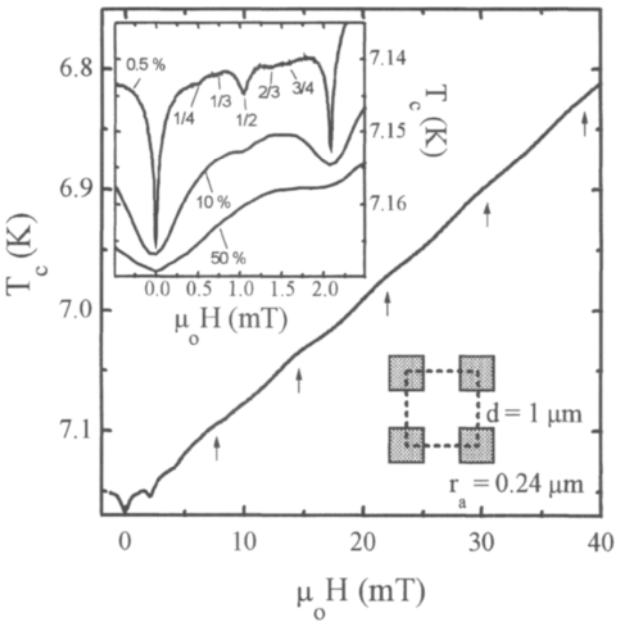


Fig. 26. Critical field of a superconducting Pb(50 nm) film measured at 10% R_n (R_n is the normal state resistance just above T_c), with $d = 1$ μm, $r_a = 0.24$ μm. The inset shows a zoom of the $T_c(H)$ data determined using different criteria 50% R_n, 10% R_n, and 0.5% R_n. (Source: Adapted from [84].)

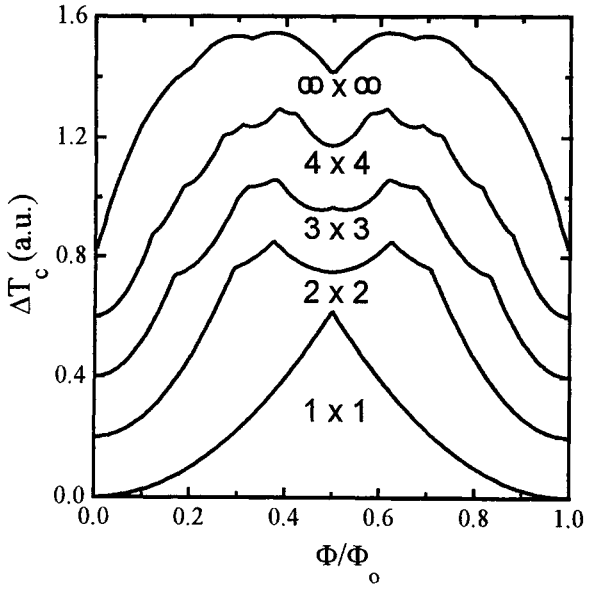


Fig. 27. Calculations of the first $T_c(H)$ period for an $N \times N$ antidot system ($N = 1, 2, 3, 4, \infty$) in the London limit. The minima at integer Φ/Φ_0 for a single loop ($N = 1$) are transformed to sharp cusps as $N \to \infty$. (Source: Adapted from [93].)

determined at 10% of the normal state resistance, R_n. In this graph, two distinct periodicities are present:

(i) Below approximately 8 mT, cusps are found with a period of 2.07 mT, corresponding to one flux quantum per lattice cell. These cusps or "collective" oscillations [88] are reminiscent of superconducting wire networks [91] and arise from the phase correlations between the different loops that constitute the network. These cusps are obtained by narrowing the minima at $n\Phi_0$ with increasing size N of the $N \times N$ antidot cluster (see the sharpening of the minima at $\Phi = 0, \Phi_0$ in Fig. 27; note that the phase boundary in the $N \to \infty$ case has a similar shape as the lowest energy level of the Hofstadter butterfly [19, 92]). An important observation is that the amplitude of these "collective" oscillations depends on the choice of the resistive criterion. This is similar to the case of Josephson junction arrays and weakly coupled wire networks [94] where phase fluctuations dominate the resistive behavior. The inset of Figure 26 shows the first collective period, measured using three different criteria. As the criterion is lowered, the cusps become sharper and the amplitude increases well above the prediction based on the mean field theory for strongly coupled wire networks [91]. At the same time, cusps appear at rational fields $\Phi/\Phi_0 = 1/4, 1/3, 1/2, 2/3$, and $3/4$ arising from the commensurability of the vortex structure with the underlying lattice.

(ii) Above approximately 8 mT, the collective oscillations die out and "single object" cusps appear, having a periodicity that roughly corresponds to one flux quantum Φ_0 per antidot area πr_a^2. These cusps are due to the transition between localized superconducting edge states [88] having a different angular momentum L. These states are formed around the antidots and are, just as the dot in Section 2.3, described by an orbital momentum quantum number L.

Figure 28 shows the same critical field as presented in Figure 26, but normalized by the upper critical field H_{c2} of a plain film without antidots, $\mu_0 H_{c2} = \Phi_0/2\pi\xi^2(T)$ [$\xi(0) =$ 36 nm]. The dashed line is the calculation of the reduced critical field for a plain film with a single circular antidot with radius $r_a = 0.24$ μm. The positions of the cusps correspond reasonably well to the experimental ones, taking into account that the model only considers

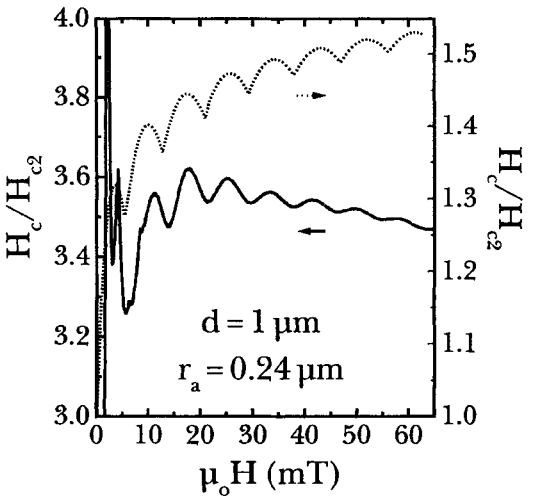


Fig. 28. The critical field of Figure 26 normalized by $\Phi_0/2\pi\xi^2(T)$ versus the applied field. The dashed line (right axis) shows the theoretical result [88] for a single circular hole with a radius $r_a = 0.24$ μm.

a single hole. From this comparison, an effective area $\pi r_a^2 = 0.18$ μm^2 is determined which is close to the experimental value 0.16 μm^2.

From Figures 26 and 28, it is possible to show that the transition from the network regime to the "single object" regime takes place at a temperature T^* approximately given by the relation $w \approx 1.6\xi(T^*)$ (where w is the width of the superconducting region between two adjacent antidots) [93].

Experiments on systems with other antidot sizes demonstrate that $w = d - r_a$ ratio determines the relative importance of the "collective regime" and changes the crossover temperature T^*. The relation $w \approx 1.6\xi(T^*)$, seems to hold reasonably well and is similar to the transition from bulk nucleation of superconductivity to surface nucleation in a thin superconducting slab parallel to the magnetic field [55], which happens at a temperature T_{cr} satisfying $w = 1.8\xi(T_{cr})$.

Comparing the bulk $H_{c2}(T)$ curve with the $T_c(H)$ boundary for films with an antidot lattice, we clearly see a qualitative difference between the two, caused by the lateral nanostructuring. For a superconducting network, $T_c(H)$ can be related to the lowest E_{LLL} level in the Hofstadter butterfly [19, 92] with pronounced cusps at $n\Phi_0$ and a substructure within each period. In the case of an antidot lattice, the size of the antidots is substantially smaller compared to a network. Here as well, $T_c(H)$ is substantially modified, but the cusps at $n\Phi_0$ are still clearly seen [84]. Note also (Fig. 28) that in films with an antidot lattice the ratio H_{c3}/H_{c2} is enhanced up to 3.4–3.6, which is substantially higher than the classical value $H_{c3}/H_{c2} = 1.695$ [23].

4.2. Pinning in Laterally Nanostructured Superconductors

Considering in the previous sections the effect of lateral nanostructuring on $T_c(H)$, we have demonstrated that this important superconducting critical parameter can be tailored by designing a proper topology to confine the superconducting condensate. This concept has been verified on individual nanostructures, clusters containing a small number of nanoplaquettes, and finally their huge arrays in laterally nanostructured superconductors. Systematic studies of the $T_c(H)$ phase boundaries for superconducting structures of the same material but with different confinement topologies have convincingly demonstrated that $T_c(H)$ is determined not only by the choice of a particular superconducting material, but is also very strongly influenced by varying the applied boundary conditions. Therefore, in

nanostructured superconductors, the upper (H_{c2}) and lower (H_{c1}) critical fields are not at all good critical parameters to characterize the material, because through nanostructuring (taking, e.g., superconductors with an antidot lattice) we can strongly increase $H_{c2}(T)$ and simultaneously decrease $H_{c1}(T)$ while keeping the thermodynamical critical field $H_c(T)$ almost constant. *As a result, it does not make any sense to define specific values of $H_{c2}(T)$ and $H_{c1}(T)$ for each given superconductor when it is further used for artificial nanostructuring. Instead, these two critical parameters can intentionally be designed by changing the confinement potential through nanostructuring of the same chosen superconducting material.* The suppression of the superconducting state is induced by an applied field (see the H–T plane in Fig. 7) as well as by the field generated by the currents running through a superconductor. When the generated field reaches the H_{c2} value, superconductivity is destroyed. This gives the maximum possible current, the depairing current [Eq. (39)].

In type II superconductors, which are most interesting for practical applications, the problem of increasing I_c up to its theoretical limit I_c^{GL} is closely related to the optimization of the pinning of flux lines (FLs). In this section, we shall focus on the advantages offered for the solution of this problem by lateral nanostructuring.

4.2.1. Pinning by an Antidot or a Columnar Defect

It has been shown experimentally and theoretically that a small hole (antidot) acts as a very efficient pinning center for flux lines. The pinning force of a single hole has been calculated by Mkrtchyan and Schmidt [95] in the London approximation (high κ). Buzdin and Feinberg [96] have obtained similar results for a nonsuperconducting columnar defect, by calculating the electromagnetic pinning interactions using a vortex–antivortex image method. An important conclusion of both studies is that, depending on the radius r_a of the defect, more than one flux line can be trapped, up to a certain saturation number, n_s, given by

$$n_s \simeq \frac{r_a}{2\xi(T)} \tag{59}$$

The radial distribution of the free energy F of a vortex around the cylindrical defect with $n_s > 1$ is schematically shown for different values of the number of pinned vortices n in Figure 29. If no vortices are pinned ($n = 0$), the force on a vortex (the gradient of the energy) from an "empty" defect is attractive at all distances. As soon as a vortex is trapped ($n = 1$), a potential barrier develops near the edge of the defect, which grows as the number n of trapped vortices increases. If n reaches the saturation number n_s, the maximum of the potential barrier reaches the edge of the defect and the force on additional vortices becomes repulsive at all distances. We should add that, in case the defect is a hole, there exists a Bean–Livingstone barrier [97] at the hole edge even if no vortices are trapped in the hole [98]. The maximum pinning force per unit length decreases with increasing n:

$$f_P^{max} \simeq \left(\frac{\Phi_0}{4\pi\lambda}\right)^2 \frac{1}{\xi}\left(1 - \frac{n}{n_s}\right) \tag{60}$$

Note that the possibility of n_s vortices being trapped by the defect does not necessarily imply that this is energetically the most favorable situation. However, because the pinning force is maximum in the hole, a vortex will remain pinned by the hole once it is there. Buzdin [99] has calculated for a triangular lattice of columnar defects that, after all defects are occupied by Φ_0 vortices, pinning of multiquanta vortices becomes energetically advantageous in case the radius r_a is larger than a critical radius r_c:

$$r_c = \sqrt[3]{\xi(T)a_v^2} \tag{61}$$

with a_v the distance between the vortices in a perfect triangular lattice. The formation of multiquanta vortices has been confirmed by means of magnetization measurements [3]

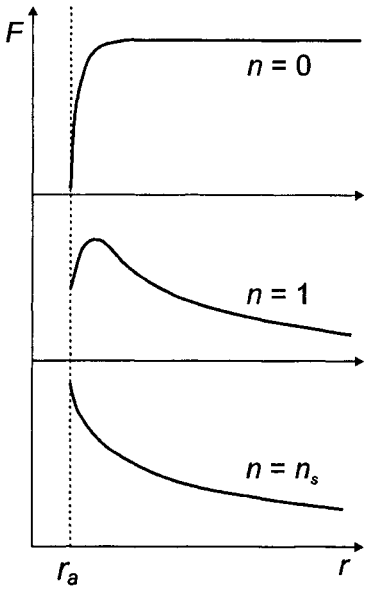


Fig. 29. Schematic presentation of the dependence of the free energy F of a vortex on its distance r from the center of a cylindrical hole with radius r_a and $n_s > 1$, showing the case with no vortex pinned by the hole ($n = 0$), and with $n = 1$, and with $n = n_s$ flux quanta trapped by the hole.

and has been directly visualized by Bitter decoration of Nb films with circular blind holes [4, 100].

From the preceding considerations of the saturation number, one expects that small antidots ($n_s = 1$) can trap only one flux line. In this case, other flux lines generated by the applied field will be forced to occupy interstitial positions. The interplay between weakly and strongly pinned flux lines at interstices and antidots, respectively, will be discussed. The presence of interstitial vortices for $n_s = 1$ makes superconductors with an antidot lattice qualitatively different from superconducting networks ($n_s \gg 1$), where the vortex configuration at integer matching fields is always the same as that of the underlying network. In contrast to that, composite vortex lattices (i.e., with vortices at antidots and at interstices) show a remarkable variety of stable patterns, quite different from the underlying antidot lattice. Large antidots ($n_s > 1$) can stabilize multiquanta vortex lattices, which do not exist in reference homogeneous superconductors without an antidot lattice. Finally, for antidot lattices with $n_s \gg 1$, the crossover to the regime of superconducting networks will be considered.

4.2.2. Regular Pinning Arrays

When arranging the pinning centers in a regular lattice, interesting *matching effects* are observed as a consequence of commensurate vortex states in the periodic pinning potential. Because, in a homogeneous superconductor, triangular and square vortex lattices are energetically most favorable (see Fig. 10), matching effects are expected to be most pronounced for pinning arrays with a triangular or square symmetry. The presence of a regular pinning array results in a huge overall enhancement of the $j_c(H)$ and $M(H)$ compared to a reference film without a pinning array. Moreover, at temperatures close to T_c, sharp *matching anomalies* are observed in the $j_c(H)$ and $M(H)$ curves at specific field values (*matching fields*) where the vortex lattice matches the lattice of pinning centers. In particular, the first matching field H_1 is defined as the field where the density of the vortices equals the density of the pinning centers, leading to a one-to-one correspondence between the vortex lattice

and the pinning array. Similarly, matching effects can also occur at integer and rational multiples of H_1, because of a commensurability between the vortex lattice and the pinning array. These matching fields can be denoted as $H_n = n \times H_1$ and $H_{p/q} = p/q \times H_1$, respectively (n, p, and q integer).

Pronounced peaks in the $j_c(H)$ occur at field values where an undistorted triangular vortex lattice matches the pinning potential, leading to enhanced coherent pinning and hence a maximum in $j_c(H)$ and $M(H)$. The resulting coherently pinned vortex lattice is very stable, which leads to the observed matching anomalies.

4.3. Regular Pinning Arrays with $n_s = 1$

4.3.1. Magnetization

The response of the flux lines to the presence of artificial pinning centers is a challenging problem of scientific [85, 101–104] and technological [105] interest. The "vortex matter" in superconductors subjected to the action of thermal fluctuations and a random or correlated pinning potential is characterized by a variety of new phases, including the vortex glass, Bose glass, and the entangled flux liquid [106–109]. These new phases are strongly influenced by the type of artificial pinning center. Especially random arrays of point defects [110–112] ("random point disorder") and columnar ("correlated disorder") defects [101, 102] have been intensively studied. The latter are convenient pins to localize the FL and enhance the critical current density j_c if the vortex density at the applied field **H** coincides with the density of the irradiation-induced columnar tracks [101].

In spite of the progress in understanding the behavior of vortex matter in the presence of columnar pins, regular arrays of well-characterized pinning centers are much less studied [85, 104]. One of the most efficient and easiest ways to produce such centers in thin films is to make submicrometer holes (antidots) [85, 104] using modern lithographic techniques [56, 113, 114].

In the case $n_s = 1$, the well-defined periodic pinning potential is formed by the antidots with a radius r_a much smaller than the period d of the array. The opposite limit ($r_a \approx d$) has been studied before in superconducting networks [19, 115, 116]. In this section, we will focus on perforated films with $r_a \ll d$, which show remarkable enhancement of the critical current at well-defined "matching" fields when the "attempted" period of the FL lattice a_v coincides with the period d of a regular pinning array and the "attempted" number of FLs per antidot, n, is an integer [56, 85, 104, 114].

An antidot of radius r_a can trap at least one FL [95, 99, 117]. If the antidots are sufficiently large, they can pin multiquanta vortices [99] with the number of the flux quanta n up to the saturation number n_s [95]. For the FL with $n > n_s$, the antidot acts as a repulsive center. Because of this saturation effect, the composite flux lattice in fields corresponding to $n > n_s$ is expected to consist of FL carrying n flux quanta Φ_0 pinned at antidots (strong pinning) as well as at the interstices (weak pinning), as has been shown theoretically [117].

The well-defined lattice of antidots ($d = 1$ μm, $r_a = 0.15$ μm) is usually obtained by a standard lift-off procedure [118]. An atomic force microscopy (AFM) study was performed that revealed a surface roughness between the antidots less than 1 nm. The very low surface roughness between the antidots ensures that the superconducting properties will mainly be influenced by the presence of the antidots. For a square antidot lattice with $d = 1$ μm, the matching fields are $\mu_0 H_n = n \times \Phi_0/d^2 = n \times 2.07$ mT, where n is an integer.

Figure 30 shows the magnetization $M(H)$ data at 6.8 K for a perforated Pb/Ge multilayer with $T_{c0} = 6.9$ K and $\xi(0) = 12$ nm. A remarkably sharp drop in $M(H)$ at the first matching field H_1 is clearly seen [1, 98] (note that the distance between the neighboring data points is only $\Delta\mu_0 H = 0.01$ mT). The presence of weaker extra peaks at $H < H_1$ is an indication of the fractional flux phases stabilized by the periodic pinning array [56]. To analyze these results, we will use the saturation number n_s and the pinning potential

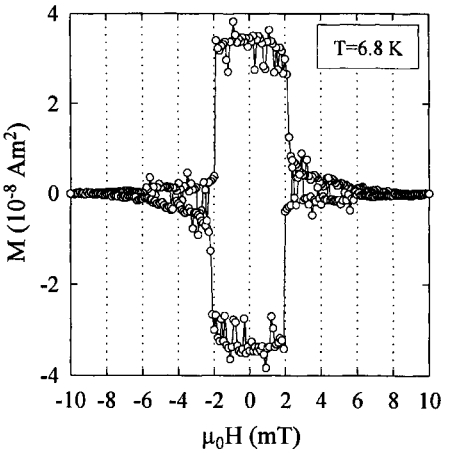


Fig. 30. Magnetization loop $M(H)$ at $T = 6.8$ K of a square antidot lattice ($d = 1$ μm, $r_a = 0.15$ μm). The loops (see also Fig. 31) were measured for $M > 0$ and symmetrized for clarity for $M < 0$. (Source: Reprinted with permission from [1]. © 1995 American Physical Society.)

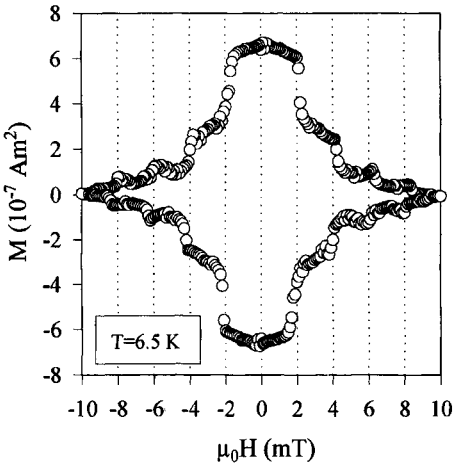


Fig. 31. Magnetization loop $M(H)$ at $T = 6.5$ K of a [Pb(15 nm)/Ge(14 nm)]$_3$ multilayer with a square lattice of submicrometer holes ($d = 1$ μm, $r_a = 0.15$ μm). (Source: Reprinted with permission from [1]. © 1995 American Physical Society.)

at interstices U_{pi} [117]. At $T = 6.8$ K, $n_s = 1$ and only one FL is attracted to the antidot while the second FL is repelled. This situation can be described by the Bose analog of the Mott–Hubbard model for correlated electrons [119]. Because the pinning potential $U_{pi} \propto d/\lambda(T) \to 0$ as $T \to T_c$ [117], the FLs repelled by the antidots are not localized, and they move freely between different very shallow U_{pi} minima at interstitial positions.

The motion of a very small number of excessive FLs at $H > H_1$ leads to a sharp field-induced first-order phase transition from fully localized FLs at $H < H_1$ ("insulator") to a collective delocalized state at $H > H_1$ ("metal") when the motion of "excessive" FLs causes an effective delocalization of all the FLs trapped by antidots. The main features of this transition correspond to the Mott metal–insulator transition for the FLs [106]. It should be noted that previously the existence of the temperature-induced first-order transition was derived from resistivity [120], magnetization [121], and heat capacity [122] measurements in high-quality high-T_c single crystals. The $M(H)$ jump at $H = H_1$ is suppressed as T goes down (see Fig. 31).

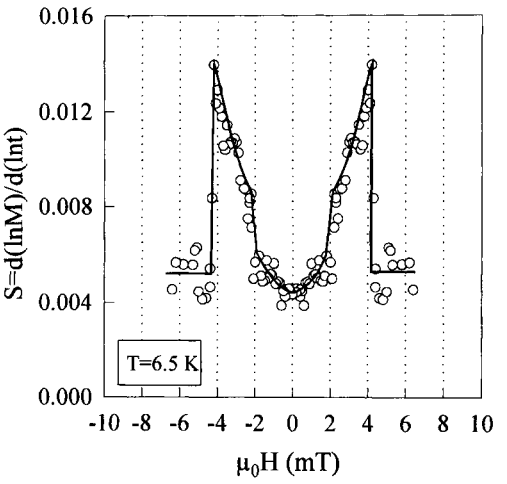


Fig. 32. Normalized relaxation rate $S(H)$ at $T = 6.5$ K of a [Pb(15 nm)/Ge(14 nm)]$_3$ multilayer with a square lattice of submicrometer holes ($d = 1$ μm, $r_a = 0.15$ μm). The solid lines are guides to the eye. The onset of the vortex formation at interstices, at $H > H_2$, leads to a much higher flux creep rate. (Source: Reprinted with permission from [1]. © 1995 American Physical Society.)

The evaluation of parameters H_m^* (matching field) and T_m^* (temperature at which matching is observed) [106] shows that, in these samples with $r_a > \sqrt{2}\xi$, H_m^* is very close to the first matching field $H_m^* \approx H_1 \equiv H_\Phi$ and T_m^* is smaller than T_c only by a few millikelvins. In this case, the Mott insulator line H_Φ terminates at temperatures extremely close to T_c, where the relaxation times are very short and, therefore, the Mott insulator can be observed. As the temperature goes down, the relaxation times increase and the $M(H)$ anomaly at H_1 is suppressed (Fig. 31) because of the equilibrium time problems. Another possibility is that there is no disorder-localized Bose-glass phase at all sandwiched between the superfluid and the Mott insulator, as shown by numerical simulations [123].

At a lower temperature (Fig. 31), $T = 6.5$ K, we still have $n_s = 1$, but the pinning potential U_{pi} increases substantially in comparison with $T = 6.8$ K (Fig. 30) and enables the localization of FLs at the interstices. For fields $H > H_1$, FLs are pushed into interstitial positions, which is confirmed by the simultaneous observation of the steplike anomaly in the $M(H)$ curve at $H = H_1$ (Fig. 31) and an abrupt increase of the flux creep rate also at $H = H_1$ (Fig. 32). In the field range $H_1 < H < H_2$, the increasing S value corresponds to FLs loosely bound at the interstices. The interstitial positions are completely occupied at $H = H_2$ and a reentrant flux creep rate anomaly shows up, indicating the onset of a strongly reduced mobility of the FLs. This reduction of mobility signals the onset of the formation of doubly quantized vortices at antidots, as shown in Figure 33. Because of the presence of interstitial vortices, the saturation value n_s is expected to increase. This leads to the formation of two-quanta vortices at the antidots at H_3 (Fig. 33). The formation of multiquanta vortices will be discussed in Section 4.4.

4.3.2. Transport Measurements

A straightforward way to obtain information about the mobility of the two types of vortices—at interstices and at antidots—is to perform low-field magnetoresistance measurements. Because flux motion leads to dissipation, the presence of the antidot lattice is expected to reduce it owing to trapping of the FLs by the antidots and hence to diminish the voltage drop over the sample. In Figure 34a, a comparison of the field dependence of the resistance $R(H)$ is made between a film with antidots and the reference film without antidots at three different temperatures near T_c (= 4.725 K) and with a fixed alternating-current (ac)

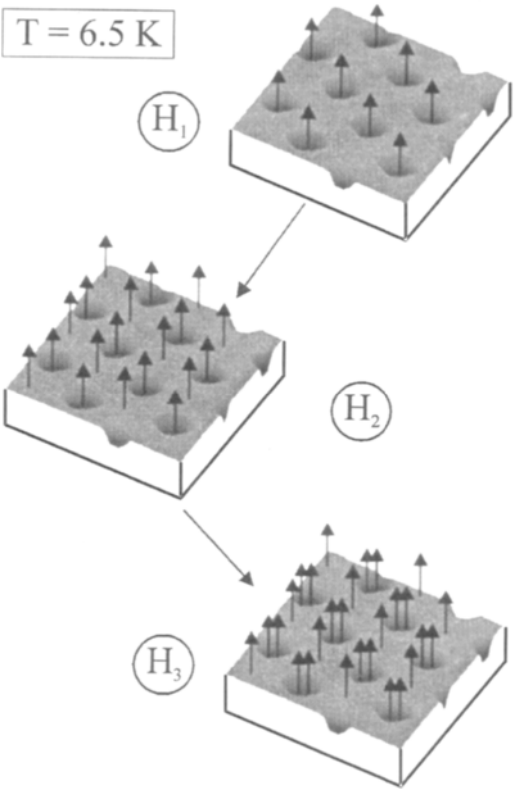


Fig. 33. Schematic representation of the evolution of the flux line lattice (arrows) for $T = 6.5$ K as a function of the magnetic field in a [Pb(15 nm)/Ge(14 nm)]$_3$ multilayer with a square antidot lattice. (Source: Adapted from [1].)

density of 41 A/cm^2. For the reference film, a linear field dependence is measured with a slope that diverges near T_c as $(T_c - T)^{-\nu}$ ($\nu \approx 1$). This behavior is typical [124] for high-κ superconductors in the presence of small fields ($H/H_{c2} < 0.1$) where the Bardeen–Stephen limit [125], $R = \beta(T)H/H_{c2}(0)$ [with $\beta(T)$ the temperature-dependent prefactor], is valid. In the case of the film with an antidot lattice, the resistance is clearly strongly suppressed when the number of FLs is less than that of available antidots ($\mu_0 H < \mu_0 H_1 = 2.07$ mT). The strong reduction with respect to the unperforated film's response is due to the efficient pinning of the FLs by the antidot lattice.

A closer look at the $R(H)$ curves for the film with the antidot lattice (see Fig. 34b) shows that there is even an additional structure present in the low-dissipation level. Besides the clear dips at $H = 0$ and $H = H_1$, less pronounced but still clearly visible R/R_n suppressions can also be found at $H = H_{p/q} = (p/q)H_1$ with $p/q = 1/4$, $1/2$, and $3/4$. The rational dips in $R(H)$ at $H < H_1$ are reminiscent of energetically stable rational flux phases [2] (such as, for example, the well-known checkerboard configuration [127] at $H = H_{1/2}$, etc.). Above H_1, all the antidots forming a lattice are filled with one flux quantum. Because the coherence length $\xi(4.71\text{ K}) \approx 0.11$ μm is quite large, the saturation number [95] $n_s \propto r_a/2\xi \leqslant 1$ is too small for the formation of two-quanta vortices at the antidots. Moreover, from a crossover in the $j_c(T)$ dependence at fixed field $H \approx H_2$ (see the inset of Fig. 36), the temperature, T_{2Q}, where two-quanta formation becomes energetically favorable is estimated to be about $T \approx 4.660$ K. As a result, at $T = 4.710$ K, the extra FLs cannot be accommodated by the antidot lattice and the FLs are forced to occupy interstices between the antidots. In this way, the interstitial FLs are caged by surrounding FLs

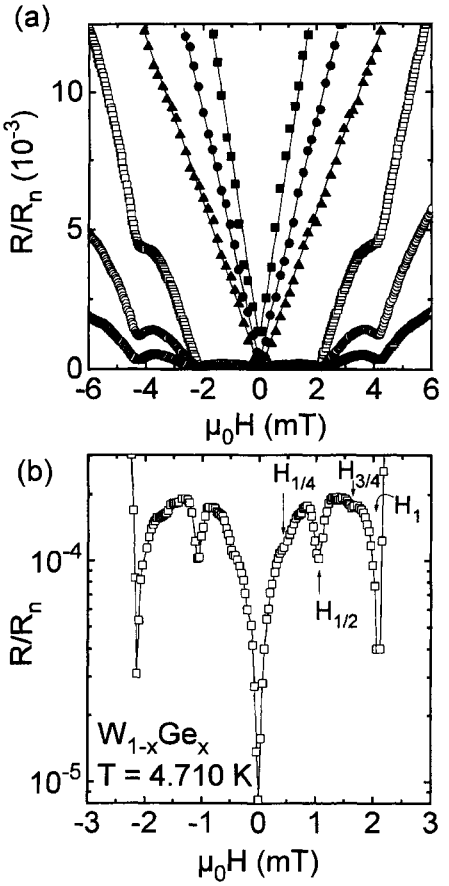


Fig. 34. (a) Comparison of the normalized resistance R/R_n (with R_n the resistance at 5 K) for a WGe film with a lattice of antidots (open symbols) and the film without antidots (filled symbols and straight guide-to-the-eye lines) at different temperatures: squares, $T = 4.710$ K; circles, $T = 4.705$ K; triangles, $T = 4.700$ K and at an ac current density of 41 A/cm^2. (b) Magnification of the low-resistance part of the $R(H)$ curve at $T = 4.710$ K (film with antidots) in a logarithmic scale. The dips in resistance at rational field values are marked with $H_{p/q} = (p/q)H_1$. (Source: Reprinted with permission from [126]. © 1996 American Physical Society.)

strongly pinned by the antidots. Under the action of the Lorentz force, $F_L \propto j\Phi_0$, perpendicular to the transport current density j, these *interstitial caged vortices are easily channeled through the rows of the FLs at the antidots, leading to a dissipation* $V \propto (H - H_1)$. As more interstitial vortices are added, the interaction between them becomes stronger and a deviation from the linear dependence can be observed.

At the second matching field, $H_2 \equiv 2H_1 = 4.14$ mT, the interstitial lines are commensurate with the underlying antidot lattice, occupying hereby the positions in the center of the squares with the antidots at the corners, which enhances the energy barrier for the motion of the interstitial FLs.

In Figure 35, E–j plots (with E the electric field and j the current density) are shown in different magnetic fields ranging from 1 to 3 mT at a fixed temperature $T = 4.690$ K. The horizontal dashed line corresponds to a voltage criterion of 5 μV/cm for the determination of the critical currents $j_c(H)$ shown in the inset of Figure 35a. For fields just below H_1, j_c seems to be rather independent of the field and the curves are reasonably well approximated by a straight line in the log(E)–log(j) plot, which corresponds to a power law relation $E \propto j^{\alpha}$. As the field exceeds the first matching field, a kink appears in the $E(j)$ curve. This kink is preceded by a tail that can also be described by a power law but with

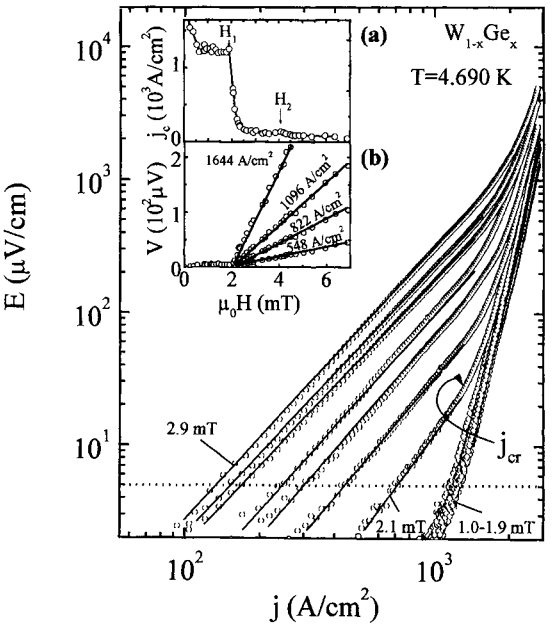


Fig. 35. $E(j)$ sweeps for different magnetic fields between 1 and 3 mT at a fixed temperature of 4.690 K. The corresponding $j_c(H)$ curve, determined using a 5-μV/cm criterion [dashed line in the $E(j)$ plot], is shown in inset a. Inset b shows the generated voltage as a function of the magnetic field for different values of the current density at a fixed temperature of 4.690 K. (Source: Reprinted with permission from [126]. © 1996 American Physical Society.)

a much smaller exponent α. Again, as for the case $H < H_1$, the slope of the curve is the same for the different fields. From the preceding observations, it is clear that at $H > H_1$ we have to distinguish between two types of dissipative processes related to vortices with a different mobility. At low currents $j < j_{cr}$ and $H > H_1$, the vortices at the antidots are pinned while the interstitial vortices are easily swept, giving rise to a dissipation:

$$E_i \propto (j - j_{ci})^{\alpha_i(T)} n_i(H) \tag{62}$$

Here j_{ci} is the critical current density for interstitial FLs motion, $\alpha_i(T)$ the temperature-dependent exponent, and $n_i(H)$ the average number of interstitial FLs taking part in the motion, per interstitial position.

From inset b in Figure 35, we can see that, for $H > H_1$, E varies linearly with H and hence we can approximate $n_i(H)$ in Eq. (62) with $(H - H_1)/H_1$. This clearly demonstrates that an increase of the magnetic field above H_1 at $T = 4.690$ K gives rise immediately to an increase of the number of FLs at interstices and their motion generates a voltage $V \propto H - H_1$. When a certain current threshold is reached ($j \equiv j_{cr} \approx j_{ca}$), the vortices at the antidots are delocalized and their motion produces an electric field:

$$E_a \propto (j - j_{ca})^{\alpha_a(T)} A(H) \tag{63}$$

with j_{ca} being the critical current density number for the vortices at the antidots, $\alpha_a(T)$ the exponent determined from the $E(j)$ curves at $H < H_1$, and $A(H)$ a factor that is weakly dependent on the field. As a result, the total field is given by $E = E_i + E_a$ and a kink is visible in the $E(j)$ curve at the moment when the additional dissipation process, related to the motion of the vortices trapped by the antidots, is initiated.

In Figure 36, the temperature dependence of the $E(j)$ exponent α is shown for fields below and above H_1. For $H > H_1$ and $j < j_{cr}(T, H)$, only the part of the $E(j)$ curve that is associated with the *interstitial* motion is taken into account for the determination of α and hence labeled α_i. When the current density exceeds $j_{cr}(T, H)$, the exponent increases

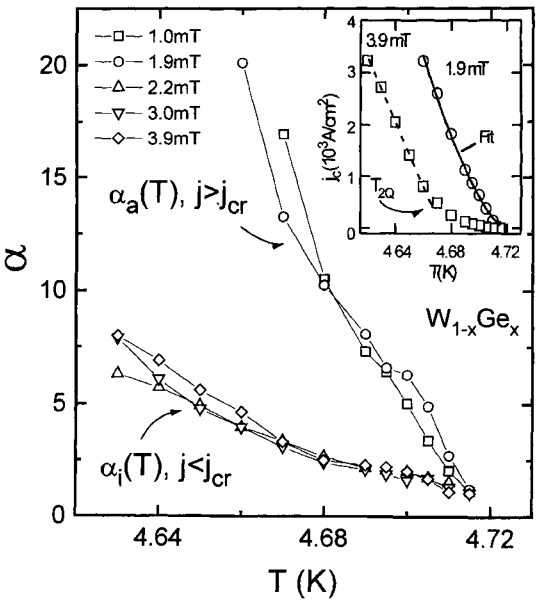


Fig. 36. Temperature dependence of the $E(j)$ exponents α [Eqs. (62) and (63)] for different fields. The subscript a refers to the vortices pinned at the antidots and i refers to the interstitial vortices. The inset shows the $j_c(T)$ dependence at $\mu_0 H = 1.9$ mT ($\approx \mu_0 H_1$) and $\mu_0 H = 3.9$ mT ($\approx \mu_0 H_2$). The solid line in the inset is a fit of the $\mu_0 H = 1.9$ mT data using the GL expression for the depairing current density with parameters: $\lambda(0) = 0.84$ μm and $T_c = 4.719$ K. The dashed line is a guide to the eye, which emphasizes the fast j_c increase below T_{2Q}. (Source: Reprinted with permission from [126]. © 1996 American Physical Society.)

rapidly from $\alpha_i(T)$ to $\alpha_a(T)$. Because both the exponent and the depinning threshold are much larger for the vortices at the antidots than at the interstices, it seems that there exists a correlation between the exponents and the different pinning potentials at the antidots (U_{pa}) and at the interstices (U_{pi}).

From a calculation based on electromagnetic pinning [117, 128], $U_{pa}(T)$ is found to be much larger than $U_{pi}(T)$ and both increase smoothly with decreasing temperature, which is also the case for $\alpha_i(T)$ and $\alpha_a(T)$. The relation between α and U_p is, however, not straightforward, though, of course one can assume that the pinning potentials are logarithmically dependent on the applied current, $U_{pi,a}(j) = U^0_{pi,a} \ln(j_{i,a}/j)$, leading to $\alpha_{i,a} = U^0_{pi,a}/k_B T$.

On the other hand, if we consider the different magnitudes for $\alpha_i(T)$ and $\alpha_a(T)$ and the fact that the generated electric field for $H < H_1$ does not scale with H as it does for the FLs at interstices (see inset b in Fig. 35), it is possible that the vortex delocalization at the interstitials and at the antidots has to be treated differently. A fit of the $j_c(T)$ dependence for $H < H_1$ with the simple GL expression for the depairing current density [27] (see the inset of Fig. 36) actually gives a fairly good result, both for the order of magnitude and for the typical $(T_c - T)^{3/2}$ dependence, thus demonstrating that *in superconductors with an antidot lattice j_c can be enhanced up to its theoretical limit—the depairing current.* Although the used formalism is probably too simple for samples with antidots, the fit may nevertheless indicate that current-induced depairing (often observed in strongly coupled wire networks [129]) is quite substantial, which might explain the steep V–I curves for $H < H_1$. If we compare the V–I behavior related to the motion of the interstitial vortices with the one observed in reference films without an antidot lattice at a comparable field $\tilde{H} = H - H_1$, it turns out that the temperature region where flux flow occurs ($\alpha = 1$) is much more extended in the latter case. Because it has been shown that in similar two-dimensional a-Nb_3Ge films [130] the pure flux flow region is a consequence of a Kosterlitz–Thouless-type melting of the vortex lattice, it seems that the presence of

the vortices at the antidots increases the shear strength of the interstitial fluid and delays the melting of the interstitial lattice with respect to the vortex lattice in the reference film. As a consequence, a peculiar $V-I$ behavior is found for the interstitial vortices.

Summarizing, we have analyzed flux motion in the presence of well-defined artificial periodic pinning arrays. A drastic reduction of the critical current for fields exceeding the first matching field H_1 has been found. From a crossover in the voltage–current ($\log(V)$–$\log(I)$) characteristics, it is clear that this reduction is caused by the coexistence of a weakly pinned interstitial fluid and a strongly pinned vortex lattice at the antidots. For recent molecular dynamics simulations by Reichhardt et al. [131] of the driven vortex lattices, we refer to the Web page:www-personal.engin.umich.edu/~nori.

4.3.3. Lorentz Microscopy on Square Pinning Arrays

The matching effect of vortices in a superconductor having regular pinning arrays, which manifested itself as the production of peaks or cusps in the critical current at specific values of the applied magnetic field [1, 104, 114, 132], has been microscopically investigated using Lorentz microscopy [133].

A coherent and penetrating electron beam of a 300-kV field emission transmission electron microscope [134] allowed a direct observation of the statics and dynamics of vortices in a superconducting thin film by Lorentz microscopy [135]. A thin film of niobium ($T_c = 9.2$ K) for transmission observation was prepared by chemically etching from a rolled niobium foil 30 μm thick, which had been annealed at 2200 °C in a vacuum to increase its grain size up to 300 μm. The film had a [110] surface and one or two holes in the middle. In the areas near the hole edges, which were approximately 100 nm thick, a square array of point defects was produced inside a region 10 μm × 10 μm by irradiation of the Nb film with a focused 30-kV Ga ion beam from a Hitachi focused ion beam machine (FB-2000). The defect consisted of a pit 30 nm in diameter and a few nm in depth and of dislocation networks 200 nm in diameter surrounding the pit. The pit with the dislocation networks is called a defect hereafter. Such square lattices of artificial pinning center regions were repeatedly produced side by side parallel to the film edge at intervals of 4 μm (see Fig. 37).

The sample prepared was set on a low-temperature stage in the microscope so that the film was tilted at an angle of 45° both to the incident electron beam and to the magnetic

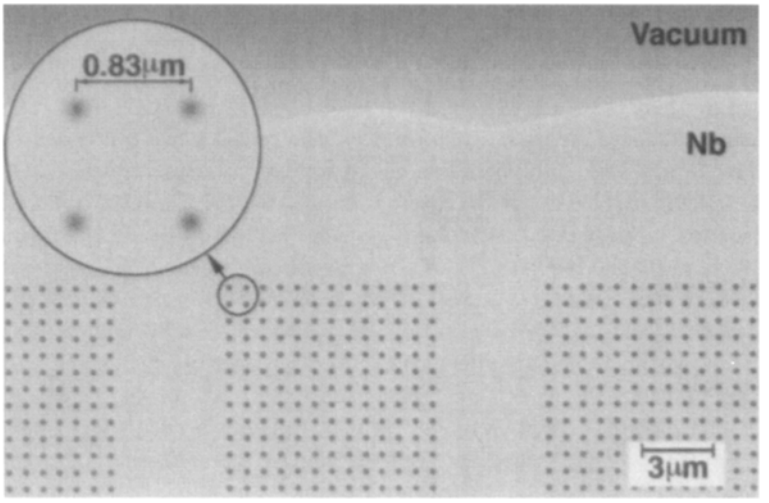


Fig. 37. Square arrays of artificial defects produced in a niobium thin film by Ga ion irradiation. (Source: Adapted from [133].)

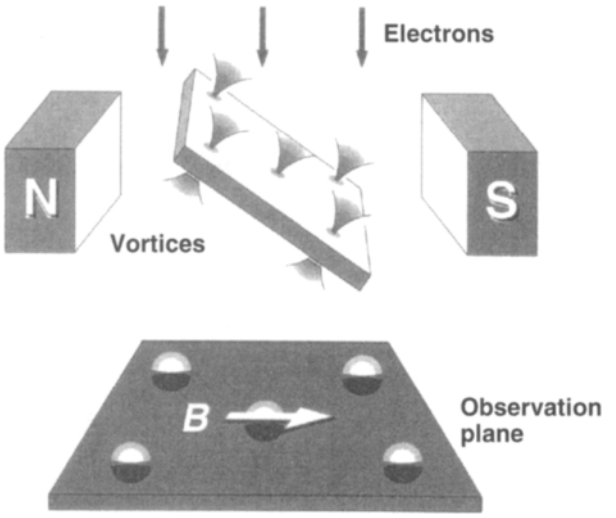


Fig. 38. Principle behind Lorentz microscopy of vortices. (Source: Adapted from [133].)

field (see Fig. 38). The vortices appeared as spots of bright and dark contrast features in an out-of-focus plane as a Lorentz micrograph, because the parallel beam of incident electrons was slightly deflected when passing through a vortex. The out-of-focus distance was 20 to 30 mm and the image magnification was about $\times 1000$.

First, the static configurations of vortices were observed at various magnetic field values to investigate what happens to vortices at specific magnetic fields. When the magnetic field was applied to the sample above $T_c = 9.2$ K and the sample was then cooled down to $T = 4.5$ K. Even under this field-cooled condition, vortices moved for a few minutes as a result of the relaxation processes related to the nonuniform film thickness until they reached an equilibrium state. We then observed the configuration of vortices inside the defect regions by Lorentz microscopy. The vortex density changed a little bit from one place to another because of changes in thickness. For the observation, the region where the film was approximately 100 nm thick was chosen and the vortex density showed no appreciable change.

The observation revealed that vortices formed regular configurations at the matching magnetic fields H_n (components perpendicular to the film plane), which are given by $\mu_0 H_n = n \times \Phi_0/d^2 = n \times 2.98$ mT, where Φ_0 is the quantized flux of a vortex.

Lorentz micrographs taken at various matching fields are shown in Figure 39. In the case of $H_{1/4}$ (Fig. 39a), vortices were located at every fourth pinning site with a spacing $4d$ in the horizontal direction (d is the spacing of the defect lattice). Such lines of vortices were stacked in the vertical direction in such a way that adjacent lines were displaced relative to each other in the horizontal direction by distance $2d$ to form a centered (4×2) structure. In this case, the vortices formed a slightly deformed $(\sqrt{5}/2)$ triangular lattice. At $H_{1/2}$, vortices occupied every other pinning site in both the horizontal and the vertical directions, forming a centered (2×2) square lattice (Fig. 39b). At the first matching field ($n = 1$), vortices occupied all of the pinning sites without any vacancies or interstices (Fig. 39c).

When $H > H_1$, vortices began to squeeze themselves at interstitial points as "quasi-bound" [117] or "caged" [126, 136] vortices. These points were the most stable places for additional vortices to penetrate a square of vortices that were already strongly pinned by defects. In the case of a pit with a larger radius than the penetration depth, $n_s > 1$, two or more vortices would be trapped at a single defect [3].

Interstitial vortices were found to be randomly distributed until H reached $H_{3/2}$, when vortices entered every other interstice in addition to the square array of vortices all pinned

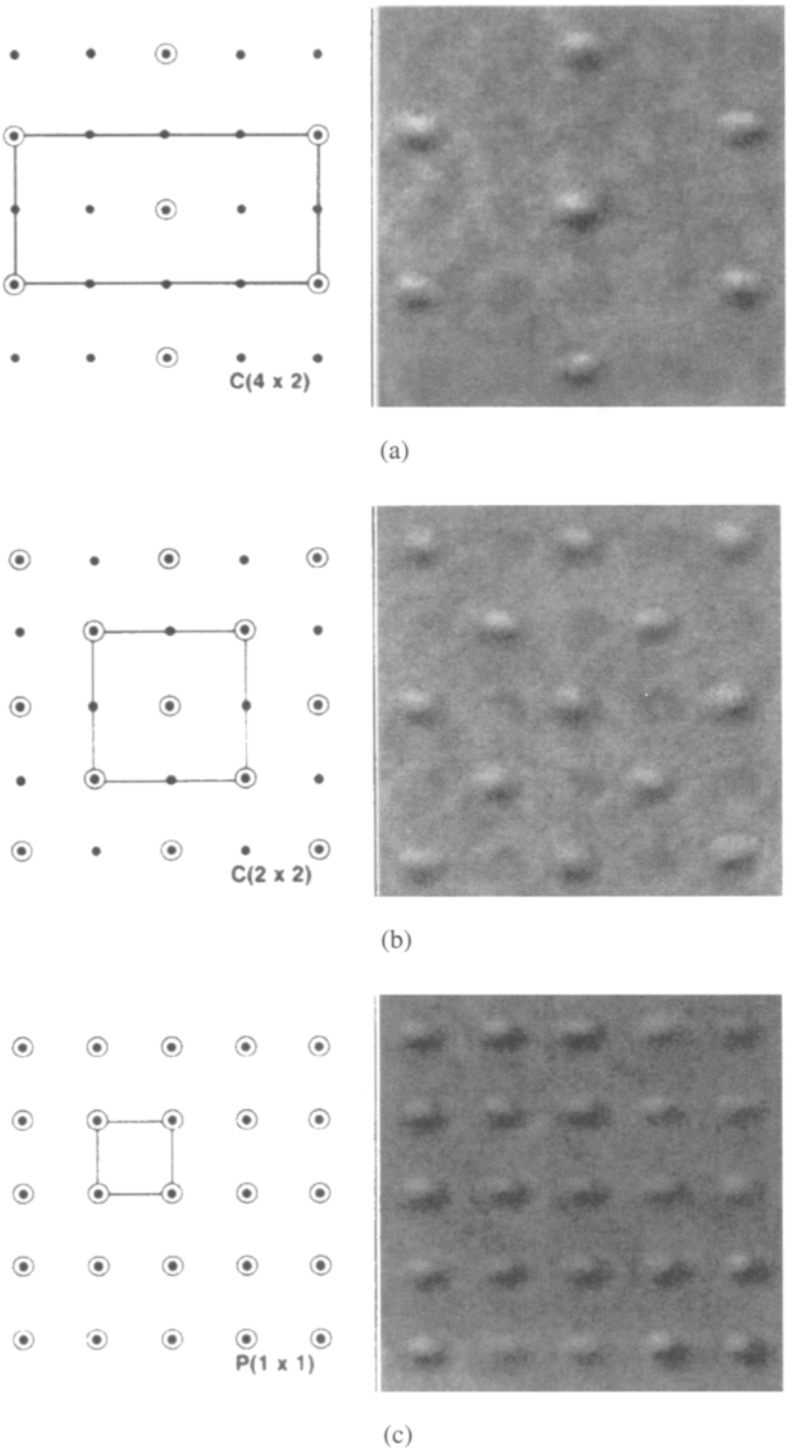
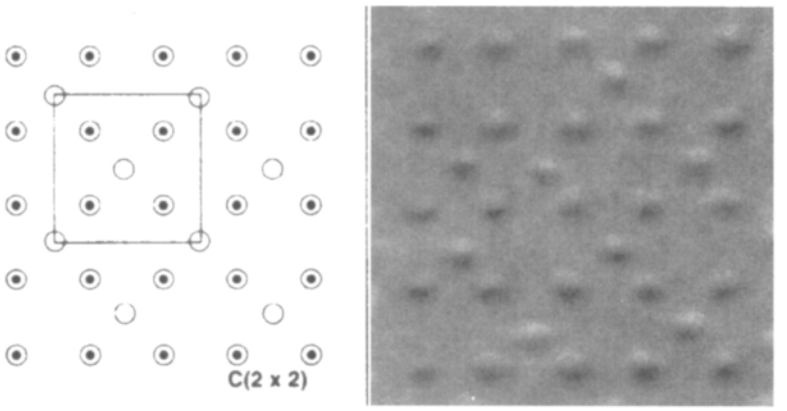
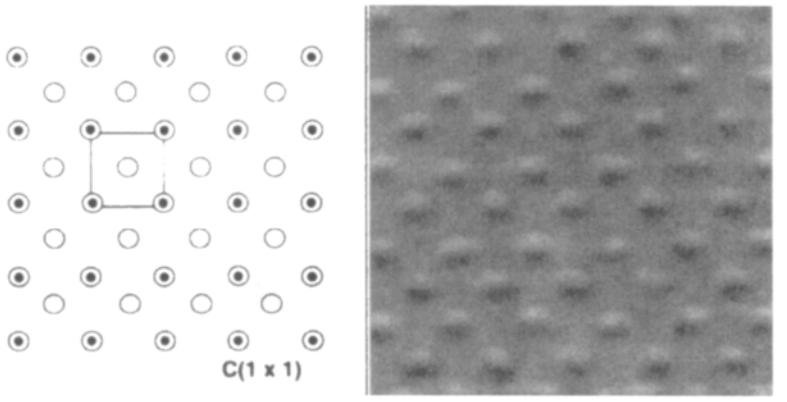


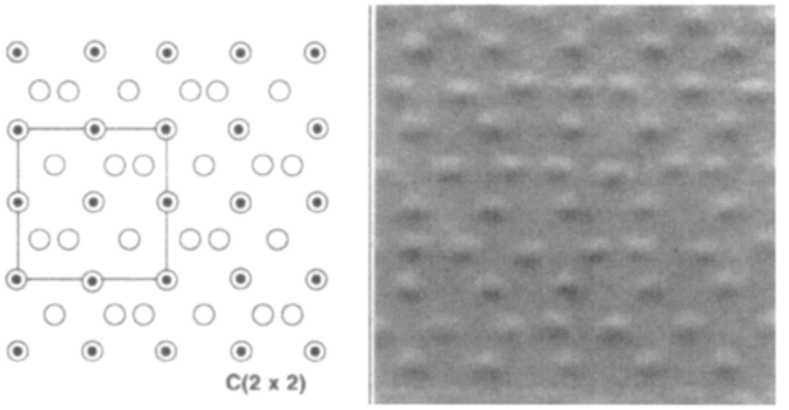
Fig. 39. Lorentz micrographs and schematics of the static stable vortex configuration in a square array of artificial defects at matching magnetic fields H_n: (a) $n = 1/4$, (b) $n = 1/2$, (c) $n = 1$, (d) $n = 3/2$, (e) $n = 2$, (f) $n = 5/2$, (g) $n = 3$, and (h) $n = 4$. Small dots and open circles in each schematic drawing to the left of the Lorentz micrographs show the positions of the defects and the vortices, respectively. Squares also indicate unit cells of the vortex lattices in each case. Vortices form regular lattices at the first matching magnetic field H_1, as well as at its multiples and its fractions. (Source: Adapted from [133].)



(d)



(e)



(f)

Fig. 39. (*Continued.*)

at defects, thus occupying just half of the available interstitial sites (Fig. 39d). Between H_1 and $H_{3/2}$, the interaction of distant interstitial vortices was too weak to form a regular lattice. Even for $H_{3/2}$, the interstitial vortex that should be situated at the top left portion of the micrograph (see Fig. 39d) is mislocated at the interstitial position one line lower. At

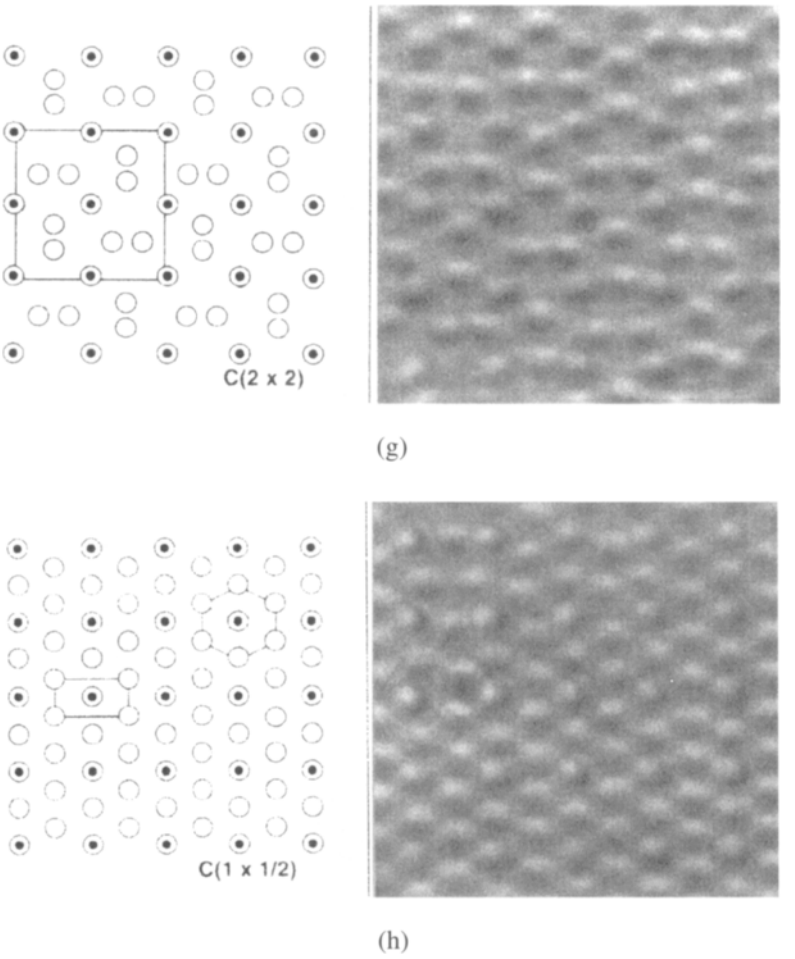


Fig. 39. (*Continued.*)

$H = H_2$, all of the interstitial sites were occupied by vortices, forming a centered (1×1) square lattice (Fig. 39e).

At $H = H_{5/2}$, additional vortices entered every other interstice of the configuration at H_2, thus forming a centered (2×2) square lattice (Fig. 39f). That is, one vortex and two vortices alternately occupied interstitial sites in both the horizontal and the vertical directions. The two interstitial vortices did not overlap but were situated side by side, separated by a distance of approximately $0.6d$. They were aligned parallel to either one of the axes of the square lattice. In the present case, the direction of the two vortices is accidentally horizontal.

When H reached H_3, two vortices were located at every interstitial site (Fig. 39g). The line connecting these two interstitial vortices was not in the same direction but switched alternately from horizontal to vertical. When $H = H_4$, all of the pairs of squeezed vortices were aligned in the vertical direction (Fig. 39h). Additionally, a vortex was inserted at every middle point between two adjacent sites in the vertical direction (Fig. 39h). As a result, vortices formed a slightly deformed triangular lattice.

Vortices form regular lattices, and consequently stable and rigid configurations at H_n. In this case, the vortices do not move easily. Especially for $n = 1$, all of the defects are occupied by vortices and therefore hopping of vortices is forbidden even when the elementary force is exerted on them. In this case, the Mott-insulator phase, introduced by Nelson and Vinokur [106] and by Blatter et al. [107] is realized. In contrast to that, interstitial vortices,

appearing at $H > H_1$, cannot be localized by a shallow pinning potential at interstices. As a result, interstitial vortices demonstrate a metallic vortex behavior. Both *localized vortices at defects* and *metallic vortices at interstices* can be more directly observed by monitoring their dynamics. The coexistence of these two species of vortices is an excellent example of the multistage melting.

For $n_s = 1$, peaks and cusps in the critical current and the magnetization were found at $H = H_{1/4}$ and $H_{1/2}$ but not at $H_{3/2}$ or $H_{5/2}$ by macroscopic measurements [114]. This is reasonable because the pinning potential at defects ($n < 1$) is deeper than that at interstices ($n > 1$). In fact, the regular lattice was partially destroyed at $H = H_{3/2}$ or $H_{5/2}$, even in the field of view shown in parts d and f of Figure 39.

The dynamic behavior of vortices was then observed in a changing magnetic field H. The sample was first cooled down to 4.5 K and H was gradually increased. At a few gauss, vortices began to penetrate the film from the film edge. They approached the defect region and soon occupied the front row of defects (Fig. 40a). Subsequent vortices approached

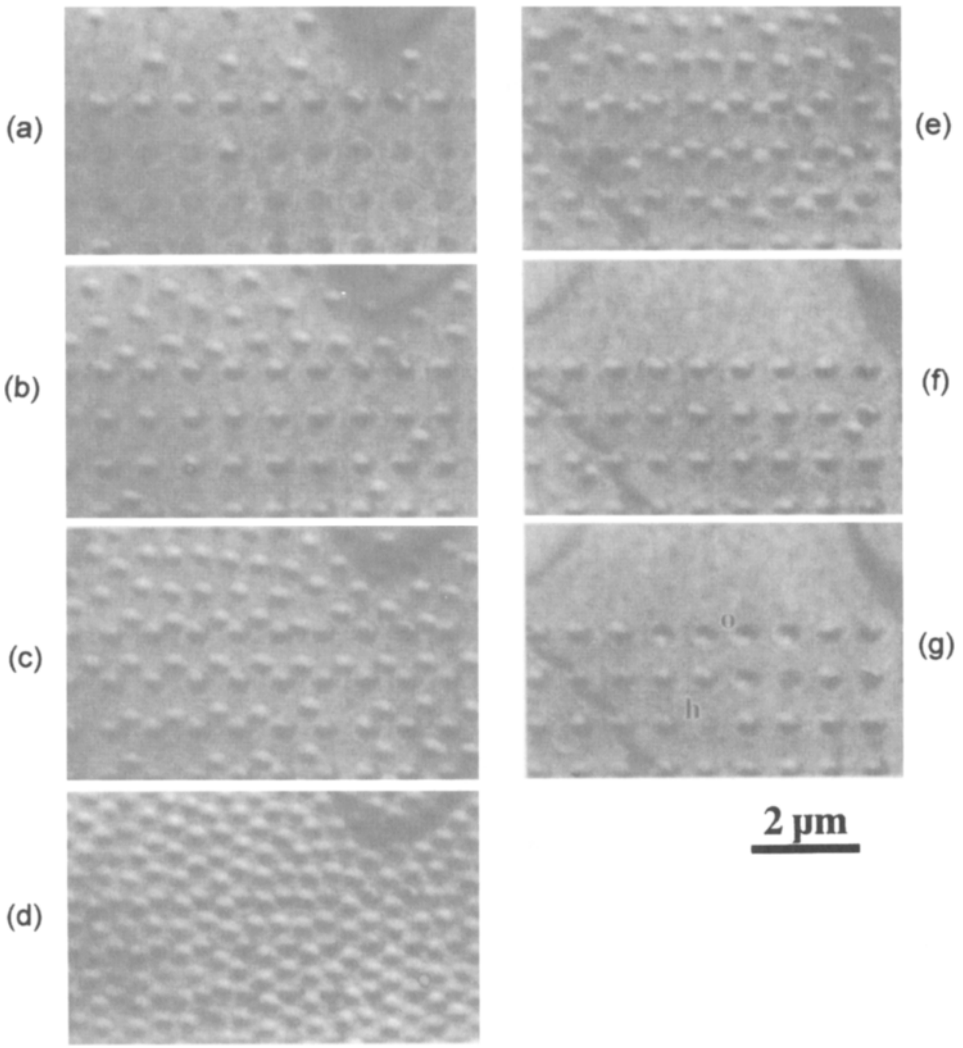


Fig. 40. Lorentz micrographs demonstrating the dynamic behavior of vortices when H is increased and then decreased gradually ($T = 4.5$ K); see text. The magnetic fields in units of H_1 were (a) 0.2, (b) 0.5, (c) 1.2, (d) 2.5, (e) 1.5, (f) 0.9, and (g) 0.6. Video clips showing the movement of the vortices under similar conditions are available at http://www.sciencemag.org/science/feature_data/harada.shl. (Source: Adapted from [133].)

this line barrier but could not easily get over it. When the vortices finally broke through the line, they jumped to defects as far away as $5d$ or more. When distant defects were occupied, vortices began to jump to nearer defects.

When all of the defects were occupied by vortices, subsequent vortices accumulated in front of the first row (Fig. 40b) because they could not enter the defect region, since they could not find vacant defect sites to jump to. Before long, however, they began to enter interstices. The vortices continued to hop from one interstitial site to another. It can be noted in Figure 40c that the positions of interstitial vortices are displaced downward from their proper central positions because of the force in the downward direction.

The manner of the vortex flow suddenly changed after all of the interstices were occupied. Without any vacant sites to hop to, they began flowing simultaneously in single lines. A few lines of vortices were flowing in the field of view in Figure 40d).

When H was decreased, a force was exerted in the opposite direction and interstitial vortices began to move upward to leave the film. Vortices were displaced upward from the proper interstitial position because of this force (Fig. 40e). Even when vortices outside the defect region disappeared, vortices forming a square lattice resisted moving (Fig. 40f).

When H was further decreased, vortices began to depin. For example, one vortex in the front row was depinned and then a vortex in the second row hopped to the vacant site to form a hole (shown as "h" in Fig. 40g). In the mean time, opposite vortices (antivortices) began to enter and to be trapped ("o" in Fig. 40g).

The preceding experiments showed that the character of the vortex flow somehow changed every time when the vortices formed closely packed regular lattices. Consequently, this indicates that the pinning force of a whole vortex lattice can change at H_n.

Peaks in the critical current could more directly be explained by the different dynamic behaviors of vortices in two cases in which H is exactly H_1 and H is slightly greater than H_1. In the sample that was field-cooled down to 4.5 K at a field of 3.1 mT, just above $\mu_0 H_1$ (2.98 mT), the interstitial vortex in Figure 41a began to hop in the downward direction when $\mu_0 H$ was increased to 3.9 mT. When T was increased to 7 K to shorten

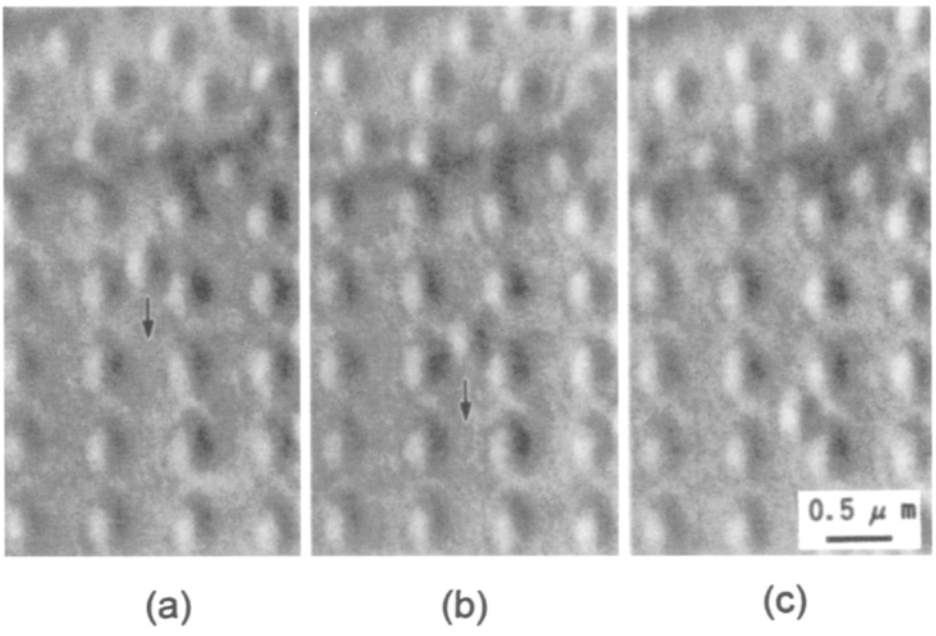


Fig. 41. Dynamics of an excess vortex. The excess vortex hopped from one interstitial site to another when H changed from 3.1 to 3.9 mT and T increased from 4.5 K (a) to 7 K (b) and then to 7.5 K (c). The arrows indicate the hopping direction. (Source: Adapted from [133].)

the time scale of the vortex hopping caused by thermal fluctuations, the interstitial vortex hopped to the next interstitial site (Fig. 41b). This micrograph was taken after the sample had been cooled down to 4.5 K, in order to obtain a high-contrast vortex image, but we confirmed that this cooling procedure did not change the configuration of the vortices. When T was further increased to 7.5 K, the vortex hopped to the next site again (Fig. 41c). The interstitial vortex hopping from one site to another reminds the hopping conductivity of charge carriers in donor-doped semiconductors.

Excess vortices in a regular vortex lattice were observed to hop easily (see also flux flow results in [126]), whereas a change in the magnetic field two times larger was required to induce hopping of the vortices forming the lattice. The hopping of holes in a vortex lattice was also observed. A stronger force was needed to cause a vortex hole to hop than to cause an excess vortex to do so, because a vortex must be depinned from a stable defect site. Similar vortex behavior was detected at other matching fields, such as H_2 and H_3, although it was not as conspicuous as in the case of $H = H_1$.

The studies by Lorentz microscopy elucidated the microscopic mechanism of the matching effect. When vortices formed a regular lattice, they could not begin to move unless a force larger than the elementary pinning force was exerted. At the same time, excess (or deficient) vortices were observed to move easily when affected by the Lorentz force, thus providing a microscopic explanation for larger critical currents at matching magnetic fields.

4.3.4. Numerical Simulations and Configuration of the Vortex Lattice in a Square Pinning Array

Static and dynamic vortex phases in superconductors with a periodic pinning array have been studied by molecular dynamics simulations by Reichhardt et al. [131]. They have performed molecular dynamics simulations of the vortex configurations in superconductors with a periodic pinning array of circular pinning centers with $n_s = 1$. In the equation of motion, the vortex–vortex interaction for a bulk superconductor [Eq. 28] is used. The vortices interact with the pinning centers only when they are within a distance λ from their edge, where the attractive force is proportional to the distance between the centers of the vortex and the pinning site. Each pinning center can only pin one vortex ($n_s = 1$). The flux-gradient-driven simulations and the simulated annealing (field-cooled) simulations result in the same vortex configurations.

Figure 42 shows the resulting vortex states at the first, second, and third matching fields for a square lattice of pinning centers that can each pin not more than one vortex ($n_s = 1$). All these simulated vortex states have also been directly observed by means of Lorentz microscopy by Harada et al. [133] in superconducting Nb films with a square lattice of small defects. At H_1, a one-to-one matching between the vortex lattice and the lattice of pinning centers is established. At H_2, a square vortex lattice is formed where one FL is

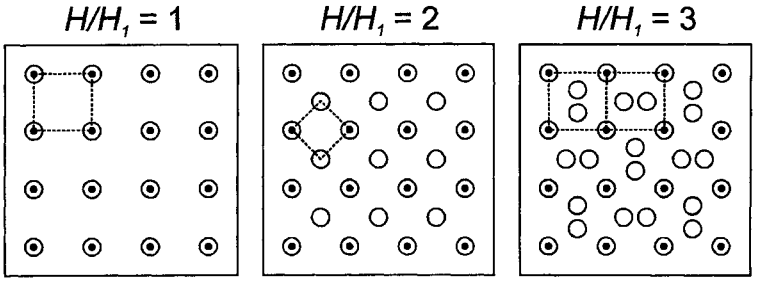


Fig. 42. Schematic presentation of the vortex configurations at integer matching fields $H/H_1 = 1, 2$, and 3 in the presence of a square lattice of pinning sites. Open circles and dots represent vortices and artificial pinning centers, respectively. (Source: Reprinted with permission from [89].)

pinned at each pinning center, and one is "caged" at each interstitial position. The vortex lattice at H_3 is highly ordered with pairs of interstitial FLs alternating in position, but has neither a square nor a triangular symmetry. The vortex configurations in a square pinning array have been simulated in [131] up to the 28th integer matching field. A variety of ordered, nearly ordered (e.g., distorted triangular), and disordered vortex lattices are found for integer matching fields up to $H/H_1 = 15$. At matching fields $H/H_1 > 15$, no overall order of the vortex lattice is found. For these high matching fields, ordered domains are observed which are separated by grain boundaries of defects.

Also at rational multiples of the first matching field, matching anomalies were found, related to a stable vortex configuration in the periodic pinning potential. Molecular dynamics simulations [131] for a square lattice of pinning centers reveal ordered vortex lattices at $H/H_1 = 1/4$ and $1/2$ and partially ordered vortex lattices at $H/H_1 = 3/2$ and $5/2$.

Experimentally, fractional matching anomalies have been observed in several types of periodic pinning arrays, for example, antidot lattices in Pb/Ge multilayers [2], or lattices of submicrometer insulating [89], metallic [89], or magnetic dots [89, 90], covered with a superconducting layer [89].

The matching anomalies at well-defined rational multiples of the first matching field

$$H_{p/q} = \frac{p}{q} H_1 \tag{64}$$

with p and q integer numbers, can be explained by the stabilization of a flux lattice with a larger unit cell than the lattice of pinning centers. We will discuss the rational matching configurations in artificial square pinning arrays with period 1.5 μm, consisting of a lattice of submicrometer rectangular dots (insulating, metallic, or magnetic), covered with a superconducting Pb film [89]. An AFM topograph of a square lattice of Au dots is shown in Figure 43.

In those systems, rational matching anomalies of two different periodicities have been observed: (i) the "binary" fractions ($q = 2^n$, with n integer) of the first matching field: $H/H_1 = 1/8$, $1/4$, $1/2$, $3/4$, $5/4$, and $3/2$; and (ii) the "threefold" ($q = 3$) fractions: $H/H_1 = 1/3, 2/3$, and $4/3$, which are only observed for $T/T_c > 0.985$.

Similar rational matching anomalies have also been observed by Baert et al. [2] in superconducting Pb/Ge multilayers with a square antidot lattice. In these antidot systems, rational matching peaks are observed only within the first period ($|H| < H_1$) at slightly different fields, namely, $H/H_1 = 1/16$, $1/8$, $1/5$, $1/4$, and $1/2$. These field values correspond exactly to those where a square lattice of flux lines with a unit cell larger than that of the antidot lattice, and if necessary rotated, can be matched onto the square lattice of pinning centers, that is, when $p = 1$ and $q = n^2 + k^2$, with n and k integer numbers. Only

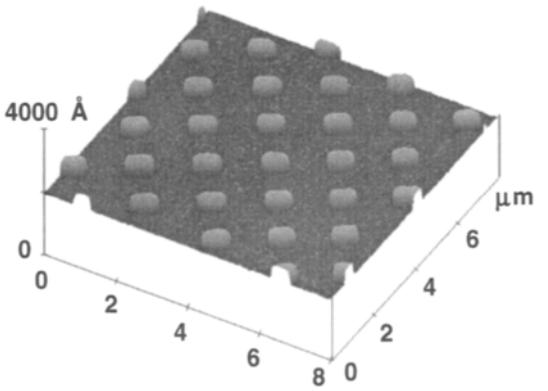


Fig. 43. AFM topograph of a square lattice of rectangular Au dots with a lattice period of $d = 1.5$ μm. (Source: Reprinted with permission from [89].)

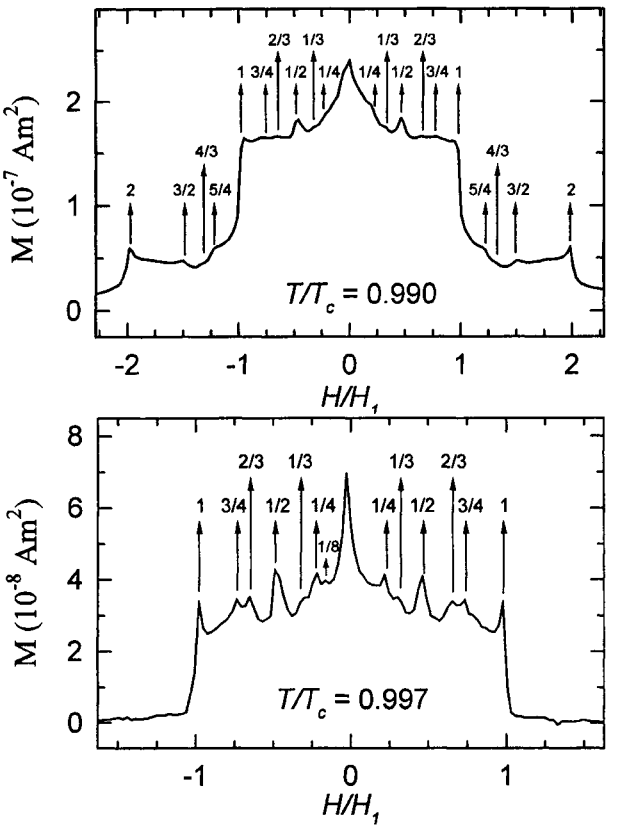


Fig. 44. Magnetization curves ($M > 0$) as a function of H/H_1 (H_1 is the first matching field) for a 50-nm Pb film on a square lattice of Ge dots ($d = 1.5$ μm), measured for T very close to T_{c0}: $T/T_{c0} = 0.990$ and $T/T_{c0} = 0.997$. The matching anomalies at $|H/H_1| = p/q$ are identified by the fraction p/q. (Source: Reprinted with permission from [89].)

when the radius of the antidots is increased, allowing pinning of multiquanta vortices, rational matching peaks are observed in the second period ($H_1 < |H| < H_2$). For very large antidot radii, a crossover to the network behavior is observed. In superconducting networks, anomalies in the critical current are present in all field periods at certain characteristic fractional numbers of flux quanta per unit cell: $H/H_1 = 1/4$, $1/3$, $2/5$, $1/2$, $3/5$, $2/3$, and $3/4$ [91]. Comparison of the series of rational matching fields found in the sample with a lattice of dots with the results obtained for superconductors with a square antidot lattice, on the one hand, and superconducting square wire networks, on the other hand, reveals that these samples exhibit a different behavior. Several of the observed anomalies ($H/H_1 = 1/3$, $2/3$, $3/4$, $5/4$, $4/3$, and $3/2$) are not present when small antidots are used as pinning centers. These specific rational matching fields are also not emerging from the simulations of Reichhardt et al. [131] for a square lattice of pinning centers. Rational anomalies in the second period have so far mainly been observed for larger antidots, related to the formation of multiquanta vortices ($n_s \geqslant 2$). The anomalies with $q = 3$ are typical for a superconducting network. Nevertheless, they are clearly visible in the $M(H)$ measurements of a Pb film with a dot lattice, although this sample consists of a continuous superconducting film, far from the network limit [91]. These interesting differences clearly demonstrate that the details and the precise nature of the lattice of pinning centers play a determining role in the pinning phenomena and the matching effects.

For the rational matching fields observed in superconducting films with a square dot lattice, the proposed stable vortex configurations are shown in Figure 45. The configuration for $H/H_1 = 1/8$ is a square vortex pattern rotated by 45° with respect to the pinning array,

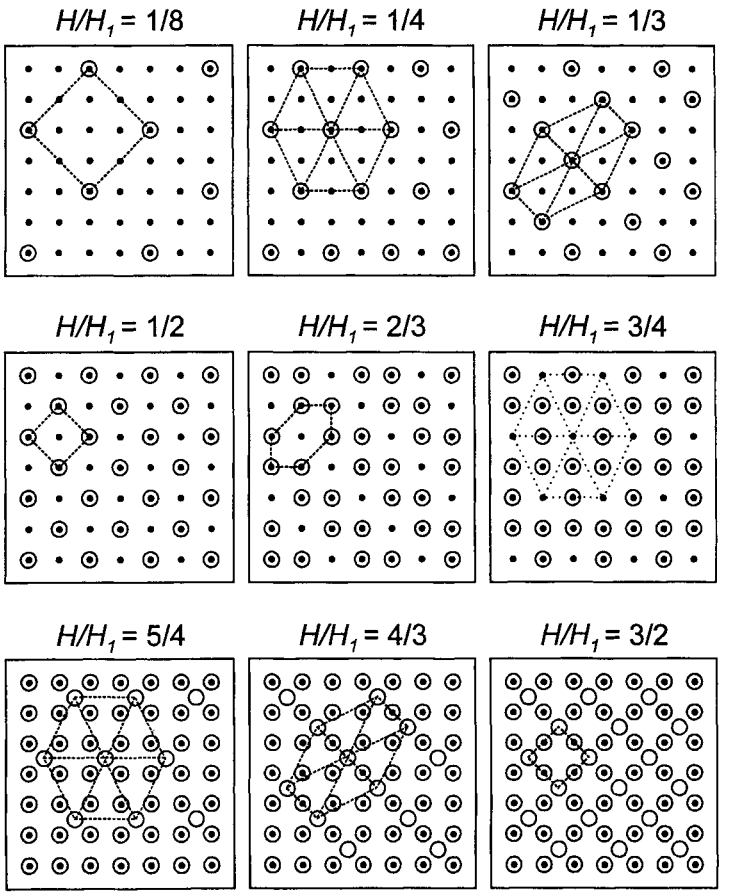


Fig. 45. Schematic presentation of the suggested stable vortex lattices at rational matching fields, indicated by $H/H_1 = p/q$, for a square lattice of pinning centers. The black dots and open circles indicate pinning centers and vortices, respectively. The dashed lines are guides to the eye, showing the symmetry of the vortex lattice. (Source: Reprinted with permission from [89].)

which also corresponds to the configuration suggested by Baert et al. [2]. For $H/H_1 = 1/4$, the flux lines can almost form a perfect triangular lattice. This configuration has been directly visualized in Lorentz microscopy measurements (see Fig. 39a) . For the rather unexpected anomaly at $H/H_1 = 1/3$, a configuration consisting of a distorted triangular lattice is suggested. This vortex configuration is similar to the one at $H/H_1 = 1/3$ in superconducting wire networks [91].

Although the considered sample is far from the limit of a wire network, it is still believed that this commensurate vortex configuration causes the matching anomaly in the $M(H)$ measurements. At $H/H_1 = 1/2$, the well-known checkerboard configuration is formed, resulting in a square vortex lattice, rotated over 45° with respect to the underlying pinning lattice. For $H/H_1 = 2/3$, an ordered vortex lattice can be formed being the inverse of the one at $H/H_1 = 1/3$, where the occupied pinning sites are replaced by empty ones, and vice versa. Similarly, the proposed configuration for $H/H_1 = 3/4$ consists of the inverse of the configuration at $H/H_1 = 1/4$. The vortex configurations at rational matching fields in the second period ($H_1 < |H| < H_2$) can be easily interpreted by using the following consideration. After single flux lines occupy all pinning centers at H_1, the minima in the pinning potential at the positions of the dots have turned into a maximum, repelling additional flux lines (Fig. 29). This results in a potential landscape characterized by minima at interstitial positions, where vortices can now be caged by the repulsive interaction with

the strongly pinned flux lines at the dot positions. The square lattice of interstitial positions now plays the role of the pinning centers in the first field period. To obtain the vortex configurations at $H/H_1 = 5/4, 4/3$, and $3/2$, we can simply superpose the rational vortex configurations for $H/H_1 = 1/4, 1/3$, and $1/2$, respectively, in the interstitial positions onto the completely filled H_1 configuration. This results in the corresponding configurations shown in Figure 45. It should be mentioned that the configuration for $H/H_1 = 3/2$ has been observed by Lorentz microscopy experiments (see Fig. 39d).

From the different configurations shown in Figures 42 and 45, all stable vortex lattices for $H \leqslant H_1$ consist of rigidly pinned vortices at the positions of the dots. On the other hand, for $H > H_1$, composite flux lattices [1, 3, 86, 87, 126, 133, 137] are formed, consisting of strongly pinned vortices at dot positions and weaker pinned or "quasi-bound" vortices at interstitial positions. These interstitial vortices can be depinned much easier, and are responsible for the markedly lower magnetization amplitude (or critical current density) compared to the $|H| \leqslant H_1$ field range, which was observed in the $M(H)$ curves, especially at relatively high temperatures where multistage melting of the composite vortex lattice can be seen (see Figs. 30 and 44).

4.3.5. Numerical Simulations and Configuration of the Vortex Lattice in a Triangular Pinning Array

Also for triangular lattices of pinning centers with $n_s = 1$, stable vortex configurations are found at integer and at certain rational multiples of the first matching field by molecular dynamics simulations [131].

Magnetization measurements on a superconducting Pb film with a triangular lattice of rectangular submicrometer magnetic dots show a series of matching anomalies that can be directly related to a stable configuration of the vortices in the periodic pinning potential. Assuming that no multiquanta vortices are formed ($n_s = 1$), we can try to identify the stable vortex lattices giving rise to an anomaly in the magnetization curves. The series of field values at which matching effects appear, and for which we will indicate a stable vortex configuration is as follows: $H/H_1 = 1/4, 1/3, 3/4, 1, 5/4, 2, 3$, and 4. The vortex configurations are schematically presented in Figures 46 and 47, where the dots and the circles indicate the pinning sites and the vortices, respectively. For some matching fields, a commensurate triangular lattice can be formed, while other stable vortex configurations are ordered but do not form a triangular lattice.

In the absence of pinning centers, the most stable vortex configuration is the triangular Abrikosov vortex lattice. When a triangular lattice of artificial pinning centers is introduced, matching effects will in the first place develop at those field values where a triangular vortex lattice with a certain period, a_v, can be formed that is commensurate with the lattice of pinning centers. This condition can be expressed mathematically as follows [131]:

$$a_v = d\sqrt{m^2 + n^2 + nm} \tag{65}$$

for the rational matching anomalies, and

$$a_v = \frac{d}{\sqrt{m^2 + n^2 + nm}} \tag{66}$$

for the integer matching anomalies. In these equations, a_v is the period of the triangular vortex lattice, d is the period of the triangular pinning array, and m and n are positive integer numbers. It is assumed that the saturation number of pinned flux quanta per pinning center $n_s = 1$. After occupation of all pinning centers, additional flux lines are trapped in minima of the pinning potential at interstitial positions. The preceding conditions are satisfied for the integer multiples $H/H_1 = 1, 3, 4, 7, 9, \ldots$ and for the rational fractions $H/H_1 = 1/3$, $1/4$, $1/7$, $1/9$, and so on. The corresponding triangular vortex lattices for the observed matching anomalies can be found in the diagrams in Figures 46 and 47. In the $M(H)$ measurements of a superconducting Pb film on a triangular lattice of submicrometer rectangular magnetic dots, no clear matching anomalies are

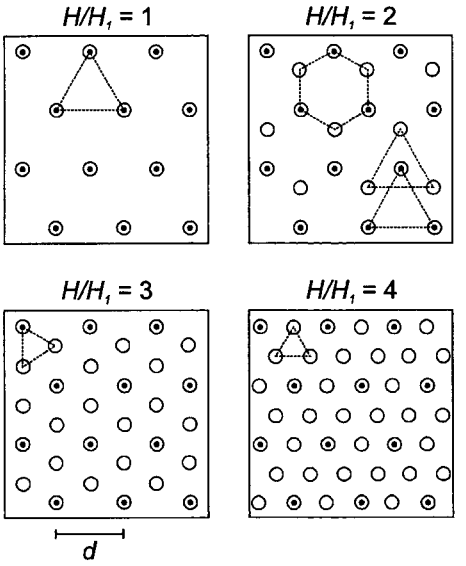


Fig. 46. Schematic presentation of stable vortex configurations at integer matching fields for a triangular lattice of pinning sites with period d. Black dots and open circles represent pinning centers and vortices, respectively. Dashed lines indicate the symmetry of the stabilized vortex lattice. (Source: Adapted from [131].)

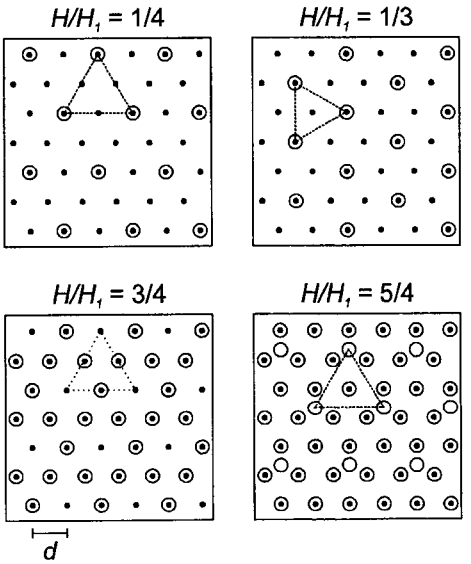


Fig. 47. Suggested vortex lattices at rational matching fields, $H/H_1 = p/q$, for a triangular pinning lattice with period d. Black dots and open circles represent pinning centers and vortices, respectively. The dashed lines are guides to the eye, showing the symmetry of the vortex lattice. (Source: Reprinted with permission from [89].)

resolved at fields smaller than $H/H_1 = 1/4$, and the highest observed matching field is $H/H_1 = 4$. Molecular dynamics simulations of the vortex lattice in a triangular pinning array indeed reveal triangular ordered vortex configurations at the integer matching fields $H/H_1 = 1, 3, 4, 7, 9, 12, 13, 16, 19, 21, 25,$ and 28 [131].

The anomalies at $H/H_1 = 3/4$, $5/4$, and 2 cannot be explained by the previous argument. However, other ordered nontriangular vortex configurations can be formed at those field values, as is shown in Figures 46 and 47. In the suggested vortex lattice for

$H/H_1 = 3/4$, a fraction of the pinning centers is occupied in such a way that the inverse of the vortex configuration at $H/H_1 = 1/4$ is formed. (A similar idea was used in the case of a square pinning array for $H/H_1 = 3/4$, and has been experimentally confirmed [133].) In this way, a triangular lattice with period $2d$ of nonoccupied pinning centers is defined. To find a stable configuration for $H/H_1 = 5/4$, let us consider the pinning potential after all pinning centers are occupied. Minima are then developed at interstitial positions in the center of each triangle of occupied pinning centers. To form a stable vortex lattice at $H/H_1 = 5/4$, the pinning centers are first occupied and the remaining flux lines can form a triangular arrangement at the interstitial positions, similar to the one at $H/H_1 = 1/4$. The resulting configuration is shown in Figure 47. For $H/H_1 = 2$, a honeycomb vortex configuration is suggested, consisting of two identical interpenetrating triangular vortex lattices, both with the same period d. In one lattice, the vortices are strongly pinned at the dot positions, while the other consists of weaker pinned interstitial vortices. This configuration was also found in the simulations of Reichhardt et al. [131], provided that the pinning at the pinning centers is sufficiently strong.

4.4. Multiquanta Vortex Lattices ($n_s > 1$)

In this section, regular arrays of relatively large antidots ($n_s > 1$), which can stabilize multiquanta vortex lattices, will be considered. Experimental evidence for the existence of such vortex lattices can be found in magnetization data. We analyze here the $M(H)$ measurements carried out on high-quality nonperforated and perforated $[Pb(10\ nm)/Ge(5\ nm)]_n$ multilayers ($n = 2$ bilayers) and amorphous $W_{1-x}Ge_x$ (60 nm) ($x \approx 0.33$) single films [93]. Both were prepared in molecular beam epitaxy apparatus using liquid-nitrogen-cooled SiO_2 substrates. The WGe films were obtained by electron beam coevaporation of W and Ge. In the same films, antidot lattices were fabricated by e-beam lithography (for details of the sample preparation, see [138]). Figure 48 shows a typical atomic force microscopy (AFM) picture of a Pb/Ge multilayer with a triangular (Fig. 48a) and a WGe single film with a square (Fig. 48b) antidot lattice. In Figure 48a, the distance d between the antidots of radius $r_a = 0.22\ \mu m$ is 1 μm and the surface between them is quite flat, the root mean square roughness σ is 4 nm on a $(0.5\ \mu m)^2$ area. The antidots obtained in the WGe single films have a radius of $r_a = 0.17\ \mu m$ and the σ of the surface between them is even less than in Pb/Ge, about 1 nm. The number of antidots per sample unit area is about $10^6/mm^2$. The matching fields H_n for these perforated films, with a triangular antidot lattice, are $n \times 2.39$ mT, while for a square antidot lattice $n \times 2.07$ mT. The coherence length and penetration depth are $\xi(0) = 12$ nm and $\lambda(0) = 260$ nm for the Pb/Ge multilayers while $\xi(0) = 6$ nm and $\lambda(0) = 490$ nm for the WGe single films.

Typical magnetization loops $M(H, T)$ of superconducting films with square and triangular antidot lattices for temperatures T close to T_c are shown in Figures 49a and 50a, with T a fixed temperature. The $M(H, T)$ curves were also measured for reference Pb/Ge and WGe nonperforated films. The width ΔM of the $M(H, T)$ loops in perforated films is strongly increased because of the efficiency of antidots as artificial pinning centers. At the used temperatures not very far from T_c, the difference between the width of the hysteresis loops ΔM (Figs. 49a and 50a) for as-grown and perforated films is so large (very high "contrast") that the $M(H, T)$ curves for the latter can be solely attributed to the contribution arising from FL pinning by an antidot lattice.

Besides an overall enhancement of ΔM, distinct cusplike $M(H, T)$ anomalies are clearly seen exactly at the expected matching fields: $\mu_0 H_n = n \times 2.39$ mT and $n \times 2.07$ mT for triangular and square antidot lattices, respectively. Strictly speaking, there is always a shift in the position of the matching field H_n extracted from increasing ($H_n\uparrow$) and decreasing ($H_n\downarrow$) field measurements of $M(H)$. However, sufficiently close to T_c ($T_c - T \approx 1$ K), where the discussed sharp matching $M(H)$ anomalies are observed, the difference $\Delta H_n = (H_n\uparrow) - (H_n\downarrow)$ is very small. At lower temperatures, matching $M(H)$ anomalies

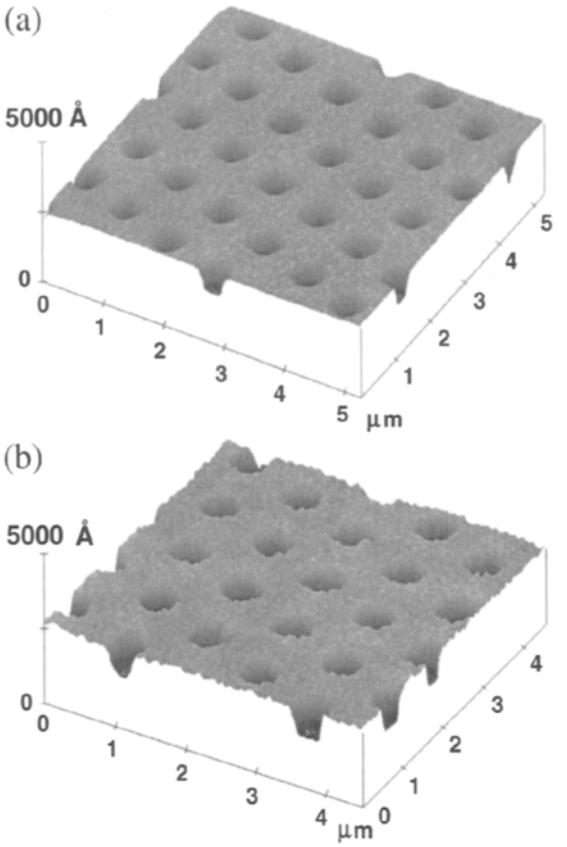


Fig. 48. AFM picture of a film with (a) a square lattice of antidots and (b) a triangular lattice of antidots.

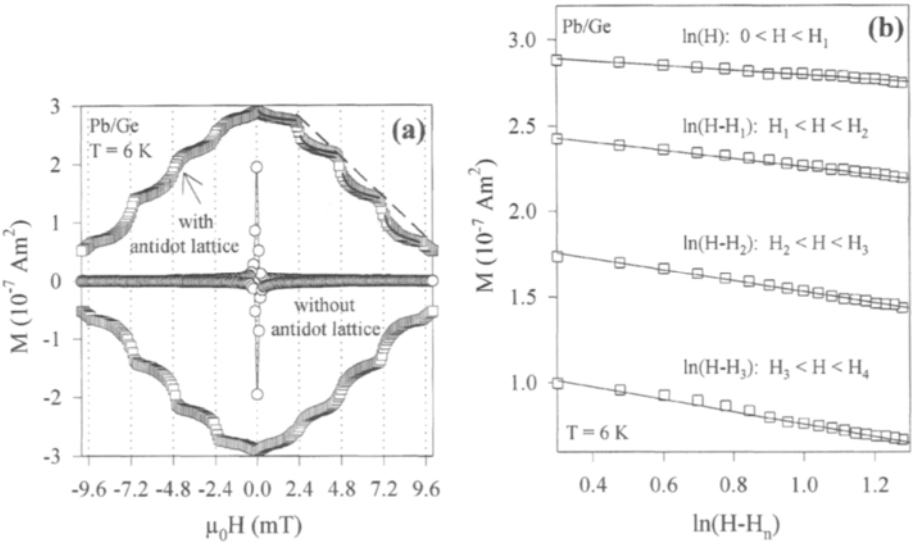


Fig. 49. (a) Magnetization loop $M(H)$ at $T = 6$ K of a [Pb(10 nm)/Ge(5 nm)]$_2$ multilayer with and without antidot lattice. The solid line is a fit with Eq. (70) (see text). The dashed line is demonstrating the validity of the linear behavior of $M(H_n)$ at the matching fields H_n [Eq. (68)]. The loops were measured for $M > 0$ and symmetrized for clarity for $M < 0$. (b) The magnetization M versus $\ln(H - H_n)$ at $T = 6$ K. The different slopes of the solid lines for the different periods are used to determine the effective flux $\tilde{\Phi}_{0n}$ in Eq. (70). (Source: Reprinted with permission from [3]. © 1996 American Physical Society.)

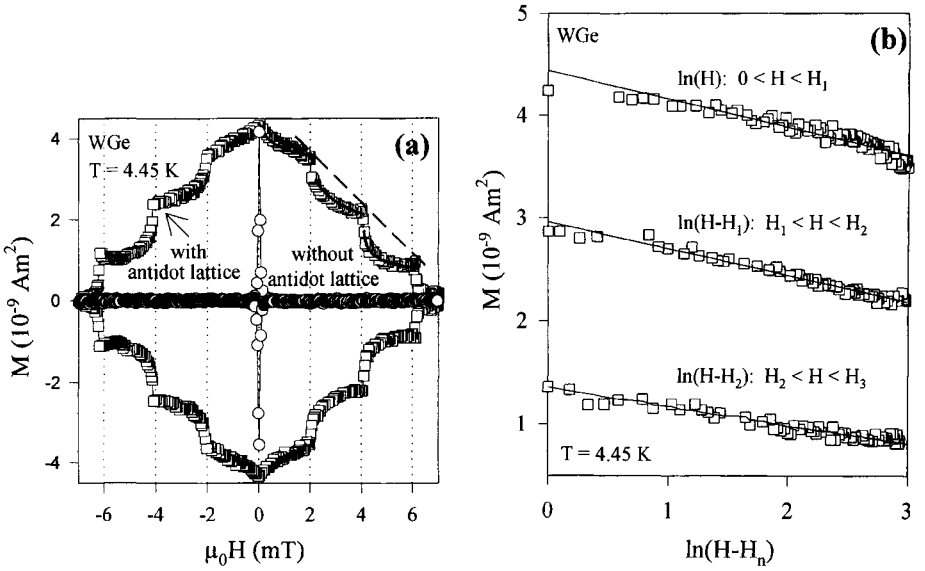


Fig. 50. (a) Magnetization loop $M(H)$ at $T = 4.45$ K of a WGe(60 nm) single film with and without antidot lattice. The solid line is a fit with Eq. (70) (see text). The dashed line is demonstrating the validity of the linear behavior of $M(H_n)$ at the matching fields H_n [Eq. (68)]. The loops were measured for $M > 0$ and symmetrized for clarity for $M < 0$. (b) The magnetization M versus $\ln(H - H_n)$ at $T = 4.45$ K. The different slopes of the solid lines for the different periods are used to determine the effective flux $\tilde{\Phi}_{0m}$ in Eq. (70). (Source: Reprinted with permission from [3]. © 1996 American Physical Society.)

are smeared out and simultaneously the difference ΔH_n strongly increases. The radii of the antidots are sufficiently large, so that the nominal calculated saturation number [95] $n_s = r/2\xi(T) \approx 3.3$ for Pb/Ge multilayers at $T = 6$ K ($T_c \approx 6.9$ K) and $n_s \approx 2$ for WGe single films at $T = 4.45$ K ($T_c \approx 4.53$ K). In this case, we can assume that cusplike $M(H, T_c)$ anomalies are related to the formation of the multiquanta vortex lattices. One should keep in mind that n_s calculated previously is only a rough estimate of the saturation number because it was derived in the limit of FLs interacting with a *single* microhole [95]. Later, we shall be able to demonstrate, however, that the assumption of the existence of multiquanta vortex lattices is fully supported by a quantitative description of the whole magnetization curve.

Let us consider first the situation when all vortices are trapped by the antidots and, as a result, there are no interstitial vortices. We begin with the estimate of the temperature-dependent penetration length $\Lambda = 2\lambda^2/\tau$ (where λ is the penetration depth and τ the total thickness of the film). The estimate of Λ shows that in this case $\Lambda(T = 6\text{ K}) \approx 5.8\ \mu\text{m} \gg d = 1\ \mu\text{m}$. This Λ value can be even further increased because of the renormalization of the penetration depth in perforated films, where superconducting volume corrections have to be taken into account [139]. Because $\Lambda \gg d$, the approximation $B =$ constant (here B is to be averaged at least over several unit cells) can be used to find the magnetization M of the superconductor with the antidot lattice in the field range $H < H_1$ at temperatures quite close to T_c.

There are at least two arguments in favor of the $B =$ constant approximation [3]. The first one is the particular profile of the calculated field distribution in thin superconducting specimens [140]. For very large Λ, the field inside the specimen is constant everywhere, except at the edges and the center. This field distribution provides a constant field not in the whole sample but at least in a very large part of its area. The second argument in favor of the approximation $B(x) =$ constant is based on the possibility of the existence of a single-terrace critical state in superconducting films with antidot lattices. Indeed, according to

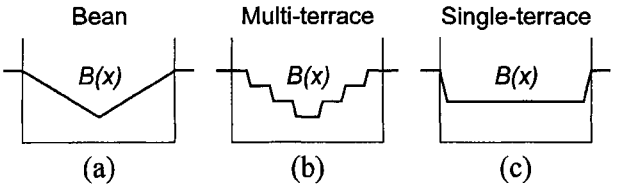


Fig. 51. Field penetration according to (a) the classical Bean model [142], (b) the multiterrace critical state [141], and (c) the single-terrace critical state. The slopes between terraces correspond to the depairing current. (Source: Reprinted with permission from [3]. © 1996 American Physical Society.)

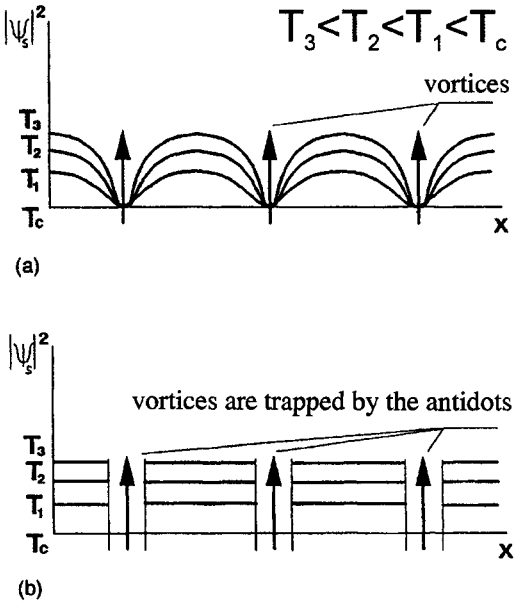


Fig. 52. The $|\Psi_s|$ modulation at different temperatures in a homogeneous superconductor in the mixed state (a) and in a superconductor with an antidot lattice (b).

Cooley and Grishin [141], the classical Bean model [142] (Fig. 51a) should be substantially modified for superconductors with a regular array of artificial pinning centers that favor a certain integer number of flux quanta pinned by each antidot. In this case, instead of a smooth sand-hill-like critical $B(x)$ profile (Fig. 51a), a multiterrace critical state with several well-defined plateaus, each having its own fixed induction $B(x) = \text{constant}$, has been predicted (Fig. 51b) [141]. The multiterrace critical state is, in a way, a quantized version of the classical Bean model [3]. The field profile with well-defined terraces is a compromise between a tendency to trap the same number $n\Phi_0$ of flux quanta by each antidot and a formation of a certain average Bean-like $B(x)$ slope. Close to T_c ($T_c - T \approx 1$ K), the latter can be quite small and then an ultimate limit of the multiterrace critical state—a single-terrace critical state (Fig. 51c)—could be established [3]. This state, especially exactly at matching fields, implies the flat field penetration profile $B(x) = \text{constant}$ may be realized in the whole sample, except its surface layer.

The next important step toward the understanding of magnetization of a sample with the multiquanta vortices can be made by taking into account a possible expansion of the London limit $|\Psi_s| = \text{constant}$ in superconducting films with antidot lattices [3]. Indeed, in homogeneous superconductors in the vicinity of the upper critical field $H_{c2}(T)$, the superconducting order parameter $\Psi_s = |\Psi_s|e^{i\varphi}$ nucleates with a very strong $|\Psi_s|$ modulation (Fig. 52a), in agreement with the classical Abrikosov model [143]. Because of this modu-

lation, the London limit can normally be used only in the range $H_{c1} \ll H \ll H_{c2}$, that is, well below the $H_{c2}(T)$ line. Contrary to that, in a superconductor with an antidot lattice, by making antidots exactly at the expected positions for the penetration of vortices, we are "helping" the superconducting order parameter to nucleate in a different way (Fig. 52b). In this case, we are forcing $|\Psi_s|$ to be nearly constant in the space between antidots, because, owing to boundary conditions at the superconductor–insulator interface [23], the surface $|\Psi_s|$ = constant can cross the cylinders, corresponding to the antidot boundaries, only at the angle 90°. Moreover, when FLs are guided to penetrate through the antidots, there is no need to create additional zeros of $|\Psi_s(r)|$ (and therefore strong $|\Psi_s|$ modulation) anywhere else. These arguments make it possible to foresee *a broader range of validity of the London limit* $|\Psi_s|$ = constant *in films with an antidot lattice.*

Following Moshchalkov et al. [3], we take into consideration the two important assumptions, B = constant and $|\Psi_s|$ = constant, and use the textbook expression for magnetization [23] with a simple substitution $\xi(T) \to r_a$ for the core radius:

$$M(H) = -\frac{\Phi_0}{4\pi\mu_0\Lambda^2}\ln\left(\frac{\beta a_v}{\sqrt{e}r_a}\right) \tag{67}$$

where a_v is the distance between Φ_0 vortices and β is a numerical constant; for a triangular vortex lattice in unperforated films, $\beta = 0.381$ [23].

First, let us consider a very interesting situation, which occurs exactly at the matching fields $H = H_n$, when we expect that the FL lattice consists of only one type of vortex, namely, $n\Phi_0$ vortices forming a regular array coinciding with the antidot lattice. In this case, in Eq. (67) $n\Phi_0$ should be used instead of Φ_0 and $a_v = d$:

$$M(H_n) = -\frac{n\Phi_0}{4\pi\mu_0\Lambda^2}\ln\left(\frac{\beta d}{\sqrt{e}r_a}\right) \propto \frac{n\Phi_0}{\Lambda^2} \tag{68}$$

The difference $M(H_n) - M(H_{n-1}) \propto -\Phi_0/\Lambda^2$ is independent of n and is determined only by Λ. All other parameters in Eq. (68) are known. Therefore, at $H = H_n$, the linear behavior of $M(H_n)$ as a function of the integer n should be seen. This behavior is in a very good agreement with the observed $M(H_n)$ variation at different temperatures (see the dashed lines in Figs. 53 and 54). The slope of the dashed lines nicely follows the expected temperature variation of $1/\Lambda^2 \propto (1 - T/T_c)^2$ (inset of Figs. 53 and 54). The two-fluid model $1/\Lambda^2 \propto (1 - (T/T_c)^4)^2$ also gives a good fit, but the Ginzburg–Landau relation $\lambda(T) \propto 1/\sqrt{1 - T/T_c}$ or $1/\lambda^2 \propto 1 - T/T_c$ provides a better linearity of the slope $\Delta M/\Delta H$ versus T (see inset of Figs. 53 and 54).

The cusps at $H = H_n$ then can be considered as analogs of the well-known $M(H)$ anomaly at H_{c1} but this time for the onset of penetration of $2\Phi_0, 3\Phi_0, \ldots, (n+1)\Phi_0$ vortices at $H_1, H_2, \ldots, H_n$, respectively. Indeed, the expected lower critical fields $H_{c1}(n\Phi_0)$ are

$$H_{c1}(n\Phi_0) = \frac{n\Phi_0}{4\pi\mu_0\Lambda^2}\ln\frac{\Lambda}{r_a} \tag{69}$$

The estimate based on Eq. (69) gives very low fields $\mu_0 H_{c1}(n\Phi_0) \approx 10^{-1}$ mT$\ll \mu_0 H_n$, which implies that the difference between $H - H_n - H_{c1}[(n+1)\Phi_0]$ and $H - H_n$ can be neglected and, therefore, one should see the logarithmic behavior $M(H) \propto -\ln(H - H_n)$ (valid for $H \gg H_{c1}$ in the London limit) in magnetic fields $H_n < H < H_{n+1}$, that is, between the matching fields. Such behavior is indeed fully supported by the experimental data [3] (Figs. 49b and 50b). This behavior is a result of inserting the relation $a_v \simeq [\Phi_0/(H - H_n)]^{1/2}$ into Eq. (67), which is a good approximation in fields $H_n < H < H_{n+1}$ for a $(n+1)\Phi_0$ vortex–vortex distance in a superconductor with an antidot lattice. In this interval, the vortex–vortex interaction terms U_{ij} [Eq. (25)] in the Gibbs potential are represented by different contributions arising from the presence of two types of vortices: $n\Phi_0$ and $(n+1)\Phi_0$. Instead of the usual $\Phi_0 \times \Phi_0$ product, these terms will contain other products: $n\Phi_0 \times n\Phi_0$, $n\Phi_0 \times (n+1)\Phi_0$, and $(n+1)\Phi_0 \times (n+1)\Phi_0$ [23]. As a result, in the

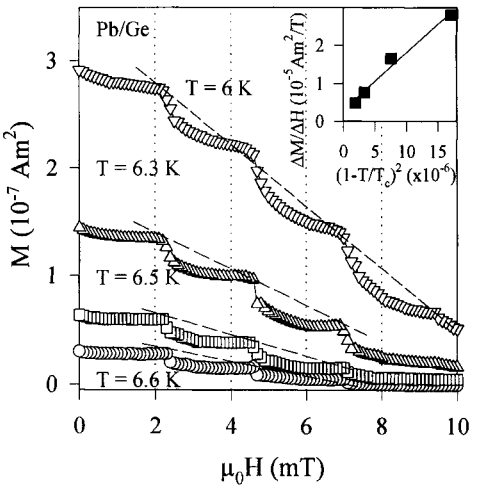


Fig. 53. Magnetization loops $M(H)$ for positive M and H at different temperatures for the [Pb(10 nm)/Ge(5 nm)]$_2$ multilayer with an antidot lattice. The dashed lines, at different temperatures, clearly indicate the linear behavior of $M(H_n)$ as a function of the integer n. The inset presents the slopes $\Delta M/\Delta H$ of the dashed lines, as a function of $[1-(T/T_c)]^2$. According to Eq. (68), these slopes follow the temperature dependence of $1/\Lambda^2$. The solid line presents the linear fit. (Source: Reprinted with permission from [3]. © 1996 American Physical Society.)

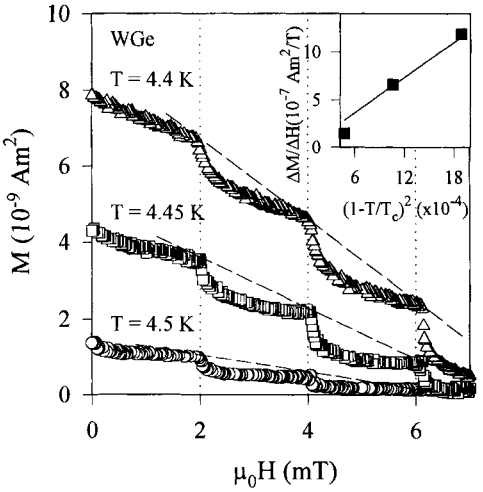


Fig. 54. Magnetization loops $M(H)$ for positive M and H at different temperatures for a WGe(60 nm) single film with an antidot lattice. The dashed lines, at different temperatures, clearly indicate the linear behavior of $M(H_n)$ as a function of the integer n. The inset presents the slopes $\Delta M/\Delta H$ of the dashed lines, as a function of $[1-(T/T_c)]^2$. According to Eq. (68), these slopes follow the temperature dependence of $1/\Lambda^2$. The solid line presents the linear fit. (Source: Reprinted with permission from [3]. © 1996 American Physical Society.)

interval between the matching fields, H_n and H_{n+1}, magnetization of the superconducting films with an antidot lattice should follow the logarithmic dependence:

$$M(H_n < H < H_{n+1}) \approx -\frac{\tilde{\Phi}_{0n}}{4\pi\mu_0\Lambda^2}\ln\left[\frac{\beta_{\text{eff}}}{\sqrt{e}r_a}\left(\frac{\Phi_0}{\mu_0(H-H_n)}\right)^{1/2}\right] \tag{70}$$

Here $\tilde{\Phi}_{0n}$ is an effective flux and β_{eff} an effective parameter appearing because of the summation of different terms in the vortex–vortex interactions U_{ij} over vortex posi-

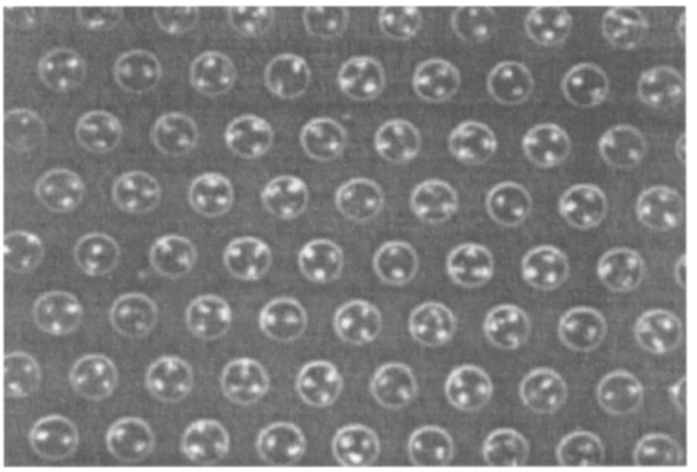


Fig. 55. Magnetic decoration of the admixture of $2\Phi_0$ and $3\Phi_0$ multiquanta vortices in the Nb film with a triangular lattice of blind antidots. (Source: Adapted from [4].)

tions i and j on the antidot lattice. For H not far from H_n, we may approximate $\tilde{\Phi}_{0n}$ as $\sqrt{n(n+1)}\Phi_0$.

Plotting M versus $\ln(H - H_n)$ (Fig. 53), from the logarithmic behavior of the magnetization (Fig. 49), the slopes of the M versus $\ln(H - H_n)$ lines defining the effective flux $\tilde{\Phi}_{0n}$ can be determined. For a triangular antidot lattice, stabilizing the multiquanta vortices, we have $\tilde{\Phi}_{01}/\Phi_0 = 1$; $\tilde{\Phi}_{02}/\Phi_0 = 1.79$; $\tilde{\Phi}_{03}/\Phi_0 = 2.45$; $\tilde{\Phi}_{04}/\Phi_0 = 2.72$, for $H_0 < H < H_1$, $H_1 < H < H_2$, $H_2 < H < H_3$, respectively. The numbers 1.79, 2.45, and 2.72 have to be compared with 1.41, 2.45, and 3.46 estimated from $[\sqrt{n(n+1)}\Phi_0]/\Phi_0$. Therefore, besides a logarithmic dependence itself, we also see a very reasonable variation of an effective parameter $\tilde{\Phi}_{0n}$ in different field intervals ($H_n < H < H_{n+1}$) with n not exceeding the saturation number n_s. At higher temperatures, the simple argument that $\tilde{\Phi}_{0n}$ should scale as $\sqrt{n(n+1)}\Phi_0$ fails, because $\lambda(T)$ is spread over many periods and U_{ij} terms, corresponding to $n\Phi_0 \times (n+1)\Phi_0$ and $(n+1)\Phi_0 \times (n+1)\Phi_0$, should be optimized numerically. These terms can also explain a small increase of magnetization when H is approaching the matching fields from below (see Fig. 49a).

We also note that the stabilization of the FL by the antidot lattice has resulted in a remarkable collective $M(H)$ behavior, typical for the presence of an $n\Phi_0$-FL lattice at $H = H_n$ ($n < n_s$) and a mixture of $n\Phi_0$ and $(n+1)\Phi_0$ vortices between the matching fields $H_n < H \leqslant H_{n+1}$.

The admixture of the $2\Phi_0$ and $3\Phi_0$ multiquanta vortices can be clearly seen in Figure 55, where the results of the magnetic decoration of the lattice of "blind" antidots [144] are presented. Blind antidots help to resolve the n individual Φ_0 vortices at the continuous bottom layer of a blind microhole, formed by trapping an $n\Phi_0$ multiquanta vortex by the antidot above the layer. This trick makes it possible to visualize an $n\Phi_0$ multiquanta vortex as a collection of n single quantum vortices [144].

Because of the introduction of the well-defined pinning potential, it is possible to obtain in a multiple-connected superconductor with an antidot lattice the logarithmic irreversible magnetization behavior that is normally observed as a reversible magnetization of the Abrikosov FL lattice in homogeneous superconductors in fields $H \gg H_c$. The irreversibility of the magnetization of the perforated film is possibly caused by its multiple connectivity. The superconducting currents flowing around antidots are similar to a supercurrent in a ring. As it has been already emphasized by Shoenberg quite some time ago (see, e.g., [145] and the references therein), a ring, as a multiply connected body, demonstrates a strong irreversible magnetization response.

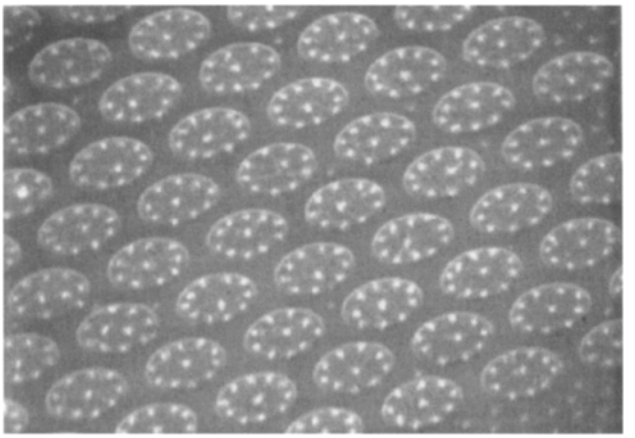


Fig. 56. Magnetic decoration of the 10-quanta vortices in a Nb film with a triangular lattice of relatively large blind holes. (Source: Adapted from [146].)

The successful interpretation of all specific features of the magnetization loops for films with an antidot lattice (Figs. 49a and 50a) gives a strong support of the assumption of the existence of the multiquanta vortex lattices. Recent magnetic decoration experiments [4] have convincingly and directly confirmed the stabilization of multiquanta vortices by the relatively large antidots (see Figs. 55 and 56). In these experiments, the use of "blind holes" has made it possible to decorate the multiquanta vortices at antidots and thus to count the number of flux quanta trapped by each antidot. Direct experimental observation of multiquanta vortex lattices [144] with no vortices pinned at the interstices confirms the conclusions based on the analysis of the magnetization data [3, 86, 87].

Figure 56 presents a beautiful example of the visualization of $10\Phi_0$ multiquanta vortices by magnetic decoration of a lattice of blind holes made in epitaxial Nb films.

4.4.1. Magnetization Curves for Different Antidot Diameters

The main experimental observations [1–3, 86, 87, 114, 132, 144] can be summarized as follows: (a) artificial arrays of submicrometer antidots can act as well-defined pinning centers with a controlled size and pattern; (b) distinct matching anomalies show up at the expected fields $\mu_0 H_n = n\Phi_0/S$, where S is the unit cell of the antidot lattice; (c) increasing the antidot diameter, clear evidence of a stronger pinning by square and triangular arrays consisting of antidots larger than $\xi(T)$ was found; and (d) similar size dependence of the pinning force is observed as well in other superconducting films, such as Pb and WGe films.

At the typical used reduced temperature $T/T_c = 0.94$ (Fig. 57), we have $\xi(T) \approx 0.1\ \mu$m. Therefore, the radius $r_a \approx 0.075\ \mu$m of the smaller antidots is quite close to $\xi(T)$ and should give the optimum pinning, if the condition $\xi(T) \approx 2r_a$ is correct in this case and the core pinning potential U_p plays a dominant role. Because for larger antidots pinning has been further enhanced, we are sure that for antidots with $2r_a \gg \xi(T)$ pinning is much stronger than that for $2r_a \approx \xi(T)$. The latter confirms that electromagnetic pinning U_p indeed gives an important contribution: According to Takezawa and Fukushima [128], the depth of U_p increases rapidly with r_a and saturates at $2r_a \approx \lambda(T)$. Unfortunately, further quantitative comparison with the theory of Takezawa and Fukushima [128] is not possible, because they have calculated the pinning potential but not the pinning force and, secondly, they have considered the limit of a single pinning center, whereas in this case the circular currents around different antidots are overlapping. In these films $\Lambda = 2\lambda^2(T)/\tau > d$. Here τ is the thickness of an individual Pb layer or the whole multilayer for decoupled or coupled superconducting layers, respectively. In these films, we have $\Lambda > d$, and, for

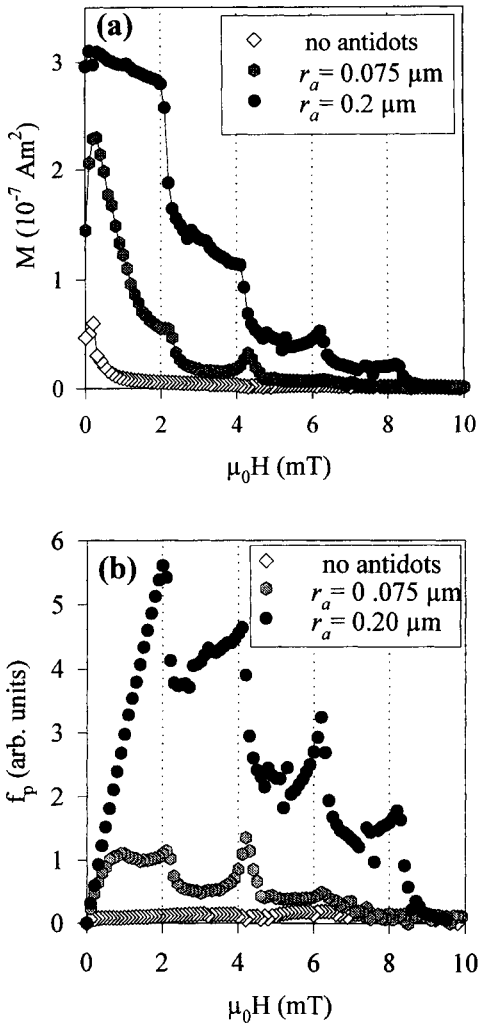


Fig. 57. (a) Magnetization curves ($T = 0.94T_c$) of the [Pb(15 nm)/Ge(14 nm)]$_3$ multilayer with a square lattice of antidots with radius $r_a = 0.075$–0.2 μm. For comparison, the data for the reference multilayers without antidots are also shown. The matching fields $\mu_0 H_n \approx n \times 2.07$ mT (where n is an integer) are indicated by dashed lines. (b) Pinning force ($T = 0.94T_c$) of the [Pb(15 nm)/Ge(14 nm)]$_3$ multilayer with a square lattice of antidots with radius $r_a = 0.075$–0.2 μm. For comparison, the data for the reference multilayers without antidots are also shown. The matching fields $\mu_0 H_n \approx n \times 2.07$ mT are indicated by dashed lines. (Source: Reprinted with permission from [87]. © 1998 American Physical Society.)

qualitative analysis of the data, lattice effects should be taken into consideration in calculations of U_p, which has not been done in [128].

The sharp magnetization anomalies at the matching field were nicely reproduced in the calculations of Cooley and Grishin [141], who showed that the appearance of the terrace critical state (Fig. 51b) results in magnetization jumps with the periodicity corresponding to Φ_0 per antidot lattice unit cell.

For small antidot radii ($n_s \approx 1$), a substantial reduction of j_c can occur when the antidots are saturated [147] and additional vortices are formed at the interstices. In this case, very weakly pinned interstitial vortices are much more mobile than the vortices pinned by the antidots [133]. As a result, the motion of interstitial vortices leads to dissipation and j_c is reduced. The dynamics and plastic flow of vortices in superconductors with coexisting interstitial FLs and vortices pinned by antidots has been recently studied by Reichhardt

et al. by numerical simulations [148]. Because of a higher mobility of interstitial vortices, larger antidots seem to be better since they can stabilize multiquanta vortices and then there is no need to have loosely bound interstitial vortices.

Concluding, we have shown that antidots with $2r_a$ considerably larger than the coherence length $\xi(T)$ are efficient pinning centers. This conclusion is valid for different superconductors. As a possible explanation for the stronger pinning by larger antidots, we refer to the electromagnetic contribution to pinning, U_p, recently analyzed by Takezawa and Fukushima [128].

4.4.2. Composite Vortex Lattices

The saturation number $n_s = r_a/2\xi(T)$ can be varied by changing both the size of the antidots and the temperature, because the coherence length $\xi(T)$ increases substantially when $T \to T_c$. Therefore, even for a fixed antidot radius r_a, different types of vortex lattices can be realized by tuning the temperature into a proper interval and thus changing n_s. The formation of a composite vortex lattice with $n_s = 2$ ($2\Phi_0$ vortices at antidots and Φ_0 vortices at interstitials) is illustrated by Figure 58, where the coexistence of these two different types of vortices is clearly seen.

We analyze now the magnetization data taken at $T = 6$ K (Fig. 59), when the width of the hysteresis loop $M(H)$ has made it possible to observe a finite loop width in a much broader field range—up to 20 mT. The $M(H)$ curve for the films with an antidot lattice demonstrates, as we have already seen before, four successive cusplike anomalies at $H = H_1, \ldots, H_4$ corresponding to the formation of multiquanta vortex lattices carrying $\Phi_0, \ldots, 4\Phi_0$ flux quanta.

Therefore, it is reasonable to assume that in this case the saturation number is at least four, which is close to the value expected from the calculated ratio $r_a/2\xi(T) \approx 3.3$ at $T = 6$ K. However, in higher fields, at $H = H_5$, the next matching anomaly does not show up (see the vertical arrow in Fig. 59). This "mysterious" disappearance of the matching cusp can be interpreted as an indication of the onset of pinning of vortices by interstices. Indeed, the position "I_2" in the center of the parallelogram $A_1A_2A_3A_4$ (see inset of Fig. 59) formed by the antidots is a saddle point in the pinning potential produced by the antidots A_1–A_3 (see Fig. 60c). As a result, interstitial flux lines will be pinned at the two equivalent positions I_1 and I_3 corresponding to the two minima of the pinning potential. The number

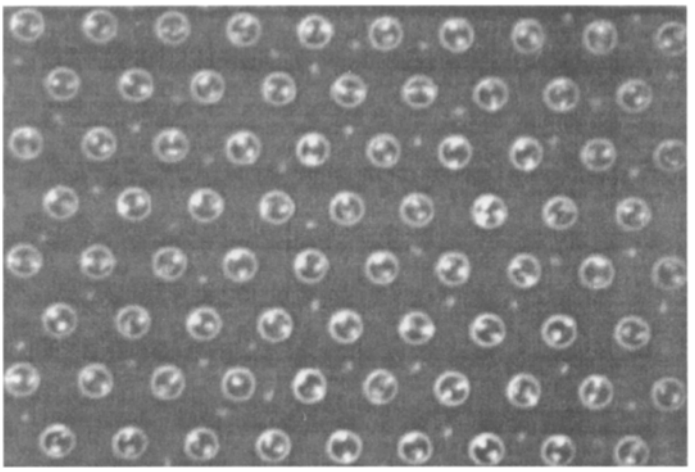


Fig. 58. Magnetic decoration pattern illustrating the coexistence of $2\Phi_0$ vortices at blind antidots and Φ_0 vortices at interstitial positions in a Nb film with a triangular lattice of blind antidots. (Source: Adapted from [4].)

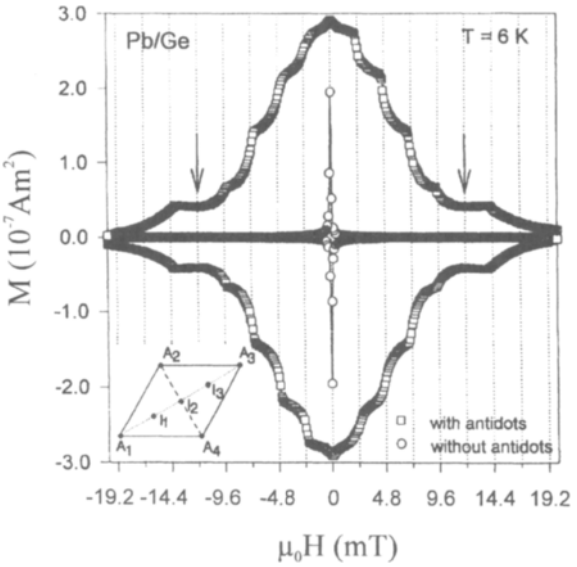


Fig. 59. Magnetization loop $M(H)$ at $T = 6$ K of a [Pb(10 nm)/Ge(5 nm)]$_2$ multilayer with and without the antidot lattice measured in a broad field range. The inset shows the parallelogram $A_1A_2A_3A_4$ formed by the antidots. Interstitial flux lines will be pinned at positions I_1 and I_3. (Source: Reprinted with permission from [3]. © 1996 American Physical Society.)

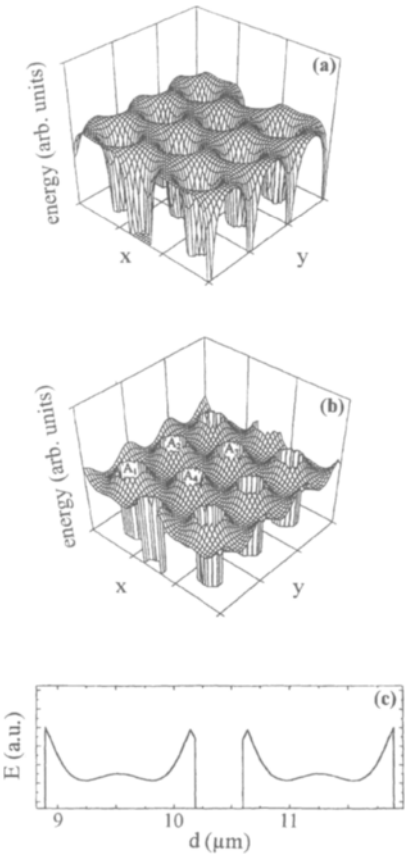


Fig. 60. Energy surface for one flux line in the antidot lattice, which was calculated with the following parameters: $\kappa = 15$, $d = \lambda$, and $r_a = 0.2$ μm for (a) empty antidots and (b) saturated antidots. In these calculations, we have used the procedure described in [117]. A line cut connecting the points A_1A_3 of the energy surface is shown in (c). (Source: Reprinted with permission from [3]. © 1996 American Physical Society.)

of flux lines required to fill in the antidot lattice all positions of the type I_1 and I_3 is twice as large as the number of antidots. All interstitial positions I_1 and I_3 will only be filled by FLs at $H = H_6$, leading to a cusp at H_6 (Fig. 59). This explains the "mystery" of the missing $M(H)$ cusp at $H = H_5$ (Fig. 59) and gives strong evidence that at $H = H_4$ antidots are indeed saturated, that is, at $T = 6$ K, $n_s = 4$.

On the other hand, the presence of interstitial vortices can also be detected from a change of the effective flux, $\tilde{\Phi}_{0m}$, which is given by the slope of the M versus $\ln(H - H_n)$ curve [see Eq. (70)]. By comparing the slopes of these plots for the different field intervals $H_n < H < H_{n+1}$, the presence of interstitials is revealed by a changed slope in the interval $H_{n_s} < H < H_{n_s+1}$ [3].

The assigned saturation number $n_s = 4$ at $T = 6$ K can also be checked by investigating the variation of the sequence of matching anomalies in magnetization curves at different temperatures. For a triangular antidot lattice, the saturation number n_s simply defines the cusplike matching anomaly at $H = H_{n_s}$ followed by the missing cusp at $H = H_{n_s+1}$. Therefore, the decrease in n_s caused by the increase of $\xi(T)$ at higher temperatures should also lead to a shift of the missing $M(H)$ cusp at H_{n_s+1}. Figure 61a ($T = 6.5$ K, $n_s = 3$) and Figure 61b ($T = 6.7$ K, $n_s = 2$) convincingly demonstrate that this is indeed the case. At $T = 6.5$ K, there is no matching peak at H_4 (therefore, $n_s = 3$) and then, at $T = 6.7$ K, a very sharp cusp at H_2 precedes a missing cusp at H_3 ($n_s = 2$). The variation of n_s with temperature is summarized in Figure 62 where the temperature dependence of n_s correlates well with the temperature dependence of $1/\xi(T) \propto (1 - T/T_c)^{1/2}$ (dashed line).

The pinning potential at antidots and at interstices is very different (Fig. 60) and it is also very sensitive to the temperature variation. As a result, as $T \to T_c$, the minima of the pinning potential at interstices become so shallow that they cannot pin any longer the interstitial vortices [2], which will then form an interstitial flux fluid. Therefore, by changing the temperature, one can induce at interstices the crossover from a flux solid to a flux fluid, thus realizing the multistage melting.

Summarizing, we would like to emphasize the unique possibilities of stabilizing novel flux phases in superconducting films by making regular arrays of pinning centers (in our case, antidots). These phases are:

1. *Multiquanta vortex lattices.* These can be realized if the antidots are sufficiently large and the field does not exceed the value H_{n_s} defined by the saturation number n_s.
2. *Composite flux lattices.* These flux lattices are observed when the normalized radii of the antidots $r_a/2\xi(T)$ are sufficiently small and H exceeds the limiting field H_{n_s}. Also the pinning potential at interstices should not be very shallow to provide a weaker, but still sufficient pinning to form a softer interstitial flux solid. The composite flux lattices are characterized by the coexistence of the two weakly and strongly pinned interpenetrating flux lattices at interstices (Φ_0 vortices) and antidots ($n\Phi_0$ vortices), respectively [1, 126].
3. *Multiquanta vortex lattices coexisting with the interstitial fluid of Φ_0 vortices.* This flux phase is formed when $T \to T_c$ and the interstitial pinning potential becomes very shallow and thus cannot prevent the melting of the caged interstitial pinning Φ_0 vortices. The melting transition as a function of magnetic field is then observed exactly at $H = H_{n_s}$. For example, in Figure 61b, $n_s = 2$ and a very abrupt first-order phase transition is observed at $H = H_2$, whereas, in Figure 30, $n_s = 1$ and the transition is observed at $H = H_1$. In other words, the homogeneous $n\Phi_0$ vortex solid with $n = n_s$ produces in this case only the $B =$ constant background while the melting of the interstitial Φ vortex phase causes the very sharp magnetization drop at $H = H_{n_s}$. The interstitial vortex fluid reversibly responds to the field variation and this results in a zero width of the hysteresis loop in fields $H > H_{n_s}$.

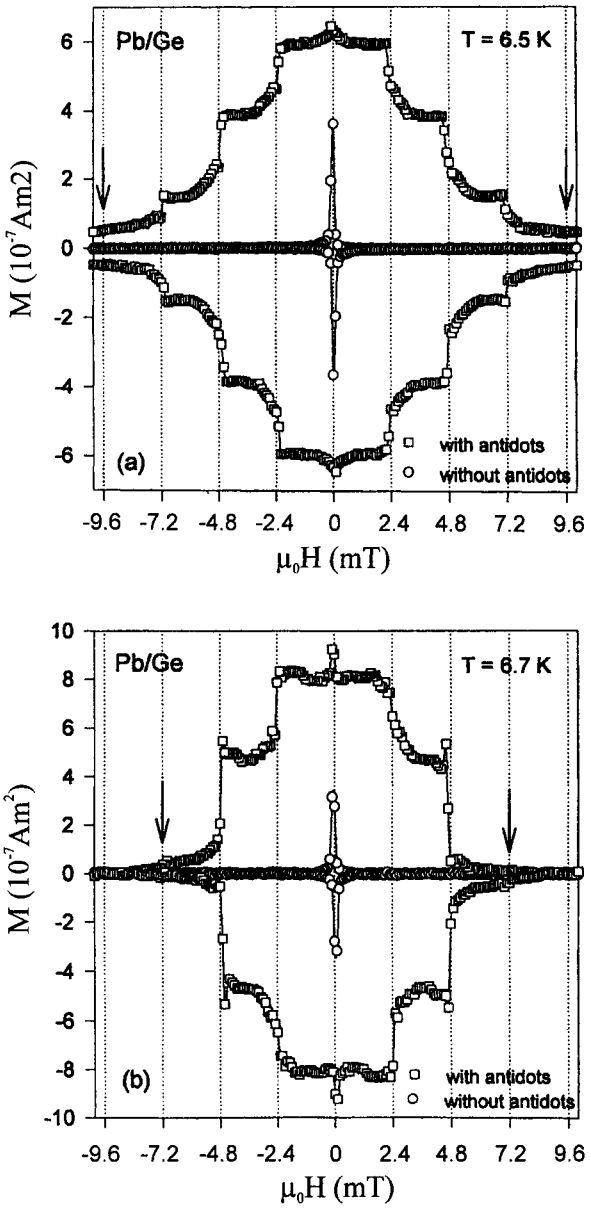


Fig. 61. Magnetization loop $M(H)$ of a [Pb(10 nm)/Ge(5 nm)]$_2$ multilayer with and without a (triangular) antidot lattice (a) at $T = 6.5$ K and (b) $T = 6.7$ K. The arrows indicate the missing $M(H)$ cusp. (Source: Reprinted with permission from [3]. © 1996 American Physical Society.)

The flux phases listed previously can exist at temperatures not too far from T_c, because at lower temperatures the tendency to form a conventional Bean profile (Fig. 51a) starts to dominate and matching anomalies are suppressed; for example, for Pb/Ge, any $M(H)$ matching anomalies below 5 K can barely be seen.

4.5. Crossover from a Pinning Array to a Network ($n_s \gg 1$)

The systematic measurements of the efficiency of antidots, as artificial pinning centers, as a function of their radius r_a (Fig. 63) have revealed [87] that for core pinning combined with the electromagnetic pinning the optimum size of the antidots is not $\xi(T)$ at all, but

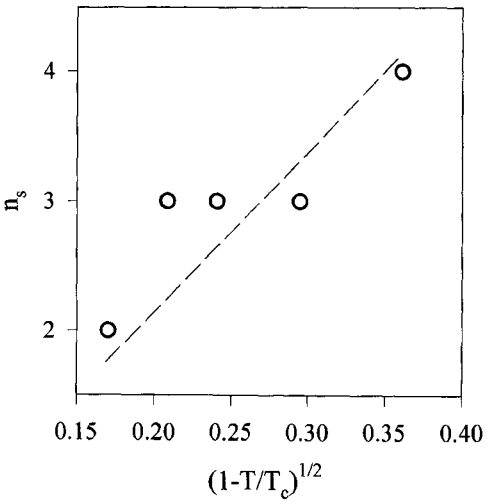


Fig. 62. Variation of the saturation number n_s with temperature. The temperature dependence of n_s correlates with the temperature dependence of $1/\xi(T) \propto (1 - T/T_c)^{1/2}$ (dashed line). (Source: Reprinted with permission from [3]. © 1996 American Physical Society.)

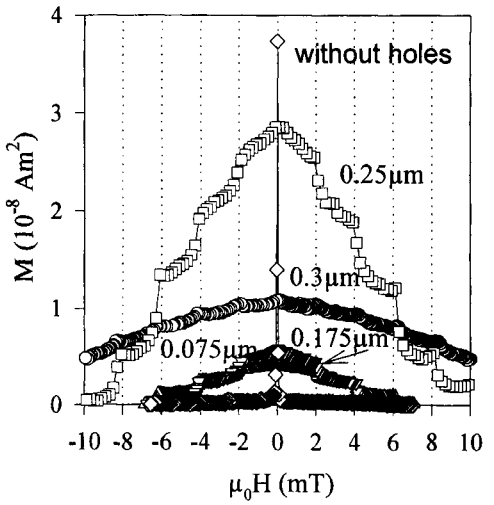


Fig. 63. Magnetization curves ($T = 0.98T_c$) of a single WGe(60 nm) film with a square lattice of antidots with radius $r_a = 0.075$–0.3 μm. For comparison, the data for the reference multilayers without antidots are also shown. The matching fields $\mu_0 H_n \approx n \times 2.07$ mT (where n is an integer) are indicated by dashed lines. (Source: Reprinted with permission from [87]. © 1998 American Physical Society.)

rather $2r_a \gg \xi(T)$ [87, 132]. As a result, the highest critical currents have been obtained for the multiquanta vortex lattices that can be stabilized by these sufficiently large antidots, because their saturation number is $n_s \approx r_a/2\xi(T) \gg 1$. At the same time, it is quite evident that by increasing the antidot diameter we are inducing a crossover to another regime (Fig. 64) when eventually $2r_a$ becomes nearly the same as the antidot lattice period d. In this case, the width of the superconducting strips w between the antidots is so small that at temperatures not too far below T_c the superconducting network regime $w \leqslant \xi(T)$ can be realized. For this regime, the M versus H curves are characterized by the presence of sharp peaklike anomalies at integer matching fields H_n (Fig. 64) and a reproducible structure between H_n, which may correspond to rational matching peaks. Both integer and rational

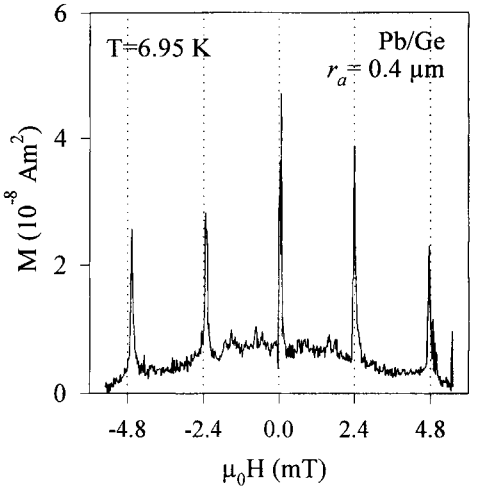


Fig. 64. Upper magnetization curve at $T = 6.95$ K of the [Pb(15 nm)/Ge(14 nm)]$_3$ multilayer with a triangular antidot lattice ($r_a = 0.4$ μm). (Source: Reprinted with permission from [87]. © 1998 American Physical Society.)

matching peaks have been observed before in various superconducting networks [19] and Josephson networks [149]. Visually, the $M(H)$ curves in the *network regime* are quite different from those in the *multiquanta vortex regime*. The former demonstrate the $M(H)$ peaks at $H = H_n$ (Fig. 64), while the latter show pronounced cusps at integer matching fields (Fig. 65b).

In the regime of a superconducting network, critical currents in moderate fields are already smaller than for the regime of the multiquanta vortex lattices (see Fig. 63). At higher fields, however, at least for the radius $r_a = 0.3$ μm, critical currents are higher for the largest studied antidot diameter, that is, *the optimum antidot size for pinning is field dependent*. The reduction of the width of the superconducting "stripes" between the antidots, needed to obtain high j_c in high fields, reflects actually a well-known designer rule for making superconducting cables, which usually consist of a bunch of very fine superconducting filaments embedded into a normal metallic matrix. Therefore, *the optimum size* of the pinning centers turns out to be *field dependent*. Smaller antidots are more efficient in low fields, while in higher fields larger antidots are needed to optimize j_c.

Summarizing the analysis of multiquanta vortices, it is worth noting that a superconducting film with a lattice of relatively large antidots seems to demonstrate the single-terrace critical state that appears because of the multiple connectivity of the film and the stabilization of the $n\Phi_0$ flux lattices. *The separation of the areas where flux penetrates from those where the superconducting order parameter nucleates provides a kind of a "peaceful coexistence" of FLs pinned by antidots with the superconducting condensate in the space between them. Fabricating an antidot lattice to let flux go through, we are thus helping the order parameter between the antidots to sustain much higher currents and magnetic fields.* The presence of the antidot lattice also broadens the validity of the London limit. Using the two essential assumptions, $B =$ constant (single-terrace critical state, especially at matching fields $H = H_n$) and $|\Psi_s| =$ constant, close to T_c, leads to a convincing quantitative description of the magnetization of the multiquanta vortex lattices, including linear behavior of $M(H)$ at matching fields $M(H_n) \propto -n\Phi_0/\Lambda^2$ and logarithmic behavior elsewhere: $M(H_n < H < H_{n+1}) \propto -\ln(H - H_n)$. By varying the saturation number $n_s = r_a/2\xi(T)$ through the use of a different $\xi(T)$, one can demonstrate that the missing matching cusp at $H = H_{n_s+1}$, signaling the onset of the formation of the interstitial vortices at $H > H_n$, is systematically shifted to lower matching fields as $T \to T_c$.

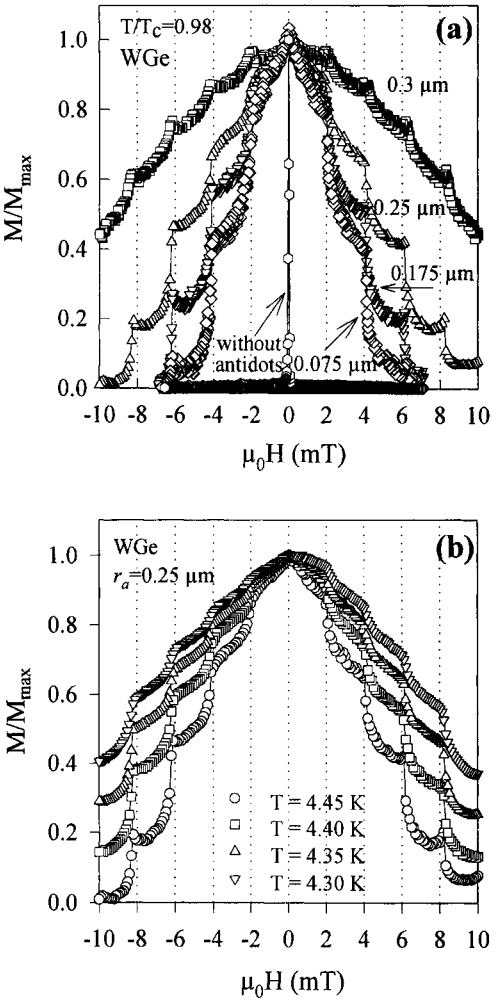


Fig. 65. (a) Normalized magnetization curves ($T = 0.98T_c$) of a single WGe(60 nm) film with a square lattice of antidots with radius $r_a = 0.075$–0.3 μm. For comparison, the data for the reference multilayers without antidots are also shown. The matching fields $\mu_0 H_n \approx n \times 2.07$ mT (where n is an integer) are indicated by dashed lines. (b) Magnetization curves at different temperatures of a single WGe(60 nm) film with a square lattice of antidots with radius $r_a = 0.25$ μm. The matching fields $\mu_0 H_n \approx n \times 2.07$ mT (where n is an integer) are indicated by dashed lines. (Source: Reprinted with permission from [87]. © 1998 American Physical Society.)

5. CONCLUSIONS

We have carried out a systematic analysis of quantization and confinement phenomena in nanostructured superconductors. The main idea of this study was to vary the boundary conditions for confining the superconducting condensate by taking samples of different topology and, through that, to modify the lowest Landau level $E_{LLL}(H)$ and, therefore, the critical temperature $T_c(H)$. Three different types of samples were used: (i) individual nanostructures (lines, loops, dots), (ii) clusters of nanoscopic elements—1D clusters of loops and 2D clusters of antidots, and (iii) films with huge regular arrays of antidots (antidot lattices). We have shown that in all these structures the phase boundary $T_c(H)$ changes dramatically when the confinement topology for the superconducting condensate is varied. The induced $T_c(H)$ variation is very well described by the calculations of $E_{LLL}(H)$ taking into account the imposed boundary conditions. These results convincingly demonstrate that the phase boundary $T_c(H)$ of nanostructured superconductors differs drastically from

that of corresponding bulk materials. Moreover, because, for a known geometry, $E_{LLL}(H)$ can be calculated a priori, the superconducting critical parameter, that is, $T_c(H)$, can be controlled by designing a proper confinement geometry. While before the optimization of the superconducting critical parameters has been done mostly by looking for different materials, we now have a unique alternative—to improve the superconducting critical parameters of *the same material* through the optimization of *the confinement topology* for the superconducting condensate and for the penetrating magnetic flux.

The critical current enhancement, resulting from the presence of the antidots, used as artificial pinning arrays, has been analyzed. Different pinning regimes can be clearly distinguished depending on the antidot size. For small antidots with a saturation number $n_s = 1$, the existence of the two species of vortices (weakly pinned at interstices and strongly pinned at antidots) should be taken into account. The motion of interstitial vortices gives rise to dissipation. To avoid dissipation and to obtain a further enhancement of j_c, larger antidots should be used. For these antidots, the saturation number becomes sufficiently large ($n_s \gg 1$) to stabilize the multiquanta vortex lattices. In this case, the highest enhancement factor for j_c can be obtained in moderate fields. The size of the antidots in this regime is considerably larger than $\xi(T)$ and, therefore, an electromagnetic contribution to pinning also plays an important role. However, the size of the antidots realizing the optimum pinning, turns out to be field dependent. For multiquanta vortex lattices, a simple approach has been applied, developed in the framework of the London limit. This approach gives an excellent fit of the $M(H, T)$ curves at different temperatures. This implies that by making antidot lattices one can substantially expand the area on the H–T plane where the London limit is still valid. In the same framework, the variation of such a fundamental parameter as $\lambda(T)$ can be achieved just by taking different antidot radii. The renormalization of $\lambda(T)$ is directly related to a different topology of films with an antidot lattice that makes the flux line penetration much easier. By a further increase of the antidot diameter, a crossover to the regime of superconducting networks can be induced, leading to the appearance of sharp $M(H)$ peaks at integer fields H_n, in contrast with the $M(H)$ cusps at H_n in the case of multiquanta vortex lattices. Finally, because the saturation number n_s, controlling the onset of different regimes (small n_s, composite flux lattices with vortices at antidots and interstices; large n_s, multiquanta vortex lattices; very large n_s, superconducting networks) is determined by the ratio $r_a/2\xi(T)$, the n_s value can be tuned not only by using different antidot radii r_a, but also by varying $\xi(T)$ by taking different temperatures. Controlling the periodic pinning potential through lateral nanostructuring, the critical current density $j_c(H)$ can be eventually enhanced up to the theoretical limit—the depairing current. Therefore, the two important superconducting critical parameters, $T_c(H)$ and $j_c(H)$, can be drastically improved by using the concept of "quantum design": creating the proper confinement topology for the superconducting condensate and the penetrating flux lines that optimizes $T_c(H)$ and $j_c(H)$.

Acknowledgments

The authors would like to thank E. Rosseel, M. Baert, K. Temst, T. Puig, V. Metlushko, C. Strunk, J. G. Rodrigo, X. Qiu, C. Van Haesendonck, A. López, H. Fink, S. Haley, A. Buzdin, J. Rubinstein, J. T. Devreese, V. Fomin, and F. Peeters for fruitful discussions. We are grateful to the Flemish Fund for Scientific Research (FWO), the Flemish Concerted Action (GOA), the Belgian Inter-University Attraction Poles (IUAP), the bilateral TOURNESOL 1998 program, the ESF Program VORTEX and the European Human Capital and Mobility (HCM) research programs for financial support. M. J. Van Bael is a Postdoctoral Research Fellow of the FWO-Vlaanderen.

References

1. M. Baert, V. V. Metlushko, R. Jonckheere, V. V. Moshchalkov, and Y. Bruynseraede, *Phys. Rev. Lett.* 74, 3269 (1995).
2. M. Baert, V. V. Metlushko, R. Jonckheere, V. V. Moshchalkov, and Y. Bruynseraede, *Europhys. Lett.* 29, 157 (1995).
3. V. V. Moshchalkov, M. Baert, V. V. Metlushko, E. Rosseel, M. J. Van Bael, K. Temst, R. Jonckheere, and Y. Bruynseraede, *Phys. Rev. B* 54, 7385 (1996).
4. A. Bezryadin and B. Pannetier, *J. Low Temp. Phys.* 102, 73 (1996).
5. V. V. Moshchalkov, V. Bruyndoncx, E. Rosseel, L. Van Look, M. Baert, M. J. Van Bael, T. Puig, C. Strunk, and Y. Bruynseraede, in "Lectures on Superconductivity in Networks and Mesoscopic Systems" (C. Giovannella and C. J. Lambert, eds.). American Institute of Physics, 1998.
6. C. S. L. Chun, G.-G. Zheng, J. L. Vicent, and I. K. Schuller, *Phys. Rev. B* 29, 4915 (1984).
7. K. Kanoda, H. Mazaki, N. Hosoito, and T. Shinjo, *Phys. Rev. B* 35, 6736 (1987).
8. V. I. Dediu, V. V. Kabanov, and A. S. Sidorenko, *Phys. Rev. B* 49, 4027 (1994).
9. H. K. Wong, B. Y. Jin, H. Q. Yang, J. B. Ketterson, and J. E. Hilliard, *J. Low Temp. Phys.* 63, 307 (1986).
10. P. Koorevaar, Y. Suzuki, R. Coehoorn, and J. Aarts, *Phys. Rev. B* 49, 441 (1994).
11. C. Strunk, C. Sürgers, U. Paschen, and H. von Löhneysen, *Phys. Rev. B* 49, 4053 (1994).
12. J. S. Jiang, D. Davidovic, D. H. Reich, and C. L. Chien, *Phys. Rev. Lett.* 74, 314 (1995).
13. Th. Mühge, N. N. Garif'yanov, Yu. V. Goryunov, G. G. Khaliullin, L. R. Tagirov, K. Westerholt, I. A. Garifullin, and H. Zabel, *Phys. Rev. Lett.* 77, 1857 (1996).
14. J. Aarts, J. M. E. Geers, E. Brück, A. A. Golubov, and R. Coehoorn, *Phys. Rev. B* 56, 2779 (1997).
15. J. E. Mattson, C. H. Sowers, A. Berger, and S. D. Bader, *Phys. Rev. Lett.* 68, 3252 (1992).
16. G. Verbanck, C. D. Potter, V. Metlushko, R. Schad, V. V. Moshchalkov, and Y. Bruynseraede, *Phys. Rev. B* 57, 6029 (1998).
17. Z. Radovic, L. Dobrosavljevic-Grujic, A. I. Buzdin, and J. R. Clem, *Phys. Rev. B* 44, 759 (1991).
18. K. Ensslin and P. M. Petroff, *Phys. Rev. B* 41, 12307 (1990); H. Fang, R. Zeller, and P. J. Stiles, *Appl. Phys. Lett.* 55, 1433 (1989); R. Schuster, K. Ensslin, D. Wharam, S. Kühn, J. P. Kotthaus, G. Böhm, W. Klein, G. Tränkle, and G. Weimann, *Phys. Rev. B* 49, 8510 (1994).
19. B. Pannetier, J. Chaussy, R. Rammal, and J. C. Villegier, *Phys. Rev. Lett.* 53, 1845 (1984).
20. A. A. Abrikosov, *Sov. Phys. JETP* 5, 1174 (1957); for a recent review see E. H. Brandt, *Rep. Prog. Phys.* 58, 1465 (1995).
21. See, for example, A. C. Rose-Innes and E. H. Rhoderick, "Introduction to Superconductivity." Pergamon Press, Oxford, U.K., 1978.
22. F. London and H. London, *Proc. R. Soc. London, Ser. A* 149, 71 (1935).
23. P. G. de Gennes, "Superconductivity of Metals and Alloys." Benjamin, New York, 1966.
24. C. P. Poole, Jr., H. A. Farach, and R. J. Creswick, " Superconductivity." Academic Press, San Diego, 1995.
25. V. V. Moshchalkov, *Solid State Commun.* 78, 711 (1991).
26. Y. B. Kim and M. J. Stephen, "Superconductivity" (R. D. Parks, ed.). Marcel Dekker, New York, 1969.
27. M. Tinkham, "Introduction to Superconductivity." McGraw–Hill, New York, 1975.
28. M. Cyrot and D. Pavuna, "Introduction to Superconductivity and High-T_c Materials." World Scientific, Singapore, 1992.
29. V. V. Moshchalkov, L. Gielen, C. Strunk, R. Jonckheere, X. Qiu, C. Van Haesendonck, and Y. Bruynseraede, *Nature* 373, 319 (1995).
30. M. Tinkham, *Phys. Rev.* 129, 2413 (1963).
31. J. Romijn, T. M. Klapwijk, M. J. Renne, and J. E. Mooij, *Phys. Rev. B* 26, 3648 (1982).
32. H. Welker and S. B. Bayer, *Akad. Wiss.* 14, 115 (1938).
33. W. A. Little and R. D. Parks, *Phys. Rev. Lett.* 9, 9 (1962); R. D. Parks and W. A. Little, *Phys. Rev. A* 133, 97 (1964).
34. R. P. Groff and R. D. Parks, *Phys. Rev.* 176, 567 (1968).
35. X. Zhang and J. C. Price, *Phys. Rev. B* 55, 3128 (1997).
36. R. Benoist and W. Zwerger, *Z. Phys. B* 103, 377 (1997).
37. H. J. Fink, A. López, and R. Maynard, *Phys. Rev. B* 26, 5237 (1982).
38. H. J. Fink, V. Grünfeld, and A. López, *Phys. Rev. B* 35, 35 (1987).
39. A. A. Abrikosov, "Fundamentals of the Theory of Metals." North-Holland, Amsterdam, 1988.
40. V. V. Moshchalkov, L. Gielen, M. Dhallé, C. Van Haesendonck, and Y. Bruynseraede, *Nature* 361, 617 (1993).
41. C. Strunk, V. Bruyndoncx, V. V. Moshchalkov, C. Van Haesendonck, Y. Bruynseraede, and R. Jonckheere, *Phys. Rev. B* 54, R12701 (1996).
42. P.-G. de Gennes, *C. R. Acad. Sci., Ser. II* 292, 279 (1981).
43. V. M. Fomin, V. R. Misko, J. T. Devreese, and V. V. Moshchalkov, *Solid State Commun.* 101, 303 (1997).
44. V. M. Fomin, J. T. Devreese, and V. V. Moshchalkov, *Europhys. Lett.* 42, 553 (1998); 46, 118 (1999).
45. E. M. Horane, J. I. Castro, G. C. Buscaglia, and A. López, *Phys. Rev. B* 53, 9296 (1996).

46. J. Berger and J. Rubinstein, *Phys. Rev. Lett.* 75, 320 (1995).
47. J. Berger and J. Rubinstein, *Philos. Trans. R. Soc. London, Ser. A* 355, 1969 (1997).
48. J. Berger and J. Rubinstein, *Physica C* 288, 105 (1997).
49. J. Berger and J. Rubinstein, *Phys. Rev. B* 56, 5124 (1997).
50. R. B. Dingle, *Proc. R. Soc. London, Ser. A* 211, 500 (1952).
51. V. V. Moshchalkov, M. Dhallé, and Y. Bruynseraede, *Physica C* 207, 307 (1993).
52. D. Saint-James, *Phys. Lett.* 15, 13 (1965); O. Buisson, P. Gandit, R. Rammal, Y. Y. Wang, and B. Pannetier, *Phys. Lett. A* 150, 36 (1990).
53. V. V. Moshchalkov, X. G. Qiu, and V. Bruyndoncx, *Phys. Rev. B* 55, 11793 (1996).
54. K. Nakamura and H. Thomas, *Phys. Rev. Lett.* 61, 247 (1988).
55. D. Saint-James, *Phys. Lett.* 16, 218 (1965).
56. V. V. Moshchalkov, L. Gielen, M. Baert, V. Metlushko, G. Neuttiens, C. Strunk, V. Bruyndoncx, X. Qiu, M. Dhallé, K. Temst, C. Potter, R. Jonckheere, L. Stockman, M. Van Bael, C. Van Haesendonck, and Y. Bruynseraede, *Phys. Scr. T* 55, 168 (1994).
57. P. S. Deo, V. A. Schweigert, F. M. Peeters, and A. K. Geim, *Phys. Rev. Lett.* 79, 4653 (1997).
58. V. A. Schweigert and F. M. Peeters, *Phys. Rev. B* 57, 13817 (1998).
59. J. J. Palacios, preprint, xxx.lanl.gov/cond-mat/9806056, 1998.
60. A. K. Geim, I. V. Grigorieva, S. V. Dubonos, J. G. S. Lok, J. C. Maan, A. E. Filippov, and F. M. Peeters, *Nature* 390, 259 (1997).
61. A. K. Geim, S. V. Dubonos, J. G. S. Lok, I. V. Grigorieva, J. C. Maan, L. Theil Hansen, and P. E. Lindelof, *Appl. Phys. Lett.* 71, 2379 (1997).
62. A. K. Geim, S. V. Dubonos, I. V. Grigorieva, J. G. S. Lok, J. C. Maan, X. Q. Li, and F. M. Peeters, *Superlattices Microstruct.* 23, 151 (1998).
63. A. I. Buzdin and J. P. Brison, *Phys. Lett. A* 196, 267 (1994).
64. V. Bruyndoncx, C. Strunk, V. V. Moshchalkov, C. Van Haesendonck, and Y. Bruynseraede, *Europhys. Lett.* 36, 449 (1996).
65. S. Alexander and E. Halevi, *J. Phys. (Paris)* 44, 805 (1983).
66. C. C. Chi, P. Santhanam, and P. E. Blöchl, *J. Low Temp. Phys.* 88, 163 (1992).
67. S. Alexander, *Phys. Rev. B* 27, 1541 (1983).
68. C. Ammann, P. Erdös, and S. B. Haley, *Phys. Rev. B* 51, 11739 (1995).
69. J. I. Castro and A. López, *Phys. Rev. B* 52, 7495 (1995).
70. R. D. Parks, *Science* 146, 1429 (1964).
71. J. Simonin, D. Rodrigues, and A. López, *Phys. Rev. Lett.* 49, 944 (1982).
72. H. J. Fink and S. B. Haley, *Phys. Rev. B* 43, 10151 (1991).
73. H. J. Fink and V. Grünfeld, *Phys. Rev. B* 31, 600 (1985).
74. H. J. Fink, O. Buisson, and B. Pannetier, *Phys. Rev. B* 43, 10144 (1991).
75. H. J. Fink, *Phys. Rev. B* 45, 4799 (1992); *Phys. Rev. B* 48, 3579 (1993).
76. S. B. Haley and H. J. Fink, *Phys. Lett. A* 102, 431 (1984).
77. H. J. Fink and S. B. Haley, *Phys. Rev. Lett.* 66, 216 (1991).
78. J. M. Simonin, C. Wiecko, and A. López, *Phys. Rev. B* 28, 2497 (1983).
79. T. M. Larson and S. B. Haley, *Physica B* 194–196, 1425 (1994).
80. T. M. Larson and S. B. Haley, *Appl. Supercond.* 3, 573 (1995).
81. T. M. Larson and S. B. Haley, *J. Low Temp. Phys.* 107, 3 (1997).
82. T. Puig, E. Rosseel, M. Baert, M. J. Van Bael, V. V. Moshchalkov, and Y. Bruynseraede, *Appl. Phys. Lett.* 70, 3155 (1997).
83. T. Puig, E. Rosseel, L. Van Look, M. J. Van Bael, V. V. Moshchalkov, Y. Bruynseraede, and R. Jonckheere, *Phys. Rev. B* 58, 5744 (1998).
84. E. Rosseel, T. Puig, M. Baert, M. J. Van Bael, V. V. Moshchalkov, and Y. Bruynseraede, *Physica C* 282–287, 1567 (1997).
85. A. F. Hebard, A. T. Fiory, and S. Somekh, *IEEE Trans. Magn.* 1, 589 (1977).
86. V. Metlushko, L. E. DeLong, M. Baert, E. Rosseel, M. J. Van Bael, K. Temst, V. V. Moshchalkov, and Y. Bruynseraede, *Europhys. Lett.* 41, 333 (1998).
87. V. V. Moshchalkov, M. Baert, V. V. Metlushko, M. J. Van Bael, K. Temst, R. Jonckheere, and Y. Bruynseraede, *Phys. Rev. B* 57, 3615 (1998).
88. A. Bezryadin and B. Pannetier, *J. Low Temp. Phys.* 98, 251 (1996); A. Bezryadin, A. Buzdin, and B. Pannetier, *Phys. Rev. B* 51, 3718 (1995).
89. M. J. Van Bael, Regular Arrays of Magnetic Dots and Their Flux Pinning Properties, Ph.D. Thesis, Katholieke Universiteit, Leuven, 1998.
90. J. I. Martín, M. Vélez, J. Nogués, and I. K. Schuller, *Phys. Rev. Lett.* 79, 1929 (1997).
91. B. Pannetier, in "Quantum Coherence in Mesoscopic Systems" (B. Kramer, ed.). Plenum Press, New York, 1991.
92. D. R. Hofstadter, *Phys. Rev. B* 14, 2239 (1976).
93. E. Rosseel, Critical Parameters of Superconductors with an Antidot Lattice, Ph.D. Thesis, Katholieke Universiteit, Leuven, 1998.

94. M. Giroud, O. Buisson, Y. Y. Wang, B. Pannetier, and D. Mailly, *J. Low Temp. Phys.* 87, 683 (1992); H. S. J. van der Zant, M. N. Webster, J. Romijn, and J. E. Mooij, *Phys. Rev. B* 50, 340 (1994).
95. G. S. Mkrtchyan and V. V. Schmidt, *Sov. Phys. JETP* 34, 195 (1972).
96. A. I. Buzdin and D. Feinberg, *Physica C* 256, 303 (1996).
97. C. P. Bean and J. D. Livingstone, *Phys. Rev. Lett.* 12, 14 (1964).
98. M. Baert, "Critical Currents, Pinning and Matching Effects in Superconducting Pb/Ge Multilayers," Ph.D. Thesis, Katholieke Universiteit, Leuven, 1995.
99. A. I. Buzdin, *Phys. Rev. B* 47, 11416 (1993).
100. A. Bezryadin, A. Buzdin, and B. Pannetier, in "Macroscopic Quantum Phenomena and Coherence in Superconducting Arrays," p. 155. World Scientific, Singapore, 1995.
101. L. Civale, A. D. Marwick, T. K. Worthington, M. A. Kirk, J. R. Thompson, L. Krusin-Elbaum, Y. Sun, J. R. Clem, and F. Holtzberg, *Phys. Rev. Lett.* 67, 648 (1991).
102. W. Gerhäuser, G. Ries, H. W. Neumüller, W. Schmidt, O. Eibl, G. Saemann-Ischenko, and S. Klaümunzer, *Phys. Rev. Lett.* 68, 879 (1992).
103. O. Daldini, P. Martinoli, J. L. Olson, and G. Berner, *Phys. Rev. Lett.* 32, 218 (1974).
104. A. N. Lykov, *Solid State Commun.* 86, 531 (1993).
105. J. E. Tkaczyk, J. A. deLuca, P. L. Karas, P. J. Bednarczyk, D. K. Christen, C. E. Klabunde, and H. R. Kerchner, *Appl. Phys. Lett.* 62, 3031 (1993); L. D. Cooley, P. J. Lee, D. C. Larbalestier, and P. M. O'Larey, *Appl. Phys. Lett.* 64, 1298 (1994).
106. D. R. Nelson and V. M. Vinokur, *Phys. Rev. B* 48, 13060 (1993).
107. G. Blatter, M. V. Feigel'man, V. B. Geshkenbein, A. I. Larkin, and V. M. Vinokur, *Rev. Mod. Phys.* 66, 1125 (1994).
108. G. Blatter and V. B. Geshkenbein, *Physica C* 282–287, 319 (1997).
109. E. H. Brandt, *Rep. Prog. Phys.* 58, 1465 (1995).
110. L. Civale, A. D. Marwick, M. W. McElfresh, T. K. Worthington, A. P. Malozemoff, F. H. Holtzberg, J. R. Thompson, and M. A. Kirk, *Phys. Rev. Lett.* 65, 1164 (1990).
111. R. B. van Dover, E. M. Gyorgy, A. E. White, L. F. Schneemeyer, R. J. Felder, and J. V. Waszczak, *Appl. Phys. Lett.* 56, 2681 (1990).
112. W. Gerhäuser, H.-W. Neumüller, W. Schmidt, G. Ries, G. Saemann-Ischenko, H. Gerstenberg, and F.-M. Sauerzopf, *Physica C* 185, 2273 (1991).
113. G. J. Dolan and J. H. Dunsmuir, *Physica B* 152, 7 (1988).
114. V. V. Metlushko, M. Baert, R. Jonckheere, V. V. Moshchalkov, and Y. Bruynseraede, *Solid State Commun.* 91, 331 (1994).
115. H. S. J. Van der Zant, H. A. Rijken, and J. E. Mooij, *J. Low Temp. Phys.* 79, 289 (1990).
116. R. Théron, J. B. Simond, Ch. Leemann, H. Beck, P. Martinoli, and P. Minnhagen, *Phys. Rev. Lett.* 71, 1246 (1993).
117. I. B. Khalfin and B. Ya. Shapiro, *Physica C* 207, 359 (1993).
118. K. Temst, M. J. Van Bael, M. Baert, E. Rosseel, V. Bruyndoncx, C. Strunk, G. Verbanck, K. Mae, C. Van Haesendonck, V. V. Moshchalkov, Y. Bruynseraede, R. Jonckheere, D. G. de Groot, N. Koeman, and R. Griessen, *J. Phys.* 6, C3-265 (1996).
119. N. E. Mott and E. A. Davis, "Electronic Processes in Non-Crystalline Materials." Clarendon Press, Oxford, U.K., 1979.
120. W. K. Kwok, J. Fendrich, S. Fleshler, U. Welp, J. Downey, and G. W. Crabtree, *Phys. Rev. Lett.* 72, 1092 (1994).
121. H. Pastoriza, M. F. Goffmann, A. Arribére, and F. de la Cruz, *Phys. Rev. Lett.* 72, 2951 (1994).
122. A. Schilling, R. Fischer, N. Phillips, U. Welp, D. Dasgupta, K. Kwok, and G. Crabtree, *Nature* 382, 792 (1996).
123. W. Krauth, N. Trivedi, and D. Ceperley, *Phys. Rev. Lett.* 67, 2307 (1991).
124. P. Berghuis and P. H. Kes, *Phys. Rev. B* 47, 262 (1993).
125. J. Bardeen and M. J. Stephen, *Phys. Rev.* 140, 1197 (1965).
126. E. Rosseel, M. Van Bael, M. Baert, R. Jonckheere, V. V. Moshchalkov, and Y. Bruynseraede, *Phys. Rev. B* 53, R2983 (1996).
127. J. P. Straley and G. M. Barnett, *Phys. Rev. B* 48, 3309 (1993).
128. N. Takezawa and K. Fukushima, *Physica C* 228, 149 (1994).
129. O. Buisson, M. Giroud, and B. Pannetier, *Europhys. Lett.* 12, 727 (1990).
130. P. Berghuis, A. L. F. van der Slot, and P. H. Kes, *Phys. Rev. Lett.* 65, 2583 (1990).
131. C. Reichhardt, C. J. Olson, S. B. Field, and F. Nori, *Phys. Rev. B* 57, 7937 (1998).
132. V. V. Moshchalkov, M. Baert, V. V. Metlushko, E. Rosseel, M. Van Bael, K. Temst, X. Qiu, R. Jonckheere, and Y. Bruynseraede, *Jpn. J. Appl. Phys.* 34, 4459 (1995).
133. K. Harada, O. Kamimura, H. Kasai, T. Matsuda, A. Tonomura, and V. V. Moshchalkov, *Science* 274, 1167 (1996).
134. T. Kawasaki, Q. Ru, T. Matsuda, Y. Bando, and A. Tonomura, *Jpn. J. Appl. Phys.* 30, L1830 (1991).
135. K. Harada, T. Matsuda, J. Bonevich, M. Igarashi, S. Kondo, G. Pozzi, U. Kawabe, and A. Tonomura, *Nature* 360, 51 (1992).

136. L. Radzihovsky, *Phys. Rev. Lett.* 74, 4923 (1995).
137. V. V. Moshchalkov, M. Baert, E. Rosseel, V. V. Metlushko, M. J. Van Bael, and Y. Bruynseraede, *Physica C* 282–287, 379 (1997).
138. Y. Bruynseraede, K. Temst, E. Osquiguil, C. Van Haesendonck, A. Gilabert, and I. K. Schuller, *Phys. Scr. T* 42, 37 (1992).
139. A. Wahl, V. Hardy, J. Provost, Ch. Simon, and A. Buzdin, *Physica C* 250, 163 (1995).
140. E. S. Bakhanova and V. M. Genkin, in "Applied Superconductivity" (H. C. Freyhardt, ed.). DGM Intoranationgesellschaft, Göttingen, Germany, 1993.
141. L. D. Cooley and A. M. Grishin, *Phys. Rev. Lett.* 74, 2788 (1995).
142. C. P. Bean, *Phys. Rev. Lett.* 8, 250 (1962).
143. A. A. Abrikosov, *Sov. Phys. JETP* 5, 1174 (1957).
144. A. Bezryadin, Yu. N. Ovchninnikov, and B. Pannetier, *Phys. Rev. B* 53, 8553 (1996).
145. D. Shoenberg, "Superconductivity." Cambridge University Press, Cambridge, MA, 1965.
146. B. Pannetier, in Publicity folder, "Centre de Recherches sur les Très Basses Températures," Grenoble, France, 1996.
147. M. Murakami, M. Morita, K. Doi, and K. Miyamoto, *Jpn. J. Appl. Phys.* 28, 1189 (1989).
148. C. Reichhardt, J. Groth, C. J. Olson, S. B. Field, and F. Nori, *Phys. Rev. B* 54, 16108 (1996).
149. W. J. Elion, H. S. J. Van der Zant, and J. E. Mooij, "Macroscopic Quantum Phenomena and Coherence in Superconducting Networks," p. 105. World Scientific, Singapore, 1995.

This Page Intentionally Left Blank

Chapter 10

PROPERTIES AND APPLICATIONS OF NANOCRYSTALLINE ELECTRONIC JUNCTIONS

Michael Grätzel

Institute of Photonics and Interfaces, Swiss Federal Institute of Technology, Lausanne, Switzerland

Contents

1. General Properties of Nanocrystalline Semiconductor Junctions 527
2. Majority Carrier Injection Devices 531
   2.1. Electrochromic Displays 531
   2.2. Cross-Surface Electron Transfer on Nanocrystalline Oxide Films 534
   2.3. Luminescent Diodes Based on Mesoscopic Oxide Cathodes 534
3. Light-Induced Charge Separation in Nanocrystalline Semiconductor Films 536
4. Nanocrystalline Injection Solar Cells 537
   4.1. Solar Light Harvesting 539
   4.2. Conversion Efficiencies 539
   4.3. Photovoltaic Performance Stability 545
   4.4. Development of Series-Connected Modules 545
   4.5. Cost and Environmental Compatibility of the New Injection Solar Cell 547
   4.6. Current Research Issues 547
5. Sensitized Solid-State Heterojunctions 548
6. Tandem Cells for the Cleavage of Water by Visible Light 550
7. Nanocrystalline Intercalation Batteries 551
   References 552

1. GENERAL PROPERTIES OF NANOCRYSTALLINE SEMICONDUCTOR JUNCTIONS

Significant advances in the fields of colloid and sol–gel chemistry in the last two decades now allow fabrication of micro- and nanosized structures using finely divided monodispersed colloidal particles [1–7]. As we approach the 21st century, there is a growing trend on the part of the scientific community to apply these concepts to develop systems of smaller dimensions. Homogeneous solid electronic devices [three-dimensional (3D)] are giving way to multilayers with quasi two-dimensional (2D) structures and quasi one-dimensional (1D) structures, such as nanowires or clusters in an insulating matrix and finally to porous nanocrystalline films.

Over the recent years, nanocrystalline materials have attracted increasing attention from the scientific community because of their spectacular physical and chemical properties. This unusual behavior results from the ultrafine structure (i.e., grain size less than 50 nm)

Handbook of Nanostructured Materials and Nanotechnology, edited by H.S. Nalwa
Volume 3: Electrical Properties
Copyright © 2000 by Academic Press
All rights of reproduction in any form reserved.
ISBN 0-12-513763-X/$30.00

of the materials. It is useful to distinguish effects related to bulk properties, such as quantum confinement [8] and monodomain grains [9], from surface effects. The latter arise from the high grain boundary to volume ratio allowing, for example, for the fabrication of ductile [10] or superplastic ceramics [11] as well as highly porous membranes [12] and electrodes [13].

Nanocrystalline electronic junctions are constituted by a network of mesoscopic oxide or chalcogenide particles, such as TiO_2, ZnO, Fe_2O_3, Nb_2O_5,WO_3, Ta_2O_5, or CdS and CdSe, which are interconnected to allow electronic conduction to take place. A paste containing the nanocrystalline semiconductor particles is applied by screen printing or doctor blading on a glass coated with a transparent conducting oxide (TCO) layer made of fluorine-doped SnO_2 (sheet resistance 8–10 Ω/square). Subsequent sintering produces a mesoporous film whose porosity varies from about 20% to 80%. The pores form an interconnected network that is filled with an electrolyte or with a solid charge transfer material, such as an amorphous organic hole transmitter or a p-type semiconductor, i.e. as CuI [14] or CuSCN [15]. In this way, an electronic junction of extremely large contact area is formed displaying very interesting and unique optoelectronic properties. The materials forming the junction are interdigitated on a length scale as minute as a few nanometers forming a bicontinuous phase. A schematic illustration of the nanocrystalline device is given in Figure 1. Some important features of such mesoporous films are:

1. An extremely large internal surface area, the roughness factors being in excess of 1000 for a film thickness of 8 μm
2. The ease of charge carrier percolation across the nanoparticle network, making this huge surface electronically addressable
3. The appearance of confinement effects for films that are constituted by quantum dots, such as 5-nm-sized ZnO particles
4. The ability to form an accumulation layer under forward bias
5. For intrinsic or weakly doped semiconductors, the inability to form a depletion layer under reverse bias

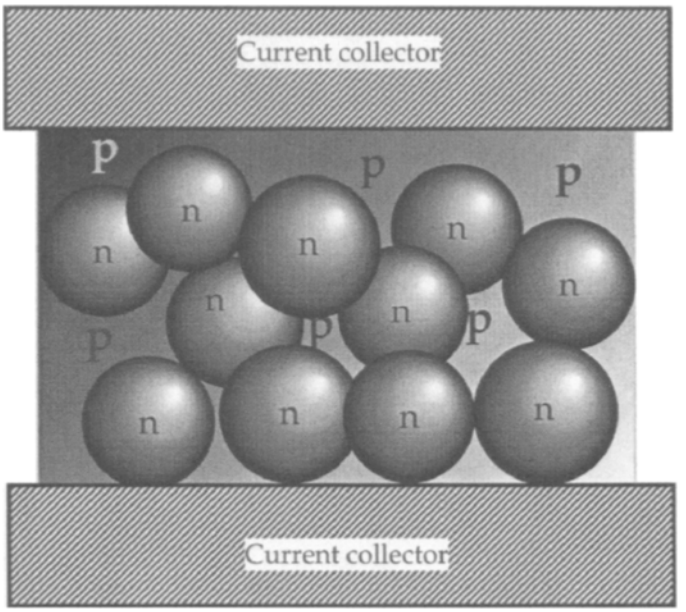


Fig. 1. Typical layout of a nanocrystalline semiconductor junction. The network of n-type particles is interpenetrated by a p-type material used to fill the pores of the film.

6. A very rapid and highly efficient interfacial charge transfer between the oxide and redox active species anchored to the particle surface
7. A fast percolative cross-surface electron transfer involving adsorbed redox relays
8. The fast intercalation and release of Li^+ ions into the oxide

Nanostructured materials offer many new opportunities to study fundamental surface processes in a controlled manner and this, in turn, leads to fabrication of new devices, some of which are summarized in Figure 2. The unique optical and electronic features of these films are being exploited to develop photochromic displays/switches, optical switches, chemical sensors, intercalation batteries, dielectrics/supercapacitors, heat-reflecting and ultraviolet (UV)-absorbing layers, coatings to improve chemical and mechanical stability of glass, and so on. Particularly intriguing is the observation of close to 100% conversion of photons in electric current made with films that are derivatized by charge transfer sensitizers adsorbed onto the surface of the oxide. This has led to the development of a new type of photovoltaic cell [16–18], which will be described in more detail later. In several recent articles [19–21], we have outlined some of these novel applications.

The oxide material of choice for many of these systems has been TiO_2. Its properties are intimately linked to the material content, chemical composition, structure, and surface morphology. Fortunately, colloid chemistry has greatly advanced in the last two decades so that it is now possible to control the processing parameters, such as precursor chemistry, hydrothermal growth temperature, binder addition, and sintering conditions, and to optimize the key parameters of the film, namely, porosity, pore size distribution, light scattering, electron percolation. On the material content and morphology, two crystalline forms of TiO_2 are important, anatase and rutile (the third form brookite is difficult to obtain). Anatase is the low-temperature stable form and gives mesoscopic films that are transparent and colorless. The predominant morphology of the particles is bipyramidal exposing well-developed (101) faces.

Preparation of mesoporous semiconductor films consists of two steps: First, a colloidal solution containing nanosized particles of the oxide is formed and this is used subsequently to produce a few micrometer-thick films with good electrical conduction properties. Figure 3 shows schematically the various steps involved in the preparation of nanocrystalline

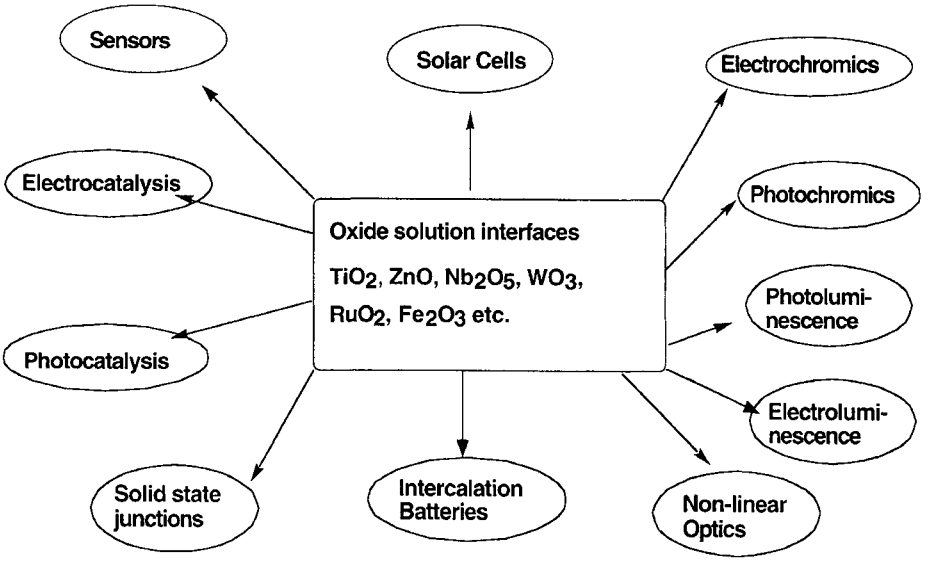


Fig. 2. Applications of nanocrystalline oxide semiconductor films.

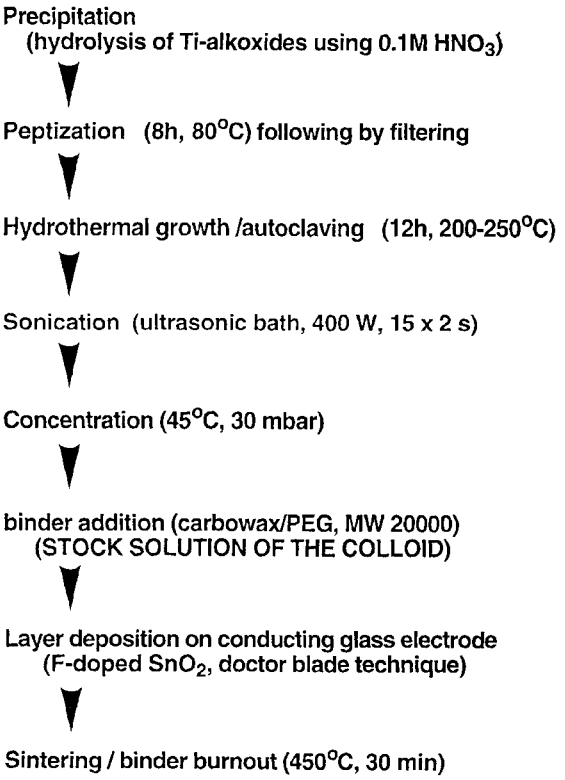


Fig. 3. Outline of the steps involved in the preparation of nanocrystalline TiO_2 films.

TiO_2 films. Only a brief summary is given, as detailed information on both the preparation and the morphology of such films has been published elsewhere [22]. The precipitation process involves hydrolysis of a Ti(IV) salt, usually an alkoxide such as Ti-isopropoxide or a chloride followed by peptization. To obtain monodispersed particles of the desired size, the hydrolysis and condensation kinetics must be controlled. Ti-alkoxides with bulky groups such as butoxy hydrolyze slowly, allowing slow condensation rates. Autoclaving of these sols (heating at 200–250 °C for 12 h) allows controlled growth of the primary particles and also, to some extent, the crystallinity. During this hydrothermal growth, smaller particles dissolve and fuse to large particles by a process known as "Ostwald ripening." After removal of the solvent and addition of a binder, the sol is now ready for deposition on the substrate. For the latter, a conducting glass sheet ($R = 8$–$10\ \Omega$/square) is often used and the sol is deposited by doctor blading or screen printing and fired in air for sintering. The film thickness is typically 5–10 μm and the film mass about 1–2 mg/cm^2. Analysis of the porous films shows the porosity to be about 50%, the average pore size being 15 nm.

Figure 4 illustrates the morphology of such a nanocrystalline TiO_2(anatase) layer deposited on a transparent conducting oxide (TCO) glass. The mean particle diameter of the oxide is 15 nm in this case. The size can be adjusted by varying the conditions of the sol–gel process used for film preparation. The optical properties of this film will be similar to those exhibited by bulk anatase. Rutile is the dominant form at high temperature and its crystals are needle shaped, similarly to those of nanocrystalline Nb_2O_5 [23].

Figure 5 shows the structure of a nanocrystalline ZnO layer composed of particles whose size is in the 5-nm range. Here, confinement effects shift the optical band gap of the semiconductor to the blue [24–26].

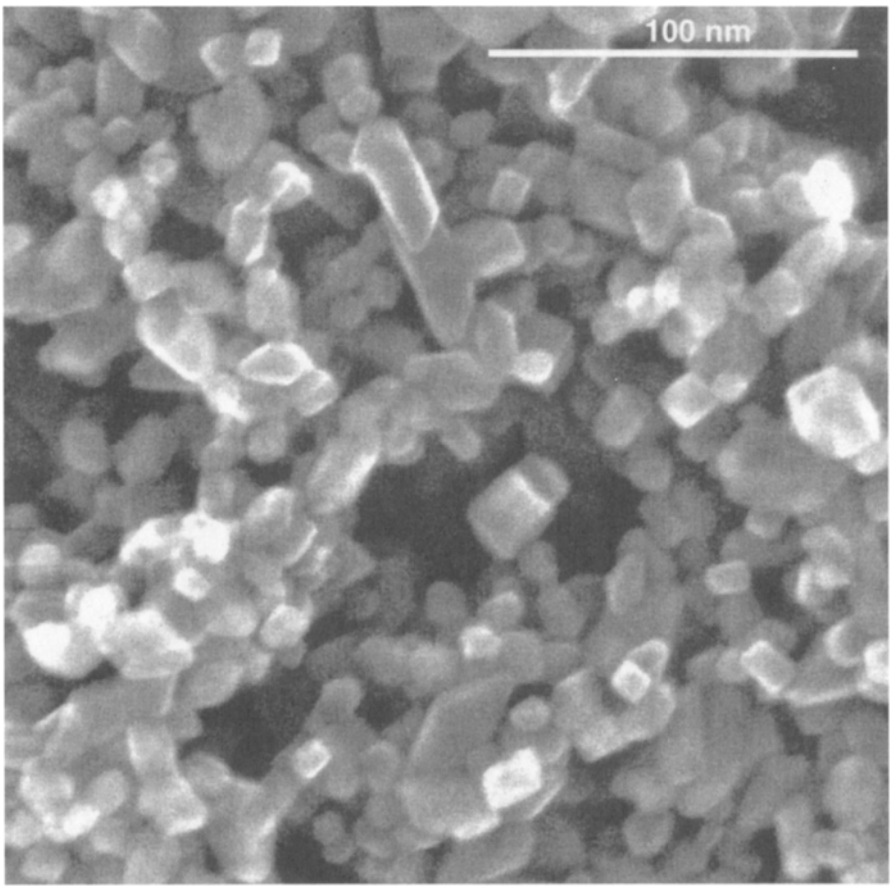


Fig. 4. Scanning electron micrograph of a nanocrystalline TiO_2 film supported on conducting glass. The magnification employed is indicated as a scale bar.

2. MAJORITY CARRIER INJECTION DEVICES

A schematic representation of a nanocrystalline junction operated in the charge injection mode is shown in Figure 6. The mesoscopic semiconductor, typically an oxide that is n-doped or left intrinsic, is deposited onto a current collector, which, in general, is constituted by a TCO glass. The pores present between the particles are filled with the contact medium constituted, for example, by an electrolyte, a hole-transmitting organic material, or a p-type semiconductor. This, in turn, is placed in contact with the second current collector, that is, the counterelectrode. Often, a thin compact layer of the oxide semiconductor is deposited between the conductive glass and the nanocrystalline film to avoid short circuiting of the two current collectors by the charge transport material that is infiltrated into the pores. Such a device can be used as an electrochromic or electroluminescent display, which will be discussed in more detail next.

2.1. Electrochromic Displays

In this case, majority carriers are injected from outside into the junction driving the nanocrystalline oxide film into accumulation. Associated with injection is an electrochromic effect produced by the accumulation of conduction band electrons in the oxide exhibiting a very broad absorption in the visible and near-infrared wavelength range [27]. This effect has been used to determine the flat band potential of such oxide films [28].

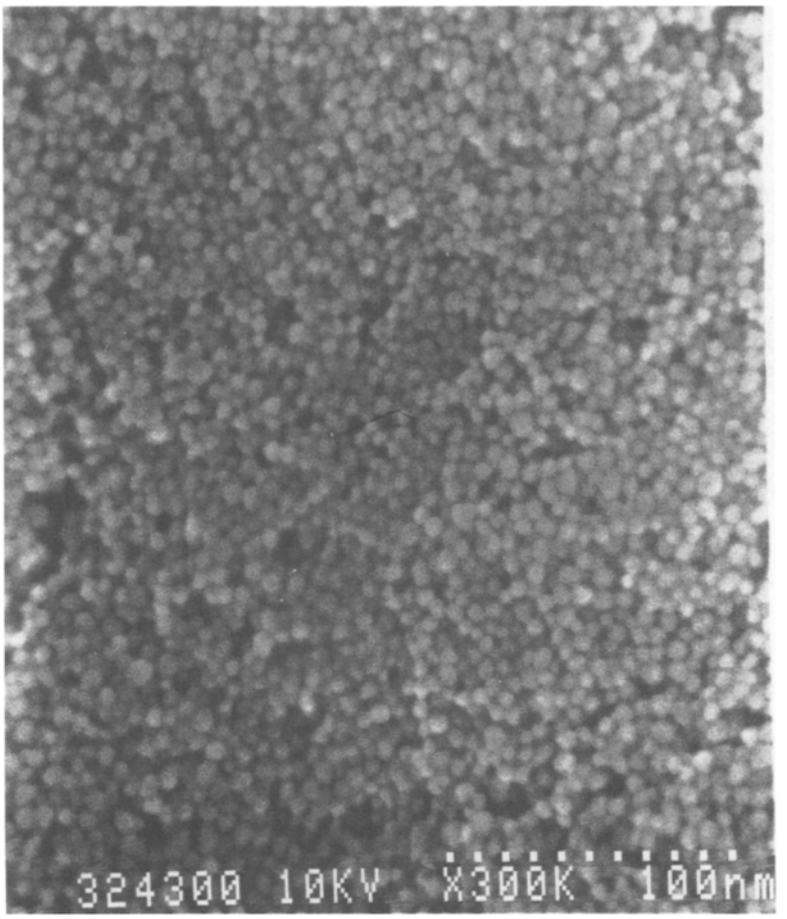


Fig. 5. Scanning electron microscope of a nanocrystalline ZnO film.

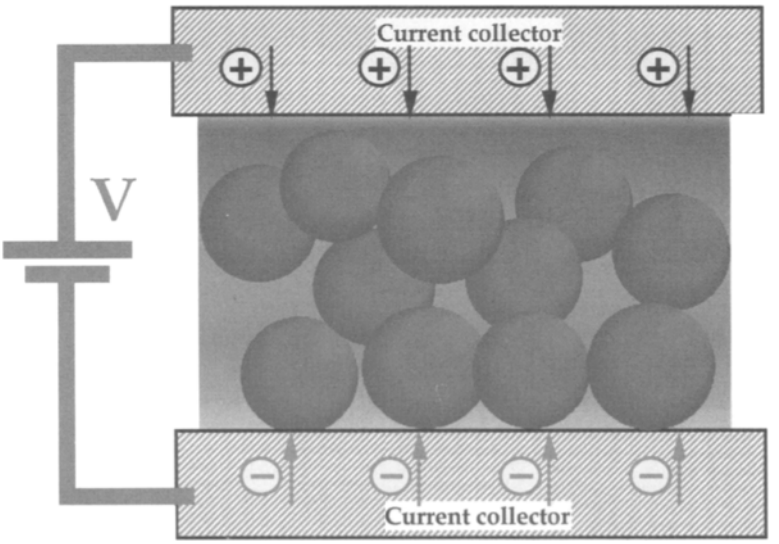


Fig. 6. General layout of a nanocrystalline majority carrier injection device.

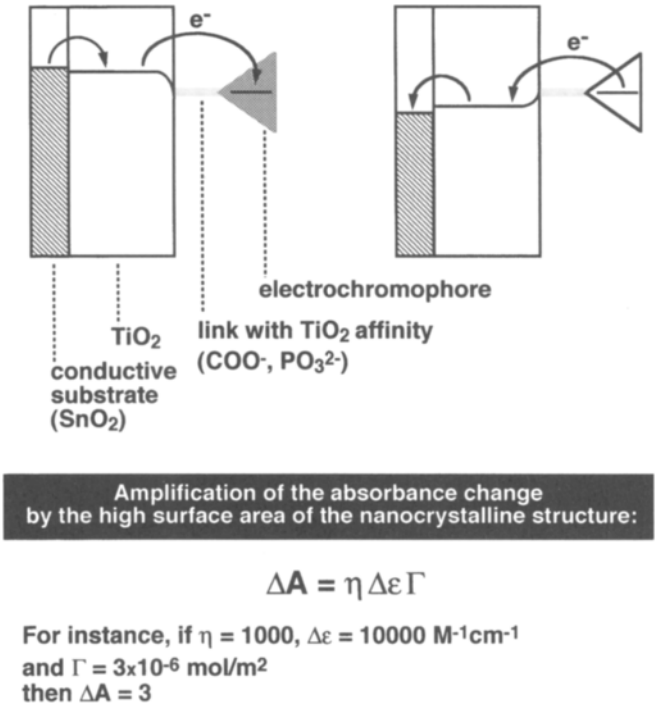


Fig. 7. n-type electrochromism on nanocrystalline oxide surfaces derivatized with a molecular redox relay.

Electrochromic switching of mesoscopic films occurs rapidly because of ready compensation of the injected space charge by ion movement in the electrolyte present in the pores and fast intercalation of lithium ions [29, 30].

Viologens form a group of redox indicators that undergo drastic color changes upon oxidation/reduction. The reduced form of methyl viologen, for example, is deep blue, while the oxidized form is colorless. Efficient reduction of anchored viologen compounds by conduction band electrons of TiO_2 can be used for the amplification of the optical signal, as shown schematically in Figure 7. The amplification is due to the high molecular extinction coefficients of these relays. Upon reduction, transparent nanocrystalline films of TiO_2 containing viologen develop strong color and the film can be decolorized by reversing the potential. Varying the chemical structure and redox potentials of the viologens makes it possible to tune the color and, hence, build a series of electrochromic display devices [19, 31]. Such surface-derivatized oxides accomplish a performance that, in terms of figure of merit, that is, the charge required to achieve an optical density change of one, is already competitive with conventional electrochromic systems and, hence, shows great promise for practical applications.

The anchoring of a redox relay, such as a viologen derivative to the surface of the oxide that turns highly colored upon reduction, allows for molecular amplification of the optical signal (see Fig. 8). The reason for this amplification is that the molecular extinction coefficient of the reduced relay is one to two orders of magnitude higher than that of the conduction band electrons. Therefore, such surface-derivatized nanocrystalline devices accomplish a performance that, in terms of figure of merit, that is, the Coulombic charge required to achieve an optical density change of one, is already competitive with conventional electrochromic systems. The exponential dependence of the change in the optical density on the applied potential allows a simple multiplexing method to be used for addressing individual pixels of the nanocrystalline film, which is important for display applications [19, 20].

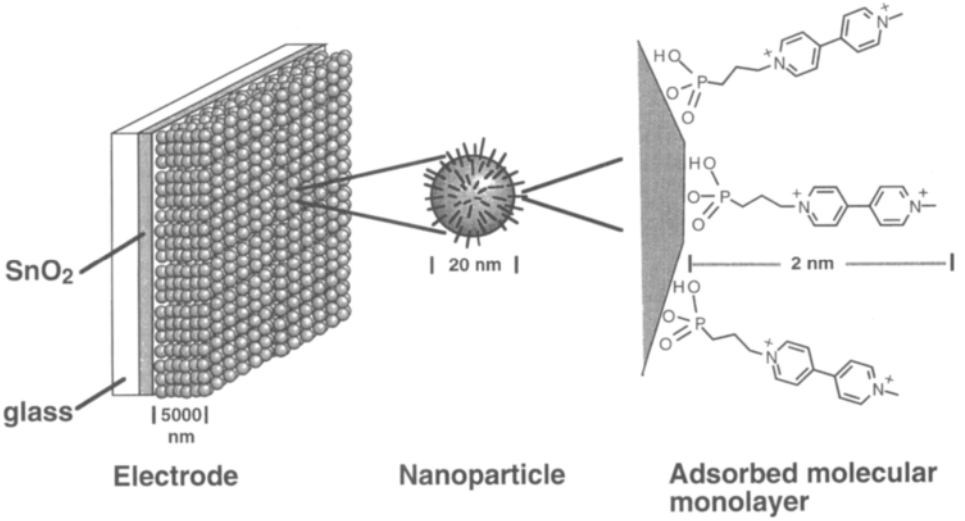


Fig. 8. Electrochromic switching with a mesoscopic TiO_2 film whose surface is derivatized with a dimeric viologen. Both the colored and the uncolored state are schematically presented.

2.2. Cross-Surface Electron Transfer on Nanocrystalline Oxide Films

A striking phenomenon of cross-surface electron transfer on nanocrystalline films of semiconducting and insulating oxides, such as TiO_2, Al_2O_3, and ZrO_2, was discovered recently [32]. These films were deposited on conducting glass and surface derivatized with a monolayer of phosphonated triarylamine acting as a redox relay. The films displayed reversible electrochemical and electrochromic behavior even though the redox potential of the triarylamine lies in the forbidden band of the semiconducting or insulating oxide. In this potential domain, the oxide is insulating, impairing any electronic charge movement across the nanocrystalline particle film. The mechanism of charge transport was found to involve hole injection from the conducting support followed by cross-surface transfer of the holes within the monolayer of the adsorbed amine. The role of the nanocrystalline oxide film is merely to support the electroactive surface layer. A sharp percolation threshold for electronic conductivity was found at about 50% coverage.

2.3. Luminescent Diodes Based on Mesoscopic Oxide Cathodes

Luminescent diodes present another important possible application of nanocrystalline junctions. In analogy to solid-state lasers, these devices operate by majority carrier injection. Organic materials have frequently been considered for the fabrication of practical electroluminescent (EL) devices. The reason for this is that a large number of organic materials are known to luminesce very efficiently in the visible region. In this respect, they are well suited for multicolor display applications.

Earlier attempts to make such devices operative were plagued by the high voltage required to drive charge transport in organic crystals. Recently, the advent of thin layer cells used in conjunction with novel diamine-type organic solids as hole-transmitting layers (HTLs) has resulted in the development of systems with much improved performance characteristics [33]. The substrate is a conducting glass covered with a layer of aromatic diamine. The diamine acts as a hole conductor. Despite their amorphous character, these charge transfer materials exhibit a respectable hole mobility, which is in the range of 10^{-5} to 10^{-2} $cm^2/V\,s$. A second layer belonging to the class of metal chelates serves as an electron conductor and light emitter. Unfortunately, the charge carrier mobility is poor in this second layer. The top electrode is an alloy of magnesium or calcium with sil-

ver. This organic diode was shown to behave as a rectifier emitting light under forward bias [34]. Although such devices do function as luminescent diodes, a major limiting factor for consumer display applications so far has been the short device lifetime. Amongst the many factors responsible for degradation, the low-work-function metal or alloy cathode has been recognized as a major source. Both the sensitivity toward water and oxygen as well as contact problems between the organic and the metal layer contribute to the observed instability.

Work initiated in our laboratory [34] makes use of the favorable properties of mesoscopic semiconductor layers for electroluminescent display applications. Instead of using low-work-function metals, nanocrystalline oxides, such as Nb_2O_5 or Ta_2O_5, are employed as cathode materials for organic light-emitting diode (LED) devices. These are attractive for several reasons: (i) They have a large band gap ($E_G > 3$ eV) assuring transmittance of visible light. (ii) Because of the small size of the oxide particles, the scattering of light is negligible. (iii) The mesoporous morphology of the such oxide film plays an important role in favoring electroluminescent processes. The high internal surface area permits the electron injection to proceed at lower overpotentials, preventing the unwanted quenching of the excited states of the light-emitter material by energy transfer to conduction band electrons. The sensitivity of oxide cathodes toward water and air is much less critical than that of the low-work-function metals.

The luminescent material may be deposited as a monomolecular layer on the nanocrystalline oxide. In such a configuration, the dye-derivatized oxide semiconductor replaces the aluminum trishydroxyquinolate film (see Fig. 9). The dye is oxidized through holes injected into a solid hole-transmitting material or a redox electrolyte. N-doping of the

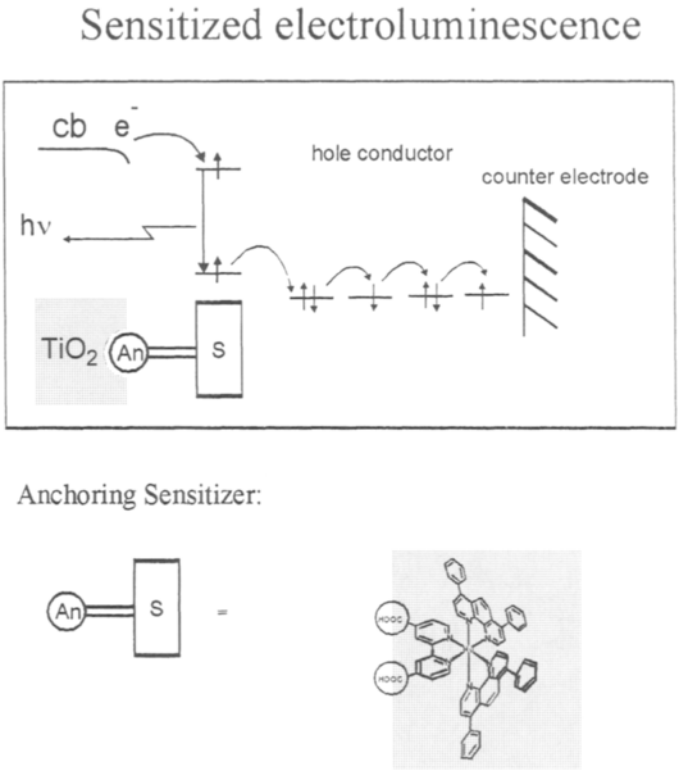


Fig. 9. Energy level diagram for an electroluminiscent device based on a nanocrystalline semiconductor oxide (SC) as an electron-injecting cathode and a counterelectrode (CE) for hole injection. The energy levels of the dye and the redox electrolyte are also indicated.

semiconductor renders it a good electron conductor. Selecting an oxide material having a low work function assures that the electron is injected in the excited state level of the dye, producing emission of light by radiative deactivation. Although this field is still in its infancy, the outlook is bright for developing luminescent diodes based on nanocrystalline films whose characteristics are superior to state-of-the-art technology.

3. LIGHT-INDUCED CHARGE SEPARATION IN NANOCRYSTALLINE SEMICONDUCTOR FILMS

The illumination of nanocrystalline junctions can be used to generate electric current from light. Because of the small size of the semiconductor oxide particles constituting the film and the fact that they are all in contact with the electrolyte, there is only a small electric field within the particles [35]. The potential gradient across the nanocrystalline film is particularly small for undoped materials [36]. The question then arises how in such a system electron–hole pairs are separated after band gap excitation. Several groups have addressed this issue and the literature has been reviewed [37]. Very recently, a detailed electrical model of nanocrystalline photovoltaic devices has been published [38]. It is now commonly agreed that charge carrier transport in the film occurs by diffusion, the rate of which is controlled by traps [39–41]. The response of the system to band gap excitation depends on the relative rate of the electron and hole reactions with the redox electrolyte present in the pores of the film. This distinguishes mesosocopic semiconductor films from conventional p/n or Schottky junction devices where the response to photoexcitation is governed by the electric field present in the junction. As an example, we consider in Figure 10 the case where the holes are scavenged more rapidly than the electrons. Here the response of the particle film to light will be that of an n-type semiconductor. In contrast, if the electrolyte contains a reactant that scavenges electrons more rapidly than holes, the film behaves like a p-type semiconductor. Thus, changing the photoresponse from n to p type becomes possible by merely modifying the composition of the electrolyte as has been shown for nanocrystalline CdSe films [42].

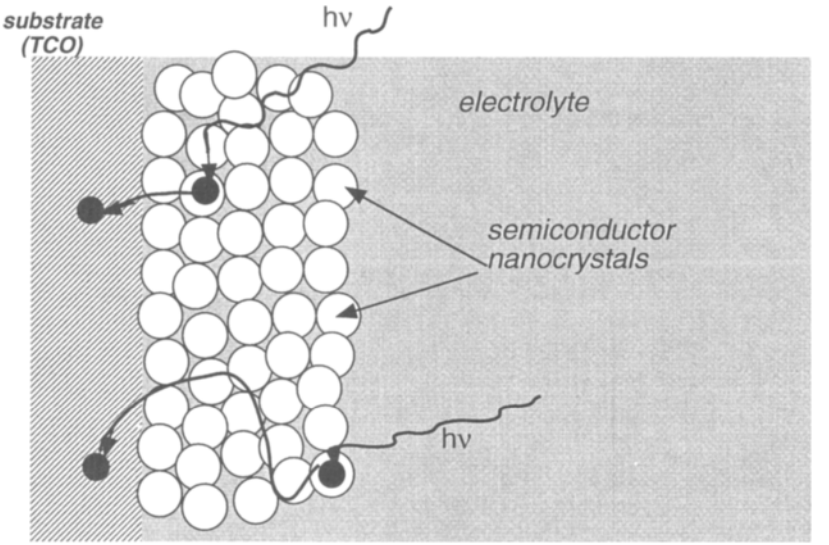


Fig. 10. Light-induced charge separation in a nanocrystalline semiconductor film where holes are scavenged more rapidly than electrons at the particle–electrolyte interface. As a consequence, the films exhibit n-type behavior.

A property that is of primary concern for applications of these systems is their efficiency of operation as a quantum converter. The film absorbs photons whose energy exceeds the energy difference between the conduction and valence band. Light absorption leads to the generation of electron–hole pairs in the solid. For oxides such as TiO_2, the electrons are majority carriers, while the holes constitute the minority carriers even though the material may not have been deliberately n-doped. This is due to the adventitious presence of defects such as oxygen vacancies. If such a nanocrystalline device is to be used for the generation of electricity from light, it is necessary that the holes can diffuse to the semiconductor/electrolyte junction before recombination with the electrons has occurred. In other words, the diffusion length of the minority carriers (l_{mc}) has to be longer than the distance these carriers have to travel before they reach the junction. This diffusion length is related to the lifetime of the holes (τ) via the mean square displacement expression:

$$l_{mc} = (2D\tau)^{0.5} \tag{1}$$

For TiO_2, the l_{mc} value is typically 100 nm. Because mesoscopic semiconductor films are constituted by 5–50-nm-sized particles, their size is smaller than the minority charge carrier diffusion length. Hence, the minority carriers can reach the electrolyte interface before recombination occurs. The operation of the thin film device as an efficient quantum converter, therefore, becomes feasible, and this has been confirmed meanwhile by a number of studies [37, 42, 43]. Conversion efficiencies of incident photons to current of nearly 100% have been achieved in the wavelength range of the band-gap absorption of the semiconductor.

In summary, the new mesoscopic films are constituted by nanometer-sized semiconductor particles forming an interconnected network. The internal surface of the film is much higher than its projected geometric surface. A network of interconnected pores is present at the same time within the film. Because of the small size of the particles, the film does not scatter visible light. Nor is visible light absorbed by such a film if it is constituted by an oxide because of its relatively large band gap. Thus, a mesoporous layer of TiO_2 (thickness 0.1–10 μm) deposited onto a conducting glass is invisible to the naked eye. This distinguishes such films from conventional photovoltaic devices.

A surprising and very important property of these nanostructured films is that a brief sintering treatment produces efficient electronic contact not only between the particles and the support but also between practically all the particles constituting the film. It has been shown that electronic charges injected into the membrane from the conducting support are able to percolate through the entire film of nanometer-sized particles at a high rate. This allows for rapid oxidation and reduction of electroactive species present at the particle surface or in the voids between particles. Alternatively, if electrons are injected into the particles from a species adsorbed at their surface or present within the voids, the injected charge can be collected with 100% efficiency at the conducting support.

Given these unique properties, the film can serve as a matrix to accommodate electroactive materials within the pores or at the particle surface and to address electronically these materials. Alternatively, the pores can be filled with a solid or liquid material that forms a junction with the semiconductor particles constituting the matrix. In this case, the film functions as a photovoltaic cell that produces electricity from light. A powerful method to enhance the visible light response of such mesoscopic oxides is their sensitization by charge transfer sensitizers. This has led to the development of a new type of injection solar cell, which will be discussed in more detail in the following section.

4. NANOCRYSTALLINE INJECTION SOLAR CELLS

The fundamental processes involved in any photovoltaic conversion process are:

1. The absorption of sunlight
2. The generation of electric charges by light
3. The collection of charge carriers to produce electricity

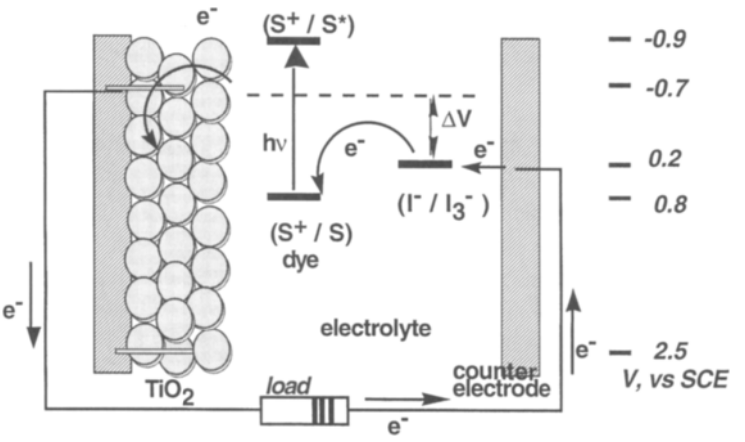


Fig. 11. Operational principle of the nanocrystalline injection solar cell.

The incident monochromatic photon-to-current conversion efficiency (IPCE) or "external quantum yield" of such a device is then given by the equation:

$$\mathrm{IPCE}(\lambda) = \mathrm{LHE}(\lambda) \times \phi_{\mathrm{inj}} \times \eta_{\mathrm{e}} \tag{2}$$

where IPCE(λ) expresses the ratio of the measured electric current to the incident photon flux for a given wavelength, LHE is the light-harvesting efficiency, ϕ_{inj} is the quantum yield for charge injection into the oxide, and η_{e} is the charge collection efficiency. Conventional solar cells convert light into electricity by exploiting the photovoltaic effect that exists at semiconductor junctions. They are thus closely related to transistors and integrated circuits. The semiconductor performs two processes simultaneously: absorption of light and separation of the electric charges (electrons and holes) that are formed as a consequence of that absorption. However, to avoid the premature recombination of electrons and holes, the semiconductors employed must be highly pure and defect free. The fabrication of this type of cell presents numerous difficulties, preventing the use of such devices for electricity production on a large industrial scale. In contrast, the solar cell developed in our group at the Swiss Federal Institute of Technology operates on a different principle, whereby the processes of light absorption and charge separation are differentiated (see Fig. 11). Light absorption is performed by a monolayer of dye (S) adsorbed chemically at the semiconductor surface. After having been excited (S*) by a photon of light, the dye—usually a transition metal complex whose molecular properties are specifically engineered for the task—is able to inject an electron into the conduction band of the oxide semiconductor. The back reaction is intercepted by transferring the positive charge from the dye (S^+) to a redox mediator R/R^+ present in the electrolyte with which the cell is filled and thence to the counterelectrode. Via this last electron transfer, in which the mediator is returned to its reduced state, the circuit is closed. The system operates as a regenerative electrochemical cell that converts light into electricity without inducing any permanent chemical transformation. The maximum voltage ΔV that such a device could deliver corresponds to the difference between the redox potential of the mediator and the Fermi level of the semiconductor. The electrolyte containing the mediator could be replaced by a p-type semiconductor, for example, cuprous thiocyanate, CuSCN [15], or cuprous iodide, CuI [14], or a hole-transmitting solid, such as the amorphous organic arylamines used in electroluminescence devices [33]. This is an attractive option that is presently being explored in our laboratory.

It should be emphasized that for all embodiments of the nanocrystalline injection cell, minority carriers, that is, holes in the case of an n-type conductor such as TiO_2, do not participate in the photoconversion process. This is a great advantage in comparison to

conventional photovoltaic devices, where, without exception, the generation and transport of minority carriers is required. The performance characteristics of the conventional device are strongly influenced by the minority carrier diffusion length, which is very sensitive to the presence of imperfections and impurities in the semiconductor lattice. By contrast, the nanocrystalline injection cell operates entirely on majority carriers whose transport is not subjected to these limitations and, hence, will be much less sensitive to lattice defects.

4.1. Solar Light Harvesting

As indicated previously, the absorption of light by a monolayer of dye is weak because the area occupied by one molecule is much larger than its optical cross section for light capture. A respectable photovoltaic efficiency, therefore, cannot be obtained by the use of a flat semiconductor surface but rather by use of a porous, nanostructured film of very high surface roughness. When light penetrates the photosensitized semiconductor "sponge", it crosses hundreds of adsorbed dye monolayers. The mesoporous structure thus fulfills a function similar to the thylakoid vesicles in green leaves, which are stacked in order to enhance light harvesting.

Apart from providing a folded surface having a very high roughness surface to enhance light harvesting by the adsorbed sensitizer, the role of the nanocrystalline oxide film is to serve as an electron conductor. The conduction band of the titanium dioxide accepts the electrons from the electronically excited sensitizer. The electron injected into the conduction band percolates very rapidly across the TiO_2 layer. Its diffusion is much faster than that of a charged ion in solution. The time required for crossing a TiO_2 film, say 5 μm thick, is at most a few milliseconds, depending on whether or not trapping of electrons is involved in the transport. During migration, the electrons maintain their high electrochemical potential, which is equal to the quasi-Fermi level of the semiconductor under illumination. Thus, the principal function of the TiO_2, apart from supporting the sensitizer, is that of charge collection and conduction. The advantage of using a semiconductor membrane rather than a biological one as employed by natural photosynthesis is that such an inorganic membrane or film is more stable and allows extremely fast transmembrane electron movement. The charge transfer across the photosynthetic membrane is less rapid because it takes about 100 μs to displace the electron across the 50-Å thick thylakoid layer. Moreover, nature has to sacrifice more than half of the absorbed photon energy to drive the transmembrane redox process at such a rate. In the case of the semiconductor film, the price to pay for the rapid vectorial charge displacement is small. It corresponds to at most 50–200 mV of voltage drop required to drive the electron injection process at the semiconductor/electrolyte junction.

In contrast to chlorophyll, which is continuously being synthesized in the leaf, the sensitizer in the nanocrystalline cell must be selected to satisfy the high stability requirements encountered in practical applications. A photovoltaic device must remain serviceable for 20 years without significant loss of performance corresponding to 50–100 million turnovers for the dye. Recent work has focused on the molecular engineering of suitable ruthenium compounds, which are known for their excellent stability. *Cis*-dithiocyanatobis(2,2′-bipyridyl)-4,4′-(dicarboxylate)- ruthenium(II), **I**, was found to be an outstanding solar light absorber and charge transfer sensitizer [18], which for a long time was unmatched by any other dyes. Only recently, has a black dye been discovered that has a superior performance to **I** as a charge transfer sensitizer in the injection solar cell [44].

4.2. Conversion Efficiencies

The use of mesoporous oxide films to support the sensitizer allows sunlight to be harvested over a broad spectral range in the visible, fulfilling the first requirement for efficient light energy conversion. In order for the device to deliver a photocurrent that matches the

performance of conventional cells, both the electron injection and the charge carrier collection must, in addition, occur with an efficiency close to unity.

4.2.1. Quantum Yield of Charge Injection

The quantum yield of charge injection (ϕ_{inj}) is the fraction of the absorbed photons that are converted into electrons injected in the conduction band. Charge injection from an electronically excited sensitizer into the conduction band of the semiconductor is in competition with other radiative or radiationless deactivation channels. Taking the sum of the rate constants of these nonproductive channels together as k_{eff} results in

$$\phi_{inj} = \frac{k_{inj}}{k_{eff} + k_{inj}} \tag{3}$$

One should remain aware that the deactivation of the electronically excited state of the sensitizer is generally very rapid. Typical k_{eff} values lie in the range of 10^3 to 10^{10} s^{-1}. To achieve a good quantum yield, the rate constant for charge injection should be at least 100 times higher than k_{eff}. This means that injection rates in the picosecond range or below have to be attained. In fact, in recent years sensitizers have been developed that satisfy these requirements. These dyes should incorporate functional groups ("interlocking groups") as, for example, carboxylate, hydroxamate or phosphonate groups [45] that are attached to the pyridyl ligands. Besides bonding to the titanium dioxide surface, these groups also effect an enhanced electronic coupling of the sensitizer with the conduction band of the semiconductor. The electronic transition is of MLCT (metal-to-ligand charge transfer) character (see Fig. 12), which serves to channel the excitation energy into the right ligand, that is, the

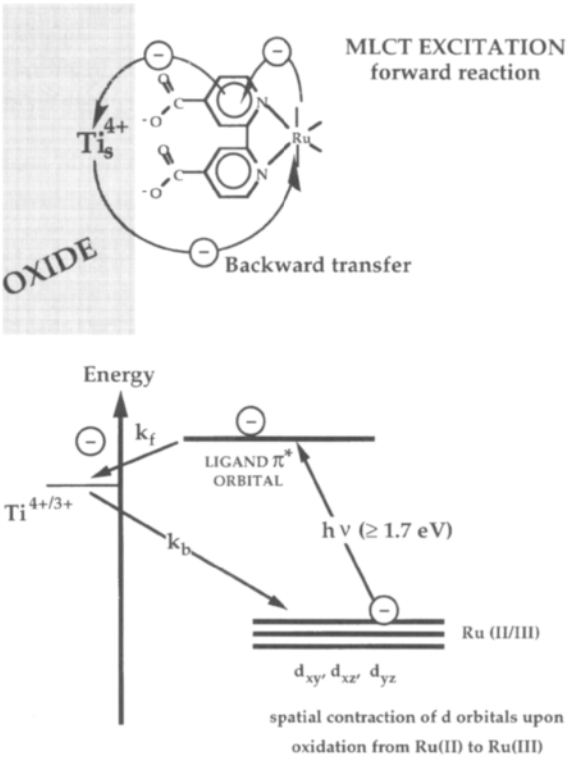


Fig. 12. Energy diagram showing the electronic orbitals involved in the MLCT excitation of a Ru(II) complex attached to the surface of the semiconducting oxide via carboxylated bipyridyl groups.

one from which electron injection into the semiconductor takes place. With molecules like these, the injection times are in the pico- or femtosecond range [46–49] and the quantum yield of charge injection generally exceeds 90%. In fact, for several sensitizers the electron transfer into the conduction band of the oxide is so rapid that it occurs from vibrationally hot excited states [50].

4.2.2. Light-Induced Charge Separation

As the next step of the conversion of light into electrical current, a complete charge separation must be achieved. On thermodynamic grounds, the preferred process for the electron injected into the conduction band of the titanium dioxide membrane is the back reaction with the oxidized sensitizer. Naturally, this reaction is undesirable, because instead of electrical current it merely generates heat. For the characterization of the recombination rate, an important kinetic parameter is the rate constant k_b. It is of great interest to develop sensitizer systems for which the value of k_{inj} is high and that of k_b low.

Fortunately, for the transition metal complexes employed as sensitizers, the ratio of the injection over that of electron recapture by the oxidized dye often exceeds one million, which significantly facilitates the charge separation. One reason for this striking behavior is that the molecular orbitals involved in the back reaction overlap less favorably with the wave function of the conduction band electron than those involved in the forward process. For the Ru complexes bound to the titanium dioxide membrane, the injecting orbital is the π^* wave function of the carboxylated bipyridyl or phosphonated terpyridyl ligand because the excited state of this sensitizer has a metal-to-ligand charge transfer character (see Fig. 12). The carboxylate groups interact directly with the surface Ti(IV) ions, resulting in good electronic coupling of the π^* wave function with the 3d orbital manifold of the conduction band of the TiO_2. As a result, the electron injection from the excited sensitizer into the semiconductor membrane is an extremely rapid process occurring in the femtosecond time domain. By contrast, the back reaction of the electrons with the oxidized ruthenium complex involves d orbitals localized on the ruthenium metal whose electronic overlap with the TiO_2 conduction band is small and is further reduced by the spatial contraction of the wave function upon oxidation of the Ru(II) to the Ru(III). Thus, the electronic coupling element for the back reaction is one to two orders of magnitude smaller for the back electron transfer as compared to injection reducing the back reaction rate by the same factor.

A second very important contribution to the kinetic retardation of charge recombination arises from the fact that this process is characterized by a large driving force and a small reorganization energy, the respective values for sensitizer **I** being 1.5 and 0.3 eV, respectively. This places the electron recapture clearly in the inverted Markus region, reducing its rate by several orders of magnitude. This provides also a rationale for the observation that this interfacial redox process is almost independent of temperature and is surprisingly insensitive to the ambient that is in contact with the film [51].

Of great significance for the inhibition of charge recombination is the existence of an electric field at the surface of the titanium dioxide film. Although there is practically no depletion layer within the oxide because of the small size of the particles and their low doping level, a dipole field is established spontaneously by proton transfer from the protonated carboxylate or phosphonate groups of the ruthenium complex to the oxide surface, producing a charged double layer. If the film is placed in contact with a protic solvent, the latter can also act as proton donor. In aprotic media, Li^+ or Mg^{2+} are potential determining ions for TiO_2 [26] and they may be used to charge the surface positively. The local potential gradient from the negatively charged sensitizer to the positively charged oxide drives the injection in the desired direction. The same field inhibits also the electrons from exiting the solid after injection has taken place.

4.2.3. Charge Carrier Percolation and Collection

The subsequent migration of electrons within the TiO_2 conduction band to the current collector involves charge carrier percolation over the mesoscopic particle network. This important process, which leads to nearly quantitative collection of injected electrons, is presently attracting a great deal of attention [20–22]. For example, the elegant experiments conceived by Hagfeldt and Lindquist [20] have given useful keys to rationalize the intriguing findings made with these films under band gap illumination.

It should be noted that apart from recapture by the oxidized dye there is an additional loss channel in the nanocrystalline injection cell involving reduction of triiodide ions in the electrolyte that is present within the mesoporous network:

$$I_3^- + 2e_{cb}^-(TiO_2) \rightarrow 3I^- \tag{4}$$

Engineering the interface to impair this unwanted heterogeneous redox process from occurring will be a challenging task for future development.

The efficient interception of recombination by the electron donor, for example, iodide:

$$2S^+ + 3I^- \rightarrow 2S + I_3^- \tag{5}$$

is crucial for obtaining good collection yields and high cycle life of the sensitizer. In the case of sensitizer **I**, our own time-resolved laser experiments have shown the interception to take place with a rate constant of about 10^9–10^8 s^{-1} at the iodide concentrations that are typically applied in the solar cell. This is about 100 times faster than the recombination rate and 10^8 times faster than the intrinsic lifetime of the oxidized sensitizer in the electrolyte in the absence of iodide. Cyclic voltammetry experiments carried out with solutions of **I** have shown its intrinsic lifetime in the oxidized state to be limited to a few seconds by intramolecular charge transfer from Ru(III) to the SCN^- group followed by irreversible oxidation of the latter ligand. The factor of 10^8 explains the fact that this sensitizer can sustain 100 million turnovers in continuous solar cell operation without loss of performance.

4.2.4. Incident Photon-to-Current Conversion Efficiencies

A graph that presents the monochromatic current output as a function of the wavelength of the incident light is known as a "photocurrent action spectrum". Figure 13 shows such spectra for four ruthenium complexes, illustrating the very high efficiency of quantum conversion with these complexes. When corrected for the inevitable reflection and absorption losses in the conducting glass serving to support the nanocrystalline film, yields of practically 100% of current flow per incident photon flux are obtained over a wide wavelength range. This implies that light harvesting, conversion of photons to electrons and collection of the injected electrons is quantative; see Eq. (2). Historically, RuL_3 (L = 2,2′-bipyridyl-4,4′-dicarboxylate) was the first efficient and stable charge transfer sensitizer to be used in conjunction with high-surface-area TiO_2 films. In a long-term experiment carried out during 1988, it sustained 9 months of intense illumination without degradation. However, the visible light absorption of this sensitizer is insufficient for solar light conversion. A significant improvement of the light harvesting was achieved with the trimeric complex of ruthenium [16] whose two peripheral ruthenium moieties were designed to serve as antennas [52]. An even more effective charge transfer sensitizer is *cis*-dithiocyanatobis(2,2′-bipyridyl)-4,4′-(dicarboxylate)-ruthenium(II). The latter achieves close to quantitative photon-to-electron conversion over the wavelength range from 350 to 600 nm [18]. Even at 700 nm, current generation is still 40% to 60% efficient depending on the thickness of the film. Its perfomance was only superseded recently by the discovery of a new black dye having a spectral onset at 900 nm, which is optimal for the conversion of amplitude-modulated (AM) 1.5 solar radiation to electric power in a single-junction photovoltaic cell [44].

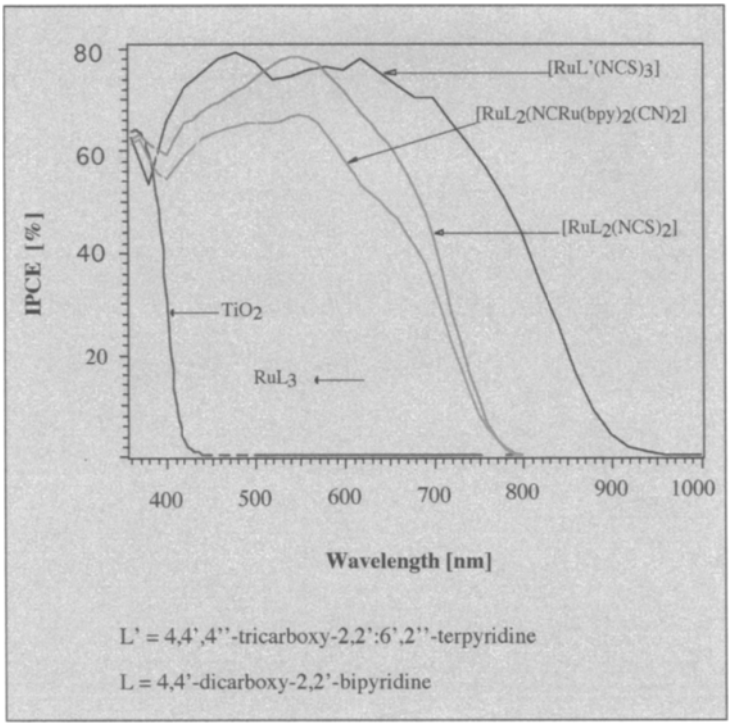


Fig. 13. Photocurrent action spectrum obtained with four different ruthenium-based sensitizers attached to the nanocrystalline TiO_2 film. Data obtained with the bare TiO_2 surface are shown for comparison.

4.2.5. Overall Solar-to-Electric Power Conversion Efficiencies

The overall efficiency (η_{global}) of the photovoltaic cell can easily be calculated from the integral photocurrent density (i_{ph}), the open-circuit photovoltage (V_{oc}), the fill factor of the cell (ff), and the intensity of the incident light (I_{s}):

$$\eta_{\text{global}} = \frac{i_{\text{ph}} \times V_{\text{oc}} \times \text{ff}}{I_{\text{s}}} \tag{6}$$

The currently obtained overall efficiencies are in the 10% to 11% range depending on the fill factor of the cell. Thus, current–voltage characteristic nanocrystalline injection cells based on sensitizer **I** were certified by the photovoltaic test laboratory at the PV Calibration Laboratory of the Fraunhofer Institute for Solar Energy in Freiburg, Germany. The photocurrent obtained at 1000 mW/cm^2 of simulated AM 1.5 global solar intensity was 19.40 mA/cm^2, the open-circuit voltage was 0.794 V, and the fill factor was 0.70, yielding for the conversion efficiency of the cell a value of 11%. This I/V curve is shown in Figure 14. Under optimal current collection geometry, minimizing ohmic losses resulting from the sheet resistance of the conducting glass resistance, cells with very high fill factors, that is, ff = 0.8, have already been fabricated.

This yield is still significantly below the value of 33% corresponding to the upper limit for conversion of standard AM 1.5 solar radiation to electricity by a single-junction cell. The main reason for the difference is the mismatch in the redox level of the dye and that of the iodide/triioide redox system used as the electrolyte, leading to a voltage loss of 0.7 V. Adjusting the redox levels to reduce this loss to a more reasonable figure of 0.3 V would allow the overall conversion efficiency to double from 10% to 20%. An improvement of the cell current by approximately 30% should be possible through better light harvesting in the 700–800-nm range where the absorption of **I** is relatively weak. Applying a dye

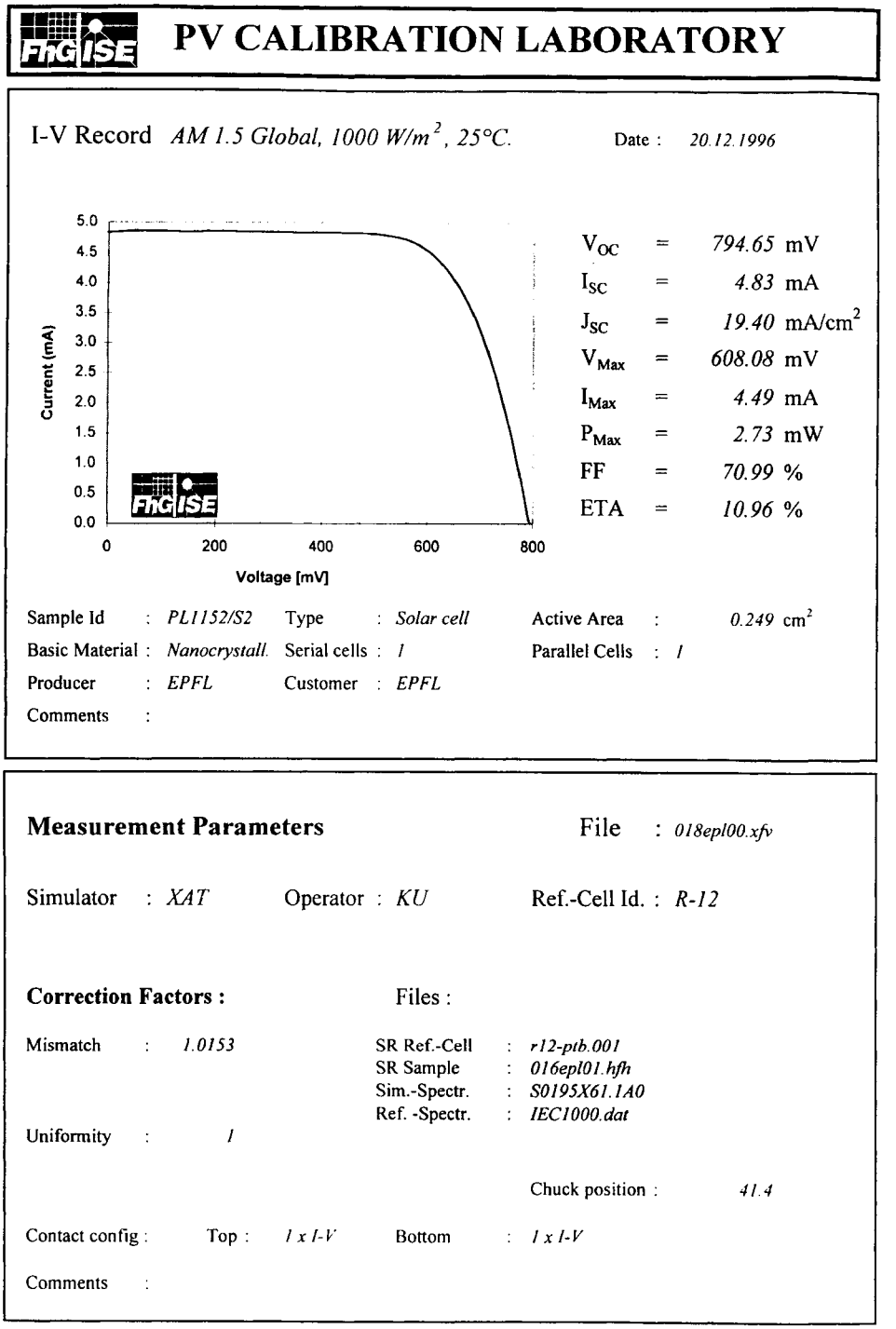


Fig. 14. Photocurrent–voltage curve for a sealed nanocrystalline injection cell based on *cis*-Ru(2,2,-bipyridyl-4,4′-dicarboxylate)$(SCN)_2$ as a sensitizer. The simulated AM 1.5 global solar radiation is 1000 W/m^2.

cocktail that is complementary in spectral response offers a straightforward way to achieve this goal. Thus, it is feasible to reach with nanocrystalline materials efficiencies around 25% that fall in the same range as those observed with top-quality, single-crystal GaAs solar cells.

An advantage of the nanocrystalline solar cell with respect to solid-state devices is that its performance is remarkably insensitive to temperature change. Thus, raising the temperature from 20 to 60 °C has practically no effect on the power conversion efficiency. In contrast, conventional silicon cells exhibit a significant decline over the same temperature range amounting to more than 25%. Because the temperature of a solar cell will reach readily 60 °C under full sunlight, this feature of the injection cell is particularly attractive for power generation under natural conditions.

4.3. Photovoltaic Performance Stability

The stability of all the constituents of the nanocrystalline injection solar cells, that is, the conducting glass, the TiO_2 film, the sensitizer, the electrolyte, the counterelectrode, and the sealant, have been subjected to close scrutiny. The stability of the TCO glass and the nanocrystalline TiO_2 film being unquestionable, investigations have focused on the four other components. On long-time illumination, complex **I** sustained 5×10^7 redox cycles without noticeable loss of performance corresponding to approximately 10 years of continuous operation in natural sunlight [53]. By contrast, practically all organic dyes tested so far underwent photobleaching after less than 10^6 cycles. This clearly outlines the exceptionally stable operation of our charge transfer sensitizers, which is of great advantage for the practical application of these devices. The reason for this astonishing stability is the very rapid deactivation of the excited triplet state via charge injection into the TiO_2 which—as was shown above—occurs in the femtosecond time domain. This is at least 8 orders of magnitude faster than any other competing channels of excited state deactivation including those leading to chemical transformation of the dye.

These tests are very important, because—apart from the sensitizer—other components of the device, such as the redox electrolyte or the sealing, may fail under long-term illumination. Indeed, a problem emerged with electrolytes based on cyclic carbonates, such as propylene or ethylene carbonate, which were found to undergo thermally activated decarboxylation in the presence of TiO_2, rendering these solvents unsuitable for practical usage. They were, therefore, replaced by a highly polar and nonvolatile liquid that does not exhibit this undesirable property. Room temperature molten salts based on imidazolium iodides and triflates have revealed very attractive stability features although their high viscosity restricts applications to the low-current regime, for example, indoor power supplies. Thus, fully assembled cells showed no decline in photovoltaic performance, that is, photocurrent, photovoltage, and fill factor, when submitted to accelerated aging performed in a sun test (AM 1) chamber at 44 and 85 °C for at least 2300 and 1000 h, respectively [53]. Direct excitation of electron–hole pairs in the anatase by $\lambda > 380$-nm light was avoided in these experiments by using a polycarbonate protective film.

Stability tests on sealed cells have progressed significantly over the last few years. These tests are very important as the redox electrolyte or the sealing may fail under long-term illumination. A recent stability test over 7000 h of continuous full-intensity light exposure has confirmed that this system does not exhibit an inherent instability [54], in contrast to amorphous silicon, which as a consequence of the Stabler–Wronski effect undergoes photodegradation.

4.4. Development of Series-Connected Modules

Meanwhile, the development and testing of the first cell module for practical applications has begun. The layout of the module is presented in Figure 15. The cell consists of two glass plates, which are coated with a transparent conducting oxide (TCO) layer. The nanocrystalline titanium dioxide film deposited on the lower plate supports the ruthenium complex acting as a charge transfer sensitizer. On illumination, this injects an electron into the titanium dioxide conduction band. The electrons pass over the collector electrode into the

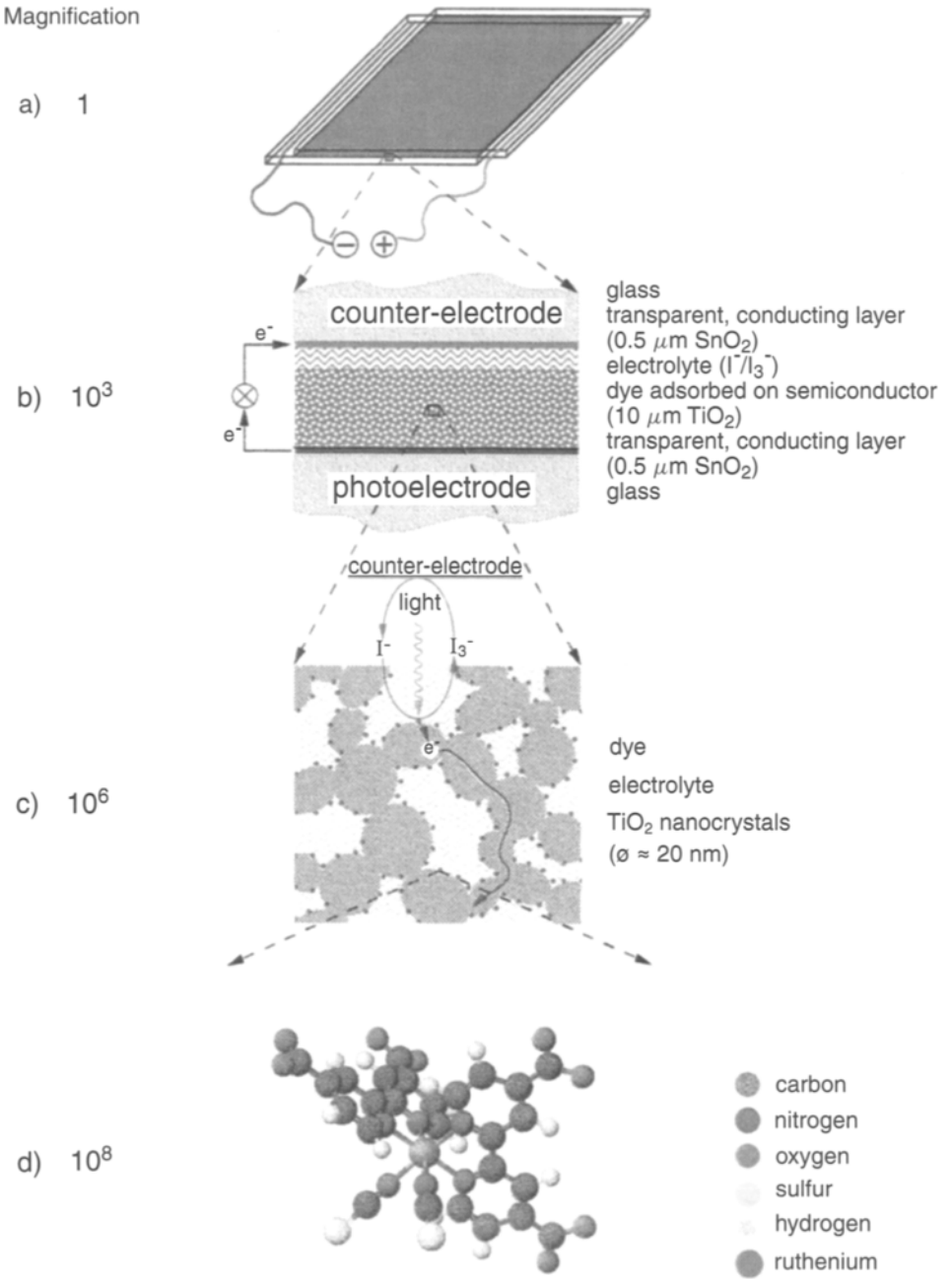


Fig. 15. Schematic presentation of the dye-sensitized nanocrystalline solar cell and its components: (a) general view, (b) cross section, (c) blowup of the mesoporous photoanode, and (d) the structure of the ruthenium complex **I** serving as the charge transfer dye.

external circuit where they perform work. They are then returned to the cell via the counterelectrode. The sensitizer film is separated from the counterelectrode by the electrolyte containing the redox couple, for example, triiodide/iodide, whose role is to transport electrons from the counterelectrode to the sensitizer layer. A small amount of platinum (5–10 $\mu g/cm^2$) is deposited onto the counterelectrode to catalyze the cathodic reduction of triiodide to iodide.

An alternative approach developed by Kay in our laboratory uses a monolithic triple-layer structure [55] where the nanocrystalline anatase film, a porous spacer, and the carbon counterelectrode are directly deposited on top of each other. A 21-cm^2-sized working interconnected module consisting of 6 Z-type interconnected cells was recently demonstrated.

Accelerated stability tests were also performed with this type of cell. Continuous exposure to full sunlight for 120 days did not result in any significant deterioriation of performance. This confirms system stability over several years of natural conditions without any indication of a decline in efficiency.

4.5. Cost and Environmental Compatibility of the New Injection Solar Cell

Several industrial sources, including Asea Brown Boveri, Strategies Unlimited, and Research Triangle Institute, have performed a cost analysis which yields U.S.$0.6/Wp and U.S.$2000/kWp for module and total systems cost, respectively. Similar values were reported by Smestad [56].

It may be argued that the presence of ruthenium renders the price of the sensitizer too high for commercial exploitation or that there is insufficient supply of it. However, the required amount is only 10^{-3} mol/m^2 of ruthenium complex corresponding to the small investment of approximately U.S.$0.2/$m^2$ for the noble metal. The world trade in ruthenium reached 10 tons in 1994 mainly because of its use as a dimensionally stable anode in electrochemical chlorine production. One ton of ruthenium alone incorporated in the charge transfer sensitizer **I** could provide 1 GW of electric power under full sunlight. This is more than twice the total photovoltaic capacity presently in use worldwide. Thus, the cost and supply of ruthenium-based sensitizers is of no real concern here. The price-determining material for this photovoltaic technology is undoubtedly the conducting glass.

Apart from efficiency and stability, any future photovoltaic technology will be valued according to its environmental and human compatibility. There is great concern about the adverse environmental effects and acute toxicity of CdTe or $CuInSe_2$, which are being considered for practical development as thin solar cells. Such concerns are unjustified for our nanocrystalline device. Titanium dioxide is a harmless, environmentally friendly material, remarkable for its very high stability. It occurs in nature as ilmenite, and is used in quantity as a white pigment and as an additive in toothpaste. Worldwide annual production is in excess of 1 million tons. Similarly, ruthenium has been used without adverse health effects as an additive for bone implants.

4.6. Current Research Issues

Current research in the field of injection solar cells focuses on the following topics:

1. The molecular design and synthesis of new sensitizers having enhanced near-infrared light response, examples being phthalocyanines or the black dye discussed previously
2. A better understanding of the interface, including experimental and theoretical work on dye adsorption processes
3. The analysis of the dynamics of interfacial electron transfer processes down to the femtosecond time domain
4. The unraveling of the factors that control electron transport in nanocrystalline oxide semiconductor films
5. The replacement of the liquid electrolyte by solid materials
6. The development of tandem cells and their use for the cleavage of water by visible light

Topics 1 through 4 have already been addressed previously. In the following, we shall, therefore, restrict ourselves to the discussion of the last two items.

5. SENSITIZED SOLID-STATE HETEROJUNCTIONS

Recently, great efforts have been undertaken to replace the electrolyte in liquid junction solar cells by a solid charge transport material. Thus, inorganic p-type semiconductors [14, 15, 58] and organic materials [57, 59, 60] have been scrutinized. These devices use hole-transmitting materials that form heterojunctions with the dye-loaded n-type nanocrystalline oxide film. Suitable solid materials to replace the liquid electrolyte in the injection solar cells are large-band-gap p-type semiconductors. Light-induced electron transfer from the excited state in the conduction band of the oxide semiconductor occurs in the same manner as with liquid electrolytes. However, the dye is regenerated by electron donation from the solid charge transfer material assuming the role of the iodide ions in the liquid junction system (see Fig. 16).

The advantage of this approach is that hole conduction to the counterelectrode occurs by hopping and does not involve mass transfer. In addition, judicious selection of the organic material allows its redox level to be matched to the ground state oxidation potential of the sensitizer. This is not the case for the triiodide/ioide redox electrolyte where typically 0.5 eV of the driving force is wasted in the regeneration of sensitizers, such as complex **I**. Judicious selection of the type of organic hole-transmitting material offers the prospect of avoiding this loss, resulting in an increased photovoltage that would permit the overall efficiency of the device to be nearly doubled. The solid nature of the cell will also foster practical applications as it avoids the technical problems associated with the use of liquid electrolytes.

So far, the incident monochromatic photon-to-current conversion efficiency (IPCE) of this type of solid-state cell has remained low. However, significant progress was achieved recently by applying the novel amorphous organic hole transport material (HTM) 2,2′,7,7′-tetrakis-(N,N-di-p-methoxyphenyl-amine)9,9′-spirobifluorene (OMeTAD) [61, 62], whose

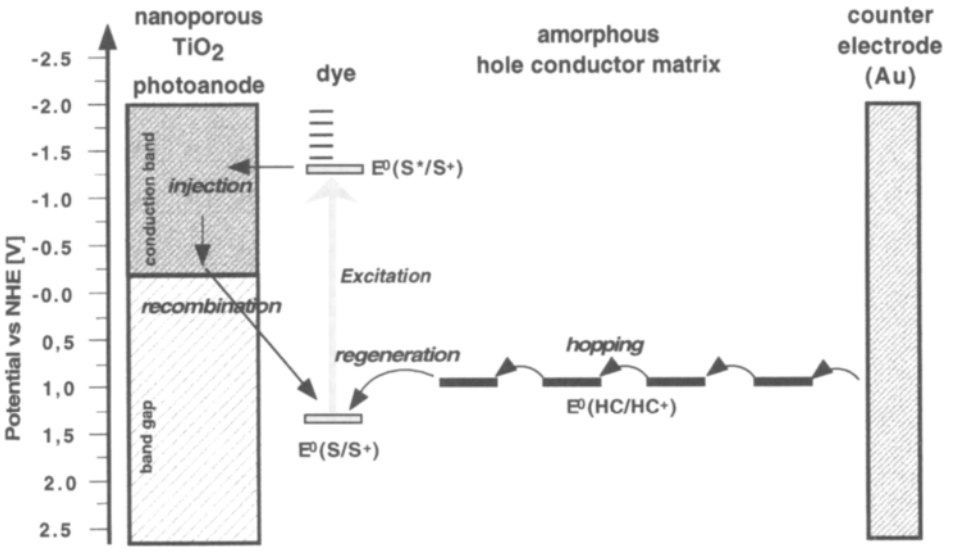


Fig. 16. Schematic outline of a dye-sensitized heterojunction device. Light-induced electron transfer processes (injection, regeneration, recapture, hopping) occurring in the dye-sensitized heterojunction, as well as the approximate redox potentials and band energies of the different components.

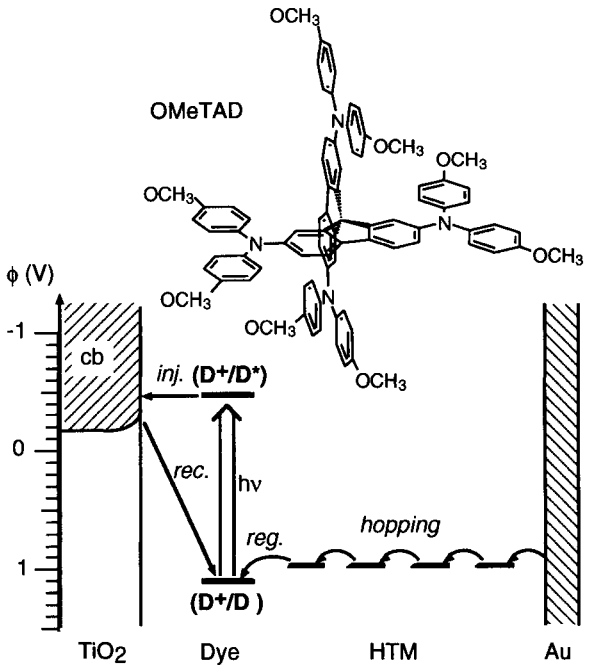


Fig. 17. Structure of arylamine used as a hole conductor in dye-sensitized heterojunctions.

structure is shown in Figure 17. Photoinduced charge carrier generation at the heterojunction is very efficient. A solar cell based on OMeTAD converts photons to electric current with a strikingly high yield of 33% [57].

The new hole conductor contains a spirocenter, which is introduced in order to improve the glass-forming properties and prevent crystallization of the organic material. Its glass transition temperature of $T_g = 120\,°C$, measured by differential scanning calorimetry, is much higher than that of the widely used hole conductor TPD ($T_g = 62\,°C$). Crystallization is undesirable as it would impair the formation of a good contact between the mesoporous surface of the TiO_2 and the hole conductor. The methoxy groups are introduced in order to match the oxidation potential of the HTM to that of the sensitizer $Ru(II)L_2(SCN)_2$(L = 4,4′-dicarboxy-2,2′-bipyridyl) used in this study.

Pulsed nanosecond laser photolysis was used in conjunction with time-resolved absorption spectroscopy to scrutinize the dynamics of the photoinduced charge separation process. It was found that electron injection from the excited sensitizer into TiO_2 is immediately followed by regeneration of the dye via hole transfer to OMeTAD [Eqs. (1) and (2)]:

$$Ru(II)L_2(SCN)_2^* \rightarrow Ru(III)L_2(SCN)_2^+ + e^-(TiO_2) \quad (7)$$

$$OMeTAD + Ru(III)L_2(SCN)_2^+ \rightarrow Ru(III)L_2(SCN)_2 + OMeTAD^+ \quad (8)$$

The latter process was too fast to be monitored with the laser equipment employed, setting an upper limit of 40 ns for the hole transfer time.

The photovoltaic performance of the dye-sensitized heterojunction was studied by means of sandwich-type cells. The working electrode consisted of conducting glass (F-doped SnO_2, sheet resistance 10 Ω/square) onto which a compact TiO_2 layer was deposited by spray pyrolysis [63]. This avoids direct contact between the HTM layer and the SnO_2, which would short-circuit the cell. A 4.2-μm-thick mesoporous film of TiO_2 was deposited by screen printing onto the compact layer [22] and derivatized with $Ru(II)L_2(SCN)_2$ by adsorption from acetonitrile. The HTM was introduced into the mesopores by spin

coating a solution of OMeTAD in chlorobenzene onto the TiO_2 film and subsequent evaporation of the solvent. The coating solution contained 3.3 mM $N(PhBr)_3SbCl_6$ and 15 mM $Li[(CF_3SO_2)_2N]$ in addition to 0.17 M OMeTAD. A semitransparent gold back contact was evaporated on top of the hole conductor under vacuum. The maximum IPCE is 33%, which is more than two orders of magnitude larger then the previously reported value for a similar dye-sensitized solid heterojunction [60] and only a factor of about 2 lower than with liquid electrolytes [18].

Further improvement of the photovoltaic performance is expected, as many parameters of the cell assembly have not yet been optimized. Preliminary stability tests performed over 80 h using the visible output of a 400-W Xe lamp showed that the photocurrent was stable within ±20%, while the open-circuit voltage and the fill factor increased. The total charge passed through the cell during illumination was 300 C/cm^2, corresponding to turnover numbers of about 8400 and 60,000 for the OMeTAD and the dye, respectively. This shows that the hole conductor can sustain photovoltaic operation without significant degradation.

From these findings, the concept of dye-sensitized heterojunctions emerges as a very interesting and viable option for future low-cost solid-state solar cells. Photodiodes based on interpenetrating polymer networks of poly(phenylene vinylene) derivatives [64, 65] present a related approach. The main difference to our system is that at least one component of the polymer network needs to function simultaneously as an efficient light absorber and a good charge transport material. The dye-sensitized heterojunction cell offers a greater flexibility inasmuch as the light absorber and charge transport material can be selected independently to obtain optimum solar energy harvesting and high photovoltaic output.

6. TANDEM CELLS FOR THE CLEAVAGE OF WATER BY VISIBLE LIGHT

A tandem device that achieves the direct cleavage of water into hydrogen and oxygen by visible light was developed in collaboration with two partner groups from the Universities of Geneva and Berne, CH [66]. This is based on the series connection of two photosystems. A thin film of nanocrystalline tungsten trioxide absorbs the blue part of the solar spectrum. The valence band holes created by band gap excitation of the WO_3 serve to oxidize water to oxygen, while the conduction band electrons are fed into the second photosystem, which consists of the dye-sensitized nanocrystalline TiO_2 film. The latter is placed directly behind the WO_3 film capturing the green and red part of the solar spectrum that is transmitted through the top electrode (see Fig. 18). The photovoltage generated by the second photosystem enables the generation of hydrogen by the conduction band electrons.

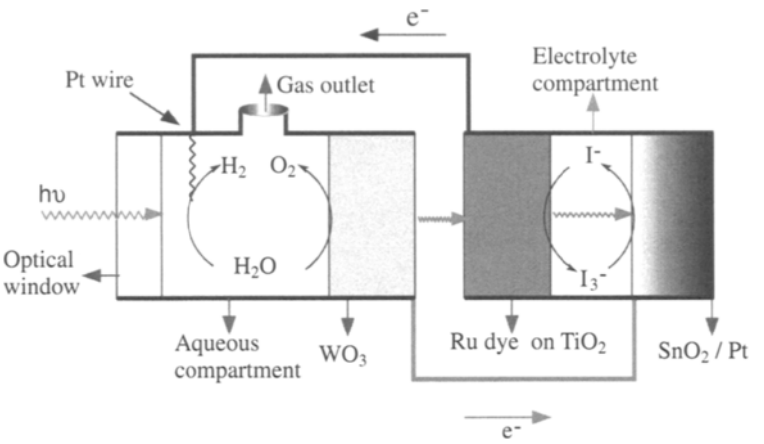


Fig. 18. Circuit diagram of the tandem cell for water cleavage by visible light.

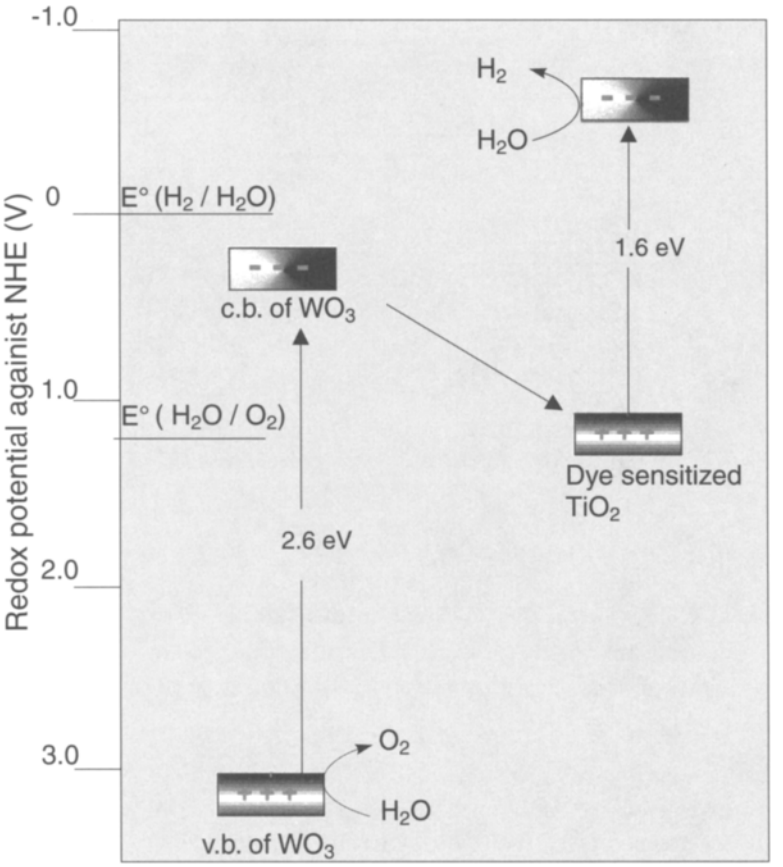


Fig. 19. The Z scheme of biphotonic water photolysis mimicks photosynthesis of green plants.

There is close analogy to the Z scheme operative in the light reaction of photosynthesis in green plants. This is illustrated by the electron flow diagram shown in Figure 19. In green plants, there are also two photosystems connected in series, one affording water oxidation to oxygen and the other generating the NADPH used in carbon dioxide fixation. The advantage of the tandem approach is that higher efficiencies than with single-junction cells can be reached if the two photosystems absorb complementary parts of the solar spectrum. At present, the overall AM 1.5 solar light to chemical conversion efficiency achieved with this device stands at 4.5%.

7. NANOCRYSTALLINE INTERCALATION BATTERIES

The diffuse and intermittent nature of sunlight renders necessary the storage of solar energy in electrical or chemical form. There is presently a thrust for improved batteries relating to electric energy storage. In this context, the so-called "rocking chair" batteries deserve particular attention. Electric power generation is associated with the migration of lithium ions from one host, that is, TiO_2, constituting the anode, to another host electrode, namely, NiO_2/CoO_2 or MnO_2, constituting the cathode. The voltage delivered by the device is simply the difference of the chemical potential of lithium in the two host materials. It was discovered that the power output of the battery is improved if the oxides employed have a nanocrystalline morphology as compared to bulk electrodes (see Fig. 20). The reason for this behavior is that the diffusion time for lithium ions in the host oxide is dramatically shortened by using oxide particles of mesoscopic dimensions as electrodes. A standard

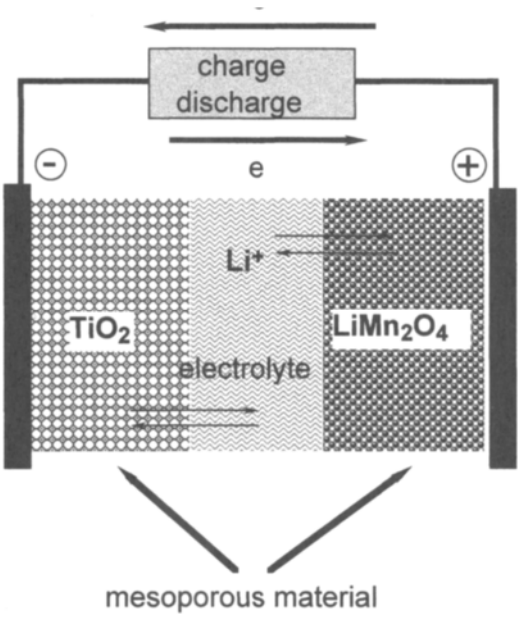


Fig. 20. Mesoporous lithium ion battery using TiO_2 and $LiMnO_4$ as the anode and cathode material, respectively.

size R921 coin cell has been developed supplying 4–4.5 mA h corresponding to 50 mA h/g capacity, which compares well with the rocking chair battery having a carbon anode. These findings provide a very promising basis for the development of a new type of rechargeable battery [67].

In conclusion, it appears that nanocrystalline electronic junctions involving transition metal oxides form not only the heart of new display and photovoltaic devices but also offer attractive perspectives for the storage of electrical energy that is generated by sunlight.

References

1. C. J. Brinker and C. W. Scherer, "Sol–Gel Science: The Physics and Chemistry of Sol–Gel Processing." Academic Press, San Diego, 1990.
2. L. C. Klein, "Sol–Gel Optics—Processing and Applications." Kluwer Academic, Boston, 1994.
3. H. D. Gesser and P. C. Goswami, *Chem. Rev.* 89, 765 (1989).
4. L. C. Klein, ed., "Sol–Gel Technology for Thin Films, Fibers, Preforms, Electronics and Special Shapes." Noyes Publications, Park Ridge, NJ, 1988.
5. (a) M. Matijevic, *Mater. Res. Soc. Bull.* 4, 18 (1989).
   (b) E. Matijevic, *Mater. Res. Soc. Bull.* 5, 16 (1990).
   (c) R. Mehrotra, *Struct. Bonding* 77, 1 (1992).
6. E. Matijevic, *Langmuir* 10, 8 (1994); ibid. 2, 12 (1986).
7. E. Matijevic, *Chem. Mater.* 5, 412 (1993); *Ann. Rev. Mater. Sci.* 15, 485 (1985).
8. W. X. Wang, D. H. Li, and S. H., *Appl. Phys. Lett.* 62, 312 (1993).
9. J. S. Foresi and T. D. Moustakas, *Mater. Res. Soc. Proc.* 256, 77 (1992).
10. T. G. Nieh, J. Wadsworth, and F. Wakai, *Int. Mat. Rev.* 36, 146 (1991).
11. M. M. Boutz, R. J. Olde-Schulthuis, A. J. Winnubst, and A. J. Burggraaf, in "Nanoceramics" (R. Freer, ed.), Vol. 51. London, 1993.
12. Q. Xu and M. A. Anderson, *J. Am. Ceram. Soc.* 77, 1939 (1994).
13. A. Hagfeldt, N. Vlachopoulos, and M. Grätzel, *J. Electrochem. Soc.* 141, L82 (1994).
14. K. Tennakone, G. R. R. A. Kumara, A. R. Kumarasinghe, K. G. U. Wijayantha, and P. M. Sirimanne, *Semicond. Sci. Technol.* 10, 1689 (1995).
15. B. O'Regan and D. T. Schwarz, *Chem. Mater.* 7, 1349 (1995).

16. B. O'Regan and M. Grätzel, *Nature (London)* 335, 737 (1991).
17. M. K. Nazeeruddin, P. Liska, J. Moser, N. Vlachopoulos, and M. Grätzel, *Helv. Chim. Acta* 73, 1788 (1990).
18. M. K. Nazeeruddin, A. Kay, I. Rodicio, R. Humphrey-Baker, E. Müller, P. Liska, N. Vlachopoulos, and M. Grätzel, *J. Am. Chem. Soc.* 115, 6382 (1993).
19. T. Gerfin, M. Grätzel, and L. Walder, *Prog. Inorg. Chem.* 44, 346 (1996).
20. M. Mayor, A. Hagfeldt, M. Grätzel, and L. Walder, *Chimia* 50, 47 (1996).
21. A. Hagfeldt and M. Grätzel, *Chem. Rev.* 95, 45 (1995).
22. Ch. J. Barbe, F. Arendse, P. Comte, M. Jirousek, F. Lenzmann, V. Shklover, and M. Grätzel, *J. Am. Ceram. Soc.* 80, 3157 (1997).
23. M. Wolf, Ph.D. Thesis, Ecole Polytechnique Fédérale de Lausanne, 1998.
24. L. E. Brus, *J. Chem. Phys.* 79, 5566 (1983).
25. L. Kavan, T. Stoto, M. Grätzel, D. Fitzmaurice, and V. Shklover, *J. Phys. Chem.* 97, 9493 (1993).
26. G. Redmond and D. Fitzmaurice, *J. Phys. Chem.* 97, 11081 (1993).
27. U. Kölle, J. Moser, and M. Grätzel, *Inorg. Chem.* 24, 2253 (1985).
28. B. Enright, G. Redmond, and D. Fitzmaurice, *J. Phys. Chem.* 97, 11081 (1994).
29. L. A. Lion and J. T. Hupp, *J. Phys. Chem.* 97, 1426 (1995).
30. S. G. Yan and J. T. Hupp, *J. Phys. Chem.* 100, 6867 (1996).
31. I. Bedja, S. Hotchandi, and P. V. Kamat, *J. Phys. Chem.* 97, 11064 (1993).
32. P. Bonhôte, E. Gogniat, S. Tingry, Ch. Barbé, N. Vlachopoulos, F. Lenzmann, P. Compte, and M. Grätzel, *J. Phys. Chem. B* 102, 1498 (1998).
33. C. W. Tang and S. A. Van Slyke, *Appl. Phys. Lett.* 51, 913 (1987).
34. J. Athanassov, F. P. Rotzinger, P. Pechy, and M. Grätzel, *J. Phys. Chem. B* 101, 2558 (1997).
35. B. O'Regan, J. Moser, M. Anderson, and M. Grätzel, *J. Phys. Chem.* 94, 98720 (1990).
36. A. Zaban, A. Meier, and B. A. Gregg, *J. Phys. Chem.* 101, 7985 (1997).
37. A. Hagfeldt, and M. Grätzel, *Chem. Rev.* 95, 45 (1995).
38. J. Ferber, R. Stangl, and J. Luther, *Sol. Energy Mater. Sol. Cells* 53, 29 (1998).
39. A. Hagfeldt, U. Björkstén, and S.-E. Lindquist, *J. Sol. Energy Mater. Sol. Cells* 27, 293 (1992).
40. K. Schwarzburg and F. Willig, *Appl. Phys. Lett.* 58, 2520 (1991).
41. R. Könenkamp and R. Henninger, *J. Appl. Phys. A* 87 (1994).
42. G. Hodes, I. D. J. Howell, and L. M. Peter, *J. Electrochem. Soc.* 139, 3136 (1992).
43. P. V. Kamat, *Prog. React. Kinet.* 19, 277 (1994).
44. Md. K. Nazeeruddin, P. Pechy, and M. Grätzel, *Chem. Commun.* 1705 (1997).
45. P. Pechy, F. Rotzinger, M. K. Nazeeruddin, O. Kohle, S. M. Zakeeruddin, R. Humphry-Baker, and M. Grätzel, *J. Chem. Soc., Chem. Commun.* 65 (1995).
46. Y. Tachibana, J. E. Moser, M. Grätzel, D. R. Klug, and J. R. Durrant, *J. Phys. Chem.* 100, 20056 (1996).
47. T. Hannapel, B. Burfeindt, W. Storck, and F. Willig, *J. Phys. Chem. B* 101, 6799 (1997).
48. J. E. Moser, D. Noukakis, U. Bach, Y. Tachibana, D. R. Klug, J. R. Durrant, R. Humphry-Baker, and M. Grätzel, *J. Phys. Chem. B* 102, 3649 (1998).
49. R. J. Ellington, J. B. Achbury, S. Ferrere, H. N. Gosh, A. J. Nozik, and T. Q. Lian, *J. Phys. Chem. B* 102, 6455 (1998).
50. J. E. Moser and M. Grätzel, *Chimia* 52, 160 (1998).
51. J. E. Moser and M. Grätzel, *Chem. Phys.* 176, 493 (1993).
52. R. Amadelli, R. Argazzi, C. A. Bignozzi, and F. Scandola, *J. Am. Chem. Soc.* 112, 7029 (1990).
53. N. Papageorgiou, Y. Athanassov, M. Armand, P. Bonhôte, H. Petterson, A. Azam, and M. Grätzel, *J. Electrochem. Soc.* 143, 3099 (1996).
54. O. Kohle, M. Grätzel, A. F. Meyer, and T. B. Meyer, *Adv. Mater.* 9, 904 (1997).
55. A. Kay and M. Grätzel, *Sol. Energy Mater. Sol. Cells* 44, 99 (1996).
56. G. Smestad, *Sol. Energy Mater. Sol. Cells* 32, 259 (1994).
57. U. Bach, D. Lupo, P. Comte, J. E. Moser, F. Weissörtel, J. Salbeck, H. Spreitzer, M. Grätzel, *Nature* 395, 583 (1998).
58. B. O'Regan and D. T. Schwarz, *Chem. Mater.* 10, 1501 (1998).
59. K. Murakoshi, R. Kogure, and S. Yanagida, *Chem. Lett.* 5, 471 (1997).
60. J. Hagen and D. Haarer, *Synth. Met.* 89, 215 (1998).
61. J. Salbeck, F. Weissörtel, and J. Bauer, *Macromol. Symp.* 125, 121 (1997).
62. J. Salbeck, N. Yu, J. Bauer, F. Weissörtel, and H. Bestgen, *Synth. Met.* 91, 209 (1997).
63. L. Kavan, and M. Grätzel, *Electrochim. Acta* 40, 643 (1995).
64. J. J. M. Halls et al., *Nature* 376, 498 (1995).
65. G. Yu, J. Gao, J. C. Hummelen, F. Wudl, and A. J. Heeger, *Science* 270, 1789 (1995).
66. J. Augustynski, G. Calzaferri, J. C. Courvoisier, M. Grätzel, and M. Ulmann, in "Proceedings of the 10th International Conference on the Photochemical Storage of Solar Energy," Interlaken, Switzerland, 1994, p. 229.
67. S. Y. Huang, K. Kavan, I. Exnar, and M. Grätzel, *J. Electrochem. Soc.* 142, L142 (1995).

This Page Intentionally Left Blank

Chapter 11

NANOSTRUCTURE FABRICATION USING ELECTRON BEAM AND ITS APPLICATION TO NANOMETER DEVICES

Shinji Matsui

Laboratory of Advanced Science and Technology for Industry, Himeji Institute of Technology, Hyogo, Japan

Contents

1. Introduction 555
2. Nanofabrication Using Electron Beam 556
   2.1. Nanometer Electron Beam Direct Writing System 556
   2.2. 10-Nanometer Lithography Using Organic Positive Resist 558
   2.3. 10-Nanometer Lithography Using Organic Negative Resist 560
   2.4. Sub-10-Nanometer Lithography Using Inorganic Resist 561
   2.5. Nanometer Fabrication Using Electron-Beam-Induced Deposition 563
3. Material Wave Nanotechnology: Nanofabrication Using a de Broglie Wave 565
   3.1. Electron Beam Holography 565
   3.2. Atomic Beam Holography 569
4. Nanometer Devices 572
   4.1. 40-Nanometer-Gate-Length Metal-Oxide-Semiconductor Field-Emitter-Transistors 572
   4.2. 14-Nanometer-Gate-Length Electrically Variable Shallow Junction MOSFETs 574
   4.3. Operation of Aluminum-Based Single-Electron Transistors at 100 Kelvins 576
   4.4. Room Temperature Operation of a Silicon Single-Electron Transistor 579
5. Summary 582
   References 582

1. INTRODUCTION

Recent years have witnessed a number of investigations concerning nanostructure technology. The objective of research on nanostructure technology is to explore the basic physics, technology, and applications of ultrasmall structures and devices with dimensions in the sub-100-nm regime. Today, the minimum size of Si and GaAs production devices is down to 0.25 μm or less. Nanostructure devices are now being fabricated in many laboratories to explore various effects, such as those created by downscaling existing devices, quantum effects in mesoscopic devices, or tunneling effects in superconductors, and so on. In addition, new phenomena are being explored in an attempt to build switching devices with dimensions down to the molecular level.

Handbook of Nanostructured Materials and Nanotechnology, edited by H.S. Nalwa
Volume 3: Electrical Properties
Copyright © 2000 by Academic Press
All rights of reproduction in any form reserved.
ISBN 0-12-513763-X/$30.00

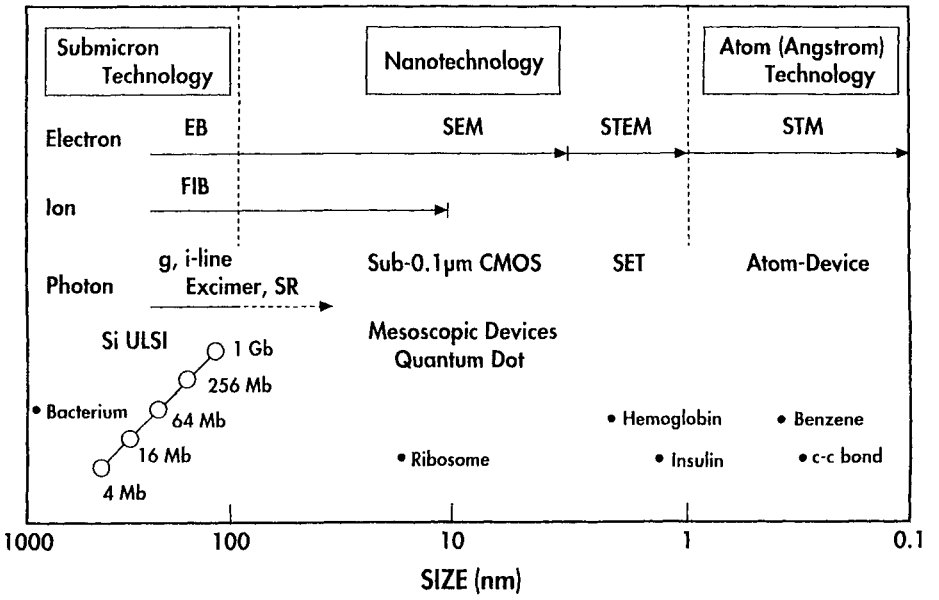


Fig. 1. Microfabrication using electrons, ions, and photons.

Figure 1 summarizes the resolution capabilities of several lithography processes that use electrons, ions, and photons. It includes the narrowest linewidth of feature size obtained with each process. Microfabrication can be classified into three regimes: submicrometer (1000–100 nm), nanometer (100–1 nm), and atom (or angstrom, less than 1 nm). A 256-Mb dynamic random-access memory (DRAM) Si ultra large scale integration (ULSI) of 0.25 μm dimension can be fabricated by using an i-line stepper with a phase shift mask or an excimer laser stepper. An excimer laser or SR lithography can be applied to a 1-Gb DRAM with a 0.15-μm feature size. Electron beam (EB) lithography is the most widely used and versatile lithography tool for fabricating nanostructure devices. Because of the availability of high-quality electron sources and optics, EB can be focused to diameters of less than 10 nm. The minimum beam diameters of scanning electron microscopes (SEMs) and scanning transmission microscopes (STEMs) are 1.5 and 0.5 nm, respectively. While a focused-ion beam (FIB) can be focused close to 8 nm, EB and FIB can be used to make nanoscale features in the 100–1-nm regime. Scanning tunneling microscopy (STM) is used for atomic technology in the range of 1 to 0.1 nm.

Figure 2 shows the resolution of various resists, which were confirmed by experiment for electrons and ions. Minimum sizes of 8 nm for poly(methyl methacrylate) (PMMA) [1, 2], 10 nm for ZEP (Nippon Zeopn Co.) positive resists [3], 20 nm for SAL601 (Shipley Co.) [4], and 10 nm for calixarene negative resists [5] have been demonstrated using EB lithography. Nanoscale patterns have also been written in inorganic resists such as AlF_3, NaCl, and SiO_2 using STEM [6, 7] and SEM [8]. Furthermore, carbon contamination patterns of 8 nm have been fabricated with SEM [9], and 8-nm PMMA patterns have been demonstrated by using Ga^+ FIB [10].

2. NANOFABRICATION USING ELECTRON BEAM

2.1. Nanometer Electron Beam Direct Writing System

There are some reports on EB nanolithography systems capable of exposure with a sub-10-nm beam in nanofabrication [3, 11–15]. Figure 3 shows a photograph and a design

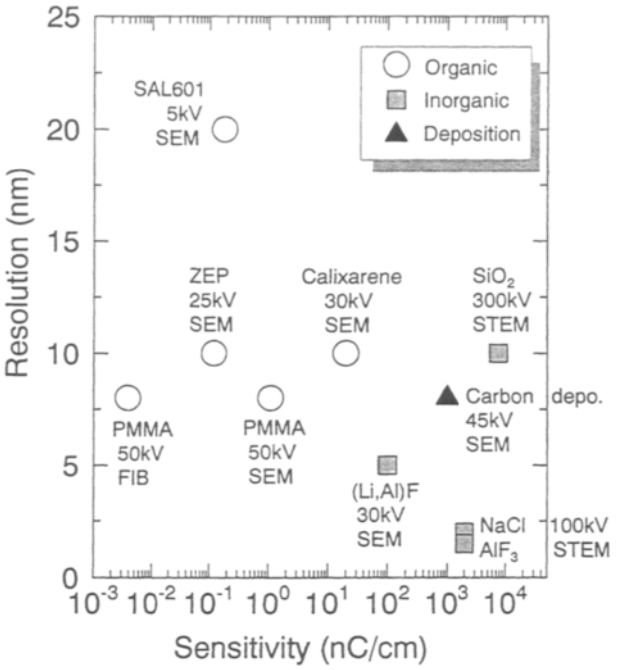
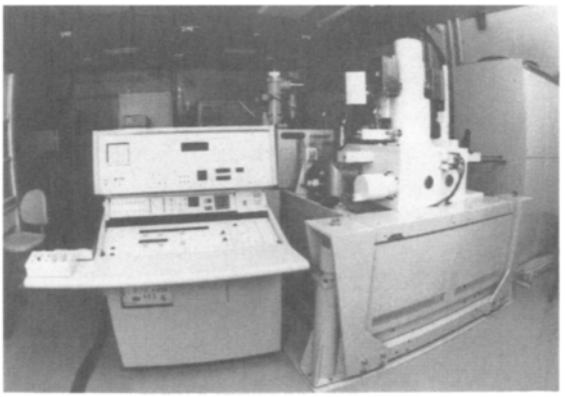


Fig. 2. Resolution of various resists for electrons and ions.



Performance

Acc = 50 kV

Beam diameter (at field center) X = 4.67 nm, Y = 4.68 nm beam current : 100 pA
Direct writing accuracy (field : 80 μm) (a) stitching : 2σ = 0.021 μm (b) overlay : 2σ = 0.016 μm beam current : 800 pA

Fig. 3. 50-kV nano-EB direct writing system.

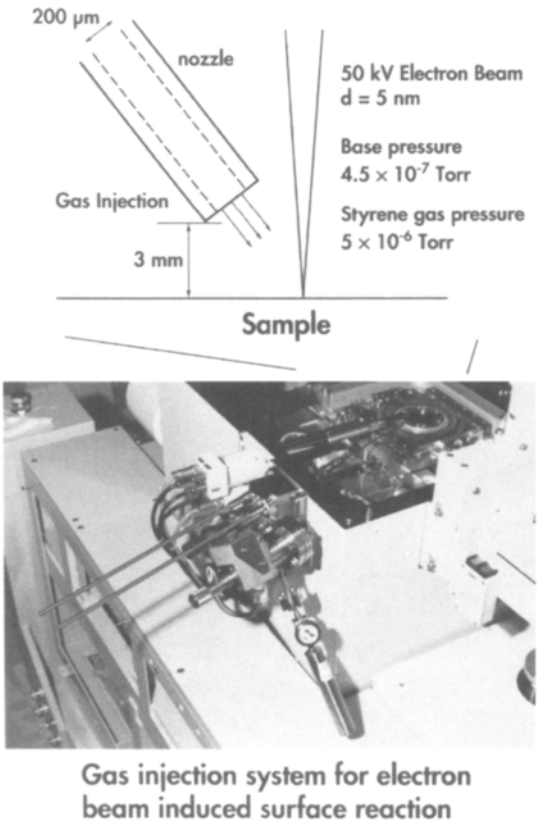


Fig. 4. Photograph and schematic diagram of gas introduction system.

target of a 50-kV EB lithography system developed by modifying the JEOL-5FE 25-kV EB system [16]. The major modified points of this EB system are acceleration voltage and a gas feed system. The acceleration voltage has been changed from 25 to 50 kV. The column design with respect to the electron gun chamber is modified to withstand the high voltage in order to avoid the field emission from the electrode surface. Because a Zr/O/W thermal field emission (TFE) electron gun is used in this system, the vacuum in the electron gun chamber must be maintained under 10^{-9} torr. The TFE gun has a small virtual source size and a high angular current intensity. Various gas species can be introduced into this specimen chamber to investigate the EB-induced surface reactions. The gas feed system is shown in Figure 4. The 50-cc-capacity gas cylinder contains the reaction gas. The gas is introduced through a variable leak valve and a fine nozzle with an inner diameter of 200 μm. The gas line nozzle is placed at a distance of 3 mm from the wafer. A carbon deposition pattern 14 nm in size was made by using styrene ($C_6H_5CH{=}CH_2$) gas. The EB diameter was measured by using a knife-edge method. The result of the measurement for both the x and the y directions was less than 5 nm. The overlay and stitching accuracy were evaluated by exposing 16 chips (4 × 4 in array) with a size of 80 × 80 μm in PMMA resist at 50 kV. The stitching accuracy and overlay accuracy were 0.021 and 0.016 μm at 2σ, respectively.

2.2. 10-Nanometer Lithography Using Organic Positive Resist

A PMMA positive resist was exposed to evaluate the fine pattern exposure characteristics using the preceding EB system. PMMA is known as the positive resist with high resolution. Thirty-nanometer-thick PMMA was spin coated on a bare thick Si wafer. After PMMA was prebaked at 170 °C for 20 min, EB exposure was carried out. The line dose was 0.8 nC/cm.

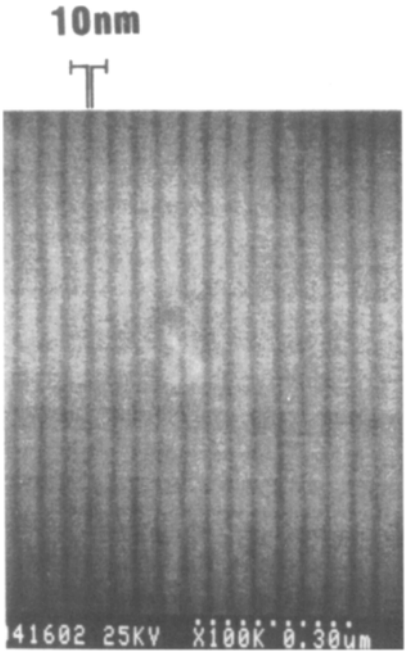


Fig. 5. 10-nm-linewidth PMMA patterns.

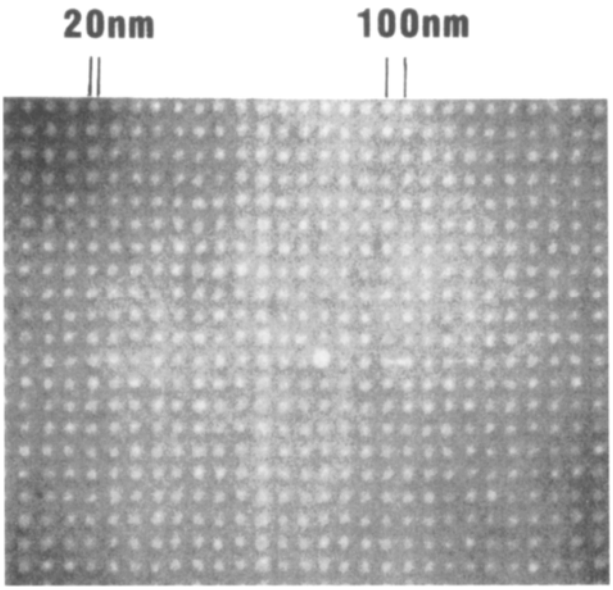


Fig. 6. 20-nm-diameter Au–Pd patterns.

The PMMA was developed in a mixture of MIBK:IPA = 1:3 for 1 min and was then rinsed in isopropyl alcohol (IPA) for 1 min. The point EB was line scanned with a period of 50 nm. Ten-nanometer-width line patterns in PMMA resist were obtained as shown in Figure 5. Fine metal patterns are useful as conductive wires or gate metals for the investigation of mesoscopic devices and other nanostructure physics. Au–Pd metal was delineated by a liftoff method. For the exposure of dot patterns, the resist was exposed with a shot time of 75 μs for each dot. After development, Au–Pd metal was deposited on the resist, at a thickness of 3 nm for dot patterns. The liftoff was performed in acetone. Figure 6 shows the

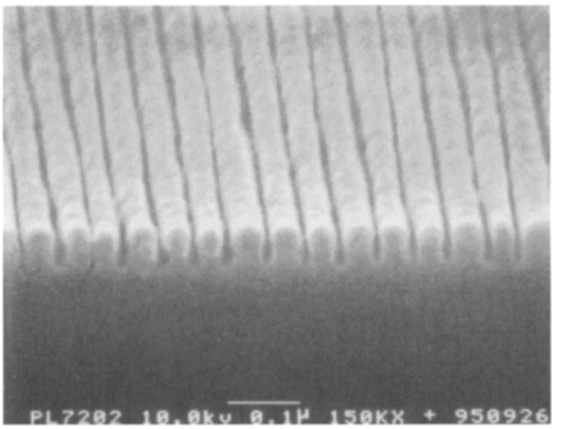


Fig. 7. 10-nm-linewidth ZEP patterns.

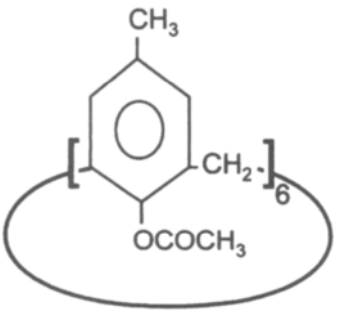


Fig. 8. Structure of calixarene.

SEM photographs of Au–Pd metal dot patterns on a Si wafer. Twenty-nanometer-diameter dot patterns with a period of 100 nm were successfully fabricated.

Nanodevice fabrication requires not only high resolution but also high overlay accuracy. High-speed exposure effectively meets the requirements because overlay accuracy is improved as a result of less beam drift on the nanometer scale. Moreover, it enables the use of a highly sensitive resist such as ZEP520 [17], which has sufficient resolution and high dry etching durability for nanolithography. A 10-nm-scale resist pattern was obtained using ZEP520 positive resist. The ZEP520 resist was spin coated onto a Si wafer to a thickness of 50 nm and prebaked at 200 °C. After EB exposure, the ZEP520 was developed with hexyl acetate for 2 min and rinsed with 2-propanol. Figure 7 shows a ZEP520 resist pattern, in which the lines are 10 nm wide and have a pitch of 50 nm [3].

2.3. 10-Nanometer Lithography Using Organic Negative Resist

Calixarene has a cyclic structure, as shown in Figure 8, and works as an ultrahigh-resolution negative EB resist. Such characteristics seem to be convenient for a nanodevice fabrication process. It is roughly a ring-shaped molecule with about a 1-nm diameter. The basic component of calixarene is a phenol derivative that seems to have high durability and stability, originating from the strong chemical coupling of the benzene ring. The threshold of sensitivity was about 800 $\mu C/cm^2$, which is almost 20 times higher than that of PMMA. Calixarene negative-resist exposure was carried out. A 30-nm-thick resist was coated on a bare Si wafer. After prebaking at 170 °C for 30 min, EB exposure was carried out and then the resist was developed in xylene for 20 s and was rinsed in IPA for 1 min.

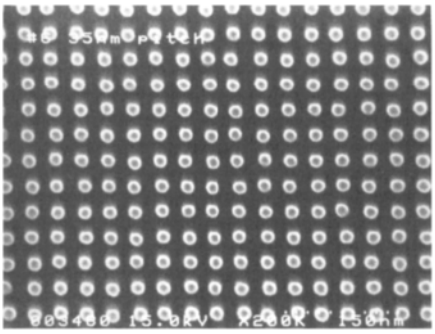


Fig. 9. Calixarene dot array patterns with 15-nm diameter and 35-nm pitch.

The etching durability of calixarene was tested using a DEM-451 (ANELVA Corp.) plasma dry-etching system with CF_4 gas. The etching rate of calixarene is almost comparable to that of Si, and the durability is about four times higher than that of PMMA. This durability seems to be sufficient to make a semiconductor or a metal nanostructure.

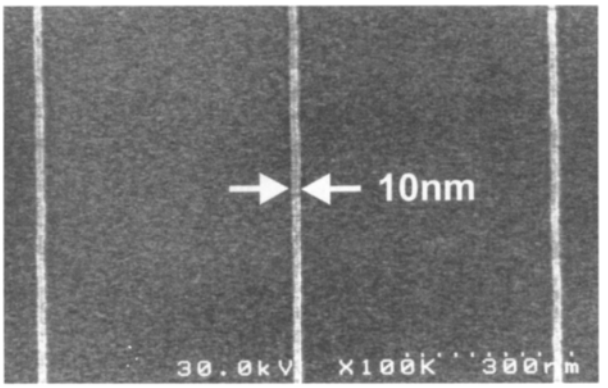
Nanodot arrays are useful not only for quantum devices but also for studying exposure properties. In this experiment, the EB current was fixed at 100 pA at 50-kV accelerating voltage, for which the spot size is estimated to be about 5 nm. All the dot arrays were fabricated on Si substrates. The typical exposure dose (spot dose) was about 1×10^5 electrons/dot. Figure 9 shows typical dot array patterns having 15-nm diameter with 35-nm pitch.

Germanium pattern transfer is shown in Figure 10. The 20-nm-thick Ge layer requires at least a 5-nm-thick calixarene layer to be etched down, and the resist thickness was 30 nm. Figure 10a shows the line patterns of the resist on Ge film exposed at a line dose of 20 nC/cm. Delineation was done using the S-5000 (Hitachi Corp.) SEM with a beam current of 100 pA at a 30-kV acceleration voltage. A 10-nm linewidth and a smooth line edge were clearly observed. This smoothness is the key point in fabricating quantum nanowires by etching processes. Figure 10b shows the transferred pattern treated by 1 min of overetching, followed by oxygen-plasma treatment to remove the resist residues. A Ge line of 7 nm width was clearly observed without short cutting. Narrowing by overetching is a standard technique to obtain a fine line; however, side-wall roughness limits the linewidth [18]. The smoothness of the calixarene side wall enables the linewidth to be narrowed below the 10-nm region by overetching. Calixarene is a single molecule and thus is monodispersed with a molecular weight of 972. In contrast, other phenol-based resists have dispersive weights ranging from 1000 to 100,000, which set a resolution limit. The molecular uniformity of calixarene and its small molecular size is the origin of such surface smoothness and the resulting ultrahigh resolution.

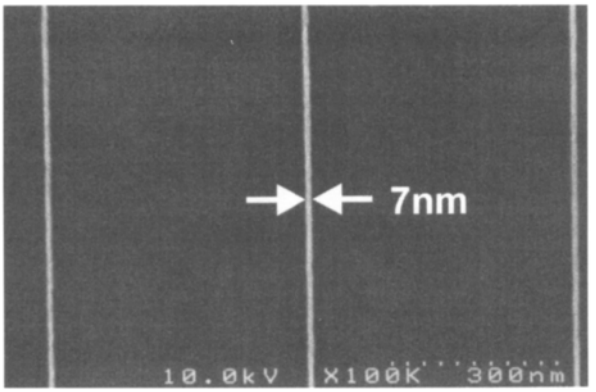
2.4. Sub-10-Nanometer Lithography Using Inorganic Resist

An inorganic resist seems to be the most promising material to achieve sub-10-nm lithography. Many previous works concerning the inorganic resist were carried out using STEM [5, 6, 19, 20], and many have attained nanometer-scale delineation. However, usage of the membrane-film substrate, which is commonly used in STEM studies, causes a crucial difficulty in device fabrication because of its delicate handling requirements. In contrast to this STEM lithography, the conventional scanning SEM should give many advantages for nanosize device fabrication if one could achieve an equally fine pattern delineation on the standard Si substrate.

In general, inorganic resists have a finer resolution than organic resists. An encouraging result, using AlF_3-doped LiF resist, was reported [21, 22]. It suggested the resist grain size



(a)



(b)

Fig. 10. Pattern transfer to Ge. (a) 10-nm-linewidth calixarene pattern and (b) transferred 7-nm-linewidth Ge pattern.

was reduced to below 10 nm on a nitrogen-cooled substrate and successfully demonstrated sub-10-nm lithography using a STEM system. Furthermore, electron-stimulated desorption should occur under relatively low energy (20–50 keV) electron irradiation in a standard SEM lithography system. The basis for the self-developing properties on LiF(AlF_3) was studied, and sub-10-nm lithography was demonstrated using a standard SEM beam writing system [8].

The AlF_3 partially doped LiF inorganic-resist films were fabricated by using conventional multitarget [LiF, $(Li_{0.9}Al_{0.1})F_x$, and $(Li_{0.7}Al_{0.3})F_x$] ion beam sputtering. The chemical composition of the films was adjusted by controlling the flux ratio from each target. The sputtered particles have energy of several electronvolts. As a result, the ion beam sputtering effectively reduced the grain size below 10 nm even at room temperature deposition and even with an extremely slow growth rate of about 1 nm/min.

The required dose for the (Li, Al)F resist in terms of AlF_3 concentration is summarized in Figure 11, where the sensitivity of the LiF and AlF_3 are cited from the STEM work, and the hatched area was obtained by extrapolating these data. A sensitivity of 0.1 C/cm^2 on the 10-nm-thick film was just below the critical dose, but the other films do not show this perfect development. The curve obtained from the 10-nm-thick films shown with solid circles are very close to those of the STEM data. This suggests that the desorption mechanism was not influenced by the electron energy, in principle, suggesting the possibility of lithography of the (Li, Al)F resist under low-energy irradiation using SEM.

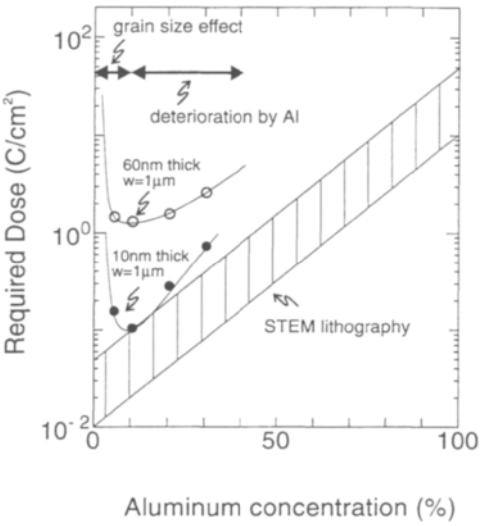


Fig. 11. Required dose versus aluminum concentration.

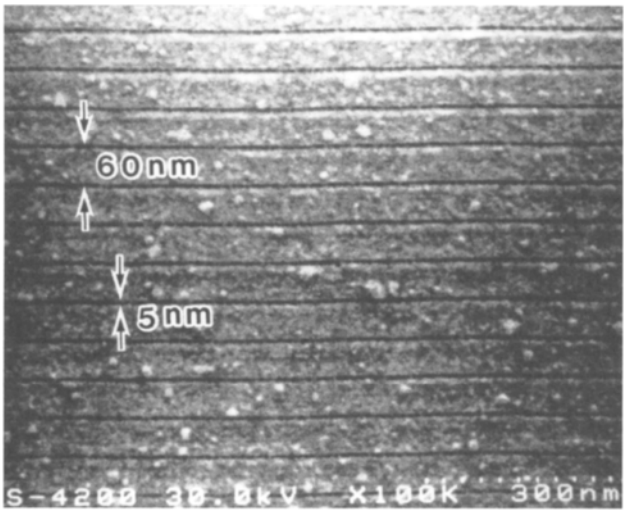


Fig. 12. 5-nm-linewidth patterns with 60-nm period fabricated at 100-nC/cm line dose by 30 kV and 1.5-nm beam diameter SEM.

By optimizing the film quality, sub-10-nm lithography was demonstrated by using a Hitachi S-4200 (Hitachi Corp.) SEM with a fine EB produced by a field emission gun. The accelerating voltage of 30 kV and the beam diameter of 1.5 nm are the specifications of the SEM. The line dose was about 100 nC/cm. Figure 12 shows the best result of the line delineation, where a fine line of 5-nm linewidth was clearly observed. This result demonstrates that sub-10-nm lithography can be achieved by SEM using an inorganic resist.

2.5. Nanometer Fabrication Using Electron-Beam-Induced Deposition

In situ processes using beam-induced chemistry are promising technologies to fabricate ultimate fine patterns and to reduce the process steps. *In situ* observation of W deposition by EB irradiation using a WF_6 gas source was carried out by transmission electron microscopy (TEM) to study the growth mechanism. The experimental arrangement is illustrated in

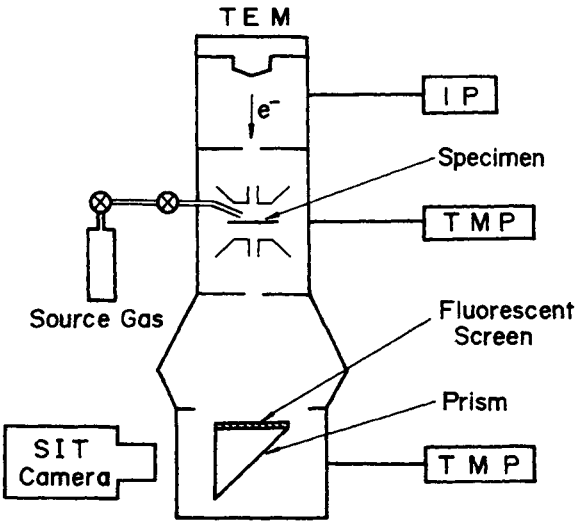


Fig. 13. *In situ* observation TEM system of EB deposition.

Figure 13. The employed electron microscope was an EM-002A (Akashi Beam Technology Corp.) equipped with a real-time TV monitor system specially improved for *in situ* observation. The microscope resolution was 0.23 nm at 120 kV, which allowed imaging individual rows of atom columns in W crystals. To reduce the problems with regard to specimen contamination, the instrument was operated under ultrahigh vacuum of 3×10^{-8} torr, attained by a dry vacuum-pumping system with turbo pumps and ion pumps. The gas injection tube had a 3-mm inner diameter and was 5 mm from the sample surface. Fine and spherical Si particles were used as TEM specimens. The small particles were made by a gas evaporation method in argon under a reduced atmosphere, where Si vapor was condensed into small particles. They were less than 100 nm in diameter and were usually covered with 1–3-nm-thick SiO_2. The gas molecules were adsorbed on the fine Si particles, which were on the TEM specimen grid. The gas molecules were excited by the TEM EB and dissociated into W and F_2 gas. Tungsten metal was deposited on the Si surface and growth was started. The growth process was observed *in situ* at the single-atom resolution level by an electron microscope equipped with a television monitor system. First, the EB was irradiated on a WF_6 adlayer, formed on the fine Si particle surface, in order to clarify the initial growth process of EB-induced deposition. Second, the focused EB was irradiated on the Si fine particle surface, while WF_6 was flowing on the surface, to study the resolution of EB-induced deposition [23, 24]. Figure 14 shows a typical series of electron micrographs of *in situ* TEM observations during EB irradiation of the WF_6 adlayer. These micrographs were selected from a video tape record (VTR) tape, which ran for 30 min. Electron beam irradiation times for parts a–d of Figure 14 were 0, 3, 15, and 30 min, respectively. These results indicated that W atoms, dissociated by EB irradiation from the WF_6 adlayer, coalesced, and grew under EB irradiation. According to the real-time observation on a television screen, moving clusters often collided with each other, causing coalescence. Figure 15 shows an electron micrograph of a W rod on a fine Si particle. The W rod was made using a focused EB (STEM mode: 3 nm in diameter) scanning manually at 1 mm/s on the Si surface under 1×10^{-6} torr source gas pressure. The W rod radius was 15 nm. This result indicated that a three-dimensional nanostructure can be fabricated using this technique. Three-dimensional STM tips as shown in Figure 16 [25] and electron field emitters as shown in Figure 17 [26] have successfully been made by EB-induced deposition with a computer-controlled writing system. Furthermore, single-electron transistor (SET) fabrication with 10-nm dimension was reported by using EB deposition with WF_6 gas [27].

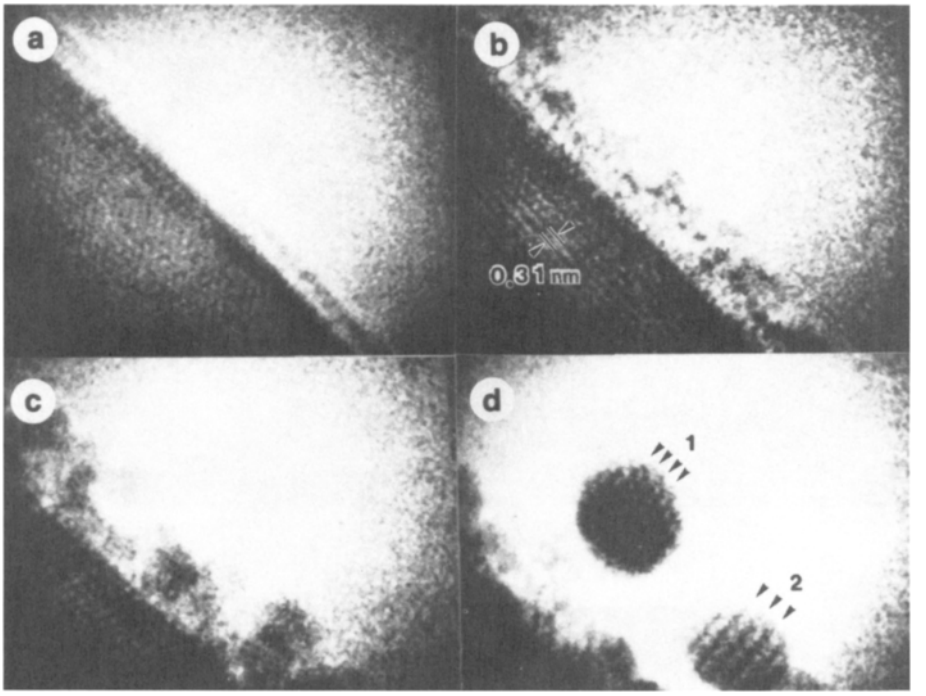


Fig. 14. EB exposure time dependence of W cluster growth on a Si particle. Exposure times: (a) 0, (b) 3, (c) 15, and (d) 30 min.

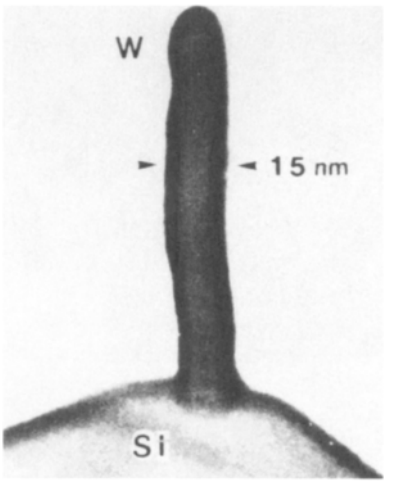


Fig. 15. W rod with 15-nm diameter.

3. MATERIAL WAVE NANOTECHNOLOGY: NANOFABRICATION USING A DE BROGLIE WAVE

3.1. Electron Beam Holography

Holographic lithography has an advantage that it can produce a number of periodic patterns simultaneously. Electron holographic lithography was applied to nanofabrication. Electron interference fringes were recorded on a PMMA resist by using W(100) TFE gun and

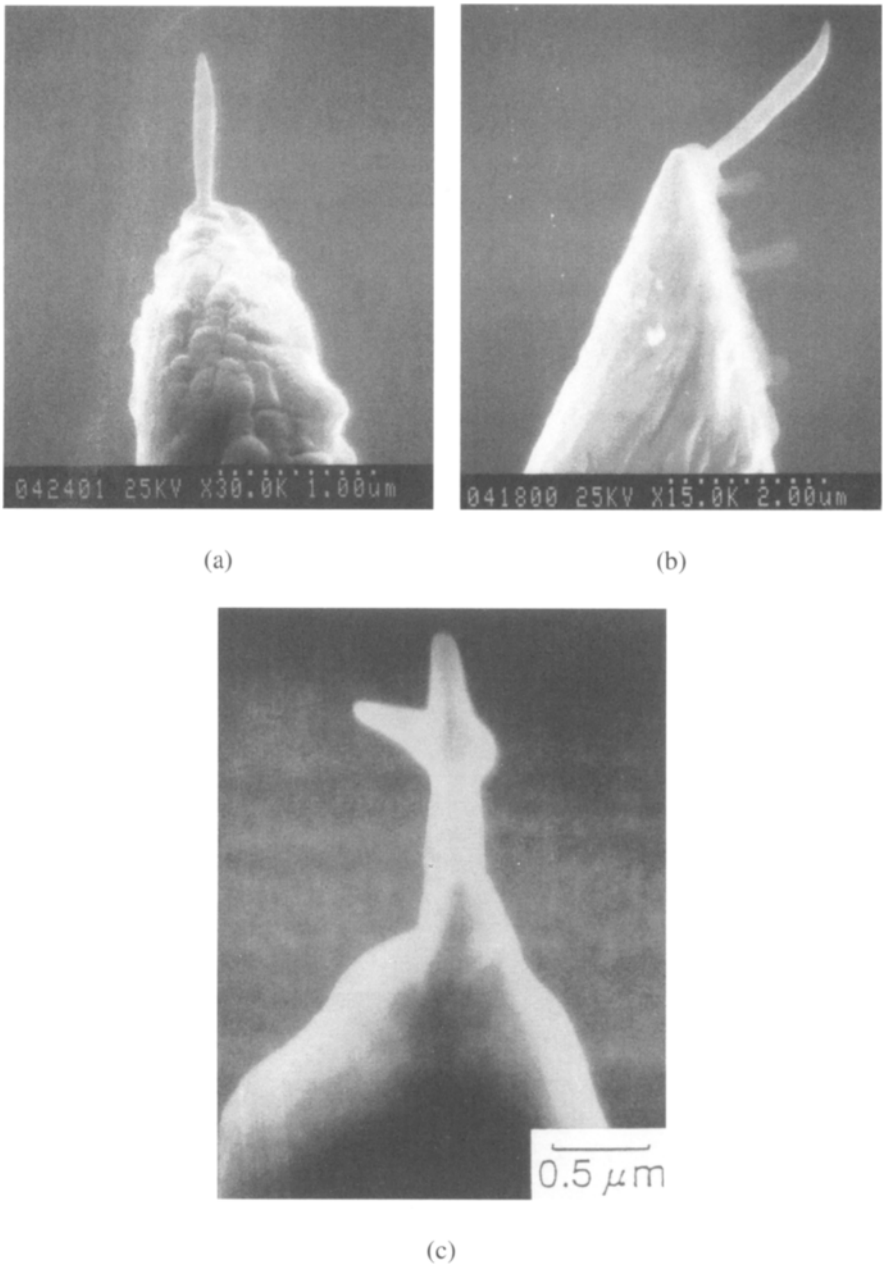


Fig. 16. SEM micrograph of a branched electron beam deposition tip.

an electron biprism, and the fabricated patterns were observed by conventional TEM and atomic force microscopy (AFM) [28, 29].

The electron optics of TEM with a W(100) TFE gun for electron holographic lithography is schematically illustrated in Figure 18. An electron beam of 40 kV is focused above an electron biprism with two condenser lenses. The Möllenstedt-type electron biprism is constructed of two grounded plane electrodes and a fine-wire electrode, called a filament, between them. When a positive voltage, V_B, is supplied to the filament, electron waves traveling on both sides of the filament are deflected and superimposed to form interference fringes on an observation plane. A Pt wire 0.6 μm in diameter was used as the filament.

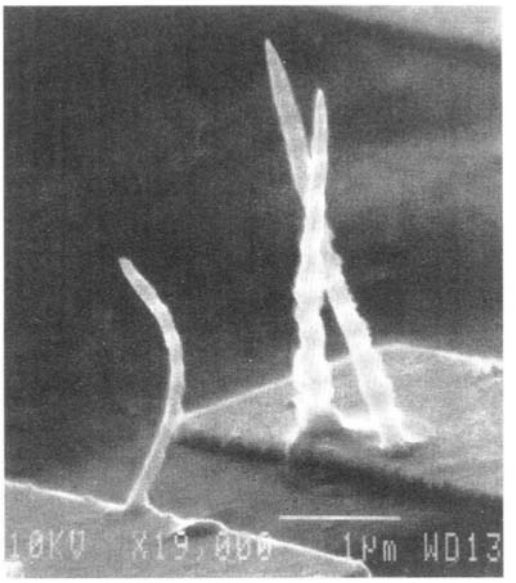


Fig. 17. Electron field emitters made by EB deposition. (Source: Reprinted with permission from [26].)

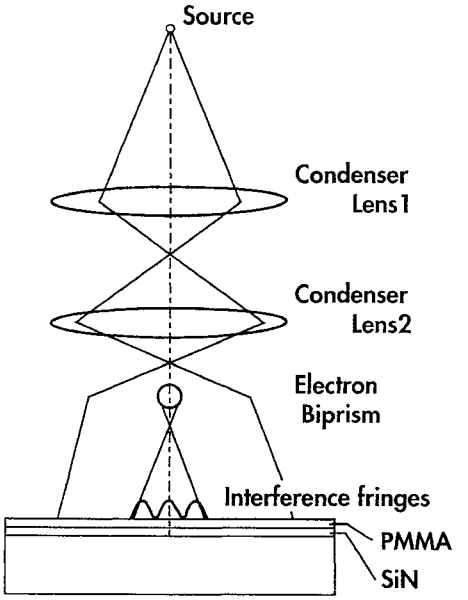


Fig. 18. Scheme of electron optics of TEM for electron holographic lithography.

As is well known, two coherence waves overlapping at an angle of θ produce interference fringes with spacing, s, represented by

$$s = \frac{\lambda/2}{\sin(\theta/2)} \tag{1}$$

where denotes the de Broglie wavelength of 6.0×10^{-3} nm in this case.

Figure 19 shows four-wave interference fringes through an X biprism. Setting an X biprism below two condenser lenses instead of the Möllenstedt-type biprism, which has two filaments placed normal to each other and both are supplied V_B, four coherent waves

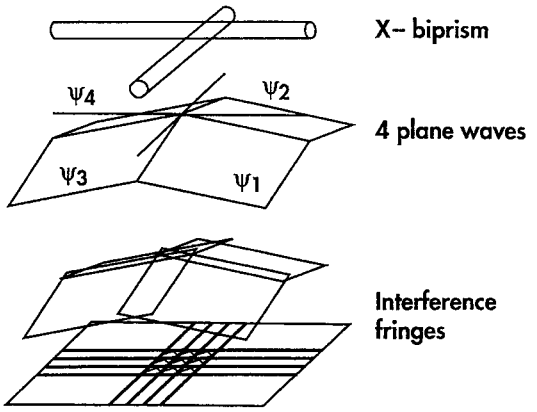


Fig. 19. Four-wave interference fringes through an X biprism.

produce fringes like a checkerboard below the intersection of filaments, with the same spacing, s, as given by Eq. (1). Thus, electron holographic lithography could, in principle, generate line and dot patterns whose minimum spacing is $\lambda/2$, which is comparable to the crystal lattice spacing.

A 30-nm-thick PMMA, spin coated on a 50-nm-thick self-supporting SiNx membrane and prebaked at 170 °C for 20 min, was set on the observation plane 70 mm below the biprism. The self-supporting nitride (SiN) membrane was about 60 μm square and used to place the PMMA below interference fringes appropriately. Electron exposure to produce line patterns was carried out for 18 s with a dose of 25 μC/cm^2, which was measured at the fringe part. Then, the PMMA was developed in MIBK:IPA = 1:3 for 1.0 min and rinsed in IPA for 30 s. Similarly, PMMA dot patterns were exposed, at half the dose as that for the line patterns, in order to maintain whole dots. The electron exposure to produce dot patterns was carried out for 9.0 s with a dose of 13 μC/cm^2. The PMMA was developed in MIBK:IPA for 3.0 min and rinsed in IPA for 1.0 min.

Figure 20a shows the interference fringes of the Möllenstedt-type electron biprism, which was magnified 530 times by the lenses below the observation plane and recorded on a photoplate with 1.0-s exposure. Figure 20b shows the AFM image of the same interference fringes as those in Figure 20a, which was recorded on PMMA. The thickness of the PMMA is represented by a photocontrast in Figure 20b, and the thicker PMMA corresponds to the brighter part of the image. The supplied voltage to the filament of electron biprism, V_B, was 5.3 V and the spacing of the fringes, s, was 108 nm in parts a and b of Figure 20. Figure 21a shows the interference fringes of the X biprism magnified and recorded on a photoplate, and Figure 21b shows the AFM image of the interference fringes recorded on PMMA. The supplied voltage to the filament, V_B, was 5.0 V and the spacing of the fringes, s, was 125 nm in parts a and b of Figure 21. In Figure 21a, dot patterns are found at the intersection where four-wave interference occurred and line patterns around the dot patterns where two-wave interference occurred. In Figure 21b, about 10 × 10 dots are recognized, but lines are not observed, owing to the reduction of the dose. Consequently, Figures 20b and 21b show that line and dot patterns were fabricated successfully, and the dose needed for lines is about twice as that for dots. More precise fabrication would be possible by optimizing the dose.

To produce finer patterns than 100 nm in period, the larger overlapping angle θ, that is, the larger supplied voltage to the filament V_B, should be selected. A simple assessment suggests that the spacing, s, becomes 1 nm when V_B is 2.4 kV with the same electron optics. Carbon contamination line patterns with a period of 23 nm were fabiricated by a 30-kV SEM [30].

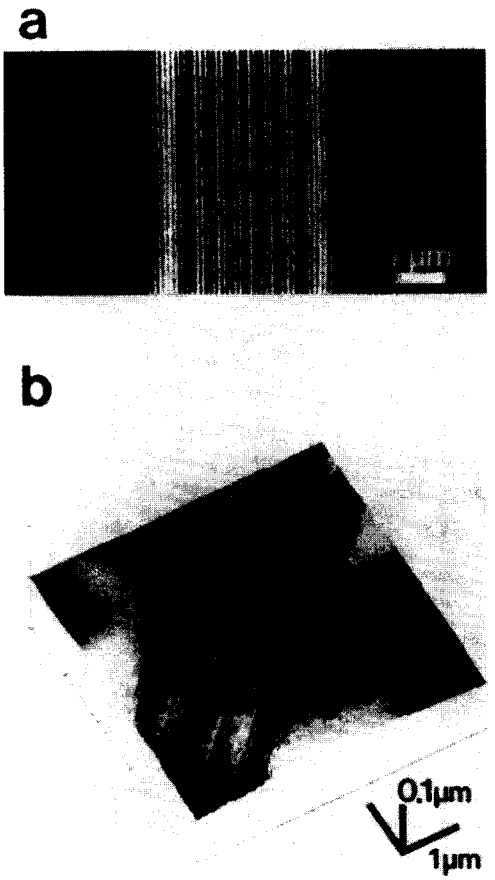


Fig. 20. (a) Two-wave interference fringes magnified and recorded on a photoplate. (b) Interference fringes corresponding to (a) recorded on PMMA. V_B: 5.3 V and s: 108 nm.

3.2. Atomic Beam Holography

Atomic manipulation based on a holographic principle has been demonstrated by using a laser trap technique and a computer-generated hologram (CGH) made by EB lithography [31]. One approximation of a CGH is the binary hologram, in which the hologram takes a binary value, either 100% transparent or 100% opaque. This hologram can be directly translated to a hologram for atomic de Broglie waves, by cutting out the pattern on a film that is equal to the pattern of the 100% transmission area of the binary hologram. A monochomatic atomic wave reconstructs an atomic pattern by passing the hologram.

The hologram used in this experiment was a Fourier hologram, which produced the Fourier-tranformed wavefront of the object. When the hologram is illustrated with a plane wave, the far-field pattern of the diffracted wave produces an image of the object. The object used in this experiment was a transparent F-shaped pattern, in which the transparent portion had a constant amplitude and random phase distribution. The object was represented by the complex transmission amplitude at points on a 128 × 128 matrix covering the F-shaped pattern. The two-dimensional array of numbers was Fourier transformed using a fast Fourier transform (FFT) algorithm, and the resulting 128 × 128 complex areas (cells) of the Fourier hologram. The transmission function of each cell of the hologram was expressed by a matrix of 4 × 4 subcells.

A 100-nm-thick SiN membrane was used for the hologram. The binary pattern was transferred to a ZEP resist on the SiN membrane by an EB writing system. Subsequent CF_4 plasma etching created through-holes in the membrane. A scanning electron micrograph

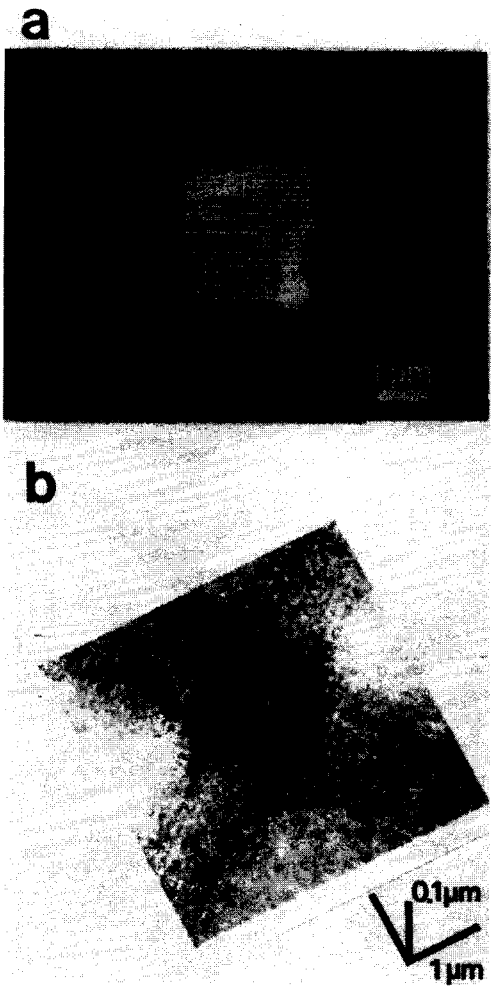


Fig. 21. (a) Two- and four-wave interference fringes magnified and recorded on a photoplate. (b) Interference fringes corresponding to (a) recorded on PMMA. V_B: 5.0 V and s: 125 nm.

of the hologram is shown in Figure 22. The size of the subcell was 0.3 × 0.3 μm square, so the size of the entire hologram was 153.6 × 153.6 μm. To increase the intensity of the deflected beam, the same pattern was repeated 10 times along the x and y directions, making the overall size of the hologram 1.5 × 1.5 mm.

A schematic diagram of this experiment is shown in Figure 23. The ultracold Ne atomic beam was generated by the reported method [32]. The cloud of Ne atoms in the trap was approximately 0.3 mm in diameter, and the one-directional average velocity of the atoms was 20 cm s^{-1}. The hologram was placed 40 cm below the trap and was mounted on top of a 0.2-mm-diameter diaphragm. The size of the diaphragm limited the resolution of the image of the Fraunhofer hologram. The position of the hologram was not adjusted because any small portion of the hologram could produce the same image. The average atomic velocity at the hologram was 2.8 m s^{-1}, corresponding to a de Broglie wavelength λ of 7.1 nm. The acceleration resulting from gravity reduced the relative velocity spread to approximately 0.28%. To detect the Fraunhofer diffracted pattern from the hologram, the multichannel plate (MCP) detector was placed 45 cm below the hologram. Figure 24a shows the reconstructed F pattern. The data were accumulated for 10 h, and the total atom number of spots on the figure was 6 × 10^4. Figure 24b shows another example of a reconstructed pattern, which represents the characters "atom, Ne, and ψ."

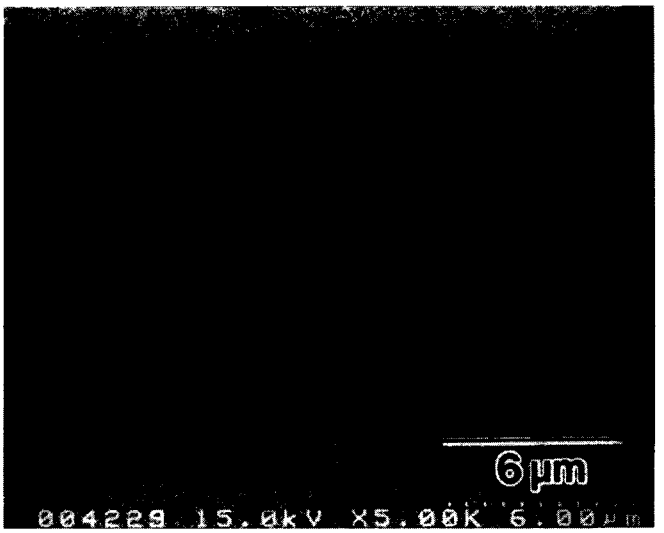


Fig. 22. Binary CGH hologram on SiN membrane made by EB lithography.

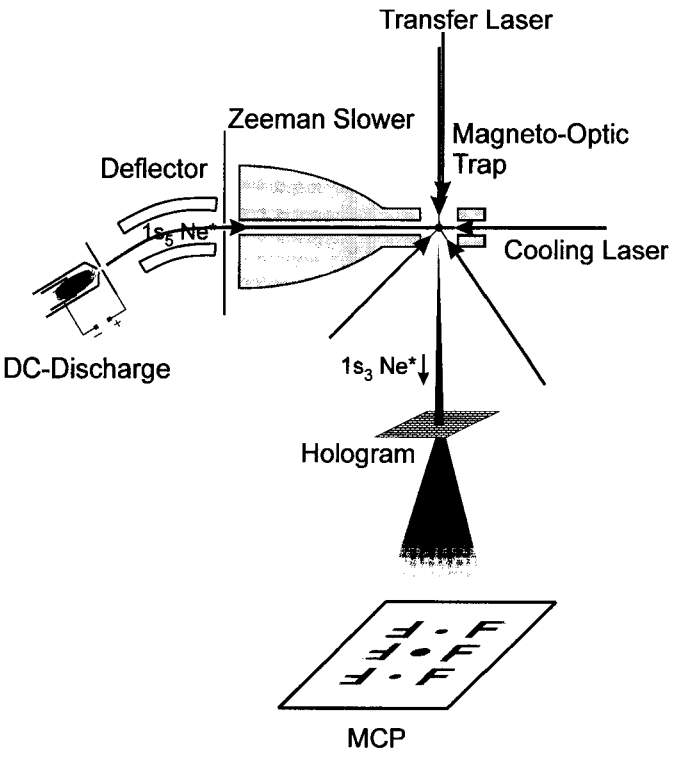
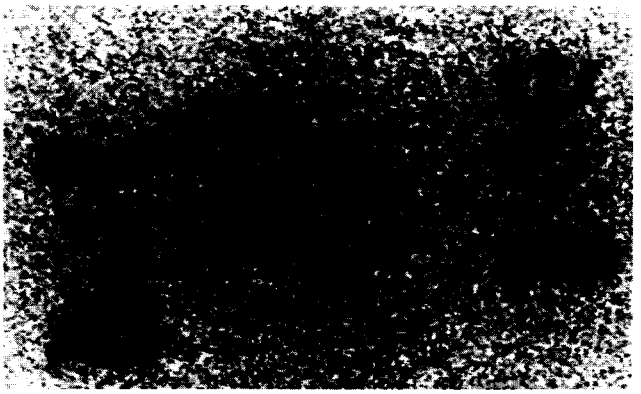


Fig. 23. Experimental apparatus of atomic beam holography.

In this experiment, a focusing lens for imaging was not used, but it is possible to combine the function of a focusing lens into the hologram [33]. In such a hologram, the resolution is determined by the same rule as applies to an optical lens. The binary hologram does not control the phase and amplitude of the wave inside a hole. When the hologram is the sole component for atomic beam manipulation, therefore, the practical limit is approximately the minimum size of the through-holes, which is in the range of 10 to 100 nm.



(a)



(b)

Fig. 24. Reconstructed image. (a) "F" pattern and (b) "atom, Ne, and Ψ" pattern.

As a next step, there is a possibility of making any three-dimensional nanostructures by using CGH with an electron/atom de Broglie wave, as shown in Figure 25.

4. NANOMETER DEVICES

4.1. 40-Nanometer-Gate-Length Metal-Oxide-Semiconductor Field-Emitter-Transistors

Minute CMOS devices with a gate length of 100 nm or less are under extensive examination [34–36]. This is because it is expected that small feature size devices do not only realize very high density integrated circuits, but also high switching speed with low power consumption. Forty-nanometer-gate MOSFETs have been fabricated using excimer laser lithography and resist thinning technology [36]. However, to accelerate investigation of these devices, it is important to develop a sub-100-nm direct EB lithography process with good linewidth control.

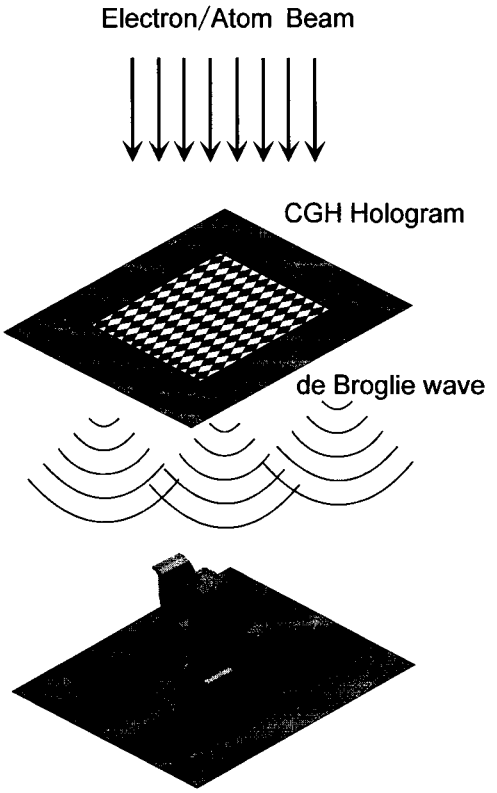


Fig. 25. Concept of three-dimensional nanofabrication by CGH with an electron/atom de Broglie wave.

A 40-nm-gate NMOS device has been demonstrated by using direct EB lithography [37]. Figure 26 shows the fabrication process of the sub-100-nm MOS transistors by EB direct writing. A 3.5-nm-thick-gate oxide was used to obtain high current drivability. The polysilicon thickness was 150 nm. The single-layer resist was adopted as a mask to make the fabrication process simple. A SAL601 (Shipley Ltd.) chemically amplified negative resist with 200-nm thickness was coated on a 6-in. Si wafer. The thickness of the resist was decided on the basis of an etching selectivity of five for polysilicon over the resist to obtain high-aspect-ratio patterns.

The gate resist patterns were exposed by a 50-kV EB lithography system as shown in Figure 3. After developing the resist, the gate pattern was transferred into polysilicon by plasma etching in which $Cl_2 + SF_6 + O_2$ etching gas was used. The etching rate of polysilicon was 130 nm/min with a uniformity of less than $\pm 5\%$. The etching selectivity of polysilicon to SiO_2 is over 40. The other lithography processes were performed using optical steppers.

Parts a and b of Figure 27 show a 40-nm-gate resist pattern on polysilicon/SiO_2/Si and on a NMOS transistor. The resist thickness was about 200 nm. A 40-nm line was exposed at 300 $\mu C/cm^2$ by a single line scan.

NMOSFETs with various gate lengths of above 40 nm on 6-in. wafers were fabricated. The source-to-drain resistance at $V_D = 0.1$ V versus the designed gate pattern width is plotted in Figure 28. The good linearity indicated that the gate length was successfully controlled even for a less-than-100-nm gate by using a proper proximity effect correction and a high-energy nanometer EB. The I_d–V_d characteristics are shown in Figure 29. Well-behaved short-channel characteristics were obtained down to a gate length of 60 nm. Operation of a 40-nm-gate FET was also confirmed, though weak punch-through occurred. Maximum transconductance (gm) at V_{DS} was 580 mS/mm for the 40-nm NMOSFET.

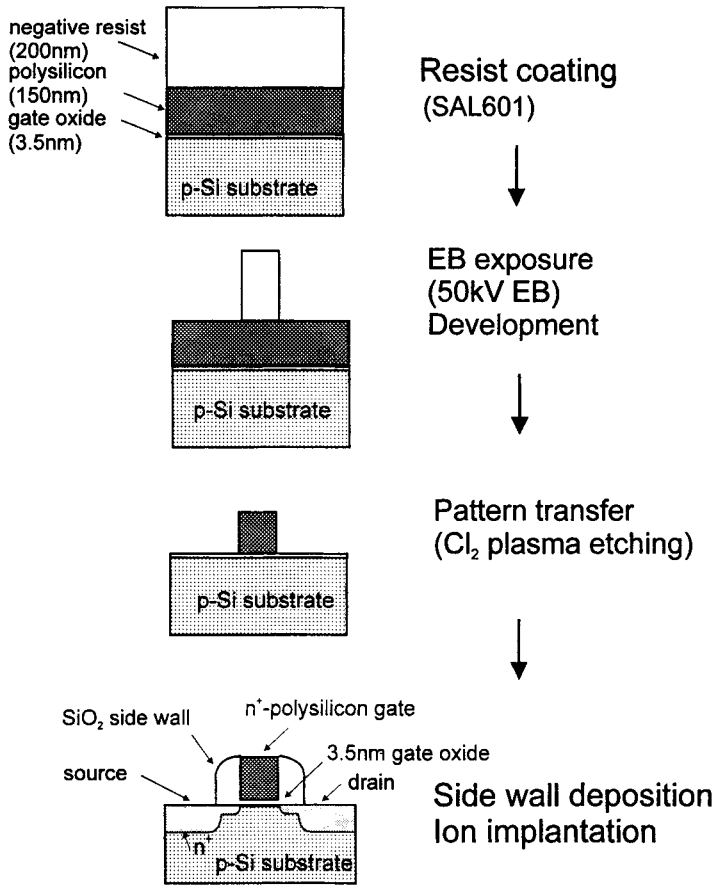


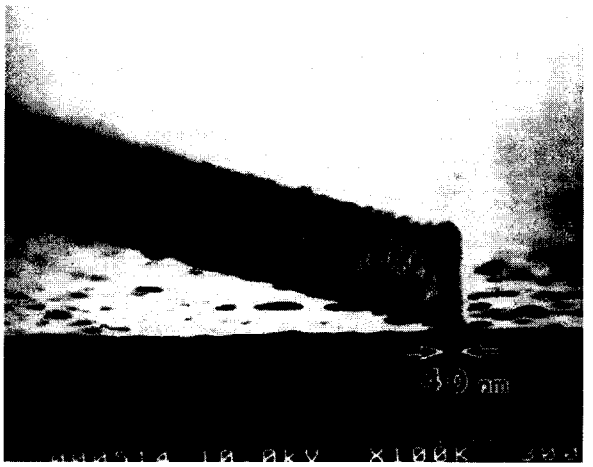
Fig. 26. Gate fabrication process of a MOSFET.

4.2. 14-Nanometer-Gate-Length Electrically Variable Shallow Junction MOSFETs

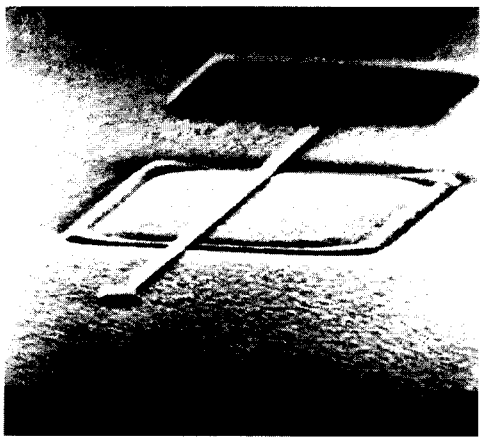
An electrically variable shallow junction MOSFET (EJ-MOSFET) with an ultra-shallow source/drain junction has been fabricated to investigate transistor characteristics and physical phenomena in ultrafine gate MOSFETs [38].

Figure 30 shows a schematic cross section of the EJ-MOSFET. The lower gate, which corresponds to the "gate" in conventional MOSFETs, controls the drain current. A positive upper-gate bias induces source/drain regions at the silicon surface. Because the source/drain regions are electrically induced, they are extremely shallow, typically 5 nm deep. The EJ-MOSFET was fabricated in a similar way as conventional Si-MOSFETs. To suppress short-channel effects (SCEs) caused by the lateral expansion of the depletion layers, a relatively high boron concentration of 2×10^{18} cm^{-3} was used within the substrate. The boron concentration was controlled by means of the boron ion implantation and the thermal drive-in. The n^+ regions were formed by arsenic ion implantation. A gate oxide ($t_{ox} = 5$ nm) was formed by thermal oxidation and a 40-nm-thick poly-Si layer was grown by chemical vapor deposition (CVD). Phosphorus was doped into the poly-Si film in a $POCl_3$ atmosphere. The ultrahigh-resolution EB resist was spin coated onto the poly-Si film and EB direct writing with a 5-nm beam diameter and a 50-kV acceleration energy was performed. After the developing procedure, the resist pattern was transferred to the poly-Si film by reactive ion etching (RIE) with CF_4 gas.

Figure 31 shows a TEM cross-sectional view of a 14-nm-long poly-Si lower gate. The lower gate was well defined. The 20-nm-thick intergate oxide layer was grown by



(a)



(b)

Fig. 27. (a) 40-nm-gate resist pattern with a height of 200 nm on a polysilicon layer and (b) on an NMOS transistor.

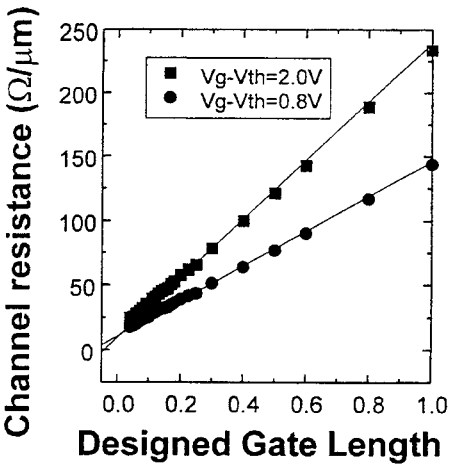


Fig. 28. Channel resistance versus designed gate length for different gate voltage.

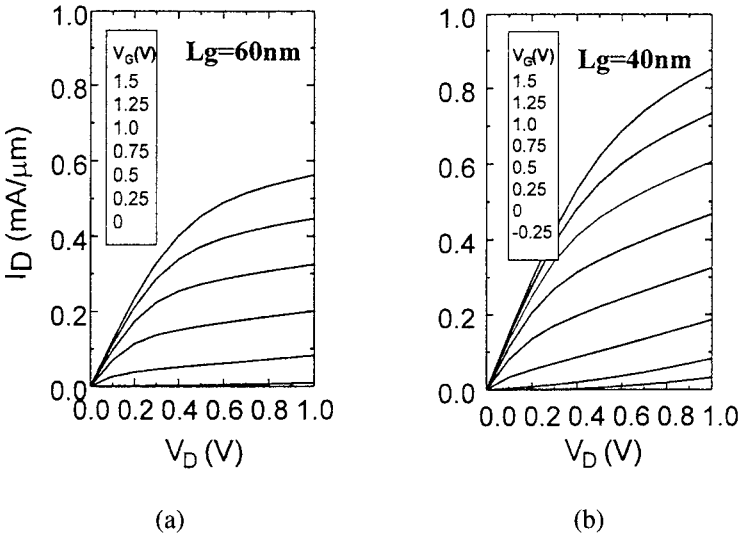


Fig. 29. I_d–V_d characteristics of NMOSFETs using direct EB exposure and a single-layer resist.

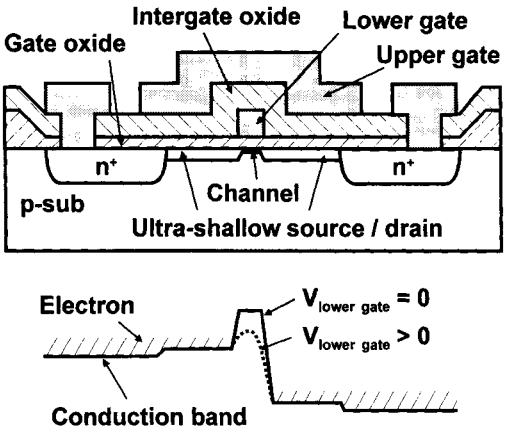


Fig. 30. Schematic cross section of an EJ-MOSFET.

CVD, which was followed by N_2 annealing and H_2 annealing. Finally, the upper gate and source/drain electrodes were formed by Au/Al evaporation.

The electrical characteristics of the fabricated devices with gate length (L_{LG}) ranged from 14 to 98 nm at 300 K. To form source/drain regions, an upper-gate voltage (V_{UG}) of 7 V was applied. Figure 32 shows the I–V characteristics of a 14-nm-gate-length device. Although the device does not exhibit clear saturation characteristics at a high drain bias, a transistor operation in the 14-nm gate length was confirmed by this experiment.

4.3. Operation of Aluminum-Based Single-Electron Transistors at 100 Kelvins

Single-electron transistors (SETs) using Al metallic systems have good-quality transport characteristics, that is, periodic gate modulation without gate-voltage-dependent background current. Nearly ideal characteristics of SETs have been observed; this has been attributed to the high quality of Al_2O_3 tunnel barriers.

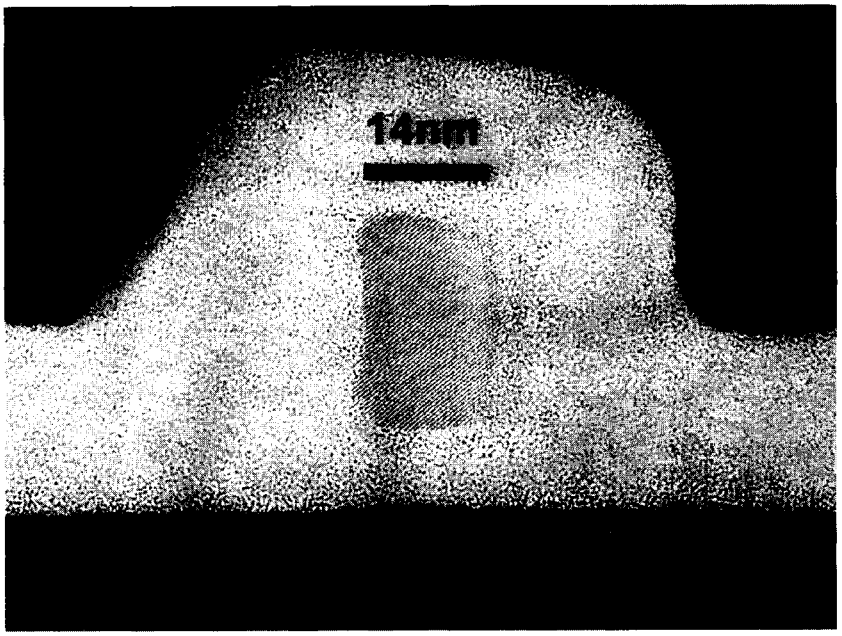


Fig. 31. TEM cross-sectional view of a 14-nm-gate-length poly-Si lower gate.

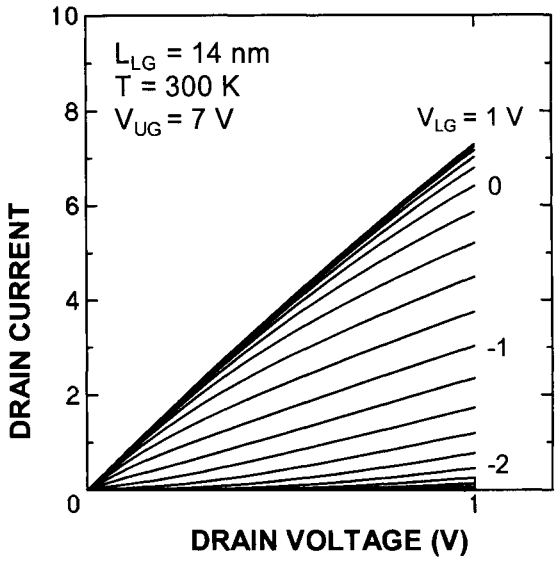


Fig. 32. *I–V* characteristics of a 14-nm-gate-length EJ-MOSFET at 300 K.

Al-based SETs operating at 100 K with a 20-nm island electrode were fabricated by EB lithography and three-angle shadow evaporation [39]. In conventional two-angle shadow evaporation, to prevent shorts between the source and the drain electrodes, the minimum possible length of the island electrode is limited by the available minimum line separation in the hanging-bridge mask, which is most likely not less than 50 nm because of the proximity effects. Thus, as illustrated in Figure 33b, three-angle shadow evaporation with two electrodes was used so that each electrode can be delineated with better accuracy.

The details of the process are as follows. A trilayer resist PMMA(50 nm)/Ge(20 nm)/PMMA(200 nm) was coated on a Si substrate covered with a 300-nm-thick thermal-oxide

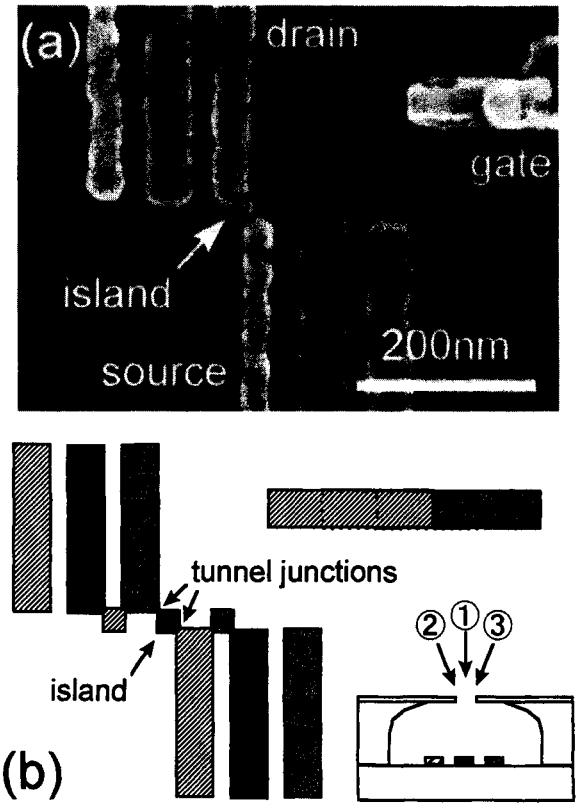


Fig. 33. (a) SEM photograph of a fabricated SET with a 20-nm island. (b) Schematic of the three-angle shadow evaporation technique. Electrodes shown in different hatches (top view) on the left side correspond to Al films evaporated from different angles as shown (cross section) on the right side. (Source: Reprinted with permission from [39].)

layer. After EB exposure and development of the upper PMMA layer, the patterns were transferred to the Ge layer by a reactive ion etching with CF_4 plasma. The underlayer PMMA was overetched by an ECR etcher with weakly accelerated O_2 plasma to form suspended Ge stencil masks. The overhang of the overetched region is about 200 nm. Al films were evaporated with an e-gun evaporator in a vacuum of 2×10^{-6} torr. The first evaporation of a 20-nm-thick Al film was made vertical to the substrate to form the island electrode, and this was followed by the oxidation of its surface for 2–3 min in 70-mtorr O_2 to make a tunnel barrier. Then, Al films with a thickness of 20–25 nm were evaporated from two different angles, $\pm 18°$, to make source and drain electrodes overlapping slightly with the island electrode. Finally, an SET was obtained after a liftoff process in butanone. From the SEM photograph shown in Figure 33a, the island electrode is estimated to have a dotlike shape with a diameter of 20 nm, while the designed EB exposure pattern is a rectangle with a dimension of 30×20 nm. The linewidth of the electrodes decreases as the total thickness of the evaporated film increases because of sticking of evaporated Al to the Ge stencil mask.

Direct-current (dc) measurements of the electrical characteristics of an SET were done in a ^{4}He continuous-flow cryostat with a temperature controller. The SET was voltage biased between the source and drain symmetrically ($V_{\text{source}} = -V_{\text{drain}} = V/2$). Higher-temperature operations of the SET are shown in Figure 34. Periodic gate voltage modulation of the current was observed up to above 100 K. The maximum modulation of the current was about 0.5% of the total current at 101 K and 3% at 81 K; this is consistent with the large charging energy $E_c \sim 130$ K. Even at high temperatures, the I–V_g

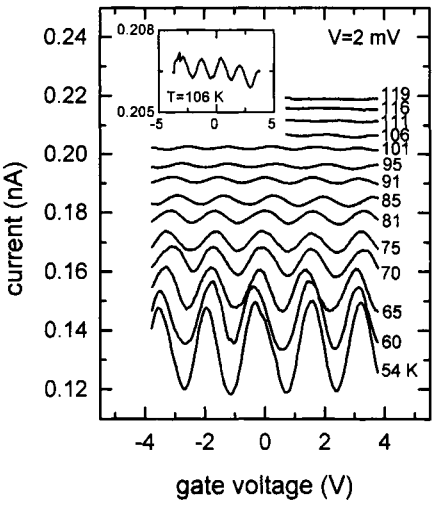


Fig. 34. Temperature dependence of the current versus gate voltage curves. The source–drain bias voltage is 2 mV. Inset shows the $I-V_g$ curve at 106 K in an enlarged current scale. (Source: Reprinted with permission from [39].)

curves were periodic and had no gate-voltage-dependent background current observed in semiconductor-based devices. The decrease in current with gate voltage at 106 K shown in the inset was not reproducible and was attributed to the temperature fluctuation resulting from poor temperature stability (±0.5 K) at this temperature.

4.4. Room Temperature Operation of a Silicon Single-Electron Transistor

A Si SET was fabricated by converting a one-dimensional Si wire on a SIMOX (separation by implanted oxygen) substrate into a small island with a tunneling barrier at the etch end by means of pattern-dependent oxidation [40–43].

A SIMOX wafer with a very smooth superficial Si/buried SiO_2 interface, which was obtained by 40-h annealing at 1350 °C, was used as the base material. A 30-nm-thick superficial Si layer with a 30-nm-thick top SiO_2 layer was prepared. The thickness of the buried SiO_2 layer was 400 nm. To fabricate the one-dimensional Si wire, EB nanolithography combined with an image-reversal process using electron cyclotron resonance (ECR) plasma oxidation was used. The SET fabrication process as shown in the schematic diagram of Figure 35 is as follows. Just after the deposition of a 40-nm-thick amorphous Si layer (a-Si) on the top SiO_2 layer, a 50-nm-thick ZEP positive resist was coated on the a-Si layer, and then the resist pattern shown in Figure 36 was formed by EB lithography [3]. Here, the resist on the one-dimensional wire and two-dimensional source and drain regions was removed and the surface of the a-Si on the area appeared because these areas were exposed on the EB. Then, the a-Si surface was oxided by an ECR O_2 plasma stream, where the lateral shrinkage of the resist pattern caused by O_2 plasma etching was very small because of the highly directional nature of the ECR plasma stream. Next, the resist was removed with acetone to avoid oxidizing the a-Si surface under the resist. The a-Si layer was etched by ECR Cl_2-based plasma using very thin plasma-oxidized SiO_2 as a mask. Then, the 30-nm-thick SiO_2 layer and the superficial Si layer were etched by RIE and ECR Cl_2-based plasma using a-Si and SiO_2 as a mask, respectively. A one-dimensional Si wire, with two-dimensional Si layers for the source and drain regions, was formed, on which the SiO_2 layer remained. However, the a-Si layer was completely removed by the final ECR etching.

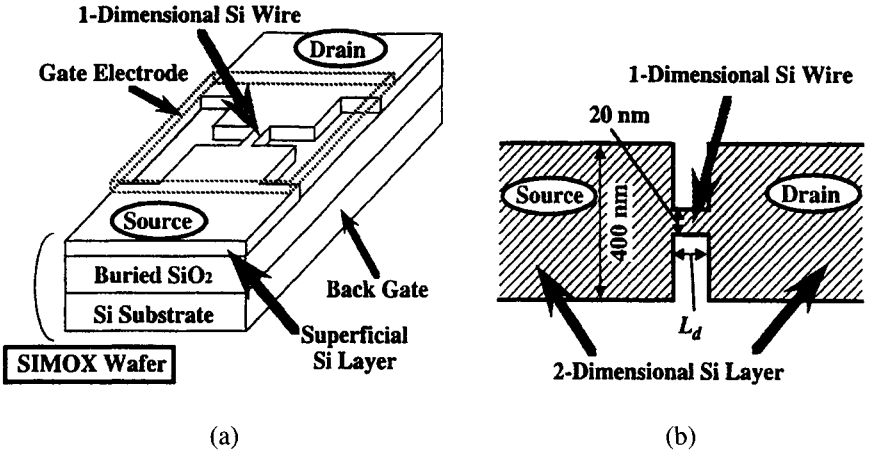


Fig. 35. (a) Schematic diagram of a Si-SET and (b) an EB pattern. (Source: Reprinted with permission from [42].)

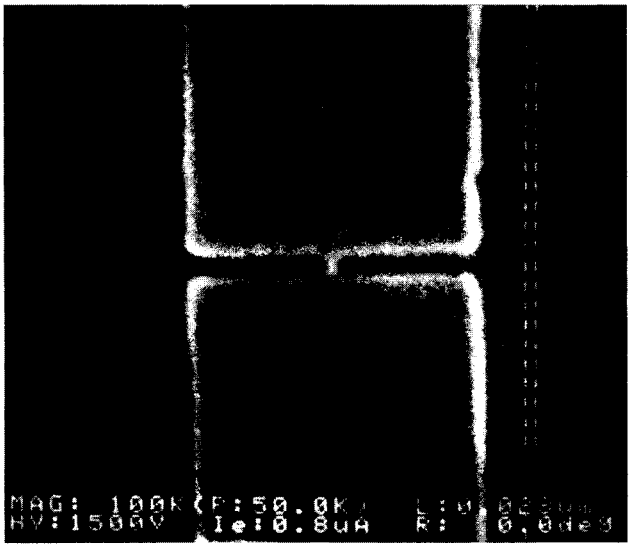


Fig. 36. SEM photograph of SET structure corresponding to Figure 35b. (Source: Reprinted with permission from [3].)

The width of the wires was 20 nm while the length L_d varied in the range of 50 to 200 nm. The width of the two-dimensional regions, which were connected to each end of the wire, was 400 nm. After the pattern was formed, the wafer was oxidized in a dry oxygen ambient at 1000 °C, which not only reduced the width and height of the wire, but constricted the wire at its ends by pattern-dependent oxidation [42]. Finally, the SET fabrication was completed after the phosphorous-doped poly-Si gate electrode was formed over the wire, followed by phosphorous ion implantation.

The source–drain conductance was derived from I–V characteristics measurement. The conductance characteristics at various temperatures for SETs with a wire length L_d of 50 nm are shown in Figure 37. Clear conductance oscillations are observed even at high temperatures of 30 K and above. These oscillations are due to the Coulomb blockade by tunneling barriers with a very small capacitance fabricated by the procedure described previously. The conductance oscillations remain even at 300 K for the SET. From these data, the total capacitance of the SETs in Figure 37 is estimated to be about 1.5 aF.

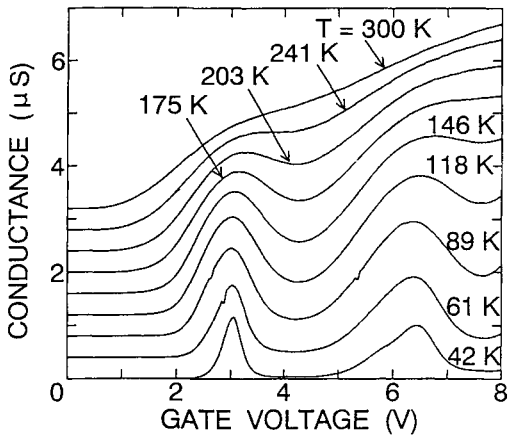


Fig. 37. Conductance oscillations of SETs with $L_d = 50$ nm at various temperatures. The curves are offset vertically. (Source: Reprinted with permission from [42].)

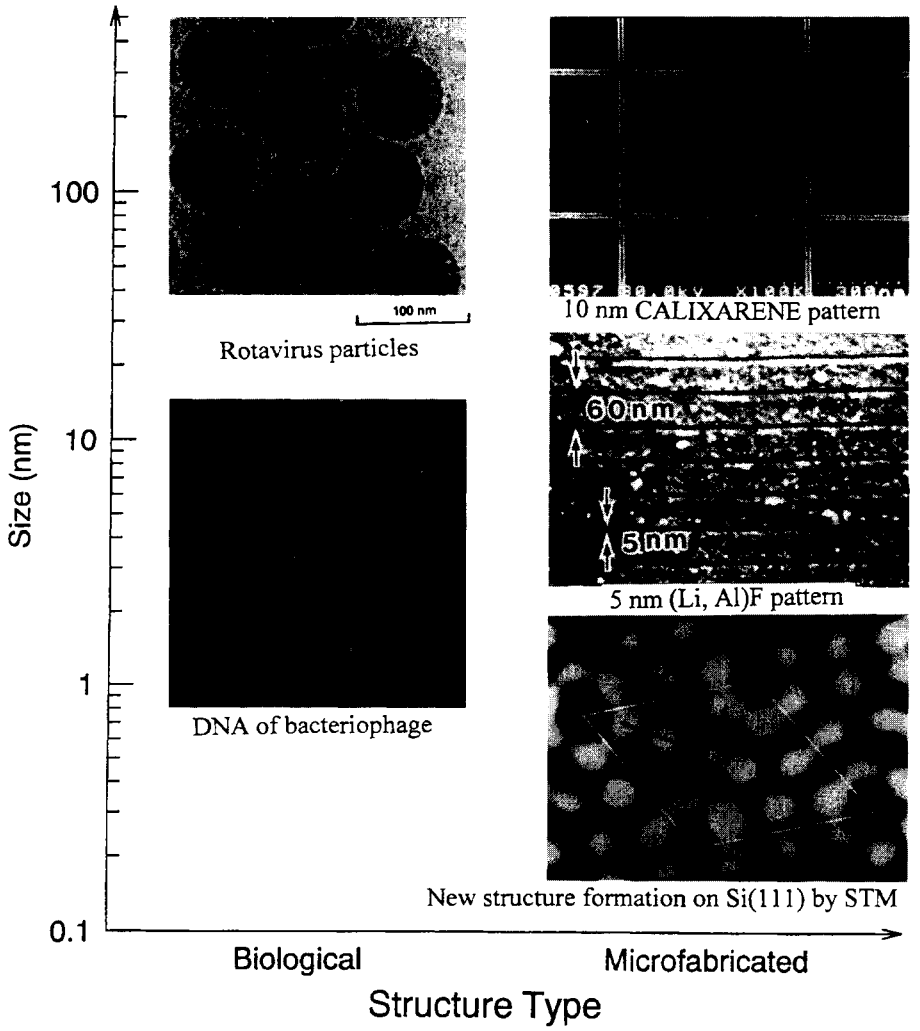


Fig. 38. Comparison of the sizes between artificial and biological structures.

5. SUMMARY

Nanofabrication and its application to nanodevices using EB have been discussed. A comparison of the sizes between artificial and biological structures is shown in Figure 38. Electron beam lithography with a commercially available machine using an organic resist has already achieved 10-nm features, which is the same size as a virus. Features 10 to 1 nm in size can also be fabricated by using inorganic resists. This indicates that even a minimum pitch of 3.4 nm of DNA can be delineated. Furthermore, a new atomic structure on a Si surface can be created by atomic manipulation with STM [44]. Electron-beam-induced surface reaction is a very interesting and promising three-dimensional process, and much progress is expected in the nanoscale regime. As a new approach, material wave nanotechnology using electron and atomic beam holography has been developed. This technique allows nano- and atomic scale structures to be produced simultaneously. Especially, atomic beam holography with CGH is promising from the point of view of making any shape and direct deposition. As applications to nanodevices of EB lithography, a 40-nm-gate-length NMOS, a 14-nm-gate-length EJ-MOSFET, and a high-temperature-operation SET have been demonstrated by EB nanolithography using an organic resist. The low cost and high throughput are very important for commercialization of electronic, optoelectronic, and magnetic nanodevices. Nanoimprinting lithography, which is expected to achieve both cost and throughput efficiencies, has been developed to fabricate practical nanodevices [45].

References

1. F. Emoto, K. Gamo, S. Namba, N. Samoto, and R. Shimizu, *Jpn. J. Appl. Phys.* 24, L809 (1985).
2. W. Chen and H. Ahmed, *Appl. Phys. Lett.* 63, 1116 (1993).
3. K. Kurihara, K. Iwadate, H. Namatsu, M. Nagase, H. Takenaka, and K. Murase, *Jpn. J. Appl. Phys.* 34, 6940 (1995).
4. T. Yoshimura, Y. Nakayama, and S. Okazaki, *J. Vac. Sci. Technol., B* 10, 2615 (1992).
5. J. Fujita, Y. Ohnishi, Y. Ochiai, and S. Matsui, *Appl. Phys. Lett.* 68, 1297 (1996).
6. M. Isaacson and A. Murray, *J. Vac. Sci. Technol.* 19, 1117 (1981).
7. D. R. Allee and A. N. Broers, *Appl. Phys. Lett.* 57, 2271 (1990).
8. J. Fujita, H. Watanabe, Y. Ochiai, S. Manako, J. S. Tsai, and S. Matsui, *Appl. Phys. Lett.* 66, 3065 (1995).
9. A. N. Broers, W. W. Molzen, J. J. Cuomo, and N. D. Wittles, *Appl. Phys. Lett.* 29, 596 (1976).
10. R. L. Kubena, J. W. Ward, F. P. Stratton, R. J. Joyce, and G. M. Atkinson, *J. Vac. Sci. Technol., B* 9, 3079 (1991).
11. H. Nakazawa, H. Takemura, M. Isobe, Y. Nakagawa, M. Hassel Shearer, and W. Thompson, *J. Vac. Sci. Technol., B* 6, 2019 (1988).
12. Z. W. Chen, G. A. C. Jones, and H. Ahmed, *J. Vac. Sci. Technol., B* 6, 2009 (1988).
13. M. Gesley, *J. Vac. Sci. Technol., B* 10, 2451 (1992).
14. B. H. Koek, T. Chisholm, J. P. Davey, J. Romijin, and A. J. V. Run, *Jpn. J. Appl. Phys.* 32, 5982 (1993).
15. H. Hiroshima, S. Okayama, M. Ogura, and M. Komuro, *J. Vac. Sci. Technol., B* 13, 2514 (1995).
16. Y. Ochiai, M. Baba, H. Watanabe, and S. Matsui, *Jpn. J. Appl. Phys.* 30, 3266 (1991).
17. T. Nishida, M. Notomi, R. Iga, and T. Tamamura, *Jpn. J. Appl. Phys.* 31, 4508 (1992).
18. T. Yoshimura, H. Shiraishi, J. Yamamoto, and S. Okazaki, *Appl. Phys. Lett.* 63, 764 (1993).
19. A. Murry, M. Isaacson, and I. Adesida, *Appl. Phys. Lett.* 45, 589 (1984).
20. E. Kratschmer and M. Isaacson, *J. Vac. Sci. Technol., B* 5, 369 (1987).
21. W. Langheinrich, A. Vescan, B. Spangenberg, and H. Beneking, *Microelectron. Eng.* 17, 287 (1992).
22. W. Langheinrich and H. Beneking, *Jpn. J. Appl. Phys.* 32, 6218 (1993).
23. S. Matsui and T. Ichihashi, *Appl. Phys. Lett.* 53, 842 (1988).
24. S. Matsui, T. Ichihashi, and M. Mito, *J. Vac. Sci. Technol.* 7, 1182 (1989).
25. A. Sato, Y. Tsukamoto, M. Baba, and S. Matsui, *Jpn. J. Appl. Phys. Ser.* 5, 409 (1991).
26. H. W. P. Koops, J. Kretz, M. Rudolph, M. Weber, G. Dahm, and K. L. Lee, *Jpn. J. Appl. Phys.* 33, 7099 (1994).
27. M. Komuro and H. Hiroshima, *Microelectron. Eng.* 35, 273 (1997).
28. K. Ogai, S. Matsui, Y. Kimura, and R. Shimizu, *Jpn. J. Appl. Phys.* 32, 5988 (1993).
29. K. Ogai, Y. Kimura, R. Shimizu, J. Fujita, and S. Matsui, *Appl. Phys. Lett.* 66, 1560 (1995).
30. S. Fujita, S. Maruno, H. Watanabe, Y. Kusumi, and M. Ichikawa, *Microelectron. Eng.* 30, 435 (1996).
31. J. Fujita, M. Morinaga, T. Kishimoto, M. Yasuda, S. Matsui, and F. Shimizu, *Nature* 380, 691 (1996).

32. F. Shimizu, K. Shimizu, and H. Takuma, *Opt. Lett.* 16, 339 (1991).
33. M. Morinaga, M. Yasuda, T. Kishimoto, F. Shimizu, J. Fijita, and S. Matsui, *Phys. Rev. Lett.* 77, 802 (1966).
34. Y. Taur, S. Wind, Y. J. Mii, Y. Lii, D. Moy, K. A. Jenkins, C. L. Chen, P. J. Coane, D. Klaus, J. Bucchignano, M. Rosenfield, M. G. R. Thomson, and M. Polcari, "IEDM93 Technical Digest," 1993, p. 127.
35. K. F. Lee, R. H. Yan, D. Y. Jeon, G. M. Chin, Y. O. Kim, D. M. Tennant, B. Razavi, H. D. Lin, Y. G. Wey, E. H. Westerwick, M. D. Morris, R. W. Johnson, T. M. Liu, M. Tarsia, M. Cerullo, R. G. Swartz, and A. Ourmarzd, "IEDM93 Technical Digest," 1993, p. 131.
36. M. Ono, M. Saito, T. Yoshitomi, C. Fiegna, T. Ohguro, and H. Iwai, "IEDM93 Technical Digest," 1993, p. 119.
37. Y. Ochiai, S. Manako, S. Samukawa, K. Takeuchi, and T. Yamamoto, *Microelectron. Eng.* 30, 415 (1996).
38. H. Kawaura, T. Sakamoto, Y. Ochiai, J. Fujita, and T. Baba, "Extended Abstract of the 1997 International Conference on Solid State Devices and Materials," Hamamatsu, Japan, 1997, pp. 572–573.
39. Y. Nakamura, C. Chen, and J. Tsai, *Jpn. J. Appl. Phys.* 35, L1465 (1996).
40. Y. Takahashi, M. Nagase, H. Namatu, K. Kurihara, K. Iwadake, Y. Nakajima, S. Horiguchi, K. Murase, and M. Tabe, *Electron. Lett.* 131, 136 (1995).
41. A. Fujiwara, Y. Takahashi, K. Murase, and M. Tabe, *Appl. Phys. Lett.* 67, 2957 (1995).
42. Y. Takahashi, M. Nagase, H. Namatsu, K. Kurihara, K. Iwadake, Y. Nakajima, S. Horiguchi, K. Murase, and M. Tabe, "Extended Abstract of the 1995 International Conference on Solid State Devices and Materials," Japan Society of Applied Physics, Osaka, Japan, 1995, p. 189.
43. Y. Takahashi, H. Namatsu, K. Kurihara, K. Iwadate, M. Nagase, and K. Murase, *IEEE Trans. Electron. Device* 43, 1213 (1996).
44. M. Baba and S. Matsui, *Appl. Phys. Lett.* 65, 1927 (1994).
45. S. Y. Chou, P. R. Krauss, and P. J. Renstrom, *Science* 72, 85 (1996).

This Page Intentionally Left Blank

This Page Intentionally Left Blank

Index

A

Abrikosov vortex lattice, 503
Absorption spectroscopy, 433–442
AC conductivity, 162
di-*n*-Alkyl sulfides, 184
n-Alkyl thiols, 184–185
Antidot diameters, magnetization curves for, 512–514
Antidot lattice, 480–482
Aryl dithiol monolayers, chemical self-assembly, 185–188
Atomic beam holography, 569–571
Atomic force microscopy (AFM), 146
  field emission and, 282–284
Au_{55}-cluster, 135
Au clusters, 192
Au dots, 500
Auger electron spectroscopy (AES), 273
$Au_{55}(Ph_2PC_6H_4SO_3H)_{12}Cl_6$ cluster, 146
$Au_{55}(PPh_3)_{12}Cl_6$, 135, 140
$Au_{55}(PPh_3)_{12}Cl_6$-clusters, 170
$Al_xGa_{1-x}As$ barriers, 120

B

Ballistic Hall magnetometry, 391–394
Bandgap, 98, 443
Bean-Livingstone barrier, 483
Bessel function, 460
Binding energy, 98
4,4′ Biphenyldithiol (BPDT), 186
Bipolar transistor, conventional, 249
Block copolymers, nanoparticles in, 141–142
Boltzmann-Drude conductivity g_0, 30
Bragg reflector, 405

C

Calixarene, 558
Capacitance, 97, 156, 159, 163, 165
Capture of clusters
  bare metal particles, 193
  colloidal particles, 193–194
C_{60} fullerenes, 151
Charge carrier percolation, 542
Charge relaxation, time scales of, 172–174
Charging effects, 97
Charging energy, tailoring of, 164–165
Chemically sticky surfaces, self-assembly, 189
Chemical vapor deposition (CVD), 235
Cluster aerosol, 191
Cluster arrays, electronic properties of, 216–224
Cluster network, 145
Clusters of loops and antidots, 473–479
Cole-Cole-like relaxation, 162
Colloidal $GaInP_2$ quantum dots, synthesis of, 431–432, 444–445
Colloidal GaP quantum dots, 431, 442
Colloidal InP quantum dots, 430–431
  arrays, 441
  etching of, 431
  n-doped, 430
  p-doped, 430
  X-ray diffraction, 432
Colloidal networks, precipitation of, 194–195
Colloidal particles, capture of clusters, 193–194
Colloidal quantum dots, 427–450
  synthesis of, 429–432
Colloidal semiconductor systems, interfacial charge transfer processes, 299–303
Coloumb gap, 74
Commensurability oscillations, 41
Condensed cluster solids, 144–145
Conduction model, 221
Conductivity tensor, 383
Confinement, 452
Conjugated polymers, 200
Conversion efficiencies, 539–545
Corboran, 172
Core pinning, 463
Coulomb blockade, 158, 280
  effect in vertical quantum dots, 75–76
  oscillations, 72
  semiconductor nanostructures, 71–77
Coulomb charging energy, 100, 123
  in impurity system, 100
Coulomb potential confinement, impurity dot system, 95–96
Coulomb staircase, 76
Coupled-dot system, 110
Crystalline phase control
  CdSe nanocrystallites, 294–296
  nanocrystallites preparation, 294–296
  phase transformation, 294–296
  ZnS nanocrystallite, 295–296
Crystalline surfaces, deposition on, 152–153
Cu_{70} cluster, 141
Cu_{147} clusters, 193
Current perpendicular to the plane magneto-transport, 418
Current-voltage characteristics, 203–206
  evolution of, 118
  fabricated quantum dots, 101–103
  vertical dot, 100–101
$Cu_{70}Se_{35}(PR)_{22}$, 141
Cutoff wavelength transistors (COW), 133
Cysteines, 184

D

DC conductivity, 162
De Broglie wavelength, 133
Debye-like relaxation, 162
Deoxyribonucleic acid-based method of self assembly, 147–149
Deoxyribonucleic acid oligonucleotides, single-stranded, 153
Design, self-assembled molecular nanostructures, 179–231
Diamagnetic shifts, 106
  and current suppression, magnetotunneling measurements, 106–113
1,4-Di(4-isocyanophenylethynl)-2-ethylbenzene(22ADI), 218
Diol molecules, 183
Discretization scheme and boundary conditions, 13–15
Donor impurity
  in bulk GaAs, energy of, 97–98
  in quantum well, energy of, 98–100
Dot, 468–473
Double barrier resonant tunneling diode (DBRTD), 62
Drude conductivity, 368

E

Ebrium-doped silicon light emitters, 240–242
Edge absorption spectroscopy (XNAES), 273
Electrical resistance, estimation of, 215–216
Electric modulations, 373
Electrochemical composition, nanoparticles in, 143
Electrochromic arrays, 175
Electrochromic displays, 531–533
Electroluminescence, 239
Electromagnetic pinning, 463, 491
Electron beam (EB)
  deposition induced by, 563–564
  holography, 565–568
  lithography, 556
  nanostructure fabrication using, 555–583
Electron diffraction, 185
Electron-electron interactions, 30
Electronic conduction
  theory of, 200–207
  through nanoparticle netwoks, 159–162
  through supported clusters, 209–211
Electronic properties
  cluster arrays, 216–224
  encapsulated gold clusters, 211–212
  individual properties, 209
  molecular nanostructures, 207–216
  self-assembled molecular nanostructures, 179–231
Electronic transport properties, quantum dots, 93–130
Electronic zone folding, 236
Electrons in microscopically inhomogeneous magnetic fields, 347–348
  Hall voltage, 347–348
  Lorentz force, 347–348
  two-dimensional electron gas, 347–348
Electron tunneling rates, 121–128
Electroreflectance spectroscopy, 237
Emitter, 110, 117
Emitter-to-well tunneling process, 126
Energy states, impurity dot, 97–100
Epitaxial growth, 262–265
Epitaxial magnetic layers, 412–413
Epitaxy, 408–413
Etching, colloidal InP quantum dots, 431
Excitation spectrum, 73–74

F

Fabricated dot states, spectroscopic analysis, 111–113
Fabrication, self-assembled molecular nanostructures, 179–231
Fermi energy, 204–205
Fermi function, 105
Fermi level, 105
Ferromagnet, 403–404, 453
Ferromagnetic materials, 372
Ferromagnetic metal epitaxy, 410
Ferromagnetic/semiconductor structures
  experimental, 408–413
  spin injection, 404–408
β-$FeSi_2$, 239
$FeSi_2$, silicon-based light emitter, 238–239
Feynman paths, 29
Field Effect Transistor (FET), 406
Field emission, AFM and, 282–284
Fine structure, magnetotunneling measurements, 113–117
Flux pinning, 462–463
FM/SC interfaces, electrical properties, 411–412
Fourier transform, 1D wave functions, 62
Full-width-at-half-maximum (FWHM), 194

G

GaAs-AlGaAs-InGaAs-AlGaAs-GaAs double barrier resonant tunneling diodes (DBRTD), 68
GaAs/AlGaAs quantum dot system, 97
GaAs-AlGaAs-GaAs heterostructure, 49
GaAs/AlGaAs quantum well, 376
GaAs quantum dots, 446
GaAs quantum well, 101
GaAs well, 97
Ga-In-P system, 445
Gas phase synthesis, 190
Giant magnetoresistance effect (GMR), 403
Ginzburg-Landau equations, 454
Gold clusters, 146, 192, 193, 194
  encapsulated, electronic properties of, 211–212
  estimation of electrical resistance, 215–216
  tethered, electronic properties of, 212–215
  thiol-encapsulated, 194
  unlinked arrays of, 198
Gold colloids, 146, 194
Gold nanoparticles, 135
Green's function, 159

H

Hall effect devices, 390–402
Hall magnetometry, 395–399

Hall resistance, 391
Heterojunction bipolar transistors (HBTs), 245
Heterojunctions, sensitized solid state, 548–550
Heterostructure bipolar transistors (HBTs), 235
Heterostructure layers, 94
Highest occupied molecular orbit (HOMO), 200
Highly oriented pyrolytic graphite (HOPG), 153
High-resolution transmission electron microscopy (HRTEM), 192
Holography
  atomic beam, 569–571
  electron beam, 565–568
Hope transport material (HTM), 548
Hybrid Hall effect device, 399–402
Hybrid magnetic-semiconductor nanostructures, 346–420

I

ID subband, 59–60
Impedance measurements, 162
Impurity dot, energy states, 97–100
Impurity dot system, 95–96
Impurity quantum dot, 103
InAs dots, 260
Inorganic resist, 561–563
In-phase modulation, 377–379
Interband transitions, 237
Interfacial charge transfer processes
  colloidal semiconductor systems, 299–303
  fullerenes, 300
  kinetics of interfacial electron transfer, 300–303
  metal chalcogenide system, 300
  oxidative process, 300–301
  reductive process, 300
Interference effects, 117
IR bands, 188
Iron disilicide, 239
β-Iron disilicide-based LED, 239
Isotropic scattering time, 48

K

Kerr microscopy, 411
Kirchoff's laws, 164
Kummer function, 469

L

Landauer-Büttiker formula, 391
Landauer formula, 171
Landau levels, 31
Landau plot, 38
Langmuir-Blodgett (LB), 145
  films, 147
  technique, 197
Lateral surface superlattice (1DSSL), 65–68
Ligand-stabilized metal clusters, intercalation of, 149–152
Ligand-stabilized nanoparticles, 139–141
Light emitters, silicon-based
  ebrium-doped, 240–242
  $FeSi_2$ as, 238–239
Light-emitting diode, 239
Light-induced charge separation, 541
Linked cluster network, 197–199
Lithography. *See also* specific type
  nanofabrication by, 249–258
  processes, 556
  STM, 278
Lorentz microscopy, 411
  square pinning arrays, 492–499
Low-dimensional electron systems, quantized states in, 4–8
Lowest unoccupied molecular orbit (LUMO), 200
Luminescence, 238
  red, 273
  spectroscopy, 433–442
Luminescent diodes, 534–536

M

Magnetic anti-dot, 393
Magnetic barriers
  single, 368
  transport of electrons through, 366–371
Magnetic depopulation, 21–25
Magnetic depopulation measurements, 36, 40
Magnetic dots, 387
Magnetic field, 113, 367
  effects, 97
  periodic sinusoidal, 381–384
  random, 388–390
  tunneling rates in, 125–126
Magnetic field profiles, 348–353
  Heaviside step function, 350
  Maxwell equation, 348–351
  one-dimensional profiles, 348–351
  periodic structures, 351–353
Magnetic flux, 29
Magnetic minibands, 380–386
Magnetic modulation
  one-dimensional, 371–386
  two-dimensional, 386–390
Magnetization, 485–487
Magnetization curves, different antidot diameters, 512–514
Magnetoconductance, 33
Magnetophonon resonances (MPR)
  experiment, 38–39
  quantum wires, 31–40
Magnetoresistance, 22
Magnetoresistive materials, 175
Magnetosize effects, 25–28
Magnetosize peak, 26
Magnetotunneling measurements
  diamagnetic shifts and current suppression, 106–113
  electron tunneling rates, 121–128
  fine structure, 113–117
  spin splitting and g^* factor, 117–121
Material wave nanotechnology, 565–571
Matrix element, 54, 63
Matrix techniques, 139
Mercaptopyridines, 184
Mesoscopic arrays, 170
Mesoscopic loop, 465
Metal cluster synthesis, 189–199

Metallic junctions, 72
Metallorganic chemical vapor deposition (MOCVD), 235
Metal-oxide-semiconductor field effect transistor (MOSFET), 282
Metal particles, bare, 193
Micelles, 141
Microelectronics, chemically tailored nanoparticles in, 131–178
Microscopy. *See* specific type
Modulation-doped field effect transistors (MODFETs), 245
Modules, series-connected, 545–547
Molecular beam epitaxy (MBE), 101, 235
Molecular beam techniques, 139
Molecular wire synthesis, 181–189
MoS_2, 217
MOS device, 278
MOSFETs, 574
Multiple expansion cluster source (MECS), 190
Multiquanta vortex lattices, 505–517
Möllenstedt-type electron biprism, 568

N

Nanocrystalline electronic junctions, 527–553
Nanocrystalline injection solar cells, 537–548
  advantage of, 545
  cost and environmental compatibility, 547
Nanocrystalline intercalation batteries, 551
Nanocrystalline junction, 531
Nanocrystalline oxide films, 534
Nanocrystalline semiconductor films, light-induced charge separation in, 536–537
Nanocrystalline TiO_2, 529–530
Nanocrystalline ZnO layer, 530
Nanocrystallites
  preparation, 293–299
    charge carriers, 298–299
    crystalline phase control, 294–296
    emission characteristics, 297–298
    nonlinear optical properties, 297
    size control, 293–294
    size quantization effect, 296–297
  silicon, 270–275
  size-controlled
    radiolysis, 293–294
    sonolysis, 293–294
Nanocrystals, silicon, 271–272
Nanofabrication
  by lithography, 249–258
  using electron beam, 556–564
Nanolithography, 282, 556
Nanometer devices, 572–581
Nanometer electron beam writing system, 556–558
14-Nanometer-gate-length EJ-MOSFETs, 574–576
40-Nanometer-gate-length MOSFETs, 572–573
10-Nanometer lithography, 558–560
Nanoparticle arrays, 158–159
Nanoparticle netwoks, electronic conduction through, 159–162
Nanoparticle/polymer superlattice films, 147
Nanoparticles
  in block copolymers, 141–142
  chemically tailored, 131–178
    applications, 174–175
    one-dimensional arrangements, 149, 158
    preparation techniques, 139–143
    three-dimensional arrangements, 144–145, 162–164
    two-dimensional arrangements, 145–146, 159–160
    zero-to-three dimensional arrangements, 154–165
  electrochemical composition, 143
  ligand-stabilized, 139–141
  metal, 169
  in polymer matrices, 143
  in porous solids, 142
  SET-junctions, 174
  single electron tunneling in, 138–139
Nanoparticle-substrate junction, 156
Nanoscale clusters, 415
Nanoscale magnetic layers, 418–419
Nanoscale magnets, 414–418
Nanostructured superconductors
  huge arrays of nanoscopic plaquettes in, 479–521
  pinning in laterally, 482–485
  quantization and confinement phenomena in, 451–525
Nanostructure fabrication, 555–583
Nanostructures
  molecular, electronic properties of, 207–216
  self-assembled molecular, 179–231
    chemistry of, 184–185
  semiconductor, 1–91
  silicon-based, 233–289
Nanostructuring, 452–454
Nanotubes, 200
Nanowires, silicon, 257
Neumann boundary conditions, 15
Nitrogen oxides decomposition, 308
Nonhomogeneous magnetic fields, quantum motion, 353–366
Nonlinear optics, 175

O

1-Octadecanethiol, 186
Oligonucleotide, 147
Oligo(1,3-phenyl-acetylenes), 182
One-dimensional clusters of loops, 473–476
One-dimensional conductivity, 28–31
One-dimensional electron system, 5–6
Organic negative resist, 558–560
Orthodox theory, of SET, 174
Ostwald ripening, 530
Out-of-phase modulations, 379–380

P

Parabolic confinement, 6–8
Pb/Cu bilayer, 477
Pd_{561} clusters, 140
$Pd_{561}phen_{36}O_{200}$, 140, 145
Periodic structures, ferromagnetic thin film, 351–353

Phonon scattering, 33
Photocatalytic applications
  fixation of carbon dioxide, 304–308
  organic synthesis, 304
  semiconductor nanoparticles, 303–309
Photocatalytic degradation organic contaminants, 308–309
Photocatalytic reduction of carbon dioxide
  metal oxides, 305
  metal sulfides, 305–308
Photocatalytic reduction of dinitrogen, 308
Photoluminescence, 237, 241, 273
  absorption and global, 433
  lifetimes, 439
  size-selected, 436–439
Photon-to-current conversion efficiencies, 542
Photovoltaic cell, 529
Photovoltaic device, 539
Photovoltaic performance stability, 545
Photovoltaics, 175
Pinning, electromagnetic, 491
Pinning arrays, 484–505
Pinning mechanisms, 463–464
Plasma etching process, 46
Plasma polymers, 143
Plunger gate, 72
p-n junction, 239
Poisson equation, 10–11, 14
Poisson-Schrödinger (PS) model, two-dimensional, 15
Polymer matrices, nanoparticles in, 143
Porous Si-based LED, 249
Porous solids, nanoparticles in, 142
Preparation techniques, chemically tailored nanostructures, 139–143
Pt_{309} clusters, 157
$Pt_{309}phen^{*}_{36}O_{30}$, 140
$Pt_{309}phen_{36}O_{20}$ metal cluster, 135, 138

Q

Quantization, 452
Quantized states, in low-dimensional systems, 4–8
Quantum coefficient, 242–277
Quantum confined states, 80
Quantum dots, 135, 428
  CdSe, 441
  colloidal, III-V semiconductors, 427–450
  colloidal InP, 430–431
  electronic transport properties of, 93–130
  fabricated, 93–96
    energy states of, 96–97
  III-V, 429
    properties of, 432–447
  II-VI, 429
  impurity, 103
  lateral and vertical transport through, 71–77
  self-assembled Si, 279
  $Si/Si_{1-x}Ge_x$, 249
  squeezable structure, 78
  three-dimensional modeling, 19–20
  vertical transport, 68–70
Quantum eigenstates, 101
Quantum lasers, 175
Quantum motion nonhomogeneous magnetic fields, 353–366
  magnetic barrier, 356–359
  magnetic dot, 363–366
  magnetic quantum well, 359–361
  magnetic step, 354–356
  Meissner effect, 363–366
  resonant tunneling structures, 361–363
  Weber function, 361–363
Quantum size confinement effects, fabricated quantum dots, 96–97
Quantum size effects, nanoparticles, 132–135
Quantum wells, 122, 428
  donor impurity in, 98–100
  GaAs/AlGaAs, 376
Quantum wires, 428
  arrays of, 22
  1D state, 55
  as emitter, 55
  magnetophonon resonances in, 31–40
  SiGe/Si, 265
  silicon, 248
  single, 51
  transport spectroscopy of, 20–40
  vertical tunneling in, 48–68
  weak localization in, 25–31
Quantum yield, 538
  charge injection, 540

R

Raman shifts, 253
Rashba mechanism, 406
Reactive ion etching (RIE), 101
Recharging time, 173
Reciprocal space mapping (RSM), 255
Red luminescence, 273
Resonant red shift
  origin, 440
  single dot, 441
Resonant tunneling diodes (RTDs), 101

S

Scanning tunneling microscopy (STM), 146
  single electron systems, 154–159
Scanning tunneling spectroscopy (STS), 207
Schottky diodes, 241
Schrödinger equation, 5, 14
  solving, 9–10
Self-assembled monolayers, 146–147
Self-consistent calculations
  in one and two dimensions, 8–20
  in two dimensions, 13–19
Self-consistent treatment, one-dimensional problems, 9–13
Semiconductor
  bulk GaP, 443
  III-V, colloidal quantum dots of, 427–450
Semiconductor colloids
  deposition of metals, 309–310
  surface modification, 309–315
Semiconductor/ferromagnetic/semiconductor multilayers, 413

Semiconductor films
CdSe quantum dots, 321–322
chemical precipitation, 320–321
colloidal suspensions, 319–320
β-CuI nanocrystallites, 321
liquid interfaces, 321–322
self-organized structure, 321–322
SnO_2 nanocrystallites, 320
solid interfaces, 321–322
Semiconductor junctions, 527–530
Semiconductor nanocrystallites
coumarine dye, 314–315
dye cation, 314–315
ultrafast charge injection, 314–315
Semiconductor nanocrystallites ordered nanostructures, 318–327
electrochromic effects, 322–323
electron storage, 322–323
large-band-gap semiconductors, 325–327
nanostructured semiconductor films, 319–322
photochromic effects, 322–323
photosensitive electrode, 323–325
single-electron tunneling devices, 327–329
Semiconductor nanoparticles, 292–329
photocatalytic applications, 303–309
Semiconductor nanostructures, 1–91
Coulomb blockade effects in, 71–77
Semiconductor surface modification
capping with inorganic molecules, 310–312
capping with organic molecules, 310–312
CdS colloids, 311
Poisson statistics, 311
sensitizing dyes, 312–314
Semiconductor systems multicomponent, 315–318
capped semiconductor colloids, 318
coupling of two semiconductor colloids, 316–318
Sensitizer, 542
Sensitizing dyes
coadsorption, 313–314
eosin, 312
phthalocyanines, 312
porphyrins, 312
rose bengal, 312
semiconductor surface modification, 312–314
squaraines, 312
Shadow masks, 266–270
Shubnikov-de Haas (SdH) oscillations, 368
Si/CaF_2 multilayers, 274
SiCGe/SiGe heterostructures, 244–246
SiGe dots, 261
SiGe/Si quantum wires, 265
Si_4Ge_4 superlattices, 237
Si/III-V light emitting nanotips, 275–277
Silicon
optical properties of, 235–242
porous, 246–249
Silicon cantilever, 282
Silicon nanocrystallites, 270–275
Silicon nanocrystals, 271–272
Silicon nanowires, 257
Silicon quantum wires, 248
Silicon tip, 282
Si_mGe_n superlattices, 237
Si nanopillars, 256
Single-electron devices, metal nanoparticles as elements for, 169
Single-electron electronics, 278–281
Single-electronics (SE), 132
Single-electron logic (SEL), 132
Single-electron MOS memory (SEM), 280–281
Single-electron transfer (SET), 564
Single-electron transistor (SET), 576
metal-based, 165–167
silicon-based, 278
silicon memory, 280
Single-electron tunneling (SET), 132, 135–137
chemically tailored nanoparticles, 156–158
devices and circuits, 165–174
in nanoparticles, 138–139
Single particle structures, 154–158
Single vortex, 459
SiO_2, thin film, 217
SiO_2/Si_3N_4 shadow mask, 266
Si-set, 579
Si-SiGe quantum wells, 244–246
Si/SiGe superlattices, 244–246
$Si/SiO_2/Si$ multilayers, 272–274
Si/SiO_2 superlattices, 272
$Si/Si_{1-x}Ge_x$ quantum dots, 249
$Si_{1-x}Ge_x$ self-assembled dots, 260
Size-induced metal-insulator transition (SIMIT), 133
Snakelike orbits, 384–386
Solar cells, 442
Solar light harvesting, 539
Solar-to-electric power conversion efficiencies, 543–545
Spectroscopy. *See also* specific type
analysis of fabricated dot states, 111–113
transport, 20–40
Spin-degeneracy, effects at zero magnetic field, 123–125
Spin field effect transistor concept, 406
Spin-polarized electric current, 404
Spin-polarized tunnel current, 404–405
Spin splitting and g^* factor, magnetotunneling measurements, 117–121
Spin switch concept, 407–408
Square pinning arrays
Lorentz microscopy on, 492–499
vortex lattice in, 499–503
Staircase, 166
Stranski-Krastanow mode, 260
Strongly modulated systems, 40–48
Subband energies, determination of, 21–25
Sub-10-nanometer lithography, 561–563
Superconducting condensate, 454–457
Superconducting films, 389, 480–482
Superconducting grains, 389
Superconducting loop, 465
Superconductor
nanostructured, 451–525
type II, vortex lattice in, 457–464
Superlattices, 418, 453
2D, 255

T

Tandem cells, 550–551
2,2′,7,7′-Tetrakis-(N,N-di-p-methoxyphenyl-amine)9,9′-spirobifluorene, 548–549
Thin film structures, STM single electron systems and, 154–155
Thiocarbamates, 184
Thiol, self-assembled monolayers, 182
Thiol-encapsulated gold clusters, 194
Thiol molecules, 183
Thiophenes, 184
Thomas-Fermi approximation, 12–13
  in two dimensions, 19
Transfer Hamiltonian formalism, 53–56
Transmission electron microscopy (TEM), 246–249
  InP quantum dots, 432
Transport spectroscopy, quantum wires, 20–40
Traps, 167–169
Trioctylphosphine oxide (TOPO), 430
Trioctylphosphine (TOP), 430
Tunneling
  processes
    1D-1D, 62–64
    2D-1D, 56–68
    2D-1D surface superlattice tunneling (SSL), 64–68
    vertical quantum dots, 75–76
  time scales of, 172–174
  zero-dimensional-2D, 82–86
  zero-dimensional donor states, 77–82
Tunneling rates, magnetic field, 125–126
Tunneling structure, 3D-0D-3D, 76, 95–96
Tunneling time, 173
Turnstiles, 167–169
Two-, one-, and zero-dimensional confinement, 242–244
Two-dimensional array, 222
Two-dimensional clusters of antidots, 477–479
Two-dimensional electron gas (2DEG), 4, 27, 49

U

Universal conductance fluctuations (UCF), 117
Unlinked arrays of gold clusters, 198
Unlinked cluster array, 195–197

V

Variable temperature measurements, 103–106
Vertical and horizontal systems, fabricated quantum dots, 93–96
Vertical dot, current-voltage characteristics, 100–101
Vertical quantum dots, 95
Vertical transport, quantum dots, 68–70
Vertical tunneling
  1D-1D, 51
  in quantum wires, 48–68
V-groove growth, 265–266
Viologens, 533
Voltage drop, 205
Voltage-to-energy conversion factor, 104
Vortex lattice
  Abrikosov, 503
  crossover, 514–517
  multiquanta, 505–517
  in square pinning array, 499–503
  in a type-II superconductor, 457–464

W

Wave functions, 55
  1D, Fourier transform of, 62
Weiss oscillations, 374

X

Xanthates, 184
X-ray diffraction, 432
X-ray photoelectron spectroscopy (XPS), 273
α, α'-Xylyldithiol, 186

Z

Zeeman effects, 107
Zero-dimensional donor states, tunneling, 77–82
Zero magnetic field, effect of spin-degeneracy, 123–125

This Page Intentionally Left Blank

HANDBOOK OF NANOSTRUCTURED MATERIALS AND NANOTECHNOLOGY

Edited by H.S. Nalwa

Volume 1. SYNTHESIS AND PROCESSING

Chapter 1. Chemical Synthesis of Nanostructured Metals, Metal Alloys, and Semiconductors
K. E. Gonsalves, S. P. Rangarajan, J. Wang

Chapter 2. Nanoparticles from Low-Pressure, Low-Temperature Plasmas
Josep Costa

Chapter 3. Synthesis of Nanostructured Coatings by High-Velocity Oxygen–Fuel Thermal Spraying
H. Jiang, M. Lau, V. L. Tellkamp, E. J. Lavernia

Chapter 4. Low-Temperature Compaction of Nanosize Powders
E. J. Gonzalez, G. J. Piermarini

Chapter 5. Kinetic Control of Inorganic Solid-State Reactions Resulting from Mechanistic Studies Using Elementally Modulated Reactants
Christopher D. Johnson, Myungkeun Noh, Heike Sellinschegg, Robert Schneidmiller, David C. Johnson

Chapter 6. Strained-Layer Heteroepitaxy to Fabricate Self-Assembled Semiconductor Islands
W. H. Weinberg, C. M. Reaves, B. Z. Nosho, R. I. Pelzel, S. P. DenBaars

Chapter 7. Nanofabrication via Atom Optics
Jabez J. McClelland

Chapter 8. Nanocomposites Prepared by Sol–Gel Methods: Synthesis and Characterization
Krzysztof C. Kwiatkowski, Charles M. Lukehart

Chapter 9. Chemical Preparation and Characterization of Nanocrystalline Materials
Qian Yitai

Chapter 10. Semiconductor Quantum Dots: Progress in Processing
David J. Duval, Subhash H. Risbud

Chapter 11. Rapid Solidification Processing of Nanocrystalline Metallic Alloys
I. T. H. Chang

Chapter 12. Vapor Processing of Nanostructured Materials
K. L. Choy

Chapter 13. Applications of Micromachining to Nanotechnology
Amit Lal

Volume 2. SPECTROSCOPY AND THEORY

Chapter 1. Nanodiffraction
J. M. Cowley, J. C. H. Spence

Chapter 2. Fourier Transform Infrared Surface Spectrometry of Nano-Sized Particles
Marie-Isabelle Baraton

Chapter 3. Specification of Microstructure and Characterization by Scattering Techniques
C. E. Krill, R. Haberkorn, R. Birringer

Chapter 4. Vibrational Spectroscopy of Mesoscopic Structures
P. Milani, C. E. Bottani

Chapter 5. Advanced Interfaces to Scanned-Probe Microscopes
Russell M. Taylor, II, Richard Superfine

Chapter 6. Microwave Spectroscopy on Quantum Dots
Robert H. Blick

Chapter 7. Tribological Experiments with Friction Force Microscopy
E. Meyer, R. Lüthi

Chapter 8. Electron Microscopy Study of Nanostructured and Ancient Materials
Miguel José-Yacamán, Jorge A. Ascencio

Chapter 9. Mesoscopic Magnetism in Metals
Kamel Ounadjela, R. L. Stamps

Chapter 10. Tools of Nanotechnology: Nanometrology
David J. Whitehouse

Chapter 11. Tunneling Time in Nanostructures
V. Gasparian, M. Ortuño, G. Schön, U. Simon

Chapter 12. Theory of Atomic-Scale Friction
Susan B. Sinnott

Chapter 13. Theoretical Aspects of Strained-Layer Quantum-Well Lasers
Doyeol Ahn

Chapter 14. Carbon-Nanotube-Based Nanotechnology in an Integrated Modeling and Simulation Environment
Deepak Srivastava, Fedor Dzegilenko, Stephen Barnard, Subhash Saini, Madhu Menon, Sisira Weeratunga

Chapter 15. Wave-Function Engineering: A New Paradigm in Quantum Nanostructure Modeling
L. R. Ram-Mohan, I. Vurgaftman, J. R. Meyer, D. Dossa

Volume 3. ELECTRICAL PROPERTIES

Chapter 1. Electron Transport and Confining Potentials in Semiconductor Nanostructures
J. Smoliner, G. Ploner

Chapter 2. Electronic Transport Properties of Quantum Dots
M. A. Reed, J. W. Sleight, M. R. Deshpande

Chapter 3. Electrical Properties of Chemically Tailored Nanoparticles and Their Application in Microelectronics
U. Simon, G. Schön

Chapter 4. The Design, Fabrication, and Electronic Properties of Self-Assembled Molecular Nanostructures
R. P. Andres, S. Datta, D. B. Janes, C. P. Kubiak, R. Reifenberger

Chapter 5. Silicon-Based Nanostructures
Tamim P. Sidiki, Clivia M. Sotomayor Torres

Chapter 6. Semiconductor Nanoparticles
Prashant V. Kamat, Kei Murakoshi, Yuji Wada, Shizo Yanagida

Chapter 7. Hybrid Magnetic–Semiconductor Nanostructures
François M. Peeters, Jo De Boeck

Chapter 8. Colloidal Quantum Dots of III–V Semiconductors
Olga I. Mićić, Arthur J. Nozik

Chapter 9. Quantization and Confinement Phenomena in Nanostructured Superconductors
V. V. Moshchalkov, V. Bruyndoncx, L. Van Look, M. J. Van Bael, Y. Bruynseraede, A. Tonomura

Chapter 10. Properties and Applications of Nanocrystalline Electronic Junctions
Michael Grätzel

Chapter 11. Nanostructure Fabrication Using Electron Beam and Its Application to Nanometer Devices
Shinji Matsui

Volume 4. OPTICAL PROPERTIES

Chapter 1. Photorefractive Semiconductor Nanostructures
D. D. Nolte, M. R. Melloch, Y. Ding, M. Dinu, K. M. Kwolek, I. Lahiri

Chapter 2. Metal Nanocluster Composite Glasses
Francesco Gonella, Paolo Mazzoldi

Chapter 3. Porous Silicon
Daniel F. Thomas

Chapter 4. Three-Dimensional Lattices of Nanostructures: The Template Approach
Sergei G. Romanov, Clivia M. Sotomayor Torres

Chapter 5. Fluorescence, Thermoluminescence, and Photostimulated Luminescence of Nanoparticles
Wei Chen

Chapter 6. Surface-Enhanced Optical Phenomena in Nanostructured Fractal Materials
Vladimir M. Shalaev

Chapter 7. Linear and Nonlinear Optical Spectroscopy of Semiconductor Nanocrystals
Victor I. Klimov

Chapter 8. Nonlinear Optical Properties of Nanostructures
S. Vijayalakshmi, H. Grebel

Chapter 9. Quantum Well Infrared Photodetectors
Sheng S. Li, Meimei Z. Tidrow

Chapter 10. Nanoscopic Optical Sensors and Probes
Weihong Tan, Raoul Kopelman

Volume 5. ORGANICS, POLYMERS, AND BIOLOGICAL MATERIALS

Chapter 1. Intercalation Compounds in Layered Host Lattices: Supramolecular Chemistry in Nanodimensions
Anton Lerf

Chapter 2. Transition-Metal-Mediated Self-Assembly of Discrete Nanoscopic Species with Well-Defined Shapes and Geometries
Peter J. Stang, Bogdan Olenyuk

Chapter 3. Molecular and Supramolecular Nanomachines
Marcos Gómez-López, J. Fraser Stoddart

Chapter 4. Functional Nanostructures Incorporating Responsive Modules
Andrew C. Benniston, Philip R. Mackie

Chapter 5. Dendritic Molecules—Historic Development and Future Applications
Andreas Archut, Fritz Vögtle

Chapter 6. Carbon Nanotubes
P. M. Ajayan

Chapter 7. Encapsulation and Crystallization Behavior of Materials Inside Carbon Nanotubes
J. Sloan, M. L. H. Green

Chapter 8. Fabrication and Spectroscopic Characterization of Organic Nanocrystals
Hitoshi Kasai, Hari Singh Nalwa, Shuji Okada, Hidetoshi Oikawa, Hachiro Nakanishi

Chapter 9. Polymeric Nanostructures
Guojun Liu

Chapter 10. Conductive Polymers as Organic Nanometals
Bernhard Wessling

Chapter 11. Biopolymer and Polymer Nanoparticles and Their Biomedical Applications
Evelyne Nakache, Nathalie Poulain, Françoise Candau, Anne-Marie Orecchioni, Juan Manuel Irache

Chapter 12. Structure, Behavior, and Manipulation of Nanoscale Biological Assemblies
Timothy Bayburt, Joseph Carlson, Bruce Godfrey, Mary Shank-Retzlaff, Stephen G. Sligar

Chapter 13. Biomimetic Thin Films
Thomas M. Cooper

This Page Intentionally Left Blank